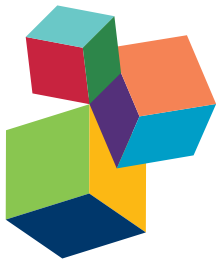


# MORPHOLOGICAL PLANT MODELING: UNLEASHING GEOMETRIC AND TOPOLOGICAL POTENTIAL WITHIN THE PLANT SCIENCES

EDITED BY: Alexander Bucksch and Dan Chitwood

PUBLISHED IN: Frontiers in Plant Science



# frontiers

## **Frontiers Copyright Statement**

© Copyright 2007-2017 Frontiers Media SA. All rights reserved.

All content included on this site, such as text, graphics, logos, button icons, images, video/audio clips, downloads, data compilations and software, is the property of or is licensed to Frontiers Media SA ("Frontiers") or its licensees and/or subcontractors. The copyright in the text of individual articles is the property of their respective authors, subject to a license granted to Frontiers.

The compilation of articles constituting this e-book, wherever published, as well as the compilation of all other content on this site, is the exclusive property of Frontiers. For the conditions for downloading and copying of e-books from Frontiers' website, please see the Terms for Website Use. If purchasing Frontiers e-books from other websites or sources, the conditions of the website concerned apply.

Images and graphics not forming part of user-contributed materials may not be downloaded or copied without permission.

Individual articles may be downloaded and reproduced in accordance with the principles of the CC-BY licence subject to any copyright or other notices. They may not be re-sold as an e-book.

As author or other contributor you grant a CC-BY licence to others to reproduce your articles, including any graphics and third-party materials supplied by you, in accordance with the Conditions for Website Use and subject to any copyright notices which you include in connection with your articles and materials.

All copyright, and all rights therein, are protected by national and international copyright laws.

The above represents a summary only. For the full conditions see the Conditions for Authors and the Conditions for Website Use.

**ISSN 1664-8714**

**ISBN 978-2-88945-297-2**

**DOI 10.3389/978-2-88945-297-2**

## **About Frontiers**

Frontiers is more than just an open-access publisher of scholarly articles: it is a pioneering approach to the world of academia, radically improving the way scholarly research is managed. The grand vision of Frontiers is a world where all people have an equal opportunity to seek, share and generate knowledge. Frontiers provides immediate and permanent online open access to all its publications, but this alone is not enough to realize our grand goals.

## **Frontiers Journal Series**

The Frontiers Journal Series is a multi-tier and interdisciplinary set of open-access, online journals, promising a paradigm shift from the current review, selection and dissemination processes in academic publishing. All Frontiers journals are driven by researchers for researchers; therefore, they constitute a service to the scholarly community. At the same time, the Frontiers Journal Series operates on a revolutionary invention, the tiered publishing system, initially addressing specific communities of scholars, and gradually climbing up to broader public understanding, thus serving the interests of the lay society, too.

## **Dedication to Quality**

Each Frontiers article is a landmark of the highest quality, thanks to genuinely collaborative interactions between authors and review editors, who include some of the world's best academicians. Research must be certified by peers before entering a stream of knowledge that may eventually reach the public - and shape society; therefore, Frontiers only applies the most rigorous and unbiased reviews.

Frontiers revolutionizes research publishing by freely delivering the most outstanding research, evaluated with no bias from both the academic and social point of view.

By applying the most advanced information technologies, Frontiers is catapulting scholarly publishing into a new generation.

## **What are Frontiers Research Topics?**

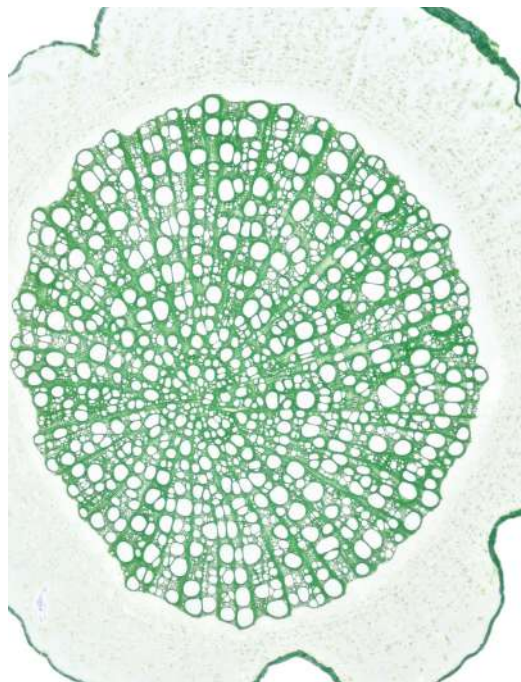
Frontiers Research Topics are very popular trademarks of the Frontiers Journals Series: they are collections of at least ten articles, all centered on a particular subject. With their unique mix of varied contributions from Original Research to Review Articles, Frontiers Research Topics unify the most influential researchers, the latest key findings and historical advances in a hot research area! Find out more on how to host your own Frontiers Research Topic or contribute to one as an author by contacting the Frontiers Editorial Office: [researchtopics@frontiersin.org](mailto:researchtopics@frontiersin.org)

# MORPHOLOGICAL PLANT MODELING: UNLEASHING GEOMETRIC AND TOPOLOGICAL POTENTIAL WITHIN THE PLANT SCIENCES

Topic Editors:

**Alexander Bucksch**, University of Georgia, United States

**Dan Chitwood**, Independent Researcher, United States



Cover image: Anna Jurkovska/Shutterstock.com

An increasing population faces the growing demand for agricultural products and accurate global climate models that account for individual plant morphologies to predict favorable human habitat. Both demands are rooted in an improved understanding of the mechanistic origins of plant development. Such understanding requires geometric and topological descriptors to characterize the phenotype of plants and its link to genotypes. However, the current plant phenotyping framework relies on simple length and diameter measurements, which fail to capture the exquisite architecture of plants.

The Research Topic “Morphological Plant Modeling: Unleashing Geometric and Topological Potential within the Plant Sciences” is the result of a workshop held at National Institute for Mathematical and Biological Synthesis (NIMBioS) in Knoxville, Tennessee. From 2.-4. September 2015 over 40 scientists from mathematics, computer science, engineering, physics and biology came together to set new frontiers in combining plant phenotyping with recent results from shape theory at the interface of geometry and topology. In doing so, the Research Topic synthesizes the views from multiple disciplines to reveal the potential of new mathematical concepts to analyze and quantify the relationship between morphological plant features. As such, the Research Topic bundles examples of new mathematical techniques including persistent homology, graph-theory, and shape statistics to tackle questions in crop breeding, developmental biology, and vegetation modeling. The challenge to model plant morphology under field conditions is a central theme of the included papers to address the problems of climate change and food security, that require the integration of plant biology and mathematics from geometry and topology research applied to imaging and simulation techniques. The introductory white paper written by the workshop participants identifies future directions in research, education and policy making to integrate biological and mathematical approaches and to strengthen research at the interface of both disciplines.

**Citation:** Bucksch, A., Chitwood, D., eds. (2017). Morphological Plant Modeling: Unleashing Geometric and Topological Potential within the Plant Sciences. Lausanne: Frontiers Media.  
doi: 10.3389/978-2-88945-297-2

# Table of Contents

- 07 Morphological Plant Modeling: Unleashing Geometric and Topological Potential within the Plant Sciences**  
Alexander Bucksch, Acheampong Atta-Boateng, Akomian F. Azihou, Dorjsuren Battogtokh, Aly Baumgartner, Brad M. Binder, Siobhan A. Braybrook, Cynthia Chang, Viktoiryia Coneva, Thomas J. DeWitt, Alexander G. Fletcher, Malia A. Gehan, Diego Hernan Diaz-Martinez, Lilan Hong, Anjali S. Iyer-Pascuzzi, Laura L. Klein, Samuel Leiboff, Mao Li, Jonathan P. Lynch, Alexis Maizel, Julin N. Maloof, R. J. Cody Markelz, Ciera C. Martinez, Laura A. Miller, Washington Mio, Wojtek Palubicki, Hendrik Poorter, Christophe Pradal, Charles A. Price, Eetu Puttonen, John B. Reese, Rubén Rellán-Álvarez, Edgar P. Spalding, Erin E. Sparks, Christopher N. Topp, Joseph H. Williams and Daniel H. Chitwood
- 23 Quantification of Overnight Movement of Birch (*Betula pendula*) Branches and Foliage with Short Interval Terrestrial Laser Scanning**  
Eetu Puttonen, Christian Briese, Gottfried Mandlburger, Martin Wieser, Martin Pfennigbauer, András Zlinszky and Norbert Pfeifer
- 36 The Application of Leaf Ultrasonic Resonance to *Vitis vinifera L.* Suggests the Existence of a Diurnal Osmotic Adjustment Subjected to Photosynthesis**  
Domingo Sancho-Knapik, Hipólito Medrano, José J. Peguero-Pina, Maurizio Mencuccini, María D. Fariñas, Tomás G. Álvarez-Arenas and Eustaquio Gil-Pelegrín
- 47 Modeling Tree Growth Taking into Account Carbon Source and Sink Limitations**  
Amaury Hayat, Andrew J. Hacket-Pain, Hans Pretzsch, Tim T. Rademacher and Andrew D. Friend
- 62 Models for Predicting the Architecture of Different Shoot Types in Apple**  
Emna Baïram, Mickaël Delaire, Christian Le Morvan and Gerhard Buck-Sorlin
- 78 Why Be a Shrub? A Basic Model and Hypotheses for the Adaptive Values of a Common Growth Form**  
Frank Götmark, Elin Götmark and Anna M. Jensen
- 92 Sweet Pepper (*Capsicum annuum L.*) Canopy Photosynthesis Modeling Using 3D Plant Architecture and Light Ray-Tracing**  
Jee Hoon Kim, Joon Woo Lee, Tae In Ahn, Jong Hwa Shin, Kyung Sub Park and Jung Eek Son
- 102 Deploying Fourier Coefficients to Unravel Soybean Canopy Diversity**  
Talukder Z. Jubery, Johnathon Shook, Kyle Parmley, Jiaoping Zhang, Hsiang S. Naik, Race Higgins, Soumik Sarkar, Arti Singh, Asheesh K. Singh and Baskar Ganapathysubramanian

- 112 Mistletoe Berry Outline Mapping with a Path Curve Function and Recording the Circadian Rhythm of Their Phenotypic Shape Change**  
Renatus Derbridge, Stephan Baumgartner and Peter Heusser
- 128 Co-ordination in Morphological Leaf Traits of Early Diverging Angiosperms Is Maintained Following Exposure to Experimental Palaeo-atmospheric Conditions of Sub-ambient O<sub>2</sub> and Elevated CO<sub>2</sub>**  
Christiana Evans-Fitz-Gerald, Amanda S. Porter, Charilaos Yiotis, Caroline Elliott-Kingston and Jennifer C. McElwain
- 139 Digital Morphometrics of Two North American Grapevines (*Vitis: Vitaceae*) Quantifies Leaf Variation between Species, within Species, and among Individuals**  
Laura L. Klein, Madeleine Caito, Chad Chapnick, Cassandra Kitchen, Regan O'Hanlon, Dan H. Chitwood and Allison J. Miller
- 149 Does Size Matter? Atmospheric CO<sub>2</sub> May Be a Stronger Driver of Stomatal Closing Rate Than Stomatal Size in Taxa That Diversified under Low CO<sub>2</sub>**  
Caroline Elliott-Kingston, Matthew Haworth, Jon M. Yearsley, Sven P. Batke, Tracy Lawson and Jennifer C. McElwain
- 161 3D Surface Reconstruction of Plant Seeds by Volume Carving: Performance and Accuracies**  
Johanna Roussel, Felix Geiger, Andreas Fischbach, Siegfried Jahnke and Hanno Scharr
- 174 Using a Structural Root System Model to Evaluate and Improve the Accuracy of Root Image Analysis Pipelines**  
Guillaume Lobet, Iko T. Koevoets, Manuel Noll, Patrick E. Meyer, Pierre Tocquin, Loïc Pagès and Claire Périlleau
- 185 A Model Analysis of Mechanisms for Radial Microtubular Patterns at Root Hair Initiation Sites**  
Pawel Krupinski, Behruz Bozorg, André Larsson, Stefano Pietra, Markus Grebe and Henrik Jönsson
- 197 Cocowood Fibrovascular Tissue System—Another Wonder of Plant Evolution**  
Oswaldo M. González and Khoi A. Nguyen
- 209 Analysis of Network Topologies Underlying Ethylene Growth Response Kinetics**  
Aaron M. Prescott, Forest W. McCollough, Bryan L. Eldreth, Brad M. Binder and Steven M. Abel
- 222 DRACO-STEM: An Automatic Tool to Generate High-Quality 3D Meshes of Shoot Apical Meristem Tissue at Cell Resolution**  
Guillaume Cerutti, Olivier Ali and Christophe Godin
- 237 Modeling the Morphometric Evolution of the Maize Shoot Apical Meristem**  
Samuel Leiboff, Christopher K. DeAllie and Michael J. Scanlon
- 247 A Bistable Switch Mechanism for Stem Cell Domain Nucleation in the Shoot Apical Meristem**  
Dorjsuren Battogtokh and John J. Tyson
- 251 Mechanical Behavior of Cells within a Cell-Based Model of Wheat Leaf Growth**  
Ulyana Zubairova, Sergey Nikolaev, Aleksey Penenko, Nikolay Podkolodnyy, Sergey Golushko, Dmitry Afonnikov and Nikolay Kolchanov
- 266 Computational Modeling of Auxin: A Foundation for Plant Engineering**  
Alejandro Morales-Tapia and Alfredo Cruz-Ramírez

**274 Morphogeometric Approaches to Non-vascular Plants**

Daniel E. Stanton and Catherine Reeb

**282 Reshaping Plant Biology: Qualitative and Quantitative Descriptors for Plant Morphology**

Mathilde Balduzzi, Brad M. Binder, Alexander Bucksch, Cynthia Chang, Lilan Hong, Anjali S. Iyer-Pascuzzi, Christophe Pradal and Erin E. Sparks



# Morphological Plant Modeling: Unleashing Geometric and Topological Potential within the Plant Sciences

## OPEN ACCESS

### Edited by:

Katrin Kahlen,  
Hochschule Geisenheim University,  
Germany

### Reviewed by:

Evelyne Costes,  
Institut National de la Recherche  
Agronomique (INRA), France  
Leo Marcelis,

Wageningen University and Research,  
Netherlands

### \*Correspondence:

Alexander Bucksch  
bucksch@uga.edu  
Daniel H. Chitwood  
dhchitwood@gmail.com

### Specialty section:

This article was submitted to  
Plant Biophysics and Modeling,  
a section of the journal  
*Frontiers in Plant Science*

**Received:** 05 October 2016

**Accepted:** 12 May 2017

**Published:** 09 June 2017

### Citation:

Bucksch A, Atta-Boateng A,  
Azihou AF, Battogtokh D,  
Baumgartner A, Binder BM,  
Braybrook SA, Chang C, Coneva V,  
DeWitt TJ, Fletcher AG, Gehan MA,  
Diaz-Martinez DH, Hong L,  
Iyer-Pascuzzi AS, Klein LL, Leiboff S,  
Li M, Lynch JP, Maizel A, Maloof JN,  
Markelz RJC, Martinez CC, Miller LA,  
Mio W, Palubicki W, Poorter H,  
Pradal C, Price CA, Puttonen E,  
Reese JB, Rellán-Álvarez R,  
Spalding EP, Sparks EE, Topp CN,  
Williams JH and Chitwood DH (2017)  
Morphological Plant Modeling:  
Unleashing Geometric  
and Topological Potential within  
the Plant Sciences.  
*Front. Plant Sci.* 8:900.  
doi: 10.3389/fpls.2017.00900

Alexander Bucksch<sup>1,2,3\*</sup>, Acheampong Atta-Boateng<sup>4</sup>, Akomian F. Azihou<sup>5</sup>, Dorjsuren Battogtokh<sup>6</sup>, Aly Baumgartner<sup>7</sup>, Brad M. Binder<sup>8</sup>, Siobhan A. Braybrook<sup>9</sup>, Cynthia Chang<sup>10</sup>, Viktoiry Coneva<sup>11</sup>, Thomas J. DeWitt<sup>12</sup>, Alexander G. Fletcher<sup>13</sup>, Malia A. Gehan<sup>11</sup>, Diego Hernan Diaz-Martinez<sup>14</sup>, Lilan Hong<sup>15</sup>, Anjali S. Iyer-Pascuzzi<sup>16</sup>, Laura L. Klein<sup>17</sup>, Samuel Leiboff<sup>18</sup>, Mao Li<sup>14</sup>, Jonathan P. Lynch<sup>19</sup>, Alexis Maizel<sup>20</sup>, Julin N. Maloof<sup>21</sup>, R. J. Cody Markelz<sup>21</sup>, Ciera C. Martinez<sup>22</sup>, Laura A. Miller<sup>23</sup>, Washington Mio<sup>14</sup>, Wojtek Palubicki<sup>9</sup>, Hendrik Poorter<sup>24</sup>, Christophe Pradal<sup>25</sup>, Charles A. Price<sup>26</sup>, Eetu Puttonen<sup>27,28</sup>, John B. Reese<sup>29</sup>, Rubén Rellán-Álvarez<sup>30</sup>, Edgar P. Spalding<sup>31</sup>, Erin E. Sparks<sup>32</sup>, Christopher N. Topp<sup>11</sup>, Joseph H. Williams<sup>29</sup> and Daniel H. Chitwood<sup>11\*</sup>

<sup>1</sup> Department of Plant Biology, University of Georgia, Athens, GA, United States, <sup>2</sup> Warnell School of Forestry and Natural Resources, University of Georgia, Athens, GA, United States, <sup>3</sup> Institute of Bioinformatics, University of Georgia, Athens, GA, United States, <sup>4</sup> School of Forestry and Environmental Studies, Yale University, New Haven, CT, United States, <sup>5</sup> Laboratory of Applied Ecology, Faculty of Agronomic Sciences, University of Abomey-Calavi, Cotonou, Benin, <sup>6</sup> Department of Biological Sciences, Virginia Polytechnic Institute and State University, Blacksburg, VA, United States, <sup>7</sup> Department of Geosciences, Baylor University, Waco, TX, United States, <sup>8</sup> Department of Biochemistry and Cellular and Molecular Biology, University of Tennessee, Knoxville, Knoxville, TN, United States, <sup>9</sup> The Sainsbury Laboratory, University of Cambridge, Cambridge, United Kingdom, <sup>10</sup> Division of Biology, University of Washington, Bothell, WA, United States, <sup>11</sup> Donald Danforth Plant Science Center, St. Louis, MO, United States, <sup>12</sup> Department of Wildlife and Fisheries Sciences–Department of Plant Pathology and Microbiology, Texas A&M University, College Station, TX, United States, <sup>13</sup> School of Mathematics and Statistics and Bateson Centre, University of Sheffield, Sheffield, United Kingdom, <sup>14</sup> Department of Mathematics, Florida State University, Tallahassee, FL, United States, <sup>15</sup> Weill Institute for Cell and Molecular Biology and Section of Plant Biology, School of Integrative Plant Sciences, Cornell University, Ithaca, NY, United States, <sup>16</sup> Department of Botany and Plant Pathology, Purdue University, West Lafayette, IN, United States, <sup>17</sup> Department of Biology, Saint Louis University, St. Louis, MO, United States, <sup>18</sup> School of Integrative Plant Science, Cornell University, Ithaca, NY, United States, <sup>19</sup> Department of Plant Science, The Pennsylvania State University, University Park, PA, United States, <sup>20</sup> Center for Organismal Studies, Heidelberg University, Heidelberg, Germany, <sup>21</sup> Department of Plant Biology, University of California, Davis, Davis, CA, United States, <sup>22</sup> Department of Molecular and Cell Biology, University of California, Berkeley, Berkeley, CA, United States, <sup>23</sup> Program in Bioinformatics and Computational Biology, The University of North Carolina, Chapel Hill, NC, United States, <sup>24</sup> Plant Sciences (IBG-2), Forschungszentrum Jülich GmbH, Jülich, Germany, <sup>25</sup> CIRAD, UMR AGAP, INRIA, VirtualPlants, Montpellier, France, <sup>26</sup> National Institute for Mathematical and Biological Synthesis, University of Tennessee, Knoxville, Knoxville, TN, United States, <sup>27</sup> Department of Remote Sensing and Photogrammetry, Finnish Geospatial Research Institute, National Land Survey of Finland, Masala, Finland, <sup>28</sup> Centre of Excellence in Laser Scanning Research, National Land Survey of Finland, Masala, Finland, <sup>29</sup> Department of Ecology and Evolutionary Biology, University of Tennessee, Knoxville, Knoxville, TN, United States, <sup>30</sup> Unidad de Genómica Avanzada, Laboratorio Nacional de Genómica para la Biodiversidad, Center for Research and Advanced Studies of the National Polytechnic Institute (CINVESTAV), Irapuato, Mexico, <sup>31</sup> Department of Botany, University of Wisconsin–Madison, Madison, WI, United States, <sup>32</sup> Department of Plant and Soil Sciences and Delaware Biotechnology Institute, University of Delaware, Newark, DE, United States

The geometries and topologies of leaves, flowers, roots, shoots, and their arrangements have fascinated plant biologists and mathematicians alike. As such, plant morphology is inherently mathematical in that it describes plant form and architecture with geometrical and topological techniques. Gaining an understanding of how to modify plant morphology, through molecular biology and breeding, aided by a mathematical perspective, is critical to improving agriculture, and the monitoring of ecosystems

is vital to modeling a future with fewer natural resources. In this white paper, we begin with an overview in quantifying the form of plants and mathematical models of patterning in plants. We then explore the fundamental challenges that remain unanswered concerning plant morphology, from the barriers preventing the prediction of phenotype from genotype to modeling the movement of leaves in air streams. We end with a discussion concerning the education of plant morphology synthesizing biological and mathematical approaches and ways to facilitate research advances through outreach, cross-disciplinary training, and open science. Unleashing the potential of geometric and topological approaches in the plant sciences promises to transform our understanding of both plants and mathematics.

**Keywords:** plant biology, plant science, morphology, mathematics, topology, modeling

## INTRODUCTION

### Morphology from the Perspective of Plant Biology

The study of plant morphology interfaces with all biological disciplines (**Figure 1**). Plant morphology can be descriptive and categorical, as in systematics, which focuses on biological homologies to discern groups of organisms (Mayr, 1981; Wiens, 2000). In plant ecology, the morphology of communities defines vegetation types and biomes, including their relationship to the environment. In turn, plant morphologies are mutually informed by other fields of study, such as plant physiology, the study of the functions of plants, plant genetics, the description of inheritance, and molecular biology, the underlying gene regulation (Kaplan, 2001).

Plant morphology is more than an attribute affecting plant organization, it is also dynamic. Developmentally, morphology reveals itself over the lifetime of a plant through varying rates of cell division, cell expansion, and anisotropic growth (Esau, 1960; Steeves and Sussex, 1989; Niklas, 1994). Response to changes in environmental conditions further modulate the abovementioned parameters. Development is genetically programmed and driven by biochemical processes that are responsible for physical forces that change the observed patterning and growth of organs (Green, 1999; Peaucelle et al., 2011; Braybrook and Jönsson, 2016). In addition, external physical forces affect plant development, such as heterogeneous soil densities altering root growth or flows of air, water, or gravity modulating the bending of branches and leaves (Moulié and Fournier, 2009). Inherited modifications of development over generations results in the evolution of plant morphology (Niklas, 1997). Development and evolution set the constraints for how the morphology of a plant arises, regardless of whether in a systematic, ecological, physiological, or genetic context (**Figure 1**).

### Plant Morphology from the Perspective of Mathematics

In 1790, Johann Wolfgang von Goethe pioneered a perspective that transformed the way mathematicians think about plant morphology: the idea that the essence of plant morphology

is an underlying repetitive process of transformation (Goethe, 1790; Friedman and Diggle, 2011). The modern challenge that Goethe's paradigm presents is to quantitatively describe transformations resulting from differences in the underlying genetic, developmental, and environmental cues. From a mathematical perspective, the challenge is how to define shape descriptors to compare plant morphology with topological and geometrical techniques and how to integrate these shape descriptors into simulations of plant development.

### Mathematics to Describe Plant Shape and Morphology

Several areas of mathematics can be used to extract quantitative measures of plant shape and morphology. One intuitive representation of the plant form relies on the use of skeletal descriptors that reduce the branching morphology of plants to a set of intersecting lines or curve segments, constituting a mathematical graph. These skeleton-based mathematical graphs can be derived from manual measurement (Godin et al., 1999; Watanabe et al., 2005) or imaging data (Bucksch et al., 2010; Aiteanu and Klein, 2014). Such skeletal descriptions can be used to derive quantitative measurements of lengths, diameters, and angles in tree crowns (Bucksch and Fleck, 2011; Raumonen et al., 2013; Seidel et al., 2015) and roots, at a single time point (Fitter, 1987; Danjon et al., 1999; Lobet et al., 2011; Galkovskyi et al., 2012) or over time to capture growth dynamics (Symonova et al., 2015). Having a skeletal description in place allows the definition of orders, in a biological and mathematical sense, to enable morphological analysis from a topological perspective (**Figure 2A**). Topological analyses can be used to compare shape characteristics independently of events that transform plant shape geometrically, providing a framework by which plant morphology can be modeled. The relationships between orders, such as degree of self-similarity (Prusinkiewicz, 2004) or self-nestedness (Godin and Ferraro, 2010) are used to quantitatively summarize patterns of plant morphology. Persistent homology (**Figure 2B**), an extension of Morse theory (Milnor, 1963), transforms a given plant shape gradually to define self-similarity (MacPherson and Schweinhart, 2012) and morphological properties (Edelsbrunner and Harer, 2010; Li et al., 2017) on the basis of topological event statistics. In the example in **Figure 2B**, topological

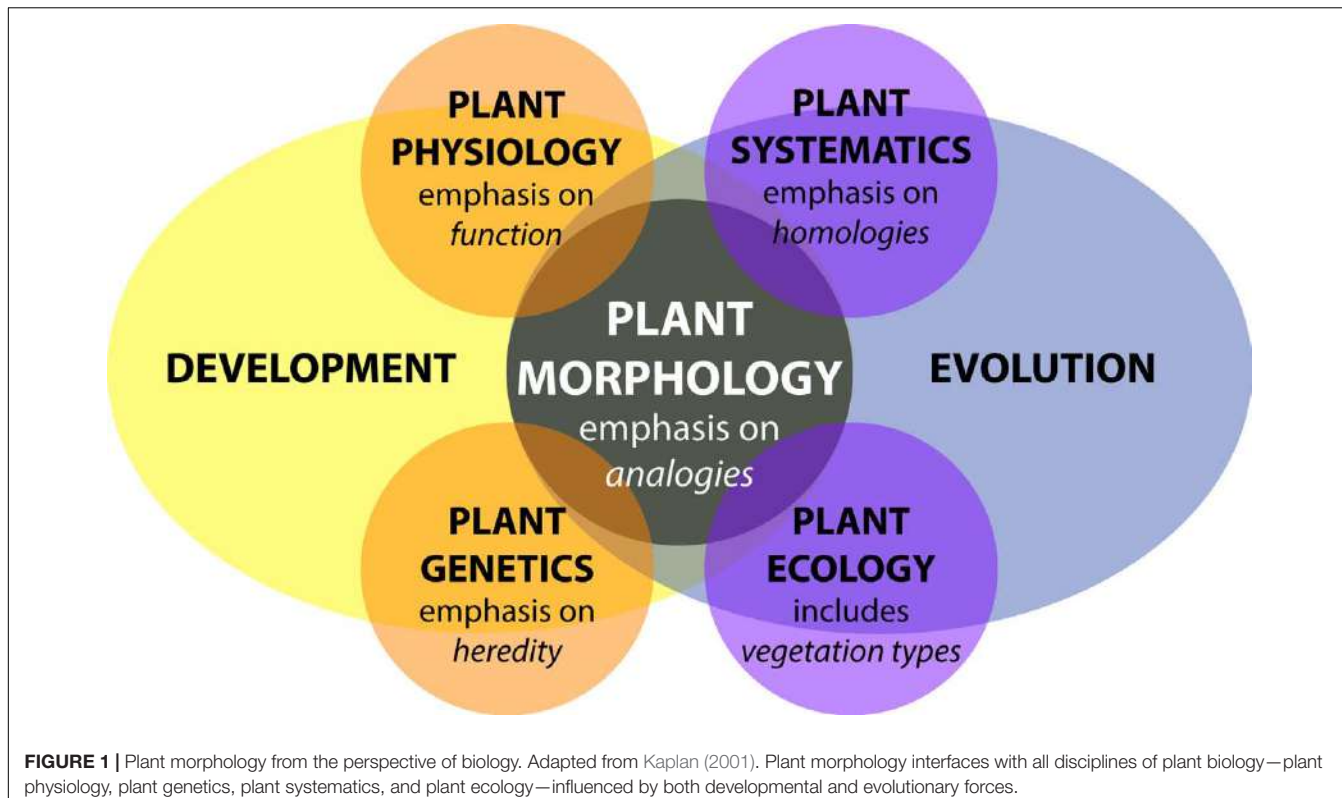


**FIGURE 1 |** Plant morphology from the perspective of biology. Adapted from Kaplan (2001). Plant morphology interfaces with all disciplines of plant biology—plant physiology, plant genetics, plant systematics, and plant ecology—influenced by both developmental and evolutionary forces.

events are represented by the geodesic distance at which branches are “born” and “die” along the length of the structure.

In the 1980s, David Kendall defined an elegant statistical framework to compare shapes (Kendall, 1984). His idea was to compare the outline of shapes in a transformation-invariant fashion. This concept infused rapidly as morphometrics into biology (Bookstein, 1997) and is increasingly carried out using machine vision techniques (Wilf et al., 2016). Kendall’s idea inspired the development of methods such as elliptical Fourier descriptors (Kuhl and Giardina, 1982) and new trends employing the Laplace Beltrami operator (Reuter et al., 2009), both relying on the spectral decompositions of shapes (Chitwood et al., 2012; Laga et al., 2014; Rellán-Álvarez et al., 2015). Beyond the organ level, such morphometric descriptors were used to analyze cellular expansion rates of rapidly deforming primordia into mature organ morphologies (Rolland-Lagan et al., 2003; Remmeler and Rolland-Lagan, 2012; Das Gupta and Nath, 2015).

From a geometric perspective, developmental processes construct surfaces in a three-dimensional space. Yet, the embedding of developing plant morphologies into a three-dimensional space imposes constraints on plant forms. Awareness of such constraints has led to new interpretations of plant morphology (Prusinkiewicz and de Reuille, 2010; Bucksch et al., 2014b) that might provide avenues to explain symmetry and asymmetry in plant organs (e.g., Martinez et al., 2016) or the occurrence of plasticity as a morphological response to environmental changes (e.g.,

Royer et al., 2009; Palacio-López et al., 2015; Chitwood et al., 2016).

#### Mathematics to Simulate Plant Morphology

Computer simulations use principles from graph theory, such as graph rewriting, to model plant morphology over developmental time by successively augmenting a graph with vertices and edges as plant development unfolds. These rules unravel the differences between observed plant morphologies across plant species (Kurth, 1994; Prusinkiewicz et al., 2001; Barthélémy and Caraglio, 2007) and are capable of modeling fractal descriptions that reflect the repetitive and modular appearance of branching structures (Horn, 1971; Hallé, 1971, 1986). Recent developments in functional-structural modeling abstract the genetic mechanisms driving the developmental program of tree crown morphology into a computational framework (Runions et al., 2007; Palubicki et al., 2009; Palubicki, 2013). Similarly, functional-structural modeling techniques are utilized in root biology to simulate the efficiency of nutrient and water uptake following developmental programs (Nielsen et al., 1994; Dunbabin et al., 2013).

Alan Turing, a pioneering figure in 20th-century science, had a longstanding interest in phyllotactic patterns. Turing’s approach to the problem was twofold: first, a detailed geometrical analysis of the patterns (Turing, 1992), and second, an application of his theory of morphogenesis through local activation and long-range inhibition (Turing, 1952), which defined the first reaction-diffusion system for morphological modeling. Combining physical experiments with computer simulations, Douady and Coudert (1996) subsequently modeled a diffusible chemical signal

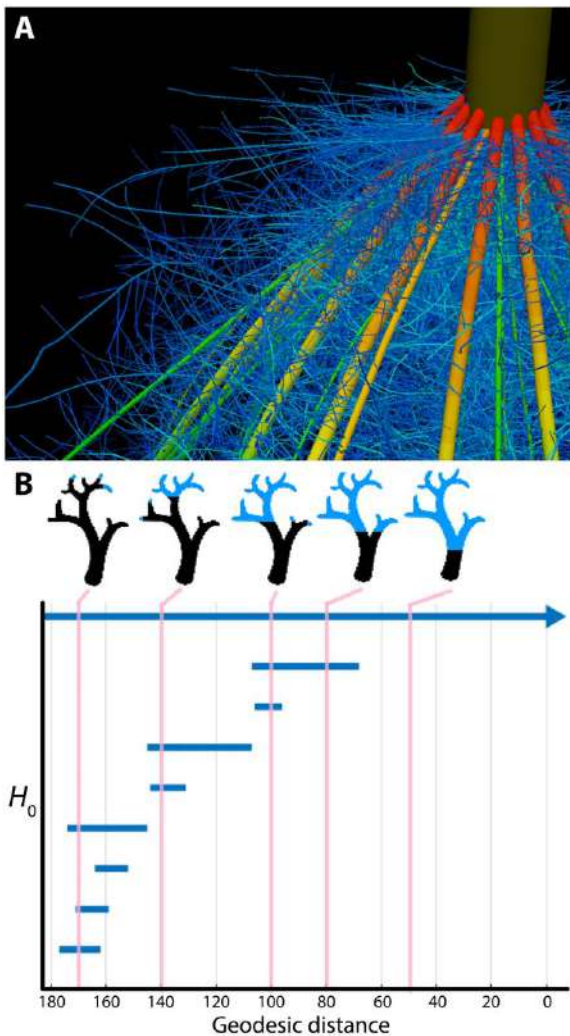


**FIGURE 2 |** Plant morphology from the perspective of mathematics. **(A)** The topological complexity of plants requires a mathematical framework to describe and simulate plant morphology. Shown is the top of a maize crown root 42 days after planting. Color represents root diameter, revealing topology and different orders of root architecture. Image by Jennifer T. Yang and provided by JPL (Pennsylvania State University). **(B)** Persistent homology deforms a given plant morphology using functions to define self-similarity in a structure. In this example, a geodesic distance function is traversed to the ground level of a tree (that is, the shortest curved distance of each voxel to the base of the tree), as visualized in blue in successive images. The branching structure, as defined across scales of the geodesic distance function is recorded as an  $H_0$  (zero-order homology) barcode, which in persistent homology refers to connected components. As the branching structure is traversed by the function, connected components are “born” and “die” as terminal branches emerge and fuse together. Each of these components is indicated as a bar in the  $H_0$  barcode, and the correspondence of the barcode to different points in the function is indicated by vertical lines, in pink. Images provided by ML (Danforth Plant Science Center).

produced by a developing primordium that would inhibit the initiation of nearby primordia, successfully recapitulating known phyllotactic patterns in the shoot apical meristem (Bernasconi, 1994; Meinhardt, 2004; Jönsson et al., 2005; Nikolaev et al., 2007;

Hohm et al., 2010; Fujita et al., 2011), the number of floral organs (Kitazawa and Fujimoto, 2015), the regular spacing of root hairs (Meinhardt and Gierer, 1974), and the establishment of specific vascular patterns (Meinhardt, 1976).

## EMERGING QUESTIONS AND BARRIERS IN THE MATHEMATICAL ANALYSIS OF PLANT MORPHOLOGY

A true synthesis of plant morphology, which comprehensively models observed biological phenomena and incorporates a mathematical perspective, remains elusive. In this section, we highlight current focuses in the study of plant morphology, including the technical limits of acquiring morphological data, phenotype prediction, responses of plants to the environment, models across biological scales, and the integration of complex phenomena, such as fluid dynamics, into plant morphological models.

### Technological Limits to Acquiring Plant Morphological Data

There are several technological limits to acquiring plant morphological data that must be overcome to move this field forward. One such limitation is the acquisition of quantitative plant images. Many acquisition systems do not provide morphological data with measurable units. Approaches that rely on the reflection of waves from the plant surface can provide quantitative measurements for morphological analyses. Time of flight scanners, such as terrestrial laser scanning, overcome unitless measurement systems by recording the round-trip time of hundreds of thousands of laser beams sent at different angles from the scanner to the first plant surface within the line of sight (Vosselman and Maas, 2010) (Figure 3). Leveraging the speed of light allows calculation of the distance between a point on the plant surface and the laser scanner.

Laser scanning and the complementary, yet unitless, approach of stereovision both produce surface samples or point clouds as output. However, both approaches face algorithmic challenges encountered when plant parts occlude each other, since both rely on the reflection of waves from the plant surface (Bucksch, 2014). Radar provides another non-invasive technique to study individual tree and forest structures over wide areas. Radar pulses can either penetrate or reflect from foliage, depending on the selected wavelength (Kaasalainen et al., 2015). Most radar applications occur in forestry and are being operated from satellites or airplanes. Although more compact and agile systems are being developed for precision forestry above- and below-ground (Feng et al., 2016), their resolution is too low to acquire the detail in morphology needed to apply hierarchy or similarity oriented mathematical analysis strategies.

Image acquisition that resolves occlusions by penetrating plant tissue is possible with X-ray (Kumi et al., 2015) and magnetic resonance imaging (MRI; van Dusschoten et al., 2016). While both technologies resolve occlusions and can even penetrate soil, their limitation is the requirement of a closed imaging

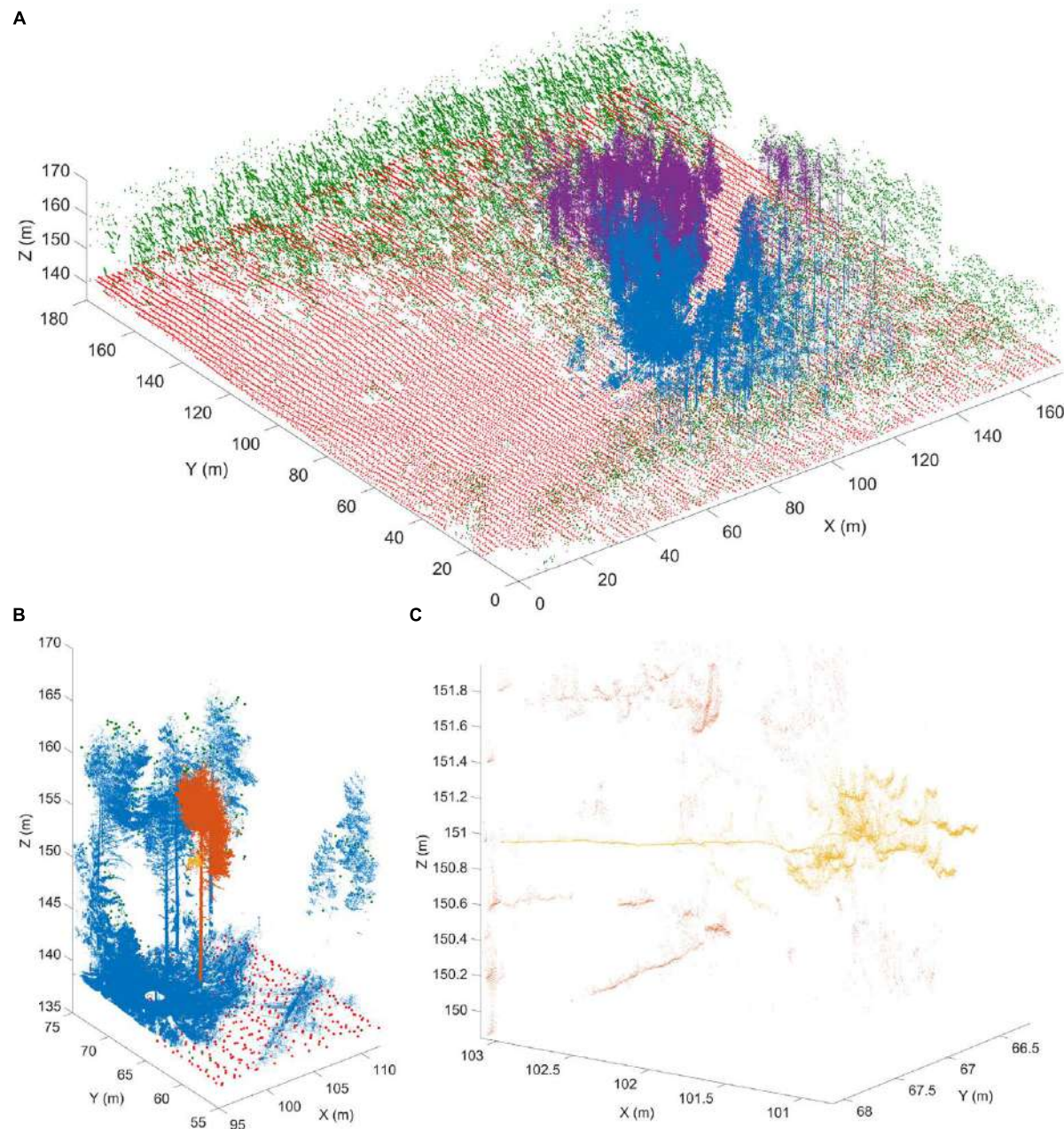


**FIGURE 3 |** Terrestrial laser scanning creates a point cloud reconstruction of a Finnish forest. **(A)** Structure of a boreal forest site in Finland as seen with airborne (ALS) and terrestrial (TLS) laser scanning point clouds. The red (ground) and green (above-ground) points are obtained from National Land Survey of Finland national ALS point clouds that cover hundreds of thousands of square kilometers with about 1 point per square meter resolution. The blue and magenta point clouds are results of two individual TLS measurements and have over 20 million points each within an area of about 500 m<sup>2</sup>. TLS point density varies with range but can be thousands of points per square meter up to tens of meters away from the scanner position. **(B)** An excerpt from a single TLS point cloud (blue). The TLS point cloud is so dense that individual tree point clouds (orange) and parts from them (yellow) can be selected for detailed analysis. **(C)** A detail from a single TLS point cloud. Individual branches (yellow) 20 m above ground can be inspected from the point cloud with centimeter level resolution to estimate their length and thickness. Images provided by EP (Finnish Geospatial Research Institute in the National Land Survey of Finland). ALS data was obtained from the National Land Survey of Finland Topographic Database, 08/2012 (National Land Survey of Finland open data license, version 1.0).

volume. Thus, although useful for a wide array of purposes, MRI and X-ray are potentially destructive if applied to mature plant organs such as roots in the field or tree crowns that are larger than the imaging volume (Fiorani et al., 2012). Interior plant

anatomy can be imaged destructively using confocal microscopy and laser ablation (Figure 4) or nano- or micro-CT tomography techniques, that are limited to small pot volumes, to investigate the first days of plant growth.

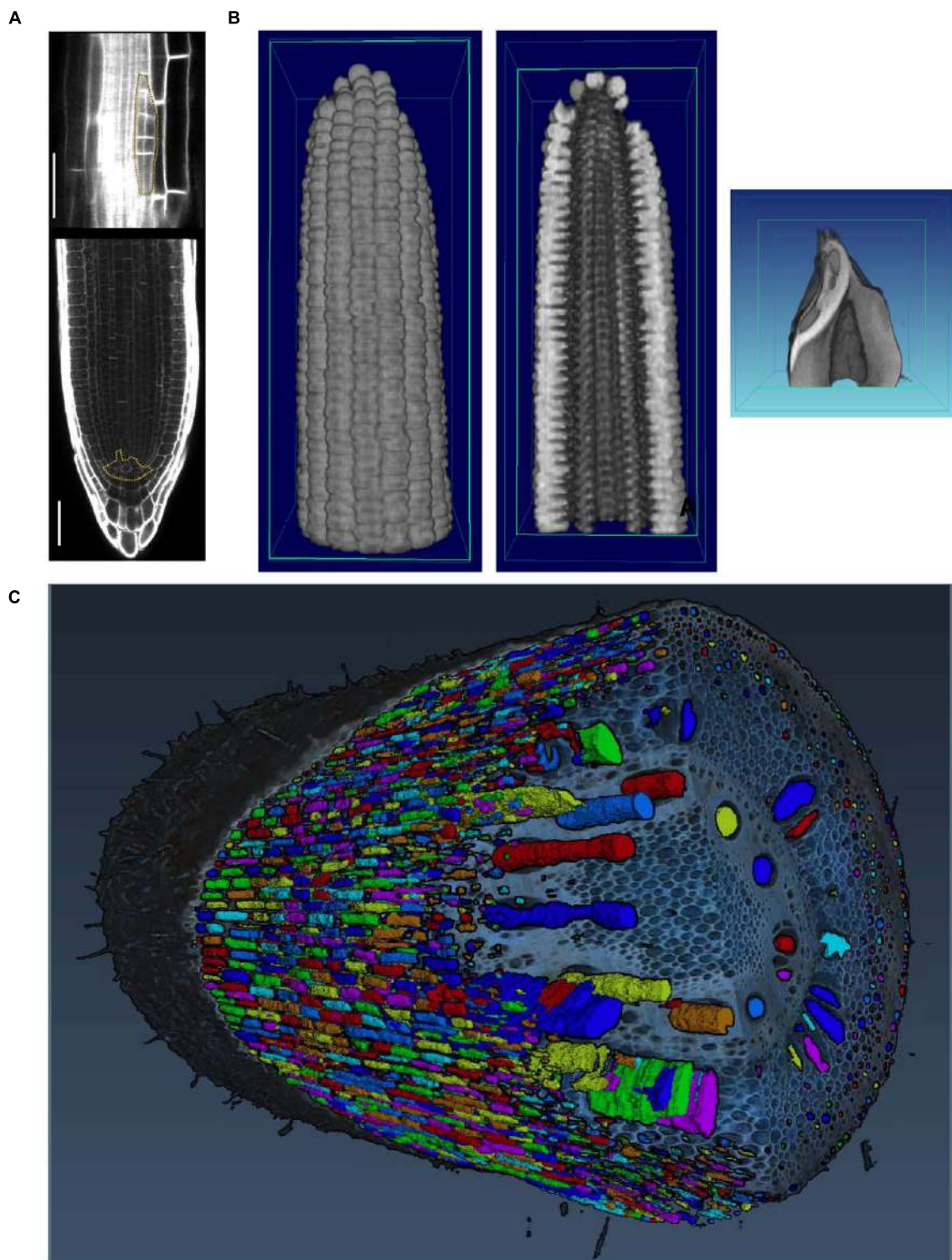


**FIGURE 4 |** Imaging techniques to capture plant morphology. **(A)** Confocal sections of an *Arabidopsis* root. The upper panel shows a new lateral root primordium at an early stage of development (highlighted in yellow). At regular intervals new roots branch from the primary root. The lower panel shows the primary root meristem and the stem cell niche (highlighted in yellow) from which all cells derive. Scale bars: 100 µm. Images provided by AM (Heidelberg University). **(B)** Computational tomographic (CT) x-ray sections through a reconstructed maize ear (left and middle) and kernel (right). Images provided by CT (Donald Danforth Plant Science Center). **(C)** Laser ablation tomography (LAT) image of a nodal root from a mature, field-grown maize plant, with color segmentation showing definition of cortical cells, aerenchyma lacunae, and metaxylem vessels. Image by Jennifer T. Yang and provided by JPL (Pennsylvania State University).

## The Genetic Basis of Plant Morphology

One of the outstanding challenges in plant biology is to link the inheritance and activity of genes with observed phenotypes. This is particularly challenging for the study of plant morphology, as both the genetic landscape and morphospaces are complex: modeling each of these phenomena alone is difficult, let alone trying to model morphology as a result of genetic phenomena (Benfey and Mitchell-Olds, 2008; Lynch and Brown, 2012; Chitwood and Topp, 2015). Although classic examples exist in which plant morphology is radically altered by the effects of a few genes (Doebley, 2004; Clark et al., 2006; Kimura et al., 2008), many morphological traits have a polygenic basis (Langlade et al., 2005; Tian et al., 2011; Chitwood et al., 2013).

Quantitative trait locus (QTL) analyses can identify the polygenic basis for morphological traits that span scales from the cellular to the whole organ level. At the cellular level, root cortex cell number (Ron et al., 2013), the cellular basis of carpel size (Frary et al., 2000), and epidermal cell area and number (Tisné et al., 2008) have been analyzed. The genetic basis of cellular morphology ultimately affects organ morphology, and quantitative genetic bases for fruit shape (Paran and van der Knaap, 2007; Monforte et al., 2014), root morphology (Zhu et al., 2005; Clark et al., 2011; Topp et al., 2013; Zurek et al., 2015), shoot apical meristem shape (Leiboff et al., 2015; Thompson et al., 2015), leaf shape (Langlade et al., 2005; Ku et al., 2010; Tian et al., 2011; Chitwood et al., 2014a,b; Zhang et al., 2014; Truong et al., 2015), and tree branching (Kenis and Keulemans, 2007; Segura et al., 2009) have been described.

Natural variation in cell, tissue, or organ morphology ultimately impacts plant physiology, and vice versa. For example, formation of root cortical aerenchyma was linked to better plant growth under conditions of suboptimal availability of water and nutrients (Zhu et al., 2010; Postma and Lynch, 2011; Lynch, 2013), possibly because aerenchyma reduces the metabolic costs of soil exploration. Maize genotypes with greater root cortical cell size or reduced root cortical cell file number reach greater depths to increase water capture under drought conditions, possibly because those cellular traits reduce metabolic costs of root growth and maintenance (Chimungu et al., 2015). The control of root angle that results in greater water capture in rice as water tables recede was linked to the control of auxin distribution (Uga et al., 2013). Similarly, in shoots, natural variation can be exploited to find genetic loci that control shoot morphology, e.g., leaf erectness (Ku et al., 2010; Feng et al., 2011).

High-throughput phenotyping techniques are increasingly used to reveal the genetic basis of natural variation (Tester and Langridge, 2010). In doing so, phenotyping techniques complement classic approaches of reverse genetics and often lead to novel insights, even in a well-studied species like *Arabidopsis thaliana*. Phenotyping techniques have revealed a genetic basis for dynamic processes such as root growth (Slovak et al., 2014) and traits that determine plant height (Yang et al., 2014). Similarly, high-resolution sampling of root gravitropism has led to an unprecedented understanding of the dynamics of the

genetic basis of plasticity (Miller et al., 2007; Brooks et al., 2010; Spalding and Miller, 2013).

## The Environmental Basis of Plant Morphology

Phenotypic plasticity is defined as the ability of one genotype to produce different phenotypes based on environmental differences (Bradshaw, 1965; DeWitt and Scheiner, 2004) and adds to the phenotypic complexity created by genetics and development. Trait variation in response to the environment has been analyzed classically using 'reaction norms,' where the phenotypic value of a certain trait is plotted for two different environments (Woltereck, 1909). If the trait is not plastic, the slope of the line connecting the points will be zero; if the reaction norm varies across the environment the trait is plastic and the slope of the reaction norm line will be a measure of the plasticity. As most of the responses of plants to their environment are non-linear, more insight into phenotypic plasticity can be obtained by analyzing dose-response curves or dose-response surfaces (Mitscherlich, 1909; Poorter et al., 2010).

Seminal work by Clausen et al. (1941) demonstrated using several clonal species in a series of reciprocal transplants that, although heredity exerts the most measureable effects on plant morphology, environment is also a major source of phenotypic variability. Research continues to explore the range of phenotypic variation expressed by a given genotype in the context of different environments, which has important implications for many fields, including conservation, evolution, and agriculture (Nicotra et al., 2010; DeWitt, 2016). Many studies examine phenotypes across latitudinal or altitudinal gradients, or other environmental clines, to characterize the range of possible variation and its relationship to the process of local adaptation (Cordell et al., 1998; Díaz et al., 2016).

Below-ground, plants encounter diverse sources of environmental variability, including water availability, soil chemistry, and physical properties like soil hardness and movement. These factors vary between individual plants (Razak et al., 2013) and within an individual root system, where plants respond at spatio-temporal levels to very different granularity (Drew, 1975; Robbins and Dinneny, 2015). Plasticity at a micro-environmental scale has been linked to developmental and molecular mechanisms (Bao et al., 2014). The scientific challenge here is to integrate these effects at a whole root system level and use different scales of information to understand the optimal acquisition in resource limited conditions (Rellán-Álvarez et al., 2016) (**Figure 5**).

## Integrating Models from Different Levels of Organization

Since it is extremely difficult to examine complex interdependent processes occurring at multiple spatio-temporal scales, mathematical modeling can be used as a complementary tool with which to disentangle component processes and investigate how their coupling may lead to emergent patterns at a systems level (Hamant et al., 2008; Band and King, 2012; Band et al., 2012; Jensen and Fozard, 2015). To be practical, a

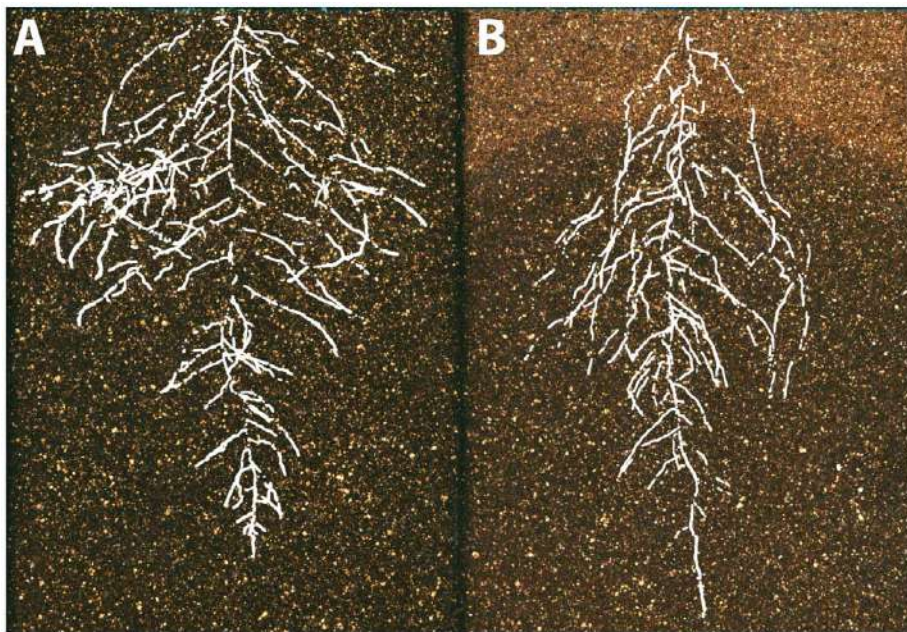


**FIGURE 5 |** The environmental basis of plant morphology. Root system architecture of *Arabidopsis* Col-0 plants expressing ProUBQ10:LUC2o growing in **(A)** control and **(B)** water-deficient conditions using the GLO-Roots system (Rellán-Álvarez et al., 2015). Images provided by RR-Á (Laboratorio Nacional de Genómica para la Biodiversidad, CINVESTAV) are a composite of a video originally published (Rellán-Álvarez et al., 2015).

multiscale model should generate well-constrained predictions despite significant parameter uncertainty (Gutenkunst et al., 2007; Hofhuis et al., 2016). It is desirable that a multiscale model has certain modularity in its design such that individual modules are responsible for modeling specific spatial aspects of the system (Baldazzi et al., 2012). Imaging techniques can validate multiscale models (e.g., Willis et al., 2016) such that simulations can reliably guide experimental studies.

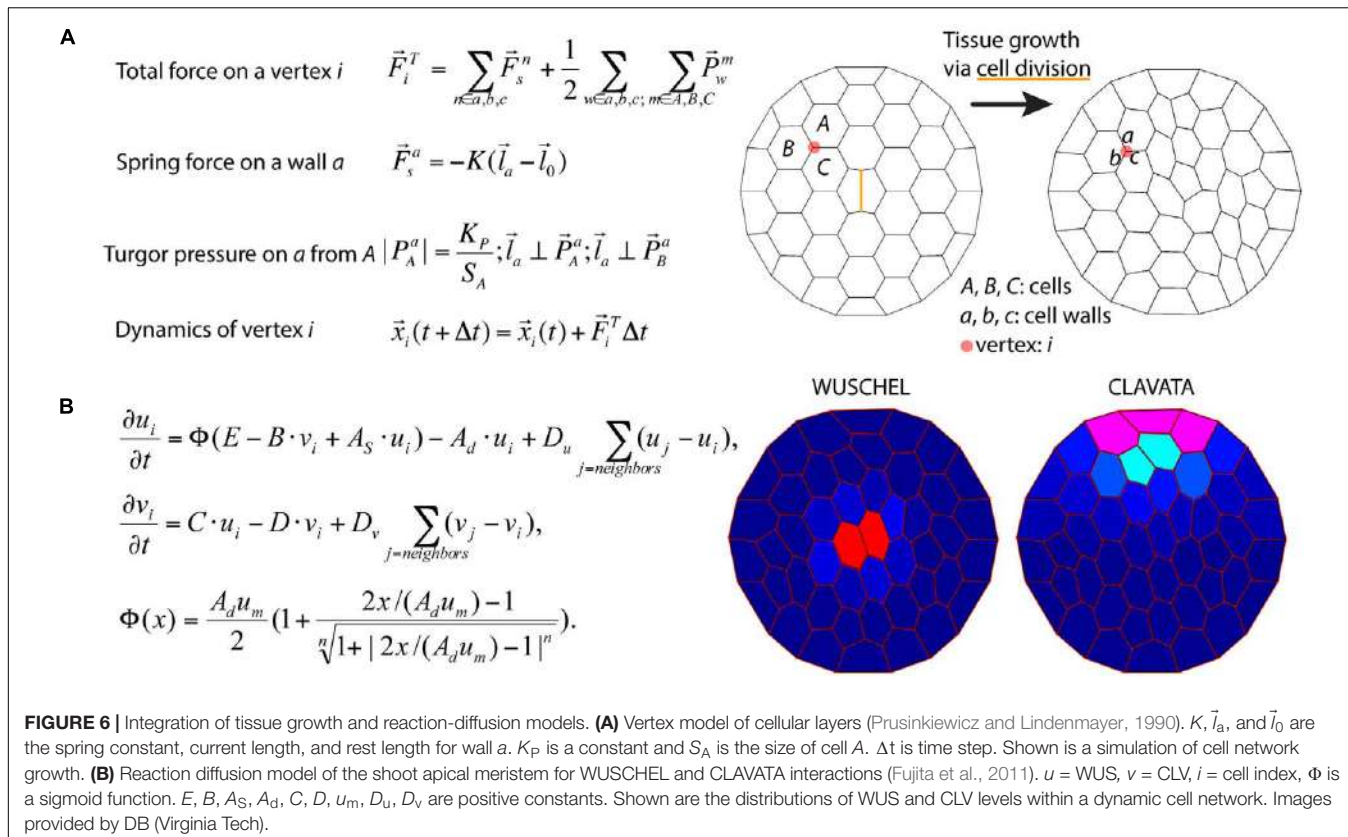
To illustrate the challenges of multi-scale modeling, we highlight an example that encompasses molecular and cellular scales. At the molecular scale, models can treat some biomolecules as diffusive, but others, such as membrane-bound receptors, can be spatially restricted (Battogtokh and Tyson, 2016). Separately, at the cellular scale, mathematical models describe dynamics of cell networks where the mechanical pressures exerted on the cell walls are important factors for cell growth and division (Jensen and Fozard, 2015) (Figure 6A). In models describing plant development in a two-dimensional cross-section geometry, cells are often modeled as polygons defined by walls between neighboring cells. The spatial position of a vertex, where the cell walls of three neighboring cells coalesce, is a convenient variable for mathematical modeling of the dynamics of cellular networks (Prusinkiewicz and Runions, 2012). A multiscale model can then be assembled by combining the molecular and cellular models. Mutations and deletions of the genes encoding the biomolecules can be modeled by changing parameters. By inspecting the effects of such modifications on the dynamics of the cellular networks, the relationship between genotypes and phenotypes can be predicted. For example, Fujita et al. (2011) model integrates the dynamics of

cell growth and division with the spatio-temporal dynamics of the proteins involved in stem cell regulation and simulates shoot apical meristem development in wild type and mutant plants (Figure 6B).

## Modeling the Impact of Morphology on Plant Function

Quantitative measures of plant morphology are critical to understand function. Vogel (1989) was the first to provide quantitative data that showed how shape changes in leaves reduce drag or friction in air or water flows. He found that single broad leaves reconfigure at high flow velocities into cone shapes to reduce flutter and drag (Figures 7A,B). More recent work discovered that the cone shape is significantly more stable than other reconfigurations such as U-shapes (Miller et al., 2012). Subsequent experimental studies on broad leaves, compound leaves, and flowers also support rapid repositioning in response to strong currents as a general mechanism to reduce drag (Niklas, 1992; Ennos, 1997; Etnier and Vogel, 2000; Vogel, 2006) (Figure 7C). It is a combination of morphology and anatomy, and the resultant material properties, which lead to these optimal geometric re-configurations of shape.

From a functional perspective, it is highly plausible that leaf shape and surface-material properties alter the boundary layer of a fluid/gas over the leaf surface or enhance passive movement that can potentially augment gas and heat exchange. For example, it has been proposed that the broad leaves of some trees flutter for the purpose of convective and evaporative heat transfer (Thom, 1968; Grant, 1983). Any movement of the leaf relative to the



movement of the air or water may decrease the boundary layer and increase gas exchange, evaporation, and heat dissipation (Roden and Pearcy, 1993). Each of these parameters may be altered by the plant to improve the overall function of the leaf (Vogel, 2012).

The growth of the plant continuously modifies plant topology and geometry, which in turn changes the balance between organ demand and production. At the organismal scale, the 3D spatial distribution of plant organs is the main interface between the plant and its environment. For example, the 3D arrangement of branches impacts light interception and provides the support for different forms of fluxes (water, sugars) and signals (mechanical constraints, hormones) that control plant functioning and growth (Godin and Sinoquet, 2005).

## MILESTONES IN EDUCATION AND OUTREACH TO ACCELERATE THE INFUSION OF MATH INTO THE PLANT SCIENCES

Mathematics and plant biology need to interact more closely to accelerate scientific progress. Opportunities to interact possibly involve cross-disciplinary training, workshops, meetings, and funding opportunities. In this section, we outline perspectives for enhancing the crossover between mathematics and plant biology.

## Education

Mathematics has been likened to “biology’s next microscope,” because of the insights into an otherwise invisible world it has to offer. Conversely, biology has been described as “mathematics’ next physics,” stimulating novel mathematical approaches because of the hitherto unrealized phenomena that biology studies (Cohen, 2004). The scale of the needed interplay between mathematics and plant biology is enormous and may lead to new science disciplines at the interface of both: ranging from the cellular, tissue, organismal, and community levels to the global; touching upon genetic, transcriptional, proteomic, metabolite, and morphological data; studying the dynamic interactions of plants with the environment or the evolution of new forms over geologic time; and spanning quantification, statistics, and mechanistic mathematical models.

Research is becoming increasingly interdisciplinary, and undergraduate, graduate, and post-graduate groups are actively trying to bridge the gap between mathematics and biology skillsets. While many graduate programs have specialization tracks under the umbrella of mathematics or biology-specific programs, increasingly departments are forming specially designed graduate groups for mathematical/quantitative biology<sup>1,2</sup> to strengthen the interface between both disciplines.

<sup>1</sup>BioQuant at University of Heidelberg, <http://www.bioquant.uni-heidelberg.de> (retrieved February 28, 2017)

<sup>2</sup>Quantitative Biosciences at Georgia Tech in Atlanta, <http://qbios.gatech.edu> (retrieved February 28, 2017)

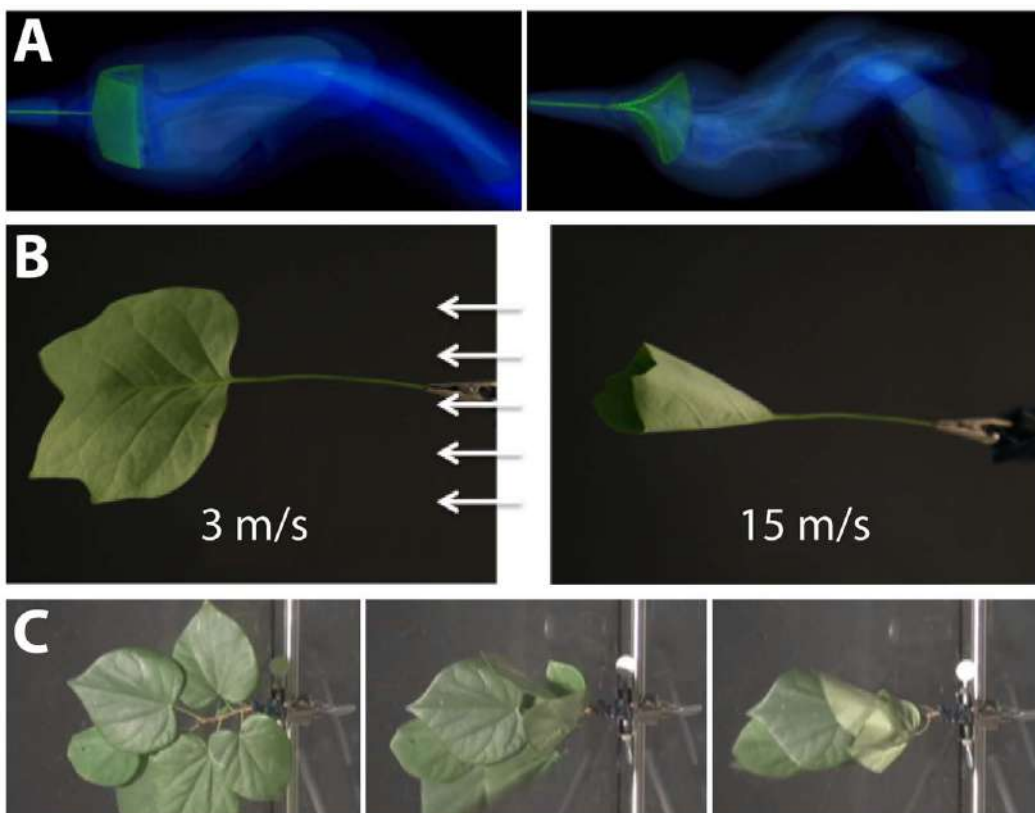


**FIGURE 7 |** Modeling the interaction between plant morphology and fluid dynamics. **(A)** 3D immersed boundary simulations of flow past a flexible rectangular sheet (left) and disk with a cut from the center to edge (right). Both structures are attached to a flexible petiole, and the flow is from left to right. The contours show the magnitude of vorticity (the rotation in the air). The circular disk reconfigures into a cone shape, similar to many broad leaves. **(B)** Reconfiguration of tulip poplar leaves in 3 m/s (left) and 15 m/s flow (right). The leaves typically flutter at lower wind speeds and reconfigure into stable cones at high wind speeds. **(C)** A cluster of redbud leaves in wind moving from right to left. The wind speed is increased from 3 m/s (left) to 6 m/s (middle) and 12 m/s (right). Note that the entire cluster reconfigures into a cone shape. This is different from the case of tulip poplars and maples where each leaf individually reconfigures into a conic shape. Images provided by LM (University of North Carolina, Chapel Hill, NC, United States).

This will necessitate team-teaching across disciplines to train the next generation of mathematical/computational plant scientists.

## Public Outreach: Citizen Science and the Maker Movement

Citizen science, which is a method to make the general public aware of scientific problems and employ their help in solving them<sup>3</sup>, is an ideal platform to initiate a synthesis between plant biology and mathematics because of the relatively low cost and accessibility of each field. Arguably, using citizen science to collect plant morphological diversity has already been achieved, but has yet to be fully realized. In total, it is estimated that the herbaria of the world possess greater than 207 million voucher specimens<sup>4</sup>, representing the diverse lineages of land plants collected over their respective biogeographies over a timespan of centuries.

Digital documentation of the millions of vouchers held by the world's botanic gardens is actively underway, allowing for researchers and citizens alike to access and study for themselves the wealth of plant diversity across the globe and centuries (Smith et al., 2003; Corney et al., 2012; Ryan, 2013).

The developmental changes in plants responding to environmental variability and microclimatic changes over the course of a growing season can be analyzed by studying phenology. Citizen science projects such as the USA National Phenology Network<sup>5</sup> or Earthwatch<sup>6</sup> and associated programs such as My Tree Tracker<sup>7</sup> document populations and individual plants over seasons and years, providing a distributed, decentralized network of scientific measurements to study the effects of climate change on plants.

<sup>5</sup><https://www.usanpn.org/#> (retrieved May 29, 2016)

<sup>6</sup><http://earthwatch.org/scientific-research/special-initiatives/urban-resiliency> (retrieved May 29, 2016)

<sup>7</sup><http://www.mytreetracker.org/cwis438/websites/MyTreeTracker/About.php?WebSiteID=23> (retrieved May 29, 2016)



**FIGURE 8 |** Milestones to accelerate the infusion of math into the plant sciences. Group photo of the authors from the National Institute for Mathematical and Biological Synthesis (NIMBioS) meeting on plant morphological models (University of Tennessee, Knoxville, September 2–4, 2015) that inspired this manuscript. Workshops such as these, bringing mathematicians and plant biologists together, will be necessary to create a new synthesis of plant morphology.

Citizen science is also enabled by low-cost, specialized equipment. Whether programming a camera to automatically take pictures at specific times or automating a watering schedule for a garden, the maker movement—a do-it-yourself cultural phenomenon that intersects with hacker culture—focuses on building custom, programmable hardware, whether via electronics, robotics, 3D-printing, or time-honored skills such as metal- and woodworking. The focus on programming is especially relevant for integrating mathematical approaches with plant science experiments. The low-cost of single-board computers like Raspberry Pi, HummingBoard, or CubieBoard is a promising example of how to engage citizen scientists into the scientific process and enable technology solutions to specific questions.

## Workshops and Funding Opportunities

Simply bringing mathematicians and plant biologists together to interact, to learn about new tools, approaches, and opportunities in each discipline is a major opportunity for further integration of these two disciplines and strengthen new disciplines at the interface of both. This white paper itself is a testament to the power of bringing mathematicians and biologists together, resulting from a National Institute for Mathematical and Biological Synthesis (NIMBioS) workshop titled “Morphological Plant Modeling: Unleashing Geometric and Topologic Potential within the Plant Sciences,” held at the University of Tennessee, Knoxville, September 2–4, 2015<sup>8</sup> (**Figure 8**). Other mathematical institutes such as the Mathematical Biology Institute (MBI) at Ohio State University<sup>9</sup>, the Statistical and Applied Mathematical Sciences Institute (SAMSI) in Research Triangle Park<sup>10</sup>, the Institute for Mathematics and Its Applications at

University of Minnesota<sup>11</sup>, and the Centre for Plant Integrative Biology at the University of Nottingham<sup>12</sup> have also hosted workshops for mathematical and quantitative biologists from the undergraduate student to the faculty level.

There are efforts to unite biologists and mathematics through initiatives brought forth from The National Science Foundation, including Mathematical Biology Programs<sup>13</sup> and the Joint DMS/NIGMS Initiative to Support Research at the Interface of the Biological and Mathematical Sciences<sup>14</sup> (DMS/NIGMS). Outside of the Mathematics and Life Sciences Divisions, the Division of Physics houses a program on the Physics of Living Systems. Societies such as The Society for Mathematical Biology and the Society for Industrial and Applied Mathematics (SIAM) Life Science Activity Group<sup>15</sup> are focused on the dissemination of research at the intersection of math and biology, creating many opportunities to present research and provide funding. We emphasize the importance that funding opportunities have had and will continue to have in the advancement of plant morphological modeling.

## Open Science

Ultimately, mathematicians, computational scientists, and plant biology must unite at the level of jointly collecting data, analyzing it, and doing science together. Open and timely data sharing to benchmark code is a first step to unite these disciplines along with building professional interfaces to bridge

<sup>8</sup>[http://www.nimbios.org/workshops/WS\\_plantmorph](http://www.nimbios.org/workshops/WS_plantmorph) (retrieved May 29, 2016)

<sup>9</sup><https://mbi.osu.edu/> (retrieved May 29, 2016)

<sup>10</sup><http://www.samsi.info/> (retrieved May 29, 2016)

<sup>11</sup><https://www.ima.umn.edu/> (retrieved May 29, 2016)

<sup>12</sup><https://www.cpib.ac.uk/outreach/cpib-summer-school/> (retrieved May 29, 2016)

<sup>13</sup>[https://www.nsf.gov/funding/pgm\\_summ.jsp?pims\\_id=5690](https://www.nsf.gov/funding/pgm_summ.jsp?pims_id=5690) (retrieved May 29, 2016)

<sup>14</sup>[https://www.nsf.gov/funding/pgm\\_summ.jsp?pims\\_id=5300&org=DMS](https://www.nsf.gov/funding/pgm_summ.jsp?pims_id=5300&org=DMS) (retrieved May 29, 2016)

<sup>15</sup><https://www.siam.org/activity/life-sciences/> (retrieved May 29, 2016)

between the disciplines (Bucksch et al., 2017; Pradal et al., 2017).

A number of platforms provide open, public access to datasets, figures, and code that can be shared, including Dryad<sup>16</sup>, Dataverse<sup>17</sup>, and Figshare<sup>18</sup>. Beyond the ability to share data is the question of open data formats and accessibility. For example, in remote sensing research it is unfortunately common that proprietary data formats are used, which prevents their use without specific software. This severely limits the utility and community building aspects of plant morphological research. Beyond datasets, making code openly available, citable, and user-friendly is a means to share methods to analyze data. Places to easily share code include web-based version controlled platforms like Bitbucket<sup>19</sup> or Github<sup>20</sup> and software repositories like Sourceforge<sup>21</sup>. Furthermore, numerous academic Journals (e.g., Nature Methods, Applications in Plant Sciences, and Plant Methods) already accept publications that focus on methods and software to accelerate new scientific discovery (Pradal et al., 2013).

Meta-analysis datasets provide curated resources where numerous published and unpublished datasets related to a specific problem (or many problems) can be accessed by researchers<sup>22</sup>. The crucial element is that data is somehow reflective of universal plant morphological features, bridging the gap between programming languages and biology, as seen in the Root System Markup Language (Lobet et al., 2015) and OpenAlea (Pradal et al., 2008, 2015). Bisque is a versatile platform to store, organize, and analyze image data, providing simultaneously open access to data and analyses as well as the requisite computation (Kvilekval et al., 2010). CyVerse<sup>23</sup> (formerly iPlant) is a similar platform, on which academic users get 100 GB storage for free and can create analysis pipelines that can be shared and reused (Goff et al., 2011). For example, DIRT<sup>24</sup> is an automatic, high throughput computing platform (Bucksch et al., 2014a; Das et al., 2015) that the public can use hosted on CyVerse using the Texas Advanced Computing Center<sup>25</sup> (TACC) resources at UT Austin that robustly extracts root traits from digital images. The reproducibility of these complex computational experiments can be improved using scientific workflows that capture and automate the exact methodology followed by scientists (Cohen-Boulakia et al., 2017). We emphasize here the importance of adopting open science policies at the individual investigator and journal level to continue strengthening the interface between plant and mathematically driven sciences.

<sup>16</sup><http://datadryad.org/> (retrieved May 29, 2016)

<sup>17</sup><http://dataverse.org/> (retrieved May 29, 2016)

<sup>18</sup><https://figshare.com/> (retrieved May 29, 2016)

<sup>19</sup><https://bitbucket.org/> (retrieved May 29, 2016)

<sup>20</sup><https://github.com/> (retrieved May 29, 2016)

<sup>21</sup><https://sourceforge.net/> (retrieved May 29, 2016)

<sup>22</sup>BAAD: a Biomass And Allometry Database for woody plants, <https://github.com/dfalster/baad> (retrieved May 29, 2016)

<sup>23</sup><http://www.cyverse.org/> (retrieved August 20, 2016)

<sup>24</sup><http://dirt.iplantcollaborative.org/> (retrieved August 20, 2016)

<sup>25</sup><https://www.tacc.utexas.edu/> (retrieved August 20, 2016)

## CONCLUSION: UNLEASHING GEOMETRIC AND TOPOLOGICAL POTENTIAL WITHIN THE PLANT SCIENCES

Plant morphology is a mystery from a molecular and quantification point of view. Hence, it fascinates both mathematical and plant biology researchers alike. As such, plant morphology holds the secret by which predetermined variations of organizational patterns emerge as a result of evolutionary, developmental, and environmental responses.

The persistent challenge at the intersection of plant biology and mathematical sciences might be the integration of measurements across different scales of the plant. We have to meet this challenge to derive and validate mathematical models that describe plants beyond the visual observable. Only then we will be able to modify plant morphology through molecular biology and breeding as means to develop needed agricultural outputs and sustainable environments for everybody.

Cross-disciplinary training of scientists, citizen science, and open science are inevitable first steps to develop the interface between mathematical-driven and plant biology-driven sciences. The result of these steps will be new disciplines, that will add to the spectrum of researchers in plant biology. Hence, to unleash the potential of geometric and topological approaches in the plant sciences, we need an interface familiar with both plants and mathematical approaches to meet the challenges posed by a future with uncertain natural resources as a consequence of climate change.

## AUTHOR CONTRIBUTIONS

AB and DC conceived, wrote, and organized the manuscript. All authors contributed to writing the manuscript.

## FUNDING

This work was assisted through participation in the *Morphological Plant Modeling: Unleashing geometric and topological potential within the plant sciences* Investigative Workshop at the National Institute for Mathematical and Biological Synthesis, sponsored by the National Science Foundation through NSF Award #DBI-1300426, with additional support from The University of Tennessee, Knoxville, Knoxville, TN, United States.

## ACKNOWLEDGMENTS

The authors are grateful to the National Institute for Mathematical and Biological Synthesis (NIMBioS, University of Tennessee, Knoxville) for hosting and funding the workshop “Morphological Plant Modeling: Unleashing geometric and topological potential within the plant sciences” that inspired this manuscript. We thank the reviewers Evelyne Costes and Leo Marcelis for creative and open discussions.

## REFERENCES

- Aiteanu, F., and Klein, R. (2014). Hybrid tree reconstruction from inhomogeneous point clouds. *Visual Comput.* 30, 763–771. doi: 10.1007/s00371-014-0977-7
- Baldazzi, V., Bertin, N., De Jong, H., and Génard, M. (2012). Towards multiscale plant models: integrating cellular networks. *Trends Plant Sci.* 17, 728–736. doi: 10.1016/j.tplants.2012.06.012
- Band, L. R., Fozard, J. A., Godin, C., Jensen, O. E., Pridmore, T., Bennett, M. J., et al. (2012). Multiscale systems analysis of root growth and development: modeling beyond the network and cellular scales. *Plant Cell* 24, 3892–3906. doi: 10.1105/tpc.112.101550
- Band, L. R., and King, J. R. (2012). Multiscale modelling of auxin transport in the plant-root elongation zone. *J. Math. Biol.* 65, 743–785. doi: 10.1007/s00285-011-0472-y
- Bao, Y., Aggarwal, P., Robbins, N. E., Sturrock, C. J., Thompson, M. C., Tan, H. Q., et al. (2014). Plant roots use a patterning mechanism to position lateral root branches toward available water. *Proc. Natl. Acad. Sci. U.S.A.* 111, 9319–9324. doi: 10.1073/pnas.1400966111
- Barthélémy, D., and Caraglio, Y. (2007). Plant architecture: a dynamic, multilevel and comprehensive approach to plant form, structure, and ontogeny. *Ann. Bot.* 99, 375–407. doi: 10.1093/aob/mcl260
- Battogtokh, D., and Tyson, J. J. (2016). A bistable switch mechanism for stem cell domain nucleation in the shoot apical meristem. *Front. Plant Sci.* 7:674. doi: 10.3389/fpls.2016.00674
- Benfey, P. N., and Mitchell-Olds, T. (2008). From genotype to phenotype: systems biology meets natural variation. *Science* 320, 495–497. doi: 10.1126/science.1153716
- Bernasconi, G. P. (1994). Reaction-diffusion model for phyllotaxis. *Physica D* 70, 90–99. doi: 10.1016/0167-2789(94)90058-2
- Bookstein, F. L. (1997). *Morphometric Tools for Landmark Data: Geometry and Biology*. New York, NY: Cambridge University Press.
- Bradshaw, A. D. (1965). Evolutionary significance of phenotypic plasticity in plants. *Adv. Genet.* 13, 115–155. doi: 10.1016/s0065-2660(08)60048-6
- Braybrook, S. A., and Jönsson, H. (2016). Shifting foundations: the mechanical cell wall and development. *Curr. Opin. Plant Biol.* 29, 115–120. doi: 10.1016/j.pbi.2015.12.009
- Brooks, T. L. D., Miller, N. D., and Spalding, E. P. (2010). Plasticity of *Arabidopsis* root gravitropism throughout a multidimensional condition space quantified by automated image analysis. *Plant Physiol.* 152, 206–216. doi: 10.1104/pp.109.145292
- Bucksch, A. (2014). A practical introduction to skeletons for the plant sciences. *Appl. Plant Sci.* 2:1400005. doi: 10.3732/apps.1400005
- Bucksch, A., Burridge, J., York, L. M., Das, A., Nord, E., Weitz, J. S., et al. (2014a). Image-based high-throughput field phenotyping of crop roots. *Plant Physiol.* 166, 470–486. doi: 10.1104/pp.114.243519
- Bucksch, A., Das, A., Schneider, H., Merchant, N., and Weitz, J. S. (2017). Overcoming the law of the hidden in cyberinfrastructures. *Trends Plant Sci.* 22, 117–123. doi: 10.1016/j.tplants.2016.11.014
- Bucksch, A., and Fleck, S. (2011). Automated detection of branch dimensions in woody skeletons of fruit tree canopies. *Photogramm. Eng. Remote Sens.* 77, 229–240. doi: 10.14358/PERS.77.3.229
- Bucksch, A., Lindenbergh, R., and Menenti, M. (2010). SkelTre. *Vis. Comput.* 26, 1283–1300. doi: 10.1007/s00371-010-0520-4
- Bucksch, A., Turk, G., and Weitz, J. S. (2014b). The fiber walk: a model of tip-driven growth with lateral expansion. *PLoS ONE* 9:e85585. doi: 10.1371/journal.pone.0085585
- Chimungu, J. G., Maliro, M. F., Nalivata, P. C., Kanyama-Phiri, G., Brown, K. M., and Lynch, J. P. (2015). Utility of root cortical aerenchyma under water limited conditions in tropical maize (*Zea mays* L.). *Field Crops Res.* 171, 86–98. doi: 10.1016/j.fcr.2014.10.009
- Chitwood, D. H., Headland, L. R., Ranjan, A., Martinez, C. C., Braybrook, S. A., Koenig, D. P., et al. (2012). Leaf asymmetry as a developmental constraint imposed by auxin-dependent phyllotactic patterning. *Plant Cell* 24, 2318–2327. doi: 10.1105/tpc.112.098798
- Chitwood, D. H., Kumar, R., Headland, L. R., Ranjan, A., Covington, M. F., Ichihashi, Y., et al. (2013). A quantitative genetic basis for leaf morphology in a set of precisely defined tomato introgression lines. *Plant Cell* 25, 2465–2481. doi: 10.1105/tpc.113.112391
- Chitwood, D. H., Ranjan, A., Kumar, R., Ichihashi, Y., Zumstein, K., Headland, L. R., et al. (2014a). Resolving distinct genetic regulators of tomato leaf shape within a heteroblastic and ontogenetic context. *Plant Cell* 26, 3616–3629. doi: 10.1105/tpc.114.130112
- Chitwood, D. H., Ranjan, A., Martinez, C. C., Headland, L. R., Thiem, T., Kumar, R., et al. (2014b). A modern ampelography: a genetic basis for leaf shape and venation patterning in grape. *Plant Physiol.* 164, 259–272. doi: 10.1104/pp.113.229708
- Chitwood, D. H., Rundell, S. M., Li, D. Y., Woodford, Q. L., Tommy, T. Y., Lopez, J. R., et al. (2016). Climate and developmental plasticity: interannual variability in grapevine leaf morphology. *Plant Physiol.* 170, 1480–1491. doi: 10.1104/pp.15.01825
- Chitwood, D. H., and Topp, C. N. (2015). Revealing plant cryptotypes: defining meaningful phenotypes among infinite traits. *Curr. Opin. Plant Biol.* 24, 54–60. doi: 10.1016/j.pbi.2015.01.009
- Clark, R. M., Wagler, T. N., Quijada, P., and Doebley, J. (2006). A distant upstream enhancer at the maize domestication gene tb1 has pleiotropic effects on plant and inflorescent architecture. *Nat. Genet.* 38, 594–597. doi: 10.1038/ng1784
- Clark, R. T., MacCurdy, R. B., Jung, J. K., Shaff, J. E., McCouch, S. R., Aneshansley, D. J., et al. (2011). Three-dimensional root phenotyping with a novel imaging and software platform. *Plant Physiol.* 156, 455–465. doi: 10.1104/pp.110.169102
- Clausen, J., Keck, D. D., and Hiesey, W. M. (1941). Regional differentiation in plant species. *Am. Nat.* 75, 231–250. doi: 10.1086/280955
- Cohen, J. E. (2004). Mathematics is biology's next microscope, only better; biology is mathematics' next physics, only better. *PLoS Biol.* 2:e439. doi: 10.1371/journal.pbio.0020439
- Cohen-Boulakia, S., Belhajjame, K., Collin, O., Chopard, J., Froidevaux, C., Gaignard, A., et al. (2017). Scientific workflows for computational reproducibility in the life sciences: status, challenges and opportunities. *Fut. Gen. Comput. Syst.* (in press). doi: 10.1016/j.future.2017.01.012
- Cordell, S., Goldstein, G., Mueller-Dombois, D., Webb, D., and Vitousek, P. M. (1998). Physiological and morphological variation in *Metrosideros polymorpha*, a dominant Hawaiian tree species, along an altitudinal gradient: the role of phenotypic plasticity. *Oecologia* 113, 188–196. doi: 10.1007/s004420050367
- Corney, D., Clark, J. Y., Tang, H. L., and Wilkin, P. (2012). Automatic extraction of leaf characters from herbarium specimens. *Taxon* 61, 231–244.
- Danjon, F., Bert, D., Godin, C., and Trichet, P. (1999). Structural root architecture of 5-year-old *Pinus pinaster* measured by 3D digitising and analysed with AMAPmod. *Plant Soil* 217, 49–63. doi: 10.1023/A:1004686119796
- Das, A., Schneider, H., Burridge, J., Ascanio, A. K. M., Wojciechowski, T., Topp, C. N., et al. (2015). Digital imaging of root traits (DIRT): a high-throughput computing and collaboration platform for field-based root phenomics. *Plant Methods* 11:51. doi: 10.1186/s13007-015-0093-3
- Das Gupta, M., and Nath, U. (2015). Divergence in patterns of leaf growth polarity is associated with the expression divergence of miR396. *Plant Cell* 27, 2785–2799. doi: 10.1105/tpc.15.00196
- DeWitt, T. J. (2016). Expanding the phenotypic plasticity paradigm to broader views of trait space and ecological function. *Curr. Zool.* 62, 463–473. doi: 10.1093/cz/zow085
- DeWitt, T. J., and Scheiner, S. M. (eds) (2004). *Phenotypic Plasticity: Functional and Conceptual Approaches*. Oxford: Oxford University Press.
- Díaz, S., Kattge, J., Cornelissen, J. H., Wright, I. J., Lavorel, S., Dray, S., et al. (2016). The global spectrum of plant form and function. *Nature* 529, 167–171. doi: 10.1038/nature16489
- Doebley, J. (2004). The genetics of maize evolution. *Annu. Rev. Genet.* 38, 37–59. doi: 10.1146/annurev.genet.38.072902.092425
- Douady, S., and Coudert, Y. (1996). Phyllotaxis as a dynamical self organizing process part I: the spiral modes resulting from time-periodic iterations. *J. Theor. Biol.* 178, 255–273. doi: 10.1006/jtbi.1996.0024
- Drew, M. C. (1975). Comparison of the effects of a localised supply of phosphate, nitrate, ammonium and potassium on the growth of the seminal root system, and the shoot, in barley. *New Phytol.* 75, 479–490. doi: 10.1111/j.1469-8137.1975.tb01409.x
- Dunbabin, V. M., Postma, J. A., Schnepf, A., Pagès, L., Javaux, M., Wu, L., et al. (2013). Modelling root-soil interactions using three-dimensional models of root growth, architecture and function. *Plant Soil* 372, 93–124. doi: 10.1007/s11004-013-1769-y

- Edelsbrunner, H., and Harer, J. (2010). *Computational Topology: An Introduction*. Providence, RI: American Mathematical Society.
- Ennos, A. R. (1997). Wind as an ecological factor. *Trends Ecol. Evol.* 12, 108–111. doi: 10.1016/S0169-5347(96)10066-5
- Esau, K. (1960). *Anatomy of Seed Plants*. New York, NY: John Wiley & Sons Inc.
- Etnier, S. A., and Vogel, S. (2000). Reorientation of daffodil (*Narcissus*: Amaryllidaceae) flowers in wind: drag reduction and torsional flexibility. *Am. J. Bot.* 87, 29–32. doi: 10.2307/2656682
- Feng, T., Bradbury, P. J., Brown, P. J., Hung, H., Sun, Q., Flint-Garcia, S., et al. (2011). Genome-wide association study of leaf architecture in the maize nested association mapping population. *Nat. Genet.* 43, 159–162. doi: 10.1038/ng.746
- Feng, Z., Chen, Y., Hakala, T., and Hyypä, J. (2016). “Range calibration of airborne profiling radar used in forest inventory,” in *Proceedings of the IEEE Geoscience and Remote Sensing Society*, Beijing.
- Fiorani, F., Rascher, U., Jahnke, S., and Schurr, U. (2012). Imaging plants dynamics in heterogenous environments. *Curr. Opin. Biotechnol.* 23, 227–235. doi: 10.1016/j.copbio.2011.12.010
- Fitter, A. H. (1987). An architectural approach to the comparative ecology of plant root systems. *New Phytol.* 106, 61–77. doi: 10.1111/j.1469-8137.1987.tb04683.x
- Frary, A., Nesbitt, T. C., Frary, A., Grandillo, S., Van Der Knaap, E., Cong, B., et al. (2000). fw2. 2: a quantitative trait locus key to the evolution of tomato fruit size. *Science* 289, 85–88. doi: 10.1126/science.289.5476.85
- Friedman, W. E., and Diggle, P. K. (2011). Charles darwin and the origins of plant evolutionary developmental biology. *Plant Cell* 23, 1194–1207. doi: 10.1105/tpc.111.084244
- Fujita, H., Toyokura, K., Okada, K., and Kawaguchi, M. (2011). Reaction-diffusion pattern in shoot apical meristem of plants. *PLoS ONE* 6:e18243. doi: 10.1371/journal.pone.0018243
- Galkovskyi, T., Mileyko, Y., Bucksch, A., Moore, B., Symonova, O., Price, C. A., et al. (2012). GiA Roots: software for the high throughput analysis of plant root system architecture. *BMC Plant Biol.* 12:116. doi: 10.1186/1471-2229-12-116
- Godin, C., Costes, E., and Sinoquet, H. (1999). A method for describing plant architecture which integrates topology and geometry. *Ann. Bot.* 84, 343–357. doi: 10.1006/anbo.1999.0923
- Godin, C., and Ferraro, P. (2010). Quantifying the degree of self-nestedness of trees: application to the structural analysis of plants. *IEEE/ACM Trans. Comput. Biol. Bioinform.* 7, 688–703. doi: 10.1109/TCBB.2009.29
- Godin, C., and Sinoquet, H., (2005). Functional-structural plant modelling. *New Phytol.* 166, 705–708. doi: 10.1111/j.1469-8137.2005.01445.x
- Goethe, J. W. (1790). *Versuch die Metamorphose der Pflanzen zu erklären*. Gotha: Carl Wilhelm Ettinger.
- Goff, S. A., Vaughn, M., McKay, S., Lyons, E., Stapleton, A. E., Gessler, D., et al. (2011). The iPlant collaborative: cyberinfrastructure for plant biology. *Front. Plant Sci.* 2:34. doi: 10.3389/fpls.2011.00034
- Grant, R. H. (1983). The scaling of flow in vegetative structures. *Boundary Layer Meteorol.* 27, 171–184. doi: 10.1007/BF00239613
- Green, P. B. (1999). Expression of pattern in plants: combining molecular and calculus-based biophysical paradigms. *Am. J. Bot.* 86, 1059–1076. doi: 10.2307/2656967
- Gutenkunst, R. N., Waterfall, J. J., Casey, F. P., Brown, K. S., Myers, C. R., and Sethna, J. P. (2007). Universally sloppy parameter sensitivities in systems biology models. *PLoS Comput. Biol.* 3:e189. doi: 10.1371/journal.pcbi.0030189
- Hallé, F. (1971). Architecture and growth of tropical trees exemplified by the Euphorbiaceae. *Biotropica* 3, 56–62. doi: 10.2307/2989706
- Hallé, F. (1986). Modular growth in seed plants. *Philos. Trans. R. Soc. B* 313, 77–87. doi: 10.1098/rstb.1986.0026
- Hamant, O., Heisler, M. G., Jönsson, H., Krupinski, P., Uyttewaal, M., Bokov, P., et al. (2008). Developmental patterning by mechanical signals in *Arabidopsis*. *Science* 322, 1650–1655. doi: 10.1126/science.1165594
- Hofhuis, H., Moulton, D., Lessinnes, T., Routier-Kierzkowska, A. L., Bomphrey, R. J., Mosca, G., et al. (2016). Morphomechanical innovation drives explosive seed dispersal. *Cell* 166, 222–233. doi: 10.1016/j.cell.2016.05.002
- Hohm, T., Zitzler, E., and Simon, R. (2010). A dynamic model for stem cell homeostasis and patterning in *Arabidopsis* meristems. *PLoS ONE* 5:e9189. doi: 10.1371/journal.pone.0009189
- Horn, H. S. (1971). *The Adaptive Geometry of Trees*, Vol. 3. Princeton, NJ: Princeton University Press.
- Jensen, O. E., and Fozard, J. A. (2015). Multiscale models in the biomechanics of plant growth. *Physiology* 30, 159–166. doi: 10.1152/physiol.00030.2014
- Jönsson, H., Heisler, M., Reddy, G. V., Agrawal, V., Gor, V., Shapiro, B. E., et al. (2005). Modeling the organization of the WUSCHEL expression domain in the shoot apical meristem. *Bioinformatics* 21, i232–i240. doi: 10.1093/bioinformatics/bti1036
- Kaasalainen, S., Holopainen, M., Karjalainen, M., Vastaranta, M., Kankare, V., Karila, K., et al. (2015). Combining lidar and synthetic aperture radar data to estimate forest biomass: status and prospects. *Forests* 6, 252–270. doi: 10.3390/f6010252
- Kaplan, D. R. (2001). The science of plant morphology: definition, history, and role in modern biology. *Am. J. Bot.* 88, 1711–1741. doi: 10.2307/3558347
- Kendall, D. G. (1984). Shape manifolds, procrustean metrics, and complex projective spaces. *Bull. Lond. Math. Soc.* 16, 81–121. doi: 10.1112/blms/16.2.81
- Kenis, K., and Keulemans, J. (2007). Study of tree architecture of apple (*Malus × domestica* Borkh.) by QTL analysis of growth traits. *Mol. Breed.* 19, 193–208. doi: 10.1007/s11032-006-9022-5
- Kimura, S., Koenig, D., Kang, J., Yoong, F. Y., and Sinha, N. (2008). Natural variation in leaf morphology results from mutation of a novel KNOX gene. *Curr. Biol.* 18, 672–677. doi: 10.1016/j.cub.2008.04.008
- Kitazawa, M. S., and Fujimoto, K. (2015). A dynamical phyllotaxis model to determine floral organ number. *PLoS Comput. Biol.* 11:e1004145. doi: 10.1371/journal.pcbi.1004145
- Ku, L. X., Zhao, W. M., Zhang, J., Wu, L. C., Wang, C. L., Wang, P. A., et al. (2010). Quantitative trait loci mapping of leaf angle and leaf orientation value in maize (*Zea mays* L.). *Theor. Appl. Genet.* 121, 951–959. doi: 10.1007/s00122-010-1364-z
- Kuhl, F. P., and Giardina, C. R. (1982). Elliptic fourier features of a closed contour. *Comput. Graph. Image Process.* 18, 236–258. doi: 10.1016/0146-664X(82)90034-X
- Kumi, F., Hanping, M., Jianping, H., and Ullah, I. (2015). Review of applying X-ray computed tomography for imaging soil-root physical and biological processes. *Int. J. Agric. Biol. Eng.* 8, 1–14.
- Kurth, W. (1994). *Growth Grammar Interpreter Grogra 2.4-A Software Tool for the 3-Dimensional Interpretation of Stochastic, Sensitive Growth Grammars in the Context of Plant Modelling*. Göttingen: Forschungszentrum Waldökosysteme der Universität Göttingen.
- Kvilekval, K., Fedorov, D., Obara, B., Singh, A., and Manjunath, B. S. (2010). Bisque: a platform for bioimage analysis and management. *Bioinformatics* 26, 544–552. doi: 10.1093/bioinformatics/btp699
- Laga, H., Kurtek, S., Srivastava, A., and Miklavcic, S. J. (2014). Landmark-free statistical analysis of the shape of plant leaves. *J. Theor. Biol.* 363, 41–52. doi: 10.1016/j.jtbi.2014.07.036
- Langlade, N. B., Feng, X., Dransfield, T., Copsey, L., Hanna, A. I., Thébaud, C., et al. (2005). Evolution through genetically controlled allometry space. *Proc. Natl. Acad. Sci. U.S.A.* 102, 10221–10226. doi: 10.1073/pnas.0504210102
- Leiboff, S., Li, X., Hu, H. C., Todt, N., Yang, J., Li, X., et al. (2015). Genetic control of morphometric diversity in the maize shoot apical meristem. *Nat. Commun.* 6:8974. doi: 10.1038/ncomms9974
- Li, M., Duncan, K., Topp, C. N., and Chitwood, D. H. (2017). Persistent homology and the branching topologies of plants. *Am. J. Bot.* 104, 349–353. doi: 10.3732/ajb.1700046
- Lobet, G., Pagès, L., and Draye, X. (2011). A novel image-analysis toolbox enabling quantitative analysis of root system architecture. *Plant physiol.* 157, 29–39. doi: 10.1104/pp.111.179895
- Lobet, G., Pound, M. P., Diener, J., Pradal, C., Draye, X., Godin, C., et al. (2015). Root system markup language: toward a unified root architecture description language. *Plant Physiol.* 167, 617–627. doi: 10.1104/pp.114.253625
- Lynch, J. P. (2013). Steep, cheap and deep: an ideotype to optimize water and N acquisition by maize root systems. *Ann. Bot.* 112, 347–357. doi: 10.1093/aob/mcs293
- Lynch, J. P., and Brown, K. M. (2012). New roots for agriculture: exploiting the root genome. *Philos. Trans. R. Soc. B* 367, 1598–1604. doi: 10.1098/rstb.2011.0243
- MacPherson, R., and Schweinhart, B. (2012). Measuring shape with topology. *J. Math. Phys.* 53, 073516. doi: 10.1063/1.4737391
- Martinez, C. C., Chitwood, D. H., Smith, R. S., and Sinha, N. R. (2016). Left-right leaf asymmetry in decussate and distichous phyllotactic systems. *Philos. Trans. R. Soc. Lond. B Biol. Sci.* 37:20150412. doi: 10.1101/043869

- Mayr, E. (1981). Biological classification: toward a synthesis of opposing methodologies. *Science* 214, 510–516. doi: 10.1126/science.214.4520.510
- Meinhardt, H. (1976). Morphogenesis of lines and nets. *Differentiation* 6, 117–123. doi: 10.1111/j.1432-0436.1976.tb01478.x
- Meinhardt, H. (2004). Out-of-phase oscillations and traveling waves with unusual properties: the use of three-component systems in biology. *Physica D* 199, 264–277. doi: 10.1016/j.physd.2004.08.018
- Meinhardt, H., and Gierer, A. (1974). Applications of a theory of biological pattern formation based on lateral inhibition. *J. Cell Sci.* 15, 321–346.
- Miller, L. A., Santhanakrishnan, A., Jones, S., Hamlet, C., Mertens, K., and Zhu, L. (2012). Reconfiguration and the reduction of vortex-induced vibrations in broad leaves. *J. Exp. Biol.* 215, 2716–2727. doi: 10.1242/jeb.064501
- Miller, N. D., Parks, B. M., and Spalding, E. P. (2007). Computer-vision analysis of seedling responses to light and gravity. *Plant J.* 52, 374–381. doi: 10.1111/j.1365-313X.2007.03237.x
- Milnor, J. W. (1963). *Morse Theory*. Princeton: Princeton University Press.
- Mitscherlich, E. A. (1909). Das gesetz des minimums und das gesetz des abnehmenden bodenertrages. *Landw. Jahrb.* 38, 537–552.
- Monforte, A. J., Diaz, A. I., Caño-Delgado, A., and van der Knaap, E. (2014). The genetic basis of fruit morphology in horticultural crops: lessons from tomato and melon. *J. Exp. Bot.* 65, 4625–4637. doi: 10.1093/jxb/eru017
- Moulia, B., and Fournier, M. (2009). The power and control of gravitropic movements in plants: a biomechanical and systems biology view. *J. Exp. Bot.* 60, 461–486. doi: 10.1093/jxb/ern341
- Nicotra, A. B., Atkin, O. K., Bonser, S. P., Davidson, A. M., Finnegan, E. J., Mathesius, U., et al. (2010). Plant phenotypic plasticity in a changing climate. *Trends Plant Sci.* 15, 684–692. doi: 10.1016/j.tplants.2010.09.008
- Nielsen, K. L., Lynch, J. P., Jablakow, A. G., and Curtis, P. S. (1994). Carbon cost of root systems: an architectural approach. *Plant Soil* 165, 161–169. doi: 10.1007/BF00009972
- Niklas, K. J. (1992). *Plant Biomechanics: An Engineering Approach to Plant form and Function*. Chicago, IL: University of Chicago Press.
- Niklas, K. J. (1994). *Plant Allometry: The Scaling of form and Process*. Chicago, IL: University of Chicago Press.
- Niklas, K. J. (1997). *The Evolutionary Biology of Plants*. Chicago, IL: University of Chicago Press.
- Nikolaev, S. V., Penenko, A. V., Lavreha, V. V., Mjolsness, E. D., and Kolchanov, N. A. (2007). A model study of the role of proteins CLV1, CLV2, CLV3, and WUS in regulation of the structure of the shoot apical meristem. *Russ. J. Dev. Biol.* 38, 383–388. doi: 10.1134/S1062360407060069
- Palacio-López, K., Beckage, B., Scheiner, S., and Molofsky, J. (2015). The ubiquity of phenotypic plasticity in plants: a synthesis. *Ecol. Evol.* 5, 3389–3400. doi: 10.1002/ece3.1603
- Palubicki, W. (2013). *A Computational Study of Tree Architecture*. Ph.D. dissertation, University of Calgary, Calgary, AB.
- Palubicki, W., Horel, K., Longay, S., Runions, A., Lane, B., Mich, R., et al. (2009). Self-organizing tree models for image synthesis. *ACM Trans. Graph.* 28, 58. doi: 10.1145/1531326.1531364
- Paran, I., and van der Knaap, E. (2007). Genetic and molecular regulation of fruit and plant domestication traits in tomato and pepper. *J. Exp. Bot.* 58, 3841–3852. doi: 10.1093/jxb/erm257
- Peaucelle, A., Braybrook, S. A., Le Guillou, L., Bron, E., Kuhlemeier, C., and Höfte, H. (2011). Pectin-induced changes in cell wall mechanics underlie organ initiation in *Arabidopsis*. *Curr. Biol.* 21, 1720–1726. doi: 10.1016/j.cub.2011.08.057
- Poorter, H., Niinemets, Ü, Walter, A., Fiorani, F., and Schurr, U. (2010). A method to construct dose-response curves for a wide range of environmental factors and plant traits by means of a meta-analysis of phenotypic data. *J. Exp. Bot.* 61, 2043–2055. doi: 10.1093/jxb/erp358
- Postma, J. A., and Lynch, J. P. (2011). Root cortical aerenchyma enhances the growth of maize on soils with suboptimal availability of nitrogen, phosphorus, and potassium. *Plant Physiol.* 156, 1190–1201. doi: 10.1104/pp.111.175489
- Pradal, C., Artz, S., Chopard, J., Dupuis, D., Fournier, C., Mielewczik, M., et al. (2017). InfraPhenoGrid: a scientific workflow infrastructure for plant phenomics on the grid. *Fut. Gen. Comput. Syst.* 67, 341–353. doi: 10.1016/j.future.2016.06.002
- Pradal, C., Dufour-Kowalski, S., Boudon, F., Fournier, C., and Godin, C. (2008). OpenAlea: a visual programming and component-based software platform for plant modelling. *Funct. Plant Biol.* 35, 751–760. doi: 10.1071/FP08084
- Pradal, C., Fournier, C., Valduriez, P., and Cohen-Boulakia, S. (2015). “OpenAlea: scientific workflows combining data analysis and simulation,” in *Proceedings of the 27th International Conference on Scientific and Statistical Database Management (SSDBM ’15)*, (New York, NY: ACM), doi: 10.1145/2791347.2791365
- Pradal, C., Varoquaux, G., and Langtangen, H. P. (2013). Publishing scientific software matters. *J. Comput. Sci.* 4, 311–312. doi: 10.1111/j.1467-8519.2009.01723.x
- Prusinkiewicz, P. (2004). “Self-similarity in plants: integrating mathematical and biological perspectives,” in *Thinking in Patterns: Fractals and Related Phenomena in Nature*, ed. M. Novak (Singapore: World Scientific), 103–118.
- Prusinkiewicz, P., and de Reuille, P. B. (2010). Constraints of space in plant development. *J. Exp. Bot.* 61, 2117–2129. doi: 10.1093/jxb/erq081
- Prusinkiewicz, P., and Lindenmayer, A. (1990). *The Algorithmic Beauty of Plants*. New York, NY: Springer Science & Business Media.
- Prusinkiewicz, P., Mündermann, L., Karwowski, R., and Lane, B. (2001). “The use of positional information in the modeling of plants,” in *Proceedings of the 28th Annual Conference on Computer Graphics and Interactive Techniques*, (New York, NY: ACM), 289–300.
- Prusinkiewicz, P., and Runions, A. (2012). Computational models of plant development and form. *New Phytol.* 193, 549–569. doi: 10.1111/j.1469-8137.2011.04009.x
- Raumonen, P., Kaasalainen, M., Åkerblom, M., Kaasalainen, S., Kaartinen, H., Vastaranta, M., et al. (2013). Fast automatic precision tree models from terrestrial laser scanner data. *Remote Sens.* 5, 491–520. doi: 10.3390/rs5020491
- Razak, K. A., Bucksch, A., Damen, M., van Westen, C., Straatsma, M., and de Jong, S. (2013). “Characterizing tree growth anomaly induced by landslides using LiDAR,” in *Landslide Science and Practice: Landslide Inventory, Susceptibility and Hazard Zoning*, eds C. Margottini, P. Canuti, and K. Sassa (Berlin: Springer), 235–241.
- Rellán-Álvarez, R., Lobet, G., and Dinneny, J. R. (2016). Environmental control of root system biology. *Annu. Rev. Plant Biol.* 67, 619–642. doi: 10.1146/annurev-plant-043015-111848
- Rellán-Álvarez, R., Lobet, G., Lindner, H., Pradier, P. L., Sebastian, J., Yee, M. C., et al. (2015). GLO-Roots: an imaging platform enabling multidimensional characterization of soil-grown root systems. *Elife* 4:e07597. doi: 10.7554/eLife.07597
- Remmeler, L., and Rolland-Lagan, A. G. (2012). Computational method for quantifying growth patterns at the adaxial leaf surface in three dimensions. *Plant Physiol.* 159, 27–39. doi: 10.1104/pp.112.194662
- Reuter, M., Biasotti, S., Giorgi, D., Patanè, G., and Spagnuolo, M. (2009). Discrete Laplace–Beltrami operators for shape analysis and segmentation. *Comput. Graph.* 33, 381–390. doi: 10.1016/j.cag.2009.03.005
- Robbins, N. E., and Dinneny, J. R. (2015). The divining root: moisture-driven responses of roots at the micro-and macro-scale. *J. Exp. Bot.* 66, 2145–2154. doi: 10.1093/jxb/eru496
- Roden, J. S., and Pearcy, R. W. (1993). Effect of leaf flutter on the light environment of poplars. *Oecologia* 93, 201–207. doi: 10.1007/BF00317672
- Rolland-Lagan, A. G., Bangham, J. A., and Coen, E. (2003). Growth dynamics underlying petal shape and asymmetry. *Nature* 422, 161–163. doi: 10.1038/nature01443
- Ron, M., Dorrity, M. W., de Lucas, M., Toal, T., Hernandez, R. I., Little, S. A., et al. (2013). Identification of novel loci regulating interspecific variation in root morphology and cellular development in tomato. *Plant Physiol.* 162, 755–768. doi: 10.1104/pp.113.217802
- Royer, D. L., Meyerson, L. A., Robertson, K. M., and Adams, J. M. (2009). Phenotypic plasticity of leaf shape along a temperature gradient in *Acer rubrum*. *PLoS ONE* 4:e7653. doi: 10.1371/journal.pone.0007653
- Runions, A., Lane, B., and Prusinkiewicz, P. (2007). “Modeling trees with a space colonization algorithm,” in *Proceedings of the 2007 Eurographics Workshop on Natural Phenomena*, eds D. Ebert and S. Merillou (Geneva: The Eurographics Association), 63–70.
- Ryan, D. (2013). The global plants initiative celebrates its achievements and plans for the future. *Taxon* 62, 417–418. doi: 10.12705/622.26

- Segura, V., Durel, C. E., and Costes, E. (2009). Dissecting apple tree architecture into genetic, ontogenetic and environmental effects: QTL mapping. *Tree Genet. Genom.* 5, 165–179. doi: 10.1111/j.1469-8137.2007.02374.x
- Seidel, D., Schall, P., Gilje, M., and Ammer, C. (2015). Relationship between tree growth and physical dimensions of *Fagus sylvatica* crowns assessed from terrestrial laser scanning. *iForest* 8, 735–742. doi: 10.3832/ifor1566-008
- Slovak, R., Göschl, C., Su, X., Shimotani, K., Shiina, T., and Busch, W. (2014). A scalable open-source pipeline for large-scale root phenotyping of *Arabidopsis*. *Plant Cell* 26, 2390–2403. doi: 10.1105/tpc.114.124032
- Smith, G. F., Steenkamp, Y., Klopper, R. R., Siebert, S. J., and Arnold, T. H. (2003). The price of collecting life. *Nature* 422, 375–376. doi: 10.1038/422375a
- Spalding, E. P., and Miller, N. D. (2013). Image analysis is driving a renaissance in growth measurement. *Curr. Opin. Plant Biol.* 16, 100–104. doi: 10.1016/j.pbi.2013.01.001
- Steeves, T. A., and Sussex, I. M. (1989). *Patterns in Plant Development*. New York, NY: Cambridge University Press.
- Symonova, O., Topp, C. N., and Edelsbrunner, H. (2015). DynamicRoots: a software platform for the reconstruction and analysis of growing plant roots. *PLoS ONE* 10:e0127657. doi: 10.1371/journal.pone.0127657
- Tester, M., and Langridge, P. (2010). Breeding technologies to increase crop production in a changing world. *Science* 327, 818–822. doi: 10.1126/science.1183700
- Thom, A. S. (1968). The exchange of momentum, mass, and heat between an artificial leaf and the airflow in a wind-tunnel. *Q. J. R. Meteorol. Soc.* 94, 44–55. doi: 10.1002/qj.49709439906
- Thompson, A. M., Yu, J., Timmermans, M. C., Schnable, P., Crants, J. C., Scanlon, M. J., et al. (2015). Diversity of maize shoot apical meristem architecture and its relationship to plant morphology. *G3* 5, 819–827. doi: 10.1534/g3.115.017541
- Tian, F., Bradbury, P. J., Brown, P. J., Hung, H., Sun, Q., Flint-Garcia, S., et al. (2011). Genome-wide association study of leaf architecture in the maize nested association mapping population. *Nat. Genet.* 43, 159–162. doi: 10.1038/ng.746
- Tisné, S., Reymond, M., Vile, D., Fabre, J., Dauzat, M., Koornneef, M., et al. (2008). Combined genetic and modeling approaches reveal that epidermal cell area and number in leaves are controlled by leaf and plant developmental processes in *Arabidopsis*. *Plant Physiol.* 148, 1117–1127. doi: 10.1104/pp.108.124271
- Topp, C. N., Iyer-Pascuzzi, A. S., Anderson, J. T., Lee, C. R., Zurek, P. R., Symonova, O., et al. (2013). 3D phenotyping and quantitative trait locus mapping identify core regions of the rice genome controlling root architecture. *Proc. Natl. Acad. Sci. U.S.A.* 110, E1695–E1704. doi: 10.1073/pnas.1304354110
- Truong, S. K., McCormick, R. F., Rooney, W. L., and Mullet, J. E. (2015). Harnessing genetic variation in leaf angle to increase productivity of *Sorghum bicolor*. *Genetics* 201, 1229–1238. doi: 10.1534/genetics.115.178608
- Turing, A. M. (1952). The chemical basis of morphogenesis. *Philos. Trans. R. Soc. B* 237, 37–72. doi: 10.1098/rstb.1952.0012
- Turing, A. M. (1992). *Collected Works of AM Turing. Morphogenesis*. ed. P.T. Saunders. Amsterdam: North-Holland Publishing.
- Uga, Y., Sugimoto, K., Ogawa, S., Rane, J., Ishitani, M., Hara, N., et al. (2013). Control of root system architecture by DEEPER ROOTING 1 increases rice yield under drought conditions. *Nat. Genet.* 45, 1097–1102. doi: 10.1038/ng.2725
- van Dusschoten, D., Metzner, R., Kochs, J., Postma, J. A., Pflugfelder, D., Buehler, J., et al. (2016). Quantitative 3D analysis of plant roots growing in soil using magnetic resonance imaging. *Plant Physiol.* 170, 1176–1188. doi: 10.1104/pp.15.01388
- Vogel, S. (1989). Drag and reconfiguration of broad leaves in high winds. *J. Exp. Bot.* 40, 941–948. doi: 10.1093/jxb/40.8.941
- Vogel, S. (2006). Drag reduction by leaf aquaplaning in *Hexastylis* (Aristolochiaceae) and other plant species in floods. *J. North Am. Benthol. Soc.* 25, 2–8. doi: 10.1899/0887-3593(2006)25[2:DRBLAI]2.0.CO;2
- Vogel, S. (2012). *The Life of a Leaf*. Chicago, IL: The University of Chicago Press.
- Vosselman, G., and Maas, H. G. (eds) (2010). *Airborne and Terrestrial Laser Scanning*. Wick: Whittles Publishing.
- Watanabe, T., Hanan, J. S., Room, P. M., Hasegawa, T., Nakagawa, H., and Takahashi, W. (2005). Rice morphogenesis and plant architecture: measurement, specification and the reconstruction of structural development by 3D architectural modelling. *Ann. Bot.* 95, 1131–1143. doi: 10.1093/aob/mci136
- Wiens, J. J. (2000). “Coding morphological variation within species and higher taxa for phylogenetic analysis,” in *Phylogenetic Analysis of Morphological Data*, ed. J. J. Wiens (Washington, DC: Smithsonian Institution Press), 115–145.
- Wilf, P., Zhang, S., Chikkerur, S., Little, S. A., Wing, S. L., and Serre, T. (2016). Computer vision cracks the leaf code. *Proc. Natl. Acad. Sci. U.S.A.* 113, 3305–3310. doi: 10.1073/pnas.1524473113
- Willis, L., Refahi, Y., Wightman, R., Landrein, B., Teles, J., Huang, K. C., et al. (2016). Cell size and growth regulation in the *Arabidopsis thaliana* apical stem cell niche. *Proc. Natl. Acad. Sci. U.S.A.* 113, E8238–E8246. doi: 10.1073/pnas.1616768113
- Woltereck, R. (1909). Weitere experimentelle untersuchungen über artveränderung, speziell über das wesen quantitativer artunterschiede bei *Daphniden*. (Further investigations of type variation, specifically concerning the nature of quantitative differences between varieties of *Daphnia*). *Verh. Deutsch. Zool. Ges.* 19, 110–173.
- Yang, W., Guo, Z., Huang, C., Duan, L., Chen, G., Jiang, N., et al. (2014). Combining high-throughput phenotyping and genome-wide association studies to reveal natural genetic variation in rice. *Nat. Commun.* 5:5087. doi: 10.1038/ncomms6087
- Zhang, J., Ku, L. X., Han, Z. P., Guo, S. L., Liu, H. J., Zhang, Z. Z., et al. (2014). The ZmCLA4 gene in the qLA4-1 QTL controls leaf angle in maize (*Zea mays* L.). *J. Exp. Bot.* 65, 5063–5076. doi: 10.1093/jxb/eru271
- Zhu, J., Brown, K. M., and Lynch, J. P. (2010). Root cortical aerenchyma improves the drought tolerance of maize (*Zea mays* L.). *Plant Cell Environ.* 33, 740–749. doi: 10.1111/j.1365-3040.2009.02099.x
- Zhu, J., Kaepller, S. M., and Lynch, J. P. (2005). Mapping of QTLs for lateral root branching and length in maize (*Zea mays* L.) under differential phosphorus supply. *Theor. Appl. Genet.* 111, 688–695. doi: 10.1007/s00122-005-2051-3
- Zurek, P. R., Topp, C. N., and Benfey, P. N. (2015). Quantitative trait locus mapping reveals regions of the maize genome controlling root system architecture. *Plant Physiol.* 167, 1487–1496. doi: 10.1104/pp.114.251751
- Conflict of Interest Statement:** The authors declare that the research was conducted in the absence of any commercial or financial relationships that could be construed as a potential conflict of interest.
- Copyright © 2017 Bucksch, Atta-Boateng, Azihou, Battogtokh, Baumgartner, Binder, Braybrook, Chang, Coneva, DeWitt, Fletcher, Gehan, Diaz-Martinez, Hong, Iyer-Pascuzzi, Klein, Leiboff, Li, Lynch, Maizel, Maloof, Markelz, Martinez, Miller, Mio, Palubicki, Poorter, Pradal, Price, Puttonen, Reese, Rellán-Álvarez, Spalding, Sparks, Topp, Williams and Chitwood. This is an open-access article distributed under the terms of the Creative Commons Attribution License (CC BY). The use, distribution or reproduction in other forums is permitted, provided the original author(s) or licensor are credited and that the original publication in this journal is cited, in accordance with accepted academic practice. No use, distribution or reproduction is permitted which does not comply with these terms.



# Quantification of Overnight Movement of Birch (*Betula pendula*) Branches and Foliage with Short Interval Terrestrial Laser Scanning

Eetu Puttonen<sup>1,2\*</sup>, Christian Briese<sup>3,4</sup>, Gottfried Mandlburger<sup>3</sup>, Martin Wieser<sup>3</sup>, Martin Pfennigbauer<sup>5</sup>, András Zlinszky<sup>6</sup> and Norbert Pfeifer<sup>3</sup>

<sup>1</sup> Department of Remote Sensing and Photogrammetry, Finnish Geospatial Research Institute, National Land Survey of Finland, Masala, Finland, <sup>2</sup> Department of Remote Sensing and Photogrammetry, Centre of Excellence in Laser Scanning Research, National Land Survey of Finland, Masala, Finland, <sup>3</sup> Department of Geodesy and GeoInformation, Technische Universität Wien, Vienna, Austria, <sup>4</sup> EODC Earth Observation Data Centre for Water Resources Monitoring, Vienna, Austria, <sup>5</sup> RIEGL Laser Measurement Systems, Horn, Austria, <sup>6</sup> Balaton Limnological Institute, Centre for Ecological Research, Hungarian Academy of Sciences, Tihany, Hungary

## OPEN ACCESS

### Edited by:

Alexander Bucksch,  
Georgia Institute of Technology, USA

### Reviewed by:

Monica Herrero-Huerta,  
Delft University of Technology,  
Netherlands  
Jean-Francois Cote,  
Natural Resources Canada, Canada

### \*Correspondence:

Eetu Puttonen  
eetu.puttonen@nls.fi

### Specialty section:

This article was submitted to  
Plant Biophysics and Modeling,  
a section of the journal  
Frontiers in Plant Science

Received: 21 November 2015

Accepted: 09 February 2016

Published: 29 February 2016

### Citation:

Puttonen E, Briese C, Mandlburger G, Wieser M, Pfennigbauer M, Zlinszky A and Pfeifer N (2016) Quantification of Overnight Movement of Birch (*Betula pendula*) Branches and Foliage with Short Interval Terrestrial Laser Scanning. *Front. Plant Sci.* 7:222.  
doi: 10.3389/fpls.2016.00222

The goal of the study was to determine circadian movements of silver birch (*Petula Bendula*) branches and foliage detected with terrestrial laser scanning (TLS). The study consisted of two geographically separate experiments conducted in Finland and in Austria. Both experiments were carried out at the same time of the year and under similar outdoor conditions. Experiments consisted of 14 (Finland) and 77 (Austria) individual laser scans taken between sunset and sunrise. The resulting point clouds were used in creating a time series of branch movements. In the Finnish data, the vertical movement of the whole tree crown was monitored due to low volumetric point density. In the Austrian data, movements of manually selected representative points on branches were monitored. The movements were monitored from dusk until morning hours in order to avoid daytime wind effects. The results indicated that height deciles of the Finnish birch crown had vertical movements between -10.0 and 5.0 cm compared to the situation at sunset. In the Austrian data, the maximum detected representative point movement was 10.0 cm. The temporal development of the movements followed a highly similar pattern in both experiments, with the maximum movements occurring about an hour and a half before (Austria) or around (Finland) sunrise. The results demonstrate the potential of terrestrial laser scanning measurements in support of chronobiology.

**Keywords:** terrestrial laser scanning, plant movement, chronobiology, circadian rhythm, time series

## INTRODUCTION

Terrestrial laser scanners have gone through rapid development during the past 10 years (Dassot et al., 2011). They produce accurate 3D point clouds of target objects often down to millimeter resolution. Thus, the point clouds provide detailed information about the structure and spatial properties of the targets.

In addition to structural modeling and scene mapping, terrestrial laser scanning (TLS) data are widely used in engineering applications to monitor possible changes in the targeted objects or in a target area. TLS-based change detection studies cover a wide range of different

applications. These include geodynamic processes such as landslide detection and monitoring (Travelletti et al., 2008; Ghuffar et al., 2013) and morphodynamic changes in coastal beaches (Lindenbergh et al., 2011), thermal karst formations (Barnhart and Crosby, 2013), or in riversides (Milan et al., 2007; Vaaja et al., 2011; Saarinen et al., 2013). Short interval scans are also used in determining dynamic structural stress (Grosse-Schwiep et al., 2013). TLS techniques are utilized to improve safety in quarries and mines by monitoring wall stability over time (Abellan et al., 2011; Hu, 2013; Kovanic and Blíštan, 2014). In vegetation studies, TLS is being actively used in static forest and forest parameter mapping (Hopkinson et al., 2004; Moskal and Zheng, 2012; Liang, 2013), tree modeling (Fleck et al., 2004; Hosoi and Omasa, 2006; Bucksch and Fleck, 2011; Eysn et al., 2013; Raumonen et al., 2013), and in estimating forest biomass (e.g., Kaasalainen et al., 2014).

Although TLS is utilized in a wide range of both temporal and vegetation studies for scientific and engineering applications, one field of study which has not yet gained wider interest in the TLS community is circadian or diurnal and nocturnal changes in vegetation. In ecology and plant physiology, these changes in plants and their driving factors have been studied intensively for a long time. It has been known for centuries that plants show diurnal cycles of leaf motion, described as “sleep” already by Darwin and Darwin (1880). It has been observed that these motions also happen if the plant is placed in darkness, therefore suggesting an internal mechanism for measuring time. The molecular mechanism of this circadian oscillator has been most extensively studied in *Arabidopsis* (Barak et al., 2000), but orthologues of the *Arabidopsis* genes controlling the diurnal rhythm of flowering time have been identified in various tree species such as Poplar (*Populus tremula*) and Chestnut (*Castanea sativa*) (Solomon et al., 2010). However, for obvious reasons, carrying out controlled experiments or even quantitative observations on fully grown trees is much more difficult, therefore both the background and the effects of sleep motions in trees are less well-understood. Circadian rhythms of leaf motion are evident for some tree species such as *Robinia pseudoacacia*. The movement of leaves is connected to changes in turgor pressure (Holmes and Shim, 1968) which is controlled by the osmotic state of the cells. Changes in water transport and in the concentration of various metabolites result in changes in osmotic flow and thus, through changes in the shape of individual plant cells, eventual movement at the scale of individual plants or plant parts. The literature identifies two common reasons that drive these changes, namely plant water balance (Chapin et al., 2002) and photoperiodism (McClung, 2006; Nozue and Maloof, 2006; Sysoeva et al., 2010). It would be plausible that the changes in turgor pressure resulting in a circadian rhythm of leaf movement also apply to the branches and thus cause a circadian rhythm of branch movements in trees. However, in an earlier case study where quantification of diurnal movement was attempted using height measurement of weighted lines attached to branches in a Walnut orchard (*Juglans regia*), diurnal change was found insignificant (Way et al., 1991). To our best knowledge, circadian movement of tree branches has never been successfully quantified before in the presented level.

Methods to monitor plant water balance at a diurnal time scale include: (a) leaf or fruit sample collection and water content measurements (Klepper, 1968; Acevedo et al., 1979); (b) sap flow monitoring (Köstner et al., 1998); (c) leaf and stem conductance measurements (García-Orellana et al., 2013); (d) leaf and stem water potential, photosynthetic capability and hydraulic conductivity measurements (Andrews et al., 2012); (e) branch growth and xylem morphometry measurements (Correia and Martins-Loucao, 1995; Correia et al., 2001). Most of these are invasive processes that involve sampling and are difficult (but possible) to carry out regularly in intervals of a few hours (Chapotin et al., 2006). Therefore, in case of trees, the most common way of observing circadian rhythms is with a dendrograph, an instrument that measures changes in tree diameter or circumference with sub-millimeter precision (e.g., Pesonen et al., 2004).

In order to monitor photoperiodism, the amount of light received by plants can be controlled by constructing external shading structures (Wayne and Bazzaz, 1993) or by using external lighting setups with selected filters (e.g., Mockler et al., 2003). Alternatively, in order to monitor the internal clock, a plant can be placed in continuously lit or dark conditions to observe periodic changes in its physiology.

Plant physiology measurements are localized and typically consider selected parts of a plant. The measurements often take place in laboratory conditions. This presents a clear challenge when results are extrapolated to model wider areas of multiple plants. Acquiring results also involves a significant amount of manual labor, as experiment setups and sample collection are hard to automatize.

TLS measurements offer a potential solution to generalize plant physiology results on larger spatial scales, like whole individual trees, or on orchard plot, and stand levels. Laser scanners can measure individual targets accurately tens of meters away with sub-centimeter point resolution. Moreover, scanning can be performed outdoors with short intervals between individual scans. Furthermore, as the scanners are active measurement devices that both produce and receive the signal, they are insensitive to varying external lighting conditions, i.e., available sunlight and cloudiness.

Laser scanning point clouds cannot provide direct biochemical parameters from plants, but they can be used in plant shape and dimension monitoring over time (e.g., branch inclination, branch, and stem swelling, leaf inclination distribution at crown level). If a clear correlation between the geometric changes in point clouds and laboratory or *in situ* results can be established and verified, the parameterized spatial changes can then act as proxies that estimate physiological changes in a plant.

Puttonen et al. (2015) detected and reported birch branch movements during a day-long classification study. The study was carried out with the Finnish Geospatial Research Institute (FGI) Hyperspectral Laser Scanner (HSL) (Hakala et al., 2012). The movements were detected from the variation of the birch Normalized Difference Vegetation Index (NDVI) response during an observation period of ca. 26 h. A more detailed inspection revealed a visible change in birch branch stances over

time. The study is to our knowledge the first to report spatial changes in tree branch geometry over a day-long cycle. However, the authors did not attempt to quantify the movement amplitude.

Hitherto, vegetation time series in TLS have been collected mainly for longer scale time series analyses, typically to determine seasonal changes in tree canopy (e.g., Hosoi and Omasa, 2009; Nevalainen et al., 2014; Hakala et al., 2014; Portillo-Quintero et al., 2014; Calders et al., 2015; Griebel et al., 2015).

In imaging, longer term time-series studies have been carried out both in the field and in a laboratory with a close range setup (e.g., more recently by Li et al., 2013; Nijland et al., 2014). However, the use of cameras inherently limits the experimental setup to daylight hours or requires the use of external light sources. Additionally, radiometry measurements and their calibration are typically rather complex. Furthermore, even a short use of external light sources may interrupt the plant photoperiod (e.g., Salisbury, 1981). Meanwhile, since laser scanners are active measurement systems their working efficiency is stable in nighttime conditions with no external light (Arslan and Kalkan, 2013). With modern laser scanners, the laser beam footprint up to a few centimeters in diameter illuminates only a localized patch of the plant surface at a time. Moreover, the footprint swipes over each spot in sub-second scale and the typically used infrared (IR) wavelengths have strong reflectance from green vegetation. Therefore, most of the transmitted energy is not absorbed by the plant. Thus, we assume that plant disturbance with a modern laser scanning system is not significant during an individual scanning measurement.

This study now aims (i) to analyze to which degree overnight birch branch movements can be measured with two different TLS scanners and (ii) whether quantifications of crown/branch movements are possible. With these goals in mind, we aim to show that TLS data provides an effective tool to detect and to monitor circadian changes in tree geometry with a centimeter scale spatial and within-hour temporal resolution. As the main focus of the study is in confirmation and quantification of geometric changes in birch branches over time, without further investigation of the cause or mechanism of these movements, the measurement setups did not include comprehensive weather or soil data.

## MEASUREMENTS AND DATA

This section is structured as follows: In section Measurement Sites and the Collected Data, descriptions of both the Finnish and the Austrian measurement sites and data collected from them are given. Section Object Point Cloud Delineation describes object delineation from the scanned point clouds. Section FGI Hyperspectral Lidar provides a detailed description of FGI HSL and its properties. Section RIEGL VZ-4000 Long Range Laser Scanner gives a detailed description of the RIEGL VZ-4000 laser scanner.

### Measurement Sites and the Collected Data

Measurements were carried out in two geographically different locations, in southern Finland (Kirkkonummi,  $60^{\circ}09'40''\text{N}$ ,  $24^{\circ}32'48''\text{W}$ ) and in northern Austria (Horn,  $48^{\circ}39'31''\text{N}$ ,

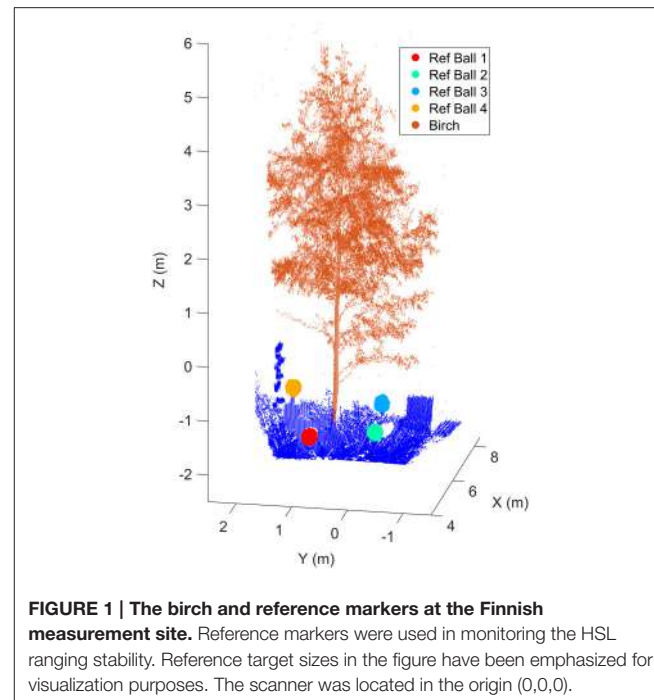


**FIGURE 1 |** The birch and reference markers at the Finnish measurement site. Reference markers were used in monitoring the HSL ranging stability. Reference target sizes in the figure have been emphasized for visualization purposes. The scanner was located in the origin (0,0,0).

$15^{\circ}39'48''\text{E}$ ). Both measurements were performed in the middle of September close to the solar equinox to guarantee approximately similar lengths of night at both sites (<http://www.timeanddate.com>, accessed on 25th February 2015). Measurement dates were 13–14 September 2013 (Finland) and 19–20 September 2014 (Austria). In both measurements, the test trees were measured from sunset to sunrise. In Finland, the nighttime measurements lasted about 11 h in total, during which 14 separate scans were collected with FGI HSL. Scan intervals were approximately 1 h. Near sunrise and sunset the scan interval was shortened to 40 min. In Austria, data acquisitions were repeated every 10 min for about 12 and half hours, resulting in 77 separate scans.

The Finnish measurement site was located on a shallow slope facing southward. The size of the test site was about  $7 \times 20 \text{ m}^2$ . The site included the main target, a small silver birch (*Betula pendula*). Low understory, a large silver birch and goat willows (*Salix caprea*) were located behind the target. The site was partially surrounded from its eastern side with a sparse, half-open canopy of full-grown birches. The nearby FGI building was located on the western side of the site. The shadow of the building shaded the target site for about half an hour before the sunset. Figure 1 illustrates the Finnish test tree and the reference markers placed around it. The markers were used to validate the distance measurement stability over the experiment. The measurement setting also included an external reference plate (Spectralon<sup>®</sup>) to calibrate laser radiometry during the experiment. The FGI HSL was mounted on a solid platform and a plastic tent was set up around the scanner to protect it from possible rain and moisture. A heating fan was kept on whole night time inside the tent. This guaranteed a constant airflow and prevented possible surface condensation.

The Austrian measurement site was located on the northern part of an outdoor test and calibration range, an open, cut grass field of size about 130 m by 100 m. The target birch had four stems and it was standing about 10 m away of a manufacturing hall. Thus, the tree was not shaded during sunrise or sunset. The scans were taken to the westward direction and the laser scanner was under a protective roof. Four white polystyrene foam spheres were attached to the birch as reference markers to detect branch movement. **Figure 2** illustrates the Austrian test tree and the branches of which movements were followed during the experiment. The branch point clouds were manually selected in CloudCompare software [Available in: <http://www.cloudcompare.org/> (Girardeau-Montaut, 2014)].

The weather conditions in both measurement sites were similar during data acquisition. The air was calm, with no wind (qualitative observation), during the night. For this reason, the time of sunset was selected as the initial point for monitoring the branch movement. There was no rainfall during either measurement. In the Finnish test site, the leaves of lower branches were verified not to have visible moisture condensation on their surfaces during nighttime.

## Object Point Cloud Delineation

A manual workflow was used to delineate birch and reference target point clouds spatially from the whole point cloud. The same procedure was used for both datasets.

The differentiation was started by viewing an object (birch or reference target) point cloud as a 2D projection from a user selected angle and then cutting the object outline by hand with a clear buffer zone. Points inside the outline were included and the rest were rejected. After the cut, a new 2D projection of the included points was taken from another angle and the manual cutting was repeated. In total, 4–5 projections were required to form a sufficiently accurate 3D delineation for the objects in both cases. As the objects had no spatial overlap in either measurement setup, there was no mixing between the object point clouds. The buffer zones in each cut were selected so wide that possible temporal movements within the object point cloud and noise point fluctuations around the object edges (e.g., due to partial hits) were captured for all measurements. All points within the selection area were kept. Intensity-based filtering was not performed.

## FGI Hyperspectral Lidar

The FGI Hyperspectral Lidar (HSL) is a laser scanning system that transmits hyperspectral (white) laser pulses with a continuous spectrum of 400–2500 nm to the target. It can measure up to eight separate wavelength bands from returning pulses. The number of bands is limited by the spectral sensitivity of the silicon detector, but the wavelengths are selectable within the transmittance range. In this study, spectral information was used only to emphasize differences between leaf and stem returns with the Normalized Difference Vegetation Index (NDVI).

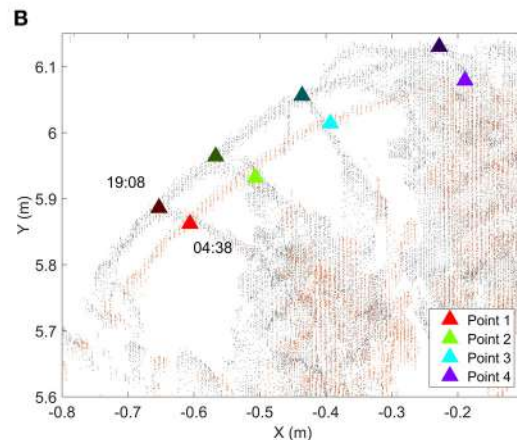
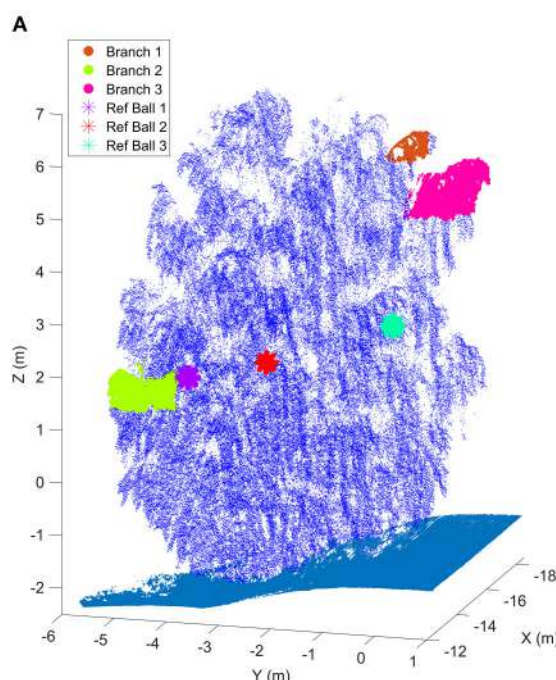


**FIGURE 2 | (A)** The birch at the Austrian test site. The selected target branches and the three detected reference markers have specific coloring. Ground points are presented with cyan. Reference target sizes have been emphasized in the figure for visualization purposes. The scanner was located in the origin (0,0,0). **(B)** A close-up of Branch 1 at two different times. Triangles represent the manually selected representative points of which total 3D movements were followed over time. Dark triangles represent the initial point locations at sunset (19:08), bright triangles the corresponding point locations at the time of the movement maximum (04:38).

The main components of the HSL system are the SM5-he supercontinuum laser source (Leukos, Limoges, France), a 2D scanning mechanism (Newport Corp., Irvine, CA, USA), the wavelength separating spectrograph (Specim, Oulu, Finland), a 16-channel high speed detector element (First Sensor AG, Berlin, Germany), and the measurement computer with digitizer cards (National Instruments Corp., Austin, Texas, USA). The HSL works by sending laser pulses to the target in a sweeping pattern and then recording returning waveforms for each wavelength band detected. The waveforms are digitized with 1 GHz frequency, thus giving the system a nominal 15 cm range resolution. However, individual laser pulses can be localized to the waveforms with a *de facto* range resolution of a few centimetres. The HSL can measure up to 5000 waveforms per second and a maximum of three discrete returns are fitted in each waveform.

A more detailed description of the HSL system, its properties, and its measurement configuration are given in articles by Hakala et al. (2012) and Nevalainen et al. (2014).

The properties of both the FGI HSL and RIEGL VZ-4000 scanners are compared in **Table 1**.

### RIEGL VZ-4000 Long Range Laser Scanner

The RIEGL VZ-4000 has been developed for surveying applications in which very long ranges are required (RIEGL, 2014). The scanner has a net measurement rate of up to 222 kHz. The maximum measurement range of the VZ-4000 is 4 km for targets with 90% reflectance at 23 kHz measurement rate. At 222 kHz the instrument is still capable of measuring targets with only 20% reflectance up to 1000 m.

The RIEGL VZ-4000 works, like the HSL, by sending laser pulses to the target, but analyses the recorded waveform internally. The nominal ranging precision is 10 mm.

The VZ-4000 can be controlled via its built-in touch screen, via WiFi or LAN. It has a built-in camera, GPS receiver, compass, and tilt sensor, and there are interfaces to attach an additional camera (e.g., IR camera) and/or a high-precision RTK GNSS.

## RESULTS

### Finnish Point Cloud Time Series

A total of 14 scans were selected from the Finnish point cloud time series in order to determine the temporal variation in the birch crown. Since the FGI HSL is a prototype device, its relative ranging precision during the experiment was first validated. Movements of the reference targets set around the birch were monitored for the duration of the experiment. **Table 2** lists the reference target distances to the scanner and their relative movements compared to the initial scan. The target ranges and movements were calculated with respect to the target center that was determined with a least squares sphere fitting (MATLAB code by Alan Jennings, available in [www.mathworks.com/matlabcentral/fileexchange/34129](http://www.mathworks.com/matlabcentral/fileexchange/34129)). The table shows that the reference targets were detected reliably and with higher precision (less than 5 mm standard deviation) than the nominal sampling frequency of the system would imply. This assumption is valid as long as the laser returns can be

**TABLE 1 | Property comparison between the laser scanners used in the Finnish and Austrian test sites.**

Laser system	FGI HSL LEUKOS-SM-X-OEM	RIEGLVZ-4000
Laser wavelength (nm)	420–2100	1550
Average output power (mW)	41	Setting dependent
Measurement rate (kHz)	5.3	23–222
Pulse width	≤1 ns	3 ns
Central wavelength of a detected channel (nm)	545.5, 641.2, 675.0, 711.0, 741.5, 778.4, 978.0	1550
Channel FWHM (nm)	20	–
Collecting optics field of view	0.2°	–
Transmit beam divergence	0.02°	0.009°
Transmit beam diameter (cm) at stem distance (m)	0.7 (7.5)	1.9 (14.7)
Scanning resolution, horizontal	0.1°	0.002°
Scanning resolution, vertical	0.02°	0.002°

expected to come from a single reflection, but cannot be directly generalized to more irregular targets, like differently positioned leaves, or to partial hits coming from edges. Nevertheless, the ranging stability test verified the HSL system accuracy for fixed target distances and that the HSL point cloud did not present a systematic drift during the measurement period.

After the range precision measurements, points were manually delineated into a new individual point cloud of the studied tree for each measurement as described in Section Finnish Point Cloud Time Series. Then, the point cloud was differentiated into crown and stem point clouds. The differentiation was based on the NDVI distribution of all birch points. The differentiation was performed using a hard NDVI threshold of 0.2, where the points with NDVI values below the threshold were classified as stem and thick branches. The bounding box of the crown point clouds had dimensions of  $3.7 \times 3.0 \times 6.6 \text{ m}^3$  (depth, width, height) when averaged over all measurements. The median point number for the crown point clouds was  $154,310 \pm 10,030$  points corresponding to 6.5% variability in the total point number.

The goal of the division was to select the returns reflecting from leaves and most of the branches of the birch and to leave the trunk and the thickest branches out of the analysis. After this, five different height percentiles were calculated for the crown point cloud for each scan (**Figure 3**). The height percentiles in the analysis were: 10th, 30th, 50th, 70th, and the 90th percentile. For example, the 90th percentile is located at the height at which 90% of the points of the whole cloud are below it. Height percentiles were calculated because a manual selection of corresponding points in consecutive scans was not possible due to the low volumetric point density. Height percentiles, on the other hand, are robust descriptions of the measurement height distribution and should therefore allow a reliable tracking of vertical movements of the crown point cloud.

The results show clear and systematic temporal variation in height statistics of the birch crown point cloud (**Figures 3, 4**,

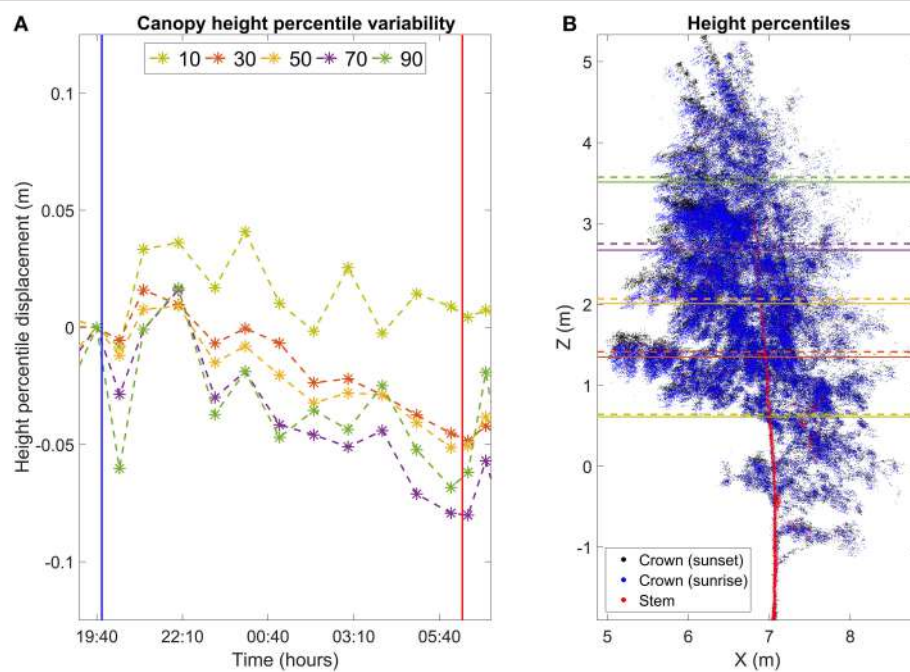


**FIGURE 3 | (A)** Movement of height percentiles of birch crown points in the Finnish dataset. Height and time are reported with respect to the scan closest to sunset. Vertical lines mark sunset (blue) and sunrise (red). **(B)** Maximum movement of height percentile positions overnight. Black points represent the birch crown at sunset. Blue points represent the birch crown at the time of sunrise. Red points represent the birch stem and the thickest branches. The stem and crown points were differentiated with NDVI thresholding. Horizontal lines represent the height percentile locations at sunset (dashed, about 19:40 o'clock) and in morning (solid, 06:40 o'clock).

**Video 1**). In **Figure 3**, all height percentiles show a declining temporal trend about 1 h after sunset (blue vertical line). The four highest percentiles also share another common trend: the height percentiles after sunrise (red line) were still lower than their sunset value. At this point, their values have decreased about 0.05 m from their sunset value. After reaching the minimum, all four percentiles show a rapid return toward the sunset value. The return takes about 3 h. The lowest percentile shows a differing temporal response compared to the others. Its value declines more slowly than the others during night, to about 0.03 m from the sunset value. Furthermore, the lowest point is reached about an hour later than for the other percentiles. The overall trend of the lowest percentile is also not as clear as with the other percentiles: the declining trend is less clear and shows more variance.

## Austrian Point Cloud Time Series

The RIEGL VZ-4000 was factory calibrated and mounted on a solid pillar throughout the experiment, and so its ranging properties were not inspected as with the Finnish datasets. The bounding box around the birch had average dimensions of  $6.0 \times 7.0 \times 9.3 \text{ m}^3$  (depth, width, height). The median point number inside the bounding box was  $9,388,000 \pm 724,000$  corresponding to 7.7% variability in the total point number.

Manual branch point selection was carried out for three branches. Reference target movement was measured from the fitted sphere center. Three of the four attached reference targets

**TABLE 2 | The ranging stability of the FGI HSL point cloud during the experiment.**

Ref Ball No.	Distance from the scanner (m)	Distance from the scanner, standard deviation (m)	Fitted radius, mean (m)	Fitted radius, standard deviation (m)
1	6.540	0.002	0.120	0.001
2	7.113	0.002	0.122	0.001
3	8.517	0.003	0.120	0.002
4	7.784	0.004	0.125	0.002

The table shows the reference target distances from the scanner and the radii fitted in their point clouds. Both the ranges and radii were compared to the initial measurement close to sunset. All standard deviation values were calculated from 14 scans.

were detected reliably. The fourth one was not detected due to it being occluded from the scan position by birch branches and leaves. **Figure 5** illustrates the total movements of the selected points on the branches and the reference target centers.

The graphs in **Figure 5** show clearly how all points measured on branches had a similar movement pattern over time. The absolute branch point movement was limited mainly to within 2 cm, with the exception of a few points, until 5 h after the sunset. Thereafter the movement trend began to increase, reaching its maximum around 9–11 h after sunset. The maximum movements varied from 5.0 to 8.5 cm for Branch 1, from 3.5 to 7.0 cm for Branch 2, and from 6.5 to 10.0 cm for Branch 3. After the movement maximum was reached, all branches returned

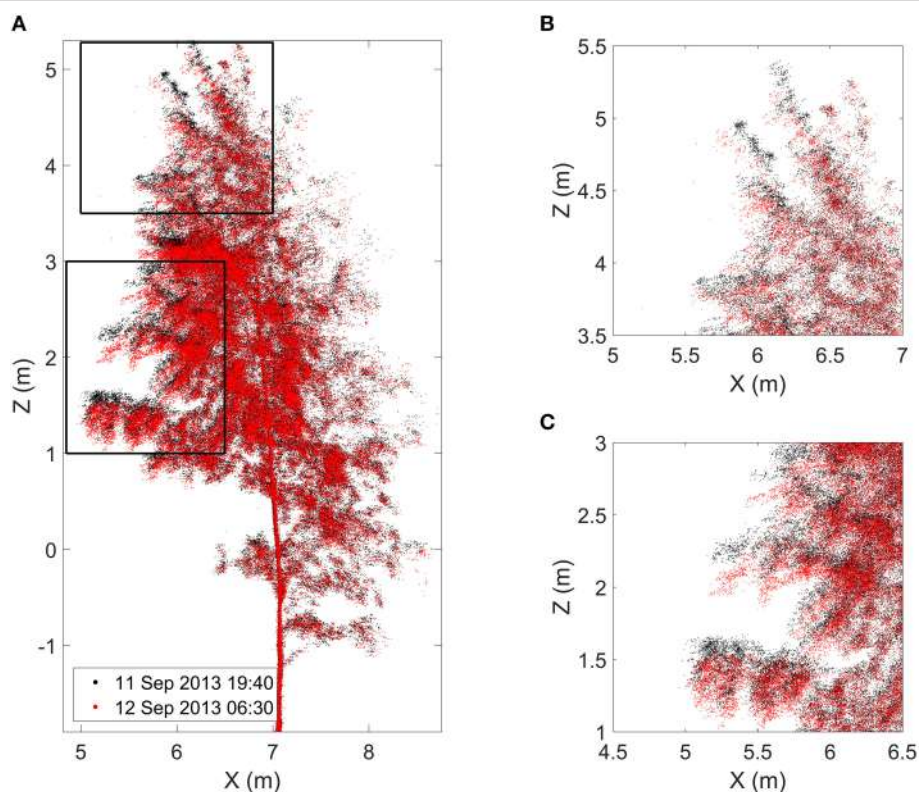


**FIGURE 4 | (A)** Finnish birch point cloud profiles at the time of sunset (black) and at the time of the maximum movement around 06:40 o'clock (red). Black frames mark zoomed in boxes in the upper (**B**) and in the lower (**C**) crown. **Video 1** visualizes the geometrical change in the Finnish birch point cloud over night. It is provided in the Supplementary Material.

rapidly toward their sunset values around sunrise (about 07:00 h in the graph). The movement was dominated by the downwards component, but included also a comparatively small radial contribution.

In addition to the similar time response, the amplitude of point movements was dependent on the point distance from the trunk in general. For every branch, the point indexing was selected so that the index increased when moving away from the trunk (Figure 2). As a general trend, points with higher index values moved more compared to points with smaller indices. The subplots show exceptions from this rule at different times, but the general trend is visible.

For reference targets attached to the branches, movement of their centers showed a similar, but attenuated, temporal trend compared to the branch points. Reference targets 1 and 3 showed relatively little movement until about 6 h after sunset, excluding occasional noise points. Then, both reference target centers showed a sharp movement with amplitude of 1 cm. The movement then increased until 05:30 o'clock, after which it diminished rapidly by about an hour after sunrise. Reference target 2 differed from the two others in that its movement amplitude was lower and the maximum movement occurred already around 05:00 o'clock. However, the movement diminished in the same way as in the case of the other reference targets.

## Considerations on Result Comparability

The results show similar temporal behavior between the two birches. This is despite the difference in location of over 12 degrees of latitude, and the difference in form of growth: the Austrian tree was a cultivar with mainly hanging branches while the Finnish study tree had more erect branches with only the branchlets hanging. Growing conditions in the measurement sites also differed from each other, the Finnish site was more covered and in a slope, whereas the Austrian site was on an open and flat grass field.

Although both experiments showed clear temporal correlation in birch branch movement overnight, the absolute branch movements cannot be compared directly. The spatial resolution obtainable with the FGI HSL was not detailed enough to determine individual branch points reliably between consecutive scans. Thus, the temporal development of the Finnish birch was treated on a crown level. The use of crown point height percentiles shows how the different parts of the crown move with respect to each other, but this level of detail was not sufficient to analyze the movement amplitude of individual branches.

The RIEGL VZ-4000 point clouds were dense enough for individual representative point monitoring. In addition, the reference markers attached to birch branches gave another point of reference to determine the movement amplitude. Since the representative points on branches were picked by hand, this

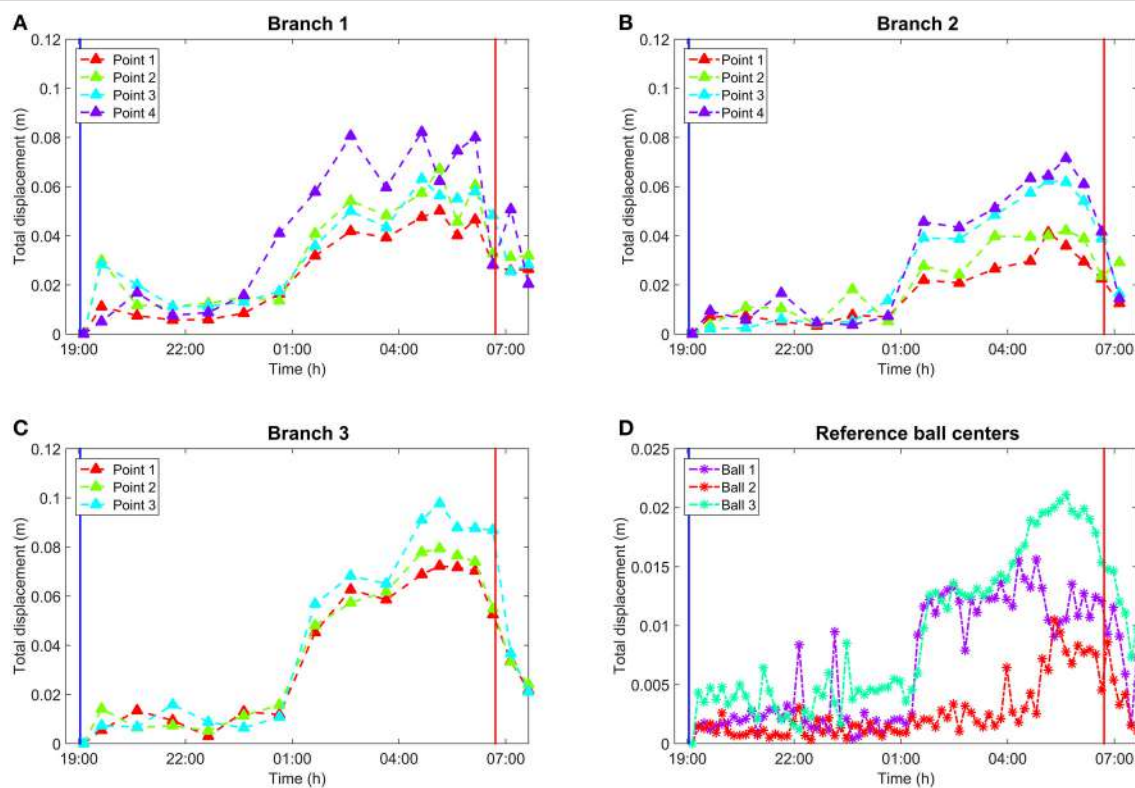


**FIGURE 5 | (A)** Total movements of the representative points on Branch 1 over time. **(B)** Total movements of the representative points on Branch 2 over time. Branch 2 is missing the last epoch due to internal occlusion. **(C)** Total movements of the representative points on Branch 3 over time. **(D)** Total movement of reference target centers over time. Vertical lines in all subplots mark sunset and sunrise. All values in **(A–D)** represent the absolute 3D movement compared to the initial point selection at the scan closest to sunset. Manual point selection in **(A–C)** was performed by picking scans once per hour which was sufficient to represent the general movement trend over time. In **(D)**, reference centers were extracted automatically for all 77 scans. The reference spheres were attached on thicker branches and closer to the stem than Branches 1–3. This resulted in smaller movement amplitudes in the sphere center movement than with the branches.

resulted in an uncertainty of about 1 cm. However, all manually selected branch points showed systematic movement amplitudes of several centimeters that was several times larger than the point ranging uncertainty and were thus interpreted as a result of changes in branch position. In the Finnish dataset, the thickest lower branches adjacent to the stem were measured to be about 15 mm in diameter. In the Austrian dataset, the selected branches were about 10–20 mm in diameter as measured from the point clouds.

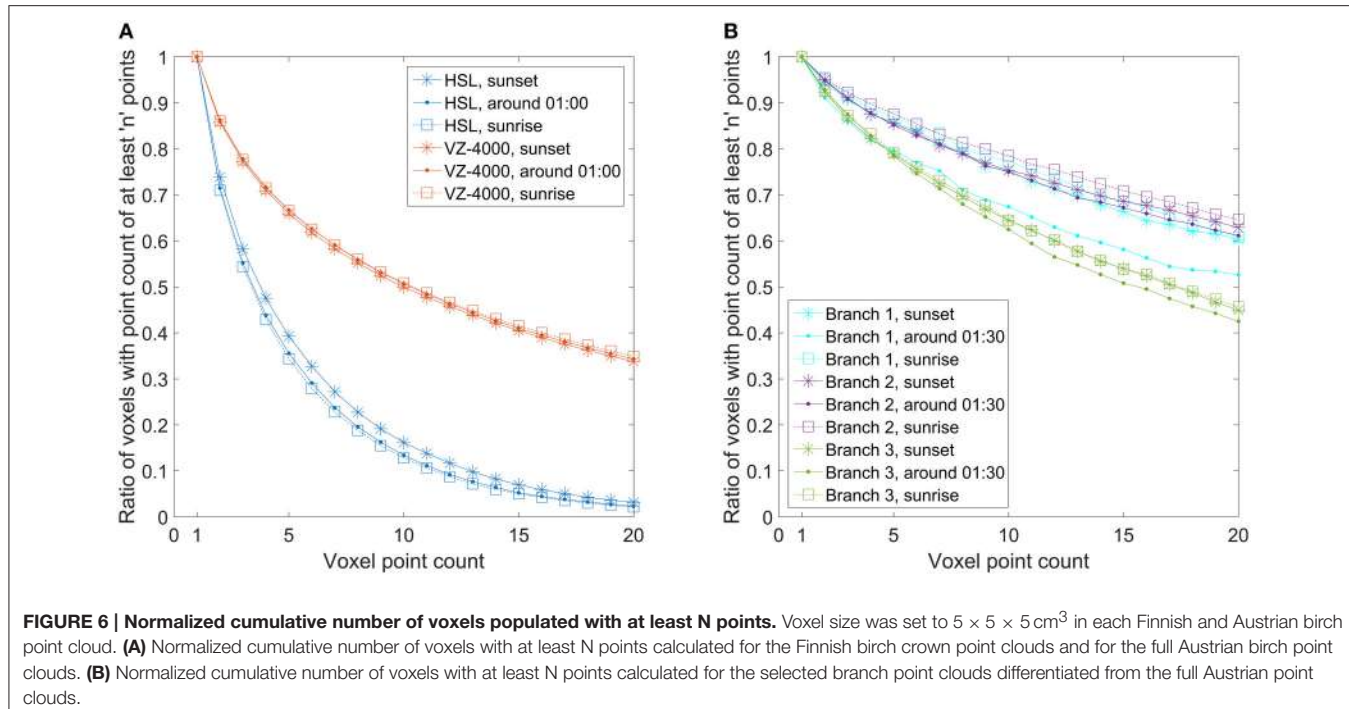
In order to better compare the results for estimating required point densities for future measurement planning, a comparative table of the two measurement setup is presented in **Table 3**. The table sums up both the differences and the similarities between the measurements.

The question arises, which density of the point cloud is required for doing the first or the second type of movement analysis, i.e., height percentiles vs. points on individual branches. To achieve this, the point density must be quantified. This was done by calculating the number of populated  $5 \times 5 \times 5 \text{ cm}^3$  voxels for the point clouds, and this was further monitored through time. The normalized cumulative number of voxels populated with at least a given number of points is illustrated in **Figure 6** for both cases. In other words, the metric shows how many voxels

contain at least n points within the voxel point cloud. This value is normalized by dividing through the number of voxels which have at least 1 point. The point density graphs were drawn at three different times in order to evaluate whether scanning time would have had a significant effect on point cloud density due to any external factors.

In the Finnish full canopy point clouds, the **Figure 5A** illustrates clearly how the cumulative point density in voxels decreases rapidly. This means that most of the populated voxels had only a few hits in them. Only about 35–40% of the populated voxels have five or more laser returns localized in them. There is also about a 5% percentage point difference between the scans taken at sunset and at night. In the Austrian point cloud, the corresponding number shows that over 65% of the populated voxels have at least five hits in them and there is no significant difference between the scans taken at different times.

The amount of voxels with one or two laser returns is important as they represent spatially isolated returns of which a significant portion may consist of noise, and partial or otherwise low quality hits on target. The graphs in **Figure 6A**) show that while there is some variation in the point density on the crown and tree level, the point densities between different scans drop



in a consistent manner for both scanners regardless of scanning time.

The graphs in **Figure 6A**) showed the point density for the full crown and tree point clouds. Thus, the inherently noisy backsides of the point clouds with lower point densities are also included. Therefore, similar graphs were also produced separately for the differentiated Austrian birch branches (**Figure 6B**) that were used for movement measurements to see if they would show different point density variations compared to the full tree point cloud. The branches were selected on the outer edge of the birch and with clear visibility to the scanner (**Figure 2**). The graphs show that about 85% of all populated voxels inside the bounding boxes of branches 1 and 2 have five or more hits, and over 75% of the voxels have 10 or more hits. The only exception here is the sunrise measurement of the branch 1, where the results are several percentage points lower. Branch 3 results show systematically lower point densities. About 80% of these voxels have at least five hits, and about 65% of the voxels have at least 10 hits. In general, the number of multi-hit branch voxels is over 10% points higher than the number of corresponding voxels in the whole birch point cloud.

Results on the point density variation in the Finnish and Austrian datasets and their effect on manual branch point selection give a rough metric to estimate required point densities for future studies. The representative point monitoring was possible with manual selection for all branches delineated from the Austrian datasets, whereas for the Finnish data similar monitoring was not possible due to lower point density. The lowest tested branch point density here had about 80% of hits coming from voxels with at least five points or more, which would correspond to a point density of at least  $40,000 \text{ pts/m}^3$ . Voxels

with 10 or more hits (at least  $80,000 \text{ pts/m}^3$ ) constituted about 65% of all voxels. In the Finnish dataset, the voxel population ratio of over 65% was obtained only when voxels with at least two points ( $16,000 \text{ pts/m}^3$ ) were included. Thus, to perform a similar point selection from a natural birch branch surface (i.e., without additional reflective material), the point densities should be at least close to  $40,000 \text{ pts/m}^3$ . This estimated value is not a universal lower limit, but it gives an initial approximation for planning new similar experiments.

Measurement settings and weather conditions were also similar between the experiments:

- Both experiments were carried out with a single scanner setup. Therefore, only one side of the test trees could be monitored over the duration of the experiments. This is sufficient to determine individual branch movements, but determination of the whole crown movement is not possible and would require a minimum of two separate scans from different positions, preferably more. Multiple scans would allow branch movement determination around the tree to get a better insight on possible directional movement differences within the crown. Multiple scans would also provide better information about effects related to growing location or sun position.
- In both experiments the weather was similar, with no observed wind and no rainfall during night. As high-resolution laser scans require typically minute-long collection times for tree-sized objects, this means that the measurements are susceptible to occasional gusts of wind and need to be accounted for in measurement planning. In order to eliminate most wind effects from point clouds, external wind covers would be needed or the scans should be performed in

an enclosed setting, for example in a greenhouse. However, in our experiments no disturbance by wind occurred.

## DISCUSSION

### The Study in Context with Previous Research

In this study we quantified a diurnal cycle of branch motion in mature birch (*Betula pendula*) trees growing under natural conditions, and therefore demonstrated the potential of TLS point clouds to monitor diurnal branch movements in birch trees. To our knowledge, the study is the first to report overnight branch and crown movement with centimeter level spatial resolution and with (less than) hourly intervals. The study approach presented here is novel in utilizing TLS point clouds with short interval outdoor scanning.

The study comprises two separate measurement settings with different equipment and geographic location, namely Finland and Austria. Target objects were individual birch trees located in the study areas and night time movements were detected by scanning their canopies for a period lasting from sunset to sunrise. The results obtained from the measurements showed that the crown movement in the Finnish and the branch movement in the Austrian study case presented similar temporal

response. Close to sunrise, the branches were hanging lower than at the time of sunset. Detected crown and branch movement amplitudes varied from a few centimeters up to 10 cm from their initial locations at sunset, depending on the position of the branch and the measurement point on it. The movements were observed to happen systematically over a time span of several hours, which ruled out occasional wind effects.

Both the molecular background of the circadian rhythm and the resulting movement of various plant parts (the leaf, stem, and flower) have been extensively described for small herbs growing under laboratory conditions. The circadian activity pattern of trees is also of interest, both for generalizing the findings of experimental chronobiology and for commercial use of tree products such as the tree sap [e.g., for the gum tree (*Hevea brasiliensis*)] and the wood (which is best harvested when it has a low water content). Understanding ecophysiological processes of individual trees, including their diurnal water use pattern and how this changes under water stress is becoming increasingly important for climate research, as near-global coverage of high-resolution remote sensing has revolutionized the up-scaling of findings from individual tree-based models to continental scale (Shugart et al., 2015). Until now, *in situ* measurements at the scale of full trees were not possible due to the lack of a non-invasive, non-contact method with high spatial accuracy. Our study demonstrates that TLS satisfies these criteria.

To our knowledge, previous and present TLS time series literature on vegetation mainly concentrates on detecting seasonal changes. The seasonal change studies have mainly focused on collecting physiological parameters, like leaf or needle chlorophyll content (Hakala et al., 2014; Nevalainen et al., 2014), or to follow the growth and phenological changes by studying changes in Leaf area index (LAI), plant area index (PAI), and Plant Area Volume Density (PAVD), e.g., in Griebel et al. (2015) and Calders et al. (2015). A study by Hosoi and Omasa (2009) determined the seasonal changes in vertical leaf area density (LAD) profiles. Measurement intervals in these studies vary from daily and weekly measurements to individual seasonal scans. These scan intervals are sufficient for detecting overall changes on crown level, but cannot capture systematic inter—and intraday dynamics as reported here.

Most of the TLS time series studies are performed during light hours, mainly due to technical restrictions that require presence of measurement staff to set up and monitor the data collection. A change to this is a new operational system, VEGNET, that has been developed and successfully applied for long-term forest monitoring (Portillo-Quintero et al., 2014; Griebel et al., 2015). The main limitation of VEGNET is its limited spatial resolution and a fixed angle rotation plane that have been designed to monitor overall crown structural dynamics around the system instead of focusing on individual trees. The VEGNET operates night time to optimize its ranging capabilities and to minimize possible wind effects. In general, any wind or local airflows present a significant source of noise in TLS point clouds and have to be accounted for either during the measurement. Another reported error source is precipitation on the scanning equipment and on target.

**TABLE 3 | Comparison between the similarities and differences in the Finnish and Austrian measurement setups.**

Similarities	
Type	Description
Tree species	Birch, <i>Betula pendula</i>
Time of the year	Finland: 13–14 of September Austria: 19–20 of September
Weather conditions	Clear weather with some overcast No observed wind (operator observation) No rainfall No visible surface condensation
Differences	
Geographic location	Separation distance: about 1500 km Difference in latitude: about 12°
Crown bounding box dimensions (depth × width × height, m <sup>3</sup> , median)	Finland: 3.7 × 3.0 × 6.6 Austria: 6.0 × 7.0 × 9.3
Total volume of the tree point cloud (sum over populated voxels, m <sup>3</sup> , median)	Finland: 4.20 Austria: 45.23
Growing spot	Finland: Semi-open, on a slope Austria: Open, flat field
Laser scanning systems	Finland: Experimental (FGI HSL) Austria: Commercial (RIEGL VZ-4000)
Year of measurement	Finland: 2013 Austria: 2014

Another feasible approach to collect longer-term time series data with high temporal resolution is short-interval photography. Li et al. (2013) performed a plant growth analysis study where they studied the structural changes in a pot plant in laboratory conditions for 35 days where the same viewing geometry was repeated every 5 min. A 4D (3D structure and time) point cloud representation was then post processed from the imagery to study geometrical changes in the plant. Nijland et al. (2014) used infrared converted consumer grade cameras to collect plant health and phenology information in an outdoor setting for several months with 1-h interval. The main weakness of the imaging approach is the requirement of external lighting and comprehensive radiometric calibration to guarantee correct radiometry between imagery taken in dynamic lighting conditions. Li et al. (2013) applied constant lighting on their targets, whereas Nijland et al. (2014) had to limit their outdoor imaging sequences to light hours. Neither solution allows studying of possible dark time dynamics in plants as reported in this study.

## SUMMARY AND FUTURE WORK

The study scope was limited to analysis and quantification of the geometric movements in birch crown and branches. The validation of possible mechanisms behind the movement was not possible within the study scope and further investigations are required. Possible mechanisms contributing to the branch and crown movement may be related to plant water balance or to plant photoperiodism, but their validation was out of the scope of this article.

Circadian changes in plants have been studied extensively in plant physiology and they can be quantified with high detail in laboratory conditions or *in-situ* for individual plants and their parts (e.g., Perämäki et al., 2001). However, extending the results to larger areas is prohibitively laborious. We conclude that whereas laser scanning point clouds are not able to give as detailed information about the physiological changes in plants as laboratory or on-the-spot measurements, they still have a significant potential to provide additional geometrical information that can be correlated with the physiological measurements, and then possibly extended to cover whole plants in their natural environment and over wider areas. Perhaps the most important open question is whether the observed branch movements take place under the influence of light from sunset and sunrise, or if they are independent from light and governed by the internal circadian clock of the plant. The fact that some branches started returning to their daytime position already before sunrise would suggest this latter hypothesis, but the temporal frequency of our investigations is not sufficient for confirming or rejecting it: ideally, measuring several full 24-h cycles of a tree isolated from natural light would be required for this.

To explore the potential of TLS-based sleep movement of trees as an indicator of water use and water stress, further studies are required with simultaneous physiological measurements of trunk diameter, water potential, and photosynthetic activity and reference comparisons. This will allow (i) quantification of the limits of reliability of different terrestrial laser scanners to detect the temporal movements in different plant and tree species and (ii) modeling and further simulation of the relationship between the detected geometric behavior and direct physiological observations of plant water use and circadian rhythms.

## AUTHOR CONTRIBUTIONS

EP is the main author and took part in the planning of both experiments, collection of Finnish data, and performed the data analysis. CB, GM, and NP planned the Austrian dataset collection and contributed to the writing. MP planned and arranged the collection of Austrian dataset and contributed to writing the manuscript. MW processed the Austrian dataset for analysis. AZ strengthened introduction and discussion from biological and ecological perspective, and commented the whole manuscript.

## FUNDING

This article received support from Academy of Finland grants no. 265949 and no. 272195, and from the Finnish foundations mobility grant “Tutkijat maailmalle, osaamista Suomeen.” AZ was supported by the OTKA grant PD 115833 of the Hungarian Research Fund.

## ACKNOWLEDGMENTS

The authors thank Sanna Kaasalainen, Teemu Hakala, Olli Nevalainen, Mika Karjalainen, Anssi Krooks, and Kati Anttila for their help with collecting the Finnish data, and Reinhard Plessl for collecting the Austrian data. We also acknowledge the support of Hermann Heilmeier, Biology and Ecology group at TU BAF in Freiberg (Germany).

## SUPPLEMENTARY MATERIAL

The Supplementary Material for this article can be found online at: <http://journal.frontiersin.org/article/10.3389/fpls.2016.00222>

**Video 1 | Animation of the overnight movement in the Finnish birch point cloud from sunset to sunrise.** Video is created by drawing birch point cloud of each scan collected during night. The point cloud scanned around sunset (19:40 o'clock) is drawn with black as a reference. The laser scanner was located in origin (0,0).

## REFERENCES

- Abellan, A., Vilaplana, J. M., Calvet, J., Garcia-Selles, D., and Asensio, E. (2011). Rockfall monitoring by Terrestrial Laser Scanning—case study of the basaltic rock face at Castellfollit de la Roca (Catalonia, Spain). *Nat. Hazards Earth Syst. Sci.* 11, 829–841. doi: 10.5194/nhess-11-829-2011
- Acevedo, E., Fereres, E., Hsiao, T. C., and Henderson, D. W. (1979). Diurnal growth trends, water potential, and osmotic adjustment of maize and sorghum leaves in the field. *Plant Physiol.* 64, 476–480. doi: 10.1104/pp.64.3.476
- Andrews, S. F., Flanagan, L. B., Sharp, E. J., and Cai, T. (2012). Variation in water potential, hydraulic characteristics and water source use in montane Douglas-fir and lodgepole pine trees in southwestern Alberta and consequences for seasonal changes in photosynthetic capacity. *Tree Physiol.* 32, 146–160. doi: 10.1093/treephys/tpr136
- Arslan, A. E., and Kalkan, K. (2013). “Comparison of working efficiency of terrestrial laser scanner in day and night conditions,” in *International Archives of the Photogrammetry, Remote Sensing and Spatial Information Sciences*, eds F. Sunar, O. Altan, S. Li, K. Schindler, and J. Jiang (Antalya: International Society for Photogrammetry and Remote Sensing), 19–21. doi: 10.5194/isprsarchives-ixl-7-w2-19-2013
- Barak, S., Tobin, E. M., Green, R. M., Andronis, C., and Sugano, S. (2000). All in good time: the *Arabidopsis* circadian clock. *Trends Plant Sci.* 5, 517–522. doi: 10.1016/S1360-1385(00)01785-4
- Barnhart, T. B., and Crosby, B. T. (2013). Comparing two methods of surface change detection on an evolving thermokarst using high-temporal-frequency terrestrial laser scanning, Selawik River, Alaska. *Remote Sens.* 5, 2813–2837. doi: 10.3390/rs5062813
- Bucksch, A., and Fleck, S. (2011). Automated detection of branch dimensions in woody skeletons of fruit tree canopies. *Photogramm. Eng. Remote Sens.* 77, 229–240. doi: 10.14358/PERS.77.3.229
- Calders, K., Schenkels, T., Bartholomeus, H., Armston, J., Verbesselt, J., and Herold, M. (2015). Monitoring spring phenology with high temporal resolution terrestrial LiDAR measurements. *Agric. For. Meteorol.* 203, 158–168. doi: 10.1016/j.agrformet.2015.01.009
- Chapin, F. S. I. I. I., Matson, P. A., and Mooney, H. A. (2002). *Principles of Terrestrial Ecosystem Ecology*. New York, NY: Springer-Verlag.
- Chapotin, S. M., Razanameharizaka, J. H., and Holbrook, N. M. (2006). Water relations of baobab trees (*Adansonia* spp. L.) during the rainy season: does stem water buffer daily water deficits? *Plant Cell Environ.* 29, 1021–1032. doi: 10.1111/j.1365-3040.2005.01456.x
- Correia, M. J., Coelho, D., and David, M. M. (2001). Response to seasonal drought in three cultivars of *Ceratonia siliqua*: leaf growth and water relations. *Tree Physiol.* 21, 645–653. doi: 10.1093/treephys/21.10.645
- Correia, P. J., and Martins-Loucao, M. A. (1995). Seasonal variations of leaf water potential and growth in fertigated carob-trees (*Ceratonia siliqua* L.). *Plant Soil.* 172, 199–206. doi: 10.1007/BF00011322
- Darwin, C., and Darwin, F. (1880). *The Power of Movement in Plants*. London, UK: John Murray. doi: 10.5962/bhl.title.102319
- Dassot, M., Constant, T., and Fournier, M. (2011). The use of terrestrial LiDAR technology in forest science: application fields, benefits and challenges. *Ann. For. Sci.* 68, 959–974. doi: 10.1007/s13595-011-0102-2
- Eysn, L., Pfeifer, N., Ressl, C., Hollaus, M., Grafl, A., and Morsdorf, F. (2013). A practical approach for extracting tree models in forest environments based on equirectangular projections of terrestrial laser scans. *Remote Sens.* 5, 5424–5448. doi: 10.3390/rs5115424
- Fleck, S., van der Zande, D., Schmidt, M., and Coppin, P. (2004). “Reconstructions of tree structure from laser-scans and their use to predict physiological properties and processes in canopies,” in *International Archives of the Photogrammetry, Remote Sensing and Spatial Information Sciences*, Vol. XXXVI-8/W2, eds M. Thies, B. Koch, H. Specker, and H. Weinacker (Freiburg), 119–123. Available online at: <http://www.isprs.org/proceedings/XXXVI/8-W2/FLECK.pdf>
- García-Orellana, Y., Ortúñoz, M. F., Conejero, W., and Ruiz-Sánchez, M. C. (2013). Diurnal variations in water relations of deficit irrigated lemon trees during fruit growth period. *Span. J. Agric. Res.* 11, 137–145. doi: 10.5424/sjar/201311-3153
- Ghuffar, S., Székely, B., Roncat, A., and Pfeifer, N. (2013). Landslide displacement monitoring using 3D range flow on airborne and terrestrial LiDAR data. *Remote Sens.* 5, 2720–2745. doi: 10.3390/rs5062720
- Girardeau-Montaut, D. (2014). *CloudCompare (Version 2.6.0) [GPL Software]*. Available online at: <http://www.cloudcompare.org/> (Accessed on Jan 16, 2015).
- Griebel, A., Bennett, L. T., Culvenor, D. S., Newham, G. J., and Arndt, S. K. (2015). Reliability and limitations of a novel terrestrial laser scanner for daily monitoring of forest canopy dynamics. *Remote Sens. Environ.* 166, 205–213. doi: 10.1016/j.rse.2015.06.014
- Grosje-Schwiep, M., Piechel, J., and Luhmann, T. (2013). Measurement of rotor blade deformations of wind energy converters with laser scanners,” in *International Annals of the Photogrammetry, Remote Sensing and Spatial Information Sciences*, eds M. Scaioni, R. C. Lindenbergh, S. Oude Elberink, D. Schneider, and F. Pirrotti (Antalya: International Society for Photogrammetry and Remote Sensing), 97–102. doi: 10.5194/isprsannals-ii-5-w2-97-2013
- Hakala, T., Nevalainen, O., Kaasalainen, S., and Mäkipää, R. (2014). Technical note: hyperspectral LiDAR time series of pine canopy physiological parameters. *Biogeosciences* 11, 15019–15035. doi: 10.5194/bg-11-15019-2014
- Hakala, T., Suomalainen, J., Kaasalainen, S., and Chen, Y. (2012). Full waveform hyperspectral LiDAR for terrestrial laser scanning. *Opt. Express.* 20, 7119–7127. doi: 10.1364/OE.20.007119
- Holmes, J. W., and Shim, S. Y. (1968). Diurnal changes in stem diameter of canary island pine trees (*Pinus canariensis*, C. Smith) caused by soil water stress and varying microclimate. *J. Exp. Bot.* 19, 219–232. doi: 10.1093/jxb/19.2.219-a
- Hopkinson, C., Chasmer, L., Young-Pow, C., and Treitz, P. (2004). Assessing forest metrics with a ground-based scanning lidar. *Canad. J. For. Res.* 34, 573–583. doi: 10.1139/x03-225
- Hosoi, F., and Omasa, K. (2006). Voxel-based 3-D modeling of individual trees for estimating leaf area density using high-resolution portable scanning lidar. *IEEE Trans. Geosci. Remote Sens.* 44, 3610–3618. doi: 10.1109/TGRS.2006.881743
- Hosoi, F., and Omasa, K. (2009). Detecting seasonal change of broadleaved woody canopy leaf area density profile using 3D portable LiDAR imaging. *Funct. Plant Biol.* 36, 998–1005. doi: 10.1071/FP09113
- Hu, H. (2013). *Deformation Monitoring and Modeling Based on LiDAR Data for Slope Stability Assessment*. Doctoral thesis (Aachen: RWTH Aachen Technical University).
- Kaasalainen, S., Krooks, A., Liski, J., Raumonen, P., Kaartinen, H., Kaasalainen, M., et al. (2014). Change detection of tree biomass with terrestrial laser scanning and quantitative structure modelling. *Remote Sens.* 6, 3906–3922. doi: 10.3390/rs6053906
- Klepper, B. (1968). Diurnal pattern of water potential in woody plants. *Plant Physiol.* 43, 1931–1934. doi: 10.1104/pp.43.12.1931
- Köstner, B., Granier, A., and Černák, C. (1998). Sapflow measurements in forest stands: methods and uncertainties. *Ann. Sci. For.* 55, 13–27. doi: 10.1051/forest:19980102
- Kovanic, L., and Blaštan, P. (2014). Quarry wall stability assessment using TLS method. *Adv. Mater. Res.* 1044–1045, 603–606. doi: 10.4028/www.scientific.net/amr.1044-1045.603
- Li, Y., Fan, X., Mitra, N. J., Chamovitz, D., Cohen-Or, D., and Chen, B. (2013). Analyzing growing plants from 4D point cloud data. *ACM Trans. Graphics Proc. SIGGRAPH Asia* 32, 10. doi: 10.1145/2508363.2508368
- Liang, X. (2013). *Feasibility of Terrestrial Laser Scanning for Plotwise Forest Inventories*. Doctoral thesis. Publications of the Finnish Geodetic Institute (Kirkkonummi: Aalto University), 150. Available online at: <https://aalto.dtic.aito.fi/handle/123456789/11355>
- Lindenbergh, R. C., Souidarissanane, S. S., de Vries, S., Gorte, B. G. H., and de Schipper, M. A. (2011). Aeolian beach sand transport monitored by terrestrial laser scanning. *Photogramm. Rec.* 26, 384–399. doi: 10.1111/j.1477-9730.2011.00659.x
- McClung, C. R. (2006). Plant circadian rhythms. *Plant Cell.* 18, 792–803. doi: 10.1105/tpc.106.040980
- Milan, D. J., Heritage, G. L., and Hetherington, D. (2007). Application of a 3D laser scanner in the assessment of erosion and deposition volumes and channel change in a proglacial river. *Earth Surf. Proc. Landforms.* 32, 1657–1674. doi: 10.1002/esp.1592
- Mockler, T., Yang, H., Yu, X., Parikh, D., Cheng, Y., Dolan, S., et al. (2003). Regulation of photoperiodic flowering by *Arabidopsis* photoreceptors. *Proc. Natl. Acad. Sci. U.S.A.* 100, 2140–2145. doi: 10.1073/pnas.0437826100

- Moskal, L. M., and Zheng, G. (2012). Retrieving forest inventory variables with terrestrial laser scanning (TLS) in urban heterogeneous forest. *Remote Sens.* 4, 1–20. doi: 10.3390/rs4010001
- Nevalainen, O., Hakala, T., Suomalainen, J., Mäkipää, R., Peltoniemi, M., Krooks, A., et al. (2014). Fast and nondestructive method for leaf level chlorophyll estimation using hyperspectral LiDAR. *Agric. For. Meteorol.* 198–199, 250–258. doi: 10.1016/j.agrformet.2014.08.018
- Nijland, W., de Jong, R., de Jong, S. M., Wulder, M. A., Bater, C. W., and Coops, N. C. (2014). Monitoring plant condition and phenology using infrared sensitive consumer grade digital cameras. *Agric. For. Meteorol.* 184, 98–106. doi: 10.1016/j.agrformet.2013.09.007
- Nozue, K., and Maloof, J. N. (2006). Diurnal regulation of plant growth. *Plant Cell Environ.* 29, 396–408. doi: 10.1111/j.1365-3040.2005.01489.x
- Perämäki, M., Nikinmaa, E., Sevanto, S., Ilvesniemi, H., Siivola, E., Hari, P., et al. (2001). Tree stem variations and transpiration in Scots pine: an analysis using a dynamic sap flow model. *Tree Phys.* 21, 889–897. doi: 10.1093/treephys/21.12.13.889
- Pesonen, E., Mielikäinen, K., and Mäkinen, H. (2004). A new girth band for measuring stem diameter changes. *Forestry* 77, 431–439. doi: 10.1093/forestry/77.5.431
- Portillo-Quintero, C., Sanchez-Azofeifa, A., and Culvenor, D. (2014). Using VEGNET *In Situ* monitoring LiDAR (IML) to capture dynamics of plant area index, structure and phenology in aspen parkland forests in Alberta, Canada. *Fores* 5, 1053–1068. doi: 10.3390/f5051053
- Puttonen, E., Hakala, T., Nevalainen, O., Kaasalainen, S., Krooks, A., Karjalainen, M., et al. (2015). Artificial target detection with a hyperspectral LiDAR over 26-h measurement. *Optic. Eng.* 54:013105, 1–15. doi: 10.1117/1.oe.54.1.013105
- Raumonen, P., Kaasalainen, M., Åkerblom, M., Kaasalainen, S., Kaartinen, H., Vastaranta, M., et al. (2013). Fast automatic precision tree models from terrestrial laser scanner data. *Remote Sens.* 5, 491–520. doi: 10.3390/rs5020491
- RIEGL (2014). *RIEGL VZ-4000: 3D Very Long Range Terrestrial Laser Scanner with Online Waveform Processing, 2014-09-19, Datasheet*. Available online at: [http://www.riegl.com/uploads/tc\\_pxprigldownloads/DataSheet\\_VZ-4000\\_2015-03-24.pdf](http://www.riegl.com/uploads/tc_pxprigldownloads/DataSheet_VZ-4000_2015-03-24.pdf) (Accessed on Feb 10, 2015).
- Saarinen, N., Vastaranta, M., Vaaja, M., Lotsari, E., Jaakkola, A., Kukko, A., et al. (2013). Area-based approach for mapping and monitoring riverine vegetation using mobile laser scanning. *Remote Sens.* 5, 5285–5303. doi: 10.3390/rs5105285
- Salisbury, F. B. (1981). Twilight effect: initiating dark measurement in photoperiodism of Xanthium. *Plant Physiol.* 67, 1230–1238. doi: 10.1104/pp.67.6.1230
- Shugart, H. H., Asner, G. P., Fischer, R., Huth, A., Knapp, N., Toan, T. L., et al. (2015). Computer and remote-sensing infrastructure to enhance large-scale testing of individual-based forest models. *Front. Ecol. Environ.* 13, 503–511. doi: 10.1890/140327
- Solomon, O. L., Berger, D. K., Myburg, A. A., and Myburg, Z. (2010). Diurnal and circadian patterns of gene expression in the developing xylem of Eucalyptus trees. *South Afr. J. Bot.* 76, 425–439. doi: 10.1016/j.sajb.2010.02.087
- Sysoeva, M. I., Markovskaya, E. F., and Shibaeva, T. G. (2010). Plants under continuous light: a review. *Plant Stress* 4, 5–17. Available online at: [http://www.globalsciencebooks.info/Online/GSBookOnline/images/2010/PS\\_4%281%29/PS\\_4%281%295-170.pdf](http://www.globalsciencebooks.info/Online/GSBookOnline/images/2010/PS_4%281%29/PS_4%281%295-170.pdf)
- Travelletti, J., Oppikofer, T., Delacourt, C., Malet, J.-P., and Jaboyedoff, M. (2008). “Monitoring landslide displacements during a controlled rain experiment using a long-range Terrestrial Laser Scanning (TLS),” in *International Archives of the Photogrammetry, Remote Sensing and Spatial Information Sciences*, eds J. Chen, J. Jiang, and H.-G. Maas (Beijing: International Society for Photogrammetry and Remote Sensing), 485–490.
- Vaaja, M., Hyppä, J., Kukko, A., Kaartinen, H., Hyppä, H., and Alho, P. (2011). Mapping topography changes and elevation accuracies using a mobile laser scanner. *Remote Sens.* 3, 587–600. doi: 10.3390/rs3030587
- Way, J., Paris, J., Dobson, M. C., McDonals, K., Ulaby, F. T., Weber, J. A., et al. (1991). Diurnal change in trees as observed by optical and microwave sensors: the EOS synergism study. *IEEE Trans. Geosci. Remote Sens.* 29, 807–821. doi: 10.1109/TGRS.1991.1019466
- Wayne, P. M., and Bazzaz, F. A. (1993). Birch seedling responses to daily time courses of light in experimental forest gaps and shadehouses. *Ecology* 74, 1500–1515. doi: 10.2307/1940078
- Conflict of Interest Statement:** The authors declare that the research was conducted in the absence of any commercial or financial relationships that could be construed as a potential conflict of interest.
- Copyright © 2016 Puttonen, Briese, Mandlburger, Wieser, Pfennigbauer, Zlinszky and Pfeifer. This is an open-access article distributed under the terms of the Creative Commons Attribution License (CC BY). The use, distribution or reproduction in other forums is permitted, provided the original author(s) or licensor are credited and that the original publication in this journal is cited, in accordance with accepted academic practice. No use, distribution or reproduction is permitted which does not comply with these terms.



# The Application of Leaf Ultrasonic Resonance to *Vitis vinifera* L. Suggests the Existence of a Diurnal Osmotic Adjustment Subjected to Photosynthesis

Domingo Sancho-Knapik<sup>1,2</sup>, Hipólito Medrano<sup>3\*</sup>, José J. Peguero-Pina<sup>1,2</sup>, Maurizio Mencuccini<sup>4</sup>, María D. Fariñas<sup>5</sup>, Tomás G. Álvarez-Arenas<sup>5</sup> and Eustaquio Gil-Pelegrín<sup>1,2</sup>

## OPEN ACCESS

### Edited by:

Daniel H. Chitwood,  
Donald Danforth Plant Science  
Center, USA

### Reviewed by:

Tobias Gebauer,  
University of Freiburg, Germany  
Tsui-Wei Chen,  
Leibniz University of Hanover,  
Germany

### \*Correspondence:

Hipólito Medrano  
hipolito.medrano@uib.es

### Specialty section:

This article was submitted to  
Plant Biophysics and Modeling,  
a section of the journal  
*Frontiers in Plant Science*

Received: 23 March 2016

Accepted: 11 October 2016

Published: 26 October 2016

### Citation:

Sancho-Knapik D, Medrano H, Peguero-Pina JJ, Mencuccini M, Fariñas MD, Álvarez-Arenas TG and Gil-Pelegrín E (2016) The Application of Leaf Ultrasonic Resonance to *Vitis vinifera* L. Suggests the Existence of a Diurnal Osmotic Adjustment Subjected to Photosynthesis. *Front. Plant Sci.* 7:1601.  
doi: 10.3389/fpls.2016.01601

<sup>1</sup> Unidad de Recursos Forestales, Centro de Investigación y Tecnología Agroalimentaria de Aragón, Gobierno de Aragón, Zaragoza, Spain, <sup>2</sup> Centro de Investigación y Tecnología Agroalimentaria de Aragón, Instituto Agroalimentario de Aragón, Universidad de Zaragoza, Zaragoza, Spain, <sup>3</sup> Research Group on Plant Biology under Mediterranean Conditions, Departament de Biología, Universitat de les Illes Balears, Palma de Mallorca, Spain, <sup>4</sup> ICREA at CREA, Barcelona, Spain, <sup>5</sup> Sensors and Ultrasonic Technologies Department, Information and Physics Technologies Institute, Spanish National Research Council, Madrid, Spain

The main objective of this study was to apply the air-coupled broad-band ultrasonic spectroscopy in attached transpiring leaves of *Vitis vinifera* L. to monitor changes in leaf water potential ( $\Psi$ ) through the measurements of the standardized value of the resonant frequency associated with the maximum transmittance ( $f/f_0$ ). With this purpose, the response of grapevine to a drought stress period was investigated in terms of leaf water status, ultrasounds, gas exchange and sugar accumulation. Two strong correlations were obtained between  $f/f_0$  and  $\Psi$  measured at predawn (pd) and at midday (md) with different slopes. This fact implied the existence of two values of  $\Psi$  for a given value of  $f/f_0$ , which was taken as a sign that the ultrasonic technique was not directly related to the overall  $\Psi$ , but only to one of its components: the turgor pressure ( $P$ ). The difference in  $\Psi$  at constant  $f/f_0$  ( $\delta$ ) was found to be dependent on net  $\text{CO}_2$  assimilation ( $A$ ) and might be used as a rough estimator of photosynthetic activity. It was then, the other main component of  $\Psi$ , osmotic potential ( $\pi$ ), the one that may have lowered the values of md  $\Psi$  with respect to pd  $\Psi$  by the accumulation of sugars associated to net  $\text{CO}_2$  assimilation. This phenomenon suggests the existence of a diurnal osmotic adjustment in this species associated to sugars production in well-watered plants.

**Keywords:** diurnal osmotic adjustment, drought, gas exchange, leaf ultrasonic frequency, *Vitis vinifera*, water potential

**Abbreviations:**  $A$ , net  $\text{CO}_2$  uptake;  $C_a$ , ambient  $\text{CO}_2$  concentration; em, early morning;  $f/f_0$ , standardized frequency;  $g_s$ , stomatal conductance; md, midday; pd, predawn;  $P$ , turgor pressure; RWC, relative water content;  $\pi$ , osmotic potential;  $\Psi$ , water potential.

## INTRODUCTION

Grapevines are one of the world's most important commercial crops, not only from an economic point of view, but also because of the extension of its worldwide cultivation. A significant proportion of these vineyards grows under Mediterranean-type climates (Tonietto and Carboneau, 2004), where *Vitis vinifera* L. has to cope with a summer water deficit that may affect berry quality (Chaves et al., 2007; Chaves et al., 2010). In such environments, climate change models (García-Mozo et al., 2010) predict an increment in extreme high temperature and drought events, which may represent a risk for the wine industry forcing it to a more frequent use of irrigation for affordable crop production (Chaves et al., 2007). The high water requirements of grapevines during the growing season (Netzer et al., 2005; Zhang et al., 2007) and the large dependence of berry quality parameters on soil water availability (Medrano et al., 2003; Keller et al., 2008; Flexas et al., 2010; Romero et al., 2010; Pou et al., 2011) justifies special attention in the optimization of water use during vineyard irrigation to achieve a more environmentally sustainable viticulture with a reasonable fruit quality (Jones, 2004).

Direct measurements of the plant stress response, 'plant stress sensing' according to Jones (2004), have been suggested as a better way to implement adequate irrigation scheduling compared to only estimating atmospheric water demand or soil moisture status (Jones, 1990, 2004, 2007). Among the methods that use the plant as an indicator, the air-coupled broad-band ultrasonic spectroscopy technique (Álvarez-Arenas et al., 2009; Sancho-Knapik et al., 2010, 2011, 2012), has been proven recently as a non-destructive, non-invasive and non-contact method for the dynamic determination of leaf water status in *V. vinifera* (Sancho-Knapik et al., 2013a; Fariñas et al., 2014). This method is based on the excitation of thickness resonances of the leaves and on the analysis of the spectral response in the vicinity of the first order thickness resonance (Álvarez-Arenas et al., 2009), and has been revealed as a good indicator of the water potential ( $\Psi$ ) and the RWC of leaves through changes in the  $f/f_0$  at the maximum transmittance (Sancho-Knapik et al., 2010, 2013a). These changes in  $f/f_0$  that occur before turgor loss can be attributed to changes in the macroscopic effective elastic constant of the leaf in the thickness direction ( $c_{33}$ ) (Sancho-Knapik et al., 2011) that are mainly associated with changes in the tautness of the microfibrils in the cell wall (Gibson and Ashby, 1997) and therefore with changes in the bulk modulus of elasticity of the cell wall ( $\epsilon$  the change in turgor pressure for a given fractional change in the weight of symplasmic water) (Tyree, 1981; Sancho-Knapik et al., 2011). As  $\epsilon$  is dependant on the variations in turgor pressure (Tyree and Jarvis, 1982), changes in  $f/f_0$  before the turgor loss point can be attributed mainly to the variations in turgor pressure.

Leaf  $\Psi$  is the sum of turgor pressure, or the outward hydrostatic pressure which is opposed by the cell wall ( $P$ , positive), osmotic potential, the component of the water potential due to the presence of solutes ( $\pi$ , negative) and matric potential, the component relative to the binding of water molecules to non-dissolved structures of the cells, which is negligible as

compared with the other two (Koide et al., 1989). Loss of water from turgid attached leaf tissues in response to transpiration can decrease  $\Psi$  not only through a significant decline in  $P$ , but also through a decline in  $\pi$ . Although variations in  $\pi$  can occur following passive concentration of solutes, this is generally less important when compared with the variation in  $P$  (Richter, 1978; Koide et al., 1989), associating the decrease in  $\Psi$  when a turgid leaf loses water, mainly with a decrease in  $P$ . In this case, the relation between  $f/f_0$  and  $\Psi$  in attached leaves may be in line with previous works where processes occurring during leaf dehydration were studied (Sancho-Knapik et al., 2010, 2013a). On the other hand, photosynthetic products, besides being uploaded immediately to the phloem or converted into starch, can be accumulated, reducing also leaf  $\pi$  by a net increase in solutes (Acevedo et al., 1979). This process, called diurnal osmotic adjustment, has been revealed as a mechanism playing a key role in leaf expansion by minimizing the opportunities for significant water loss from leaf tissues (Acevedo et al., 1979; Girma and Krieg, 1992). Diurnal osmotic adjustment induces a significant reduction in  $\Psi$  without any decrease in  $P$ , so that, a variation in  $\Psi$  caused only by a net increase of solutes in the leaf may not induce a variation neither in RWC nor in  $f/f_0$ . In this second case, the air-coupled broad-band ultrasonic spectroscopy technique may be used to appreciate mechanisms at leaf level that have been interpreted as the consequence of diurnal osmotic adjustment associated to photosynthesis when no changes in  $f/f_0$  occur during a decrease in  $\Psi$ . In this sense, the aim of this study is to apply the air-coupled broad-band ultrasonic spectroscopy on *V. vinifera* to (i) monitor changes in  $f/f_0$  with changes in leaf water potential on attached transpiring leaves and (ii) analyse the mechanisms that can suggest the existence of a diurnal osmotic adjustment associated with photosynthesis.

## MATERIALS AND METHODS

### Plant Material and Experimental Conditions

Two-year-old rooted cuttings of *Vitis vinifera* cv. Grenache were planted in 75-L containers with a mixture of 80% compost (Neuhaus Humin Substrat N6; Klasman-Deilmann GmbH, Geeste, Germany) and 20% perlite. Plants grew during 2 years in a common garden located at CITA de Aragón (41°39'N, 0°52'W, Zaragoza, Spain; mean annual temperature 15.4°C, total annual precipitation 298 mm) with irrigation employed when necessary. Two weeks before the beginning of the experiment (starting date on 16 July 2014), three pots of each variety were placed under a transparent greenhouse tunnel of alveolar polycarbonate that allowed passing 90% of PPFD. The use of covers in water-stress experiments had the advantage of performing measurements in more controlled environmental conditions, avoiding re-watering by storms or unwanted rainfall events.

Watering was stopped on 15 July 2014 and measurements in well watered plants started on 16 July 2014. During the following days, measurements of water potential, gas exchange and ultrasounds were performed every 2 or 3 days with increasing levels of drought stress. pd measurements of ultrasounds and

water potential ( $\Psi^{pd}$ ) were conducted strictly between 3 and 4 h (solar time), while md measurements of ultrasounds and water potential ( $\Psi^{md}$ ) were made at 12 h (solar time). Measurements of gas exchange were made at 8 h solar time (em) and at md. Drought stress was imposed during 20 days. Finally, after the last measurement under drought stressed conditions, plants were rewatered and measurements were performed again after 2 days. In addition, leaves were collected at pd, em, and md for the measurement of sugars concentration, osmolality and RWC during the first and the last days of the drought period (when plants were well watered and just before rewetting, respectively). Leaves for RWC were previously measured with ultrasounds and water potential was also measured at em.

A second complementary experiment was carried out during summer 2015 on a well watered specimen located inside a plant chamber at low CO<sub>2</sub> concentration (40–80  $\mu\text{mol mol}^{-1}$ ). Water potential, ultrasounds and sugars concentration were measured on 10 leaves at pd and at md in order to obtain the response of a well watered plant when photosynthetic activity was impaired due to the almost complete absence of CO<sub>2</sub>. Under these conditions, the decrease of water potential at midday ( $\Psi^{md}$ ) with respect to that measured at predawn ( $\Psi^{pd}$ ) would be only affected by concentration of solutes due to the loss of water through transpiration and not by the accumulation of photosynthates. For more details of the plant chamber, see section below. The effect of low CO<sub>2</sub> concentration on plant photosynthesis was previously checked on the same specimen during the previous day by measuring gas exchange at controlled cuvette CO<sub>2</sub> concentration (C<sub>a</sub>) between 30 and 90  $\mu\text{mol mol}^{-1}$ .

## Air-Coupled Ultrasonic Measurements

Two attached mature leaves per plant from three plants were selected and marked at the beginning of the experiment in order to perform all the pd and md ultrasonic measurements systematically on the same leaves. Magnitude and phase of the transmission coefficient were measured in the frequency domain (Sancho-Knapik et al., 2012). Then, in real time, the computer program adjusted theoretical curves to the measured curves of magnitude and phase and gave the value of the resonant frequency associated with the maximum transmittance at the peak curve ( $f$ , Hz) (Sancho-Knapik et al., 2010, 2012). One ultrasonic measurement was taken between 30 and 60 s. Afterward each value of  $f$  was divided by the value obtained before dawn at the beginning of the experiment when the plants were well watered ( $f_0$ , Hz). The  $f/f_0$  (non-dimensional) associated with the maximum transmittance at the peak curve was then obtained (Sancho-Knapik et al., 2011).

The air-coupled ultrasonic system used to obtain the resonant frequency of the leaves in this study was a more portable and easy-to-handle device (Álvarez-Arenas et al., 2016) compared to the one used in previous physiological studies (Sancho-Knapik et al., 2013a,b). The new device (Figure 1) consists in one pair of air-coupled transducers embedded in a U-shaped holder which was connected to a small pulser/receiver and to a laptop. The transducers were developed, designed and built at the Spanish

National Research Council with a center frequency of 650 kHz, frequency band of 350–950 kHz and area diameter of 20 mm (see Álvarez-Arenas, 2004 for further details). The U-shaped holder maintains the transducers facing each other at a distance of 20 mm providing the necessary robustness that can be easily manipulated without affecting the integrity of the signal. The holder also had a slot in which leaves could be easily positioned between the transducers for the measurements (see Álvarez-Arenas, 2013 and Fariñas et al., 2014 for further details). The pulser/receiver is a commercial device (ULTRASCOPE USB, Dasel Sistemas, Madrid, Spain) which was used to drive the transmitter transducer with a semicycle of square wave (200 V amplitude), tuned to the transducers centre frequency, to amplify (40 dB) the electrical signal provided by the receiver transducer and to digitize this received signal for further processing. It includes pass-band digital (filtering) and extraction of the Fourier transform (using a built-in FFT algorithm). The measurement process was controlled via a graphical user interface (GUI) managed in LABVIEW and also designed by the Spanish National Research Council for this purpose.

## Water Potential, Gas Exchange and Relative Water Content

Predawn and midday leaf water potentials ( $\Psi^{pd}$  and  $\Psi^{md}$ , MPa) were measured in one mature leaf per plant of *V. vinifera* with a Scholander pressure chamber following the methodological procedure described by Turner (1988). Briefly, in this technique a leaf was cut and placed in the pressure chamber with the cut end of the petiole just protruding from the chamber. The pressure inside the chamber was gradually increased by compressed nitrogen gas until the sap just returned to the severed ends of the xylem vessels. In this moment the pressure inside the chamber was recorded and taken as the value of water potential with the opposite sign. Net CO<sub>2</sub> uptake ( $A$ , mol CO<sub>2</sub> m<sup>-2</sup> s<sup>-1</sup>) and  $g_s$  (mmol H<sub>2</sub>O m<sup>-2</sup> s<sup>-1</sup>) were measured in two mature leaves per plant located along the middle of the stem with a portable gas exchange system (CIRAS-2, PP-Systems, Herts, UK). Measurements were performed at controlled cuvette CO<sub>2</sub> concentration (C<sub>a</sub> = 400 mol mol<sup>-1</sup>), PPFD incident on the leaf surface [ $\sim$ 1300 and 1800 mol photons m<sup>-2</sup> s<sup>-1</sup> at em and md, respectively] and ambient relative humidity. RWC was calculated at the beginning and the end of the drought period as a ratio of the difference between leaf fresh weight (FW) minus leaf dry weight (DW) and the difference between leaf turgid weight (TW) minus leaf DW. To obtain RWC, 5 discs per leaf (1.8 cm in diameter) from one half of each blade from two leaves per plant were obtained with a cork borer and subsequently weighed (FW). Afterward discs were introduced in a stove (70°C, 72 h) to obtain DW. The other half of the blade was rehydrated to full turgor by cutting carefully their petioles and submerging them in distilled water. Leaves were wrapped in plastic seal and stored in the fridge overnight. TW was then obtained from 5 disks per leaf.

## Pressure-Volume Curves

Pressure-Volume (P-V) curves were determined using a Scholander pressure chamber following the free-transpiration

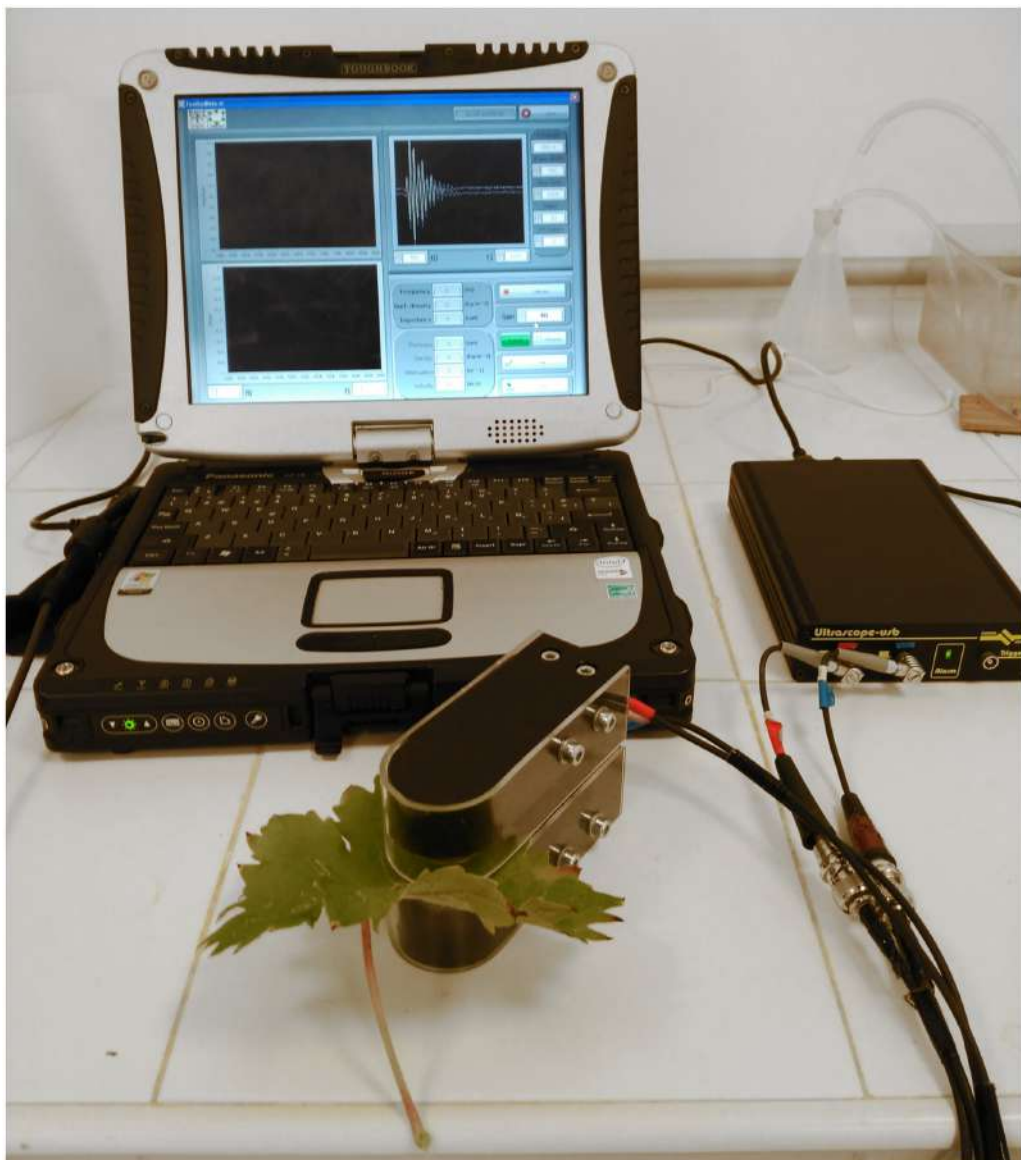


**FIGURE 1 | Schematic picture of the portable air-coupled broadband ultrasonic device.**

method described in previous studies (Turner, 1988; Dreyer et al., 1990). The weight and water potential were measured at different levels of RWC, starting at full turgor (TW) and until close to  $-2.5$  MPa were reached. Two leaves per plant were collected at pd from well watered plants. Their petioles were carefully cut and submerged in distilled water until full rehydration. Afterward, leaves were wrapped in plastic seal and left overnight in the refrigerator. After the measurements, leaf DW was obtained by keeping the plant material in a stove ( $70^{\circ}\text{C}$ , 72 h). RWC was then calculated as explained above being FW the sample fresh weight at any moment. Additionally, ultrasounds measurements were simultaneously performed in order to relate the values of turgor pressure ( $P$ ) derived from P-V curves with  $f/f_0$ .

### Leaf Sugars Analysis and Osmolality

Two leaves per plant of three different plants were collected at pd, at em and at md from well watered plants (at the beginning of the experiment) and from drought stressed plants (just before rewetting). Leaves were cut from the plants and were introduced in glass tubes closed hermetically and kept in ice for leaf preservation. Immediately after, tubes were carried to the laboratory and were stored in a freezer at  $-80^{\circ}\text{C}$  until analysis. To obtain the expressed leaf sap, frozen leaves were easily broken with a glass rod and they were centrifuged at 5000 rpm for 20 min (Yu et al., 1999). For sugars analysis, 20  $\mu\text{L}$  of the expressed sap extract was filtered by 0.45  $\mu\text{m}$  nylon filters and injected in a HPLC 360 (Kontron, Milan, Italy), equipped with a double piston pump, self-sampler, and regulated furnace at  $40^{\circ}\text{C}$ . The column

used was a 250 mm × 4.6 mm i.d., 5 mm, Kromasil Amine. The mobile phase was an isocratic elution of acetonitrile:water (75/25). Detection of sugars (fructose, glucose, and sucrose) was based on a liquid chromatographic method (AOAC, 1990) using a differential refractive index (RI) detector model ERC-7512 (Erma Inc., Tokyo, Japan) at 40°C temperature. The linear range for the concentration determination of each compound was 0.05–2 g/100 ml. Identification of chromatographic peaks was based on retention times by comparison with known standards (Merck, Darmstadt, Germany). An external calibration curve was prepared for each carbohydrate standard to calculate the amount of these compounds present in the leaf extract. The percentage weight:volume (% w:v) of sugars (fructose, glucose and sucrose) was finally obtained. On the other hand, another aliquot (10 µl) was used for measuring the osmolality (mmol Kg<sup>-1</sup>) of expressed sap of em and md samples with a calibrated vapor pressure osmometer (Wescor Vapro model 5500, Wescor, Logan, UT). Osmotic potential of the expressed sap was then calculated from the osmolality using the Van't Hoff equation (Callister et al., 2006).

## Plant Chamber

The chamber consisted of a Teflon FEP (Fluorinated Ethylene Propylene copolymer) film rolled and stapled into a wood rectangular frame (80 cm × 80 cm × 150 cm). A tape was used to seal the chamber and a 10-cm<sup>2</sup> hole was left in one of the upper corners to have an open flow. Teflon FEP was used because of its low permeability to liquids and gasses and its excellent transmission in the infrared and visible range of the solar spectrum (Liu et al., 2000). The plant chamber was screwed on a wood base (100 cm × 100 cm) where a few holes were cut to accommodate the plant stem (3.8 cm in diameter) and the air inlet tubes (10 mm in diameter). The base was then cut in half through the stem opening so that it could be moved on and off the plant. Two chest-latches held the base together during operation. A sleeve of sealed-cell foam was placed around the plant stem. The foam was slightly larger in diameter than the opening for the vine stem, enabling the chamber base to compress the sleeve and form a tight seal around the stem. This design separated the plant from the potting soil to eliminate the effects of soil and root respiration on CO<sub>2</sub> determinations (Miller et al., 1996). Finally, the joining between the chamber and the base was sealed with a plastic adhesive tape.

The air-supply system consisted of an air compressor (model LX 108, Atlas Copco AB, Stockholm, Sweden) with an output of c.a. 2000 l/min and a maximum pressure of 10 bar. This compressor was attached to a "T" connector through an 8-mm-i.d. polyamide tube. From the connector, two polyamide tubes ended in two clear acrylic pipes (38-mm-i.d., and 1.30 m in length) that were filled up with soda lime and molecular sieve (90:10) in order to lower the air CO<sub>2</sub> concentration inside the chamber. Two more polyamide tubes connected the end of the pipes to the base of the plant chamber. CO<sub>2</sub> concentration was measured during the experiment with a Carbon Dioxide Probe (GMP343, Vaisala CARBOCAP, Helsinki, Finland) obtaining concentrations levels inside the chamber between 40 and 80 ppm. Two small electric fans (12 cm × 12 cm × 3.8 cm) were located on

the wood base to stir the air throughout the chamber. Finally, a small rocking piston (model ROA-P201-BN; Gast Manufacturing Inc., Benton Harbor, MI, USA) with an output of 35 l/min and a maximum pressure of 6.9 bar was used to recirculate the chamber air through another acrylic pipe filled with silica gel in order to dry the chamber air and avoid a water-saturated atmosphere.

## Statistical Analysis

Relationships between mean values of  $f/f_0$  and water potential obtained at predawn ( $f/f_0^{pd}$ ,  $\Psi^{pd}$ ) and at md ( $\Psi^{md}$ ,  $f/f_0^{md}$ ) were adjusted to a linear function. One-way ANOVAs were performed to compare  $\Psi$ ,  $f/f_0$ ,  $A$ ,  $g_s$ , RWC,  $\pi$  and sugars concentration among the different times of the day (pd, em, and md) for plants well watered and drought stressed plants just before rewetting. Multiple comparisons were carried out among the different times of the day using the *post hoc* Tukey's Honestly Significant Difference test. A Student's *t*-test was used to compare the same parameters between well watered and drought stressed plants. All statistical analyses were performed with the program SAS version 8.0 (SAS, Cary, NC, USA).

## RESULTS

The evolution of pd water potential ( $\Psi^{pd}$ ) and  $f/f_0$  ( $f/f_0^{pd}$ ) for *Vitis vinifera* cv. Grenache showed that plants started the drought period with values close to full turgor ( $\Psi^{pd} = -0.01 \pm 0.00$  MPa,  $f/f_0^{pd} = 1.00 \pm 0.00$ ) (Figure 2). Six days after the last watering,  $\Psi^{pd}$  and  $f/f_0^{pd}$  became slightly lower, reaching values of  $-0.06 \pm 0.03$  MPa and  $0.994 \pm 0.007$  respectively. From here,  $\Psi^{pd}$  and  $f/f_0^{pd}$  dropped to  $-1.14 \pm 0.05$  MPa and  $0.872 \pm 0.014$ , respectively, at the end of the drought period. Two days after rewetting, values of  $\Psi^{pd}$  and  $f/f_0^{pd}$  became similar to those obtained at the beginning of the experiment. Midday measurements for water potential and ultrasounds showed a similar trend than that found at pd (Figure 2). Thus, plants experienced a slight decrease of  $\Psi^{md}$  and  $f/f_0^{md}$  during the first days of the experiment followed by a drop at the end of the dry period and a recovery to the initial values after rewetting. Regarding gas exchange measurements, plants started the drought period with values of  $A$  and  $g_s$  at em of  $13.0 \pm 0.5$  mol CO<sub>2</sub> m<sup>-2</sup> s<sup>-1</sup> and  $148.8 \pm 17.1$  mmol H<sub>2</sub>O m<sup>-2</sup> s<sup>-1</sup>, respectively (Figure 3). The values of  $A$  and  $g_s$  measured at md at the beginning of the experiment were very similar than those measured at em (Figure 3). These values remained practically constant at em and md during the first 6 days of the experiment. Since this day, both  $A$  and  $g_s$  started to decline, especially at md, until they reached values close to zero at md (Figure 3). A recovery was observed at em and md two days after rewetting, with values of  $A$  and  $g_s$  at em of  $10.98 \pm 0.54$  mol CO<sub>2</sub> m<sup>-2</sup> s<sup>-1</sup> and  $96.2 \pm 8.1$  mmol H<sub>2</sub>O m<sup>-2</sup> s<sup>-1</sup>, respectively (Figure 3).

Plants well watered – at the beginning of the drought period – did not show statistically significant differences at  $p < 0.05$  between pd and md for  $f/f_0$  and RWC (Figure 4). However, significative variations between pd and md ( $p < 0.05$ ) were found for  $\Psi$  (from  $-0.07 \pm 0.02$  to  $-0.84 \pm 0.12$  MPa) and sugars (from

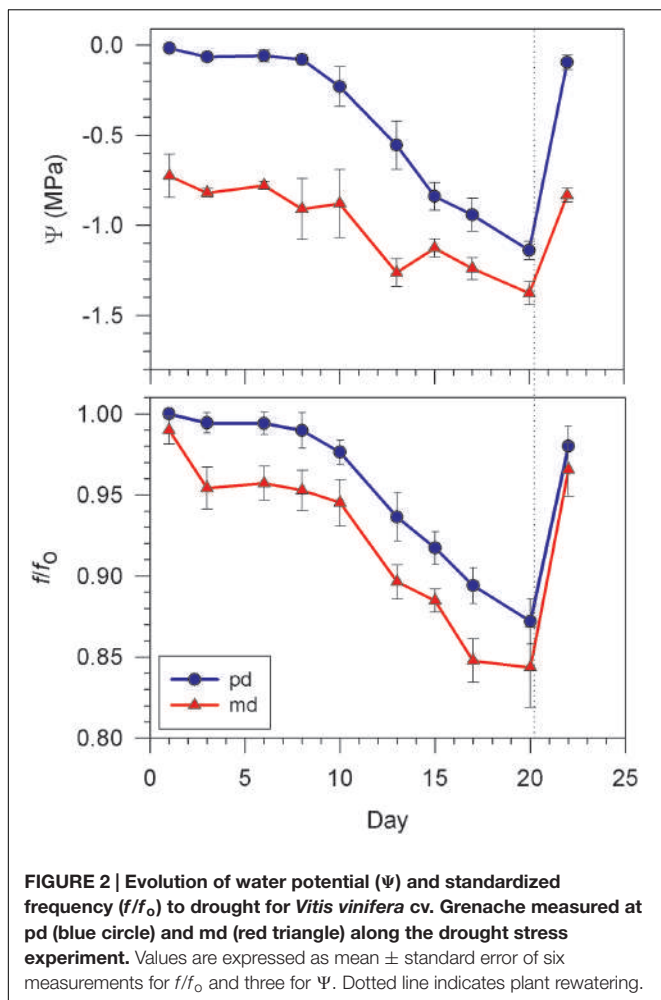


**FIGURE 2 |** Evolution of water potential ( $\Psi$ ) and standardized frequency ( $f/f_0$ ) to drought for *Vitis vinifera* cv. Grenache measured at pd (blue circle) and md (red triangle) along the drought stress experiment. Values are expressed as mean  $\pm$  standard error of six measurements for  $f/f_0$  and three for  $\Psi$ . Dotted line indicates plant rewatering.

$1.99 \pm 0.06$  to  $3.17 \pm 0.23$  in % w:v) (Figure 4). Differences in  $\pi$  obtained from the osmolality of the expressed sap were also found between em and md ( $p < 0.05$ ) (Table 1). On the other hand, at the end of the drought period plants did not show statistically significant differences at  $p < 0.05$  between pd, em, and md for  $f/f_0$ , RWC,  $\Psi$ , sugars (Figure 4) and between em and md for  $\pi$  (Table 1). In other words, although  $f/f_0$  and RWC did not show changes between pd and md neither for well watered nor for drought stressed plants, plants well watered showed a great decrease in  $\Psi$  and a great increase in sugars between pd and md when compared to drought stressed plants (Figure 4).

Two linear relationships between  $f/f_0$  and  $\Psi$  at pd and md were obtained with the values of both parameters measured during the drought cycle (Figure 5;  $R^2 = 0.99$ ,  $p < 0.001$  for pd and  $R^2 = 0.91$ ,  $p < 0.001$  for md). It was observed that a decrease in  $f/f_0$  was associated with a decrease in  $\Psi$  and a convergence between the relationships at pd and at md toward lower values of  $f/f_0$ . In addition, Figure 5 shows that for a given value of  $f/f_0$  there was a corresponding value of  $\Psi$  at pd and a different value at md. The difference between the two values of water potential for a given  $f/f_0$  ( $\delta$  was related to the value of net  $\text{CO}_2$  uptake measured at midday ( $A^{\text{md}}$ ) (Figure 6). This relationship showed that the

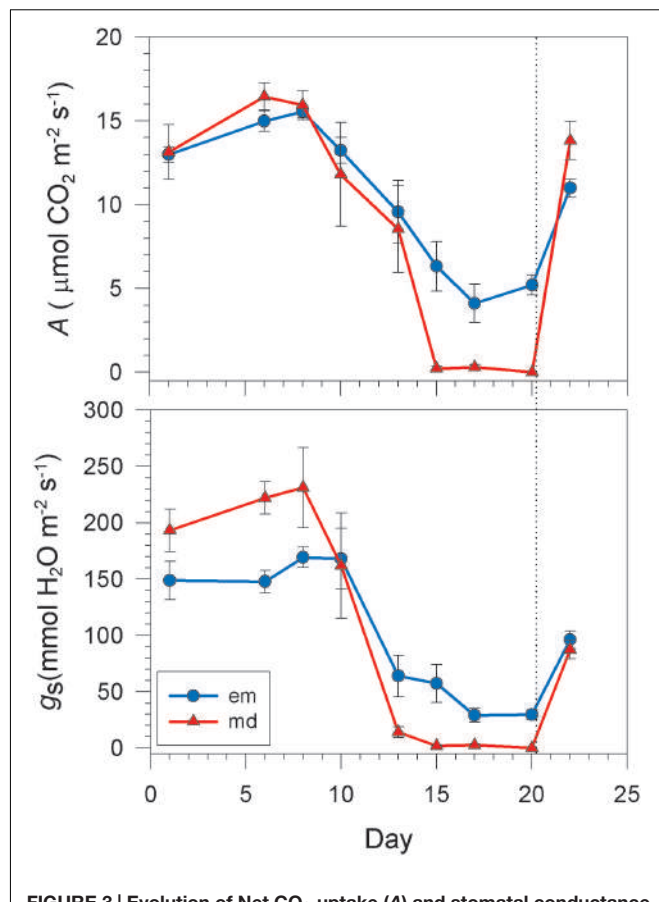


**FIGURE 3 |** Evolution of Net  $\text{CO}_2$  uptake ( $A$ ) and stomatal conductance ( $g_s$ ) to drought for *Vitis vinifera* cv. Grenache measured at early morning (blue circle) and md (red triangle) along the drought stress experiment. Values are expressed as mean  $\pm$  standard error of six measurements.

highest value of  $\delta$  ( $0.4 \pm 0.1$  MPa) occurred at the time of the highest value of  $A^{\text{md}}$  ( $16.2 \pm 0.2$  mol  $\text{CO}_2 \text{ m}^{-2} \text{ s}^{-1}$ ). When  $A^{\text{md}}$  became lower due to drought stress,  $\delta$  also decreased, reaching values of zero when  $A^{\text{md}}$  also reached zero.

Finally, the grapevine plant forced to live for 1 day under a  $\text{CO}_2$  concentration (between 40 and 80 mol  $\text{mol}^{-1}$ ) lower than the atmospheric one ( $p < 0.05$ ) showed statistically significant differences at  $p < 0.05$  between pd and md for  $\Psi$  (from  $-0.11 \pm 0.01$  to  $-0.56 \pm 0.05$  MPa) and  $f/f_0$  (from  $0.990 \pm 0.002$  to  $0.939 \pm 0.006$ ) (Table 2). However, the concentration of leaf sap sugars under low  $\text{CO}_2$  concentration did not show statistically significant differences between pd and md (Table 2). The measurement of gas exchange at md under low  $\text{CO}_2$  concentrations during the previous day confirmed the absence of net  $\text{CO}_2$  uptake ( $-0.2 \pm 0.6$  mol  $\text{CO}_2 \text{ m}^{-2} \text{ s}^{-1}$ ).

## DISCUSSION

The air-coupled broad-band ultrasonic spectroscopy has proved useful in this study to monitor how changes in the  $f/f_0$  varied with water potential ( $\Psi$ ) in attached transpiring leaves of *Vitis*

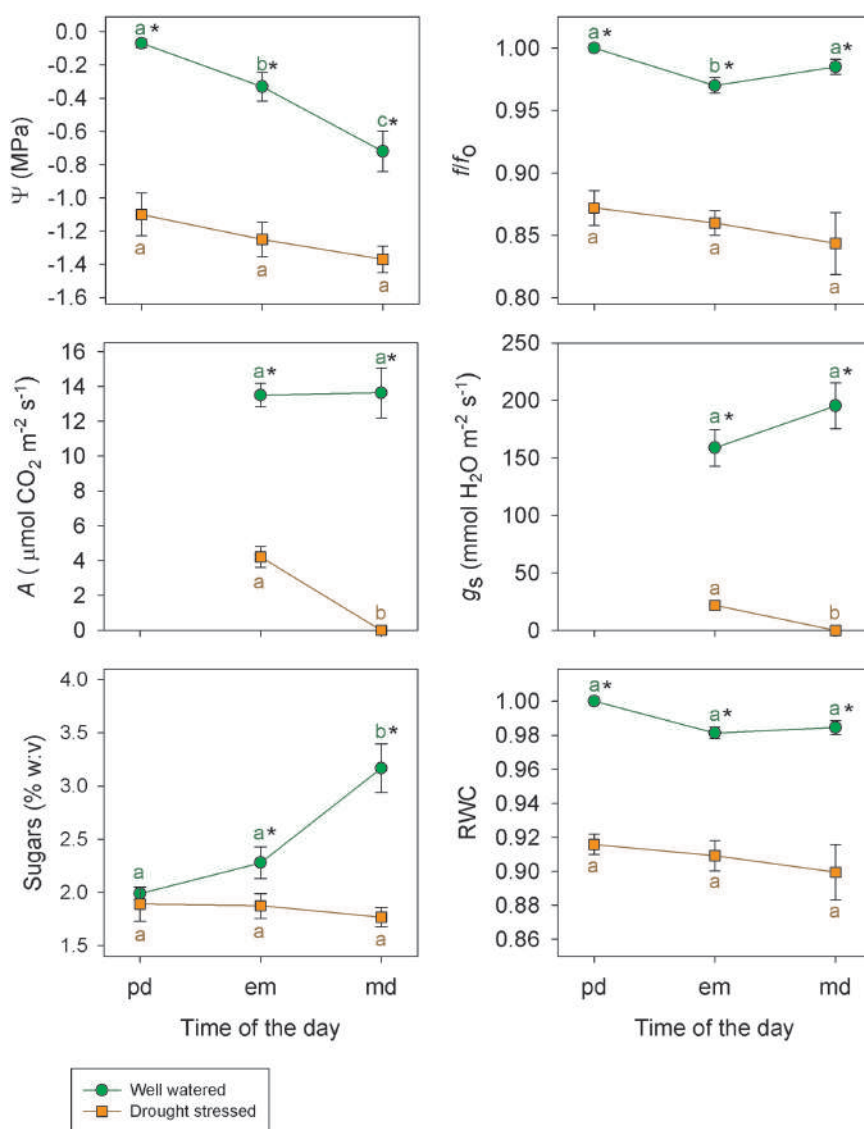


**FIGURE 4 |** Water potential ( $\Psi$ ), standardized frequency ( $f/f_0$ ), Net  $\text{CO}_2$  uptake ( $A$ ), stomatal conductance ( $g_s$ ), percentage weight:volume (% w:v) of leaf sap sugars (fructose, glucose and sucrose) and relative water content (RWC) for well watered (green circle) and drought stressed (orange square) plants of *Vitis vinifera* cv. Grenache during three moments of the day: pd, em, and md. Measurements on well watered and drought stressed plants were taken the first and the last day of the drought period, respectively. Values are expressed as mean  $\pm$  standard error. Asterisks indicate statistically significant differences between well watered and drought stressed plants (Student's  $t$ -test,  $p < 0.05$ ). Different letters indicate significant differences among pd, em, and md for well watered and drought stressed plants (Tukey test,  $p < 0.05$ ).

*vinifera*. When plants became drought stressed,  $\Psi$  and  $f/f_0$  varied simultaneously (Figure 2) resulting in good correlations between the two variables (Figure 5), as shown for detached leaves during previous dehydration studies (Sancho-Knapik et al., 2010, 2013a). The development of a new smaller and easy-to-use ultrasonic device used in this work provided the possibility of measuring attached leaves under field conditions, in contrast to previous studies made under laboratory conditions with a more complex and non-portable apparatus (Sancho-Knapik et al., 2010, 2011, 2013a,b). It should be noted that, at present, this device cannot be used for plant species with small leaves due to the size of

the transducers. This is a matter that deserves further technical improvements.

The methodology used in this study is based in two main assumptions which were validated by the results obtained. On the one hand, the ultrasonic technique was only measuring one of the components of  $\Psi$  the turgor pressure ( $P$ ), and on the other hand, *Vitis vinifera* plants developed diurnal osmotic adjustments that facilitated the maintenance of leaf turgor during md. Both assumptions have emerged from the occurrence of two different  $\Psi$  values, one at pd and other at md, for a given value of  $f/f_0$  (Figure 5). Regarding the first assumption, the positive

**TABLE 1 |** Osmotic potential ( $\pi$ , MPa) obtained from the osmolality of the expressed leaf sap measured on well watered and drought stressed plants of *Vitis vinifera* cv. Grenache during two moments of the day: em and md.

	em	md
$\pi$ (Well watered)	$-1.17 \pm 0.05$ a	$-1.33 \pm 0.06$ b*
$\pi$ (Drought stressed)	$-1.19 \pm 0.05$ a	$-1.18 \pm 0.05$ a

Measurements on well watered and drought stressed plants were taken the first and the last day of the drought period, respectively. Values are expressed as mean  $\pm$  standard error. Asterisks indicate statistically significant differences between well watered and drought stressed plants (Student's t-test,  $p < 0.05$ ). Different letters indicate significant differences among em and md for well watered and drought stressed plants (Tukey test,  $p < 0.05$ ).

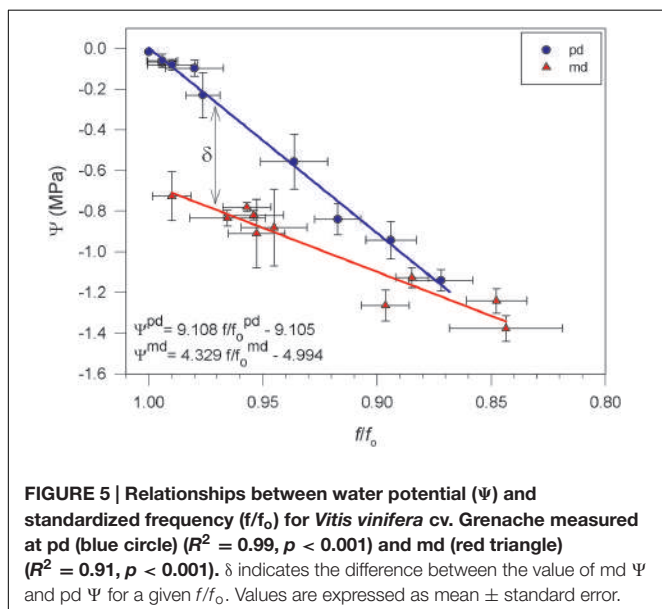


**FIGURE 5 |** Relationships between water potential ( $\Psi$ ) and standardized frequency ( $f/f_0$ ) for *Vitis vinifera* cv. Grenache measured at pd (blue circle) ( $R^2 = 0.99$ ,  $p < 0.001$ ) and md (red triangle) ( $R^2 = 0.91$ ,  $p < 0.001$ ).  $\delta$  indicates the difference between the value of md  $\Psi$  and pd  $\Psi$  for a given  $f/f_0$ . Values are expressed as mean  $\pm$  standard error.

linear relationship found between  $P$  and  $f/f_0$  (Figure 7) showed that a higher  $f/f_0$  value can be related to an increased  $P$ -value, independently of the time of the day when measurements were carried out (i.e., pd or md). Taking this into account, plants with low values of water potential at md ( $\Psi^{md}$ ) but with relatively higher values of  $f/f_0^{md}$ , would have  $P$ -values close to full turgor. Therefore, the difference between both  $\Psi$  values ( $\delta$ ) could not be associated with changes in  $P$  because  $f/f_0$  remained constant.

Concerning the second assumption, we found that  $\delta$  was dependent on net  $\text{CO}_2$  uptake ( $A$ ) (Figure 6), which could be used as a rough estimator of photosynthetic activity. To the extent of our knowledge, this is indeed the first time in which a quantitative relationship between  $\delta$  and  $A$  has been described, and this relation might change for other cultivars (e.g., Syrah, data not shown) or species with different photosynthetic rates. Considering (i) that  $P$  was not the factor leading to the occurrence of  $\delta$  in Figure 5, and (ii) the actual existence of a relationship between  $\delta$  and  $A$ , we propose that the remaining component of  $\Psi$ , i.e., the osmotic potential ( $\pi$ ), may have induced the decrease of  $\Psi^{md}$  with respect to  $\Psi^{pd}$  through the synthesis of carbohydrates. Indeed, we have found a significant decrease in  $\pi$  between em and md

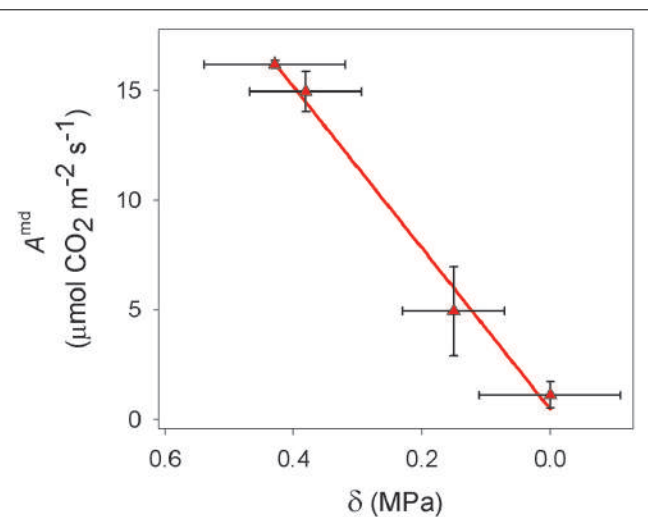


**FIGURE 6 |** Relationship of the difference between the value of md and pd water potential for a given standardized frequency ( $\delta$ ) and Net  $\text{CO}_2$  uptake measured at midday ( $A^{md}$ ) for *Vitis vinifera* cv. Grenache. Values are expressed as mean  $\pm$  standard error.

**TABLE 2 |** Leaf water potential ( $\Psi$ ), standardized frequency ( $f/f_0$ ), net  $\text{CO}_2$  uptake ( $A$ ) and percentage weight:volume (% w:v) of leaf sap sugars measured on well watered plants of *Vitis vinifera* cv. Grenache at low  $\text{CO}_2$  concentration ( $C_a = 40\text{--}80 \mu\text{mol mol}^{-1}$ ).

	pd	md
$\Psi$ (MPa)	$-0.11 \pm 0.01$	$-0.56 \pm 0.05$
$f/f_0$	$0.990 \pm 0.002$	$0.939 \pm 0.006$
$A$ ( $\mu\text{mol CO}_2 \text{ m}^{-2} \text{ s}^{-1}$ )	0	$-0.2 \pm 0.6$
Sugars (% w:v)	$5.31 \pm 0.25$	$4.98 \pm 0.19$

Measurements were performed at pd and md. Values are expressed as mean  $\pm$  standard error ( $n = 10$ ). For sugar analysis, no significant differences ( $P < 0.05$ ) were found between pd and md.

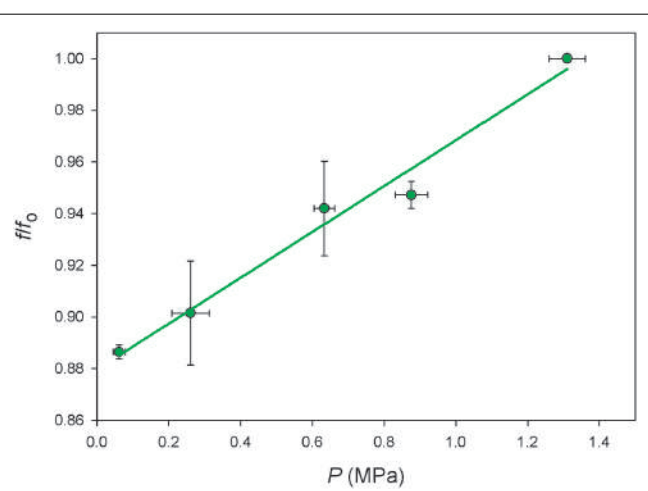


**FIGURE 7 |** Relationship between turgor pressure ( $P$ ) and standardized frequency ( $f/f_0$ ) measured on six leaves of *Vitis vinifera* cv. Grenache ( $R^2 = 0.98$ ,  $p < 0.01$ ). Values are expressed as mean  $\pm$  standard error.

estimated with the osmometer (**Table 1**), despite the discrepancy between this and other methods for the measurement of  $\pi$  (Callister et al., 2006). These dynamic changes in  $\pi$  can be explained through the daily accumulation of solutes due to photosynthesis in order to maintain  $P$  (i.e., the so-called “diurnal osmotic adjustment” according to Acevedo et al., 1979). The solutes that can lower  $\pi$  are divided in four classes (Sanders and Arndt, 2012): (i) sugars, that are considered the main component for the change in diurnal osmotic adjustment (Acevedo et al., 1979); (ii) organic acids, which could represent less than  $-0.01$  MPa according to Acevedo et al. (1979); (iii) inorganic ions which play a minor influence in osmotic adjustment (Warren et al., 2011) and (iv) free amino acids (specially proline) which mainly increase at higher drought stress levels in prolonged dry periods (Irigoyen et al., 1992; Aranjuelo et al., 2011; Masoudi-Sadaghiani et al., 2011). In this study, the high photosynthetic activity measured in fully irrigated plants induced the production and accumulation of sugars at md (**Figure 4**). These solutes may have induced a decrease in  $\pi$  between pd and md (the diurnal osmotic adjustment), which was noticeable due to the decrease of the water potential at midday ( $\Psi^{md}$ ) with respect to that measured at predawn ( $\Psi^{pd}$ ) without any significant reduction in  $f/f_0$  and RWC (**Figure 4**). That is, water loss by transpiration did not induce a significant reduction in  $\Psi^{md}$ . Furthermore, when RWC at md in well watered plants (**Figure 4**) is expressed in terms of the value of  $\Psi$  given by the P-V curves (data not shown), this value ( $-0.30 \pm 0.06$  MPa) is less negative than the one measured during the experiment ( $-0.72 \pm 0.12$  MPa, **Figure 4**). The difference between both values may then represent the diurnal osmotic adjustment due to the effect of solute accumulation due to photosynthesis. Moreover, this difference is similar to the one estimated with sugar concentrations for well watered plants (**Figure 4**) using the equation of Acevedo et al. (1979), which yielded a theoretical change of ca.  $0.3$  MPa in the osmotic potential between pd and md. The adjustment observed was larger at the beginning of the experiment, when plants had higher values of net CO<sub>2</sub> uptake ( $A$ ) and increased sugar concentrations (**Figures 3** and **4**, respectively) than at the end of the drought period when net CO<sub>2</sub> assimilation was almost negligible (**Figure 3**). Consequently, in drought stressed plants it was not detected neither an accumulation of sugars in leaves (**Figure 4**) nor an increment in  $\pi$  (**Table 1**) and, therefore,  $\Psi$  was not lowered between pd and md. In this situation, the expected values of  $\Psi$  based on the measurements of  $f/f_0^{md}$  corresponded with the measured  $\Psi^{md}$  values.

The measurements obtained from the experiment of a well-watered Grenache plant under low CO<sub>2</sub> concentration inside a chamber confirmed that changes in  $f/f_0$  were associated to changes in  $P$ . The low CO<sub>2</sub> concentration inside the plant chamber induced close-to-zero net CO<sub>2</sub> uptake. Despite pd values of sugar content higher than those seen in the previous experiment, here an accumulation of sugars at md was not seen (**Table 2**). Acevedo et al. (1979) also reported a lack of accumulation in sugars and

a lack of  $\pi$  diurnal change when a close-to-zero net CO<sub>2</sub> uptake was induced in sorghum leaves by artificial plant shading, suggesting an association between photosynthesis and the observed diurnal osmotic adjustment. Therefore, it is then logical to assume that in *V. vinifera* under low CO<sub>2</sub> concentration no decrease occurred in  $\pi$  between pd and md, leaving  $P$  as the only responsible component of the decrease in  $\Psi$ . Observed changes in  $\Psi^{md}$  were indeed very small and compared to those seen in water-stressed plants. Under these circumstances, measured values of  $f/f_0^{md}$  should reflect measured values in  $\Psi^{md}$  without the confounding factor of diurnal osmotic adjustment. Consistent with this idea, if  $f/f_0$  and  $\Psi$  values of the Grenache specimen at low CO<sub>2</sub> concentration measured at md (**Table 2**) are plotted over the relationships between  $f/f_0$  and  $\Psi$  for that appears in **Figure 5**, it can be observed that values at md from **Table 2** fitted the relationship obtained at pd.

It should be noted that, although the seasonal osmotic adjustment may be a common phenomenon in many plant species (Hsiao et al., 1976) including *V. vinifera* (Martorell et al., 2015), the diurnal osmotic adjustment has been studied and detected only in a few species during the last decades (Acevedo et al., 1979; Rada et al., 1985; Koroleva et al., 2002). This physiological response has been interpreted as an adaptive mechanism for plants that may experience drought stress by means of an active increase in the concentration of cell solutes that may maintain positive turgor potentials above thresholds for stomatal closure and growth cessation (Rada et al., 1985). In contrast with these previous studies that detected the osmotic adjustment through the direct measurement of  $\pi$  in the laboratory, our investigation has served to suggest this phenomenon on attached transpiring leaves under field conditions.

## CONCLUSION

This study demonstrates for the first time that plant water status of *V. vinifera* can be monitored on transpiring leaves under field conditions through the measurement of ultrasonic frequencies. Moreover, our results suggest the existence of a diurnal osmotic adjustment in this species associated to sugars production, which plays a key role in the decrease found in  $\Psi$  between pd and md in well-watered plants. These facts, together with the possibility of measuring ultrasonic frequencies continuously (Fariñas et al., 2014) make the ultrasonic technique a promising tool to be used in plant sciences.

## AUTHOR CONTRIBUTIONS

DS-K, HM, JP-P, and EG-P conceived the study and participated in its design. MF and TA-A developed and applied the ultrasonic system. All authors analyzed and interpreted the data. DS-K

drafted the manuscript and JP-P, MM, TA-A and EG-P critically revised the manuscript. All authors read and approved the final version of the manuscript.

## FUNDING

This study was supported by the Spanish Ministry of Economy and Competitiveness (IPT-2012-1022-310000) and by Gobierno

de Aragón (research group H38). Work of DS-K is supported by a DOC INIA contract co-funded by INIA and ESF.

## ACKNOWLEDGMENT

The authors are grateful to José Sánchez for his help in the construction of the plant chamber.

## REFERENCES

- Acevedo, D., Fereres, E., Hsiao, T. C., and Henderson, D. W. (1979). Diurnal growth trends, water potential, and osmotic adjustment of maize and sorghum leaves in the field. *Plant Physiol.* 64, 476–480. doi: 10.1104/pp.64.3.476
- Álvarez-Arenas, T. E. G. (2004). Acoustic impedance matching of piezoelectric transducers to the air. *IEEE Trans. Ultrason. Ferroelectr. Freq. Control* 51, 624–633. doi: 10.1109/TUFFC.2004.1320834
- Álvarez-Arenas, T. E. G. (2013). Air-coupled piezoelectric transducers with active polypropylene foam matching layer. *Sensors* 13, 5996–6013. doi: 10.3390/s130505996
- Álvarez-Arenas, T. E. G., Gil-Pelegrin, E., Ealo Cuello, J., Fariñas, M. D., Domingo Sancho-Knapik, D., Collazos Burbano, D. A., et al. (2016). Ultrasonic sensing of plant water needs for agriculture. *Sensors* 16:1089. doi: 10.3390/s16071089
- Álvarez-Arenas, T. E. G., Sancho-Knapik, D., Peguero-Pina, J. J., and Gil-Pelegrín, E. (2009). Noncontact and noninvasive study of plant leaves using air-coupled ultrasounds. *Appl. Phys. Lett.* 95:193702. doi: 10.1063/1.3263138
- AOAC (1990). “Sugars and sugar products,” in *Official Methods of Analysis*, 15th Edn, Vol. II, ed. K. Helrich (Arlington, Virginia, USA: Association of official analytical chemists Inc.).
- Aranjuelo, I., Molero, G., Erice, G., Avíce, J. C., and Nogue, S. (2011). Plant physiology and proteomics reveals the leaf response to drought in alfalfa (*Medicago sativa* L.). *J. Exp. Bot.* 62, 111–123. doi: 10.1093/jxb/erq249
- Callister, A. N., Arndt, S. K., and Adams, M. A. (2006). Comparison of four methods for measuring osmotic potential of tree leaves. *Physiol. Plant.* 12, 383–392. doi: 10.1111/j.1399-3054.2006.00652.x
- Chaves, M. M., Santos, T. P., Souza, C. R., Ortúñoz, M. F., Rodrigues, M. L., Lopes, C. M., et al. (2007). Deficit irrigation in grapevine improves water-use efficiency while controlling vigour and production quality. *Ann. Appl. Biol.* 150, 237–252. doi: 10.1111/j.1744-7348.2006.00123.x
- Chaves, M. M., Zarrouk, O., Francisco, R., Costa, J. M., Santos, T., Regalado, A. P., et al. (2010). Grapevine under deficit irrigation: hints from physiological and molecular data. *Ann. Bot.* 105, 661–676. doi: 10.1093/aob/mcq030
- Dreyer, E., Bousquet, F., and Ducrey, M. (1990). Use of pressure volume curves in water relation analysis on woody shoots: influence of rehydration and comparison of four European oak species. *Ann. Sci. For.* 47, 285–297. doi: 10.1051/forest:19900401
- Fariñas, M. D., Sancho-Knapik, D., Peguero-Pina, J. J., Gil-Pelegrín, E., and Gómez Álvarez-Arenas, T. (2014). Ultrasonic monitoring of plants response to environmental stimuli. *Ultrasound. Med. Biol.* 40, 2183–2194. doi: 10.1016/j.ultrasmedbio.2014.04.004
- Flexas, J., Galmés, J., Gallé, A., Gulías, J., Pou, A., Ribas-Carbo, M., et al. (2010). Improvement of water use efficiency in grapevines. *Aust. J. Grape Wine Res.* 16, 106–121. doi: 10.1111/j.1755-0238.2009.00057.x
- García-Mozo, H., Mestre, A., and Galán, C. (2010). Phenological trends in southern Spain: a response to climate change. *Agric. For. Meteorol.* 150, 575–580. doi: 10.1016/j.agrformet.2010.01.023
- Gibson, L. J., and Ashby, M. F. (1997). *Cellular Solids*, 2nd Edn. Cambridge: Cambridge University Press.
- Girma, S. F., and Krieg, D. R. (1992). Osmotic adjustment in sorghum. I. Mechanisms of diurnal osmotic potential changes. *Plant Physiol.* 99, 577–582. doi: 10.1104/pp.99.2.577
- Hsiao, T. C., Acevedo, E., Fereres, E., and Henderson, D. W. (1976). Water stress, growth and osmotic adjustment. *Philos. Trans. R. Soc. Lond. B Biol. Sci.* 273, 479–500. doi: 10.1098/rstb.1976.0026
- Irigoyen, J. J., Emerich, D. W., and Sanchez-Diaz, M. (1992). Water stress induced changes in concentrations of proline and total soluble sugars in nodulated alfalfa (*Medicago sativa*) plants. *Physiol. Plant.* 84, 55–60. doi: 10.1111/j.1399-3054.1992.tb08764.x
- Jones, H. G. (1990). Plant water relations and implications for irrigation scheduling. *Acta Hortic.* 278, 67–76. doi: 10.17660/ActaHortic.1990.278.4
- Jones, H. G. (2004). Irrigation scheduling: advantages and pitfalls of plant-based methods. *J. Exp. Bot.* 55, 2427–2436. doi: 10.1093/jxb/erh213
- Jones, H. G. (2007). Monitoring plant and soil water status: established and novel methods revisited and their relevance to studies of drought tolerance. *J. Exp. Bot.* 58, 119–130. doi: 10.1093/jxb/erl118
- Keller, M., Smithyman, R. P., and Mills, L. J. (2008). Interactive effects of deficit irrigation and crop load on Cabernet Sauvignon in an arid climate. *Am. J. Enol. Vitic.* 59, 221–234.
- Koide, R. T., Robichaux, R. H., Morse, S. R., and Smith, C. M. (1989). “Plant water status, hydraulic resistance and capacitance,” in *Plant Physiological Ecology*, eds R. W. Pearcy, J. Ehleringer, H. A. Mooney, and P. W. Rundel (London: Chapman and Hall), 161–184.
- Koroleva, O. A., Tomos, A. D., Farrar, J., and Pollock, C. J. (2002). Changes in osmotic and turgor pressure in response to sugar accumulation in barley source leaves. *Planta* 215, 210–219. doi: 10.1007/s00425-002-0744-2
- Liu, L., Hoogenboom, G., and Ingram, K. T. (2000). Controlled-environment sunlit plant growth chambers. *Crit. Rev. Plant. Sci.* 19, 347–375. doi: 10.1080/07352680091139268
- Martorell, S., Diaz-Espejo, A., Tomás, M., Pou, A., El Aou-ouad, H., Escalona, J. M., et al. (2015). Differences in water-use efficiency between two *Vitis vinifera* cultivars (Grenache and Tempranillo) explained by the combined response of stomata to hydraulic and chemical signals during water stress. *Agric. Water Manag.* 156, 1–9. doi: 10.1016/j.agwat.2015.03.011
- Masoudi-Sadaghiani, F., Abdollahi Mandoulakani, B., Zardoshti, M. R., Rasouli-Sadaghiani, M. H., and Tavakoli, A. (2011). Response of proline, soluble sugars, photosynthetic pigments and antioxidant enzymes in potato (*Solanum tuberosum* L.) to different irrigation regimes in greenhouse condition. *Aust. J. Crop Sci.* 5, 55–60.
- Medrano, H., Escalona, J. M., Cifre, J., Bota, J., and Flexas, J. (2003). A ten-year study on the physiology of two Spanish grapevine cultivars under field conditions: effects of water availability from leaf photosynthesis to grape yield and quality. *Funct. Plant Biol.* 30, 607–619. doi: 10.1071/FP02110
- Miller, D. P., Howell, G. S., and Flore, J. A. (1996). A whole-plant, open, gas-exchange system for measuring net photosynthesis of potted woody plants. *Hortscience* 31, 944–946.
- Netzer, Y., Yao, C., Shenker, M., Bravdo, B., Schwartz, A., and Cohen, S. (2005). Water consumption of “superior” grapevines grown in a semiarid region. *Acta Hortic.* 689, 399–405. doi: 10.17660/ActaHortic.2005.689.47
- Pou, A., Gulias, J., Moreno, M., Tomas, M., Medrano, H., and Cifre, J. (2011). Cover cropping in *Vitis vinifera* L. cv Manto Negro vineyards under Mediterranean conditions: effects on plant vigour, yield and grape quality. *J. Int. Sci. Vigne Vin* 45, 223–234.
- Rada, F., Goldstein, G., Azocar, A., and Meinzer, F. (1985). Daily and seasonal osmotic changes in a tropical treeline species. *J. Exp. Bot.* 36, 989–1000. doi: 10.1093/jxb/36.6.989
- Richter, H. (1978). A diagram for the description of water relations in plant cells and organs. *J. Exp. Bot.* 29, 1197–1203. doi: 10.1093/jxb/29.5.1197
- Romero, P., Fernández-Fernández, J. I., and Martínez-Cutillas, A. (2010). Physiological thresholds for efficient regulated deficit-irrigation management in winegrapes grown under semiarid conditions. *Am. J. Enol. Vitic.* 61, 300–312.

- Sancho-Knapik, D., Álvarez-Arenas, T., Peguero-Pina, J. J., Fernandez, V., and Gil-Pelegrín, E. (2011). Relationship between ultrasonic properties and structural changes in the mesophyll during leaf dehydration. *J. Exp. Bot.* 62, 3637–3645. doi: 10.1093/jxb/err065
- Sancho-Knapik, D., Álvarez-Arenas, T., Peguero Pina, J. J., and Gil-Pelegrín, E. (2010). Air-coupled broadband ultrasonic spectroscopy as a new non-invasive and non-contact method for the determination of leaf water status. *J. Exp. Bot.* 61, 1385–1391. doi: 10.1093/jxb/erq001
- Sancho-Knapik, D., Calás, H., Peguero-Pina, J. J., Ramos-Fernández, A., Gil-Pelegrín, E., and Álvarez-Arenas, T. (2012). Air-coupled ultrasonic resonance spectroscopy for the study of the relationship between plant leaves' elasticity and their water content. *IEEE Trans. Ultrason. Ferroelectr. Freq. Control* 59, 319–325. doi: 10.1109/TUFFC.2012.2194
- Sancho-Knapik, D., Peguero-Pina, J. J., Medrano, H., Fariñas, M. D., Álvarez-Arenas, T., and Gil-Pelegrín, E. (2013a). The reflectivity in the S-Band and the broadband ultrasonic spectroscopy as new tools for the study of water relations in *Vitis vinifera* L. *Physiol. Plant.* 148, 512–521. doi: 10.1111/ppl.12007
- Sancho-Knapik, D., Peguero-Pina, J. J., Medrano, H., Fariñas, M. D., Álvarez-Arenas, T., and Gil-Pelegrín, E. (2013b). Ultrasonic spectroscopy allows a rapid determination of the relative water content at the turgor loss point. A comparison with pressure-volume curves in 13 woody species. *Tree Physiol.* 33, 695–700. doi: 10.1093/treephys/tpt052
- Sanders, G. J., and Arndt, S. K. (2012). "Osmotic adjustment under drought conditions," in *Plant Responses to Drought Stress*, ed. R. Aroca (Berlin: Springer-Verlag), 199–230.
- Tonietto, J., and Carboneau, A. (2004). A multicriteria climatic classification system for grape-growing regions worldwide. *Agric. For. Meterol.* 124, 81–97. doi: 10.1016/j.agrformet.2003.06.001
- Turner, N. C. (1988). Measurement of plant water status by pressure chamber technique. *Irrigation Sci.* 9, 289–308. doi: 10.1007/BF00296704
- Tyree, M. T. (1981). The relationship between the bulk modulus of elasticity of a complex tissue and the mean modulus of its cells. *Ann. Bot.* 47, 547–559.
- Tyree, M. T., and Jarvis, P. G. (1982). "Water in tissues and cells," in *Encyclopaedia of Plant Physiology, New Series*, Vol. 12b, eds O. L. Lange, P. S. Nobel, C. B. Osmond, and H. Ziegler (Berlin: Springer-Verlag), 33–77.
- Warren, C. R., Aranda, I., and Cano, F. J. (2011). Responses to water stress of gas exchange and metabolites in *Eucalyptus* and *Acacia* spp. *Plant Cell Environ.* 34, 1609–1629. doi: 10.1111/j.1365-3040.2011.02357.x
- Yu, Q., Tang, C., Chen, Z., and Kuo, J. (1999). Extraction of apoplastic sap from plant roots by centrifugation. *New Phytol.* 143, 299–304. doi: 10.1046/j.1469-8137.1999.00454.x
- Zhang, B. Z., Kang, S. Z., Zhang, L., Du, T. S., Li, S. E., and Yang, X. Y. (2007). Estimation of seasonal crop water consumption in a vineyard using Bowen ratio-energy balance methods. *Hydrol. Process.* 21, 3635–3641. doi: 10.1002/hyp.6568

**Conflict of Interest Statement:** The authors declare that the research was conducted in the absence of any commercial or financial relationships that could be construed as a potential conflict of interest.

Copyright © 2016 Sancho-Knapik, Medrano, Peguero-Pina, Mencuccini, Fariñas, Álvarez-Arenas and Gil-Pelegrín. This is an open-access article distributed under the terms of the Creative Commons Attribution License (CC BY). The use, distribution or reproduction in other forums is permitted, provided the original author(s) or licensor are credited and that the original publication in this journal is cited, in accordance with accepted academic practice. No use, distribution or reproduction is permitted which does not comply with these terms.



# Modeling Tree Growth Taking into Account Carbon Source and Sink Limitations

Amaury Hayat<sup>1\*</sup>, Andrew J. Hacket-Pain<sup>2,3</sup>, Hans Pretzsch<sup>4</sup>, Tim T. Rademacher<sup>5</sup> and Andrew D. Friend<sup>5\*</sup>

<sup>1</sup> Department of Pure Mathematics and Mathematical Statistics, Centre for Mathematical Sciences, University of Cambridge, Cambridge, UK, <sup>2</sup> Fitzwilliam College, Cambridge, UK, <sup>3</sup> St Catherine's College, Oxford, UK, <sup>4</sup> Technical University of Munich, Munich, Germany, <sup>5</sup> Department of Geography, University of Cambridge, Cambridge, UK

## OPEN ACCESS

### Edited by:

Alexander Bucksch,  
University of Georgia, USA

### Reviewed by:

Gerhard Buck-Sorlin,  
Agrocampus Ouest, France  
Simone Fatichi,  
ETH Zurich, Switzerland

### \*Correspondence:

Amaury Hayat  
amaury.hayat@cantab.net  
Andrew D. Friend  
adf10@cam.ac.uk

### Specialty section:

This article was submitted to  
Plant Biophysics and Modeling,  
a section of the journal  
*Frontiers in Plant Science*

**Received:** 21 September 2016

**Accepted:** 30 January 2017

**Published:** 21 March 2017

### Citation:

Hayat A, Hacket-Pain AJ, Pretzsch H, Rademacher TT and Friend AD (2017)  
Modeling Tree Growth Taking into Account Carbon Source and Sink Limitations. *Front. Plant Sci.* 8:182.  
doi: 10.3389/fpls.2017.00182

Increasing CO<sub>2</sub> concentrations are strongly controlled by the behavior of established forests, which are believed to be a major current sink of atmospheric CO<sub>2</sub>. There are many models which predict forest responses to environmental changes but they are almost exclusively carbon source (i.e., photosynthesis) driven. Here we present a model for an individual tree that takes into account the intrinsic limits of meristems and cellular growth rates, as well as control mechanisms within the tree that influence its diameter and height growth over time. This new framework is built on process-based understanding combined with differential equations solved by numerical method. Our aim is to construct a model framework of tree growth for replacing current formulations in Dynamic Global Vegetation Models, and so address the issue of the terrestrial carbon sink. Our approach was successfully tested for stands of beech trees in two different sites representing part of a long-term forest yield experiment in Germany. This model provides new insights into tree growth and limits to tree height, and addresses limitations of previous models with respect to sink-limited growth.

**Keywords:** tree growth, vegetation modeling, sink limitation, source limitation, height growth

## 1. INTRODUCTION

Forests are an important component of the global carbon cycle and are currently thought to be a major sink of atmospheric CO<sub>2</sub> (Bonan, 2008; Pan et al., 2011). Being able to predict the future responses of forests is therefore of great interest. Many models have been used to address this issue, but they are almost exclusively carbon source-driven, with plants at any particular location treated as a pool, or pools, of carbon mainly driven by photosynthesis (e.g., Cramer et al., 2001; Anav et al., 2013; Friend et al., 2014). However, it is likely that many other factors, such as the intrinsic limits of meristems and cellular growth rates, as well as control mechanisms within the tree, have large influences on forest responses (Körner, 2003; Fatichi et al., 2014). A few research groups have addressed the issue of sink-limited growth in a modeling context with respect to carbon sequestration. The potential for sink-limited growth to affect carbon storage and treeline position was addressed by Leuzinger et al. (2013) using a global vegetation model. However, their approach was highly empirical and only addressed temperature limitations. A more mechanistic approach was presented by Schiestl-Aalto et al. (2015), in which a tree-level carbon balance model was constructed with both carbon source and sink parameterizations. The sink

parameterizations were based on thermal-time and included different ontogenetic effects between tissue types and xylogenetic processes for secondary growth. However, while this paper makes a significant contribution, the various parameterizations were very simply incorporated, with no effect of moisture on wood growth, fixed durations for xylem enlargement, and no overall tree growth across years. Gea-Izquierdo et al. (2015) also presented a tree-level model parameterization that addressed the effect of growth processes independently of photosynthesis, and in this case looked particularly at soil moisture effects. However, they did not explicitly treat meristem growth, but instead used modified allocation coefficients depending on temperature and soil water.

Grossman and DeJong (1994) examined the consequences of explicit consideration of sink-limited growth for growth partitioning through the growing season in fruit trees. Sink growth was parameterized using a priority order and as a function of carbohydrate supply up to potential rates for different tissues, which were modulated by daily temperature and season. It was concluded that source and sink limit at different times of the year, with carbohydrate supply limiting stem growth during the spring and autumn periods, presumably related to the total sink strength being maximal at those times. Derived from this type of approach, a number of so-called “Functional-Structural Plant Models” (FSPMs) have been developed which typically explicitly consider both source and sink functions (Allen et al., 2005). While the emphasis of these models has been on allocation to plant form, the focus on sinks makes them relevant for the sink-source debate, and potentially useful tools to address it. However, as far as we know they have not been directly used for this purpose. The LIGNUM model (Perttunun, 2009), for example, computes stem growth using available photosynthate in order to conform to the pipe model, based on foliage area. The tree grows as a coordinated whole, and storage is not considered. It has primarily been used to study the three-dimensional aspects of crown shape and light capture.

Most of the published growth and yield models that are routinely applied to forest ecosystem management and scenario analyses are based on statistical relationships between tree growth and environmental conditions (Pretzsch et al., 2007). Thus, they inherently consider the sink aspect of growth, in terms of parameterized resource-growth relationships, more than the source approach. Examples are the individual tree models TASS (Purves et al., 2008), SILVA (Pretzsch et al., 2002), PROGNAUS (Sterba and Monserud, 1997), SORTIE (Pacala and Deutschman, 1995), MELA (Hynynen, 2002), and HEUREKA (Wikström et al., 2011). They represent successful but maybe too exclusively sink-oriented models, in which new knowledge of tree responses to environmental conditions is difficult to integrate due to their empirical nature. In contrast, the generation of mainly source-driven models such as BALANCE (Grote and Pretzsch, 2002), TREEDYN (Bossel, 1991), and 3PG (Landsberg and Waring, 1997) represent hypotheses about biogeophysiological mechanisms, but so far are little established beyond scientific applications. This is mainly due to the lack of evaluation and comparison with empirical growth and yield records. In response to this current one-sided focus on modeling either

taking the sink or the source aspect into account, an integration of both seems most promising for taking forward understanding and prognosis of tree and stand growth.

Here we present a new framework for addressing tree growth responses to environmental change, building on knowledge of tree physiology to develop approaches for predicting the development of an individual tree, and thereby enabling a better understanding of forest responses to environmental change than purely source-driven models can achieve, as well as addressing the limitations of previous sink-limited approaches. Our aim is to derive an approach that can be applied in global models, specifically Dynamic Global Vegetation Models (DGVMs). Therefore, we seek the minimal level of detail necessary in order to compute behavior at the global scale, and to be compatible with the other highly aggregated process representation in DGVMs.

In this paper we suggest that this objective can be realized using differential models, that is to say growth models using differential equations. We propose here a first differential model taking into account control mechanisms and the intrinsic limits of meristems and cellular growth within trees together with the carbon balance, as well as direct environmental controls on meristematic activity. The paper is presented as follows. First we make several hypotheses concerning physiological considerations, then we give a description of the model. We show how the model is used to predict tree height and stem volume in two sets of three different stands of beech trees. Finally, we discuss the results and the behavior of the model in several situations.

## 2. MODEL AND FRAMEWORK

### 2.1. General Considerations

To describe the development of the tree, we suppose that it has two types of meristems, apical and lateral, and that the apical meristem increases the height through sustaining primary growth, while the lateral meristem (i.e., the vascular cambium) increases the radius through sustaining secondary growth. We recognize that trees will usually have many separate apical meristems distributed across many branches, but for convenience we treat these together as one apical meristem; we also ignore apical root growth for now. We further assume that the stem can be represented by a cylinder and that the crown (i.e., the branches and foliage) occupies a cylindrical volume and has dimensions that are proportional to the stem dimensions, i.e., the crown depth is proportional to the height of the tree stem and its radius to the radius of the tree stem. In this way we need only obtain information about the radius  $r$  and the height  $h$  of the stem to describe the growth of the tree. Future developments will include introducing other crown and stem shapes, as well as root meristems. Here our objective is to keep the model as simple as possible in order to explore the realism of its fundamental assumptions.

In order to derive the dynamics of  $r$  and  $h$  we need three types of equations:

- constitutive equations—related to the structure of the tree;

- control equations—representation(s) of the intrinsic controls that the tree has on itself;
- carbon balance equations—related to the balance of carbon between the tree and its environment, and the balance within the tree.

## 2.2. Constitutive Equations: Allometric Relationships

Physiologically, plant growth is sustained by meristems producing new cells which subsequently enlarge and increase in mass (Aloni, 1987). We suppose that for each type of meristem, growth is proportional to its volume, that is to say that the mass of carbon allocated to a meristematic region will depend proportionally on the volume of meristem, which determines the maximum potential production rate of new cells.

We also suppose that a tree controls the activities of the meristems and therefore the relative demand for carbon between the meristematic regions: it can favor either height or diameter growth in this way, depending on environmental signals. Moreover, we suppose that this is the only control the tree has on its growth. With this hypothesis we soon get:

$$\frac{dh}{h} = 2\alpha_2 \frac{dr}{r} \quad (1)$$

where  $\alpha_2$  is the ratio of activities between the apical and lateral meristems, i.e., when the activity of the lateral meristem produces 1 g of carbon growth,  $\alpha_2$  g of carbon growth occurs from the apical meristem. It is the control parameter.

Note that we suppose here that the volume of the apical meristem is proportional to the top surface area of the (cylindrical) stem and that the volume of the lateral meristem is proportional to the lateral surface area of the stem. This hypothesis is used as it is more realistic than assuming that the volume of the lateral and apical meristems are proportional to the volume of the tree, i.e., that the thickness of the lateral meristem area increases proportionally with the radius and the thickness of apical meristem increases proportionally with height. Although even under this alternative hypothesis we would get the same type of equation with  $\alpha_2$  being the proportion of growth per unit of volume of apical meristem relative to proportional lateral growth, only adding a numerical coefficient in front of  $\alpha_2$ .

Knowing the definition of the volume and integrating we get the following constitutive equations:

$$h = \gamma r^{2\alpha_2} \quad (2)$$

$$M_c = g_1 r^2 h \quad (3)$$

We recognize Equation (2) as the usual allometric relationship where  $\gamma$  is a constant. As it is true for any time  $t$ , it can be expressed as  $h_0/r_0^{2\alpha_2}$ , with  $h_0$  and  $r_0$  the height and radius at some time origin  $t = 0$ .

Equation (3) is simply the definition of the volume of the stem plus canopy (containing the branches and leaves) in relation to its mass,  $M_c$ . We assume naturally that branches, stem, and leaves have different densities, but for each of them we suppose that their mass is proportional to  $r^2 \times h$  with potentially a geometrical

coefficient. That implies that the general mass is proportional to  $r^2 \times h$ , and in Equation (3),  $g_1$  is the global proportionality coefficient. Therefore,  $g_1$  takes into account the density of the stem, the density of the branches and foliage, their contribution to the mass of the tree, and geometric factors.  $g_1$  can therefore be found using the proportionality coefficients we assumed between crown radius and stem radius and crown height and stem height, and their relative densities. Or if we call  $a$  the geometrical factors and  $d$  the densities:  $g_1 = a_{foliage}d_{foliage} + a_{branches}d_{branches} + a_{stem}d_{stem}$ . Here  $a$  takes into account the geometry and the volume of each element.

## 2.3. Control Mechanism of the Tree

We want now to take into account the intrinsic control that the tree has on itself, parameterized in our model by  $\alpha_2$ , the ratio between the activities of the apical and lateral meristems. For this we need to consider what happens physiologically (for convenience we use teleological terminology): the tree uses internal controls to be able to adapt its shape and physiology to the surrounding environment, for instance other competing trees (e.g., Ritchie, 1997), through phytohormonal signaling networks (Brackmann and Greb, 2014; Aloni, 2015). Many behaviors could be taken into account, but here we focus on the behavior of a tree competing for light by trying to grow taller faster than its competitors by increasing  $\alpha_2$ . The modeled tree is assumed to detect the presence of surrounding trees by sensing the ratio of downwelling red radiation (i.e., wavelengths between 655 and 665 nm) to downwelling far-red radiation (i.e., wavelengths between 725 and 735 nm). A low ratio signals potentially more neighboring trees and therefore a potential threat of shading. In that case the tree reacts by increasing the activity of the apical meristem relative to the lateral meristem, while a higher ratio potentially means no threat and so the tree reacts by balancing the activities of the two meristems as it needs to compete less for light (Franklin, 2008). We hypothesize that this reaction can be modeled as:

$$\alpha_2 = \alpha_0 \exp(-\alpha_3 R_a) \quad (4)$$

Where  $\alpha_0$  is the highest limit for  $\alpha_2$  beyond which the tree breaks due to mechanical failure, and  $R_a$  is the ratio of received downwelling red:far-red ratio.  $\alpha_3$  is a scaling parameter such that  $\alpha_0 \exp(-\alpha_3)$  is the value of  $\alpha_2$  when the tree is unshaded (i.e., when it detects no other tree around).

This approach is based on the findings of several studies (e.g., Morgan and Smith, 1976; Franklin, 2008). In particular, Morgan and Smith (1976) observed the laboratory behavior of two similar young trees grown for 21 days with the same intensity of photosynthetically active radiation (PAR), but different red:far-red ratios. They experimentally obtained a relationship which, extended by limited development for short trees, is coherent with the relationship we give in Equation (4).

A potential limitation to our approach is that we may not have access to direct measurements of  $R_a$ . For a lone tree this would not be a real problem: the allometric relationship would be constant in our model and the red:far-red ratio maximal. For individual trees growing in a stand in a forest, however, the situation is different as the trees shade each other.

Finding a dependency rule of the red:far-red ratio for trees in a stand is therefore a challenge that does not seem to be overcome yet. Because of this and our desire to keep the model simple<sup>1</sup>, when we do not have access to measurements of the red:far-red ratio we make the assumption that  $\alpha_2$  is constant for each stand, as it would be for a lone tree. When the value of this constant is required, it will be estimated as a typical value consistent with the empirical allometric relationship. This is likely to be our most limiting factor as we are here trying to model the internal control that the tree has on itself, which is probably the most complicated phenomenon to take into account, and likely the least-well understood component of our model (cf. Li et al., 2011; Aloni, 2015). Although the model seems to work realistically, further work may require a more precise dependency of the red:far red ratio.

## 2.4. Carbon Balance

The variation of carbon in the tree over time can be written as the sum of the carbon used for volume growth and the carbon stored:

$$\frac{dM_{\text{tot}}}{dt} = \frac{dM_c}{dt} + \frac{d((S - S_1) \frac{g_1}{(1+S_1)} \pi h r^2)}{dt} \quad (5)$$

where  $M_c$  is the carbon used for volume growth,  $S_c = S \frac{g_1}{(1+S_1)} \pi h r^2$  the carbon stored,  $S$  is defined as carbon stored per unit volume of stem,  $S_{c0} = (S - S_1) \frac{g_1}{(1+S_1)} \pi h r^2$  is the carbon stored above the storage limit  $S_1$  under which the tree is considered in danger. This distinction has a physical interpretation and therefore in this model the density of the tree can then be seen as a standard density related to the carbon used for growth plus an increase of density due to the storage.

We also know that the variation of carbon is given by:

$$\frac{dM_{\text{tot}}}{dt} = A(Q1, C_g, T, \psi, h, r) - C_1 h r^2 - \frac{C_2(1 + S_1)}{g_1 \pi} S_c \quad (6)$$

where  $A$  is the carbon assimilation due to gross photosynthesis minus a foliage respiration part proportional to photosynthesis, while  $C_1$  is a constant grouping a part of the respiration and a litter component proportional to the volume, together with the geometrical factor  $g_1 \pi$  (such that  $C_1/g_1 \pi$  is the respiration and litter component constant). We assume here that there is no other litter component, that is to say that litter is completely proportional to the volume of the stem. We note that this also means that the litter is proportional to the volume of the crown with our previous assumptions. Also we assumed here that we are dealing with trees where the living volume can be approximated as proportional to the total volume. This is an approximation and further work could include a variable corrective coefficient, however this is a secondary issue compared to the main advance of this model concerning sink-limited growth. Finally,  $C_2$  is the same type of constant but for the carbon storage.  $A$  is assumed to depend on PAR (Q1), the concentration of CO<sub>2</sub> in

the atmosphere ( $C_g$ ), temperature ( $T$ ), water potential ( $\psi$ ), and the dimensions of the tree ( $h$  and  $r$ ).

Therefore:

$$\frac{dM_c}{dt} + \frac{dS_{c0}}{dt} = A(Q1, C_g, T, \psi, h, r) - Chr^2 - \frac{C_2(1 + S_1)}{g_1 \pi} S_c \quad (7)$$

The system is so far incomplete as there needs to be a relationship that controls which part of the carbon is allocated to growth and which part is allocated to storage. Also, the volume growth of the tree is sustained by meristematic cell division and enlargement, with a maximal rate determined by intrinsic physiological limits or environmental controls.

We assume that the tree grows in volume as much as it can, as long as it keeps enough storage to avoid being in danger, such as for repairing damage and surviving poor growing seasons. We assume that there is one tree specific storage pool, although we acknowledge that localized storage with various turnover times are more realistic (Sprugel et al., 1991; Palacio et al., 2014; Richardson et al., 2015). Therefore, if there is enough carbon assimilation then the rate of growth is equal to the meristem-sustained growth-rate limit and the storage can increase using the difference of these two. Also, if the carbon assimilation rate becomes too low but there is enough storage, then the storage delivers carbon to the meristematic region to maintain a rate of growth equal to its maximal sustainable rate. Then density decreases as the carbon of the storage is used to maintain the volume growth. This is likely to occur for instance when buds appear while photosynthesis is not yet high enough to support the maximal growth potential due to meristem reactivation (note that bud-burst and other seasonal phenological phenomena are not yet treated by the model). However, if there is not enough carbon assimilation or storage then the rate of growth is equal to the carbon assimilation rate and the storage per unit volume remains constant.

This behavior can be translated into evolution equations. As growth occurs at a cellular level we can assume that the maximal meristem growth is proportional to the volume of meristems. We denote this maximal meristem-sustained growth per volume by  $R_{\text{max}}$ , the volume of the meristems by  $V_{\text{me}}$ .

If there is enough photosynthesis or storage, i.e.,

$$\text{if } A(Q1, C_g, T, \psi, h, r) - Chr^2 - C_2 Sh r^2 > R_{\text{max}} V_{\text{me}} \text{ or } S > S_1 \quad (8)$$

then:

$$\frac{dM_c}{dt} = \frac{R_{\text{max}} V_{\text{me}}}{1 + \frac{(S - S_1)}{(1 + S_1)}} \quad (9)$$

$$\frac{d((S - S_1) \pi \frac{g_1}{(1 + S_1)} h r^2)}{dt} = A(Q1, C_g, T, \psi, h, r) - Chr^2 - C_2 Sh r^2 - \frac{dM_c}{dt} \quad (10)$$

$$\text{but if } A(Q1, C_g, T, \psi, h, r) - Chr^2 - C_2 Sh r^2 \leq R_{\text{max}} V_{\text{me}} \text{ and } S = S_1 \quad (11)$$

<sup>1</sup>Variation of  $\alpha_2$  could strongly increase the complexity of the equations as  $\alpha$  is an exponent in our model.

then

$$\frac{dM_c}{dt} = A(Q_1, Cg, T, \psi, h, r) - Chr^2 - C_2 Shr^2 \quad (12)$$

$$\frac{dS}{dt} = 0 \quad (13)$$

Note that the case where for some reason the carbon assimilation by photosynthesis is insufficient even to cover the cost of maintenance is treated by Equations (8–10). In that case there will be a depletion of storage to sustain the maintenance cost until the storage reaches a critical level or until the photosynthesis rate increases sufficiently.

## 2.5. Modeling Photosynthesis

We assume the following dependencies of photosynthesis on water potential, atmospheric CO<sub>2</sub> concentration (C<sub>g</sub>), PAR (Q<sub>1</sub>), temperature, radius, and height:

1. Photosynthesis increases with CO<sub>2</sub> concentration and PAR exponentially and tends to saturate:

$$A \propto (1 - \exp(-\frac{Cg}{Cr})) \quad (14)$$

$$A \propto (1 - \exp(-\frac{Q_1}{Q_r})) \quad (15)$$

Cr and Q<sub>r</sub> refers to the critical constants.

2. As a first approximation photosynthesis of each leaf decreases linearly with a reduction in soil water potential. We also suppose that water potential and hence photosynthesis decreases linearly with height (Friend, 1993):

$$A_{\text{leaf}} \propto \frac{h_1 - h}{h_1} \quad (16)$$

Where:

$$h_1 = \frac{(\psi_{\text{soil}} - \psi_{\text{lim}})}{R_h} \quad (17)$$

With  $\psi_{\text{soil}}$  the water potential in the soil and  $\psi_{\text{lim}}$  the limit water potential below which any photosynthesis cannot be performed due to a lack of turgor pressure in the leaves and increased probability of xylem cavitation. R<sub>h</sub> is the hydraulic resistance per unit length. Overall for the whole canopy we suppose a dependency of the form:

$$A \propto (\frac{h_1 - \beta h}{h_1}) \quad (18)$$

In particular this means that there are two antagonist effects: one that tend to increase photosynthesis with the depth of the canopy due to more leaves and another that tends to make photosynthesis decrease with height due to the decline in water potential. Note that  $\beta$  is a numerical coefficient that depends on the ratio between the crown depth and the height. We assumed in our simulations that  $\beta = 3/4$ . Also, the dependency of both height and water potential is given above.

3. We assume a dependency with temperature given by an asymmetric parabola:

$$A \propto (1 - (\frac{|T - T_{\text{opt}}|}{T_i})^2) \quad (19)$$

With T<sub>i</sub> being 21°C if  $T > T_{\text{opt}}$  and 25°C otherwise. We set here  $T_{\text{opt}} = 18^\circ\text{C}$ . These values are inspired by previous studies (e.g., Precht et al., 1973).

4. We suppose that photosynthesis is proportional to the surface area of the crown, and so proportional to  $r^2$ .

Overall we get:

$$A = A_{\max}(1 - e^{-\frac{Cg}{Cr}})(1 - e^{-\frac{Q_1}{Q_r}})(1 - (\frac{|T - T_{\text{opt}}|}{T_i})^2) \left( \frac{h_1 - 3h/4}{h_1} \right) r^2 h \quad (20)$$

## 2.6. Maximal Meristem-Sustained Growth

Intuitively, as meristem-sustained growth occurs at a cellular level, we assume that the limit to meristem-sustained growth per volume increases with temperature up to a certain temperature and increases with water potential (cf. Deleuze and Houllier, 1998). Therefore, we assume the following dependencies:

1. The meristem-sustained growth limit decreases with height as:

$$R_{\max} \propto \frac{(h_2 - h)}{h_2}$$

$$h_2 = \frac{(\psi_{\text{soil}} - \psi_{\text{lim2}})}{R_h} \quad (21)$$

With  $\psi_{\text{soil}}$  the water potential in the soil and  $\psi_{\text{lim2}}$  the limit water potential below which meristem-sustained growth cannot occur. Physically this gives us a maximal height h<sub>2</sub> due to the limit on meristematic growth.

We define therefore R<sub>max0</sub> the reference maximal meristem-sustained growth per volume independant of water potential by:  $R_{\max} = R_{\max0} \frac{(h_2 - h)}{h_2}$

We could also suppose that the limit to meristem-sustained growth per volume increases with temperature using a standard Q<sub>10</sub> formulation:  $R_{\max} \propto Q_{10}^{\frac{T-T_2}{10}}$ . However, seen the difficulty to know precisely Q<sub>10</sub> and in order to keep the model as simple as possible we assumed that R<sub>max0</sub> remains constant with time.

2. As stated previously, we suppose that the volume of meristems is expressed as:  $V_{\text{me}} = (t_1 \pi r^2 + 2\pi r h t_2)$ , where t<sub>1</sub> is the effective thickness of the apical meristem and t<sub>2</sub> is the effective thickness of the lateral meristem.

## 2.7. Final Evolution Equations

Using the previous elements we finally get:

$$\frac{dM_c}{dt} = \frac{R_{\max0}(\frac{h_2 - h}{h_2}) V_{\text{me}}}{1 + \frac{(S - S_1)}{(1 + S_1)}} \quad (22)$$

$$\frac{dS_{c_0}}{dt} = (A_{\max}(1 - e^{-\frac{Cg}{Cr}})(1 - e^{-\frac{Q_1}{Qr}})(1 - (\frac{|T - T_{\text{opt}}|}{T_i})^2) - (\frac{h_1 - 3h/4}{h_1}) - C)hr^2 - C_2Shr^2 - \frac{dM_c}{dt} \quad (23)$$

or

$$\frac{dM_c}{dt} = (A_{\max}(1 - e^{-\frac{Cg}{Cr}})(1 - e^{-\frac{Q_1}{Qr}})(1 - (\frac{|T - T_{\text{opt}}|}{T_i})^2) - (\frac{h_1 - 3h/4}{h_1}) - C)r^2h - C_2Shr^2 \quad (24)$$

$$\frac{dS}{dt} = 0 \quad (25)$$

depending on whether carbon supply from photosynthesis plus storage is sufficient to meet demand for growth (Equations 22 and 23) or not (Equations 24 and 25).

## 2.8. Deriving the Values of the Parameters

So far we need to know the values of the following physiological parameters to use the model (**Table 1**):

$$A_{\max}, g_1, C, C_2, S_1, Cr, Qr, h_1, h_2, t_2R_{\max_0}$$

The most accessible are probably  $Cr$  and  $Qr$ . These are usually well known and can be obtained from the curve of photosynthesis activity as a function of atmospheric  $\text{CO}_2$  mixing ratio (in ppmv) or as a function of PAR, respectively.

$A_{\max}$  can be obtained by direct measurements of the carbon exchange at a given height, ambient  $\text{CO}_2$  concentration, temperature, PAR, and compensating for respiration as in Campioli et al. (2011). Acting similarly and measuring litter with litter traps gives access to  $C$ . These values can also be deduced from net primary production and gross primary production and the typical litter flux rates. Note that here we use data coming from forest stands, although in the model we suppose that we have an individual tree without shading because data for lone standing trees are seldom available. This means that we may underestimate the growth of isolated trees, but at the same time the values of  $A_{\max}$  and  $C$  obtained enable to take into account the shading effect by neighbors of a forest with the same density, which is a hidden parameter of this model (i.e., not explicitly taken into account). Also, depending on the typical time length of the study, we choose a model timestep and therefore we use averaged values of the parameters on this timestep. In this analysis, we chose 1 year as the timestep although smaller timesteps could be considered.

Finding  $h_1$  is equivalent to finding the minimal water potential that can sustain photosynthesis.  $h_2$  is its equivalent with respect to growth. Combined, these two parameters take into account all water potential-dependant limits in trees such as cavitation in the xylem conduits, minimal turgor potential to maintain the shape of the leaf and enable stomatal opening, etc. While  $h_1$  (or equivalently  $\psi_{\max 1}$ ) has been extensively studied (e.g., Friend, 1993; Koch et al., 2004; Du et al., 2008), and is believed to be equal to around 90 m for redwood trees (Koch et al., 2004),  $h_2$  seems to

**TABLE 1 | Numeric values of the parameters used in the model.**

Symbol	Value	Quantity
$g_1$	$365 \text{ kg.m}^{-3}$	Density of carbon of the equivalent cylinder representing the tree
$C/\pi$	$73 \text{ kg.m}^{-3} \cdot \text{y}^{-1}$	Respiration and litter coefficient
$C_2/\pi$	$73 \text{ kg.m}^{-3} \cdot \text{y}^{-1}$	Respiration coefficient for the storage
$t_2R_{\max 0}/g_1$	$0.0201 \text{ m.y}^{-1}$ corresponds to a maximal radius expansion of $1.5 \text{ cm.y}^{-1}$	Reference maximal meristem-sustained lateral growth per area independent of water potential
$t_2/t_1$	1	Ratio between lateral and apical meristem thickness
$\beta h_1$	$67.5 \text{ m}$	Limit height of occurrence for photosynthesis
$h_2$	$47 \text{ m}$	Limit height of occurrence for meristem-sustained growth
$S_1$	0.2	Critical value of the storage per unit mass
$A_{\max}/\pi$	$206 \text{ kg.m}^{-3} \cdot \text{y}^{-1}$	Maximal assimilation of carbon per unit volume by photosynthesis
$Q_r$	$1000 \text{ W.m}^{-2}$	Characteristic PAR dependency
$\alpha_2$	0.34–0.43	Ratio of meristematic activity
$Cr$	500 ppm	Characteristic $\text{CO}_2$ mixing ratio dependency
$\beta$	3/4	Geometrical integrand for $h_1$
$T_{\text{opt}}$	$18^\circ\text{C}$	Optimal temperature for carbon assimilation

be less known. However, knowing  $h_1$  and the other parameters, as well as the effective limit height for the considered species,  $h_2$  can be estimated by assuming that it is the limiting parameter in regions with very good conditions for photosynthesis. Therefore, looking at the effective limit height would give access to  $h_2$  for these particular regions. Using Equation (22) and regressing on the water potential we would have access to  $\psi_{\lim}$  and  $R_h$  and therefore we would be able to estimate  $h_2$  in any region from a measure of  $\psi_{soil}$ .

We can find  $R_{\max 0}$ , at least approximately, by looking at the tree rings of many trees across several geographical locations and assuming that the largest ones correspond to the maximal increment  $dr$  achievable in a year, which is directly linked to  $R_{\max 0}$ , the maximal meristem-sustained growth rate under perfect water potentials. Then we can deduce the value of  $R_{\max 0}$ , or at least its order of magnitude.

## 3. RESULTS

The model described above is ordinary, first order, non-linear, and has no widely known explicit analytical solution in the case where  $2\alpha_2$  is not an integer. Therefore, it was solved numerically

by the Runge-Kutta-Fehlberg (RK45) method (Dormand and Prince, 1980). Coherence both with the analytical solution in simplified cases and with other solving methods (i.e., the trapezoidal rule and numerical differentiation formula) was tested.

As some parameters can depend, *a priori*, on the considered species, we derived the parameters explained previously for beech trees from the data provided in Campioli et al. (2011) and Zianis and Mencuccini (2005). Beech trees were chosen because of their importance in European forests, especially in Germany where they represent more than 15% of the forest and in France where they comprise 15% of the non-conifer forest. Therefore, a great number of studies have focussed on beech trees, enabling easier comparisons with our current study.

As the computation of the parameters is based on independent measurements that have sometimes a non-negligible margin of error, we allowed the parameters thus obtained to vary with a 20% margin to account for this error, and to allow a small adaptation of the model (as it is only a simplification of reality) by fitting them with reference measurements of a standard beech tree stand in Fabrikschleihach, Germany that we refer to as “first stand” in the following. As  $R_{\max 0}$  was more coarsely estimated we allowed it a variation of 50% in order to maintain the right order of magnitude. Also, as no precise data on the soil water potentials over the tested period A.D. 1870–2010 were available for these stands, we allowed a 50% variation of  $h_2$ , the height where meristem-sustained growth cannot occur due to cell turgor limits. We obtained then a final vector of parameters for our model using a non-linear least-square method (trust-region-reflective algorithm: <http://uk.mathworks.com/help/optim/ug/equation-solving-algorithms.html>).

We then used our model to predict the time variation of height and volume of an average tree in other stands of beech trees. It should be emphasized that there is a substantial difference between fitting and prediction. Fitting a model to some data gives a partial understanding of the data but does not usually enable prediction for another tree or even for future data points as the fitting is done on a restricted set of measurements. Prediction, on the other hand, is much harder to achieve as it supposes the use of previously-derived parameters and environmental information (e.g., air temperature, soil moisture,  $\text{CO}_2$  concentration, etc.) to predict the measurements. Usually most models are fitted rather than predicting as it is much harder to predict anything without any fitting, although when it works it gives much more information: a better understanding and a reliable way to deduce future measurements before they occur even for other trees (e.g., height or volume prediction).

On these stands the model was tested without any additional fitting. In that sense it is, at least partially, a prediction. Of course a fitting on these stands would give a better result than the (still good) results we obtain, however it is not the goal of our approach. This is the reason why in the figures, to emphasize the difference of treatment between the standard stand and the others, two labels appear: “partial fit” and “prediction.”

We first considered three stands of beech trees that are part of a long-term experiment on forest yield science performed by the Chair of Forest Growth and Yield Science at the Technische Universität München. The stands are in southern Germany, about 60 km from Würzburg in the heart of the Steigerwald, a richly forested hillside, near a small village named Fabrikschleihach ( $49.9^{\circ}\text{N}$ ;  $10.5^{\circ}\text{E}$ ). They cover roughly 0.37 ha, are located within immediate proximity of each other (i.e., they have experienced the same environmental conditions), and differ only in silvicultural management, especially thinning with consequences for the development of stem densities during the experiment. The beech trees were planted and then measured at irregular intervals averaging  $8 \pm 3$  (mean  $\pm$  standard deviation) years from an age of 48 y in A.D. 1870 to 188 y in A.D. 2010. For each stand we considered the average height of the 100 trees with the largest stem diameter at breast height. The first stand was the reference stand used to partially fit the parameters (within the 20% margin). As the model needs initial values for both  $h_0$  and  $r_0$ , and as measurements only started at an age of 48 y, all the computations were run starting at an age of 48 y as can be seen in Figure 1.

As expected, our partially fitted model agrees well with the measurements from this stand (Figure 1A;  $R^2 = 0.924$ ). Predictions with the model were then performed for the two other stands (Figures 1B,C).

The results give a very good prediction for the second stand ( $R^2 > 0.925$ ), and a small, although non-negligible, error for the third one ( $R^2 = 0.89$ ). However, this could be at least partially explained by the change in the density of trees during the 120 y due to different rates of thinning in the different stands (i.e., from 3,500 tree  $\text{ha}^{-1}$  to 200 tree  $\text{ha}^{-1}$  in the first stand, 6,400 tree  $\text{ha}^{-1}$  to 200 tree  $\text{ha}^{-1}$  in the second, and 2,400 tree  $\text{ha}^{-1}$  to 200 tree  $\text{ha}^{-1}$  in the third). Therefore, the red:far-red radiation ratio changes with time in the real forest while it was assumed constant in our model.

To complete the analysis by testing the model thus calibrated on another site where the conditions may be different, it was also used to predict the height of dominant trees in three other stands at a different site in the Spessart, Hain ( $50.0^{\circ}\text{N}$ ;  $9.3^{\circ}\text{E}$ ), a low wooded mountain range in central Germany, located approximately 100 km from the first site where the beech trees were also planted and then measured from an age of 48 y in A.D. 1870 to 188 y in A.D. 2010 (Figure 2). As data were missing concerning the water potential during the growth period from A.D. 1870 to compare with the first stand, we allowed the model to adapt its value of  $h_2$  within 20% by keeping the calibration derived previously and fitting only this one parameter on the first of the three new stands. Then the new calibration was used to predict the heights of the three stands according to the model. To avoid the potential error induced by the different variations of the red:far-red ratios within the stands, we restrict our analysis to data when the density was lower than 1,000 tree  $\text{ha}^{-1}$  and started the simulations from these ages. As before, the predictions are in strong accordance with the observations for all three stands, with a nearly exact correspondence with the measurements ( $R^2 = 0.99$ ,  $R^2 = 0.92$ ,  $R^2 = 0.99$  respectively), except for the second stand.

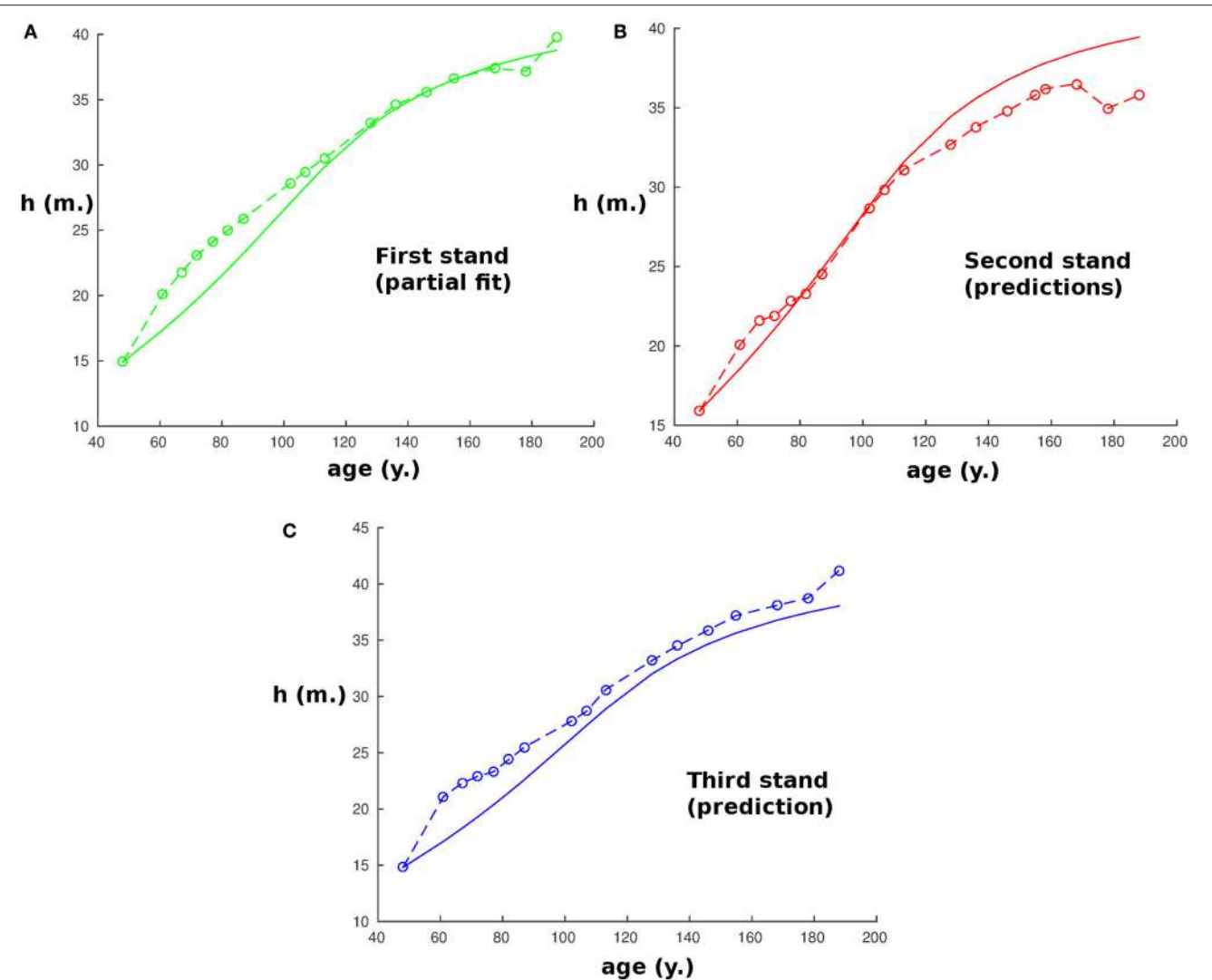
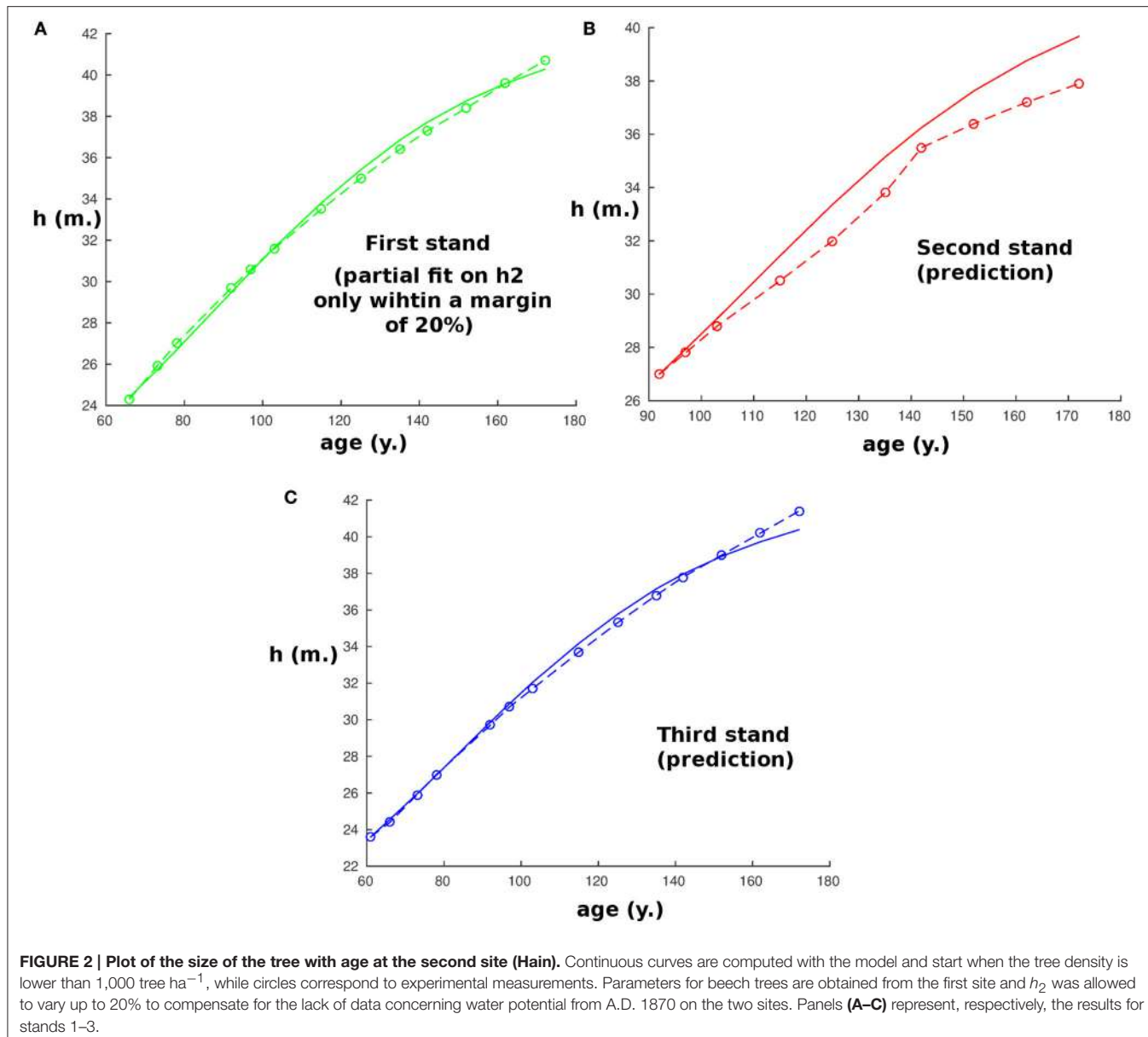


**FIGURE 1 | Size of the modeled tree with age at the first site (Fabrikschleichach).** Continuous curves are computed with the model while circles correspond to experimental measurements. **(A)** Represents the results of the partial fit on the reference stand. **(B,C)** Represent the results of the prediction with the parameters obtained by partial fitting.

We should note that the correspondence is very close but not exact, and that the data we have might limit the accuracy: firstly, from our equations we can see that there is a propagation of error from the initial conditions. An error on the initial height of 1 m could imply an error of the predicted height of up to 2.5 m after 50 years even if the model were perfect. Also, no data were available for the difference of water potentials between the stands on a same site, while it seems logical that for a certain density of trees, the stands with higher density will have less water available per tree. Therefore, this could induce a small error in  $h_2$  and  $h_1$  that could be corrected if we knew the average water potential during the growth period in each stand.

To exam the sensitivity of the model to the initial condition, we investigated how this impacts its predicting potential. **Figure 3A** shows predictions by the model for the second stand of the first site (Fabrikschleichach) when we add an error on the

initial condition for  $r_0$  between  $-20\%$  and  $+20\%$  (in blue) with an increment of 4%. We also show the effect of combining this error on  $r_0$  with a  $-20\%$  error on  $h_0$  (in cyan) and a  $+20\%$  error on  $h_0$  (in magenta). Experimental measurements are represented in red. In **Figure 3B** we show the result of the model with a full range of error for  $r_0$  and  $h_0$  between  $-20\%$  and  $+20\%$  with an increment of 4%, while the experimental measurements are again represented in red. In these simulations some knowledge on the experimental measurement is still necessary as we need to known the allometric relationship *a priori*. However, we could avoid this assumption by estimating it for instance using the allometric relationship of the first stand used for partial fitting. **Figure 3B** would not change much: the result of this procedure is given in **Figure 3C**. Of course the prediction is likely to be more precise if we knew more than the single initial point. The existing but small dispersion of the model prediction

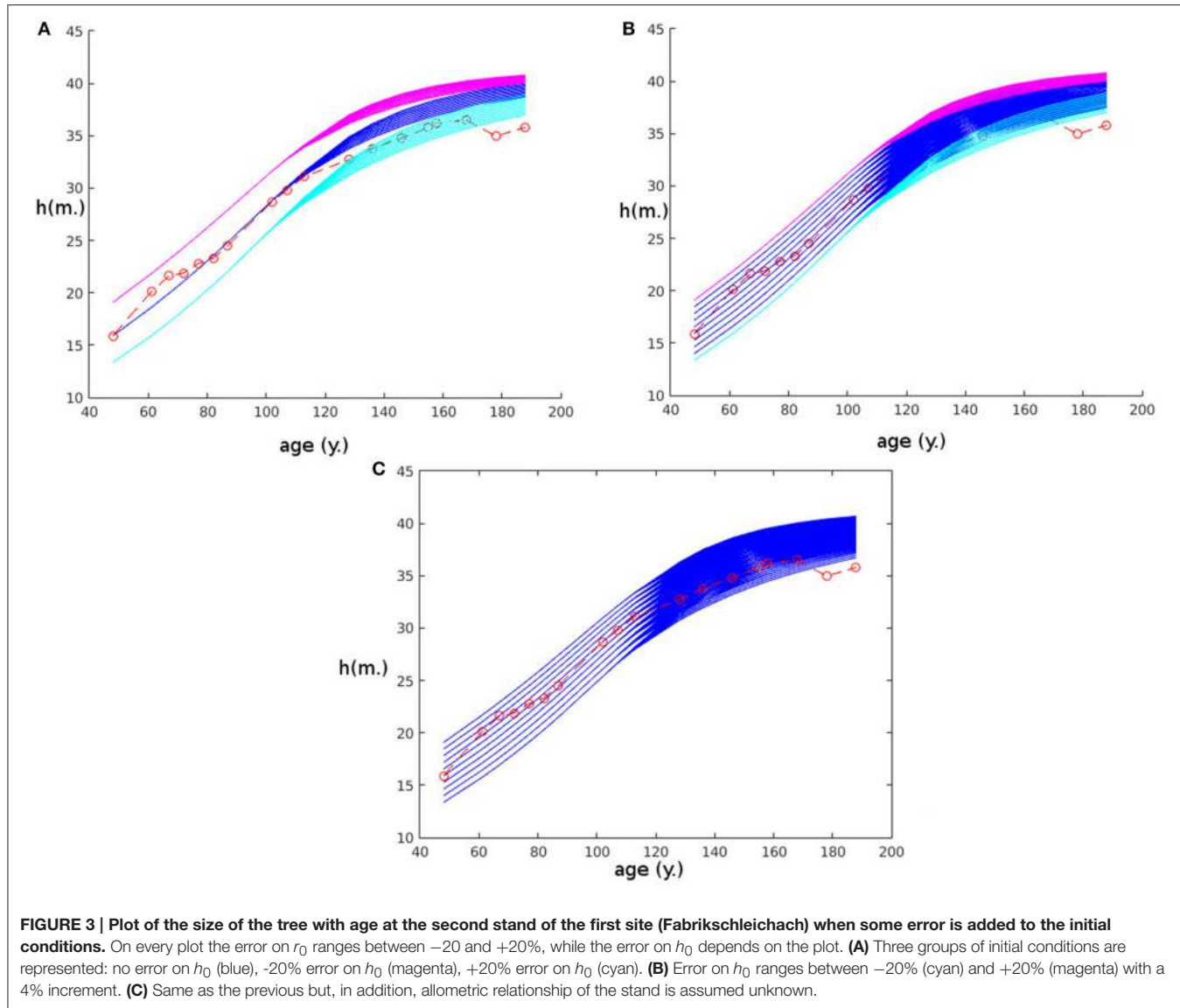


due to variation in the initial condition as demonstrated by the panels in **Figure 3**, is encouraging. It appears that the sensitivity of our model to the initial condition is not a significant concern regarding the ability of the model to reproduce actual behavior.

Finally, mortality is not addressed by the model, although the model does produce cessation of growth under stressful circumstances. Therefore, tree mortality due to critical events (e.g., disturbance, pathogens, etc.) other than a limit on growth due to the external conditions, can create discontinuities in the data which are not captured by the model. Although the continual use of the 100 trees with largest DBHs tends to average this discontinuity (as the probability that a large change in those 100 trees occurs in 1 year is low), this might have created another limit to the accuracy. For instance, we note that we have observed

in the 2010 measurements, i.e., after 188 years, the death of several of the 100 trees with the largest DBHs, which seems to have caused a decline of the average height of the 100 living trees with the largest DBHs as taller trees were replaced by smaller trees in this group, which is a result of size-related mortality dynamics (cf. Holzwarth et al., 2013).

If we wanted to address further this question, especially if we wanted to simulate many individual trees that interact together in a forest, we could multiply the height  $h$  by a random process  $M(t)$  that would be equal to 1 when the tree is alive and 0 when the tree is dead. Then the probability  $p(M(t) = 0|M(s < t) = 1)$  of transition between a living tree and a dead tree could be derived using experimental measurements and even be a function of the size of the tree. So far, though, this doesn't seem to be needed in the present application.



So far, the only things we assumed to be known for predicting the height are the external variables (i.e., temperature, water potential, PAR, and  $\text{CO}_2$  concentration), the species of the tree, and the allometric relationships for each stand. No other knowledge about the trees was used to perform the predictions. Measurements in themselves were used to compare our predictions with reality.

We chose to predict height as there is usually a relatively small error of measurement in height compared to other variables. It should be noted that the same procedure is possible taking instead the stem volume as the quantity to predict. However, the results would be less precise because they will be susceptible to cumulative measurement errors of the radius and the stem height, among other reasons, but they would still be accurate (the highest error is around  $25\%$  after 75 years) and are presented in **Figure 4**. As in **Figure 1**, we find again between 168 and 188 years that the effect of thinning reduces the precision and explains

the apparently strange experimental values. Also, we chose to predict height instead of radius or diameter as the measurements performed on the radius were the DBH which might be different from the equivalent cylindrical diameter, especially for the 100 trees with the largest DBH, and this would have added an artificial error of measurement.

### 3.1. Notable Behavior

The results of this model are very encouraging and are not limited to predicting the height of dominant trees but show notable qualitative behaviors in other respects.

Firstly, it is known that forest stand growth dynamics have significantly changed since 1870, as shown in Pretzsch et al. (2014), and many experiments have been conducted to measure the impact of climate and  $\text{CO}_2$  change on forests. Climate and  $\text{CO}_2$  change also shows an impact on this individual tree model, as the model depends on external conditions such as temperature

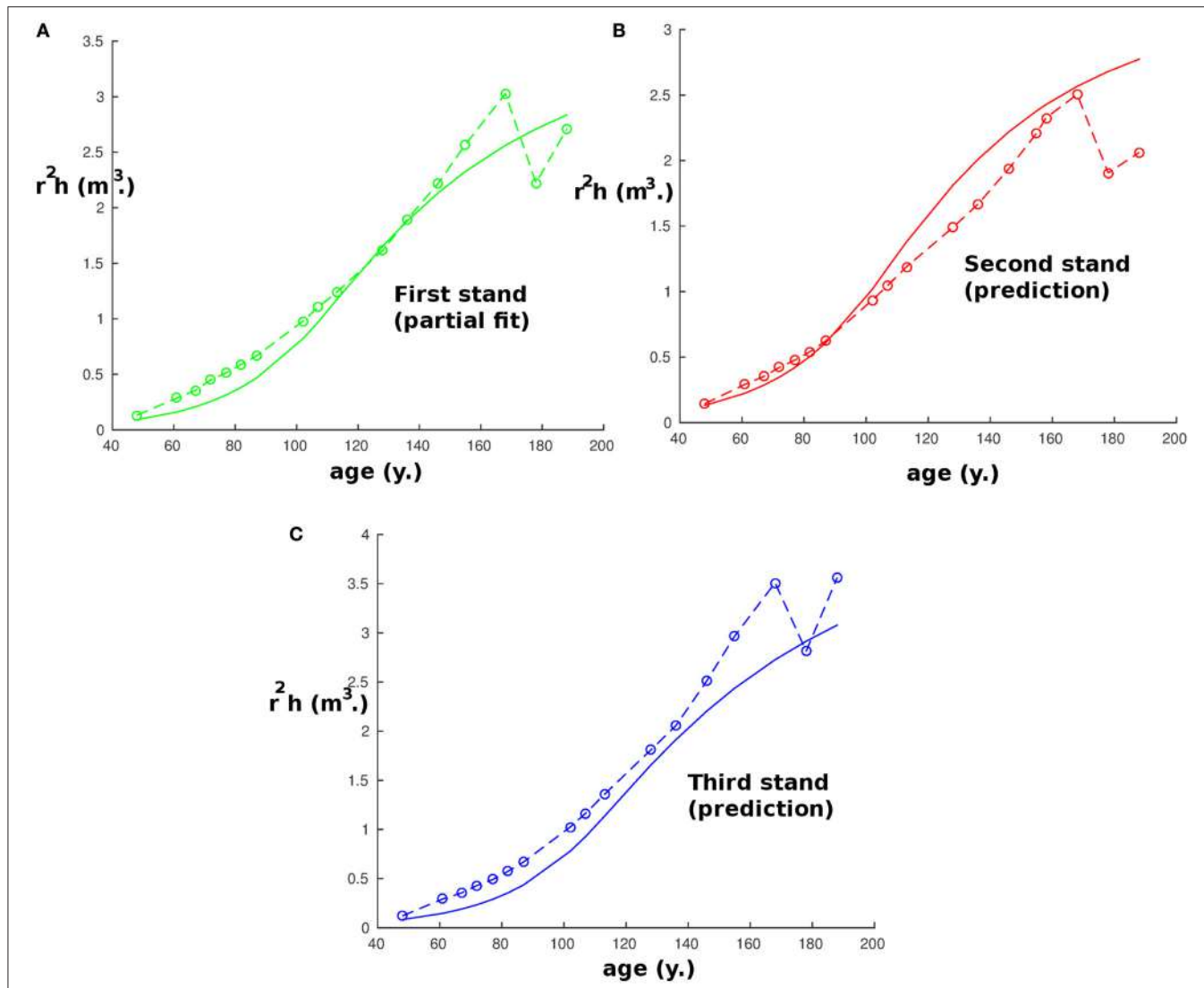


**FIGURE 4 | Plot of the stem volume with age at the first site (Fabrikschleichach).** Continuous curves are computed with the model and start when the tree density is lower than 1,000 tree  $ha^{-1}$ , while circles correspond to experimental measurements. Panel (A) represents the partial fit on the reference stand. Panels (B) and (C) represent the results of the prediction with the parameters obtained by partial fitting.

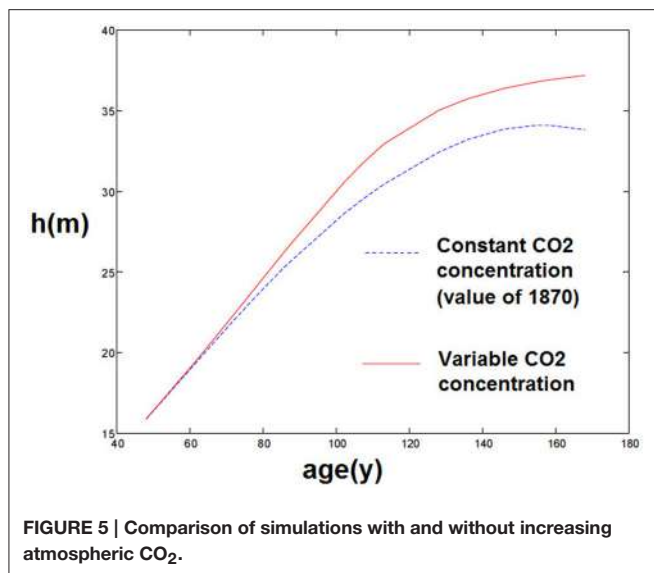
and soil moisture, as well as  $CO_2$  concentration. For instance, using the model with a constant  $CO_2$  concentration (from 1870) rather than the actual  $CO_2$  concentrations gives biased results and a slower growth of trees (Figure 5)<sup>2</sup>. This seems coherent with both the idea that atmospheric  $CO_2$  had an impact on forest stand growth and that present forest stands are growing more rapidly than comparable stands before.

Also, if we consider a small tree in a forest, shaded by the canopy above, it would receive only a small amount of light. Therefore, the model would predict a very limited maximum height and the tree would remain near this height with very small growth until a big tree nearby falls. Then the light received would

be higher and enough for the tree to grow taller very quickly. If the tree were very close to the dead big tree then the aperture is large enough and the tree would reach the canopy. If not, and if the tree is still significantly partially shaded compared to the rest of the trees, then its limit height would be lower than the forest height and it would reduce its growth progressively until it were close to this height. This behavior would seem to be qualitatively in accordance with reality Nagel et al. (2007), but due to a lack of data we have not been able to test this quantitatively.

Finally, we have examined the response of our model to a wide range of maximal carbon assimilation parameter values ( $A_{max}$ ) in order to investigate the conditions under which sink-limited growth dominates (Figure 6). Under the reference simulation, the growth of the tree was source-limited when young, but

<sup>2</sup>The three last experimental points are likely to be decreasing because of the thinning.



switched to being sink-limited when it reached 84 y old (this simulation is equivalent to that presented in **Figure 1B**, with  $A_{\max}$  obtained after a partial fit on the first stand from the value in **Table 1**). At low values of  $A_{\max}$  (i.e., approximately < 80% of the reference value), the tree remained source-limited to maturity, whereas at high values it was sink-limited for most of its life.

To examine further the idea of the importance of considering the sink limit in this model we performed a similar simulation but we switched off the sink limit, letting photosynthesis being the only limiting factor. We then computed the difference of the two simulations. This difference is shown in **Figure 7**. As we can see for regions where  $A_{\max}$  is large, the difference in tree heights between the two simulations can reach around 40 m after several 100 years.

## 4. DISCUSSION

Our aim in developing this model has been to provide a means of representing realistic tree growth and forest/vegetation dynamics at the global scale. To simulate individual tree competition our preferred method is to use a gap model of succession. Our global gap-model, HYBRID (Friend and White, 2000), computes individual-level photosynthesis and allocates photosynthate to leaves, stems, and roots, without consideration of sink limitations. All other DGVMs do something similar (Fatichi et al., 2014), usually at the big-leaf level (i.e., they do not consider individuals at all). The motivation of the new model described here is to explore a framework for introducing, in DGVMs, sink-limited growth. We have suggested as simple a scheme as possible to avoid reaching the point where we can no longer simulate dynamics at the global scale due to limited computing resources. The approach to modeling photosynthesis in DGVMs is similar to ours, in that the whole canopy is typically simulated as one leaf, and so it seems appropriate to simulate the meristems with a similar approach. We have chosen

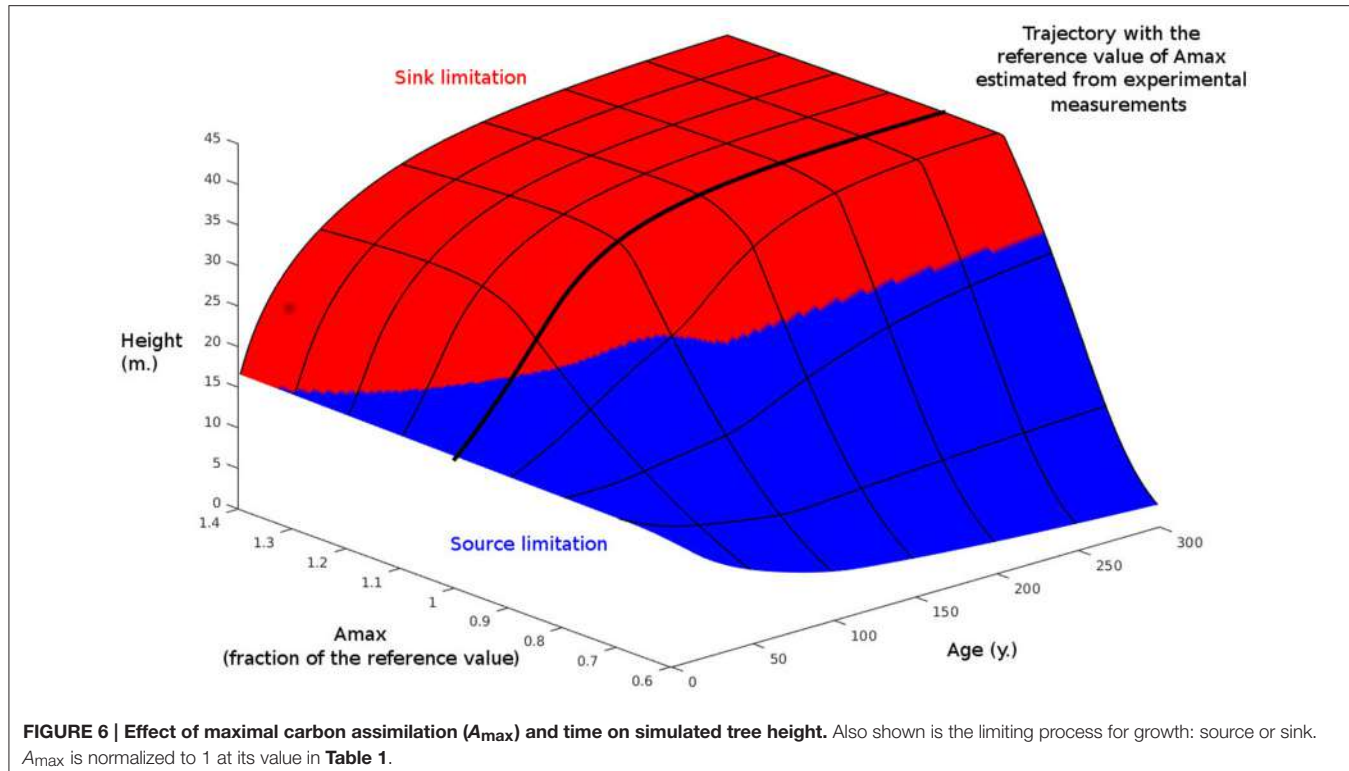
two meristem types—apical and lateral, in order to simulate the essential properties of height and diameter growth. Our new model is a major advance over current global models, and we expect that it could have significant consequences for our understanding of the historical and future global terrestrial carbon sink.

Our model starts from physiological considerations about trees and several hypotheses to derive differential equations that are solved over time to obtain the growth of a tree and predict its size. Although the model is fairly simple and far from taking every possible parameter of the tree into account, it seems to obtain very good results and predictions which agree closely with observations from different stands of trees with different environmental conditions.

Interestingly, our approach gives rise to two limiting tree heights:  $h_1$ , the limit height above which photosynthesis cannot occur, and  $h_2$ , the height above which growth is limited by the capacity of the meristematic regions themselves to grow at low water potential. These two heights represent different processes:  $h_1$  includes the factors that limit photosynthesis such as minimal turgor potential and possible xylem cavitation (i.e., source limitations), whereas  $h_2$  takes into account intrinsic meristem factors such as the physiological limits of cell division and growth limits such as cell wall extension when the water potential is too low (i.e., sink limitations).

While  $h_1$  (and, more generally, source processes) is often considered as the only limiting height to explain the maximal height of trees (e.g., Koch et al., 2004), under some external conditions of light and temperature it could be that  $h_2$  (i.e., sink activity) becomes limiting (cf. Friend, 1993). Although in this model, water potential is still the critical factor which limits the height of trees, the amount of light received and the temperature during the growth period also play roles that could produce one or other limit and influence its value. Hence, our approach could give a new and more complete understanding of the limits of tree height, and growth more generally, through a balanced consideration of both source and sink limitations.

Concerning the derivation of the results, we could have avoided assuming known allometric relationships for each stand and tried to estimate them as described in Section 2.3 ("Control mechanism of the tree"). Another way to estimate the allometric relationship on the second and third stand could be to estimate it close to the allometric relationship of the first stand used for partial fitting. In that case we would still get good results with  $R^2$  around 0.8 – 0.9. The small difference of accuracy between this case and the previous one is mainly due to the model becoming more sensitive to measurement error when we estimate the allometric relationship, and also to the estimated allometric relationship being a constant as explained in Section 2.3, whereas the allometric relationship in reality changes with changes in tree density and therefore time. Lastly, our model for  $\alpha_2$  is probably too simple as we also explained in Section 2.3. Nevertheless, we can note that the accuracy of the results is still very good considering that we try here to predict the heights of three stands without knowing anything but the species, the CO<sub>2</sub> concentration, the temperature, the soil moisture, the PAR, the



number of trees per ha, and the initial tree dimensions. This last point also underscores an additional motivation to build such a relatively simple model: collecting data about the external variables can be difficult. Therefore, data can be limiting and in order to be practical the model should stay as simple as it can relative to the required data, provided that it can still give accurate results.

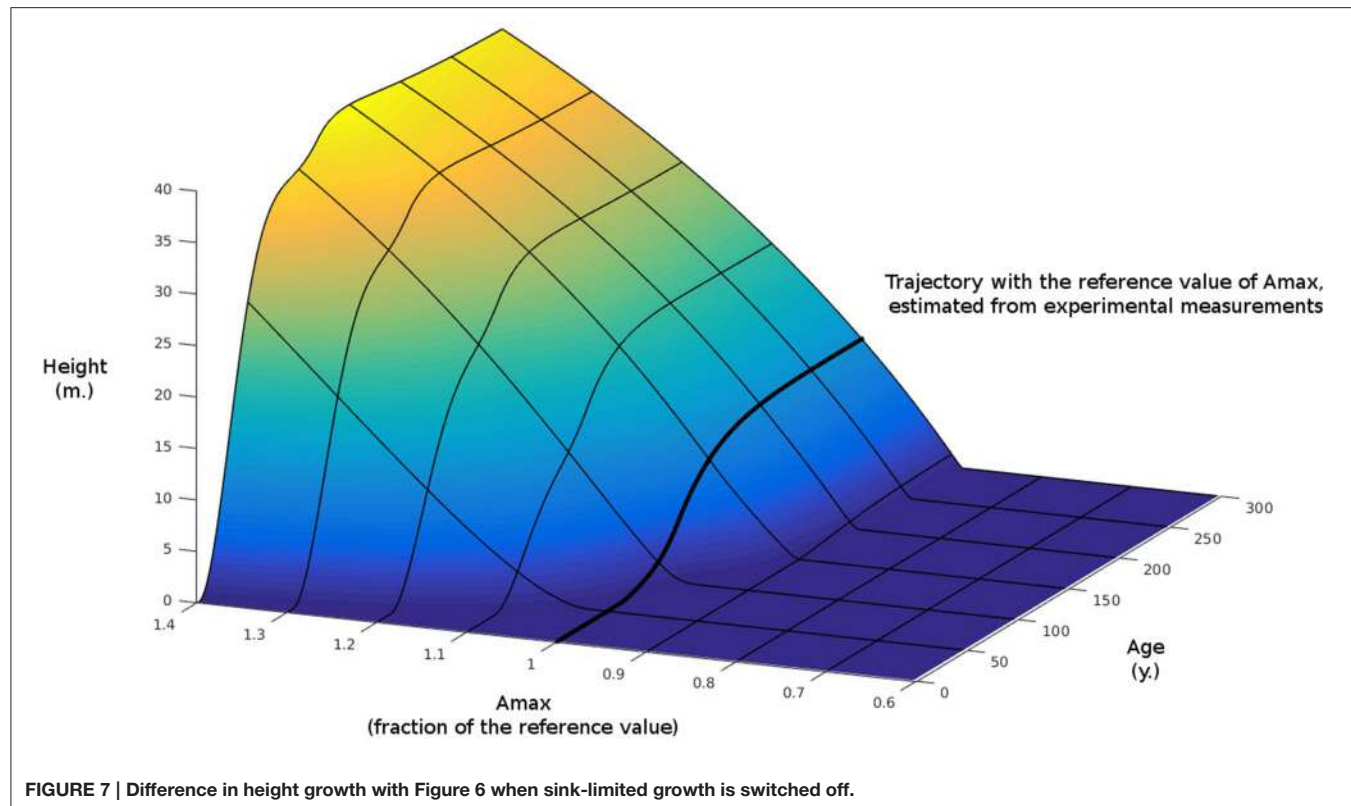
As a first dynamic model for an individual tree using such considerations about control mechanism and the maximal meristem-sustained limited rate of growth, improvements could probably be made by introducing additional parameters, especially taking the roots into account explicitly, and improving the function of the red:far-red ratio. Nevertheless, the model already gives very good results while being relatively simple, allowing its wider use such as through allowing many trees to interact with each other via shading, water potential, etc., and obtaining a model for the whole forest. So far the partial fitting of the parameters within bounds of 20% takes less than 120 s on a desk-top computer, and computing height over 100 y less than 0.1 s, which suggests that its use as a growth simulator within a forest model could be achieved with today's computer resources.

Our model makes the interesting prediction that under standard conditions/parameterization, trees shift from being source- to sink-limited as they mature. This behavior is consistent with field and experimental evidence for a lack of stem growth response to elevated  $\text{CO}_2$  in mature trees, despite increased photosynthesis (e.g., Körner, 2005; van der Sleen et al., 2014), whereas young fast growing trees show significant responses (e.g.,

Norby et al., 1999). In our model, the cause of the change in growth limitation as trees grow appears to be a combination of the effect of the limiting height for meristem activity,  $h_2$ , and the dependency of the balance of photosynthesis and respiration on height.

The relative simplicity of the model and its extremely encouraging results should stimulate further use of similar differential models in the future. Starting from physiological considerations to derive differential equations and an individual tree model as a cornerstone for simulating a whole forest may considerably improve our understanding of forest behavior, including, but not limited to, the prediction of overall responses of forests to increasing  $\text{CO}_2$  concentrations in order to address the future terrestrial carbon sink.

A number of other models have the potential to address the issues considered in this paper. For example, the L-PEACH FSPM (Allen et al., 2005) contains a number of features that make it applicable to the source-sink debate, including carbohydrate storage dynamics, product inhibition of photosynthesis, a transport-resistance framework for sugar partitioning, a sink growth control from available carbon, a direct effect of water supply, and an intrinsic size limit. The pipe model constraint is used, making overall growth a strong function of leaf growth, which itself is determined by carbon supply. However, it is not clear the extent to which this model would predict either source- or sink-limitations under different environmental conditions and/or timescales. This would be a very interesting exercise. FSPMs are also relevant to the calculation of canopy red:far red



ratios as they explicitly treat light interception throughout the canopy. In fact, some herbaceous crop models already compute the canopy red:far red ratio distribution and its influence on morphogenesis (e.g., Chelle et al., 2007). Such approaches could be simplified for implementing dynamic red:far red ratio responses in our model.

To conclude, we have proposed a differential model for modeling tree growth over time under external conditions such as temperature, soil moisture, and CO<sub>2</sub> concentration. This model takes into account not only photosynthesis and the carbon balance but also meristem behavior and cellular growth limits. We established a procedure to parametrize the model with measurable quantities and reference measurements. This model seems not only to fit data very well but also to give accurate predictions for tree height and tree volume.

## REFERENCES

- Allen, M. T., Prusinkiewicz, P., and DeJong, T. M. (2005). Using L-systems for modeling source-sink interactions, architecture and physiology of growing trees: the L-PEACH model. *New Phytol.* 166, 869–880. doi: 10.1111/j.1469-8137.2005.01348.x
- Aloni, R. (1987). Differentiation of Vascular Tissues. *Ann. Rev. Plant Physiol.* 38, 179–204. doi: 10.1146/annurev.pp.38.060187.001143
- Aloni, R. (2015). Ecophysiological implications of vascular differentiation and plant evolution. *Trees* 29, 1–16. doi: 10.1007/s00468-014-1070-6
- Anav, A., Friedlingstein, P., Kidston, M., Bopp, L., Ciais, P., Cox, P., et al. (2013). Evaluating the land and ocean components of the global carbon cycle in the CMIP5 earth system models. *J. Clim.* 26, 6801–6843. doi: 10.1175/JCLI-D-12-00417.1
- Bonan, G. B. (2008). Forests and climate change: forcings, feedbacks, and the climate benefits of forests. *Science* 320, 1444–1449. doi: 10.1126/science.1155121
- Bossel, H. (1991). Modelling forest dynamics: moving from description to explanation. *For. Ecol. Manage.* 42, 129–142. doi: 10.1016/0378-1127(91)90069-8
- Brackmann, K., and Greb, T. (2014). Long- and short-distance signaling in the regulation of lateral plant growth. *Physiol. Plant.* 151, 134–141. doi: 10.1111/ppl.12103
- Campioli, M., Gielen, B., Göckede, M., Papale, D., Bouriaud, O., and Granier, A. (2011). Temporal variability of the NPP-GPP ratio at seasonal and interannual

## AUTHOR CONTRIBUTIONS

AH executed the study designed by AF with input from AH-P and TR. HP provided data for model evaluation. AH initially wrote the manuscript and all authors commented on and edited the manuscript.

## FUNDING

AH wishes to thank the Cambridge Faculty of Mathematics for support via the PMP scheme.

## ACKNOWLEDGMENTS

All authors thank those involved in the measurements of the plot data at the two experimental sites.

- time scales in a temperate beech forest. *Biogeosciences* 8, 2481–2492. doi: 10.5194/bg-8-2481-2011
- Chelle, M., Evers, J. B., Combes, D., Varlet-Grancher, C., Vos, J., and Andrieu, B. (2007). Simulation of the three-dimensional distribution of the red: far-red ratio within crop canopies. *New Phytol.* 176, 223–234. doi: 10.1111/j.1469-8137.2007.02161.x
- Cramer, W., Bondeau, A., Woodward, F. I., Prentice, I. C., Betts, R. A., Brovkin, V., et al. (2001). Global response of terrestrial ecosystem structure and function to CO<sub>2</sub> and climate change: results from six dynamic global vegetation models. *Global Change Biol.* 7, 357–373. doi: 10.1046/j.1365-2486.2001.00383.x
- Deleuze, C., and Houllier, F. (1998). A simple process-based xylem growth model for describing wood microdensitometric profiles. *J. Theor. Biol.* 193, 99–113. doi: 10.1006/jtbi.1998.0689
- Dormand, J., and Prince, P. (1980). A family of embedded Runge-Kutta formulae. *J. Comput. Appl. Math.* 6, 19–26. doi: 10.1016/0771-050X(80)90013-3
- Du, N., Fan, J., Chen, S., and Liu, Y. (2008). A hydraulic, Aiphotosynthetic model based on extended HLH and its application to Coast redwood (*Sequoia sempervirens*). *J. Theor. Biol.* 253, 393–400. doi: 10.1016/j.jtbi.2008.03.016
- Fatici, S., Leuzinger, S., and Körner, C. (2014). Moving beyond photosynthesis: from carbon source to sink-driven vegetation modeling. *New Phytol.* 201, 1086–1095. doi: 10.1111/nph.12614
- Franklin, K. A. (2008). Shade avoidance. *New Phytol.* 179, 930–944. doi: 10.1111/j.1469-8137.2008.02507.x
- Friend, A. D. (1993). "The prediction and physiological significance of tree height," in *Vegetation Dynamics and Global Change*, eds A. M. Solomon, and H. H. Shugart (Springer), 101–115. doi: 10.1007/978-1-4615-2816-6\_5
- Friend, A. D., Lucht, W., Rademacher, T. T., Keribin, R., Betts, R., Cadule, P., et al. (2014). Carbon residence time dominates uncertainty in terrestrial vegetation responses to future climate and atmospheric CO<sub>2</sub>. *Proc. Natl. Acad. Sci. U.S.A.* 111, 3280–3285. doi: 10.1073/pnas.1222477110
- Friend, A. D., and White, A. (2000). Evaluation and analysis of a dynamic terrestrial ecosystem model under preindustrial conditions at the global scale. *Global Biogeochem. Cycles* 14, 1173–1190. doi: 10.1029/1999GB900085
- Gea-Izquierdo, G., Guibal, F., Joffre, R., Ourcival, J. M., Simioni, G., and Guiot, J. (2015). Modelling the climatic drivers determining photosynthesis and carbon allocation in evergreen Mediterranean forests using multiproxy long time series. *Biogeosciences* 12, 3695–3712. doi: 10.5194/bg-12-3695-2015
- Grossman, Y. L., and DeJong, T. M. (1994). PEACH: a simulation model of reproductive and vegetative growth in peach trees. *Tree Physiol.* 14, 329–345. doi: 10.1093/treephys/14.4.329
- Grote, R., and Pretzsch, H. (2002). A model for individual tree development based on physiological processes. *Plant Biol.* 4, 167–180. doi: 10.1055/s-2002-25743
- Holzwarth, F., Kahl, A., Bauhus, J., and Wirth, C. (2013). Many ways to die – partitioning tree mortality dynamics in a near-natural mixed deciduous forest. *J. Ecol.* 101, 220–230. doi: 10.1111/1365-2745.12015
- Hyynynen, J., (ed.). (2002). *Models for Predicting Stand Development in MELA System*. Number 835 in *Metsätutkimuslaitoksen Tiedonantaja*. Vantaa: Vantaa Research Center. OCLC: 248970310.
- Koch, G. W., Sillett, S. C., Jennings, G. M., and Davis, S. D. (2004). The limits to tree height. *Nature* 428, 851–854. doi: 10.1038/nature02417
- Körner, C. (2003). Carbon limitation in trees. *J. Ecol.* 91, 4–17. doi: 10.1046/j.1365-2745.2003.00742.x
- Körner, C. (2005). Carbon flux and growth in mature deciduous forest trees exposed to elevated CO<sub>2</sub>. *Science* 309, 1360–1362. doi: 10.1126/science.1113977
- Landsberg, J., and Waring, R. (1997). A generalised model of forest productivity using simplified concepts of radiation-use efficiency, carbon balance and partitioning. *For. Ecol. Manage.* 95, 209–228. doi: 10.1016/S0378-1127(97)00026-1
- Leuzinger, S., Manusch, C., Bugmann, H., and Wolf, A. (2013). A sink-limited growth model improves biomass estimation along boreal and alpine tree lines. *Global Ecol. Biogeogr.* 22, 924–932. doi: 10.1111/geb.12047
- Li, J., Li, G., Wang, H., and Wang Deng, X. (2011). Phytochrome signaling mechanisms. *Arabidopsis Book* 9:e0148. doi: 10.1199/tab.0148
- Morgan, D. C., and Smith, H. (1976). Linear relationship between phytochrome photoequilibrium and growth in plants under simulated natural radiation. *Nature* 262, 210–212. doi: 10.1038/262210a0
- Nagel, T. A., Levanic, T., and Diaci, J. (2007). A dendroecological reconstruction of disturbance in an old-growth *Fagus*-*Abies* forest in Slovenia. *Ann. For. Sci.* 64, 891–897. doi: 10.1051/forest:2007067
- Norby, R. J., Wullschleger, S. D., Gunderson, C. A., Johnson, D. W., and Ceulemans, R. (1999). Tree responses to rising CO<sub>2</sub> in field experiments: implications for the future forest. *Plant Cell Environ.* 22, 683–714. doi: 10.1046/j.1365-3040.1999.00391.x
- Pacala, S. W., and Deutschman, D. H. (1995). Details that matter: the spatial distribution of individual trees maintains forest ecosystem function. *Oikos* 74:357. doi: 10.2307/3545980
- Palacio, S., Hoch, G., Sala, A., Körner, C., and Millard, P. (2014). Does carbon storage limit tree growth? *New Phytol.* 201, 1096–1100. doi: 10.1111/nph.12602
- Pan, Y., Birdsey, R. A., Fang, J., Houghton, R., Kauppi, P. E., Kurz, W. A., et al. (2011). A large and persistent carbon sink in the world's forests. *Science* 333, 988–993. doi: 10.1126/science.1201609
- Perttunun, J. (2009). *The LIGNUM Functional-Structural Tree Model*. Ph.D. thesis, Aalto University.
- Precht, H., Christoffersen, J., Hensel, H., and Larcher, W. (1973). *Temperature and Life*. New York; Heidelberg; Berlin: Springer-Verlag.
- Pretzsch, H., Biber, P., Schütze, G., Uhl, E., and Rötzer, T. (2014). Forest stand growth dynamics in Central Europe have accelerated since 1870. *Nat. Commun.* 5:4967. doi: 10.1038/ncomms5967
- Pretzsch, H., Biber, P., and Dürsý, J. (2002). The single tree-based stand simulator SILVA: construction, application and evaluation. *For. Ecol. Manage.* 162, 3–21. doi: 10.1016/S0378-1127(02)00047-6
- Pretzsch, H., Grote, R., Reineking, B., Rotzer, T., and Seifert, S. (2007). Models for forest ecosystem management: a European perspective. *Ann. Bot.* 101, 1065–1087. doi: 10.1093/aob/mcm246
- Purves, D. W., Lichstein, J. W., Strigul, N., and Pacala, S. W. (2008). Predicting and understanding forest dynamics using a simple tractable model. *Proc. Natl. Acad. Sci. U.S.A.* 105, 17018–17022. doi: 10.1073/pnas.0807754105
- Richardson, A. D., Carbone, M. S., Huggett, B. A., Furze, M. E., Czimczik, C. I., Walker, J. C., et al. (2015). Distribution and mixing of old and new nonstructural carbon in two temperate trees. *New Phytol.* 206, 590–597. doi: 10.1111/nph.13273
- Ritchie, G. A. (1997). Evidence for red:far red signaling and photomorphogenic growth response in Douglas-fir (*Pseudotsuga menziesii*) seedlings. *Tree Physiol.* 17, 161–168. doi: 10.1093/treephys/17.3.161
- Schiestl-Aalto, P., Kulmala, L., Mäkinen, H., Nikinmaa, E., and Mäkelä, A. (2015). CASSIA - a dynamic model for predicting intra-annual sink demand and interannual growth variation in Scots pine. *New Phytol.* 206, 647–659. doi: 10.1111/nph.13275
- Sprugel, D., Hinckley, T., and Schaap, W. (1991). The theory and practise of branch autonomy. *Ann. Rev. Ecol. Systemat.* 22, 309–334. doi: 10.1146/annurev.es.22.110191.001521
- Sterba, H., and Monserud, R. A. (1997). Applicability of the forest stand growth simulator prognaus for the Austrian part of the Bohemian Massif. *Ecol. Model.* 98, 23–34. doi: 10.1016/S0304-3800(96)01934-5
- van der Sleen, P., Groenendijk, P., Vlam, M., Anten, N. P. R., Boom, A., et al. (2014). No growth stimulation of tropical trees by 150 years of CO<sub>2</sub> fertilization but water-use efficiency increased. *Nat. Geosci.* 8, 24–28. doi: 10.1038/ngeo2313
- Wikström, P., Edénius, L., Elfving, B., Eriksson, L. O., Lämås, T., Sonesson, J., et al. (2011). The heureka forestry decision support system: an overview. *Mathematical and computational forestry & natural-resource sciences (MCFNS)*. *Math. Comput. For. Nat. Resour. Sci.* 3, 87–94.
- Zianis, D., and Mencuccini, M. (2005). Aboveground net primary productivity of a beech (*Fagus moesiaca*) forest: a case study of Naousa forest, northern Greece. *Tree Physiol.* 25, 713–722. doi: 10.1093/treephys/25.6.713

**Conflict of Interest Statement:** The authors declare that the research was conducted in the absence of any commercial or financial relationships that could be construed as a potential conflict of interest.

Copyright © 2017 Hayat, Hacket-Pain, Pretzsch, Rademacher and Friend. This is an open-access article distributed under the terms of the Creative Commons Attribution License (CC BY). The use, distribution or reproduction in other forums is permitted, provided the original author(s) or licensor are credited and that the original publication in this journal is cited, in accordance with accepted academic practice. No use, distribution or reproduction is permitted which does not comply with these terms.



# Models for Predicting the Architecture of Different Shoot Types in Apple

Emna Bairam <sup>\*</sup>, Mickaël Delaire, Christian Le Morvan and Gerhard Buck-Sorlin <sup>\*</sup>

Unité Mixte de Recherche 1345, Institut de Recherche en Horticulture et Semences (Institut National de la Recherche Agronomique-Agrocampus Ouest-Université d'Angers), Angers, France

## OPEN ACCESS

**Edited by:**

Alexander Bucksch,  
University of Georgia, USA

**Reviewed by:**

David Ford,  
University of Washington, USA

Guillaume Loyer,  
Forschungszentrum Jülich, Germany

**\*Correspondence:**

Emna Bairam  
emna.bairam@gmail.com  
Gerhard Buck-Sorlin  
gerhard.buck-sorlin@  
agrocampus-ouest.fr

**Specialty section:**

This article was submitted to  
Plant Biophysics and Modeling,  
a section of the journal  
*Frontiers in Plant Science*

**Received:** 27 September 2016

**Accepted:** 12 January 2017

**Published:** 01 February 2017

**Citation:**

Bairam E, Delaire M, Le Morvan C and  
Buck-Sorlin G (2017) Models for  
Predicting the Architecture of Different  
Shoot Types in Apple.  
*Front. Plant Sci.* 8:65.  
doi: 10.3389/fpls.2017.00065

In apple, the first-order branch of a tree has a characteristic architecture constituting three shoot types: bourses (rosettes), bourse shoots, and vegetative shoots. Its overall architecture as well as that of each shoot thus determines the distribution of sources (leaves) and sinks (fruits) and could have an influence on the amount of sugar allocated to fruits. Knowledge of architecture, in particular the position and area of leaves helps to quantify source strength. In order to reconstruct this initial architecture, rules equipped with allometric relations could be used: these allow predicting model parameters that are difficult to measure from simple traits that can be determined easily, non-destructively and directly in the orchard. Once such allometric relations are established they can be used routinely to recreate initial structures. Models based on allometric relations have been established in this study in order to predict the leaf areas of the three different shoot types of three apple cultivars with different branch architectures: "Fuji," "Ariane," and "Rome Beauty." The allometric relations derived from experimental data allowed us to model the total shoot leaf area as well as the individual leaf area for each leaf rank, for each shoot type and each genotype. This was achieved using two easily measurable input variables: total leaf number per shoot and the length of the biggest leaf on the shoot. The models were tested using a different data set, and they were able to accurately predict leaf area of all shoot types and genotypes. Additional focus on internode lengths on spurs contributed to refine the models.

**Keywords:** *Malus x domestica* Borkh., apple, leaf surface, shoot architecture, allometry, modeling, apple branch

## INTRODUCTION

The study of plant architecture is a discipline that attempts to understand and explain plant form and structure and the processes underlying its formation (Barthélémy, 1991). Vascular plants have developed different architectures as part of their genetic blueprint and in response to a changing environment (Sussex and Kerk, 2001). The size, shape and spatial orientation of plant organs are, therefore, not pure coincidence but the result of a morphogenetic program which is carried out by a whole range of physiological processes. Therefore, "reading" the architecture could be a starting point for a better understanding of this underlying program. Of these architectural traits, leaf area has a particular impact on fruit quality as it is directly involved in several physiological processes such as light interception and photosynthesis (Björkman and Demmig-Adams, 1995; Štampar et al., 1999).

Studies on the influence of tree architecture on physiological functioning can be conducted in several ways: Two suitable tools are ecophysiological experimentation and functional-structural plant modeling (FSPM) (Vos et al., 2010; Buck-Sorlin, 2013). Ecophysiological experiments aim at changing the microenvironment of a selected plant and its organs and even at pushing it to an extreme limit, in order to obtain knowledge about the growth and developmental potential in a certain parameter space. FSPM aims at the integration of the dynamics of known physiological processes with information about the topology and geometry of organs (plant architecture) using mainly rule-based mathematical modeling (Buck-Sorlin, 2013).

In order to represent initial architecture there are several methods at hand and it is worthwhile to invest some time in developing a work flow to obtain “good” plant architecture with reduced effort. Casella and Sinoquet (2003) name several approaches: (1) describe architecture as a collection of individual 3-D geometric shapes; (2) model 3D architecture of a population of plants using stochastic, fractal or Lindenmayer-system (Lindenmayer, 1968a,b) methods or (3) describe architecture using a 3D digitizing method. All these methods have their advantages and disadvantages (for a review see Prusinkiewicz, 1998): The first method is suitable for the representation of the context of a detailed tree model, but too coarse for the modeling of leaf photosynthesis. The second one, despite being relatively quickly put into place, can still turn out to be too inaccurate for the description of leaf-scale photosynthesis since due to the stochastic method of architecture construction the reproducibility of a given real architecture is difficult. Apart from that, this method requires extensive calibration with measured data sets. The third method, though the most accurate one, is unsuitable for logistic reasons in the orchard: in the absence of a socket an electricity generator needs to be used, and there might be interference with the steel wires used for fixing the drip irrigation system, quite apart from the fact that digitizing is a tedious task and the structure to be digitized is often too complex to be acquired in 1 day.

Yet another, alternative approach is to use allometric relations between traits at the organ and intermediate (shoot, branch) scales: The principle is to obtain faithful models for the prediction of traits that are difficult to measure or that involve destruction of the organ, e.g., leaf area, by traits that are more readily measured (e.g., leaf blade length) or easily and non-destructively scored in the orchard (leaf number, rank, order). Once such allometric relations are established they can be used routinely to recreate initial structures. As with all indirect measures they need to be well tested as they bear the risk of cumulative error.

In apple two types of buds are distinguished: the mixed and the vegetative bud. The mixed bud, independent of its position on the shoot (apical or lateral), contains primordia of vegetative and reproductive organs and will develop into a spur. Thus the spur consists of a short shoot called “bourse” on which the primordia of preformed leaves will extend, as well as one or two sylleptic shoots called “bourse shoots” and the inflorescence (Fanwoua et al., 2014). The vegetative bud develops into a vegetative shoot. In temperate species, short axes are composed

of preformed organs only whereas long axes are composed of both preformed and neoformed organs successively (Costes et al., 2014); therefore, branch architecture is essentially determined by the developmental fate of these two bud types (**Figure 1**).

In this study we decided to concentrate on the prediction of leaf area: of all the traits contributing to branch architecture (leaf area, leaf blade and petiole orientation in space), it is the one that is most easily determined (as will be shown below) and yet very influential for light interception (Falster and Westoby, 2003). It was shown for apple that leaf area was the second most influential trait for light interception, after internode length (Da Silva et al., 2014). The distribution of leaves on the shoot and their size distribution clearly have an influence on light interception and leaf photosynthesis at the branch scale (Massonnet et al., 2008).

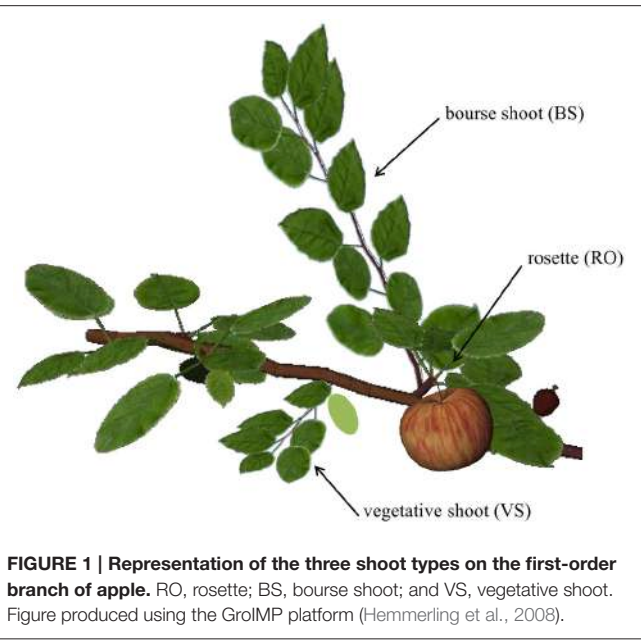
Any good model should be minimal in terms of number of input variables and the time invested in measurements but also efficient in simulating the output variable of interest. Therefore, the main aim of this study was to find models predicting the area of leaves of the three main shoot types of apple: bourse shoot (BS), rosette (RO) and vegetative shoot (VS), and this as a function of other traits on the same shoot that were either easy to score (total leaf number per shoot) or relatively quickly measured (length of the longest leaf of a given shoot). A secondary aim was to model the position of leaves on the shoot (length of the internodes) as a function of simple measured traits (length of the shoot). Such leaf area distributions can then serve to reconstruct the architecture of an apple branch used as an input for a functional-structural plant model of the first-order branch of apple, with emphasis on sugar transport (Bairam et al., unpubl.).

## MATERIALS AND METHODS

### Plant Material and Experiments

All experiments were performed on apple trees planted in 2008 in an experimental orchard at the INRA experimental unit in Beaucazé, France. The cultivars selected for this experiment were “Ariane,” “Fuji,” and “Rome Beauty” (in the following abbreviated as AR, FU, and RB, respectively). The main purpose of this study was to develop an allometric model for the prediction of the distribution of individual leaf areas along a certain shoot type, as well as of the total leaf area for a given shoot, namely the bearing spurs and vegetative shoots as they are the most cumbersome to be measured in the orchard. The models presented here were developed to take into account the impact of the genotype (G, with values AR, FU, and RB, see above) and the type of the shoot (j, which has the value “BS” for the bourse shoot, “RO” for the rosette and “VS” for the vegetative shoot). Shoots of each type were collected, and the leaves were scanned using a flatbed scanner (HP Scanjet G4010) with a resolution of 150 dpi and saved in portable network graphics (png) format. Leaf blade area, length and width were measured using ImageJ 1.48v software, assuming that leaf shape is elliptical (Freeman and Bolas, 1956). Total leaf area on each shoot was calculated as the sum of its individual leaves.

The models predicting individual/total leaf area use allometric relations between easily recorded input variables such as the length of the ellipse of the biggest leaf on the shoot ( $L_{max}$ ), the



number of leaves ( $nl$ ) and the acropetal leaf rank ( $R$ ). These models were built using different parameters and each of them was estimated using regression models. For rosettes and bourse shoots, enough data was available to be split into training and testing sets: the first data set was used for the estimation of the parameters and the second one for the testing of the model (Snee, 1977; Montgomery et al., 2015). Therefore, models were parameterized, calibrated and tested. For vegetative shoots, a simple model was built as there was not enough data for testing it.

## Modeling the Leaf Area of Bourse Shoots and Rosettes

Data used in this study consisted of a first data set from an experiment conducted in 2014 and a second, complementary data set collected in 2015 (Bairam et al., unpublished). The variables describing architectural traits of bourse shoots and rosettes [shoot length, number of leaves, leaf individual surface, leaf length, leaf width, and leaf rank (the latter only for bourse shoots)] extracted from the two sets were used for modeling total shoot leaf area and individual leaf area distribution along the stem. In the 2014 experiment, spurs of AR and RB were collected at eight different developmental stages from full bloom to harvest, and spurs of FU were collected at full bloom, 2 weeks after full bloom and at harvest. The experiment conducted in 2014 aimed at studying the impact of removing bourse shoot leaves, rosette leaves or both of them at full bloom and 2 weeks after full bloom, on fruit quality, bourse shoot and rosette (bourse) morphological traits. To develop an allometric model for the prediction of final leaf area, we needed a sufficiently large data set. However, the data set available in this study (2014 experiment, Bairam et al., unpublished) already included three defoliation treatments. In order to enlarge the database for the parameterization of our model beyond the control data, we checked whether the defoliation treatments had a significant impact on the following variables used in the model: total

leaf area and number of leaves of bourse shoot and rosette, respectively. The statistical tests were carried out separately, on each genotype for each sampling date and each type of shoot. Results (ANOVA, Kruskal-Wallis) showed that there was no significant influence of the defoliation treatments (Bairam et al., unpublished). This allowed us to pool the data available for these variables, involving all defoliation treatments, and to use them in the model. 174, 49, and 134 rosettes of AR, FU and RB, respectively, as well as 336, 80, and 280 bourse shoots of AR, FU and RB, respectively, were retained from the 2014 experiment. Afterwards, for AR and RB, tests (ANOVA, Kruskal-Wallis) were conducted on 2014 data in order to establish the phenological stage of development expressed in growing degree days (GDD) since FB from which onwards each type of shoot for each genotype was fully developed in terms of number of leaves and total leaf area. This developmental time was first measured using growing degree hours [GDH, base temperature  $T_b = 7^\circ\text{C}$  (Anderson and Richardson, 1982)] calculated using hourly air temperatures ( $^\circ\text{C}$ ) obtained from the weather station of Beaucouzé ( $47^\circ 28' \text{N}, 0^\circ 37' \text{W}$ , 50 m a.s.l.) and accessed from the INRA Climatik platform, [https://intranet.inra.fr/climatik\\_v2/](https://intranet.inra.fr/climatik_v2/):

$$GDH_i = \sum_{h=1}^{24} (HT_h - T_b) \quad (1)$$

Here,  $HT_h$  is replaced by  $T_b$  if  $HT_h < T_b$ ;  $HT_h$  is the hourly air temperature at hour  $h$ ; and  $GDH_i$  are the growing degree hours on day  $i$ . Cumulated GDD ( $GDD_{cum}$ ) for each sampling day were calculated using Equation 2. The starting point of  $GDD_{cum}$  is full bloom (FB) which, in 2014, occurred for AR on April 10th, for FU on April 14th and for RB on April 22nd while in 2015, full bloom occurred for FU on April 20th.

$$GDD_{cum} = \sum_{i=FB}^D \frac{GDH_i}{24} \quad (2)$$

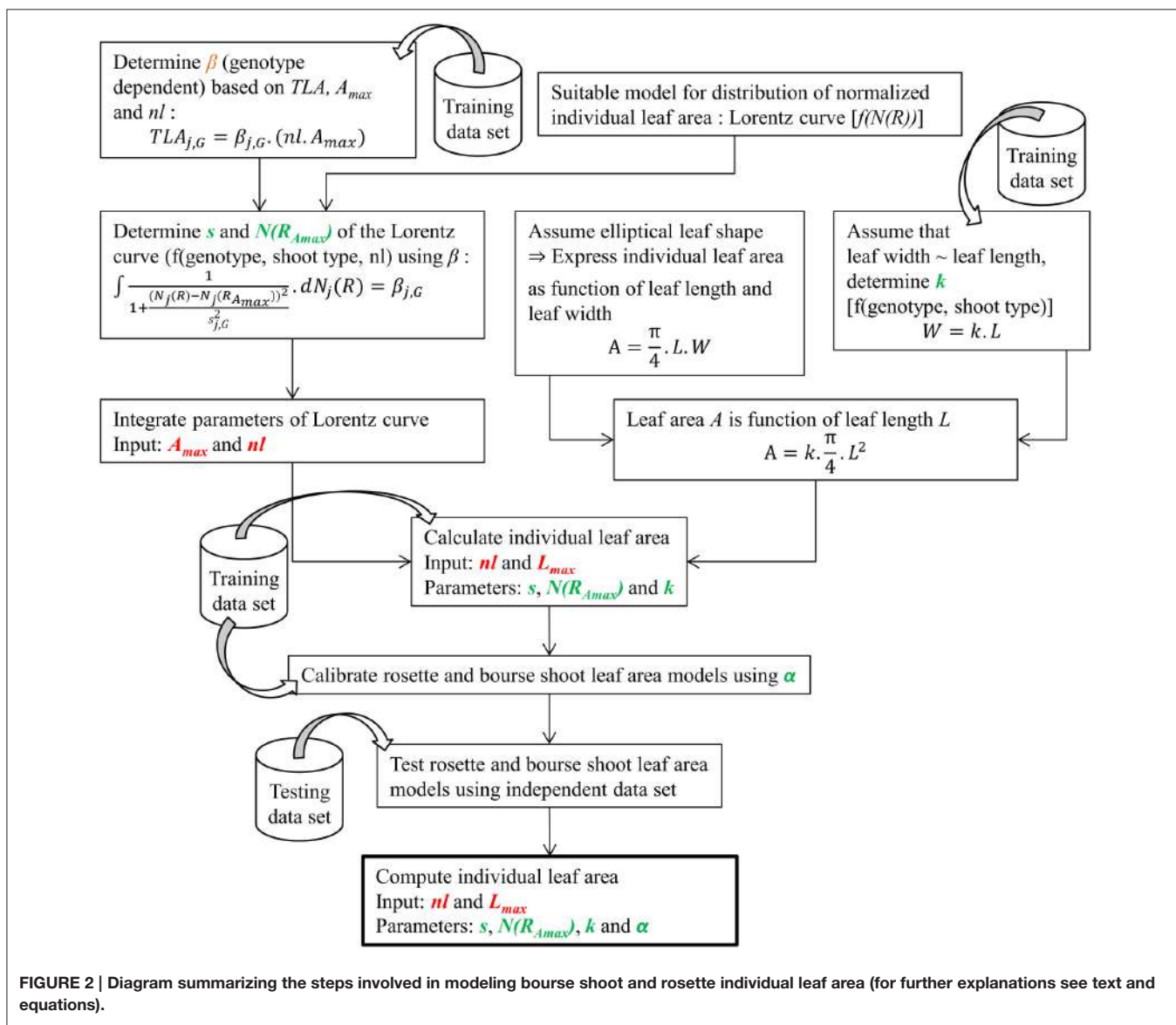
where  $FB$  is day of full bloom and  $D$  is the number of days since  $FB$ .

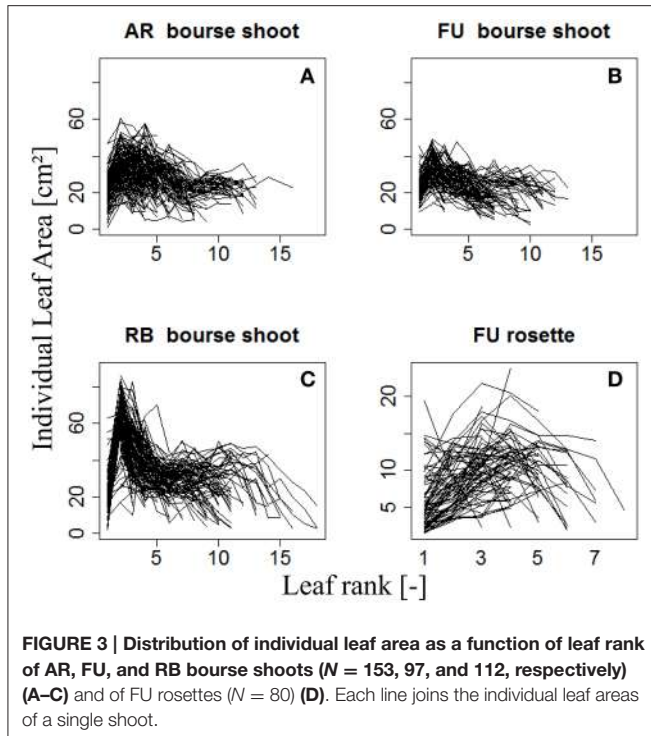
During the second experiment conducted in 2015, the same variables as in 2014 were recorded plus the ranks of rosette leaves; however, based on the results of the 2014 experiment no defoliation treatments were applied and only spurs of FU at different phenological stages (FB, FB+2, FB+4, FB+6, FB+9 weeks) were considered. For FU, ANOVA and Kruskal-Wallis analysis were carried out on 2015 and 2014 data to compare total leaf area and number of leaves (rosettes and bourse shoots) as a function of developmental stages (expressed in GDD) in order to establish the sampling stages at which the spur shoots were fully developed. Therefore, fully developed bourse shoots and rosette shoots, respectively, were pooled for each genotype. All shoots of the same type and the same genotype considered to be fully developed in terms of total leaf area and numbers of leaves were used in this study for building the allometric models. Total leaf areas and numbers of leaves of bourse shoots of AR, FU, and RB, were fully developed at 345, 201, and 275 GDD, respectively. Groups of bourse shoots of each genotype were selected from these physiological ages

onwards, until harvest. Rosette shoots were assumed to be fully developed at full bloom as the mean total leaf areas for the three genotypes were the highest at the earliest sampled spurs. However, even if a significant difference was found between groups of rosettes sampled at different phenological stages for a same genotype, still the means are not correlated with phenological sampling dates and the only group really apart in terms of rosette total leaf area and number of leaves for the three genotypes, respectively, was the one collected at harvest (Bairam et al., unpublished). Therefore, only rosettes collected before harvest were retained for the rest of the study. Only selected spurs were used for the rest of this study and data selected for each genotype and each shoot type was split randomly into a training set (2/3 of data) and a testing set (the remaining 1/3 of data) for setting up the models. The procedure to build the models for predicting bourse shoot and rosette individual leaf area is summarized in **Figure 2**. In the following, the steps

followed for building the models described in the flow chart are explained.

The variation of individual leaf areas of 153, 97, and 112 bourse shoots, respectively, of AR, FU, and RB, as a function of leaf rank is shown in (**Figures 3A–C**), and of 80 rosettes of FU considered to be fully grown shoots in (**Figure 3D**). Based on these observations, it was assumed that leaf size follows a rank-specific pattern typical for both bourse shoots and rosettes. In this study, we aimed to establish the pattern and parameterize it for each genotype and each type of shoot. However, the total leaf area of the shoot which can be calculated by integrating the sum of the areas of individual leaves of each rank seemed to be correlated with the number of leaves per shoot and the area of the biggest leaf (**Figure 3**). Furthermore, if this hypothesis would prove to be true, the result would confirm the existence of an allometric relation between the total leaf area on the one hand and the number of leaves and individual leaf area on the other.





Moreover, if individual leaf areas follow a stable pattern along the shoot, this would mean that only one of these areas would be necessary as an input to the model, and that then the biggest leaf area would be an appropriate variable. Therefore, the assumption made and expressed in (Equation 3) implies that total leaf area (TLA) of the shoot is somehow related to the area of the biggest leaf ( $A_{max}$ ) and the number of leaves ( $nl$ ).

$$TLA_{j,G} = \beta_{j,G} \cdot (nl \cdot A_{max}) \quad (3)$$

ANOVA and Kruskal-Wallis tests were carried out on the selected data set in order to check if there is a significant difference of the parameter  $\beta_{j,G}$  among genotypes for a same shoot type. Groups of samples showing no significant difference were pooled and the training set established before were used in order to fix  $\beta_{j,G}$  using linear regressions between the variable TLA and the variable  $nl \cdot A_{max}$ .

Therefore, total leaf area of a shoot can be estimated by two variables: the area of the biggest leaf on the shoot ( $A_{max}$ ) and the number of leaves ( $nl$ ) it bears. Thus, we made the assumption that the normalized individual leaf area [ $N(A_R)$ , expressed as the ratio of the individual leaf area by the biggest leaf area on the shoot (Equation 4a)] is a function of the normalized leaf rank [ $N(R)$ ], calculated as the ratio of the rank of the leaf divided by the number of leaves on the shoot (Equation 4b). However, we could observe that in bourse shoots, the leaf with the biggest area was by far the most often the second one (Table 1). Hence, in order to adjust a maximum of the curves describing  $N(A_R)$  as a function of  $N(R)$ , the normalized rank for bourse shoots was calculated by dividing [the rank ( $R$ ) minus 2] by the number of leaves (Equation 4c). Indeed, subtracting two from the rank of

**TABLE 1 | Distribution of the leaves with the biggest area on bourse shoots with respect to their rank for AR, FU, and RB genotypes.**

Genotype	Rank					
	1	2	3	4	5	6
AR	0.65%	50.00%	26.62%	15.58%	5.84%	1.30%
FU	8.08%	68.69%	14.14%	3.57%	0.89%	—
RB	—	87.50%	8.04%	3.57%	0.89%	—

the biggest leaf (2) will result in a normalized rank which is always zero and will lead to a very good alignment of the curves. Besides, with this method, the entire curve is just shifted to the left without being stretched or compressed.

$$N(A_R) = \frac{A_R}{A_{max}} \quad (4a)$$

$$N_{RO}(R) = \frac{R}{nl} \quad (4b)$$

$$N_{BS}(R) = \frac{R - 2}{nl} \quad (4c)$$

The models were established from predicting the normalized area of each leaf  $N(A_R)$  as a function of the normalized leaf rank  $N_j(R)$  by using the area of the biggest (in terms of leaf area) leaf ( $A_{max}$ ) on each shoot as a predictor of the other leaf areas. This hypothesis is expressed by Equation (5).

$$N(A_R) = f_{j,G}(N_j(R)) \quad (5)$$

For each type of shoot and each genotype, we looked for a function  $f_{j,G}$  that models the normalized area of each leaf on the shoot as a function of its normalized rank.  $N(A_R)$  was plotted as a function of  $N_j(R)$ , giving a certain pattern (Figure 4). We then tried to find a model that best described this relationship: a bilinear (broken stick) model and a Lorentz function. The first model requires five parameters while the second one only needs three. The Lorentz function has been successfully used by other workers (Buck-Sorlin, 2002; Evers et al., 2005, 2007; Gu et al., 2014) to predict leaf length in cereals and cotton. In this study, this function was chosen to model leaf areas of bourse shoots and rosettes.

$$f_{j,G}(x) = \frac{M}{1 + \frac{(x - x_0)^2}{s^2}} ; j \in \{BS; RO\} \quad (6)$$

The maximum is reached for  $x = x_0$ , with  $M$  being the maximum value.  $s$  defines the slope of the curve of the function  $f_{j,G}$ . For both bourse shoots and rosettes,  $f_{j,G}(x)$  corresponds to the normalized leaf area and  $x$  to the normalized leaf rank.  $x_0$  is the normalized rank of the leaf with highest area on the shoot [ $N_j(R_{Amax})$ ]. Consequently, the maximum of the function has the value of the normalized biggest area, i.e.,  $M = 1$  (Equation 7).

$$f_{j,G}(N_j(R)) = N(A_R) = \frac{1}{1 + \frac{(N_j(R) - N_{j,G}(R_{Amax}))^2}{s_{j,G}^2}} ; j \in \{BS; RO\} \quad (7)$$

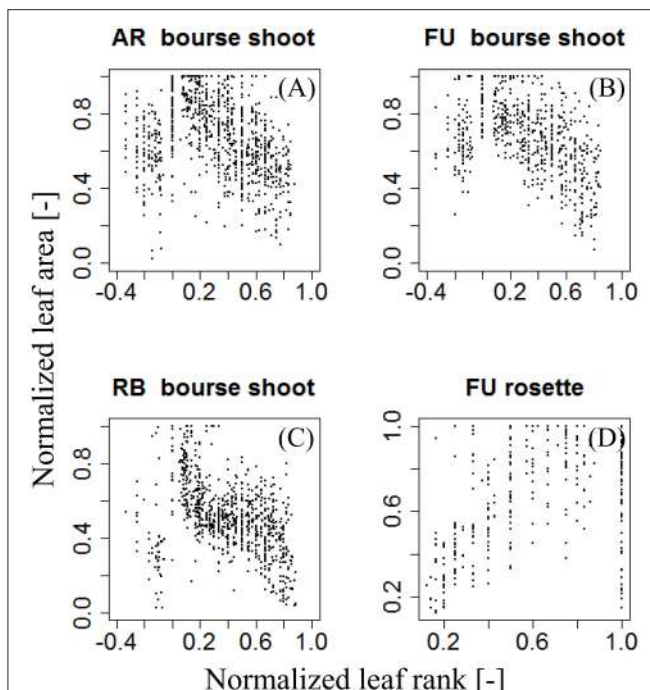


**FIGURE 4 | Distribution of individual normalized leaf area plotted against normalized leaf rank of AR, FU, and RB bourse shoots ( $N = 153, 97$ , and  $112$ ) (A–C) and FU rosettes ( $N = 80$ ) (D).**

After normalization for each type of shoot, Equations 7a and 7b are obtained:

$$f_{BS,G}(N_{BS}(R)) = N(A_R) = \frac{1}{1 + \frac{(N_{BS}(R))^2}{s_{BS,G}^2}} \quad (7a)$$

$$f_{RO,G}(N_{RO}(R)) = N(A_R) = \frac{1}{1 + \frac{(N_{RO}(R) - N_{RO,G}(R_{Amax}))^2}{s_{RO,G}^2}} \quad (7b)$$

Therefore, based on the fact that (i) the total leaf area ( $TLA_{j,G}$ ) of a shoot of type “ $j$ ” is the sum of the individual areas  $A_R$  of leaves and (ii) its value depends on the pattern described by Equations 7a and 7b, the models (Equation 3) were derived as follows:

$$\begin{aligned} TLA_{j,G} &= \beta_{j,G} \cdot (nl \cdot A_{max}) \\ \sum_{R=1}^{nl} A_R &= \beta_{j,G} \cdot (nl \cdot A_{max}) \\ \sum_{R=1}^{nl} \frac{A_R}{A_{max}} \cdot \frac{1}{nl} &= \beta_{j,G} \\ \sum_{R=1}^{nl} \frac{N(A_R)}{nl} &= \beta_{j,G} \\ \int f_{j,G}(N_j(R)) \cdot dN_j(R) &= \beta_{j,G} \\ \left\{ \begin{array}{l} \int_{-\frac{nl-2}{nl}}^{\frac{nl-2}{nl}} \frac{1}{1 + \frac{(N_{BS}(R))^2}{s_{BS,G}^2}} \cdot dN_{BS}(R) = \beta_{BS,G} \\ \int_0^1 \frac{1}{1 + \frac{(N_{RO}(R) - N_{RO,G}(R_{Amax}))^2}{s_{RO,G}^2}} \cdot dN_{RO}(R) = \beta_{RO,G} \end{array} \right. \end{aligned}$$

$$[s_{BS,G} \cdot \text{atan}\left(\frac{N_{BS}(R)}{s_{BS,G}}\right)]_{-\frac{nl-2}{nl}}^{\frac{nl-2}{nl}} = \beta_{BS,G} \quad (8a)$$

$$[s_{RO,G} \cdot \text{atan}\left(\frac{N_{RO}(R) - N_{RO,G}(R_{Amax})}{s_{RO,G}}\right)]_0^1 = \beta_{RO,G} \quad (8b)$$

When solving Equation 8a used for the bourse shoot leaf area model, the only parameter to fix was  $s_{BS,G}$  and its different values were calculated as a function of the value of  $\beta_{BS,G}$  (which is unique for a same genotype and shoot type) and  $nl$  (from 1 to 18). Equation 8b used for parameterizing the rosette leaf area model does not take into account the number of leaves and it was solved using only  $\beta_{RO,G}$ . However, in this second equation two parameters of the model [ $s_{RO,G}$  and  $N_{RO,G}(R_{Amax})$ ] had to be fixed. Both equations 8a and 8b were solved using the solver functionality of Microsoft Excel software (Microsoft, Redmond, WA, USA).

Starting from Equation 7, the model is expressed as:

$$\begin{aligned} N(A_R) &= \frac{1}{1 + \frac{(N_j(R) - N_j(R_{Amax}))^2}{s_{j,G}^2}} ; j \in \{BS; RO\} \\ A_R &= \frac{A_{max}}{1 + \frac{(N_j(R) - N_j(R_{Amax}))^2}{s_{j,G}^2}} ; j \in \{BS; RO\} \end{aligned} \quad (9)$$

$$\begin{aligned} A_R &= \frac{A_{max}}{\frac{(R - R_{Amax})^2}{(R - R_{Amax})^2 + s_{j,G}^2}} ; j \in \{BS; RO\} \\ A_R &= \frac{A_{max}}{1 + \frac{(R - R_{Amax})^2}{nl^2 \cdot s_{j,G}^2}} ; j \in \{BS; RO\} \end{aligned} \quad (10)$$

By fixing the latter parameters, it was possible to calculate the normalized area of each leaf, using only the number of leaves on the shoot and the area of its biggest leaf. However, as the leaf area is not easily measurable non-destructively, further allometric relations are required for predicting leaf areas using variables that are more easily accessible. Leaf length and width seem to be the most obvious candidates for modeling the leaf area as we consider the leaf blade to be elliptical (Equation 11). Observations of leaves indicate that the length/width ratio is constant for a same genotype and shoot type (Equation 12). Assuming this is confirmed, only the variable “length of the leaf” ( $L$ ) could be retained for calculating the individual leaf area. This assumption is stated as follows: (i) the ratio between the length ( $L$ ) and the width ( $W$ ) of a leaf is a constant parameter ( $k_{j,G}$ ) for the same shoot type ( $j$ ) and the same genotype ( $G$ ) and (ii) apple leaves have the shape of an ellipse (Freeman and Bolas, 1956). These two hypotheses are captured by Equations 11 and 12.

$$A = \pi \frac{L \cdot W}{4} \quad (11)$$

$$\frac{W}{L} = k_{j,G} \quad (12)$$

The Shape of an ellipse is defined by its eccentricity  $e$ , i.e., the ratio between the distance from the center to a focus and the distance between that focus to a vertex (Equation 13a). Therefore,  $k_{j,G}$  can be expressed as a function of  $e_{j,G}$  (Equation 13b). If  $e_{j,G}$  is proven

to be invariant for a same genotype and a same type of shoot, it could be used in the model as the constant for leaves on shoots of type  $j$  and of cultivar  $G$ ;  $0 < k_{j,G} \leq 1$

$$e_{j,G} = \frac{\sqrt{L^2 - W^2}}{L} \quad (13a)$$

$$k_{j,G} = \sqrt{1 - e_{j,G}^2} \quad (13b)$$

Therefore,  $e_{j,G}$  was calculated for each leaf used in this study using Equation 13a, as it is an indicator of the shape of the ellipse defined by the leaf. Then, a first test was done in order to check if there is a significant difference in  $e_{j,G}$  among the leaves of different ranks in a shoot within the same cultivar for each type of shoot. A second test was conducted to verify if there is a significant difference of  $e_{j,G}$  among the three genotypes for each type of shoot. Moreover, even if the leaf shape is genotype dependent, the environment can influence it during the last stages of leaf development (Tsukaya, 2004). Therefore, a test was done in order to check if there is a significant difference of  $e_{j,G}$  between 2014 ( $N = 323$  and  $N = 159$ , for bourse shoots and rosettes, respectively) and 2015 ( $N = 385$  and  $N = 363$ , for bourse shoots and rosettes, respectively) leaves of FU. Leaf data with no significant difference in  $e$  were pooled and the training set of the bearing spurs was used to fix  $k_{j,G}$  using a linear model.

Combining Equations (11) and (12), the following relation (14) is obtained:

$$A = \frac{\pi}{4} \cdot k_{j,G} \cdot L^2 \quad (14)$$

By combining Equation (10) and Equation (14), equation (15) is obtained.

$$A_R = \frac{\frac{\pi}{4} \cdot k_{j,G} \cdot L_{max}^2}{1 + \frac{(R - R_{Amax})^2}{nl^2 \cdot s_{j,G}^2}}; j \in \{BS; RO\} \quad (15)$$

In this way,  $L_{max}$  (the length of the biggest leaf on the shoot) and  $nl$  are the only two required input variables.

Using the models established we calculated individual leaf area and total leaf area on a shoot as the sum of the calculated individual leaf areas on the training set. Comparisons were made using the linear model between measured and calculated total leaf areas on each type of shoot and each genotype separately. Then, calibrations were made using a parameter  $\alpha_{j,G}$  referring to the slope of the axis defined by measured total leaf area on a shoot ( $TLA_{j,G}$ ) as a function of calculated total leaf area on a shoot ( $CTLA_{j,G}$ ) of the training set.  $\alpha_{j,G}$  was calculated for each type of shoot and each genotype separately.

The final model calculating individual leaf area is:

$$A_R = \alpha_{BS,G} \frac{\frac{\pi}{4} \cdot k_{BS,G} \cdot L_{max}^2}{1 + \frac{(R - 2)^2}{nl^2 \cdot s_{BS,G}^2}} \quad (16a)$$

$$A_R = \alpha_{RO,G} \frac{\frac{\pi}{4} \cdot k_{RO,G} \cdot L_{max}^2}{1 + \frac{(R - nl \cdot N_{RO,G} \cdot (R_{Amax}))^2}{nl^2 \cdot s_{RO,G}^2}} \quad (16b)$$

The testing set was then used for calculating individual and total leaf areas. Using the testing data set, comparisons were made between measured and calculated data (i) for each established parameter, (ii) for individual leaf area and (iii) total leaf area on each shoot of each genotype using the linear model.  $P$ -values and coefficients of determination  $R^2$  were calculated in order to analyze and interpret the significance and the goodness of fit of the models. For rosettes, as the ranks of leaves on the bourse were not recorded in the 2014 experiment, comparisons between measured and calculated values of individual area were done only on data from 2015.

## Modeling the Leaf Area of Vegetative Shoots

For modeling the leaf area of vegetative shoots, 20 vegetative shoots each of AR and FU were collected on July 3rd, 2015 when they were considered to be fully developed, then scanned and analyzed as described for bourse shoots and rosettes. Total leaf area on each vegetative shoot was calculated as the sum of areas of individual leaves. Leaf ranks on each shoot were recorded, and lengths and dry weights of the shoots and the leaves measured. The variation of individual leaf areas of the 20 vegetative shoots of AR and FU as a function of leaf rank is shown in (Figures 5A,B): leaf area increases with rank for both genotypes. However, the pattern is heterogeneous when based on absolute leaf length measurements and ranks. We therefore normalized both leaf areas (Equation 4a) and ranks (Equation 4b). On visual inspection, the distribution of  $N(A_R)$  as a function of  $N(R)$  on vegetative shoots of both genotypes (Figures 5C,D) seems to describe a linear pattern (Equation 17). We made the assumption that  $A_R$  is proportional to the square of leaf length  $L_R^2$  as for bourse shoots and rosettes (Equation 14). Eccentricity ( $e_{VS,G}$ ) of the ellipse was calculated for each leaf and comparison tests were made between the two genotypes, then  $k_{VS,G}$  (ratio between width and length of the leaf blade) was fixed for the model. Afterwards and using the previously fixed  $k_{VS,G}$ , a parameter  $p$  which describes the slope of the curve was calculated for each leaf using Equation 17 and a statistical comparison was carried out between the two cultivars in order to check if they were different with respect to  $p$ . Based on this comparison,  $p$  was fixed using a linear regression model. The vegetative shoot model (Equation 18) is a descriptive model allowing calculating the individual leaf areas of AR and FU vegetative shoots using only two variables,  $L_{max}$  and  $nl$ . A regression test was carried out using the linear model between the calculated individual areas and the measured ones.

$$N(A_R) = p \cdot N(R) \quad (17)$$

$$\frac{A_R}{A_{max}} = p \cdot \frac{R}{nl}$$

$$A_R = p \cdot \frac{R}{nl} \cdot A_{max}$$

$$A_R = p \cdot \frac{R}{nl} \cdot \frac{\pi}{4} \cdot k_{j,G} \cdot L_{max}^2 \quad (18)$$

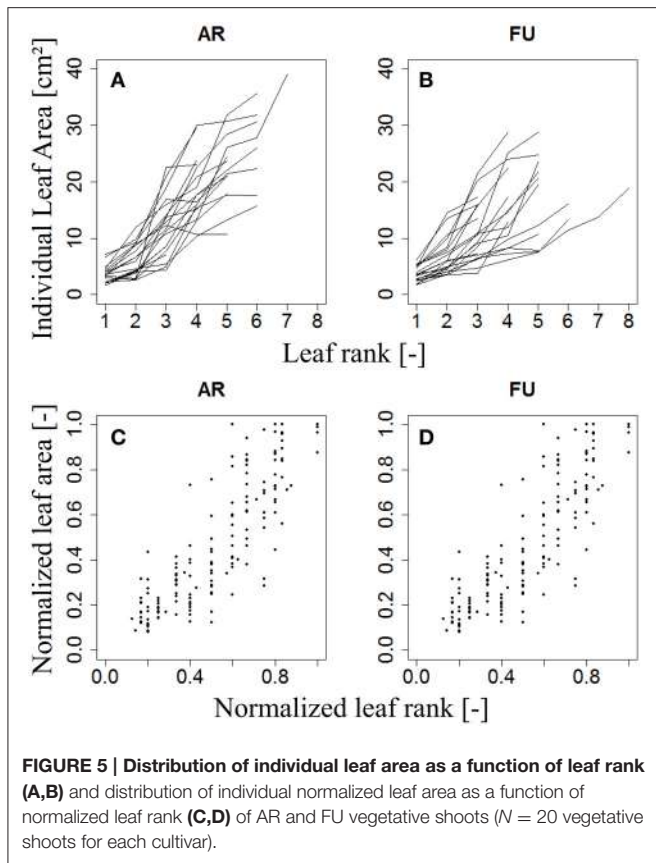


**FIGURE 5 |** Distribution of individual leaf area as a function of leaf rank (**A,B**) and distribution of individual normalized leaf area as a function of normalized leaf rank (**C,D**) of AR and FU vegetative shoots ( $N = 20$  vegetative shoots for each cultivar).

## Modeling Length of Spur Internodes

The internode lengths of 20 spurs of “FU” were measured in the orchard in July 2016. As the bourse internodes are very short, we assigned to each one the mean value of the bearing spur calculated as the ratio of “Length of the bourse”/“Number of internodes on the bourse.” For each spur, a “cumulative shoot length”  $D_I$  between the base of the bourse (rosette) and the node (leaf insertion point) for each bourse and bourse shoot leaf was measured. For bourse shoot nodes, this cumulative shoot length is equal to the sum of the lengths of the rosette internodes from the base of the bourse to the node on which is inserted the bourse shoot ( $BL$ ) and the sum of the internode lengths from the base of the bourse shoot to the considered node. The rank of each internode, on each spur, was also recorded from the first rosette leaf to the last bourse shoot leaf, assuming that the rank of the first internode of the bourse shoot has the value of the rank of the bourse internode on which it is inserted, plus one. Among the 20 spurs, 16 were bearing only one bourse shoot and the remaining ones were bearing two bourse shoots. Plotting this cumulative shoot length  $D_I$  as a function of cumulative (bourse and bourse shoot) rank  $R_I$  corresponded to a logistic pattern for each spur (Figure 6). However, the pattern seemed to be dependent upon the length of the shoot (bourse plus bourse shoot). Therefore, normalized cumulative internode lengths [ $N(D_I)$ ] between each leaf base and the base of the bourse (Equation 19a) and normalized rank [ $N(R_I)$ ] (Equation 19b) were calculated assuming that the bourse and the bourse shoot are the same shoot unit (and that, therefore, the bourse shoot is a

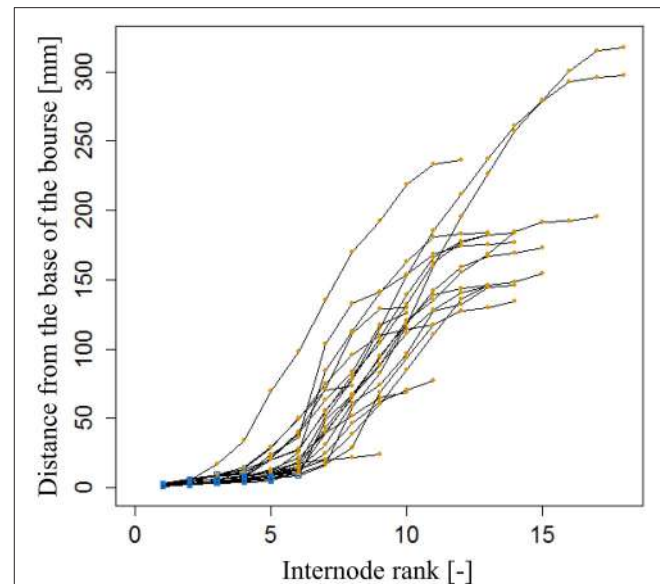


**FIGURE 6 |** Cumulated length of bourse and bourse shoots, expressed as the distance from the base of the bourse to the point of insertion of a bourse or a bourse shoot leaf of internode rank 1–18 in FU [ $N = 24$ , continuum: bourse (●) - bourse shoot (○)].

sylleptic extension of the bourse). The normalized cumulative shoot length was calculated as a function of the sum of  $BL$  and the bourse shoot length ( $BSL$ ).

$$N(D_I) = \frac{D_I}{BL + BSL} \quad (19a)$$

$$N(R_I) = \frac{R_I}{nl} \quad (19b)$$

Afterwards, the parameters  $qi$  and  $si$  of the internode model were fixed by fitting a logistic model (Equation 20) to the distribution of the  $N(D_I)$  as a function of  $N(R_I)$ .

$$N(D_I) = \frac{1}{1 + \exp\left(\frac{qi - N(R_I)}{si}\right)} \quad (20)$$

Once established, this descriptive model would estimate the cumulative shoot length of each leaf insertion point of rank  $R_I$  on the bourse or the bourse shoot from the bottom of the bourse providing 3 input variables:  $nl$ ,  $(BL + BSL)$  and  $R_I$  (Equation 21).

$$D_I = \frac{1}{1 + \exp\left(\frac{qi - R_I}{si}\right)} \cdot (BL + BSL) \quad (21)$$

## Statistical Analyses

Statistical analyses were done using R Studio software version 0.98.1062.0 running R version 3.2.2, and the statistical computing environment of the R-package “agricolae,” version 1.2-2. Normality of data used for each analysis was tested on residuals using the Shapiro-Wilk test for data sets with more than 50 samples per group or sample distributions considered to be

normal ( $P > 0.05$ ); ANOVA tests were used to check if there was a significant difference among groups ( $P < 0.05$ ). Otherwise differences between groups were tested with the Kruskal-Wallis test ( $P < 0.05$ ), or both ANOVA and Kruskal-Wallis. Fit of data to selected models was checked using the *lm* function in R software for linear distribution models. The logistic model was parameterized using the *SSlogis* function in R software and coefficients of determination ( $R^2$ ) and root mean squared errors (RMSE) were calculated to test the fit of the model.

## RESULTS

### Modeling the Leaf Area of Bourse Shoots (BS)

ANOVA made on  $\beta_{BS,G}$  of bourse shoots showed there was no significant difference between AR (mean  $\beta_{BS,AR} = 0.71$ ) and FU (mean  $\beta_{BS,FU} = 0.70$ ). However, bourse shoots of both AR and FU were significantly different from RB with respect to  $\beta_{BS,G}$  (mean  $\beta_{BS,RB} = 0.53$ ). Therefore, the same value of  $\beta_{BS,G}$  was used for the training data set of AR and FU bourse shoots, while for RB bourse shoots a separate training data set was used, thus necessitating the parameterization of two linear regression models (Figures 7A,B). For both groups, the linear model was significant ( $P < 2.10^{-16}$ ). The coefficients of determination for both the AR|FU model and the RB model were sufficiently high ( $R^2 = 0.95$  and  $R^2 = 0.89$ ) to support the assumption that the values of  $\beta_{BS,G}$  ( $\beta_{BS,AR/FU} = 0.67$  and  $\beta_{BS,RB} = 0.50$ ) were robust.

Using the values of  $\beta_{BS,G}$  Equation 8a was solved and  $s_{BS,AR|FU}$  and  $s_{BS,RB}$  were established as a function of the number of leaves on the bourse shoot. The number of leaves recorded on bourse shoots sampled varied from 1 to 16, 13 and 18, respectively, for AR, FU and RB. Thus 18 values for  $s_{BS,G}$  were established for each one of the two groups of genotypes (Table 2).

$e_{BS,G}$  was significantly different among genotypes ( $p < 2.2.10^{-16}$ ), with means of  $e_{BS,G}$  equal to 0.79, 0.76, and 0.74 for AR, FU and RB, respectively. ANOVA tests showed no significant differences among the shapes of leaves of different ranks on

a bourse shoot ( $e_{BS,G}$ ). However, leaves above rank 14 in AR and leaves above rank 15 in RB seemed to indicate a significant difference, but based on the weak frequencies of these leaf ranks (only one bourse shoot of AR and 15 bourse shoots of RB having more than 13 and 15 leaves, respectively), it was decided not to take into account this difference. Furthermore,  $e_{BS,FU}$  was not significantly different between 2014 and 2015 ( $p = 0.59$ ). Therefore, it was considered that the impact of the factor year was not significant.

$k_{BS,G}$  was fixed for AR, FU and RB using linear regression models on the training set of each genotype (Figures 8A–C) and the leaf length of each genotype was significantly correlated with its width ( $P < 2.10^{-16}$  for all the genotypes' models), with coefficients of determination of 0.68, 0.73, and 0.72 for AR, FU

**TABLE 2 | Parameterization of  $s_{BS,G}$ .**

NL	AR & FU	RB
1	2.13	1.48
2	0.70	0.43
3	0.38	0.23
4	0.35	0.22
5	0.36	0.22
6	0.38	0.23
7	0.40	0.24
8	0.42	0.25
9	0.44	0.25
10	0.46	0.26
11	0.48	0.27
12	0.49	0.28
13	0.51	0.29
14	0.52	0.30
15	0.53	0.31
16	0.54	0.31
17	0.55	0.32
18	0.55	0.32

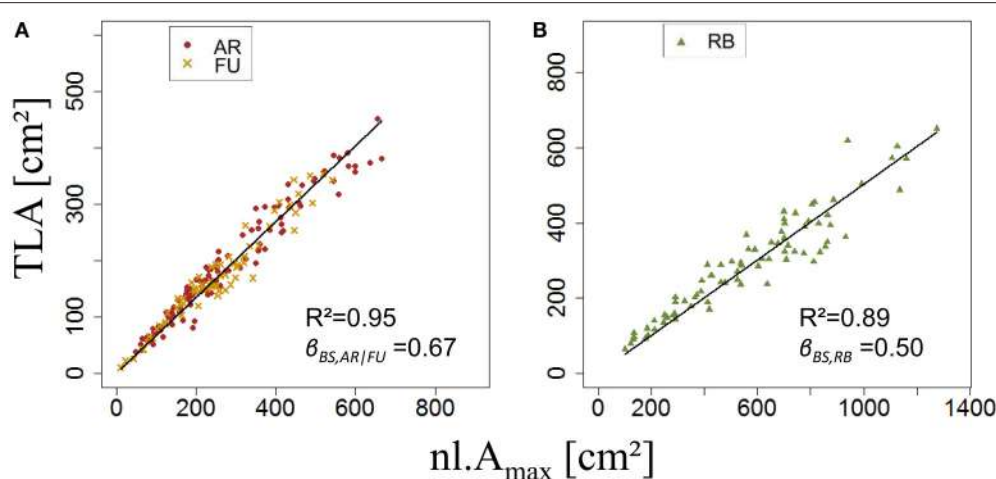


**FIGURE 7 |** Parameterization of  $\beta_{BS,G}$  ( $N = 180$  and  $80$  bourse shoots, respectively; A,B).

and RB, respectively.  $k_{BS,G}$  values were fixed to 0.60, 0.64, 0.66 for AR, FU and RB, respectively.

Once  $s_{BS,G}$  and  $k_{BS,G}$  were fixed, all leaf areas of the bourse shoot training set were calculated using Equation 15, with the rank of the leaf and the variables  $L_{max}$  and  $nl$  of each bourse shoot as input. Total leaf area on each shoot was calculated as the sum of individual leaves. Calculated and measured total leaf areas ( $CTLA_{BS,G}$  and  $TLA_{BS,G}$ ) of the bourse shoots were compared for each genotype using a linear regression where the slope  $\alpha_{BS,G}$  of each regression model of  $TLA_{BS,G}$  as a function of  $CTLA_{BS,G}$  was expected to be equal to 1 if the calculated and the measured area were identical. The slope parameter was equal to 1.2, 0.99 and 1.87 for AR, FU and RB, respectively (Figures 9A–C), which led us to assume that the parameter  $\alpha_{BS,G}$  was genotype dependent. Therefore, values of  $\alpha_{BS,G}$  fixed using the training set were retained for calibrating the model. The model defined in Equation 15 and built for bourse shoots including the three parameters ( $s_{BS,G}$ ,  $k_{BS,G}$  and  $\alpha_{BS,G}$ ) and using the variables  $L_{max}$  and  $nl$  for the prediction of individual leaf areas was used to calculate individual areas for each leaf of the testing set and the comparison with measured individual data was conducted using a linear model. In the testing set, though linear models of calculated individual leaf area as a function of measured individual leaf area were significant for all genotypes

( $P < 2.10^{-12}$ ), the coefficients of determination were very small ( $R^2 = 0.17, 0.20, 0.30$  for AR, FU and RB, respectively). In contrast to this, linear regression modeling of  $TLA_{BS,G}$  as a function of  $CTLA_{BS,G}$  yielded significant results for all genotypes ( $R^2 = 0.84, 0.67$  and  $0.64$ ; slope = 1.02, 1.05 and 0.95 for AR, FU and RB, respectively; Figures 10A–C).

## Modeling the Leaf Area of Rosettes (RO)

Both ANOVA and Kruskal-Wallis test showed there was no significant difference between the three genotypes with respect to  $\beta_{RO,G}$ . Thus  $\beta_{RO,G}$  was fixed to 0.69 using a linear regression model on the training set of rosette data of bourses sampled before harvest of the three genotypes (Figure 11A). The model was significant ( $P < 2.10^{-16}$ ) and the coefficient of determination was high ( $R^2 = 0.97$ ). Afterwards, the values of parameters  $s_{RO,G}$  and  $N_{RO,G}(R_{Amax})$  were fixed to 0.38 and 0.63, respectively.

$e_{RO,G}$  was significantly different among genotypes ( $P = 3.46.10^{-8} < 0.05$ ), with means of  $e_{RO,G}$  equal to 0.65, 0.66 and 0.68 for AR, FU and RB, respectively. When comparing  $e_{BS}$  of different ranks on rosettes of FU sampled in 2015, both ANOVA and Kruskal –Wallis test showed there were no significant differences among the shapes of leaves of different ranks on the bourse.  $e_{RO,FU}$  did in fact significantly vary between the 2 years ( $P = 2.162.10^{-7}$ ).

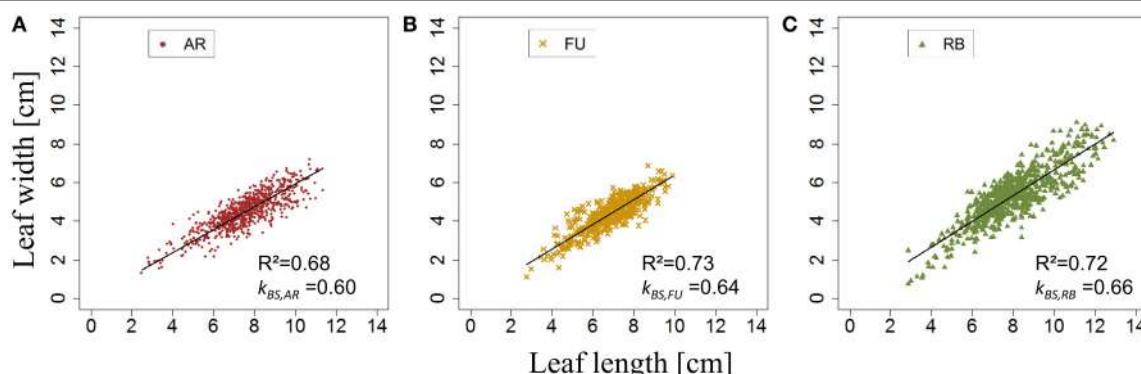


FIGURE 8 | Parameterization of  $k_{BS,G}$  ( $N = 763, 465$ , and  $655$  bourse shoot leaves, respectively; A–C).

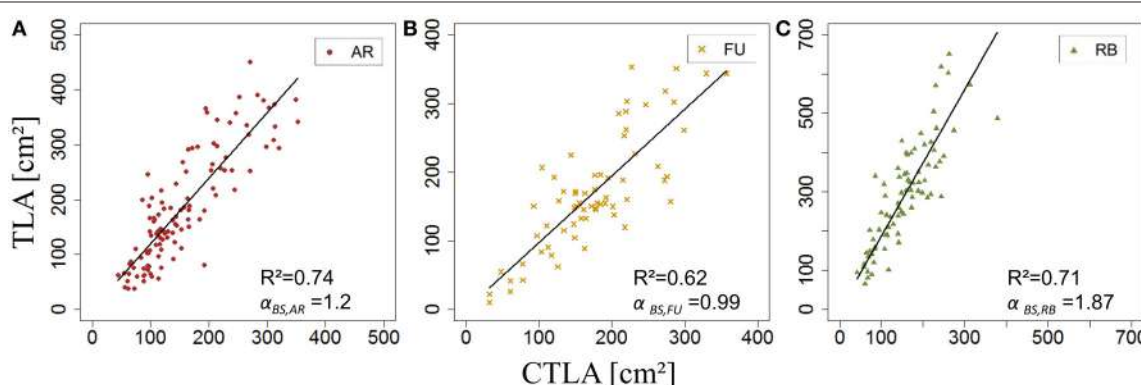
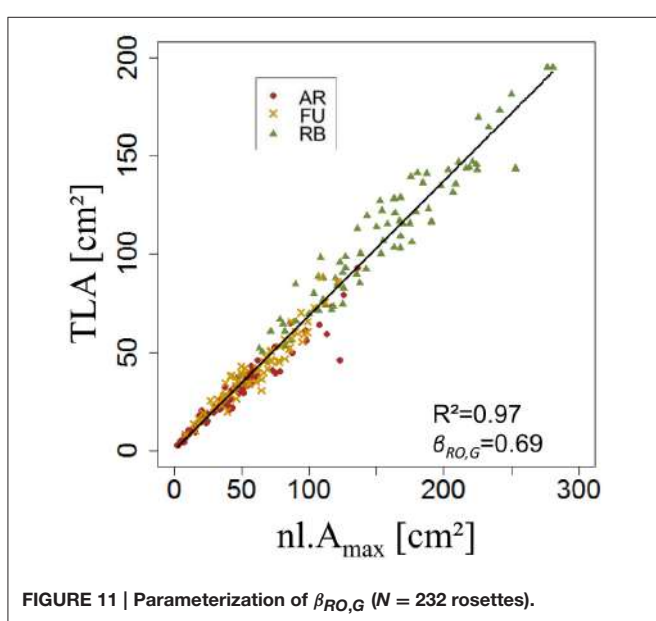
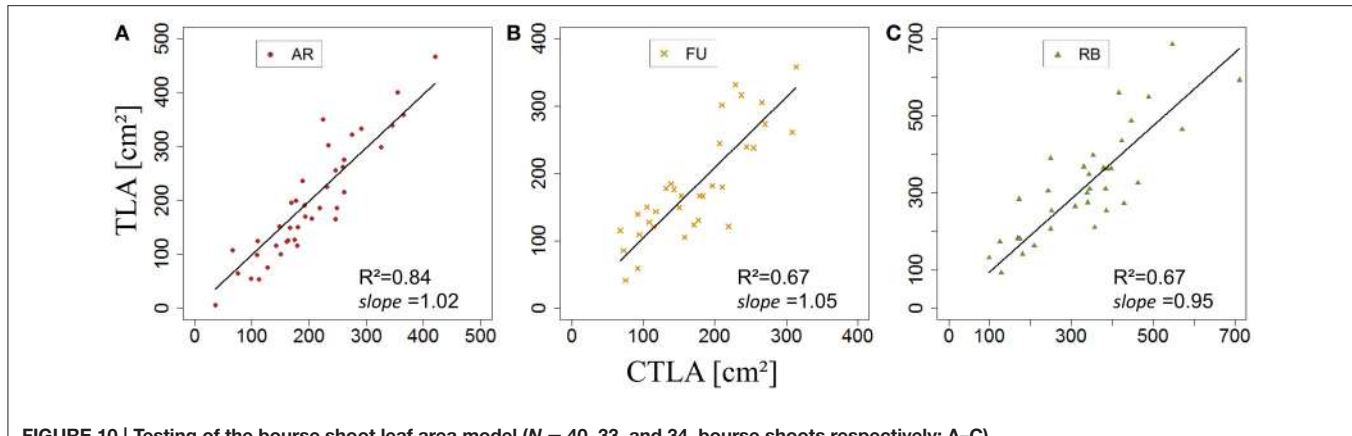


FIGURE 9 | Calibration of the bourse shoot leaf area model: parameterization of  $\alpha_{BS,G}$  ( $N = 114, 66$ , and  $80$  bourse shoots, respectively; A–C).



$k_{RO,G}$  was established for AR, FU, and RB using linear regression models on the training set of each genotype (Figures 12A–C) and the leaf lengths of each genotype were significantly correlated with leaf width ( $P < 2.10^{-16}$  for all the genotypes' models) with  $R^2 = 0.86, 0.85$  and  $0.85$  for AR, FU and RB, respectively.  $k_{RO,G}$  values were fixed to  $0.75, 0.74$  and  $0.71$  for AR, FU and RB, respectively. Regression models of  $TLA_{RO,G}$  as a function of  $CTLA_{RO,G}$  conducted on the training data set showed a significant relationship ( $P < 2.10^{-16}$ ) for the three genotypes with  $R^2$  of  $0.83, 0.88$  and  $0.91$  for AR, FU and RB, respectively. However, the  $CTLA_{RO,G}$  were bigger than the  $TLA_{RO,G}$  as can be seen from the slopes. Therefore, their values were assigned to  $\alpha_{RO,G}$  ( $0.86, 0.92, 0.92$ , respectively) to calibrate the rosette model (Figure 13). After that, individual and total leaf areas for each rosette were established for the testing set. The linear regression model of measured individual leaf area as a function of calculated individual leaf area showed a significant relationship ( $P < 2.10^{-16}$ ) for FU samples of 2015 ( $R^2 = 0.52$ ). The slope of the regression model (ratio between measured and calculated leaf area) was equal to  $0.92$ . Linear

models simulating  $TLA_{RO,G}$  as a function of  $CTLA_{RO,G}$  were all significant ( $P < 2.10^{-16}$ ). The predictive models (Figure 14) had high coefficients of determination ( $0.88, 0.85$  and  $0.70$  for AR, FU and RB, respectively) and the slopes were equal to  $1$  for the three genotypes ( $1.06, 1$  and  $1$ , respectively).

## Modeling the Leaf Area of Vegetative Shoots (VS)

Neither ANOVA nor Kruskall-Wallis tests showed any significant difference in  $e_{VS,G}$  between AR and FU ( $P = 0.54$  and  $0.49$ , for each test, respectively). Thus,  $k_{VS,G}$  was fixed ( $k_{VS,G} = 0.56$ ) using a linear regression model using data of both genotypes. The regression model showed a significant relationship between leaf length and width ( $P < 2.10^{-16}$ ) and  $R^2$  was equal to  $0.79$ . Besides, neither ANOVA nor Kruskal-Wallis test showed any significant difference in the variable  $p$  between genotypes AR and FU. The linear model used to fix  $p_{VS,G}$  ( $p_{VS,G} = 0.95$ ) was significant ( $P < 2.10^{-16}$ ) with  $R^2 = 0.83$ .

## Modeling Internode Lengths of Spurs

Parameterization of the internode model fixed the value of  $q_i$  to  $0.62$  and that of  $si$  to  $0.12$  (Figure 15). Both the coefficient of determination and the RMSE indicated a very good fit of the model to the distribution of measured data ( $R^2 = 0.96$ ; RMSE =  $0.08$ ). Indeed, the model exhibited a common pattern involving bourse and bourse shoot internodes. Moreover, the model showed that rosette internodes correspond to the first part of the logistic equation (exponential phase), while bourse shoot internodes belong to the second part (linear phase).

## DISCUSSION

Several studies show the determinism of plant architecture traits (Lauri and Trottier, 2004; Kahlen and Stützel, 2007; Massonnet et al., 2008). In this study we assumed that the distribution of normalized individual leaf area as a function of normalized rank is described by a similar pattern regardless of shoot size and, therefore, that the total leaf area of a shoot is proportional to the product of the leaf number times the area of the biggest leaf. Spann and Heerema (2010) also showed relationships between shoot leaf area and the product of the number of leaves and

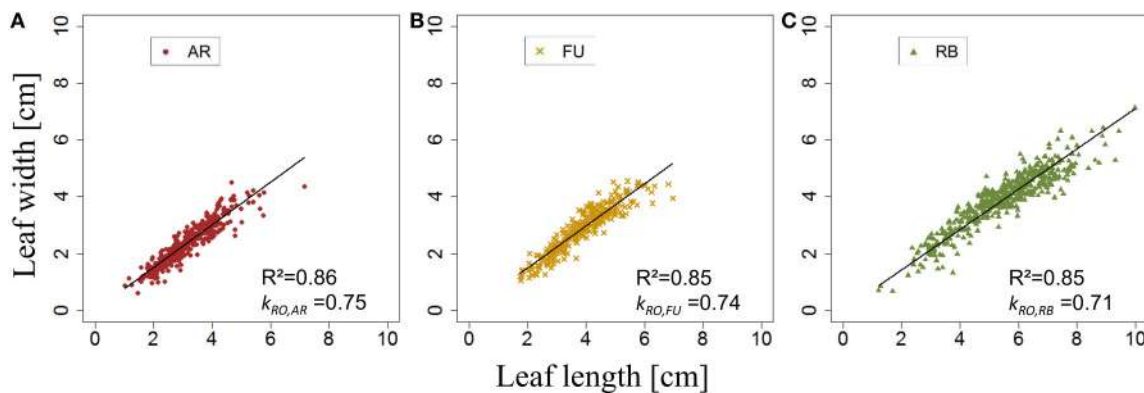


**FIGURE 12 |** Parameterization of  $k_{RO,G}$  ( $N = 375, 303$ , and  $475$  rosette leaves, respectively; A–C).

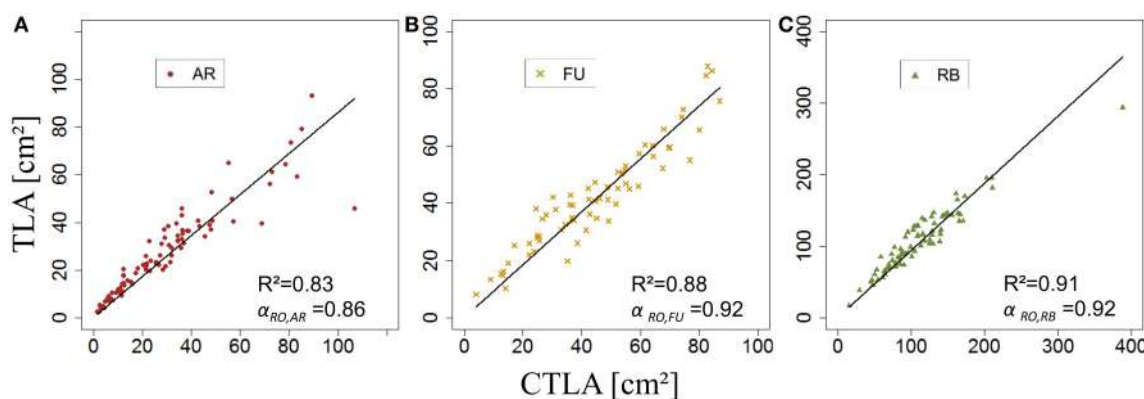


**FIGURE 13 |** Calibration of the rosette leaf area model: parameterization of  $\alpha_{RO,G}$  ( $N = 87, 67$ , and  $78$  rosettes, respectively; A–C).

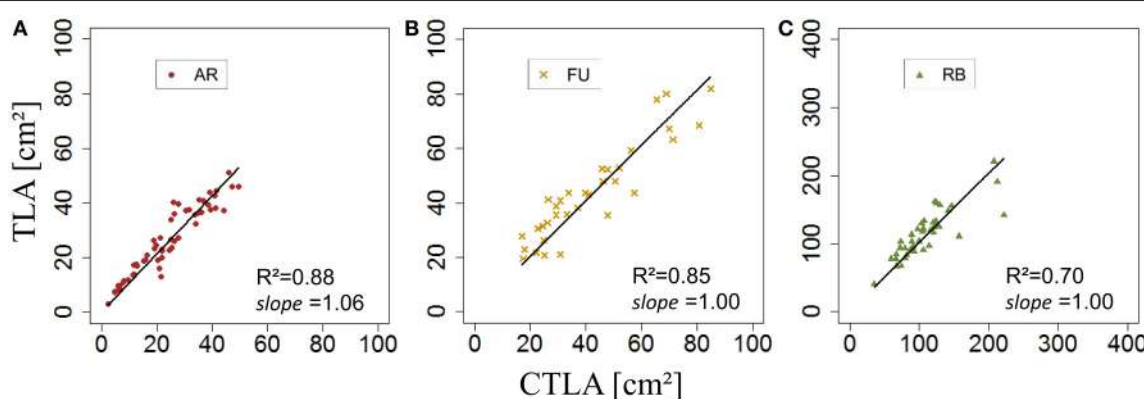


**FIGURE 14 |** Testing of the rosette leaf area model ( $N = 57, 33$ , and  $40$  rosettes, respectively; A–C).

length of longest leaf, for different species. However, the models presented here were conceived with the aim to link parameters that have the same unit (i.e.,  $\text{cm}^2$ ), both being expressions of surface. This is also the reason why in our final model, which only takes into account leaf lengths and numbers, leaf length is expressed as the square of itself. What is more, the linear model linking measured shoot total leaf area ( $TLA$ ) with the product of

leaf number ( $nl$ ) and area of the biggest leaf ( $A_{max}$ ), exhibits a larger coefficient of determination than the regression between  $TLA$  and the product of  $nl$  and the length of the longest leaf ( $L_{max}$ ) (data not shown). Although the predictive capacity of our models with respect to individual leaf area was not optimal, the model was nevertheless based on a very good prediction of the total shoot leaf area. Indeed, in the case of the rosette and the bourse

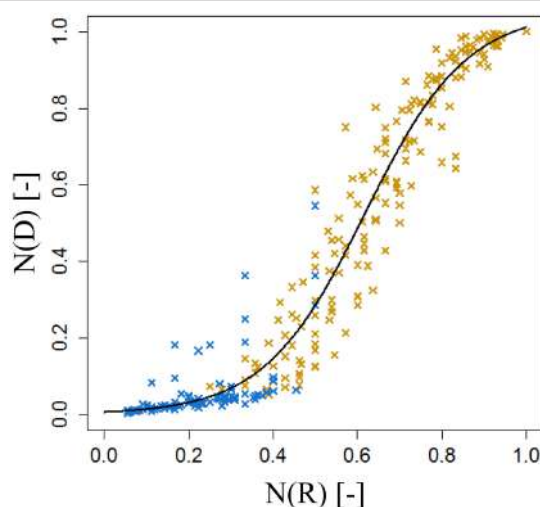


**FIGURE 15 | Parameterization of the cumulative shoot length model on FU spurs.**  $N(R_i)$ , normalized rank;  $N(D_i)$ , normalized cumulative shoot length from the base of the bourse [ $N = 24$ , continuum: bourse ( $\times$ ) – bourse shoot ( $x$ )].

shoot, we have chosen to construct our model as a function of the parameter  $\beta$  which is described by the slope of TLA versus  $nL.A_{max}$ , and not by parameterizing a Lorentz function, on the distribution of the point cloud which describes the normalized individual leaf surface as a function of the normalized rank. This choice was made on the one hand because of the absence of a particular pattern and therefore, the scatter of data points was considered to be too big; on the other hand, because of the proven robustness of  $\beta$  which we wanted to conserve for the development of the model. Besides, it is not unlikely that the fact that we had to use a calibration parameter ( $\alpha$ ) for each genotype and each shoot type (rosette and bourse shoot) is due to the way the point cloud deviates from the chosen Lorentz equation according to the genotype. Furthermore, even if the prediction of individual leaf area is not ideal, it is still faithful to an existing pattern of distribution of individual leaf area as a function of rank. Similar patterns were described for wheat (Pararajasingham and Hunt, 1996; Bos and Neuteboom, 1998; Hotsonyame and Hunt, 1998) and for rice (Tivet et al., 2001; Zhu et al., 2009). As an alternative to the Lorentz equation, we tested a bilinear equation with five parameters. However, apart from the higher number of parameters compared to Lorentz, this equation also yielded a higher RMSE.

Furthermore, the models developed were thought to go beyond predicting only shoot total leaf area. Indeed, the prediction of individual leaf area is more relevant if we aim to use this in an FSPM because in this approach parameterization takes place at the organ scale. Moreover, unlike the rosette which can be considered a compact functional unit in terms of leaf area, the bourse shoot usually exhibits a more open structure conveying more importance to the individual leaf with respect to light interception or exposure to liquids or dusts (in the case of chemical treatments: Dekeyser et al., 2013; Duga et al., 2015). However, even in a rosette, individual leaf area and its distribution along the shoot will determine the mutual shading of leaves and, therefore, light interception. Furthermore, in an

FSPM, the position, shape and orientation of each organ are required as an input. The model proposed in this study is an attempt to optimize and simplify the reconstruction of branch architecture which is needed as an input for many FSPMs. As pointed out by Fisher (1984), the leaf surface of the crown is determined by phyllotaxis of the shoot, leaf orientation, clustering of new leaves on short shoots, internode lengths, and distribution of leaves along a branch (Fisher, 1984). Therefore, besides predicting leaf area (and its distribution along the shoot) our model also integrated internode lengths distribution and phyllotactic leaf angles (data not shown).

The data set used for the establishment of the leaf length model for bourse shoots was based on leaves sampled from shoots from a wide range of dates. This was justified as we determined the time (in GDD) from which onwards shoot leaf areas did no longer differ significantly from final leaf areas in the three different genotypes. This time roughly coincides with the date found by Da Silva et al. (2014), who indicated the 30th of June of each year as the end of annual primary shoot extension for most shoot types.

We found that the shape of rosette leaves, independent of genotype, was always more circular than that of bourse shoots which is not surprising as rosette leaves are preformed (Lauri, 2007). In this study, AR exhibited extreme values for the parameter that describes leaf shape ( $k$ ), with bourse shoot leaves being much more elongated ( $k_{BS,AR} = 0.60$ ) than rosette leaves ( $k_{RO,AR} = 0.75$ ). This was in sharp contrast to RB where bourse shoot leaves ( $k_{BS,RB} = 0.66$ ) and rosette leaves ( $k_{RO,RB} = 0.71$ ) were much more similar in shape. FU was intermediary between AR and RB. An interesting observation made in this study was that the descriptive model of internode lengths could be optimized if we considered the bourse rosette and the bourse shoot as one single continuous morphogenetic unit. The bourse shoot being a sylleptic extension of the bourse, it in fact represents the continuation of the rosette. We can thus state that the base of the rosette up to the insertion point of the bourse shoot, plus the bourse shoot itself, is forming a unit that is characterized by a basal zone with short internodes, followed by a median zone with longer internodes (base of the bourse shoot), and a subapical zone with short internodes (Buck-Sorlin and Bell, 2000). This tentative conclusion gives rise to the idea that leaf length prediction could be further improved by considering leaf length distribution of the continuum of rosette plus bourse shoot instead of treating the two shoots separately. It would furthermore be interesting to see if there are allometric relations between the length of an internode and the area of the leaf that is inserted on it, given the fact that both have been produced by the vegetative meristem during the same developmental event. According to Da Silva et al. (2014) it is unlikely that leaf area changes independently from internode length, as metamers exhibit a strong allometry (Fisher, 1986).

In the present study we chose to split our data into training and testing sets: the first one was used to calibrate our model while the latter was employed to test it. Admittedly, some aspects of this procedure are arguable: first of all, it could be claimed that the splitting (two thirds training to one third testing) was arbitrary. However, enough data was available to have sufficiently large training and testing sets and more data was needed for calibration than for testing. Secondly, we confounded the FU data

sets of the two experimental years (2014 and 2015)—whereas for AR and RB only data of 2014 was available—and randomly distributed the data into the two sets, instead of using 1 year's data set for calibration and the other one for testing. However, the data sets revealed no significant inter-annual variation, except for the shape of rosettes in FU. As the 2015 data set was smaller than the one from 2014 and contained data only for FU, future testing with independent data sets has to be conducted to further prove the robustness of our models. Thirdly, as an alternative we could have neglected model testing and just have included a description of the variance (as was in fact done for the leaf area of vegetative shoots in this study). However, this would have meant neglecting the clearly robust and stable patterns that emerged among some of the meristic (leaf number) and continuous (length of the biggest leaf, total and individual leaf area) traits. In this study, the use of a test data set was necessary to check the fit of the final model. Indeed, the final model cumulates all the errors of the intermediate steps of parameterization and calibration, and the testing allowed us to quantify this cumulated error.

An accurate prediction of total shoot leaf area for each shoot type, and of the distribution of single leaf area as a function of leaf rank, in connection with individual internode length, are the first steps toward the faithful reconstruction of architecture, to be used in an FSPM to compute light interception or even to estimate the percentage of hidden surfaces in simulations of the efficiency of pesticide spray applications (Dekeyser et al., 2013; Duga et al., 2015). With respect to light interception, leaf area and internode length are in fact the two most important traits contributing to plant architecture whereas branching angle seems to have only little impact on this functional trait (Han et al., 2012; Da Silva et al., 2014). It also appears that in order to explain leaf distribution within the tree the shoot scale is the most appropriate one (Da Silva et al., 2014). This justifies the choice we have made in this study, namely to concentrate on the modeling of leaf area distribution along different shoot types and to neglect divergence angles. As the spatial distribution of leaves in apple trees is not random (Da Silva et al., 2014) but rather characterized by a certain clumpiness (also reported for other tree species by Cohen et al., 1995; Chen et al., 1997; Da Silva et al., 2008), the next step in the reconstruction of branch architecture has to be to position and orient the different shoot types. In doing so, it has to be considered that the proportion of long and short shoots differs among genotypes (Lauri et al., 1995). The genotypes used in this study exhibited such a numerical variability at the scale of the first-order branch, with bourse shoots in AR being much more important than in RB (data not shown). The analysis of the distribution of shoots within the branch will be the subject of a follow-up study (Bairam et al., unpubl.). In any case, it is thus necessary to count the number of shoots of the different types or better still, create a topological map of the branch and its different organs (see Buck-Sorlin and Bell, 2000, for an example) in order to finalize the reconstruction of branch architecture.

## CONCLUSIONS AND PERSPECTIVES

In the present study, we provided a new model allowing the reconstruction of the initial branch architecture as an input for

a Functional Structural Plant Model of apple, with an emphasis on the prediction of leaf area at the shoot and leaf scale, using allometric relations among shoot architecture variables. The model was calibrated and tested using sufficiently large training and testing data sets, proving that it is robust enough for the prediction of leaf area of the three apple cultivars used in this study, which exhibit a contrasting leaf and shoot morphology. Combined with light response curves measured in 2015 (Bairam et al., unpubl.), the initial architecture thus modeled will help to create a mapping of photosynthetic potential for each leaf. Furthermore, the combination of this information with the developmental kinetics of each fruit on such a branch (Bairam et al., unpubl.) will then allow finding coefficients for daily sugar transport rates from source leaves to fruits.

This study has shown that the distribution of leaves along a shoot of the same type follows certain clear endogenous regularities that seem to be genotype dependent (cf. Lauri, 2007), with rather little phenotypic plasticity. Further experimental and modeling studies will be conducted to try to decipher and quantify the physiological mechanisms behind these regularities, in order to improve the modeling of apple fruit quality in the context of the first-order branch as an experimental system.

## AUTHOR CONTRIBUTIONS

EB, MD, and GBS conceived and designed the work; EB, MD, and CLM collected the experimental data; EB developed the mathematical models, and did the programming in R; EB and GBS analyzed and interpreted the data; EB and GBS wrote the paper; MD revised it critically; all authors approved the final version.

## FUNDING

The doctoral thesis of EB was funded by a strategic bourse of the Région Pays de la Loire, France, convention no. 2011-12596. All financial help is duly acknowledged.

## ACKNOWLEDGMENTS

Sylvain Hanteville and Julienne Fanwoua helped with measurements in the field and the laboratory, and Gilles Hunault gave valuable statistical advice. Michael Henke developed the initial ImageJ script for the automatic measurement of leaf surfaces from scanned images. Antoine Roche helped with scanning leaves and saving images for leaf area analysis. Julienne Fanwoua helped to improve the readability of the manuscript. The staff of the experimental unit at Beaucouzé provided day-to-day maintenance of the orchard. All help is gratefully acknowledged.

## SUPPLEMENTARY MATERIAL

The leaf data can be accessed here: <https://zenodo.org/record/215977>. The R scripts used can be found here: [https://github.com/EmnaBairam/Apple\\_leaf\\_surface](https://github.com/EmnaBairam/Apple_leaf_surface)

## REFERENCES

- Anderson, J. L., and Richardson, E. A. (1982). "Utilizing meteorological data for modeling crop and weed growth," in *Biometeorology in integrated pest management*, eds J. L. Hatfield and I. J. Thomason (New York, NY: Academic), 449–461.
- Barthélémy, D. (1991). Levels of organization and repetition phenomena in seed plants. *Acta Biotheor.* 39, 309–323. doi: 10.1007/BF00114184
- Björkman, O., and Demmig-Adams, B. (1995). "Regulation of photosynthetic light energy capture, conversion, and dissipation in leaves of higher plants," in *Ecophysiology of Photosynthesis* (Berlin Heidelberg, NY: Springer), 17–47.
- Bos, H. J., and Neuteboom, J. H. (1998). Growth of individual leaves of spring wheat (*Triticum aestivum* L.) as influenced by temperature and light intensity. *Ann. Bot.* 81, 141–149. doi: 10.1006/anbo.1997.0532
- Buck-Sorlin, G. H. (2002). "L-system model of the vegetative growth of winter barley," in Fifth German Workshop on Artificial Life, eds D. Polani, J. Kim, and T. Martinetz (Lübeck: Akademische Verlagsgesellschaft Aka GmbH), 53–64.
- Buck-Sorlin, G. H. (2013). "Functional-structural plant modeling," in *Encyclopedia of Systems Biology*, eds W. Dubitzky, O. Wolkenhauer, K. Cho, and H. Yokota (New York, NY: Springer), 778–781. doi: 10.1007/978-1-4419-9863-7
- Buck-Sorlin, G. H., and Bell, A. D. (2000). Models of crown architecture in *quercus petraea* and *q.robur*: shoot lengths and bud numbers. *Forestry* 73, 1–19. doi: 10.1093/forestry/73.1.1
- Casella, E., and Sinoquet, H. (2003). A method for describing the canopy architecture of coppice poplar with allometric relationships. *Tree Physiol.* 23, 1153–1170. doi: 10.1093/treephys/23.17.1153
- Chen, K., Hu, G. Q., and Lenz, F. (1997). Training and shading effects on vegetative and reproductive growth and fruit quality of apple. *Gartenbauwiss* 5, 207–213.
- Cohen, S., Mosoni, P., and Meron, M. (1995). Canopy clumpiness and radiation penetration in a young hedgerow apple orchard. *Agric. For. Meteorol.* 76, 185–200. doi: 10.1016/0168-1923(95)02226-N
- Costes, E., Crespel, L., Denoyes, B., Morel, P., Demene, M. N., Lauri, P. E., et al. (2014). Bud structure, position and fate generate various branching patterns along shoots of closely related Rosaceae species: a review. *Front. Plant Sci.* 5:666. doi: 10.3389/fpls.2014.00666
- Da Silva, D., Boudon, F., Godin, C., and Sinoquet, H. (2008). Multiscale framework for modeling and analyzing light interception by trees. *Multiscale Model. Sim.* 7, 910–933. doi: 10.1137/08071394X
- Da Silva, D., Han, L., Faivre, R., and Costes, E. (2014). Influence of the variation of geometrical and topological traits on light interception efficiency of apple trees: sensitivity analysis and metamodeling for ideotype definition. *Ann. Bot.* 114, 739–752. doi: 10.1093/aob/mcu034
- Dekeyser, D., Duga, A. T., Verboven, P., Hendrickx, N., and Nuyttens, D. (2013). Assessment of orchard sprayers using laboratory experiments and CFD modelling. *Biosyst. Eng.* 114, 157–169. doi: 10.1016/j.biosystemseng.2012.11.013
- Duga, A. T., Ruysen, K., Dekeyser, D., Nuyttens, D., Bylemans, D., Nicolai, B. M., et al. (2015). Spray deposition profiles in pome fruit trees: effects of sprayer design, training system and tree canopy characteristics. *Crop Protec.* 67, 200–213. doi: 10.1016/j.cropro.2014.10.016
- Evers, J. B., Vos, J., Fournier, C., Andrieu, B., Chelle, M., and Struik, P. C. (2005). Towards a generic architectural model of tillering in Gramineae, as exemplified by spring wheat (*Triticum aestivum*). *New Phytol.* 166, 801–812. doi: 10.1111/j.1469-8137.2005.01337.x
- Evers, J. B., Vos, J., Fournier, C., Andrieu, B., Chelle, M., and Struik, P. C. (2007). An architectural model of spring wheat: evaluation of the effects of population density and shading on model parameterization and performance. *Ecol. Model.* 200, 308–320. doi: 10.1016/j.ecolmodel.2006.07.042
- Falster, D. S., and Westoby, M. (2003). Leaf size and angle vary widely across species: what consequences for light interception? *New Phytol.* 158, 509–525. doi: 10.1046/j.1469-8137.2003.00765.x
- Fanwoua, J., Bairam, E., Delaire, M., and Buck-Sorlin, G. (2014). The role of branch architecture in assimilate production and partitioning: the example of apple (*Malus domestica*). *Front. Plant Sci.* 5:338. doi: 10.3389/fpls.2014.00338
- Fisher, J. B. (1984). "Tree architecture: relationships between structure and function," in *Contemporary Problems in Plant Anatomy*, eds R. A. White, and W. C. Dickson (New York, NY: Academic Press), 541–589.
- Fisher, J. B. (1986). "Branching patterns and angles in trees," in *The Economy of Plant Form and Function*, ed T. J. Givnish (Cambridge: Cambridge University Press), 493–523.
- Freeman, Freeman, G. M., and Bolas, B. D. (1956). A method for the rapid determination of leaf area in the field. *Rep. East Malling Res. Stn.* 1955, 104–107.
- Gu, S., Evers, J. B., Zhang, L., Mao, L., Zhang, S., Zhao, X., et al. (2014). Modelling the structural response of cotton plants to mepiquat chloride and population density. *Ann. Bot.* 114, 877–887. doi: 10.1093/aob/mct309
- Han, L., Costes, E., Boudon, F., Cokelaer, T., Pradal, C., Da Silva, D., et al. (2012). "Investigating the influence of geometrical traits on light interception efficiency of apple trees: a modelling study with MAappleT," in 2012 IEEE Fourth International Symposium on Plant Growth Modeling, Simulation, Visualization and Applications (PMA), eds M. Z. Kang, Y. Dumont, and Y. Guo (Shanghai: IEEE Press), 152–159.
- Hemmerling, R., Kniemeyer, O., Lanwert, D., Kurth, W., and Buck-Sorlin, G. (2008). The rule-based language XL and the modelling environment GroIMP illustrated with simulated tree competition. *Funct. Plant Biol.* 35, 739–750. doi: 10.1071/FP08052
- Hotsonyame, G. K., and Hunt, L. A. (1998). Effects of sowing date, photoperiod and nitrogen on variation in main culm leaf dimensions in field-grown wheat. *Can. J. Plant Sci.* 78, 35–49. doi: 10.4141/P97-027
- Kahlen, K., and Stützel, H. (2007). Estimation of geometric attributes and masses of individual cucumber organs using three-dimensional digitizing and allometric relationships. *J. Am. Soc. Hortic. Sci.* 132, 439–446.
- Lauri, P. E. (2007). Differentiation and growth traits associated with acrotony in the apple tree (*Malus domestica*, Rosaceae). *Am. J. Bot.* 94, 1273–1281. doi: 10.3732/ajb.94.8.1273
- Lauri, P. E., Térouanne, E., Lespinasse, J. M., Regnard, J. L., and Kelner, J. J. (1995). Genotypic differences in the axillary bud growth and fruiting pattern of apple fruiting branches over several years—an approach to regulation of fruit bearing. *Sci. Hortic.* 64, 265–281. doi: 10.1016/0304-4238(95)00836-5
- Lauri, P. É., and Trottier, C. (2004). Patterns of size and fate relationships of contiguous organs in the apple (*Malus domestica*) crown. *New Phytol.* 163, 533–546. doi: 10.1111/j.1469-8137.2004.01136.x
- Lindenmayer, A. (1968a). Mathematical models for cellular interactions in development. I. Filaments with one-sided inputs. *J. Theor. Biol.* 18, 280–299. doi: 10.1016/0022-5193(68)90079-9
- Lindenmayer, A. (1968b). Mathematical models for cellular interactions in development II. Simple and branching filaments with two-sided inputs. *J. Theor. Biol.* 18, 300–315. doi: 10.1016/0022-5193(68)90080-5
- Massonet, C., Regnard, J. L., Lauri, P. E., Costes, E., and Sinoquet, H. (2008). Contributions of foliage distribution and leaf functions to light interception, transpiration and photosynthetic capacities in two apple cultivars at branch and tree scales. *Tree Physiol.* 28, 665–678. doi: 10.1093/treephys/28.5.665
- Montgomery, D. C., Peck, E. A., and Vining, G. G. (2015). *Introduction to Linear Regression Analysis*. New Jersey, NJ: J. Wiley and Sons.
- Pararajasingham, S., and Hunt, L. A. (1996). Effects of photoperiod on leaf appearance rate and leaf dimensions in winter and spring wheats. *Can. J. Plant Sci.* 76, 43–50. doi: 10.4141/cjps96-008
- Prusinkiewicz, P. (1998). Modeling of spatial structure and development of plants: a review. *Sci. Hortic.* 74, 113–149.
- Snee, R. D. (1977). Validation of regression models: methods and examples. *Technometrics* 19, 415–428. doi: 10.1080/S0304-4238(98)00084-3

- Spann, T. M., and Heerema, R. J. (2010). A simple method for non-destructive estimation of total shoot leaf area in tree fruit crops. *Sci. Hortic.* 125, 528–533. doi: 10.1016/j.scienta.2010.04.033
- Štampar, F., Hudina, M., Usenik, V., Šturm, K., Marn, V., and Batič, F. (1999). Influence of leaf area on net photosynthesis, yield and flower-bud formation in apple (*Malus domestica* Borkh.). *PlantPhysiol.* 39, 101–106.
- Sussex, I. M., and Kerk, N. M. (2001). The evolution of plant architecture. *Curr. Opin. Plant Biol.* 4, 33–37. doi: 10.1016/S1369-5266(00)00132-1
- Tivet, F., Pinheiro, B. D. S., Raïssac, M. D., and Dingkuhn, M. (2001). Leaf blade dimensions of rice (*Oryza sativa* L. and *Oryza glaberrima* Steud.). Relationships between tillers and the main stem. *Ann. Bot.* 88, 507–511. doi: 10.1006/anbo.2001.1447
- Tsukaya, H. (2004). Leaf shape: genetic controls and environmental factors. *Int. J. Dev. Biol.* 49, 547–555. doi: 10.1387/ijdb.041921ht
- Vos, J., Evers, J. B., Buck-Sorlin, G. H., Andrieu, B., Chelle, M., and de Visser, P. H. B. (2010). Functional-structural plant modelling: a new versatile tool in crop science. *J. Exp. Bot.* 61, 2102–2115. doi: 10.1093/jxb/erp345
- Zhu, Y., Chang, L., Tang, L., Jiang, H., Zhang, W., and Cao, W. (2009). Modelling leaf shape dynamics in rice. *NJAS* 57, 73–81. doi: 10.1016/j.njas.2009.11.001

**Conflict of Interest Statement:** The authors declare that the research was conducted in the absence of any commercial or financial relationships that could be construed as a potential conflict of interest.

Copyright © 2017 Baïram, Delaire, Le Morvan and Buck-Sorlin. This is an open-access article distributed under the terms of the Creative Commons Attribution License (CC BY). The use, distribution or reproduction in other forums is permitted, provided the original author(s) or licensor are credited and that the original publication in this journal is cited, in accordance with accepted academic practice. No use, distribution or reproduction is permitted which does not comply with these terms.



# Why Be a Shrub? A Basic Model and Hypotheses for the Adaptive Values of a Common Growth Form

Frank Götmark<sup>1\*</sup>, Elin Götmark<sup>2</sup> and Anna M. Jensen<sup>3</sup>

<sup>1</sup> Department of Biological and Environmental Sciences, University of Gothenburg, Göteborg, Sweden, <sup>2</sup> Mathematical Sciences, Chalmers University of Technology and University of Gothenburg, Göteborg, Sweden, <sup>3</sup> Department of Forestry and Wood Technology, Linnaeus University, Växjö, Sweden

## OPEN ACCESS

### Edited by:

Alexander Bucksch,  
Georgia Institute of Technology, USA

### Reviewed by:

Gerald Schoenknecht,  
Oklahoma State University–Stillwater,  
USA

Roman Zweifel,

Swiss Federal Institute for Forest,  
Snow and Landscape Research,  
Forest Dynamics, Switzerland

Masha Van Der Sande,  
Wageningen University and Research  
Centre, Netherlands

### \*Correspondence:

Frank Götmark  
frank.gotmark@gu.se

### Specialty section:

This article was submitted to  
Plant Biophysics and Modeling,  
a section of the journal  
*Frontiers in Plant Science*

Received: 08 April 2016

Accepted: 11 July 2016

Published: 26 July 2016

### Citation:

Götmark F, Götmark E and Jensen AM (2016) Why Be a Shrub? A Basic Model and Hypotheses for the Adaptive Values of a Common Growth Form. *Front. Plant Sci.* 7:1095.  
doi: 10.3389/fpls.2016.01095

Shrubs are multi-stemmed short woody plants, more widespread than trees, important in many ecosystems, neglected in ecology compared to herbs and trees, but currently in focus due to their global expansion. We present a novel model based on scaling relationships and four hypotheses to explain the adaptive significance of shrubs, including a review of the literature with a test of one hypothesis. Our model describes advantages for a small shrub compared to a small tree with the same above-ground woody volume, based on larger cross-sectional stem area, larger area of photosynthetic tissue in bark and stem, larger vascular cambium area, larger epidermis (bark) area, and larger area for sprouting, and faster production of twigs and canopy. These components form our Hypothesis 1 that predicts higher growth rate for a small shrub than a small tree. This prediction was supported by available relevant empirical studies (14 publications). Further, a shrub will produce seeds faster than a tree (Hypothesis 2), multiple stems in shrubs insure future survival and growth if one or more stems die (Hypothesis 3), and three structural traits of short shrub stems improve survival compared to tall tree stems (Hypothesis 4)—all hypotheses have some empirical support. Multi-stemmed trees may be distinguished from shrubs by more upright stems, reducing bending moment. Improved understanding of shrubs can clarify their recent expansion on savannas, grasslands, and alpine heaths. More experiments and other empirical studies, followed by more elaborate models, are needed to understand why the shrub growth form is successful in many habitats.

**Keywords:** woody plants, stem, multi-stemmed, shrubland, scrub, tree, growth, canopy

“...since Theophrastus (born c. 370 BC), botanists have generally distinguished between trees, shrubs, and herbs.” (Petit and Hampe, 2006, p. 189)

“Shrubiness is such a remarkable adaptive design that one may wonder why more plants have not adopted it.” (Stutz, 1989, p. 325)

## INTRODUCTION

Trees and shrubs are two major growth forms in many natural and semi-natural habitats. Here, we focus on shrubs, a widespread category of woody plants, and elucidate their adaptive significance. We present a model based on scaling relationships where shrubs are compared with trees, outline hypotheses for the adaptiveness of shrubs, and test one of the hypotheses, based on the literature.

Many theoretical and empirical studies of trees address their adaptive significance, for instance variability in height among species, and maximum height (e.g., Horn, 1971; Ryan and Yoder, 1997; Loehle, 2000). In contrast, the adaptive significance of shrubs is only discussed briefly in the literature. For instance, Whittaker and Woodwell (1968, p. 11) stated that shrubs “may have high production per unit leaf weight and surface... and smaller expenditure of this production on supporting stem and branch tissue than is the case in forest trees.” Givnish (1984, p. 78) suggested that shrubs are favored in open habitats where tree crowns have been destroyed, by having “more meristems active, [and] more potential points for stem regeneration.”

Another suggestion is that the shrub growth form is “a design strategy of relatively small, low-investment, low risk, “throwaway” stems that are expendable in high-stress environments” (Wilson, 1995, p. 92). Stutz (1989) stated that shrubs usually are tall enough to dominate herbs and do not need to rebuild as much biomass each year as herbs. On the other hand, shrubs often occur in grassland, for instance savanna, where grasses and/or fires may control woody vegetation, including shrubs (Bond and van Wilgen, 1996; Sholes and Archer, 1997). Shrubs are sometimes discussed on the basis of their low, broad canopy in disturbed habitats, and Givnish (1984) argued that such a canopy is favored by multiple stems. It is often suggested that shrubs are associated with disturbed and stressful environments (e.g., Rundel, 1991; Givnish, 1995; Sheffer et al., 2014). However, elaborate hypotheses and models for the adaptive significance of the shrub growth form seem to be lacking. Moreover, the recent expansion of shrubs in several regions globally (e.g., Naito and Cairns, 2011; Formica et al., 2014) motivates more basic research about shrubs.

Below, we first define “tree” and “shrub.” Because shrubs have been neglected compared to herbs and trees (see Discussion), we briefly outline their importance. We then describe our basic model and four hypotheses that potentially can explain the adaptive significance of shrubs, compared to trees. Our main contributions are the basic model (Section The Basic Model and Hypotheses), and Hypothesis 1 and the preliminary test of it (Section Hypothesis 1: The Multiple Stems of a Small Shrub Give Faster Growth than for a Small Tree). The Hypotheses 2, 3 and 4 (Sections Hypothesis 2: The Fast Maturity of Shrubs Enables Earlier Seed Production Compared to Trees, Hypothesis 3: The Multiple Stems in Shrubs Insure Future Survival and Growth if One or More Stems Die, and Hypothesis 4: The Short Stems of Shrubs Improve Survival through Three Traits, Compared to Tall Tree Stems) are complementary and also important ideas, supported by some evidence. Finally, we discuss ecological aspects of shrubs and trees, and identify research needs.

## Delimitation and Definition

It is sometimes difficult to identify a woody plant as a tree or a shrub, and intermediate forms exist (see Rundel, 1991; Wilson, 1995). Sheffer et al. (2014) stated “In contrast to shrubs, trees have a single stem, but this distinction is not absolute... 9.2% of the tree species we analyzed were also qualified as shrubs by some contributors in the trait database.” In tropical rainforest, the woody growth forms are diverse, with more forms than just

tree/shrub (see Givnish, 1984, Table 4; Rundel, 1991). In South African savanna, in a study of 23 woody species, Zizka et al. (2014) recognized shrubs (mean value: 13 stems), SSTs (“shrubs sometimes small trees,” 3.6 stems) and trees (2.2 stems). Some shrubs are semi-woody, being woody in the lower stem parts and herbaceous in the upper (trees also have herb-like shoots that become woody with time).

Here, we define a tree as a tall perennial plant with a single self-supporting woody stem, and a shrub as a short perennial plant with multiple self-supporting woody stems, branching at or near the ground. However, trees can have multiple stems, and the shrubs we discuss below range from very small (e.g., *Vaccinium* spp., about 0.2 m tall) to large *Corylus* spp. (up to about 10 m tall). **Figure 1** illustrates a shrub of a common type (about 50 cm tall); a tree with one central stem (many conifers and angiosperms); a tree with one short stem, branching early to produce a broad canopy forming >50% of the height of the tree (e.g., *Ulmus* spp., savanna trees); and a tree with multiple stems which we suggest may be distinguished by stem form as well as height (see Discussion). Photographs in **Figure 2** illustrate two types of shrubs and two multi-stemmed trees. Shrub-like bamboos are also relevant, some of which have strong stems more than 25 m tall (Wang et al., 2014) and may also dominate trees (Griscom and Ashton, 2003), but we did not include them in our literature review below.

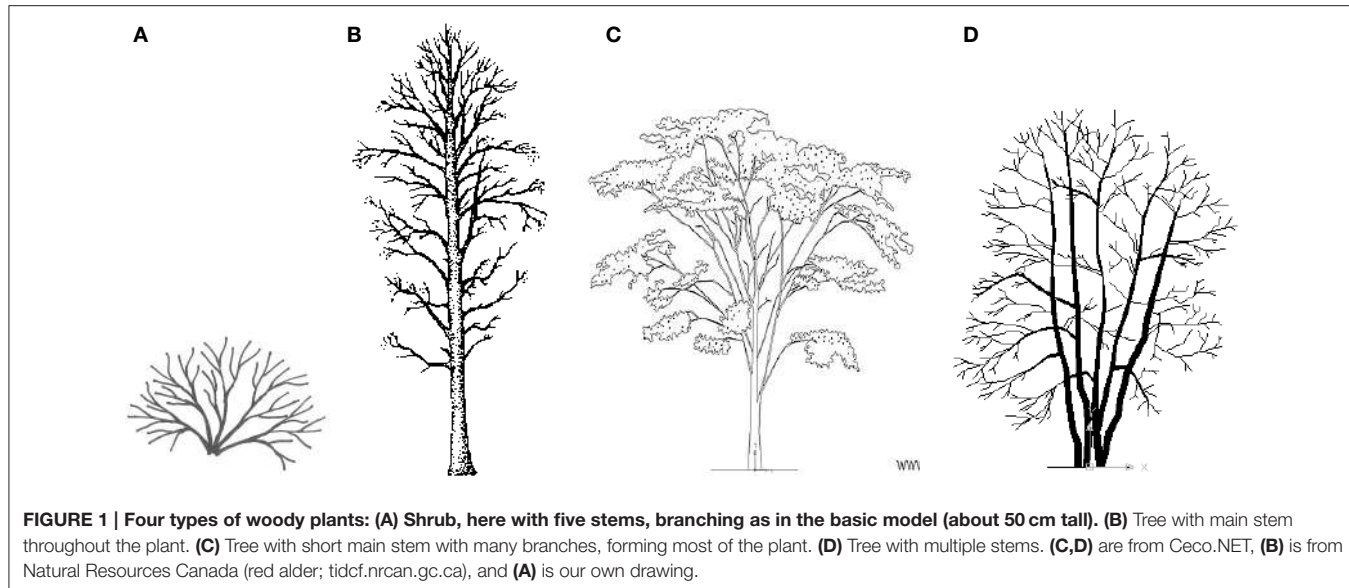
Despite problems in defining some species as shrubs, the term shrub is widely used and shrubs are important in many ecosystems (see next section). In addition, biology and ecology contain many terms that are difficult to define precisely (e.g., “forest”) but useful in research and management.

## The Occurrence and Ecological Importance of Shrubs

Shrubs are important components in at least 9 of 11 global biomes (Archibald, 1995; see also McKell, 1989), forming much of the vegetation in tropical savannas, arid regions, Mediterranean ecosystems, and polar and high mountain tundras. They are also frequent in terrestrial wetlands and in the understory and canopy gaps in forests, where both shade-tolerant and pioneer (shade-intolerant) shrubs occur (e.g., Denslow et al., 1990).

Olson et al. (2001) classified 14 terrestrial biomes, and “shrubland” or “scrub” occur in the name of 5 biomes. Shrubs occur in at least 13 of the 14 biomes. Gong et al. (2013) used satellite data to estimate global land-cover types; forest covered 28.4% of the land and shrubland covered 11.5%. Because shrubs also occur in forest, they grow, or can grow, on about 40% of the land surface. Shrubland was defined as having a vegetation cover of >15%, but some bare land with sparse vegetation also contains shrubs (see Gong et al., 2013), so the total area where they can grow might be close to 45% of the global land surface.

Given the vast global distribution of shrubs, they are important for climate control, soil stabilization and production, ecosystem water balance, carbon uptake and storage, and for many associated species such as grazing and browsing mammals



and livestock, birds, fungi, and invertebrates. “Nurse plants” favor other plants, including trees, and in a review of such plants “shrubs were the dominant nurse life-form” (Filazzola and Lortie, 2014). Moreover, shrubs exhibit high species richness in several regions on the earth (Qian, 2015; Qian and Ricklefs, 2015; see also Rundel, 1991). Currently, shrubs and “shrubification” are much studied in tropical and temperate grassland and in arctic and other cold habitats that lack trees, often in relation to climate change (e.g., Hallinger et al., 2010; Ratajczak et al., 2012; Formica et al., 2014; Ogden, 2015).

The next section describes our basic model, which is relevant for Hypothesis 1 in Section Hypothesis 1: The Multiple Stems of a Small Shrub Give Faster Growth than for a Small Tree. All our four hypotheses focus on the adaptive value of shrubs compared with trees. For trees, we assume that their main adaptive value or advantage is height development, leading to elevated canopies that shade competitors (including shrubs) and large root systems that also help dominate shrubs. In addition, a tall tree with a large canopy can potentially produce more seeds and disperse pollen and seeds more widely.

## THE BASIC MODEL AND HYPOTHESES

To explore functional trait differences between single- and multi-stemmed woody plants (trees vs. shrubs), we built a basic volume-based growth model. Biomass partitioning occurs only between above-ground woody parts, thus foliage and roots are not included in the model. The following traits were studied: cross-sectional stem area, bark surface area, branching, canopy development (branching), and stem bending moment (intuitively, the strain when forces act on the stem so that it bends). We modeled above-ground woody biomass [that is, stem(s) and branches] using the functions  $V_t(h_t)$  and  $V_s(h_s, n)$ , which give the volumes of a tree of height  $h_t$ , and a shrub of height

$h_s$ , and number of stems  $n$ . For a given volume  $v$  we can solve  $V_t(x) = v$  and  $V_s(x, n) = v$  numerically and obtain heights  $h_t(v)$  and  $h_s(v, n)$ , compared in Figure 3A.

For simplicity, tree and shrub volumes  $V_t(h_t)$  and  $V_s(h_s, n)$  are calculated by modeling stems and branches as truncated cones with basal radius proportional to length, or as cylinders when the basal radius is small enough. We explain the parameters in Table 1; all are constants which can be varied freely. When a stem reaches the length  $l_{min}$ , branches of length  $p^*l_{min}$  are added, which then grow proportionally in length with the main stem. We add  $a_t$  branches per stem for a tree and  $a_s$  for a shrub, corresponding to Whitney (1976) branching coefficients  $a_t+1$  and  $a_s+1$ , respectively (Whitney counts the stem tip as a child branch; we do not). These branches in turn get “child branches” in the same way when they grow long enough. The model does not include thinning within individuals during growth, so we only apply it to small trees and shrubs.

Note that the above description is simplified: to avoid child branches  $p^*l_{min}$  cm long appearing out of nowhere when parent branches reach the length  $l_{min}$  cm (making the volume functions discontinuous), child branches begin to grow when parent branches are  $2/3^*l_{min}$  cm long, and grow linearly to reach the length  $p^*l_{min}$  cm when the parent branch is  $l_{min}$  cm long. The number  $2/3$  is rather arbitrary, but affects the results very little—it only specifies how the discontinuous parts of the function are “glued together.” The parameters  $r_{tip}$  (the radius of a branch tip),  $b_t$ , and  $b_s$  (the ratio of the basal radius of a stem or branch and its length for trees and shrubs, respectively),  $l_{min}$ , and  $p$  were chosen from inspection of small trees and shrubs of several species, to be:  $a_t = a_s = 2$ ,  $p = 0.5$ ,  $l_{min} = 20$  cm,  $r_{tip} = 0.1$  cm,  $b_t = b_s = 0.0075$ ,  $g_s = 1$ . All parameters probably vary among species and habitats, but we have tried different realistic values and the scaling relationships between trees and shrubs seen in Figure 3 still hold. Note that to reach the same

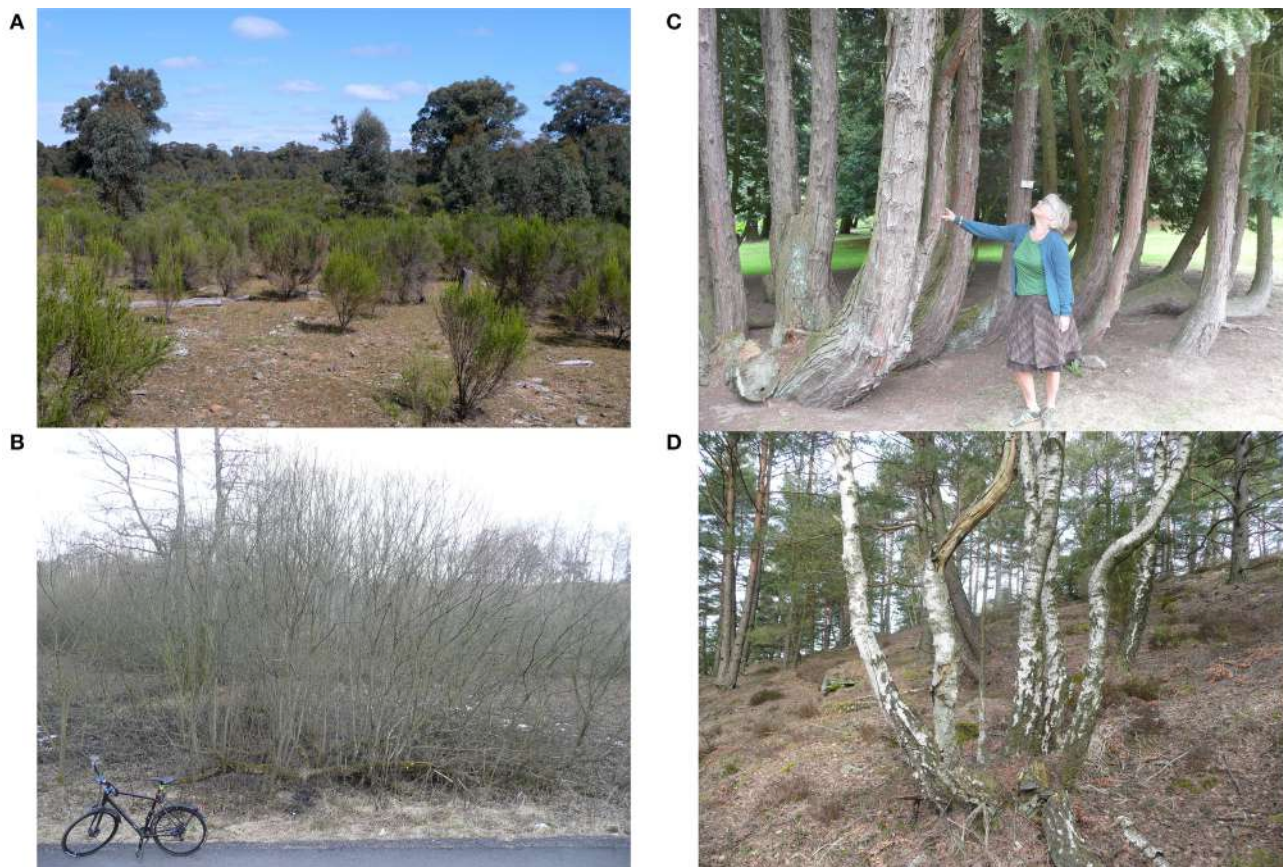


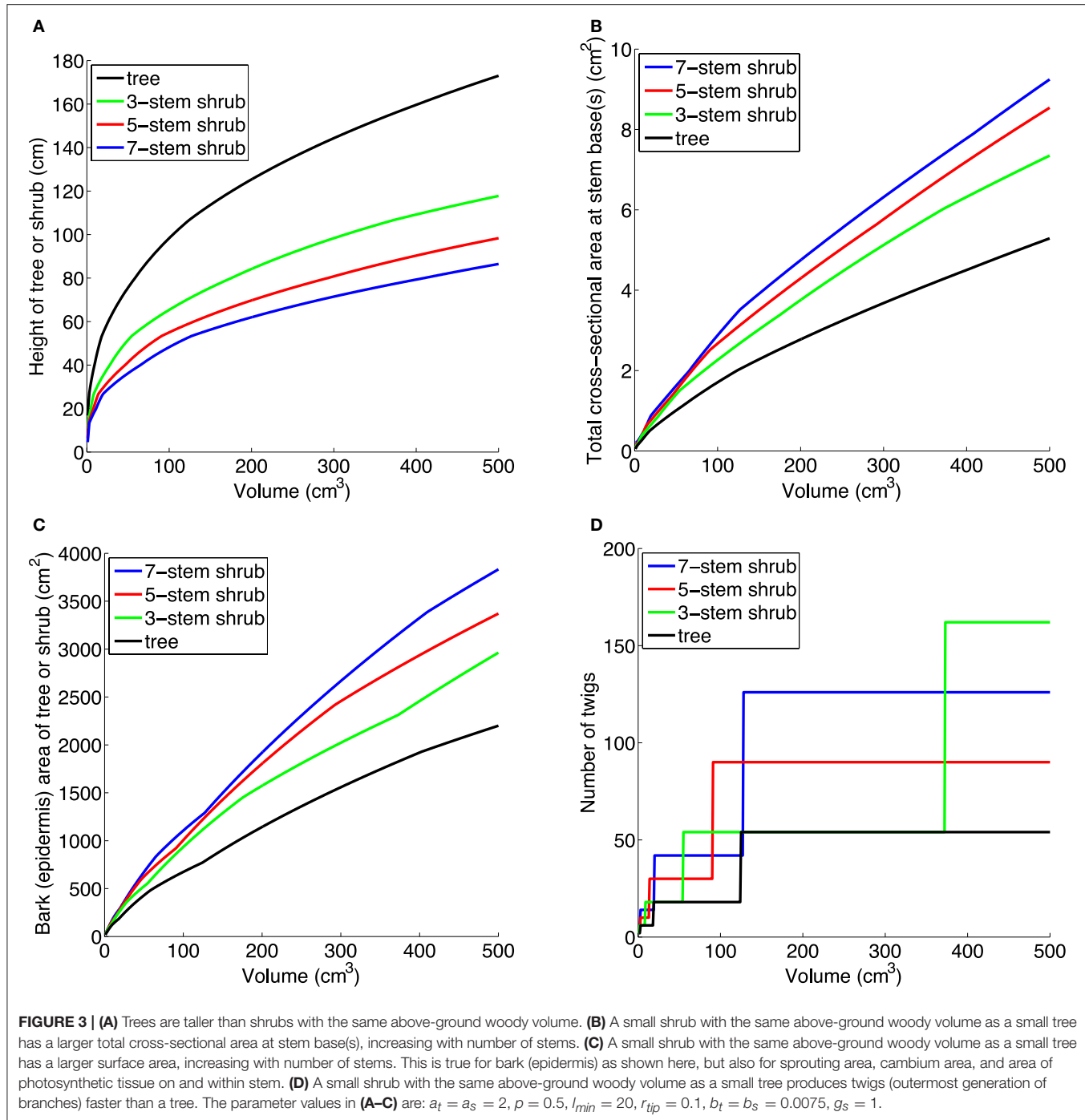
**FIGURE 2 | Two species of shrubs and two species of trees, multi-stemmed:** (A) *Cassinia arcuata* (Asteraceae), Drooping Cassinia or Chinese Scrub, an evergreen shrub in central Victoria, Australia. This species has colonized thousands of hectares in the area during the last 40 years, when land use changed (see Lunt, 2011). The trees are *Eucalyptus sideroxylon* (Red Ironbark). (B) A large *Salix* sp. shrub (probably a hybrid) in winter on moist ground in Sweden, with horizontal growth by sprouts on lying stems. Deciduous *Salix* spp. are common especially on moist soils in cold and temperate regions in the northern hemisphere. (C) *Chamaecyparis lawsoniana* (Cupressaceae) or Port-Orford-cedar, an evergreen conifer from western North America. It is normally single-stemmed but may become multi-stemmed after damages, e.g., from browsing (picture from botanical garden, Sweden). (D) *Betula pendula* (Betulaceae), Silver Birch or Warty Birch in multi-stemmed version probably caused by browsing or cutting damage on seedling/sapling (Pixbo, SW Sweden). Note self-thinning (dead stems). Normal single-stem birches grow in the background. Note also uprising stems of the multi-stemmed trees in (C,D), which would reduce the bending moment of heavy leaning stems (see Discussion and Figure 4). Photographs: Ian Lunt (A) and Frank Götmark (B–D).

height as a tree, a shrub with  $n$  stems and with  $a_t = a_s$ ,  $b_t = b_s$ , must increase in above-ground woody volume  $n$  times as fast as a tree (that is,  $g_s = n$ ). This follows since one shrub stem with its branches is modeled the same as a tree stem with branches.

Once we have  $h_t(v)$  and  $h_s(v,n)$  we can calculate other important traits, for example the basal radius of a stem and thus the total cross-sectional area at stem base(s). Investing in multiple stems, compared to a single stem, gives a greater total cross-sectional area at the stem base(s), increasing with  $n$  (Figure 3B). We can also calculate the total surface area of stem(s) and branches. Investing in multiple stems gives a greater total bark surface area, increasing with  $n$  (Figure 3C). The same holds for the stem-photosynthetic area, the area of vascular cambium, and area for sprouting, e.g., on the lower 25% of the stems (all graphs would be similar to Figure 3C). All these results are illustrations of the general mathematical principle that volume and area

scale differently. The number of twigs (outermost generation of branches) is larger for shrubs than for trees, given the same above-ground woody volume (Figure 3D). A more realistic twig model requires knowledge of the relative thinning and allocation strategies of trees and shrubs.

Our model uses a simple proportional relationship between stem height and basal radius for small stems (Whittaker and Woodwell, 1968; Niklas, 1994). In Equation (5) in Niklas and Spatz (2004) a relationship  $L = k_5 D^{2/3} - k_6$  is derived between height  $L$ , basal stem diameter  $D$ , and empirically determined constants  $k_5$  and  $k_6$ . This relationship is a good model for both small and large trees (as opposed to the common model  $L = kD^{2/3}$  for large trees). Substituting this relationship instead of the simple proportional function in our model, the functions  $V_t(h_t)$  and  $V_s(h_s, n)$  will change, but the height and area comparison between trees and shrubs will not be much affected (see graphs in Data Sheet 1 in



Supplementary Material). That is, the graphs in **Figure 3** would be similar.

The bending moment around the origin of a point-mass at location  $\mathbf{a}$  is  $|\mathbf{F}| \cdot |\mathbf{b}|$ , where  $\mathbf{F}$  is the force applied to the mass, and  $\mathbf{b}$  is the component of  $\mathbf{a}$  which is at right angles to  $\mathbf{F}$ . We set the origin at the stem base. In our case the force will be gravity which acts vertically, so that the bending moment increases the farther we get from the origin horizontally. This is why a straight stem will have higher

bending moment the more it leans outwards. Since a stem is not a point mass, we have to add all the contributions along its length, which leads to an integral. For simplicity, we omit the branches, and we use the stem taper function from Niklas and Spatz (2004; **Figure 4**; calculations in Data Sheet 1 in Supplementary Material). We use these results in Hypothesis 4.

All calculations are implemented in Matlab (see Supporting Information).

**TABLE 1 | Definition of parameters used in the basic model.**

Parameter	Definition
$n$	The number of stems.
$a_t$ and $a_s$	The number of child branches added in each step to each parent branch/stem for trees and shrubs, respectively.
$p$	The ratio of the length of a child branch and the length of its parent branch/stem.
$l_{min}$	The length at which a branch or stem gets child branches (in cm).
$r_{tip}$	The radius of the outermost tip of a branch or stem (in cm).
$b_t$ and $b_s$	The ratio of the basal radius of a stem or branch and its length $h$ for trees and shrubs, respectively (an exception is made when $b_t \cdot h$ or $b_s \cdot h$ is less than $r_{tip}$ ; the basal radius is then set to $r_{tip}$ , making the stem or branch a cylinder).
$g_s$	The ratio of the growth rate of the above-ground woody volume of a shrub and that of a tree (we set $g_s = 1$ , but in case of e.g., known faster growth rate in a shrub, it could be changed).

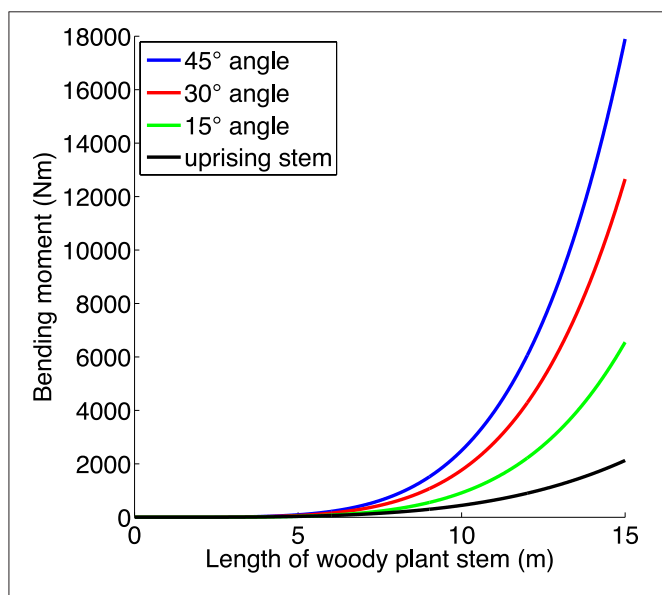


**FIGURE 4 |** The bending moment (Nm) as a function of the length of a straight stem (neglecting branches and foliage) growing in an angle of 15, 30, and 45° from the vertical, and the bending moment for a more uprising stem such as a multi-stemmed tree often has (cf. Figures 1D, 2C,D). The latter stem first grows at an angle of 20° off vertical, and when it has reached a horizontal distance of 1 m from its starting point, it grows straight upwards. Taper function from Niklas and Spatz (2004). (For calculations, see Supporting Information).

## Hypothesis 1: The Multiple Stems of a Small Shrub Give Faster Growth than for a Small Tree

We suggest that a small shrub has at least six functional traits that lead to higher growth rate than in a small tree with the same above-ground woody volume and grown under similar conditions.

*First*, shrubs have greater sapwood area compared to trees of the same above-ground woody volume. When partitioning biomass to multiple stems instead of height growth (Figure 3A),

shrubs develop a larger total stem cross-sectional area than in a tree (Figure 3B). Assuming similar heartwood proportions and sapwood efficiency in shrubs and trees, a larger total stem cross-sectional area would give a larger functional stem sapwood area. As hydraulic conductance scales positively with leaf area and mass (see Mencuccini, 2003; Rance et al., 2014), this indicates that a small multi-stemmed shrub may produce more leaves than a small tree with a single stem. While a greater sapwood area would result in greater rate of respiration (Lavigne and Ryan, 1997), we argue that this is negligible compared to the potential greater canopy C assimilation in shrubs. For plants of the same size, for example 500 cm<sup>3</sup> volume, our model predicts a 39, 61, and 75% greater total cross-sectional sapwood area in shrubs with 3, 5, and 7 stems, compared to a single-stemmed tree (Figure 3B). Although slope (sapwood area to leaf area ratios) depends on species, growth conditions, and leaf water conductance (Whitehead et al., 1984; McDowell et al., 2002), recent work on different tropical trees suggests that cross-sectional sapwood area is a critical morphological trait for growth and biomass accumulation (van der Sande et al., 2015). Further, there is evidence that shrubs have higher canopy density than trees in savanna (total leaf area in m<sup>2</sup> per canopy volume in m<sup>3</sup>; Zizka et al., 2014) and have higher leaf area index (LAI, m<sup>2</sup> m<sup>-2</sup>) than trees in several mesic forests (Knapp et al., 2008: p. 620). Put differently, the larger sapwood area of a small shrub could potentially support a greater leaf area/mass than in a small tree, leading to higher C uptake and growth rate.

*Second*, shrubs have greater stem-photosynthetic area for additional C acquisition compared to trees. Although foliage in most shrubs and trees is the primary producer of photosynthates, C assimilation also occurs in stems and twigs (Stutz, 1989; Nilsen, 1995; Pfanz et al., 2002; Vick and Young, 2009; Avila et al., 2014). Our model predicts a 35, 53, and 74% greater total epidermis area in shrubs with 3, 5, and 7 stems, compared to a single-stemmed tree (for 500 cm<sup>3</sup> above-ground woody volume, see Figure 3C). Reported light-saturated rates of bark photosynthesis ( $A_{sat}$ ) at ambient CO<sub>2</sub> (360–400 ppm) are lower (0.6–2.2 μmol CO<sub>2</sub> m<sup>-2</sup> s<sup>-1</sup>) than foliage rates (7–35 μmol CO<sub>2</sub> m<sup>-2</sup> s<sup>-1</sup>; Wullschleger, 1993; Wittmann and Pfanz, 2007; Jensen et al., 2012, 2015), but this related stem area advantage for shrubs may be especially beneficial during leafless periods such as early spring and late autumn, after severe droughts (Maurits et al., 2015), or after insect defoliation events. However, the primary function of corticular photosynthesis may not be net photosynthetic uptake of CO<sub>2</sub> but rather sustaining physiologically active tissues by re-assimilation of respired CO<sub>2</sub> (Pfanz et al., 2002; Wittmann and Pfanz, 2007; Teskey et al., 2008). Multi-stemmed shrubs may thereby be able to maintain a greater cambium area than small single-stemmed trees.

*Third*, shrubs have greater total cambium area than trees with the same above-ground woody volume, facilitating greater secondary xylem and phloem growth in all emerging stems and branches. However, a greater active cambium area requires additional C investment both in cambium development and maintenance. A greater total cambium

area *per se* does not ensure higher growth rates, but is a precondition for accelerated growth. So shrubs have an advantage over trees for plants grown without resource limitations.

*Fourth*, especially after disturbances, shrubs have greater bark area for sprouting and potential development of new organs compared to trees with the same above-ground woody volume. Epicormic and dormant adventitious buds underneath the bark of stems, stem bases, and branches can contribute to growth. Assuming that a small tree and a small shrub have equal density of such buds on their stems above ground, a shrub with its greater bark area may gain a growth advantage by higher sprouting potential. Sprouts will also have more space available for growth on the spread-out stems of a shrub than if they all grow on a single-stem tree. However, as both external conditions (e.g., light, water availability, disturbances) and internal conditions (e.g., growth hormones and stored resources) may trigger sprouting, the role of bark area *per se* remains to be clarified.

*Fifth*, assuming the same branching pattern ( $a_s = a_t$ ), a small shrub can produce more branches and twigs than a small tree (**Figure 3D**) and its canopy can expand horizontally to capture more light than a small tree that tends to grow mainly upwards (see also Pickett and Kempf, 1980; Givnish, 1984; Küppers, 1989; Sun et al., 2010).

*Sixth*, multiple stems in a shrub may allow continued horizontal growth. The stems can grow close to the ground; as their length and mass increase, some stems lean against the ground allowing new roots and vertical shoots to develop, further horizontally expanding the canopy (one example in **Figure 2B**). Pickett and Kempf (1980) suggested that “shrubs represent a horizontally oriented strategy for reduction of [self-]shading,” referring to clones and root suckers in the shrubs they studied (see Discussion).

Based on the six traits and the mechanisms described above, we predicted higher above-ground growth rate in small shrubs than in small trees with the same woody volume, and tested this prediction by a review of the literature. Using the Web of Science database and reference lists in published articles and books, we searched for articles containing the term “shrub” where the authors had quantified growth in both shrubs and trees. After exhaustive search, we found 14 such studies. We also looked for evidence for Hypotheses 2–4, but not systematically.

We categorized the 14 studies into those with (1) disturbed habitat and mainly resprouting plants—five studies, (2) disturbed habitat and mainly seeders (pioneer plants)—one study, (3) laboratory experiments—three studies, (4) field experiments—two studies, and (5) natural colonization and growth—one study. Two studies were not easy to categorize. The 14 studies are presented in **Table 2**. Studies of both absolute and relative growth rate were included. Overall, we find support for our prediction in 12 studies (good support in three studies), while two studies were inconclusive (see **Table 2**). For a description of the 14 studies with additional information, see Data Sheet 2 in Supplementary Material.

## Hypothesis 2: The Fast Maturity of Shrubs Enables Earlier Seed Production Compared to Trees

Because a shrub does not grow tall, it will reach reproductive size earlier (e.g., Hoffmann and Solbrig, 2003), and produce seeds earlier than a tree (e.g., Hermann et al., 2012). This gives shrubs an extra fitness benefit after processes that reduce tree dominance. Early seed production should facilitate seed dispersal to new, unoccupied patches. A tall tree with a large canopy can produce many more seeds than a shrub, but for most trees, the time lag in seed set is a disadvantage. This hypothesis may be less relevant for tropical rain forests where small tree species also occur (e.g., understory treelets), with apparently fewer multi-stemmed shrubs.

## Hypothesis 3: The Multiple Stems in Shrubs Insure Future Survival and Growth if One or More Stems Die

A single-stemmed tree faces a lethal risk if the stem breaks and dies due to e.g., harsh weather conditions, falling trees/branches, drought, disease, or browsing, and trampling animals. In contrast, a shrub can afford to lose some of its stems and still survive (Wilson, 1995; Sheffer et al., 2014). Loss of a stem during the growth season will result in loss of foliage, reducing C uptake. A tree would lose its entire canopy, whereas a shrub would only lose part of it. In the dormant season, if a single-stemmed tree breaks it loses all its dormant terminal and lateral buds, delaying foliage, and canopy development and C uptake the following year. Further, woody plants may store resources (e.g., nitrogen, water, and non-structural carbohydrates) within the stems for re-growth, and a tree loses all such stored resources if its stem breaks near the ground. Multi-stemmed shrubs may also have an advantage over single-stemmed trees if a stem suffers hydraulic failure. This may be especially true for hydraulically modular shrubs, such as *Ambrosia dumosa* in arid ecosystems in California, USA (Espino and Schenk, 2009).

## Hypothesis 4: The Short Stems of Shrubs Improve Survival through Three Traits, Compared to Tall Tree Stems

We suggest that short shrubs have at least three structural traits that improve survival, compared to taller trees. Being short or tall is a trade-off; trees gain other advantages from being tall, as mentioned at the end of Section The Occurrence and Ecological Importance of Shrubs.

*First*, shrubs can bend and thus survive storms, snow load, avalanches, etc., which may otherwise result in stem breakage. In cold and alpine areas, low vegetation survives extreme weather and strong winds better, due to better aerodynamic resistance and improved temperature conditions (Grace, 1988; Hallinger et al., 2010; Neuner, 2014). In areas with landslides and avalanches, shrubs are favored by short and flexible stems compared to trees, which may fall (review in Givnish, 1995; Stokes et al., 2012). Recently, Larjavaara (2015) emphasized the advantages of stem flexibility in shrubs, and suggested that this limits their height.

**TABLE 2 | Result of literature review to test the prediction from Hypothesis 1: higher above-ground growth rate in small shrubs than in small trees.**

Category and country	Habitat	Comparison	Main result	Type of evidence for Hypothesis 1 (++, +, +/-, -)	References
<b>DISTURBED HABITAT, MAINLY RESPROUTING</b>					
Brazil	Grassland	2 shrub and 3 tree species	Shrubs regained more basal area and height than trees after fire/cutting	++	Hermann et al., 2012
Brazil	Forest-grassland ecotone	38 shrub and 42 larger woody species	Shorter multi-stemmed shrubs dominated early regrowth after fire	+	Müller et al., 2007
Brazil	Savanna (Cerrado)	4 shrubs/subshrubs and 3 tree species	Diameter growth <sup>a</sup> ; basal area, biomass, and heights not given	+/-	Hoffmann and Solbrig, 2003
Sweden	Mixed forest with Quercus	1 shrub and 13 tree species	Shrubs had higher growth rate and survival rate than trees after partial cutting	+	Leonardsson and Götmark, 2015
Japan	Mixed forest with Quercus and Carpinus	7 shrub and 24 larger woody species	Shrubs had stronger resprouting than the other species	+	Shibata et al., 2014
<b>DISTURBED HABITAT, MAINLY SEEDERS</b>					
Mexico	Tropical deciduous forest	47 species; mix, but more trees than shrubs	Shrubs and trees did not differ in height growth after clear-cut and burn <sup>b</sup>	+/-	Miller and Kauffman, 1998
<b>LABORATORY EXPERIMENTS</b>					
Lab	Species from British isles and northern Spain	25 shrub/sub-shrub and 55 tree species	Shrubs had higher relative growth rate than trees (only tested up to day 21)	+	Cornelissen et al., 1996
Lab	The tropics; meta-analysis of 15 studies	17 shrub, 12 intermediate and 61 tree species	Shrubs accumulated more biomass than trees after nutrient addition ( $P < 0.07$ ) <sup>c</sup>	+	Lawrence, 2003
Lab	Karst habitats, SW China	2 shrub and 4 tree species	Shrubs had higher biomass increase than "most of the trees" <sup>d</sup>	+	Liu et al., 2011
<b>FIELD EXPERIMENTS</b>					
Mexico	Tropical oak forest: open, edge, and interior habitat	2 shrub and 3 tree species (seedlings planted)	Shrubs had higher biomass growth, larger root systems, and higher survival than trees <sup>d</sup>	++	Asbjørnsen et al., 2004
Spain, highlands	Forest, shrub-land and open	4 shrub <sup>e</sup> , and 4 tree species (seeds sown)	Shrubs tended to survive better than trees, especially under dry conditions <sup>d</sup>	+	Matias et al., 2012
<b>NATURAL COLONIZATION AND GROWTH</b>					
USA, New York state	Abandoned fields	2 shrub and 2 tree species	Shrubs emerged better per seed, survived better, grew better, and became taller than the trees	++	Gardescu and Marks, 2004
<b>OTHER STUDIES</b>					
Lab, and experiments <sup>f</sup> (also herbs)	Diverse conditions	9 studies of shrubs, 27 studies of trees	Shrubs had higher median relative growth rate than trees	+	Houghton et al., 2013
Australia	Post-fire successional habitat	17 shrub-like, 2 taller tree-like species	Shrub-like outpaced tree-like species in height growth (early growth)	+	Falster and Westoby, 2005

<sup>a</sup>Difficult to compare growth data in publication.<sup>b</sup>Similar height growth of shrubs and trees generally implies higher (above-ground) biomass growth in the shrubs, since they have more stems.<sup>c</sup>Bonferroni-test that may be considered conservative.<sup>d</sup>Tested drought tolerance, or related the study to drought tolerance.<sup>e</sup>Two species referred to as scrub and broom by authors are considered shrubs here.<sup>f</sup>Controlled studies (laboratory and field experiments); studies of only trees, and of only shrubs, also included. Shrubs vs. trees not directly tested (their Figure 1).

Types of evidence: ++, good support for prediction; +, support; +/-, inconclusive; -, contradicts the prediction.

Second, shrubs can have a wide canopy with leaning stems to capture more light, since low height reduces the cost of the bending moment of leaning stems. Bending moment increases with increasing stem length and stem angle (Figure 4), so that the cost is much higher for a tree with leaning stems. We neglect branches for simplicity, so the actual bending moment of a stem

with its canopy would be greater than in Figure 4, and it would also be increased by snow and wind (e.g., Spatz and Bruechert, 2000). Falster and Westoby (2005) commented that "Multiple stems are thought to limit maximum height since they emerge at an angle and are less securely attached to the roots" (see also Kruger et al., 1997).

Third, the lower height of shrubs compared to trees should reduce the risk of cavitation due to drought and freezing. The maximum height of trees is partly determined by the problem of getting water to tall canopies. Water shortage can cause embolism in the xylem (Tyree and Sperry, 1989), and the risk of cavitation increases with stem height because of gravity (Ryan and Yoder, 1997). Freeze-thaw cycles during winter can cause similar problems (Tyree and Sperry, 1989; Zhu et al., 2000). This may be common in alpine and arctic habitats, where trees are disfavored especially in windy conditions, when temperatures drop. Because shrubs are shorter, they are less likely than trees to suffer from these problems, which occur in many habitat types. In addition, snow can more easily cover a shrub than a tree and protect it against low temperatures.

A possible further component of Hypothesis 4 might be: since shrubs are generally lower than trees, they may invest relatively less in support structure, and can invest more in e.g., foliage and roots, as suggested by Whittaker and Woodwell (1968). However, an overview and analysis of this suggestion is needed, including a definition of “support structure.” One would need to compare small trees and shrubs, as well as large trees and shrubs.

## DISCUSSION

We found support for our basic model, Hypothesis 1, and the prediction of higher growth rate in small shrubs than in small trees. Since shrubs occur in several biomes and many habitats and include numerous species, multiple hypotheses are needed to fully clarify their adaptive significance. Shrubs exhibit striking morphological diversity and adaptations within regions and across gradients (e.g., Schenk et al., 2008). Many studies relate shrubs and multi-stemmed trees to disturbed and low-productive habitats (e.g., Rundel, 1991; Wilson, 1995; Hoffmann and Moreira, 2002; Bellingham and Sparrow, 2009). Our Hypotheses 1 and 2 are independent of habitat, while the advantages predicted by Hypotheses 3 and 4 depend on disturbances, morphology, extreme weather, and climate. Shrubs seem to survive by combinations of fast growth and persistence (e.g., Kanno et al., 2001; Tanentzap et al., 2012), including early seed production and long-distance dispersal (e.g., by wind and birds).

An important result from our model, and the first functional trait under Hypothesis 1, was that shrubs have greater total sapwood area compared to single-stemmed trees of similar size. For an individual tree or shrub stem, the cross-sectional area of the sapwood is correlated with its total leaf area and mass (Waring et al., 1982; Meadows and Hodges, 2002; Wang, 2005; Rance et al., 2014; Issoufou et al., 2015) and thus with C uptake. Most studies focus on trees, and for shrubs we found only a handful of studies relating sapwood area to leaf area/mass, or the Huber value (HV, conductive xylem per leaf area) (Gartner, 1991; Wang, 2005; Issoufou et al., 2015). Wang (2005) reported data for shrubs and trees within the same site; he studied hydraulic conductivity and the ratio of sapwood cross-sectional area and leaf area (HV) in 10 trees and four shrubs in Canada and reported similar values in trees and shrubs. His study supports

our assumption of a similar ratio of sapwood cross-sectional area and leaf area in trees and shrubs, giving shrubs growth advantages over trees of similar size (i.e., of the same above-ground woody volume, as in our model).

One mechanism in Hypothesis 1 was that shrubs should sprout better than small trees from buds because of their larger surface area and widespread stems with more space for sprouts. Sprouting is involved in the fast growth of shrubs (Table 2) but we found no study that directly compared bud density or bud numbers and the initiation of sprouts on shrubs and small trees. Bond and van Wilgen (1996) distinguished basal and crown sprouting in woody plants in response to fire. The positions of buds and sprouts on woody plants are rarely described in published studies. In South African savanna after fire, sprouting near the ground dominated for shrubs (A. Zizka, pers. com.), presumably because fire kills buds higher up (see also Bond and van Wilgen, 1996; Hoffmann and Solbrig, 2003). Sprouting varies much among shrub species and with height growth (Bond and Midgley, 2001); some shrubs also sprout along stems (Figure 2B, and e.g., Lunt, 2011).

Shrubs may also flower and set seeds earlier than trees (Hypothesis 2); although this seems likely (e.g., Hoffmann and Solbrig, 2003; Hermann et al., 2012), a review and more empirical studies are desirable. Hypothesis 3 predicts that shrubs should survive stem breakage better than trees, for which there is little evidence (but see Shibata et al., 2014; Leonardsson and Götmark, 2015). In general, Hypotheses 3 and 4 would predict lower mortality in shrubs than trees. Condit et al. (1995) studied the mortality of tropical trees and shrubs during and after a drought on Barro Colorado Island (BCI), Panama; shrubs had higher overall mortality rates than trees, but shrubs had mortality rates less affected by the drought than trees. Lopez et al. (2005) analyzed xylem vulnerability to cavitation in five tree species and four shrub species on BCI (all shrubs were shade-tolerant). The four shrubs were on average less vulnerable to cavitation than the trees (Lopez et al., 2005; Table 2), and a shrub was the least vulnerable.

One contributing factor for fast growth in shrubs could be lower investment in wood, i.e., lower xylem density. If there is less need for structural strength in short shrub stems, they can invest more in growth. Castro-Diez et al. (1998) found that “shrub seedlings had less dense stem tissues than tree seedlings,” and added “possibly because they need less investment in long-term strength and stature.” However, two groups of 65 shrub species and 135 tree species from Argentina, Mexico, and the US did not differ in wood density (Martínez-Cabrera et al., 2011). Moreover, in a recent study of three co-occurring woody species that differed in maximum height (McCulloh et al., 2015), the shortest (a *Corylus* shrub) had the highest stem wood density, and the tallest (an *Alnus* tree) had lowest wood density (stems compared at similar plant heights).

Martínez-Cabrera et al. (2011) reported that shrubs had lower vessel diameter, and a higher density of vessels than trees. This was in addition reported for alpine shrubs compared to trees (Noshiro and Suzuki, 2001), and such vessels may reduce the risk of embolism—see also Lopez et al. (2005). McCulloh et al. (2015, see previous paragraph) suggested that vulnerability to embolism

increases with maximum potential height in the species. A reviewer suggested that plants “might be short (and shrubby) because they have inefficient, short, narrow vessels... which alone would make them less vulnerable to cavitation,” but it is also possible that both vessel traits and low height reduce the risk of embolism in shrubs. Worth noting is that Maherli et al. (2004), using data from a global database, found a large overlap in cavitation risk between major groups, life- and growth-forms, where shrubs on average were less vulnerable to cavitation than trees.

After severe damage or sudden increased light availability, a small tree or tree stump can sprout and change into shrub growth form. We suggest that our hypotheses contribute to explaining this response in trees, and thus may form parts of a theory of multi-stemming in woody plants. In trees, a change to a multi-stemmed growth form may be an attempt to survive a difficult situation and may sometimes fail and increase mortality, depending on tree size, species, and conditions (e.g., Del Tredici, 2001; Leonardsson and Götmark, 2015). One study of single- and multi-stemmed large *Pinus strobus* is consistent with our Hypothesis 1, since the latter, of a given age, grew better (higher volume production) than individuals with a single stem (Chamberlin and Aarssen, 1996). In addition, based on long-term data, Bellingham and Sparrow (2009) reported lower mortality (and lower recruitment) in multi-stemmed than in single-stemmed trees in montane rain forest.

Hypothesis 4 posits that low height in shrubs allows the stems to spread wide, since the bending moment of short stems is low even if they lean outward. The same bending moment calculations (see **Figure 4**) may also help explain why tall trees usually have a single stem and why multi-stemmed trees tend not to have the same shape as shrubs. A tall multi-stemmed tree with wide-spread leaning stems would need to invest much in stem strength (including reaction wood, Du and Yamamoto, 2007) to counteract the large bending moment; for very tall trees this would even likely be impossible. Such trees are therefore rare. Instead, a multi-stemmed tree might seek to lessen the bending moment with upward-tending stems (see “uprising stem” in **Figures 2C,D, 4**). But such stems would be close to each other and would each have a canopy smaller than that of an isolated stem, leading to an increased proportion of support structure for the tree as a whole. The tree would therefore not gain much in C uptake by having multiple stems. This may help to define and distinguish trees (single- and multi-stemmed) from shrubs, and help explain why shrubs do not evolve to “trubs,” intermediate in size between trees and shrubs (Sheffer et al., 2014). More detailed models, with empirical tests, are needed to clarify the growth form of stems in multi-stemmed trees.

Shrubs are often subjected to browsing. Zizka et al. (2014) suggested that the dense growth form of shrubs could protect the inner crown parts and their foliage from herbivory (a dilution effect). In the understory of temperate forest, deer grazing had little effect on growth and stem survival in the shrubs *Corylus avellana* and *Crataegus* sp. (Tanentzap et al., 2012). Livestock and grazing may also spread shrubs (Naito and Cairns, 2011). Possibly, small trees may be more susceptible to browsing than shrubs.

To assess and improve our model and hypotheses, the root systems of small shrubs and small trees are of considerable interest. Shrub roots can grow deep into the ground (Jackson et al., 1996; Schenk and Jackson, 2002). Whittaker and Woodwell (1968) suggested that shrubs, with smaller expenditure on supporting stem and branch tissue than trees, can allocate “a larger fraction of production [to] root growth,” to “survive fire, browsing, and drought.” A large tree must invest in structurally strong roots to support its size, while a shrub might develop relatively finer roots. But it is unclear whether small trees invest much in roots, and if they do so when they compete with shrubs. If a shrub can grow fast, it will be able to invest much in roots. In Asbjornsen’s et al. (2004) study, the two shrubs grew better, and produced longer and more branched roots than the three trees. In Whittaker and Woodwell’s (1968) study, the mean root/shoot ratio was clearly higher for four shrub species than for three tree species (p. 7), but in contrast to Asbjornsen et al. (2004), they report values for large trees (exact sizes not given) and for (small) shrubs.

Clonal growth is more common among trees and shrubs in “very harsh, resource-poor, or highly disturbed habitats” (Peterson and Jones, 1997). Some authors regard clumped stems of a single shrub individual as a clone, but it is important to distinguish clonal shrubs that grow by root suckers or runners and form new distant stems or stem clumps. To judge from the literature, it is unclear whether shrubs are clonal in this way more often than trees. Shrubs, compared to trees, may more often be clonal through layering, where nodes of lying stems root and sprout (one component in Hypothesis 1).

Finally, a comprehensive review of the adaptive significance of the shrub growth form seems non-existent (or is hard to find). Trees and herbs dominate the scientific literature: a search in the Web of Science for “tree\* AND leaf\*” gave 40,324 publications (18 March, 2016), and for “shrub\* AND leaf\*” 5658 publications (“tree\* AND shrub\* AND leaf\*”: 1839). Classical and much-cited publications on woody plants usually exclude shrubs, or focus strongly on trees (e.g., Horn, 1971; Connell, 1978; Loehle, 2000; Petit and Hampe, 2006; Thomas, 2014; but see Bond and van Wilgen, 1996 and recent studies of shrubland and climate change). The literature on woody plants in fire-prone ecosystems includes studies of shrubs, though with focus on fire or sprouting (e.g., Bond and Midgley, 2001).

Why is the shrub growth form neglected? Partly perhaps because it is difficult to define shrubs precisely or because of their often low direct economic value, but aesthetical aspects are probably also involved: many of the shrub-covered areas do not attract people. Negative words are common, such as “scrubby,” “thicket,” “encroachment,” “broussaille” (French), “sly” (Swedish); even “shrub” may sound negative. Many shrubs reduce the view of the surroundings, and good view is important for humans that hunt prey or seek charismatic species (Orians, 1986; Gray and Bond, 2013). Raunkiaer (1934) did not classify shrubs separately, but listed five other categories in the “most widely used system” of plant life forms (Archibold, 1995, p. 2) which may have led botanists to overlook shrubs. In contrast, shrubs are popular in horticulture, and the interest in shrubs increases.

## CONCLUSIONS AND FUTURE STUDIES

We have attempted to clarify why shrubs are successful in many habitats, including those where trees grow. Hypothesis 1 predicts that small shrubs should have higher growth rates than small trees, and we find evidence for that. Shrubs, compared to trees, should have earlier seed set and dispersal (Hypothesis 2), should have higher survival in extreme conditions and weather, and can benefit from having several stems and low height (Hypotheses 3 and 4). Although all hypotheses have some support, more studies and more detailed models are needed, including laboratory and field experiments where shrubs and trees are sown or planted in different habitat types and followed at least until the shrubs are fully grown. Growth rates, morphological traits, and ecophysiology should be analyzed in detail, and parts of the plant populations should be harvested at two or more stages to analyze whole plants.

Trees are more successful than shrubs in many areas under certain climatic conditions, where tall trees can dominate or control shrubs. The large distributions of some shrub-dominated communities may partly be due to pre-historical and historical human overexploitation of such areas, and of trees (Williams, 2006). Examples include Iceland (Diamond, 2005) and the West European heathlands dominated by the shrub *Calluna vulgaris* (Vandvik et al., 2014, and references therein). A review of the historical role of humans in the distribution of shrublands globally would be valuable.

Currently, our results are of interest for studies of shrubs expanding into savannas, rangelands, and grasslands, and for studies related to climate change, C pools, and habitat management (see e.g., Knapp et al., 2008; Naito and Cairns, 2011; Ratajczak et al., 2012; Gray and Bond, 2013; Conti et al., 2014; Ogden, 2015). Studies on “shrubification” in such open habitats (Naito and Cairns, 2011; Formica et al., 2014) can be reviewed: did the study areas lack trees, or did trees occur there but did not increase? A related, much studied and old theme is that shrubs

may facilitate tree regeneration by providing protection for small tree plants (e.g., Jefferies, 1885; Filazzola and Lortie, 2014). Researchers in this field should also ask: what made the shrubs more successful than the trees initially? Moreover, some genera contain both trees and shrubs, e.g., *Salix*, *Quercus*, *Camellia*, *Acacia*, and *Juniperus*. The species may be closely related, or one species may be highly variable, existing both as shrub and tree. A review of such species, their occurrence, and existing studies of them is of interest, and may clarify selection pressures acting on species and growth forms.

## AUTHOR CONTRIBUTIONS

FG conceived the topic and problem, and the initial approach. EG constructed the models and ran the calculations. FG, EG, and AJ developed hypotheses, partly from a review of the literature (made by FG, to some extent also EG and AJ). FG, EG, and AJ wrote the manuscript together.

## ACKNOWLEDGMENTS

Our research was supported by salary from the University of Gothenburg, the Chalmers University of Technology, and the Linnaeus University. We thank Heidi Asbjørnsen, Åslög Dahl, Craig Loehle, Shuichi Noshiro, Harry T. Valentine, and the reviewers for comments and suggestions on the manuscript, and Alexander Zizka and participants in three seminars for additional comments on our ideas about shrubs. Also, we thank Ian Lunt for permission to use his photograph.

## SUPPLEMENTARY MATERIAL

The Supplementary Material for this article can be found online at: <http://journal.frontiersin.org/article/10.3389/fpls.2016.01095>

## REFERENCES

- Archibold, O. W. (1995). *Ecology of World Vegetation*. London: Chapman and Hall.
- Asbjørnsen, H., Vogt, K. A., and Ashton, M. S. (2004). Synergistic responses of oak, pine and shrub seedlings to edge environments and drought in a fragmented tropical highland oak forest, Oaxaca, Mexico. *For. Ecol. Manage.* 192, 313–334. doi: 10.1016/j.foreco.2004.01.035
- Avila, E., Herrera, A., and Tezara, W. (2014). Contribution of stem CO<sub>2</sub> fixation to whole-plant carbon balance in nonsucculent species. *Photosynthetica* 52, 3–15. doi: 10.1007/s11099-014-0004-2
- Bellingham, P. J., and Sparrow, A. D. (2009). Multi-stemmed trees in montane rain forests: their frequency and demography in relation to elevation, soil nutrients and disturbance. *J. Ecol.* 97, 472–483. doi: 10.1111/j.1365-2745.2009.01479.x
- Bond, W. J., and Midgley, J. J. (2001). Ecology of sprouting in woody plants: the persistence niche. *Trends Ecol. Evol.* 16, 45–51. doi: 10.1016/S0169-5347(00)02033-4
- Bond, W. J., and van Wilgen, W. (1996). *Fire and Plants*. London: Chapman and Hall.
- Castro-Diez, P., Puyravaud, J. P., Cornelissen, J. H. C., and Villar-Salvador, P. (1998). Stem anatomy and relative growth rate in seedlings of a wide range of woody plant species and types. *Oecologia* 116, 57–66. doi: 10.1007/s004420050563
- Chamberlin, E. A., and Aarssen, L. W. (1996). The cost of apical dominance in white pine (*Pinus strobus* L.): growth in multi-stemmed versus single-stemmed trees. *Bull. Torrey Bot. Club* 123, 268–272. doi: 10.2307/296774
- Condit, R., Hubbell, S. P., and Foster, R. B. (1995). Mortality rates of 205 neotropical tree and shrub species and the impact of a severe drought. *Ecol. Monogr.* 65, 419–439. doi: 10.2307/2963497
- Connell, J. H. (1978). Diversity in tropical rain forests and coral reefs. High diversity of trees and corals is maintained only in a nonequilibrium state. *Science* 199, 1302–1310. doi: 10.1126/science.199.4335.1302
- Conti, G., Pérez-Harguindeguy, N., Quétier, F., Gorné, L. D., Jaureguiberry, P., Bertone, G. A. et al. (2014). Large changes in carbon storage under different land-use regimes in subtropical seasonally dry forests of southern South America. *Agric. Ecosyst. Environ.* 197, 68–76. doi: 10.1016/j.agee.2014.07.025
- Cornelissen, J. H. C., Castro Diez, P., and Hunt, R. (1996). Seedling growth, allocation and leaf attributes in a wide range of woody plant species and types. *J. Ecol.* 84, 755–765. doi: 10.2307/2261337
- Del Tredici, P. (2001). Sprouting in temperate trees: a morphological and ecological review. *Bot. Rev.* 67, 121–140. doi: 10.1007/BF02858075
- Denslow, J. S., Schultz, J. C., Vitousek, P. M., and Strain, B. R. (1990). Growth responses of tropical shrubs to treefall gap environments. *Ecology* 71, 165–179. doi: 10.2307/1940257

- Diamond, J. (2005). *Collapse. How Societies Choose to Fail or Survive*. London: Allen Lane.
- Du, S., and Yamamoto, F. (2007). An overview of the biology of reaction wood formation. *J. Integr. Plant Biol.* 49, 131–143. doi: 10.1111/j.1744-7909.2007.00427.x
- Espino, S., and Schenk, H. J. (2009). Hydraulically integrated or modular? Comparing whole-plant-level hydraulic systems between two desert shrub species with different growth forms. *New Phytol.* 183, 142–152. doi: 10.1111/j.1469-8137.2009.02828.x
- Falster, D. S., and Westoby, M. (2005). Tradeoffs between height growth rate, stem persistence and maximum height among plant species in a post-fire succession. *Oikos* 111, 57–66. doi: 10.1111/j.0030-1299.2005.13383.x
- Filazzola, A., and Lortie, C. J. (2014). A systematic review and conceptual framework for the mechanistic pathways of nurse plants. *Global Ecol. Biogeogr.* 23, 1335–1345. doi: 10.1111/geb.12202
- Formica, A., Farrer, E. C., Ashton, I. W., and Suding, K. N. (2014). Shrub expansion over the past 62 years in Rocky Mountain alpine tundra: possible causes and consequences. *Arctic Antarctic Alp. Res.* 46, 616–631. doi: 10.1657/1938-4246.46.3.616
- Gardescu, S., and Marks, P. L. (2004). Colonization of old fields by trees vs. shrubs: seed dispersal and seedling establishment. *J. Torrey Bot. Soc.* 131, 53–68. doi: 10.2307/4126928
- Gartner, B. L. (1991). Stem hydraulic-properties of vines vs. shrubs of western poison oak, *Toxicodendron diversilobum*. *Oecologia* 87, 180–189. doi: 10.1007/BF00325255
- Givnish, T. J. (1984). “Leaf and canopy adaptations in tropical forests,” in *Physiological Ecology of Plants of the Wet Tropics*, eds E. Medina, H. A. Mooney and C. Vazquez-Yanez (The Hague: Dr. W. Junk Publishers), 51–84.
- Givnish, T. J. (1995). “Plant stems: biomechanical adaptation for energy capture and influence on species distributions,” in *Plant Stems: Physiology and Functional Morphology*, ed B. L. Gartner (San Diego, CA: Academic Press), 3–49.
- Gong, P., Wang, J., Yu, L., Zhao, Y., Zhao, Y., Liang, L., et al. (2013). Finer resolution observation and monitoring of global land cover: first mapping results with Landsat TM and ETM+ data. *Int. J. Remote Sensing* 34, 2607–2654. doi: 10.1080/01431612.2012.748992
- Grace, J. (1988). “The functional significance of short stature in montane vegetation,” in *Plant form and Vegetation Structure*, ed M. J. A. Werger (The Hague: SPB Academic Publishing), 201–209.
- Gray, E. F., and Bond, W. J. (2013). Will woody plant encroachment impact the visitor experience and economy of conservation areas? *Koedoe* 55, e1–e9. doi: 10.4102/koedoe.v55i1.1106
- Griscom, B. W., and Ashton, P. M. S. (2003). Bamboo control of forest succession: *Guadua sarcocarpa* in Southeastern Peru. *For. Ecol. Manage.* 175, 445–454. doi: 10.1016/S0378-1127(02)00214-1
- Hallinger, M., Manthey, M., and Wilmking, M. (2010). Establishing a missing link: warm summer and winter snow cover promote shrub expansion into alpine tundra in Scandinavia. *New Phytol.* 186, 890–899. doi: 10.1111/j.1469-8137.2010.03223.x
- Hermann, J.-M., Haug, S., Depatta Pillar, V., and Pfadenhauer, J. (2012). Shrubs versus ‘gullivers’: woody species coping with disturbance in grassland. *Plant Ecol.* 213, 1757–1768. doi: 10.1007/s11258-012-0131-4
- Hoffmann, W. A., and Moreira, A. G. (2002). “The role of fire in population dynamics of woody plants,” in *The Cerrados of Brazil. Ecology and Natural History of a Neotropical Savanna*, eds P. S. Oliviera, and R. J. Marquis (New York, NY: Columbia University Press), 159–177.
- Hoffmann, W. A., and Solbrig, O. T. (2003). The role of topkill in the differential response of savanna woody species to fire. *For. Ecol. Manage.* 180, 273–286. doi: 10.1016/S0378-1127(02)00566-2
- Horn, H. S. (1971). *The Adaptive Geometry of Trees*. Princeton, NJ: Princeton University Press.
- Houghton, J., Thompson, K., and Rees, M. (2013). Does seed mass drive the differences in relative growth rate between growth forms? *Proc. R. Soc. B.* 280: 20130921. doi: 10.1098/rspb.2013.0921
- Issoufou, H. B., Rambal, S., Le Dantec, V., Oi, M., Laurent, J.-P., Saadou, M. et al. (2015). Is the WBE model appropriate for semi-arid shrubs subjected to clear cutting? *Tree Physiol.* 35, 197–208. doi: 10.1093/treephys/tpv002
- Jackson, R. B., Canadell, J., Ehleringer, J. R., Mooney, H. A., Sala, O. E., and Schulze, E. D. (1996). A global analysis of root distributions for terrestrial biomes. *Oecologia* 108, 389–411. doi: 10.1007/BF00333714
- Jefferies, R. (1885). *After London, or Wild England. Chapter 1, paragraph seven*. Available online at: <https://www.gutenberg.org/ebooks/13944> (Accessed May 23, 2016).
- Jensen, A. M., Gardiner, E. S., and Vaughn, K. C. (2012). High-light acclimation in *Quercus robur* L. seedlings upon over-topping a shaded environment. *Env. Exp. Bot.* 78, 25–32. doi: 10.1016/j.envexpbot.2011.12.020
- Jensen, A. M., Warren, J. M., Hanson, P. H., Childs, J., and Wullschleger, S. D. (2015). Needle age and season influence photosynthetic temperature response and total annual carbon uptake in mature *Picea mariana* trees. *Ann. Bot.* 116, 821–832. doi: 10.1093/aob/mcv115
- Kanno, H., Hara, M., Hirabuki, Y., Takehara, A., and Seiwa, K. (2001). Population dynamics of four understorey shrub species during a 7-yr period in a primary beech forest. *J. Veg. Sci.* 12, 391–400. doi: 10.2307/3236853
- Knapp, A. K., Briggs, J. M., Collins, S. L., Archers, S. L., Bret-Harte, M. S., Ewers, B. E., et al. (2008). Shrub encroachment in North American grasslands: shifts in growth form dominance rapidly alters control of ecosystem carbon inputs. *Global Change Biol.* 14, 615–623. doi: 10.1111/j.1365-2486.2007.01512.x
- Kruger, L. M., Midgley, J. J., and Cowling, R. M. (1997). Resprouters vs reseeders in South African forest trees; a model based of forest canopy height. *Funct. Ecol.* 11, 101–105.
- Küppers, M. (1989). Ecological significance of above-ground architectural patterns in woody plants: a question of cost-benefit relationships. *Trends Ecol. Evol.* 4, 375–379. doi: 10.1016/0169-5347(89)90103-1
- Larjavaara, M. (2015). Trees and shrubs differ biomechanically. *Trends Ecol. Evol.* 30, 499–500. doi: 10.1016/j.tree.2015.07.007
- Lavigne, M. B., and Ryan, M. G. (1997). Growth and maintenance respiration rates of aspen, black spruce and jack pine stems at northern and southern BOREAS sites. *Tree Physiol.* 17, 543–551. doi: 10.1093/treephys/17.8-9.543
- Lawrence, D. (2003). The response of tropical tree seedlings to nutrient supply: meta-analysis for understanding a changing tropical landscape. *J. Trop. Ecol.* 19, 239–250. doi: 10.1017/S0266467403003274
- Leonardsson, J., and Götmark, F. (2015). Differential survival and growth of stumps in 14 woody species after conservation thinning in mixed oak-rich temperate forests. *Eur. J. For. Res.* 134, 199–209. doi: 10.1007/s10342-014-0843-1
- Liu, C.-C., Liu, Y. G., Guo, K., Li, G.-Q., Zheng, E. R., Yu, L.-F., et al. (2011). Comparative ecophysiological responses to drought of two shrub and four tree species from karst habitats of southwestern China. *Trees* 25, 537–549. doi: 10.1007/s00468-010-0533-7
- Loehle, C. (2000). Strategy space and the disturbance spectrum: a life-history model for tree species coexistence. *Am. Nat.* 156, 14–33. doi: 10.1086/303369
- Lopez, O. R., Kursar, T. A., Cochard, H., and Tyree, M. T. (2005). Interspecific variation in xylem vulnerability to cavitation among tropical tree and shrub species. *Tree Physiol.* 25, 1553–1562. doi: 10.1093/treephys/25.12.1553
- Lunt, I. (2011). *Growing Old in a Shrubland: Gravity Always Wins*. Available online at: <http://ianlunt ecology.com/2011/09/18/growing-old-in-a-shrubland/> (Accessed March 18, 2016).
- Maherali, H., Pockman, W., and Jackson, R. (2004). Adaptive variation in the vulnerability of woody plants to xylem cavitation. *Ecology* 85, 2184–2199. doi: 10.1890/02-0538
- Martínez-Cabrera, H. I., Schenk, H. J., Cevallos-Ferriz, S. R. S., and Jones, C. S. (2011). Integration of vessel traits, wood density, and height in angiosperm shrubs and trees. *Am. J. Bot.* 98, 915–922. doi: 10.3732/ajb.100335
- Matias, L., Quero, J. L., Zamora, R., and Castro, J. (2012). Evidence for plant traits driving specific drought resistance. A community field experiment. *Env. Exp. Bot.* 81, 55–61. doi: 10.1016/j.envexpbot.2012.03.002
- Maurits, W., Vandegheuchte, M. W., Jasper Bloemen, J., Vergeynst, L. L., and Steppe, K. (2015). Woody tissue photosynthesis in trees: salve on the wounds of drought? *New Phytol.* 208, 998–1002. doi: 10.1111/nph.13599
- McCulloh, K. A., Johnson, D. M., Petitmermet, J., McEllis, B., Meinzer, F. C., and Lachenbruch, B. (2015). A comparison of hydraulic architecture in three similarly sized woody species differing in their maximum potential height. *Tree Physiol.* 35, 723–731. doi: 10.1093/treephys/tpv035

- McDowell, N., Barnard, H., Bond, B. J., Hinckley, T., Hubbard, R. M., Ishii, H., et al. (2002). The relationship between tree height and leaf area: sapwood area ratio. *Oecologia* 132, 12–20. doi: 10.1007/s00442-002-0904-x
- McKell, C. M., (ed.) (1989). *The Biology and Utilization of Shrubs*. San Diego, CA: Academic Press.
- Meadows, J. S., and Hodges, J. D. (2002). Sapwood area as an estimator of leaf area and foliar weight in cherrybark oak and green ash. *For. Sci.* 48, 69–76.
- Mencuccini, M. (2003). The ecological significance of long-distance water transport: short-term regulation, long-term acclimation and the hydraulic costs of stature across plant life forms. *Plant Cell Environ.* 26, 163–182. doi: 10.1046/j.1365-3040.2003.00991.x
- Miller, P. M., and Kauffman, J. B. (1998). Seedling and sprout response to slash-and-burn agriculture in a tropical deciduous forest. *Biotropica* 30, 538–546. doi: 10.1111/j.1744-7429.1998.tb00094.x
- Müller, S., Overbeck, G. E., Pfadenhauer, J., and Pillar, V. D. (2007). Plant functional types of woody species related to fire disturbance in forest–grassland ecotones. *Plant Ecol.* 189, 1–14. doi: 10.1007/s11258-006-9162-z
- Naito, A. T., and Cairns, D. M. (2011). Patterns and processes of global shrub expansion. *Progr. Phys. Geogr.* 35, 423–442. doi: 10.1177/0309133311403538
- Neuner, G. (2014). Frost resistance in alpine woody plants. *Front. Plant Sci.* 5:654. doi: 10.3389/fpls.2014.00654
- Niklas, K. J. (1994). *Plant Allometry. The Scaling of Form and Process*. Chicago, IL: University of Chicago Press.
- Niklas, K. J., and Spatz, H.-C. (2004). Growth and hydraulic (not mechanical) constraints govern the scaling of tree height and mass. *Proc. Natl. Acad. Sci. U.S.A.* 44, 15661–15663. doi: 10.1073/pnas.0405857101
- Nilson, E. T. (1995). “Stem photosynthesis: extent, patterns, and role in plant carbon Economy,” in *Plant Stems: Physiology and Functional Morphology*, ed. B. L. Gartner (San Diego, CA: Academic Press), 223–240.
- Noshiro, S., and Suzuki, M. (2001). Ontogenetic wood anatomy of tree and subtree species of Nepalese Rhododendron (Ericaceae) and characterization of shrub species. *Am. J. Bot.* 88, 560–569. doi: 10.2307/2657054
- Ogden, L. E. (2015). Plants duke it out in a warming arctic. *BioScience* 65, 220. doi: 10.1093/biosci/biu209
- Olson, D. M., Dinerstein, E., Wikramanayake, E. D., Burgess, N. D., Powell, G. V. N., Underwood, E. C., et al. (2001). Terrestrial ecoregions of the World: a new map of life on Earth. *BioScience* 51, 1–6. doi: 10.1641/0006-3568(2001)051[0933:TEOTWA]2.0.CO;2
- Orians, G. H. (1986). “An ecological and evolutionary approach to landscape aesthetics,” in *Landscape Meanings and Values*, eds G. C. Penning-Roswell and D. Lowenthal (London: Allen and Unwin), 3–25.
- Peterson, C. J., and Jones, R. H. (1997). “Clonality in woody plants: a review and comparison with clonal herbs,” in *The Ecology and Evolution of Clonal Plants*, eds H. Kroon, and J. van Groenendaal (Leiden: Backhuys Publishers), 263–289.
- Petit, R. J., and Hampe, A. (2006). Some evolutionary consequences of being a tree. *Ann. Rev. Ecol. Evol. Syst.* 37, 187–214. doi: 10.1146/annurev.ecolsys.37.091305.110215
- Pfanz, H., Aschan, G., Langenfeld-Heyser, R., Wittman, C., and Loose, M. (2002). Ecology and ecophysiology of tree stems: corticular and wood photosynthesis. *Naturwissenschaften* 89, 147–162. doi: 10.1007/s00114-002-0309-z
- Pickett, S. T. A., and Kempf, J. S. (1980). Branching patterns in forest shrubs and understory trees in relation to habitat. *New Phytol.* 86, 219–228. doi: 10.1111/j.1469-8137.1980.tb03191.x
- Qian, H. (2015). Patterns of frequency distribution of woody plant heights: a response to Scheffer et al. *Trends Ecol. Evol.* 30, 497–498. doi: 10.1016/j.tree.2015.02.006
- Qian, H., and Ricklefs, R. E. (2015). Bimodality of plant height: fact or artifact? A response to Scheffer et al. *Trends Ecol. Evol.* 30, 6–7. doi: 10.1016/j.tree.2014.09.010
- Rance, S. J., Mendham, D. S., and Cameron, D. M. (2014). Assessment of leaf mass and leaf area of tree crowns in young *Eucalyptus grandis* and *E. globulus* plantations from measurements made on the stems. *New For.* 45, 523–542. doi: 10.1007/s11056-014-9416-x
- Ratajczak, Z., Nippert, J. B., and Collins, S. L. (2012). Woody encroachment decreases diversity across North American grasslands and savannas. *Ecology* 93, 697–703. doi: 10.1890/11-1199.1
- Raunkiaer, C. (1934). *The Life Form of Plants and Statistical Plant Geography*. London: Clarendon.
- Rundel, P. W. (1991). “Shrub life forms,” in *Response of Plants to Multiple Stress*, eds H. A. Mooney, W. E. Winner, and E. J. Pell (San Diego, CA: Academic Press), 345–371.
- Ryan, M. G., and Yoder, B. J. (1997). Hydraulic limits to tree height and tree growth. *Bioscience* 47, 235–242. doi: 10.2307/1313077
- Schenk, H. J., Espino, S., Goedhart, C. M., Nordenstahl, M., Martinez Cabrera, H. I., and Jones, C. S. (2008). Hydraulic integration and shrub growth form linked across continental aridity gradients. *Proc. Natl. Acad. Sci. U.S.A.* 105, 11248–11253. doi: 10.1073/pnas.0804294105
- Schenk, H. J., and Jackson, R. B. (2002). The global biogeography of roots. *Ecol. Monogr.* 72, 311–328. doi: 10.1890/0012-9615(2002)072[0311:TGBOR]2.0.CO;2
- Sheffer, M., Vergnon, R., Cornelissen, H. C., Hantson, S., Holmgren, M., van Nes, E. H., et al. (2014). Why trees and shrubs but rarely trubs? *Trends Ecol. Evol.* 29, 433–434. doi: 10.1016/j.tree.2014.06.001
- Shibata, R., Shibata, M., Tanaka, H., Lida, S., Masaki, T., Hatta, F., et al. (2014). Interspecific variation in the size-dependent resprouting ability of temperate woody species and its adaptive significance. *J. Ecol.* 102, 209–220. doi: 10.1111/1365-2745.12174
- Sholes, R. J., and Archer, S. R. (1997). Tree-grass interactions in savanna. *Ann. Rev. Ecol. Syst.* 28, 517–544. doi: 10.1146/annurev.ecolsys.28.1.517
- Spatz, H.-C., and Bruechert, F. (2000). Basic biometrics of self-supporting plants: wind loads and gravitational loads on a Norway spruce tree. *For. Ecol. Manage.* 135, 33–44. doi: 10.1016/S0378-1127(00)00296-6
- Stokes, A., Mine, F.-C., Mao, Z., and Brancheriau, L. (2012). Multi-stemming and mechanical traits ensure persistence of subalpine woody plants exposed to a disturbance gradient. *J. Veg. Sci.* 23, 325–338. doi: 10.1111/j.1654-1103.2011.01349.x
- Stutz, H. C. (1989). “Evolution of shrubs,” in *The Biology and Utilization of Shrubs*, ed C. M. McKell (San Diego, CA: Academic Press), 323–340.
- Sun, S., Niklas, K. J., Fang, F., Xiang, S., Wu, X., and Yang, X. (2010). Is branching intensity interspecifically related to biomass allocation? A survey of 25 dicot shrub species from an open-growing dry valley. *Int. J. Plant Sci.* 171, 615–625. doi: 10.1086/653544
- Tanentzap, A., Mountford, E. P., Cooke, A. S., and Coomes, D. A. (2012). The more stems the merrier: advantages of multi-stemmed architecture for the demography of understorey trees in a temperate broadleaf woodland. *J. Ecol.* 100, 171–183. doi: 10.1111/j.1365-2745.2011.01879.x
- Teskey, R. O., Saveyn, A., Steppe, K., and McGurie, M. A. (2008). Origin, fate and significance of CO<sub>2</sub> in tree stems. *New Phytol.* 177, 17–32. doi: 10.1111/j.1469-8137.2007.02286.x
- Thomas, P. A. (2014). *Trees. Their Natural History*, 2nd Edn. Cambridge: Cambridge University Press.
- Tyree, M. T., and Sperry, J. S. (1989). Vulnerability of xylem to cavitation and embolism. *Ann. Rev. Plant Physiol. Plant Mol. Biol.* 40, 19–38. doi: 10.1146/annurev.pp.40.060189.000315
- van der Sande, M. T., Zuidema, P. A., and Sterck, F. (2015). Explaining biomass growth of tropical canopy trees: the importance of sapwood. *Oecologia* 177, 1145–1155. doi: 10.1007/s00442-015-3220-y
- Vandvik, V., Töpper, J. P., Cook, Z., Daws, M. I., Heegaard, E., Måren, I. E. et al. (2014). Management-driven evolution in a domesticated ecosystem. *Biol. Lett.* 10: 20140156. doi: 10.1098/rsbl.2014.0156
- Vick, J. K., and Young, D. R. (2009). Corticular photosynthesis: a mechanism to enhance shrub expansion in coastal environments. *Photosynthetica* 47, 26–32. doi: 10.1007/s11099-009-0006-7
- Wang, J. R. (2005). Spring and summer hydraulic conductivity of 14 woody species of the sub-boreal forest in British Columbia. *Can. J. For. Res.* 35, 2727–2733. doi: 10.1139/x05-176
- Wang, X. O., Keplinger, T., Gierlinger, N., and Burgert, I. (2014). Plant material features responsible for bamboo’s excellent mechanical performance: a comparison of tensile properties of bamboo and spruce at the tissue, fibre and cell wall levels. *Ann. Bot.* 114, 1627–1635. doi: 10.1093/aob/mcu180
- Waring, R. H., Schroeder, P. E., and Oren, R. (1982). Application of the pipe model theory to predict canopy leaf area. *Can. J. For. Res.* 12, 556–560. doi: 10.1139/x82-086
- Whitehead, D., Edwards, W. R. N., and Jarvis, P. G. (1984). Conducting sapwood area, foliage area, and permeability in mature trees of *Picea sitchensis* and *Pinus contorta*. *Can. J. For. Res.* 14, 940–947. doi: 10.1139/x84-166

- Whitney, G. G. (1976). The bifurcation ratio as an indicator of adaptive strategy in woody plant species. *Bull. Torrey Bot. Club* 103, 67–72. doi: 10.2307/2484833
- Whittaker, R. H., and Woodwell, G. M. (1968). Dimension and production relations of trees and shrubs in the Brookhaven Forest, New York. *J. Ecol.* 56, 1–25. doi: 10.2307/2258063
- Williams, M. (2006). *Deforesting the Earth. From Prehistory to Global Crisis, An Abridgement*. Chicago, IL: University of Chicago Press.
- Wilson, B. F. (1995). "Shrub stems: form and function," in *Plant Stems: Physiology and Functional Morphology*, ed B. L. Gartner (San Diego, CA: Academic Press), 91–102.
- Wittmann, C., and Pfanz, H. (2007). Temperature dependency of bark photosynthesis in beech (*Fagus sylvatica* L.) and birch (*Betula pendula* Roth.) trees. *J. Exp. Bot.* 58, 4293–4306. doi: 10.1093/jxb/erm313
- Wullschleger, S. D. (1993). Biochemical limitations to carbon assimilation in C3 plants – A retrospective analysis of the A/Ci curves from 109 species. *J. Exp. Bot.* 44, 907–920. doi: 10.1093/jxb/44.5.907
- Zhu, X. B., Cox, R. M., and Arp, P. A. (2000). Effects of xylem cavitation and freezing injury on dieback of yellow birch (*Betula alleghaniensis*) in relation to simulated winter thaw. *Tree Physiol.* 20, 541–547. doi: 10.1093/treephys/20.8.541
- Zizka, A., Govender, N., and Higgins, S. I. (2014). How to tell a shrub from a tree: a life-history perspective from a South African savanna. *Austral Ecol.* 39, 767–778. doi: 10.1111/aec.12142

**Conflict of Interest Statement:** The authors declare that the research was conducted in the absence of any commercial or financial relationships that could be construed as a potential conflict of interest.

Copyright © 2016 Götmark, Götmark and Jensen. This is an open-access article distributed under the terms of the Creative Commons Attribution License (CC BY). The use, distribution or reproduction in other forums is permitted, provided the original author(s) or licensor are credited and that the original publication in this journal is cited, in accordance with accepted academic practice. No use, distribution or reproduction is permitted which does not comply with these terms.



# Sweet Pepper (*Capsicum annuum* L.) Canopy Photosynthesis Modeling Using 3D Plant Architecture and Light Ray-Tracing

Jee Hoon Kim<sup>1†</sup>, Joon Woo Lee<sup>1†</sup>, Tae In Ahn<sup>1</sup>, Jong Hwa Shin<sup>2</sup>, Kyung Sub Park<sup>3</sup> and Jung Eek Son<sup>1\*</sup>

<sup>1</sup> Department of Plant Science and Research Institute of Agriculture and Life Sciences, Seoul National University, Seoul, South Korea, <sup>2</sup> Department of Horticulture and Breeding, Andong National University, Andong, South Korea, <sup>3</sup> Protected Horticulture Research Institute, National Institute of Horticultural and Herbal Science, Haman, South Korea

## OPEN ACCESS

### Edited by:

Alexander Bucksch,  
University of Georgia, USA

### Reviewed by:

Tsu-Wei Chen,  
Leibniz University of Hanover,  
Germany  
Malia Gehan,  
Donald Danforth Plant Science Center,  
USA

### \*Correspondence:

Jung Eek Son  
sjeenv@snu.ac.kr

<sup>†</sup>These authors have contributed  
equally to this work.

### Specialty section:

This article was submitted to  
Plant Biophysics and Modeling,  
a section of the journal  
*Frontiers in Plant Science*

Received: 17 March 2016

Accepted: 18 August 2016

Published: 09 September 2016

### Citation:

Kim JH, Lee JW, Ahn TI, Shin JH, Park KS and Son JE (2016) Sweet Pepper (*Capsicum annuum* L.) Canopy Photosynthesis Modeling Using 3D Plant Architecture and Light Ray-Tracing. *Front. Plant Sci.* 7:1321.  
doi: 10.3389/fpls.2016.01321

Canopy photosynthesis has typically been estimated using mathematical models that have the following assumptions: the light interception inside the canopy exponentially declines with the canopy depth, and the photosynthetic capacity is affected by light interception as a result of acclimation. However, in actual situations, light interception in the canopy is quite heterogenous depending on environmental factors such as the location, microclimate, leaf area index, and canopy architecture. It is important to apply these factors in an analysis. The objective of the current study is to estimate the canopy photosynthesis of paprika (*Capsicum annuum* L.) with an analysis of by simulating the intercepted irradiation of the canopy using a 3D ray-tracing and photosynthetic capacity in each layer. By inputting the structural data of an actual plant, the 3D architecture of paprika was reconstructed using graphic software (Houdini FX, FX, Canada). The light curves and A/C<sub>i</sub> curve of each layer were measured to parameterize the Farquhar, von Caemmerer, and Berry (FvCB) model. The difference in photosynthetic capacity within the canopy was observed. With the intercepted irradiation data and photosynthetic parameters of each layer, the values of an entire plant's photosynthesis rate were estimated by integrating the calculated photosynthesis rate at each layer. The estimated photosynthesis rate of an entire plant showed good agreement with the measured plant using a closed chamber for validation. From the results, this method was considered as a reliable tool to predict canopy photosynthesis using light interception, and can be extended to analyze the canopy photosynthesis in actual greenhouse conditions.

**Keywords:** FvCB model, light interception, paprika, photosynthetic rate, vertical position

## INTRODUCTION

Canopy photosynthesis is one of the important factors for estimating crop growth and establishing the strategy of CO<sub>2</sub> fertilization inside a greenhouse. Because crop yield is closely related to the seasonal integral of the total canopy photosynthesis, it can be used as base data to predict the crop production in a greenhouse (Monteith, 1965). Additionally, by estimating the attenuation of CO<sub>2</sub> concentration with time, supply rates of CO<sub>2</sub> fertilization in a cultivation system could

be determined. In general, canopy photosynthesis is primarily determined by the light regime inside the greenhouse, and several factors such as meteorological and greenhouse structural factors, must be considered. Scaling up from the leaf to the canopy, the vertical pattern of the intercepted irradiation can be affected by the vertical structure of the whole plant and additional shading effects would occur from neighboring plants in the canopy (Caldwell et al., 1986; Chen et al., 1999). Other variances such as the direction of the sunlight, the ratio of the diffuse light, the greenhouse structure, the plant growth stage, and the plant density also affect the intercepted irradiation inside the canopy (Elifis et al., 1989; Lieth and Pasian, 1990; Stirling et al., 1994; Buck-Sorlin et al., 2011). Therefore, in estimating the canopy photosynthesis, it is important to investigate the light interception of the plant caused by these variances.

It is difficult to measure the actual light interception of the plant surface because of technical limitations. Therefore, previous research has estimated the canopy photosynthesis by various modeling approaches. Among the various approaches, the single leaf models, such as the FvCB model (Farquhar et al., 1980), represent the leaf level biochemical mechanism, and the whole canopy models, including the sunlit-shaded model (de Pury and Farquhar, 1997), are the most well-known models for photosynthesis (Zhu et al., 2012). Although these models are useful, they have been seldom used in greenhouse crop species (Gonzalez-Real and Baille, 2000; Yin and Struik, 2009; excepting cucumber Chen et al., 2014a; tomato de Visser et al., 2014; and rose Buck-Sorlin et al., 2011). Primary assumptions are that the absorbed photosynthetic active radiation affects the photosynthetic capacity of each canopy layer and contributes to the entire canopy photosynthesis (Field, 1983; de Pury and Farquhar, 1997; Roux et al., 1998; Drecer et al., 2000; Johnson et al., 2010). Additionally, to simplify the calculation procedures, models have assumed that the vertical distribution of light interception has a negative exponential pattern from the top to the bottom of the canopy (Monsi and Saeki, 1953; Norman, 1980). The high level of spatial and temporal heterogeneity of the light interception is not considered in these models, for example, the shading by upper leaves on the lower part of the canopy, diffuse radiation which penetrates deep into the canopy (de Pury and Farquhar, 1997; Hikosaka, 2014), and the plant architecture affected by the leaf shape and angle in the light interception (Kim et al., 2010; Tang et al., 2015).

For analysis of the canopy photosynthesis rate, precise light distribution, and leaf photosynthesis are prerequisites (Chen et al., 2015). From this perspective, the construction of a 3D graphic plant is necessary to reflect the precise physical properties of the plant structure. Ray-tracing technique is a reasonable solution to incorporate optical properties such as the reflectance and transmittance of a leaf and other structures into the light simulation. Recently, there are increasing amount of studies where the light interceptions of crops have been estimated by using 3D plant models and light ray-tracing methods (Mabrouk et al., 1997; Buck-Sorlin et al., 2011; Sarlikioti et al., 2011; der Zande et al., 2011; Chen et al., 2014a,b; de Visser et al., 2014; Tang et al., 2015; Kang et al., 2016). To estimate canopy photosynthetic rates by combining above methods and photosynthetic models

would be helpful for designing greenhouse crop production system. Thus, the objectives of the current study are to analyze accurate light interceptions using a 3D ray-tracing method, determine the vertical distributions of photosynthetic parameters, calculate the photosynthesis rate of each layer, and validate the canopy photosynthesis of paprika.

## MATERIALS AND METHODS

### Cultivation Conditions

This experiment was conducted in a Venlo-type glasshouse located at the experimental farm of the Seoul National University in Suwon, Korea ( $37.3^{\circ}\text{N}$ ,  $127^{\circ}\text{E}$ ). Paprika plants (*Capsicum annuum* L.) were transplanted after 3 months (20 July–15 October 2014) in rock wool cubes with a plant density of 3 plants/ $\text{m}^2$  and the distance between rows was 80 cm. Air conditioners were installed in each wall of the glasshouse to maintain a temperature between  $25^{\circ}$  and  $35^{\circ}\text{C}$  inside the greenhouse during the summer season and the relative humidity was controlled to be within a range of 60–80% using fogging systems. Nutrient solutions were irrigated 4 times a day at 10:00, 12:00, 14:00, and 16:00. To prevent a deficit of N related to the biosynthesis of chlorophylls, the total N concentration in the nutrient solution was  $\text{NO}_3\text{-N}$  1.45 mM. The other concentrations of macro-elements in the nutrient solution included P 1.61, K 3.59, Ca 4.00, Mg 1.88, and S 1.88 mM. The EC and pH ranges of the nutrient solutions were  $2.6\text{--}3.0 \text{ dS m}^{-1}$  and 5.5–6.5, respectively. The plants were pruned to form two main stems, which were vertically trellised to a "V" canopy system (Jovicich et al., 2004).

### Leaf Photosynthesis and Leaf Nitrogen Measurements

Eight layers were determined within each plant to investigate the vertical pattern of the leaf photosynthetic capacity. Each layer consists of four leaves and layer number was counted acropetally.

The leaf photosynthesis was measured with a portable photosynthesis system (LI-6400, LI-COR, USA). A closed chamber on the photosynthesis system was set at  $25^{\circ}\text{C}$  for the leaf temperature and 60–70% for the relative humidity to obtain the photosynthetic parameters on the standard temperature condition. Additionally, a red 8:blue 2 light quality of an LED light source similar to the sun spectrum was used inside the closed chamber. By using the auto program of the light curve and an  $A/C_i$  curve that measures 20 points for each program, photosynthesis were measured at (1) photosynthetic photon flux density (PPFD) =  $1000 \mu\text{mol m}^{-2} \text{ s}^{-1}$  under varying external  $\text{CO}_2$  partial pressure ( $p_a$ ) = 0–120 Pa and (2) external  $\text{CO}_2$  partial pressure (Pa) = 100 Pa with varying PPFD ( $50\text{--}1000 \mu\text{mol m}^{-2} \text{ s}^{-1}$ ). The calculated values of the internal  $\text{CO}_2$  partial pressure ( $C_i$ ) were provided by the LI-COR system inside the device.

After the photosynthesis measurement, each sample leaf was collected to determine the leaf nitrogen content. An average value of the leaf nitrogen content per layer was investigated after the Kjeldahl digestion of the leaves, which were oven-dried at  $80^{\circ}\text{C}$  for 5 days and then grounded (Kjeldahl, 1883).

## Entire-Plant Photosynthesis Measurements

To measure the daily CO<sub>2</sub> consumption of an entire plant, a closed chamber ( $1 \times 1 \times 2$  m) was designed and constructed using transparent polycarbonate. A closed chamber on the photosynthesis system was set at 25°C for the leaf temperature and 60–70% for the relative humidity (Figure 1); this is referred to as an open chamber system (Garcia et al., 1990). The CO<sub>2</sub> concentration inside the chamber was set to range between 80 and 200 Pa to measure the photosynthesis rate of the entire plant while maintaining a CO<sub>2</sub> level above the saturation points (Shin et al., 2011). An additional supply of CO<sub>2</sub> gas was implemented when the CO<sub>2</sub> concentration in the chamber was ~80 Pa. The CO<sub>2</sub> concentrations inside the chamber were detected using a CO<sub>2</sub> analyser (LI-820, LI-COR, USA). CO<sub>2</sub> leakage of the chamber was about 0.2–0.3  $\mu\text{mol CO}_2 \text{ s}^{-1}$  under the experimental CO<sub>2</sub> condition (Figure S1). Irradiance inside the chamber was measured using an irradiation sensor (BF5, Delta-T Devices, UK) and the diffuse ratio was also determined. To maintain the temperature and CO<sub>2</sub> concentration inside the chamber, two radiators circulating cool water were placed along each sidewall. A fan was passed through the radiators and blown toward the chamber wall to maintain equal ventilation. The temperature inside the chamber was maintained at 25°C by circulating cooled water controlled by a condenser (DH-003A, Daeho-condenser, Korea). The CO<sub>2</sub> concentration, irradiance, and temperature inside the chamber were stored in a data logger every 10 s. Silica gel was used in the air circulation process to control increased humidity from the transpiration of the plant. A plant was selected from among five samples and was placed in the chamber from 9:00 to 18:00. Whenever the CO<sub>2</sub> concentration reached approximately 100 Pa, additional CO<sub>2</sub> was supplied to retain a saturated CO<sub>2</sub> condition (Figure 2).

## Construction of the 3D Virtual Plant

Before sealing the chamber for measuring the entire plant's photosynthesis, a sample plant free from disorders was chosen to design the 3D virtual plant. The structure of the sample plant was measured using a ruler and protractor to transpose the real structure of the plant to a 3D graphic. The architect parameters consisted of three major parts (leaf, petiole, and stem) and the detailed measurements included the following: (1) leaf area and leaf angle; (2) petiole length and petiole angle; and (3) stem length, stem diameter, and stem angle. The area of each leaf within the sample plant was measured using a leaf area meter (LI-3100, LI-COR, USA). Structural characteristics of leaves and stems by layer were measured as Table 1.

A 3D plant model was developed using graphic software (Houdini FX, FX, Canada), as shown in Figure 3. Using an

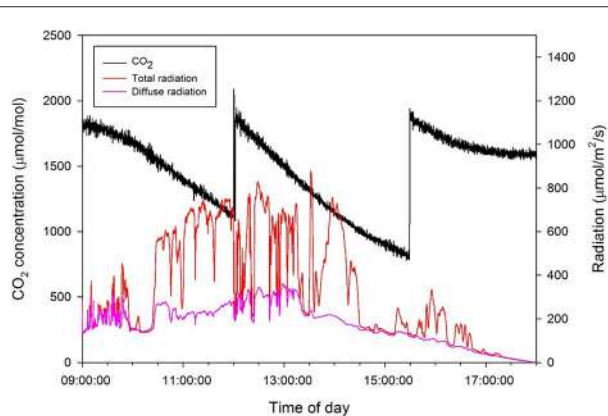


**FIGURE 2 |** Daily changes in CO<sub>2</sub> concentration in the closed chamber with light intensity above the plant on 15 October 2014.

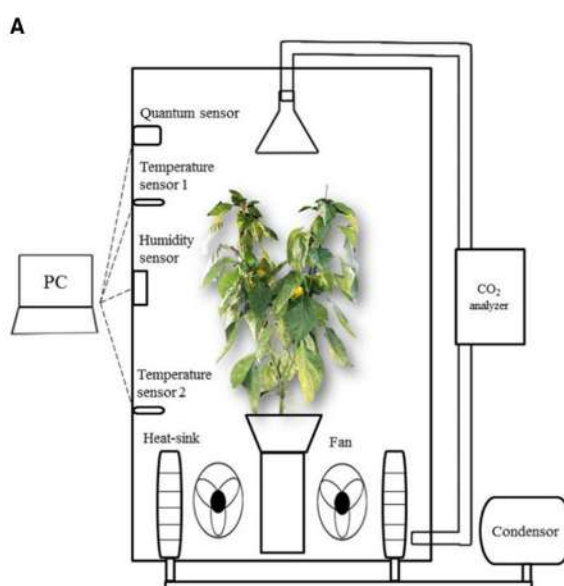


**FIGURE 1 |** A schematic diagram (A), and actual installation (B) of a closed growth chamber for measuring CO<sub>2</sub> consumption of paprika plant.

**TABLE 1 | Structural characteristics of leaves and stems by layer.**

Layer	Leaf				Stem		
	Leaf area (cm <sup>2</sup> )	Petiole length (cm)	Dropness (°)	n <sup>z</sup>	Radius (mm)	Length (cm)	n <sup>z</sup>
1	181.4	7.0	30.33	4	4.3	8.3	2
3	189.9	6.3	37.08	4	4.5	7.5	2
5	200.3	5.3	34.92	4	4.1	9.2	2
7	220.0	6.1	29.25	4	4.2	8.8	2
9	200.2	5.0	45.72	4	4.0	7.9	2
11	269.8	5.4	36.18	4	4.4	9.0	2
13	243.8	5.1	57.78	4	4.4	8.5	2
15	181.1	3.8	51.84	6	4.2	3.4	4

<sup>z</sup>replicates.

L-system formalism, which is useful in the construction of a plant's growth pattern, the plant structure could be built up from the bottom to the top in the tree window (**Figure 3D**) by applying structure values for each part of the plant. For the validation procedure, the actual plant inside the closed chamber was virtualized as a 3D graphic plant that referred to the measured values of the plant structure and the digitized data using a 3D digitizer (Sense, 3D systems, Inc., USA). The virtual plant consisted of two primary stems having 15 nodes each. The calculation of the leaf area (LA) is determined using the length (L) and width (W). The leaf area equation is embedded inside the graphic tool,  $LA = 0.6034 LW + 0.0732$  ( $R^2 = 0.994$ ,  $p < 0.001$ ; Tai et al., 2009). The leaves with an accurate leaf area were simultaneously shown on the graphic window when the users input the values of L and W (**Figure 3D**). The petiole and leaf angles were also applied by inputting the angles (x, y, z) of the directions (**Figures 3A,B**).

## Simulation of the Intercepted Irradiation

Redesigning the 3D plant was accomplished using 3D CAD software (SOLIDWORKS, Dassault Systemes, FRANCE), and light interception analysis was simulated using ray-tracing software (OPTISWORKS, OPTIS Inc., FRANCE). Light illuminance on the surface of the leaves of the 3D plant model was calculated to investigate the intercepted irradiance in specific conditions and values of light intensity were obtained on the 3D leaf surface. The growth chamber was modeled with the 3D CAD software and assembled with the 3D plant model. With the simulation software it was possible to input microclimate parameters: sun directions (coordinates, date, time, zenith, north direction), and sunlight properties (ratio of direct light and diffuse light); and material parameters: optical properties of the leaf, chamber, and glasshouse structure. Optical properties (transmittance and reflectance) were measured using an integrating sphere (IC2, StellarNet Inc., CANADA) with a spectrometer (BLUE-Wave, StellarNet Inc., CANADA) and a light source (SL1 Tungsten Halogen, StellarNet Inc., CANADA) and entered in the preferences section for the leaves in the simulation program (**Figure 4**). In the leaf optical measurements, the optical properties of the leaves have little

differences in the vertical position within the plant. The reflectance and transmittance of both sides of leaf were used as 0.1 and 0.07, respectively, in our simulation; Ray-tracing simulations were conducted with 10 giga rays and the number of max impacts was set to be 10 for all conditions. Identifying the applicability for expanding to a canopy situation, plant arrays of  $1 \times 1$  and  $3 \times 3$  with a distance of 0.8 m between plants were set to investigate the different patterns of intercepted radiation. Detectors were placed on the surface of a single plant located in the center of the canopy. Four cases were simulated at 9:00, 12:00, 15:00, and 18:00 and the intercepted irradiance was analyzed for each layer.

## Calculation of the Photosynthetic Parameters

$A/C_i$  curve fitting utility was used to calculate the photosynthetic parameters (Sharkey et al., 2007). The prediction of the leaf photosynthesis rate was based on the FvCB model (Equation 1).

$$A_l = \min \left\{ \frac{A_v, f(V_{lm}, c_i, T_l)}{A_j, f(I, f, J_m, c_i, T_l)} \right\} - R_l, f(T_l) \quad (1)$$

where  $A_l$  is the rate of the leaf's net assimilation, and  $A_v$  and  $A_j$  indicate the rates of the leaf gross assimilation limited by ribulose biphosphate-carboxylase-oxygenase (Rubisco) activity and ribulose biphosphate (RuBP) regeneration, respectively.  $A_l$  is determined by the minimum value of the two rates (Equation 1). Each rate can be expressed as various leaf characteristics (the maximum photosynthetic Rubisco capacity,  $V_{lm}$ , and the maximum rate of electron transport,  $J_m$ ). All of the temperature conditions in the current experiment were fixed at 25°C to neglect the effect of temperature on the parameters and, therefore, on the temperature-related functions in the model.

The maximum photosynthesis rate ( $A_{max}$ ) was calculated from the light curve at each layer by using a non-rectangular hyperbolic function. The photosynthetic Rubisco capacity ( $V_l$ ) was also obtained from the  $A/C_i$  curve by using a non-linear regression. Assuming that the CO<sub>2</sub> fixation rate is limited only by Rubisco activity in a low CO<sub>2</sub> condition, and  $V_l$  value of each layer was estimated from the  $A/C_i$  curve of each layer within the range  $C_i < 30$  Pa (Equation 2). Similarly, the potential rate of the electron transport ( $J_m$ ) values was determined from the  $A/C_i$  curve at a range above 40 Pa for  $C_i$  (Equations 3, 4).

$$V_l = A_v \frac{(c_i + K')}{(c_i - \Gamma_*)} \quad (2)$$

$$J = 4A_j \frac{(c_i + 2\Gamma_*)}{(c_i - \Gamma_*)} \quad (3)$$

$$J_m = J \frac{(I_{le} - \theta_l J)}{(I_{le} - J)} \quad (4)$$

where  $I_{le}$  is the photosynthetic active radiation (PAR) effectively absorbed by PSII, and  $J$  is the rate of electron transport. Detailed model equations and constants are shown in **Tables 2, 3**.  $I_l$  is the total absorbed PAR per unit leaf area. Calculation of all the parameters were followed by de Pury and Farquhar (1997) and Kim and Lieth (2003).

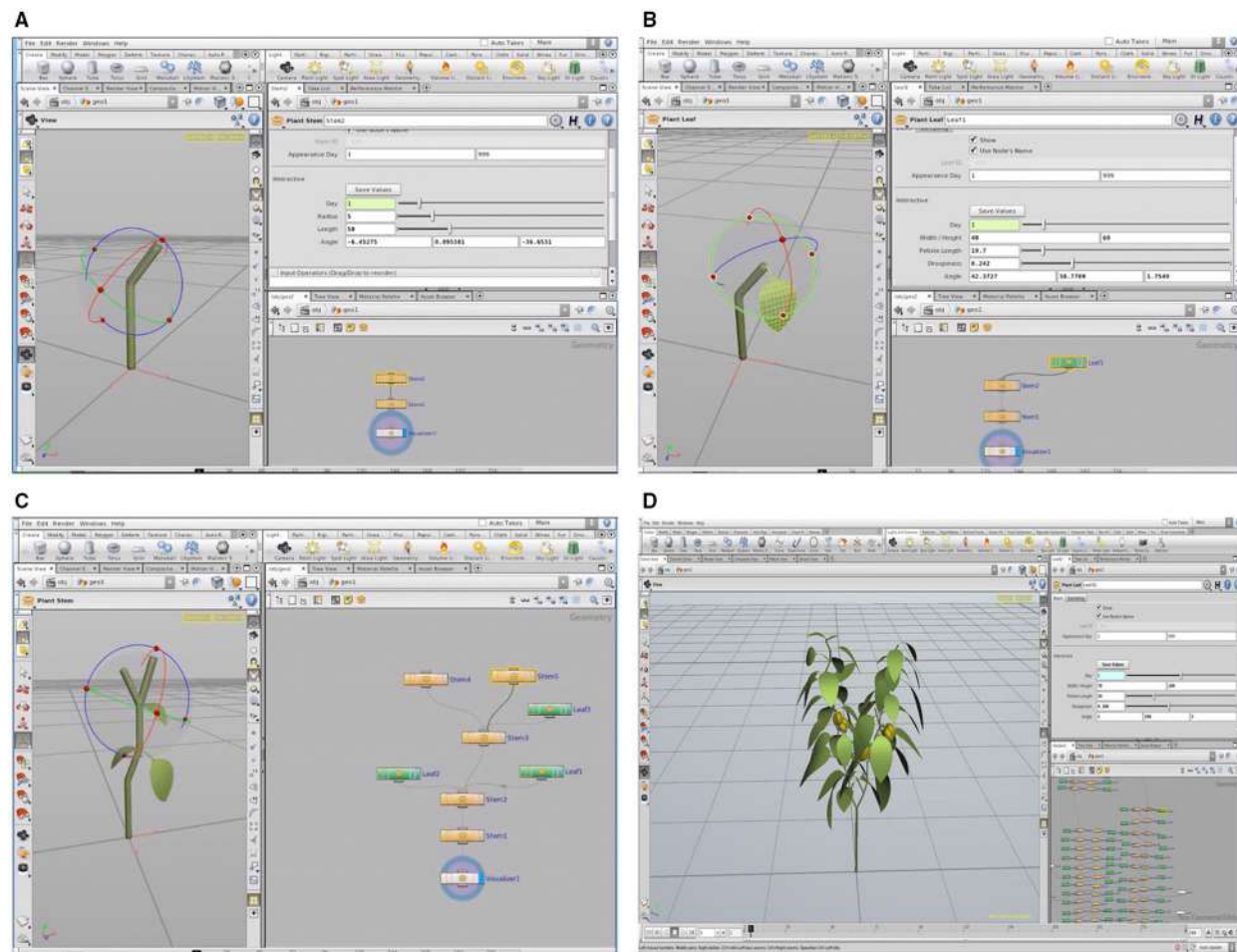


**FIGURE 3 |** A 3D virtual plant constructed in the L-system using the Houdini FX graphic software: construction of paprika stem (A) and leaf (B), the process of modeling the paprika (C), and tree window of L-system formalism and graphic window of the completed paprika structure (D).

## Validation of Whole Plant Photosynthetic Rate

With an average value of intercepted irradiation from the simulation and photosynthetic parameters from the measurements at each layer, the leaf photosynthesis rate was calculated for each layer. To apply the actual light intensity from the logged data to an estimate, the average values of light intensity and the diffuse ratio for 30 min were used. By integrating the photosynthesis rate at each layer, the photosynthesis rate of the entire plant was calculated using the sum of  $A_l$  in each layer.

According to this method, the estimated data were calculated every half hour and these data of the entire plant's photosynthesis rate were compared with actual data from 9:00 to 18:00 on October 15, 2014, for validation. From an actual measurement of the CO<sub>2</sub> concentration in a sealed chamber, the reduction of the CO<sub>2</sub> concentration was converted to a photosynthesis rate assuming that the slope of the CO<sub>2</sub> concentration is the same as the photosynthesis rate. A work flow for construction of 3D plant model, calculation, and validation of a whole plant photosynthesis rate was described as Figure 4.

## RESULTS

### Distribution of the Maximum Photosynthesis Rate and Leaf Nitrogen Content within the Entire Plant

The maximum photosynthesis rate,  $A_{max}$ , at each layer was measured to be within 1000  $\mu\text{mol m}^{-2} \text{s}^{-1}$  of the light intensity and 100 Pa of the CO<sub>2</sub> saturation condition as shown in Figure 5. The mean values of  $A_{max}$  decreased from the top (layer 15) to the bottom (layer 1), from 37.04 to 12.41  $\mu\text{mol m}^{-2} \text{s}^{-1}$ , respectively. The standard variations of  $A_{max}$  were somewhat higher in the upper part than the bottom, indicating that the range of  $A_{max}$  appeared broader in the younger leaves compared to the older leaves at the bottom. Unlike the exponential patterns generally assumed in many photosynthesis models, the distribution of  $A_{max}$  for an individual plant showed a linear pattern on all of the five sample plants.

In the case of nitrogen distribution, the total nitrogen content in each leaf increased with an increase in the leaf layer number. Although the standard deviation in the middle layer was greater,

**TABLE 2 | Equations of the FvCB model.**

Equation	Description	Number
$A_l = \min \{A_v, A_j\} - R_l$	Rate of leaf net photosynthesis	(A1)
$A_v = V_l \frac{(C_l - I^*)}{(C_l + K')}$	Rubisco-limited photosynthesis	(A2)
$K' = K_C (1 + \frac{O}{K_O})$	Effective Michaelis-Menten constant	(A3)
$A_j = J \frac{(C_l - I^*)}{4(C_l + 2I^*)}$	Electron-transport limited rate of photosynthesis	(A4)
$\theta_l J^2 - (I_{le} + J_m) J + I_{le} J_m = 0$	Irradiance dependence of electron transport	(A5)
$I_{le} = \frac{I_l(1-f)}{2}$	PAR effectively absorbed by PSII	(A6)
$\frac{R_l}{V_l} = \frac{I^* - I^*}{I^* + K'}$	Ratio of leaf respiration to photosynthetic Rubisco capacity	(A7)

\*Temperature condition, 25°C; other temperature-related functions are omitted.

**TABLE 3 | Photosynthetic parameters and constants of the FvCB model at 25°C.**

Symbol	Value	Unit	Description
$K_C$	40.4	Pa	Michaelis-Menten constant of Rubisco for CO <sub>2</sub>
$K_O$	$24.8 \times 10^3$	Pa	Michaelis-Menten constant of Rubisco for O <sub>2</sub>
$O$	$20.5 \times 10^3$	Pa	Oxygen partial pressure
$R_{lo}$	$0.0089V_{lo}$	$\mu\text{mol m}^{-2} \text{s}^{-1}$	Dark leaf respiration rate
$I^*$	4.4	Pa	CO <sub>2</sub> compensation point of photosynthesis
$I^{*+}$	3.69	Pa	$I^*$ in the absence of mitochondrial respiration
$f$	0.15	–	Spectral correction factor
$\theta_l$	0.68–0.83	–	Curvature of leaf response of electron transport to irradiance

\*Values of the photosynthetic parameters are given at 25°C.

the total nitrogen content in the uppermost layer was more than double that in the bottom layer, similar to  $A_{max}$ , and it was apparent that most of the nitrogen was allocated to the upper layer, which retained higher light use efficiency (Figure 5). Decreasing patterns of  $A_{max}$  and  $N_{tot}$  were very similar in the vertical distribution, indicating that the nitrogen content is strongly correlated with the photosynthetic capacity. Converting a leaf nitrogen content on a dry mass basis ( $\text{mg g}^{-1}$ ) to a leaf nitrogen concentration on a leaf area basis ( $\text{g m}^{-2}$ ), the spatial distribution of the nitrogen content on a leaf area basis was not significantly meaningful.

## Distribution of Photosynthetic Parameters, $V_{lo}$ and $J_{mo}$ , within an Entire Plant

Comparing the light curves and  $A/C_i$  curves at each layer, the photosynthetic capacity in a certain position varied considerably among the layers, resulting in different light use efficiencies.

Changes in  $V_{lo}$  and  $J_{mo}$  were identified by the leaf position using the measured value of  $A_l$  for each layer at 25°C (Table 4). The range of  $\theta$  is between 0.68 and 0.83 regardless of the leaf layer number. By increasing the leaf layer number, both the average values of  $V_{lo}$  and  $J_{mo}$  decreased from 88.62 and 175.42 (layer 15) to 20.31 and 50.83  $\mu\text{mol m}^{-2} \text{s}^{-1}$  (layer 1), respectively. Despite significant variations, both average values of the parameters showed linear patterns in the vertical distribution rather than exponential patterns within the plant, similar to  $A_{max}$  and  $N_{tot}$ . Average values of photosynthetic parameters were selected to use in the calculation of the photosynthesis rate at each layer.

## Validation of an Entire Plant's Photosynthesis and Expansion to the Canopy Situation

Half hour-photosynthesis rates of the sample plant were compared with estimated rates and showed good agreement with a coefficient of determination ( $R^2$ ) of 0.85 and a root mean square error (RMSE) of 0.47 (Figure 6). The estimation values were slightly lower than actual values at 9:00 to 10:30 and upper at 11:30 to 15:00. Daily variations in the photosynthesis rates were clearly shown in the estimated data. For the canopy situation, the 3D simulated data explicitly shows the shading effect of the neighboring plants, which mostly appeared in the middle and bottom layers (Figure 7). From an overhead view the intercepted irradiance within the plant was primarily affected by the plant, which was oriented toward the sun. The total intercepted radiation of the center plant surrounded by eight plants did not decrease significantly regardless of the number of neighboring plants and the shade time determined by the height of the neighboring plants. In estimating the intercepted irradiation at each layer, linear decay appeared at the top and middle layers, and the variations in the intercepted irradiation occurred as a result of the changes in sun direction (Figure 8).

## DISCUSSION

Canopy photosynthesis is such a complex mechanism that the correlation of various environmental factors engaged in the photosynthesis process should be considered. Furthermore, scaling up from leaf to canopy, intercepted radiation and the optical and physiological properties related to the photosynthetic capacity should be considered, including leaf age, leaf acclimation to light, and nitrogen distribution within the canopy. However, it is necessary to clarify the relationship between light acclimation and nitrogen distribution, which is also heterogeneous within the canopy. Intercepted radiation is sensitively affected by leaf shape, leaf angle, and plant position inside the canopy architecture (Gonzalez-Real and Baille, 2000; Sarlikioti et al., 2011); therefore, precise measurement of intercepted radiation on the plant surface is not easy because of technical limitations.

Accordingly, 3D model is necessary for analysis of intercepted irradiation (Figure 3). To obtain the precise architecture for a plant in a 3D model, advanced technology for scanning the material is required to simulate the intercepted radiation on the plant surface, and the supporting hardware should be

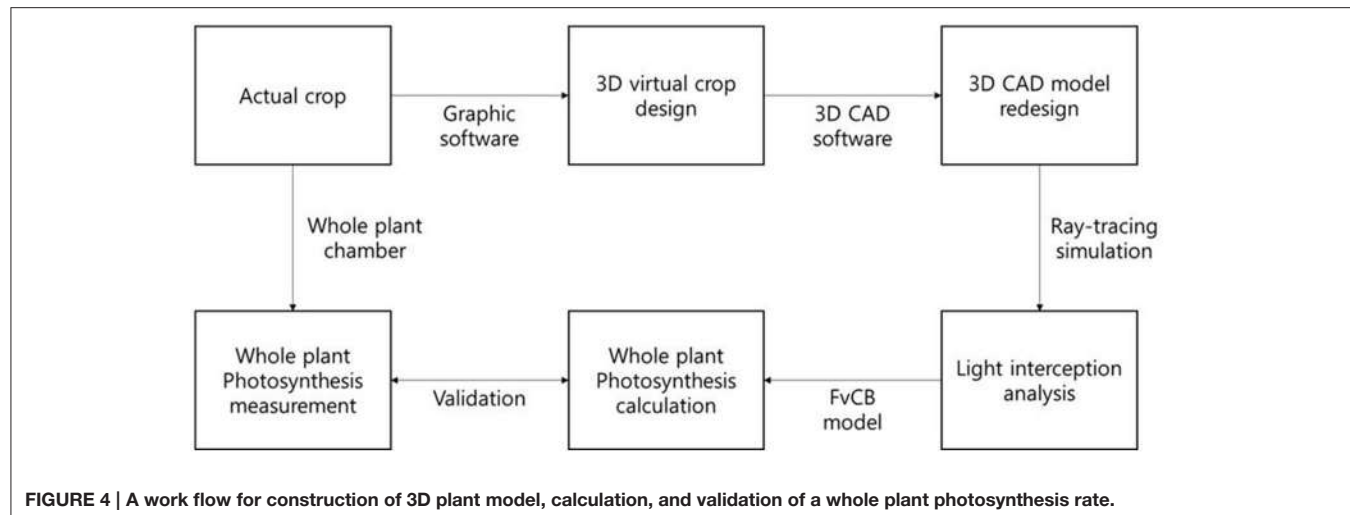


**FIGURE 4 |** A work flow for construction of 3D plant model, calculation, and validation of a whole plant photosynthesis rate.

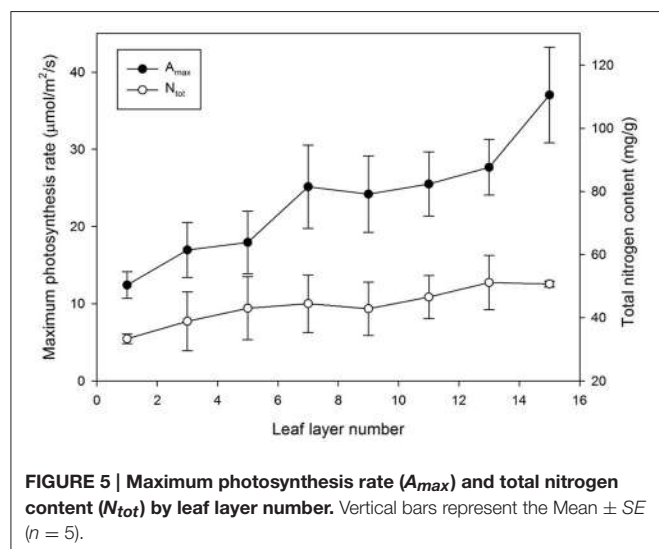


**FIGURE 5 |** Maximum photosynthesis rate ( $A_{\max}$ ) and total nitrogen content ( $N_{\text{tot}}$ ) by leaf layer number. Vertical bars represent the Mean  $\pm$  SE ( $n = 5$ ).

accompanied by an increased number of rays in the optical simulation. In actual canopy conditions, the heterogeneity of plant architecture still exists such that the compromise between precision and simplicity is inevitable in analyzing canopy photosynthesis. A simplified analysis method with guarantee of its accuracy is strongly required to perceive dynamic changes of the canopy photosynthesis rate in real-time.

There are still many possibilities to improve the analysis by (1) parameterization by using chlorophyll fluorescence as input (Bellasio et al., 2016), (2) development of dynamic architectural models related with physiological events (Chen et al., 2014b, 2015), (3) analysis of horticultural practices on the model behavior (de Visser et al., 2014), (4) specification of the relationships between nitrogen content and photosynthetic parameters, (5) analysis of photosynthesis as influenced by stomatal conductance and  $\text{CO}_2$  concentration (Kim and Lieth, 2003), and (6) reduction of  $\text{CO}_2$  leakage and inhomogeneous air mixing in the chamber.

**TABLE 4 |** Estimation of the photosynthetic parameters  $V_{lo}$  (= value of  $V_l$  at 25°C) and  $J_{mo}$  (= value of  $J_m$  at 25°C).

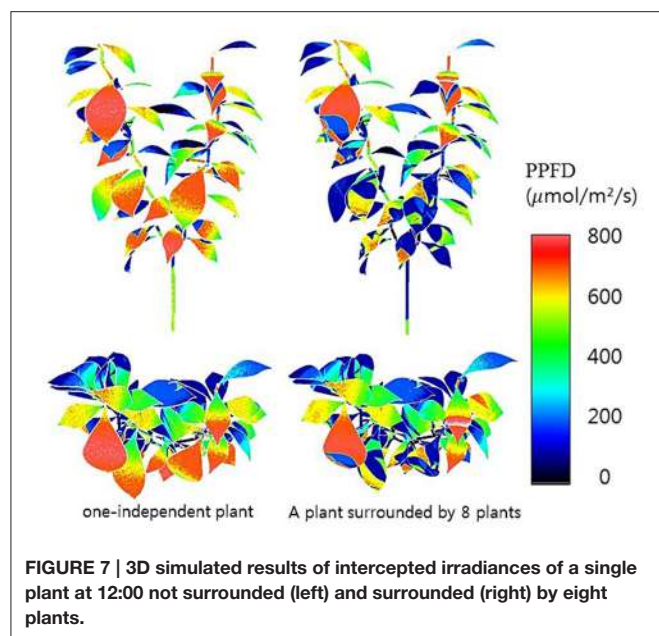
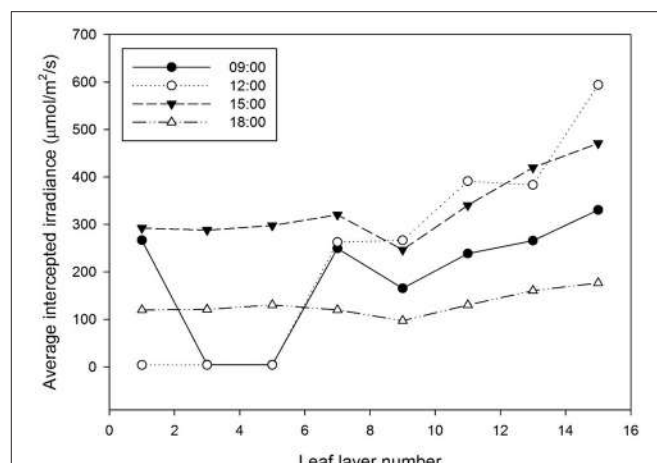
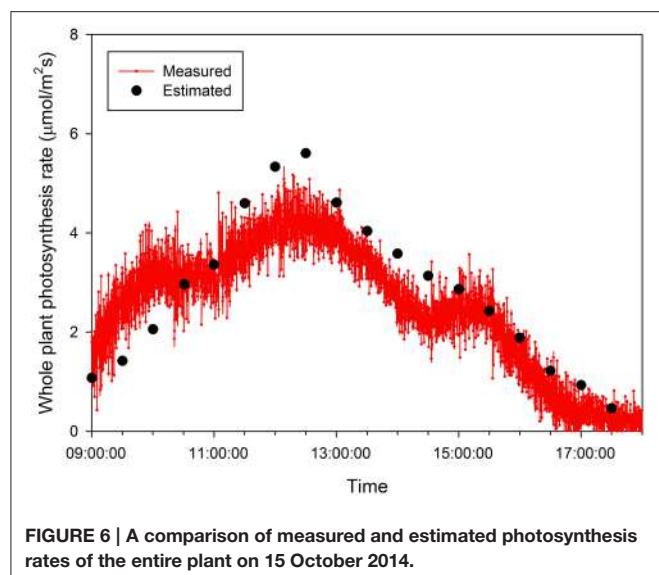
Layer	$V_{lo}$	$n^y$	$R^2$	$J_{mo}$	$n^y$	$R^2$
15	$88.62 \pm 8.20^z$	5	0.76	$175.42 \pm 13.17$	5	0.71
13	$81.72 \pm 5.74$	5	0.83	$123.97 \pm 9.77$	5	0.78
11	$77.93 \pm 6.24$	5	0.70	$119.64 \pm 9.87$	5	0.85
9	$71.25 \pm 5.60$	5	0.80	$107.64 \pm 11.84$	5	0.75
7	$68.56 \pm 6.88$	5	0.69	$88.63 \pm 12.47$	5	0.69
5	$56.08 \pm 7.09$	5	0.73	$72.62 \pm 14.08$	5	0.73
3	$32.82 \pm 7.70$	5	0.66	$67.49 \pm 14.66$	5	0.67
1	$20.31 \pm 2.57$	5	0.88	$50.83 \pm 10.69$	5	0.73

<sup>z</sup>Mean  $\pm$  SE.

<sup>y</sup>replicates.

$n$  and  $R^2$  are the number of observed  $A/C_l$  curves per layer and the coefficient of determination by fitting non-rectangular hyperbolae functions, respectively.

Especially, the spatial distribution of nitrogen allocation provides another method for estimating canopy photosynthesis with regards to the photosynthetic capacity. Standard deviations of the nitrogen content exist primarily in the middle layers, indicating that the heterogeneity of the light environment in the canopy primarily occurred as a result of additional influences such as a sun fleck or shading effect by neighboring plants. Although many researchers determined the optimal distribution of nitrogen in nature to be a method for maximizing canopy photosynthesis (Hirose and Werger, 1987; Schieving et al., 1992), the detailed mechanism of leaf acclimation to the light environment remains under investigation including the quantitative analyzes of photosynthetic capacity (Ellsworth and Reich, 1993; Ito et al., 2005; Anten and During, 2011). The spatial distribution of nitrogen within the canopy is greatly simplified by models to calculate the canopy photosynthesis, and fixing the pattern of the photosynthetic parameters may cause errors in the precise estimation of canopy photosynthesis. In the current study, the leaf layer criteria of paprika were simplistically established because of the plant architecture pattern. However,



additional criteria might be required for other species such as leafy vegetables that have a horizontal structure rather than a vertical structure.

In addition, other environmental factors such as the external CO<sub>2</sub> concentration, temperature, and leaf age also affect the leaf properties of photosynthesis (Thornley, 2002; Escudero and Mediavilla, 2003). It was assumed in this research that the spatial distributions of the external CO<sub>2</sub> concentration and temperature are identical within the canopy. Paprika transplanted after 3 months were chosen in the current analysis because of the closed chamber's size limitations. In applying later growth stages, the conditions for the analysis should be modified because the intercepted radiation is changed by neighboring plants whose heights are greater. Furthermore, leaf age functions should be

incorporated into the FvCB model (Irving and Robinson, 2006) to estimate the photosynthesis of each leaf for different growth stages within the canopy.

By measuring the actual photosynthetic rates of a whole plant in the growth chamber, we could validate the canopy photosynthetic results estimated with the 3D plant model and light ray-tracing method. Interestingly, the measured canopy photosynthesis (Figure 6) did not simultaneously reflect the fluctuating light condition (Figure 2). This might be due to that, technically, the air in the chamber could not be homogeneously mixed. Estimated values were around 5–10% different from measured. In spite of several existing limitations in estimating the canopy's photosynthesis, the simulation method developed is quite suitable for precisely predicting the canopy's photosynthesis rate by applying microclimatic factors such as the location, date, time, diffuse ratio, and optical properties of the materials. From the simulated data, the sun fleck inside the canopy was found to change with time and the average light intensity of a certain layer depends on the amount of direct sunlight. Furthermore, fractions of sunlit and shaded areas changed through time (Figure 2), with the result that the vertical distributions of intercepted radiation did not always follow the pattern of the Lambert-Beer's law that irradiation is exponentially decayed (Figure 8). An increase in the diffuse ratio of sunlight reduces light variations among the leaves at different locations in the canopy. The current simulation results identified that the pattern of intercepted irradiation within the entire plant was strongly determined by sun direction and its optical properties.

In the current study, an analysis method to determine the canopy photosynthesis was developed using graphic software based on a 3D model and ray-tracing simulation (Figure 7). The photosynthetic capacity within the plant was significantly different among the vertical positions (Table 4). With the intercepted irradiation data and photosynthetic parameters of each layer, the values of an entire plant's photosynthesis rate were estimated by integrating the calculated photosynthesis rate

at each layer. The estimated photosynthesis rate of an entire plant showed good agreement with the measured plant using a closed chamber for validation (**Figure 6**). The advantages of this method are the availability of precise analysis of canopy photosynthesis considering various environmental factors and the expendability to a greenhouse cultivation condition. By expanding this approach to canopy conditions, it is possible to analyze the canopy's photosynthesis as a key factor in a cultivation system. By supplementing plant physiological aspects, the method could be a powerful tool to predict the mass production of horticultural crops in greenhouses.

## AUTHOR CONTRIBUTIONS

JK and JL developed the 3D model, conducted the measurement and simulation. TA, JHS, and KP constructed the growth chamber and controlled the environments. JES designed the

experiment, developed the 3D model, and conducted the total analysis.

## ACKNOWLEDGMENTS

This research was supported by the MSIP (Ministry of Science, ICT and Future Planning), Korea, under the ITRC (Information Technology Research Center) support program (IITP-2016-H8601-16-1007) supervised by the IITP (Institute for Information and Communications Technology Promotion).

## SUPPLEMENTARY MATERIAL

The Supplementary Material for this article can be found online at: <http://journal.frontiersin.org/article/10.3389/fpls.2016.01321>

**Figure S1 | Change in CO<sub>2</sub> concentration in the closed chamber without plant for 9 h.**

## REFERENCES

- Anten, N. P. R., and During, H. J. (2011). Is analyzing the nitrogen use at the plant canopy level a matter of choosing the right optimization criterion? *Oecologia* 16, 293–303. doi: 10.1007/s00442-011-2011-3
- Bellasio, C., Beerling, D. J., and Griffiths, H. (2016). An Excel tool for deriving key photosynthetic parameters from combined gas exchange and chlorophyll fluorescence: theory and practice. *Plant Cell Environ.* 39, 1180–1197. doi: 10.1111/pce.12560
- Buck-Sorlin, G., de Visser, P. H. B., Henke, M., Sarlikioti, V., van der Heijden, G. W. A. M., Marcelis, L. F. M., et al. (2011). Towards a functional-structural plant model of cut-rose: simulation of light environment, light absorption, photosynthesis and interference with the plant structure. *Ann. Bot.* 108, 1121–1134. doi: 10.1093/aob/mcr190
- Caldwell, M. M., Meister, H. P., Tenhunen, J. D., and Lange, O. L. (1986). Canopy structure, light microclimate and leaf gas exchange of *Quercus coccifera* L. in a Portuguese macchia: measurements in different canopy layers and simulations with a canopy model. *Trees* 1, 25–41. doi: 10.1007/BF00197022
- Chen, J. M., Liu, J., Cihlar, J., and Goulden, M. L. (1999). Daily canopy photosynthesis model through temporal and spatial scaling for remote sensing applications. *Ecol. Model.* 124, 99–119. doi: 10.1016/S0304-3800(99)00156-8
- Chen, T. W., Henke, M., de Visser, P. H. B., Buck-Sorlin, G., Wiechers, D., Kahlen, K., et al. (2014a). What is the most prominent factor limiting photosynthesis in different layers of a greenhouse cucumber canopy? *Ann. Bot.* 114, 677–688. doi: 10.1093/aob/mcu100
- Chen, T. W., Nguyen, T. M., Kahlen, K., and Stützel, H. (2015). High temperature and vapor pressure deficit aggravate architectural effects but ameliorate non-architectural effects of salinity on dry mass production of tomato. *Front. Plant Sci.* 6:887. doi: 10.3389/fpls.2015.00887
- Chen, T. W., Nguyen, T. M. N., Kahlen, K., and Stützel, H. (2014b). Quantification of the effects of architectural traits on dry mass production and light interception of tomato canopy under different temperature regimes using a dynamic functional-structural plant model. *J. Exp. Bot.* 65, 6399–6410. doi: 10.1093/jxb/eru136
- de Pury, D. G. G., and Farquhar, G. D. (1997). Simple scaling of photosynthesis from leaves to canopies without the errors of big-leaf models. *Plant Cell Environ.* 20, 537–557. doi: 10.1111/j.1365-3040.1997.00094.x
- der Zande, D. V., Struckens, J., Verstraeten, W. W., Mereu, S., Muys, B., and Coppin, P. (2011). 3D modeling of light interception in heterogeneous forest canopies using ground-based LiDAR data. *Int. J. Appl. Earth Observ. Geoinf.* 13, 792–800. doi: 10.1016/j.jag.2011.05.005
- de Visser, P. H., Buck-Sorlin, G. H., and Van Der Heijden, G. W. (2014). Optimizing illumination in the greenhouse using a 3D model of tomato and a ray tracer. *Front. Plant Sci.* 5:48. doi: 10.3389/fpls.2014.00048
- Dreccer, M. F., Oijen, M. V., Schapendonk, A. H. C. M., Pot, C. S., and Rabbinge, R. (2000). Dynamics of vertical leaf nitrogen distribution in a vegetative wheat canopy, impact on canopy photosynthesis. *Ann. Bot.* 86, 821–831. doi: 10.1006/anbo.2000.1244
- Elifis, P., Kratochvilová, I., Janous, D., Marek, M., and Masarovcová, E. (1989). Stand microclimate and physiological activity of tree leaves in an oak-hornbeam forest I. Stand microclimate. *Trees* 4, 227–233.
- Ellsworth, D. S., and Reich, P. B. (1993). Canopy structure and vertical patterns of photosynthesis and related leaf traits in a deciduous forest. *Oecologia* 96, 169–178. doi: 10.1007/BF00317729
- Escudero, A., and Mediavilla, S. (2003). Decline in photosynthetic nitrogen use efficiency with leaf age and nitrogen resorption as determinants of leaf life span. *J. Ecol.* 91, 880–889. doi: 10.1046/j.1365-2745.2003.00818.x
- Farquhar, G. V., von Caemmerer, S. V., and Berry, J. A. (1980). A biochemical model of photosynthetic CO<sub>2</sub> assimilation in leaves of C3 species. *Planta* 149, 78–90. doi: 10.1007/BF00386231
- Field, C. (1983). Allocating leaf nitrogen for the maximization of carbon gain: leaf age as a control on the allocation program. *Oecologia* 56, 341–347. doi: 10.1007/BF00379710
- Garcia, R. L., Norman, J. M., and Mcdermitt, D. K. (1990). Measurements of canopy gas exchange using an open chamber system. *Remote Sens. Rev.* 5, 141–162. doi: 10.1080/02757259009532126
- Gonzalez-Real, M. M., and Baille, A. (2000). Changes in leaf photosynthetic parameters with leaf position and nitrogen content within a rose plant canopy (*Rosa hybrid*). *Plant Cell Environ.* 23, 351–363. doi: 10.1046/j.1365-3040.2000.00559.x
- Hikosaka, K. (2014). Optimal nitrogen distribution within a leaf canopy under direct and diffuse light. *Plant Cell Environ.* 37, 2077–2085. doi: 10.1111/pce.12291
- Hirose, T., and Werger, M. J. A. (1987). Maximizing daily canopy photosynthesis with respect to the leaf nitrogen allocation pattern in the canopy. *Oecologia* 72, 520–526. doi: 10.1007/BF00378977
- Iio, A., Fukasawa, H., Nose, Y., Kato, S., and Kakubari, Y. (2005). Vertical, horizontal and azimuthal variations in leaf photosynthetic characteristics within a *Fagus crenata* crown in relation to light acclimation. *Tree Physiol.* 25, 533–544. doi: 10.1093/treephys/25.5.533
- Irving, L. J., and Robinson, D. (2006). A dynamic model of Rubisco turnover in cereal leaves. *New Phytol.* 169, 493–504. doi: 10.1111/j.1469-8137.2005.01584.x
- Johnson, I. R., Thornley, J. H. M., Frantz, J. M., and Bugbee, B. (2010). A model of canopy photosynthesis incorporating protein distribution through the canopy and its acclimation to light, temperature and CO<sub>2</sub>. *Ann. Bot.* 106, 735–749. doi: 10.1093/aob/mcq183

- Jovicich, E., Cantliffe, D. J., and Stoffella, P. J. (2004). Fruit yield and quality of greenhouse-grown bell pepper as influenced by density, container, and trellis system. *HortTechnology* 14, 507–513.
- Kang, W. H., Zhang, F., Lee, J. W., and Son, J. E. (2016). Improvement of canopy light distribution, photosynthesis, and growth of lettuce (*Lactuca Sativa L.*) in plant factory conditions by using filters to diffuse light from LEDs. *Korean J. Hortic. Sci. Technol.* 34, 84–93. doi: 10.12972/kjhst.20160015
- Kim, H. S., Palmroth, S., Thérezién, M., Stenberg, P., and Oren, R. (2010). Analysis of the sensitivity of absorbed light and incident light profile to various canopy architecture and stand conditions. *Tree Physiol.* 31, 30–47. doi: 10.1093/treephys/tpq098
- Kim, S. H., and Lieth, J. H. (2003). A coupled model of photosynthesis, stomatal conductance and transpiration for a rose leaf (*Rosa hybrida L.*). *Ann. Bot.* 91, 771–781. doi: 10.1093/aob/mcg080
- Kjeldahl, J. (1883). A new method for the determination of nitrogen in organic matter. *Z. Anal. Chem.* 22, 366–382. doi: 10.1007/BF01338151
- Lieth, J. H., and Pasian, C. C. (1990). A model of net photosynthesis of rose leaves as a function of photosynthetically active radiation, leaf temperature, and leaf age. *J. Amer. Soc. Hort. Sci.* 115, 486–491.
- Mabrouk, H., Sinoquet, H., and Carboneau, A. (1997). Canopy structure and radiation regime in grapevine. II. Modeling radiation interception and distribution inside the canopy. *Vitis* 36, 125–132.
- Monsi, M., and Saeki, T. (1953). The light factor in plant communities and its significance for dry matter production. *J. Bot.* 14, 22–52.
- Monteith, J. L. (1965). Light distribution and photosynthesis in field crops. *Ann. Bot.* 29, 17–37.
- Norman, J. M. (1980). Interfacing leaf and canopy light interception models in predicting photosynthesis for ecosystem models. *CRC Press* 2, 49–67.
- Le Roux, X., Sinoquet, H., and Vandame, M. (1998). Spatial distribution of leaf dry weight per area and leaf nitrogen concentration in relation to local radiation regime within an isolated tree crown. *Tree Physiol.* 19, 181–188. doi: 10.1093/treephys/19.3.181
- Sarlikioti, V., de Visser, P. H. B., Buck-Sorlin, G. H., and Marcelis, L. F. M. (2011). How plant architecture affects light absorption and photosynthesis in tomato: towards an ideotype for plant architecture using a functional-structural plant model. *Ann. Bot.* 108, 1065–1073. doi: 10.1093/aob/mcr221
- Schieving, F., Pons, T. L., Werger, M. J. A., and Hirose, T. (1992). The vertical distribution of nitrogen and photosynthetic activity at different plant densities in *Carex acutiformis*. *Plant Soil* 14, 9–17.
- Sharkey, T. D., Bernacchi, C. J., Farquhar, G. D., and Singsaas, E. L. (2007). Fitting photosynthetic carbon dioxide response curves for C3 leaves. *Plant Cell Environ.* 30, 1035–1040. doi: 10.1111/j.1365-3040.2007.01710.x
- Shin, J. W., Ahn, T. I., and Son, J. E. (2011). Quantitative measurement of carbon dioxide consumption of a whole Paprika plant (*Capsicum annuum L.*) using a large sealed chamber. *Korean J. Hortic. Sci. Technol.* 29, 211–216.
- Stirling, C. M., Aguilera, C., Baker, N. R., and Long, S. P. (1994). Changes in the photosynthetic light response curve during leaf development of field grown maize with implications for modelling canopy photosynthesis. *Photosyn. Res.* 42, 217–225. doi: 10.1007/BF00018264
- Tai, N. G., Hung, T. T., Ahn, T. I., Park, J. S., and Son, J. E. (2009). Estimation of leaf area, fresh weight, and dry weight of Paprika (*Capsicum annuum L.*) using leaf length and width in rockwool-based soilless culture. *Hortic. Environ. Biotechnol.* 50, 422–426.
- Tang, L., Hou, C., Huang, H., Chen, C., Zou, J., and Lin, D. (2015). Light interception efficiency analysis based on three-dimensional peach canopy models. *Ecol. Inform.* 30, 60–67. doi: 10.1016/j.ecoinf.2015.09.012
- Thornley, J. H. M. (2002). Instantaneous canopy photosynthesis: analytical expressions for sun and shade leaves based on exponential light decay down the canopy and an acclimated non-rectangular hyperbola for leaf photosynthesis. *Ann. Bot.* 89, 451–458. doi: 10.1093/aob/mcf071
- Yin, X., and Struijk, P. C. (2009). C3 and C4 photosynthesis models: An overview from the perspective of crop modelling. *NJAS Wageningen J. Life Sci.* 57, 27–38. doi: 10.1016/j.njas.2009.07.001
- Zhu, X. G., Song, Q., and Ort, D. R. (2012). Elements of a dynamic systems model of canopy photosynthesis. *Curr. Opin. Plant Biol.* 15, 237–244. doi: 10.1016/j.pbi.2012.01.010

**Conflict of Interest Statement:** The authors declare that the research was conducted in the absence of any commercial or financial relationships that could be construed as a potential conflict of interest.

Copyright © 2016 Kim, Lee, Ahn, Shin, Park and Son. This is an open-access article distributed under the terms of the Creative Commons Attribution License (CC BY). The use, distribution or reproduction in other forums is permitted, provided the original author(s) or licensor are credited and that the original publication in this journal is cited, in accordance with accepted academic practice. No use, distribution or reproduction is permitted which does not comply with these terms.



# Deploying Fourier Coefficients to Unravel Soybean Canopy Diversity

Talukder Z. Jubery<sup>1</sup>, Johnathon Shook<sup>2</sup>, Kyle Parmley<sup>2</sup>, Jiaoping Zhang<sup>2</sup>, Hsiang S. Naik<sup>1</sup>, Race Higgins<sup>2</sup>, Soumik Sarkar<sup>1</sup>, Arti Singh<sup>2</sup>, Asheesh K. Singh<sup>2\*</sup> and Baskar Ganapathysubramanian<sup>1, 3, 4\*</sup>

<sup>1</sup> Department of Mechanical Engineering, Iowa State University, Ames, IA, USA, <sup>2</sup> Department of Agronomy, Iowa State University, Ames, IA, USA, <sup>3</sup> Department of Electrical and Computer Engineering, Iowa State University, Ames, IA, USA, <sup>4</sup> Plant Sciences Institute, Iowa State University, Ames, IA, USA

## OPEN ACCESS

### Edited by:

Daniel H. Chitwood,  
Donald Danforth Plant Science Center,  
USA

### Reviewed by:

Carmelo Fruciano,  
Queensland University of Technology,  
Australia  
Mao Li,  
Donald Danforth Plant Science Center,  
USA

### \*Correspondence:

Asheesh K. Singh  
singhak@iastate.edu  
Baskar Ganapathysubramanian  
baskarg@iastate.edu

### Specialty section:

This article was submitted to  
Plant Biophysics and Modeling,  
a section of the journal  
*Frontiers in Plant Science*

Received: 07 October 2016

Accepted: 26 December 2016

Published: 19 January 2017

### Citation:

Jubery TZ, Shook J, Parmley K, Zhang J, Naik HS, Higgins R, Sarkar S, Singh A, Singh AK and Ganapathysubramanian B (2017) Deploying Fourier Coefficients to Unravel Soybean Canopy Diversity. *Front. Plant Sci.* 7:2066.  
doi: 10.3389/fpls.2016.02066

Soybean canopy outline is an important trait used to understand light interception ability, canopy closure rates, row spacing response, which in turn affects crop growth and yield, and directly impacts weed species germination and emergence. In this manuscript, we utilize a methodology that constructs geometric measures of the soybean canopy outline from digital images of canopies, allowing visualization of the genetic diversity as well as a rigorous quantification of shape parameters. Our choice of data analysis approach is partially dictated by the need to efficiently store and analyze large datasets, especially in the context of planned high-throughput phenotyping experiments to capture time evolution of canopy outline which will produce very large datasets. Using the Elliptical Fourier Transformation (EFT) and Fourier Descriptors (EFD), canopy outlines of 446 soybean plant introduction (PI) lines from 25 different countries exhibiting a wide variety of maturity, seed weight, and stem termination were investigated in a field experiment planted as a randomized complete block design with up to four replications. Canopy outlines were extracted from digital images, and subsequently chain coded, and expanded into a shape spectrum by obtaining the Fourier coefficients/descriptors. These coefficients successfully reconstruct the canopy outline, and were used to measure traditional morphometric traits. Highest phenotypic diversity was observed for roundness, while solidity showed the lowest diversity across all countries. Some PI lines had extraordinary shape diversity in solidity. For interpretation and visualization of the complexity in shape, Principal Component Analysis (PCA) was performed on the EFD. PI lines were grouped in terms of origins, maturity index, seed weight, and stem termination index. No significant pattern or similarity was observed among the groups; although interestingly when genetic marker data was used for the PCA, patterns similar to canopy outline traits was observed for origins, and maturity indexes. These results indicate the usefulness of EFT method for reconstruction and study of canopy morphometric traits, and provides opportunities for data reduction of large images for ease in future use.

**Keywords:** canopy outline, elliptic Fourier, diversity panel, image processing

## INTRODUCTION

Soybean [*Glycine max* (L.) Merr.] is a leguminous plant and an important source of protein and oil for a wide range of end users across the world. Given the recent rate of climatic change and predictions for worsening environmental conditions, coupled with a growing global population (O'Neill et al., 2010), breeders are pressed to meet multi-objective requirements (increasing yield, decreasing resource requirement, increasing stress resiliency) during breeding. A promising approach to breeding involves rapid and accurate screening of a large number of plots under various conditions, in order to identify genotypes that maximize production potential under specific or broad environments and allow mapping the genes conditioning adaptation to varying stresses.

A critical aspect to this approach is accurate measurement of traits important to key physiological processes of the plant, which will enable breeders to evaluate and select from the pool of genetic diversity. It also follows that starting from a large, diverse pool of genetic diversity is important to efficiently attain these multi-objective requirements. It is imperative to note that the amount of genetic diversity used in modern soybean breeding is severely limited (Gizlice et al., 1994); therefore, the potential for finding useful alleles for traits of interest is very high by looking at the larger collection of soybean diversity. However, to characterize the genetic diversity present in germplasm, methods that are amenable to high throughput as well as automated applications are required. This is because quantifying traits manually/visually is difficult (especially when considering large, diverse planting populations), and is often done with high error or user bias. High throughout phenotyping along with computer vision has enabled a revolution in crop phenotype collection to reduce reliance on visual ratings while improving accuracy (Singh et al., 2016). Image based phenotyping allows the collection of plant and canopy morphological traits on spatial and temporal scales enabling the monitoring of physiological development and to quantify abiotic and biotic stresses (Pauli et al., 2016).

In this context, our focus is on evaluating the soybean canopy outline. Yield potential is a function of products of incident solar radiation, conversion, and partitioning efficiencies, and linear improvements have been observed in each of the three efficiencies (Koester et al., 2014). For continued yield increase these three efficiencies need to be increased, therefore, necessitating continued research on canopy traits. Canopy outline is important to evaluate light interception ability. Light interception, measured as a function of ground surface area shaded by at least one leaf, directly factors in to the yield potential equation (Koester et al., 2014). Canopy closure rates will affect the light interception rate of soybean by capturing incident sunlight sooner over a greater area. Increased canopy closure rates also have secondary effects by inhibiting weed species germination and emergence, which may provide a source of protection against difficult to control weeds (Harder et al., 2007; Evers and Bastiaans, 2016). We therefore, focus on traits that quantify soybean canopy outline and structure that are important to evaluate differences in light interception ability, canopy closure rates, and row spacing response. To analyze the canopy outline,

generally, digital image of a canopy is captured by high resolution cameras. Traditional morphometric traits including aspect ratio, roundness, circularity, and solidity (Olson, 2011; Chitwood et al., 2014a), while useful are not sufficient to capture the complexity of shapes, especially when considering shape evolution. In this manuscript, we utilize a methodology [based on Elliptic Fourier descriptors (EFD)] that provides reduction in data, enables visualization of diversity and results in a rigorous quantification of shape. The EFD has been used in various studies in past for plant species identification (Neto et al., 2006), tomato leaf shape (Chitwood et al., 2014a), leaf shape and venation (Chitwood et al., 2014b), flower petal shape (Iwata and Ukai, 2002; Yoshioka et al., 2004) and soybean pod diversity (Truong et al., 2005). In the present study EFD is used for soybean canopy outline diversity analysis.

We collected canopy images in a replicated field experiment using 446 soybean PI lines acquired from the USDA soybean germplasm collection. This is a very diverse set of germplasm, from over 25 different countries exhibiting a wide variety of maturity, seed weight, and stem termination. Digital images of the canopy were available for analysis, which were taken using a standard imaging protocol (Zhang et al., submitted). The images produced 8 GB of data. We deployed the analysis framework to reduce the useful storage size required while retaining information related with canopy outline, and evaluate shape descriptors/trait to investigate shape diversity among the lines. This paper represents the first stage of our analysis program. After evaluating and quantifying the shape diversity exhibited by this set of lines, we envision (in subsequent work) utilizing this framework to analyze and evaluate time-dependent geometric canopy traits to isolate genetic pathways that control various stress adaptation mechanisms.

## MATERIALS AND METHODS

### Plant Material, Field Phenotyping and Data Acquisition

A total of 446 soybean PI lines from 25 different countries acquired from the USDA soybean germplasm collection, grown near Ames, IA, in 2015, were used for this study (Figure 1). These lines also differ from one another in terms of maturity, seed weight, and stem termination. The field experiment was organized as a randomized complete block design with four replications. The germplasm accessions were planted in hill plots of five seeds per plot at one foot between plots and two feet between rows. The images were taken at 2 weeks after second trifoliolate leaf stage using a Canon EOS REBEL T5i camera with the Scene Intelligent Auto model. All images were stored in RAW image quality. An umbrella was always used to shade the area under the camera view, and the flash function was kept off to maintain consistent illumination. Also, at the beginning of imaging operations and every 20 min thereafter or whenever the light condition changed (e.g., cloud cover), a picture of the X-Rite Color Checker Color Rendition Chart was taken to calibrate the illumination and the color of canopy image. Whenever possible, weeds and other plant residuals, connected

to the plant canopy in the view of camera, were removed for easy image processing and enhanced efficiency of subsequent image processing. After checking for quality of image (removing images that did not follow the imaging protocol, that exhibited disease symptoms or that did not have an intact canopy), around 1200 images were used for subsequent analysis. The single nucleotide polymorphism (SNP) dataset for the panel was prepared in a previous study (Song et al., 2013) and was acquired from the SoyBase site (<http://soybase.org/>).

## Image Data Processing

First, each image was segmented. Then they were converted from native RGB to hue-saturation-value format to efficiently segment the foreground (the plant) from the background. The background of an image (soil) contains more gray pixels than the foreground (plant) and lacks in green and yellow hue values; therefore, most of the background was removed by excluding pixels that had a saturation value below a predefined threshold and hue values outside of a predefined range. The saturation threshold value was obtained by identifying the saturation values of the background in 148 diverse images. The hue range was simply obtained from the hue color wheel, removing pixels that were neither green nor brown.

Once segmentation was done, the connected components labeling method (Suzuki et al., 2003; Gonzales and Woods, 2008; Wodo et al., 2012; Samudrala et al., 2013; Pace et al., 2014) was used on the processed image to remove spurious outliers and noise from the image (e.g., plant debris on soil). This was accomplished by identifying clusters of pixels that connected to one another, followed by labeling them, and identifying the largest connected component (i.e., plants in a plot). Cleaning was done by removing any other connected components that contained fewer pixels than the largest connected component. Then, a mask of the isolated plant was applied to the binary image. In contrast to other commonly used thresholding

methods (Otsu, 1975; Browning and Browning, 2009; Lee et al., 2016; Naik et al., submitted), no significant pixel loss was observed.

Next, contour/outline of canopy was defined from the locations of boundary pixels of the image. Any empty space inside the canopy was filled, and the outline of the canopy was obtained from the filled binary image. The extracted outline of the canopy was represented as a sequence of x and y coordinates of boundary pixels (see Figure 2 for a schematic of the operation).

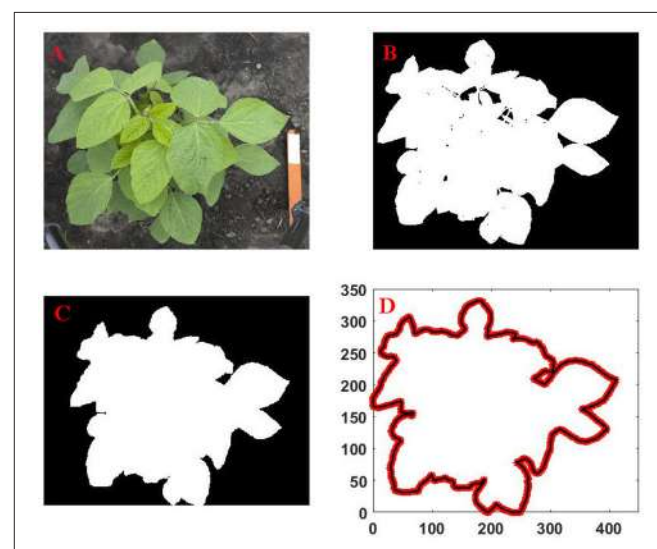


**FIGURE 2 | Sequence of the canopy outline extraction process from an image captured by digital camera:** (A) original image; (B) cleanup, segmentation and conversion of the RGB image to binary image; (C) filling of empty spaces inside the binary image; (D) extraction of outline from the filled image.

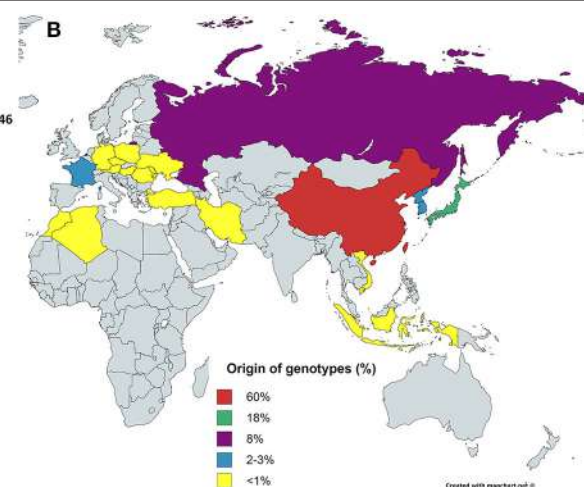
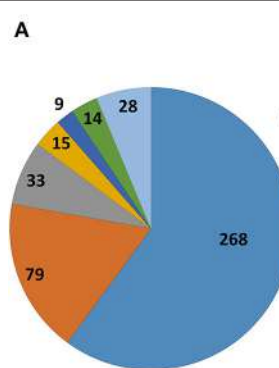


**FIGURE 1 | Origins of the lines.** (A) Shows the distribution of the 446 lines/genotypes based on origins, collected from USDA soybean line collection. China and Japan are the highest contributors in the selected collection. (B) Shows the origins in terms of percentage contribution from different countries. Yellow shows countries with <1% contribution, i.e., four genotypes or less.

The MATLAB image processing toolbox was used for all image data processing operations.

## Geometric and Shape Descriptors Details

Both traditional and EFD are utilized for subsequent analysis. The traditional shape descriptors/traits, including aspect ratio, roundness, circularity, and solidity are defined as follows:

- aspect ratio = the ratio of the major to minor axis of the best-fitted ellipse on the canopy;
- roundness =  $4 \frac{\text{Area}}{\pi (\text{Major axis})^2}$ ; it indicates closeness of the shape of the canopy to a circle;
- circularity =  $4\pi \frac{\text{Area}}{(\text{Perimeter})^2}$ ; it indicates closeness of the form of the canopy to a circle;
- solidity =  $\frac{\text{Area}}{\text{Convex Area}}$ .

For EFD, the extracted outline was chain coded and expanded into a shape spectrum by obtaining the Fourier coefficients. Summations of the harmonics of the resulting series approximate the outline of the original shape. Each harmonic was represented by four set of Fourier coefficients. The coefficients are descriptors of the shape of the canopy outline/contour. Finally, the descriptors were made invariant of shape, rotation and starting-point of the contour by standardization (Kuhl and Giardina, 1982).

Each contour was chain coded following standard practice (Freeman, 1974). Then linear interpolation was used to represent contour between the two chain-coded points [e.g.,  $(i-1)^{\text{th}}$  and  $i^{\text{th}}$ ]. The x and y coordinates of any point,  $p^{\text{th}}$ , were expressed as

$$x_p = \sum_{i=1}^p \Delta x_i \text{ and } y_p = \sum_{i=1}^p \Delta y_i \quad (1)$$

where  $\Delta x_i$  and  $\Delta y_i$  are the differences along the x and y axes between the  $(i-1)^{\text{th}}$  and the  $i^{\text{th}}$  points.

The length of the contour from the starting point to the  $p^{\text{th}}$  point and the perimeter of the contour are denoted by  $t_p$  and  $T$ , respectively.

$$t_p = \sum_{i=1}^p \Delta t_i \text{ and } T = t_s \quad (2)$$

where  $\Delta t_i$  is the distance between  $i-1^{\text{th}}$  and  $i^{\text{th}}$  points, and  $s$  is the total number of the chain coded points on the contour.

The co-ordinates in Equation (1) were expressed using elliptic Fourier expansion as

$$x_p = A_0 + \sum_{N=1}^{\infty} \left( a_N \cos \frac{2N\pi t_p}{T} + b_N \sin \frac{2N\pi t_p}{T} \right) \quad (3)$$

and

$$y_p = C_0 + \sum_{N=1}^{\infty} \left( c_N \cos \frac{2N\pi t_p}{T} + d_N \sin \frac{2N\pi t_p}{T} \right) \quad (4)$$

where the coefficients of the  $N^{\text{th}}$  harmonic were

$$a_N = \frac{T}{2N^2\pi^2} \sum_{p=1}^k \frac{\Delta x_p}{\Delta t_p} \left( \cos \frac{2N\pi t_p}{T} - \cos \frac{2N\pi t_{p-1}}{T} \right) \quad (5)$$

$$b_N = \frac{T}{2N^2\pi^2} \sum_{p=1}^k \frac{\Delta x_p}{\Delta t_p} \left( \sin \frac{2N\pi t_p}{T} - \sin \frac{2N\pi t_{p-1}}{T} \right) \quad (6)$$

$$c_N = \frac{T}{2N^2\pi^2} \sum_{p=1}^k \frac{\Delta y_p}{\Delta t_p} \left( \cos \frac{2N\pi t_p}{T} - \cos \frac{2N\pi t_{p-1}}{T} \right) \quad (7)$$

$$d_N = \frac{T}{2N^2\pi^2} \sum_{p=1}^k \frac{\Delta y_p}{\Delta t_p} \left( \sin \frac{2N\pi t_p}{T} - \sin \frac{2N\pi t_{p-1}}{T} \right) \quad (8)$$

For a shape representation using  $N$  harmonics,  $4N$  coefficients were evaluated and were subsequently used as descriptors of the shape. The original shape of canopy outline was reconstructed using inverse Fourier transform from these shape descriptors. The accuracy of the reconstruction depends on the number of harmonics ( $N$ ) used. We defined the deviation of the reconstructed shape from the original as

$$E_N = \frac{\max \left[ \sqrt{(x_p - x_{N_p})^2 + (y_p - y_{N_p})^2} \right]}{2L} \times 100\% \quad (9)$$

where  $x_{N_p}$  and  $y_{N_p}$  are the approximated co-ordinates using  $N$  harmonics, and  $L$  is half of the length of the major axis (semi-major axis) of the best-fitted ellipse to the shape (estimation of  $L$  is presented in the standardized shape descriptors section). As with any approximation scheme, increase in the number of harmonics results in high accuracy of reconstruction, but requires more processing time and storage. We next detail an approach of identification of the optimal number of harmonics to use that represents a balance between accuracy and computational requirement.

## Choice of Number of Harmonic Descriptors

We first identified the most complex canopy (that would require the most number of harmonics to accurately represent) from the set of all available canopies. We then evaluated the optimal number of harmonics,  $N$ , needed to represent this canopy and subsequently utilize this number  $N$  for all other canopy descriptors. This ensures consistency while ensuring that a desired threshold of accuracy is met. **Figure 3** illustrates this idea using a flowchart format.

To identify the most complex canopy, error between outline from each original image and the Fourier approximation using the first ten harmonics of that image was calculated using Equation 9. The canopy with the highest deviation exhibits the most complex shape (and is shown in **Figure 4A**). Harmonic representation of this canopy outline using increasing number of harmonics (from 10 to 1000 in steps of 10) was constructed and the error was computed. **Figure 4B** shows how the error decreases as the number of harmonics used for shape representation is increased. We chose  $N = 500$  as this is where the

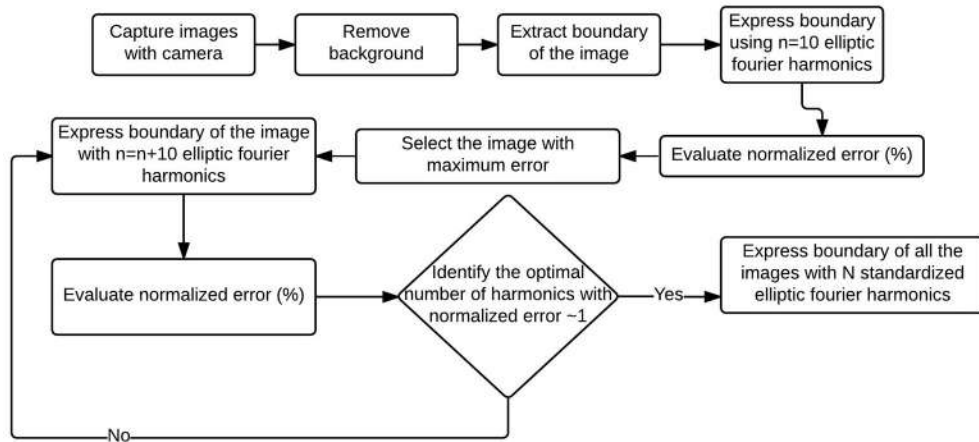


**FIGURE 3 | Flowchart to evaluate EFDs for a set of images.** First canopy outline/boundary from all the images were captured and expressed using 10 elliptic Fourier harmonics. The worst (in terms of deviation from the original outline) reconstructed outline (which is also the most complex outline) from the EFDs was identified. Optimal number of harmonics of the complex outline was identified, and all the outlines were expressed using that optimal number of harmonics.

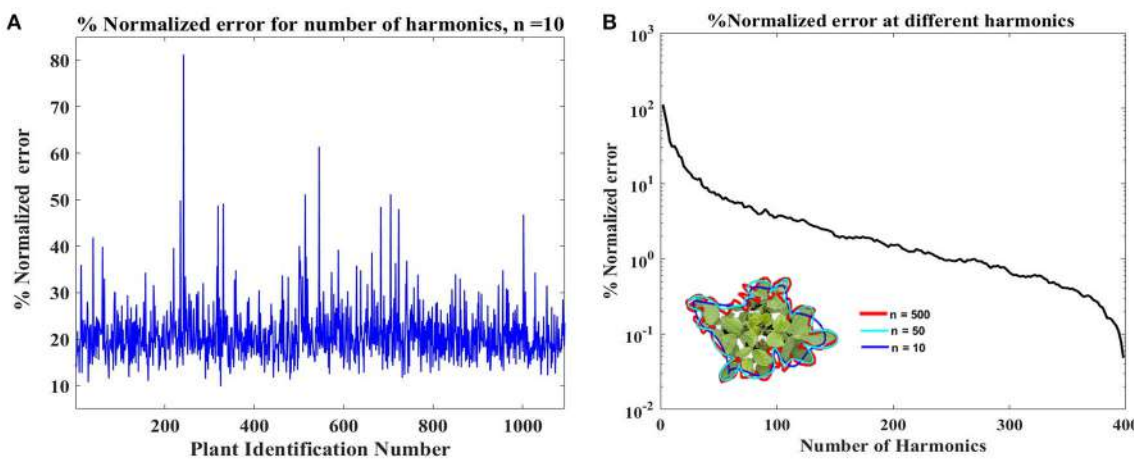


**FIGURE 4 | (A)** Identification of the complex canopy outline in the dataset. The identification was performed by evaluating deviation of the reconstructed outlines using ten harmonics from the original outline (Equation 9). Plant with Id# 246 shows the highest deviation/error and was considered as the most complex canopy outline. **(B)** Identification of optimal harmonics for the plant Id# 246, shown in inset. The % normalized error value reaches near 1% around 500 harmonics, and the inset shows that 500 harmonics (red line) outlines is in good agreement with the original outline. This value, 500, was considered as the optimal number of harmonics.

normalized error reaches around 1%. Thus, each canopy outline is subsequently represented using a 500 harmonic representation.

## Standardized Shape Descriptors

The descriptors were made invariant in size, rotation, shift by standardizing the coefficients (Kuhl and Giardina, 1982), using the size and spatial location on the ellipse represented by the first harmonic. The standardized coefficients are

$$\begin{bmatrix} a_N^* & b_N^* \\ c_N^* & d_N^* \end{bmatrix} = \frac{1}{L} \begin{bmatrix} \cos \psi & \sin \psi \\ -\sin \psi & \cos \psi \end{bmatrix} \begin{bmatrix} a_N & b_N \\ c_N & d_N \end{bmatrix} \begin{bmatrix} \cos N\theta & \sin N\theta \\ -\sin N\theta & \cos N\theta \end{bmatrix} \quad (10)$$

where  $L = \sqrt{(A_0 - x_m)^2 + (C_0 - y_m)^2}$  is half of the length of the major axis of the ellipse from 1st harmonic,  $(A_0, C_0)$  is the center of the ellipse,  $(x_m, y_m)$  is the location of modified starting point (point on the major axis of the ellipse),  $\theta = \frac{2\pi t_m}{T}$  and  $\psi = \tan^{-1} \left[ \frac{y_m - C_0}{x_m - A_0} \right]$ , is the angle between the major axis of the ellipse and x axis. After standardization, three Fourier coefficients became constant ( $a_1^* = 1$ ,  $b_1^* = 0$  and  $c_1^* = 0$ ). An in-house code was developed (using MATLAB) to implement the above methods. This code is available upon request.

## Analysis Procedure

After each canopy outline is represented using 500 Fourier shape descriptors, traditional morphometric traits are evaluated from

the shape. For comparative assessment of the utility of Fourier shape descriptors, the traits obtained from EFD reconstructed canopy outlines are compared with traits obtained from the original images. Diversity of the traits among the lines/genotypes based on the country of origin is investigated. For visualization and interpretation of diversity, PCA on the EFD is next deployed. Data visualization based on the first two principle components is performed with a focus on four classifications including country of origin, maturity index, stem termination index and seed weight. Finally, the canopy descriptors that are suitable for genetic improvement were suggested.

## Trait Heritability Estimate

The model for the phenotypic trait with a single trial of randomized complete block design was  $y_{ik} = \mu + g_i + b_k + e_{ik}$ , where  $y_{ik}$  is the trait observation/estimate of the  $i^{\text{th}}$  genotype at the  $k^{\text{th}}$  block,  $\mu$  is the total mean,  $g_i$  is the genetic effect of the  $i^{\text{th}}$  genotype,  $b_k$  is the block effect, and  $e_{ik}$ , is a random error following  $N(0, \sigma_e^2)$ . Accordingly, the broad-sense heritability on an entry-mean basis of each trait was calculated as  $H^2 = \sigma_g^2 / [\sigma_g^2 + \sigma_e^2/k]$ , where  $\sigma_g^2$  is the genotypic variance,  $k$  is the number of replications. The analysis of variance was implemented in R via the ANOVA function. The variance components were calculated with all effects considered to be random.

## RESULTS AND DISCUSSION

### Traditional Morphometric Traits Evaluation and Their Fidelity

The accuracy of reconstruction was checked by comparing traits obtained from original images and traits evaluated from the reconstructed outlines using 500 harmonics. **Figure 5** shows excellent agreement with the traits evaluated from original images and reconstructed outlines. In our study, data size of an image captured by camera is  $\sim 15$  MB (RAW format), and size of the 500 harmonics used for reconstruction is  $\sim 5$  kB. In other words, EFD requires *two orders of magnitude* less memory with minimal computational overhead to evaluate traditional traits.

### Shape Diversity Based on the Traditional Traits

To investigate the shape diversity based on the traditional traits, the traits are grouped based the origin of the lines, and presented in box plots (**Figure 6A**). The plots indicate that lines from France have less spread in all the traits. Lines from North Korea have the highest spread in aspect ratio and circularity. In brief, there is considerable variation in traits regardless of country of origin. Roundness has almost three times more spread than the other traits for all countries (**Figure 6B**). Fifty-five individual plants were identified as canopy outline outliers (red "+" symbol in **Figure 6A**). Fifty lines were outliers in only one of the four replications, suggesting that non-genetic factors including differences in growth stage at imaging (such as due to delayed emergence) as well as unequal number of seeds per plot could be

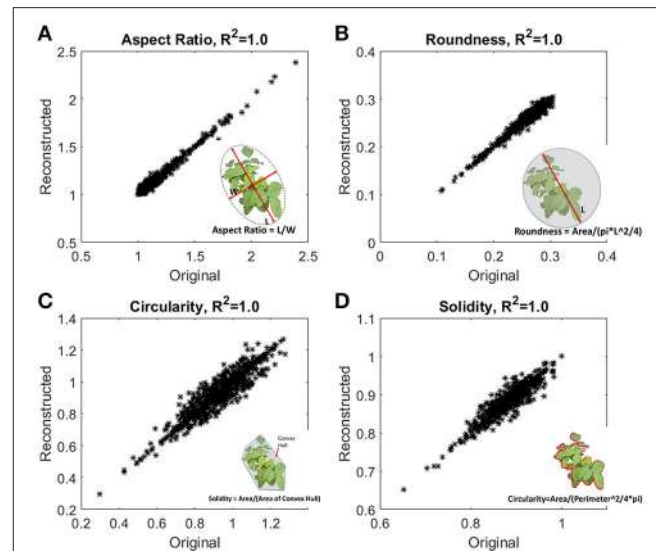


**FIGURE 5 | Fidelity checks of the reconstructed outlines.** Traditional morphometric traits, (A) aspect ratio, (B) roundness, (C) circularity, and (D) solidity were evaluated from the reconstructed outlines, and also from the original images. Inset shows the definition of the traits. Aspect ratio and circularity are related with the shape of the outline, and roundness and solidity are related with the form or area enclosed by the outline.

the causal factors for the observed variation. These fifty plants are removed from the data set for subsequent analysis.

Two lines are outliers for solidity, and occur as outliers in two of three reps (**Figures 6C,D**), i.e., around 67%. Six canopies were outliers for two traits simultaneously. These traits were paired as circularity with either solidity or aspect ratio, with two thirds of the circularity outliers also showing up as outliers for another trait. In spite of this, when comparing trait relationships using the complete data set, the pairings of (1) roundness with solidity, and (2) aspect ratio with circularity were the only two combinations with an  $|r|$  (correlation coefficient)  $> 0.75$ . The genotypes lines with these outliers are strong candidates for extreme variation among canopy traits, and are interesting for additional studies to determine if they may provide unique ideotypes for practical applications. Furthermore, the study of genetic variation in canopy traits on a temporal and spatial scale will require inclusion of diverse germplasm in environments that may differ in latitude, longitude, water and nutrient stresses, planting date, and row spacing, in order to ultimately associate canopy traits with productivity and resiliency.

### Shape Diversity Based on EFDs

We perform principal component analysis (PCA) on the EFD. PCA facilitates dimension reduction of the data set and permits efficient summarization of the information contained by the coefficients. The first 30 principal components express around 90% of the total variability, and first and second components describe, respectively, around 17 and 10% of the total variability. These two components are used in the subsequent sections for diversity visualization and interpretation. **Figure 7** illustrates the first two PCA coefficients, color-coded according to four different

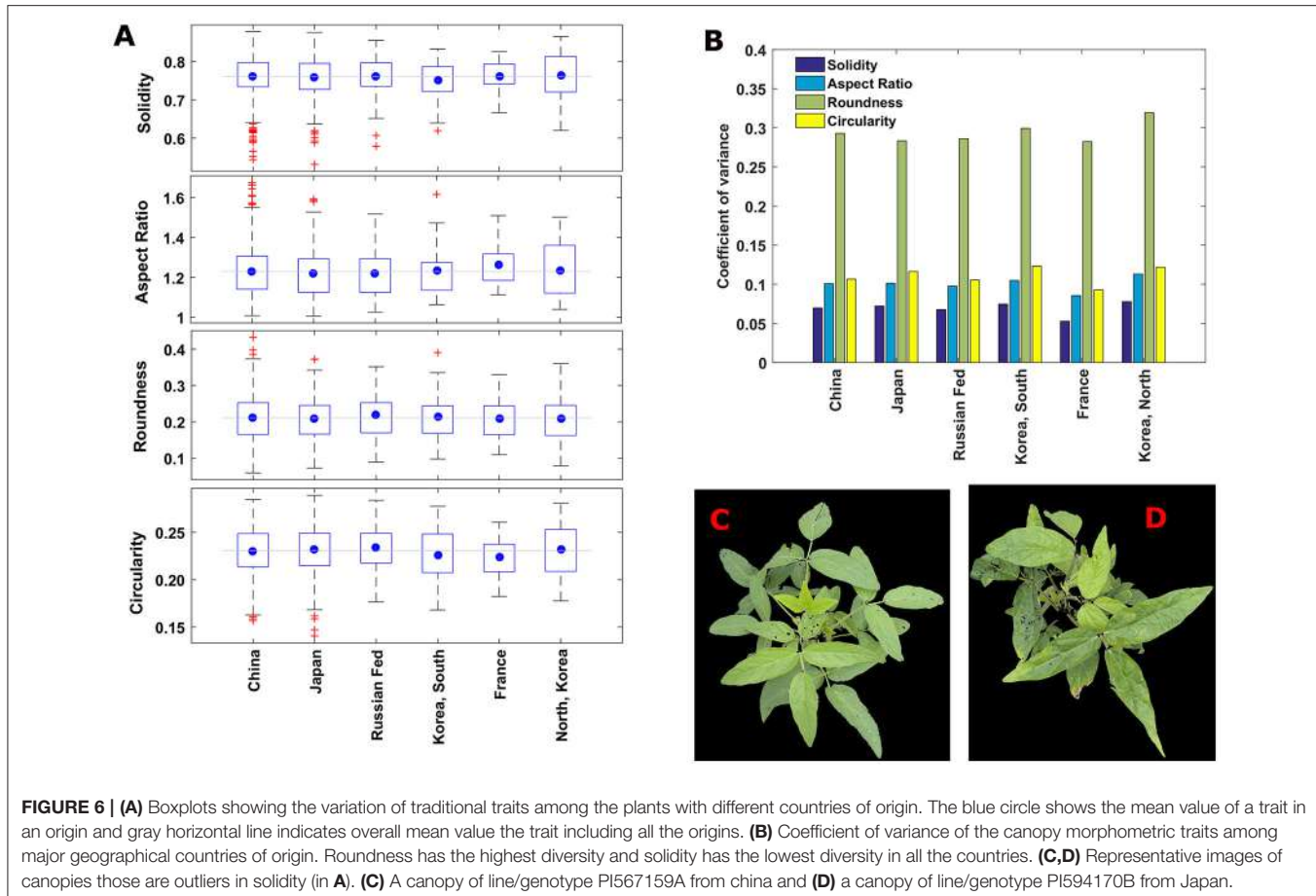


**FIGURE 6 | (A)** Boxplots showing the variation of traditional traits among the plants with different countries of origin. The blue circle shows the mean value of a trait in an origin and gray horizontal line indicates overall mean value of the trait including all the origins. **(B)** Coefficient of variance of the canopy morphometric traits among major geographical countries of origin. Roundness has the highest diversity and solidity has the lowest diversity in all the countries. **(C,D)** Representative images of canopies those are outliers in solidity (in **A**). **(C)** A canopy of line/genotype PI567159A from china and **(D)** a canopy of line/genotype PI594170B from Japan.

classes (**Figure 7A**), country of origin; (**Figure 7B**), maturity index; (**Figure 7C**), stem termination index; and (**Figure 7D**), seed weight.

In **Figure 7A**, lines from China and Japan show the most variation. This is consistent with their status as centers of diversity for the domesticated soybean (Hymowitz and Harlan, 1983; Zhou et al., 2015; Valliyodan et al., 2016). No significant pattern/classification among the countries is observed in the PCs representation in **Figure 7A**. The reconstructed canopy outlines from 30 PCs, did not show significant diversity among the countries of origin (Figure S1). When grouped in terms of maturity indexes (I, II, or III), our results showed that each maturity group has similar variation of canopy outline, and soybean maturity is not correlated with the canopy outline (**Figure 7B**). Likewise, similar results were observed for the PCA using SNP genetic marker when country origin and maturity were used to cluster (Figure S2). One possible explanation to this phenomena was that the panel in this study is a subgroup of the USDA soybean core collection and it was designed to maximize the representative of the diversity of all the germplasm lines of maturity index I, II, and III, (Oliveira et al., 2010; Valliyodan et al., 2016). Based on the stem growth habit, the lines are classified into three major categories: determinate (D), semi-determinate (S) and indeterminate (N). For the determinate soybean cultivars,

the stem elongation stops soon after photoperiod-induced floral transition of the shoot apical meristem (SAM) from vegetative growth to reproductive growth (Bernard, 1972). In contrast, the transition of SAM to reproductive growth is suppressed in indeterminate cultivars and vegetative growth continues until a cessation is caused by the demand of developing seeds (Tian et al., 2010). Therefore, stem growth habit has broad effects on soybean canopy architecture. Although there is no clear border among subpanels of different stem growth habit, we observed a wide variation of canopy outline in semi-determinate soybean germplasm lines followed by determinate and indeterminate subpanels (**Figure 7C**). Also, in this study, these images were taken at relatively early vegetative stages of the plants, and differences in canopy architecture related to stem growth habit is less apparent before reproductive stages. **Figure 7D** indicates that large seeded varieties have significantly less variation in the PC factors, indicating a specific type of ideotype.

## Genetic Control of the Soybean Canopy Outline

Genetic improvement of plant canopy has long been a challenge of soybean genetic improvement programs because of the complexity of the trait and the difficulty of measurement. We

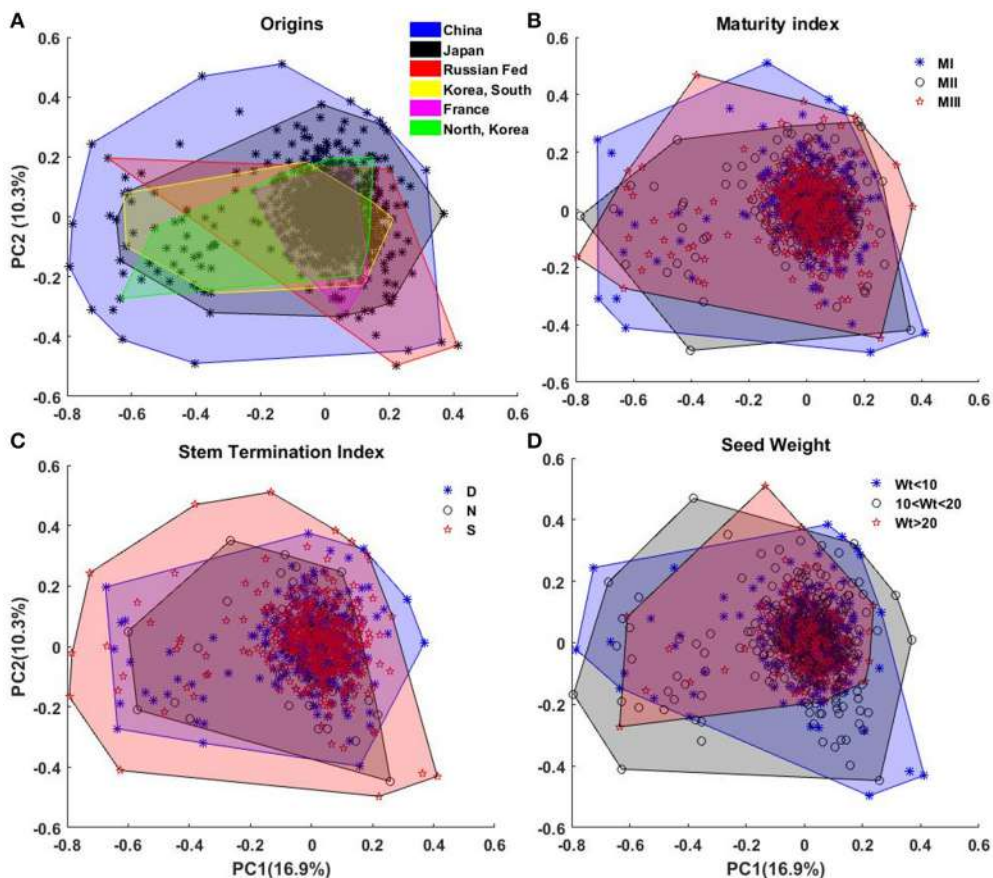


**FIGURE 7 | Representation of the diversity of canopy outline among (A) the origins, (B) maturity index, (C) stem termination index, and (D) weight of 100 seeds (in grams). In (A) the black \* shows all the plants. Areas of different colors represent the diversity. The areas were generated from the convex hull of the plants belonging to a diversity group.**

investigated the genetic effect underlying each of the four shape traits/descriptors. The analysis of variance implied that the genetic effect of all traits, except aspect ratio, were significant (Table 1). Further analysis showed that solidity and roundness have similar, large broad sense heritability, much higher than that of circularity (Table 1). These results suggest that performance of solidity and roundness, rather than aspect ratio and circularity, is predominated by the genetic effects and thus are suitable indexes of soybean canopy improvement. Further dissecting the genetic basis of canopy solidity and roundness will be of great interest.

## CONCLUSIONS

Characterizing and understanding canopy outline variations is important for breeding. This work discusses a framework for efficient representation of complex canopy outlines using EFD. We detail how the choice of the number of harmonics is made to ensure consistency while ensuing a balance with computational effort. We rigorously show that traditional traits/descriptors can be easily, and very accurately reconstructed from the elliptic Fourier representation of the canopy outline. We utilized this

**TABLE 1 | Heritability estimates of the canopy outline descriptors.**

Trait	$F_G^{\dagger}$	Heritability <sup>‡</sup>
Aspect ratio	1.10	0.03
Roundness	3.13***	0.68
Circularity	1.27*	0.22
Solidity	3.46***	0.71

<sup>†</sup> $F_G$  represents the F value for genotypic effects.

<sup>‡</sup>The estimates are based on 154 lines that have 3 replications.

\* $P < 0.05$ , \*\*\* $P < 0.001$ .

framework to explore the diversity in canopy outline using a diverse panel of soybean plants.

In the near term, we envision that this approach will allow for design and utilization of a high throughput canopy morphology phenotyping platform. Such a platform will allow systematic canopy outline analysis while maintaining the integrity of the shape. The use of EFD provides an attractive alternative to conventional canopy phenotypes. Genotypic differences within a species, as well as morphological differences under differing environmental and management conditions, can be characterized

without bias, allowing identification of desirable lines/genotypes, as well as providing a proxy for rapidly measuring important plant canopy and growth traits. The approach presented in our paper may also find applications in the hyperspectral and multispectral imaging of disease and other causal damage that is observable on canopy during the crop growing season (Roschera et al., 2016). We also anticipate that this framework will find utility for time series analysis of the canopy throughout the growing season. Our future work is targeted toward providing biological relevance of these canopy traits to soybean productivity and stress tolerance, and thereby their utilization in genetic enhancement. Finally, we think that the approaches presented in this paper can be translated to investigations on canopy traits in other crops with similar canopy characteristics to soybean.

## AUTHOR CONTRIBUTIONS

TJ, BG, AKS, and AS formulated research problem and designed approaches. AKS and AS directed field efforts and phenotyping. HN, TJ, JZ, and BG developed processing workflow. BG, AKS, SS, TJ, JS, KP, and JZ performed data analytics. All authors contributed to the writing and development of the manuscript.

## REFERENCES

- Bernard, R. (1972). Two genes affecting stem termination in soybeans. *Crop Sci.* 12, 235–239. doi: 10.2135/cropscl1972.0011183X001200020028x
- Browning, B. L., and Browning, S. R. (2009). A unified approach to genotype imputation and haplotype-phase inference for large data sets of trios and unrelated individuals. *Am. J. Hum. Genet.* 84, 210–223. doi: 10.1016/j.ajhg.2009.01.005
- Chitwood, D. H., Ranjan, A., Kumar, R., Ichihashi, Y., Zumstein K., Headland, L. R., et al. (2014a). Resolving distinct genetic regulators of tomato leaf shape within a heteroblastic and ontogenetic context. *Plant Cell* 26, 3616–3629. doi: 10.1105/tpc.114.130112
- Chitwood, D. H., Ranjan, A., Martinez, C. C., Headland, L. R., Thiem, T., Kumar, R., et al. (2014b). A modern ampelography: a genetic basis for leaf shape and venation patterning in grape. *Plant Physiol.* 164, 259–272. doi: 10.1104/pp.113.229708
- Evers, J. B., and Bastiaans, L. (2016). Quantifying the effect of crop spatial arrangement on weed suppression using functional-structural plant modelling. *J. Plant Res.* 129, 339–351. doi: 10.1007/s10265-016-0807-2
- Freeman, H. (1974). Computer processing of line-drawing images. *ACM Comput. Surv.* 6, 57–97. doi: 10.1145/356625.356627
- Gizlice, Z., Carter, T., and Burton, J. W. (1994). Genetic base for North American public soybean cultivars released between 1947 and 1988. *Crop Sci.* 34, 1143–1151. doi: 10.2135/cropscl1994.0011183X003400050001x
- Gonzales, R. C., and Woods, R. E. (2008). *Digital Image Processing*. New Jersey: Pearson Prentice Hall.
- Harder, D. B., Sprague, C. L., and Renner, K. A. (2007). Effect of soybean row width and population on weeds, crop yield, and economic return. *Weed Technol.* 21, 744–752. doi: 10.1614/WT-06-122.1
- Hymowitz, T., and Harlan, J. R. (1983). Introduction of soybean to North America by Samuel Bowen in 1765. *Econ. Bot.* 37, 371–379. doi: 10.1007/BF02904196
- Iwata, H., and Ukai, Y. (2002). SHAPE: a computer program package for quantitative evaluation of biological shapes based on elliptic Fourier descriptors. *J. Hered.* 93, 384–385. doi: 10.1093/jhered/93.5.384
- Koester, R. P., Skoneczka, J. A., Cary, T. R., Diers, B. W., and Ainsworth, E. A. (2014). Historical gains in soybean (*Glycine max* Merr.) seed yield are driven by linear increases in light interception, energy conversion, and partitioning efficiencies. *J. Exp. Bot.* 65, 3311–3321. doi: 10.1093/jxb/eru187
- Kuhl, F. P., and Giardina, C. R. (1982). Elliptic Fourier features of a closed contour. *Comput. Graph. Image Process.* 18, 236–258. doi: 10.1016/0146-664X(82)90034-X
- Lee, N., Chung, Y. S., Srinivasan, S., Schnable, P., and Ganapathysubramanian, B. (2016). “Fast, automated identification of tassels: Bag-of-features, graph algorithms and high throughput computing,” in *International Conference on Knowledge Discovery & Data Mining, The ACM SIGKDD Conference Series* (San Francisco, CA).
- Neto, J. C., Meyer, G. E., Jones, D. D., and Samal, A. K. (2006). Plant species identification using Elliptic Fourier leaf shape analysis. *Comput. Electron. Agric.* 50, 121–134. doi: 10.1016/j.compag.2005.09.004
- Oliveira, M. F., Nelson, R. L., Geraldic, I. O., Cruzd, C. D., and de Toledoa, J. F. F. (2010). Establishing a soybean germplasm core collection. *Field Crops Res.* 119, 277–289. doi: 10.1016/j.fcr.2010.07.021
- Olson, E. (2011). Particle shape factors and their use in image analysis part II: practical applications. *J. GXP Compl.* 15:77.
- O’Neill, B. C., Dalton, M., Fuchs, R., Jiang, L., Pachauri, S., and Zigova, K. (2010). Global demographic trends and future carbon emissions. *Proc. Natl. Acad. Sci. U.S.A.* 107, 17521–17526. doi: 10.1073/pnas.1004581107
- Otsu, N. (1975). A threshold selection method from gray-level histograms. *Automatica* 11, 23–27.
- Pace, J., Lee, N., Naik, H. S., Ganapathysubramanian, B., and Lübbertsd, T. (2014). Analysis of Maize (*Zea mays* L.) seedling roots with the high-throughput image analysis tool ARIA (Automatic Root Image Analysis). *PLoS ONE* 9:e108255. doi: 10.1371/journal.pone.0108255
- Pauli, D., Andrade-Sánchez, P., Carmo-Silva, A. E., Gazave, E., French, A. N., Heun, J., et al. (2016). Field-based high-throughput plant phenotyping reveals the temporal patterns of quantitative trait loci associated with stress-responsive traits in cotton. *G3 (Bethesda)* 6, 865–879. doi: 10.1534/g3.115.023515
- Roschera, R., Behmann, J., Mahlein, A.-K., Dupuis, J., Kuhlmann, H., and Plümer, L. (2016). Detection of disease symptoms on hyperspectral 3D plant models. *ISPRS Ann. Photogramm. Remote Sens. Spatial Inf. Sci.* III-7, 89–96. doi: 10.5194/isprs-annals-III-7-89-2016
- Samudrala, S., Wodola, O., Suramb, S. K., Broderickb, S., Rajanb, K., and Ganapathysubramaniana, B. (2013). A graph-theoretic approach for characterization of precipitates from atom probe tomography data. *Comput. Mater. Sci.* 77, 335–342. doi: 10.1016/j.commatsci.2013.04.038

## FUNDING

Partial funding for this work came from Iowa Soybean Association, ISU Plant Science Institute Faculty Fellow (BG), ISU Presidential Initiative for Interdisciplinary Research (PIIR) in Data Driven Science (DDS) project, Monsanto Chair in Soybean Breeding at ISU (AKS), R F Baker Center for Plant Breeding; USDA CRIS project #IOW04314, and the USDA NIFA grant “A multi-scale data assimilation framework for layered sensing and hierarchical control of disease spread in field crops.”

## ACKNOWLEDGMENTS

Teshale Mamo, Jae Brungardt, Brian Scott for field experimentation. Members of AKS soybean breeding group with imaging, field experimentation.

## SUPPLEMENTARY MATERIAL

The Supplementary Material for this article can be found online at: <http://journal.frontiersin.org/article/10.3389/fpls.2016.02066/full#supplementary-material>

- Singh, A., Ganapathysubramanian, B., Singh, A. K., and Sarkar, S. (2016). Machine learning for high-throughput stress phenotyping in plants. *Trends Plant Sci.* 21, 110–124. doi: 10.1016/j.tplants.2015.10.015
- Song, Q., Hyten, D. L., Jia, G., Quigley, C. V., Fickus, E. W., Nelson, R. L., et al. (2013). Development and evaluation of SoySNP50K, a high-density genotyping array for soybean. *PLoS ONE* 8:e54985. doi: 10.1371/journal.pone.0054985
- Suzuki, K., Horiba, I., and Sugie, N. (2003). Linear-time connected-component labeling based on sequential local operations. *Comput. Vis. Image Understand.* 89, 1–23. doi: 10.1016/S1077-3142(02)00030-9
- Tian, Z., Wang, X., Lee, R., Li, Y., Specht, J. E., Nelson, R. L., et al. (2010). Artificial selection for determinate growth habit in soybean. *Proc. Natl. Acad. Sci. U.S.A.* 107, 8563–8568. doi: 10.1073/pnas.1000088107
- Truong, N. T., Gwag, J.-G., Park, Y.-J., and Lee, S.-H. (2005). Genetic diversity of soybean pod shape based on elliptic Fourier descriptors. *Korean J. Crop Sci.* 50, 60–66.
- Valliyodan, B., Qiu, D., Patil, G., Zeng, P., Huang, J., Dai, L., et al. (2016). Landscape of genomic diversity and trait discovery in soybean. *Sci. Rep.* 6:23598. doi: 10.1038/srep23598
- Wodo, O., Tirthapura, S., Chaudhary, S., and Ganapathysubramanian, B. (2012). Computational characterization of bulk heterojunction nanomorphology. *J. Appl. Phys.* 112, 064316. doi: 10.1063/1.4752864
- Yoshioka, Y., Iwata, H., Ohsawa, R., and Ninomiya, S. (2004). Analysis of petal shape variation of *Primula sieboldii* by elliptic Fourier descriptors and principal component analysis. *Ann. Bot.* 94, 657–664. doi: 10.1093/aob/mch190
- Zhou, Z., Jiang, Y., Wang, Z., Gou, Z., Lyu, J., Li, W., et al. (2015). Resequencing 302 wild and cultivated accessions identifies genes related to domestication and improvement in soybean. *Nat. Biotechnol.* 33, 408–414. doi: 10.1038/nbt.3096

**Conflict of Interest Statement:** The authors declare that the research was conducted in the absence of any commercial or financial relationships that could be construed as a potential conflict of interest.

The reviewer ML and handling Editor declared their shared affiliation, and the handling Editor states that the process nevertheless met the standards of a fair and objective review.

Copyright © 2017 Jubery, Shook, Parmley, Zhang, Naik, Higgins, Sarkar, Singh, Singh and Ganapathysubramanian. This is an open-access article distributed under the terms of the Creative Commons Attribution License (CC BY). The use, distribution or reproduction in other forums is permitted, provided the original author(s) or licensor are credited and that the original publication in this journal is cited, in accordance with accepted academic practice. No use, distribution or reproduction is permitted which does not comply with these terms.



# Mistletoe Berry Outline Mapping with a Path Curve Function and Recording the Circadian Rhythm of Their Phenotypic Shape Change

Renatus Derbridge<sup>1,2\*</sup>, Stephan Baumgartner<sup>1,3</sup> and Peter Heusser<sup>1</sup>

<sup>1</sup> Institute of Integrative Medicine, University of Witten/Herdecke, Witten, Germany, <sup>2</sup> Research Institute at the Goetheanum, Science Section, Dornach, Switzerland, <sup>3</sup> Hiscia Institute, Society for Cancer Research, Arlesheim, Switzerland

## OPEN ACCESS

### Edited by:

Alexander Bucksch,  
University of Georgia, USA

### Reviewed by:

Eetu Puttonen,  
National Land Survey of Finland,  
Finland

Ernst Rudolf Zuercher,  
Bern University of Applied Sciences,  
Switzerland

### \*Correspondence:

Renatus Derbridge  
renatus.derbridge@goetheanum.ch

### Specialty section:

This article was submitted to  
Plant Biophysics and Modeling,  
a section of the journal  
*Frontiers in Plant Science*

Received: 16 June 2016

Accepted: 07 November 2016

Published: 25 November 2016

### Citation:

Derbridge R, Baumgartner S and Heusser P (2016) Mistletoe Berry Outline Mapping with a Path Curve Function and Recording the Circadian Rhythm of Their Phenotypic Shape Change. *Front. Plant Sci.* 7:1749.  
doi: 10.3389/fpls.2016.01749

This paper presents a discovery: the change of the outline shape of mistletoe (*Viscum album* ssp. *album*) berries *in vivo* and *in situ* during ripening. It was found that a plant organ that is usually considered to merely increase in size actually changes shape in a specific rhythmic fashion. We introduce a new approach to chronobiological research on a macro-phenotypic scale to trace changes over long periods of time (with a resolution from hours to months) by using a dynamic form-determining parameter called Lambda ( $\lambda$ ).  $\lambda$  is known in projective geometry as a measure for pertinent features of the outline shapes of egg-like forms, so called path curves. Ascertained circadian changes of form were analyzed for their correlation with environmental factors such as light, temperature, and other weather influences. Certain weather conditions such as sky cover, i.e., sunshine minutes per hour, have an impact on the amplitude of the daily change in form. The present paper suggests a possible supplement to established methods in chronobiology, as in this case the dynamic of form-change becomes a measurable feature, displaying a convincing accordance between mathematical rule and plant shape.

**Keywords:** mistletoe, plant movement, circadian rhythm, change of shape, shape mapping, form and function, phenotypic study

## INTRODUCTION

In the present research project we were interested in analyzing the form or shape of a plant organ *in vivo* and *in situ* and recording how it changes over time. The main focus in recent biology is on phenomena on a cellular and genetic level. To our thinking the link between biological forms on a phenotypic level with chronobiological findings deserves more attention, since form and shapes of biological organs are such apparent and pertinent features. We applied mathematical functions to the outline shape of mistletoe berries (*Viscum album* ssp. *album* L.). These so-called “path curves” accord accurately with the shape of mistletoe berries (Flückiger and Baumgartner, 2003; Baumgartner et al., 2004). Furthermore, path curves are suited to revealing even small phenotypic changes and rhythms of form. A parameter called Lambda ( $\lambda$ ) defines the outline shape of path curves (Edwards, 2003; Klein, 2006, 2013; Derbridge et al., 2013).  $\lambda$  allows exact determination of the form derived from the profiles of the plant organs in question.

Our work is related to the research of the Scottish mathematician Edwards (1912–2004). For decades he measured the form of plant leaf buds, in particular those of trees during dormancy. He observed a fortnightly change of shape in almost all species, discovering that winter dormancy is not a static state, but that it also exhibits rhythmical phenomena (Clopper, 1994; Edwards, 2006). We refined his method to meet the needs and standards of current science by developing corresponding software (Derbridge et al., 2013).

In a previous publication we described the mathematical background of the path curves applied for fitting berry outlines, the software developed and the technical intra- and interrater variability to determine the shape-defining parameter  $\lambda$  (Derbridge et al., 2013). The present publication focuses on the non-mathematical methods applied in this study (mostly technical procedures for outdoor photography) and furthermore presents detailed results of four independent data sets (from four consecutive years) to identify any circadian rhythms present and to investigate the biological variability over 4 years. In this context, a possible modulation by weather effects is analyzed. The detected circadian rhythm seems to be independent from temperature but triggered by the condition of sky cloudiness, i.e., blue sky or cloud cover.

Developing a method to trace phenotypic changes in outline shape introduces a new approach to chronobiology, whereby rhythms in morphological change can be detected. In this way, a salient biological feature can be mapped in a non-invasively phenotypic way.

## MATERIALS AND METHODS

In separate sections below, we describe the sequence of steps involved in the study: observations of the living, untouched berries still attached to their branches, digital photography, the artificial lighting situation for day and night photography, computerized image analysis to reveal the state of form (determination of the  $\lambda$ -value) and statistical analysis and correlations of  $\lambda$  with weather data. A separate section briefly explains what  $\lambda$  is and how it is used. The methodology combines two areas usually kept distinct: outdoor observations and (indoor) laboratory precision. The objects studied grow in a natural habitat in the open. Little huts around the area of interest shield a small space for “laboratory-like” conditions. The balance established here between usually separate approaches accords with the need to observe the plants in nature, but may also be problematic, as will be discussed.

### Mistletoe Biology

European mistletoe (*Viscum album* ssp. *album* L.) is an indeciduous, perennial, dioecious, half parasitic dicotyledonous plant growing on varied trees mainly in middle Europe. After 4–7 years (depending on the host tree and vitality of the mistletoe bush) it starts to flower. Flowering season is in late winter (February/March). After pollination (mainly by flies) a green berry develops. Inside the berry the new plant develops as an embryo without a hard shell or the usual dormancy period

associated with seed producing plants. The full ripening time requires almost a year. This is congruent with the generally slow growth of mistletoe. In autumn, around September or October, the full size is reached (average of 9 mm in height and 8 mm in width, having a shape of a very round egg). It then turns white and transparent, so the green and photosynthetically active embryo can just barely be seen through the outer skin of the berry. According to unpublished data (Urech, personal communication) mistletoe berries gain weight until the end of December. Unpublished observations from the current study show that rhythmic fluctuations of form finishes in December or January, also corresponding to the time of year when the berries are fully ripe. The berries then remain on the plant until they are removed by external influences like extreme weather conditions or being eaten by birds. Berries can be found on the bush until summer of the following year. Quite often they are still in good shape, but clearly they gradually begin to wilt after December, indicating that the tension of the skin is decreasing (see Sallé, 1983; Büsing, 2000 for whole section).

### Mistletoe and Host Trees

We chose bushes of European mistletoe (*Viscum album* ssp. *album* L.) of at least 5–6 years in age, these being mature enough to develop berries. Since mistletoe grows on trees we chose bushes on lower branches that were in reach for easy handling. In a natural habitat this rarely happens. At the mistletoe research institute Hiscia in Arlesheim, Switzerland, mistletoe is artificially seeded on various host trees and also on lower branches. After testing the reaction of the mistletoe plants to growing on different host trees such as apple (*Malus domestica*), lilac (*Syringa vulgaris*), oak (*Quercus robur*), and pine (*Pinus sylvestris*) under surveillance in rain-protected conditions, we decided to concentrate on the oak host tree since the altered, semi-artificial observation environment (huts during observation period built around them with greenhouse effects) did neither affect mistletoe nor the host tree. In contrast fungal infections developed on mistletoe growing on apple and on the apple tree itself. Mistletoe growing on oaks (along with the oak branch itself) showed a resistant and robust behavior, i.e., the berries were stable in their ripening until the end of the observation period.

### Mistletoe and Huts

In order to protect the digital cameras and the control equipment for regular photographing, huts were built around bushes of mistletoe growing on low branches of oak trees in the gardens of the Hiscia Institute in Arlesheim, Switzerland. Chosen for reasons of easy handling, the branches with the mistletoe bushes were positioned 1–2 m above the ground (Figure 1). The huts were constructed from untreated wood and corrugated PVC sheets that keep out rain and protect bush and equipment from wind. Since the PVC sheets are transparent, light conditions were not substantially altered. Roofs and sides were constructed so as to make air circulation possible. At least one side (pointing away from the main wind direction) and large openings above the ground and below the roof allow air to circulate and warm air to escape.



**FIGURE 1 | A mistletoe hut. (Left)** The cabin shelters a branch with a bush of mistletoe on an oak tree (*Quercus robur*), approximately 35 years old. **(Right)** An isolated and sheltered mistletoe bush without any additional technical equipment.

The observations start with the onset of berry ripening in September and are completed with the end of berry maturation in December. Thus, from January until September – when no observations take place – roofs and sides are removed. Otherwise, insects and fungi find favorable conditions that cause harm to the mistletoe plants due to the artificial situation, especially during summer with elevated temperature due to the greenhouse effect of the hut.

## The Camera-Support Construction and the Fixed Position of Mistletoe Berries

The huts' robust wooden structure allows a construction of metal rods and clamps used in chemical labs to maintain a flexible yet solid position to which the necessary camera and equipment can be attached. Mistletoe branches are also held in a fixed position. Thus, the camera can be adjusted at an exact angle of 90° to the main axis of the berry and at a distance of 3 cm from lens to the berry's axis. Camera, lights and technical devices are shown in **Figure 2**.

## The Camera

We use Nikon Coolpix E5000 cameras, which have a large set of features, most importantly a close-up focus of up to 2 cm from lens to object. The flexible LCD-monitor allows excellent visibility control of the picture. All the features are separately and manually programmable. Triggerable electro-mechanical shutter release “fingers” (see Automatic Photography) allowed photographing in programmed intervals (see **Figure 2**).

The camera settings used were as follows:

- No flash
- Fixed aperture setting: shutter speed of 1/250 or 1/500 s (ensuring that the background, i.e., the light dispenser screen was always lighter than the focused object); focal length of 63 mm, focused at 3 cm

- 2560 × 1920 Pixels, average size between 800 and 1200 kilobytes
- Pictures saved as JPEG

All the above settings, as well as the time and date of the picture taken were saved in the JPEGs exif data.

## The Lighting

We use 9 Volt LED flashlights for lighting (see **Figure 2**). LEDs are a good alternative to other light sources (Jeong et al., 2012). They produce almost no warmth and only moderate electric and magnetic fields. To reduce influences as much as possible, the flashlight is switched on for only 3 s during photography. The light spectrum for LEDs shows a maximum in blue light wavelength but has an equal distribution (all visible colors in its spectrum) as measured by spectroscope (Carl Zeiss, Hand Spectroscopic Nr. 9931).

To get equal light situations during day and night and to achieve optimal contrast for a clearly defined berry outline, the lighting was passive, i.e., via a reflector (**Figures 2** and **3**). Short exposure time (1/250 or 1/500 s) combined with flashlight reflection gave black silhouettes of the berry at any time of day (**Figure 3**).

## Automatic Photography

We use a programmable relay (Logo! 230Rco by Siemens). This triggers the lighting by switching the flashlight on for 3 s and, with a delay of 1 s, activates the shutter release (“finger”) of the camera, causing the camera to take a picture (in a lit situation). The scheme of programming is shown in **Figure 4**.

## Measurements

The pictures are imported in the “LambdaFit” software, which is programmed to semi-automatically fit the outline shape of the object with its specific path curve situation (Derbidge et al., 2013).



**FIGURE 2 | Cabin and camera in use.** The hut (**Figure 1**) shelters the technical equipment as well as the berries to achieve a stable situation for the period of measurements (September to December). (**Left**) The camera with externally programmed electro-mechanical “finger” on the camera’s trigger; the LED flashlight (yellow) that switches on whenever a picture is taken. Lamp, camera and light reflection screen are attached and held by a solid metal structure with clamps and flexible but stable metal arms. The power cables are needed to run the camera, the “finger” (trigger) and the flashlight. (**Right**) A mistletoe berry between lens and light reflector screen.



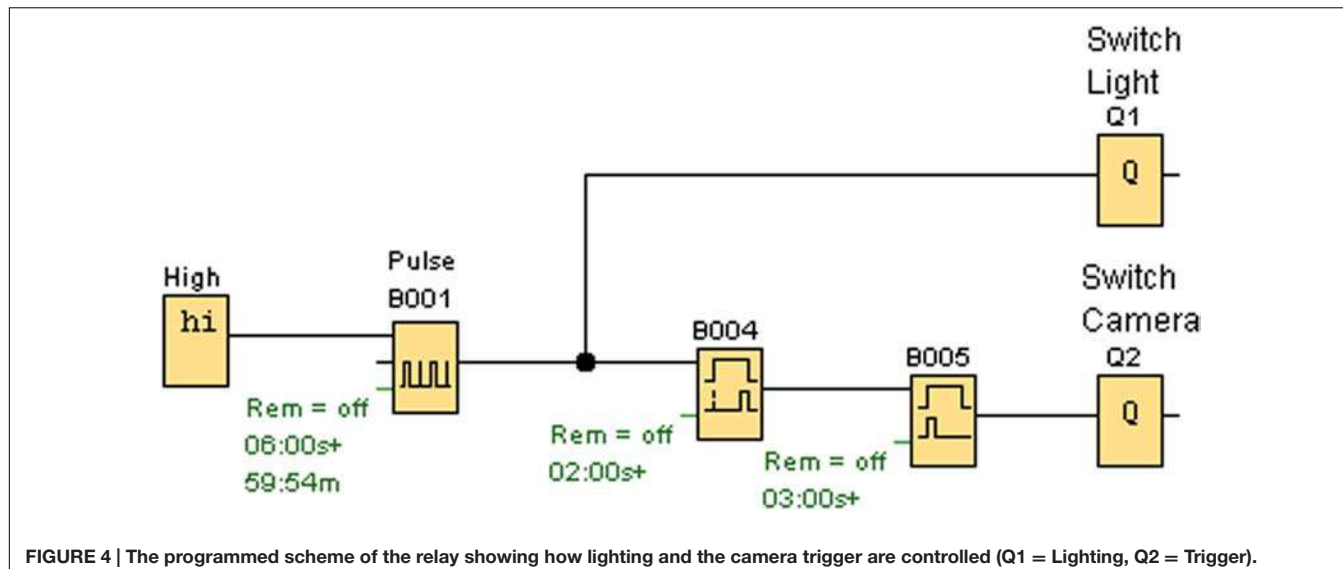
**FIGURE 3 | The lighting situation.** (**Left**) Direct lighting produces somewhat blurry contrasts and unequal reflections. The indirect, passive lighting via a reflector screen produces “black” berries with equally lit (i.e., shaded) edges at night (**middle**) and daytime (**right**). The LED flashlight is pointed at a light reflector. The indirect lighting results in comparable pictures both during the night and day.

The software determines the contour of the shape and calculates a path curve starting from a set of predefined parameters (top and bottom of the object, and  $\lambda$ ). The software further calculates the difference between the path curve and that of the outline shape, and minimizes this difference by iteration, varying the free parameters  $\lambda$ , width, length and the angle of the symmetry axis according to a defined mathematical procedure. The result of one such process is called a measurement, yielding data values for  $\lambda$ , and also width and length of the object. Due to the multi-parameter fit procedure, results of such measurements may vary slightly depending on the starting values of the curve fitting process. Due to this fact, multiple measurements are performed on one photograph in order to get stable mean fitting parameters and to determine variability of the fitting procedure (see Data Sets and Lambda Values). To avoid systematic errors randomized sets of pictures were subjected to measurements [e.g., sets of 144 photographs (6 days  $\times$  24

pictures); each picture measured 10 times]. The outline shape described by  $\lambda$  is independent of the size of the photographed object and of the distance between lens and object. As long as the position (90° from lens to growing-axis of the plant organ) is constant, the absolute distance is of no importance. The final result of the analyzing process by “LambdaFit” is the parameter  $\lambda$ , which represents the state of the object’s form and is used for further analysis of form change over time.

### The Lambda Parameter

Since path curve geometry and in particular  $\lambda$  as the form-defining parameter play prominent roles in the present study design, we will very briefly and qualitatively describe the definition of  $\lambda$ . The mathematical background of  $\lambda$  and all necessary formulae are explained in detail elsewhere (Derbridge et al., 2013).



Since we are interested in the outline, we reduce the rather complicated mathematics to a two-dimensional system. An organ following a path curve (an egg-like shape) is a bi-symmetrical form with a mirror axis XY, with top (X) and bottom (Y) of the organ, which must be clearly defined, as in mistletoe berries. Every point on XY has two corresponding points (a and a') 90° to the axis on both sides of the outline of the organ. Any two points a and a' define a cross section through the organ at a certain level, which gives a diameter for this level.  $T = XY/2$  cuts the line XY in half. For any chosen level, a  $\lambda_{\text{level}}$  can be defined as ratio of the chosen level diameter to the T level diameter. The parameter  $\lambda$  of the whole path curve then is defined as the ratio of the mean of all  $\lambda_{\text{level}}$  on XT to mean of all  $\lambda_{\text{level}}$  on YT. The parameter  $\lambda$  thus is an approach to describe the ratio of the curvature of the upper half to the curvature of the lower half of the objects outline shape. In other words,  $\lambda$  is a measure indicating the flatness or sharpness of an egg-like shaped form.  $\lambda = 1$  thus describes outline shapes that are equally rounded on the top and bottom.  $\lambda$ -values > 1 describes egg forms that are more acuminated on the top and flatter on the bottom.  $\lambda < 1$  but > 0 will be the opposite, flat on the top and peaked on the bottom.  $\lambda = 0$  is the point of transformation to a new set of path-curve forms: for  $\lambda < 0$  the path curves turn into vortex-like forms (see Figure 5 for a range of  $\lambda$  shapes relevant to mistletoe berries). Mistletoe berries change their shape during ripening which  $\lambda$  slowly decreasing from  $\lambda \approx 1.2$  in September to  $\approx 0.9$  in December (see Figure 6). Their overall shape change, so to speak, is the inversion of an egg-like shape “standing upright” (i.e., flat on the bottom part and sharp at the top end) which moves toward the opposite: flatter on top and sharper at the bottom, where the berry is attached to the stem (egg standing upside down).

## Data Sets and Lambda Values

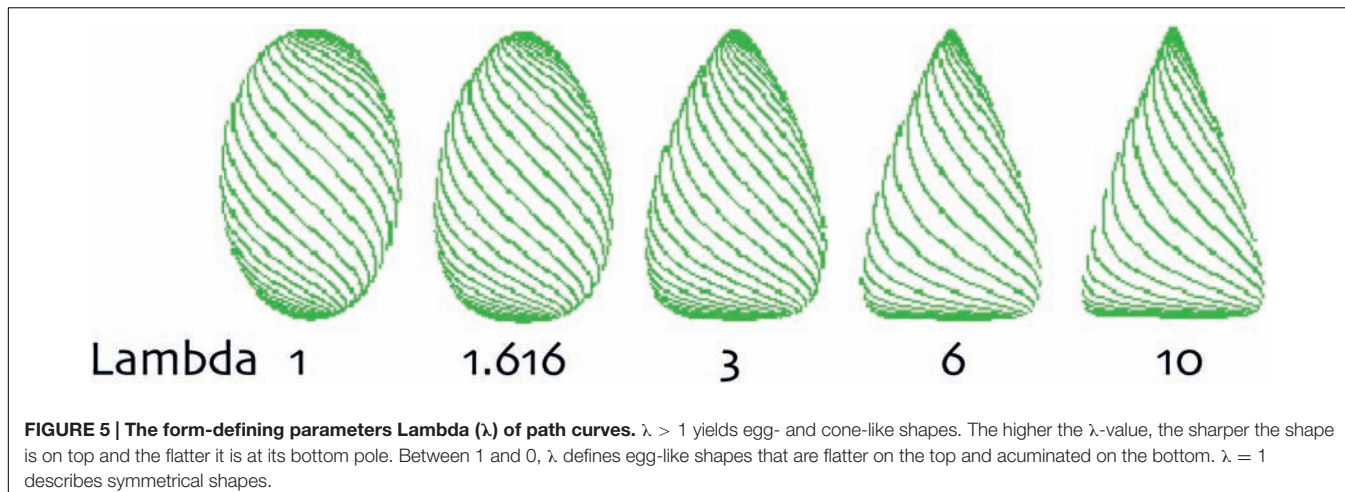
The  $\lambda$ -values represent the state of form for a certain picture extracted from the pictures via the software we use (Derbridge et al., 2013). The  $\lambda$ -values we use are mean values of 10

independent measurements of the same photograph (except for 2010 where it is the mean value of only six independent measurements). These 10 (6) measurements, performed in randomized order within a set of several pictures, allow calculation of a mean value and a corresponding standard deviation (Derbridge et al., 2013). This mean value is used in all further calculations.

To assess circadian rhythms, one photograph per hour H1, H2 ... H24 was taken. Thus, 1 day yields 24  $\lambda_j$  data points ( $j = 1, 2 \dots 24$ ). In order to calculate mean circadian rhythms over several days, data from each day was normalized to the experimental mean of the corresponding day. A circadian data set for a given period of time (day 1-i) was calculated by averaging the normalized  $\lambda_j$  data for each hour  $j$  of the 24 data points for all the experimental days of the given period with the corresponding standard deviation (SD) or standard error (SE).

## Environmental Data

Weather data were obtained from the weather station run by “Meteo Swiss” in Binningen (BIN), Basel, Switzerland, situated approximately 7 km northwest from our location at a similar altitude (316 m above sea level). In addition, the temperature was recorded in the actual place where the berries were growing and compared with the temperature from BIN. No irregularities between the two measurements were found, except that range of temperature in the mistletoe huts was proportionally higher on warm sunny days (greenhouse effect). The site of observation is geomorphologically and meteorologically comparable with that of the weather station. Basically there are three meteorologically relevant weather situations: a weather front coming from the west; an inversion with fog; a stable high pressure (good weather) situation. All three will be the same in both places. No meteorologically relevant barriers separate both places. For the statistical correlation analysis we used the BIN data exclusively, since they are representative of our location and are recorded at



the same time as the other weather data from BIN. All data from BIN are means or sums of the previous hour (see Table 1).

### Deviation between Path Curve Form (Lambda) and Shape of Plant Organ as Represented in the Energy Value

The “energy” value, used in the software’s algorithms, is an operation analogous to the standard deviation and gives the average distance between the path curve and the berry’s contour. For each pixel  $t$  ( $0 \leq t \leq n$ ) of the path curve, the distance to the respectively closest pixel of the plant contour  $dist_t$  is measured. The squares of all  $dist_t$  are summed up and divided

by  $n$ , whereupon the square root is extracted. The formula is Equation 1:

$$e = \sqrt{\frac{\sum_{t=1}^n dist_t^2}{n}} \quad (1)$$

This “energy” value  $e$  estimates the agreement between the actual contour of the mistletoe berry and the mathematical path curve fitted to that shape. Further details on the formula and the operations done are given elsewhere (Derbridge et al., 2013).

Notice that the pixel distance and hence the “energy” value depends on the picture’s resolution. For instance, if the height of a berry is 500 pixels and  $e$  is 3 pixels, there is a 0.6% deviation. For a real berry’s height of 10 mm the average deviation between berry outline and path curve is 0.06 mm.

### Statistical Analysis

Basic data reduction (for the operations mentioned see Data Sets and Lambda Values) were performed using Excel 12.3.2 (Microsoft, Redmond, WA, USA) data sheets. Data smoothing was done with LOWESS (locally weighted regression scatter plot smoothing) fits (Chambers et al., 1983), calculated with KaleidaGraph 4.0 (Synergy Software, Reading, PA, USA). This operation defines for each data point a linear regression equation, in which a variable percentage  $P$  of neighboring data points can be included. The function thus calculates a smoothed curve; the larger the percentage  $P$  of included

**TABLE 1 | List of weather factors recorded at the BIN weather station for the correlation analysis with  $\lambda$ .**

Weather factor	Unit	Definition
Temperature (2 m above ground)	°C or K	Mean of previous hour
Air humidity	%	Mean of previous hour
Sunshine	min	Sum of previous hour
Global radiation	W/m <sup>2</sup>	Mean of previous hour
Atmospheric pressure	hPa	Mean of previous hour

For some calculations we transferred temperature (°C) into K to avoid calculations with minus degree.

**TABLE 2 |** Average  $\lambda$  and energy values (mean  $\pm$  standard error SE) for four series of measurements in 4 years.

Type of measurement series	Average $\lambda$ (mean $\pm$ SE)	Average energy value [pixel] (mean $\pm$ SE)
Mistletoe berry 2010 (lilac); n Pictures = 380; n Measurements = 2280	1.1309 $\pm$ 0.0165	1.5022 $\pm$ 0.1008
Mistletoe berry 2011 (oak); n Pictures = 144; n Measurements = 1440	1.0553 $\pm$ 0.0320	0.9740 $\pm$ 0.1140
Mistletoe berry 2012 (oak); n Pictures = 144; n Measurements = 1440	0.9823 $\pm$ 0.0299	1.2844 $\pm$ 0.1651
Mistletoe berry 2013 (oak); n Pictures = 144; n Measurements = 1440	1.0804 $\pm$ 0.0146	0.8797 $\pm$ 0.0605

$\lambda$  is the form-determining parameter of the path curve, and the energy value corresponds to the deviation between the mathematical path curve and the outline shape of the mistletoe berry (expressed in pixels). 144 photographs (380 in the year 2010) of a mistletoe berry were taken during 6 days (16 days in the year 2010, with 4 single photos missing due to technical problems) at hourly intervals.  $\lambda$  was measured in randomized order within a given experimental series ( $n = 10$  independent measurements per photo ( $n = 6$  in the year 2010)).

neighboring data points, the smoother and straighter the curve. Correlation analyses were done using the Pearson product moment correlation test, calculated with Statistica 6.0 (StatSoft, Tulsa, OK, USA).

## RESULTS

### Outline Shape of Mistletoe Berries Show a Correlation with Path Curves

Mistletoe berries show an almost perfect congruence with mathematical path curves. The “energy” value, as implemented in the algorithms of the software used to optimize the fit of the path curves to the outline shape of the mistletoe berries, is closely related to the standard deviation of the distance between fitted curve and outline (see Methods for details). The “energy” value depends on the picture’s resolution, since it is calculated based on the deviation in pixels. The average “energy” value is between 0.9 and 1.5 pixels (see Table 2 for the average  $\lambda$  and energy values of all the circadian rhythm photo-series used in this study), which corresponds to an average “deviation” between fitted path curve and berry outline shape of 1.6–2.7  $\mu\text{m}$  for the average height of a berry of 9 mm. Thus, the outline of mistletoe berries corresponded almost perfectly to mathematical path curves for all four measurement series between 2010 and 2013 (for a visual impression see Figure 7).

### Circadian Rhythm

Once it was clear that the outline shape of mistletoe berries could be mapped as path curves, four series of pictures from the years 2010–2013 were assessed in order to identify potential circadian rhythms. Each series consisted of 6 days in October of uninterrupted data (16 days in 2010). Statistical analysis revealed highly significant circadian rhythms in 2010 and 2011, and no significant rhythms in 2012 and 2013 (Table 3; Figure 8). A correlation analysis of the circadian data from 2010 to 2011 revealed a highly significant correlation between circadian rhythms from both years ( $r = 0.7829$ ;  $p = < 0.0001$ ;  $n = 24$ ). The daily rhythms of 2010 and 2011 are in congruence. Compared to the data of 2010/2011, the standard deviations of the hourly mean values of the 2012/2013 daily data are much higher, an indication that there is no daily rhythm or signal in those 2 years (see Table 3).

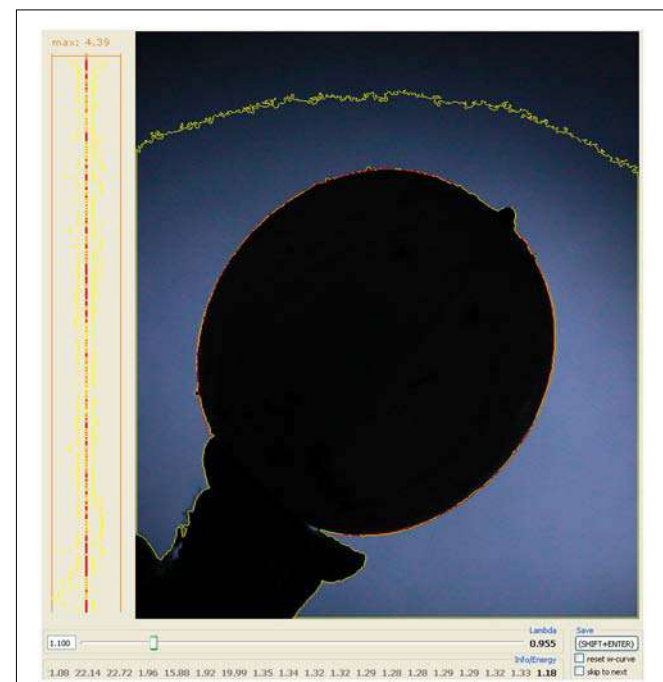


**FIGURE 7 |** Congruency between the mathematical (path curve, red) and the actual form (outline shape, yellow) of a mistletoe berry. The yellow line is the outline of the black object determined by the LambdaFit software [ $\lambda$ ] and the red line is the best fitting mathematical path curve to that given shape. On the left-hand frame the path curve is set as a straight line from top to bottom, and the deviation to the plant organ’s contour is shown for every pixel on the line for both sides. The number above that graph gives the maximum deviation. On some parts of the graph the red and the yellow line overlap, i.e., the path curve exactly fits the berry’s outline. The bottom part and the tip of the path curve are “cut off”, since the stem and the top (where the wilted petals are) must be excluded.

### Determining Weather Influence

To search for possible causes for the circadian rhythms in the berries’ change of outline shape in the years 2010 and 2011, a number of correlation analyses were performed with factors known to have an impact on circadian rhythms (Dunlap et al., 2004; Yakir et al., 2007; Pfeuty et al., 2012). The weather data of the days with  $\lambda$  data were normalized for each day and averaged. Correlations between all weather factors with  $\lambda$  were calculated (Table 4).

**TABLE 3 | Results of the ANOVA analysis (24 groups) investigating possible circadian rhythms (data of Figure 2 and respective measurements for the stated years).**

Year	Month	Host-tree	Groups	F	p
2010	Oct	Lilac	0–23 (each hour) over 16 days	2.269	0.001
2011	Oct	Oak	0–23 (each hour) over 6 days	5.498	<0.001
2012	Oct	Oak	0–23 (each hour) over 6 days	1.233	0.231
2013	Oct	Oak	0–23 (each hour) over 6 days	0.117	1.000

F: F-test values; p: significance levels.

Temperature and humidity (humidity in reciprocal relationship with temperature) show highly significant correlations with the berries' outline form ( $\lambda$ ). This corresponds to wave patterns similar to the  $\lambda$  wave when viewed in a graphic representation for 2010 and 2011 (see Figure 9 for 2011). Sunshine hours and global radiation show a significant correlation in the 2011 data set (see Figure 10).

## External Factors for a Strong Diurnal Movement

The fact that we found significant circadian rhythmic change in mistletoe berries in 2010 and 2011 but not in 2012 and 2013 (see above and Table 3) raised questions that we investigated by looking at weather conditions that might trigger or suppress the rhythm.

Therefore all data were further analyzed. A histogram of all 24 h data blocks with regard to sunshine minutes per day showed a distribution with three distinct groups. We separated the 24 h data blocks of all years into these three groups as

follows: (a) “clear sky,” i.e., good weather with a high number of sunshine minutes (>400 min per day); (b) “partly cloudy,” i.e., moderately good weather (with sunshine minutes between 100 and 400 per day); and (c) “overcast sky” i.e., bad weather (<100 sunshine minutes per day or no direct sun at all). Those “bad weather days” were rainy, foggy or overcast because of weather changes. This grouping corresponds to the range or amplitude of temperature (high amplitude = no clouds; medium amplitude = partly clouded days; and low amplitude = clouds or fog or mist; see Figure 11).

The graphs of the circadian rhythms of  $\lambda$  show: a significant change of form for group (b) (“partly cloudy”) in a rhythm that accords with Figure 10 for 2010 and 2011; a visually clear but statistically just near significant change ( $p = 0.06$ ) of form in group (a) (“clear sky”); and no pronounced change in  $\lambda$  in group (c) (“overcast sky”).

Analysis of variance tests showed that an intermediate weather situation with medium amplitude of temperature and a medium number of sunshine minutes per day are the necessary condition for the strongest rhythmic change in  $\lambda$ . This result indicates that the change of form is sensitive and cannot be fully expressed by the berries when sunshine is strong (i.e., high global radiation [ $\text{W/m}^2$ ]) and also when the sky is under full cloud cover. As these are indirect assumptions, the results elicit certain questions rather than answering them. But a hypothesis that change of form is in this case dependent on “nice weather” (a not too extreme temperature amplitude, and also a not fully overcast sky) seems reasonable. Some parts of the sky must be blue (but no direct sun, at least not all the time) for the emergence of this change of form as a statistically distinct feature (see Table 5).

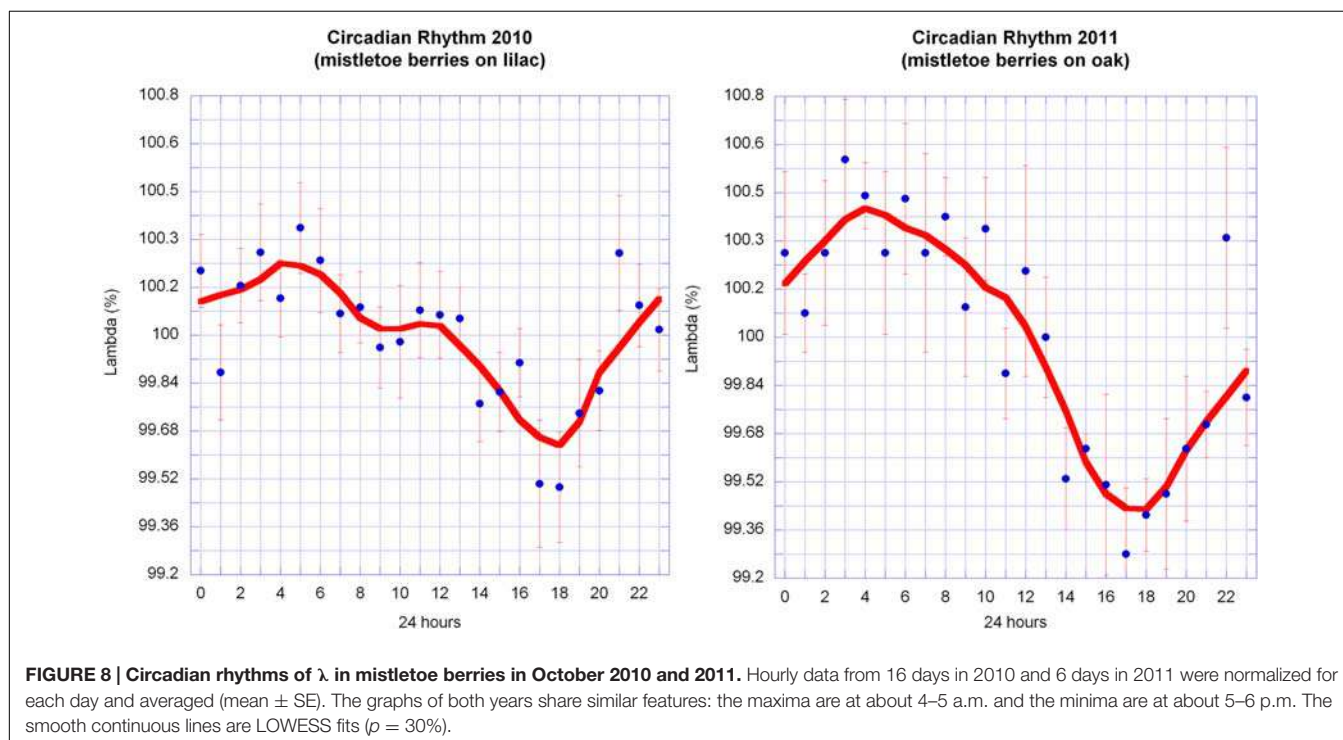


**FIGURE 8 | Circadian rhythms of  $\lambda$  in mistletoto berries in October 2010 and 2011.** Hourly data from 16 days in 2010 and 6 days in 2011 were normalized for each day and averaged (mean  $\pm$  SE). The graphs of both years share similar features: the maxima are at about 4–5 a.m. and the minima are at about 5–6 p.m. The smooth continuous lines are LOWESS fits ( $\rho = 30\%$ ).

**TABLE 4 | Pearson correlation coefficients  $r$  and corresponding significance levels  $p$  between circadian rhythms ( $\lambda$ ) and the different weather factors.**

Correlations Lambda ( $\lambda$ ) with weather factors	2010 $N = 380$		2011 $N = 144$		2012 $N = 144$		2013 $N = 144$	
	$r$	$p$	$r$	$p$	$r$	$p$	$r$	$p$
Temperature	-0.2098	<b>&lt;0.0001</b>	-0.5737	<b>&lt;0.0001</b>	0.0418	0.6185	0.0865	0.3042
Air humidity	0.2528	<b>&lt;0.0001</b>	0.6226	<b>&lt;0.0001</b>	0.0269	0.7485	-0.1006	0.2318
Sunshine	-0.0987	0.0547	-0.3940	<b>&lt;0.0001</b>	0.1489	0.0749	-0.1207	0.1511
Global radiation	-0.0655	0.2026	-0.3243	<b>0.0001</b>	0.1034	0.2175	-0.1088	0.1959
Atmospheric pressure	-0.0258	0.6165	0.1216	0.1466	-0.0093	0.9122	-0.4703	<b>&lt;0.0001</b>

Significant values ( $p < 0.05$ ) are printed in bold.

## DISCUSSION

### Research Design and Methodology

We measured circadian morphological changes affecting the outer skin of a berry, something that has not been previously studied to the best of our knowledge. The only research with similarity to our approach is on diurnal changes in leaf hyponasty or growing rates, studies that are summed up under the topic of plant movements (Klein, 2007; Asanidze et al., 2011; Dornbusch et al., 2012; Chitwood, 2014). The rationale for those studies is, largely, to describe phenological findings and relate them to physiological and molecular processes and structures within the plants. But additionally phenological change detection from pictures is used with modern techniques to, for instance, trace growth (Li and Gu, 2004). The focus on exact form change in berry phenology in our approach *in vivo* and *in situ* using mathematics from projective geometry is new. The rhythms found are phenological changes in outline shape that are strictly mathematical and yet dynamic in nature (path curves). The outline as well as the detected outline variance can be accurately mapped with the  $\lambda$  parameter.  $\lambda$  thus becomes the key value to trace the change of shape. One formula can trace changes in form because only one parameter ( $\lambda$ ) is changing its value. Since our focus is change of form, we cannot say anything about anatomical or physiological reasons for the changes, or corresponding metabolism within the berries. We strictly analyze the correlation between a mathematical law and a biological object to demonstrate their correlation in this study.

### Findings Relating to the Path Curves of Mistletoe Berries

To the best of our knowledge, forms or outline shapes have not yet been used in plant biology or in any research involving living organs in the manner we applied them in our study. In projective geometry, path curves are a set of dynamic forms with determining parameters accessible to exact measurement (Edwards, 2003; Klein, 2006; Derbidge et al., 2013; Klein, 2013). This new method of shape recognition using mathematics derived from projective geometry works under different outdoor conditions (like day and night, change in temperature, change of relative humidity) and detects a difference of just a few pixels between formula and real object (see Results, Table 2; how to convert pixels into actual berry size, which is depended on the pictures resolution, is exemplified in Derbidge et al., 2013).

Form as such is used to describe objects at all levels, i.e., from whole organisms, through organs to small units such as cells, or even molecular structures that can be reconstructed as two- or three-dimensional forms (Thompson, 1992; Pivar, 2009; Schwartz, 2013). Forms of plant organs such as leaf forms have been classified and are used to determine species but rarely to detect circadian or other rhythms.

Using  $\lambda$  in the algorithm to define the state of the outline shape of mistletoe berries might open a new line of thought in chronobiology. This feature, visible to the eye, makes studying the phenomena accessible without the aid of complex and expensive apparatus. The method described in this publication thus is an *in vivo* and *in situ* observation during the long ripening season of mistletoe berries.

The approach we seek to introduce here, if proven to be of value, could re- engender something of a more direct, phenotypic relationship to nature while at the same time continuing to pursue current biological questions such as those of rhythmic interactions or behavior.

Form, in its common usage, is about static features: proportions, length, width, number of features, etc. (Lonergran, 1985; Ji-xiang et al., 2013; Schwartz, 2013). Path curves, by contrast, are dynamic in nature (see Figure 7). There was a significant correlation between a path curve's outline shape and that of mistletoe berries. Here, we demonstrated that it is promising to pursue this approach further and to extend it to chronobiology.

### Findings Relating to the Circadian Rhythm

It was not completely unexpected that mistletoe berries exhibit a circadian rhythm since almost all living organs so far studied do so (Kondo and Ishiura, 1999). Almost, all biological functions find an expression in rhythms. When plotted in graphs, the circadian rhythm of the berry's outline shape (change of  $\lambda$  over time) appears to be quite close to a harmonious wave, i.e., a sine wave without any disruptive features such as asymmetry or certain peaks. Thus, it expresses a common rhythmic behavior found in many organs or organisms (Kondo and Ishiura, 1999; Dunlap et al., 2004).

Circadian rhythms are well-understood by means of circadian clocks – genetic oscillators that generate biochemical rhythms with a free-running period (FRP) close to 24 h (Roenneberg and Foster, 1997; Somer et al., 1998; Dunlap, 1999; Young and

### Mistletoe Berries on Oak 2011

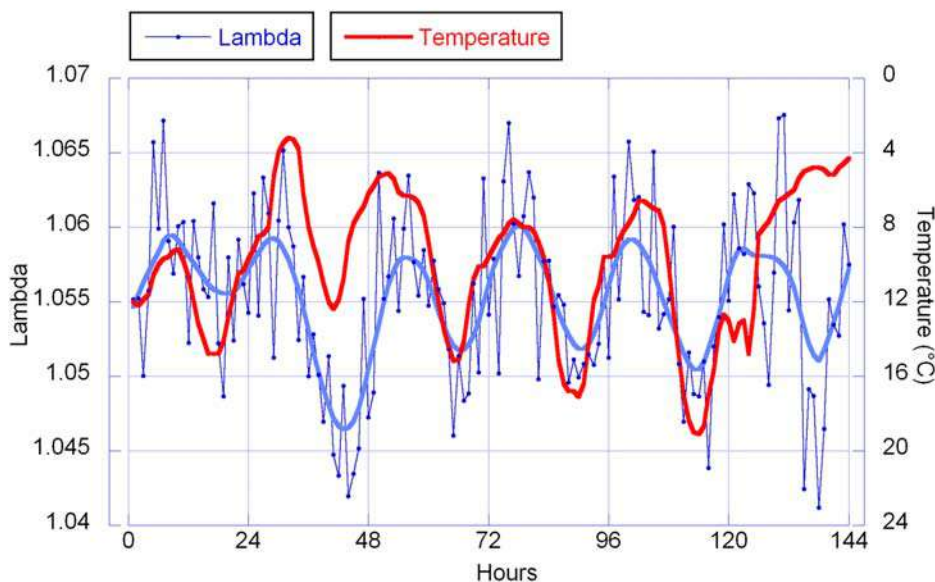
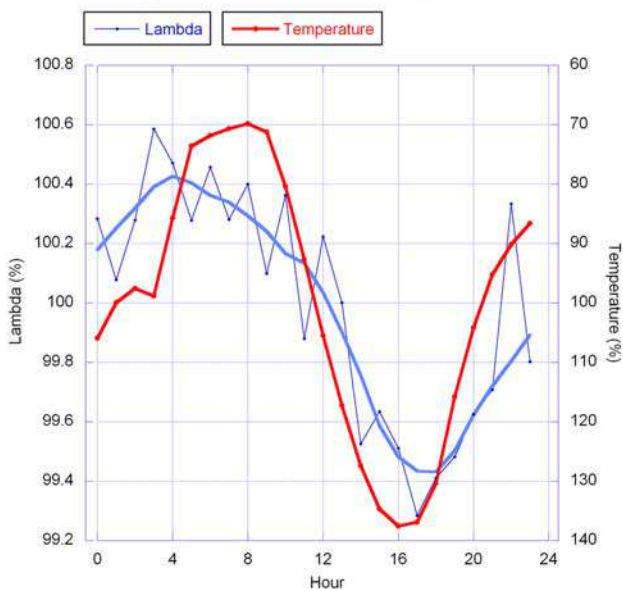


**FIGURE 9 | Lambda values and temperature.** Hourly  $\lambda$ -values in blue (6 days = 144 h) and temperature values in red (reverse axis). For  $\lambda$ , every data point represents the mean of 10 measurements. For the temperature each dot represents the average of that hour. The smooth continuous line represents a LOWESS fit for the  $\lambda$  data with  $p = 10\%$ .

### Circadian Rhythm of Lambda 2011 with Temperature



### Circadian Rhythm of Lambda 2011 with Sunshine and Radiation

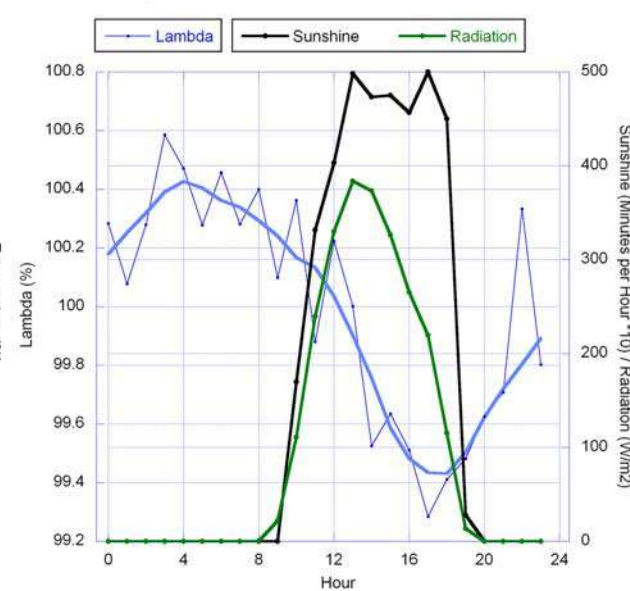
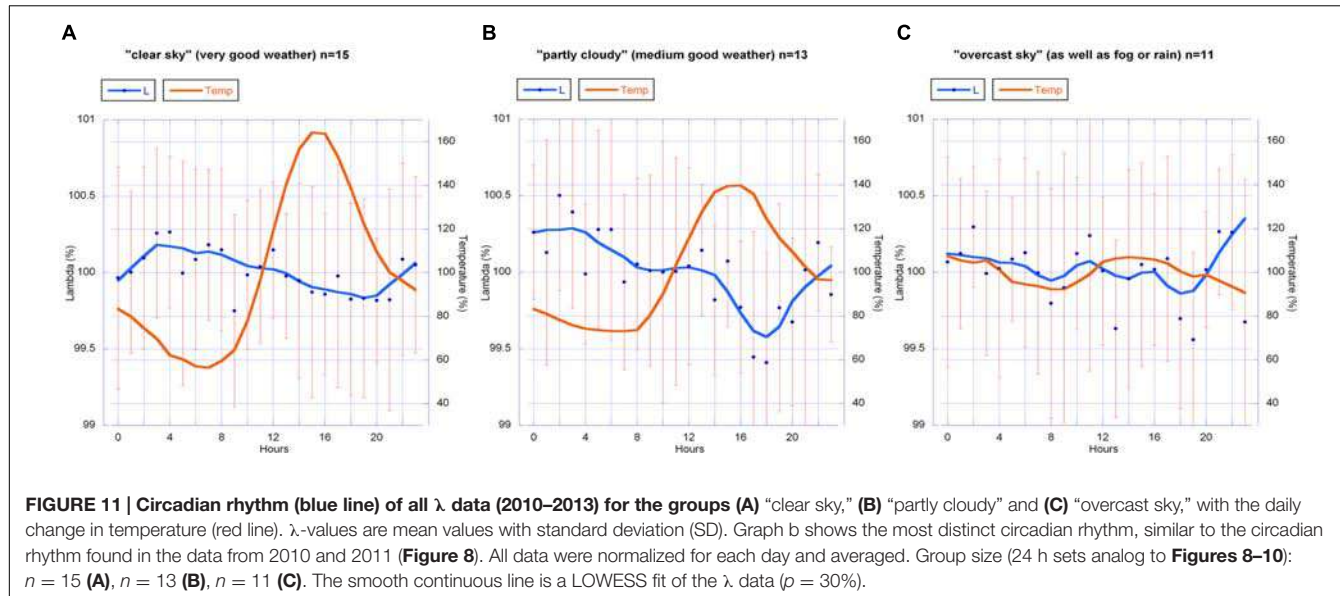


**FIGURE 10 | Circadian rhythms of  $\lambda$  in mistletoe berries (error bars omitted for clarity) in October 2011 together with, left: the daily change in temperature (reverse axis), and right: sunshine minutes and global radiation.** The smooth continuous lines for  $\lambda$  (blue thick line) are LOWESS fits ( $p = 30\%$ ).  $\lambda$  and temperature data were normalized for each day and averaged. They are expressed as relative percentage change whereby sunshine [minutes/hour] and global radiation [ $\text{W}/\text{m}^2$ ] are the average of the 6 days in regard to the specific hour.

Kay, 2001; Bell-Pedersen et al., 2005; Pfeuty et al., 2012). To achieve synchronization with the day/night cycle, a circadian oscillator integrates a complex set of environmental signals such as changes in daylight quantity or quality (Young and

Kay, 2001; Bell-Pedersen et al., 2005) or in temperature (Yoshii et al., 2009). The effect of those signals usually alters the reactions, i.e., the characteristics of the rhythm. In particular, light signaling pathways play a major role in coupling the clock to its



environment as they provide information about the day–night status.

## Findings Relating to Weather Influences

The observation of the mistletoe berries and the detection of their change of form in four consecutive years took place under different specific weather conditions. All weather data were taken from the nearest official and validated weather station (7 km distance from our study site). We correlated those weather data (temperature from BIN) with local data (temperature measured in the hut around the observed berry). Correlation analysis showed that both weather situations were highly significant in agreement. So we decided to use the more reliable “official” data from a state weather station. The host tree’s leaves shaded the study site, so no direct sunlight reached the hut construction that allows good air circulation and statistically, the rather small greenhouse effects could be neglected. Humidity always correlates reciprocally with temperature and all other weather factors we used do not differ locally from the nearby weather station, which, meteorologically, is in a very comparable location.

A certain circadian rhythm of the mistletoe berry’s shape was observed in 2010 and 2011, but not in 2012 and 2013. Correlations to  $\lambda$  were observed in the data of 2010 and 2011 for temperature and humidity, and in 2011 also for sunshine

hours and global radiation (graphs of these data of all 4 years are available as Supplementary Figure A).

The  $\lambda$  correlations in 2010 and 2011 with temperature and sunshine minutes or radiation don’t match ideally.  $\lambda$  and temperature both show a wave, close to a sine wave in its rise and fall, with almost equidistant periods. Thus both waves have a similar sine curve, but with a phase shift. The  $\lambda$  wave has a maximum at about 5 a.m., 2 h before sunrise (which is around 7 a.m. in October at the place of observation). The temperature drops to its minimum a bit later (minimum at 8 a.m. which is a 3 h shift from the  $\lambda$  wave). In the afternoon the  $\lambda$  wave minimum is at 5 p.m., 1 h later than the temperature maximum but running earlier than the decline of radiation (sunset at 7 p.m.).

Temperature and light influences are fundamental causes of circadian rhythms but the rhythmical change of form in the present case do not correspond to these factors in an unambiguous way.

In plants it seems to be usual for effects to follow the timekeeper and not the other way around (Roenneberg and Foster, 1997; Beersma et al., 1999; Pfeuty et al., 2012).

An exploratory analysis identified predominantly blue vs. overcast sky as being correlated to the presence of a circadian phenotypic shape change. During “nice” weather the diurnal  $\lambda$  rhythm was observed, but not in “bad” weather. Most of the

**TABLE 5 | Analysis of variance (ANOVA) results for the circadian rhythm analysis of form change as a function of three characteristic weather groups.**

Group	Analysis of variance		Weather features	
	F	p	Temperature Amplitude	Sunshine minutes (total per day)
(a) “clear sky”	2.219	0.0665	very high	>400
(b) “partly cloudy”	3.636	0.0065	pronounced but intermediate	100–400
(c) “overcast sky”	0.459	0.8063	small	<100

Group size: a ( $n = 15$ ), b ( $n = 13$ ), and c ( $n = 11$ ). The data correspond to Figure 11. The group b (“partly cloudy”) with medium amplitude in temperature yields the most pronounced result for circadian rhythms.



**FIGURE 12 | Longitudinal section of a ripe mistletoe berry in November.** The green embryo with its clearly visible hypocotyl and surrounding endosperm is encircled by the white pericarp. The otherwise strong tension of the skin has collapsed because of the cutting needed for the section (Photo: H. Ramm).

2012 and 2013 weather was foggy or the sky was overcast at the time of measurements, which seemed to suppress the rhythmic expression in  $\lambda$  change.

## The Influence of Light

In our research the “usual suspect,” light, as major influence on circadian rhythms, has not been exhaustively studied yet. For instance, it would be necessary to further study the influence of day length. Since we studied rhythm in a seasonal context the impact of the light situation (for instance total sunshine minutes per day) on the characteristic circadian pattern found, could be of significance. Especially, in October and November when the duration of daylight changes rapidly (in Middle Europe). The time of minima and maxima might therefore vary from the beginning to the end of the measurement period: in September, for instance, there is at least one additional hour of light compared with November. We measured berries only once per hour (24 measurements per day), and therefore did not obtain a high enough resolution for change in day length to resolve this question. Measurements would be needed every 10 min or less to detect possible (and most likely small) changes during the twilight hours.

Knowledge of circadian rhythms is extensive and sophisticated. Modifications to rhythms during the season as an adaptation to changes in habitat conditions, or during the day, for example when overcast sky situations can rapidly alter the quality and quantity of light, have been discussed for different organisms (Beersma et al., 1999; Dunlap, 1999; Pfeuty et al., 2012).

The mistletoe berry has no testa, being a pseudo-fruit and bearing a pseudo-seed with mostly one, but sometimes 2 and rarely 3 to 5 embryos, each with a haustorium that emerges from the endosperm, a hypocotyl and two rudimentary cotyledons. As such it is probably sensitive to alterations in light quantity and quality, since the new organism growing within the ripening berry is already active in photosynthesis (Becker, 1986). Our discovery that full sun exposure flattens the peak shape of the 24 h-wave, contradicts an explanation of the rhythm as an adaptation to photosynthesis of the embryo. Half-clouded skies – conditions where the sun is not at full strength – seem to be optimum for expression of the circadian rhythm. These conditions are comparable with conditions in the morning and evening, when the sun is lower, but light is present.

Daylight is the key factor for circadian clock entrainment. But it changes in quality and quantity seasonally and during the day due to changes in weather such as cloud-cover, and is therefore neither a reliable nor a uniform environmental cue (Beersma et al., 1999; Troein et al., 2011). Plants and other organisms need to be adapted to such changes (Stoleru et al., 2004; Trivedi et al., 2013). It is likely that a physiological study of mistletoe berries will discover the effect of these influences (Büssing, 2000; Urech et al., 2006; Dorka et al., 2007), but our findings tend to show that the outline form is not clearly dependent on such factors. Light, by means of direct sunlight and radiation is linked to temperature, a major possible influence on form change as discussed in Section “Findings Relating to Weather Influences.”

## Mistletoe Physiology and Anatomy

The results presented here should be contextualized with the berries’ anatomy and physiology, which we refer to collectively as “internal” biotic factors. Anatomical structure and physiological activities of the mistletoe berry are of great interest, since the changes of shape must be accompanied by anatomical rearrangements and alterations in physiological processes (Azuma et al., 2000; Dorka et al., 2007).

Sap flow has been studied as a rhythmic circadian and seasonal phenomenon especially in regard to the metabolism of plants, which is subject to external influences (Zürcher et al., 1998; Zürcher, 2001; Barbetta et al., 2012; Forster, 2014). Sap flow has been studied in many species including various oak subspecies (Čermák et al., 1982; Granier et al., 1994; Barbetta et al., 2012). Recently the topic gained attention in regard to nocturnal sap flow (Dodd et al., 2005; Pfautsch et al., 2011; Forster, 2014). In general the strong increase in xylem sap rise from roots to leaves starts at sunrise (when light meets the leaves and photosynthesis starts). In the broadly recognized cohesion-tension theory, the factors responsible for this mechanism are driven by transpiration, i.e., the sap flow rhythm is correlated with sunlight and modified by temperature as well as humidity in the environment. On a hot day or during a dry hot summer (with light), as for example in Mediterranean countries, water flow is reduced due to stomata aperture regulation to avoid dehydration (Pfautsch et al., 2011; Barbetta et al., 2012). But even under these conditions the diurnal change in water volume rising in the tree starts at sunrise and rapidly decreases at dusk

(Pfautsch et al., 2011). This is a rhythm quite different from the one we found in the change of form in mistletoe berries. **Figure 4** shows the sine like rhythm of change of form of the berries' outline shape together with sunlight (sunshine minutes per hour) and global radiation. According to the literature on sap flow, these two parameters should quite accurately correlate with sap flow, but they don't correlate well with the change of form. Thus tree xylem flow most probably is not the cause for the rhythmic form change observed. The rhythm of the tides, i.e., the moon's influence, has also been subject of some studies and would be worth looking at, especially since it has generated much controversial discussion (Zürcher et al., 1998; Vesala et al., 2000; Zürcher, 2001; Barlow et al., 2010). Causes of any detected rhythms in sap flow would demand a similar or even synchronous study of sap flow in the host tree and the mistletoe growing on it. To our knowledge no such study yet exists and it would be a good candidate for further research where the interaction of host tree and mistletoe (mutual or parasitic relationship) could be the focus.

Little is known about transpiration of mistletoe berries. They seem to have a cuticle that effectively prevents evapotranspiration (Sallé, 1983; Büsing, 2000). Still, in principle, it could be possible that sap or water flow from the host tree into the mistletoe bush (stem and leaves) also affects the mistletoe berry even though the latter most probably doesn't need water for transpiration. However, as discussed above, tree sap flow cannot be the only cause of the change of form of the mistletoe berries.

A mistletoe berry exhibits specific anatomical features. The green embryo and endosperm lie in the berry's center and are surrounded by the pericarp. The mesocarp develops as the main substance of the berry – a whitish, transparent, soft, and glue-like material. The mesocarp is composed of inner elongated cells and outer vacuolated cells. The elastic and flexible skin (epicarp) has a thick cuticle (Sallé, 1983) (see **Figure 12**). These anatomical features, in principle, should enable the occurrence of a dynamic form change. Further detailed investigations of the underlying changes in the anatomical structures and the physiological processes are needed to provide a rationale for the specific shape changes observed.

The germination of a mistletoe embryo starts by end of September. The hypocotyl then begins to grow toward the epicarp. In cross sections one can see that it breaks through the endocarp and, after January, changes the outline shape of the berry (its skin) since it pushes from inside against it. In December the hypocotyls (there can be one, in some cases two or even 3–5 embryos per berry) can be clearly seen through the transparent skin. Unpublished measurements about the weight of the berries show a steady increase of weight until the end of December (Urech, personal communication). This probably is due to the embryos' growth. Whether this weight gain is paralleled by a growth in size of the whole berry, cannot be stated ( $\lambda$  is a dimensionless ratio). Increase in weight could also be explained by an increase in density. But this result suggests that the mistletoe berries we observed in October were still in a ripening phase. If the change of form has to do with the ripening process, it might be a rhythmical growing process or be induced by the physiological activity of the embryo.

## Methods

Within the present research project a new method for studying rhythms on a macro-phenotypic scale was developed: the detection of rhythmic changes in living objects *in situ* by controlled outdoor photography and mathematical processing to fit the projective geometrical forms. In a former publication (Derbidge et al., 2013) we reported on the algorithms and software used for this study. The present paper focuses on the handling of mistletoe, the photography and the equipment used. Overall the results demonstrate the robustness and reliability of the method itself. Questions and problems of the newly developed method will be identified and discussed below.

The procedure used allows photography to be undertaken in a situation as natural as possible, and guarantees the comparability and uniformity of picture series, i.e., equal lighting of pictures taken in daylight and in artificial lighting at night, for purposes of comparison. Most importantly, it minimizes the variation of angle and distance between lens and object.

The outdoor situation sometimes results in unpredictable elements. Extreme weather situations such as storms or a sudden drop of temperature can bias the data or lead to missing data due to damage to the plant. For example, a very sudden drop in temperature, associated with a rapid increase in relative air humidity, can fog the lens. Storms can make the tree shake so much that the fixed stem with the berry can change position or even break; and identical repositioning is not possible. In addition, natural "hazards" can occur, such as the berries being eaten by birds. Flies and other insects were seen on some pictures, making them useless for measurements. Fungi and insects find favorable conditions in the sheltered situation during summertime, which means that the roof and side protection of the hut have to be removed in summer.

The cameras and the other outside equipment need to function in a temperature range from  $-15$  to  $+35^{\circ}\text{C}$ . This is quite a technical challenge. Thus the status quo described is a compromise, yet one that meets our needs and proved successful.

The hut construction leads to very small, but measurable greenhouse effects on warm, sunny days. A possible influence could not be estimated in the present experimental setting; a closed, air-conditioned system would be necessary for comparison.

Certain other influences could not or cannot easily be detected. For instance, do the LED flashlights (Jeong et al., 2012) or the electromagnetic fields around the berries (arising from the camera, the light and the "trigger-finger") influence or distort the biological object? And if so, how severe is the influence and/or is it negligible?

To reduce the influence of the artificial lighting, it is set to turn on each hour for only 3 s with a smooth run-in and fade-out phase. Nevertheless it is not possible to eliminate the possibility of light influence since light is regarded as the most important trigger in chronobiology (Young and Kay, 2001; Dunlap et al., 2004).

The need to obtain optimum photographic contours of the berries with negligible biological effects necessitated a long sequence of experiments, and some aspects could still be improved. However, the methods used are well-suited to the

task and yielded robust results. As shown elsewhere (Derbridge et al., 2013) and confirmed here, a compromise between external observation and repeatable and comparable results is possible.

## Research Questions Raised by the Results

The demonstrated fact, that the change in profile form of a biological organ (a mistletoe berry) can be accurately described with a particular mathematical form (a path curve from projective geometry), and about using path curves in describing the dynamics of form in phenotype, invite questions about the link between form and biology. The phenomena observed could open up new aspects in this field, which is a highly topical one in current biology (Müller and Newman, 2003; Dornbusch et al., 2012; Newman and Linde-Medina, 2013). A next step could be to enquire further into the physiological origin of the change of form.

Many scientific and laymen authors have been fascinated by the occurrence of mathematical form in biology (Arber, 1950; Kapraff, 2002), yet they rarely explain scientifically how that correlation comes about. In some cases, such as golden section geometry in the seed order of a sunflower, the phenomenon can be explained by means of optimum space use as a useful adaptation. Yet the precise adaptation values of those forms or patterns has not, or cannot be explained, because many other options would lead to similar success (Müller and Newman, 2003; Dornbusch et al., 2012; Newman and Linde-Medina, 2013). Ultimately the old questions (e.g., “what is form?”) remain, and we will probably continue to ponder them for as long as scientists seek to understand how form and structure arise in evolution in an ordered and purposeful way (West-Eberhard, 1989; Waldrop, 1992; Carroll, 2005; Kirschner and Gerhart, 2006; Holland, 2010).

## Future Research

The results presented here are pertinent and raise a wide range of questions for future studies. Ongoing research will continue to focus on rhythms and their correlations at a macro-phenotypic level. Further research is needed to explain and better understand the connection between form and function in the case of rhythmic change of shapes. As yet we do not know how general it is for plant organs to follow a mathematical or projective geometrical form. But clearly, “form follows function” is not a satisfying answer here, since there is no recognizable function prior to the phenomenon. If fruiting and ripening have a biological function alongside the obvious and well-studied function of seed production, further research may change how we look at plants in many ways. The empirical data introduced here need to be integrated into a theoretical context, which could open up a novel field of potential inquiries. One of the first

steps would be, for instance, to examine other plants (fruits) to discover whether the phenomenon of rhythmic change of form in mistletoe is an exception or not. Likewise, it would be of great interest to study morphological change in different species to ascertain differences from or similarities to the phenomena identified here.

The results of the present study set a clear path to continue the investigation and extend its applications to different objects that follow path curves, such as other berries, buds, and to other research. As showed by Edwards (2006), the heartbeat can be also modeled with path curves. This may be true of other living organisms and processes that have not yet been explored in this way.

## AUTHOR CONTRIBUTIONS

RD and SB conceived and designed the study, with suggestions from PH. RD performed the experiment set-up, collected the data and analyzed them. RD and SB did the statistics. RD wrote the main manuscript, and all authors reviewed the manuscript.

## FUNDING

This paper is part of a research project partly funded by the “Software AG Stiftung,” Darmstadt, Germany (<http://www.software-ag-stiftung.com/>). The funder had no role in study design, data collection and analysis, decision to publish, or preparation of the manuscript.

## ACKNOWLEDGMENTS

Special thanks are due to the late Joan Davis and Johannes Wirz for helpful comments on the manuscript. We also thank Nick Thomas for letting us use his graph of a path curve and of Lambda in path curves (Figure 5) and Hartmut Ramm for contributing the longitudinal-section photo of a mistletoe berry (Figure 12). Thanks to Laura Liska and Matthew Barton for improving style and language of the manuscript. We also would like to attribute our gratitude to the reviewers who substantially helped to improve the manuscript.

## SUPPLEMENTARY MATERIAL

The Supplementary Material for this article can be found online at: <http://journal.frontiersin.org/article/10.3389/fpls.2016.01749/full#supplementary-material>

## REFERENCES

- Arber, A. (1950). *Natural Philosophy of Plant Form*. Cambridge: Cambridge University Press.  
Asanidze, Z., Akhalkatsi, M., and Gvritishvili, M. (2011). Comparative morphometric study and relationships between the Caucasian species of

- wild pear (*Pyrus* spp.) and local cultivars in Georgia. *Flora* 206, 974–986. doi: 10.1016/j.flora.2011.04.010  
Azuma, J. I., Kim, N. H., Heux, L., Vuong, R., and Chanzy, H. (2000). The cellulose system in viscin from mistletoe berries. *Cellulose* 7, 3–19. doi: 10.1023/A:1009223730317

- Barbeta, A., Ogaya, R., and Penuelas, J. (2012). Comparative study of diurnal and nocturnal sap flow of *Quercus ilex* and *Phillyrea latifolia* in a Mediterranean holm oak forest in Prades (Catalonia, NE Spain). *Trees* 26, 1651–1659. doi: 10.1007/s00468-012-0741-4
- Barlow, P. W., Mikulecký, M., and Střestík, J. (2010). Tree-stem diameter fluctuates with the lunar tides and perhaps with geomagnetic activity. *Protoplasma* 247, 25–43. doi: 10.1007/s00709-010-0136-6
- Baumgartner, S., Flückiger, H., and Ramm, H. (2004). Mistletoe berry shapes and the zodiac. *Archetype* 10, 1–20.
- Becker, H. (1986). Botany of European mistletoe (*Viscum album* L.). *Oncology* 43(Suppl. 1), 2–7. doi: 10.1159/000226413
- Beersma, D. G., Daan, S., and Hut, R. A. (1999). Accuracy of circadian entrainment under fluctuating light conditions: contributions of phase and period response. *J. Biol. Rhythms* 14, 320–329. doi: 10.1177/074873099129000858
- Bell-Pedersen, D., Cassone, V. M., Earnest, D. J., Golden, S. S., Hardin, P. E., Thomas, T. L., et al. (2005). Circadian rhythms from multiple oscillators: lessons from diverse organisms. *Nat. Rev. Genet.* 6, 544–556. doi: 10.1038/nrg1633
- Büssing, A. (2000). *Mistletoe. The Genus Viscum*. Reading: Harwood Academic Publishers.
- Carroll, S. (2005). *Endless Forms Most Beautiful: The New Science of Evo Devo*. New York City, NY: W. W. Norton & Company.
- Čermák, J., Ulehla, J., Kučera, J., and Penka, M. (1982). Sap flow rate and transpiration dynamics in the full-grown oak (*Quercus robur* L.) in floodplain forest exposed to seasonal floods as related to potential evapotranspiration and tree dimensions. *Biol. Plant.* 24, 446–460. doi: 10.1007/BF02880444
- Chambers, J. M., Cleveland, W. S., Kleiner, B., and Tukey, P. A. (1983). “Smoothing by lowess in graphical methods for data analysis,” in *Graphical Methods for Data Analysis*, eds J. M. Chambers, W. S. Cleveland, B. Kleiner, and P. A. Tukey (Belmont, CA: Wadsworth International Group), 94–104.
- Chitwood, D. H. (2014). A modern ampelography: a genetic basis for leaf shape and venation patterning in grape. *Plant Physiol.* 164, 259–272. doi: 10.1104/pp.113.229708
- Clopper, A. (1994). Path curves, an introduction to the work of L. Edwards on bud forms. *Open Syst. Inf. Dyn.* 2, 265–277. doi: 10.1007/BF02228852
- Deridge, R., Feiten, L., Conradt, O., Heusser, P., and Baumgartner, S. (2013). Assessment of shape changes of mistletoe berries: a new software approach to automatize the parameterization of path curve shaped contours. *PLoS ONE* 8:e60522. doi: 10.1371/journal.pone.0060522
- Dodd, A. N., Salathia, N., Hall, A., Kévei, E., Tóth, R., Nagy, F., et al. (2005). Plant circadian clocks increase photosynthesis, growth, survival, and competitive advantage. *Science* 309, 630–633. doi: 10.1126/science.1115581
- Dorka, R., Miersch, O., Wasternack, C., and Weik, P. (2007). Chronobiological phenomena and seasonal changes in jasmonate levels during the course of the year and under constant conditions in mistletoe (*Viscum album* L.). *Phytomedicine* 14, 7–15.
- Dornbusch, T., Lorrain, S., Kuznetsov, D., Fortier, A., Liechti, R., Xenarios, I., et al. (2012). Measuring the diurnal pattern of leaf hyponasty and growth in *Arabidopsis* – a novel phenotyping approach using laser scanning. *Funct. Plant Biol.* 39, 860–869. doi: 10.1071/FP12018
- Dunlap, J., Loros, J., and DeCoursey, P. (2004). *Chronobiology: Biological Timekeeping*. Sunderland: Sinauer Associates.
- Dunlap, J. C. (1999). Molecular bases for circadian clocks. *Cell* 96, 271–290. doi: 10.1016/S0092-8674(00)80566-8
- Edwards, L. (2003). *Projective Geometry*. Edinburgh: Floris Books.
- Edwards, L. (2006). *The Vortex of Life: Nature's Patterns in Space and Time*. Edinburgh: Floris Books.
- Flückiger, H., and Baumgartner, S. (2003). Shape changes of ripening mistletoe berries. *Archetype* 9, 1–13.
- Forster, M. (2014). How significant is nocturnal sap flow? *Tree Physiol.* 34, 757–765. doi: 10.1093/treephys/tpu051
- Granier, A., Anfodillo, T., Sabatti, M., Cochard, H., Dreyer, E., Tomasi, M., et al. (1994). Axial and radial water flow in the trunks of oak trees: a quantitative and qualitative analysis. *Tree Physiol.* 14, 1383–1396. doi: 10.1093/treephys/14.12.1383
- Holland, J. H. (2010). *Emergence from Chaos to Order*. Oxford: Oxford University Press.
- Jeong, S. W., Park, S., Jin, J. S., Seo, O. N., Kim, G. S., Kim, Y. H., et al. (2012). Influences of four different light-emitting diode lights on flowering and polyphenol variations in the leaves of *Chrysanthemum* (*Chrysanthemum morifolium*). *J. Agric. Food Chem.* 60, 9793–9800. doi: 10.1021/jf302272x
- Ji-xiang, D. J., Zhai, C., and Wang, Q. (2013). Recognition of plant leaf image based on fractal dimension features. *Neurocomputing* 116, 150–156. doi: 10.1016/j.neucom.2012.03.028
- Kappraff, J. (2002). *Beyond Measure: A Guided Tour Through Nature, Myth, and Number*. River Edge, NJ: World Scientific.
- Kirschner, M., and Gerhart, J. (2006). *The Plausibility of Life*. New Haven, CT: Yale University Press.
- Klein, F. (2006). *Einleitung in die höhere Geometrie . . . Von F Klein. Ausgearb. Von Fr. Schilling*. Ann Arbor, MI: University of Michigan Library.
- Klein, F. (2013). *Vorlesungen über Nicht-Euklidische Geometrie*, Vol. 26. Berlin: Springer-Verlag.
- Klein, G. (2007). *Farewell to the Internal Clock. A Contribution in the Field of Chronobiology*. New York, NY: Springer Science+Business Media.
- Kondo, T., and Ishiura, M. (1999). The circadian clocks of plants and cyanobacteria. *Trends Plant Sci.* 4, 171–176. doi: 10.1016/S1360-1385(99)01410-7
- Li, Y., and Gu, P. (2004). Free-form surface inspection techniques state of the art review. *Comput. Aided Des.* 36, 1395–1417. doi: 10.1016/j.cad.2004.02.009
- Lonergran, T. A. (1985). Regulation of cell shape in *Euglena gracilis*. *J. Cell Sci.* 77, 197–208.
- Müller, G., and Newman, S. (2003). *Origination of Organismal Form: Beyond the Gene in Developmental and Evolutionary Biology*. Cambridge: MIT Press.
- Newman, S., and Linde-Medina, M. (2013). Physical determinants in the emergence and inheritance of multicellular form. *Biol. Theory* 8, 274–285. doi: 10.1007/s13752-013-0116-0
- Pfautsch, S., Keitel, C., Turnbull, T. L., Braimbridge, M. J., Wright, T. E., Simpson, R. R., et al. (2011). Diurnal patterns of water use in *Eucalyptus viminalis* indicate pronounced desiccation-rehydration cycles despite unlimited water supply. *Tree Physiol.* 31, 1041–1051. doi: 10.1093/treephys/tp082
- Pfeuty, B., Thommen, Q., Corellou, F., Djouani-Tahri, el B., Bouget, F. Y., and Lefranc, M. (2012). Circadian clocks in changing weather and season: lessons from the picoalgae *Ostreococcus tauri*. *Bioessays* 34, 781–790. doi: 10.1002/bies.201200012
- Pivar, S. (2009). *On the Origin of Form: Evolution by Self-Organization*. Berkeley, CA: North Atlantic Books.
- Roenneberg, T., and Foster, R. G. (1997). Twilight times: light and circadian system. *Photochem. Photobiol.* 66, 549–561. doi: 10.1111/j.1751-1097.1997.tb03188.x
- Sallé, G. (1983). “Germination and establishment of *Viscum album* L.” in *The Biology of Mistletoes*, eds M. Calder and P. Bernhardt (Sydney, NSW: Academic Press), 145–159.
- Schwartz, J. (2013). Emergence of shape. *Biol. Theory* 8, 209–210. doi: 10.1007/s13752-013-0133-z
- Somer, D. E., Devin, P. F., and Kay, S. A. (1998). Phytochromes and cryptochromes in the entrainment of the *Arabidopsis* circadian clock. *Science* 282, 1488–1490. doi: 10.1126/science.282.5393.1488
- Stoleru, D., Peng, Y., and Rosbach, M. (2004). Coupled oscillators control morning and evening locomotor behaviour of *Drosophila*. *Science* 31, 862–864.
- Thompson, D. (1992). *On Growth and Form*. Mineola, NY: Dover Publications.
- Trivedi, A. K., Rani, S., and Kumar, V. (2013). Circadian adaptation to seasons: effects on activity behavior in subtropical house sparrow, *Passer domesticus*. *Biol. Rhythm Res.* 45, 465–475. doi: 10.1080/09291016.2013.850888
- Troein, C., Corellou, F., Dixon, L. E., van Ooijen, G., O'Neill, J. S., Bouget, F. Y., et al. (2011). Multiple light inputs to a simple clock circuit allow complex biological rhythms. *Plant J.* 66, 375–385. doi: 10.1111/j.1365-313X.2011.04489.x
- Urech, K., Schaller, G., and Jäggy, C. (2006). Viscotoxins, mistletoe lectins and their isoforms in mistletoe (*Viscum album* L.) extracts Iscador. *Arzneimittelforschung* 56, 428–434.
- Vesala, T., Sevanto, S., Paatero, P., Nikinmaa, E., Peramaki, M., Ala-Nissila, T., et al. (2000). Do tree stems shrink and swell with the tides? *Tree Physiol.* 20, 633–635. doi: 10.1093/treephys/20.9.633
- Waldrop, M. M. (1992). *Complexity. The Emerging Science at the Edge of Order and Chaos*. New York City, NY: Simon & Schuster.
- West-Eberhard, M. J. (1989). Phenotypic plasticity and the origins of diversity. *Annu. Rev. Ecol. Syst.* 20, 249–278. doi: 10.1146/annurev.es.20.110189.001341

- Yakir, E., Hilman, D., Harir, Y., and Green, R. M. (2007). Regulation of output from the plant circadian clock. *FEBS J.* 274, 335–345. doi: 10.1111/j.1742-4658.2006.05616.x
- Yoshii, T., Vanin, S., Costa, R., and Helfrich-Förster, C. (2009). Synergic entrainment of *Drosophila*'s circadian clock by light and temperature. *J. Biol. Rhythms* 6, 452–464. doi: 10.1177/0748730409348551
- Young, M. W., and Kay, S. A. (2001). Time zones: a comparative genetics of circadian clocks. *Nat. Rev. Genet.* 2, 702–715. doi: 10.1038/35088576
- Zürcher, E. (2001). “Lunar rhythms in forestry traditions – lunar-correlated phenomena in tree biology and wood properties,” in *Earth-Moon Relationships*, eds C. Barbieri and F. Rampazzi (Dordrecht: Springer), 463–478.
- Zürcher, E., Cantiani, M. G., Sorbetti-Guerri, F., and Michel, D. (1998). Tree stem diameters fluctuate with tide. *Nature* 392, 665–666. doi: 10.1007/s00709-010-0136-6

**Conflict of Interest Statement:** The authors declare that the research was conducted in the absence of any commercial or financial relationships that could be construed as a potential conflict of interest.

Copyright © 2016 Derbridge, Baumgartner and Heusser. This is an open-access article distributed under the terms of the Creative Commons Attribution License (CC BY). The use, distribution or reproduction in other forums is permitted, provided the original author(s) or licensor are credited and that the original publication in this journal is cited, in accordance with accepted academic practice. No use, distribution or reproduction is permitted which does not comply with these terms.



# Co-ordination in Morphological Leaf Traits of Early Diverging Angiosperms Is Maintained Following Exposure to Experimental Palaeo-atmospheric Conditions of Sub-ambient O<sub>2</sub> and Elevated CO<sub>2</sub>

Christiana Evans-Fitz.Gerald<sup>1,2\*</sup>, Amanda S. Porter<sup>1,2</sup>, Charilaos Yiotis<sup>1,2</sup>, Caroline Elliott-Kingston<sup>3</sup> and Jennifer C. McElwain<sup>1,2</sup>

<sup>1</sup> Earth Institute, O'Brien Centre for Science, University College Dublin, Dublin, Ireland, <sup>2</sup> School of Biology and Environmental Science, University College Dublin, Dublin, Ireland, <sup>3</sup> School of Agriculture and Food Science, University College Dublin, Dublin, Ireland

## OPEN ACCESS

### Edited by:

Daniel H. Chitwood,  
Donald Danforth Plant Science  
Center, USA

### Reviewed by:

Victoria Fernandez,  
Technical University of Madrid, Spain  
Stanislaus Josef Schymanski,  
ETH Zurich, Switzerland

### \*Correspondence:

Christiana Evans-Fitz.Gerald  
crissyevans@gmail.com

### Specialty section:

This article was submitted to  
Plant Biophysics and Modeling,  
a section of the journal  
*Frontiers in Plant Science*

Received: 31 May 2016

Accepted: 29 August 2016

Published: 15 September 2016

### Citation:

Evans-Fitz.Gerald C, Porter AS,  
Yiotis C, Elliott-Kingston C and  
McElwain JC (2016) Co-ordination  
in Morphological Leaf Traits of Early  
Diverging Angiosperms Is Maintained  
Following Exposure to Experimental  
Palaeo-atmospheric Conditions of Sub-ambient O<sub>2</sub> and Elevated  
CO<sub>2</sub>. *Front. Plant Sci.* 7:1368.  
doi: 10.3389/fpls.2016.01368

In order to be successful in a given environment a plant should invest in a vein network and stomatal distribution that ensures balance between both water supply and demand. Vein density ( $D_v$ ) and stomatal density (SD) have been shown to be strongly positively correlated in response to a range of environmental variables in more recently evolved plant species, but the extent of this relationship has not been confirmed in earlier diverging plant lineages. In order to examine the effect of a changing atmosphere on the relationship between  $D_v$  and SD, five early-diverging plant species representing two different reproductive plant grades were grown for 7 months in a palaeo-treatment comprising an O<sub>2</sub>:CO<sub>2</sub> ratio that has occurred multiple times throughout plant evolutionary history. Results show a range of species-specific  $D_v$  and SD responses to the palaeo-treatment, however, we show that the strong relationship between  $D_v$  and SD under modern ambient atmospheric composition is maintained following exposure to the palaeo-treatment. This suggests strong inter-specific co-ordination between vein and stomatal traits for our study species even under relatively extreme environmental change. This co-ordination supports existing plant function proxies that use the distance between vein endings and stomata ( $D_m$ ) to infer plant palaeo-physiology.

**Keywords:** vein density, stomatal density, co-ordination, plant growth chambers, palaeo-atmosphere

## INTRODUCTION

Global diversity in plant and leaf architecture reflects a plasticity in morphology that allows plants to survive in a range of environments (Díaz et al., 2016). In this current era of rapid climate change, understanding the relationships between plant morphological traits and how they might be influenced by the surrounding environment is of the utmost importance, enabling predictions of plant responses over the coming decades as atmospheric carbon dioxide (CO<sub>2</sub>) rises. Plants

are a critical component of the hydrological cycle, influencing the amount of water vapor that is returned to the atmosphere via the process of transpiration (Rodell et al., 2015). The predicted future increases in CO<sub>2</sub> and global temperatures will have an impact on plant physiological function and morphological traits and will consequently influence the hydrological cycle (Gedney et al., 2006; Betts et al., 2007). The present study focuses on vein and stomatal density (SD), two plant morphological traits that play a pivotal role in the transpirational pathway, and attempts to understand how one may influence the other as a plant encounters environmental change.

Stomata are microscopic pores on a leaf surface that regulate gas exchange. CO<sub>2</sub> from the atmosphere which is essential for photosynthesis is exchanged for water vapor from the inside of the leaf (Jones, 1992). Stomata respond to environmental cues, opening in response to increasing light, low carbon dioxide, and high humidity (Assmann, 1999; Outlaw, 2003; See review by Roelfsema and Hedrich, 2005; Vavasseur and Raghavendra, 2005; Shimazaki et al., 2007; Lawson, 2009). Stomatal opening results in an increase in stomatal pore aperture which leads to an increase in both carbon uptake and water loss from the leaf. SD is the number of stomata per mm<sup>2</sup> of leaf tissue and it is determined by various genetic (Nadeau and Sack, 2002; Shpak et al., 2005) and environmental factors (McElwain and Chaloner, 1995; Woodward and Kelly, 1995; Casson and Gray, 2008). A change in SD alters gas exchange along the plants' diffusional pathway, influencing transpiration and therefore water demand. Veins are found in the leaves of plants, and are differentiations of the vascular bundles that transport water and nutrients from the soil to leaves, as well as sucrose from leaves to the storage sites of the plant (Sack and Holbrook, 2006). A network of major and minor veins (some species only have major veins) carries water throughout the leaf tissue to the stomata where it is lost to the atmosphere as water vapor. Vein density ( $D_v$ ) is the length of veins per leaf area (mm mm<sup>-2</sup>), and in angiosperms it is determined predominantly by the minor veins, as they make up >80% of the total vein length of the leaf (Sack et al., 2012). Minor vein density has been shown to be an important functional plant trait, exerting a strong influence over xylem conductivity ( $K_x$ ) and outside xylem conductivity ( $K_{ox}$ ), parameters that determine leaf hydraulic conductance ( $K_{leaf}$ ) (Sack and Frole, 2006; McKown et al., 2010). Thus it could be said that in the same way that SD and size influence the water demands of a plant, the vein architecture influences its water supply.

In order to be successful in a given environment a plant should invest in a vein network and stomatal distribution that ensures balance between both water supply and demand. Maintaining this balance via co-ordinated shifts in venation and stomatal traits should ensure that the plant is operating at optimal efficiency in terms of carbon uptake and water loss, conforming to the optimality principle (Sack and Scoffoni, 2013). Previous studies have found a strong relationship between  $D_v$  and SD in response to light (Brodribb and Jordan, 2011) and vapor pressure deficit (Carins Murphy et al., 2014) in certain derived plant species and between SD and transpiration ( $T$ ) across a range of ferns, conifers, and angiosperms from both tropical and temperate ecosystems (Boyce et al., 2009).  $D_v$  and SD have been shown

to be strongly correlated with modeled maximum theoretical stomatal conductance ( $g_{max}$ ) in a diverse range of Proteaceae species (Brodribb et al., 2013). Furthermore, a recent study using a range of modern and basal plant species grown in greenhouse conditions has also reported a strong correlation between  $D_v$  and  $g_{max}$  (McElwain et al., 2016b), suggesting that this balance does indeed exist. Moreover, other studies combine anatomical and physiological measurements to uncover the links between the architectural properties of a leaf and photosynthetic potential. For example, a proxy for leaf photosynthetic capacity has been developed based on the mesophyll path length ( $D_m$ ) between vein endings and stomata. In multi-veined species, veins should be optimally placed to minimize  $D_m$  ensuring maximum photosynthetic capacity (Brodribb et al., 2007). These results together demonstrate the potential link between leaf hydraulic morphology and photosynthetic physiology and also highlight the ability of plants to maintain a balance between leaf phenotypic traits under environmental change.

The co-ordination between water supply ( $D_v$ ) and demand (SD) traits is critical to plant success and the relationship between the two seems to be conserved across the major plant groups under present day atmospheric conditions (Boyce et al., 2009; Brodribb and Jordan, 2011; Brodribb et al., 2013; Carins Murphy et al., 2014; McElwain et al., 2016b). However, it is not known whether this relationship is maintained when levels of oxygen (O<sub>2</sub>) and CO<sub>2</sub> in the atmosphere change. Co-ordination between these two morphological traits may have been critical throughout the past 400 million years during times of fluctuating atmospheric O<sub>2</sub> and CO<sub>2</sub>. Maintaining this balance between water supply and demand may have allowed certain species to operate more efficiently in their environment. For example, it has been widely proposed that the co-evolution of leaf traits (an increase in  $D_v$  and SD) during the Cretaceous decline in atmospheric CO<sub>2</sub> allowed angiosperms to outcompete other plant groups as they transitioned from predominantly moist to drier habitats (Boyce and Zwieniecki, 2012; de Boer et al., 2012; McElwain et al., 2016b).

Stomatal density has been shown to be inversely proportional to atmospheric CO<sub>2</sub> (McElwain and Chaloner, 1995; Woodward and Kelly, 1995; Beerling and Woodward, 1996; Royer, 2001; Konrad et al., 2008; Franks and Beerling, 2009a,b) and it has been accepted as a palaeo-environmental proxy for CO<sub>2</sub> on this basis. Studies examining SD responses to concurrent changes in atmospheric O<sub>2</sub> and CO<sub>2</sub> are scarce, as are those investigating  $D_v$  responses to atmospheric change. In one of the few studies, examining both living and herbarium material of *Acer monspessulanum* L. and *Quercus petraea* Liebl, no change was observed in  $D_v$  in response to an increase in CO<sub>2</sub> from 280 to 350 ppm (Uhl and Mosbrugger, 1999). However, in other studies  $D_v$  has been shown to respond to environmental change (Brodribb and Jordan, 2011; Sack and Scoffoni, 2013; Carins Murphy et al., 2014) and has also been used in models to predict both atmospheric carbon dioxide partial pressure and temperature (Blonder and Enquist, 2014). Furthermore,  $D_v$  has the potential to be a useful palaeo-environmental proxy, as venation networks are often preserved in fossilized plant material. For example, studies have shown an increase in  $D_v$

in angiosperms during the Cretaceous period when CO<sub>2</sub> was declining (Feild et al., 2011a; Boyce and Zwieniecki, 2012).

Using a range of early diverging plant species (**Figure 1**), this study examines for the first time the effect of changing atmospheric conditions on the relationship between  $D_v$ , SD, and  $g_{\max}$ . Using four angiosperm and one fern species, the plasticity and co-ordination of these morphological plant traits was assessed in a low O<sub>2</sub>/high CO<sub>2</sub> atmosphere. In the context of this study, co-ordination in plant traits refers to either inter-specific or intra-specific co-ordination. Inter-specific co-ordination is taken to mean an observable trend in morphological plant traits across the experimental species. Intra-specific co-ordination on the other hand, is when the direction of change of plant traits is the same within a single species. We acknowledge that the number of species studied here is relatively small and experimental conditions limited to one palaeo-treatment, and as such, results discussed here are merely intended to be a suggestion of the possible behavior of early diverging plant species under changing atmospheric conditions. Further studies using a wider range of species and palaeo-treatments will build on the current study and will allow more robust conclusions to be drawn.

Results were used to determine the robustness of plant function proxies that rely on co-ordination in morphological traits (such as the use of  $D_m$  as a proxy for palaeo-assimilation rate (Brodribb et al., 2007; Wilson et al., 2015)), specifically when applied at times of the geological past when the atmospheric composition was different from that of today. Theoretical maximum stomatal conductance ( $g_{\max}$ ) is a plant functional trait calculated using both SD and anatomical measurements of stomatal geometry (Franks and Beerling, 2009a). This trait has

been used in palaeo-CO<sub>2</sub> proxy models (Franks et al., 2014) to infer past CO<sub>2</sub> levels from the stomatal conductance ( $g_s$ ) of ancient fossil species. The extent of the relationship between  $g_{\max}$  and operational stomatal conductance ( $g_{op}$ ) has been shown in two angiosperm species (Franks et al., 2009; Dow et al., 2014) and more recently in a range of basal angiosperm, gymnosperm, and fern species (McElwain et al., 2016b). Across this range of basal species  $g_{\max}$  and  $g_{op}$  were found to be strongly related ( $r^2 = 0.54$ ), with a scaling relationship of  $g_{op} = 0.25 g_{\max}$ . Therefore  $g_{\max}$  was used in the current study as a means to infer changes in physiological behavior with a change in the concentration of O<sub>2</sub> and CO<sub>2</sub> and to relate this to changes in  $D_v$ .

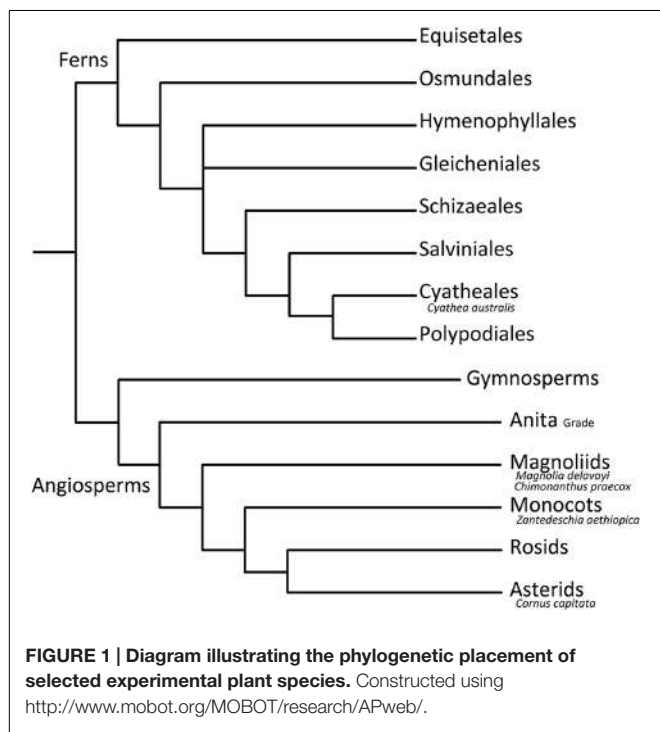
## MATERIALS AND METHODS

### Species and Growth Conditions

Plant species from two different evolutionary plant groups, ferns (*Cyathea australis*) and angiosperms (*Chimonanthus praecox*, *Magnolia delavayi*, *Cornus capitata*, and *Zantedeschia aethiopica*), were grown for approximately 7 months in Conviron (Winnipeg, MB, Canada) BDW-40 walk-in plant growth chambers at PÉAC (Programme for Experimental Atmospheres and Climate), Rosemount Environmental Research Station, University College Dublin. For each of these plant groups, the earliest diverging species obtainable from each plant family was used in order to follow the nearest living relative (NLR) protocol (Mosbrugger, 2009), whereby the responses of extant plant species can be said to reflect the responses of their extinct relatives. Growth conditions were set to ambient (two chambers at 21% O<sub>2</sub> and 400 ppm CO<sub>2</sub>, O<sub>2</sub>:CO<sub>2</sub> ratio of 525) and a palaeo-treatment of low O<sub>2</sub>/high CO<sub>2</sub> (three chambers at 16% O<sub>2</sub> and 1900 ppm CO<sub>2</sub>, O<sub>2</sub>:CO<sub>2</sub> ratio of 84.21). These conditions represent prehistoric modeled atmospheres (Bergman et al., 2004; Berner, 2009) that likely occurred multiple times throughout the last 400 million years, for example in the Devonian (~ 419–359 mya), the late Triassic (~ 218–201 mya), and Jurassic periods (~ 201–145 mya) (Willis and McElwain, 2014). Plants were given water and nutrients according to the individual species requirements (See Supplementary Table S1). Chambers were set to a 16 h day/8 h night schedule, with day/night temperatures of 20°C/15°C, relative humidity of 65% and a photosynthetic photon flux density (PPFD) of 600 μmol m<sup>-2</sup> s<sup>-1</sup>.

### SD, $D_v$ , and $g_{\max}$ Quantification

SD and  $D_v$  were quantified on three leaves per plant, and three to four plants per species per treatment using a modified vein density protocol (Berlyn and Miksche, 1976; Perez-Harguindeguy et al., 2013). Leaves were cleared in 5% NaOH, bleached, and then brought through a series of 30, 50, 70, and 100% ethanol. Leaves were then stained using Safranin and Fast Green before being brought back through the ethanol series in the reverse order (100–30% ethanol). Leaves were then suspended in distilled water before being mounted on glass slides for microscopy. For SD quantification, multiple images (on average six images) were taken over an area of approximately 1 cm<sup>2</sup> per leaf and stomatal counts performed using Image J software inside



a superimposed grid of 0.09 mm<sup>2</sup> on each image (this area was already determined to be the most representative of the entire leaf using the protocol of Poole and Kürschner (1999) from Jones and Rowe (1999)). For  $D_v$  quantification, images were taken on three areas of each leaf (an area of approximately 2 mm<sup>2</sup> near the tip, center, and bottom of the leaf near the petiole) and using Image J software the length of veins in these areas was manually traced (using a Wacom Intuos4 pen tablet) and  $D_v$  calculated in Excel. Minor  $D_v$  is independent of leaf size and accounts for the majority (>80%) of total vein length per area in most angiosperms (Sack et al., 2012), therefore vein length per area was calculated only on minor veins (quaternary orders upward), major veins being excluded from analysis. Images were taken using a Leica DM2500 microscope with Leica DFC300FX camera (Leica® Microsystems, Wetzlar, Germany) attached and Syncroscopy Automontage (Syncroscopy, Cambridge, UK) digital imaging software was used to impose grids and scale bars on each image.

For  $g_{\max}$  quantification, anatomical measurements of 90 to 120 stomata per species and per treatment were obtained using the same images used for SD determination (See Table 1 for parameter values).  $g_{\max}$  was calculated using the following diffusion equation (Parlange and Waggoner, 1970; Franks and Beerling, 2009a):

$$g_{\max} = \frac{\left(\frac{dw}{v} \cdot SD \cdot pa_{\max}\right)}{pd + \frac{\Pi}{2} \cdot \sqrt{\frac{pa_{\max}}{\Pi}}} \quad (1)$$

$dw$  = diffusivity of water vapor at 25°C (0.0000249 m<sup>2</sup> s<sup>-1</sup>),  $v$  = molar volume of air (0.0224 m<sup>3</sup> mol<sup>-1</sup>),  $SD$  = Stomatal density (m<sup>-2</sup>),  $pa_{\max}$  = max stomatal pore area (m<sup>2</sup>),  $pd$  = stomatal pore depth (m). The maximum stomatal pore area was calculated (treating the pore as an ellipse) by using stomatal pore length as the long axis, pore length/2 as the short axis and taking the stomatal pore depth as being equal to the width of a fully turgid guard cell (Franks and Beerling, 2009a,b). It is important to note here that guard cells examined in the current study were not experimentally maintained at maximum turgor before anatomical measurements were made. Even though this might lead to a slight underestimation of  $g_{\max}$ , this approach is in line with that used in many other palaeo-studies (Franks and Beerling, 2009a,b).

## Vein density responses of a selection of non-angiosperm species from 2009 palaeo-experiment

In order to assess whether other non-angiosperm species show a change in  $D_v$  under different atmospheric compositions, dried plant material from a previous palaeo-experiment was analyzed for  $D_v$ . Representatives of both the gymnosperms (*Agathis australis*, *Lepidozamia peroffskyana*, and *Ginkgo biloba*) and ferns (*Osmunda regalis*) were grown for 18 months in walk-in Conviron growth chambers in both an ambient and low O<sub>2</sub>/high CO<sub>2</sub> atmosphere (Ambient treatment: 20.9% O<sub>2</sub> and 380 ppm CO<sub>2</sub>, low O<sub>2</sub>/high CO<sub>2</sub> treatment: 13% O<sub>2</sub> and 1500 ppm CO<sub>2</sub>,

	$SD \text{ mm}^{-2}$		$D_v \text{ mm mm}^{-2}$		$Pore length \mu\text{m}$		$Pore depth \mu\text{m}$		$g_{\max} \text{ mmol m}^{-2}\text{s}^{-1}$	
	Ambient (n = 12)	Palaeo (n = 12)	Ambient (n = 12)	Palaeo (n = 12)	Ambient (n = 12)	Palaeo (n = 12)	Ambient (n = 12)	Palaeo (n = 12)	Ambient (n = 12)	Palaeo (n = 12)
<i>Chimonanthus praecox</i>	513 ± 103.2	390 ± 102.2	8.3 ± 0.8	7.0 ± 1.0	10.4 ± 1.0	10.9 ± 1.0	3.8 ± 0.3	3.4 ± 0.3	2300 ± 279.0	1923 ± 298.9
<i>Magnolia delavayi</i>	343 ± 48.2	316 ± 72.7	6.6 ± 0.5	6.7 ± 1.1	8.9 ± 0.9	8.7 ± 0.8	5.8 ± 0.9	5.6 ± 0.9	1018 ± 210.8	908 ± 201.3
<i>Conus capitata</i>	193 ± 21.8	210 ± 34.6	4.4 ± 0.3	5.1 ± 0.5	10.3 ± 0.5	10.3 ± 0.5	6.5 ± 0.6	5.9 ± 0.6	671 ± 74.3	774 ± 156.5
<i>Zantedeschia aethiopica</i>	104 ± 20.4	68 ± 14.7	4.3 ± 0.5	3.8 ± 0.2	15.9 ± 1.7	16.0 ± 0.9	8.6 ± 0.5	8.3 ± 0.5	599 ± 108.6	406 ± 75.0
<i>Cyathea australis</i>	171 ± 50.3	145 ± 50.5	3.3 ± 0.2	2.8 ± 0.2	12.4 ± 1.4	13.6 ± 1.7	9.4 ± 0.8	9.4 ± 0.5	649 ± 213.4	635 ± 216

TABLE 1 | Measured parameters (± standard deviation) for experimental species.

$O_2:CO_2$  ratios 552.63 and 86.67, respectively). These species have either parallel or dichotomously branching major veins, therefore it was not necessary to clear and stain leaves for  $D_v$  observation.  $D_v$  was calculated on one leaf per plant and three plants per species per treatment. Leaves were imaged using a Nikon SMZ1000 stereomicroscope with Leica DFC490 camera attached (Leica® Microsystems, Wetzlar, Germany), and using Image J software the length of veins was manually traced and  $D_v$  calculated in Excel in an area between 20 mm<sup>2</sup> and 60 mm<sup>2</sup>.

## Statistical Analysis

Data were first checked for normal distribution and Generalized Linear Models were run in Minitab (version 16.1.1) statistical software to investigate differences in SD,  $D_v$ , and  $g_{max}$  between treatments. Minitab (version 16.1.1) statistical software was also used for correlation tests, boxplot representation of data, and to graphically display percent changes in SD,  $D_v$ , and  $g_{max}$ . RStudio (version 0.99.489) was used for Standardised Major Axis (SMA) regression analysis and for scatterplot representation of data.

## RESULTS

Species show a varied and species-specific response in SD,  $D_v$ , and  $g_{max}$  to the palaeo-treatment (**Figure 2**; **Table 1**). A significant decrease in SD is seen in two species (*Chimonanthus praecox* shows a 24% and *Zantedeschia aethiopica* a 34% decrease), *Magnolia delavayi* and *Cyathea australis* show a non-significant yet noticeable decrease (8 and 15%, respectively), and another angiosperm (*Cornus capitata*) shows a small (9%), but non-significant increase (**Figures 2A** and **3**).  $D_v$  shows a similar mix of responses, three of the species show a significant decrease (*Chimonanthus praecox*, *Zantedeschia aethiopica*, and *Cyathea australis* decrease by 15, 12, and 17%, respectively), *Magnolia delavayi* shows a very slight (2%) yet non-significant increase, and *Cornus capitata* shows a significant (14%) increase (**Figures 2B** and **3**). Two of the angiosperm species (*Chimonanthus praecox* and *Zantedeschia aethiopica*) show a significant decrease in  $g_{max}$  (16 and 32%, respectively) in response to the palaeo-treatment, with *Magnolia delavayi* showing a non-significant decrease (11%), *Cornus capitata* a non-significant increase (15%), and *Cyathea australis* a non-significant decrease (2%) (**Figures 2C** and **3**). See Supplementary Table S2 for results of generalized linear models (*F* and associated *p*-values).

Three out of four angiosperm species (*Chimonanthus praecox*, *Cornus capitata*, and *Zantedeschia aethiopica*) and the fern species *Cyathea australis* demonstrate intra-specific co-ordination of  $D_v$ , SD, and  $g_{max}$  in response to the palaeo-treatment (**Figure 3**). This co-ordination is evident even though one angiosperm species (*Cornus capitata*) shows an increase in all three parameters while the remaining species show a decrease. *Magnolia delavayi* shows co-ordination in two plant traits in response to the palaeo-treatment (SD and  $g_{max}$ ), however, co-ordination is lacking between both of these parameters and  $D_v$ .

The positive relationship between  $D_v$  and SD (**Figure 4A**) is strong under ambient conditions (Pearson's correlation coefficient:  $r = 0.91$ , SMA regression:  $r^2 = 0.82$ ) and it persists

in the palaeo-treatment ( $r = 0.86$ ,  $r^2 = 0.73$ ). Similarly,  $D_v$  and  $g_{max}$  (**Figure 4B**) show a strong relationship under both the ambient ( $r = 0.87$ ,  $r^2 = 0.76$ ) and palaeo-treatment ( $r = 0.73$ ,  $r^2 = 0.53$ ). The slopes of the regression lines between  $D_v$  and SD and  $D_v$  and  $g_{max}$  are not significantly different in the ambient and palaeo-treatments ( $D_v = 0.01SD + 2.53$  for ambient and  $D_v = 0.01SD + 2.39$  for palaeo-treatment;  $D_v = 0.003g_{max} + 2.85$  for ambient and  $D_v = 0.003g_{max} + 2.66$  for palaeo-treatment).

## DISCUSSION

### SD, $D_v$ , and $g_{max}$ Responses to Low $O_2$ /High $CO_2$

Results of the current study reflect variability in SD responses to atmospheric change. The inverse relationship between SD and  $CO_2$  has been well documented in the literature using both fossil, herbarium, and living plant material (Woodward and Kelly, 1995; McElwain and Chaloner, 1995; Beerling and Woodward, 1996; Royer, 2001; Konrad et al., 2008; Franks and Beerling, 2009a,b). However, this inverse relationship is not universal across all species (Beerling and Kelly, 1997; Haworth et al., 2013). Stomatal responses to  $O_2$  are not well documented in the literature to date. The few existing studies, however, show an increase in stomatal index (ratio of stomata to epidermal cells or SI) in response to growth in 35%  $O_2$  (Beerling et al., 1998), and a range of SD and SI responses to growth in a combined low  $O_2$ /high  $CO_2$  treatment, as well as to separate low  $O_2$  and high  $CO_2$  treatments (Haworth et al., 2013).

The observed decrease in  $D_v$  in the majority of species exposed to the palaeo-treatment is likely a consequence of an overall lower water demand due to stomatal optimisation in a high  $CO_2$  atmosphere. Reduced  $g_s$  in response to high  $CO_2$  has been shown in previous studies (Haworth et al., 2013). This overall reduction in SD and  $D_v$  reflects a balance between water supply and demand in the palaeo-treatment, and the overall result would likely be a reduction in allocation of resources to non-essential veins and stomata, and a maximization of resource use. It is important to acknowledge that the SD and  $D_v$  responses observed in the current study cannot be attributed to either low  $O_2$  or high  $CO_2$  alone without undertaking additional and separate sub-ambient  $O_2$  and elevated  $CO_2$  growth experiments using the same species. For the purposes of this analysis, suffice it to say that any SD and  $D_v$  responses are the result of the specific  $O_2:CO_2$  ratio in the palaeo-treatment growth chambers.

It is noteworthy that only two of the studied species (*Chimonanthus praecox* and *Magnolia delavayi*) have vein densities higher than 6 mm mm<sup>-2</sup> (**Figure 2B**), the 'critical vein density' (Feild et al., 2011a; de Boer et al., 2012) that angiosperms are thought to have surpassed as they rose to dominance in the Cretaceous. This emphasizes the similarity between our chosen study species and those very early evolving angiosperms that had vein densities as low as non-angiosperms (Brodribb and Feild, 2010; Boyce and Zwieniecki, 2012). The significant  $D_v$  decrease seen in the fern species (*Cyathea australis*) is interesting (**Figure 2B**), as it is thought that non-angiosperm species are

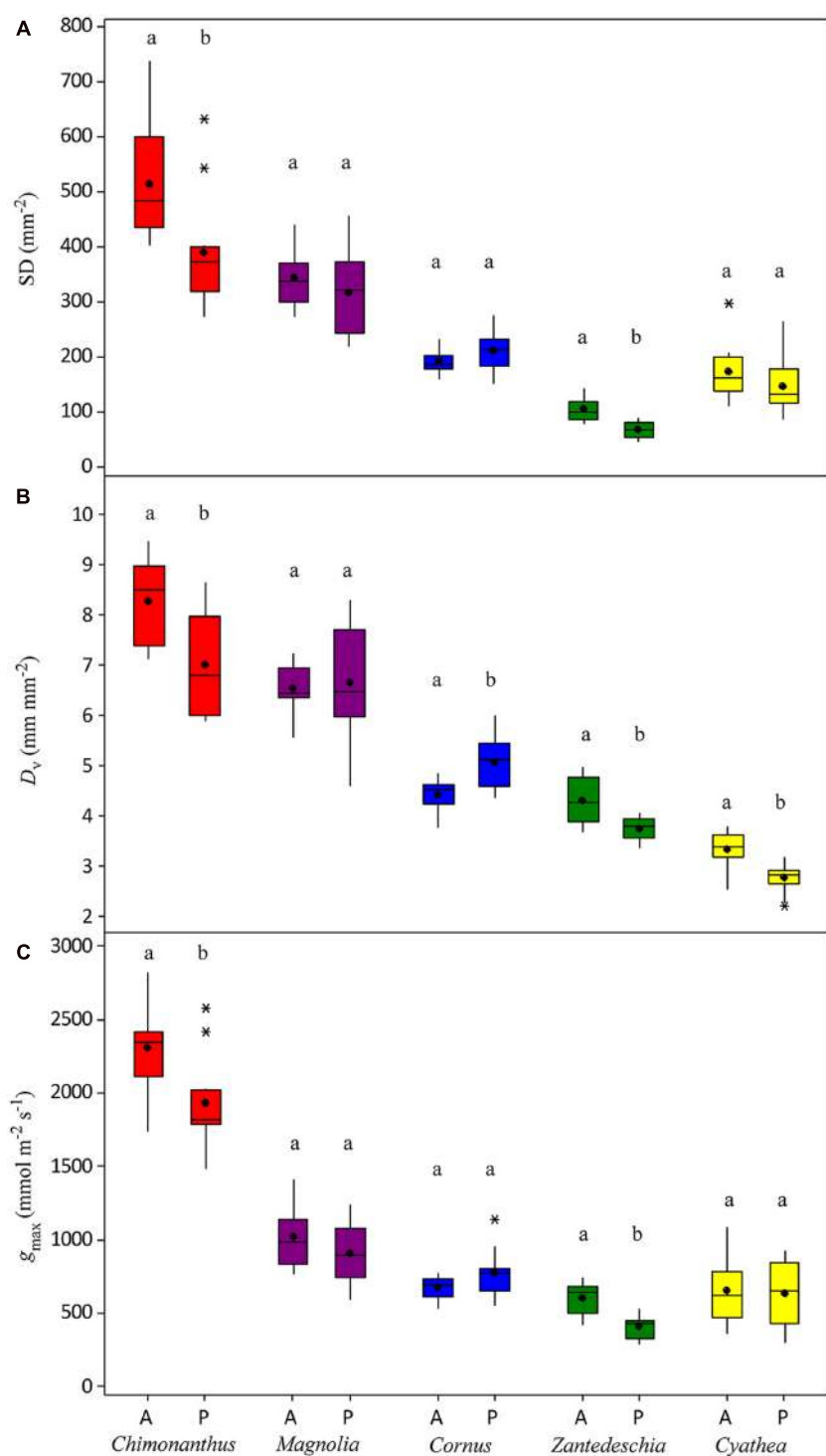


**FIGURE 2 | Changes in (A) SD, (B)  $D_v$ , and (C)  $g_{\max}$  of experimental species in response to the palaeo-treatment.** Different letters signify a significant difference between treatments. A, ambient treatment; P, palaeo-treatment. \*symbols denote outliers.

incapable of altering their vein architecture in the same way that angiosperm species can (Boyce et al., 2009; de Boer et al., 2012). Non-angiosperms seem to exhibit limited plasticity in  $D_v$  when exposed to a long-term palaeo-atmospheric treatment (Figure 5).

Examination of archived leaf material of three gymnosperms and one fern species from a 2009 palaeo-experiment (Haworth et al., 2013) shows that growth in a low O<sub>2</sub>/high CO<sub>2</sub> atmosphere results in a change in  $D_v$  in one gymnosperm species (*Agathis*

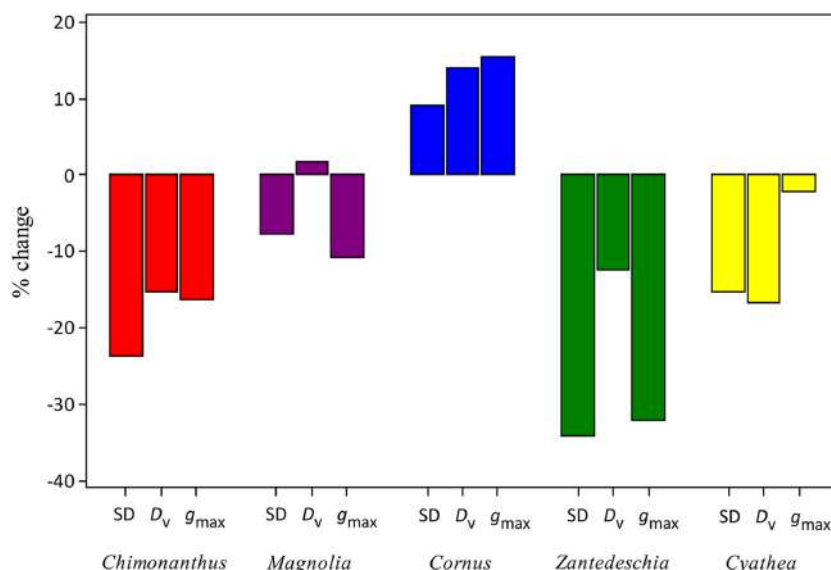


**FIGURE 3 |** Percent change in SD,  $D_v$ , and  $g_{\max}$  of experimental species.

*australis*), but has no effect on  $D_v$  in the remaining species (two gymnosperms and one fern). These non-angiosperms have vein densities below  $2 \text{ mm mm}^{-2}$  and all have either parallel or dichotomously branching major vein networks, implying that this vein configuration may lack developmental plasticity. The major veins of non-angiosperms are generally thicker in diameter and their xylem anatomy is distinct from that of the angiosperms, lacking an important feature that is believed to be paramount in the proliferation of minor veins, vessels with simple perforation plates. Only angiosperms evolved these less resistive perforation plates, and this in conjunction with the development of thinner minor veins may have allowed this plant group to outperform non-angiosperms (Feild and Brodribb, 2013). Angiosperms also possess vein endings that are diffuse or dispersed throughout the leaf allowing them to develop more reticulate venation patterns, whereas gymnosperms with their marginal vein endings lack this ability (Boyce, 2005). An important implication of the current findings is that some angiosperm species are able to alter their vein density on a developmental time-scale in response to a change in atmospheric composition; studies to date have only discussed CO<sub>2</sub>-driven  $D_v$  changes across evolutionary time-scales (Brodribb and Feild, 2010; Boyce and Zwieniecki, 2012; McElwain et al., 2016b). Results of the current study indicate that at least in some early diverging species,  $D_v$  is a plant functional trait that can respond dynamically to atmospheric change.

### Relationship between $D_v$ , SD, and $g_{\max}$

The strong relationship observed in both the ambient and palaeo-treatment between  $D_v$  and SD (**Figure 4A**) demonstrates inter-specific co-ordination in two morphological plant traits that determine hydraulic supply and demand across different plant lineages and under a changing atmosphere. Furthermore, the robust relationship observed between  $D_v$  and  $g_{\max}$  (**Figure 4B**)

demonstrates that morphology has the potential to influence the physiological behavior of these species, via the strong relationship already found between  $g_{\max}$  and  $g_{op}$  (Franks et al., 2009; Dow et al., 2014; McElwain et al., 2016b). Examining the direction of change in the morphological traits for each species it is clear that a high degree of intra-specific co-ordination is also occurring (**Figure 3**). Three out of four angiosperm species and the fern species show intra-specific co-ordination in SD,  $D_v$ , and  $g_{\max}$  in response to the palaeo-treatment. Co-ordination between traits that determine the water relations (supply and demand) of a plant is critical for its survival. For example, an increase in SD and/or  $g_{\max}$  would increase the evaporative demands of the plant and without a corresponding increase in  $D_v$  (to match the increase in water demand with an increase in hydraulic supply) the plant would be maladapted to its environment and would most likely not survive. The opposite scenario would not be as detrimental to plant survival, however, a decrease in SD and/or  $g_{\max}$  without a corresponding decrease in  $D_v$  would result in a waste of resources, the construction of veins being costly to the plant (Sack and Scoffoni, 2013). This ability to co-ordinate morphological traits under a changing atmosphere likely occurred throughout plant evolutionary history as the composition of atmospheric O<sub>2</sub> and CO<sub>2</sub> fluctuated, allowing certain plant species to adapt and survive. During the Cretaceous decline in atmospheric CO<sub>2</sub> for example, it is thought that angiosperms were able to increase their gas exchange capacity (thereby increasing photosynthetic rates) by evolving smaller stomata (Franks and Beerling, 2009a), and by increasing both the density of stomata on the leaf surface and the density of veins (Boyce et al., 2009; Brodribb and Feild, 2010; de Boer et al., 2012; McElwain et al., 2016b). Furthermore, angiosperms that surpassed the ‘critical vein density’ of  $6 \text{ mm mm}^{-2}$  were able to out-compete the gymnosperms and ferns in niches with high evapotranspirational

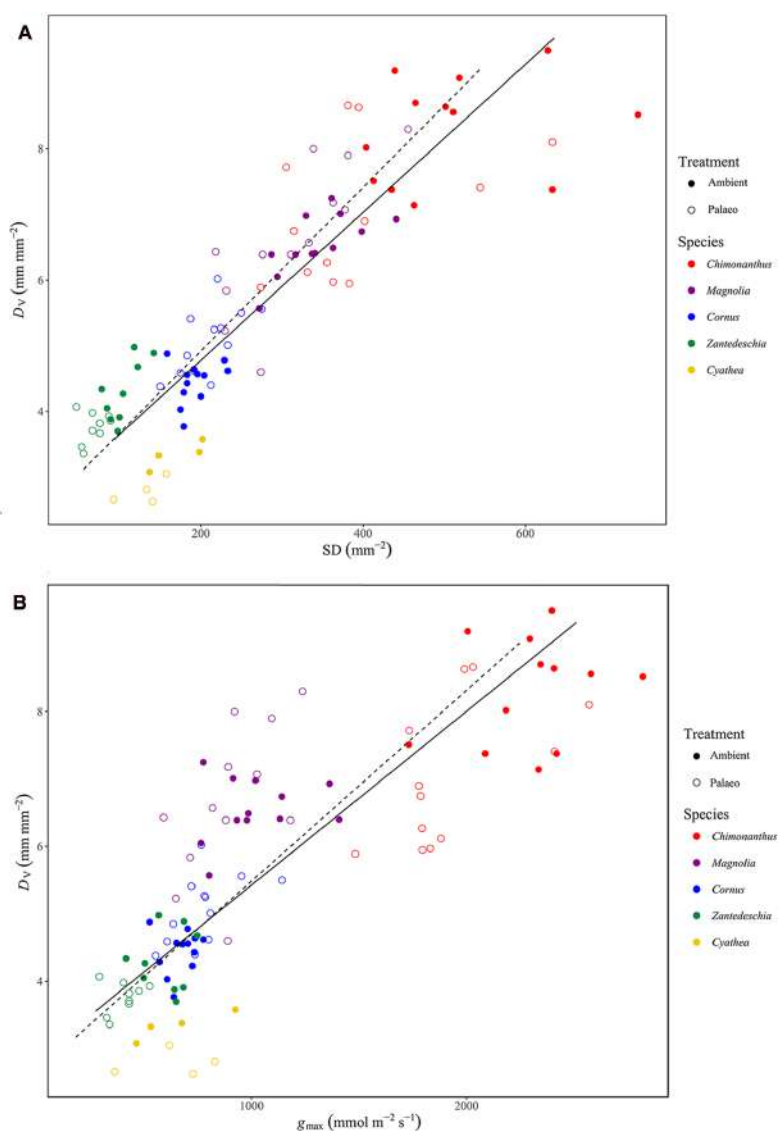


**FIGURE 4 | SMA regression showing the relationship between (A)  $D_V$  and SD,  $D_V = 0.01SD + 2.53$  for ambient and  $D_V = 0.01SD + 2.39$  for palaeo-treatment, and (B)  $D_V$  and theoretical maximum stomatal conductance ( $g_{max}$ ),  $D_V = 0.003g_{max} + 2.85$  for ambient and  $D_V = 0.003g_{max} + 2.66$  for palaeo-treatment. Each data point represents a single leaf with the exception of *Cyathea* where data points represent the average per plant.**

demand where an increase in water supply to the leaf would have been necessary for survival (de Boer et al., 2012). Higher vein densities have been suggested to confer a higher capacity for CO<sub>2</sub> uptake and an increased range of  $g_{op}$ ; this would explain the ability of angiosperms to expand to such diverse habitats and to outcompete species that are more constrained in their venation and hence gas exchange capacity (McElwain et al., 2016b). A recent study suggests that angiosperms are indeed hydraulically optimized for a diverse range of environments, achieving this by maintaining an equal vein to vein and vein to evaporative surface distance in the leaf (Zwieniecki and Boyce, 2014). Ferns are under-invested hydraulically due to their thin leaves and large vein to vein distances, and while some gymnosperms do approach optimal investment by producing

thicker leaves in more water-demanding environments, they are as a group sub-optimal in terms of vein placement (Zwieniecki and Boyce, 2014).

The current study supports these theories by demonstrating a higher degree of plasticity in  $D_V$  in some early diverging angiosperms in response to a changing O<sub>2</sub>:CO<sub>2</sub> ratio, compared to the studied gymnosperms and ferns (Figure 5). It is interesting, however, that examined non-angiosperm species from the 2009 palaeo-experiment show limited plasticity in  $D_V$  as well as in SD (see SD results for these non-angiosperm species reported in Haworth et al., 2013). This demonstrates that while these species do not show a high degree of morphological plasticity in response to a changing atmosphere on experimental time-scales comparable to the studied angiosperms,

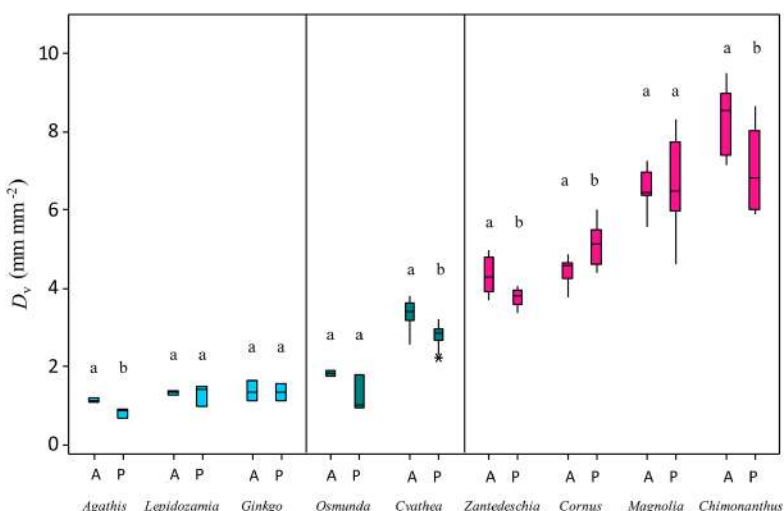


**FIGURE 5 | Comparison of the  $D_v$  responses of gymnosperms, ferns, and angiosperms to growth in low  $O_2$ /high  $CO_2$  conditions.** Different letters signify a significant difference between treatments. A, ambient treatment; P, palaeo-treatment. \*symbols denote outliers.

they do demonstrate similar co-ordination in leaf morphological traits.

Furthermore, these results suggest that angiosperms are not only capable of showing morphological plasticity in response to rising  $O_2$  and declining  $CO_2$  (Boyce et al., 2009; Feild et al., 2011a; de Boer et al., 2012), but also to declining  $O_2$  and high  $CO_2$  conditions. The robust positive relationship observed here between the density of veins and stomata strongly supports the theory suggested by Brodribb et al. (2007), whereby multi-veined leaves optimize the placement of veins in relation to stomata so that the distance water needs to travel through the resistive mesophyll ( $D_m$ ) is minimized. Although  $D_m$  was not directly measured in this study, the morphological co-ordination observed suggests that any change in  $D_v$  will elicit a corresponding change in SD or vice versa, allowing the leaf to minimize the distance between veins and stomata, and to maximize photosynthetic performance and operational efficiency of the leaf.

## Implications for Past Plant–Atmosphere Interactions

The experimental species examined show a species-specific and varied response to growth in the palaeo-treatment, yet the strong positive relationship between  $D_v$  and SD persists (Figure 4A). Furthermore, the positive relationship observed between  $D_v$  and  $g_{\max}$  (Figure 4B) demonstrates the link between hydraulic and gas exchange/diffusional processes in these species, as shown in previous studies (Sack et al., 2003; Boyce et al., 2009; Brodribb and Feild, 2010; Feild et al., 2011b; McElwain et al., 2016b). The finding that  $D_m$  is most likely maintained under changing atmospheric conditions (due to the intra-specific co-ordination between  $D_v$  and SD) has important implications when attempting to understand plant–atmosphere interactions throughout the last 400 million years of plant evolution.

A lack of co-ordination in  $D_v$  and SD on developmental time-scales would result in a plant that is morphologically and physiologically out of sync, negatively impacting operational efficiency and overall fitness under changing atmospheric conditions. Furthermore, plant species that exhibited plasticity in these morphological traits under a changing atmosphere would likely have had an ecological advantage over plant species that were morphologically inflexible, being able to maximize their photosynthetic capacity as the surrounding environment changed (McElwain et al., 2016b). The finding that a proxy for photosynthetic capacity ( $D_m$ ) (Brodribb et al., 2007) remains stable under changing atmospheric conditions is important for accurate initial parameterisation of mechanistically based models used to predict palaeo- $CO_2$  (Franks et al., 2014) since these require robust estimates of palaeo-assimilation (Franks et al., 2014; McElwain et al., 2016a). The current study focuses on plant responses to an experimentally imposed low  $O_2$ /high  $CO_2$  atmosphere. This  $O_2$ : $CO_2$  ratio occurred multiple times throughout plant evolutionary history based on model and proxy estimates (Royer, 2001; Bergman et al., 2004; Royer et al., 2004; McElwain et al., 2005; Berner, 2006, 2009; Steinhorsdottir et al., 2016), however, it would be beneficial to investigate the effect of other atmospheric  $O_2$ : $CO_2$  ratios on these plant trait relationships in order to test their linearity. Further experiments examining plant responses to a range of palaeo-atmospheric conditions will build on these results, providing a better picture of plant-atmosphere interactions over the past 400 million years and allowing predictions of future plant responses to global climate change.

## CONCLUSION

Species show a varied response in SD,  $D_v$ , and  $g_{\max}$  to growth in an experimental low  $O_2$ /high  $CO_2$  palaeo-atmosphere.

Regardless of this variation in responses, a strong relationship is observed between  $D_v$  and SD and  $D_v$  and  $g_{max}$  under both the ambient and palaeo-atmosphere. Gymnosperms studied here appear to lack the same degree of developmental plasticity in  $D_v$  compared to the angiosperms, at least on short experimental time-scales. The ability to increase their range of  $D_v$  values may have contributed to the success of angiosperms during the Cretaceous decline in CO<sub>2</sub>; a high degree of plasticity in this trait possibly provided early diverging angiosperms with a competitive advantage over other seed plant groups in more changeable environments. The tight relationship observed between  $D_v$  and SD in the palaeo-treatment suggests that  $D_m$  is likely maintained under environmental change and lends confidence to existing palaeo-CO<sub>2</sub> proxies that use this parameter in their models. Further studies examining the robustness of these plant trait relationships under a range of O<sub>2</sub>:CO<sub>2</sub> ratios are needed in order to elucidate the full spectrum of plant-atmosphere interactions throughout the last 400 million years.

## AUTHOR CONTRIBUTIONS

CE-F carried out vein density and SD analysis, anatomical stomatal measurements for  $g_{max}$  calculation, statistical analysis, and drafted the manuscript. AP contributed SD and  $g_{max}$  data

## REFERENCES

- Assmann, S. M. (1999). The cellular basis of guard cell sensing of rising CO<sub>2</sub>. *Plant Cell Environ.* 22, 629–637. doi: 10.1046/j.1365-3040.1999.00408.x
- Bearling, A. D. J., Woodward, F. I., Lomas, M. R., Wills, M. A., Quick, W. P., Valdes, P. J., et al. (1998). The influence of Carboniferous palaeoatmospheres on plant function: an experimental and modelling assessment. *Phil. Trans. R. Soc. Lond. B* 353, 131–140. doi: 10.1098/rstb.1998.0196
- Bearling, D. J., and Kelly, C. K. (1997). Stomatal density responses of woodland plants over the past seven decades of CO<sub>2</sub> increase: a comparison of Salisbury (1927) with contemporary data. *Am. J. Bot.* 84, 1572–1583. doi: 10.2307/2446619
- Bearling, D. J., and Woodward, F. I. (1996). Palaeo-ecophysiological perspectives on plant responses to global change. *Trends Ecol. Evol.* 11, 20–23. doi: 10.1016/0169-5347(96)81060-3
- Bergman, N., Lenton, T., and Watson, A. (2004). COPSE: a new model of biogeochemical cycling over Phanerozoic time. *Am. J. Sci.* 304, 397–437. doi: 10.2475/ajs.304.5.397
- Berlyn, G. P., and Miksche, J. P. (1976). *Botanical Microtechnique and Cytochemistry*. Ames, IA: Iowa State University Press.
- Berner, R. A. (2006). GEOCARBSULF: a combined model for Phanerozoic atmospheric O<sub>2</sub> and CO<sub>2</sub>. *Geochim. Cosmochim. Acta* 70, 5653–5664. doi: 10.2475/07.2009.03
- Berner, R. A. (2009). Phanerozoic atmospheric oxygen: new results using the GEOCARBSULF model. *Am. J. Sci.* 309, 603–606. doi: 10.2475/07.2009.03
- Betts, R. A., Boucher, O., Collins, M., Cox, P. M., Falloon, P. D., and Gedney, N. (2007). Projected increase in continental runoff due to plant responses to increasing carbon dioxide. *Nature* 448, 1037–1041. doi: 10.1038/nature06045
- Blonder, B., and Enquist, B. J. (2014). Inferring climate from angiosperm leaf venation networks. *New Phytol.* 204, 116–126. doi: 10.1111/nph.12780
- Boyce, C. K. (2005). Patterns of segregation and convergence in the evolution of fern and seed plant leaf morphologies. *Paleobiology* 31, 117–140. doi: 10.1666/0094-8373(2005)031<0117:POSACI>2.0.CO;2
- Boyce, C. K., Brodribb, T. J., Feild, T. S., and Zwieniecki, M. A. (2009). Angiosperm leaf vein evolution was physiologically and environmentally transformative. *Proc. R. Soc. B* 276, 1771–1776. doi: 10.1098/rspb.2008.1919
- for *Cyathea australis*. CE-K was involved in the 2009 palaeo-experiment and therefore provided dried leaf material for vein density analysis. JM is the principal investigator. All authors read, revised, and approved the final manuscript.

## FUNDING

We gratefully acknowledge funding from a European Research Council grant (ERC-279962-OXYEVOL).

## ACKNOWLEDGMENTS

We thank Mr. G. Kavanagh and Ms. B. Moran (UCD, Ireland) for their technical assistance. We would also like to thank both J. D. Fitz. Gerald and Dr. S. P. Batke for their assistance with statistical analysis. Finally, we thank the Editor and both reviewers for their valuable comments and suggestions.

## SUPPLEMENTARY MATERIAL

The Supplementary Material for this article can be found online at: <http://journal.frontiersin.org/article/10.3389/fpls.2016.01368>

- Boyce, C. K., and Zwieniecki, M. A. (2012). Leaf fossil record suggests limited influence of atmospheric CO<sub>2</sub> on terrestrial productivity prior to angiosperm evolution. *Proc. Natl. Acad. Sci. U.S.A.* 109, 10403–10408. doi: 10.1073/pnas.1203769109
- Brodribb, T. J., and Feild, T. S. (2010). Leaf hydraulic evolution led a surge in leaf photosynthetic capacity during early angiosperm diversification. *Ecol. Lett.* 13, 175–183. doi: 10.1111/j.1461-0248.2009.01410.x
- Brodribb, T. J., Feild, T. S., and Jordan, G. J. (2007). Leaf maximum photosynthetic rate and venation are linked by hydraulics. *Plant Physiol.* 144, 1890–1898. doi: 10.1104/pp.107.101352
- Brodribb, T. J., and Jordan, G. J. (2011). Water supply and demand remain balanced during leaf acclimation of *Nothofagus cunninghamii* trees. *New Phytol.* 192, 437–448. doi: 10.1111/j.1469-8137.2011.03795.x
- Brodribb, T. J., Jordan, G. J., and Carpenter, R. J. (2013). Unified changes in cell size permit coordinated leaf evolution. *New Phytol.* 199, 559–570. doi: 10.1111/nph.12300
- Carins Murphy, M. R., Jordan, G. J., and Brodribb, T. J. (2014). Acclimation to humidity modifies the link between leaf size and the density of veins and stomata. *Plant Cell Environ.* 37, 124–131. doi: 10.1111/pce.12136
- Casson, S., and Gray, J. E. (2008). Influence of environmental factors on stomatal development. *New Phytol.* 178, 9–23. doi: 10.1111/j.1469-8137.2007.02351.x
- de Boer, H. J., Eppinga, M. B., Wassen, M. J., and Dekker, S. C. (2012). A critical transition in leaf evolution facilitated the Cretaceous angiosperm revolution. *Nature Commun.* 3, 1221. doi: 10.1038/ncomms2217
- Díaz, S., Kattge, J., Cornelissen, J. H. C., Wright, I. J., Lavorel, S., Dray, S., et al. (2016). The global spectrum of plant form and function. *Nature* 529, 1–17. doi: 10.1038/nature16489
- Dow, G. J., Bergmann, D. C., and Berry, J. A. (2014). An integrated model of stomatal development and leaf physiology. *New Phytol.* 201, 1218–1226. doi: 10.1111/nph.12608
- Feild, T. S., and Brodribb, T. J. (2013). Hydraulic tuning of vein cell microstructure in the evolution of angiosperm venation networks. *New Phytol.* 199, 720–726. doi: 10.1111/nph.12311
- Feild, T. S., Brodribb, T. J., Iglesias, A., Chatelet, D. S., Baresch, A., Upchurch, G. R., et al. (2011a). Fossil evidence for Cretaceous escalation in angiosperm

- leaf vein evolution. *Proc. Natl. Acad. Sci. U.S.A.* 108, 8363–8366. doi: 10.1073/pnas.1014456108
- Feild, T. S., Upchurch, G. R., Chatelet, D. S., Brodribb, T. J., Grubbs, K. C., Samain, S., et al. (2011b). Fossil evidence for low gas exchange capacities for early Cretaceous angiosperm leaves. *Paleobiology* 37, 195–213. doi: 10.1666/10015.1
- Franks, P. J., and Beerling, D. J. (2009a). Maximum leaf conductance driven by CO<sub>2</sub> effects on stomatal size and density over geologic time. *Proc. Natl. Acad. Sci. U.S.A.* 106, 10343–10347. doi: 10.1073/pnas.0904209106
- Franks, P. J., and Beerling, D. J. (2009b). CO<sub>2</sub>-forced evolution of plant gas exchange capacity and water-use efficiency over the Phanerozoic. *Geobiology* 7, 227–236. doi: 10.1111/j.1472-4669.2009.00193.x
- Franks, P. J., Drake, P. L., and Beerling, D. J. (2009). Plasticity in maximum stomatal conductance constrained by negative correlation between stomatal size and density: an analysis using *Eucalyptus globulus*. *Plant Cell Environ.* 32, 1737–1748. doi: 10.1111/j.1365-3040.2009.002031.x
- Franks, P. J., Royer, D. L., Beerling, D. J., Van de Water, P. K., Cantrill, D. J., Barbour, M. M., et al. (2014). New constraints on atmospheric CO<sub>2</sub> concentration for the Phanerozoic. *Geophys. Res. Lett.* 41, 4685–4694. doi: 10.1002/2014GL060457
- Gedney, N., Cox, P. M., Betts, R. A., Boucher, O., Huntingford, C., and Stott, P. A. (2006). Detection of a direct carbon dioxide effect in continental river runoff records. *Nature* 439, 835–838. doi: 10.1038/nature04504
- Haworth, M., Elliott-Kingston, C., and McElwain, J. C. (2013). Co-ordination of physiological and morphological responses of stomata to elevated [CO<sub>2</sub>] in vascular plants. *Oecologia* 171, 71–82. doi: 10.1007/s00442-012-2406-9
- Jones, H. G. (1992). *Plants and Microclimate: A Quantitative Approach to Environmental Plant Physiology*, 2nd Edn. Cambridge: Cambridge University Press.
- Konrad, W., Roth-Nebelsick, A., and Grein, M. (2008). Modelling of stomatal density response to atmospheric CO<sub>2</sub>. *J. Theor. Biol.* 253, 638–658. doi: 10.1016/j.jtbi.2008.03.032
- Lawson, T. (2009). Guard cell photosynthesis and stomatal function. *New Phytol.* 181, 13–34. doi: 10.1111/j.1469-8137.2008.02685.x
- McElwain, J. C., and Chaloner, W. G. (1995). Stomatal density and index of fossil plants track atmospheric carbon dioxide in the Palaeozoic. *Ann. Bot.* 76, 389–395. doi: 10.1006/anbo.1995.1112
- McElwain, J. C., Wade-Murphy, J., and Hesselbo, S. P. (2005). Changes in carbon dioxide during an oceanic anoxic event linked to intrusion into Gondwana coals. *Nature* 435, 479–482. doi: 10.1038/nature03618
- McElwain, J. C., Montañez, I., White, J. D., Wilson, J. P., and Yiotis, C. (2016a). Was atmospheric CO<sub>2</sub> capped at 1000 ppm over the past 300 million years? *Palaeogeogr. Palaeoclimatol. Palaeoecol.* 441, 653–658. doi: 10.1016/j.palaeo.2015.10.017
- McElwain, J. C., Yiotis, C., and Lawson, T. (2016b). Using modern plant trait relationships between observed and theoretical maximum stomatal conductance and vein density to examine patterns of plant macroevolution. *New Phytol.* 209, 94–103. doi: 10.1111/nph.13579
- McKown, A. D., Cochard, H., and Sack, L. (2010). Decoding leaf hydraulics with a spatially explicit model: principles of venation architecture and implications for its evolution. *Am. Nat.* 175, 447–460. doi: 10.1086/650721
- Mosbrugger, V. (2009). “Nearest-living-relative method,” in *Encyclopedia of Palaeoclimatology and Ancient Environments*, ed. V. Gorin (Berlin: Springer), 607–609.
- Nadeau, J. A., and Sack, F. D. (2002). Control of stomatal distribution on the *Arabidopsis* leaf surface. *Science* 296, 1697–1700. doi: 10.1126/science.1069596
- Outlaw, W. H. (2003). Integration of cellular and physiological functions of guard cells. *Water* 22, 503–529. doi: 10.1080/07352680390253511
- Parlange, J., and Waggoner, P. E. (1970). Stomatal dimensions and resistance to diffusion. *Plant Physiol.* 46, 337–342. doi: 10.1104/pp.46.2.337
- Perez-Harguindequy, N., Díaz, S., Garnier, E., Lavorel, S., Poorter, H., Jaureguiberry, P., et al. (2013). New handbook for standardised measurement of plant functional traits worldwide. *Aust. J. Bot.* 61, 167–234. doi: 10.1071/BT12225
- Poole, I., and Kürschner, W. (1999). “Stomatal density and index: the practice,” in *Fossil Plants and Spores: Modern Techniques*, eds T. P. Jones and N. P. Rowe (London: Geological Society), 257–260.
- Rodell, M., Beaudoing, H. K., L'Ecuyer, T. S., Olson, W. S., Famiglietti, J. S., Houser, P. R., et al. (2015). The observed state of the water cycle in the early twenty-first century. *J. Clim.* 28, 8289–8318. doi: 10.1175/JCLI-D-14-00555.1
- Roelfsema, M. R. G., and Hedrich, R. (2005). In the light of stomatal opening: new insights into ‘the Watergate’. *New Phytol.* 167, 665–691. doi: 10.1111/j.1469-8137.2005.01460.x
- Royer, D. L. (2001). Stomatal density and stomatal index as indicators of paleoatmospheric CO<sub>2</sub> concentration. *Rev. Palaeobot. Palynol.* 114, 1–28. doi: 10.1016/S0034-6667(00)00074-9
- Royer, D. L., Berner, R. A., Montanez, I. P., Tabor, N. J., and Beerling, D. J. (2004). CO<sub>2</sub> as a primary driver of Phanerozoic climate. *GSA Today* 14, 4–10. doi: 10.1130/1052-5173(2004)014<4:CAAPDO>2.0.CO;2
- Sack, L., Cowan, P., Jaikumar, N., and Holbrook, N. (2003). The ‘hydrology’ of leaves: co-ordination of structure and function in temperate woody species. *Plant Cell Environ.* 26, 1343–1356. doi: 10.1046/j.0016-8025.2003.01058.x
- Sack, L., and Frole, K. (2006). Leaf structural diversity is related to hydraulic capacity in tropical rain forest trees. *Ecology* 87, 483–491. doi: 10.1890/05-0710
- Sack, L., and Holbrook, N. M. (2006). Leaf Hydraulics. *Annu. Rev. Plant Biol.* 57, 361–381. doi: 10.1146/annurev.applant.56.032604.144141
- Sack, L., and Scoffoni, C. (2013). Leaf venation: structure, function, development, evolution, ecology and applications in the past, present and future. *New Phytol.* 198, 983–1000. doi: 10.1111/nph.12253
- Sack, L., Scoffoni, C., McKown, A. D., Frole, K., Rawls, M., Havran, J. C., et al. (2012). Developmentally based scaling of leaf venation architecture explains global ecological patterns. *Nature Commun.* 3, 1–10. doi: 10.1038/ncomms1835
- Shimazaki, K., Doi, M., Assmann, S. M., and Kinoshita, T. (2007). Light regulation of stomatal movement. *Annu. Rev. Plant Biol.* 58, 219–247. doi: 10.1146/annurev.applant.57.032905.105434
- Shpak, E. D., McAbee, J. M., Pillitteri, L. J., and Torii, K. U. (2005). Stomatal patterning and differentiation by synergistic interactions of receptor kinases. *Science* 309, 290–293. doi: 10.1126/science.1109710
- Steinhorst, M., Porter, A. S., Holohan, A., Kunzmann, L., Collinson, M., and McElwain, J. C. (2016). Fossil plant stomata indicate decreasing atmospheric CO<sub>2</sub> prior to the Eocene-Oligocene boundary. *Clim. Past* 12, 439–454. doi: 10.5194/cp-12-439-2016
- Uhl, D., and Mosbrugger, V. (1999). Leaf venation density as a climate and environmental proxy: a critical review and new data. *Palaeogeogr. Palaeoclimatol. Palaeoecol.* 149, 15–26. doi: 10.1016/S0031-0182(98)00189-8
- Vavasseur, A., and Raghavendra, A. S. (2005). Guard cell metabolism and CO<sub>2</sub> sensing. *New Phytol.* 165, 665–682. doi: 10.1111/j.1469-8137.2004.01276.x
- Willis, K. J., and McElwain, J. C. (2014). *The Evolution of Plants*, 2nd Edn. Oxford: Oxford University Press.
- Wilson, J. P., White, J. D., Dimichele, W. A., Hren, M. T., Poulsen, C. J., McElwain, J. C., et al. (2015). Reconstructing extinct plant water use for understanding vegetation-climate feedbacks: methods, synthesis, and a case study using the Paleozoic-era medullosan seed ferns. *Paleontol. Soc. Pap.* 21, 167–195.
- Woodward, F. I., and Kelly, C. K. (1995). The influence of CO<sub>2</sub> concentration on stomatal density. *New Phytol.* 131, 311–327. doi: 10.1111/j.1469-8137.1995.tb03067.x
- Zwieniecki, M. A., and Boyce, C. K. (2014). Evolution of a unique anatomical precision in angiosperm leaf venation lifts constraints on vascular plant ecology. *Proc. R. Soc. B* 281, 1–7. doi: 10.1098/rspb.2013.2829
- Conflict of Interest Statement:** The authors declare that the research was conducted in the absence of any commercial or financial relationships that could be construed as a potential conflict of interest.
- Copyright © 2016 Evans-Fitz.Gerald, Porter, Yiotis, Elliott-Kingston and McElwain. This is an open-access article distributed under the terms of the Creative Commons Attribution License (CC BY). The use, distribution or reproduction in other forums is permitted, provided the original author(s) or licensor are credited and that the original publication in this journal is cited, in accordance with accepted academic practice. No use, distribution or reproduction is permitted which does not comply with these terms.



# Digital Morphometrics of Two North American Grapevines (*Vitis*: Vitaceae) Quantifies Leaf Variation between Species, within Species, and among Individuals

Laura L. Klein<sup>1,2\*</sup>, Madeleine Caito<sup>1</sup>, Chad Chapnick<sup>1</sup>, Cassandra Kitchen<sup>1</sup>, Regan O'Hanlon<sup>1</sup>, Dan H. Chitwood<sup>3</sup> and Allison J. Miller<sup>1,2\*</sup>

<sup>1</sup> Department of Biology, Saint Louis University, St. Louis, MO, USA, <sup>2</sup> Science and Conservation Department, Missouri Botanical Garden, St. Louis, MO, USA, <sup>3</sup> Independent Researcher, St. Louis, MO, USA

## OPEN ACCESS

### Edited by:

Andrea Michelle Smith-Moritz,  
University of California, Davis, USA

### Reviewed by:

Tsu-Wei Chen,  
Leibniz University of Hanover,  
Germany

Stefanie M. Ickert-Bond,  
University of Alaska Fairbanks, USA

### \*Correspondence:

Laura L. Klein  
lklein10@slu.edu  
Allison J. Miller  
amille75@slu.edu

### Specialty section:

This article was submitted to  
Plant Biophysics and Modeling,  
a section of the journal  
*Frontiers in Plant Science*

Received: 06 September 2016

Accepted: 03 March 2017

Published: 17 March 2017

### Citation:

Klein LL, Caito M, Chapnick C, Kitchen C, O'Hanlon R, Chitwood DH and Miller AJ (2017) Digital Morphometrics of Two North American Grapevines (*Vitis*: Vitaceae) Quantifies Leaf Variation between Species, within Species, and among Individuals. *Front. Plant Sci.* 8:373. doi: 10.3389/fpls.2017.00373

Recent studies have demonstrated that grapevine (*Vitis* spp.) leaf shape can be quantified using digital approaches which indicate phylogenetic signal in leaf shape, discernible patterns of developmental context within single leaves, and signatures of local environmental conditions. Here, we extend this work by quantifying intra-individual, intraspecific, and interspecific variation in leaf morphology in accessions of North American *Vitis riparia* and *V. rupestris* in a common environment. For each species at least four clonal replicates of multiple genotypes were grown in the Missouri Botanical Garden Kemper Center for Home Gardening. All leaves from a single shoot were harvested and scanned leaf images were used to conduct generalized Procrustes analysis, linear discriminant analysis, and elliptical Fourier analysis. Leaf shapes displayed genotype-specific signatures and species distinctions consistent with taxonomic classifications. Leaf shape variation within genotypes and among clones was the result of pest and pathogen-induced leaf damage that alters leaf morphology. Significant trends in leaf damage caused by disease and infestation were non-random with respect to leaf position on the shoot. Digital morphometrics is a powerful tool for assessing leaf shape variation among species, genotypes, and clones under common conditions and suggests biotic factors such as pests and pathogens as important drivers influencing leaf shape.

**Keywords:** digital morphometrics, leaf shape, *Vitis*, generalized Procrustes analysis, elliptical Fourier descriptors, linear discriminant analysis

## INTRODUCTION

The diversity of leaf morphologies reflects the multifaceted interplay of genetics, development, and environment. The genetic basis of leaf morphology is currently understood to be influenced both through variation in gene sequence and expression patterns but much remains unknown (Ichihashi et al., 2014; Chitwood and Sinha, 2016). Developmental biology has made great strides in explaining leaf shape variation, identifying constraints on heteroblasty, cell expansion, polar development, and metabolic pathways (Dkhar and Pareek, 2014; Chitwood and Sinha, 2016).

Particularly in the case of angiosperms, these genetic and developmental constraints are intertwined with the life history of the organism. Traits such as plant architecture, venation patterns, or total leaf area represent functional tradeoffs that evolved in response to water distribution, drought and freezing tolerance, transpiration efficiency, light exposure, and many other challenges (Kaplan, 2001; Nicotra et al., 2011).

In addition to genetic and developmental effects, aspects of the abiotic and biotic environments influence leaf shape. For example, environments with greater temperature fluctuations correlate with higher incidences of plasticity in leaf shape (Little et al., 2010), and colder climates are associated with higher incidences of larger-toothed, more highly dissected leaf margins (Boyce, 2008; Royer et al., 2009; Peppe et al., 2011). Biotic influences including leaf-borne pests and pathogens add additional complexity to leaf shape. Fungal and viral infections or insects can affect the health of a plant often through leaf and tissue deformity (e.g., Kadioglu et al., 2012). In response to these infections, a series of physical and biochemical processes within the plant (e.g., stomatal closure, changes in ion concentration, induction of reactive oxygen species, up-regulation of genes, etc.; Boyd et al., 2013) result in the expression of a diseased phenotype. Thus, it is important to account for local environmental conditions when interpreting complex phenotypes.

Within the genus *Vitis*, leaf morphology has proven so informative a trait for cultivated varieties that an entire discipline, ampelography, has been devoted to the description of grape leaves (Rendu, 1854). Ampelography was originally developed to identify leaves of cultivated *V. vinifera* L. varieties. The technique has evolved from manually acquired measurements of veins, sinuses, and teeth (Galet, 1979), to a more precise, digital approach utilizing scanned leaf images and rigorous statistical analyses (Chitwood et al., 2014). Recently, digital morphometrics has been employed to describe leaf shape in hundreds of *V. vinifera* varieties (Chitwood et al., 2014), as well as *V. vinifera* hybrids, and among *Vitis* and *Ampelopsis* species (Chitwood et al., 2016a). This work demonstrated that subtle shape variation is unique to different taxa and developmental stages. These important contributions demonstrate that, under common conditions, genetics, and development interact to influence leaf shape in individual vines.

A persistent question among plant morphologists is the extent to which leaf shape varies within and among genotypes. Because grapevines are easily cloned, it is possible to assess intra- and inter-individual variation in a statistically explicit fashion by examining multiple replicates of the same genotype(s) under common and unique environmental conditions (e.g., Atlan et al., 2015). Phenotypic plasticity research indicates that plants respond to their environments at the sub-genotype level, and that there is variation among genotypes in phenotypic response to light (e.g., a shade leaf may be phenotypically different from a sun leaf on the same plant; De Kroon et al., 2005). In grapevines and many other clonally propagated perennial crops, leaf shape plasticity serves as a proxy indicating the range of variation exhibited by genotypes in response

to climate. Through morphology we can observe the range of variation expressed by an individual, and can quantify how traits vary not only in different parts of the same plant, but among individuals, populations, and ultimately species.

In this study, we explored intra-and inter-individual variation in leaf shape in two North American *Vitis* species, *V. riparia* Michx. and *V. rupestris* Scheele. These species are closely related and are differentiated morphologically, genetically, and with respect to the environmental variables characterizing their native ranges (Miller et al., 2013; Callen et al., 2016). We quantified leaf shape in at least four clonal replicates of multiple *V. riparia* and *V. rupestris* genotypes growing in a common garden housed at the Missouri Botanical Garden (MBG; St. Louis, MO). Our goals were to: (1) assess variation in leaf shape among the species *V. riparia* and *V. rupestris*, as well as among genotypes within these species, and among clones within genotypes; (2) investigate effects of naturally occurring pests and pathogens on leaf morphology.

## MATERIALS AND METHODS

### Assessing Leaf Shape Variation among Species, among Genotypes within Species, and among Clones within Genotypes

#### Study System and Research Vineyards

To investigate differences in leaf shape within and among genotypes, and among species, we selected multiple genotypes of two closely related native North American grapevine species, *V. riparia* and *V. rupestris* (Miller et al., 2013; Wan et al., 2013). These species differ in the climatic variables characterizing their environmental niches, in growth habit, and habitat preference (Callen et al., 2016; Moore and Wen, 2016). Both species can be propagated vegetatively with ease and are commonly used for rootstock breeding.

A research vineyard was established at the Missouri Botanical Garden's William T. Kemper Center for Home Gardening in 2013 (MBG common garden) using canes (dormant shoot clippings) obtained from accessions housed in the USDA Agricultural Research Service Grape Genetics Research Unit germplasm reserve (USDA-ARS-GGRU; Geneva, NY, USA). The garden plot was open to observation in the public area of the botanical garden grounds, with a center experimental plot and a side experimental plot, divided by a pathway (Supplementary Figure S1). Four genotypes of *Vitis riparia* and five genotypes *V. rupestris* were planted in a randomized design in the MBG common garden, each with at least four clonal replicates per genotype (clones) (Table 1). The *V. riparia* and *V. rupestris* genotypes in the MBG common garden represent a subset of the variation preserved at the USDA-ARS-GGRU germplasm.

Leaf collections were made June 29, 2014 from single shoots directly spawned from buds on the previous year's spurs whenever possible. We selected well-established axillary vines in the event primary shoots were previously pruned. Leaf blades

**TABLE 1 | Summary of MBG common garden germplasm accessions.**

Species	Genotype	No. clones at MBG	Sex	Genotype origin
<i>Vitis riparia</i>	588347	7	Female	Illinois
	588354	8	Male	Illinois
	588439	7	Female	Missouri
	588653	7	Female	Iowa
<i>Vitis rupestris</i>	588160	7	Female	Illinois or Texas
	588224	4	Female	Arkansas
	588181	5	Male	Missouri
	588188	6	Male	Missouri
	588333	7	Male	Missouri
Total	9	58		

Genotype represents the USDA-ARS-GGRU germplasm accession from which canes were harvested. Genotype origin is the putative location from where accessions were originally harvested.

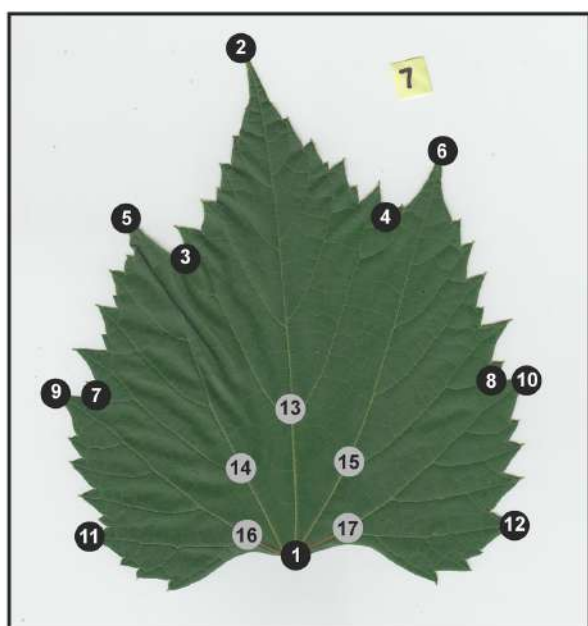


**FIGURE 1 | Example of a scanned *Vitis riparia* leaf, with 17 landmark points applied.** Black dots correspond to 12 “outer landmarks” that capture leaf outline, sinuses, and lobes. Gray dots correspond to five “inner landmarks” that capture aspects vein architecture.

were harvested from the shoots and placed into plastic bags with ventilation holes. To preserve the order of developmental leaf stage along a selected shoot, leaves were stacked from youngest (open, fully developed at the tip of the shoot, ~1 cm in diameter; numbered as one) to oldest leaf at the base of the vine. Leaves were digitally imaged using a Canon CanoScan LiDE 110 color image scanner within 24 h of harvest. Occasionally some leaves were damaged or missing from a shoot as the result of tissue damage from weather or herbivory and were thus excluded in the numbering process. All images are available on the Dryad Digital Repository<sup>1</sup>.

<sup>1</sup><https://dataverse.harvard.edu/dataverse/VitisLeafVariation>

## Analyses

To identify leaf shape variation, we utilized generalized Procrustes analysis (GPA), a method of shape comparison that scales the data equally to eliminate the effects of different-sized objects, resulting in an analysis that examines differences among shapes only (Viscosi and Cardini, 2011). GPA is applied to landmark data that represent homologous points of shape, in this case important grapevine leaf features. Following Chitwood et al. (2014, 2016a) we applied 17 landmark points on each leaf to capture details of the leaf outline such as lobes and sinuses (12 “outer landmarks”) and vein architecture (5 “inner landmarks”) (Figure 1). Landmarks were placed on leaf images using the software package ImageJ (Abràmoff et al., 2004). Following landmark dataset assembly, GPA was implemented in R (R Core Team, 2016) using the ‘procGPA’ function in the “shapes” package (Dryden, 2017), generating 34 principal component (PC) scores for each leaf and percent variance explained by each PC. Eigenleaves were visualized using the ‘shapePCA’ function.<sup>2</sup> Visualization of average shape outlines extracted from Procrustes coordinates for each genotype were plotted using custom R scripts and in the R package ggplot2 (Wickham, 2009). All code is available on GitHub<sup>2</sup>.

In order to further investigate differences in leaf shape within genotypes among clones, among genotypes, and among species, we performed linear discriminants analysis (LDA) on the landmark data using R. LDA is a statistical classification method consisting of mechanized pattern detection that can be used to distinguish two or more classes of objects in a dataset (e.g., species, genotypes, or disease). Linear discriminants were determined using the ‘lda’ function in the R package MASS (Venables and Ripley, 2002). Those linear discriminants, which are multivariate classifications similar to PCs, are then used to classify the leaves in the data set, blind to their assigned identity, according to class (i.e., species, genotype, or disease) using the ‘predict’ function. The end result is visualized as a table of predicted vs. actual class (i.e., species, genotype, disease) identity.

A second approach using elliptical Fourier descriptors (EFDs) was employed to look at differences in overall leaf shape within and among genotypes and species. Individual scanned leaves were converted to binary images (i.e., black leaf image on a white background) using custom macros in ImageJ for chain coding. Occasionally, some leaves were damaged or diseased, resulting in deformed leaf shapes (see below); these leaves were removed from the EFD dataset. Each binary image was converted into chain code using the program SHAPE v1.3 (Iwata and Ukai, 2002). EFD analysis begins by building chain code along the perimeter of each leaf to create a harmonic series (Chitwood and Sinha, 2016). Chain code contours were converted to normalized EFDs for Fourier analysis. In the R package Momocs (Bonhomme et al., 2014), function ‘nef2coe’ was used to convert normalized EFDs to harmonic coefficients, or ‘coe’ objects. The ‘coe’ objects were analyzed for differences in leaf shape outline using PCA and visualized using the ‘dudi.plot’ function. For each genotype, an average outline shape was calculated using the ‘meanShapes’

<sup>2</sup><https://github.com/lklein/VitisDigitalMorphometricAnalysis>

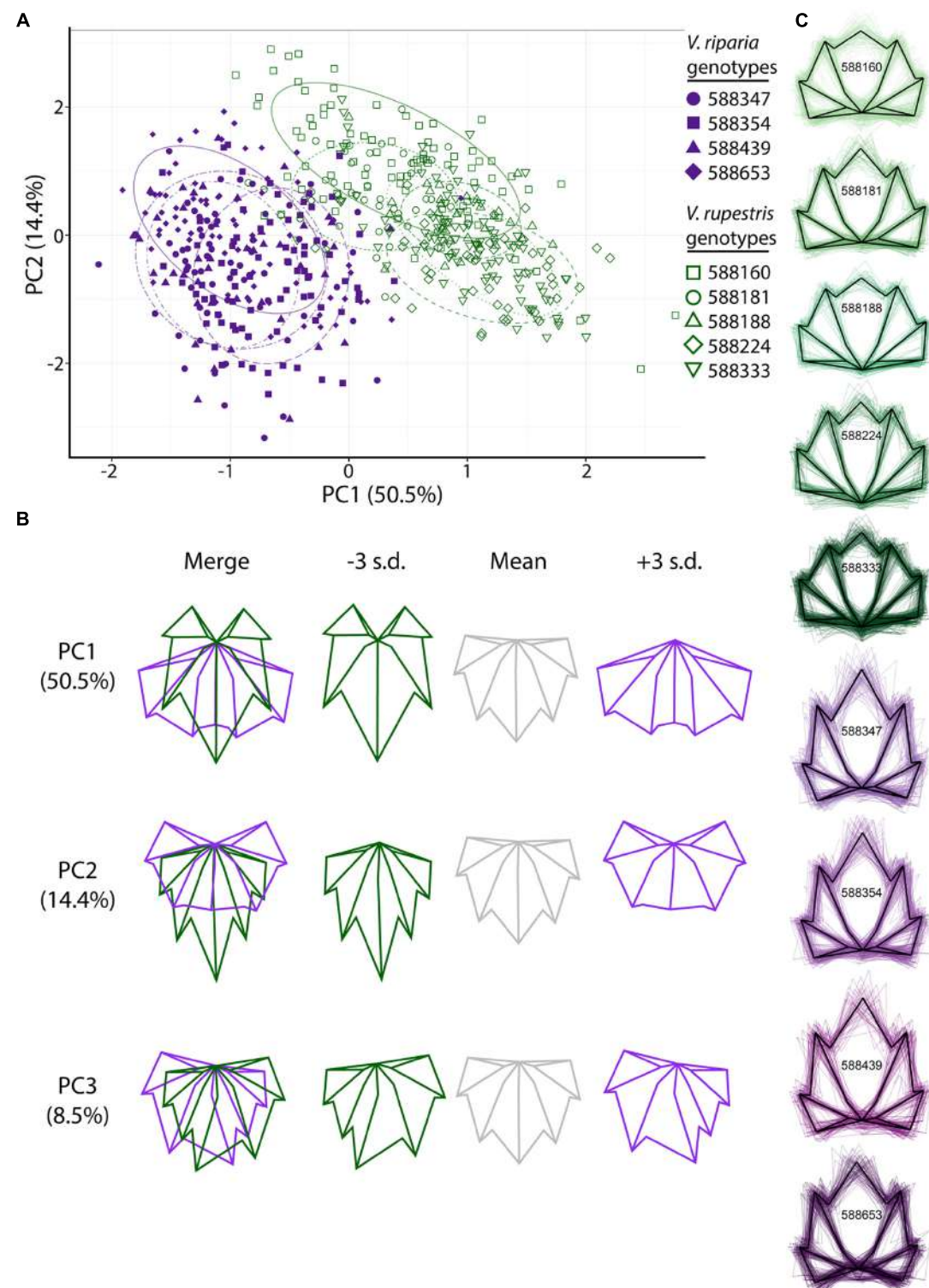


**FIGURE 2 | Generalized Procrustes analysis (GPA) of 17 landmark points applied to leaves harvested from the MBG common garden principal components (PC) morphospace. (A)** PCs 1 and 2 of *Vitis riparia* (purple, filled) and *V. rupestris* (green, open) leaves. Different shapes represent genotypes (see legend). The 95% confidence ellipses drawn around each genotype are designated by different dashed patterns for each genotype. **(B)** ‘Eigenleaves’ display differences among mean leaf morphologies in PCs 1–3 at  $\pm 3$  SD and percent shape variance for each. **(C)** Black outline represents the average shape outline of each *V. riparia* and *V. rupestris* genotype, with all outlines super imposed beneath in purple and green, respectively.

function, then visualized using function ‘tps.iso’ in the Momocs R package.

## Signatures of Pest and Pathogen Interaction

The MBG common garden included North American grapevines grown within their natural geographic distribution and were not treated with pesticides or fungicides in the common garden. Consequently, several individuals became infested with phylloxera (*Daktulosphaira vitifoliae* Fitch) and infected with grape fan-leaf virus (GFLV), among potential others. Both are common issues among native North American *Vitis* species and are generally non-fatal, but these pests and pathogens can have significant effects on the morphology of grapevine leaves and are disastrous in the grape industry (Andret-Link et al., 2004; Nabity et al., 2013). During our preliminary analyses, we detected leaf morphologies atypical of *V. riparia* or *V. rupestris*; subsequently, we determined these leaves were infected with phylloxera galls and/or GFLV. While this is an interesting aspect of phenotype, it reduces the accuracy with which we can interpret differences between species and within and among genotypes. Therefore, we removed those individuals expressing the diseased phenotype for examining differences between healthy individuals and performed separate analyses on a dataset including the diseased phenotype.

Two resulting data sets and analyses were designed to assess these aspects of leaf shape: (1) a phenotypically disease-free dataset to address overall differences in leaf shape using GPA, LDA, and EFDs, with individual leaves that expressed the GFLV phenotype as well as any leaves laden with phylloxera galls that severely deformed leaf morphology removed; (2) the total dataset (i.e., including diseased and non-diseased phenotypes) to assess the impact of disease on morphology. Leaves in the total dataset were scored based on the presence of a phylloxera- or GFLV-infected genotype, and correlation tests between shoot position and those leaves expressing the diseased phenotypes were performed using Spearman’s rank correlation rho and visualized with ggplot2 (Wickham, 2009).

## RESULTS

### Assessing Leaf Shape Variation among Species, among Genotypes within Species, and among Clones within Genotypes

To assess variation in leaf shape among species, among genotypes within species, and among clones within genotypes, we first looked at leaf shapes of the phenotypically disease-free *V. riparia* and *V. rupestris* leaves in the MBG common garden. GPA of the landmark points demonstrates observable differences between the leaves of *V. riparia* and *V. rupestris*: the first two PCs explain 64.9% of the variance in the data, with discernible clouds representing *V. riparia* (purple) and *V. rupestris* (green; Figure 2A). Low PC1 (Figure 2A x-axis, Figure 2B top panel) scores are reflective of longer than wide leaf blades, deeper

petiolar sinuses, and major and minor vein axes (i.e., the inner five landmarks) that vary from the branch point of the midvein being the most distal from the petiolar junction to the midvein branch point and the branch point of both major distal veins being nearly equally distal from the petiolar junction. High PC1 scores describe those leaves that are wider than long, with shallower petiolar sinuses, which is representative of *V. rupestris* leaf morphology. Similar to PC1, low PC2 scores are representative of cordate leaves, but the petiolar sinus largely absent, more convex. High PC1 and PC2 scores also detect wider than long leaf blades, but with shallow yet deeper petiolar sinus lobes characterizing high PC2 scores (Figure 2A y-axis, Figure 2B middle panel).

Generalized Procrustes analysis also detected differences among genotypes within species in the MBG common vineyard. Genotypes (Figure 2A) are represented as different shapes (i.e., *V. riparia* genotypes are filled shapes, *V. rupestris* are open), and appear to occupy distinct groups within each species. PC3 detects mostly asymmetrical leaf shape variation (Figure 2B bottom panel), a relatively common phenomenon in grape leaves (Wolf et al., 1986). Figure 2C represents the mean shape of each genotype extracted from Procrustes coordinates (black outline), as well as all leaf shape outlines (colored), demonstrating that within a species, there are subtle variations within genetically distinct individuals.

We used LDA to examine if phenotypically disease-free leaf morphology patterns among species and among genotypes in the MBG common garden vary predictably. Six of 263 *V. riparia* leaves (2%) and three of 315 *V. rupestris* leaves (0.9%) were wrongly classified (Table 2; >98% leaves correctly assigned to species). Accuracy decreased when we used LDA to predict genotype for each leaf: 385 of 578 leaves were predicted to be the correct genotype (66%; Supplementary Table S1). Five of the nine genotypes had leaves that were assigned to the wrong species. Two leaves of a single *V. riparia* genotype 588653 clone were incorrectly predicted to be *V. rupestris*. These misclassifications are likely because the genotype tends to be characterized by a shorter midvein, thus appearing more similar to the *V. rupestris* morphology (e.g., Figures 2C, 3A). Further, two misclassified leaves from the same individual, among other leaves from this genotype, suggests interclonal variation within this genotype. Out of five clones, two clones of *V. rupestris* genotype 588181 each had one leaf incorrectly predicted to be *V. riparia*. Compared to other *V. rupestris* genotype average shape outlines (Figures 2C, 3A), *V. rupestris* genotype 588181

**TABLE 2 |** LDA-generated species identity predictions for 263 *V. riparia* leaves and 315 *V. rupestris* leaves.

	Predicted Species Identity	
	<i>V. riparia</i>	<i>V. rupestris</i>
Species identity	<i>V. riparia</i>	257
	<i>V. rupestris</i>	3

Rows represent species identity according to USDA-ARS-GGRU germplasm accession records, and columns are the predicted species identity based on algorithms the program uses to discern shape features as different categories.

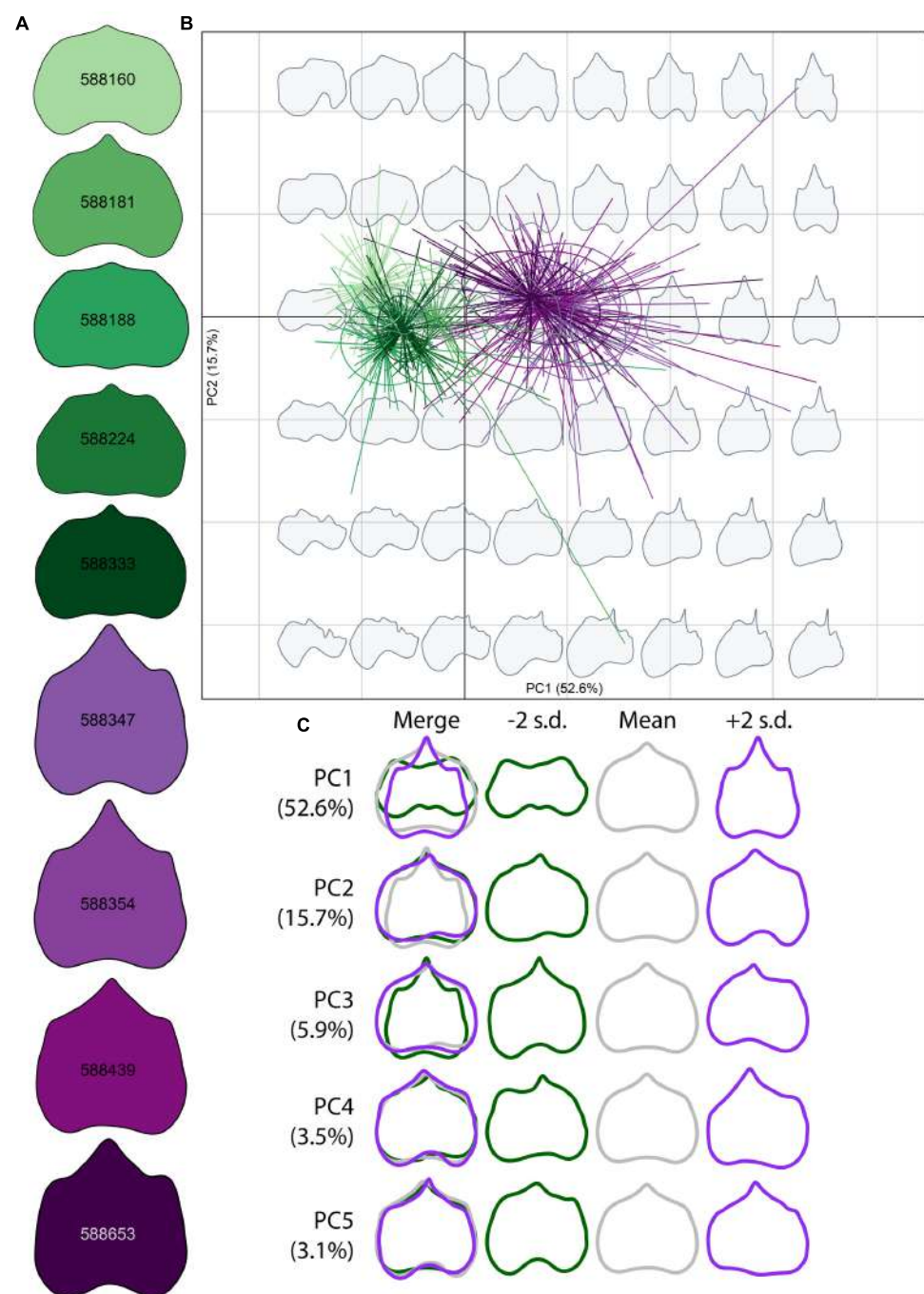


**FIGURE 3 | Morphospace of elliptical Fourier descriptors (EFDs).** **(A)** Average leaf shape outline for each genotype. Different shades of purple and green correspond to different genotypes. **(B)** PCs 1 and 2 of harmonic coefficients for *V. riparia* (purple) and *V. rupestris* (green). Different shades of purple and green correspond with genotypes in **(A)**. Gray leaf outlines on the background represent shapes drawn on the positions on the factorial map. **(C)** ‘Eigenleaves’ display differences among mean leaf morphologies in PCs 1–5 at  $\pm 2$  SD and percent shape variance for each, with overlay in the left column.

is characterized by a comparatively deeper petiolar sinus, which may have contributed to the incorrect prediction of these leaves. Overall, LDA performed well at identifying leaf shape features at the species level, but accuracy was limited in the classification of leaf shape features at the level of genotype.

Elliptical Fourier descriptor analysis, which compares total shape variation through the use of shape outlines (**Figure 3**), largely supports among-species and among-genotype shape variation detected using GPA (**Figure 2**). Low PC1 (**Figure 3B** x-axis, **Figure 3C** top panel) values describe those leaf blades

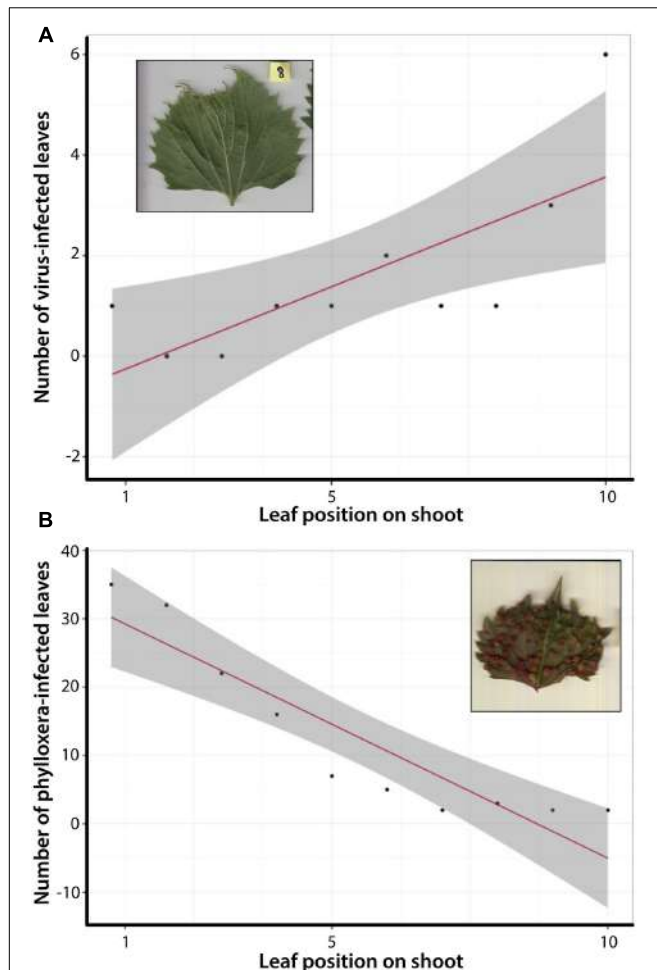


**FIGURE 4 | Correlation tests between shoot position and number of leaves expressing an infected phenotype. (A)** Total number of leaves expressing the GFLV phenotype occurs more often in older, more developed leaves. **(B)** Total number of leaves expressing phylloxera galls is more common in newly developed leaves.

that are wider and long, while high PC1 values describe leaf longer than wide blades, for a total of 52.6% of the variation explained in the total dataset. PC2 (**Figure 3B** y-axis, **Figure 3C** second panel), describing 15.7% of the variation, captures shallow petiolar sinuses in low PC2 values, versus deeper petiolar sinuses represented by high PC2 values. PCs three through five (**Figure 3C** bottom three panels) detect the asymmetry that characterizes some malformed leaves in the MBG common garden, much like GPA (**Figure 2B**). Asymmetry in leaf shape is common among *Vitis* species (Wolf et al., 1986).

## Signatures of Pest and Pathogen Interaction

During initial analysis of the total MBG vineyard dataset, we observed several leaves expressing phenotypes congruent with deformities caused by GFLV or galls indicative of phylloxera

infestation. Leaves infected with GFLV, a common viral infection among grapevines, exhibit crowding of the major veins into a fan-like shape, with vein tips elongating past the leaf blade at termination (**Figure 4A**). The petiolar sinus, which is concave in healthy leaves of both *V. riparia* and *V. rupestris*, instead becomes convex at the petiolar junction. Phylloxera, also specific to grapevines, is a parasitic insect that forms galls in the leaf and root tissues, causing malformations in the surrounding tissues and structures (**Figure 4B**). Diseased leaf phenotypes resulted in several LDA misidentifications in the total dataset (Supplementary Figure S1). Moreover, we observed that certain genotypes appeared to be more susceptible to pests (e.g., 588347, 588181) or pathogens (e.g., 588439, 588188) while others maintain a healthy phenotype (e.g., 588333, 588160; Supplementary Figure S1). The pattern of incorrect assignment suggests certain genotypes were more susceptible leaf shape modification as a result of pests or pathogens.

We quantified the diseased phenotype further by looking at the relationship between leaf development (position of the leaf along a shoot) and infected leaf phenotypes. For the total dataset of 640 leaves correlation tests demonstrated a significant relationship between older, more developed leaves and the expression of the GFLV phenotype (**Figure 4A**). In contrast, the opposite trend was observed for phylloxera galls, which were more common in younger leaves (**Figure 4B**). These data suggest not only are certain genotypes within a species more susceptible to pathogens than others, but that the expression of unique leaf phenotypes associated with disease varies along the shoot within an individual.

## DISCUSSION

This study advances current understanding of shape differences in the context of species, development, and biotic interaction through the use of clonal replicates of multiple genotypes in a common environment. Digital morphometric techniques offer great utility for future research in *Vitis*, but also serve as an example for other biological systems that seek to make sense of morphological variation.

## Leaf Shape Variation among Species, among Genotypes within Species, and among Clones within Genotypes

Detailed analyses of leaf shape variation have applications in viticulture (Galet, 1979; Chitwood et al., 2014) and also in biodiversity research. Our results indicate that inter- and intra-specific leaf shape variation is discernible in a common garden containing multiple genotypes of *V. riparia* and *V. rupestris*. Distinct clusters of *V. riparia* and *V. rupestris* visualized with GPA (**Figure 2A**) and EFD (**Figure 3B**) confirm existing species distinctions based on morphological and phylogenetic data (Moore, 1991; Ren et al., 2011). Researchers already combine genetic and morphological data to generate strong phylogenetic hypotheses (Cannon and Manos, 2001; Wortley and Scotland, 2006; Fouquet et al., 2012). Increasingly, the utility of digital morphometrics for evolutionary and ecological research is

becoming more apparent (Neto et al., 2006; Cope et al., 2012; Wilf et al., 2016), and has promising applications as museum collections become digitized and publicly available. Our analyses also show distinct, averaged leaf shapes among genotypes that are clonally replicated (**Figures 2C, 3A**). In addition, interclonal variation was detected, as LDA identified several individual leaves that were incorrectly assigned (**Table 2**). The ability to quantify discrete phenotypes across multiple levels of organization (within genotype, among genotype, among species) could be serviceable in the identification of adaptive phenotypes linked with genetic or environmental data (e.g., Lande, 2009).

The resolution with which our study identified inter- and intra-specific leaf shape variation is valuable to ecological questions that attempt to discern predictable patterns among complex systems. For example, community interaction or phenotypic plasticity research regularly seeks to make use of functional traits (traits related to increased fitness), which can be related to morphological features. Several studies have identified relationships between leaf shape and altitudinal or temperature gradients using more traditional, length and width leaf measurements or anatomical traits (e.g., *Metrosideros*, Cordell et al., 1998; *Nothofagus*, Hovenden and Vander Schoor, 2004; *Oryza*, Zhou et al., 2013). Applying GPA, LDA, or EFD analysis to morphological data in combination with environmental and genetic data is increasingly feasible as bioinformatic capability increases, thus increasing the potential to uncover acute character linkages between or among species, populations, or individuals. Recently, digital morphometrics was employed to compare *Vitis* leaves from USDA-ARS-GGRU germplasm from two different growing seasons (Chitwood et al., 2016b). In this work, growing season was accurately predicted from leaf shape using LDA. Large-scale digital morphometric datasets have the potential to identify subtle evolutionary and ecological relationships.

## Signatures of Pest and Pathogen Interaction

Digital morphometrics is an effective method for identifying and characterizing biotic stress in plants. Consistent with previous work, we observed that pest and pathogen infestation in grapevines affects specific genotypes more than others (Andret-Link et al., 2004; Granett et al., 2001; Omer et al., 1999b; Supplementary Figure S1). Further, our data suggest there is developmental context to the disease phenotype expressed within a single individual (**Figure 4**). Individuals infected with GFLV expressed the diseased phenotype in more developed leaves; whereas individuals infected with phylloxera expressed the diseased phenotype (leaf galls) in younger leaves. Primary goals of grape breeding include the development of biotic stress resistant scions and rootstocks, and *V. riparia* and *V. rupestris* surveyed here have been used to breed both the rootstock and the scion (Warschefsky et al., 2016). North American grapevines have evolved resistance to native pests and pathogens such as GFLV and phylloxera, but several studies (including ours) suggest variation in resistance response (e.g., Omer et al., 1999a; McKenry et al., 2001). As such it is useful to examine the range of natural

variation in native grapevines that could be harnessed to maintain pest and pathogen resistance in grapevines. As researchers continue to investigate these patterns, detailed phenotyping paired with molecular and ecological data could provide deeper insight to these challenges to the grapevine industry.

## CONCLUSION

In this study, we analyzed leaf shape variation between *V. riparia* and *V. rupestris*, as well as within and among genetically identical individuals of those species. Patterns of morphological differentiation were consistent with species boundaries and displayed genotype-specific signatures. Further, we observed leaf shape variation among clones, some of which was the result of pest and pathogen-induced leaf damage at predictable developmental stages. These data provide a window into how leaf shape varies among species, genotypes, and clones under common conditions, and offers a unique opportunity to look at the effect of abiotic effects on cloned individuals.

## AUTHOR CONTRIBUTIONS

LK, DC, and AM contributed to the conception of the work and the interpretation of data. LK, MC, CK, and RO contributed to data acquisition, and LK, CC, and DC contributed to analysis. LK drafted the manuscript, and all authors revised several drafts. All authors agree to be accountable for accuracy and integrity of the work.

## FUNDING

The Saint Louis University Center for Sustainability funded the development of the research vineyard. A Saint Louis University Graduate Research Assistantship supported LK throughout this work. The National Science Foundation Research Experiences for Undergraduates program at the Missouri Botanical Garden supported CK under the direction of Dr. David Bogler.

## ACKNOWLEDGMENTS

We appreciate Dr. Jason Londo for providing dormant canes for propagation from the USDA-ARS-GGRU germplasm. We are grateful to the Missouri Botanical Garden for propagating the canes, installing and maintaining the common garden under the direction of Mr. Andrew Wyatt. Special thanks goes to members of the Miller lab for providing valuable feedback on previous versions of the manuscript.

## SUPPLEMENTARY MATERIAL

The Supplementary Material for this article can be found online at: <http://journal.frontiersin.org/article/10.3389/fpls.2017.00373/full#supplementary-material>

## REFERENCES

- Abràmoff, M. D., Magalhães, P. J., and Ram, S. J. (2004). Image processing with ImageJ. *BioPhotonics Int.* 11, 36–42.
- Andret-Link, P., Laprote, C., Valat, L., Ritzenthaler, C., Demangeat, G., Vigne, E., et al. (2004). Grapevine fanleaf virus: still a major threat to the grapevine industry. *J. Plant Pathol.* 86, 183–195.
- Atlan, A., Hornoy, B., Delerue, F., Gonzalez, M., Pierre, J. S., and Tarayre, M. (2015). Phenotypic plasticity in reproductive traits of the perennial shrub *Ulex europaeus* in response to shading: a multi-year monitoring of cultivated clones. *PLoS ONE* 10:e0137500. doi: 10.1371/journal.pone.0137500
- Bonhomme, V., Picq, S., Gaucherel, C., and Claude, J. (2014). Momocs: outline analysis using R. *J. Stat. Softw.* 56, 1–24. doi: 10.18637/jss.v056.i13
- Boyce, C. K. (2008). The fossil record of plant physiology and development: what leaves can tell us. *Paleontol. Soc. Pap.* 14, 133–146.
- Boyd, L. A., Ridout, C., O'Sullivan, D. M., Leach, J. E., and Leung, H. (2013). Plant-pathogen interactions: disease resistance in modern agriculture. *Trends Genet.* 29, 233–240. doi: 10.1016/j.tig.2012.10.011
- Callen, S. T., Klein, L. L., and Miller, A. J. (2016). Climatic niche characterization of 13 North American *Vitis* species. *Am. J. Enol. Viticul.* 52, 304–309. doi: 10.5344/ajev.2016.15110
- Cannon, C. H., and Manos, P. S. (2001). Combining and comparing morphometric shape descriptors with a molecular phylogeny: the case of fruit type evolution in Bornean *Lithocarpus* (Fagaceae). *Syst. Biol.* 50, 860–880. doi: 10.1080/106351501753462849
- Chitwood, D. H., Klein, L. L., O'Hanlon, R., Chacko, S., Greg, M., Kitchen, C., et al. (2016a). Latent developmental and evolutionary shapes embedded within the grapevine leaf. *New Phytol.* 210, 343–355. doi: 10.1111/nph.13754
- Chitwood, D. H., Ranjan, A., Martinez, C. C., Headland, L. R., Thiem, T., Kumar, R., et al. (2014). A modern ampelography: a genetic basis for leaf shape and venation patterning in grape. *Plant Physiol.* 164, 259–272. doi: 10.1104/pp.113.229708
- Chitwood, D. H., Rundell, S. M., Li, D. Y., Woodford, Q. L., Yu, T. T., Lopez, J. R., et al. (2016b). Climate and developmental plasticity: interannual variability in grapevine leaf morphology. *Plant Physiol.* 170, 1480–1491. doi: 10.1104/pp.15.01825
- Chitwood, D. H., and Sinha, N. R. (2016). Evolutionary and environmental forces sculpting leaf development. *Curr. Biol.* 26, R297–R306. doi: 10.1016/j.cub.2016.02.033
- Cope, J. S., Corney, D., Clark, J. Y., Remagnino, P., and Wilkin, P. (2012). Plant species identification using digital morphometrics: a review. *Expert Syst. Appl.* 39, 7562–7573. doi: 10.1016/j.eswa.2012.01.073
- Cordell, S., Goldstein, G., Mueller-Dombois, D., Webb, D., and Vitousek, P. M. (1998). Physiological and morphological variation in *Metrosideros polymorpha*, a dominant Hawaiian tree species, along an altitudinal gradient: the role of phenotypic plasticity. *Oecologia* 113, 188–196. doi: 10.1007/s004420050367
- De Kroon, H., Huber, H., Stuefer, J. F., and Van Groenendaal, J. M. (2005). A modular concept of phenotypic plasticity in plants. *New Phytol.* 166, 73–82. doi: 10.1111/j.1469-8137.2004.01310.x
- Dkhar, J., and Pareek, A. (2014). What determines a leaf's shape? *EvoDevo* 5:47. doi: 10.1186/2041-9139-5-47
- Dryden, I. L. (2017). *R Foundation for Statistical Computing. Contributed Package Version 1.2.0*. Vienna: R Foundation for Statistical Computing.
- Fouquet, A., Recoder, R., Teixeira, M. Jr., Cassimiro, J., Amaro, R. C., Camacho, A., et al. (2012). Molecular phylogeny and morphometric analyses reveal deep divergence between Amazonia and Atlantic Forest species of *Dendrophryniscus*. *Mol. Phylogenet. Evol.* 62, 826–838. doi: 10.1016/j.ympev.2011.11.023
- Galet, P. (1979). *A Practical Ampelography*. Ithaca, NY: Cornell University Press.
- Granett, J., Walker, M. A., Kocsis, L., and Omer, A. D. (2001). Biology and management of grape phylloxera. *Annu. Rev. Entomol.* 46, 387–412. doi: 10.1146/annurev.ento.46.1.387
- Hovenden, M. J., and Vander Schoor, J. K. (2004). Nature vs nurture in the leaf morphology of Southern beech, *Nothofagus cunninghamii* (Nothofagaceae). *New Phytol.* 161, 585–594. doi: 10.1046/j.1469-8137.2003.00931.x
- Ichihashi, Y., Aguilar-Martínez, J. A., Farhi, M., Chitwood, D. H., Kumar, R., Millon, L. V., et al. (2014). Evolutionary developmental transcriptomics reveals a gene network module regulating interspecific diversity in plant leaf shape. *Proc. Natl. Acad. Sci. U.S.A.* 111, E2616–E2621. doi: 10.1073/pnas.1402835111
- Iwata, H., and Ukai, Y. (2002). SHAPE: a computer program package for quantitative evaluation of biological shapes based on elliptic Fourier descriptors. *J. Hered.* 93, 384–385. doi: 10.1093/jhered/93.5.384
- Kadioglu, A., Terzi, R., Saruhan, N., and Saglam, A. (2012). Current advances in the investigation of leaf rolling caused by biotic and abiotic stress factors. *Plant Sci.* 182, 42–48. doi: 10.1016/j.plantsci.2011.01.013
- Kaplan, D. R. (2001). The science of plant morphology: definition, history, and role in modern biology. *Am. J. Bot.* 88, 1711–1741. doi: 10.2307/3558347
- Lande, R. (2009). Adaptation to an extraordinary environment by evolution of phenotypic plasticity and genetic assimilation. *J. Evol. Biol.* 22, 1435–1446. doi: 10.1111/j.1420-9101.2009.01754.x
- Little, S. A., Kembel, S. W., and Wilf, P. (2010). Paleotemperature proxies from leaf fossils reinterpreted in light of evolutionary history. *PLoS ONE* 5:e15161. doi: 10.1371/journal.pone.0015161
- McKenry, M. V., Kretsch, J. O., and Anwar, S. A. (2001). Interactions of selected rootstocks with ectoparasitic nematodes. *Am. J. Enol. Vitic.* 52, 304–309.
- Miller, A. J., Matasci, N., Schwaninger, H., Aradhya, M. K., Prins, B., Zhong, G. Y., et al. (2013). Vitis phylogenomics: hybridization intensities from a SNP array outperform genotype calls. *PLoS ONE* 8:e78680. doi: 10.1371/journal.pone.0078680
- Moore, M. O. (1991). Classification and systematics of eastern North American *Vitis* L. (Vitaceae) north of Mexico. *SIDA Contrib. Bot.* 14, 339–367.
- Moore, M. O., and Wen, J. (2016). "Vitaceae," in *Flora of North America North of Mexico*, Vol. 12, ed. Flora of North America Editorial Committee (New York, NY: Oxford University Press).
- Nabity, P. D., Haus, M. J., Berenbaum, M. R., and DeLucia, E. H. (2013). Leaf-galling phylloxera on grapes reprograms host metabolism and morphology. *Proc. Natl. Acad. Sci. U.S.A.* 110, 16663–16668. doi: 10.1073/pnas.1220219110
- Neto, J. C., Meyer, G. E., Jones, D. D., and Samal, A. K. (2006). Plant species identification using Elliptic Fourier leaf shape analysis. *Comput. Electron. Agric.* 50, 121–134. doi: 10.1016/j.compag.2005.09.004
- Nicotra, A. B., Leigh, A., Boyce, C. K., Jones, C. S., Niklas, K. J., Royer, D. L., et al. (2011). The evolution and functional significance of leaf shape in the angiosperms. *Funct. Plant Biol.* 38, 535–552. doi: 10.1098/rspb.2012.1110
- Omer, A. D., Granett, J., Kocsis, L., and Downie, D. A. (1999a). Preference and performance responses of California grape phylloxera to different *Vitis* rootstocks. *J. Appl. Entomol.* 123, 341–346. doi: 10.1046/j.1439-0418.1999.00394.x
- Omer, A. D., Granett, J., and Wakeman, R. J. (1999b). Pathogenicity of *Fusarium oxysporum* on different *Vitis* rootstocks. *J. Phytopathol.* 147, 433–436. doi: 10.1111/j.1439-0434.1999.tb03846.x
- Peppe, D. J., Royer, D. L., Cariglino, B., Oliver, S. Y., Newman, S., Leight, E., et al. (2011). Sensitivity of leaf size and shape to climate: global patterns and paleoclimate applications. *New Phytol.* 190, 724–739. doi: 10.1111/j.1469-8137.2010.03615.x
- R Core Team (2016). *R: A Language and Environment for Statistical Computing*. Vienna: R Foundation for Statistical Computing.
- Ren, H., Lu, L. M., Soejima, A., Luke, Q., Zhang, D. X., Chen, Z. D., et al. (2011). Phylogenetic analysis of the grape family (Vitaceae) based on the noncoding plastid trnC-petN, trnH-psbA, and trnL-F sequences. *Taxon* 60, 629–637.
- Rendu, V. (1854). *Ampélographie Française: Description des Principaux Cépages, des Procédés de Culture et de Vinification Usités dans les Meilleurs Crus de France*. Paris: V. Bouchard-Huzard.
- Royer, D. L., Meyerson, L. A., Robertson, K. M., and Adams, J. M. (2009). Phenotypic plasticity of leaf shape along a temperature gradient in *Acer rubrum*. *PLoS ONE* 4:e7653. doi: 10.1371/journal.pone.0007653
- Venables, W. N., and Ripley, B. D. (2002). *Modern Applied Statistics with S*, 4th Edn. New York, NY: Springer. doi: 10.1007/978-0-387-21706-2
- Viscosi, V., and Cardini, A. (2011). Leaf morphology, taxonomy and geometric morphometrics: a simplified protocol for beginners. *PLoS ONE* 6:e25630. doi: 10.1371/journal.pone.0025630
- Wan, Y., Schwaninger, H. R., Baldo, A. M., Labate, J. A., Zhong, G.-Y., and Simon, C. J. (2013). A phylogenetic analysis of the grape genus (*Vitis* L.) reveals broad reticulation and concurrent diversification during neogene and quaternary climate change. *BMC Evol. Biol.* 13:141. doi: 10.1186/1471-2148-13-141

- Warschefsky, E. J., Klein, L. L., Frank, M. H., Chitwood, D. H., Londo, J. P., von Wettberg, E. J. B., et al. (2016). Rootstocks: diversity, domestication, and impacts on shoot phenotypes. *Trends Plant Sci.* 21, 418–437. doi: 10.1016/j.tplants.2015.11.008
- Wickham, H. (2009). *Ggplot2: Elegant Graphics for Data Analysis*. Berlin: Springer Science & Business Media. doi: 10.1007/978-0-387-98141-3
- Wilf, P., Zhang, S., Chikkerur, S., Little, S. A., Wing, S. L., and Serre, T. (2016). Computer vision cracks the leaf code. *Proc. Natl. Acad. Sci. U.S.A.* 113, 3305–3310. doi: 10.6084/m9.figshare.1521157
- Wolf, S. D., Silk, W. K., and Plant, R. E. (1986). Quantitative patterns of leaf expansion: comparison of normal and malformed leaf growth in *Vitis vinifera* cv. Ruby Red. *Am. J. Bot.* 73, 832–846. doi: 10.2307/2444294
- Wortley, A., and Scotland, R. (2006). The effect of combining molecular and morphological data in published phylogenetic analyses. *Syst. Biol.* 55, 677–685. doi: 10.1080/10635150600899798
- Zhou, W., Wang, Z., Davy, A. J., and Liu, G. (2013). Geographic variation and local adaptation in *Oryza rufipogon* across its climatic range in China. *J. Ecol.* 101, 1498–1508. doi: 10.1111/1365-2745.12143

**Conflict of Interest Statement:** The authors declare that the research was conducted in the absence of any commercial or financial relationships that could be construed as a potential conflict of interest.

Copyright © 2017 Klein, Caito, Chapnick, Kitchen, O'Hanlon, Chitwood and Miller. This is an open-access article distributed under the terms of the Creative Commons Attribution License (CC BY). The use, distribution or reproduction in other forums is permitted, provided the original author(s) or licensor are credited and that the original publication in this journal is cited, in accordance with accepted academic practice. No use, distribution or reproduction is permitted which does not comply with these terms.



# Does Size Matter? Atmospheric CO<sub>2</sub> May Be a Stronger Driver of Stomatal Closing Rate Than Stomatal Size in Taxa That Diversified under Low CO<sub>2</sub>

Caroline Elliott-Kingston<sup>1\*</sup>, Matthew Haworth<sup>2</sup>, Jon M. Yearsley<sup>3</sup>, Sven P. Batke<sup>3</sup>, Tracy Lawson<sup>4</sup> and Jennifer C. McElwain<sup>3</sup>

<sup>1</sup> School of Agriculture and Food Science, University College Dublin, Dublin, Ireland, <sup>2</sup> Italian National Research Council, Institute of Tree and Timber IVALSA, Rome, Italy, <sup>3</sup> Earth Institute, Science Centre East, School of Biology and Environmental Science, University College Dublin, Dublin, Ireland, <sup>4</sup> School of Biological Science, University of Essex, Colchester, UK

## OPEN ACCESS

### Edited by:

Daniel H. Chitwood,  
Donald Danforth Plant Science  
Center, USA

### Reviewed by:

Nava Moran,  
Hebrew University of Jerusalem, Israel  
Hugo J. De Boer,  
Utrecht University, Netherlands

### \*Correspondence:

Caroline Elliott-Kingston  
carolineelliottkingston@gmail.com

### Specialty section:

This article was submitted to  
Plant Biophysics and Modeling,  
a section of the journal  
Frontiers in Plant Science

Received: 16 March 2016

Accepted: 08 August 2016

Published: 24 August 2016

### Citation:

Elliott-Kingston C, Haworth M, Yearsley JM, Batke SP, Lawson T and McElwain JC (2016) Does Size Matter? Atmospheric CO<sub>2</sub> May Be a Stronger Driver of Stomatal Closing Rate Than Stomatal Size in Taxa That Diversified under Low CO<sub>2</sub>. *Front. Plant Sci.* 7:1253.  
doi: 10.3389/fpls.2016.01253

One strategy for plants to optimize stomatal function is to open and close their stomata quickly in response to environmental signals. It is generally assumed that small stomata can alter aperture faster than large stomata. We tested the hypothesis that species with small stomata close faster than species with larger stomata in response to darkness by comparing rate of stomatal closure across an evolutionary range of species including ferns, cycads, conifers, and angiosperms under controlled ambient conditions (380 ppm CO<sub>2</sub>; 20.9% O<sub>2</sub>). The two species with fastest half-closure time and the two species with slowest half-closure time had large stomata while the remaining three species had small stomata, implying that closing rate was not correlated with stomatal size in these species. Neither was response time correlated with stomatal density, phylogeny, functional group, or life strategy. Our results suggest that past atmospheric CO<sub>2</sub> concentration during time of taxa diversification may influence stomatal response time. We show that species which last diversified under low or declining atmospheric CO<sub>2</sub> concentration close stomata faster than species that last diversified in a high CO<sub>2</sub> world. Low atmospheric [CO<sub>2</sub>] during taxa diversification may have placed a selection pressure on plants to accelerate stomatal closing to maintain adequate internal CO<sub>2</sub> and optimize water use efficiency.

**Keywords:** stomata, half-closure time in response to darkness, stomatal size, atmospheric CO<sub>2</sub> concentration, time of taxa diversification

## INTRODUCTION

Stomata are microscopic pores on aerial surfaces of land plants, surrounded by guard cells that adjust turgor in order to regulate pore size, thus controlling gas exchange between the plant interior and atmosphere. Fossil records show that stomata evolved more than 400 million years ago (Ma) and their morphology remains largely unchanged (Edwards et al., 1998), apart from the evolution of dumbbell-shaped guard cells in grasses (Franks and Farquhar, 2007). Extant species have evolved from ancestors that originated under diverse environmental conditions; therefore, a simple expectation is that stomata in extant plants will exhibit morphological and functional diversity. Stomatal conductance governs gas exchange, photosynthesis, water loss and evaporative

cooling and is determined by density and size of stomata along with functional responses such as rate of aperture change. Stomatal density (SD) and size also determine maximum gas diffusion rate (Brown and Escombe, 1900; Parlange and Waggoner, 1970; Raschke, 1976; Wong et al., 1979; McElwain and Chaloner, 1995; Hetherington and Woodward, 2003; Franks and Beerling, 2009; McElwain et al., 2016). Density and size are linked and both are often correlated with atmospheric carbon dioxide concentration ( $[CO_2]_{atm}$ ; Hetherington and Woodward, 2003; McElwain et al., 2005; Franks and Beerling, 2009).

In an investigation into how morphological diversity in stomatal complexes influences stomatal function, Franks and Farquhar (2007) determined that morphological structure of the stomatal complex (guard cell shape and presence or absence of subsidiary cells) impacts mechanical opening and closing of stomata. In particular, the mechanical advantage of fully turgid subsidiary cells constrains guard cell lateral movement, limiting maximum aperture and leaf diffusive conductance. They showed that morphological and mechanical diversity ultimately translated into functional diversity. They concluded that the combination in grasses of dumbbell-shaped guard cells and the ability to quickly shuttle osmotica between subsidiary and guard cells facilitated swift alteration of turgor pressure, allowing rapid stomatal movements, which conferred a functional advantage upon grasses (Hetherington and Woodward, 2003; Franks and Farquhar, 2007). Another aspect of morphological diversity is number and size of stomata. On a geological timescale, a trend has been suggested with recently evolved species having high densities of small stomata compared to species with fewer, larger stomata in the past (Hetherington and Woodward, 2003; Franks and Beerling, 2009). Leaves with short lifespans, built for higher rates of gas exchange, are thought to have small stomata and faster stomatal response times to offset the risks associated with large tissue water potential gradients that may result in xylem cavitation (Drake et al., 2013). It has been suggested that the ability of angiosperms to sustain high stomatal conductance rates may be due to the possession of large numbers of small stomata (Hetherington and Woodward, 2003; Franks and Beerling, 2009). In addition, high densities of small stomata allow exploitation of the “edge effect” as small pores have a greater proportion of edge than large pores, resulting in a shorter diffusion pathway from the pore (Jones, 1992). In contrast to angiosperms, ferns and gymnosperms tend to have large stomata in small numbers (Franks and Beerling, 2009). For the same total pore area, a leaf with few large stomata will have a lower maximum stomatal conductance than a leaf with many small stomata because of the longer diffusion pathway through the stomatal pore. Thus, Franks and Beerling (2009) have proposed that high numbers of small stomata are necessary in low  $CO_2$  atmospheres, such as pertains today, to achieve high maximum diffusive conductance to  $CO_2$ . In addition, they suggest that small stomata respond faster than large stomata, enhancing their ability to function effectively in dynamic environments (Franks and Beerling, 2009). Robinson (1994) hypothesized that certain factors, such as declining atmospheric  $CO_2$  and water limitation, place selection pressures on plants to develop compensating mechanisms, including improved stomatal efficiency. Since

atmospheric  $[CO_2]$  has declined over the past 20 million years, Robinson (1994) suggested that the most recently evolved group, angiosperms, with faster rates of evolution, have more efficient stomata than ferns and gymnosperms. This hypothesis was tested on angiosperm and coniferous gymnosperm species; however, ferns and cycads were excluded (Robinson, 1994). In contrast to angiosperms, cycads are an ancient plant group (Jones, 2002; Nagalingum et al., 2011) with slow reproductive biology, long leaf lifespan, and relatively large stomata (Haworth et al., 2011); the question remains whether their large stomata are less efficient than the smaller stomata of angiosperms in our currently low  $CO_2$  world.

Cowan (1977) and Cowan and Farquhar (1977) hypothesized that plants display optimal stomatal behavior, defined as maximizing photosynthetic gain to water loss. It is reasonable to suppose that different taxa have developed diverse strategies for optimization. For example, a strategy for optimizing water use efficiency via stomatal behavior is to open stomata rapidly to take advantage of irradiance for photosynthetic gain, and to close them again quickly when conditions become unfavorable (Lawson and Blatt, 2014), for example, under limited water availability. The rate of stomatal opening and closing response is, therefore, one method of stomatal optimization (Katul et al., 2010; Lawson et al., 2010; Lawson and Blatt, 2014). In a study on stomatal opening and closing rate in different plant functional types, including graminoids, forbs, woody angiosperms and gymnosperms, in both wet and dry climates, graminoids were shown to have the fastest stomatal responses (Vico et al., 2011). The long pore length in grass stomata combined with narrow, dumbbell-shaped guard cells means that very small changes in guard and subsidiary cell turgor cause comparatively large changes in aperture and stomatal conductance (Hetherington and Woodward, 2003). Therefore, in grasses, large stomata (in terms of stomatal pore length, SPL) are not an impediment to efficient stomatal response to changing environmental conditions. Perhaps the evolutionary trend toward higher numbers of small stomata from few, large stomata has led to the common perception that small stomata are more efficient than large stomata, and that rate of stomatal response is directly linked to stomatal size (SS). “Small stomata can open and close more rapidly...” (Hetherington and Woodward, 2003). “Smaller stomata are capable of faster response times...” (Franks and Beerling, 2009). “...leaves with smaller and more numerous stomata exhibit faster absolute rates of response of stomatal conductance to water vapour” (Drake et al., 2013). Logically, this might be expected to be the case given that changes in osmotic potential are needed for guard cell swelling and smaller stomata have a greater surface area to volume ratio than larger stomata; changes in osmotic potential therefore affect small stomata relatively more than they affect large stomata. The assumption or perception that small stomata are faster may hold across related species within the same genus (Drake et al., 2013). However, this hypothesis has not been comprehensively tested across a range of phylogenetic groups. Here we test the hypothesis that small stomata are more efficient than large stomata with respect to rate of stomatal closure in response to a changing environmental signal, in this case,

darkness. To test this hypothesis, an evolutionary range of species including one fern, four gymnosperms and two angiosperms, including one cereal grass, were grown under identical controlled ambient conditions, and rate of stomatal closure in response to darkness was measured.

## MATERIALS AND METHODS

A range of plants representing all major vascular plant groups was selected for determining stomatal closure rate in response to darkness. These include: *Osmunda regalis* L. (Osmundaceae), a perennial, rhizomatous, deciduous fern; *Lepidozamia peroffskyana* von Regel (Zamiaceae), an evergreen cycad; *Ginkgo biloba* L. (Ginkgoaceae), a deciduous gymnosperm tree; two broad-leaved, evergreen conifers in the order Pinales, including *Podocarpus macrophyllus* (Thunb.) D. Don (Podocarpaceae) and *Agathis australis* (D. Don) Loudon (Araucariaceae); *Solanum lycopersicum* L. (Solanaceae), a dicotyledonous, herbaceous, perennial angiosperm; and *Hordeum vulgare* L. (Poaceae), a monocotyledonous, graminaceous, annual angiosperm. All species were individually planted into 4 l square pots (15 cm × 15 cm × 23 cm) in a growing medium comprising 80% compost (Shamrock® Multi-Purpose compost; Scotts Horticulture Ltd., Co. Kildare, Ireland), 20% vermiculite (2–5 mm horticultural grade; William Sinclair Horticulture Ltd., UK) and 7 kg/m<sup>-3</sup> Osmocote® Exact® 16–18 months slow release fertilizer (15% N, 8% P<sub>2</sub>O<sub>5</sub>, 11% K<sub>2</sub>O, 2.5% MgO plus trace elements; Scotts International BV, Netherlands).

Cycad seeds were initially scarified, soaked for 24 h in 3% potassium nitrate solution to encourage germination (Bradbeer, 1988), then placed in plastic bags containing a damp mixture of 50:50 perlite and vermiculite (2–5 mm Sinclair Standard; William Sinclair Horticulture Ltd., UK). To prevent fungal infection, the seeds were sprayed fortnightly with 0.06 g l<sup>-1</sup> Doff Systemic Fungus Control spray (Doff, UK) containing myclobutanil. Following the first appearance of the radical, seeds were sown in seed trays containing a 80:20 mixture of compost and vermiculite and placed in well-ventilated propagators under atmospheric treatment conditions (380 ppm CO<sub>2</sub>; 20.9% O<sub>2</sub>) in a Conviron BDW40 growth control chamber. After radicle development but just before emergence of the plumule, the seeds were planted individually into 4 l square pots (15 cm × 15 cm × 23 cm) using the growing medium described above. *H. vulgare* (barley) seeds were germinated in seed trays in the growing medium detailed above and potted up individually in the same medium 14 days after emergence of the coleoptile. After 18 months (or 3 months in the case of tomato and barley), plants were liquid fed with Osmocote® Plus Multi-Purpose Plant Food. One application feeds for up to 6 months, contains 15% N, 9% P<sub>2</sub>O<sub>5</sub>, 12% K<sub>2</sub>O plus nine other essential nutrients, and is suitable for all plant types and all soil conditions. All plants were grown in controlled environment chambers under identical conditions (see below).

## Controlled Growth Chambers

Six plants of each species were grown in two Conviron (Winnipeg, MB, Canada) BDW-40 walk-in growth rooms

(internal chamber size 3.7 m<sup>2</sup>) with atmospheric control of [CO<sub>2</sub>] at ambient (380 ppm) and [O<sub>2</sub>] at ambient (20.9%) in the Program for Experimental Atmospheres and Climate (PÉAC) facility at Rosemount Environmental Research Station, University College Dublin. Carbon dioxide concentration was maintained at 380 ppm by injection of compressed CO<sub>2</sub> (BOC UK, Surrey, England) and was continuously monitored with a PP-systems WMA-4 IRGA (Amesbury, MA, USA); injection of CO<sub>2</sub> gas was controlled by opening and closing a solenoid valve. Oxygen concentration was monitored and maintained at 20.9% by a PP-systems OP-1 Oxygen Sensor. All other growth conditions remained constant, with 16 h day length (0500–0600 hours, light intensity rose from 0 to 300 μmol m<sup>-2</sup> s<sup>-1</sup>; 0600–0900 hours, light intensity increased from 300 to 600 μmol m<sup>-2</sup> s<sup>-1</sup>; 0900–1700 hours, photosynthetic photon flux density (PPFD) maintained at 600 μmol m<sup>-2</sup> s<sup>-1</sup>; 1700–2000 hours, light intensity decreased from 600 to 300 μmol m<sup>-2</sup> s<sup>-1</sup>; 2000–2100 hours, light intensity decreased from 300 to 0 μmol m<sup>-2</sup> s<sup>-1</sup>), temperature regime (nighttime temperature of 18°C rising to a midday peak of 28°C), relative humidity of 80%, downward ventilation to ensure mixing of atmospheric gases; with each plant receiving 30 ml of water per day in the 1st year of growth, and 60 ml thereafter, except for ferns, which received 60 ml of water day<sup>-1</sup> in the 1st year and 120 ml day<sup>-1</sup> thereafter. In order to avoid mutual shading, plants were randomized within areas of identical canopy height in the growth chambers (Hammer and Hopper, 1997; Sager and McFarlane, 1997). *O. regalis*, *L. peroffskyana*, *G. biloba*, *P. macrophyllus*, and *A. australis* were grown for a minimum of 18 months before analysis. *S. lycopersicum* and *H. vulgare* were grown for a minimum of 3 months before analysis. To avoid chamber effects, plants were rotated between chambers every 3 months (Hirano et al., 2012).

## Measuring Rate of Stomatal Closure in Response to Darkness

Rate of stomatal closure in response to darkness (0 μmol m<sup>-2</sup> s<sup>-1</sup> PPFD) was measured using a PP-Systems CIRAS-2 portable photosynthesis system (Amesbury, MA, USA) from saturating light intensity calculated from photosynthesis response curves (Parsons et al., 1998) to 0 μmol m<sup>-2</sup> s<sup>-1</sup> PPFD in a single step decrease in PPFD. Measurements were performed on intact, mature, fully expanded leaves on three replicates of each species between 9 am and 11 am each day. Within the leaf cuvette, temperature was set to 25°C and water vapor pressure deficit was maintained at 1.0 ± 0.2 kPa. Cuticular conductance was assumed to be negligible. After  $g_s$  had reached steady state, irradiance was removed in the leaf cuvette chamber. To ensure no light leaked into the chamber from external sources, the room lights were also extinguished. Measurements of stomatal conductance ( $g_s$ ) were recorded every 10 s for 90 min, during which time all species reduced  $g_s$  to a minimum value. The half-closure time (minutes) was calculated; this was defined as the time taken for  $g_s$  to reach 50% of the difference between the first and final values. The first  $g_s$  value was taken 1–12 min, depending on species, after lights were extinguished to exclude the fluctuation in  $g_s$  that occurs due to a

change in energy balance in the CIRAS-2 when it recalculates  $g_s$  in darkness (as distinct from full light previously). The technical nature of the fluctuation is caused by temperature recalculation in the CIRAS-2 and is an artifact of the machine. The rate at which stomatal conductance declined can be quantified by the value of the half-closure time of the stomata: the shorter the time of half-closure, the faster the rate.

## Stomatal Morphology Measurements

Following completion of stomatal conductance ( $g_s$ ) measurements, the leaves on which  $g_s$  measurements were recorded were removed from the plants. Leaf impressions were taken from the abaxial leaf surface using dental impression material (Coltene PRESIDENT light body) and nail varnish “positives” were mounted onto glass slides (Weyers and Johansen, 1985). In the case of *H. vulgare*, leaf impressions were taken from both the abaxial and adaxial leaf surfaces. Five photomicrographs per leaf impression were recorded at  $\times 200$  magnification using a Leica (DMLB) epifluorescent microscope. SD was counted on each photomicrograph using AcQuis (version 4.0.1.10, Syncroscopy Ltd, Cambridge, UK) by placing a  $0.09\text{ mm}^2$  grid on the image (half-way down the leaf between midrib and leaf edge) and counting the number of stomata within the box and those touching two of the border lines and the corner where they intersect, on five micrographs for each of three leaves per plant and on three plants, giving a total of 45 counts. Mean SD (number of stomata per  $\text{mm}^2$ ) for the abaxial surfaces of all hypostomatous species was recorded. For amphistomatic *H. vulgare*, the average of both surfaces was recorded as one measurement. SPL ( $\mu\text{m}$ ) and guard cell width measurements ( $\mu\text{m}$ ) were taken for 5–20 open stomata per photomicrograph using the hand tool in AcQuis.

Stomatal geometry was calculated from guard cell width, stomatal pore depth, pore length and density of stomata when fully open ( $g_{\max}$ ; Table 1). Maximum stomatal pore area ( $\text{m}^2$ ) when the guard cells were fully turgid was calculated as an ellipse using SPL (m) multiplied by the width of the guard cell pair with maximum aperture defined as a fraction  $\beta$  of the stomatal pore; in the case of a circular pore with diameter equal to pore length,  $\beta = 1.0$  while in long narrow stomata  $\beta = 0.2$ . Maximum aperture was calculated with  $\beta$  values of 0.2, 0.4, 0.5, 0.6, 0.8, and 1.0. Theoretical maximum stomatal conductance ( $g_{s\max}$ ) was then calculated using the morphological measurements of fully open stomata and the following diffusion equation (Parlange and Waggoner, 1970; Franks and Beerling, 2009):

$$g_{\max} = \frac{\frac{dw}{v} \cdot SD \cdot pa_{\max}}{pd + \frac{\pi}{2} \sqrt{\frac{pa_{\max}}{\pi}}} \quad (1)$$

where  $dw$  = diffusivity of water vapor at  $25^\circ\text{C}$  ( $0.0000249\text{ m}^2\text{ s}^{-1}$ ) and  $v$  = molar volume of air ( $0.0224\text{ m}^3\text{ mol}^{-1}$ ) are both constants;  $SD$  is stomatal density ( $\text{m}^{-2}$ );  $pa_{\max}$  is maximum stomatal pore area ( $\text{m}^2$ ) calculated as an ellipse using SPL (l in m) as the long axis and  $1/2$  as the short axis; and  $pd$  is stomatal pore depth (m) considered to be equivalent to the width of an inflated, fully turgid guard cell (Franks and Beerling, 2009).

## Paleo-Carbon Dioxide Concentration (Paleo-[CO<sub>2</sub>])

Best estimates of origination date and last diversification date for each of the seven taxa were gathered from the literature. Atmospheric CO<sub>2</sub> concentration ([CO<sub>2</sub>]<sub>atm</sub>) over Phanerozoic time was taken from Bergman et al. (2004) COPSE model and from Berner and Kothavala (2001) GEOCARB III model. The relationship between estimated [CO<sub>2</sub>]<sub>atm</sub> at the time of each taxon's origination date and last known diversification date was tested against the log<sub>e</sub> of each species' half-closure time to determine whether [CO<sub>2</sub>]<sub>atm</sub> was correlated with rate of stomatal closing.

## Statistical Analysis

The decrease of stomatal conductance ( $g_s$ ;  $\text{mmol m}^{-2}\text{ s}^{-1}$ ) over time ( $t$ , minutes) was fitted to the following exponential decay curve:

$$g_s(t) = g_s(\infty) + (g_s(0) - g_s(\infty)) \cdot \exp(-\exp(A) \cdot t) \quad (2)$$

where  $g_s(0)$  is the stomatal conductance at time  $t = 0$ ,  $g_s(\infty)$  is the long-term residual stomatal conductance and  $A$  is a parameter related to the half-closure time response,  $t_{1/2}$ , by  $\log_e(t_{1/2}) = \log_e[\log_e(2)] - A$ . The fit was performed for each replicate of each of the seven species using generalized non-linear least squares with an error structure that allowed for first-order autoregressive temporal autocorrelation (implemented using the nlme package in R version 3.1.1; R Core Team, 2014); as shown in Figure 1. Each fit gave best-estimates and standard errors for  $g_s(0)$ ,  $g_s(\infty)$ , and  $A$ . From the fitted values of  $A$ , the half-closure time response was calculated for each replicate and the median, maximum and minimum half-closure time (min) calculated across replicates for a species. The half-closure time response is defined as the time taken for the stomatal conductance to decrease to half of its value at time  $t$ . For exponential decay, this half-time is a constant, independent of the initial stomatal conductance. ANOVA with Tukey's honest significant difference (HSD) post hoc analysis was used to test for differences between species in the  $\log_e$ (half-closure times). It was only possible to perform a between-species variance analysis, as the low number of replicates did not permit satisfactory analysis of the variability within species. Differences between species in the mean SD, SPL, and half-closure time were analyzed using a one-way ANOVA with Tukey's HSD pairwise comparison. Data were  $\log_e(SD)$  and square root (SPL) transformed prior to analysis. Generalized linear mixed-effects models were implemented using the lmer package in R to describe the relationship between the response variable,  $\log_e(\text{median half-closure time})$  and the fixed variables, SD, SPL, plant functional type, shade tolerance, drought tolerance, and climate, as defined by Vico et al. (2011). Species was treated as a random variable. ANOVA and Akaike information criterion (AIC) were used to identify the model with the best fit. Linear models (LM) were used to test for correlations between  $\log_e(\text{half-closure time})$  and estimated atmospheric CO<sub>2</sub> concentration at time of taxa origination and diversification. Moreover, LM were also used to test the correlations between  $\log_e(\text{half-closure time})$ , SD, and SPL.

**TABLE 1 |** Median and mean stomatal half-closure time (minutes) from maximum stomatal conductance ( $g_s$ ;  $\text{mmol m}^{-2} \text{s}^{-1}$ ) under illumination to minimum  $g_s$  in the dark; estimated time of taxa diversification (millions of years ago);  $[\text{CO}_2]$  (ppm) at time of taxa diversification; mean maximum  $g_s$  under illumination to mean minimum  $g_s$  in the dark ( $\text{mmol m}^{-2} \text{s}^{-1}$ ); mean reduction in  $g_s$  ( $\text{mmol m}^{-2} \text{s}^{-1}$ ; %) from maximum to minimum; mean stomatal pore length ( $\mu\text{m}$ ); mean stomatal density ( $\text{mm}^{-2}$ ); and mean theoretical maximum conductance ( $g_{s\max}$ ;  $\text{mmol m}^{-2} \text{s}^{-1}$ ) for seven species grown under controlled ambient atmosphere (380 ppm  $\text{CO}_2$ ; 20.9%  $\text{O}_2$ ).

Species	Median estimated half-closure time (minutes) (minimum and maximum in brackets)	Mean estimated half-closure time (minutes $\pm$ SEM)	Estimated time of taxa diversification (millions years ago)	$[\text{CO}_2]$ (ppm) at time of taxa diversification COPSE <sup>8</sup>	$[\text{CO}_2]$ (ppm) at time of taxa diversification GEOCARB III <sup>9</sup>	Mean maximum $g_s$ ( $\text{mmol m}^{-2} \text{s}^{-1}$ )	Mean minimum $g_s$ ( $\text{mmol m}^{-2} \text{s}^{-1}$ )	Mean change in $g_s$ ( $\text{mmol m}^{-2} \text{s}^{-1}$ ) from maximum to minimum	Mean stomatal pore length ( $\mu\text{m}$ ) $\pm$ SD	Mean stomatal density ( $\text{mm}^{-2}$ ) $\pm$ SD	Mean maximum conductance ( $g_{s\max}$ ) ( $\text{mmol m}^{-2} \text{s}^{-1}$ )
<i>Hordeum vulgare</i>	4.83 (4.25, 12.41)	7.16 $\pm$ 2.63	10,000 years <sup>1</sup>	333–280 ppm (low)	300 ppm (low)	558–53	505 (90.5)	28.1 $\pm$ 6.2	79.8 $\pm$ 30.7	1347.33	
<i>Lepidium sativum perofskiana</i>	6.53 (4.30, 19.96)	10.26 $\pm$ 4.89	12–6 Ma <sup>2</sup>	401–363 ppm (low)	300 ppm (low)	61–0	61 (100.0)	35.6 $\pm$ 5.5	33.3 $\pm$ 7.9	519.16	
<i>Podocarpus macrophyllus</i>	12.74 (11.71, 29.41)	17.96 $\pm$ 5.74	33–2.6 Ma <sup>3</sup>	718–346 ppm (declining)	420–300 ppm (low)	97–26	71 (73.2)	14.7 $\pm$ 2.3	145.4 $\pm$ 24.9	476.62	
<i>Agathis australis</i>	15.02 (7.35, 18.05)	13.47 $\pm$ 3.18	39–11 Ma <sup>4</sup>	805–394 ppm (declining)	630–300 ppm (declining)	85–41	44 (51.8)	18.8 $\pm$ 4.2	119.4 $\pm$ 43.3	669.58	
<i>Solanum lycopersicum</i>	16.86 (14.60, 41.94)	24.47 $\pm$ 8.76	16 Ma <sup>5</sup>	439 ppm (low)	360–300 ppm (low)	377–103	274 (72.7)	15.4 $\pm$ 3.5	316.8 $\pm$ 92.4	1793.94	
<i>Osmunda regalis</i>	25.27 (19.57, 45.55)	30.13 $\pm$ 7.88	100–66 Ma <sup>6</sup>	1283–912 ppm (high)	1590–960 ppm (high)	386–210	176 (45.6)	29.8 $\pm$ 6.5	56.3 $\pm$ 16.5	621.57	
<i>Ginkgo biloba</i>	78.69 (25.70, 212.07)	105.49 $\pm$ 55.45	146–100 Ma <sup>7</sup>	1443–876 ppm (high)	2280–1590 (high)	42–6	36 (85.7)	24.3 $\pm$ 5.0	76.8 $\pm$ 20.6	689.19	

Species listed from fastest to slowest median stomatal half-closure time (minutes). <sup>1</sup>Badr et al. (2000), <sup>2</sup>Nagalingum et al. (2011), <sup>3</sup>Bliffen et al. (2011), <sup>4</sup>Bliffen et al. (2010), <sup>5</sup>Bremer et al. (2004), <sup>6</sup>Jud et al. (2008), <sup>7</sup>Crane (2013), <sup>8</sup>Bergman et al. (2004), <sup>9</sup>Berner and Kothavala (2001).

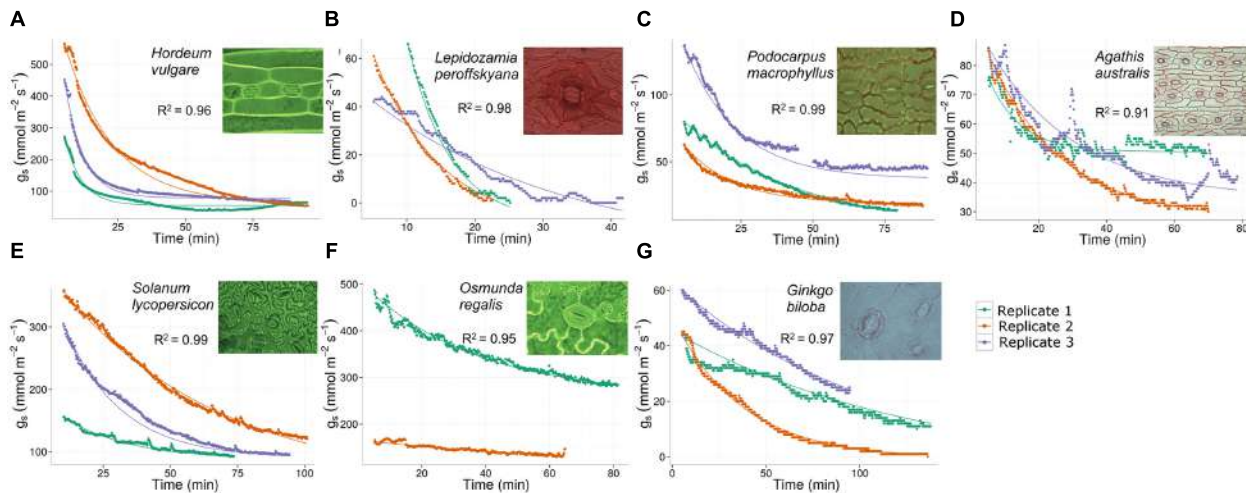


**FIGURE 1 | Change in stomatal conductance ( $g_s$ ;  $\text{mmol m}^{-2} \text{s}^{-1}$ ) over time (minutes) in response to darkness in an evolutionary range of species grown at 380 ppm  $\text{CO}_2$  and 20.9%  $\text{O}_2$  fitted to an exponential decay curve.** The fit was performed for each replicate of seven species. Species listed from fastest to slowest median half-closure time. (A) *Hordeum vulgare*; (B) *Lepidozamia perofskyana*; (C) *Podocarpus macrophyllus*; (D) *Agathis australis*; (E) *Solanum lycopersicum*; (F) *Osmunda regalis*; (G) *Ginkgo biloba*. Light microscope images of stomata  $\times 630$ .

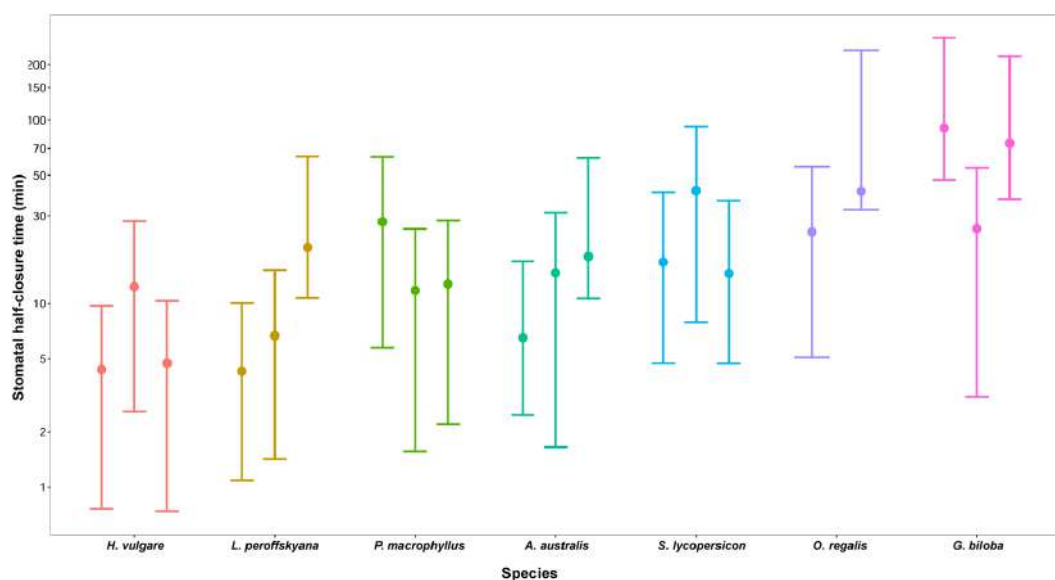


**FIGURE 2 |  $\log_e$ (median stomatal half-closure time) of seven species.** *H. vulgare* = *Hordeum vulgare* (graminaceous angiosperm); *L. perofskyana* = *Lepidozamia perofskyana* (cycad); *P. macrophyllus* = *Podocarpus macrophyllus* (conifer); *A. australis* = *Agathis australis* (conifer); *S. lycopersicum* = *Solanum lycopersicum* (angiosperm); *O. regalis* = *Osmunda regalis* (fern); *G. biloba* = *Ginkgo biloba* (ginkgophyte). The fastest species to close stomata in response to darkness was *Hordeum vulgare*; the slowest was *Ginkgo biloba*.

## RESULTS

The stomatal conductance ( $g_s$ ;  $\text{mmol m}^{-2} \text{s}^{-1}$ ) change in response to darkness was measured in the seven species (Figure 1). From these measurements  $\log_e$ (stomatal half-closure time) was calculated (Figure 2). Of the species studied, the fastest responder with respect to stomatal closing response was barley, *H. vulgare* (median half-closure time: 4.83 min; mean  $7.16 \pm 2.63$  min;  $R^2$  fit = 0.96; Figure 2; Table 1), a species

with comparatively large stomata (SPL:  $28.1 \pm 6.2 \mu\text{m}$ ; Table 1). The second fastest responder was the cycad *L. perofskyana* (median half-closure time: 6.53 min; mean  $10.26 \pm 4.89$  min;  $R^2$  fit = 0.98; Figure 2; Table 1), which had the largest stomata of all species studied (SPL:  $35.6 \pm 5.5 \mu\text{m}$ ; Table 1). The next three species in order of decreasing rate of closure were two conifers: *P. macrophyllus* (median half-closure time: 12.74 min; mean  $17.96 \pm 5.74$  min;  $R^2$  fit = 0.99); *A. australis* (median half-closure time: 15.02 min; mean  $13.47 \pm 3.18$  min;  $R^2$  fit = 0.91); and the

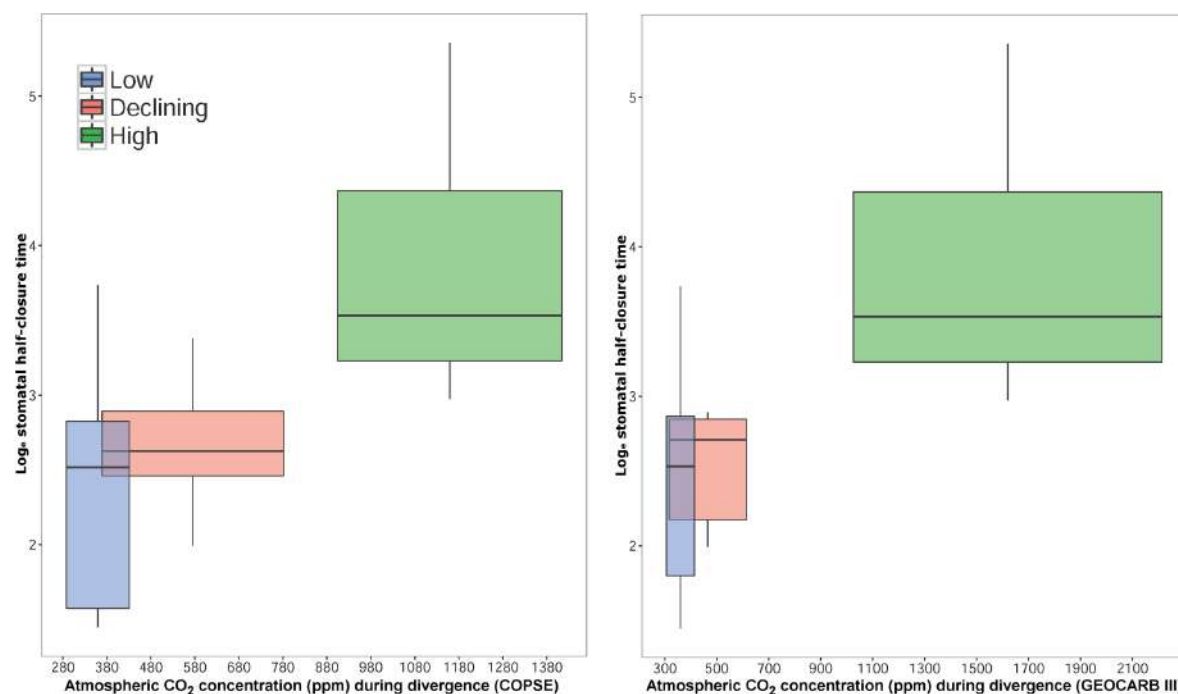


**FIGURE 3 |**  $\log_e$ (median stomatal half-closure time) of seven species, grouped by estimated atmospheric  $\text{CO}_2$  concentration at time of taxa diversification into low, declining or high  $\text{CO}_2$  groups. For COPSE model (Bergman et al., 2004), low  $\text{CO}_2$  (280–439 ppm) includes *Hordeum vulgare*, *Lepidozamia peroffskyana*, and *Solanum lycopersicon*; declining  $\text{CO}_2$  (346–805 ppm) includes *Podocarpus macrophyllus* and *Agathis australis*; high  $\text{CO}_2$  (876–1443 ppm) includes *Osmunda regalis* and *Ginkgo biloba* (see Table 1). For GEOCARB III model (Berner and Kothavala, 2001), low  $\text{CO}_2$  (300–420 ppm) includes *Hordeum vulgare*, *Lepidozamia peroffskyana*, *Podocarpus macrophyllus*, and *Solanum lycopersicon*; declining  $\text{CO}_2$  (300–630 ppm) includes *Agathis australis*; high  $\text{CO}_2$  (960–2280 ppm) includes *Osmunda regalis* and *Ginkgo biloba* (see Table 1).

angiosperm *S. lycopersicon* (median half-closure time: 16.86 min; mean  $24.47 \pm 8.76$  min;  $R^2$  fit = 0.99; Figure 2; Table 1). All three species have the smallest stomata of those measured (SPL:  $14.7 \pm 2.3$   $\mu\text{m}$ ;  $18.8 \pm 4.2$   $\mu\text{m}$ ; and  $15.4 \pm 3.5$   $\mu\text{m}$ , respectively; Table 1). Finally, the two slowest species to close in response to darkness had large stomata: the fern *O. regalis* (median half-closure time: 25.27 min; mean  $30.13 \pm 7.88$  min;  $R^2$  fit = 0.95; SPL:  $29.8 \pm 6.5$   $\mu\text{m}$ ) and *G. biloba* (median half-closure time: 78.69 min; mean  $105.49 \pm 55.45$  min;  $R^2$  fit = 0.97; SPL:  $24.3 \pm 5.0$   $\mu\text{m}$ ; Figure 2; Table 1).

Mean differences in SD ( $\text{mm}^2$ ) and SPL ( $\mu\text{m}$ ) of all seven species were tested using ANOVA with pairwise comparison. Differences in SD at alpha 0.05 were observed for one pairwise comparison, namely *H. vulgare* versus *G. biloba* (overall comparison: DF = 6, 880,  $F = 629.4$ ,  $p < 0.05$ ). The remaining pairwise comparisons showed no differences. Differences in SPL were observed for two pairwise comparisons (*O. regalis* versus *H. vulgare* and *S. lycopersicon* versus *P. macrophyllus*; overall comparison: DF = 6, 880,  $F = 344.8$ ,  $p < 0.05$ ). The remaining pairwise comparisons showed no differences.

The differences in half-closure time between species were tested using ANOVA comparison (overall comparison: DF = 6, 13,  $F = 4.453$ ,  $p < 0.05$ ). Post hoc analysis revealed that four comparisons were different, namely *G. biloba* versus *A. australis*; *G. biloba* versus *H. vulgare*; *G. biloba* versus *L. peroffskyana*; and *G. biloba* versus *P. macrophyllus*.

Generalized linear mixed models were used to describe the relationship between  $\log_e(\text{half-closure time})$  and SD, SPL, plant functional type, shade tolerance, drought tolerance, and climate. The best fit model following AIC comparison was  $\log_e(\text{half-closure time})$  as a function of species (AIC = 174.81,  $R^2 = 0.52$ ).

Maximum stomatal aperture ( $\mu\text{m}$ ) was calculated with  $\beta$  values of 0.2, 0.4, 0.5, 0.6, 0.8, 1.0; the relationship between theoretical maximum stomatal conductance ( $g_{\max}$  in  $\text{mmol m}^{-2} \text{s}^{-1}$ ) and  $\log_e(\text{half-closure time})$  was tested for all  $\beta$  values. No relationship was found between  $g_{\max}$  and rate of stomatal closing in the case of  $\beta = 0.5$  (linear model: DF = 1, 5,  $F = 0.069$ ,  $R^2 = -0.18$ ,  $p > 0.05$ ).

Correlations between  $\log_e(\text{half-closure time})$  and estimated paleo- $\text{CO}_2$  concentration (ppm) at the time when taxa originated (Ma) for the COPSE model (Bergman et al., 2004) and GEOCARB III model (Berner and Kothavala, 2001; Table 1) demonstrated no correlations between rate of closing and atmospheric  $\text{CO}_2$  concentration at time of taxa origination (COPSE:  $R^2 = 0.07$ ,  $p > 0.05$ ; GEOCARB III:  $R^2 = 0.08$ ,  $p > 0.05$ ).

Correlations between  $\log_e(\text{half-closure time})$  and estimated paleo- $\text{CO}_2$  concentration (ppm) at the time when taxa last diversified (Ma) for the COPSE model (Bergman et al., 2004) and GEOCARB III model (Berner and Kothavala, 2001; Figure 3; Table 1) were tested. The correlations showed evidence for a relationship (COPSE: DF = 6, 18,  $F = 4.45$ ,  $R^2 = 0.52$ ,  $p < 0.05$ ; GEOCARB III: DF = 6, 18,  $F = 5.71$ ,  $R^2 = 0.55$ ,

$p < 0.05$ ). For both models, species that diversified under low or declining [CO<sub>2</sub>] (280–805 ppm) were different from species that diversified under high [CO<sub>2</sub>] (912–2280 ppm); (overall comparison:  $F = 14.57$ , DF = 2, 39,  $p < 0.05$ ) in their log<sub>e</sub>(half-closure time; **Figure 3**). However, no differences were found between species that diversified in low or declining atmospheric [CO<sub>2</sub>].

## DISCUSSION

### Stomatal Efficiency in Relation to Stomatal Size and Density

It has been assumed in the past that small stomata respond faster in terms of opening and closing than large stomata. Rate of stomatal opening and closing response to environmental signals is an essential characteristic of stomatal efficiency, required to maintain optimum CO<sub>2</sub> assimilation to transpiration rate (Lawson et al., 2010; Lawson and Blatt, 2014). The evolutionary trend toward high densities of small stomata from few large stomata (Hetherington and Woodward, 2003; Franks and Beerling, 2009) is thought to represent a move toward increased efficiency in stomatal function under low or declining [CO<sub>2</sub>] atmospheres over geological time. This is because it is believed that species with high densities of small stomata achieve greater maximum stomatal conductance due to reduced pore depth in small stomata, decreasing the distance for diffusion of gas molecules through the stomatal pore (Franks and Farquhar, 2007; Franks and Beerling, 2009). However, Monda et al. (2016) have shown that *Arabidopsis thaliana* ecotype Me-0, whose stomata are significantly larger than those of the wild type Columbia (Col), had higher stomatal conductance ( $g_s$ ) than Col, confirming that the longer diffusion pathway in the larger stomata did not restrict conductance. Therefore, the commonly accepted assumption that smaller stomata attain higher conductance did not hold in this case (Monda et al., 2016). In this study, we defined stomatal efficiency in terms of half-closure time in response to darkness. Therefore, if the evolutionary trend in SS and density represents a move toward more efficient stomata, it could be expected that the fastest responders in this study would be those species with the smallest stomata. In a study by Drake et al. (2013), SS was found to be negatively correlated with the maximum rate of stomatal opening in response to light within the genus *Banksia*, indicating that leaves with many, small stomata exhibit faster stomatal conductance to water vapor than leaves with few, large stomata; however, that study measured five species within a single genus. So, while it has been shown that smaller stomata are faster over a range of SSs within a single genus, this finding cannot be said to apply generally across plant taxa. In contrast to the study by Drake et al. (2013) where stomatal opening in response to light was measured, our study measured stomatal closing in response to darkness. Our results, in comparison, suggest that smaller stomata are not always faster as we show that rate of stomatal closure in response to darkness is not correlated with SS, measured as SPL, nor with stomatal geometry, measured as guard cell width, stomatal pore depth, pore length and density for

calculation of maximum theoretical conductance in the species studied (**Table 1**).

Of seven species under study, the two species with largest stomata, *H. vulgare* (barley) and *L. peroffskyana* (cycad; SPL > 24  $\mu\text{m}$ ), closed their stomata faster in response to darkness than the remaining five species (**Figure 2**; **Table 1**). While both have large stomata, their morphology is different; barley stomatal guard cells are modified into the narrow, dumbbell-shape typical of grasses and are situated level with the leaf surface; cycad kidney-shaped guard cells are broad and are sunken below the leaf surface. Dumbbell-shaped stomata have a higher diffusible area of stomatal pore than kidney-shaped stomata because they require a much smaller change in volume to produce a unit change in aperture width (Raschke, 1976) with resultant higher conductance rates (Aasamaa et al., 2001; Hetherington and Woodward, 2003; Franks and Farquhar, 2007; Franks and Beerling, 2009). Indeed, maximum stomatal conductance ( $g_s$ ) observed under saturating light in *H. vulgare* was 558 mmol m<sup>-2</sup> s<sup>-1</sup> compared to *L. peroffskyana*, which was only 61 mmol m<sup>-2</sup> s<sup>-1</sup> (**Table 1**), illustrating that maximum operational  $g_s$  and rate of closing response are not correlated. In the absence of light,  $g_s$  reduced to 0 mmol m<sup>-2</sup> s<sup>-1</sup> in *L. peroffskyana* indicating that all stomata were tightly closed, in contrast to *H. vulgare* where  $g_s$  decreased to a minimum of 53 mmol m<sup>-2</sup> s<sup>-1</sup> (**Table 1**), confirming that stomata do not close completely in this grass in the dark, or possibly that cuticular conductance was greater in this species. In addition, it is known that conducting at night occurs in many species (Daley and Phillips, 2006; Caird et al., 2007; Dawson et al., 2007).

The next three species in order of decreasing rate of closure were two conifers, *P. macrophyllus* and *A. australis*, followed by the angiosperm *S. lycopersicum*; these species have the smallest stomata (SPL < 19  $\mu\text{m}$ ) of the seven species measured (**Figure 2**; **Table 1**). The two slowest species to close in response to darkness have large stomata, *O. regalis* and *G. biloba* (SPL > 24  $\mu\text{m}$ ; **Figure 2**; **Table 1**). If rate of stomatal closure is taken as a proxy for stomatal efficiency, then small stomata are not more efficient than larger stomata in response to removal of irradiance, at least with respect to the species examined. Stomata optimize behavior in order to maximize photosynthetic gain to water loss and this optimization can take many forms. In this study, barley is efficient in terms of response time but may be considered inefficient in terms of water loss during the night, if nighttime conductance is considered a wasteful process, whereas the cycad is efficient in terms of both rate and effectiveness of stomatal closure by rapidly reducing conductance through the aperture to 0 mmol m<sup>-2</sup> s<sup>-1</sup>.

### Other Factors that May Impact Stomatal Efficiency

We confirmed the notion that SS and SD are inversely correlated (Hetherington and Woodward, 2003; Franks and Beerling, 2009; Franks et al., 2009). In the present study, the two fastest and the two slowest species examined all have large stomata and low SD compared with the remaining three species, which have smaller stomata and higher density (**Table 1**). Thus, half-closure time in response to darkness in these seven species is neither correlated

with SS ( $r^2 = 0.01$ ) nor SD ( $r^2 = 0.02$ ). Since our results found that half-closure time in these species is not correlated with size or density, we attempted to identify other factors correlated with half-closure time. It is not likely linked to phylogeny because the two fastest stomatal responders are phylogenetically removed from each other by millions of years. Stem group cycads, the oldest lineage of extant seed plants, evolved in the Permian (~298–252 Ma) during a time of increasing global warmth and aridity (Eyles, 2008; Tabor and Poulsen, 2008; Montañez and Poulsen, 2013). Extant crown group cycad species result from a radiation that began approximately 12 Ma during the Miocene (Nagalingum et al., 2011). Grasses evolved during the late Cretaceous/early Paleogene (70–60 Ma), when the climate was warm and relatively wet (Wolfe and Upchurch, 1987; Pearson et al., 2001). They subsequently radiated and diversified in a climate of decreasing temperatures and increasing seasonally aridity (Ruddiman, 2001), occupying early grassland open habitats in South America by ~40 Ma and grassland habitats globally during the early to middle Miocene (~20–10 Ma; Jacobs et al., 1999; Kellogg, 2001; Strömberg, 2011). The two species with the largest stomata also represent two separate plant divisions, that is, gymnosperms and angiosperms. Additionally, rate of closure is not likely linked with life strategy; *L. peroffskyana* is a woody, evergreen cycad, endemic to coastal and near-coastal regions of New South Wales and Queensland in Australia, where it grows in wet sclerophyll forest, littoral rainforest or open scrubby forest (Jones, 2002; Whitelock, 2002), whereas *H. vulgare* is an herbaceous, annual grass descended from wild barley, *H. vulgare* subsp. *spontaneum* from Western Asia (Badr et al., 2000). It must also be noted that neither species is under strong selection pressure to have fast-closing stomata in response to drought as neither usually grows in water-limited environments.

## Effect of Atmospheric CO<sub>2</sub> Concentration on Stomatal Closure Rate

We explored the possibility that the concentration of atmospheric CO<sub>2</sub> ([CO<sub>2</sub>]<sub>atm</sub>) at the time of taxa origination and/or latest diversification event may have impacted stomatal function, bearing in mind that Robinson (1994) suggested that “plants evolving under declining CO<sub>2</sub> tended to develop increased stomatal efficiency.” The difficulty in ascertaining exactly when taxa originated and last diversified, along with accurate determination of atmospheric [CO<sub>2</sub>] during those times, limits the accuracy with which the impact of past [CO<sub>2</sub>] on stomatal function can be studied. Nonetheless, using current information available for origination and diversification dates for the seven taxa, along with modeled atmospheric carbon dioxide concentration at the time (Berner and Kothavala, 2001; Bergman et al., 2004), we tested for a relationship between half-closure time and [CO<sub>2</sub>]. Half-closure time was not found to be correlated with estimated concentration of CO<sub>2</sub> in the atmosphere when the taxa originated but correlation between half-closure time and estimated [CO<sub>2</sub>]<sub>atm</sub> during the time of taxa diversification was observed (Figure 3); species whose ancestors underwent their last major diversification event in low or declining [CO<sub>2</sub>]<sub>atm</sub> closed

their stomata faster in response to darkness than species whose ancestors last diversified under high [CO<sub>2</sub>]<sub>atm</sub>. Therefore, we suggest that the concentration of CO<sub>2</sub> in the atmosphere during diversification events may impact stomatal function, specifically, rate of stomatal closure.

The rapid half-closure time exhibited by the cycad, a member of an ancient plant order that has persisted over millions of years with little morphological change, was unexpected. With the aid of DNA sequence data and fossil-calibrated phylogenies it is now known, however, that living cycad species are not relictual taxa (Treutlein and Wink, 2002; Crisp and Cook, 2011; Nagalingum et al., 2011). All extant cycad genera diversified in the last 12–6 million years (Nagalingum et al., 2011); therefore, despite their ancient origins, extant cycads last diversified with the grasses in a low CO<sub>2</sub> world. Using the same techniques, Biffin et al. (2011) have shown that despite the ancient origins of Podocarpaceae in the Triassic–Jurassic, extant species within the family are likely to be of more recent evolutionary origin (mid-to-late Cenozoic). While extant Podocarp leaves can be scale-like, needle-like or broad, reconstructions of leaf morphology indicate that the ancestral state was scale-like, suggesting that modern broad leaves in Podocarps are an adaptation to compete with angiosperm radiation in shady canopies of newly developing rainforests (Biffin et al., 2012). The Podocarp species included in this study, *P. macrophyllus*, has broad leaves analogous to angiosperms. Similarly, Crisp and Cook (2011) have concluded that conifers in the Araucariaceae family, despite their ancient origins, have a crown age estimated at only 36 Ma, while Biffin et al. (2010) have suggested the estimated age of the *A. australis* lineage to be 39–11 Ma. Thus, it appears that the cycad and conifer species in this study diversified at a similar time to angiosperms under a relatively low or declining atmospheric CO<sub>2</sub> composition (Table 1). In contrast, the two slowest stomatal responders, *O. regalis* and *G. biloba*, diversified much earlier in a high CO<sub>2</sub> world (Table 1). The fern family, Osmundaceae, originated in the Permian and radiated in the Triassic (Jud et al., 2008). Phipps et al. (1998) established that crown group Osmundaceae has a minimum age of 220 million years, with fossil evidence of the genus *Osmunda* from the Late Triassic. Osmundaceous ferns diverged as early as the Carboniferous (Schneider et al., 2004) and living species began to appear no later than the Late Cretaceous (Jud et al., 2008), suggesting that some extant genera and species could be remarkably ancient. The order Ginkgoales also originated in the Permian (Royer et al., 2003) and diversified during the Jurassic and Early Cretaceous (Royer et al., 2003; Crane, 2013). The sole survivor of this order, *G. biloba*, has persisted through millions of years of environmental and atmospheric change but last diversified in a high CO<sub>2</sub> world. In contrast, the two angiosperm species in this study *S. lycopersicum* and *H. vulgare* originated much later in time. Solanales originated in the mid-Cretaceous (Bremer et al., 2004). Solanaceae crown group divergence times vary from c. 51 Ma (Paape et al., 2008) to c. 40 Ma (Wikström et al., 2001), while crown age of the genus *Solanum* is estimated at c. 16 Ma (Paape et al., 2008). Grasses (Poaceae) originated in the latest Cretaceous to early Tertiary (Jacobs et al., 1999; Kellogg, 2001; Piperno and Sues, 2005; Prasad et al., 2005) and

increased in abundance during the middle Tertiary (Jacobs et al., 1999).

Using current knowledge on the date of diversification of the seven species studied, and estimated atmospheric composition at that time, we showed that the five species that diversified under low or declining atmospheric CO<sub>2</sub> concentration (280–805 ppm) had faster stomatal closing response times (median half-closure time 4.83–16.86 min; mean half-closure time 7.16–24.47 min) than the two species that diversified under high atmospheric CO<sub>2</sub> concentration (912–2280 ppm; median half-closure time 25.27–78.69 min; mean half-closure time 30.13–105.49 min; **Figures 2 and 3; Table 1**). This trend may suggest that, in these seven species at least, atmospheric [CO<sub>2</sub>] during taxa diversification is a more important driver of stomatal closing rate than SS, SD, phylogeny or life strategy. However, intriguing this idea, it must be viewed with caution as the number of species used was moderate and the sample size small for each species so an overall trend in all land plants cannot be assumed from such a preliminary study. Additionally, only one cycad species was included, thus the possibility exists that fast and tight stomatal closure in *L. peroffskyana* represents a species-specific response that is not typical of all cycads. It is possible that cycad species that diversified in a low CO<sub>2</sub> world were placed under selection pressure to optimize stomatal efficiency; perhaps species that could not adapt became extinct, whilst those that could adapt, survived. Nagalingum et al. (2011) have suggested that a shift from a globally warm, equatorial climate to cooler temperatures with increasing aridity and seasonality during the Late Miocene may explain the dramatic extinction of many cycad species; the reduction in atmospheric [CO<sub>2</sub>] during the Miocene may have selected for cycad species with fast responding stomata while cycad species with slow stomata became extinct. Therefore, perhaps other extant cycad species also close their stomata quickly when irradiance is removed and this remains to be tested.

To our knowledge, no previous study has compared measured stomatal response rate and measured SS in species with ancient stem lineages from a high CO<sub>2</sub> world to species with more recent stem lineages from a low CO<sub>2</sub> world. It is likely that several factors combine to drive optimal stomatal function and, under stressful circumstances, some factors may become more dominant in terms of driving optimality than others. We recommend further detailed studies on stomatal closing rates in a much wider phylogenetic range of species, especially those where time of diversification has been established with reasonable certainty, in order to provide more insight into this interesting topic. Vico et al. (2011) have shown that stomatal opening and closing times are strongly correlated, with opening faster than closing. Therefore, in our future studies, we will test whether stomatal opening rate in response to light, and in particular to sun flecks, is correlated with rate of closing and with atmospheric CO<sub>2</sub> concentration at time of diversification in these same species, and will also broaden the number of species and increase replication.

## CONCLUSION

Small stomata do not always close faster than large stomata when compared across a phylogenetic range of genera and plant functional groups and thus are not more efficient than large stomata if stomatal closing time is taken as a proxy for stomatal efficiency. We suggest that atmospheric concentration of CO<sub>2</sub> at the time of taxa diversification, and not SS, may be a stronger driver of stomatal closing time in response to darkness in the seven species studied. We recommend that future studies testing whether small stomata are faster than large stomata should consider other adverse factors that may place a strong selection pressure on plants to optimize stomatal function. In such adverse circumstances, guard cell size may not be the most dominant driver of stomatal function.

## AUTHOR CONTRIBUTIONS

CE-K (primary researcher) carried out all stomatal conductance and speed of stomatal closing measurements. Wrote the manuscript. Awarded an Irish Research Council funding grant to undertake the research. MH carried out stomatal pore length and stomatal density measurements. JY created the model to work out half-time closing from raw data. Wrote the R Script for the model. SB provided considerable statistical help. Produced **Figures 1 and 3**. TL visited at beginning of project and co-designed study. Provided instructive comments on the original manuscript. JM (principal investigator) designed the study and edited the manuscript. Awarded funding from European Research Council to undertake the research.

## FUNDING

We gratefully acknowledge funding from: IRCSET Embark scholarship (R10679); EU Marie Curie Excellence Grant (MEXT-CT-2006-042531); EU Marie Curie Intra-European Fellowship (PEA-IEF-2010-275626); ERC grant (ERC-279962-OXYEVOL).

## ACKNOWLEDGMENTS

We thank the following for technical assistance: Ms. Bredagh Moran, Mr. Ray O'Haire, Mr. Liam Kavanagh (UCD, Ireland); Mr. Matthew Gilroy (Conviron, UK); Mr. Aidan Blake (Aaron Refrigeration, Ireland). We greatly appreciate the comments and suggestions of the two reviewers which improved the quality of this manuscript.

## REFERENCES

- Asamaa, K., Sober, A., and Rahi, M. (2001). Leaf anatomical characteristics associated with shoot hydraulic conductance, stomatal conductance and stomatal sensitivity to changes of leaf water status in temperate deciduous trees. *Aust. J. Plant Physiol.* 28, 765–774.
- Badr, A., Müller, K., Schäfer-Pregl, R., El Rabey, H., Effgen, S., Ibrahim, H. H., et al. (2000). On the origin and domestication history of Barley (*Hordeum vulgare*). *Mol. Biol. Evol.* 17, 499–510. doi: 10.1093/oxfordjournals.molbev.a026330
- Bergman, N. M., Lenton, T. M., and Watson, A. J. (2004). COPSE: A new model of biogeochemical cycling over Phanerozoic time. *Am. J. Sci.* 304, 397–437. doi: 10.2475/ajs.304.5.397
- Berner, R. A., and Kothavalav, Z. (2001). GEOCARB III: A revised model of atmospheric CO<sub>2</sub> over Phanerozoic time. *Am. J. Sci.* 301, 182–204. doi: 10.2475/ajs.301.2.182
- Biffin, E., Brodrribb, T. J., Hill, R. S., Thomas, P., and Lowe, A. J. (2012). Leaf evolution in Southern Hemisphere conifers tracks the angiosperm ecological radiation. *Proc. Biol. Sci.* 279, 341–348. doi: 10.1098/rspb.2011.0559
- Biffin, E., Conran, J. G., and Lowe, A. J. (2011). Podocarp evolution: a molecular phylogenetic perspective. *Smithson. Contrib. Bot.* 95, 1–20. doi: 10.5479/si.0081024X.95.1
- Biffin, E., Hill, R. S., and Lowe, A. J. (2010). Did Kauri (*Agathis*: Araucariaceae) really survive the Oligocene drowning of New Zealand? *Syst. Biol.* 59, 594–602. doi: 10.1093/sysbio/syq030
- Bradbeer, J. W. (1988). *Seed Dormancy and Germination*. Glasgow: Blackie and Son Ltd.
- Bremer, K., Friis, E., and Bremer, B. (2004). Molecular phylogenetic dating of Asterid flowering plants shows early cretaceous diversification. *Syst. Biol.* 53, 496–505. doi: 10.1080/10635150490445913
- Brown, H. T., and Escombe, F. (1900). Static diffusion of gases and liquids in relation to the assimilation of carbon and translocation in plants. *Philos. Trans. R. Soc. B* 193, 223–291. doi: 10.1098/rstb.1900.0014
- Caird, M. A., Richards, J. H., and Donovan, L. A. (2007). Nighttime stomatal conductance and transpiration in C3 and C4 plants. *Plant Physiol.* 143, 4–10. doi: 10.1104/pp.106.092940
- Cowan, I. R. (1977). Stomatal behaviour and environment. *Adv. Bot. Res.* 4, 117–228. doi: 10.1016/S0065-2296(08)60370-5
- Cowan, I. R., and Farquhar, G. D. (1977). Stomatal function in relation to leaf metabolism and environment. *Soc. Exp. Biol. Symp.* 31, 471–505.
- Crane, P. (2013). *Ginkgo: the Tree That Time Forgot*. New Haven, CT: Yale University Press.
- Crisp, M. D., and Cook, L. G. (2011). Cenozoic extinctions account for the low diversity of extant gymnosperms compared with angiosperms. *New Phytol.* 192, 997–1009. doi: 10.1111/j.1469-8137.2011.03862.x
- Daley, M. J., and Phillips, N. G. (2006). Interspecific variation in nighttime transpiration and stomatal conductance in a mixed New England deciduous forest. *Tree Physiol.* 26, 411–419. doi: 10.1093/treephys/26.4.411
- Dawson, T. E., Burgess, S. S. O., Tu, K. P., Oliveira, R. S., Santiago, L. S., Fisher, J. B., et al. (2007). Nighttime transpiration in woody plants from contrasting ecosystems. *Tree Physiol.* 27, 561–575. doi: 10.1093/treephys/27.4.561
- Drake, P. L., Froend, R. H., and Franks, P. J. (2013). Smaller, faster stomata: scaling of stomatal size, rate of response, and stomatal conductance. *J. Exp. Bot.* 64, 495–505. doi: 10.1093/jxb/ers347
- Edwards, D., Kerp, H., and Hass, H. (1998). Stomata in early land plants: an anatomical and ecophysiological approach. *J. Exp. Bot.* 49, 255–278. doi: 10.1093/jxb/49.Special\_Issue.255
- Eyles, N. (2008). Glacio-epochs and the supercontinent cycle after ~3.0 Ga: tectonic boundary conditions for glaciation. *Palaeogeogr. Palaeoclimatol. Palaeoecol.* 258, 89–129. doi: 10.1016/j.palaeo.2007.09.021
- Franks, P. J., and Beerling, D. J. (2009). Maximum leaf conductance driven by CO<sub>2</sub> effects on stomatal size and density over geologic time. *Proc. Nat. Acad. Sci. U. S. A.* 106, 10343–10347. doi: 10.1073/pnas.0904209106
- Franks, P. J., Drake, P. L., and Beerling, D. J. (2009). Plasticity in maximum stomatal conductance constrained by negative correlation between stomatal size and density: an analysis using *Eucalyptus globulus*. *Plant Cell Environ.* 32, 1737–1748. doi: 10.1111/j.1365-3040.2009.002031.x
- Franks, P. J., and Farquhar, G. D. (2007). The mechanical diversity of stomata and its significance in gas-exchange control. *Plant Physiol.* 143, 78–87. doi: 10.1104/pp.106.089367
- Hammer, P. A., and Hopper, D. A. (1997). “Experimental design,” in *Plant Growth Chamber Handbook*, eds R. W. Langhans and T. W. Tibbits (Ames, IA: Iowa State University), 177–187.
- Haworth, M., Fitzgerald, A., and McElwain, J. C. (2011). Cycads show no stomatal-density and index response to elevated carbon dioxide and subambient oxygen. *Austr. J. Bot.* 59, 629–638. doi: 10.1071/BT11009
- Hetherington, A. M., and Woodward, F. I. (2003). The role of stomata in sensing and driving environmental change. *Nature* 424, 901–908. doi: 10.1038/nature01843
- Hirano, A., Hongo, I., and Koike, T. (2012). Morphological and physiological responses of Siebold’s beech (*Fagus crenata*) seedlings grown under CO<sub>2</sub> concentrations ranging from pre-industrial to expected future levels. *Landsc. Ecol. Eng.* 8, 59–67. doi: 10.1007/s11355-011-0149-0
- Jacobs, B. F., Kingston, J. D., and Jacobs, L. L. (1999). The origin of grass-dominated ecosystems. *Ann. Missouri Bot. Gard.* 86, 590–643. doi: 10.2307/2666186
- Jones, D. L. (2002). *Cycads of the World, Ancient Plants in Today’s Landscape*. Washington, DC: Smithsonian Institution Press.
- Jones, H. G. (1992). *Plants and Microclimate: a Quantitative Approach to Environmental Plant Physiology*. Cambridge: Cambridge University Press.
- Jud, N. A., Rothwell, G. W., and Stockey, R. A. (2008). *Todea* from the Lower Cretaceous of western North America: implications for the phylogeny, systematics, and evolution of modern Osmundaceae. *Am. J. Bot.* 95, 330–339. doi: 10.3732/ajb.95.3.330
- Katul, G., Manzoni, S., Palmroth, S., and Oren, R. (2010). A stomatal optimization theory to describe the effects of atmospheric CO<sub>2</sub> on leaf photosynthesis and transpiration. *Ann. Bot.* 105, 431–442. doi: 10.1093/aob/mcp292
- Kellogg, E. A. (2001). Evolutionary history of the grasses. *Plant Physiol.* 125, 1198–1205. doi: 10.1104/pp.125.3.1198
- Lawson, T., and Blatt, M. R. (2014). Stomatal size, speed, and responsiveness impact on photosynthesis and water use efficiency. *Plant Physiol.* 164, 1556–1570. doi: 10.1104/pp.114.237107
- Lawson, T., VonCaemmerer, S., and Baroli, I. (2010). Photosynthesis and stomatal behaviour. *Prog. Bot.* 72, 265–304. doi: 10.1007/978-3-642-13145-5\_11
- McElwain, J. C., and Chaloner, W. G. (1995). Stomatal density and index of fossil plants track atmospheric carbon dioxide in the Palaeozoic. *Ann. Bot.* 76, 389–395. doi: 10.1006/anbo.1995.1112
- McElwain, J. C., Wade-Murphy, J., and Hesselbo, S. P. (2005). Changes in carbon dioxide during an oceanic anoxic event linked to intrusion into Gondwana coals. *Nature* 435, 479–482. doi: 10.1038/nature03618
- McElwain, J. C., Yiotsis, C., and Lawson, T. (2016). Using modern plant trait relationships between observed and theoretical maximum stomatal conductance and vein density to examine patterns of plant macroevolution. *New Phytol.* 209, 94–103. doi: 10.1111/nph.13579
- Monda, K., Araki, H., Kuhara, S., Ishigaki, G., Akashi, R., Negi, J., et al. (2016). Enhanced stomatal conductance by a spontaneous *Arabidopsis* tetraploid, Me-0, results from increased stomatal size and greater stomatal aperture. *Plant Physiol.* 170, 1435–1444. doi: 10.1104/pp.15.01450
- Montañez, I. P., and Poulsen, C. J. (2013). The Late Paleozoic ice age: an evolving paradigm. *Annu. Rev. Earth Planet. Sci.* 41, 629–656. doi: 10.1146/annurev.earth.031208.100118
- Nagalingum, N. S., Marshall, C. R., Quental, T. B., Rai, H. S., Little, D. P., and Mathews, S. (2011). Recent synchronous radiation of a living fossil. *Science* 334, 796–799. doi: 10.1126/science.1209926
- Paape, T., Igic, B., Smith, S. D., Olmstead, R., Bohs, L., and Kohn, J. R. (2008). A 15-Myr-old genetic bottleneck. *Mol. Biol. Evol.* 25, 655–663. doi: 10.1093/molbev/msn016
- Parlange, J.-Y., and Waggoner, P. E. (1970). Stomatal dimensions and resistance to diffusion. *Plant Physiol.* 46, 337–342. doi: 10.1104/pp.46.2.337
- Parsons, R., Weyers, J. D. B., Lawson, T., and Godber, I. M. (1998). Rapid and straightforward estimates of photosynthetic characteristics using a portable gas exchange system. *Photosynthetica* 34, 265–279. doi: 10.1023/A:1006800909651
- Pearson, P. N., Ditchfield, P. W., Singano, J., Harcourt-Brown, K. G., Nicholas, C. J., Olsson, R. K., et al. (2001). Warm tropical sea surface temperatures in

- the Late Cretaceous and Eocene epochs. *Nature* 413, 481–487. doi: 10.1038/35097000
- Phipps, C. J., Taylor, T. N., Taylor, E. L., Cuneo, N. R., Boucher, L. D., and Yao, X. (1998). *Osmunda* (Osmundaceae) from the Triassic of Antarctica: an example of evolutionary stasis. *Am. J. Bot.* 85, 888–895. doi: 10.2307/2446424
- Piperno, D. R., and Sues, H.-D. (2005). Dinosaurs dined on grass. *Science* 310, 1126–1128. doi: 10.1126/science.1121020
- Prasad, V., Strömborg, C. A. E., Alimohammadian, H., and Sahni, A. (2005). Dinosaur coprolites and the early evolution of grasses and grazers. *Science* 310, 1177–1180. doi: 10.1126/science.1118806
- R Core Team (2014). *R: A Language and Environment for Statistical Computing*. Available at: <http://www.r-project.org/>
- Raschke, K. (1976). How stomata resolve the dilemma of opposing priorities. *Philos. Trans. R. Soc. B* 273, 551–560. doi: 10.1098/rstb.1976.0031
- Robinson, J. M. (1994). Speculations on carbon dioxide starvation, Late Tertiary evolution of stomatal regulation and floristic modernization. *Plant Cell Environ.* 17, 345–354. doi: 10.1111/j.1365-3040.1994.tb00303.x
- Royer, D. L., Hickey, L. J., and Wing, S. L. (2003). Ecological conservatism in the “living fossil” Ginkgo. *Paleobiology* 29, 84–104. doi: 10.1666/0094-8373(2003)029<0084:ECITLF>2.0.CO;2
- Ruddiman, W. F. (2001). *Earth's Climate*. New York, NY: W H Freeman.
- Sager, J. C., and McFarlane, J. C. (1997). “Radiation,” in *Plant Growth Chamber Handbook*, eds R. W. Langhans and T. W. Tibbitts (Ames, IA: Iowa State University), 1–29.
- Schneider, H., Schuettpelz, E., Pryer, K. M., Cranfill, R., Magallon, S., and Lupia, R. (2004). Ferns diversified in the shadow of angiosperms. *Nature* 428, 553–557. doi: 10.1038/nature02361
- Strömborg, C. A. E. (2011). Evolution of grasses and grassland ecosystems. *Annu. Rev. Earth Planet. Sci.* 39, 517–544. doi: 10.1146/annurev-earth-040809-52402
- Tabor, N. J., and Poulsen, C. J. (2008). Palaeoclimate across the Late Pennsylvanian-Early Permian tropical palaeolatitudes: a review of climate indicators, their distribution, and relation to palaeophysiographic climate factors. *Palaeogeogr. Palaeoclimatol. Palaeoecol.* 268, 293–310. doi: 10.1016/j.palaeo.2008.03.052
- Treutlein, J., and Wink, M. (2002). Molecular phylogeny of cycads inferred from rbcL sequences. *Naturwissenschaften* 89, 221–225. doi: 10.1007/s00114-002-0308-0
- Vico, G., Manzoni, S., Palmroth, S., and Katul, G. (2011). Effects of stomatal delays on the economics of leaf gas exchange under intermittent light regimes. *New Phytol.* 192, 640–652. doi: 10.1111/j.1469-8137.2011.03847.x
- Weyers, J. D. B., and Johansen, L. G. (1985). Accurate estimation of stomatal aperture from silicone rubber impressions. *New Phytol.* 101, 109–115. doi: 10.1111/j.1469-8137.1985.tb02820.x
- Whitelock, L. M. (2002). *The cycads*. Portland, OR: Timber Press Inc.
- Wikström, N., Savolainen, V., and Chase, M. W. (2001). Evolution of the angiosperms: calibrating the family tree. *Proc. Biol. Sci. R. Soc.* 268, 2211–2220. doi: 10.1098/rspb.2001.1782
- Wolfe, J. A., and Upchurch, G. R. J. (1987). North American nonmarine climates and vegetation during the Late Cretaceous. *Palaeogeogr. Palaeoclimatol. Palaeoecol.* 61, 33–77. doi: 10.1016/0031-0182(87)90040-X
- Wong, S. C., Cowan, I. R., and Farquhar, G. D. (1979). Stomatal conductance correlates with photosynthetic capacity. *Nature* 282, 424–426. doi: 10.1038/282424a0

**Conflict of Interest Statement:** The authors declare that the research was conducted in the absence of any commercial or financial relationships that could be construed as a potential conflict of interest.

Copyright © 2016 Elliott-Kingston, Haworth, Yearsley, Batke, Lawson and McElwain. This is an open-access article distributed under the terms of the Creative Commons Attribution License (CC BY). The use, distribution or reproduction in other forums is permitted, provided the original author(s) or licensor are credited and that the original publication in this journal is cited, in accordance with accepted academic practice. No use, distribution or reproduction is permitted which does not comply with these terms.



# 3D Surface Reconstruction of Plant Seeds by Volume Carving: Performance and Accuracies

Johanna Roussel, Felix Geiger, Andreas Fischbach, Siegfried Jahnke and Hanno Scharr \*

Institute of Bio- and Geo-sciences, IBG-2: Plant Sciences, Forschungszentrum Jülich GmbH, Jülich, Germany

We describe a method for 3D reconstruction of plant seed surfaces, focusing on small seeds with diameters as small as 200 µm. The method considers robotized systems allowing single seed handling in order to rotate a single seed in front of a camera. Even though such systems feature high position repeatability, at sub-millimeter object scales, camera pose variations have to be compensated. We do this by robustly estimating the tool center point from each acquired image. 3D reconstruction can then be performed by a simple shape-from-silhouette approach. In experiments we investigate runtimes, theoretically achievable accuracy, experimentally achieved accuracy, and show as a proof of principle that the proposed method is well sufficient for 3D seed phenotyping purposes.

## OPEN ACCESS

### Edited by:

Alexander Bucksch,  
Georgia Institute of Technology, USA

### Reviewed by:

Randy Clark,  
DuPont Pioneer, USA  
Nathan Miller,  
University of Wisconsin-Madison,  
USA

### \*Correspondence:

Hanno Scharr  
h.scharr@fz-juelich.de

### Specialty section:

This article was submitted to  
Plant Biophysics and Modeling,  
a section of the journal  
*Frontiers in Plant Science*

Received: 18 March 2016

Accepted: 17 May 2016

Published: 07 June 2016

### Citation:

Roussel J, Geiger F, Fischbach A, Jahnke S and Scharr H (2016) 3D Surface Reconstruction of Plant Seeds by Volume Carving: Performance and Accuracies. *Front. Plant Sci.* 7:745.  
doi: 10.3389/fpls.2016.00745

## 1. INTRODUCTION

Making image analysis methods available for plant phenotyping applications is currently a driving force in plant sciences (Spalding and Miller, 2013). In many such applications the absence of suitable image processing is even a bottleneck (Minervini et al., 2015). More than 100 specialized methods (Lobet et al., 2013) and software packages are available for image-based analysis of different plant parts, e.g., fruit shape (Brewer et al., 2006), single or multiple leaves (Bylesjö et al., 2008; Weight et al., 2008; Alenya et al., 2011; De Vylder et al., 2011; Wallenberg et al., 2011; Dellen et al., 2015; Müller-Linow et al., 2015; Pape and Klukas, 2015), hypocotyl and seedlings (Koenderink et al., 2009; Wang et al., 2009; Silva et al., 2013; Golbach et al., 2015), shoot (Augustin et al., 2015; Santos and Rodrigues, 2015; Pound et al., 2016), rosettes (Arvidsson et al., 2011; Aksoy et al., 2015) and many more. Such analysis tools are needed in robotic imaging platforms for high-throughput plant phenotyping (Granier et al., 2006; Jansen et al., 2009; Hartmann et al., 2011; Nagel et al., 2012; van der Heijden et al., 2012; Fahlgren et al., 2015), but also in affordable systems (Tsaftaris and Noutsos, 2009; Minervini et al., 2014; Santos and Rodrigues, 2015).

Plant seed phenotyping is needed by seed banks for quality management e.g., concerning breeding purposes, linking to germination rate or plant growth. For this, 2D scanning is a popular, affordable technique (Herridge et al., 2011; Tanabata et al., 2012; Moore et al., 2013; Whan et al., 2014). Several commercial software packages are available for seed investigations using flat-bed scanners (e.g., Regent Instruments, 2000; Next Instruments, 2015). It has been applied to different seed types, like *Arabidopsis*, soybean, barley, or rice. Typically parameters like width, length, or area are calculated from the 2D images, but also more complex shape measures like Fourier descriptors (Iwata and Ukai, 2002; Iwata et al., 2010).

However, to the best of our knowledge, no affordable 3D imaging technique has been presented so far designed for seed measurements. Correspondence-based techniques (Quan et al., 2006; Paproki et al., 2012; Pound et al., 2014, 2016; Santos and Rodrigues, 2015) reconstructing 3D models from multiple images, or other low-cost techniques like laser scanning or the Kinect can be used for 3D whole plant reconstruction (Paulus et al., 2014) or root systems in transparent gel (Fang et al., 2009). However, such techniques are not suitable for much smaller objects like seeds of rapeseed plants ( $\sim 2$  mm diameter) or even *Arabidopsis* seeds ( $\sim 0.2\text{--}0.4$  mm length).

Here we investigate volume carving, a well-known shape-from-silhouette technique (Martin and Aggarwal, 1983; Potmesil, 1987; Laurentini, 1994), for 3D seed shape reconstruction. It is a fast, reliable, and simple but robust method, having been used in plant phenotyping before, e.g., 3D seedling reconstruction (Koenderink et al., 2009; Golbach et al., 2015) or root system investigations (Clark et al., 2011; Zheng et al., 2011; Topp et al., 2013). Depending on the selected viewpoints it approximates the convex hull of an object or reconstructs even valleys and saddle-points, but cannot reconstruct true concavities. Most seeds are, however, relatively smooth, convex objects. For the seed types investigated here (*Arabidopsis*, barley, and maize, see **Figure 1**), true concavities seem to be of low relevance for volume estimation. For non-smooth seeds, like e.g., seeds of the plant parasites *Phelipanche aegyptiaca*, or *Orobanche cernua* the proposed method may be less suitable.

This paper is an extension of our conference publication (Roussel et al., 2015), thus theory (Section 2 and 3), and some experiments from Section 4 are mainly repeated from there. We extend the theory by an accuracy check and iterative camera position correction procedure, and the experiments by a numerical and experimental investigation of achievable accuracy vs. number of images in Sections 4.2 and 4.3. Further we updated references and discussion.

## 2. RECONSTRUCTING SEED SHAPE FROM SILHOUETTES

Aiming at relatively simple, mostly convex seed shapes, target voxel resolutions needed to describe such shapes are comparably low—as we will show in the experiments below, see Section 4. Therefore, for this study, it is sufficient to apply one of the most basic volume carving approaches.

We get the intrinsic camera matrix  $\mathbf{K}$  (Hartley and Zisserman, 2004) and the distance between the origin of our working volume and the camera center from calibration (*cmp.* Section 3.2). The origin of the working volume is selected to be the tool center point (TCP) of the robot system handling the seeds, i.e., rotating them in front of the camera for imaging (*cmp.* Section 3.1).

We acquire  $N$  images, showing a seed under (equidistantly spaced) rotation angles  $\alpha_i$  where  $i \in \{1, \dots, N\}$ , see **Figure 1**. Rotation is around the vertical axis through the TCP, being parallel to the  $y$ -axis of the camera. We segment by gray-value thresholding each image into a binary mask  $\mathbf{M}_i$  being one at the foreground, i.e., seed and tool tip, and zero at background locations. Small objects like noise are removed and small holes (e.g., the reflection of the tool) filled.

For each image and thus segmentation mask we calculate the homogeneous camera projection matrix  $\mathbf{P}_i$ , from the rotation angle  $\alpha_i$  by

$$\mathbf{P}_i = \mathbf{K}(\mathbf{R}_i | \vec{t}_i) \quad (1)$$

where  $\mathbf{R}_i$  is the rotation matrix corresponding to the given angle  $\alpha_i$ , and translation vector  $\vec{t}_i$  is calculated using the distance of the world origin to the camera center, also known from calibration (see e.g., Hartley and Zisserman, 2004). By this, the world coordinate frame rotates with the object, i.e., the seed.

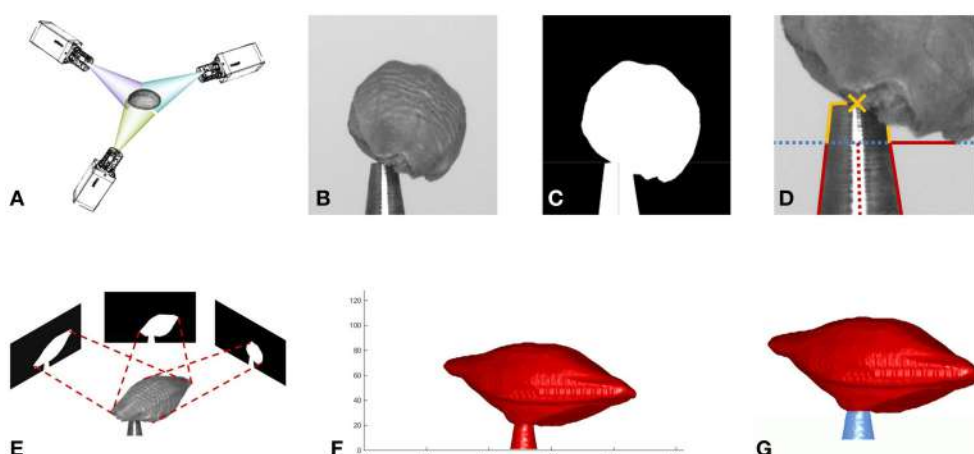


**FIGURE 1 |** Overview of the reconstruction method. **(A)** Image acquisition from multiple viewing angles. **(B)** One of the acquired gray value images. **(C)** Mask image. **(D)** Estimation of tool center point (TCP). **(E)** Estimate shape from silhouette by volume carving. **(F)** Surface of reconstructed volume. **(G)** Tool removed from volume: seed red, tool blue.

We define an equidistantly spaced, cubic voxel grid around the world origin, being large enough to contain the seed. The thus defined working volume depends on the seed type. For *Arabidopsis* we use  $(1 \text{ mm})^3$ , for rapeseed  $(2.9 \text{ mm})^3$ , and for barley and maize  $(13 \text{ mm})^3$ .

Each voxel center with homogeneous world coordinates  $\vec{X}$  is projected to a point  $\vec{x}_i$  in each mask  $\mathbf{M}_i$  by

$$\vec{x}_i = \mathbf{P}_i \vec{X} \quad (2)$$

If  $\vec{X}$  is projected to the background region of at least one of the  $N$  masks  $\mathbf{M}_i$ , then this voxel does not belong to the foreground object and its value  $\mathbf{V}(\vec{X})$  is set to 0, i.e.,

$$\mathbf{V}(\vec{X}) = \prod_{i=1}^N \mathbf{M}_i(\vec{x}_i) \quad (3)$$

Thus, if a voxel belongs to the foreground object, its value  $\mathbf{V}(\vec{X})$  is set to 1.

When higher voxel resolution is desired, and thus runtimes increase, parallelization of the carving algorithm (Brenscheidt, 2014) is feasible (see Section 4.1). Even higher resolutions become available on current desktop computer hardware, when hierarchically representing the voxel grid, e.g., as an octree (Szeliski, 1993; Klodt and Cremers, 2015).

One of the main drawbacks of this simple carving algorithm is its sensitivity to imprecise external camera calibration. When a mask  $\mathbf{M}_i$  is misaligned and thus does not well overlap with the “true” object volume, the non-overlapping parts are deleted from the volume without further testing or corrections. We therefore apply an image-based camera pose calibration step, as described next.

## 2.1. Correcting Camera Pose

Methods not adapting camera pose by estimating extrinsic parameters from the acquired images are known to be particularly sensitive to (extrinsic) calibration errors, thereby requiring precise positioning of the cameras (see e.g., Yezzi and Soatto, 2003). For relatively large objects in the multiple centimeter-range, say 20 cm long and filling most of an image, and typical pixel resolutions, say  $2000 \times 2000$ , a pixel covers an object area  $0.1 \times 0.1 \text{ mm}^2$ . Position repeatability of industrial-grade robotic systems, typically  $\leq 20 \mu\text{m}$  and  $\leq 0.05^\circ$  (Denso Robotics Europe, 2015), is therefore high enough for precise reconstruction. However, for objects being few millimeter in size or even in the sub-millimeter range additional care has to be taken. The mathematical TCP coordinates known to the robot control software may not coincide precisely with the physical TCP at the tool tip, due to mechanical calibration inaccuracies, wear and tear, or small deformations of the tool. In our case, instead of being at a fixed location in the camera images, the TCP moves on a more or less reproducible, elliptic trajectory of up to  $200 \mu\text{m}$  diameter, varying with room temperature.

Before projecting the voxels to the mask images, we therefore adapt projection matrices  $\mathbf{P}_i$ . If a suitable non-changing target moving with the TCP is visible in all images, image registration

can be done using simple normalized cross-correlation (see Figure 2).

In our robotic application, in order to adapt projection matrices  $\mathbf{P}_i$ , the truncated cone shape of the gripping tool has to be found, see Figure 3. As larger seeds may partly occlude the tool tip, we search for a region of the tool being reliably visible in the images. The tool enters the image vertically from below and becomes smaller in diameter toward the true TCP, being the center point of the very tip of the tool. As we can robustly find the tool’s left and right edges, we apply a simple and very fast procedure. We calculate the visible width of the tool line by line starting at the bottom of the image, moving upwards, i.e., in negative  $y$ -direction. We iterate while the width decreases and is larger than the minimum tool width (being at the tip). The thus reached  $y$ -coordinate is taken as first estimate of the TCP  $y$ -coordinate  $y_{\text{TCP}}$ . A reliable estimate of the TCP’s  $x$ -coordinate  $x_{\text{TCP}}$  is established as the mean of all found left and right edge  $x$ -positions. As the tool tip may be partly occluded by the seed,  $y_{\text{TCP}}$  needs refinement. For this the left and right tool edges are independently tracked further until the narrowest point is reached, i.e., the rightmost point of the left edge, and the leftmost point of the right edge. The smallest  $y$ -value (highest point) of the two points is taken as new  $y_{\text{TCP}}$ .

For small seeds like *Arabidopsis* this procedure works reliably, as the seeds are too small to occlude the whole tool tip in an image. For larger seeds, we use the observation that the TCP’s elliptic trajectory results in its  $y$ -coordinates to describe a sinusoidal curve over the rotation angle. We therefore robustly fit a sin-curve to the  $y$ -coordinates and correct outliers according to the fit result.

For such small objects, the optical lens setup (*cmp.* Section 3) features a narrow opening angle (i.e., large zoom), like a microscope at 1-to-1 magnification. This means lines of sight are almost parallel and thus depth effects are negligible. This allows to update  $\mathbf{P}_i$  with  $\vec{x}_{\text{TCP}}$  by simply setting the principal point (Hartley and Zisserman, 2004) to  $\vec{x}_{\text{TCP}}$ .

In our experiments we observed that  $\vec{x}_{\text{TCP}}$  can be estimated reliably with pixel accuracy, when no disturbances like small dust particles are present. Maximum offset in locating TCP from an unoccluded tool tip was 2 pixel.

In situations, where larger inaccuracies in locating  $\vec{x}_{\text{TCP}}$  occur, testing consistency of results and correcting  $\vec{x}_{\text{TCP}}$  is recommended. Back-projection of the reconstructed 3d object is a simple procedure allowing to test whether or not  $\mathbf{P}_i$  is correct and the selected segmentation procedure is suitable. For this test, each surface voxel of the found 3d object is projected to a mask image  $\tilde{\mathbf{M}}_i$ , initially filled with zeros. A voxel is projected to  $\tilde{\mathbf{M}}_i$  by projecting its corners to  $\tilde{\mathbf{M}}_i$  using  $\mathbf{P}_i$  and filling the respective convex hull with ones. If no errors occurred, the thus generated foreground mask should be identical to the segmentation mask  $\mathbf{M}_i$  (up to ignored subpixel effects when filling the convex hull, leading to a potentially slightly dilated mask  $\tilde{\mathbf{M}}_i$ ). Measuring overlap between the two masks can be done using well established measures, e.g., the *Overlap Ratio Criterion* =  $|\tilde{\mathbf{M}}_i \cap \mathbf{M}_i| / |\tilde{\mathbf{M}}_i \cup \mathbf{M}_i|$  (see e.g., Everingham et al., 2010), or *Dice Similarity Coefficient* =  $2|\tilde{\mathbf{M}}_i \cap \mathbf{M}_i| / (|\tilde{\mathbf{M}}_i| + |\mathbf{M}_i|)$  established by Dice (1945) and Sørensen (1948), where  $|\cdot|$  denotes set cardinality. These measures are

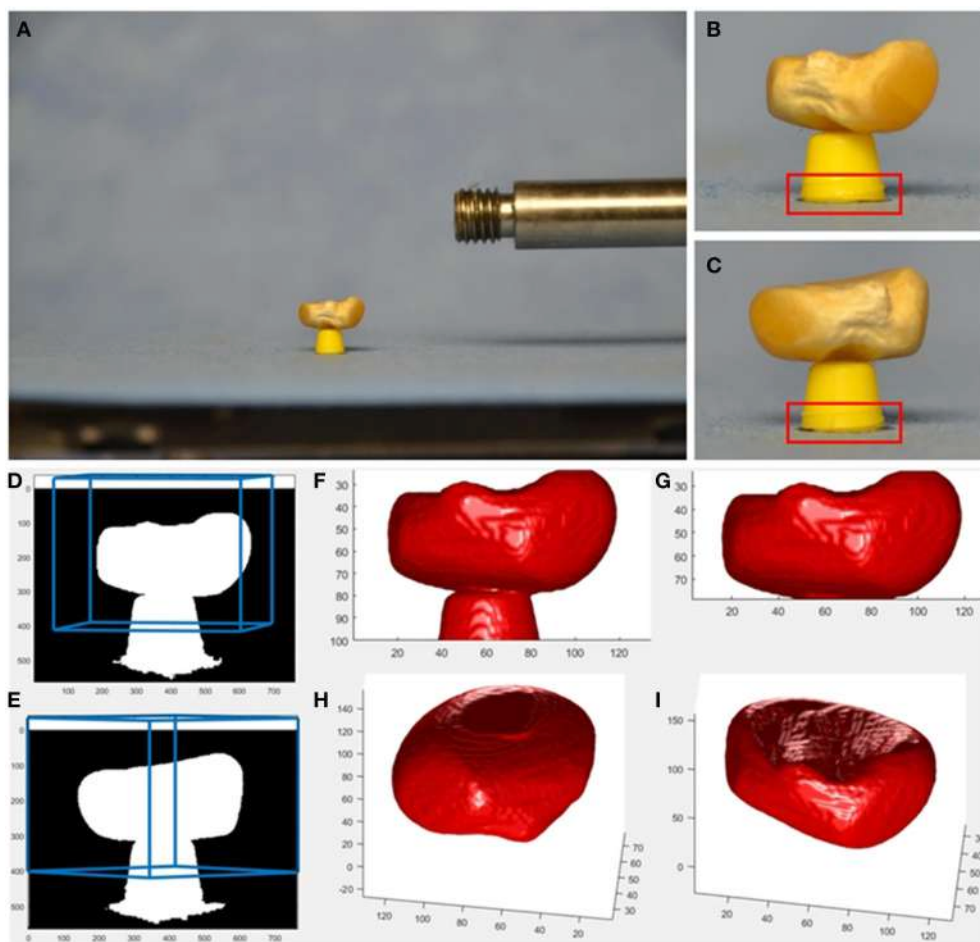


**FIGURE 2 | Example provided together with source code as supplemental material.** Imaging is done using affordable hardware, i.e., a usual SLR camera (Nikon D7000, AF-S Nikkor 16–85 mm 1:3.5–5.6 GED lens at  $f = 85$  mm) and a motorized turntable (Steinmeyer DT130-360°-SM01) for rotating the seed. As tool keeping the seed above the turntable's plane, we use a cut-off ball-pen-tip. A smaller tool, like in our robotic setup, allows for better seed visibility and reconstruction, however it is not easy to build. Even though the SLR is mounted on a sturdy tripod and released by a remote control, the camera center moves from image to image. In this setup, the base of the tool is visible in each image and can be used as target for correlation-based image registration. From the calculated image shifts, projection matrices  $\mathbf{P}_i$  are adapted accordingly. See provided source code for more details. **(A)** SLR image showing a maize seed, **(B,C)** cropped 760×564-image with 293×100 target for cross correlation indicated in red, **(D,E)** mask image with borders of the user-defined reconstruction volume projected back into the image in blue, **(F)** reconstructed seed and tool, **(G)** reconstructed seed with tool removed, **(H,I)**, reconstructed seed from a more bottom and more top view.

used throughout image analysis and are common in plant imaging as well (Minervini et al., 2014).

In case the achieved mask overlap is too small but larger than zero, iterative procedures can be applied to increase accuracy. Straight forward is to (1) shift the principal point in each projection matrix  $\mathbf{P}_i$  such that the center of mass of  $\tilde{\mathbf{M}}_i$  coincides with the center of mass of  $\mathbf{M}_i$  and (2) recarve, and iterate both steps until convergence or suitably large overlap. Alternatively, gradient descent-based algorithms optimizing camera pose may be applied as a refinement step (e.g., Yezzi and Soatto, 2003).

## 2.2. Removing the Tool from the Seed

For small seeds not overlapping with the tool, the TCP lies precisely in the world origin, i.e., the origin of the reconstructed voxel block. Thus, voxel above the TCP contain the seed, voxel

below (which in that case we do not reconstruct) contain the tool. In cases where seed and tool may overlap (see e.g., Figure 3), the tool tip is also reconstructed. It can be removed from the volume data using its known position, orientation, and physical size by deleting the corresponding voxel volume.

Alternatively, at high voxel resolutions, where the reconstructed volume covered by the tool may be affected by noise, one can estimate the tool position from the reconstruction. Summing up voxel values of horizontal planes in the bottom region of the volume gives reliable estimates of the area of horizontal cuts through the tool. While the areas decrease when summing over higher and higher planes, the planes are deleted from the data. Then, when areas no longer decrease, using these areas, we estimate the  $y$ -position of the truncated cone using a least squares fit and remove the thus covered volume.

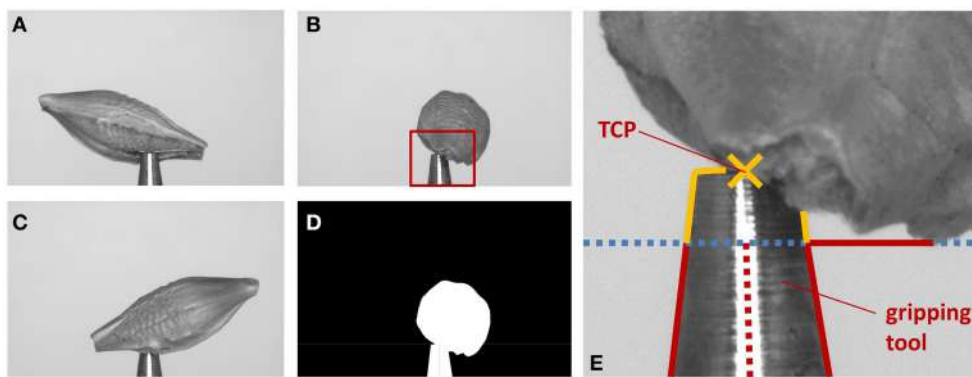


**FIGURE 3 | Illustration of the extrinsic camera calibration correction.** (A–C) Images of the same barley seed taken from different angles. (D) Mask image generated from (B). (E) Steps to find the TCP: (1) find edges of gripping tool (red lines), stop when lines diverge (blue dotted line). (2)  $x_{TCP}$  is average of middle between found edge positions (red dotted line). (3) Trace edges further as long as they come closer to  $x_{TCP}$  (yellow lines). (4) Top most position is  $y_{TCP}$ . The found TCP is indicated by a yellow cross.

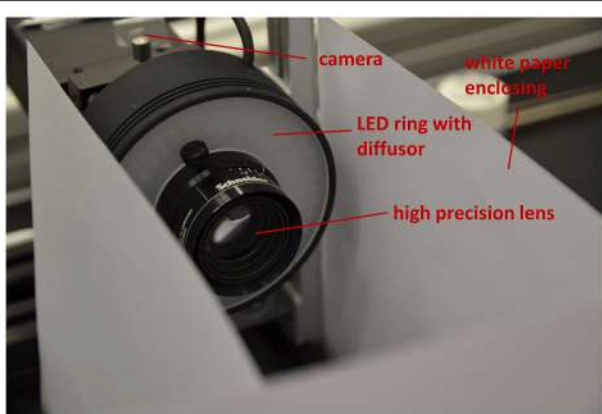


**FIGURE 4 | Camera setup for 3D imaging.**

### 3. MATERIALS AND METHODS

#### 3.1. Imaging

Depending on seed size for 3D reconstruction we use two different setups for image acquisition. Both setups consist of an industrial-grade c-mount camera (PointGrey Grasshopper, GRAS-50S5M-C, Mono, 5.0 MP, Sony ICX625 CCD, 2/3", square pixels of size  $\mu = 3.45 \mu\text{m}$ , global shutter, 2448 × 2048, 15 FPS), 35 mm high precision lens (Schneider KMP APO-XENOPLAN 35/1,9) and a white LED ring with diffusor (CCS LDR2-70-SW2) shown in **Figure 4**. For small seeds (e.g., *Arabidopsis*, tobacco, rapeseed) a 36 mm spacer is mounted between camera and lens. For larger seeds (e.g., barley, maize) only a 15 mm spacer is needed. Spacers reduce the minimum working distance of the lens ( $d = 69.9 \text{ mm}$  for the 36 mm spacer,  $128.0 \text{ mm}$  for the other) and thus are responsible for suitable magnification. This allows to measure seeds in a range between  $\approx 0.2$  and  $12 \text{ mm}$ . White paper is used as background.

For image acquisition seeds are picked by a cone-shaped vacuum nozzle and held in front of the camera at optimal

working distance using a robotic system to be described elsewhere. The robot rotates the seed in configurable angles and triggers the camera. We use  $10^\circ$  steps and take 36 images, if not stated differently. Image acquisition times are mainly limited by the robot's rotation typically  $\gtrsim 2.7 - 5 \text{ s}$  per  $360^\circ$ , depending on the motion type. We perform 36 stop-and-go steps resulting in an overall acquisition time of  $\approx 6 - 7 \text{ s}$ .

#### 3.2. Camera Calibration

We use the OpenCV implementation (Bradski and Kaehler, 2008) of Bouguet's calibration method (Bouguet, 1999) and an asymmetric  $4 \times 11$  dot-pattern target with a total size of  $5.8 \times 4.3 \text{ mm}$ . It was printed using a professional, high resolution film recorder, as usual office printers even on good paper do not achieve a printing precision suitable for camera calibration at such small spatial scales.

Using this toolbox, estimation of the focal length  $f$  is not precise enough for our purposes. We therefore use a ball-bearing ball (steel, precision according to DIN5401 G20) with  $r_0 = 1.50 \text{ mm} \pm 0.25 \mu\text{m}$  radius as calibration object, in order to estimate the working distance  $d$  (or equivalently focal length  $f$  from working distance  $d$ ) of our system precisely. From a mask image of the ball acquired with our system, we estimate its area  $A$  in pixel. This allows to estimate its radius  $r$  in the image by  $r = \mu\sqrt{A/\pi}$ , where  $\mu$  is the pixel size. From basic geometric reasoning working distance  $d$  can be derived as  $d = \sqrt{f^2 + r^2} r_0/r$ .

#### 3.3. Software Implementation

The software framework is implemented in C++ on a Windows 7 operating system with Visual Studio 2013. The application programming interface Open Graphics Library (OpenGL OpenGL.org, 2015) was used for the GPU implementation.

As supplemental material (Roussel et al., 2016) we provide both, a suite of *Matlab* (Mathworks, 2015) routines as well as a Python implementation suitable for volume carving of not too

small seeds using an affordable imaging setup. Such setups may e.g., use a turntable and a consumer SLR camera. In our example (see **Figure 2**) we use normalized cross-correlation for image registration, as the bottom of the tool is always visible as a suitable registration target.

## 4. EXPERIMENTS

### 4.1. Resolution and Runtime

The complexity of the volume carving algorithm is proportional to the number  $N_V$  of voxels and number  $N$  of images acquired. For our equidistantly spaced cubic  $R \times R \times R$  grids the voxel number is  $N_V = R^3$  and thus complexity is  $O(R^3 N)$ . In addition

time for loading (or acquiring) the images (with  $N_P$  pixels) and, for the GPU implementation, transferring the data to and from the graphics card is needed. Complexity of this data transfer and preprocessing of the images is  $O(N_P N)$ , or  $O(N_P N) + O(R^3)$  for the GPU implementation.

Runtimes shown in **Figure 5D** have been measured on a PC with Intel Core i5-3470 CPU, 8GB DDR3 RAM and an NVIDIA GeForce GTX 580 GPU with 4047MB GDDR5 RAM (*cmp. Brenscheidt, 2014* for further details). We observe that for low resolutions  $R$  of the voxel grid, runtime contributions by the  $O(N_P N)$  components dominate, as no dependence on  $R$  is visible. For increasing  $R$ , these parts become negligible. While for the CPU implementation a significant increase of the runtime vs.

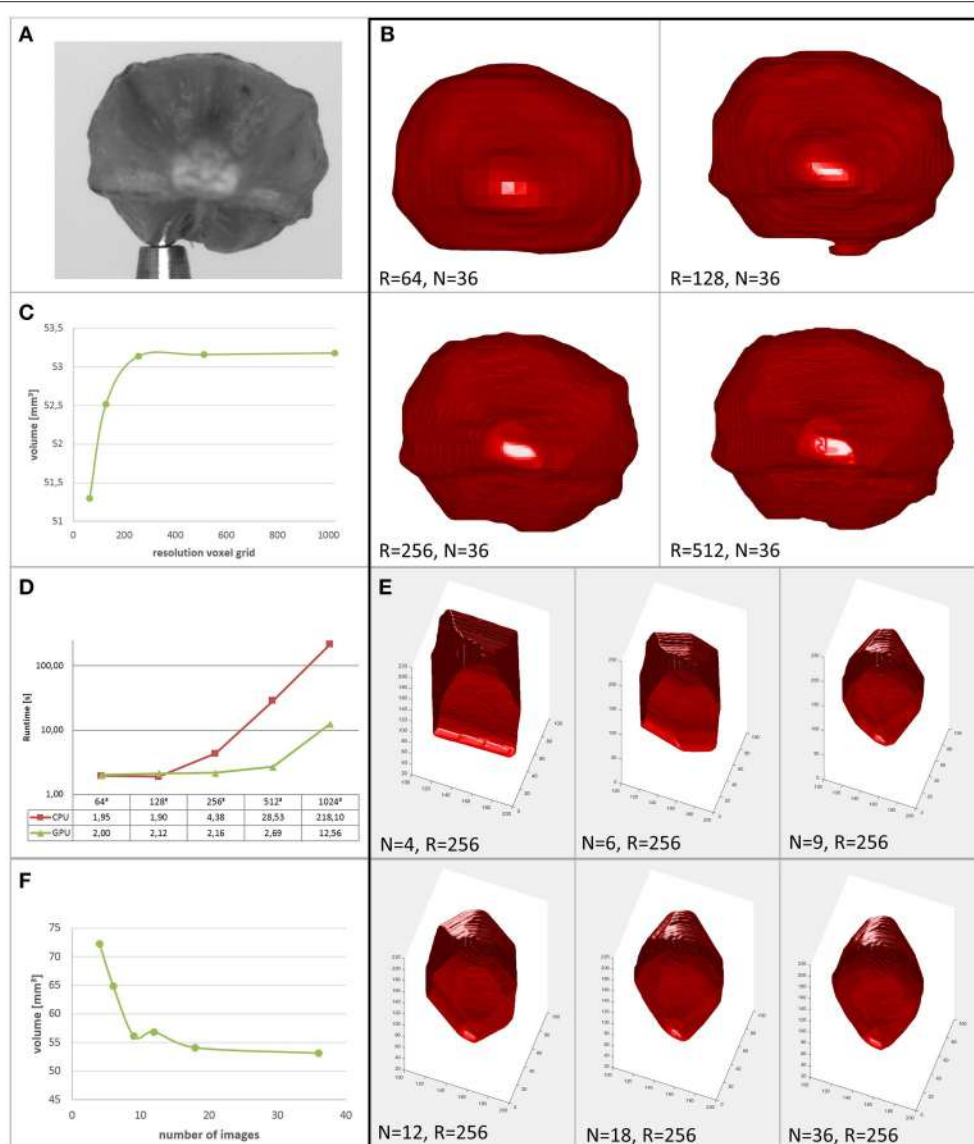


**FIGURE 5 | Performance of the proposed method.** **(A)** Original image of a barley seed. **(B)** Reconstructions of the seed at different grid resolutions. **(C)** Reconstructed volume vs. resolution of the voxel grid. **(D)** Runtimes in seconds of serial CPU and parallel GPU implementations (reproduced from *Brenscheidt, 2014*). **(E)** Reconstructions of the seed using different numbers of images. **(F)** Reconstructed volume vs. number of images used.

the 2 s runtime for smallest voxel resolutions can be noticed at  $R = 256$  (4 s), the parallel GPU implementation stays at comparable runtimes even at  $R = 512$ .

When interested in a seed's volume as a trait used for high throughput phenotyping, rather than in subtle surface details, voxel resolution can be selected comparably low. In **Figures 5A–C** we show a barley seed and its reconstructions together with its derived volume for different grid resolutions  $R$ . We observe that above  $R = 256$  the estimated volume is approximately constant. Thus, for this phenotyping task, runtime is limited mainly by file-IO, transfer and preprocessing. Sophisticated speed-up mechanisms for the carving provide rather low benefits in this application, as their main potential lies in higher achievable volume resolutions.

Speedup using fewer images may be paid by lower accuracy (see Section 4.2). We show reconstructions of the same barley seed in **Figure 5E** and the corresponding volumes in **Figure 5F**. Images are selected equidistantly. We observe that reducing image number rapidly reduces reconstruction quality. Interesting to note is that the reconstruction using  $N = 9$  images is more accurate than with  $N = 12$  images. This is due to the fact that for  $N = 12$  the selected angle between images is  $\alpha = 30^\circ$ , thus  $180^\circ$  is a multiple of  $\alpha$  (the same is true for  $N \in \{4, 6, 12, 18, 36\}$ , *cmp.* also **Figure 8** and Section 4.2). However, as the opening angle of our lens is small, complementary information content in masks coming from cameras looking in opposite direction is low. We conclude that for shorter runtimes with comparable

or even higher reconstruction accuracy investigating alternative viewing directions is promising. We do this in the next section for the restricted possibilities of our robotic, turntable-like, single camera acquisition system.

## 4.2. Accuracy vs. Number of Images

We numerically investigate the influence of the number  $N$  of equidistantly acquired images on the accuracy of volume estimation in an ideal turntable setting. To do so, we calculate the volume  $V_{\text{num}}$  of a sphere with radius  $r_0$  derived as cut of tangent cones, *cmp.* **Figures 6A,B,D**: Each ideal camera is represented by its camera center  $C_i$ , known from the selected working distance and rotation angle. A sphere projects to a circle on the sensor plane. A volume carving step for each image of this sphere thus corresponds to testing for each point of the working volume, if it lies inside or outside a cone spanned by  $C_i$  and the outline of the projected sphere (transparent cones in **Figure 6B**). The cone is independent of the focal length  $f$  of the ideal camera, but depends on the working distance  $d$ , i.e., the distance between each camera center and the center of the sphere. We select  $r_0 = 1.5$  mm, as we use a highly accurate, spherical bearing ball of this size as ground truth object in real experiments (see Section 4.4).

As we did not find a closed form solution for the volume of an object derived by a cut of  $N$  cones for arbitrary  $N$ , we numerically integrate the volume by a Monte-Carlo method:

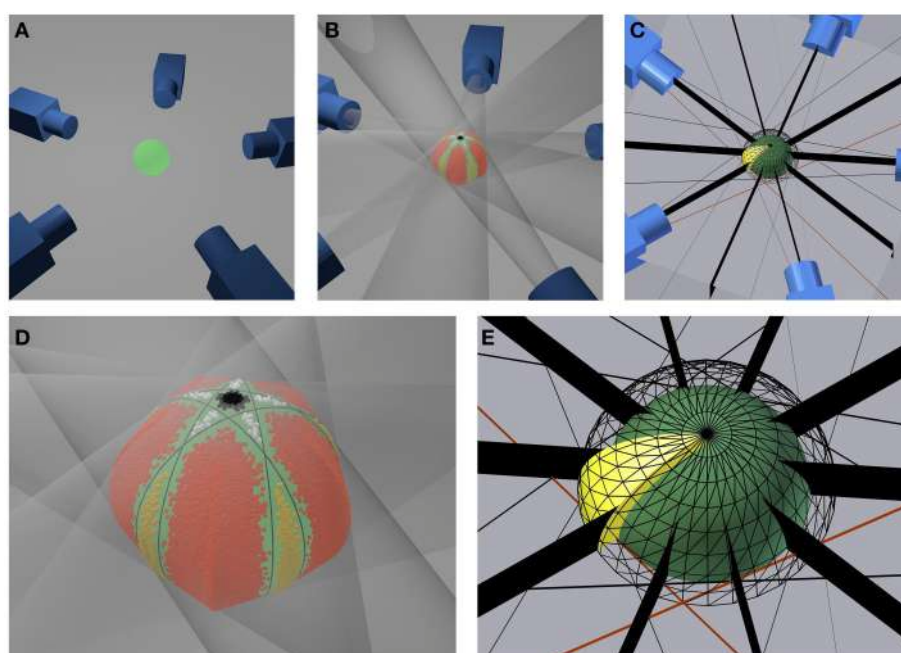


**FIGURE 6 | Setup for the numerical accuracy analysis.** **(A)** Exemplary geometrical setup for five cameras. **(B)** Same configuration with transparent projection cones touching the green sphere and colored inlier sampling points. **(D)** Close up of the sphere (green) and a visualization of the sampled inlier points. Red, yellow, black, and white points indicate the four different types of surplus volumes not taken away by carving. Black lines indicate where cones touch the sphere. **(C)** Symmetry planes (black) for each camera and section of a spherical shell indicating the geometry of the sampling region (yellow). **(E)** Close up of the sampling region (yellow). The inner sphere (green) represents the inner border of the volume, the meshed sphere the outer border. Black stripes indicate symmetry planes.

1. We randomly select  $K$  points in a region with known volume  $V_{\text{reg}}$  including the complete test volume.
2. For each point we test, if it lies in *all* cones spanned by the cameras. If yes, the point lies in the volume, if no, not. The number of all inliers is  $K_{\text{in}}$ .
3. The sought-for volume  $V_{\text{num}}$  is then  $V_{\text{num}} \approx V_{\text{reg}} * K_{\text{in}} / K$ .

The smaller  $V_{\text{reg}}$  can be selected, the more accurate  $V_{\text{num}}$  can be approximated with a fixed number  $K$  of sampling points. We observe that the selected turntable camera configuration (**Figures 6A,C**) is symmetric with respect to

- the plane spanned by the cone centers i.e., the equator of the sphere,
- each plane spanned by the rotation axis and a camera center,
- each plane spanned by the rotation axis and cutting the rotation angle between two adjacent camera centers in half, i.e., the vertical plane between two cameras.

Furthermore, we observe that

- the inner of the sphere lies completely in the carved volume, i.e., we carve the sphere from the outside; and finally that
- the sought-for volume lies in a concentric sphere with a somewhat larger radius than the carved sphere.

This allows to restrict numerical calculations to a region with known volume  $V_{\text{reg}}$  being box interval in spherical coordinates (*cmp.* **Figure 6E**, yellow region), in order to benefit optimally

from symmetries in the problem. We restrict the altitude angle to  $\theta \in [0, \pi/2]$ , azimuth to  $\phi \in [0, \pi/(2N)]$ , and the radius to  $r \in [r_0, r_1]$ . Radius  $r_1$  is calculated by (1) intersecting all cones with the plane spanned by the camera centers, yielding a pair of lines for each cone, (2) selecting the right lines of two adjacent cones (*cmp.* example red lines in **Figures 6C,E**) (3) calculating the intersection between these lines, and (4) selecting  $r_1$  as radius of the point given in polar coordinates.

This geometry is depicted in **Figures 6C,E**. The selection correspond to one section of a spherical shell, cut in half by the plane spanned by the cone centers (i.e., at the equator of the sphere) and cut in  $2N$  sections by the half-planes starting at the axis of rotation symmetry (i.e., the axis through the poles of the sphere) and each including one cone center; as well as their angle bisector planes.

Randomly sampling points in spherical coordinates produces higher point densities toward the origin in Euclidean coordinates and toward the north-south-axis of the sphere. We correct for these density differences combining two approaches. To understand this we need to calculate the Jacobian of the spherical coordinate transformation from Euclidean coordinates. Using the convention

$$x = r \sin \theta \cos \phi \quad (4)$$

$$y = r \sin \theta \sin \phi \quad (5)$$

$$z = r \cos \theta \quad (6)$$

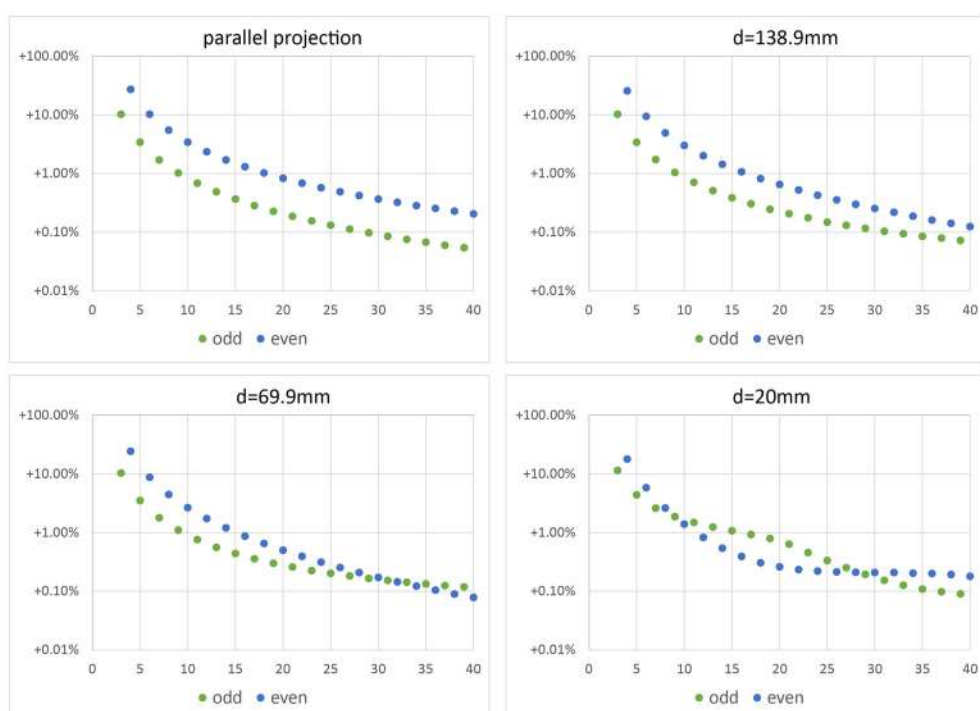


**FIGURE 7 | Error of volume vs. number  $N$  of camera positions.** Top left: error when using parallel projection (telecentric lens). The other plots show errors for different working distances  $d$  and central projection. In real experiments we use working distance  $d = 69.9$  mm.

we get the Jacobian  $J$

$$\begin{aligned} J &= \det \frac{\partial(x, y, z)}{\partial(r, \theta, \phi)} \\ &= \det \begin{pmatrix} \sin \theta \cos \phi & r \cos \theta \cos \phi & -r \sin \theta \sin \phi \\ \sin \theta \sin \phi & r \cos \theta \sin \phi & r \sin \theta \cos \phi \\ \cos \theta & -r \sin \theta & 0 \end{pmatrix} = r^2 \sin \theta. \end{aligned} \quad (7)$$

As long as  $r_0$  and  $r_1$  do not differ too much, as in our case, it is sufficient to consider the radial part of  $J$  by weighing sampling points  $p$  by their radius value  $r_p$

$$V_{\text{num}} \approx V_{\text{reg}} * \tilde{K}_{\text{in}} / \tilde{K} \quad (8)$$

where  $\tilde{K}_{\text{in}} = \sum_{p \in P_{\text{in}}} r_p^2$  and  $\tilde{K} = \sum_{p \in P} r_p^2$ .  $P$  is the set of all sampling points and  $P_{\text{in}} \subset P$  the set of all inliers.

Density variations due to altitude  $\theta$  are compensated by transforming the sampling probability density from the uniform distribution  $p(\chi)$  (with  $\chi \in [0, 1]$ ) a random number generator delivers to a  $\sin(\theta)$ -shaped distribution  $p_\theta(\theta)$ . This is achieved by the transform  $\theta = g(\chi)$ , where  $g(\chi) = \arccos(1 - \chi)$ . This can be easily verified using the transform law for densities  $p_\theta(\theta) = |\frac{d}{d\theta}g^{-1}(\theta)|p(g^{-1}(\theta))$ , where  $g^{-1}$  denotes the inverse function of  $g$ .

In **Figure 7** relative error  $E = (V_{\text{num}} - V_0)/V_0$  with  $V_0 = 4/3\pi r_0^3$  is depicted vs. the number  $N$  of images used for reconstruction of  $V_{\text{num}}$ . We observe that for parallel projection, using an even number of cameras (or images) yields the same result as using half the number of images. This makes sense, as for an even number of cameras, pairs of cameras are in an  $180^\circ$ -configuration, looking at the same object contour from different sides. This does not add additional information to the reconstruction. However, when considering central projection also images from an  $180^\circ$ -configuration add additional information, as cameras do not look at the same contour.

**Figure 8** shows volumes reconstructed using different camera configurations. We observe that using  $N = 5$  or  $N = 10$  camera positions yields identical results for parallel projection in **Figure 8**, left. However, for central projection  $N = 10$  camera positions yields a much better reconstruction than using  $N = 5$  images. This is in full agreement with the plot given in **Figure 7**, bottom right, where we also observe, that using odd  $N$  is not always better than using even  $N$  with one additional camera position. It depends on object size in relation to working distance, which camera position configuration yields better results in theory. We observe, that in the cases tested here, a minimum of  $N = 11$  or  $N = 12$  images is needed to stay below 1% relative error. A limit of less than 0.1% error is reached using  $N = 33$ ,  $N = 36$ , or  $N = 37$  images. In practice, however, given a sufficiently high  $N$ , other error sources may dominate (see next Sections).

### 4.3. Accuracy Loss Due to Position Inaccuracies

We performed experiments using synthetic images in order to test the different error sources in our method. The images

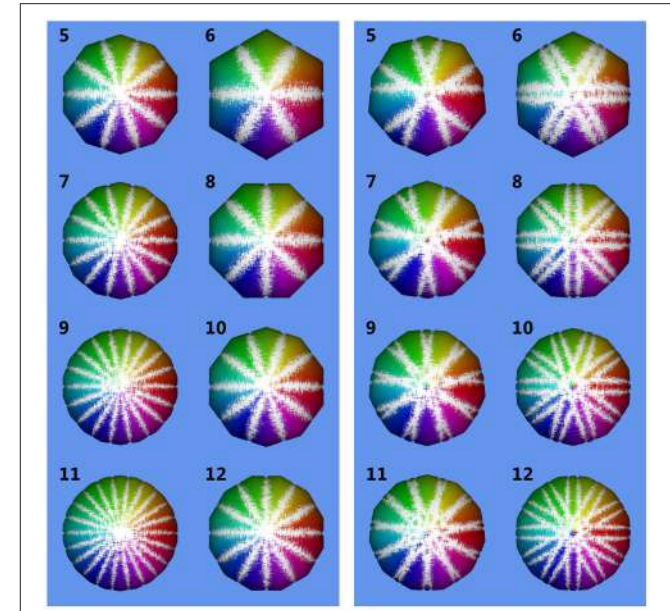


**FIGURE 8 | Reconstructed volumes for different numbers  $N$  of camera positions.** Numbers in the upper left corner of each subimage are  $N$ . Inlier sampling points are color-coded, where hue indicates  $\phi$  and brightness  $\theta$ . The underlying ground truth sphere is white. **Left:** reconstruction using parallel projection (telecentric lens). **Right:** reconstruction using central projection with working distance  $d = 20\text{mm}$  and sphere radius  $r_0 = 1.5\text{ mm}$ .

showed a perfect sphere as projection of a synthetic ball of same size as our bearing-ball. Geometrical setup was as for the experiments in Section 4.2, with working distance  $d = 69.9\text{ mm}$ . We reconstructed the ball using volume carving, a voxel grid resolution of  $256^3$  and  $(12\text{ }\mu\text{m})^3$  voxel size. Results were very similar to the ones shown in **Figure 7** for the same  $d$ , e.g., relative error at 36 images was approximately 0.14% instead of 0.1%. We do not show this plot. We conclude, that volume carving on a fine enough grid comes close to the theoretical performance of the simulation from Section 4.2, in agreement with our observations in **Figure 5C**.

Estimating TCP locations in the images is critical for reconstruction accuracy. To test the influence of a TCP wrongly located in an image, we add a relatively large offset of 7 pixel in  $y$ -direction to  $\vec{x}_{\text{TCP}}$  in the first image and leave the TCP locations in all other images untouched. The carving result is shown in **Figure 9**. The volume loss due to the misaligned TCP is in the order of 0.001 to 0.002  $\text{mm}^3$ , and thus reduces the positive volume error due to non-carved regions (as described in Section 4.2). For image configurations with relatively low positive initial error, i.e., here  $N > 36$ , the error due to the TCP offset dominates, such that overall relative error is negative. Please note that **Figure 9** shows absolute values of the relative errors due to the log-scale.

### 4.4. Seed Types and Overall Accuracy

Using the proposed method we reconstructed different seed types, namely *Arabidopsis* (length, i.e., longest dimension  $\lesssim 0.5\text{ mm}$ ), rapeseed ( $\approx 2\text{ mm}$ ), barley ( $\approx 8\text{ mm}$ ),

and maize ( $\approx 11$  mm). See **Figure 10** to get an impression of the usually achieved reconstruction accuracy.

Absolute accuracy is validated experimentally using two different test objects. The first one is the ball-bearing ball we used for working distance calibration with  $3.00 \text{ mm} \pm 0.5 \mu\text{m}$

diameter, i.e., 0.02% diameter tolerance, and thus a precisely known volume of  $14.137 \text{ mm}^3 \pm 0.007 \text{ mm}^3$ , i.e., 0.05% volume tolerance. Clearly, as we used this object for calibration, scaling of the mask images exactly fit to the respective projection matrices  $\mathbf{P}_i$ . However, the overall performance of the system for volume reconstruction can still be evaluated using this object, as the volume derived has *not* been used for calibration and still accumulates all errors and imperfections the method has. The second object is an ink cartridge ball with  $2.45 \text{ mm} \pm 0.02 \text{ mm}$  diameter, i.e., 0.4% diameter measurement error, measured with a digital sliding caliper, and thus a volume of  $7.70 \text{ mm}^3 \pm 0.19 \text{ mm}^3$ , i.e., 2.5% volume error.

In **Figure 11** volume error vs. number  $N \in \{27, \dots, 36\}$  of imaging positions is shown for the ball-bearing ball experiment. Comparing results to **Figure 7**, lower left (values repeated in **Figure 11** for easy reference), we observe that negative reconstruction errors due to positioning inaccuracies are in the same range as the positive theoretical errors and increase with increasing number of images. Please note that the plot shows absolute values of relative errors, as negative errors can not be displayed in log-scale.

Reconstructing the ball using 36 images as used for seed reconstruction, a voxel grid resolution of  $256^3$  and  $(12 \mu\text{m})^3$  voxel size, i.e., a volume tightly surrounding the object,

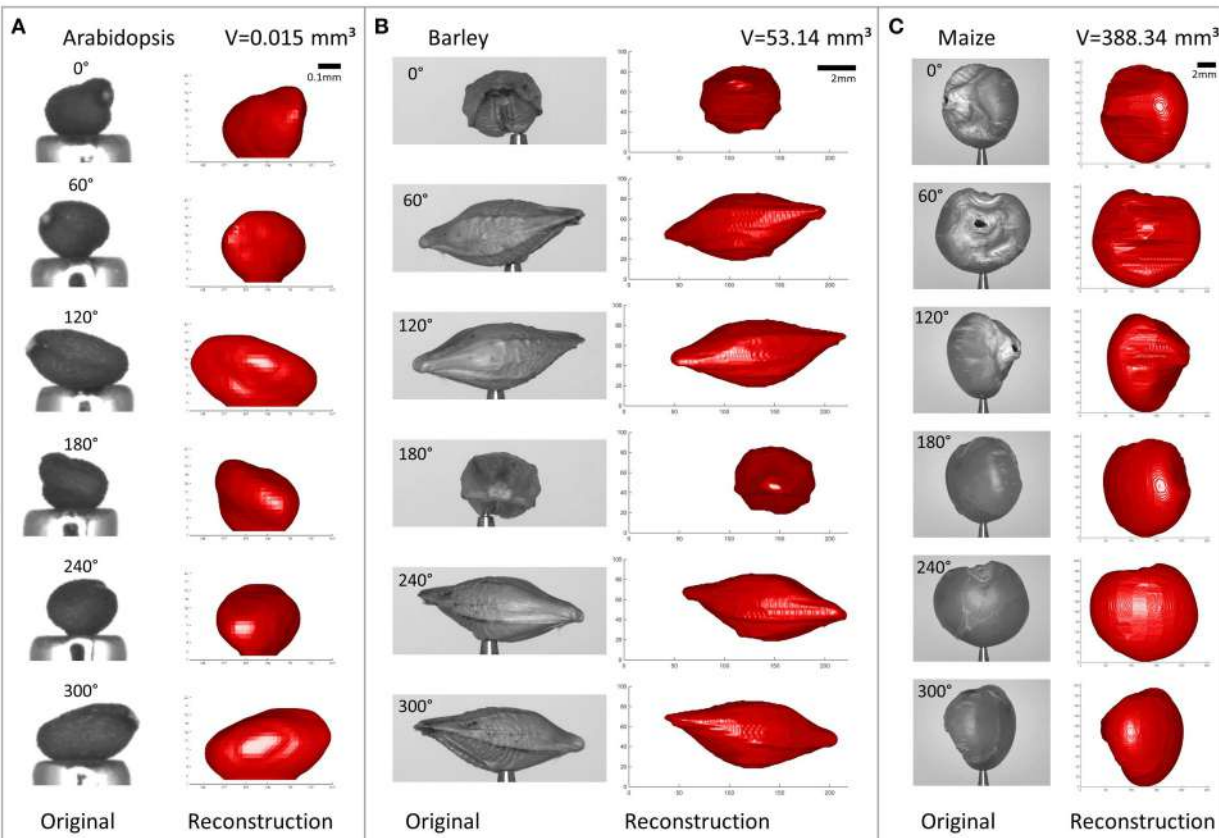
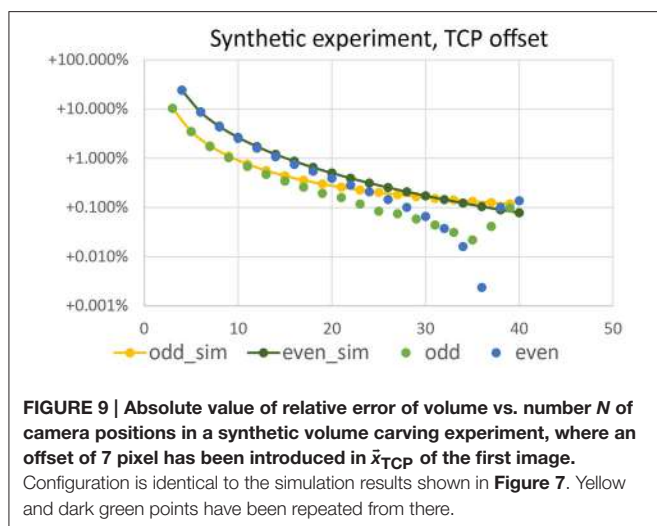


**FIGURE 10 |** Reconstructed seeds shown from different angles, side-by-side with the original images ( $R = 256$ ,  $N = 36$ ). **(A)** Arabidopsis. **(B)** Barley. **(C)** Maize. Please note the different scalings.

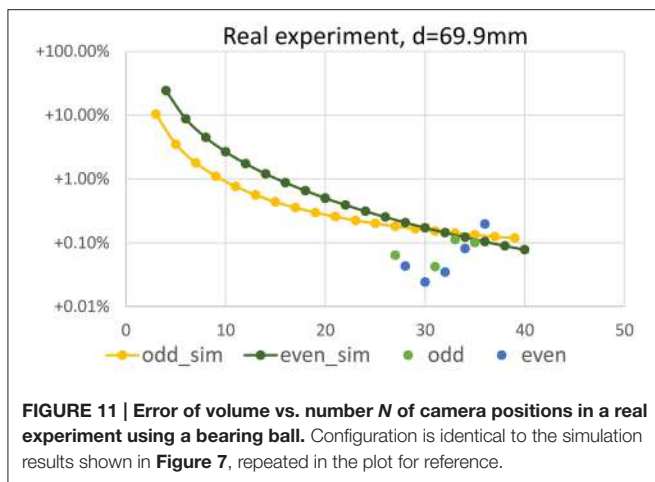


**FIGURE 11 | Error of volume vs. number  $N$  of camera positions in a real experiment using a bearing ball.** Configuration is identical to the simulation results shown in Figure 7, repeated in the plot for reference.

yields a volume of  $14.11 \text{ mm}^3$  and thus a mean diameter of  $2.998 \text{ mm}$  for the bearing ball. This is a relative error of  $-0.19\%$  wrt. the specified volume, and of  $-0.06\%$  wrt. the diameter, when calculating the diameter from the measured volume, assuming a perfect sphere. For the ink cartridge ball we measure  $7.83 \text{ mm}^3$  corresponding to a mean diameter of  $2.46 \text{ mm}$ , being well within the measuring error of our caliper measurement.

We conclude that the overall accuracy of our method, including camera calibration error, mechanical imperfections, TCP finding error, imprecision due to the simple carving approach etc. is high enough to compete with or even beat a precise slide caliper for length measurements. Absolute values of measurement errors of volume and lengths are in the range of few per mill.

## 5. CONCLUSION AND OUTLOOK

Simple volume carving combined with a method for extrinsic camera pose estimation from images is sufficiently accurate for size measurements of even tiny seeds. To optimize our system for runtime and accuracy, we investigated its performance using different parameter settings. Surprisingly, the main performance gain potential does currently not lie in using more sophisticated reconstruction methods allowing for higher achievable voxel resolutions  $R$ , e.g., achievable by the highly accurate method presented by Klodt and Cremers (2015) and necessary for reconstruction of more complex surfaces. Our findings allow reducing preprocessing and transfer times by selecting a suitable image number  $N$  and comparably low voxel resolution of  $256^3$ .

The optimal number  $N$  of acquisition positions used in a turntable setting depends on the selected projection geometry. In

our case using  $N = 36$  images yields a theoretical overestimation of the reconstructed volume of a sphere by  $+0.1\%$  relative error.

The method's achievable accuracy has been tested experimentally using a highly accurate spherical object. Systematic errors are much lower than we expected, between  $+0.06\%$  for  $N = 27$  and  $-0.19\%$  for  $N = 36$ . This means that volume losses due to inaccurate positioning of the object are truly negligible for our purposes. Clearly, as seeds are not well represented by a ball, such accuracy studies give insight in the accuracy potential of the method—if it fails on a ball, it will also fail on more complex shapes.

Seed-shape-specific errors are not well captured by a ball and may vary from seed type to seed type. Alternative simple volume measurement methods for ground truthing, e.g., Archimedes' principle, are not accurate enough for such small objects, but high-resolution CT may be an option.

Many factors influence the accuracy, e.g., segmentation errors, small dust particles or camera pose errors. Most critical are inaccuracies of  $\bar{x}_{TCP}$  in the image, leading to parts of a seed being erroneously carved away. To detect such errors, suitable error estimation methods can be implemented to complement the method proposed here, e.g., summing back-projection error. When positioning accuracy is an issue, more elaborated, iterative, optimization-based but also more costly to calculate methods may be applied. However, as we have seen in our experiments, achieved accuracies are well high enough for seed phenotyping even without such corrections.

Overall we conclude that the presented method yields highly accurate seed reconstructions being accurate enough when interested in seed volume.

## AUTHOR CONTRIBUTIONS

SJ and HS designed the robotic system used for seed handling and image acquisition. JR and AF implemented robot and acquisition hard and software. JR performed all lab experiments. FG performed all numerical experiments and implemented the supplemental Python code. HS implemented the baseline method, the supplemental Matlab code, and drafted the manuscript. All authors contributed to text and figures of the manuscript and approved the final manuscript.

## ACKNOWLEDGMENTS

Parts of this work was performed within the German-Plant-Phenotyping Network which is funded by the German Federal Ministry of Education and Research (project identification number: 031A053).

## REFERENCES

- Aksoy, E. E., Abramov, A., Wörgötter, F., Scharr, H., Fischbach, A., and Dellen, B. (2015). Modeling leaf growth of rosette plants using infrared stereo image sequences. *Comput. Electron. Agric.* 110, 78–90. doi: 10.1016/j.compag.2014.10.020

- Alenya, G., Dellen, B., and Torras, C. (2011). “3D modelling of leaves from color and ToF data for robotized plant measuring” in *IEEE International Conference on Robotics and Automation* (Shanghai), 3408–3414. doi: 10.1109/icra.2011.5980092
- Arvidsson, S., Pérez-Rodríguez, P., and Mueller-Roeber, B. (2011). A growth phenotyping pipeline for *Arabidopsis thaliana* integrating image analysis and

- rosette area modeling for robust quantification of genotype effects. *New Phytol.* 191, 895–907. doi: 10.1111/j.1469-8137.2011.03756.x
- Augustin, M., Haxhimusa, Y., Busch, W., and Kropatsch, W. G. (2015). “Image-based phenotyping of the mature arabidopsis shoot system,” in *Computer Vision - ECCV 2014 Workshops*, Vol. 8928 of *Lecture Notes in Computer Science* (Zurich: Springer International Publishing), 231–246.
- Bougjet, J.-Y. (1999). *Visual Methods for Three-dimensional Modeling*. Ph.D thesis, California Institute of Technology, Pasadena, CA, USA.
- Bradski, G., and Kaehler, A. (2008). *Learning OpenCV*. Sebastopol, CA: O'Reilly Media.
- Brenschmidt, M. (2014). Rekonstruktion der visuellen Hülle von Pflanzensamen mithilfe der OpenGL. Bachelor's thesis, Fachhochschule Aachen Campus Jülich, Germany.
- Brewer, M. T., Lang, L., Fujimura, K., Dujmovic, N., Gray, S., and van der Knaap, E. (2006). Development of a controlled vocabulary and software application to analyze fruit shape variation in tomato and other plant species. *Plant Physiol.* 141, 15–25. doi: 10.1104/pp.106.077867
- Bylesjö, M., Segura, V., Soolanayakanahally, R. Y., Rae, A. M., Trygg, J., Gustafsson, P., et al. (2008). Lamina: a tool for rapid quantification of leaf size and shape parameters. *BMC Plant Biol.* 8:82. doi: 10.1186/1471-2229-8-82
- Clark, R. T., MacCurdy, R. B., Jung, J. K., Shaff, J. E., McCouch, S. R., Aneshansley, D. J., et al. (2011). Three-dimensional root phenotyping with a novel imaging and software platform. *Plant Physiol.* 2, 455–465. doi: 10.1104/pp.110.169102
- De Vylder, J., Ochoa, D., Philips, W., Chaerle, L., and Van Der Straeten, D. (2011). “Leaf segmentation and tracking using probabilistic parametric active contours,” in *International Conference on Computer Vision/Computer Graphics Collaboration Techniques* (Rocquencourt), 75–85.
- Dellen, B., Scharr, H., and Torras, C. (2015). Growth signatures of rosette plants from time-lapse video. *IEEE/ACM Trans. Comput. Biol. Bioinf.* 12, 1470–1478. doi: 10.1109/tcbb.2015.2404810
- Denso Robotics Europe (2015). Denso Main Brochure. EN\_Global\_EU\_042015\_V1, Accessed June 2015.
- Dice, L. (1945). Measures of the amount of ecologic association between species. *Ecology* 26, 297–302. doi: 10.2307/1932409
- Everingham, M., Van Gool, L., Williams, C. K. I., Winn, J., and Zisserman, A. (2010). The Pascal Visual Object Classes (VOC) challenge. *Int. J. Comput. Vis.* 88, 303–338. doi: 10.1007/s11263-009-0275-4
- Fahlgren, N., Gehan, M. A., and Baxter, I. (2015). Lights, camera, action: high-throughput plant phenotyping is ready for a close-up. *Curr. Opin. Plant Biol.* 24, 93–99. doi: 10.1016/j.pbi.2015.02.006
- Fang, S., Yan, X., and Liao, H. (2009). 3d reconstruction and dynamic modeling of root architecture *in situ* and its application to crop phosphorus research. *Plant J.* 60, 1096–1108. doi: 10.1111/j.1365-313X.2009.04009.x
- Golbach, F., Kootstra, G., Damjanovic, S., Otten, G., and Zedde, R. (2015). Validation of plant part measurements using a 3d reconstruction method suitable for high-throughput seedling phenotyping. *Mach. Vis. Appl.* doi: 10.1007/s00138-015-0727-5. [Epub ahead of print].
- Granier, C., Aguirrezabal, L., Chenu, K., Cookson, S. J., Dauzat, M., Hamard, P., et al. (2006). PHENOPSIS, an automated platform for reproducible phenotyping of plant responses to soil water deficit in *Arabidopsis thaliana* permitted the identification of an accession with low sensitivity to soil water deficit. *New Phytol.* 169, 623–635. doi: 10.1111/j.1469-8137.2005.01609.x
- Hartley, R. I., and Zisserman, A. (2004). *Multiple View Geometry in Computer Vision, 2nd Edn*. Canberra: Cambridge University Press.
- Hartmann, A., Czauderna, T., Hoffmann, R., Stein, N., and Schreiber, F. (2011). HTPheo: an image analysis pipeline for high-throughput plant phenotyping. *BMC Bioinform.* 12:148. doi: 10.1186/1471-2105-12-148
- Herridge, R. P., Day, R. C., Baldwin, S., and Macknight, R. C. (2011). Rapid analysis of seed size in *Arabidopsis* for mutant and QTL discovery. *Plant Methods* 7, 3. doi: 10.1186/s11032-009-9319-2
- Iwata, H., Ebana, K., Uga, Y., Hayashi, T., and Jannink, J.-L. (2010). Genome-wide association study of grain shape variation among *oryza sativa* l. germplasms based on elliptic fourier analysis. *Mol. Breeding* 25, 203–215. doi: 10.1007/s11032-009-9319-2
- Iwata, H., and Ukai, Y. (2002). SHAPE: a computer program package for quantitative evaluation of biological shapes based on elliptic fourier descriptors. *J. Hered.* 93, 384–385. doi: 10.1093/jhered/93.5.384
- Jansen, M., Gilmer, F., Biskup, B., Nagel, K., Rascher, U., Fischbach, A., et al. (2009). Simultaneous phenotyping of leaf growth and chlorophyll fluorescence via GROWSCREEN FLUORO allows detection of stress tolerance in *Arabidopsis thaliana* and other rosette plants. *Funct. Plant Biol.* 36, 902–914. doi: 10.1071/FP09095
- Klodt, M., and Cremers, D. (2015). “High-resolution plant shape measurements from multi-view stereo reconstruction,” in *Computer Vision - ECCV 2014 Workshops*, Vol. 8928 of *Lecture Notes in Computer Science*, eds L. Agapito, M. M. Bronstein, and C. Rother (Zurich: Springer International Publishing), 174–184.
- Koenderink, N. J. J. P., Wigham, M., Golbach, F., Otten, G., Gerlich, R., and van de Zedde, H. J. (2009). “MARVIN: high speed 3d imaging for seedling classification,” in *Seventh European Conference on Precision Agriculture 2009* (Wageningen), 279–286.
- Laurentini, A. (1994). The visual hull concept for silhouette-based image understanding. *Pattern Anal. Mach. Intell. IEEE Trans.* 16, 150–162. doi: 10.1109/34.273735
- Lobet, G., Draye, X., and Périlleux, C. (2013). An online database for plant image analysis software tools. *Plant Methods* 9, 38. doi: 10.1186/1746-4811-9-38
- Martin, W. N., and Aggarwal, J. K. (1983). Volumetric descriptions of objects from multiple views. *IEEE Trans. Pattern Anal. Mach. Intell.* 5, 150–158. doi: 10.1109/TPAMI.1983.4767367
- Mathworks (2015). *Mathlab r2015b* (Natick, MA). Accessed May 2016.
- Minervini, M., Abdelsamea, M. M., and Tsafaris, S. A. (2014). Image-based plant phenotyping with incremental learning and active contours. *Ecol. Inf.* 23, 35–48. doi: 10.1016/j.ecoinf.2013.07.004
- Minervini, M., Scharr, H., and Tsafaris, S. A. (2015). Image analysis: the new bottleneck in plant phenotyping [applications corner]. *Signal Process. Mag. IEEE* 32, 126–131. doi: 10.1109/MSP.2015.2405111
- Moore, C. R., Gronwall, D. S., Miller, N. D., and Spalding, E. P. (2013). Mapping quantitative trait loci affecting *Arabidopsis thaliana* seed morphology features extracted computationally from images. *Genes Genomes Genet.* 3, 109–118. doi: 10.1534/g3.112.003806
- Müller-Linow, M., Pinto-Espinosa, F., Scharr, H., and Rascher, U. (2015). The leaf angle distribution of natural plant populations: assessing the canopy with a novel software tool. *Plant Methods* 11, 11. doi: 10.1186/s13007-015-0052-z
- Nagel, K., Putz, A., Gilmer, F., Heinz, K., Fischbach, A., Pfeifer, J., et al. (2012). GROWSCREEN-Rhizo is a novel phenotyping robot enabling simultaneous measurements of root and shoot growth for plants grown in soil-filled rhizotrons. *Funct. Plant Biol.* 39, 891–904. doi: 10.1071/FP12023
- Next Instruments (2015). *Seedcount*. Accessed June 2015.
- OpenGL.org (2015). *OpenGL Overview*. Beaverton: The Khronos Group, Accessed June 2015.
- Pape, J.-M., and Klukas, C. (2015). “3-D histogram-based segmentation and leaf detection for rosette plants,” in *Computer Vision - ECCV 2014 Workshops*, Vol. 8928 of *Lecture Notes in Computer Science* (Zurich: Springer International Publishing), 61–74.
- Paproki, A., Sirault, X., Berry, S., Furbank, R., and Fripp, J. (2012). A novel mesh processing based technique for 3d plant analysis. *BMC Plant Biol.* 12:63. doi: 10.1186/1471-2229-12-63
- Paulus, S., Behmann, J., Mahlein, A.-K., Plümer, L., and Kuhlmann, H. (2014). Low-cost 3d systems: Suitable tools for plant phenotyping. *Sensors* 14:3001. doi: 10.3390/s140203001
- Potmesil, M. (1987). Generating octree models of 3d objects from their silhouettes in a sequence of images. *Comput. Vis. Graph. Image Process.* 40, 1–29. doi: 10.1016/0734-189X(87)90053-3
- Pound, M. P., French, A. P., Fozard, J. A., Murchie, E. H., and Pridmore, T. P. (2016). A patch-based approach to 3d plant shoot phenotyping. *Mach. Vis. Appl.* doi: 10.1007/s00138-016-0756-8. [Epub ahead of print].
- Pound, M. P., French, A. P., Murchie, E. H., and Pridmore, T. P. (2014). Automated recovery of three-dimensional models of plant shoots from multiple color images. *Plant Physiol.* 166, 1688–1698. doi: 10.1104/pp.114.248971
- Quan, L., Tan, P., Zeng, G., Yuan, L., Wang, J., and Kang, S. B. (2006). Image-based plant modeling. *ACM Trans. Graph.* 25, 599–604. doi: 10.1145/1141911.1141929
- Regent Instruments (2000). *Winseedle*. Ville de Québec: Instruments Regent Inc., Accessed June 2015.

- Roussel, J., Fischbach, A., Jahnke, S., and Scharr, H. (2015). “3D surface reconstruction of plant seeds by volume carving,” in *Computer Vision Problems in Plant Phenotyping 2015* (Swansea).
- Roussel, J., Geiger, F., Fischbach, A., Jahnke, S., and Scharr, H. (2016). *Supplemental Material on “3D Surface Reconstruction of Plant Seeds by Volume Carving: Performance and Accuracies”*. Available online at: <http://www.fz-juelich.de/ibg/ibg-2/software>
- Santos, T. T., and Rodrigues, G. C. (2015). Flexible three-dimensional modeling of plants using low-resolution cameras and visual odometry. *Mach. Vis. Appl.* doi: 10.1007/s00138-015-0729-3. [Epub ahead of print].
- Silva, L. O. L. A., Koga, M. L., Cugnasca, C. E., and Costa, A. H. R. (2013). Comparative assessment of feature selection and classification techniques for visual inspection of pot plant seedlings. *Comput. Electron. Agricult.* 97, 47–55. doi: 10.1016/j.compag.2013.07.001
- Sørensen, T. (1948). A method of establishing groups of equal amplitude in plant sociology based on similarity of species content and its application to analyses of the vegetation on danish commons. *Biol. Skr* 5, 1–34.
- Spalding, E. P., and Miller, N. D. (2013). Image analysis is driving a renaissance in growth measurement. *Curr. Opin. Plant Biol.* 16, 100–104. doi: 10.1016/j.pbi.2013.01.001
- Szeliski, R. (1993). Rapid octree construction from image sequences. *CVGIP: Image Underst.* 58, 23–32. doi: 10.1006/ciu.1993.1029
- Tanabata, T., Shibaya, T., Hori, K., Ebana, K., and Yano, M. (2012). Smartgrain: High-throughput phenotyping software for measuring seed shape through image analysis. *Plant Physiol.* 160, 1871–1880. doi: 10.1104/pp.112.205120
- Topp, C. N., Iyer-Pascuzzi, A. S., Anderson, J. T., Lee, C.-R., Zurek, P. R., Symonova, O., et al. (2013). 3d phenotyping and quantitative trait locus mapping identify core regions of the rice genome controlling root architecture. *Proc Natl. Acad. Sci. U.S.A.* 110, E1695–E1704. doi: 10.1073/pnas.1304354110
- Tsaftaris, S., and Noutsos, C. (2009). “Plant phenotyping with low cost digital cameras and image analytics,” in *Information Technologies in Environmental Engineering*, eds I. N. Athanasiadis, A. E. Rizzoli, P. A. Mitkas, and J. M. Gómez (Berlin: Springer), 238–251.
- van der Heijden, G., Song, Y., Horgan, G., Polder, G., Dieleman, A., Bink, M., et al. (2012). SPICY: towards automated phenotyping of large pepper plants in the greenhouse. *Funct. Plant Biol.* 39, 870–877. doi: 10.1071/FP12019
- Wallenberg, M., Felsberg, M., and Forssén, P.-E. (2011). “Leaf segmentation using the Kinect.” in *SSBA’11 Symposium on Image Analysis* (Linköping), 1–4.
- Wang, L., Uilecan, I. V., Assadi, A. H., Kozmik, C. A., and Spalding, E. P. (2009). HYPOTrace: image analysis software for measuring hypocotyl growth and shape demonstrated on *Arabidopsis* seedlings undergoing photomorphogenesis. *Plant Physiol.* 149, 1632–1637. doi: 10.1104/pp.108.134072
- Weight, C., Parnham, D., and Waites, R. (2008). LeafAnalyser: a computational method for rapid and large-scale analyses of leaf shape variation. *Plant J.* 53, 578–586. doi: 10.1111/j.1365-313X.2007.03330.x
- Whan, A. P., Smith, A. B., Cavanagh, C. R., Ral, J.-P. F., Shaw, L. M., Howitt, C. A., et al. (2014). GrainScan: a low cost, fast method for grain size and colour measurements. *Plant Methods* 10, 1–10. doi: 10.1186/1746-4811-10-23
- Yezzi, A. J., and Soatto, S. (2003). “Structure from motion for scenes without features,” in *Computer Vision and Pattern Recognition, 2003. Proceedings. 2003 IEEE Computer Society Conference on* (Madison), 525–532.
- Zheng, Y., Gu, S., Edelsbrunner, H., Tomasi, C., and Benfey, P. (2011). “Detailed reconstruction of 3d plant root shape,” in *Proceedings of the 2011 International Conference on Computer Vision, ICCV ’11*, (Washington, DC: IEEE Computer Society), 2026–2033.

**Conflict of Interest Statement:** The authors declare that the research was conducted in the absence of any commercial or financial relationships that could be construed as a potential conflict of interest.

Copyright © 2016 Roussel, Geiger, Fischbach, Jahnke and Scharr. This is an open-access article distributed under the terms of the Creative Commons Attribution License (CC BY). The use, distribution or reproduction in other forums is permitted, provided the original author(s) or licensor are credited and that the original publication in this journal is cited, in accordance with accepted academic practice. No use, distribution or reproduction is permitted which does not comply with these terms.



# Using a Structural Root System Model to Evaluate and Improve the Accuracy of Root Image Analysis Pipelines

Guillaume Lobet<sup>1,2\*</sup>, Iko T. Koevoets<sup>3†</sup>, Manuel Noll<sup>1†</sup>, Patrick E. Meyer<sup>1</sup>, Pierre Tocquin<sup>1</sup>, Loïc Pagès<sup>4</sup> and Claire Périlleux<sup>1</sup>

<sup>1</sup> InBioS-PhytoSYSTEMS, University of Liège, Liège, Belgium, <sup>2</sup> Institut für Bio-und Geowissenschaften: Agrosphäre, Forschungszentrum Jülich, Jülich, Germany, <sup>3</sup> Plant Cell Biology, Swammerdam Institute for Life Sciences, University of Amsterdam, Amsterdam, Netherlands, <sup>4</sup> INRA, Centre d'Avignon, UR 1115 PSH, Avignon, France

## OPEN ACCESS

### Edited by:

Alexander Bucksch,  
University of Georgia, USA

### Reviewed by:

Christopher N. Topp,  
Donald Danforth Plant Science Center,  
USA

Tony Pridmore,  
University of Nottingham, UK

### \*Correspondence:

Guillaume Lobet  
g.lobet@fz-juelich.de

<sup>†</sup>These authors have contributed  
equally to this work.

### Specialty section:

This article was submitted to  
Plant Biophysics and Modeling,  
a section of the journal  
Frontiers in Plant Science

Received: 14 September 2016

Accepted: 15 March 2017

Published: 03 April 2017

### Citation:

Lobet G, Koevoets IT, Noll M, Meyer PE, Tocquin P, Pagès L and Périlleux C (2017) Using a Structural Root System Model to Evaluate and Improve the Accuracy of Root Image Analysis Pipelines. *Front. Plant Sci.* 8:447. doi: 10.3389/fpls.2017.00447

Root system analysis is a complex task, often performed with fully automated image analysis pipelines. However, the outcome is rarely verified by ground-truth data, which might lead to underestimated biases. We have used a root model, ArchiSimple, to create a large and diverse library of ground-truth root system images (10,000). For each image, three levels of noise were created. This library was used to evaluate the accuracy and usefulness of several image descriptors classically used in root image analysis softwares. Our analysis highlighted that the accuracy of the different traits is strongly dependent on the quality of the images and the type, size, and complexity of the root systems analyzed. Our study also demonstrated that machine learning algorithms can be trained on a synthetic library to improve the estimation of several root system traits. Overall, our analysis is a call to caution when using automatic root image analysis tools. If a thorough calibration is not performed on the dataset of interest, unexpected errors might arise, especially for large and complex root images. To facilitate such calibration, both the image library and the different codes used in the study have been made available to the community.

**Keywords:** image analysis, root structural model, benchmarking, image library, machine learning

## INTRODUCTION

Roots are of utmost importance in the life of plants and hence selection on root systems represents great promise for improving crop tolerance to biotic and abiotic stresses (as reviewed in Koevoets et al., 2016). As such, their quantification is a challenge in many research projects. This quantification is usually two-fold. The first step consists in acquiring images of the root system, either using classic imaging techniques (CCD cameras) or more specialized ones (microCT, X-Ray, fluorescence,...). The next step is to analyse the pictures to extract meaningful descriptors of the root system.

To paraphrase the famous Belgian surrealist painter, René Magritte: “**Figure 1A** is not a root system.” **Figure 1A** is an image of a root system and that distinction is important. An image is indeed a two-dimensional representation of an object, which is usually three-dimensional.

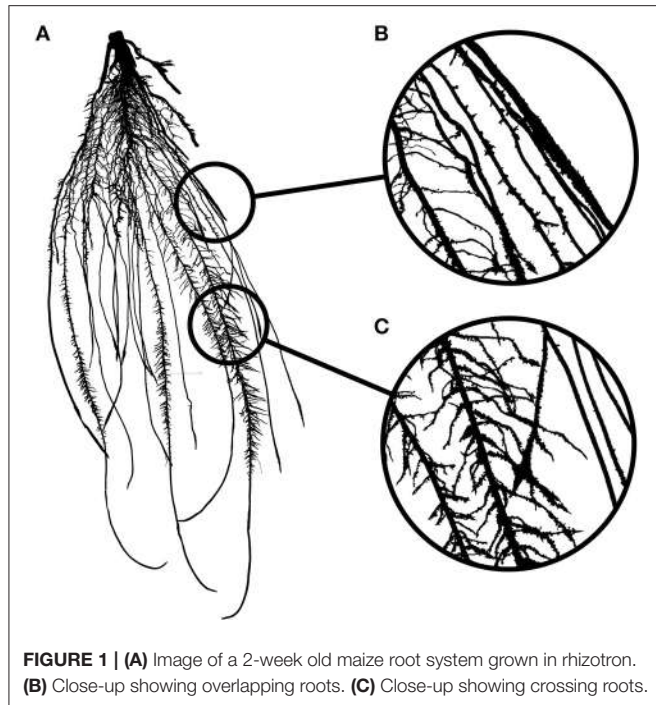


**FIGURE 1 | (A)** Image of a 2-week old maize root system grown in rhizotron. **(B)** Close-up showing overlapping roots. **(C)** Close-up showing crossing roots.

Nowadays, measurements are generally not performed on the root systems themselves, but on the images, and this raises some issues.

Image analysis is the acquisition of traits (or descriptors) describing the objects contained in a particular image. In a perfect situation, these descriptors would accurately represent the biological object of the image with negligible deviation from the biological truth (or data). However, in many cases, artifacts might be present in the images so that the representation of the biological object is not accurate anymore. These artifacts might be due to the conditions under which the images were taken or to the object itself. Mature root systems, for instance, are complex branched structures, composed of thousands of overlapping (Figure 1B), and crossing segments (Figure 1C). These features are likely to impede image analysis and create a gap between the descriptors and the data.

Root image descriptors can be separated into two main categories: morphological and geometrical descriptors. Morphological descriptors refer to the shape of the different root segments forming the root system (Table 1). They include, among others, the length and diameter of the different roots. For complex root system images, morphological descriptors are difficult to obtain and are prone to error as mentioned above. Geometrical descriptors give the position of the different root segments in space. They summarize the shape of the root system as a whole. The simplest geometrical descriptors are the width and depth of the root system. Since these descriptors are mostly defined by the external envelope of the root system, crossing and overlapping segments have little impact on their estimation and hence they can be considered as relatively errorless. Geometrical descriptors are expected to be loosely linked to the actual root system topology, since identical shapes could be obtained from

**TABLE 1 | Root system parameters used as ground-truth data.**

Name	Description	Unit
tot_root_length	The cumulative length of all roots	mm
tot_1_order_length	The cumulative length of all root axes	mm
tot_2+_order_length	The cumulative length of all lateral roots	mm
mean_1_order_length	The mean first-order roots length	mm
mean_2+_order_length	The mean lateral root length	mm
n_1_orders	The total number of first order roots	-
n_2+_orders	The total number of lateral roots	-
mean_2+_order_density	The mean lateral root density: for each first-order root, the number of lateral roots divided by the axis length (total length).	mm <sup>-1</sup>
mean_1_order_diam	The mean diameter of the first-order roots	mm
mean_2+_order_diam	The mean diameter of the lateral roots	mm
mean_2+_order_angle	The mean insertion angle of the lateral roots	°

different root systems (the opposite is true as well). They are usually used in genetic studies, to identify genetic bases of root system shape and soil exploration.

Several automated analysis tools were designed in the last few years to extract both types of descriptors from root images (Armengaud et al., 2009; Galkovskyi et al., 2012; Pierret et al., 2013; Bucksch et al., 2014). However, the validation of such tools is often incomplete and/or error prone. For technical reasons, the validation is usually performed on a small number of ground-truth images of young root systems. In agreement, most analysis tools are specifically designed for this kind of root systems. In the few cases where validation is performed on large and complex root systems, it is usually not on ground-truth images, but in comparison with previously published tools (measurement of X with tool A compared with the same measurement with tool B). This might seem a reasonable approach, regarding the scarcity of ground-truth images of large root systems. However, the inherent limitations of these tools, such as scale or root system type (fibrous- vs. tap-roots) are often not known. Users might not even be aware that such limitations exist and apply the provided algorithm without further validation on their own images. This can lead to unexpected errors in the final measurements.

One strategy to address the lack of in-depth validation of image analysis pipelines would be to use synthetic images generated by structural root models (models designed to recreate the physical structure and shape of root systems). Many structural root models have been developed, either to model specific plant species (Pagès et al., 1989), or to be generic (Pagès et al., 2004, 2013). These models have been repeatedly shown to faithfully represent the root system structure (Pagès and Pellerin, 1996). In addition, they can provide the ground-truth data for each synthetic root system generated, independently of its complexity. However, they have not been used for validation of image analysis tools (Rellán-Álvarez et al., 2015), with one exception performed on young seedling unbranched roots (Benoit et al., 2014).

Here we (i) illustrate the use of a structural root model, Archisimple, to systematically analyse and evaluate an image analysis pipeline and (ii) use the model-generated images to improve the estimation of root traits.

## MATERIALS AND METHODS

### Nomenclature Used in the Paper

**Ground-truth data:** The real (geometrical and morphometrical) properties of the root system as a biological object. They are determined by either manual tracking of roots or by using the output of simulated root systems.

**(Image) Descriptor:** Property of the root image. It does not necessarily have a biological meaning.

**Root axes:** First order roots, directly attached to the shoot.

**Lateral roots:** Second- (or lower) order roots, attached to another root.

### Creation of a Root System Library

We used the model ArchiSimple, which was shown to allow the generation of a large diversity of root systems with a minimal amount of parameters (Pagès et al., 2013). To produce a large library of root systems, we ran the model 10,000 times, each time with a random set of parameters (Figure 2A). For each simulation, the growth and development of the root system were constrained in two dimensions.

The simulations were divided into two main groups: fibrous and tap-rooted. For the fibrous simulations, the model generated a random number of root axes and secondary (radial) growth was disabled. For tap-root simulations, only one root axis was produced and secondary growth was enabled (the extent of which was determined by a random parameter).

The root system created in each simulation was stored in a Root System Markup Language (RSML) file. Each RSML file was then read by the RSML Reader plugin from ImageJ to extract ground-truth data for the library (Lobet et al., 2015). These ground-truth data included geometrical and morphological parameters (Table 1). For each RSML data file, the RSML Reader plugin also created three JPEG images (at a resolution of 300 DPI) for each root system. To simulate one type of image degradation, we added different levels of noise to the images (using the Salt and Pepper Filter in ImageJ) (Figure 2D). For each root system, we computed overlapping index as the number of root segments having an overlap with other root segments over the total number of root segments.

### Root Image Analysis

Each generated image was analyzed using a custom-made ImageJ plugin, Root Image Analysis-J (or RIA-J). For each image, we extracted a set of classical root image descriptors, such as the total root length, the projected area, and the number of visible root tips (Figure 2E). In addition, we included shape descriptors such as the convex-hull area or the exploration ratio (see Supplemental File 1 for details of RIA-J). The list of traits and algorithms used by our pipeline is listed in Table 2. Distribution of the different descriptors is given in the Supplemental Figure 2.

### Data Analysis

Data analysis was performed in R (R Core Team)<sup>1</sup>. Plots were created using *ggplot2* (Wickham, 2009) and *lattice* (Sarkar, 2008).

The Mean Relative Errors (MRE) were estimated using the equation:

$$MRE = \frac{\sum_1^n \frac{|\bar{y}_i - y_i|}{\bar{y}_i}}{n}$$

where  $n$  is the number of observations,  $\bar{y}_i$  is the ground-truth and  $y_i$  is the estimated ground-truth.

### Random Forest Framework

A *random forest* is a state-of-the-art machine learning algorithm typically used for making new predictions (in both classification and regression tasks). Random Forests can perform non-linear predictions and, thus, often outperform linear models. Since its introduction by Breiman (2001), Random Forests have been widely used in many fields from gene regulatory network inference to generic image classification (Huynh-Thu et al., 2013; Marée et al., 2016). Random Forest relies on growing a multitude of decision trees, a prediction algorithm that has shown good performances by itself but, when combined with other decision trees (hence the name forest), returns predictions that are much more robust to outliers and noisy data (see bootstrap aggregating, Breiman, 1996).

In a machine learning setting one is given a set  $D = \{(x_1, y_1), (x_2, y_2), \dots, (x_n, y_n)\}$ ,

where  $x_i = (x_i^1, x_i^2, \dots, x_i^s)$  is an element of a  $s$ -dimensional feature space  $X$ ,

and  $y_i = (y_i^1, y_i^2, \dots, y_i^t)$  an element of a  $t$ -dimensional response space  $Y$ .

The learning task is to find a model

$$M : X \rightarrow Y$$

that predicts the data in a good way, where goodness is measured with regard to an error function  $L$ .

A decision tree  $T_D$  is a machine learning method that, for a dataset  $D$ , constructs a binary tree with each node representing a binary question and each leaf a value of the response space. In other words, a prediction can be made from an input value by looking at the set of binary questions that leads to a leaf (e.g., is the first-order root bigger than q1 and if yes is the number of second-order roots smaller than q2 and if no, ...).

Each decision is based upon exactly one feature and is used for deciding which branch of the tree a given input value must take. Hence a decision tree splits successively the set  $D$  into smaller subsets and assigns them a value  $y_i = T_D(x_i)$  of the response space.

The choice of the feature used for splitting depends on a relevance criterion. In our setting, the default relevance criterion from the *randomForest* R package (CRAN randomForest, 2015), namely the Gini index, has been used.

A Random Forest

$$F_D = (T_{D,k})_{k \in I} \text{ where } I = \{1, 2, \dots, l\} \quad (1)$$

<sup>1</sup>R Core Team R: A Language and Environment for Statistical Computing.

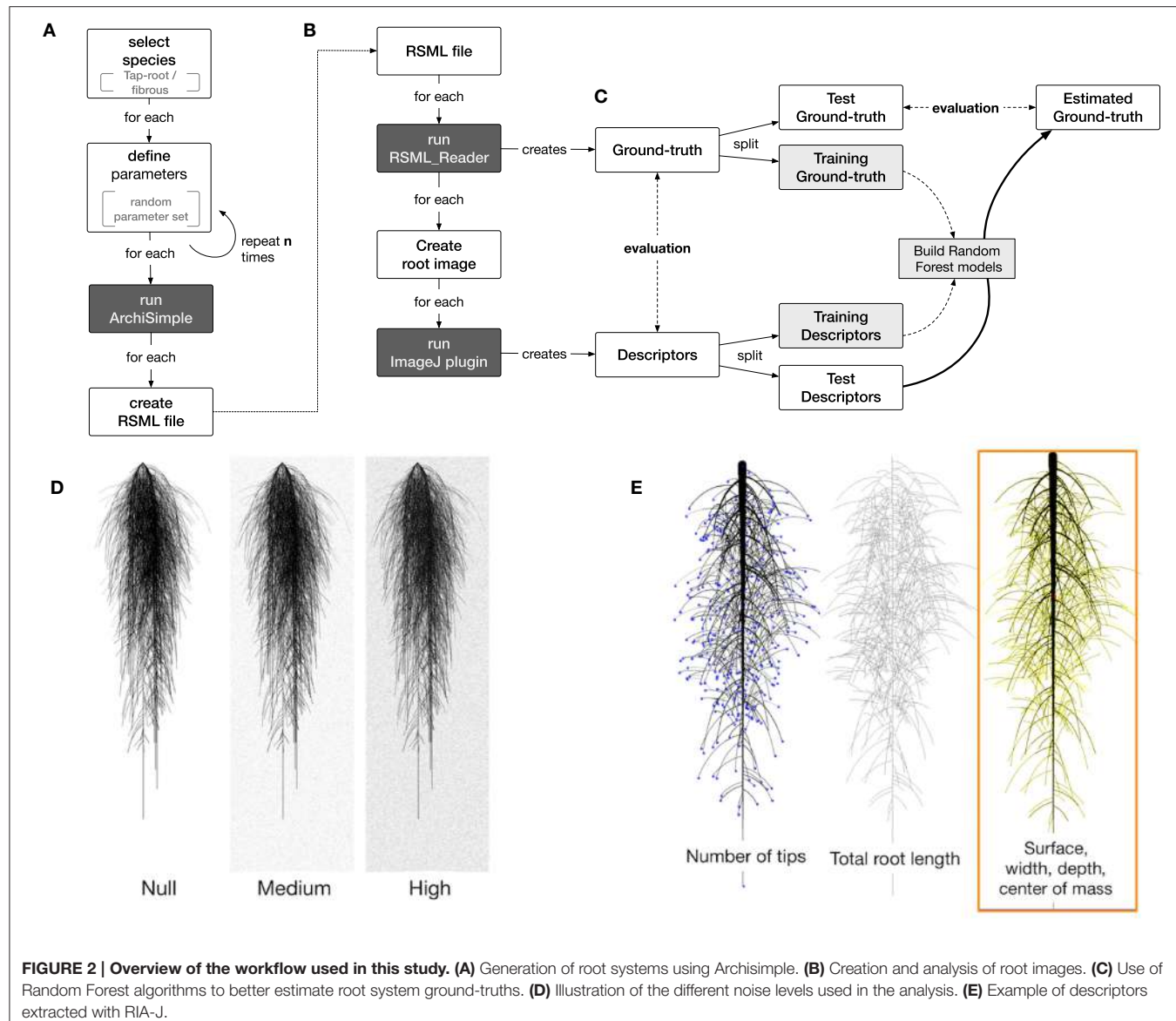


**FIGURE 2 | Overview of the workflow used in this study. (A)** Generation of root systems using Archisimple. **(B)** Creation and analysis of root images. **(C)** Use of Random Forest algorithms to better estimate root system ground-truths. **(D)** Illustration of the different noise levels used in the analysis. **(E)** Example of descriptors extracted with RIA-J.

**TABLE 2 | Root image descriptors extracted by RIA-J.**

Name	Description	Unit	Reference
<b>MORPHOLOGY</b>			
area	Projected area of the root system	mm <sup>2</sup>	Galkovskyi et al., 2012
length	Length of the skeleton of the root system image	mm	Galkovskyi et al., 2012
tip_count	Number of end branches in the root system skeleton	–	
diam_mean	Mean diameter of the root object in the image	mm	
<b>GEOMETRY</b>			
width	The maximal width of the root system	mm	–
depth	The maximal depth of the root system	mm	–
width_depth_ratio	Ratio between the width and the depth of the root system	–	Galkovskyi et al., 2012
com_x-com_y	Relative coordinates of the center of mass of the root system	–	Galkovskyi et al., 2012
convexhull	Area of the smallest convex shape encapsulating the root system	mm <sup>2</sup>	Galkovskyi et al., 2012
exploration	Ratio between the convex hull area and the projected area	–	Galkovskyi et al., 2012

consists of  $l$  decision trees  $T_{D,k}$ , where several key parameters such as the feature space, are chosen randomly (hence the word Random in the algorithm name). While using a random subspace strongly accelerates the growth of a single tree, it can also decrease its accuracy. However, the use of large number of trees counterbalance advantageously those two effects. The final prediction for each input value  $x_i$  corresponds to the majority vote of all the decision trees of the forest  $T_{D,k}(x_i)$  in a classification setting while an average of all predicted values is used in a regression task.

## Framework Description

Our method consists of three typical steps:

1. A preprocessing step, where we replace missing values of the training set.
2. A model generation step where, for each response variable, we generate different models according to two Random Forest parameters (number of trees and number of splits).
3. A model selection step, where we choose the best performing pair of parameters of the previous step for each one of the response variable.

## Preprocessing

Missing values in our dataset might arise due to highly noisy images, where the measurement of certain descriptors has been infeasible. To deal with this issue, we first replaced missing values.

This is done using the imputation function of the randomForest R package. It replaces all missing values of a response variable by the median and then a Random Forest is applied on the completed data to predict a more accurate value. We favored 10 trees for computing the new value over the default value of 300 as we found that it offered sufficiently accurate results for our application while being much faster.

## Model Generation

In the model generation step, for each of the response variables, several forests with different number of trees and different number of splits ( $t_i, m_j$ ) are tested. In practice, the training set  $D_{train}$  is divided into  $m_j$  disjunct subsets  $D_{train}^{m_j}$  and on each of those, a Random Forest  $F_{D_{train}^{m_j}}$  is trained on a growing number of  $t_i$  random trees.

## Model Selection

Given a new data point  $x$ , each model predicts a response variable  $y$  by averaging the predicted values  $F_{D_{train}}^m(x)$ , i.e.,

$$\hat{y} = M_{D_{train}}^{t,m}(x) = \frac{1}{m} \sum_{k=1}^m F_{D_{train}^k}(x)$$

Then in a final step an estimate of the root-mean-square (RMSE) generalized error on the test set  $D_{test}$  is computed, where RSME is defined as

$$RMSE = \sqrt{\sum_{i=1}^n (y_i - \bar{y}_i)^2}$$

for  $D_{test} = \{(x_1, y_1), (x_2, y_2), \dots, (x_n, y_n)\}$ .

Finally, the model with the parameter pair  $(t, m)$  having the minimal error (on the separate test set) is chosen in order to make the predictions.

## Data Availability

All data used in this paper (including the image and RSML libraries) are available at the address <http://doi.org/10.5281/zenodo.208214>

An archived version of the codes used in this paper is available at the address <http://doi.org/10.5281/zenodo.208499>

An archived version of the machine learning framework is available at the address <https://github.com/FaustFrankenstein/RandomForestFramework/releases/tag/v1.0>

## RESULTS AND DISCUSSIONS

### Production of a Large Library of Ground-Truth Root System Images

We combined existing tools into a single pipeline to produce a large library of ground-truth root system images. The pipeline combines a root model (ArchiSimple, Pages et al., 2013), the Root System Markup Language (RSML) and the RSML Reader plugin from ImageJ (Lobet et al., 2015). In short, ArchiSimple was used to create a large number of root systems, based on random input parameter sets. Each output was stored as an RSML file (**Figure 2A**), which was then used by the RSML Reader plugin to create a graphical representation of the root system (as a jpeg file) and a ground-truth dataset (**Figure 2B**). Details about the different steps are presented in the Materials and Methods section.

We used the pipeline to create a library of 10,000 root system images, separated into fibrous (multiple first order roots and no secondary growth) and tap-root systems (one first order root and secondary growth). The ranges of the different ground-truth data are shown in **Table 3** and their distribution is shown in the **Supplemental Figure 1**.

We started by evaluating whether fibrous and tap-root systems should be separated during the analysis. We performed a Principal Component Analysis on the ground-truth dataset to reduce its dimensionality and assess if the *type* grouping influenced the overall dataset structure (**Figure 3A**). Fibrous and tap-root systems formed distinct groups (MANOVA  $p < 0.001$ ), with limited overlap. The first principal component, which represented 30.9% of the variation within the dataset, was mostly influenced by the number of first-order axes. The second principal component (19.1% of the variation) was influenced, in part, by the root diameters. These two effects were consistent with the clear root system type grouping, since they expressed the main difference between the two groups of root-system *types*. Therefore, since the *type* grouping had such a strong effect on the overall structure, we decided to separate them for the following analyses.

To demonstrate the utility of a synthetic library of ground-truth root systems, we analyzed every image of the library using a custom-built root image analysis tool, RIA-J. We decided to do so since our purpose was to test the usefulness of the synthetic analysis and not to

**TABLE 3 |** Ranges of the different ground-truth data from the root systems generated using ArchiSimple.

Variable	Minimum value	Maximum value	Unit
<b>FIBROUS</b>			
tot_root_length	110	73971	mm
width	0.76	302	mm
depth	50	505	mm
n_1_order	1	20	-
tot_1_order_length	79	5409	mm
mean_1_order_length	27	470	mm
mean_1_order_diameter	0.2	0.4	mm
mean_2+_order_density	0	5	root/mm
n_2+_orders	0	4448	-
tot_2+_order_length	0	71556	mm
mean_2+_order_length	0	50	mm
mean_2+_order_diameter	0	0.3	mm
mean_2+_order_angle	0	88	°
<b>TAP ROOTED</b>			
tot_root_length	78	41870	mm
width	0.1	173	mm
depth	55	505	mm
n_1_order	1	1	-
tot_1_order_length	59	509	mm
mean_1_order_length	59	509	mm
mean_1_order_diameter	0.2	16	mm
mean_2+_order_density	0	2.3	root/mm
n_2+_orders	0	3353	-
tot_2+_order_length	0	40225	mm
mean_2+_order_length	0	51	mm
mean_2+_order_diameter	0	2.2	mm
mean_2+_order_angle	0	97	°

assess the accuracy of existing tools. Nonetheless, RIA-J was designed using known and published algorithms, often used in root system quantification. A detailed description of RIA-J can be found in the Materials and Methods section and **Supplemental File 1**.

We extracted 10 descriptors from each root system image (**Table 2**) and compared them with the ground-truth data. For each pair of descriptor-data, we performed a linear regression and computed its r-squared value. Different types of information are highlighted in **Figure 4**. First, using a ground-truth image library allows for a quick and systematic analysis of all the descriptors extracted by the image analysis pipeline. Second, it allows researchers to identify which traits can be accurately evaluated (or not) and by which descriptors. Third, for some ground-truth data, such as the mean length of second order roots or the number of first order roots, it shows that none of the classical descriptors gave a good estimation (**Figure 4**, highlighted with arrows). Finally, the figure highlights that some correlations were different for fibrous- and tap-root systems. As an example, the correlation found between the *mean\_2+\_order\_diameter* and *diam\_mean* estimators was better for fibrous roots than within the tap-root dataset. Consequently, validation of the

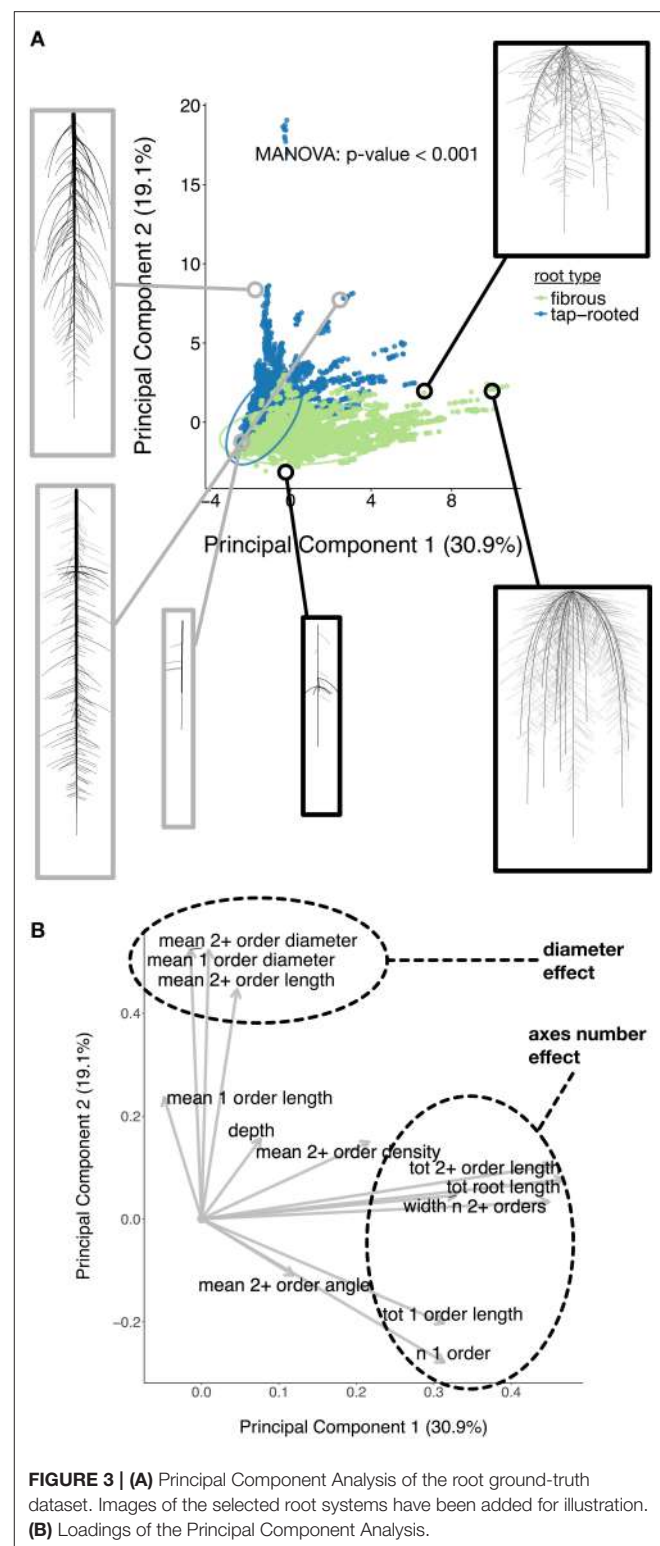


**FIGURE 3 | (A)** Principal Component Analysis of the root ground-truth dataset. Images of the selected root systems have been added for illustration. **(B)** Loadings of the Principal Component Analysis.

different image analysis algorithms should be performed, at least, for each group. An algorithm giving good results for a fibrous root system might fail when applied to tap-rooted ones.

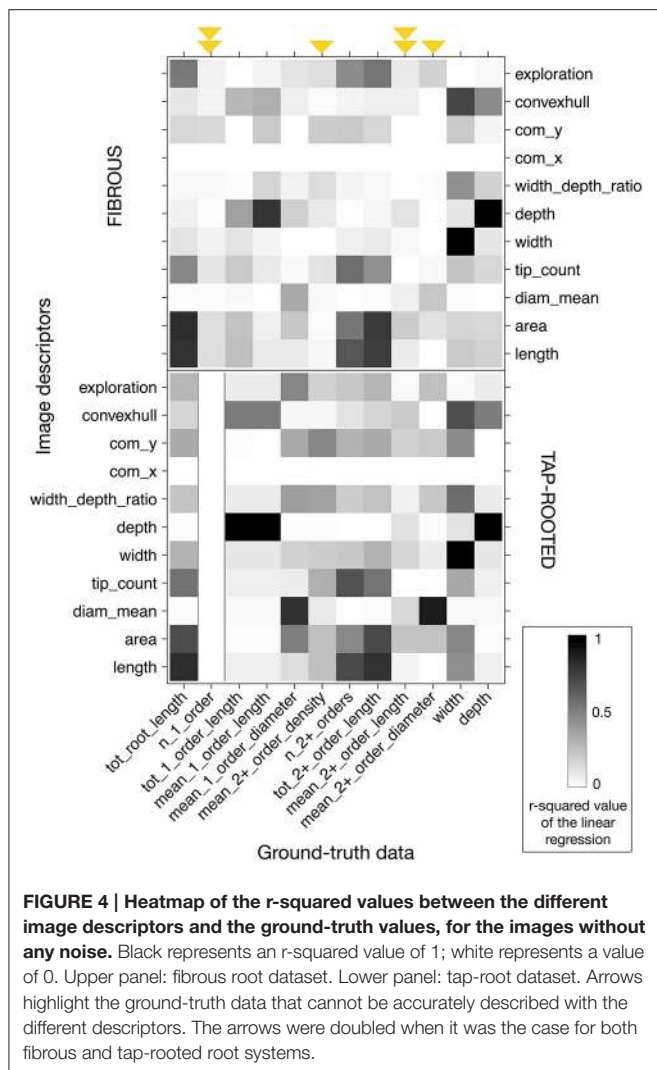


**FIGURE 4 | Heatmap of the r-squared values between the different image descriptors and the ground-truth values, for the images without any noise.** Black represents an r-squared value of 1; white represents a value of 0. Upper panel: fibrous root dataset. Lower panel: tap-root dataset. Arrows highlight the ground-truth data that cannot be accurately described with the different descriptors. The arrows were doubled when it was the case for both fibrous and tap-rooted root systems.

## Errors from Image Descriptors Are Likely to Be Non-linear across Root System Sizes and Image Qualities

In addition to being related to the species of study, estimation errors are likely to increase with the root system size. As the root system grows and develops, the number of crossing and overlapping segments increases (Figure 5A), making the subsequent image analysis potentially more difficult and prone to error. However, a systematic analysis of such error is seldom performed.

Estimation errors are also likely to increase as the image quality decreases. Here we artificially added one type of noise (random “salt and pepper” particles) to the images, with two intensity levels. It should be noted that virtually any type of image degradation could be added to the original images using custom image filters (e.g., using ImageJ). Different types of degradation are expected to generate different levels of estimation errors.

**Figure 5** shows the relationship between the ground-truth and descriptor values for three parameters: the total root length (Figure 5B), the number of roots (Figure 5C), and the root system depth (Figure 5D). For each of these variables, we quantified the Mean Relative Error (see Materials and Methods for details) as a function of the overlap index. This was done for three levels of noise added to the images (“null,” “medium,” and “high”). We can observe that for the estimation of both the total root length and the number of lateral roots, the Mean Relative Error increased with the size of the root system (Figures 5B–C). As stated above, such increase of the error was somehow expected with increasing complexity. Moreover, depending on the metric of interest, such as the number of root tips, low image quality can result in high level of error. For other traits, such as the root system depth, no errors were expected (*depth* is supposedly an error-less variable) and the Mean Relative Error was close to 0 whatever the size of the root system and image quality.

The results presented here are tightly dependent on the specific algorithms used for image analysis and hence might be different for other published tools. However, they are a call for caution when analyzing root images: unexpected errors in ground-truth estimation can arise. Our image library can be used to better identify the errors generated by other analysis tools, current or future.

## Roadmap for Root Image Analysis Tools Calibration

To improve the calibration and validation of future root image analysis tools, we propose the following procedure:

1. Develop the new root image analysis pipeline;
2. Use it to analyse the images from the synthetic root library described here;
3. Compare the results from the new analysis with the corresponding ground-truth;
4. Identify, and clearly state, the type of root systems for which the pipeline works accurately;
5. When releasing the new pipeline, inform the users about the possible errors identified.

## Using the Synthetic Library to Train Machine Learning Algorithms

The main advantage of creating a synthetic library is to generate paired datasets of image descriptors and their corresponding ground-truth values. Having information on both can, in theory, be used to either calibrate the image analysis pipeline or to identify the best descriptors for the ground-truth traits of interest. Here, we explored the second approach and used a Random Forest algorithm to find which combination of descriptors would best describe each ground-truth data (see Material and Methods for details). In short, we randomly divided the whole dataset into training (3/4) and testing subsets (1/4). The training set was used to create a Random Forest model for each ground-truth data, which was then applied to the test set. The accuracy of these new predictions was then compared to the accuracy of the direct method (single descriptors) (Figure 2C).

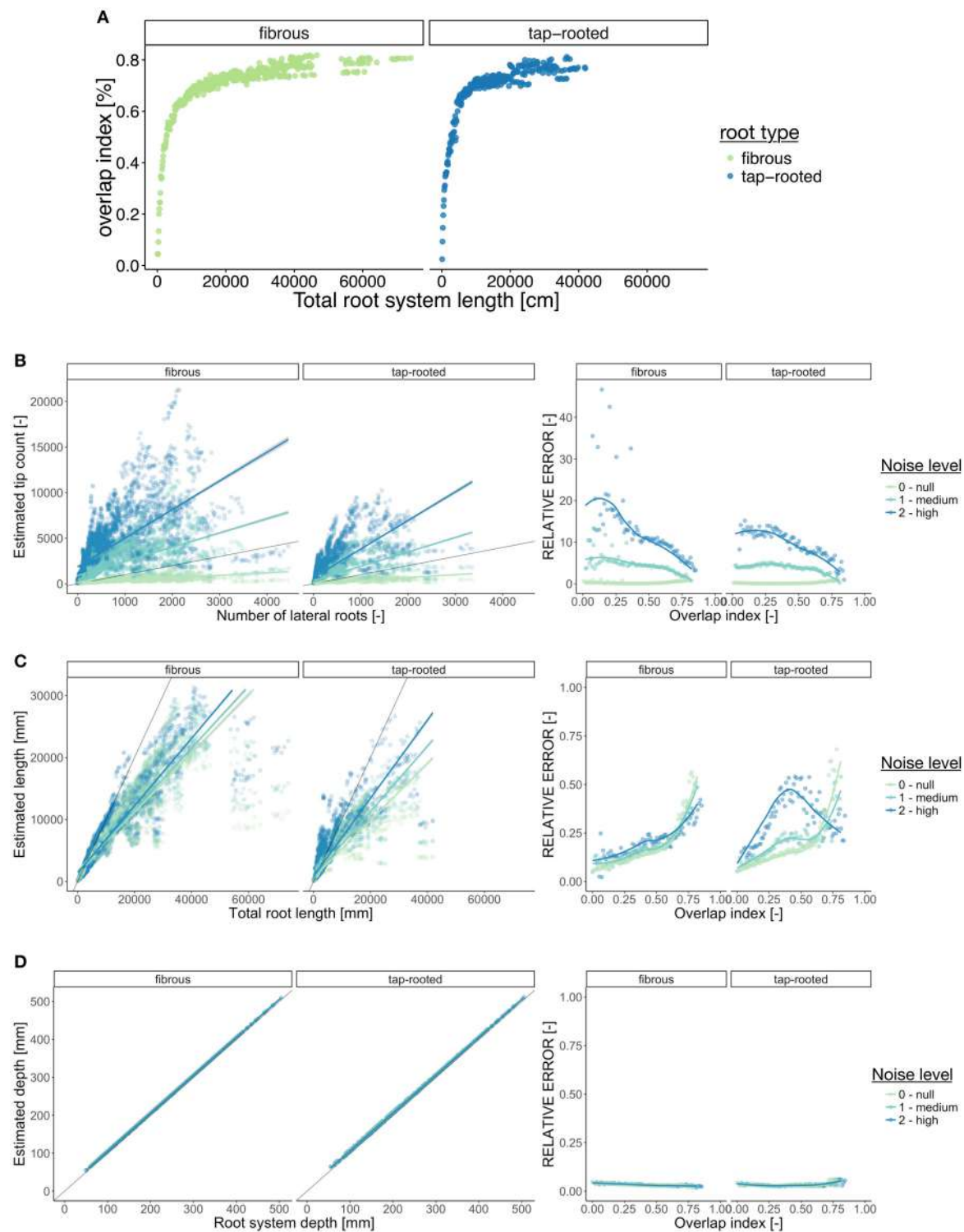


**FIGURE 5 | Error estimation for three ground-truth parameters. (A)** Evolution of the overlap index (proportion of root overlapping) with the root system size. **(B–D)** Left panel shows the relationship between the descriptors and the corresponding ground-truth variables. Right panels show the evolution of the Mean Relative Error (MRE) as a function of the overlap index. For the MRE calculations, the continuous variables were discretized in groups. **(B)** Number of lateral roots. **(C)** Total root length. **(D)** Root system depth. In the left panels, the gray line indicates the diagonal (1:1 relation).

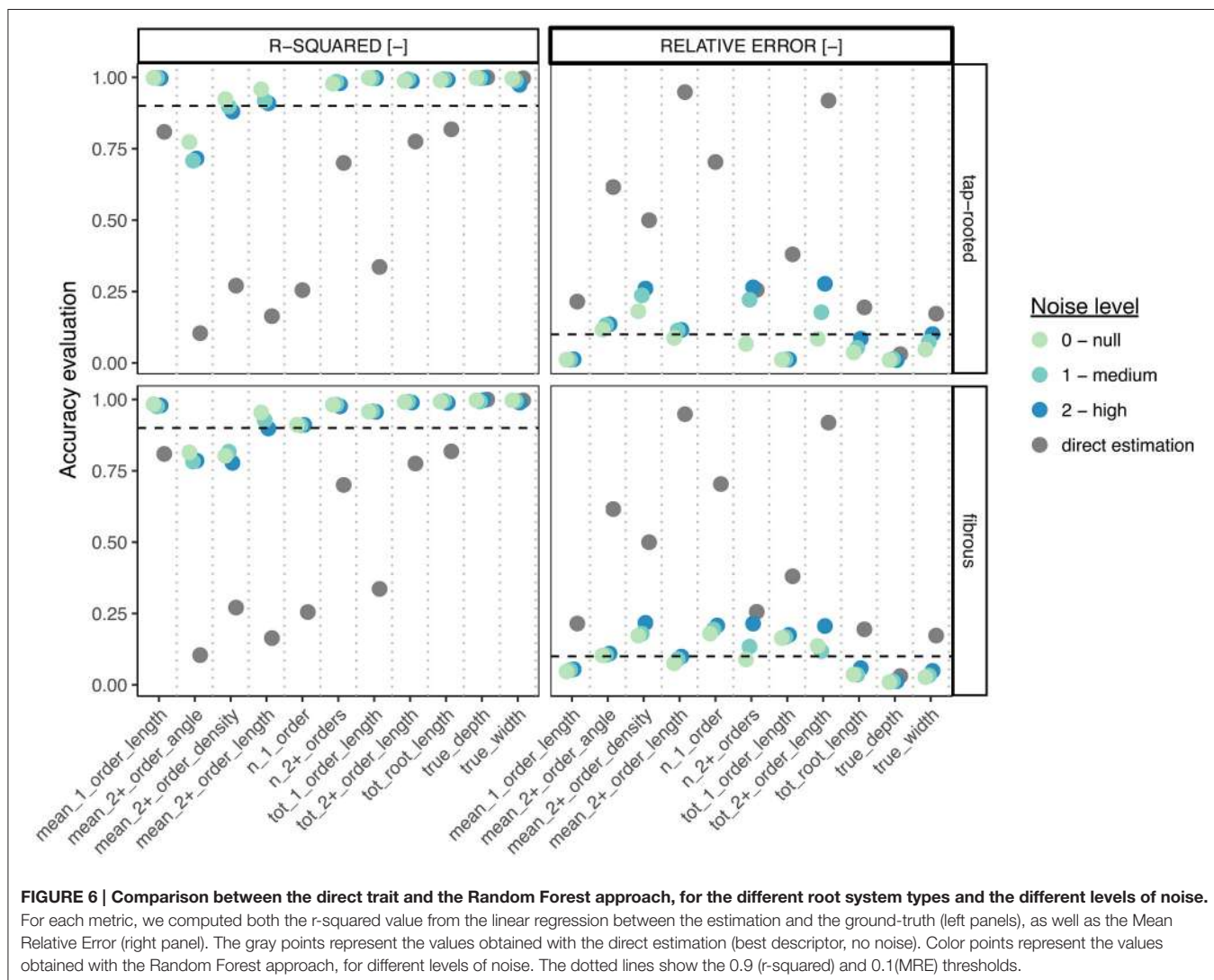
**Figure 6** shows the comparison of the accuracy (both the r-squared values from linear regressions and the Mean Relative Error, MRE) of both methods for each ground-truth data. We can clearly see that the Random Forest approach performed always better (sometimes substantially) than the direct approach, even for images with high level of noise. In addition, for most traits, the r-squared and MRE values were above 0.9 and below 0.1 respectively, which is very good, especially for such a wide range of images. In addition, the Random Forest approach allowed the correct estimation of traits that were difficult to estimate with the direct approach (such as the number of first-order axes or the mean second-order root density).

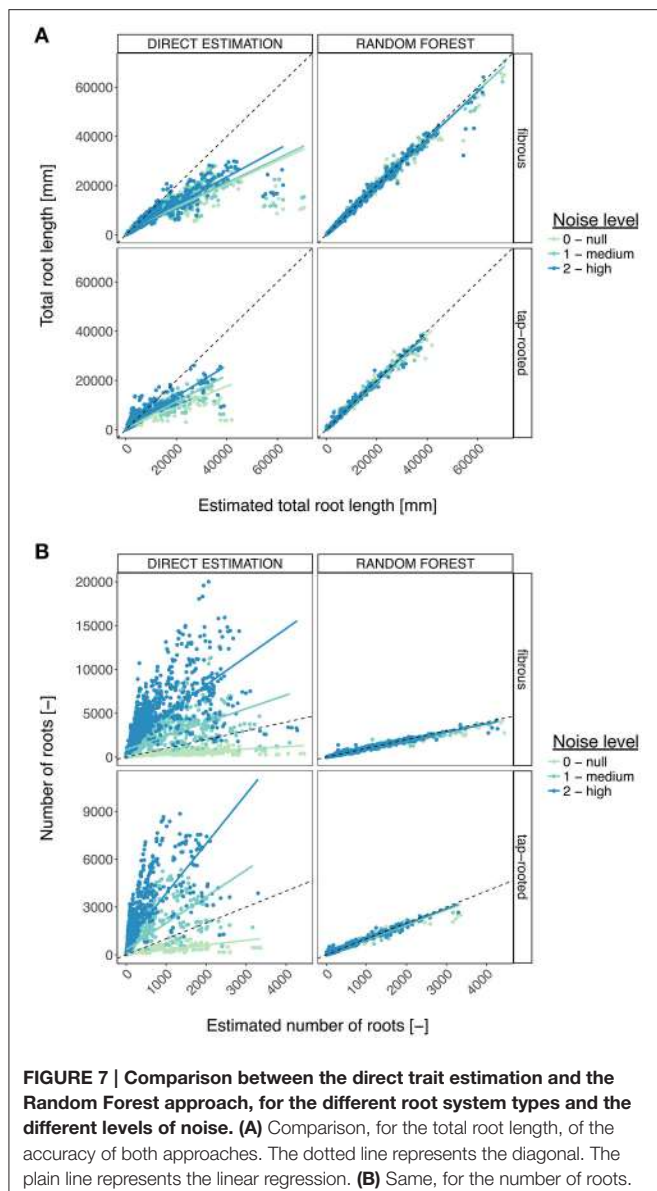
**Figure 7** shows the detailed comparison of both methods for the estimation of the total root length. Again, a clear improvement was visible with the Random Forest method, leading to small errors, even with large root systems and noisy images.

Here we presented how machine learning algorithms (Random Forest), could be used in combination with a

synthetic image library to improve the estimation of root system traits. Although both the training and test datasets used were made of synthetic images, we believe this approach presents an interesting perspective for the analysis of experimental images.

Indeed, a root architectural model can be used to build a custom library of synthetic images from a set of parameters evaluated on a small number of plants from the experimental dataset. Such library could then be used to train the machine learning model which, in turn, will enable the automatic evaluation of root traits from the remaining experimental images. Alternatively, the algorithm could be directly trained on a subset of experimental data obtained by manual or semi-automatic analyses to be then automatically applied to the rest of the dataset. One must keep in mind that the output of the machine learning strongly depends upon the quality of the dataset used for its training and hence must be analyzed carefully.





## CONCLUSIONS

The automated analysis of root system images is routinely performed in many research projects. Here we used a library of 10,000 synthetic images to estimate the accuracy and usefulness

of different image descriptors extracted with a homemade root image analysis pipeline. Our study highlighted some limitations and biases of the image analysis process.

We found that the type of root system (fibrous vs. tap-rooted), its size and complexity, as well as the quality of the images had a strong influence on the accuracy of some commonly used image descriptors and their meaning and relevance for ground-truth extraction. So far, a large proportion of the root research has been focused on seedlings with small root systems and has *de facto* avoided such errors.

However, as the research questions are likely to focus more on mature root systems in the future, these limitations will become critical. We showed that synthetic datasets can be used for calibration or modeling (machine learning) steps that allow ground-truth extraction from comparable images. We then hope that our library will be helpful for the root research community to evaluate and improve other image analysis pipelines.

## AUTHOR CONTRIBUTIONS

GL, LP, PT, IK, MN, and CP designed the study. IK developed the image analysis pipeline RIA-J. MN and PM developed the Random Forest framework. GL generated the image library and did the data analysis. LP developed the Archisimple model. All authors have participated in the writing of the manuscript.

## FUNDING

This research was funded by the Interuniversity Attraction Poles Programme initiated by the Belgian Science Policy Office, P7/29. GL and MN are grateful to the F.R.S.-FNRS for a postdoctoral research grant (1.B.237.15F) and doctoral grant (1.A.320.16F), respectively.

## SUPPLEMENTARY MATERIAL

The Supplementary Material for this article can be found online at: <http://journal.frontiersin.org/article/10.3389/fpls.2017.00447/full#supplementary-material>

**Supplemental Figure 1 | Distribution of the properties of the modeled root images.**

**Supplemental Figure 2 | Distribution of the descriptors of the modeled root images.**

**Supplemental File 1 | Definitions of the different descriptors extracted by RIA-J.**

## REFERENCES

- Armengaud, P., Zambaux, P., Hills, A., Sulpice, R., Pattison, R. J., Blatt, M. R., et al. (2009). EZ-Rhizo: integrated software for the fast and accurate measurement of root system architecture. *Plant J.* 57, 945–956. doi: 10.1111/j.1365-313X.2008.03739.x
- Benoit, L., Rousseau, D., Belin, É., Demilly, D., and Chapeau-Blondeau, F. (2014). Simulation of image acquisition in machine vision dedicated to seedling elongation to validate image processing root segmentation algorithms. *Comput. Electron. Agric.* 104, 84–92. doi: 10.1016/j.compag.2014.04.001
- Breiman, L. (1996). Bagging predictors. *Mach. Learn.* 24, 123–140. doi: 10.1007/BF00058655
- Breiman, L. (2001). Random Forests. *Mach. Learn.* 45, 5–32. doi: 10.1023/A:1010933404324
- Bucksch, A., Burridge, J., York, L. M., Das, A., Nord, E., Weitz, J. S., et al. (2014). Image-based high-throughput field phenotyping of crop roots. *Plant Physiol.* 166, 470–486. doi: 10.1104/pp.114.243519

- CRAN randomForest (2015). Available online at: <https://cran.r-project.org/web/packages/randomForest/randomForest.pdf>
- Galkovskyi, T., Mileyko, Y., Bucksch, A., Moore, B., Symonova, O., Price, C. A., et al. (2012). GiA Roots: software for the high throughput analysis of plant root system architecture. *BMC Plant Biol.* 12:116. doi: 10.1186/1471-2229-12-116
- Huynh-Thu, V. A., Wehenkel, L., and Geurts, P. (2013). *Gene Regulatory Network Inference from Systems Genetics Data Using Tree-Based Methods*. New York, NY: Springer.
- Koevoets, I. T., Venema, J. H., Elzenga, J. T., and Testerink, C. (2016). Roots withstanding their environment: exploiting root system architecture responses to abiotic stress to improve crop tolerance. *Front. Plant Sci.* 7:1335. doi: 10.3389/fpls.2016.01335
- Lobet, G., Pound, M. P., Diener, J., Pradal, C., Draye, X., Godin, C., et al. (2015). Root system markup language: toward a unified root architecture description language. *Plant Physiol.* 167, 617–627. doi: 10.1104/pp.114.253625
- Marée, R., Geurts, P., and Wehenkel, L. (2016). Towards generic image classification using tree-based learning: an extensive empirical study. *Pattern Recognit. Lett.* 74, 17–23. doi: 10.1016/j.patrec.2016.01.006
- Pagès, L., Bécel, C., Boukçim, H., Moreau, D., Nguyen, C., and Voisin, A.-S. (2013). Calibration and evaluation of ArchiSimple, a simple model of root system architecture. *Ecol. Modell.* 290, 76–84. doi: 10.1016/j.ecolmodel.2013.11.014
- Pagès, L., Jordan, M. O., and Picard, D. (1989). A simulation model of the three-dimensional architecture of the maize root system. *Plant Soil* 119, 147–154. doi: 10.1007/BF02370279
- Pagès, L., and Pellerin, S. (1996). Study of differences between vertical root maps observed in a maize crop and simulated maps obtained using a model for the three-dimensional architecture of the root system. *Plant Soil* 182, 329–337. doi: 10.1007/BF00029063
- Pagès, L., Vercambre, G., Drouet, J.-L., Lecompte, F., Collet, C., and LeBot, J. (2004). RootTyp: a generic model to depict and analyze the root system architecture. *Plant Soil* 258, 103–119. doi: 10.1023/B:PLSO.0000016540.47134.03
- Pierret, A., Gonkhamdee, S., Jourdan, C., and Maeght, J.-L. (2013). IJ-Rhizo: an open-source software to measure scanned images of root samples. *Plant Soil* 373, 531–539. doi: 10.1007/s11104-013-1795-9
- Rellán-Álvarez, R., Lobet, G., Lindner, H., Pradier, P.-L., Sebastian, J., Yee, M.-C., et al. (2015). GLO-Roots: an imaging platform enabling multidimensional characterization of soil-grown root systems. *Elife* 4:e07597. doi: 10.7554/eLife.07597
- Sarkar, D. (2008). *Lattice: Multivariate Data Visualization with R*. New York, NY: Springer.
- Wickham, H. (2009). *ggplot2*. New York, NY: Springer New York.

**Conflict of Interest Statement:** The authors declare that the research was conducted in the absence of any commercial or financial relationships that could be construed as a potential conflict of interest.

Copyright © 2017 Lobet, Koevoets, Noll, Meyer, Tocquin, Pagès and Périlleux. This is an open-access article distributed under the terms of the Creative Commons Attribution License (CC BY). The use, distribution or reproduction in other forums is permitted, provided the original author(s) or licensor are credited and that the original publication in this journal is cited, in accordance with accepted academic practice. No use, distribution or reproduction is permitted which does not comply with these terms.



# A Model Analysis of Mechanisms for Radial Microtubular Patterns at Root Hair Initiation Sites

Pawel Krupinski<sup>1\*</sup>, Behruz Bozorg<sup>1</sup>, André Larsson<sup>1</sup>, Stefano Pietra<sup>2†</sup>, Markus Grebe<sup>2,3</sup> and Henrik Jönsson<sup>1,4,5</sup>

<sup>1</sup> Computational Biology and Biological Physics, Department of Astronomy and Theoretical Physics, Lund University, Lund, Sweden, <sup>2</sup> Department of Plant Physiology, Umeå Plant Science Centre, Umeå University, Umeå, Sweden, <sup>3</sup> Institute of Biochemistry and Biology, Plant Physiology, University of Potsdam, Potsdam, Germany, <sup>4</sup> Sainsbury Laboratory, University of Cambridge, Cambridge, UK, <sup>5</sup> Department of Applied Mathematics and Theoretical Physics, University of Cambridge, Cambridge, UK

## OPEN ACCESS

### Edited by:

Alexander Bucksch,  
University of Georgia, USA

### Reviewed by:

Joakim Sundnes,  
Simula Research Laboratory, Norway  
Patompeng Saengwilai,  
Mahidol University, Thailand

### \*Correspondence:

Pawel Krupinski  
pawel.krupinski@thep.lu.se

### †Present Address:

Stefano Pietra,  
Department of Zoology, University of  
Cambridge, Cambridge, UK

### Specialty section:

This article was submitted to  
Plant Biophysics and Modeling,  
a section of the journal  
*Frontiers in Plant Science*

Received: 16 May 2016

Accepted: 04 October 2016

Published: 28 October 2016

### Citation:

Krupinski P, Bozorg B, Larsson A,  
Pietra S, Grebe M and Jönsson H  
(2016) A Model Analysis of  
Mechanisms for Radial Microtubular  
Patterns at Root Hair Initiation Sites.  
*Front. Plant Sci.* 7:1560.  
doi: 10.3389/fpls.2016.01560

Plant cells have two main modes of growth generating anisotropic structures. Diffuse growth where whole cell walls extend in specific directions, guided by anisotropically positioned cellulose fibers, and tip growth, with inhomogeneous addition of new cell wall material at the tip of the structure. Cells are known to regulate these processes via molecular signals and the cytoskeleton. Mechanical stress has been proposed to provide an input to the positioning of the cellulose fibers via cortical microtubules in diffuse growth. In particular, a stress feedback model predicts a circumferential pattern of fibers surrounding apical tissues and growing primordia, guided by the anisotropic curvature in such tissues. In contrast, during the initiation of tip growing root hairs, a star-like radial pattern has recently been observed. Here, we use detailed finite element models to analyze how a change in mechanical properties at the root hair initiation site can lead to star-like stress patterns in order to understand whether a stress-based feedback model can also explain the microtubule patterns seen during root hair initiation. We show that two independent mechanisms, individually or combined, can be sufficient to generate radial patterns. In the first, new material is added locally at the position of the root hair. In the second, increased tension in the initiation area provides a mechanism. Finally, we describe how a molecular model of Rho-of-plant (ROP) GTPases activation driven by auxin can position a patch of activated ROP protein basally along a 2D root epidermal cell plasma membrane, paving the way for models where mechanical and molecular mechanisms cooperate in the initial placement and outgrowth of root hairs.

**Keywords:** plant cell wall, finite element modeling, computational morphodynamics, root hair initiation, microtubules, cellulose fibers, composite material

## 1. INTRODUCTION

Most higher plants do not display cell migration and need to generate optimal shapes by adjusting growth both in terms of magnitude and directions. Two main modes of growth are prevailing across the plant kingdom (Baskin, 2005; Rounds and Bezanilla, 2013). The first is diffuse growth where whole cells or tissues are expanding quite homogeneously, although often anisotropically. The other mode of growth is tip growth, where expansion appears in a focused region of a cell. The growth is

dependent on environmental signals and guided by cells, genetic and hormonal interactions (Chen et al., 2016). Still, to effectuate the growth, manipulation of the stiff cell walls surrounding all cells is necessary (Cosgrove, 2005).

The plant cell wall can be seen as a complex composite material composed mainly of cellulose microfibrils, pectins and xyloglucans (Baskin, 2005; Cosgrove, 2005). Intricate connections between these wall components and their effect on the mechanical properties of the cell wall are not yet completely understood. Similarly, the way in which the plant dynamically controls composition and properties of its cell walls to form different organs to their appropriate shape is a matter of extensive research (Braybrook and Jönsson, 2016). Cortical microtubules serve as the guiding tracks for deposition of cellulose microfibrils and in consequence cells can control anisotropy of their wall stiffness (Arioli et al., 1998; McFarlane et al., 2014). This in turn relates to directionality of anisotropic growth of a tissue and influences stresses at subcellular to tissue scales (Green, 1962; Heath and Geitmann, 2000; Baskin, 2005). For tip-growing root hairs, the cellulose fibers have been shown to be randomly oriented at the very tip, while organized longitudinally away from the tip where there is also a formation of a secondary wall (Newcomb and Bonnet, 1965; Park et al., 2011; Akkerman et al., 2012). In tip growth, high rates of wall material deposition are promoting the localized growth (Geitmann et al., 2000).

Several signals regulating the dynamic orientations of the cortical microtubules have been suggested, including environmental, molecular and mechanical regulation (Hogetsu, 1986; Zandomeni and Schopfer, 1993; Hamant et al., 2008; Lindeboom et al., 2013; Chen et al., 2014, 2016), and for diverse input signals microtubule severing is an important part of the orientation process as shown by katanin mutants (Uyttewaal et al., 2012; Lindeboom et al., 2013; Chen et al., 2014; Sampathkumar et al., 2014; Sassi et al., 2014). The *Arabidopsis* hypocotyl displays a strong growth response to light. Hypocotyl microtubules were recently shown to quickly reorient from transverse to longitudinal after being exposed to blue light and this reorganization was dependent on katanin (Lindeboom et al., 2013). Treatment with the phytohormone auxin has been shown to induce changes in microtubule orientations (Zandomeni and Schopfer, 1993), which more recently has also been reported for *Arabidopsis* roots and hypocotyls (Chen et al., 2014). Again the reorientation is quick (Chen et al., 2014), but it is yet to be understood whether growth is affected in such treatments (Baskin, 2015).

For several of the suggested input cues orienting microtubules it is unclear how the input provides a directional signal. Mechanical stresses and strains could serve that purpose. Mechanical stresses in the walls have been suggested to provide a directional signal where cortical microtubules orient along the maximal principal stress direction (Hejnowicz et al., 2000), both at the tissue and at the subcellular levels in shoots, leaves and flowers in *Arabidopsis* (Hamant et al., 2008; Sampathkumar et al., 2014; Hervieux et al., 2016). Such feedback loop between stress and direction of material anisotropy has been implemented in models which have verified its ability to produce robust regulation of anisotropic growth (Bozorg et al., 2014). In

particular, such a model correctly predicts the circumferential arrangement of microtubules (and tissue scale stresses) around the sites of primordia outgrowth in the shoot apical meristem and toward the stem tissue. The question of how plant cells can sense mechanical stress remains unanswered. In principle stresses can be measured through deformation of microscopic cell wall or membrane components, but the direct confirmation of such mechanism is still lacking.

In tip growing cells, the growth is much more localized to a specific site of the cell wall. As mentioned above, the microtubules are randomly organized at the tip, and growth is rather promoted by vigorous local deposition of the new material to the site of outgrowth. At the tip there is a region of the cytosol less abundant in large organelles and with targeted secretion of wall material seen by enriched presence of secretory vesicles (Galway et al., 1997; Lovy-Wheeler et al., 2007; Rounds and Bezanilla, 2013). Pectin deposited to the tip is further de-esterified and rigidified by calcium cross-linking, promoted by high levels of calcium at the tip (Sanati Nezhad et al., 2014). In particular, the addition of wall material, and hence the cell wall thickness at the tip, is oscillating and is out of phase with growth rates, alternating thick walls with high growth rates (McKenna et al., 2009). Also actin has been shown to play a prominent role in wall elongation processes (Geitmann et al., 2000). When measuring the rigidity of pollen tubes using cellular force microscopy, the apparent reduced stiffness at the tip was attributed to the respective geometrical change (Vogler et al., 2013). Computational models of tip growth connect deformation to the addition of material, the use of anisotropic wall material, and strain-based growth (Dumais et al., 2006). In addition, the inclusion of pectin chemistry provides means to have parameter space regions determining steady and oscillatory growth in such model (Rojas et al., 2011). Moreover, models including details of osmotic pressure alterations discuss possible roles of pressure as a driving force for oscillatory tip growth (Hill et al., 2012), as suggested by experimental data (Zonia, 2010), although controversial (Winship et al., 2010).

We are particularly interested in the process of root hair initiation. A transcriptional network for root hair cell differentiation in *Arabidopsis* has been identified (Schiefelbein et al., 2009), defining alternating cell files of root hair cells (trichoblasts) and non root hair cells (atrichoblasts). The differentiation of root hair cells has been modeled, suggesting different mechanisms (Savage et al., 2008; Benítez and Alvarez Buylla, 2010; Benítez et al., 2011). While root hair initiation often fails in genetic perturbations of components of these networks, these proteins are not known to provide information on the polar position of root hair initiation sites on the lateral membrane of epidermal cells. Similarly, auxin has been suggested to identify files of root hair cells. Its supply is facilitated, at least in part, by auxin influx mediators throughout non root hair cells files (Jones et al., 2009).

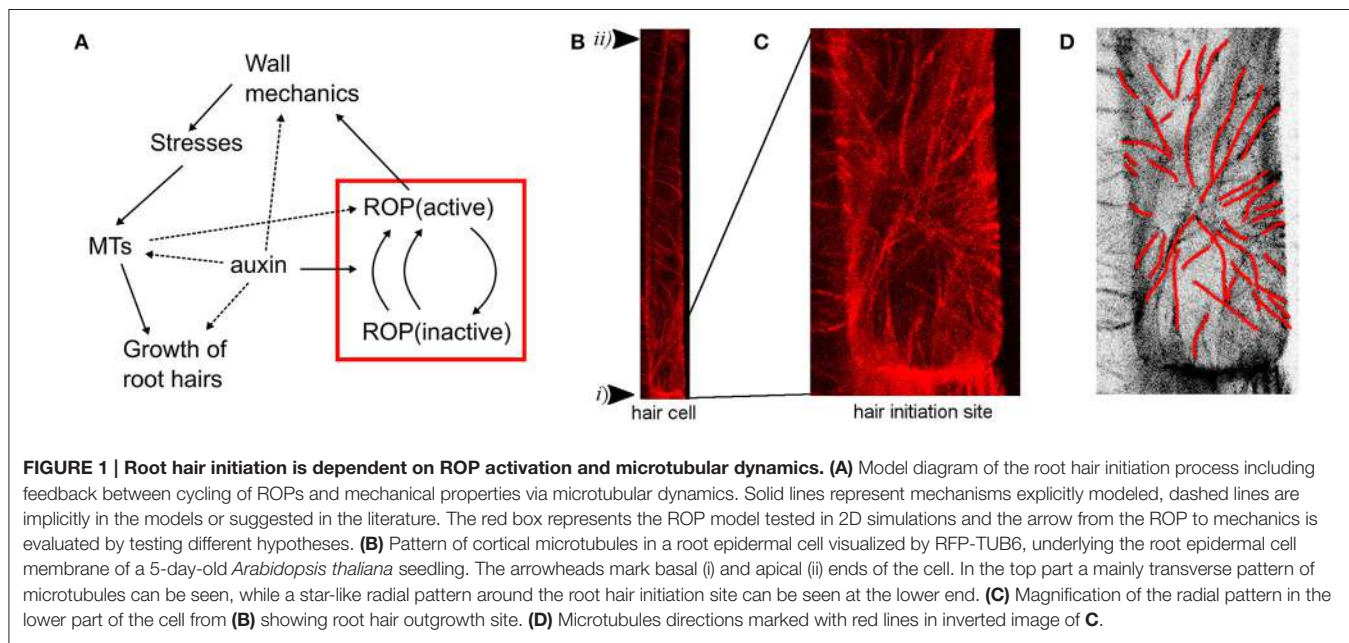
More interesting for the subcellular localization of the root hair is that an intracellular auxin gradient has been proposed to be informative in the positioning of root hairs on the lateral membrane of hair cells, close to their basal (rootward) end (Fischer et al., 2006). One of the earliest markers of the basal initiation site are the activated Rho-of-plants (ROP) GTPases

(Molendijk et al., 2001; Jones et al., 2002; Xu and Scheres, 2005; Fischer et al., 2006). The ROP localization has also been found to correlate with positioning of lobes and necks in pavement cells where ROP is activated by auxin (Xu et al., 2010). The ROP proteins are likely to be important for the correct placement and outgrowth of root hairs as suggested by dominant-interference and overexpression studies (Molendijk et al., 2001; Jones et al., 2002). The activation dynamics of ROP proteins in root hair cells has been modeled using a reaction-diffusion type of model where auxin at the subcellular level is assumed to promote activation of ROP (Payne and Grierson, 2009), similar to models of Rho GTPases generating spontaneous intracellular patterns in other organisms (Jilkine et al., 2007; Goryachev and Pokhilko, 2008). In the former, reaction-diffusion model, ROP was explicitly divided into an active and an inactive form. Active ROP was further assumed to be bound to the membrane, while the inactive form was assumed to be located in the cytosol, implemented as a lower diffusion rate of the active form of ROP compared to the inactive form of ROP. Together with a positive self-feedback of ROP-activation this was sufficient to generate peaks of activated ROPs at the root-tip oriented (basal) end of cells in a 1D model, predicting the positioning of root hair initiation in wild type as well as in selected mutants. Detailed investigations of the ROP patterning model have revealed a possibility for more complex dynamics, where ROP peaks can move transiently, and the patterning dynamics of the model have been shown to exhibit hysteresis behavior (Brena-Medina et al., 2014).

Also the actin and microtubular cytoskeleton networks are important for correct root hair formation (Bao et al., 2001; Ringli et al., 2002; Kiefer et al., 2015). When microtubules were imaged together with PIP5K3, an early root hair initiation marker (Kusano et al., 2008), microtubules were reported to orient into a radial pattern surrounding the root hair initiation site

(Pietra et al., 2013). Similar to other microtubule organizing events, this was disrupted in mutants defective in the SABRE and CLASP genes required for microtubule organization. Also, the basal positioning of root hairs as well as the polar localization of the ROP patches were perturbed in different combinations of loss-of-function mutants, indicating a regulatory role of microtubular patterning for polar ROP placement. Consistent with this view, the *procuste1/cesa6* mutant defective in a cellulose synthase subunit displays alterations in polar ROP and root hair placement (Singh et al., 2008), resembling the defects in *sabre* mutants and suggesting a requirement for both correct microtubule organization and cellulose microfibril synthesis during polar root hair initiation. In addition, ROPs have been reported to be activated by auxin and regulate microtubular patterning in pavement cells (Fu et al., 2009; Xu et al., 2010). Hence, an intricate feedback mechanism between ROPs and microtubules connecting also auxin and wall mechanics seems to be at the core of root hair initiation and growth (**Figure 1A**).

Altogether, the ROP and microtubular data indicate a complex feedback between molecular and cytoskeletal dynamics during root hair initiation, and computational modeling is essential to understand the behavior. In particular, current data raise the question if a correlation between microtubule organization and principal stress direction is sustained in the case of the root hair initiation, as has been observed before in diffuse growth (**Figure 1A**). In diffuse growth of organ formation, auxin is accumulated at the site of outgrowth, leading to the loosening of cell wall material. In effect, we observe around the outgrowth region circumferential stress orientation and corresponding microtubule pattern. Here, we extend the previously published 1D ROP model to 2D to confirm it can provide a mechanism for correct placing of an activated ROP patch along a root hair cell. We then investigate whether the previously suggested



mechanical stress feedback on microtubule directions can predict the patterns seen at root hair initiation sites by analyzing mechanical scenarios of tip growth that can produce radial stress patterns.

## 2. METHODS

### 2.1. Plant Growth and Imaging

Plant growth medium and conditions were as described (Fischer et al., 2006). Seeds were surface sterilized and stratified at 4°C for 3 days before plating on MS plates (1× MS medium, 1% sucrose, 0.8% plant agar, 1 M morpholinoethanesulfonic acid, pH 5.7). Seedlings were grown vertically at 23°C day and 18°C night under 16 h light/8 h dark photoperiod and subjected to analysis after 5 days. Confocal imaging followed (Pietra et al., 2013). Cortical microtubules were imaged in epidermal cells of seedlings expressing pUBQ1:RFP-TUB6 (Ambrose et al., 2011). Z stacks of planes at 0.53  $\mu\text{m}$  distance intersecting the periclinal face of the cell were acquired and employed to generate maximum intensity projections.

### 2.2. ROP Activation Model

We developed a ROP activation model based on a previously published model (Payne and Grierson, 2009). The model describes the ROP dynamics in 2D close to the epidermal cell membrane of a root trichoblast. The ROP activation is influenced by an auxin ( $A$ ) gradient, which in our case is produced by a source-sink model in which auxin is allowed to diffuse and is subject to a constant degradation rate. Based on the assumption of a basipetal auxin flow in the epidermis (due to reported fluxes and gradients), auxin is produced in the basal part of the cell, representing auxin influx, and degraded at the apical side of the cell, representing auxin outflux. The auxin dynamics are described by

$$\frac{dA}{dt} = D_a \Delta A + t + s_{in} - s_{out}A - qA \quad (1)$$

where  $s_{in}$  is the auxin production at the source and  $s_{out}$  is the auxin degradation at the sink. Further,  $q$  is the auxin degradation rate,  $D_a$  is the rate of auxin diffusion and  $t$  is a general auxin production. For the simulation with an auxin gradient, the parameter  $t$  is set to zero (Table 1). In the simulations with constant auxin levels, all parameters are zero except for the general production rate  $t$  and the degradation rate  $q$ . The ROPs can be in an “inactive” form ( $R_i$ ) moving in the cytosol, or in an “activated” form ( $R_a$ ) where they sit in the membrane less prone to move. In addition to a constant activation of the ROPs with rate  $k_1$  and an inactivation with rate  $c$  there is also an auxin-dependent activation with the rate  $k_2$  that depends also on the active ROP concentration, creating a positive feedback. The full ROP dynamics are described by

$$\frac{dR_a}{dt} = \begin{cases} D_1 \Delta R_a + a + R_i \cdot (k_1 + k_2 R_a^2 A) - cR_a - (r + p)R_a & \text{if boundary} \\ D_1 \Delta R_a + a + R_i \cdot (k_1 + k_2 R_a^2 A) - cR_a - rR_a & \text{otherwise} \end{cases} \quad (2)$$

**TABLE 1 | Model parameters for the ROP activation model.**

Symbol	Value	Description	Figures
$D_a$	5.0 length <sup>2</sup> /s	Diffusion rate of auxin	<b>Figure 2A</b>
$t$	0 conc/s	Production of auxin throughout the cell	<b>Figure 2A</b>
$t$	0.11 conc/s	Production of auxin throughout the cell	<b>Figure 2B</b>
$t$	0.12 conc/s	Production of auxin throughout the cell	<b>Figure 2C</b>
$t$	0.13 conc/s	Production of auxin throughout the cell	<b>Figure 2D</b>
$s_{in}$	0.25 conc/s	Auxin source production rate	<b>Figure 2A</b>
$s_{out}$	0.31/s	Auxin sink degradation rate	<b>Figure 2A</b>
$q$	$2.0 \cdot 10^{-5}$ 1/s	Degradation rate of auxin	<b>Figure 2A</b>
$q$	0.1 1/s	Degradation rate of auxin	<b>Figures 2B–D</b>
$D_1$	0.01 length <sup>2</sup> /s	Diffusion rate of active ROP	<b>Figures 2A–D</b>
$a$	0 conc/s	Production rate of active ROP	<b>Figures 2A–D</b>
$r$	0.01 1/s	Degradation rate of active ROP	<b>Figures 2A–D</b>
$p$	0.01 1/s	Rate of boundary degradation of active ROP	<b>Figures 2A–D</b>
$k_1$	0.01 1/s	Rate of constant ROP activation	<b>Figures 2A–D</b>
$k_2$	0.015 1/(conc <sup>3</sup> s)	Rate of auxin-dependent ROP-autoactivation	<b>Figures 2A–D</b>
$c$	0.1 1/s	Rate of constant ROP inactivation	<b>Figures 2A–D</b>
$D_2$	1.0 length <sup>2</sup> /s	Diffusion rate of inactive ROP	<b>Figures 2A–D</b>
$b$	0.01 conc/s	Production rate of inactive ROP	<b>Figures 2A–D</b>
$e$	0 1/s	Degradation rate of inactive ROP	<b>Figures 2A–D</b>

For the simulations with constant auxin gradient in Figures 2B–D, the parameters  $D_a, s_{in}, s_{out}$  are all set to zero.

$$\frac{dR_i}{dt} = D_2 \Delta R_i + b - eR_i - R_i \cdot (k_1 + k_2 R_a^2 A) + cR_a \quad (3)$$

where  $D_1$  and  $D_2$  are the diffusion rates of active and inactive ROP, respectively.  $a$  is the production rate of active ROP,  $b$  the production rate of inactive ROP while  $r$  is the degradation rate of active ROP and  $e$  is the degradation rate of inactive ROP. Further, we have also included a degradation of active ROPs at the cell boundary (compartments that have the background as a neighbor) with a rate  $p$ , corresponding to active ROPs diffusing to the anticlinal sides or out of the cell. We assume that ROP is only produced in its inactive form and only degraded in its active form (Table 1). Transport between compartments is assumed to be proportional to the difference in concentrations, with spatial factors being included in the diffusion constant. The auxin simulation was run first, and the resulting auxin gradient was used in the ROP simulation. Both simulations were run until the system was in equilibrium. We discretized the 2D surface into 286 polygonal compartments, and spatial factors are added to the transport rates given the different sizes of the compartments and their neighbor cross sections. All simulations use a 4th order Runge-Kutta solver and were implemented in an in-house developed open source software (<http://dev.thep.lu.se/organism>), available upon request. Files defining the models, the initial configuration,

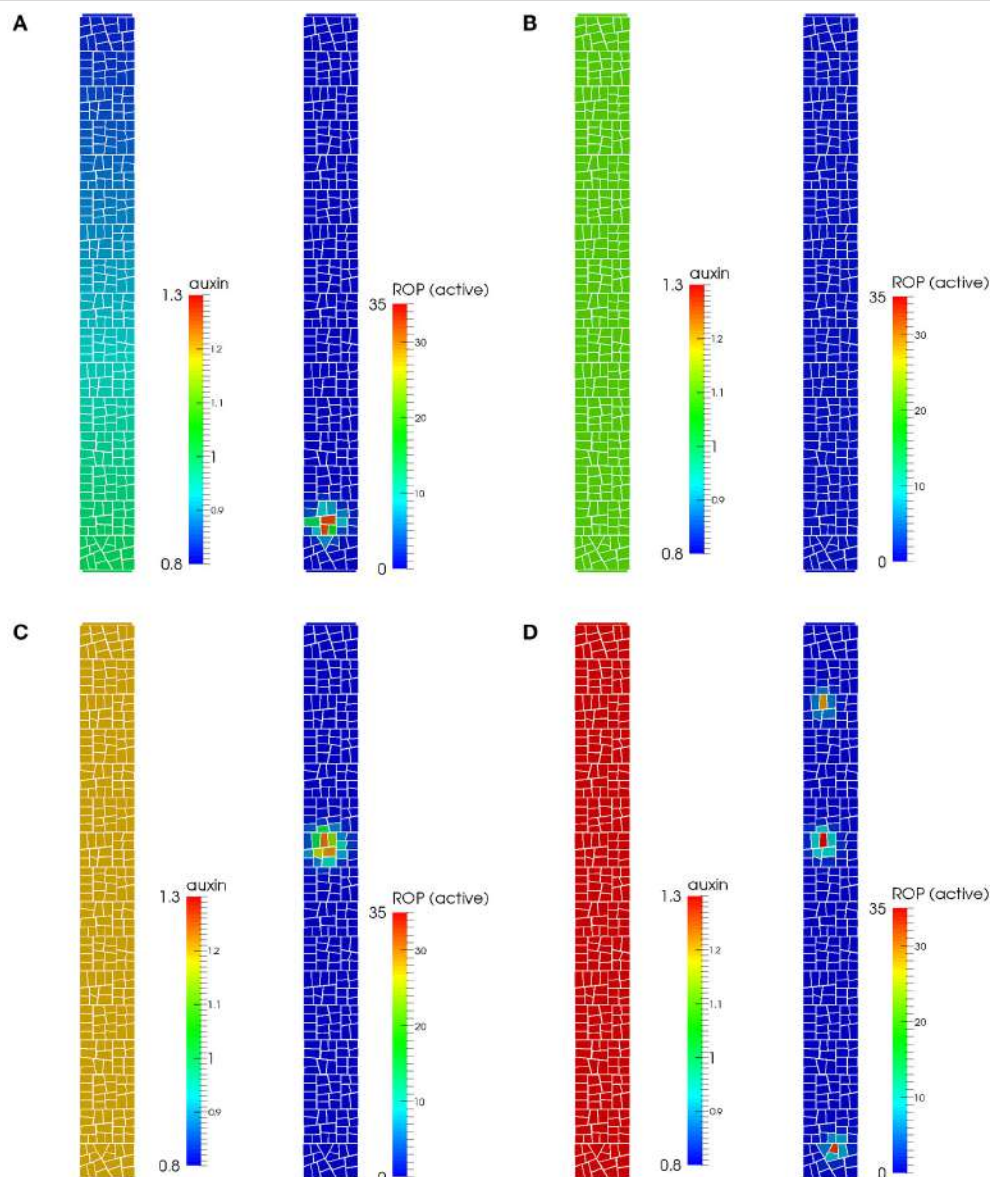


**FIGURE 2 | Auxin gradient and pattern of active ROP in a model of auxin-driven ROP-activation.** **(A)** When an auxin gradient is present, active ROPs can localize centrally toward the basal end along the outer membrane of the epidermal cell, similar to the experimentally observed pattern. **(B)** A low activation of ROPs is seen for a constant auxin level of 1.1, with no clear peaks of active ROP forming. **(C)** For a constant auxin level of 1.2, the active ROP peak localizes closer to a middle position along the cells apical-basal axis. **(D)** For a constant auxin level of 1.3, several ROP peaks appear throughout the cell.

and the solver parameters are provided as Supplementary Information.

### 2.3. Mechanical Simulations and Material Model

The model treats the epidermal wall of a root cell as a thin shell under turgor pressure. We want to focus on the site of root hair outgrowth and analyze the trends in the stress pattern around the root hair outgrowth site under different hypotheses. Thus, the model consists of a square patch of dimensions  $20 \times 20 \mu\text{m}$  and thickness of  $0.5 \mu\text{m}$ . The boundaries of the patch

were fixed in place and the patch was under pressure load perpendicular to its surface at all times. We used finite element models for all mechanical simulations using linear quadrilateral (S4R) and triangular (S3) shell elements in Abaqus (Dassault Systemes, 2012). We employed general static analysis with adaptive stabilization and included nonlinear geometric effects.

The finite element method is based on linearization of the virtual work,  $\delta W$ , equation

$$\delta W = \int_V \mathbf{S} : \delta \dot{\mathbf{E}} dV - \int_V \mathbf{f}_0 \cdot \delta \mathbf{v} dV - \int_{\partial V} \mathbf{t}_0 \cdot \delta \mathbf{v} dA = 0, \quad (4)$$

where  $S$  is a second Piola-Kirchhoff stress tensor and  $\dot{E}$  is the rate of change of its work conjugate Green-Lagrange strain tensor. The two last terms of Equation (4) contribute to the external virtual work component and  $f_0$  and  $t_0$  represent body force per undeformed unit volume and traction per undeformed unit area, respectively. For hyperelastic materials second Piola-Kirchhoff stress tensor can be calculated from strain energy function  $U$  as a derivative with respect to Green-Lagrange strain tensor

$$S = \frac{\partial U}{\partial E}. \quad (5)$$

In Saint Venant-Kirchhoff model strain energy function takes the form

$$U = \frac{1}{2}\lambda(\text{tr}E)^2 + \mu E : E, \quad (6)$$

where  $\lambda$  and  $\mu$  are Lamé coefficients related to Young's modulus  $E_Y$  and Poisson ratio  $\nu$  by formulas

$$E_Y = \frac{\mu}{\lambda + \mu}(2\mu + 3\lambda), \quad (7)$$

$$\nu = \frac{\lambda}{2(\lambda + \mu)}. \quad (8)$$

We applied standard isotropic elastic material in Abaqus with elastic modulus of 100 MPa. In softened regions we used Young's modulus of 70 MPa and in stiffened regions 130 MPa. We assumed turgor pressure of 0.2 MPa and increased turgor pressure in central region of 0.4 MPa. In all cases we used Poisson ratio of 0.2. The experimental estimates of plant cell wall elasticity from *in vivo* samples (Suslov et al., 2009; Hayot et al., 2012; Nezhad et al., 2013) and synthetic bio-composites (Chanliaud et al., 2002) cover the large range 100 kPa to 1 GPa depending on the type of plant tissue and measurement method. Similarly the turgor pressure measurements can vary from 2 to 10 atm. For simulations we have chosen elastic modulus in the middle of this range. The turgor pressure was chosen such that the wall deformation is macroscopic but not exaggerated and turned out to be on a lower side of the experimental range. We took into account the influence of the atmospheric pressure so the load pressure in the simulation is a turgor lowered by 1 atm.

The Saint Venant-Kirchhoff material model is in principle a simplistic model of a real plant wall material in the sense that it does not reflect its complicated nonlinear visco-elastic and plastic properties. However, in this case we are interested rather in general stress pattern changes than in the accurate description of deformations and thus the linear material model presents a simple alternative with a well understood notion of elastic modulus.

### 3. RESULTS

The results reported in this communication present two connected mechanisms concerning root hair outgrowth. Firstly we consider the process by which the site of the root hair outgrowth can be specified within a cell, by the localization of activated ROP into a small patch. Secondly we examine if the

initiation of root hair growth can be explained by mechanical perturbations in such a patch. We consider several scenarios and analyze the emerging pattern of stresses in comparison with experimentally observed microtubule organization.

### 3.1. An Auxin-Driven ROP-Activation Model Can Guide the Activated Membrane-Localized ROP Into A Basally Localized Patch in the 2D Epidermal Outer Cell Membrane

We developed a 2D single cell model where the cycling of ROP from an inactive to an active form is influenced by an auxin gradient (Methods, Red box in **Figure 1A**). The model is an extension of a previously published 1D model of ROP cycling (Payne and Grierson, 2009). We discretize the cell into several compartments between which the ROPs are allowed to diffuse, assuming a faster movement of inactive ROPs, which reside in the cytosol, compared to the active ROPs which are connected to the membrane. In contrast to the model which it is based on, we have explicitly modeled the auxin gradient as resulting from diffusion of the auxin molecule with a source of auxin production at the basal end of the cell and an auxin sink, where auxin is degraded, at the apical end. We assume that ROPs are created in their inactive form and subsequently activated by auxin to become the active membrane-bound form. Further, the active form of ROP is subject to constant degradation. Also included in the model is a non-linear self-activation of ROP. All reactions follow simple mass action and diffusion descriptions (Equations 1–3).

First we tested whether such a molecular model is able to create a peak of active ROP, marking the site of root hair outgrowth, at the correct location in the epidermal cell membrane. We expect the peak to locate close to the basal end of the lateral membrane, even when considering a full 2D description of this membrane. Indeed, a patch of active ROP localizes at the basal end of the lateral membrane (**Figure 2A**), slightly away from the cell wall, consistent with previous experimental findings (Molendijk et al., 2001; Jones et al., 2002; Fischer et al., 2006). The patch first appears near the cell boundary where the level of auxin is predicted to be highest, after which it moves a small distance away from the cell boundary where it becomes stable. To confirm the importance of the auxin gradient for the localization of the peak, we simulated the model with constant auxin in the cell (**Figures 2B–D**). The basal bias for the ROP patch is lost, and depending on the auxin level, a single central peak, several peaks spread across the cell, or a low activation of ROP throughout the cell was found. Interestingly, phenotypes as multiple hairs, more apical root hair positions and loss of root hairs have been found in mutants suggested to alter intracellular auxin levels and/or gradients (Masucci and Schiefelbein, 1994; Grebe et al., 2002; Fischer et al., 2006; Ikeda et al., 2009). The model parameters of the simulation with a gradient were set such that they generate a gradient of about 20%, showing that the gradient does not need to be steep to generate enough bias for the ROP dynamics. While the intracellular gradient has yet to be measured in

experiments, the gradient is well within ranges suggested in tissue models of auxin in the root (Swarup et al., 2005; Jones et al., 2009).

Our model confirms, in a 2D setting, that a sub-cellular auxin-independent activation of ROPs promoted by an intracellular auxin gradient together with intracellular transport is sufficient to create convergence of active ROPs, placing the site of root hair formation to the center close to the basal end of the outer epidermal cell plasma membrane. The active ROP is an early marker of root hair initiation and we will use this to investigate how such a patch may influence mechanical properties of the cell wall such that a root hair can be initiated, and whether this can lead to a star-like pattern of stresses.

### 3.2. Altering Mechanical Stiffness Locally at the Root Hair Initiation Site Can Guide Stresses from Circumferential to Radial

The mechanical aspects of root hair growth are analyzed by means of a finite element model of the epidermal wall of a rectangular cell and from changing material properties in a small region representing an activated ROP patch.

A simulation of rectangular epidermal wall under turgor pressure results in a stress pattern in which the first principal stress component is mostly oriented perpendicularly to the long axis of the cell (**Figure 3A**). This pattern correlates well with the orientation of microtubules observed in close to rectangular epidermal cells of the *Arabidopsis* root (**Figure 1B**, Pietra et al., 2013). Note that this result pertains to the cell scale stresses and is independent of the root tissue curvature where a pressurized cylindrical root shape would also produce highest stresses in the circumferential direction, e.g., Bozorg et al. (2014). Hence, the simulation suggests that cellular stresses can complement tissue scale stresses to provide a directional cue for microtubules in roots and other elongated tissues with elongated cells. Note that there are deviations in the general stress patterns in the proximity of basal and apical ends of the outer wall of the root hair cell (**Figure 3A**). Such a pattern could provide a mechanical bias for root hair initiation, but the effect can be dependent on the specific choice of material model.

More intriguingly, in experiments deviation from this pattern of microtubule orientation appears at the site of subsequent root hair outgrowth, where a star-like pattern around the initiation point can be observed (**Figures 1C,D**, Pietra et al., 2013). We extended the model to analyze whether mechanical perturbations in a localized patch can reconcile the experimental observations of microtubule organization with stress patterns surrounding the patch. We localize the site of the root hair outgrowth to a circular region, which can have different mechanical properties. We assume that the outer edges of the cell are fixed in space and the loading forces arise from turgor pressure. We have previously shown that an assumption of local loosening of the pressurized cell wall(s) leads to a circumferential pattern of tissue scale stresses surrounding the loosened region (Hamant et al., 2008). A similar principle applies for the simulation of local loosening of a root epidermal cell wall (**Figure 3B**), which shows circumferential maximal principal stress around

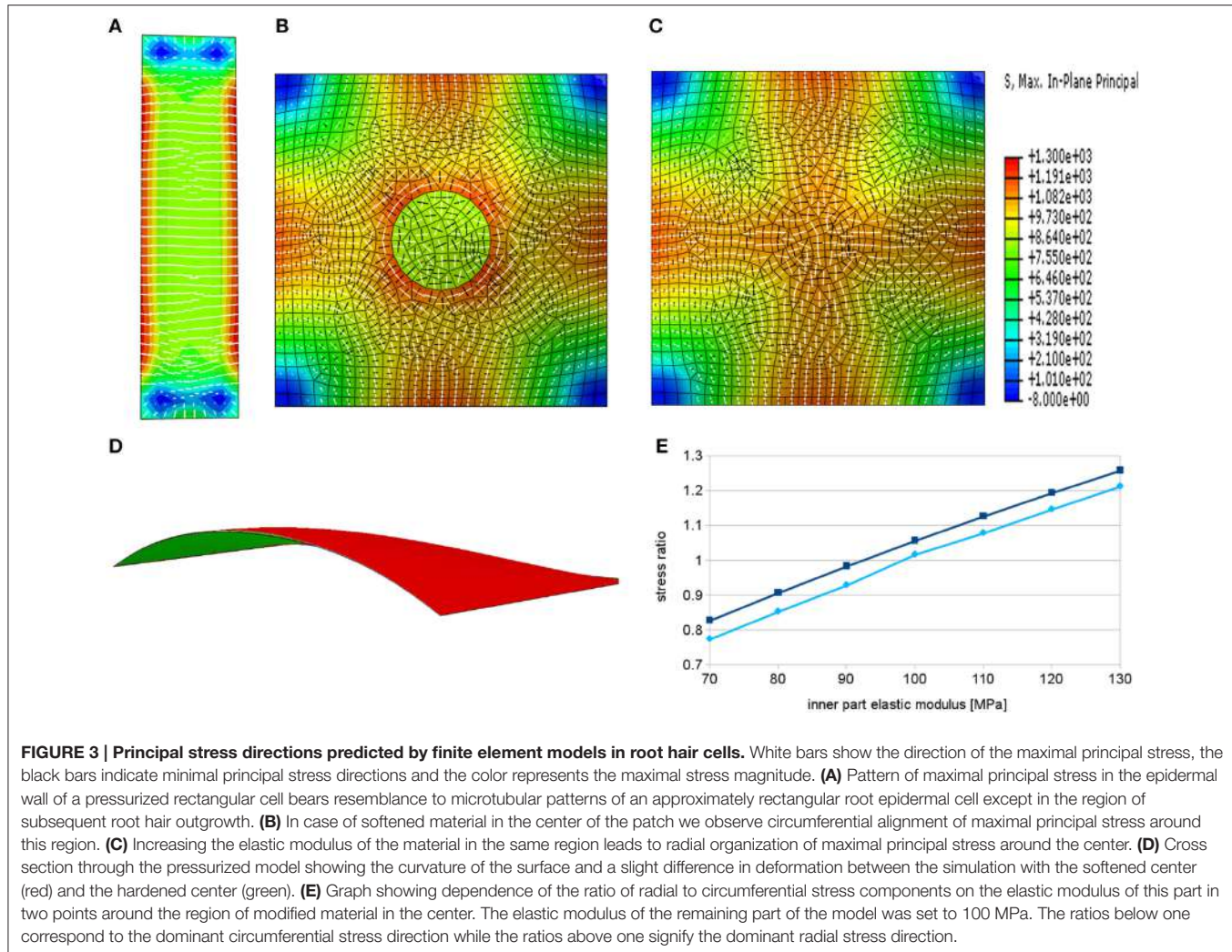
the loosened region. Such loosening is suggested to be a prerequisite, for example, for the diffuse growth in plant meristems and it is supposed to be a result of breaking the bonds that link the cellulose fibers or of processes that affect the pectin matrix (Cosgrove, 2005; Braybrook and Jönsson, 2016).

In tip growing cells rapid deposition of new wall material and complex pectin chemistry may alter mechanical properties at the tip (Bosch, 2005; Pang et al., 2010; Rounds and Bezanilla, 2013). We hypothesize that such rapid deposition of new material and reorganization of cell wall components can, at least temporarily, lead to local stiffening of the cell wall. Indeed, under the assumption of local stiffening of the material we obtain a radial pattern of maximal stress in the surrounding region (**Figures 3C,E**), which is matching the microtubule pattern seen *in vivo* (**Figure 1C**, Pietra et al., 2013). This simulation suggests a phase of local stiffening, by addition of more wall material or by changes to the wall properties, preceding the localized growth phase of the root hair. Interestingly, such suggestion is in parallel with observations of changes in thickness of the cell wall in pollen tube tips, which show oscillatory behavior and thickening prior to the growth phase (McKenna et al., 2009). It is worth to point out that the opposing hypotheses about the change of material stiffness at the outgrowth site would produce different types of elastic deformation. In case of softening of the material, we would expect bulging out of the surface of the tip and in case of hardening of the material, we should observe flattening of the surface. This effect could be small and transient, as it can be overshadowed by the rapid growth process, and thus hard to observe experimentally, but potentially it could be used to discern between the two cases (**Figure 3D**).

We explored the idea that the quick addition of material connected to root hair initiation might, at least transiently, lead to stiffer walls at the initiation site, and our model predicted radial stresses surrounding such a region. In such scenario stresses correlate with the star-like microtubule patterns seen in root hair cells before root hairs grow out.

### 3.3. Heterogeneous Forces Can Generate Radial Stress Patterns Surrounding a Root Hair Initiation Site

Another mechanism that may contribute to tip growth is a differential pressure model (Winship et al., 2010; Zonia, 2010), possibly driven by strong cytosolic streaming together with heterogeneous cytoskeletal crowding. While a pressure difference within a root epidermal cell might be hard to envision, a heterogeneous force distribution at the wall might still be possible, where for example the cytoskeleton could exert forces on the site of outgrowth leading to increased loading of this region. Application of increased outward forces in a patch can lead to radial stresses around the outgrowth site in simulations (**Figure 4A**). We increase loading forces by increasing pressure in the small region in the simulations up to 200% of the pressure value in the remaining part of the cell. This large pressure difference that is required to change the main principal stress



pattern to radial around the outgrowth site (**Figure 4D**) might be hard to justify biologically by just cytosolic streaming and makes this hypothesis questionable.

Next we test a combination of the previously analyzed mechanisms of local material or loading force changes during root hair initiation. Strikingly, locally increased forces at the site of outgrowth can lead to radial stress pattern even in the case of elastically softened material in the outgrowth region (**Figure 4B**, cf. **Figure 3B**). This however depends on the relation between the difference in Young's modulus and pressure in both regions in such a way that there exists a threshold where radial stress pattern occurs. This possibility of combining local material softening with locally increased forces at a tip growth site allows for a mechanism in which the structure of the cell wall changes, allowing greater wall extensibility similarly to the scenario suggested for diffuse wall growth and, at the same time, local forces exerted by the cytoskeleton contribute to tip growth.

Finally, if locally increased forces and local material stiffening are combined, a slightly stronger (more anisotropic) radial stress pattern results (**Figure 4C**). This scenario can be of interest since

there is the possibility that cytoskeleton reorganization during tip growth itself leads to local stiffening of the cell wall material.

In summary, the finite element model predicts that radial stress patterns are possible surrounding a small region where increased forces are applied. This can be realized independently of any heterogeneous or anisotropic material properties in such a region.

## 4. DISCUSSION

The importance of growth for morphogenesis in plants has led to a large interest in how cortical microtubules organize into patterns regulating cellulose deposition and subsequent growth. The classic model is that the microtubules organize like hoops around a barrel to generate anisotropic growth (Green, 1962).

Our study was inspired by the strikingly different pattern of microtubules seen at the initiation of root hairs, where a radial pattern is found around the initiation site (**Figure 1**, Pietra et al., 2013). Importantly, we acknowledge that the root hair initiation process involves a complex combination of molecular

and mechanical patterning (**Figure 1A**). Hence, our first aim was to investigate a mechanism for marking the site of the root hair outgrowth in a molecular 2D model based on a previous 1D effort (Payne and Grierson, 2009). An early marker for the site where a root hair is initiated is a peak of active ROP protein (Jones et al., 2002). Our simulations demonstrate that an internal auxin gradient promoting ROP activation together with self-activating feedback is sufficient to correctly place the peak centrally at the basal side of the lateral membrane (**Figure 2A**).

We then investigated how a localized change in mechanical properties affects stresses surrounding this region, in particular if a radial star-like pattern of microtubules (**Figure 1C**, Pietra et al., 2013) can be predicted by stress patterns. This appeared plausible since it has previously been reported that microtubular patterns correlate with maximal stress directions at subcellular and at

tissue scales (Hamant et al., 2008; Sampathkumar et al., 2014). For example, the outgrowth of primordia at the shoot apical meristem leads to a circumferential pattern of microtubules and the intracellular patterns of stresses can be used to predict microtubular patterns in the complex shapes of leaf epidermal pavement cells (Sampathkumar et al., 2014). Of course this correlation does not mean that the microtubules organize according to stress patterns in all cases and systems. It is possible and likely that other mechanisms not involving mechanical inputs are involved in microtubule organization. Here we analyze which mechanical conditions have to be realized to explain the available microtubule data on the basis of a microtubule-stress alignment hypothesis.

We presented two different scenarios that could lead to a radial pattern of stresses during tip growth, reconciling the

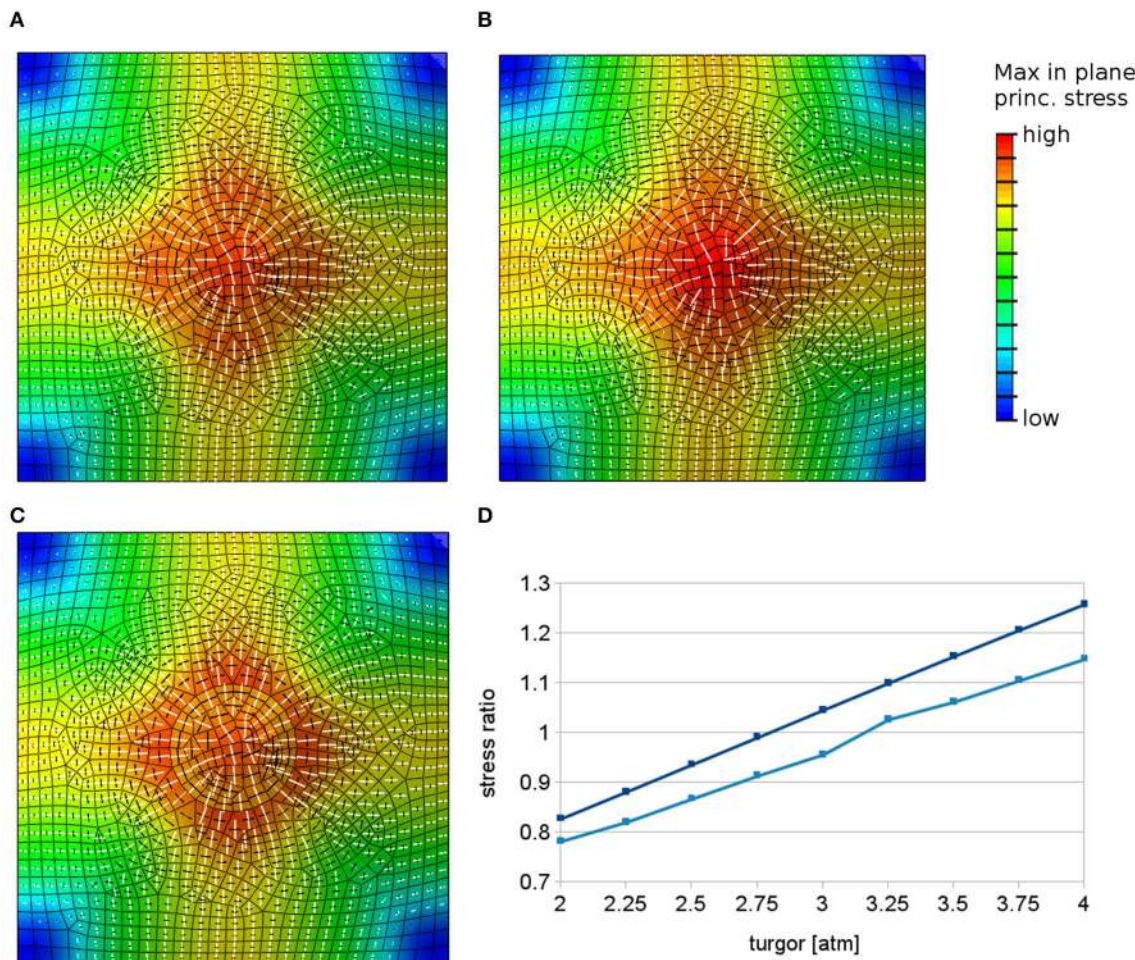


**FIGURE 4 | Simulations with heterogeneous loading forces.** White and black bars show respectively maximal and minimal principal stress directions in finite element models when loading forces are locally increased in the region of predicted root hair outgrowth. The color represents the maximal stress magnitude. **(A)** Principal stress directions predicted by finite element models in the case of locally increased pressure in the center when material properties are kept constant. **(B)** The radial pattern can appear also when the material in the patch is made elastically softer. **(C)** The mechanisms yielding radial stress alignment can be combined without destruction of the radial stress pattern. The image presents a combination of elastically stronger center with locally increased forces. The radial pattern of maximal principal stress is still evident. **(D)** Graph showing the trend of the stress anisotropy vs. the inner region pressure value measured at two different points on the boundary of the circular region, where the pressure is increased and the material is made softer with respect to the rest of the surface. The principal stresses change from circumferential (values below 1) to radial (values above 1).

alignment of microtubules and stresses in the case of root hair initiation. Firstly, the quick addition of material could lead to a stiffening of the wall, and we could show that this can lead to radial stress patterns (**Figure 3C**). This can be related to observations of alternating phases of tip growth and wall thickening at the tip (McKenna et al., 2009). Although this may occur at a different time scale during root hair initiation, only about 50% of analyzed cells showed a radial pattern, which could indicate that it represents a transient state (Pietra et al., 2013). A competing idea suggested for tip growth is that the forces exerted on the wall at the tip are changing (Zonia, 2010). When applied to a model of a patch in the epidermal wall, this was also able to generate radial patterns of stresses (**Figure 4**), but the required difference in forces was high and might be hard to realize in reality in an epidermal root cell (**Figure 4D**, Winship et al., 2010).

Since our results show that either local alteration of material properties of the cell wall or the active interaction with cytoskeleton may lead to the radial pattern of stresses around the place of root hair outgrowth, it would be interesting to measure wall stiffness at this site for example by using atomic force microscopy.

While we have stressed the importance of looking at several processes when analyzing root hair initiation (**Figure 1A**), our computational simulations have been divided into the processes of ROP patch formation (**Figure 2**) and of ongoing mechanical changes (**Figures 3, 4**). A main challenge will be to integrate these into a single model where both ROP activation is necessary for root hair initiation (Jones et al., 2002), and correct microtubular

dynamics are necessary for correct ROP positioning (Pietra et al., 2013). Induced chemical or genetic perturbations followed by live imaging can provide additional dynamical data to generate improved insight into the process, and computational modeling of the interactions will be essential to understand the consequences of direct or indirect mechanisms of several combined feedback regulations.

## AUTHOR CONTRIBUTIONS

SP and MG designed and analyzed experiments. PK, AL, BB, HJ designed and analyzed models and simulations. PK and BB developed and simulated mechanical models. AL developed and simulated the molecular model. All authors wrote and edited the paper.

## FUNDING

This work was funded by the Knut and Alice Wallenberg Foundation via grant ShapeSystems (KAW 2012.0050) to MG and HJ, the Swedish Research Council (VR2013-4632) to HJ, and the Gatsby Charitable Foundation (GAT3395/PR4) to HJ.

## SUPPLEMENTARY MATERIAL

The Supplementary Material for this article can be found online at: <http://journal.frontiersin.org/article/10.3389/fpls.2016.01560/full#supplementary-material>

## REFERENCES

- Akkerman, M., Franssen-Verheijen, M. A. W., Immerzeel, P., Hollander, L. D. E. N., Schel, J. H. N., and Emons, A. M. C. (2012). Texture of cellulose microfibrils of root hair cell walls of *Arabidopsis thaliana*, *Medicago truncatula*, and *Vicia sativa*. *J. Microsc.* 247, 60–67. doi: 10.1111/j.1365-2818.2012.03611.x
- Ambrose, C., Allard, J. F., Cytrynbaum, E. N., and Wasteneys, G. O. (2011). A CLASP-modulated cell edge barrier mechanism drives cell-wide cortical microtubule organization in *Arabidopsis*. *Nat. Commun.* 2:430. doi: 10.1038/ncomms1444
- Arioli, T., Peng, L., Betzner, A. S., Burn, J., Wittke, W., Herth, W., et al. (1998). Molecular analysis of cellulose biosynthesis in *Arabidopsis*. *Science* 279, 717–720. doi: 10.1126/science.279.5351.717
- Bao, Y., Kost, B., and Chua, N. H. (2001). Reduced expression of alpha-tubulin genes in *Arabidopsis thaliana* specifically affects root growth and morphology, root hair development and root gravitropism. *Plant J.* 28, 145–157. doi: 10.1046/j.1365-313X.2001.01142.x
- Baskin, T. I. (2005). Anisotropic expansion of the plant cell wall. *Annu. Rev. Cell Dev. Biol.* 21, 203–222. doi: 10.1146/annurev.cellbio.20.082503.103053
- Baskin, T. I. (2015). Auxin inhibits expansion rate independently of cortical microtubules. *Trends Plant Sci.* 20, 471–472. doi: 10.1016/j.tplants.2015.05.008
- Benítez, M., and Alvarez-Buylla, E. R. (2010). Dynamic-module redundancy confers robustness to the gene regulatory network involved in hair patterning of *Arabidopsis* epidermis. *Biosystems* 102, 11–15. doi: 10.1016/j.biosystems.2010.07.007
- Benítez, M., Monk, N. A. M., and Alvarez-Buylla, E. R. (2011). Epidermal patterning in *Arabidopsis*: models make a difference. *J. Exp. Zool. B* 316B, 241–253. doi: 10.1002/jezb.21398
- Bosch, M. (2005). Pectin methylesterases and pectin dynamics in pollen tubes. *Plant Cell* 17, 3219–3226. doi: 10.1105/tpc.105.037473
- Bozorg, B., Krupinski, P., and Jönsson, H. (2014). Stress and strain provide positional and directional cues in development. *PLoS Comput. Biol.* 10:e1003410. doi: 10.1371/journal.pcbi.1003410
- Braybrook, S. A., and Jönsson, H. (2016). Shifting foundations: the mechanical cell wall and development. *Curr. Opin. Plant Biol.* 29, 115–120. doi: 10.1016/j.pbi.2015.12.009
- Brena-Medina, V., Champneys, A. R., Grierson, C., and Ward, M. J. (2014). Mathematical modeling of plant root hair initiation : dynamics of localized. *SIAM J. Appl. Dyn. Syst.* 13, 210–248. doi: 10.1137/120902264
- Chanliaud, E., Burrows, K. M., Jeronimidis, G., and Gidley, M. J. (2002). Mechanical properties of primary plant cell wall analogues. *Planta* 215, 989–996. doi: 10.1007/s00425-002-0783-8
- Chen, X., Grandont, L., Li, H., Hauschild, R., Paque, S., Abuzeineh, A., et al. (2014). Inhibition of cell expansion by rapid ABP1-mediated auxin effect on microtubules. *Nature* 516, 90–93. doi: 10.1038/nature13889
- Chen, X., Wu, S., Liu, Z., and Friml, J. (2016). Environmental and endogenous control of cortical microtubule orientation. *Trends Cell Biol.* 26, 409–419. doi: 10.1016/j.tcb.2016.02.003
- Cosgrove, D. J. (2005). Growth of the plant cell wall. *Nat. Rev. Mol. Cell Biol.* 6, 850–861. doi: 10.1038/nrm1746
- Dumais, J., Shaw, S. L., Steele, C. R., Long, S. R., and Ray, P. M. (2006). An anisotropic-viscoplastic model of plant cell morphogenesis by tip growth. *Int. J. Dev. Biol.* 50, 209–222. doi: 10.1387/ijdb.052066jd
- Fischer, U., Ikeda, Y., Ljung, K., Serralbo, O., Singh, M., Heidstra, R., et al. (2006). Vectorial information for *Arabidopsis* planar polarity is mediated by combined aux1, ein2, and gnom activity. *Curr. Biol.* 16, 2143–2149. doi: 10.1016/j.cub.2006.08.091
- Fu, Y., Xu, T., Zhu, L., Wen, M., and Yang, Z. (2009). A ROP GTPase signaling pathway controls cortical microtubule ordering and cell expansion in *Arabidopsis*. *Curr. Biol.* 19, 1827–1832. doi: 10.1016/j.cub.2009.08.052

- Galway, M. E., Heckman, J. W. Jr., and Schiefelbein, J. W. (1997). Growth and ultrastructure of *Arabidopsis* root hairs: the *rhd3* mutation alters vacuole enlargement and tip growth. *Planta* 201, 209–218. doi: 10.1007/BF01007706
- Geitmann, A., Snowman, B. N., Emons, A. M. C., and Franklin-Tong, V. E. (2000). Alterations in the actin cytoskeleton of pollen tubes are induced by the self-incompatibility reaction in *Papaver rhoeas*. *Plant Cell* 12, 1239–1251. doi: 10.1105/tpc.12.7.1239
- Goryachev, A. B., and Pokhilko, A. V. (2008). Dynamics of Cdc42 network embodies a Turing-type mechanism of yeast cell polarity. *FEBS Lett.* 582, 1437–1443. doi: 10.1016/j.febslet.2008.03.029
- Grebe, M., Friml, J., Swarup, R., Ljung, K., Sandberg, G., Terlou, M., et al. (2002). Cell polarity signaling in *Arabidopsis* involves a bfa-sensitive auxin influx pathway. *Curr. Biol.* 12, 329–334. doi: 10.1016/S0960-9822(02)00654-1
- Green, P. B. (1962). Mechanism for plant cellular morphogenesis. *Science* 138, 1404–1405. doi: 10.1126/science.138.3548.1404
- Hamant, O., Heisler, M. G., Jönsson, H., Krupinski, P., Uyttewaal, M., Bokov, P., et al. (2008). Developmental patterning by mechanical signals in *Arabidopsis*. *Science* 322, 1650–1655. doi: 10.1126/science.1165594
- Hayot, C. M., Forouzesh, E., Goel, A., Avramova, Z., and Turner, J. A. (2012). Viscoelastic properties of cell walls of single living plant cells determined by dynamic nanoindentation. *J. Exp. Bot.* 63, 2525–2540. doi: 10.1093/jxb/err428
- Heath, I. B., and Geitmann, A. (2000). Cell biology of plant and fungal tip growth—getting to the point. *Plant Cell* 12, 1513–1517. doi: 10.1105/tpc.12.9.1513
- Hejnowicz, Z., Rusin, A., and Rusin, T. (2000). Tensile tissue stress affects the orientation of cortical microtubules in the epidermis of sunflower hypocotyl. *J. Plant Growth Regul.* 19, 31–44. doi: 10.1007/s003440000005
- Hervieux, N., Dumond, M., Sapala, A., Routier-Kierzkowska, A.-L., Kierzkowski, D., Roeder, A. H. K., et al. (2016). A mechanical feedback restricts sepal growth and shape in *Arabidopsis*. *Curr. Biol.* 26, 1019–1028. doi: 10.1016/j.cub.2016.03.004
- Hill, A. E., Shachar-Hill, B., Skepper, J. N., Powell, J., and Shachar-Hill, Y. (2012). An osmotic model of the growing pollen tube. *PLoS ONE* 7:e36585. doi: 10.1371/journal.pone.0036585
- Hogetsu, T. (1986). Re-formation of microtubules in closterium ehrenbergii meneghinii after cold-induced depolymerization. *Planta* 167, 437–443. doi: 10.1007/BF00391218
- Ikeda, Y., Men, S., Fischer, U., Stepanova, A. N., Alonso, J. M., Ljung, K., et al. (2009). Local auxin biosynthesis modulates gradient-directed planar polarity in *Arabidopsis*. *Nat. Cell Biol.* 11, 731–738. doi: 10.1038/ncb1879
- Jilkine, A., Marée, A. F. M., and Edelstein-Keshet, L. (2007). Mathematical model for spatial segregation of the Rho-family GTPases based on inhibitory crosstalk. *Bull. Math. Biol.* 69, 1943–1978. doi: 10.1007/s11538-007-9200-6
- Jones, A. R., Kramer, E. M., Knox, K., Swarup, R., Bennett, M. J., Lazarus, C. M., et al. (2009). Auxin transport through non-hair cells sustains root-hair development. *Nat. Cell Biol.* 11, 78–84. doi: 10.1038/ncb1815
- Jones, M., Shen, J.-J., Fu, Y., Li, H., Yang, Z., and Grierson, C. S. (2002). The *Arabidopsis* rop2 gtpase is a positive regulator of both root hair initiation and tip growth. *Plant Cell* 14, 763–776. doi: 10.1105/tpc.010359
- Kiefer, C. S., Claes, A. R., Nzayisenga, J.-C., Pietra, S., Stanislaski, T., Huser, A., et al. (2015). *Arabidopsis* AIP1-2 restricted by WER-mediated patterning modulates planar polarity. *Development* 142, 151–161. doi: 10.1242/dev.111013
- Kusano, H., Testerink, C., Vermeer, J. E. M., Tsuge, T., Shimada, H., Oka, A., et al. (2008). The *Arabidopsis* phosphatidylinositol phosphate 5-kinase PIP5K3 is a key regulator of root hair tip growth. *Plant Cell* 20, 367–380. doi: 10.1105/tpc.107.056119
- Lindeboom, J. J., Nakamura, M., Hibbel, A., Shundyak, K., Gutierrez, R., Ketelaar, T., et al. (2013). A mechanism for reorientation of cortical microtubule arrays driven by microtubule severing. *Science* 342:1245533. doi: 10.1126/science.1245533
- Lovy-Wheeler, A., Cárdenas, L., Kunkel, J. G., and Hepler, P. K. (2007). Differential organelle movement on the actin cytoskeleton in lily pollen tubes. *Cell Motil. Cytoskeleton* 64, 217–232. doi: 10.1002/cm.20181
- Masucci, J. D., and Schiefelbein, J. W. (1994). The *rhd6* mutation of *Arabidopsis thaliana* alters root-hair initiation through an auxin- and ethylene-associated process. *Plant Physiol.* 106, 1335–1346.
- McFarlane, H. E., Döring, A., and Persson, S. (2014). The cell biology of cellulose synthesis. *Ann. Rev. Plant Biol.* 65, 69–94. doi: 10.1146/annurev-arplant-050213-040240
- McKenna, S. T., Kunkel, J. G., Bosch, M., Rounds, C. M., Vidali, L., Winship, L. J., et al. (2009). Exocytosis precedes and predicts the increase in growth in oscillating pollen tubes. *Plant Cell* 21, 3026–3040. doi: 10.1105/tpc.109.069260
- Molendijk, A. J., Bischoff, F., Rajendrakumar, C. S. V., Friml, J., Braun, M., Gilroy, S., et al. (2001). *Arabidopsis thaliana* rop gtpases are localized to tips of root hairs and control polar growth. *EMBO J.* 20, 2779–2788. doi: 10.1093/emboj/20.11.2779
- Newcomb, E. H., and Bonnet, H. T. (1965). Cytoplasmic microtubule and wall microfibril orientation in root hairs of radish. *J. Cell Biol.* 27, 575–589. doi: 10.1083/jcb.27.3.575
- Nezhad, A. S., Naghavi, M., Packirisamy, M., Bhat, R., and Geitmann, A. A. (2013). Quantification of the Young's modulus of the primary plant cell wall using Bending-Lab-On-Chip (BLOC). *Lab Chip* 13, 2599–608. doi: 10.1039/c3lc00012e
- Pang, C.-Y., Wang, H., Pang, Y., Xu, C., Jiao, Y., Qin, Y.-M., et al. (2010). Comparative proteomics indicates that biosynthesis of pectic precursors is important for cotton fiber and *Arabidopsis* root hair elongation. *Mol. Cell. Proteom.* 9, 2019–2033. doi: 10.1074/mcp.M110.000349
- Park, S., Szumlanski, A. L., Gu, F., Guo, F., and Nielsen, E. (2011). A role for CSLD3 during cell-wall synthesis in apical plasma membranes of tip-growing root-hair cells. *Nat. Cell Biol.* 13, 973–980. doi: 10.1038/ncb2294
- Payne, R. J. H., and Grierson, C. S. (2009). A theoretical model for rop localisation by auxin in *Arabidopsis* root hair cells. *PLoS ONE* 4:e8337. doi: 10.1371/journal.pone.0008337
- Pietra, S., Gustavsson, A., Kiefer, C., Kalmbach, L., Hörstedt, P., Ikeda, Y., et al. (2013). *Arabidopsis* SABRE and CLASP interact to stabilize cell division plane orientation and planar polarity. *Nat. Commun.* 4:2779. doi: 10.1038/ncomms3779
- Ringli, C., Baumberger, N., Diet, A., Frey, B., and Keller, B. (2002). ACTIN2 is essential for bulge site selection and tip growth during root hair development of *Arabidopsis*. *Plant Physiol.* 129, 1464–1472. doi: 10.1104/pp.005777
- Rojas, E. R., Hotton, S., and Dumais, J. (2011). Chemically mediated mechanical expansion of the pollen tube cell wall. *Biophys. J.* 101, 1844–1853. doi: 10.1016/j.bpj.2011.08.016
- Rounds, C. M., and Bezanilla, M. (2013). Growth mechanisms in tip-growing plant cells. *Annu. Rev. Plant Biol.* 64, 243–265. doi: 10.1146/annurev-arplant-050312-120150
- Sampathkumar, A., Krupinski, P., Wightman, R., Malini, P., Berquand, A., Boudaoud, A., et al. (2014). Subcellular and supracellular mechanical stress prescribes cytoskeleton behavior in *Arabidopsis* cotyledon pavement cells. *eLife* 3:e01967. doi: 10.7554/eLife.01967
- Sanati Nezhad, A., Packirisamy, M., and Geitmann, A. (2014). Dynamic, high precision targeting of growth modulating agents is able to trigger pollen tube growth reorientation. *Plant J.* 80, 185–195. doi: 10.1111/tpj.12613
- Sassi, M., Ali, O., Boudon, F., Cloarec, G., Abad, U., Cellier, C., et al. (2014). An auxin-mediated shift toward growth isotropy promotes organ formation at the shoot meristem in *Arabidopsis*. *Curr. Biol.* 24, 2335–2342. doi: 10.1016/j.cub.2014.08.036
- Savage, N. S., Walker, T., Wieckowski, Y., Schiefelbein, J., Dolan, L., and Monk, N. A. M. (2008). A mutual support mechanism through intercellular movement of CAPRICE and GLABRA3 can pattern the *Arabidopsis* root epidermis. *PLoS Biol.* 6:e235. doi: 10.1371/journal.pbio.0060235
- Schiefelbein, J., Kwak, S.-H., Wieckowski, Y., Barron, C., and Bruex, A. (2009). The gene regulatory network for root epidermal cell-type pattern formation in *Arabidopsis*. *J. Exp. Bot.* 60, 1515–1521. doi: 10.1093/jxb/ern339
- Singh, S. K., Fischer, U., Singh, M., Grebe, M., and Marchant, A. (2008). Insight into the early steps of root hair formation revealed by the procustel cellulose synthase mutant of *Arabidopsis thaliana*. *BMC Plant Biol.* 8:57. doi: 10.1186/1471-2229-8-57
- Suslov, D., Verbelé, J.-P., and Vissenberg, K. (2009). Onion epidermis as a new model to study the control of growth anisotropy in higher plants. *J. Exp. Bot.* 60, 4175–4187. doi: 10.1093/jxb/erp251
- Swarup, R., Kramer, E. M., Perry, P., Knox, K., Leyser, H. M. O., Haseloff, J., et al. (2005). Root gravitropism requires lateral root cap and epidermal cells for transport and response to a mobile auxin signal. *Nat. Cell Biol.* 7, 1057–1065. doi: 10.1038/ncb1316

- Yttewaal, M., Burian, A., Alim, K., Landrein, B., Borowska-Wykret, D., Dedieu, A., et al. (2012). Mechanical stress acts via katanin to amplify differences in growth rate between adjacent cells in *Arabidopsis*. *Cell* 149, 439–451. doi: 10.1016/j.cell.2012.02.048
- Vogler, H., Draeger, C., Weber, A., Feleki, D., Eichenberger, C., Routier-Kierzkowska, A.-L., et al. (2013). The pollen tube: a soft shell with a hard core. *Plant J.* 73, 617–627. doi: 10.1111/tpj.12061
- Winship, L. J., Obermeyer, G., Geitmann, A., and Hepler, P. K. (2010). Under pressure, cell walls set the pace. *Trends Plant Sci.* 15, 363–369. doi: 10.1016/j.tplants.2010.04.005
- Xu, J., and Scheres, B. (2005). Dissection of *Arabidopsis* ADP-RIBOSYLATION FACTOR 1 function in epidermal cell polarity. *Plant Cell* 17, 525–536. doi: 10.1105/tpc.104.028449
- Xu, T., Wen, M., Nagawa, S., Fu, Y., Chen, J.-G., Wu, M.-J., et al. (2010). Cell surface- and rho GTPase-based auxin signaling controls cellular interdigitation in *Arabidopsis*. *Cell* 143, 99–110. doi: 10.1016/j.cell.2010.09.003
- Zandomeni, K., and Schopfer, P. (1993). Reorientation of microtubules at the outer epidermal wall of maize coleoptiles by phytochrome, blue-light photoreceptor, and auxin. *Protoplasma* 173, 103–112. doi: 10.1007/BF01378999
- Zonia, L. (2010). Spatial and temporal integration of signalling networks regulating pollen tube growth. *J. Exp. Bot.* 61, 1939–1957. doi: 10.1093/jxb/erq073

**Conflict of Interest Statement:** The authors declare that the research was conducted in the absence of any commercial or financial relationships that could be construed as a potential conflict of interest.

Copyright © 2016 Krupinski, Bozorg, Larsson, Pietra, Grebe and Jönsson. This is an open-access article distributed under the terms of the Creative Commons Attribution License (CC BY). The use, distribution or reproduction in other forums is permitted, provided the original author(s) or licensor are credited and that the original publication in this journal is cited, in accordance with accepted academic practice. No use, distribution or reproduction is permitted which does not comply with these terms.



# Cocowood Fibrovascular Tissue System—Another Wonder of Plant Evolution

Oswaldo M. González<sup>1,2\*</sup> and Khoi A. Nguyen<sup>2</sup>

<sup>1</sup> Research Department, Universidad de las Fuerzas Armadas ESPE, Sangolqui, Ecuador, <sup>2</sup> Griffith School of Sciences and Engineering, Griffith University, Gold Coast, QLD, Australia

## OPEN ACCESS

### Edited by:

Daniel H. Chitwood,  
Donald Danforth Plant Science Center,  
USA

### Reviewed by:

Gerhard Buck-Sorlin,  
Agrocampus Ouest, France  
Artem Kulachenko,  
Royal Institute of Technology, Sweden

### \*Correspondence:

Oswaldo M. González  
omgonzalez@espe.edu.ec;  
mauricio.gonzalezmosquera@  
griffithuni.edu.au

### Specialty section:

This article was submitted to  
Plant Biophysics and Modeling,  
a section of the journal  
Frontiers in Plant Science

Received: 19 April 2016

Accepted: 18 July 2016

Published: 09 August 2016

### Citation:

González OM and Nguyen KA (2016)  
Cocowood Fibrovascular Tissue  
System—Another Wonder of Plant  
Evolution. *Front. Plant Sci.* 7:1141.  
doi: 10.3389/fpls.2016.01141

The coconut palm (*Cocos nucifera L.*) stem tissue (referred to as cocowood in this study) is a complex fibrovascular system that is made up of fibrovascular bundles embedded into a parenchymatous ground tissue. The complex configuration of fibrovascular bundles along with the non-uniform distribution of the material properties likely allow senile coconut stems to optimize their biomechanical performance per unit mass (i.e., mechanical efficiency) and grow into tall, slender, and very flexible plants with minimum resources of biomass and water. For the first time, to the best of the authors' knowledge, this paper examines, from the integral (i.e., stem structure) and macroscopic (i.e., tissue structure) levels of hierarchy, the characteristic triple helix formation depicted by the fibrovascular bundles within the monocotyledon cocowood. The natural course of the tangential orientation of the axial fibrovascular bundles is mapped for the whole cocowood structure by quantifying 264 cocowood discs, corresponding to 41 senile coconut palms estimated to be >70 years old. The observed variations were modeled in this paper by simple equations that partially enabled characterization of the cocowood fibrovascular tissue system. Furthermore, 11 finite element analyses (FEA) were performed over a three dimensional (3D) finite element (FE) model resembling a characteristic coconut palm stem of 25 m in height to analyze the biomaterial reactions produced by the progressive deviation of the tangential fibrovascular bundles on the cocowood mechanical response (i.e., on the material compressive strength and the bending stiffness). The analyses in this study were carried out for the critical wind speed of 23 m/s (i.e., Gale tornado according to the Fujita tornado scale). For each analysis, the characteristic average maxima degree of orientation of the cocowood fibrovascular bundles was varied from 0° to 51°. The acquired results provided a deep understanding of the cocowood optimum fibrovascular tissue system that denotes the natural evolution of the material through millions of years. The knowledge advanced from this study may also serve as concept generators for innovative biomimetic applications to improve current engineered wood products.

**Keywords:** coconut palm stem tissue (cocowood), monocotyledon plant, fibrovascular bundle degree of orientation, mechanical efficiency, finite element analysis, integral and macroscopic levels of hierarchical structure

## INTRODUCTION

### Cocowood Fibrovascular Tissue System

According to botanical taxonomy, coconut palms (*Cocos nucifera L.*) belong to the palm tree family (*Arecaceae*), a family of monocotyledon plants whereas hardwoods and softwoods are woody plants with similar stem characteristics from the point of view of structural mechanics, but different tissue properties (e.g., quasi-uniform vs. non-uniform density distribution; Bahtiar et al., 2010). The main differences between palmwoods, hardwoods, and softwoods are summarized by Butterfield et al. (1997). The coconut palm stem is composed of two anatomical components: the cortex and the central cylinder. The cortex is a fibrous tissue covering the entire outer circumference of the stem. It is typically 1–1.5 cm thick and plays a similar function to that of the bark in woody plants (Tomlinson, 1990). The central cylinder is a plant tissue (referred to as cocowood herein) that constitutes more than 96% of the palm stem. Cocowood is a complex tissue that depicts a cellular structure (Gibson, 2005) comprising two different tissues as shown in **Figure 1**.

The fibrovascular tissue system (i.e., the assemblage of conducting tissues and associated supportive fibers) of monocotyledonous palms has been extensively investigated from different levels of hierarchy (Zimmermann and Tomlinson, 1972; Tomlinson et al., 1984, 2001, 2011; Tomlinson, 1990, 2006; Rüggeberg et al., 2008, 2009; Thomas and De Franceschi, 2013). The system is essentially made up of three elements: axial fibrovascular bundles, leaf traces, and fibrous cortical traces (Zimmermann and Tomlinson, 1972). The axial fibrovascular bundles remain within the stem tissue and provide longitudinal continuity to the palm structure (Tomlinson, 1990). Both leaf and cortical traces connect the stem fibrovascular system with that of the leaves and petioles (Rüggeberg et al., 2009). Moreover, the leaf traces are connected to the axial fibrovascular bundles within the stem central cylinder by narrow bundles called bridges (Tomlinson, 1990).

The fibrovascular bundles are made of fibers, xylem, phloem, and axial parenchyma. The fibers constitute over half of the volume of each fibrovascular bundle (Butterfield et al., 1997). In monocotyledonous palms, the fibers have thin walls and large lumens (cavities inside the fibers) toward the stem core, and thick walls and small highly lignified lumens toward the stem periphery (Fathi et al., 2014). This implies denser and stronger fibers at the stem periphery likely influencing the biomechanical performance of palm stems, in terms of bending strength (Sudo, 1980; Rich, 1986, 1987; Butterfield et al., 1997; Fathi and Frühwald, 2014) and bending stiffness (Rüggeberg et al., 2009). The fiber walls are commonly multi-layered (e.g., similar to cell wall layers of hardwood fibers) and the thickness and microfibril orientation of each layer are clearly visible under light microscopy (Butterfield et al., 1997).

Thousands of fibrovascular bundles (e.g., 20,000 approximately) are scattered within a single transverse section of a senile (i.e., <60 years old) coconut palm stem (Zimmermann and Tomlinson, 1972; Tomlinson, 1990). Radial density and fibrovascular bundle distribution develop non-homogeneously throughout the palm stem, with denser

tissue toward the periphery and base, where the biomechanical performance of the material shows maximum bending stresses (Rüggeberg et al., 2009; Gibson, 2012). According to Killmann and Fink (1996), the distribution of fibrovascular bundles within coconut stems can be classified into three different zones: (a) the dermal zone, close to the cortex, with a high density distribution of about 68 fibrovascular bundles per  $\text{cm}^2$ , (b) the sub-dermal zone, with a medium density distribution of about 42 fibrovascular bundles per  $\text{cm}^2$ , and (c) the central zone, with a low density distribution of about 18 fibrovascular bundles per  $\text{cm}^2$ . The average cross-cut area of the single fibrovascular bundle within cocowood stems was found to vary from  $0.30 \text{ mm}^2$  at the central zone to  $0.53 \text{ mm}^2$  at the dermal zone (Fathi et al., 2014). The high and low distributions of fibrovascular bundles toward the palm stem periphery (dermal zone) and core (central zone), respectively, reflect an efficient structure that is not excessively overbuilt (Tomlinson, 1990).

### Fibrovascular Bundle Degree of Orientation in Palmwoods

In plant species, fibers can be oriented in various directions within the structure to adapt the structural response to the external loading conditions (Zhang et al., 2012). The fibrovascular development (i.e., the method of construction of the fibrovascular tissue system described in Section Cocowood Fibrovascular Tissue System) of monocotyledon palms was thoroughly analyzed by Tomlinson (1990), especially for that of *Rhapis excelsa* palms. The course of the fibrovascular bundles was found to follow a helical path as they ascend the stem, but also vary progressively toward the center of the stem before bending rapidly outwards toward a leaf trace at the periphery of the stem. While the observed pattern is typical, it is not a consistent attribute for all palm species. According to Tomlinson (1990), the longitudinal helical pattern seems to have been observed in the nineteenth century by both Meneghini (1836) and De Mirbel (1843). Tomlinson (1990) pointed out that the helical formation “probably adds to the mechanical efficiency of the stem by minimizing longitudinal splitting.”

The natural course of axial fibrovascular bundles within monocot palm stems was further described by Rüggeberg et al. (2008) as a feature that follows both a “screw-like pathway” (i.e., a longitudinal–helical course) while running up the stem, and a “zigzag” pattern across the stem diameter, thereby deviating in tangential and radial directions as they run back and forth within the palm stem. Butterfield et al. (1997) called attention to “an understanding of the three dimensional path-ways traced out by the fibrovascular bundles within the stem that is fundamental to a full understanding of the structure of palmwood.”

Rüggeberg et al. (2009) by studying the structure–function relationships of different vascular bundle types in one 33 year-old *Washingtonia robusta* palm at an elevation of 5 m graphically reported the radial degree of orientation of the fibrovascular bundles. The bundles were found to move toward the periphery of the stem, with the higher degree of orientation reported in the dermal zone of the stem.

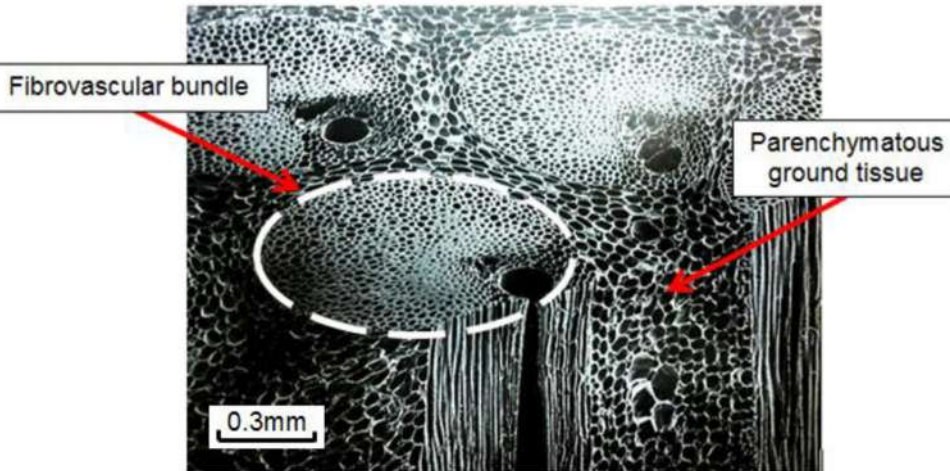


**FIGURE 1 | Cocowood is a complex vascular tissue system that depicts a cellular structure that can be described as parallel stiff fibers embedded in foam.** Its simple botanical description is a blend of two structurally and functionally divergent cell tissues: (a) the fibrovascular bundles with a honeycomb-like structure, which are rounded and dense groups of long fibers surrounding vessel elements for sap circulation, mainly orientated in the longitudinal axis of the stem, and (b) the ground tissue made up of foam-like polyhedral parenchyma cells.

From the literature review, it appears that, only one study performed by Kuo-Huang et al. (2004) has reported a partial degree of orientation of axial fibrovascular bundles within juvenile coconut stems (20–25 years old), average heights of 6 m. Kuo-Huang et al. (2004) graphically showed a tangential degree of orientation of fibrovascular bundles across the stem diameter that varied from 4° to 12° at the bottom of the studied stems.

Although the development of the fibrovascular system of monocotyledonous tissues has been investigated at different hierarchical levels, and the triple helix formation of cocowood fibrovascular bundles (Figure 2) has been observed, they have not yet been characterized and modeled for the whole cocowood structure. Furthermore, the extent to which the degrees of orientation of the fibrovascular bundles influence on the cocowood stem biological function has remained unknown up to now. These observations were the driving forces behind the work in this study.

## MATERIALS AND METHODS

### Tangential Fibrovascular Bundle Degree of Orientation

A total of 41 senile coconut palms with average stem heights ranging from 18.8 to 25 m, sourced during the Project FST/2004/054: “Improving value and marketability of coconut wood” by the Australian Centre for International Agricultural Research (ACIAR) in 2010, from the Pacific islands of Fiji (29 palms) and Samoa (12 palms), were used to measure the tangential orientation of the cocowood axial fibrovascular bundles. For each palm, nominal 50 mm thick discs were cut at the key stem elevations of 0.2, 3.2, 6.2, 9.4, 12.4, 15.8, 18.8, 22.0, and 25.0 m. The fibrovascular bundle degrees of orientation were acquired by measuring the tangential deviation of the

fibrovascular bundles after splitting the discs along their diameter (Figure 3A). One of the two split half-disc was positioned on a white paper sheet to project the two lines in the same plane (i.e., the straight split line and the undulated split line). The straight line (SL) was projected perpendicularly onto the paper and the undulated line (UL) was directly drawn on the paper sheet. Each line was divided into 100 points equally spaced along the disc diameter to take measurements. The tangential fibrovascular bundle degree of orientation  $\theta$  at a radial position  $R$  from the disc center was calculated for each point as,

$$\theta(R) = \tan^{-1} \left( \frac{x}{h_b} \right) \quad (1)$$

where  $x$  is the distance between the lines UL and SL, and  $h_b$  is the measured disc height of break, as shown in Figure 3B.

As mentioned before, the tangential fibrovascular bundle degree of orientation of the coconut stem tissue describes a triple helix structure. Observations from the collected data showed that the fibrovascular bundle degree of orientation is typically not vertical at the periphery of the palm. As the distribution of the fibrovascular bundle degree of orientation is axisymmetric (i.e., symmetrical about the palm stem’s main axis), the fibrovascular bundles at the center of the stem must be vertical when considered analytically. The following periodic equation is proposed to characterize the fibrovascular bundle degree of orientation  $\theta$  as function of the radial position  $R$  from the center of the stem and the palm height  $h$ ,

$$\theta(R, h) = \theta_{max}(h) \times \sin \left( 2\pi \times f \times \frac{R}{R_{max}(h)} \right) \quad (2)$$

where  $R_{max}$  is the palm maximum radius,  $f$  is the natural frequency of the triple helix, and  $\theta_{max}$  is the average maxima

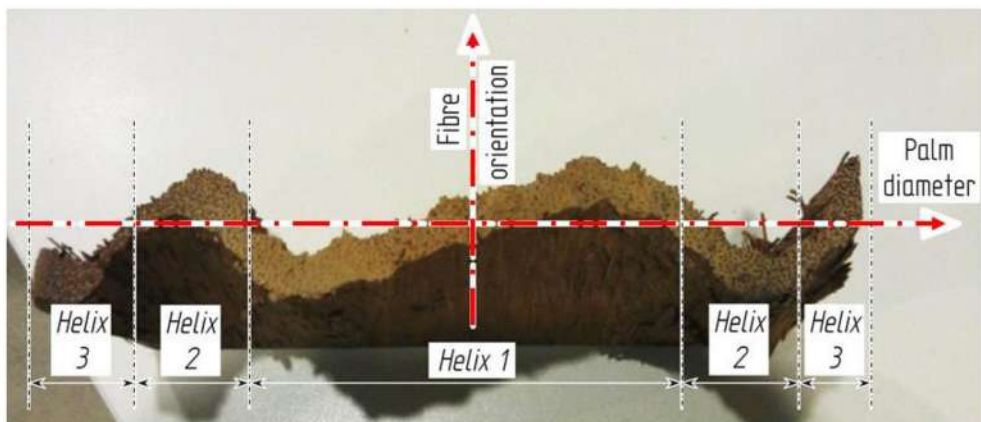


**FIGURE 2 | Cocowood triple helix pattern shown in a radially split disc.** Similar to the zigzag pattern described by Rüggeberg et al. (2008) for *Washingtonia robusta* palms, the cocowood fibrovascular bundle architecture follows an axisymmetric and triple helix configurations across the palm stem diameter.

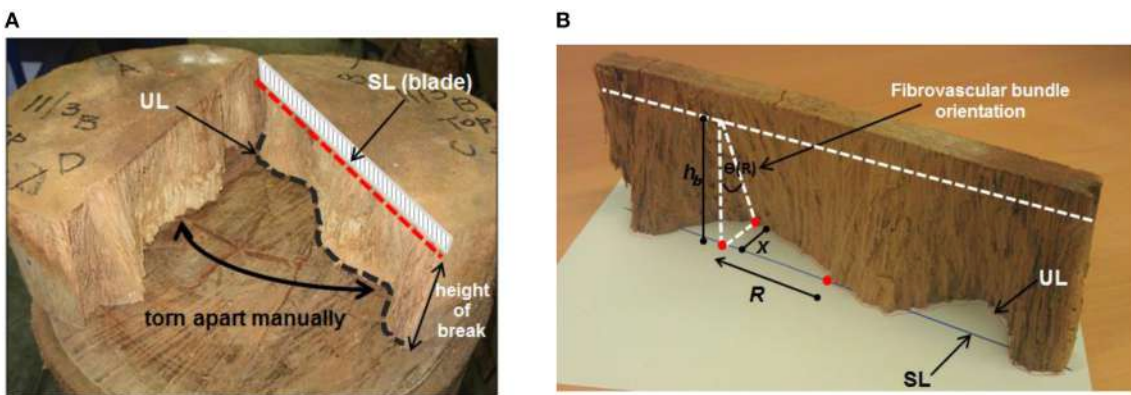


**FIGURE 3 | (A)** Each disc was split up to a depth of 10 mm with a 1100 mm long lathe-blade and manually torn apart. This left a straight split line (SL) on the upper face of the disc, where the blade was driven, and an undulated split line (UL) on the lower face that followed the fibrovascular bundles. **(B)** Measurement of the tangential fibrovascular bundle degree of orientation.

tangential fibrovascular bundle degree of orientation. Average measured maximum radiiuses of the studied cocowood discs (see Table 1) allowed determining the characteristic palm radius  $R_{max}$  (in mm) in terms of the palm stem height  $h$  (in m) as,

$$R_{max}(h) = \frac{4035}{h + 25.5} \quad (3)$$

**Figure 4** plots a typical measured fibrovascular bundle degree of orientation  $\theta$  across the palm stem diameter, showing the axisymmetric distribution and the triple helix pattern for the palm 13 at 12.4 m of stem height. To suppress the noise inherent to the fibrovascular bundle degree of orientation measurements, a discrete Fourier transform (FT) was applied to all measurements. The FT function allows transforming the discrete fibrovascular bundle degree of orientation signal from the length domain to the frequency domain. It expresses the signal as a sum of sinusoids of different frequency and magnitude (Winter David, 1997). To smooth the curves resulting

from the raw measurements of fibrovascular bundle degrees of orientation, the high frequency noise was removed by applying a low-pass filter to the transformed signal, with a cutoff frequency of 5 mm/mm (**Figure 5**). The inverse Fourier transform was subsequently applied to obtain the smoothed fibrovascular bundle degree of orientation curve. A typical smoothed fibrovascular bundle degree of orientation curve is shown above in **Figure 4**. The representative average maxima tangential fibrovascular bundle degree of orientation  $\theta_{max}$  was then calculated for each cocowood disc on the smoothed curve (see **Figure 4**) as the arithmetic mean value of the three local minimum and the three local maximum fibrovascular bundle degrees of orientation,

$$\theta_{max} = \frac{1}{6} \left( \sum_{i=1}^3 \theta_{max,i} + \sum_{i=1}^3 |\theta_{min,i}| \right) \quad (4)$$

where  $\theta_{min,i}$  and  $\theta_{max,i}$  are the values of the  $i$ th local minimum and maximum, respectively. The natural frequency  $f$  of the

triple helix was calculated from the frequency spectrum of the discrete FT applied to the tangential fibrovascular bundle degree of orientation measurements of each disc. With the discretization of 100 measurements, two different types of frequency spectra occurred: (i) two distinct dominant frequencies with no clear peak were observed, as shown in **Figure 5A**, and (ii) only one dominant frequency was observed, as shown in **Figure 5B**. When no clear peak was observed, the two dominant frequencies were

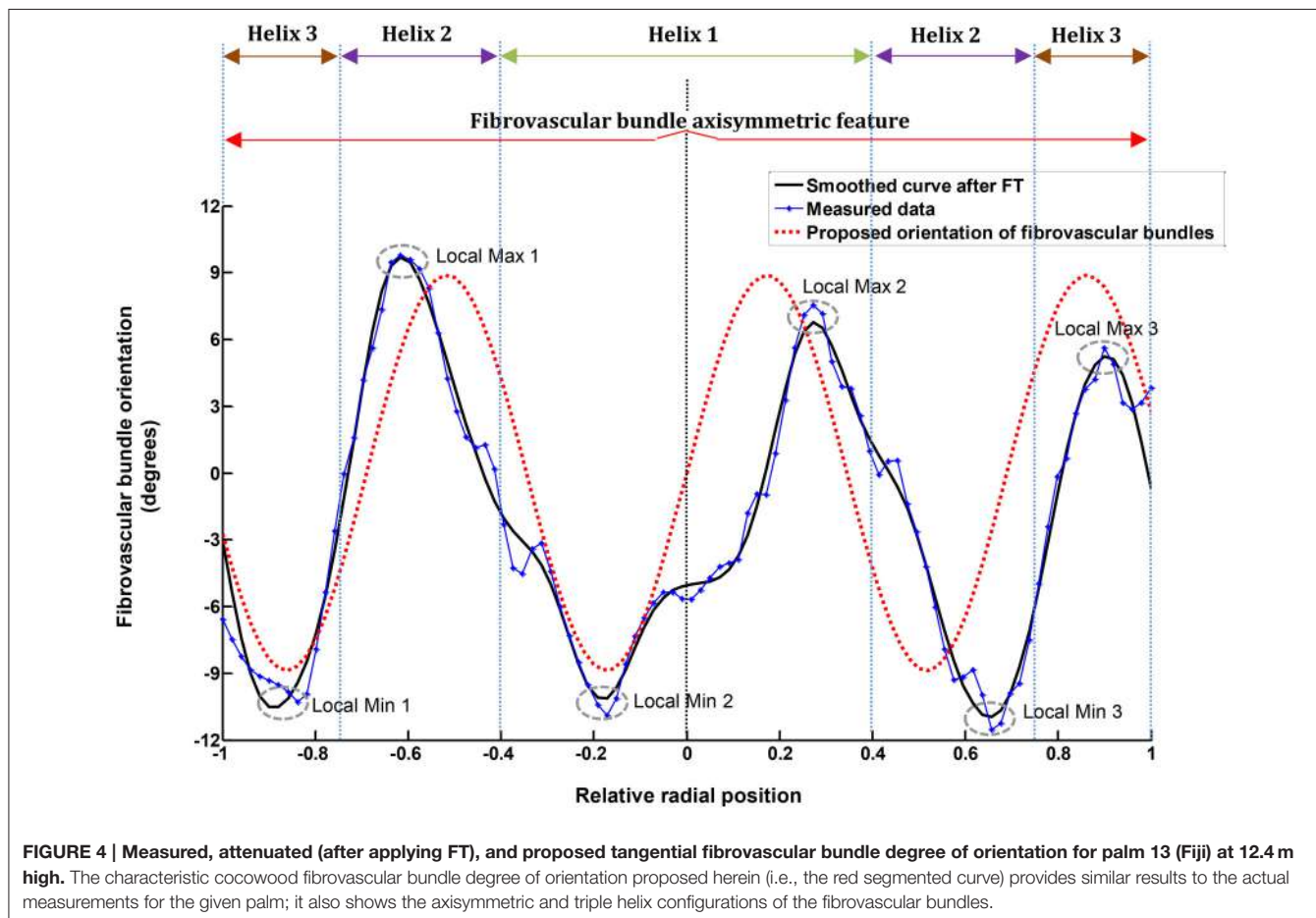
**TABLE 1 |** Measured maximum radiiuses at the studied key stem elevations.

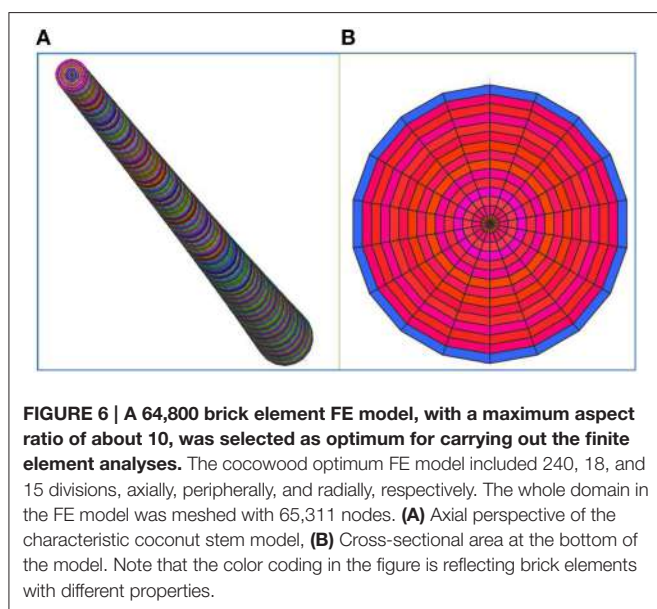
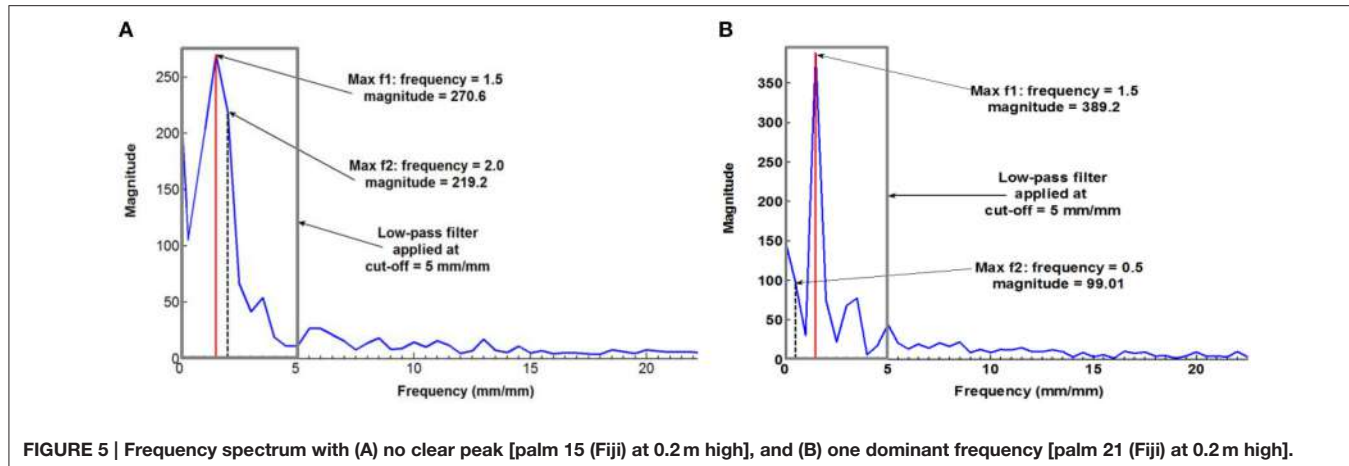
Palm stem height (m)	Number of measurements (discs)	Average radius (mm)	CoV
0.2	34	164.88	0.14
3.2	32	134.14	0.08
6.2	30	124.04	0.11
9.4	30	115.92	0.10
12.4	30	107.43	0.11
15.8	28	96.63	0.12
18.8	28	90.35	0.15
22.0	26	87.78	0.11
25.0	26	79.11	0.16

considered to both contribute to the signal if their magnitudes do not differ by more than 25%. In this case, the triple helix frequency  $f$  was approximated as the average of these two dominant frequencies. Otherwise, the frequency with the higher magnitude was considered to predominantly contribute to the signal and the helix frequency  $f$  was taken as this frequency.

## Finite Element Modeling

The 3D FE model of a characteristic senile coconut palm stem shown in **Figure 6** was built using the commercial finite element software Strand7 (2005). From the structural mechanics point of view, palm stems can be considered as composite, hierarchically structured, and fiber-reinforced beams (Speck and Burgert, 2011). Therefore, the cocowood FE model herein bears a resemblance to a fully fixed (i.e., all the model bottom surface nodes were constrained to the ground) cantilever tapered beam or pole with foliage but no branches. The structural modeled system has consequently one degree of freedom. In the FE model, the characteristic form, complex structure of the coconut stem-tissue and the cocowood properties were all derived from previous findings by the author (Gonzalez et al., 2014, 2015; Gonzalez, 2015). **Table 2** gives characteristic green properties [i.e., basic density ( $d_b$ ), modulus of elasticity (MOE), compressive modulus of rupture (MOR), shear modulus ( $G$ ), and shear





strength ( $\tau_{max}$ )] at key locations of the cocowood FE model, in the longitudinal (L), radial (R), and tangential (T) directions.

The orthotropic material behavior and the radial triple helix configuration depicted by the tangential deviation of the axial fibrovascular bundles were captured in the cocowood FE model by using the 3D brick orthotropic element property from Strand7 (i.e., 8-node brick elements have different properties for the L, R, and T directions, depending on their location within the FE model). The number of brick elements along the radius, height, and perimeter of the cocowood FE model, was tested until reaching the most appropriate mesh for the analyses. Thus, a regular solid mesh was generated to uniformly distribute the nodes in the FE model that allowed a uniform application of the wind pressure profile. Besides, the stresses developed within the cocowood model by the applied loading conditions described below, were calculated by Strand7 at the centroid of each brick element (i.e., the resultant brick stress value reflected the average of the corresponding eight brick Gauss points). Specifically, eight finite element models were analyzed at the

acute wind speed of 60 m/s (i.e., Significant tornado according to the Fujita tornado scale; Cullen, 2002) to define the most appropriate FE model for the current analyses. **Table 3** gives detailed information about each analyzed model. Two aspects were considered when defining the optimum model in this study: (i) an aspect ratio no >10 for each brick element, and (ii) a time no >1 h 15 min to process the model. Additionally, three parameters were considered to find the point of convergence when the total number of brick elements was varied in the model: (i) the maximum stress occurring in the axial direction of the model; (ii) the vertical displacement at the top/middle node of the FE model, and (iii) the displacement at the top/middle node of the model in the wind direction.

A Python program code was used to integrate the typical coconut stem form, complex structure, material properties, and loads acting on the model. The program code automatically reproduced the palm stem model, which in turn was exported to Strand7 to perform the analyses, and the relevant results were retrieved again by the Python program for easy of data evaluation and presentation. The code also considered the progressive reduction of the stem projected area due to higher deflections experienced as the wind speed increased up to 23 m/s.

No damping or swaging effects (i.e., dynamic analyses) during extended high wind events were considered herein as a pilot study showed a relative low-frequency response of about 0.2 Hz for the first natural frequency bending mode of vibration; the modal analysis was done around the equilibrium position (i.e., the non-deformed stem position) from the static geometry calculated around the unloaded state. The vortex-shedding effect was also disregarded due to two main reasons: (i) the high bending capacity (i.e., nearly to quarter circle for wind speeds >23 m/s) and the marked streamlining effect [i.e., foliage moves into alignment with the wind direction (flag) as the wind force increases] allowed reducing the palm crown/stem projected areas and the pressure drag. Hence, the whole structure reduced the wind surface, the bending moments and the vortex shedding phenomenon. (ii) The vortex shedding frequency was found to be very low (i.e., about 0.077 Hz) for an average slender coconut stem diameter of 237.8 mm, and the critical wind speed under investigation (i.e., 23 m/s), and thereby the quasi-static state portion of the movement dominated the analyses. Thus,

**TABLE 2 |** Green material properties for a characteristic senile coconut palm stem.

Stem's key location	Radial position	$d_b$ (kg/m <sup>3</sup> )	MOE <sub>L</sub> (MPa)	MOE <sub>R</sub> (MPa)	MOE <sub>T</sub> (MPa)	MOR <sub>L</sub> (MPa)	MOR <sub>R</sub> (MPa)	MOR <sub>T</sub> (MPa)	G <sub>LT</sub> (MPa)	G <sub>TR</sub> (MPa)	G <sub>RL</sub> (MPa)	$\tau_{max\_LT}$ (MPa)	$\tau_{max\_TR}$ (MPa)	$\tau_{max\_RL}$ (MPa)
Bottom (0 m)	Periphery	901	8608	463.9	352.3	40.2	16.8	15.3	783.2	154.9	930.3	9.9	2.3	10.2
	Core	223	1313	87.6	88.9	6.0	1.2	0.8	79.4	37.2	161.2	1.0	0.2	1.2
Top (25 m)	Periphery	595	5315	294.1	233.4	24.8	9.8	8.8	465.6	104.6	588.2	5.9	1.1	6.1
	Core	112	118.3	26.0	45.8	0.4	0.0	0.0	0.0	14.8	25.5	0.0	0.0	0.0

non-linear static analyses (NLA) were performed taking into account the cocowood stem's geometric non-linear effect (GNL) produced by the large deflections in the model.

The finite element model of the coconut stem-tissue was investigated under the influence of the non-uniform distributed wind pressure ( $P_w$ ), the top wind force ( $F_{top}$ ), and the self-weight ( $P$ ) of the whole structure. The  $P_w$  profile (in N/m<sup>2</sup>) acting along the cocowood FE model was derived from the Australian Standards AS/NZS 4676 (2000) and AS/NZS 1170.2 (2011), and calculated as,

$$P_w = (0.5\rho_{air})(f_h W_s)^2 \times 1.2 \quad (5)$$

where  $\rho_{air}$  is the density of air equal to 1.225 kg/m<sup>3</sup> (i.e., at sea level and 15°C),  $f_h$  is a coefficient that varies from 0.99 to 1.22 depending on the stem height (i.e., from 0 to 25 m) at which  $P_w$  is applied, and  $W_s$  is the wind speed in m/s.

Even though wind exerts a distributed non-uniform pressure all over the tree stem together with its crown (i.e., the tree's projected area), the bulk of the wind pressure acts primarily on the center of the crown (Niklas, 1992) and, therefore, a top wind force  $F_{top}$ , also known as "drag force" (Mayhead, 1973; Rudnicki et al., 2004; Vollsinger et al., 2005) was calculated (in N) as,

$$F_{top} = P_w(25m) \times A_{proj} \times C_D \quad (6)$$

where  $P_w$  in N/m<sup>2</sup> was considered at the palm stem top (25 m in this analysis),  $A_{proj}$  (in m<sup>2</sup>) is the projected area by the coconut leaves at the palm stem's crown, and  $C_D$  is the drag coefficient assumed to be constant and equal to 1. The coconut palm projected area  $A_{proj}$ , equal to 1.2 m<sup>2</sup> in this study, was derived from related studies (Rich et al., 1995; Rudnicki et al., 2004; Vollsinger et al., 2005). The vertical self-weight load ( $P$ ) was calculated in terms of gravity and mass of the cocowood structure.

## Finite Element Analyses

To fulfil the purposes in this study, a total of 11 finite element analyses (FEA) were carried out over the 3D cocowood FE model exposed to the wind speed of 23 m/s (i.e., Gale tornado, according to the Fujita tornado scale; Cullen, 2002); the wind speed that was determined in Gonzalez (2015) as the critical wind speed (i.e., the wind at which the material tissue starts reaching stress at failure) under the equivalent bending moment of 64.4 kN.m.

The analyses were performed by varying the characteristic cocowood average maxima fibrovascular bundle degree of

orientation  $\theta_{max}$  from 0° to 51°. It thus changed the characteristic cocowood fibrovascular tissue system in terms of  $\theta$ , given by Equation (2). Higher  $\theta_{max}$  variations were not examined as the results from the above-mentioned range showed well-defined trends for both the material stress at failure and the palm bending stiffness. Furthermore, the optimal average maxima fibrovascular bundle degree of orientation was determined by the point at which the cocowood tissue endured high load without considerably reducing its compressive strength and bending stiffness.

The bending stiffness is defined herein as the force required to produce a unit deflection of the coconut palm stem. The palm bending stiffness  $k$  was calculated (in kN/m) as (Ugural, 2008),

$$k = \frac{F_{th}}{\delta_h} \quad (7)$$

where  $F_{th}$  (in kN) is the horizontal reaction force acquired from the FEA in Strand7, and  $\delta_h$  (in m) is the maximum horizontal displacement in the wind direction at the top/middle point of the cocowood model.

Due to the orthotropic nature of the coconut stem-tissue, the Tsai-Hill failure criterion (Jones, 1999; Rao et al., 2008), which is a variation of the von Mises criterion (Hull and Clyne, 1996) and the Tsai-Wu criterion (Cabrero and Gebremedhin, 2010), was used to predict and evaluate the circumstances under which stress at failure was likely to occur (i.e., the material damage when the stresses produced by the progressive loading conditions rose beyond the material strength). Specifically, the material failure was predicted by this method when the failure index ( $FI$ ) was  $\geq 1$ . The referred failure index ( $FI$ ) was calculated as (Jones, 1999; Rao et al., 2008),

$$FI = \left( \frac{\sigma_L}{MOR_L} \right)^2 + \left( \frac{\sigma_R}{MOR_R} \right)^2 + \left( \frac{\sigma_T}{MOR_T} \right)^2 - \sigma_L \sigma_R \left[ \frac{1}{MOR_L^2} + \frac{1}{MOR_R^2} - \frac{1}{MOR_T^2} \right] - \sigma_L \sigma_T \left[ \frac{1}{MOR_L^2} - \frac{1}{MOR_R^2} + \frac{1}{MOR_T^2} \right] - \sigma_R \sigma_T \left[ \frac{-1}{MOR_L^2} + \frac{1}{MOR_R^2} + \frac{1}{MOR_T^2} \right] + \left( \frac{\tau_{LR}}{\tau_{max_{LR}}} \right)^2 + \left( \frac{\tau_{RT}}{\tau_{max_{RT}}} \right)^2 + \left( \frac{\tau_{TL}}{\tau_{max_{TL}}} \right)^2 \quad (8)$$

**TABLE 3 |** Results of the mesh and convergence studies.

FE model	Analyzed wind speed	Total brick elements	Number of divisions in the FE model		Brick size		(P)	(L/R)	(L/P)	Brick aspect ratio	Time to process the FE model	Max axial stress	Top/middle node displacements
			Radially (R)	Axially (L)	(R)	(L)							
1	60	2100	15	10	14	10.53	2500.00	70.91	6.7	237.3	35.3	11 s	17.08
2	60	4200	15	20	14	10.53	1250.00	70.91	6.7	118.7	17.6	46 s	44.50
3	60	8400	15	40	14	10.53	625.00	70.91	6.7	59.3	8.8	3 min 40 s	68.05
4	60	21,600	15	80	18	10.53	312.50	55.15	5.2	29.7	5.7	17 min 51 s	77.87
5	60	43,200	15	160	18	10.53	156.25	55.15	5.2	14.8	2.8	44 min 34 s	80.19
6	60	54,000	15	200	18	10.53	125.00	55.15	5.2	11.9	2.3	57 min 51 s	80.45
<b>7*</b>	<b>60</b>	<b>64,800</b>	<b>15</b>	<b>240</b>	<b>18</b>	<b>10.53</b>	<b>104.17</b>	<b>55.15</b>	<b>5.2</b>	<b>9.9</b>	<b>1.9</b>	<b>1 h 15 min 57 s</b>	<b>80.58</b>
8	60	79,200	15	240	22	10.53	104.17	45.12	4.3	9.9	2.3	3 h 30 min 3 s	80.60
													17.978.32
													11,092.49

\*Highlighted (Bold) results corresponding to the most appropriate cocowood FE model for this study.

**TABLE 4 |** Average maxima tangential fibrovascular bundle degree of orientation ( $\theta_{max}$ ) for the studied coconut palms.

Stem height (m)	Local max/min		$\theta_{max}$	
	Average max (deg)	Average min (deg)	Average (deg)	CoV
0.2	7.14	-10.02	8.58	0.37
3.2	5.63	-6.77	6.20	0.39
6.2	4.84	-7.65	6.25	0.35
9.4	5.97	-10.07	8.02	0.29
12.4	6.45	-8.89	7.67	0.29
15.8	6.92	-10.38	8.65	0.34
18.8	7.07	-9.31	8.19	0.38
22.0	7.01	-11.30	9.15	0.35
25.0	8.75	-9.04	8.89	0.40

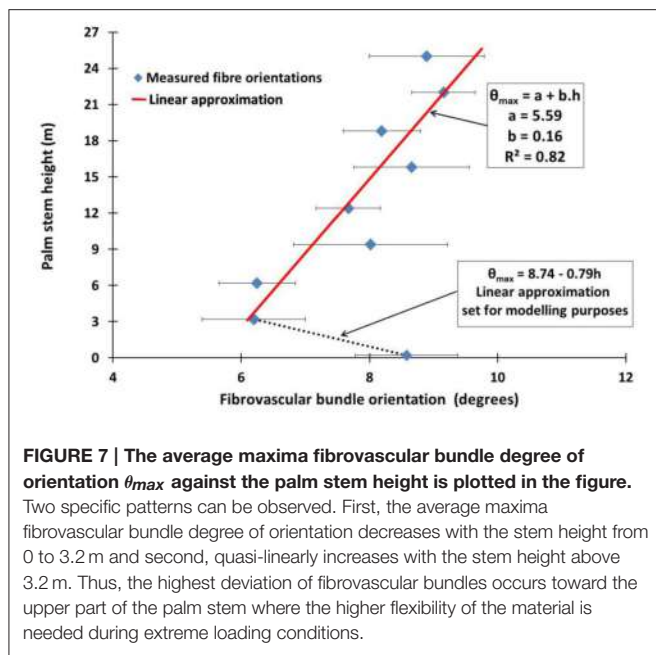
where  $\sigma_L$ ,  $\sigma_R$ , and  $\sigma_T$  (in MPa) are stresses in the  $L$ ,  $R$ , and  $T$  directions, respectively.  $MOR_L$ ,  $MOR_R$ , and  $MOR_T$  (in MPa) are the compressive strengths in the  $L$ ,  $R$ , and  $T$  directions, respectively.  $\tau_{LR}$ ,  $\tau_{RT}$ , and  $\tau_{TL}$  (in MPa) are shear stresses in the longitudinal-radial ( $LR$ ), radial-tangential ( $RT$ ), and tangential-longitudinal ( $TL$ ) planes, respectively.  $\tau_{maxLR}$ ,  $\tau_{maxRT}$ , and  $\tau_{maxTL}$  (in MPa) are the material shear strengths in the  $LR$ ,  $RT$ , and  $TL$  planes, respectively.

## RESULTS

### Tangential Fibrovascular Bundle Degree of Orientation

The results for this part of the study are based on 26,400 fibrovascular bundle degree of orientation measurements corresponding to 264 cocowood discs. Preliminary analysis showed no significant differences in the acquired global measurements between the different coconut growing sites (i.e., Fiji and Samoa). Thus, the results in this section represent the analysis of the coconut palms sourced from Fiji and Samoa islands altogether.

**Table 4** gives the average values of the local maximum and minimum fibrovascular bundle degree of orientations, as the average maxima fibrovascular bundle degree of orientation  $\theta_{max}$  at all investigated stem heights. The average maxima fibrovascular bundle degree of orientation  $\theta_{max}$  is found to vary with the palm stem height and range from a minimum degree of  $6.20^\circ$  at 3.2 m high to a maximum value of  $9.15^\circ$  at 22 m of stem height.  $\theta_{max}$  is found to be  $8.58^\circ$  at the bottom of the coconut palm stem (see **Figure 7**). Based on these observations and, as no clear correlation can be found in **Figure 7** between the measurement at the ground elevation and all subsequent measurements, two linear equations are chosen in this study to characterize the average maxima fibrovascular bundle degree of orientation  $\theta_{max}$  for senile coconut stem tissues. Note that the linear approximation that characterizes the tangential degree of orientation up to the stem height of 3.2 m, was set only for modeling and discussion purposes.  $\theta_{max}$  (in degrees) is then



expressed as function of the palm stem height  $h$  (in m) as,

$$\begin{cases} \theta_{max}(h) = 8.74 - 0.79 \times h & \text{for } h \leq 3.2 \text{ m} \\ \theta_{max}(h) = 5.59 + 0.16 \times h & \text{for } h > 3.2 \text{ m} \end{cases} \quad (9)$$

**Table 5** gives the average values of natural frequencies found at the investigated stem heights. No clear correlation between the natural frequency of the tangential fibrovascular bundle degree of orientation and the palm stem height can be found and, therefore, a unique natural frequency  $f$  of 1.45 mm/mm is considered herein for the entire palm. Thus, the proposed tangential fibrovascular bundle degree of orientation presented in **Figure 4** was calculated by using Equation (2) with inputs from Equation (3), Equation (9), and the above mentioned natural frequency  $f$ . Similarly, **Figure 8** maps the proposed tangential fibrovascular bundle degree of orientation for the whole structure of a characteristic coconut stem of 25 m in height.

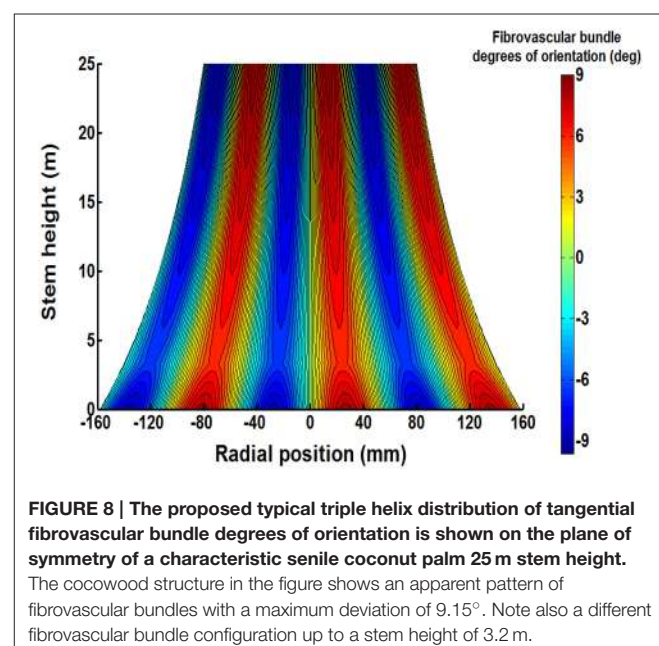
## Effects Produced by the Variation of the Tangential Fibrovascular Bundle Degrees of Orientation on the Cocowood Mechanical Performance

**Table 6** gives the results from the FEA for every variation of the average maxima fibrovascular bundle degrees of orientation ( $0^\circ$ – $51^\circ$ ) when the wind speed of 23 m/s is acting on the whole cocowood structure. **Figure 9** shows both the palm stiffness  $k$  and the maximum failure stress  $FI$ , plotted against the variation of average maxima fibrovascular bundle degrees of orientation ( $0^\circ$ – $51^\circ$ ) for the analyzed wind speed. In the main, the research findings show a significant increase in material failure index and a severe decrease of the palm bending stiffness for fibrovascular bundle degrees of orientation  $>9^\circ$ . It can also be noticed that both factors (i.e.,  $FI$  and  $k$ ) are critically

**TABLE 5 |** Average values of natural frequencies at all investigated heights and the representative natural frequency  $f$  for all the studied cocowood discs.

Stem height (m)	$f$ (mm/mm)	CoV	Total number of discs
0.2	1.49	0.208	34
3.2	1.41	0.202	28
6.2	1.53	0.159	38
9.4	1.46	0.250	26
12.4	1.53	0.175	40
15.8	1.40	0.185	29
18.8	1.41	0.263	37
22.0	1.42	0.229	15
25.0	1.29	0.267	17
Average (weighed)	<b>1.45</b>	0.215	264

*Bold result corresponding to the representative natural frequency of the whole coconut palm stem-tissue.*



reduced when the average maxima fibrovascular bundle degrees of orientation become  $\geq 33^\circ$ .

## DISCUSSION

Similar to some monocotyledonous palms (e.g., *W. robusta* palms), senile coconut palms are tall and slender with an aspect ratio (about 80) that tends to indicate excellent stability (Slodick and Novak, 2006) with a high bending capacity during strong wind conditions (Fratzl and Weinkamer, 2007). Indeed, from the acquired results it has been revealed a cocowood structure that is, from the structural mechanics point of view, stronger toward the palm stem's bottom-periphery, where the greater concentration of fibrovascular bundles were found. Interestingly,

**TABLE 6 | FEA results for the variation of  $\theta_{max}$  at the critical wind speed of 23 m/s.**

FEA no.	$\theta_{max}$ (deg)	Max FI	FI increment (%)	$F_{th}$ (kN)	$\delta_h$ (m)	$k$ (kN/m)	K drop (%)
1	0	1.021		3.036	10.046	0.302	
2	3	1.029	0.76	3.033	10.101	0.300	0.66
3	6	1.052	2.21	3.021	10.262	0.294	1.94
4	9	1.091	3.60	3.002	10.526	0.285	3.12
5	15	1.219	10.53	2.941	11.333	0.260	9.01
6	21	1.416	13.90	2.844	12.450	0.228	11.98
7	27	1.646	13.96	2.689	13.687	0.196	13.98
8	33	1.931	14.76	2.518	15.109	0.167	15.20
9	39	2.268	14.87	2.374	16.689	0.142	14.64
10	45	2.718	16.54	2.145	17.531	0.122	13.96
11	51	3.406	20.20	1.954	18.137	0.108	11.97

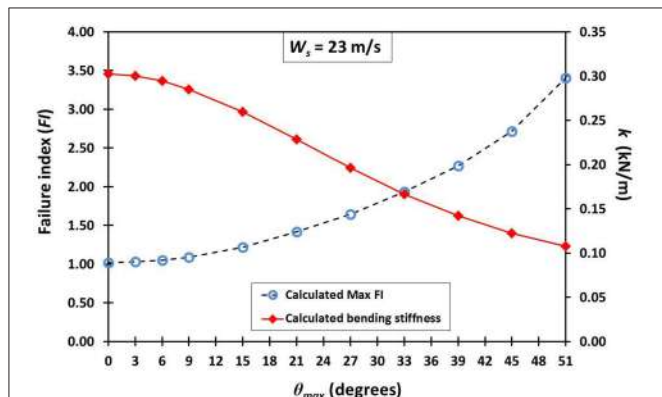


**FIGURE 9 |** An insignificant increase in material failure index FI (segmented line with blue circles) is observed for fibrovascular bundle degrees of orientation up to  $9^\circ$ . Beyond this point, the slope of the FI curve starts to drastically increase reaching a FI of about 3.5 when the angle varied to  $51^\circ$ . For the  $\theta_{max}$  of  $15^\circ$ , there is a sudden FI increment that is three times higher than the previous value at  $9^\circ$ . Similarly, the palm bending stiffness  $k$  (red line with rhombi) is sharply reduced by nearly three times from  $9^\circ$  to  $15^\circ$ . The identified trends become higher and lower, respectively, for the greater values of  $\theta_{max}$ .

the cocowood structure at the stem's top part close to the leaves has the minimum diameter and is the least dense part of the stem with the highest deviation of fibrovascular bundles, which structurally means it is the most flexible part of the whole structure. This strategy may likely permit the palm stem to better bend or efface itself under high wind conditions with the leaves streamline effect offering a very low resistance to wind pressure. Yet, it is a hypothesis that might be proved by future studies.

The calculated average maxima fibrovascular bundle degree of orientation at the bottom part of the stem (see Figure 7) markedly differs from those for the higher elevations. It clearly reflects a different configuration of the cocowood fibrovascular tissue system at this section of the palm stem. This occurs due to the transition between the stem-tissue and root systems,

both having structurally and functionally different configurations (Niklas, 1992). For modeling purposes, these properties have been represented in this study by simple linear equations that match the dissimilar property regions. However, the atypical pattern found close to the bottom of the palm stem needs further investigation, likely from a different approach (e.g., microscopic), in order to accurately depict the structure at this region of the coconut stem.

Note that the average maxima fibrovascular bundle degree of orientation  $\theta_{max}$  of  $8.58^\circ$  was found in this study at the bottom of the characteristic senile coconut palm stem whereas the  $\theta_{max}$  of  $12^\circ$  was reported by Kuo-Huang et al. (2004) for juvenile palms ( $6\text{ m}$  high) at the same stem location. It can be inferred that tangential fibrovascular bundles likely become less deviated in senile cocowood due to the structural adaptation process experienced as coconut palm stems grow taller and have to resist higher external loading conditions; a common phenomenon in plant species (Zhang et al., 2012).

The cocowood mechanical response observed when varying the degrees of orientation of fibrovascular bundles has in principle (i.e., the greater the fiber orientation, the inferior the tree stem mechanical response, and vice versa) some similarity to that of hardwoods and softwoods. For example, the woody stem spiral configuration of the southern Utah's Ponderosa pine (*Pinus ponderosa*) species was studied by Leelavanichkul and Cherkav (2004) to determine the influence of fiber orientations (varying from  $21.2^\circ$  to  $90^\circ$ ) on the trunk strength under three progressive wind forces expressed in terms of bending moments ( $2.26$ ,  $22.59$ , and  $90.39\text{ kN}\cdot\text{m}$ ). The results showed that the Ponderosa pine trunk failed when the critical fiber angle was set at  $37^\circ$ . The critical average maxima fibrovascular bundle degree of orientation of  $33^\circ$  was found herein. The reason of such similar findings may have its foundations on (i) the similar fibrovascular-cellular structure (i.e., an assembly of prismatic or polyhedral cells with solid edges and faces packed together to fill space; Gibson, 2005) that both cellular solids (i.e., woody plants and palmwoods) have in common, and (ii) the related mechanical characteristics that are mutual for tree stems in order to support static and dynamic loads, store and release elastic energy, bend through large angles, and resist buckling and fracture.

When the fibrovascular bundle degrees of orientation varied between  $0^\circ$  and  $9^\circ$ , a superior cocowood biomechanical response was identified in terms of the stem bending stiffness and the material capacity to undergo failure due to generated stresses and strengths. Average maxima fibrovascular bundle degrees of orientation beyond this limit ( $\theta_{max}$  of  $9^\circ$ ) significantly reduced the palm bending stiffness and weakened its compressive strength with a consequent increase in material failure (FI). Thus, a  $\theta_{max} = 9^\circ$  is identified as the maximal fibrovascular bundle degree of orientation, defined in Leelavanichkul and Cherkav (2004) as the maximum fiber angle that does not substantially reduce/weaken the stiffness and strength of a tree. It can thus be concluded that senile cocowood fibrovascular tissue systems are optimally arranged complex structures, partially because of the typical variation of average maxima fibrovascular bundle degrees of orientation (i.e.,  $6.2^\circ$  to  $9.1^\circ$ ) that was found herein

to be within the limits of the *maximal* fibrovascular bundle degree of orientation defined above. Where nature has already optimized the structure of a living organism, it is assumed there must be a reason for it. In fact, what has been observed in the current analysis is not just a random causality of the biomechanical behavior produced by the cocowood fibrovascular tissue system; on the contrary, it is without doubt, a phenomenon that reflects an optimized cocowood fibrovascular development resulting from the natural adaptation of the material to resist varying conditions of external forces [e.g., gravity (biomass), wind, and rain water], during the course of millions of years of evolution. Wind forces, for example, become critical as trees age and grow taller, particularly because, during high wind episodes, the forces induced on the stems, foliage, and roots can reach critical bounds. If surpassed, these forces will result in failure. Further, while strong winds may occur only a few times in a tree's life, its resistance capability to overturning or breaking during these extreme weather conditions is critical to its survival (Vogel, 1989, 1996).

The acquired results in this study evidenced an efficient cocowood fibrovascular tissue system that highlighted its optimal local design in terms of the tangential deviation of the axial fibrovascular bundles. The present analyses significantly advanced the understanding of the cocowood fibrovascular tissue system and, concomitantly, of the monocotyledonous palms. The research findings have a significant future potential for innovative material/structure concepts; e.g., the representative cocowood fibrovascular bundle degrees of orientation proposed herein may serve as a biomimetic inspiration to produce

superior engineered wood products (EWPs) such as coconut fiber reinforced polyethylene composites (Brahmakumar et al., 2005) and/or spirally wood-laminated composite poles (Piao et al., 2008; Berard et al., 2011). Yet, further research from a multidisciplinary approach should be carried out to reveal other properties and underlying principles of the biomaterial at the macroscopic, microscopic, ultrastructural, and biochemical levels of hierarchical structure. Such studies would also improve our understanding of the cocowood fibrovascular development; a system that has evolved in accordance with engineering principles long before these principles were known.

## AUTHOR CONTRIBUTIONS

Dr. OG performed the measurements and analyses, derived the equations, drew the figures, and wrote the paper. Dr. KN supervised the work, reviewed the analyses, and wrote the paper.

## ACKNOWLEDGMENTS

The authors gratefully acknowledge the constructive comments on this paper offered by Professor Luis Cumbal, Professor Jorge Zuñiga (Universidad de las Fuerzas Armadas ESPE—Ecuador) and Dr. Hongyu Qin (Griffith University—Australia). The authors would like to also thank the Department of Agriculture and Fisheries (DAF), Queensland Government, for supplying the material and data collected during the ACIAR project, FST/2004/054 and Universidad de las Fuerzas Armadas ESPE in Ecuador for funding us to publish this paper.

## REFERENCES

- AS/NZS 1170.2 (2011). *Structural Design Actions, Part 2: Wind Actions*. Australian/New Zealand Standard.
- AS/NZS 4676 (2000). *Structural Design Requirements for Utility Services Poles*. Australian/New Zealand Standard.
- Bahtiar, E., Nugroho, N., and Surjokusumo, S. (2010). Estimating Young's modulus and modulus of rupture of coconut logs using reconstruction method. *Civil Eng. Dimens.* 12, 65–72. doi: 10.9744/ced.12.2.65-72
- Berard, P., Yang, P., Yamauchi, H., Umemura, K., and Kawai, S. (2011). Modeling of a cylindrical laminated veneer lumber I: mechanical properties of hinoki (*Chamaecyparis obtusa*) and the reliability of a nonlinear finite elements model of a four-point bending test. *J. Wood Sci.* 57, 100–106. doi: 10.1007/s10086-010-1150-1
- Brahmakumar, M., Pavithran, C., and Pillai, R. (2005). Coconut fibre reinforced polyethylene composites: effect of natural waxy surface layer of the fibre on fibre/matrix interfacial bonding and strength of composites. *Compos. Sci. Technol.* 65, 563–569. doi: 10.1016/j.compscitech.2004.09.020
- Butterfield, B. G., Meylan, B. A., and Peszlen, I. M. (1997). *Three Dimensional Structure of Wood*. London: Chapman and Hall Ltd.
- Cabrero, J., and Gebremedhin, K. (2010). "Evaluation of failure criteria in wood members" in *Electronic Proceedings of the World Conference on Timber Engineering (WCTE2010)* (Trentino).
- Cullen, S. (2002). Trees and wind: wind scales and speeds. *J. Arboricul.* 28, 237–242.
- De Mirbel, C. (1843). Recherches anatomiques et physiologiques sur quelques végétaux monocotylédones. *C. R. Paris* 19, 689–695.
- Fathi, L., and Frühwald, A. (2014). The role of vascular bundles on the mechanical properties of coconut palm wood. *Wood Mater. Sci. Eng.* 9, 214–223. doi: 10.1080/17480272.2014.887774
- Fathi, L., Frühwald, A., and Koch, G. (2014). Distribution of lignin in vascular bundles of coconut wood (*Cocos nucifera*) by cellular UV-spectroscopy and relationship between lignification and tensile strength in single vascular bundles. *Holzforschung* 68, 915–925. doi: 10.1515/hf-2013-0213
- Fratzl, P., and Weinkamer, R. (2007). Nature's hierarchical materials. *Prog. Mater. Sci.* 52, 1263–1334. doi: 10.1016/j.pmatsci.2007.06.001
- Gibson, L. J. (2005). Biomechanics of cellular solids. *J. Biomech.* 38, 377–399. doi: 10.1016/j.jbiomech.2004.09.027
- Gibson, L. J. (2012). The hierarchical structure and mechanics of plant materials. *J. R. Soc. Interface* 9, 2749–2766. doi: 10.1098/rsif.2012.0341
- Gonzalez, O. M. (2015). *An Engineering Approach to Understand Senile Coconut Palms as Foundation for Biomimetic Applications*. Ph.D. thesis, Griffith School of Engineering, Griffith University, Gold Coast Campus, Australia.
- Gonzalez, O. M., Gilbert, B. P., Bailleres, H., and Guan, H. (2014). "Compressive strength and stiffness of senile coconut palms stem green tissue," in *Proceedings of the 23rd Australasian Conference on the Mechanics of Structures and Materials (ACMSM23)*, Southern Cross University, Byron Bay (Byron Bay, NSW), 881–886.
- Gonzalez, O. M., Gilbert, B. P., Bailleres, H., and Guan, H. (2015). "Shear mechanical properties of senile coconut palms at stem green tissue," in *Proceedings of the 4th International Conference on Natural Sciences and Engineering (2015ICNSE)*, Higher Education Forum, Kyoto Research Park, Japan (Kyoto), 529–543.
- Hull, D., and Clyne, T. (1996). *An Introduction to Composite Materials*. New York, NY: Cambridge University Press.
- Jones, R. M. (1999). *Mechanics of Composite Materials*. Philadelphia, PA: Taylor & Francis, Inc.
- Killmann, W., and Fink, D. (1996). *Coconut Palm Stem Processing. A Technical Handbook*. Eschborn: Protrade, GTZ.

- Kuo-Huang, L. L., Huang, Y. S., Chen, S. S., Huang, Y. R. (2004). Growth stresses and related anatomical characteristics in coconut palm trees. *IAWA J.* 25, 297–310. doi: 10.1163/22941932-90000367
- Leelavanichkul, S., and Cherkaev, A. (2004). Why the grain in tree trunks spirals: a mechanical perspective. *Struct. Multidiscipl. Optim.* 28, 127–135. doi: 10.1007/s00158-003-0311-x
- Mayhead, G. (1973). Some drag coefficients for British forest trees derived from wind tunnel studies. *Agric. Meteorol.* 12, 123–130. doi: 10.1016/0002-1571(73)90013-7
- Meneghini, G. (1836). *Ricerche Sulla Struttura del Caule Nelle Piante Monocotiledoni*. Padua: Minerva.
- Niklas, K. J. (1992). *Plant Biomechanics: An Engineering Approach to Plant Form and Function*. Chicago, IL: University of Chicago Press.
- Piao, C., Shupe, T. F., Tang, R., and Hse, C. Y. (2008). Finite element modeling of small-scale tapered wood-laminated composite poles with biomimicry features. *Wood Fiber Sci.* 40, 3–13.
- Rao, G. V. G., Mahajan, P., and Bhatnagar, N. (2008). Three-dimensional macro-mechanical finite element model for machining of unidirectional-fiber reinforced polymer composites. *Mater. Sci. Eng. A* 498, 142–149. doi: 10.1016/j.msea.2007.11.157
- Rich, P. M. (1986). Mechanical architecture of arborescent rain forest palms. *Principes* 30, 117–131.
- Rich, P. M. (1987). Mechanical structure of the stem of arborescent palms. *Bot. Gaz.* 148, 42–50. doi: 10.1086/337626
- Rich, P. M., Holbrook, N. M., and Luttinger, N. (1995). Leaf development and crown geometry of two *Iriarteoid* palms. *Am. J. Bot.* 82, 328–336. doi: 10.2307/2445578
- Rudnicki, M., Mitchell, S. J., and Novak, M. D. (2004). Wind tunnel measurements of crown streamlining and drag relationships for three conifer species. *Can. J. For. Res.* 34, 666–676. doi: 10.1139/x03-233
- Rüggeberg, M., Speck, T., and Burgert, I. (2009). Structure–function relationships of different vascular bundle types in the stem of the Mexican fanpalm (*Washingtonia robusta*). *New Phytol.* 182, 443–450. doi: 10.1111/j.1469-8137.2008.02759.x
- Rüggeberg, M., Speck, T., Paris, O., Lapierre, C., Pollet, B., Koch, G., et al. (2008). Stiffness gradients in vascular bundles of the palm *Washingtonia robusta*. *Proc. R. Soc. B Biol. Sci.* 275, 2221–2229. doi: 10.1098/rspb.2008.0531
- Slodicka, M., and Novak, J. (2006). Silvicultural measures to increase the mechanical stability of pure secondary Norway spruce stands before conversion. *For. Ecol. Manage.* 224, 252–257. doi: 10.1016/j.foreco.2005.12.037
- Speck, T., and Burgert, I. (2011). Plant stems: functional design and mechanics. *Annu. Rev. Mater. Res.* 41, 169–193. doi: 10.1146/annurev-matsci-062910-100425
- Strand7 (2005). *Theoretical Manual: Theoretical Background to the Strand7 Finite Element Analysis System*. Sydney, NSW: Strand7 Pty Limited.
- Sudo, S. (1980). Some anatomical properties and density of the stem of coconut palm (*Cocos nucifera*), with consideration for pulp quality. *IAWA Bull.* 1, 161–171. doi: 10.1163/22941932-90000716
- Thomas, R., and De Franceschi, D. (2013). Palm stem anatomy and computer-aided identification: the Coryphoideae (Arecaceae). *Am. J. Bot.* 100, 289–313. doi: 10.3732/ajb.1200242
- Tomlinson, P. B. (1990). *The Structural Biology of Palms*. New York, NY: Oxford University Press.
- Tomlinson, P. B. (2006). The uniqueness of palms. *Bot. J. Linn. Soc.* 151, 5–14. doi: 10.1111/j.1095-8339.2006.00520.x
- Tomlinson, P. B., Fisher, J. B., Spangler, R. E., and Richer, R. A. (2001). Stem vascular architecture in the rattan palm Calamus (Arecaceae-Calamoideae-Calaminae). *Am. J. Bot.* 88, 797–809. doi: 10.2307/2657032
- Tomlinson, P. B., Horn, J. W., and Fisher, J. B. (2011). *The Anatomy of Palms: Arecaceae-Palmae*. Oxford, UK: Oxford University Press.
- Tomlinson, P. B., Forest, H., and Petersham, M. (1984). *Contemporary Problems in Plant Anatomy - Development of the Stem Conducting Tissues in Monocotyledons*. New York, NY: Academic Press.
- Ugural, A. C. (2008). *Mechanics of Materials*. Newark, NJ; Hoboken, NJ: New Jersey Institute of Technology; John Wiley & Sons Inc.
- Vogel, S. (1989). Drag and reconfiguration of broad leaves in high winds. *J. Exp. Bot.* 40, 941–948. doi: 10.1093/jxb/40.8.941
- Vogel, S. (1996). Blowing in the wind: storm-resisting features of the design of trees. *J. Arboricul.* 22, 92–98.
- Vollsinger, S., Mitchell, S. J., Byrne, K. E., Novak, M. D., and Rudnicki, M. (2005). Wind tunnel measurements of crown streamlining and drag relationships for several hardwood species. *Can. J. For. Res.* 35, 1238–1249. doi: 10.1139/x05-051
- Winter David, P. A. (1997). *Signal Processing and Linear Systems for the Movement Sciences*. Waterloo, ON: University of Waterloo.
- Zhang, Y., Yao, H., Ortiz, C., Xu, J., and Dao, M. (2012). Bio-inspired interfacial strengthening strategy through geometrically interlocking designs. *J. Mech. Behav. Biomed. Mater.* 15, 70–77. doi: 10.1016/j.jmbbm.2012.07.006
- Zimmermann, M. H., and Tomlinson, P. B. (1972). The vascular system of monocotyledonous stems. *Bot. Gaz.* 133, 141–155. doi: 10.1086/336628

**Conflict of Interest Statement:** The authors declare that the research was conducted in the absence of any commercial or financial relationships that could be construed as a potential conflict of interest.

Copyright © 2016 González and Nguyen. This is an open-access article distributed under the terms of the Creative Commons Attribution License (CC BY). The use, distribution or reproduction in other forums is permitted, provided the original author(s) or licensor are credited and that the original publication in this journal is cited, in accordance with accepted academic practice. No use, distribution or reproduction is permitted which does not comply with these terms.



# Analysis of Network Topologies Underlying Ethylene Growth Response Kinetics

Aaron M. Prescott<sup>1</sup>, Forest W. McCollough<sup>2</sup>, Bryan L. Eldreth<sup>1</sup>, Brad M. Binder<sup>2\*</sup> and Steven M. Abel<sup>1,3\*</sup>

<sup>1</sup> Department of Chemical and Biomolecular Engineering, University of Tennessee, Knoxville, TN, USA, <sup>2</sup> Department of Biochemistry and Cellular and Molecular Biology, University of Tennessee, Knoxville, TN, USA, <sup>3</sup> National Institute for Mathematical and Biological Synthesis, University of Tennessee, Knoxville, TN, USA

## OPEN ACCESS

### Edited by:

Daniel H. Chitwood,  
Donald Danforth Plant Science Center,  
USA

### Reviewed by:

Tsu-Wei Chen,  
Leibniz University of Hanover,  
Germany  
Ashok Prasad,  
Colorado State University, USA

### \*Correspondence:

Brad M. Binder  
[bbinder@utk.edu](mailto:bbinder@utk.edu)  
Steven M. Abel  
[abel@utk.edu](mailto:abel@utk.edu)

### Specialty section:

This article was submitted to  
Plant Biophysics and Modeling,  
a section of the journal  
Frontiers in Plant Science

Received: 25 June 2016

Accepted: 16 August 2016

Published: 30 August 2016

### Citation:

Prescott AM, McCollough FW, Eldreth BL, Binder BM and Abel SM (2016) Analysis of Network Topologies Underlying Ethylene Growth Response Kinetics. *Front. Plant Sci.* 7:1308.  
doi: 10.3389/fpls.2016.01308

Most models for ethylene signaling involve a linear pathway. However, measurements of seedling growth kinetics when ethylene is applied and removed have resulted in more complex network models that include coherent feedforward, negative feedback, and positive feedback motifs. The dynamical responses of the proposed networks have not been explored in a quantitative manner. Here, we explore (i) whether any of the proposed models are capable of producing growth-response behaviors consistent with experimental observations and (ii) what mechanistic roles various parts of the network topologies play in ethylene signaling. To address this, we used computational methods to explore two general network topologies: The first contains a coherent feedforward loop that inhibits growth and a negative feedback from growth onto itself (CFF/NFB). In the second, ethylene promotes the cleavage of EIN2, with the product of the cleavage inhibiting growth and promoting the production of EIN2 through a positive feedback loop (PFB). Since few network parameters for ethylene signaling are known in detail, we used an evolutionary algorithm to explore sets of parameters that produce behaviors similar to experimental growth response kinetics of both wildtype and mutant seedlings. We generated a library of parameter sets by independently running the evolutionary algorithm many times. Both network topologies produce behavior consistent with experimental observations, and analysis of the parameter sets allows us to identify important network interactions and parameter constraints. We additionally screened these parameter sets for growth recovery in the presence of sub-saturating ethylene doses, which is an experimentally-observed property that emerges in some of the evolved parameter sets. Finally, we probed simplified networks maintaining key features of the CFF/NFB and PFB topologies. From this, we verified observations drawn from the larger networks about mechanisms underlying ethylene signaling. Analysis of each network topology results in predictions about changes that occur in network components that can be experimentally tested to give insights into which, if either, network underlies ethylene responses.

**Keywords:** ethylene, signal transduction, network topologies, computational modeling, evolutionary algorithm

## 1. INTRODUCTION

Ethylene is the simplest of olefin gases and functions as a plant hormone, affecting many processes throughout the lifetime of a plant including seed germination, growth, formation of the apical hook, senescence, fruit ripening, abscission, and responses to various stresses (Mattoo and Suttle, 1991; Abeles et al., 1992). Ethylene inhibits the growth of dark-grown eudicot seedlings (Abeles et al., 1992), and sustained exposure to ethylene leads to a growth-inhibition response that has been used to screen for mutants and to provide information about the ethylene signaling network (Bleecker et al., 1988; Guzman and Ecker, 1990). Most proposed models of ethylene signaling consist of a linear pathway (**Figure 1**), where in air, ethylene receptors signal to the CONSTITUTIVE RESPONSE1 (CTR1) protein kinase which functions as a negative regulator of ethylene signaling (Kieber et al., 1993). CTR1 prevents ethylene signaling by phosphorylating the ETHYLENE INSENSITIVE2 (EIN2) protein, leading to its ubiquitination and proteolysis (Chen et al., 2011; Ju et al., 2012; Qiao et al., 2012). The binding of ethylene to ethylene receptors reduces the activity of the receptors, leading to reduced activity of CTR1 kinase and reduced phosphorylation of EIN2 protein (Chen et al., 2011; Ju et al., 2012; Qiao et al., 2012). The reduction in EIN2 phosphorylation leads to a decrease in ubiquitination of EIN2, causing a rise in EIN2 protein levels and allowing for proteolytic release of the C-terminal portion (EIN2-C) of the protein (Qiao et al., 2009; Ju et al., 2012; Qiao et al., 2012; Wen et al., 2012). EIN2-C affects the levels of two transcription factors, EIN3 and EIN3-Like1 (EIL1), in part by regulating their ubiquitination via S-PHASE KINASE-ASSOCIATED1-CULLIN-F-BOX (SCF) ubiquitin ligase complexes containing EIN3-BINDING F-BOX1 and 2 (EBF1 and 2) F-box proteins (Guo and Ecker, 2003; Potuschak et al., 2003; Yanagisawa et al., 2003; Gagne et al., 2004; Binder et al., 2007; An et al., 2010). In the presence of ethylene, ubiquitination of EIN3 and EIL1 is reduced, leading to accumulation of these transcription factors causing most ethylene responses (Guo and Ecker, 2003; Potuschak et al., 2003; Yanagisawa et al., 2003; Binder et al., 2004a, 2007; Gagne et al., 2004; An et al., 2010).

The above model was developed based on end-point analyses. Even though end-point analysis of ethylene responses continues to be an instructive bioassay, it is limited because transient events are overlooked. Time-lapse imaging has provided information about the kinetics of ethylene growth responses. The kinetics of ethylene responses have been studied for several plant species (Laan, 1934; Warner and Leopold, 1971; Burg, 1973; Goeschl and Kays, 1975; Rauser and Horton, 1975; Jackson, 1983) and most extensively studied in the model flowering plant, *Arabidopsis thaliana* (Binder et al., 2004a,b; Potuschak et al., 2006; Binder et al., 2007; Gao et al., 2008; Christians et al., 2009;

Vandenbussche et al., 2010; van Zanten et al., 2010; Žádníková et al., 2010; Kim et al., 2011, 2012; McDaniel and Binder, 2012; Bakshi et al., 2015; Merchant et al., 2015; Rai et al., 2015).

Studies of ethylene growth kinetics in *Arabidopsis* have revealed two phases of growth inhibition at saturating ethylene levels (1 ppm or above, see **Figure 2A**) (Binder et al., 2004b). The first phase is rapid, with a decrease in growth rate beginning approximately 10 min after the application of ethylene and lasting approximately 10 min, at which point the growth rate reaches a plateau. This plateau lasts approximately 30 min when a second, slower phase of growth inhibition is observed. Approximately 90 min after the application of ethylene, the growth rate reaches a minimum that lasts for as long as saturating levels of ethylene are present. If ethylene is removed after 2 h, seedlings recover to pre-treatment growth rates in approximately 90 min (**Figure 2A**).

The two phases of growth inhibition are genetically separable (Binder et al., 2004a). Mutants lacking EIN3 and EIL1 (*ein3;eil1*) have a normal first phase of growth inhibition but fail to have a second phase response and over time return to pre-treatment growth rates in the continued presence of ethylene (**Figure 2B**). This demonstrates that the first phase of growth inhibition is EIN3/EIL1-independent. Mutants lacking EIN2 (*ein2*) have no response to ethylene. Additionally, in wild type plants, adaptation is observed at sub-saturating levels of ethylene. At intermediate to high sub-saturating levels (e.g., 100 ppb), seedlings initially show both phases of growth inhibition but then have a partial recovery to an intermediate growth rate. At lower levels of ethylene (e.g., 2 and 10 ppb), only the first phase of growth inhibition occurs and is followed by recovery of the growth rate (**Figure 2C**) (Binder et al., 2004a).

The experiments described above and other observations that indicate possible alternative pathways and feedback control (Kieber et al., 1993; Roman et al., 1995; Larsen and Chang, 2001; Hall and Bleecker, 2003; Qiu et al., 2012; Rai et al., 2015) suggest that ethylene signal transduction is not simply a linear pathway. Several network models have been proposed that involve more complicated topologies (Binder et al., 2004a; Gao et al., 2008; Kim et al., 2012). These and related networks are the focus of this paper.

A study comparing the time-dependent growth responses of several plant species led to a proposed network that included both coherent feedforward and negative feedback (CFF/NFB) signaling motifs (**Figure 3A**; Kim et al., 2012). In the CFF/NFB model, in air (i.e., without ethylene) the receptors signal to CTR1, which in turn inhibits downstream signaling. This leads to fast growth with feedback on growth occurring via the modulation of gibberellin (GA), a hormone known to stimulate growth. Application of ethylene inhibits the receptors, leading to a reduction of CTR1 activity and hence an increase in EIN2 levels. EIN2 is predicted to cause an initial growth inhibition response



**FIGURE 1 |** Basic linear ethylene signaling network.

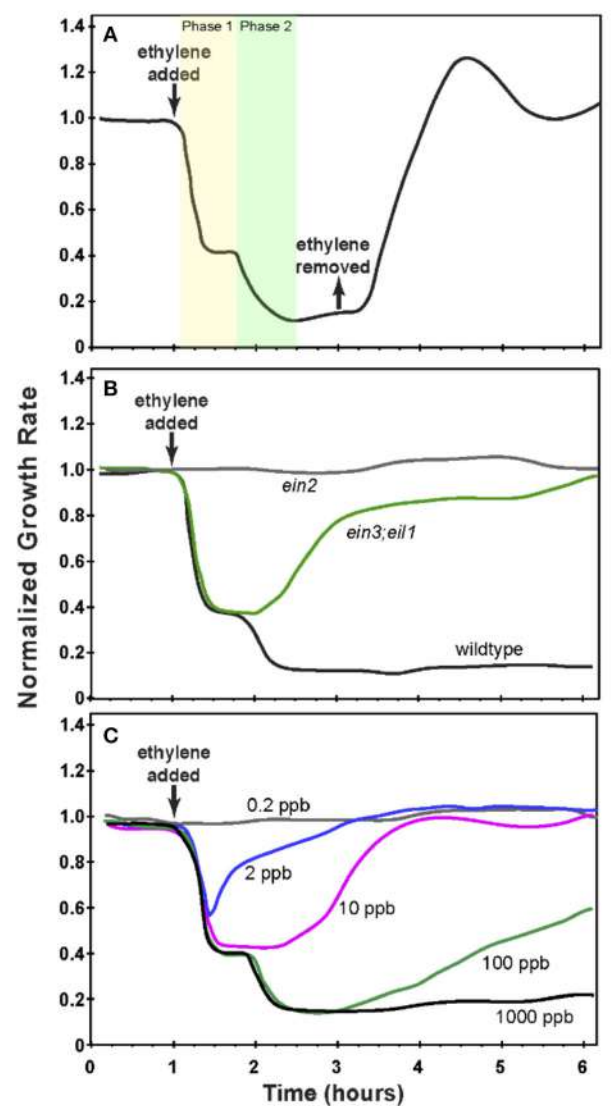


**FIGURE 2 |** Growth response kinetics of dark-grown *Arabidopsis* seedling hypocotyls. **(A)** The normalized growth rate of wildtype *Arabidopsis*. Seedlings were grown in air for 1 h at which time 10 ppm ethylene was applied for 2 h at which time ethylene-free air was used to replace the ethylene. **(B)** The normalized growth rate of wildtype *Arabidopsis* compared to *ein3;eil1* and *ein2* mutants. Seedlings were grown in air for 1 h at which time 10 ppm ethylene was applied. **(C)** The normalized growth rate of wildtype *Arabidopsis* treated with varying concentrations of ethylene as indicated. Seedlings were grown in air for 1 h prior to application of ethylene. In all panels, the growth rate was normalized to the growth rate in air prior to treatment with ethylene. Based on data from Binder et al. (2004a,b).

independently of EIN3 and EIL1. EIN2 also inhibits the EBF1 and EBF2 F-box proteins, leading to increases in EIN3 and EIL1. In the CFF/NFB network model, EIN3 and EIL1 inhibit growth via a GA-dependent and GA-independent pathway. The indirect inhibition of growth from EIN2 through EIN3 and EIL1 is hypothesized to be responsible for the second phase of growth inhibition. Qualitatively, this network topology provides a framework to understand the molecular basis for phase 1 and

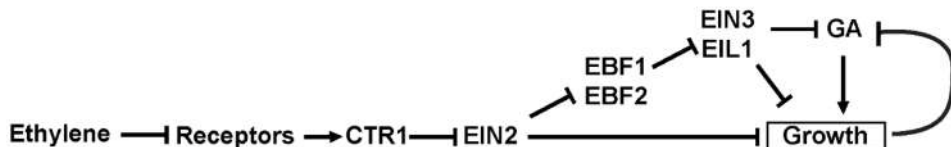
phase 2 growth inhibition and its regulation by the coherent feedforward signal. It also provides a mechanism for transient growth inhibition in the absence of EIN3 and EIL1 that is regulated by negative feedback components.

We were curious to determine whether other network topologies would yield response kinetics similar to experiments. We previously proposed a model where one function of EIN3 and EIL1 is to provide feedback to regulate growth (Binder et al., 2004a). More recent data has shown that ethylene signaling requires the accumulation of EIN2 followed by the proteolytic cleavage of the EIN2 C-terminal tail (Alonso et al., 1999; Ju et al., 2012; Qiao et al., 2012; Wen et al., 2012). This accumulation of EIN2 protein is reduced in *ein3;eil1* double mutants (Qiao et al., 2009) suggesting a mechanism for feedback by EIN3 and EIL1. We therefore developed a network topology where the function of EIN3 and EIL1 is to provide feedback stimulation in the form of increased synthesis of EIN2 (Figure 3B). EIN2-C feeds back through EBF1/2 and EIN3 to promote EIN2. Without accumulation of EIN2, the prediction is that the levels of EIN2-C would decrease, resulting in growth reversal. We refer to this network as the cleavage with positive feedback (PFB) network.

Few computational models of ethylene signaling have been published (Díaz and Álvarez-Buylla, 2006; Díaz and Alvarez-Buylla, 2009), and none take into account the dynamical information obtained from kinetic studies of ethylene response. Considering experimental results of this nature provides an opportunity to identify network features underlying the observed growth responses. Therefore, we developed computational models that account for proposed interactions within the CFF/NFB and PFB networks described above. These networks are modeled as sets of coupled ordinary differential equations (ODEs) describing the time evolution of network components. We are interested in (i) whether the proposed networks are capable of producing dynamical growth-response behavior consistent with experiments, and (ii) mechanisms underlying the network response when it does recapitulate experimental results. The CFF/NFB and PFB networks we consider have relatively high-dimensional parameter spaces (35 and 26 parameters, respectively). The parameters regulate numerous coupled, nonlinear ODEs describing the dynamics of the network, and changing the value of one parameter can have unexpected effects on network responses. Few *in vivo* measurements of network parameters are available. As such, we used an evolutionary algorithm (EA) to search for sets of parameters that produce network behavior consistent with experimental growth response kinetics. EAs are a class of numerical optimization techniques and have been used to investigate networks in a variety of biochemical applications (Bäck and Schwefel, 1993; Bray and Lay, 1994; François and Hakim, 2004; Patil et al., 2005; Auliac et al., 2008; Sun et al., 2012; Spirov and Holloway, 2013; Feng et al., 2015). For example, time-course data has been used to determine parameters of small genetic networks (Kikuchi et al., 2003) and parameters associated with signal transduction in neurons (Arisi et al., 2006).

We used an EA to evolve parameter sets that produce ethylene growth responses similar to those observed in experiments. In particular, we focused on evolving two-phase growth

### A Coherent Feedforward Loop with Negative Feedback (CFF/NFB)



### B EIN2 Cleavage with Positive Feedback (PFB)

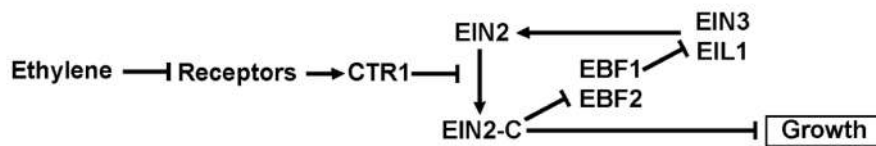


**FIGURE 3 |** Diagrams illustrating proposed network topologies.

inhibition (2-PGI) and *ein3;eil1* mutant partial growth recovery (MPGR). By repeatedly performing independent runs of our EA, we created libraries of evolved parameter sets. We gain insight into mechanisms underlying network responses by analyzing the dynamics of individual network components and the distributions of parameters governing the network. We additionally screen the parameter sets for partial growth recovery in the presence of sub-saturating ethylene doses, which is a property that emerges in some of the evolved parameter sets. We further explore each network by identifying simplified networks producing both 2-PGI and MPGR.

## 2. METHODS

### 2.1. Kinetics of the Ethylene Response Network

We model the ethylene growth-response networks proposed above using systems of coupled ordinary differential equations (ODEs). Ethylene concentration is treated as an input variable that is varied to mimic experimental conditions. We treat the growth rate, denoted by [Growth], as a concentration-like variable that measures the fraction of maximal growth rate. The unbound ethylene receptor concentration is described by a production term and a mass-action binding term representing ethylene binding. The time-dependence of all other components is described by production and degradation terms. As an example, the ODE describing CTR1 dynamics is written

$$\frac{d[CTR1]}{dt} = \left( k_{prod} \frac{[R]^N}{K_{prod}^N + [R]^N} \right)_R (1 - [CTR1]) - k_{degr}^{CTR1} [CTR1]$$

Concentrations are denoted by square brackets,  $k$  denotes a reaction rate,  $K$  denotes an activation coefficient in a

Hill equation, and  $N$  is the associated Hill coefficient. All concentrations are restricted to the range of 0 to 1 and can be interpreted as the fraction of the maximum concentration for each species. The concentration range is constrained by describing the production as a logistic production term, with production vanishing when the concentration approaches 1. Interactions between network components are described with Hill-like kinetics. For example, in the above equation, CTR1 is promoted by receptors ( $R$ ), which is captured by the Hill equation in the production term on the right-hand side. Inhibitory interactions promote the rate of degradation (e.g., EBF increases the degradation rate of EIN3 and EIL1). Stimulatory interactions promote the rate of production. The complete sets of ODEs for the networks studied are included in the Supplementary Material. We initially equilibrate the system with no ethylene present, allowing it to reach steady state. We then introduce a step-change in ethylene to mimic experimental conditions. We treat EIN3 and EIL1 as a single entity, and therefore, to model the *ein3;eil1* mutant, the production rate for EIN3 is set equal to zero.

### 2.2. Evolutionary Algorithm

Given the system of ODEs describing network dynamics, we use an evolutionary algorithm (EA) to identify sets of parameters that produce growth-response behavior similar to that observed experimentally. EAs are a class of optimization techniques that utilize the principle of inherited fitness to optimize parameters. A population of parameter sets is evolved over multiple generations. At each generation, each parameter set is evaluated by a fitness function and ranked by its fitness. Parameter sets with better rankings are modified in order to produce a new population of parameter sets for evaluation. The modifications consist of mutation and crossover operations. Mutations change a parameter value within a set to a new, randomly sampled value. Crossovers are events in which subsets from two high-performing parameter sets are recombined to form a new parameter set. Details of the mutations and crossovers depend on

the specific implementation of the EA. Each iteration in which the population of parameter sets is updated is termed a generation.

We used the following fitness function for all proposed ethylene signaling networks:

$$\text{fitness} = \sum_{i=1}^{N_{\text{wt}}} \alpha_i ([\text{Growth}]_{\text{calc}}(t_i) - [\text{Growth}]_{\text{targ}}(t_i))_{\text{wt}}^2 + \sum_{i=1}^{N_{\text{mt}}} \beta_i ([\text{Growth}]_{\text{calc}}(t_i) - [\text{Growth}]_{\text{targ}}(t_i))_{\text{mt}}^2$$

Calculated growth values ( $[\text{Growth}]_{\text{calc}}(t_i)$ ) are determined by numerically solving the system of ODEs in MATLAB using the ode45 numerical solver. Target values ( $[\text{Growth}]_{\text{targ}}(t_i)$ ) were obtained using experimentally-determined growth rates at select times (Figures 2A,B). Target values were selected from wildtype (wt) and *ein3;eil1* mutant (mt) experiments, with the index  $i$  in each sum indexing the target values (there are  $N_{\text{wt}}$  target values for the wildtype response and  $N_{\text{mt}}$  target values for the mutant response). For each time point, the squared deviation of the calculated growth rate from the target value is multiplied by a weighting factor ( $\alpha_i$ ,  $\beta_i$ ) that emphasizes important regimes of the growth response. Specifically, we emphasize pre-ethylene steady state values, the wildtype two-phase growth inhibition response, minimal growth rate following ethylene introduction, and maximum growth recovery levels. Target values and weighting factors are provided in Supplemental Tables 2.1.1, 2.1.2. Target growth rates were scaled by dividing all experimental growth rates by the maximum observed growth rate under both wildtype and mutant conditions. This gives a pre-ethylene growth rate target value that is less than one, in contrast with Figure 2 in which growth rates were scaled so that pre-ethylene growth rates were unity. The evolutionary algorithm was designed to minimize the fitness function.

In our EA, we use a population size of 200 parameters sets at each generation. The initial parameter sets are generated by selecting uniformly distributed random values for each parameter from allowed parameter ranges (see Supplemental Table 2.1.3). Hill coefficients (N) are restricted to integer values. After evaluating each parameter set, the 50 parameter sets with the lowest fitness scores are selected as source parameter sets. These source sets are used to generate the population of parameter sets for the next generation. New parameter sets are produced by performing a two-point crossover followed by mutations. The crossover events and mutations allow a balance of global and local exploration of parameter space, and the algorithm converged to local minima of the fitness function for the signaling networks studied. Two-point crossovers are performed by randomly selecting two source parameter sets with replacement (i.e., the same set can be chosen twice). Two crossover points are chosen at random from the list of parameters. Two blocks of parameters are taken from the first source and the other block is taken from the second source, leading to a newly constructed set of parameters. Additionally, the probability of mutation for each parameter is chosen such that on average three parameters within the crossover product are mutated (the probability is 3/35 for the CFF/NFB

network and 3/26 for the PFB network). When a parameter is selected for mutation, the decision to increase or decrease the value is made with equal probability. The parameter is then multiplied or divided, respectively, by a uniformly distributed value between 1 and 2. When this decision would result in a parameter exceeding its upper bound, a uniform random value between the current parameter value and its upper limit is used instead. The source parameter sets are updated each generation by replacing 25 randomly selected source sets with parameter sets having the lowest fitness scores from the current population.

We ran the EA for 400 generations and recorded the parameter set with the lowest fitness score for additional analysis. This evolutionary process was repeated independently 500–4000 times depending on the network topology. Each parameter set was screened for the targeted network behavior and the resulting data was used to characterize ethylene response kinetics and identify features of the evolved parameters.

### 2.3. Screening for Targeted Responses

After running the EA, we check whether the resulting growth responses exhibit wildtype two-phase growth inhibition and/or *ein3;eil1* mutant partial growth recovery. Specifically, network responses are checked to ensure that the wildtype response meets the following conditions:

1. With no ethylene, steady state growth is sufficiently high.
2. After applying ethylene, the minimal growth rate is sufficiently low.
3. A plateau-like region separates the first and second phases of growth inhibition.
4. Following removal of ethylene, growth recovers to a sufficiently high level.

Logic diagrams for discriminant functions are included in Supplemental Figures S1, S2. For mutant behavior, traits 1 and 2 were used to check for proper behavior. The discriminant functions were designed to make the inclusion of false positives unlikely.

### 2.4. Ethylene Dose Response

We additionally screen evolved parameters sets to identify whether they exhibit sub-saturating ethylene dose response kinetics similar to experimental observations (see Figure 2C). The level of ethylene that leads to a sub-saturating response depends on the parameters of the network. Thus, we first identify the range of ethylene concentrations over which the network is responsive to concentration variations. For each evolved parameter set, we use a binary search method to identify the ethylene concentration range in which (i) the maximum dose produces long-time growth rate between 0.5 and 1.0% above minimum growth observed in the saturated response and (ii) the minimum dose produces a minimum growth rate between 0.5 and 1.0% below pre-ethylene steady state growth. We consider 20 evenly distributed ethylene concentrations between these bounds to test for partial growth recovery in the presence of sustained ethylene exposure. A parameter set is considered to exhibit sub-saturating growth recovery if there exists at least one ethylene concentration at which the growth maximum

that occurs 1 h or longer after the introduction of ethylene exceeds the minimum growth observed within the first hour of ethylene exposure by at least 0.1 (maximum possible growth is unity).

### 3. RESULTS

#### 3.1. Coherent Feedforward/Negative Feedback Network

The CFF/NFB network (**Figure 3A**) was proposed by Kim et al. (2012) based on growth kinetics in response to the addition and removal of ethylene. It can be broken down into three distinct regions: (i) the initial linear signaling cascade consisting of ethylene receptors, CTR1, and EIN2; (ii) a coherent feedforward loop with EIN2 as the initial node that inhibits growth both directly and indirectly (via EBF and EIN3); (iii) a negative feedback loop consisting of growth and GA. The coherent feedforward cascade interacts with the negative feedback loop as a result of the inhibitory effect of EIN3 on GA. As indicated in **Figure 3A**, we treat EBF1 and EBF2 as well as EIN3 and EIL1 as single entities. We refer to these nodes as EBF and EIN3, respectively. This reduces the complexity of the model and the dimensionality of the parameter space while keeping key topological features of the network. Additionally, with existing experimental data, it is difficult to elucidate differences between these individual components, which could be included in a more detailed computational model.

We conducted multiple independent trials of the EA, obtaining 3774 sets of optimized parameters. Using the discriminant functions described previously, each evolved parameter set was screened for wildtype two-phase growth inhibition (2-PGI) and *ein3;eil1* mutant partial growth recovery

(MPGR). **Figure 4** shows examples of results that exhibit both 2-PGI and MPGR, as well as those that exhibit only one of the responses. Approximately 36% of the evolved parameter sets exhibit both 2-PGI and MPGR, 20% exhibit only 2-PGI, and 23% exhibit only MPGR. The large number of parameter sets yielding one or both of the targeted growth responses provides a large data set for analysis.

#### 3.1.1. Dynamical Response of Network Components

In **Figure 5**, we plot the time dependence of each network component. This provides insight into how the feedforward and feedback loops shape growth response dynamics. For each component, we plot the mean response of the 1344 parameter sets exhibiting both 2-PGI and MPGR behavior. We also display the standard deviation about the mean (shaded regions) to characterize the heterogeneity of the response. Analogous results for parameter sets exhibiting only 2-PGI or MPGR behavior are provided in Supplemental Figures S3, S4.

The response of the linear portion of the signaling cascade is identical for the wildtype (shown in **Figure 5A**) and *ein3;eil1* mutant (not shown) topologies upon addition of ethylene. In response to the addition of ethylene at 1 h, the concentration of unbound receptors rapidly declines to levels near zero. This results in a decrease of CTR1 from a relatively high pre-ethylene concentration to a much lower concentration. Following this, EIN2 is no longer inhibited by active CTR1 and rapidly increases in concentration. There is a slight delay in the EIN2 response to ethylene due to the time required for the signal to propagate through the upstream components of the linear signaling cascade. Upon removal of ethylene at 3 h in the wildtype response, components return to their pre-ethylene levels.

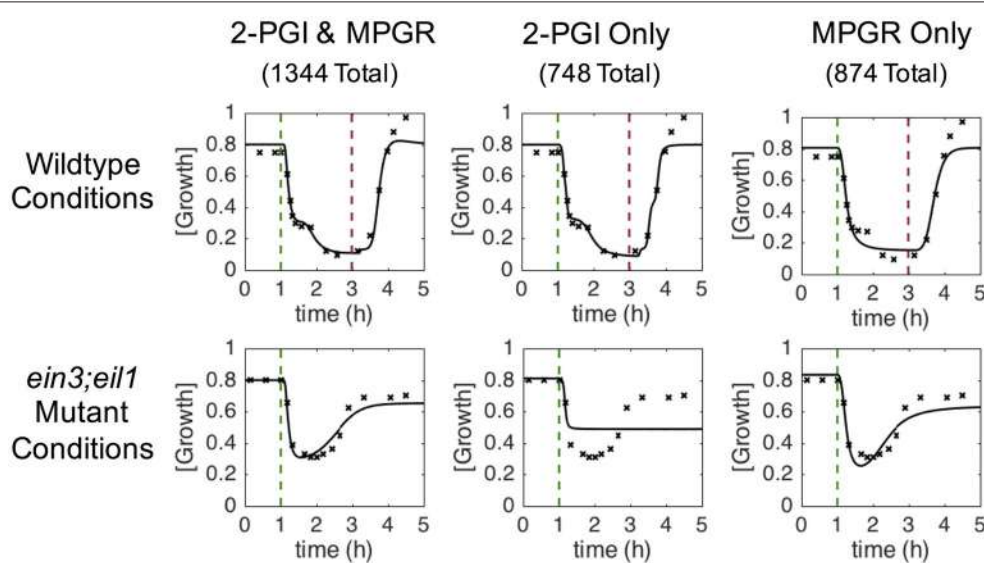
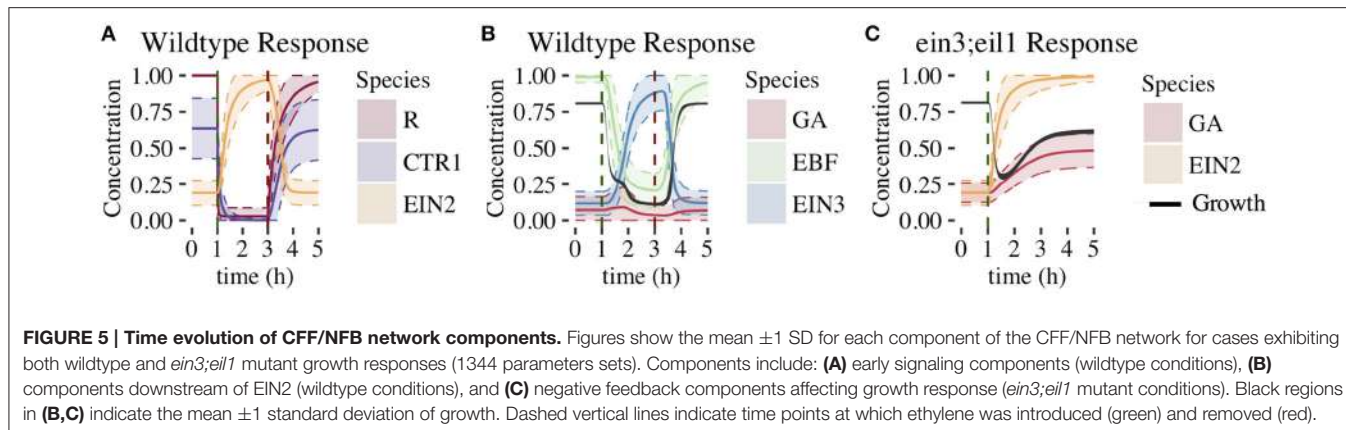


**FIGURE 4 | Characteristic growth responses at saturating ethylene doses.** Columns show examples of time-dependent growth responses passing different combinations of screening criteria. Each column corresponds to a single set of evolved parameters. Rows show different simulated conditions (wildtype and *ein3;eil1* mutant). Targeted growth rates are denoted by x and the evolved response is shown by solid lines. Dashed vertical lines indicate time points at which ethylene was introduced (green) and removed (red).



The remaining network connections differentiate the wildtype response from the *ein3;eil1* mutant response. Components of the wildtype network are shown in **Figure 5B**. Increasing EIN2 concentration acts to inhibit both growth and EBF, which is part of the indirect feedforward loop. The direct inhibitory effect of EIN2 on growth is responsible for the first phase of growth inhibition. In response to decreasing EBF concentration, EIN3 concentration increases from an initially low value approximately 30 min after ethylene is introduced. Once EIN3 reaches a sufficiently high concentration, a pronounced second phase of growth inhibition begins. Thus, the coherent feedforward loop leads to the desired 2-PGI.

The effect of the negative feedback loop can be understood by examining the dynamics of growth and GA. For the wildtype topology, GA is inhibited by both EIN3 and growth. A limited increase in GA levels accompanies the first phase of growth inhibition, and is driven by decreasing growth rates. During the second phase of growth inhibition, increasing EIN3 concentration inhibits GA, with EIN3 inhibition outcompeting the effect of decreasing growth rate. This drives GA to a low concentration, minimizing the effect of the negative feedback loop on growth. Thus, in the presence of increased EIN3, the effects of the negative feedback loop are suppressed. In the *ein3;eil1* mutant, however, the inhibitory action of EIN3 on the negative feedback loop is lost. Thus, the negative feedback loop plays a more prominent role since GA is not inhibited by EIN3 (**Figure 5C**). Additionally, the indirect path of growth inhibition is removed, eliminating the second phase of growth inhibition. **Figure 5C** shows the response of key network components under these conditions. When increasing EIN2 levels cause a decrease in growth, GA levels increase in response, promoting growth and leading to partial growth recovery. This illustrates the importance of the negative feedback loop for partial growth recovery in the *ein3;eil1* mutant.

After the removal of ethylene at 3 h, it is interesting to note that the average growth rate does not exhibit a large overshoot compared with pre-ethylene levels (**Figure 5B**). When analyzing individual parameter sets, none of the responses exhibit an overshoot that exceeds pre-ethylene levels by more than 10%, only 5 of 1344 exhibit  $>5\%$  overshoot, and only 44 of 1344 exhibit  $>1\%$  overshoot. This is in contrast with experimental

results and suggests that modifications of the network or additional components might be needed to adequately capture the overshoot behavior. However, as discussed above, our results show that the core CFF/NFB topology generates key features of the 2-PGI and MPGR responses.

### 3.1.2. Analysis of Parameter Sets

The roles of the feedforward and feedback loops can be further understood by examining evolved parameters. In particular, it is instructive to characterize the distributions of evolved parameter values for the CFF/NFB network, as certain parameters are constrained to small ranges or excluded from certain parameter regimes. In **Figure 6**, we compare the distributions of select parameters when the evolved parameter sets are categorized by their behavior (both 2-PGI and MPGR, only 2-PGI, or only MPGR). The distributions of all parameters are shown in Supplemental Figure S5. Parameter values are scaled by normalizing the maximum value to one, and the width of each distribution is scaled such that the maximum width is equal in each distribution. Comparing the distributions for specific parameters highlights key network features leading to each response.

The parameter distributions in **Figure 6** provide additional evidence that the feedforward loop plays a key role in generating 2-PGI. The activation coefficient for EIN2-regulated growth degradation of EBF ( $K_{\text{degr}}^{\text{EIN2}}$ ) is excluded from low values in evolved parameter sets exhibiting 2-PGI. As a consequence, EIN2 concentration must reach high levels to significantly inhibit EBF, which contributes to a delay before the second phase of growth inhibition. Interestingly, this parameter is most significantly constrained in evolved parameter sets exhibiting both 2-PGI and MPGR. This is in contrast with the broader distributions seen for the cases exhibiting only one of the targeted responses. Additionally, in parameter sets exhibiting 2-PGI, the rate constant associated with basal production of EIN3 ( $k_{\text{prod}}^{\text{basal}}$ ) occurs at low values. This also contributes to a time delay in the feedforward loop, which is needed for a second phase of growth inhibition.

It is also informative to consider the parameters governing the negative feedback loop (**Figure 6**). Parameter sets exhibiting

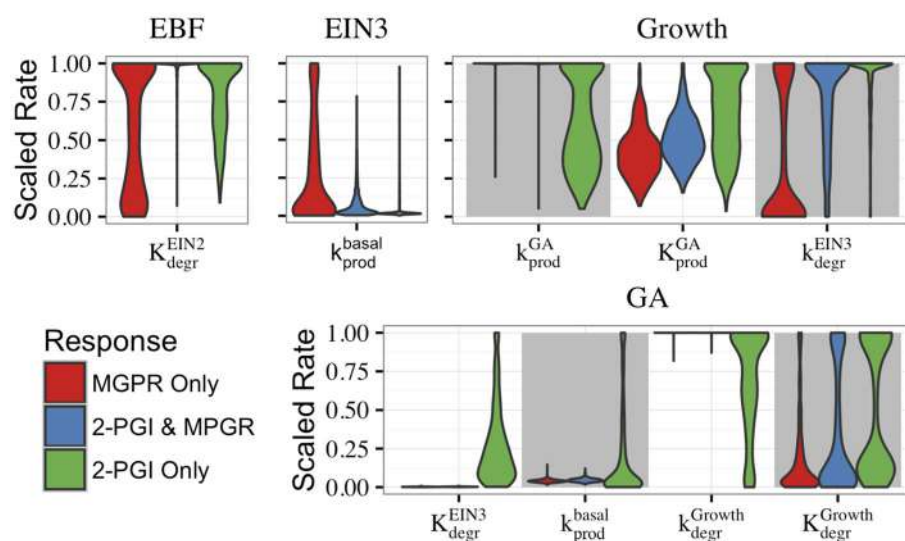


**FIGURE 6 | Distributions of parameters from evolved sets of CFF/NFB network parameters.** Parameter sets exhibiting different combinations of responses are shown. Parameter labels K and k indicate activation coefficients and rate constants, respectively, that are associated with the ODEs governing the species labeled above each figure. Subscripts indicate if the parameter regulates degradation (degr) or production (prod) and superscripts indicate the network component regulating the reaction. Basal rates indicate that the parameter is not regulated by another network component. All parameters were unit normalized using range rescaling.

MPGR have highly restricted ranges associated with the rate constant for basal production of GA and the parameters for GA inhibition by growth. These restrictions lead to low pre-ethylene levels of GA and a reasonable response of GA as growth declines following ethylene exposure. In cases exhibiting MPGR, the rate constant governing promotion of growth by GA is also restricted to high values and the activation coefficient for the promotion of growth by GA is excluded from the lowest values. Thus, a moderate increase in GA concentration will result in a significant increase in growth. However, excluding the activation coefficient from low values prevents increases from occurring with small changes in GA. Thus, tight regulation of parameters of the negative feedback loop is most readily apparent in parameter sets exhibiting MPGR. This further suggests the importance of the negative feedback loop for MPGR.

### 3.1.3. Ethylene Dose Response

Given that our network parameters were evolved to target only 2-PGI and MPGR behavior, we were interested in whether other experimentally observed behavior emerged as well. As such, we examined the sub-saturating ethylene dose-response behavior of evolved parameter sets exhibiting both 2-PGI and MPGR. **Figure 7A** shows an example of sub-saturating ethylene growth recovery (SSGR) that passes our screening criteria. **Figure 7B** shows an example of a typical growth response failing to exhibit SSGR behavior. Here, there is no growth recovery observed at any ethylene concentration. Of the evolved parameter sets exhibiting both 2-PGI and MPGR, 26% also exhibit SSGR. Partial growth recovery at large sub-saturating ethylene concentrations was observed experimentally (e.g., at 100 ppb in **Figure 2C**) but was not observed in the CFF/NFB network model. However, the observed adaptive behavior occurring at lower ethylene

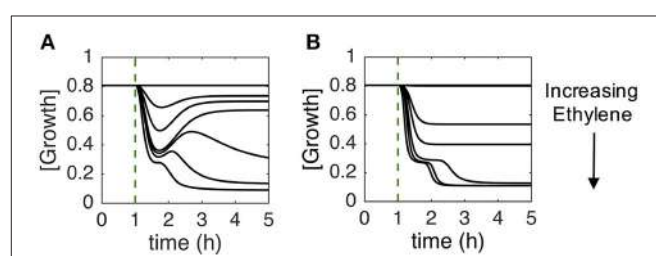


**FIGURE 7 | Characteristic growth responses at sub-saturating ethylene doses.** Parameter sets exhibiting both 2-PGI and MPGR were screened for partial growth recovery to sustained sub-saturating ethylene doses (SSGR). Figures show typical growth responses for parameter sets: **(A)** passing SSGR screening and **(B)** failing SSGR screening.

concentrations is qualitatively consistent with experiments. This emergent property provides additional support for the proposed CFF/NFB network topology.

To gain insight into features that lead to SSGR, we compared the parameter distributions that passed SSGR screening to those that failed SSGR screening. Surprisingly, this revealed nearly identical parameter distributions except for the activation coefficient for GA inhibition by EIN3 and the rate constant associated with inhibition of growth by EIN3 (**Figure 8** and Supplemental Figure S6). The activation coefficient regulating GA inhibition by EIN3 occurs at higher values in sets producing SSGR. The rate constant for growth inhibition by EIN3 occurs at lower values more frequently in cases giving SSGR. The distributions of these parameters across all evolved sets exhibiting 2-PGI and/or MPGR are shown in **Figure 6**. Higher values of the activation coefficient for GA inhibition by EIN3 are found primarily in parameter sets exhibiting 2-PGI, while lower values

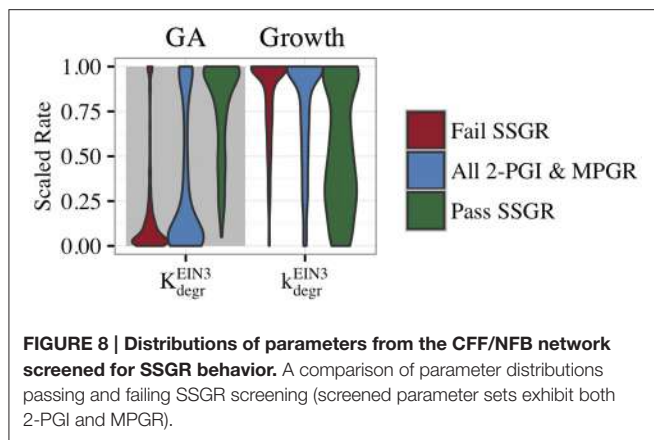


**FIGURE 8 | Distributions of parameters from the CFF/NFB network screened for SSGR behavior.** A comparison of parameter distributions passing and failing SSGR screening (screened parameter sets exhibit both 2-PGI and MPGR).

of the rate constants for inhibition of growth by EIN3 occur primarily in parameter sets exhibiting MPGR. These restrictions apply to the regulation of EIN3 on components of the negative feedback loop. This again suggests that inhibition of the negative feedback loop by the coherent feedforward loop may play a key role in ethylene signaling.

### 3.1.4. Simplified CFF/NFB Networks

We have shown that the CFF/NFB network can produce multiple experimentally-observed features of *Arabidopsis* growth responses to ethylene. Using this network topology as a guide, we probed simplified networks containing coherent feedforward and negative feedback motifs. The networks explored are shown in **Figure 9**. Ethylene (E) acts as either the first node of the coherent feedforward loop (**Figures 9A–C**) or as a direct input into the first node of the loop (**Figures 9D,E**). Additionally, EBF and EIN3 are combined into a single node (Y) which acts to inhibit growth. In the simplest network (**Figure 9A**), we remove the GA node and allow growth to directly inhibit its own production. For the remaining networks, the role of GA in the negative feedback loop is performed by node Z. To probe the inhibition of the negative feedback loop by the coherent feedforward loop, we tested network topologies with and without the inhibition of Z by Y. Approximately 500 independent optimization runs were performed for each simplified network topology. *Ein3;eil1* mutants were simulated by eliminating node Y. Evolved parameter sets were screened for 2-PGI and MPGR responses and a summary of results are shown in **Table 1**.

The simplest network (**Figure 9A**) failed to produce any parameter sets passing 2-PGI or MPGR screening procedures. Examining the dynamical response of evolved parameter sets revealed two phases of growth inhibition that occurred too early and above the desired growth range. Additionally, no growth recovery was observed upon removal of Y. The addition of node Z to the negative feedback loop (**Figure 9B**) produced two parameter sets exhibiting 2-PGI but none showing MPGR. When the inhibition of Z by Y is included (**Figure 9C**), we begin to observe substantial numbers of parameter sets exhibiting either 2-PGI or MPGR. However, no parameter sets simultaneously produced both responses. 2-PGI and MPGR were observed together only when ethylene promoted the first node of the

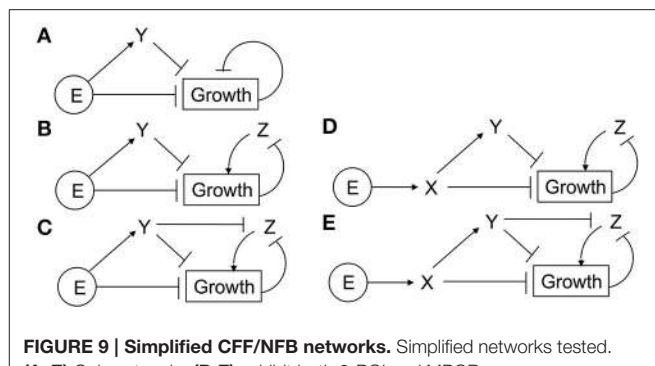


**FIGURE 9 | Simplified CFF/NFB networks.** Simplified networks tested. **(A–E)** Only networks **(D,E)** exhibit both 2-PGI and MPGR.

**TABLE 1 | Screening results for ethylene growth responses of simplified CFF/NFB networks.**

Network	Total	2-PGI & MPGR	2-PGI only	MPGR only
A	504	0	0	0
B	500	0	2	0
C	500	0	80	18
D	499	5	1	3
E	500	92	73	37

coherent feedforward cascade, which more closely mimics the initial linear signaling cascade. In networks in which Z is not directly inhibited by Y (**Figure 9D**), 1.0% of parameter sets exhibit both 2-PGI and MPGR responses. When Y regulates Z (**Figure 9E**), 18.4% of parameter sets exhibit both targeted growth responses. These results suggest the importance of (i) the initial linear cascade in achieving proper timing of growth inhibition and (ii) the inhibition of negative feedback by the coherent feedforward loop in expanding the parameter space in which 2-PGI and MPGR are observed.

### 3.2. EIN2 Cleavage with Positive Feedback

In this section, we consider the second proposed network topology with EIN2 cleavage and a positive feedback loop (PFB network, **Figure 3B**). The network was evolved with the same target responses as before. We obtained evolved parameter sets that produced both 2-PGI and MPGR behavior, but the number was substantially lower than in the CFF/NFB network. Out of 1247 independent runs of the EA, only 5 evolved parameter sets produce both 2-PGI and MPGR. Parameter sets exhibiting only 2-PGI were also uncommon (3 sets). However, a significant proportion of parameter sets exhibited only MPGR (726 sets). Two of the 5 parameter sets exhibiting both 2-PGI and MPGR also display sub-saturating ethylene growth response (SSGR). The limited number of parameter sets exhibiting both targeted responses precludes analysis of parameter distributions. However, studying the dynamic response of the best-performing parameter set exhibiting 2-PGI, MPGR, and SSGR provides valuable insight (**Figure 10**). Results are representative of the other parameter sets exhibiting 2-PGI and MPGR. Complete results of evolved sets exhibiting 2-PGI, MPGR, and SSGR are presented in the Supplemental Figure S7.

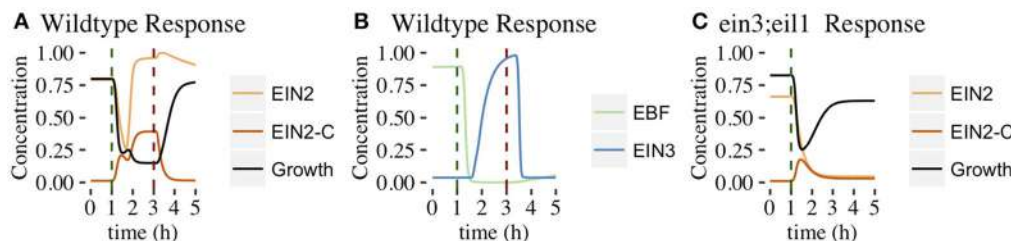


**FIGURE 10 | Time evolution of PFB network components.** Figures show the behavior of the best-performing evolved parameter set that passed 2-PGI, MPGR, and SSGR screening. **(A)** Response of growth, EIN2, and EIN2-C (wildtype conditions). **(B)** Response of components in the positive feedback loop (wildtype conditions). **(C)** Response of growth, EIN2, and EIN2-C (*ein3;eil1* mutant conditions).

### 3.2.1. Dynamical Response of Network Components

As in the CFF/NFB network, the introduction of ethylene decreases CTR1 levels (Figure 10A). In the PFB network, the cleavage of EIN2 is no longer inhibited and EIN2-C is produced (Figure 10A). As EIN2-C increases in concentration it inhibits both growth and EBF (Figures 10A,B). EIN2 levels drop during this phase of network response as basal production of EIN2 cannot compensate for the rapid conversion of EIN2 to EIN2-C. EIN2 reaches low concentrations, limiting the resources available for production of EIN2-C. This leads to a transient decline in EIN2-C, which causes the plateau-like region of growth inhibition. Within the feedback loop, lower EBF levels decrease the inhibition of EIN3, which rises and promotes production of EIN2. The rapid rise of EIN2 provides more resources for EIN2-C production. This leads to the second phase of growth inhibition.

Within the *ein3;eil1* mutant, the positive feedback loop is absent. The addition of ethylene leads to EIN2 being converted to EIN2-C, resulting in a decline of EIN2. Without the positive feedback loop, there is no mechanism to further increase EIN2 production and its concentration monotonically decreases. EIN2-C initially increases but then declines as basal degradation eventually dominates the low rates of EIN2-C production associated with low levels of EIN2. As EIN2-C concentration decreases, partial growth recovery is observed (Figure 10C).

### 3.2.2. Simplified PFB Network

We again explored a simplified network topology that keeps key features of the PFB network. We found that a four component network in which ethylene directly promotes the conversion of X (EIN2) to Y (EIN2-C) can produce both 2-PGI and MPGR (Figure 11). In the network, Y directly inhibits growth and promotes the production of X. We performed 500 optimizations of this network and obtained 142 evolved parameter sets exhibiting both 2-PGI and MPGR. The marked increase in the fraction of parameter sets exhibiting both 2-PGI and MPGR suggests parameter evolution in the full PFB network is hindered by interactions in the positive feedback loop. Three parameters regulate the positive feedback from Y to X in the simplified network, while 9 parameters govern the positive feedback loop in the full network (associated with interactions between EIN2-C, EBF, EIN3, and EIN2). This apparently makes it difficult for our

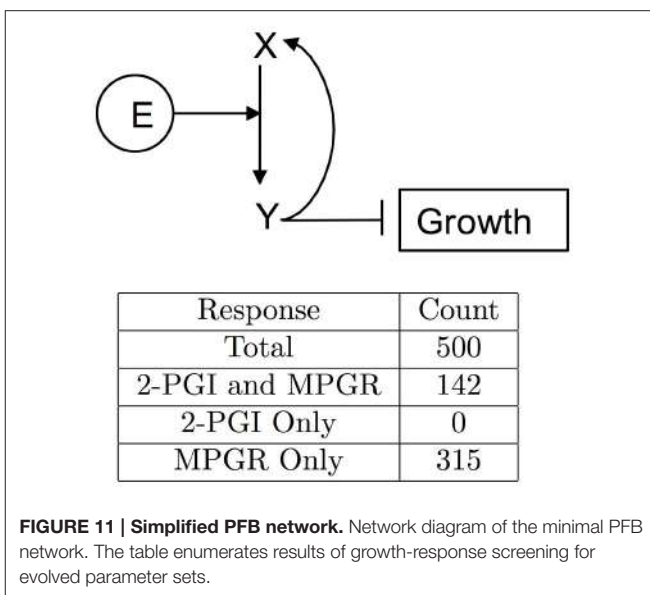


**FIGURE 11 | Simplified PFB network.** Network diagram of the minimal PFB network. The table enumerates results of growth-response screening for evolved parameter sets.

EA to evolve large numbers of parameter sets producing both 2-PGI and MPGR. The large fraction of simplified PFB networks exhibiting both 2-PGI and MPGR again provides support for EIN2 cleavage with positive feedback as a viable network topology.

## 4. CONCLUSIONS

We used computational methods to explore hypothesized network topologies underlying ethylene signaling responses in *Arabidopsis*. We focused on two core networks that are topologically distinct. Using an evolutionary algorithm to explore parameter space, we showed that both network topologies can produce dynamical responses consistent with experimental time-dependent growth data. The core topologies are (i) a coherent feedforward loop that inhibits growth and a negative feedback from growth onto itself (CFF/NFB), and (ii) a network in which ethylene promotes the cleavage of EIN2, with the product of the cleavage inhibiting growth and promoting the production of EIN2 through a positive feedback loop (PFB).

For the CFF/NFB network, high-throughput use of the evolutionary algorithm led to a large number of parameter sets producing responses consistent with experimental growth kinetics under various conditions and genotypes. The results emphasize the importance of various network features for regulating dynamic responses. For example, the two branches of the coherent feedforward loop collectively produce two-phase growth inhibition (2-PGI), and the negative feedback loop is critical for mutant partial growth recovery (MPGR). Our study additionally suggests that 2-PGI and MPGR coexist in a broader parameter regime when the negative feedback loop is suppressed by an intermediate component of the coherent feedforward cascade. The large number of parameter sets producing 2-PGI and MPGR behavior provide insight into important regimes of parameter space. Additionally, a large fraction of these parameter sets also exhibit sub-saturating ethylene growth response (SSGR), even though this was not a targeted response by the evolutionary algorithm. Taken together, these results provide support for the CFF/NFB network as a viable network topology underlying ethylene signaling.

For the PFB network, the evolutionary algorithm led to far fewer parameter sets producing both 2-PGI and MPGR behavior, yet the dynamics of their responses provided insight into the mechanisms underlying the network topology. A key feature of the network is that EIN2 is converted to EIN2-C and its transient depletion upon the addition of ethylene is responsible for the plateau phase of growth inhibition. Two of the evolved parameter sets also exhibited SSGR, indicating that this emergent behavior is also possible in the PFB network. Although we generated far more parameter sets producing 2-PGI and MPGR for the CFF/NFB network, this does not necessarily imply that it is biologically more likely. For example, the region of parameter space for the PFB network that gives the desired behavior may be smaller or more difficult to identify with our EA, but this does not exclude the PFB network as biologically feasible.

It is interesting to note that different plant species have qualitatively different ethylene response kinetics (Kim et al., 2012). For example, some plant species (millet) have only a transient first phase response and some (rice) have only a prolonged second phase response. The paper by Kim et al. first proposed the CFF/NFB network studied here. For millet, Kim et al. proposed that the circuit controlled by EIN3/EIL1 was missing to give the transient response; for rice, it was proposed that the rapid, EIN3/EIL1-independent output of EIN2 is missing. The first case was analyzed in this paper when we analyzed the MPGR response. An interesting feature of the CFF/NFB model is that there is a simple conceptual way to modify the network to generate responses consistent with other species. It is less clear how the PFB network could be modified in an analogous manner to generate growth response kinetics consistent with the rice and millet studies. Further exploration of the network topology across species is an interesting area for future exploration.

Even though both models exhibited SSGR behavior that was similar to what has been observed experimentally, the

kinetics of the computational responses are subtly different from experimental observations. In particular, there was no long-time recovery at high sub-saturating ethylene concentrations and incomplete recovery at low concentrations. It has been suggested that responses to low levels of ethylene are in large part a result of receptor clustering, where ligand occupancy of one receptor affects the signaling state of surrounding receptors through direct interactions and results in signal amplification at low ethylene levels (Gamble et al., 2002; Binder and Bleeker, 2003; Binder et al., 2004b). Computational models invoking receptor clustering indicate this element can affect both sensitivity and adaptation (Bray et al., 1998). Our models did not incorporate this feature, which would likely affect features of the SSGR. Additionally, our models do not incorporate spatial information. For instance, it is now known that EIN2-C translocates to the nucleus to affect ethylene signaling (Ju et al., 2012; Qiao et al., 2012; Wen et al., 2012). Cleavage of EIN2 was not incorporated into the CFF/NFB network and translocation of EIN2-C was not explicitly incorporated into either model. This translocation also may have diverse functions since it has recently been found that EIN2-C in the cytosol also has a role in ethylene signaling (Li et al., 2015; Merchant et al., 2015). It is likely that spatial changes in important components such as EIN2-C have a role in adaptation.

Despite these differences, our calculations show that several simple networks can recapitulate the ethylene growth responses observed experimentally. The dynamic responses observed provide opportunities for experimental exploration. A comparison of the dynamical response of individual components for each network is shown in Supplemental Figure S7. For example, the PFB network shows that when ethylene is added there is a transient decrease in EIN2 levels followed by accumulation of EIN2. By contrast, the CFF/NFB model predicts qualitatively different accumulation kinetics for EIN2, with no transient decrease. Thus, one avenue of experimentation can be to obtain more detailed spatio-temporal information about the accumulation of EIN2 (and EIN2-C) to determine if the details predicted by the calculations in either model occur when saturating levels of ethylene are added. For example, a detailed time-course of EIN2-C accumulation or EIN2 full-length protein is lacking. Such information would help determine which, if either, model correctly predicts the accumulation pattern for EIN2. Additionally, removing EIN3 from the CFF/NFB model has minimal effect on the time-course of EIN2 accumulation when ethylene is added, but has a profound effect on both EIN2 and EIN2-C levels in the PFB model. Thus, experiments examining EIN2 and EIN2-C levels in *ein3;eil1* double mutants would also be informative. Another example is the involvement of GA in the CFF/NFB network where it plays a larger role in the growth kinetics observed in the *ein3;eil1* mutants. Detailed information about changes in GA levels would provide a test of this model and whether the negative feedback loop needs to be incorporated into the PFB network. Such experimental details will help determine which network topology, if either, could serve as the ethylene signaling transduction network of Arabidopsis. It is also possible that a combination of the two models or different network topologies will yield emergent properties that are closer

to experimental observations. Additional experimental details about the spatio-temporal changes that occur in each component of the pathway will allow us to refine the above models or develop additional network topologies.

In summary, these calculations show that a basic mechanistic understanding of ethylene growth response and recovery kinetics is possible without detailed knowledge of the molecular mechanisms or enzymatic kinetic parameters. Given that ethylene signal transduction has been highly studied for several decades, we anticipate that major advances in our understanding about this pathway will be to provide details about network interactions, reaction kinetics, and changes in the spatial distribution of proteins in the pathway. Our hope is that with more refined experimental input, we can refine the network models to provide insights into how plants respond to ethylene.

## REFERENCES

- Abeles, F. B., Morgan, P. W., and Saltveit, M. E. Jr. (1992). *Ethylene in Plant Biology*. San Diego, CA: Academic Press.
- Alonso, J. M., Hirayama, T., Roman, G., Nourizadeh, S., and Ecker, J. R. (1999). EIN2, a bifunctional transducer of ethylene and stress responses in arabidopsis. *Science* 284, 2148–2152. doi: 10.1126/science.284.5423.2148
- An, F., Zhao, Q., Ji, Y., Li, W., Jiang, Z., Yu, X., et al. (2010). Ethylene-induced stabilization of ETHYLENE INSENSITIVE3 and EIN3-LIKE1 is mediated by proteasomal degradation of EIN3 binding F-box 1 and 2 that requires EIN2 in arabidopsis. *Plant Cell* 22, 2384–2401. doi: 10.1105/tpc.110.076588
- Arisi, I., Cattaneo, A., and Rosato, V. (2006). Parameter estimate of signal transduction pathways. *BMC Neurosci.* 7(Suppl. 1):S6. doi: 10.1186/1471-2202-7-S1-S6
- Auliac, C., Frouin, V., Gidrol, X., and d'Alché Buc, F. (2008). Evolutionary approaches for the reverse-engineering of gene regulatory networks: a study on a biologically realistic dataset. *BMC Bioinformatics* 9:91. doi: 10.1186/1471-2105-9-91
- Bäck, T., and Schwefel, H.-P. (1993). An overview of evolutionary algorithms for parameter optimization. *Evol. Comp.* 1, 1–23. doi: 10.1162/evco.1993.1.1.1
- Bakshi, A., Wilson, R. L., Lacey, R. F., Kim, H., Wupalapati, S. K., and Binder, B. (2015). Identification of regions in the receiver domain of the ETHYLENE RESPONSE1 ethylene receptor of arabidopsis important for functional divergence. *Plant Physiol.* 169, 219–232. doi: 10.1104/pp.15.00626
- Binder, B. M., and Bleecker, A. B. (2003). A model for ethylene receptor function and 1-methylcyclopentene action. *Acta Hortic.* 628, 177–187. doi: 10.17660/ActaHortic.2003.628.21
- Binder, B. M., Mortimore, L. A., Stepanova, A. N., Ecker, J. R., and Bleecker, A. B. (2004a). Short-term growth responses to ethylene in arabidopsis seedlings are EIN3/EIL1 independent. *Plant Physiol.* 136, 2921–2927. doi: 10.1104/pp.104.050393
- Binder, B. M., O'Malley, R. C., Wang, W., Moore, J. M., Parks, B. M., Spalding, E. P., et al. (2004b). Arabidopsis seedling growth response and recovery to ethylene. A kinetic analysis. *Plant Physiol.* 136, 2913–2920. doi: 10.1104/pp.104.050369
- Binder, B. M., Walker, J. M., Gagne, J. M., Emborg, T. J., Hemmann, G., Bleecker, A. B., et al. (2007). The arabidopsis EIN3 binding F-box proteins EBF1 and EBF2 have distinct but overlapping roles in ethylene signaling. *Plant Cell* 19, 509–523. doi: 10.1105/tpc.106.048140
- Bleecker, A. B., Estelle, M. A., Somerville, C., and Kende, H. (1988). Insensitivity to ethylene conferred by a dominant mutation in *Arabidopsis thaliana*. *Science* 241, 1086–1089. doi: 10.1126/science.241.4869.1086
- Bray, D., and Lay, S. (1994). Computer simulated evolution of a network of cell-signaling molecules. *Biophys. J.* 66, 972–977. doi: 10.1016/S0006-3495(94)80878-1
- Bray, D., Levin, M. D., and Morton-Firth, C. J. (1998). Receptor clustering as a cellular mechanism to control sensitivity. *Nature* 393, 85–88. doi: 10.1038/30018
- Burg, S. P. (1973). Ethylene in plant growth. *Proc. Natl. Acad. Sci. U.S.A.* 70, 591–597. doi: 10.1073/pnas.70.2.591
- Chen, R., Binder, B. M., Garrett, W. M., Tucker, M. L., Chang, C., and Cooper, B. (2011). Proteomic responses in *Arabidopsis thaliana* seedlings treated with ethylene. *Mol. Biosyst.* 7, 2637–2650. doi: 10.1039/c1mb05159h
- Christians, M. J., Gingerich, D. J., Hansen, M., Binder, B. M., Kieber, J. J., and Vierstra, R. D. (2009). The BTB ubiquitin ligases ETO1, EOL1 and EOL2 act collectively to regulate ethylene biosynthesis in arabidopsis by controlling type2 ACC synthase levels. *Plant J.* 57, 332–345. doi: 10.1111/j.1365-313X.2008.03693.x
- Díaz, J., and Álvarez-Buylla, E. R. (2006). A model of the ethylene signaling pathway and its gene response in *Arabidopsis thaliana*: pathway cross-talk and noise-filtering properties. *Chaos* 16:023112. doi: 10.1063/1.2189974
- Díaz, J., and Alvarez-Buylla, E. R. (2009). Information flow during gene activation by signaling molecules: ethylene transduction in arabidopsis cells as a study system. *BMC Syst. Biol.* 3:48. doi: 10.1186/1752-0509-3-48
- Feng, S., Ollivier, J. F., Swain, P. S., and Soyer, O. S. (2015). Biojazz: *in silico* evolution of cellular networks with unbounded complexity using rule-based modeling. *Nucleic Acids Res.* 43:e213. doi: 10.1093/nar/gkv595
- François, P., and Hakim, V. (2004). Design of genetic networks with specified functions by evolution *in silico*. *Proc. Natl. Acad. Sci. U.S.A.* 101, 580–585. doi: 10.1073/pnas.0304532101
- Gagne, J. M., Smalle, J., Gingerich, D. J., Walker, J. M., Yoo, S.-D., Yanagisawa, S., et al. (2004). Arabidopsis EIN3-binding F-box 1 and 2 form ubiquitin-protein ligases that repress ethylene action and promote growth by directing EIN3 degradation. *Proc. Natl. Acad. Sci. U.S.A.* 101, 6803–6808. doi: 10.1073/pnas.0401698101
- Gamble, R. L., Qu, X., and Schaller, G. E. (2002). Mutational analysis of the ethylene receptor ETR1. Role of the histidine kinase domain in dominant ethylene insensitivity. *Plant Physiol.* 128, 1428–1438. doi: 10.1104/pp.010777
- Gao, Z., Wen, C.-K., Binder, B. M., Chen, Y.-F., Chang, J., Chiang, Y.-H., et al. (2008). Heteromeric interactions among ethylene receptors mediate signaling in arabidopsis. *J. Biol. Chem.* 283, 23801–23810. doi: 10.1074/jbc.M800641200
- Goeschl, J. D., and Kays, S. J. (1975). Concentration dependencies of some effects of ethylene on etiolated pea, peanut, bean, and cotton seedlings. *Plant Physiol.* 55, 670–677. doi: 10.1104/pp.55.4.670
- Guo, H., and Ecker, J. R. (2003). Plant responses to ethylene gas are mediated by SCF EBF1/EBF2-dependent proteolysis of EIN3 transcription factor. *Cell* 115, 667–677. doi: 10.1104/pp.55.4.670
- Guzman, P., and Ecker, J. R. (1990). Exploiting the triple response of arabidopsis to identify ethylene-related mutants. *Plant Cell* 2, 513–523. doi: 10.1105/tpc.2.6.513

## AUTHOR CONTRIBUTIONS

AP, BB, and SA designed research. AP, FM, and BE performed research. AP, BB, and SA analyzed data and wrote the paper.

## FUNDING

This work was funded by NSF Grants (IOS-1254423, MCB-1517032) to BB.

## SUPPLEMENTARY MATERIAL

The Supplementary Material for this article can be found online at: <http://journal.frontiersin.org/article/10.3389/fpls.2016.01308>

- Hall, A. E., and Bleeker, A. B. (2003). Analysis of combinatorial loss-of-function mutants in the arabidopsis ethylene receptors reveals that the ERS1 ETR1 double mutant has severe developmental defects that are EIN2 dependent. *Plant Cell* 15, 2032–2041. doi: 10.1105/tpc.013060
- Jackson, M. B. (1983). “Regulation of root growth and morphology by ethylene and other externally applied growth substances,” in *Growth Regulators in Root Development*, Monograph No. 10, eds M. B. Jackson and A. D. Stead (London: British Plant Growth Regulator Group), 103–116.
- Ju, C., Yoon, G. M., Shemansky, J. M., Lin, D. Y., Ying, Z. I., Chang, J., et al. (2012). CTR1 phosphorylates the central regulator EIN2 to control ethylene hormone signaling from the er membrane to the nucleus in arabidopsis. *Proc. Natl. Acad. Sci. U.S.A.* 109, 19486–19491. doi: 10.1073/pnas.1214848109
- Kieber, J. J., Rothenberg, M., Roman, G., Feldmann, K. A., and Ecker, J. R. (1993). CTR1, a negative regulator of the ethylene response pathway in arabidopsis, encodes a member of the raf family of protein kinases. *Cell* 72, 427–441. doi: 10.1016/0092-8674(93)90119-B
- Kikuchi, S., Tominaga, D., Arita, M., Takahashi, K., and Tomita, M. (2003). Dynamic modeling of genetic networks using genetic algorithm and s-system. *Bioinformatics* 19, 643–650. doi: 10.1093/bioinformatics/btg027
- Kim, H., Helmbrecht, E. E., Stalans, M. B., Schmitt, C., Patel, N., Wen, C.-K., et al. (2011). Ethylene receptor ethylene receptor1 domain requirements for ethylene responses in arabidopsis seedlings. *Plant Physiol.* 156, 417–429. doi: 10.1104/pp.110.170621
- Kim, J., Wilson, R. L., Case, J. B., and Binder, B. M. (2012). A comparative study of ethylene growth response kinetics in eudicots and monocots reveals a role for gibberellin in growth inhibition and recovery. *Plant Physiol.* 160, 1567–1580. doi: 10.1104/pp.112.205799
- Laan, P. (1934). *Der Einfluss von Aethylen auf die Wuchsstoffbildung bei Avena und Vicia*. Ph.D. thesis, Utrecht: Van der Laan.
- Larsen, P. B., and Chang, C. (2001). The arabidopsis EER1 mutant has enhanced ethylene responses in the hypocotyl and stem. *Plant Physiol.* 125, 1061–1073. doi: 10.1104/pp.125.2.1061
- Li, W., Ma, M., Feng, Y., Li, H., Wang, Y., Ma, Y., et al. (2015). EIN2-directed translational regulation of ethylene signaling in arabidopsis. *Cell* 163, 670–683. doi: 10.1016/j.cell.2015.09.037
- Mattoo, A. K., and Suttle, J. C. (1991). *The Plant Hormone Ethylene*. Boca Raton, FL: CRC Press.
- McDaniel, B. K., and Binder, B. M. (2012). Ethylene receptor 1 (ETR1) is sufficient and has the predominant role in mediating inhibition of ethylene responses by silver in *Arabidopsis thaliana*. *J. Biochem.* 287, 26094–26103. doi: 10.1074/jbc.M112.383034
- Merchante, C., Brumos, J., Yun, J., Hu, Q., Spencer, K. R., Enríquez, P., et al. (2015). Gene-specific translation regulation mediated by the hormone-signaling molecule EIN2. *Cell* 163, 684–697. doi: 10.1016/j.cell.2015.09.036
- Patil, K. R., Rocha, I., Förster, J., and Nielsen, J. (2005). Evolutionary programming as a platform for *in silico* metabolic engineering. *BMC Bioinformatics* 6:308. doi: 10.1186/1471-2105-6-308
- Potuschak, T., Lechner, E., Parmentier, Y., Yanagisawa, S., Grava, S., Koncz, C., et al. (2003). EIN3-dependent regulation of plant ethylene hormone signaling by two arabidopsis F box proteins: EBF1 and EBF2. *Cell* 115, 679–689. doi: 10.1016/S0092-8674(03)00968-1
- Potuschak, T., Vansiri, A., Binder, B. M., Lechner, E., Vierstra, R. D., and Genschik, P. (2006). The exoribonuclease XRN4 is a component of the ethylene response pathway in arabidopsis. *Plant Cell* 18, 3047–3057. doi: 10.1105/tpc.106.046508
- Qiao, H., Chang, K. N., Yazaki, J., and Ecker, J. R. (2009). Interplay between ethylene, ETP1/ETP2 F-box proteins, and degradation of EIN2 triggers ethylene responses in arabidopsis. *Gene Dev.* 23, 512–521. doi: 10.1101/gad.1765709
- Qiao, H., Shen, Z., Huang, S.-S. C., Schmitz, R. J., Urich, M. A., Briggs, S. P., et al. (2012). Processing and subcellular trafficking of er-tethered ein2 control response to ethylene gas. *Science* 338, 390–393. doi: 10.1126/science.1225974
- Qiu, L., Xie, F., Yu, J., and Wen, C.-K. (2012). Arabidopsis RTE1 is essential to ethylene receptor ETR1 amino-terminal signaling independent of CTR1. *Plant Physiol.* 159, 1263–1276. doi: 10.1104/pp.112.193979
- Rai, M. I., Wang, X., Thibault, D. M., Kim, H. J., Bombyk, M. M., Binder, B. M., et al. (2015). The argos gene family functions in a negative feedback loop to desensitize plants to ethylene. *BMC Plant Biol.* 15:157. doi: 10.1186/s12870-015-0554-x
- Rausler, W. E., and Horton, R. F. (1975). Rapid effects of indoleacetic acid and ethylene on the growth of intact pea roots. *Plant Physiol.* 55, 443–447. doi: 10.1104/pp.55.3.443
- Roman, G., Lubarsky, B., Kieber, J. J., Rothenberg, M., and Ecker, J. R. (1995). Genetic analysis of ethylene signal transduction in *Arabidopsis thaliana*: five novel mutant loci integrated into a stress response pathway. *Genetics* 139, 1393–1409.
- Spirov, A., and Holloway, D. (2013). Using evolutionary computations to understand the design and evolution of gene and cell regulatory networks. *Methods* 62, 39–55. doi: 10.1016/j.ymeth.2013.05.013
- Sun, J., Garibaldi, J. M., and Hodgman, C. (2012). Parameter estimation using metaheuristics in systems biology: a comprehensive review. *IEEE ACM Trans. Comput. Biol. Bioinf.* 9, 185–202. doi: 10.1109/TCBB.2011.63
- van Zanten, M., Basten Snoek, L., van Eck-Stouten, E., Proveniers, M. C., Torii, K. U., Voesenek, L. A., et al. (2010). Ethylene-induced hyponastic growth in *Arabidopsis thaliana* is controlled by erecta. *Plant J.* 61, 83–95. doi: 10.1111/j.1365-313X.2009.04035.x
- Vandenbussche, F., Petrásek, J., Žádníková, P., Hoyerová, K., Pešek, B., Raz, V., et al. (2010). The auxin influx carriers AUX1 and LAX3 are involved in auxin-ethylene interactions during apical hook development in arabidopsis thaliana seedlings. *Development* 137, 597–606. doi: 10.1242/dev.040790
- Warner, H., and Leopold, A. (1971). Timing of growth regulator responses in peas. *Biochem. Biophys. Res. Commun.* 44, 989–994. doi: 10.1016/0006-291X(71)90809-6
- Wen, X., Zhang, C., Ji, Y., Zhao, Q., He, W., An, F., et al. (2012). Activation of ethylene signaling is mediated by nuclear translocation of the cleaved EIN2 carboxyl terminus. *Cell Res.* 22, 1613–1616. doi: 10.1038/cr.2012.145
- Yanagisawa, S., Yoo, S.-D., and Sheen, J. (2003). Differential regulation of ein3 stability by glucose and ethylene signalling in plants. *Nature* 425, 521–525. doi: 10.1038/nature01984
- Žádníková, P., Petrásek, J., Marhavý, P., Raz, V., Vandenbussche, F., Ding, Z., et al. (2010). Role of pin-mediated auxin efflux in apical hook development of *Arabidopsis thaliana*. *Development* 137, 607–617. doi: 10.1242/dev.041277
- Conflict of Interest Statement:** The authors declare that the research was conducted in the absence of any commercial or financial relationships that could be construed as a potential conflict of interest.
- Copyright © 2016 Prescott, McCollough, Eldreth, Binder and Abel. This is an open-access article distributed under the terms of the Creative Commons Attribution License (CC BY). The use, distribution or reproduction in other forums is permitted, provided the original author(s) or licensor are credited and that the original publication in this journal is cited, in accordance with accepted academic practice. No use, distribution or reproduction is permitted which does not comply with these terms.*



# DRACO-STEM: An Automatic Tool to Generate High-Quality 3D Meshes of Shoot Apical Meristem Tissue at Cell Resolution

Guillaume Cerutti<sup>1\*</sup>, Olivier Ali<sup>1,2</sup> and Christophe Godin<sup>1\*</sup>

<sup>1</sup> Virtual Plants INRIA Team, UMR AGAP, CIRAD, INRIA, INRA, Montpellier, France, <sup>2</sup> Laboratoire de Reproduction et Développement des Plantes, Université de Lyon, ENS-Lyon, INRA, Centre National de la Recherche Scientifique, Lyon, France

## OPEN ACCESS

### Edited by:

Alexander Bucksch,  
University of Georgia, USA

### Reviewed by:

Soeren Strauss,  
University of Birmingham, UK  
Giovanni Sena,  
Imperial College London, UK  
Pawel Krupinski,  
Lund University, Sweden

### \*Correspondence:

Guillaume Cerutti  
guillaume.cerutti@inria.fr  
Christophe Godin  
christophe.godin@inria.fr

### Specialty section:

This article was submitted to  
Plant Biophysics and Modeling,  
a section of the journal  
Frontiers in Plant Science

Received: 27 September 2016

Accepted: 28 February 2017

Published: 29 March 2017

### Citation:

Cerutti G, Ali O and Godin C (2017) DRACO-STEM: An Automatic Tool to Generate High-Quality 3D Meshes of Shoot Apical Meristem Tissue at Cell Resolution. *Front. Plant Sci.* 8:353.  
doi: 10.3389/fpls.2017.00353

**Context:** The shoot apical meristem (SAM), origin of all aerial organs of the plant, is a restricted niche of stem cells whose growth is regulated by a complex network of genetic, hormonal and mechanical interactions. Studying the development of this area at cell level using 3D microscopy time-lapse imaging is a newly emerging key to understand the processes controlling plant morphogenesis. Computational models have been proposed to simulate those mechanisms, however their validation on real-life data is an essential step that requires an adequate representation of the growing tissue to be carried out.

**Achievements:** The tool we introduce is a two-stage computational pipeline that generates a complete 3D triangular mesh of the tissue volume based on a segmented tissue image stack. DRACO (Dual Reconstruction by Adjacency Complex Optimization) is designed to retrieve the underlying 3D topological structure of the tissue and compute its dual geometry, while STEM (SAM Tissue Enhanced Mesh) returns a faithful triangular mesh optimized along several quality criteria (intrinsic quality, tissue reconstruction, visual adequacy). Quantitative evaluation tools measuring the performance of the method along those different dimensions are also provided. The resulting meshes can be used as input and validation for biomechanical simulations.

**Availability:** DRACO-STEM is supplied as a package of the open-source multi-platform plant modeling library OpenAlea (<http://openalea.github.io/>) implemented in Python, and is freely distributed on GitHub (<https://github.com/VirtualPlants/draco-stem>) along with guidelines for installation and use.

**Keywords:** morphogenesis, shoot apical meristem, triangular mesh, topological optimization, mechanical simulation, python

## 1. MOTIVATION

With the ongoing advances in digital microscopy for the monitoring of plant cell development, and the emergence of computational pipelines analyzing such complex 4D data, the understanding of molecular and biophysical processes controlling plant morphogenesis appears closer and closer (Bassel and Smith, 2016). The emerging field of *computational morphodynamics* proposes more and

more complex multicellular models simulating growth and shape emergence, with a crucial need for validation (Jönsson et al., 2012).

Image analysis on time-lapse sequences of 3D *z*-stacks (be it confocal laser scanning microscopy or light-sheet microscopy) provides an unprecedented way to access morphometric data of a living tissue at ever-growing spatial and temporal resolutions (Keller, 2013). In plants, such approach generally requires segmenting the cells in membrane-marked images to extract their individual geometry (Fernandez et al., 2010; Federici et al., 2012; Barbier de Reuille et al., 2014; Bassel et al., 2014) and track their shapes in time along with their division events, either automatically (Fernandez et al., 2010) or with the assistance of a human user (Barbier de Reuille et al., 2015). This results in very rich 4D data, and a considerable source of information for validating biological hypotheses transferred into computational models.

However, manipulating voxel-based representations such as 3D images might be inconvenient given the necessary volume of information, and for some applications (visualization, physical simulation) lighter representations are preferred. The geometry of the cells can be represented by their common surfaces, under the form of a (generally triangular) mesh. In the case of biomechanical modeling of the plant tissue, the interactions located at the interfaces between cells are determinant components of the morphogenesis (Hamant et al., 2008), and a representation of the geometry of those interfaces in the most realistic way is essential for the validation of the underlying models (Bassel et al., 2014; Bozorg et al., 2014; Boudon et al., 2015). For approaches based on the classical Finite Element Methods (FEM) the mesh representing the tissue has an additional constraint of containing only regular elements, for a good numerical behavior and valid outputs.

Converting the segmented 3D cell shapes into triangular meshes appears as the best way to obtain those geometries. However, common approaches of isosurface generation such as marching cubes (Lorensen and Cline, 1987) do not create junctions between more than two cells and produce unrealistic, discontinuous, tissue configurations. Non-manifold generalizations have been developed (Hege et al., 1997) but their efficient implementation remains a challenge. Other meshing techniques based for instance on tetrahedral meshes (Shewchuk, 1998) also fail to reconstruct realistic cell shapes and need further processing to be used.

Some other methods have been used to convert tissues into meshes, mostly taking into account the resemblance of plant tissue in the meristematic zone with a Voronoi diagram (Barbier de Reuille et al., 2005) to study the possibility of computing cell geometry as a regular tessellation, which proved to work mostly in 2D (Shapiro et al., 2008). To go to 2.5D (surfacic mesh) (Barbier de Reuille et al., 2015) or to a 3D tessellation (Chakraborty et al., 2013) is possible but results in highly simplified meshes. An optimal conversion that will bridge the gap between experimental acquisitions and computational models is still an open challenge (Bassel and Smith, 2016).

## 2. ALGORITHMS AND IMPLEMENTATION

Our objective is to reconstruct 3D, non-manifold, FEM-ready triangular meshes of plant cell tissue from confocal microscopy images, using a dual reconstruction method (as depicted in **Figure 1**). Our input of the whole pipeline is a segmented shoot apical meristem tissue 3D image stack, obtained using either the MARS-ALT segmentation pipeline (Fernandez et al., 2010), an active region segmentation (Federici et al., 2012) or any 3D

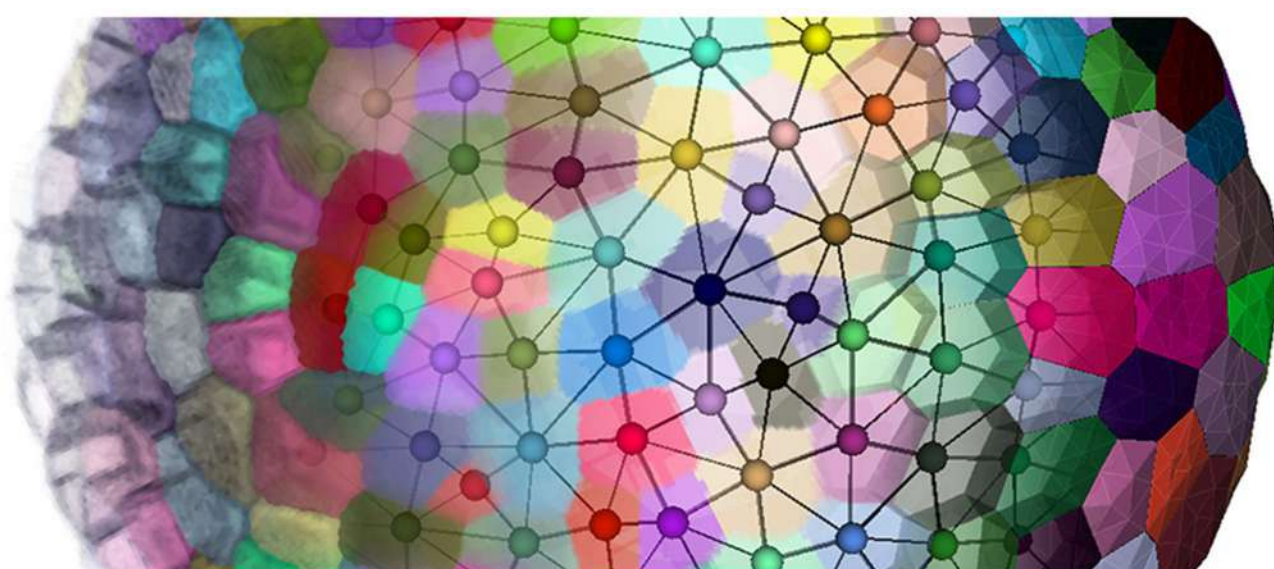


**FIGURE 1 |** Going from confocal microscopy image to cell tissue triangular mesh with DRACO-STEM.

watershed (Barbier de Reuille et al., 2015) or convenient 3D segmentation method creating adjacent labeled cell regions.

## 2.1. Definitions and Duality

In all the following, we consider that the tissue is a **collection of connected regions** representing the cells. In a first approximation, we assume that these regions form **convex polytopes** (polygons in 2D or polyhedra in 3D) subdividing the space of the tissue. For the sake of simplicity we will first expose our reasoning for the case of a 2-dimensional tissue, where polygonal cells are connected through single edges that represent **cell interfaces**. The vertices where several edges are connected are the **cell corners** where at least three tissue cells meet.

Such a representation falls within the scope of the geometrical notion of **cellular complex** (Agoston, 2005) (Chapter 7: *Algebraic Topology*), naturally used in earlier works to represent cell tissues (Pradal et al., 2009). A cellular complex of dimension  $N$  is a collection of  $n$ -dimensional elements (with  $n \leq N$ ) called  **$n$ -cells**, topologically connected together in such way that:

- Any  $n$ -cell of the complex has a boundary formed of  $k$ -cells ( $k < n$ ) that are all part of the complex.
- The intersection of two  $n$ -cells is either empty or  $k$ -cells ( $k < n$ ) belonging to both their boundaries.

In 2D, the tissue is then represented by a set of vertices, edges and convex polygons (respectively 0, 1 and 2-cells) where polygons intersect only at their boundary edges, and edges at their boundary vertices. A simple vision of how meristematic plant tissue can be represented as a cellular complex is given in **Figure 2**.

We add an even more restrictive hypothesis for cellular complexes representing plant tissue geometry, stating that only **exactly 3** polygonal 2-cells (representing the cells of the tissue) can meet at vertices of the complex. From a biological point of view, this could be interpreted as the assumption that a plant cell always shares a wall (at least a tiny portion) with all of its neighbors, so that the interface between two cells could not be reduced to a single vertex. In the tissues, ambiguous junctions implying 4 or more cells can occur, but they are not preserved in time and the evolution of adjacency provides information on which cells were neighbors.

Through the notions of shared boundaries and interfaces, such cellular complex representation also provides information on the

**adjacency** between tissue cells. An interface between two 2-cells defines an adjacency link between the tissue cells they represent, and the vertices where three 2-cells meet can be seen as **triangles of adjacency** linking the three concerned tissue cells. Considering the adjacency between cells is another way of looking at the tissue structure and the **adjacency object** formed by adjacency links and triangles constitutes a complementary view to the **geometry object**.

More precisely, we consider that those two objects are the **dual** of each other. The notion of duality refers to the idea that lowest dimension elements of a topological object correspond the highest dimension elements in its dual, and *vice versa*. For instance, 2-cells, the highest dimension elements in the geometry complex, representing tissue cells, are converted into points in the dual. Interfaces between tissue cells (edges, or 1-cells in the geometry) are converted into adjacency edges (dimension 1), and cell corners (vertices, or 0-cells in the geometry) correspond to triangles linking tissue cells in the adjacency (dimension 2). The vertices representing tissue cells in the adjacency object can for instance be placed at the center of the region of their corresponding cell. If we consider adjacency edges connected to only one adjacency triangle to be dual to infinite cell interfaces, this produces a reversible mapping between the two objects, illustrated in **Figure 3**. Consequently, we consider that the adjacency complex contains the same topological information as the geometry complex, and it might be a more suitable representation of the tissue depending on the application.

The vertices where cells meet in the geometry complex are mapped in the dual adjacency object to triangles which are **2-simplices**. A  $n$ -simplex is a  $n$ -dimensional element that is the convex hull of its  $n + 1$  vertices, generalizing the notion of triangle to any dimension. The consequence is that the dual of the cellular complex of geometry constitutes a **simplicial complex** of

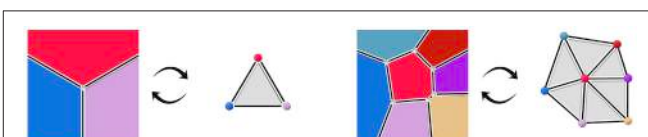


**FIGURE 3 |** Dualization of cellular complexes representing cells the geometry of tissue cells into simplicial complexes representing their adjacency.

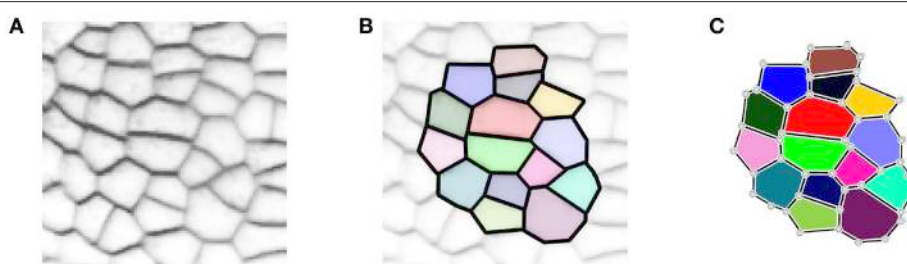


**FIGURE 2 |** A two-dimensional cell tissue (A) where cells are seen as a collection of connected polygons (B) that can be represented as a cellular complex (C).

adjacency, a special case of cellular complex where all  $n$ -cells are  $n$ -simplices. In 2D, simplicial complexes are triangulations, and the **Delaunay triangulation** of the cell center points constitutes an example of adjacency simplicial complex (De Berg et al., 2008) (Chapter 9: *Delaunay Triangulations*). It is a complex of triangles built on a set of vertices such that no vertex lies inside the circumscribed center of any triangle; its dual geometry is the **Voronoi diagram** of the center points, where cells are the volume of space closer to the point they represent than to any other.

In this setting, our problem consists then of reconstructing the cellular complex representing the geometry of the tissue given a **segmented image** as input. We consider segmented images as connected labeled regions, each label representing one tissue cell. Such an image encompasses all the information on the geometry of the tissue under the form of a connected grid of pixels, but the abstraction which is necessary to extract the cellular complex is not obvious to perform. An image directly defines a cellular complex in which 2-cells are pixels, and converting it into a complex with tissue cells as highest dimension elements requires a merging process in which it is difficult to ensure that topological properties will be preserved.

However, it is much easier to perform an abstraction of the adjacency relationships from the segmented image. A lot of useful information can be extracted from this pixel-based representation: cell center points can be computed as the center of mass of the regions, neighbor pixels of different labels can create adjacency links between the corresponding cells, and pixel squares containing at least three different labels can be extracted to define adjacency triangles.

This collection of simplices does not necessarily form a simplicial complex, as shown in **Figure 4C** where 4 triangles are overlapping in the ambiguous area, thus not partitioning the space. But if we use them to reconstruct a simplicial complex of adjacency (therefore forcing a choice in the ambiguous junctions), computing its dual is a straightforward way to obtain an approximated geometry of the tissue as a cellular complex. This is the key idea that drives our reconstruction method. The **Figure 4** illustrates this process of extracting adjacency simplices from pixel data to reconstruct a simplicial complex for which the dualization is direct.

These notions of cellular complexes of geometry and their dual simplicial complexes of adjacency extend very well to 3D. Tissue cells are then represented as polyhedra sharing polygonal interfaces, bounded by edges, and cell corners where

exactly 4 cells meet. Consequently, those points convert to **adjacency tetrahedra** in the dual domain, 3-simplices, that define a simplicial complex. Cell interfaces still correspond to adjacency links, and interface edges to adjacency triangles, ensuring that cells share a surface of wall with their neighbors. Here as well, the **Delaunay tetrahedrization** is the dual of the 3D Voronoi diagram. The **Figure 5** shows this extension of 2D duality to 3D.

3D segmented image stacks are defined over a grid of voxels that makes neighborhood between labeled regions more complex. But all adjacency simplices can still be extracted considering neighborhood relationships between voxels of different labels, up to the adjacency tetrahedra detected in voxel cubes where at least 4 different labels meet. Constructing a simplicial complex of such tetrahedra and computing its dual produces a 3D geometry simplicial complex. Then, the only step left is to triangulate the faces of such structure to obtain a **3D triangular mesh** of the tissue, the very object we aim to produce.

## 2.2. Data Structure

As we just saw, the 3D triangular meshes and polyhedral complexes representing the tissue geometry, as well as the adjacency simplicial complexes, may all be represented by the topological structure of cellular complex. In the case of tissue meshes, the 3-cells (elements of dimension 3) of this complex are the actual cells of the tissue, whereas in adjacency complexes, they correspond to tetrahedra linking 4 tissue cells adjacent to each other in the tetrahedrization.

We implement cellular complexes as incidence graphs, a graph-like boundary representation in which the nodes are the 0, 1, 2, and 3-cells of the complex (respectively vertices, edges, faces, and polyhedra) and the links define the boundary relationship between elements of consecutive dimensions. For instance an element of dimension 1 will generally be linked to two elements

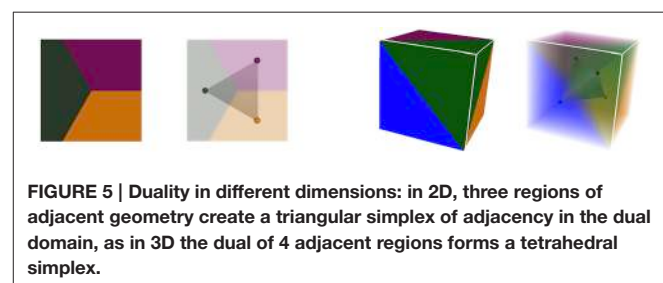


**FIGURE 5 |** Duality in different dimensions: in 2D, three regions of adjacent geometry create a triangular simplex of adjacency in the dual domain, as in 3D the dual of 4 adjacent regions forms a tetrahedral simplex.

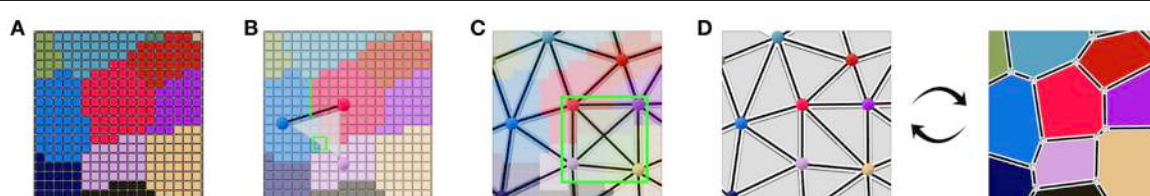


**FIGURE 4 |** Abstracting an adjacency simplicial complex from a 2D segmented image: cells as connected regions of labeled pixels (**A**), extraction of adjacency simplices from pixel neighborhoods (**B**), the set of adjacency simplices not necessarily forming a simplicial complex (**C**), and the reconstructed valid simplicial complex converting directly into the geometry cellular complex through dualization (**D**).

of dimension 0, the two vertices that define it as an edge. The nodes of the graph can bear additional properties to make the data structure a rich representation of annotated cell complexes. An example of such a representation used in a triangular mesh is given in **Figure 6**.

All the connectivity information between the elements is included in the graph structure, a great advantage to perform topological operations. Another advantage is that generally, the dualization operation applied on an incidence graph simply consists in flipping over the graph: all the elements are preserved, as well as their topological relationships, but their dimensions are swapped (elements of dimension 3 converting into elements of dimension 0 in the dual graph, dimension 2 into dimension 1, and so on).

In such topological representations, the geometry of the structure relies on the spatial positions affected to the vertices (elements of dimension 0) that will define the shapes of all higher dimension elements. The topological relationships constraint the overall shape of the object, but in the end the local appearance of its components depends entirely on the geometry. In particular, to obtain triangular meshes usable for FEM applications, it is required to adjust the positions of the vertices with a high concern for regularity of the triangles.

### 2.3. Methods

The DRACO-STEM algorithm aims at computing a 3D triangular mesh of the tissue by the dualization of a simplicial complex of adjacency, and the triangulation and optimization of the resulting polyhedral geometry. As stated earlier, adjacency simplices can be extracted from the segmented image. However, due to segmentation errors, local noise, or converging regions, they do not necessarily form a simplicial complex (see **Figure 4C**). Some might intersect, or even be included in another, or holes may exist inside the tissue. To perform the dual reconstruction, it is then necessary to build a valid simplicial complex that includes as many image-extracted simplices as possible, which is the idea behind our method.

The mesh construction algorithm can then be split into two independent steps illustrated in **Figure 7**:

- The first one (DRACO) starts by extracting cell neighborhood relationships from the segmented image to reconstruct a

simplicial complex of cell adjacencies that optimally matches them. This adjacency complex is either optimized from a valid initial guess for the whole tissue, or, if limited to the outermost cell layers, constructed by aggregation of simplices extracted from the image. The resulting complex can directly be dualized into a valid topological representation of the tissue. Its geometry is defined by setting cell corners to their position in the image, and possibly triangulating the cell interfaces.

- The second step (STEM) starts from such a 3D triangular mesh of the tissue, obtained from the DRACO algorithm, or from another topologically accurate meshing method [interfaces of tetrahedral image mesh (Shewchuk, 1998) or decimated multi-label marching cubes mesh (Hege et al., 1997)]. The algorithm performs a specific optimization of the geometry of the mesh to improve simultaneously the regularity of the triangles and the shape of the cells while keeping the topological and geometrical consistency with the segmented image in the best compromise possible.

The proposed mesh generation pipeline relies on a set of original mesh processing algorithms operating on cellular complexes and trying to optimize both their topology and their geometry along several criteria, through energy minimization. Such complex optimization processes are necessary to obtain a faithful mesh of the original tissue, with convex polygonal cell interfaces and triangles regular enough to be used as an input to simulation methods.

#### 2.3.1. Dual Reconstruction by Adjacency Complex Optimization (DRACO)

The first component (DRACO) works on the dual adjacency object to later reconstruct a geometry, using the method detailed in Cerutti et al. (2015). This idea initially comes from the fact that the geometry of the meristematic tissue forms a regular tessellation (Shapiro et al., 2008) that strongly evokes a Voronoi diagram of the cell centers. However, the tissue presents strong local anisotropy in the shapes of its cells that can not be well approximated by a Voronoi diagram. This anisotropy can be explained by the local mechanical constraints on the cells and by the directed growth and division processes that create highly variable shapes. The very isotropic Voronoi diagram would end up creating walls between cells that are not actual neighbors.

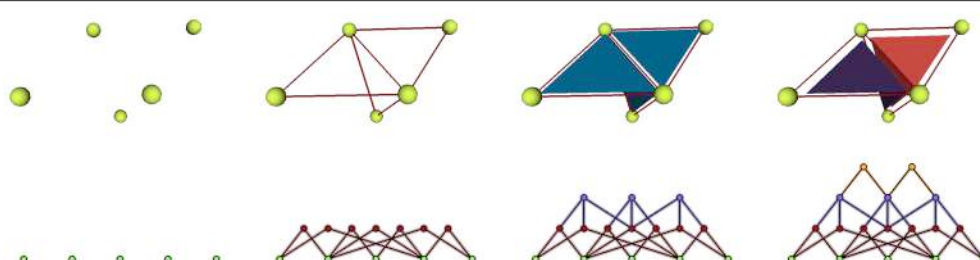
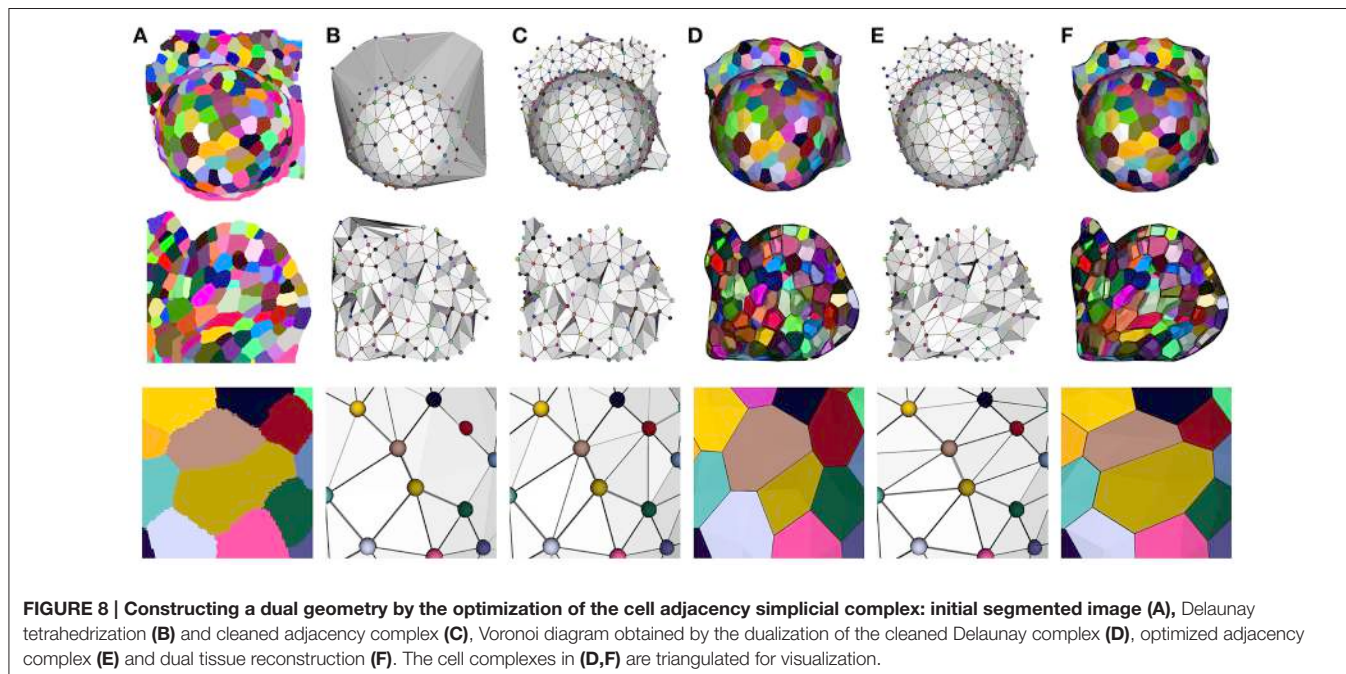
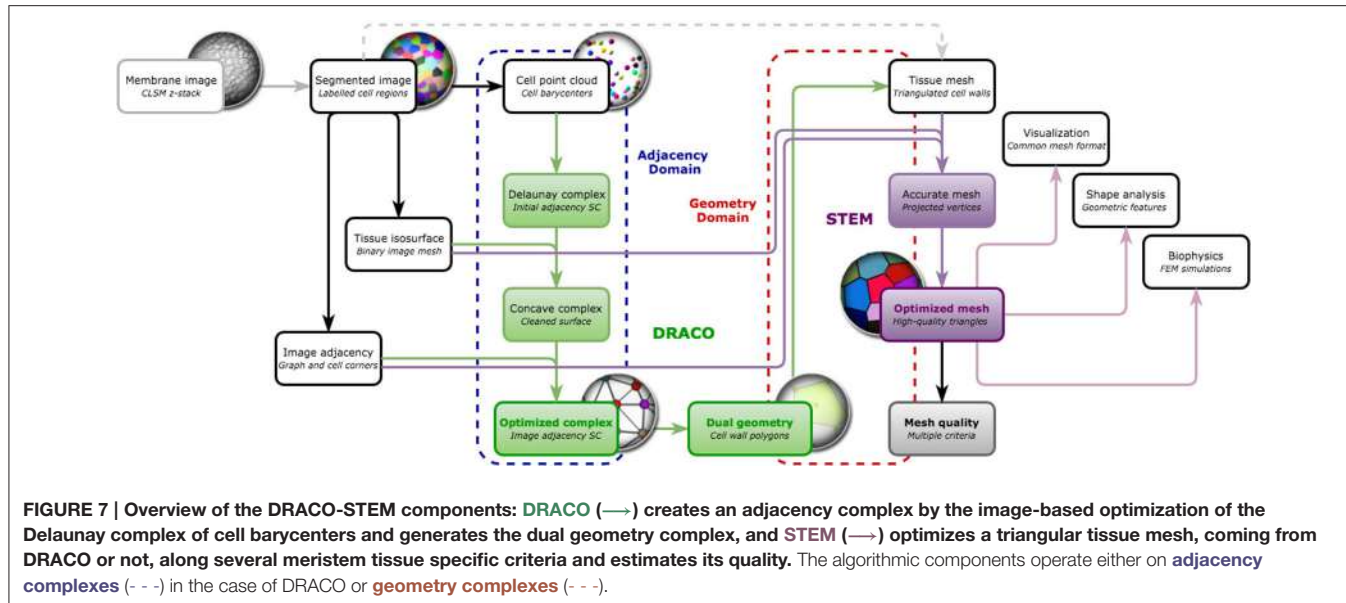


**FIGURE 6 |** Representation of a mesh containing 2 cells defined by 3 triangular faces as an incidence graph: 3D mesh on the first line, incidence graph representation on the second; the edges defining the triangles are linked to their two extremities, the triangles to their respective edges, and the cells to their boundary triangles.



Since this tessellation is the dual of a simplicial complex (the Delaunay tetrahedrization) in which tetrahedral units define adjacencies between cells by their edges, the fact that the Voronoi diagram creates wrong walls can be related to the fact that some adjacency edges are wrong in the Delaunay complex. The Delaunay criterion creates edges between non-adjacent cells of the tissue. In consequence, if we correct this adjacency simplicial complex so that it fits the actual adjacencies observed in the tissue, the resulting dual geometry will be a much better approximation of the cell walls.

Our optimization method reflects this idea, and takes the Delaunay tetrahedrization of the cell centers as a valid starting

point. This complex is then optimized by a two step process to fit the adjacencies extracted from the image. The first one consists in getting rid of the excessive triangles due to the constraint of convexity of the Delaunay complex (see Figure 8B). This is done by successively removing exterior triangles that either cross the surface of the tissue, present too long edges or form flat tetrahedra (or slivers).

Then the actual tissue adjacencies are optimized following an iterative process performing local topological operations (triangle swaps and edge removals, Shewchuk, 2002) in order to minimize an energy functional. This energy defined on the adjacency simplicial complex  $\mathcal{T}$  is composed of several terms to

take into account the adjacencies extracted from the segmented image  $\mathcal{S}$ , the prior knowledge about the number of possible neighbors for a cell, and the regularity constraints preventing elongated tetrahedra so that distant cells do not end up as neighbors. Each term is weighted by a coefficient so that its relative influence can be fine-tuned:

$$\begin{aligned} E(\mathcal{T}, \mathcal{S}) = & \omega_{image} E_{image}(\mathcal{T}, \mathcal{S}) + \omega_{prior} E_{prior}(\mathcal{T}) \\ & + \omega_{regularity} E_{regularity}(\mathcal{T}) \end{aligned} \quad (1)$$

The content and formulation of those three energy components can be found in Section 1.2 of Supplementary Material. The energy minimization takes the form of an iterative simulated annealing process, with successive temperature cycles, high temperatures allowing non-optimal transformations, in order to reach non-trivial optimal configurations when the temperature lowers. This method shows a great improvement in the adjacency estimation, recovering nearly 90% correct adjacency links when the Delaunay complex only reached 76% (Cerutti et al., 2015).

However, due to the hypotheses made on cell adjacency detailed in Section 2.1, the method might create incorrect adjacencies in the ambiguous cell junctions where 5 cells or more come close together. Considering that the adjacency complex forms a tetrahedralization of the cell centers structurally forces the method to get rid of the ambiguity by making a decision on which 4 cells are actually going to be adjacent in the tissue development. Any choice would be correct based on the image, since in these cases all the cells will have voxels in contact, and the decision will then be mostly made based on geometry and number of neighbors. As shown in **Figure 9**, the only way to ensure that the decision made at this point is right would be to compute cell lineages between consecutive time points to know which groups of daughter cells will be adjacent.

The dualization of the resulting adjacency complex provides a simple polyhedral representation of the cells. An important point for the accuracy of this polygonal mesh is to determine the position of its vertices, and we chose, as in a Voronoi diagram, to place them at the center of the circumscribed sphere of their dual adjacency tetrahedron. However, since the Delaunay constraint no longer holds, we had to force them to remain inside their tetrahedra by projection on the nearest face, to avoid geometrical

artifacts (face intersection notably), using a process detailed in Section 1.3 of Supplementary Material. The result of this step is a very simple tissue mesh composed of polyhedral cells but reflecting faithfully the topological structure of the tissue with accurate cell walls, as shown in **Figure 8**.

### 2.3.2. Layer Dual Reconstruction

In the general case, the adjacency object formed using the adjacency simplices extracted from the image does not constitute a valid simplicial complex. But it is possible to take advantage of the specific layered structure of the meristem tissue to reconstruct only the two outermost layers of cells. The epidermal layer L1 and the one right underneath L2 are very well separated and constitute independent sets of cells. This means that if we consider the simplicial complex of adjacency of L1 and L2 cells, the set of triangles linking only L1 cells forms a simplicial complex, as well as set of triangles linking only L2 cells. Consequently, the adjacency complex between L1 and L2 cells will only contain tetrahedra either composed of a triangle of L1 cells and one L2 cell, a triangle of L2 cells and one L1 cell, or two L1 cells and two L2 cells.

This is a very strong prior information, not valid further down in the tissue, that can be used to create a valid simplicial complex by aggregation of tetrahedra that correspond to the structure of these tissue layers. To do so, we added a way of iteratively constructing the complex from a set of candidate tetrahedra extracted from the segmented image. Each tetrahedron is assigned a weight taking into account the distances between the cells it links and the area of the wall they share. The process starts from the tetrahedron achieving the best weight and adds to the complex its neighbors that do not create intersections, selecting the highest weights and unambiguous configurations first. The added tetrahedra are placed into a queue to continue the exploration, until no new candidate can be added.

The resulting complex is a single layer of tetrahedra that makes it possible to reconstruct accurately the L1 and L2 cells by dualization. The same aggregation process can also be used to reconstruct a single layer of cells by building a simplicial complex made of triangles representing the cell adjacencies inside the L1 or L2 layer. This allows us to reconstruct a surfacic 2.5D polygonal mesh of the cell layer. **Figure 10** gives an illustration of these two alternative methods.

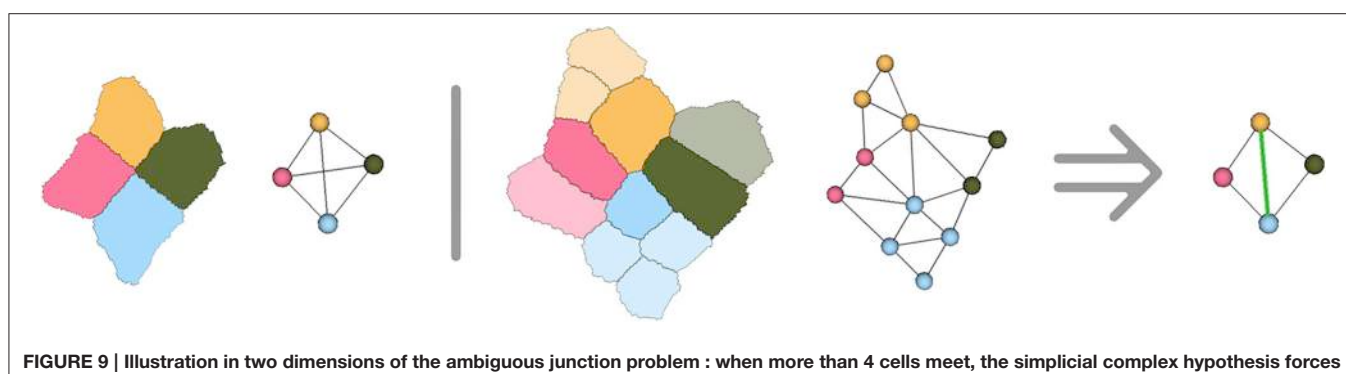


**FIGURE 9 |** Illustration in two dimensions of the ambiguous junction problem : when more than 4 cells meet, the simplicial complex hypothesis forces to make a choice concerning cell adjacency, that might only be verified by looking at the further evolution of the ambiguous junction.

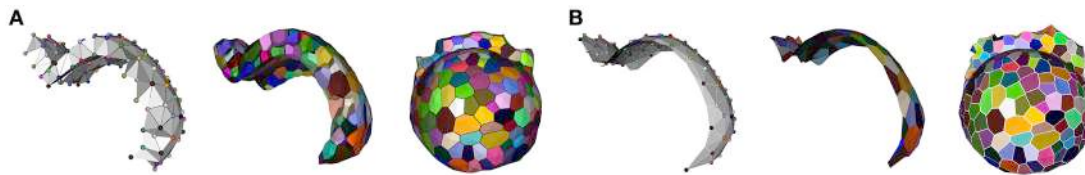


**FIGURE 10 |** Layer reconstruction using adjacency complexes: L1-L2 tetrahedrization and its dual 2-layer 3D geometry (A) and L1 triangulation and its dual 2.5D geometry (B).

### 2.3.3. SAM Tissue Enhanced Mesh (STEM)

A triangular mesh obtained out of the DRACO pipeline may be too coarse and present too many irregular triangles for a use in FEM-based simulations. It is therefore required to provide a way of enhancing such structures. The second stage of our mesh generation pipeline consists then of a multi-objective optimization algorithm for non-manifold triangular meshes, based on the methodology described in Cerutti and Godin (2015). It takes as input a triangular mesh such as the one obtained by triangulating the DRACO geometry (either by Delaunay, or more simply placing an additional vertex at the center of each cell interface, a process referred as “Star” triangulation from now on) or by another coarse, topologically accurate meshing method.

The mesh is first passed through optional pre-processing steps to refine it (and make it more precise), enhance its topological properties and its local accuracy:

- Simple triangle split refinement (creating 4 identical triangular faces for each input face).
- Isotropic remeshing with target edge length for global refinement (Botsch and Kobbelt, 2004).
- Surface vertex projection onto the surface of the meshed object (extracted as a binary isosurface).
- Cell corner identification and positioning based on the positions extracted from the segmented image.

Then, the core optimization process can be applied. Here again, it is implemented as an iterative energy minimization process performing local operations to improve several criteria simultaneously. This time, the local operations are vertex shifting (relocation of the vertex points in a small sphere around their current position) and interface triangle edge flips. The energy minimized by the process has the same form as Equation (1), with an image attachment term tying vertices to actual cell interfaces, a shape prior term producing polygonal flat cell walls, and a regularization term ensuring regularly shaped triangles and isotropic vertex neighborhoods (more details in Section 1.5 of Supplementary Material). The Figure 11 gives an example of the application of this tissue specific mesh enhancement algorithm.

### 2.3.4. Quantitative Quality Estimation

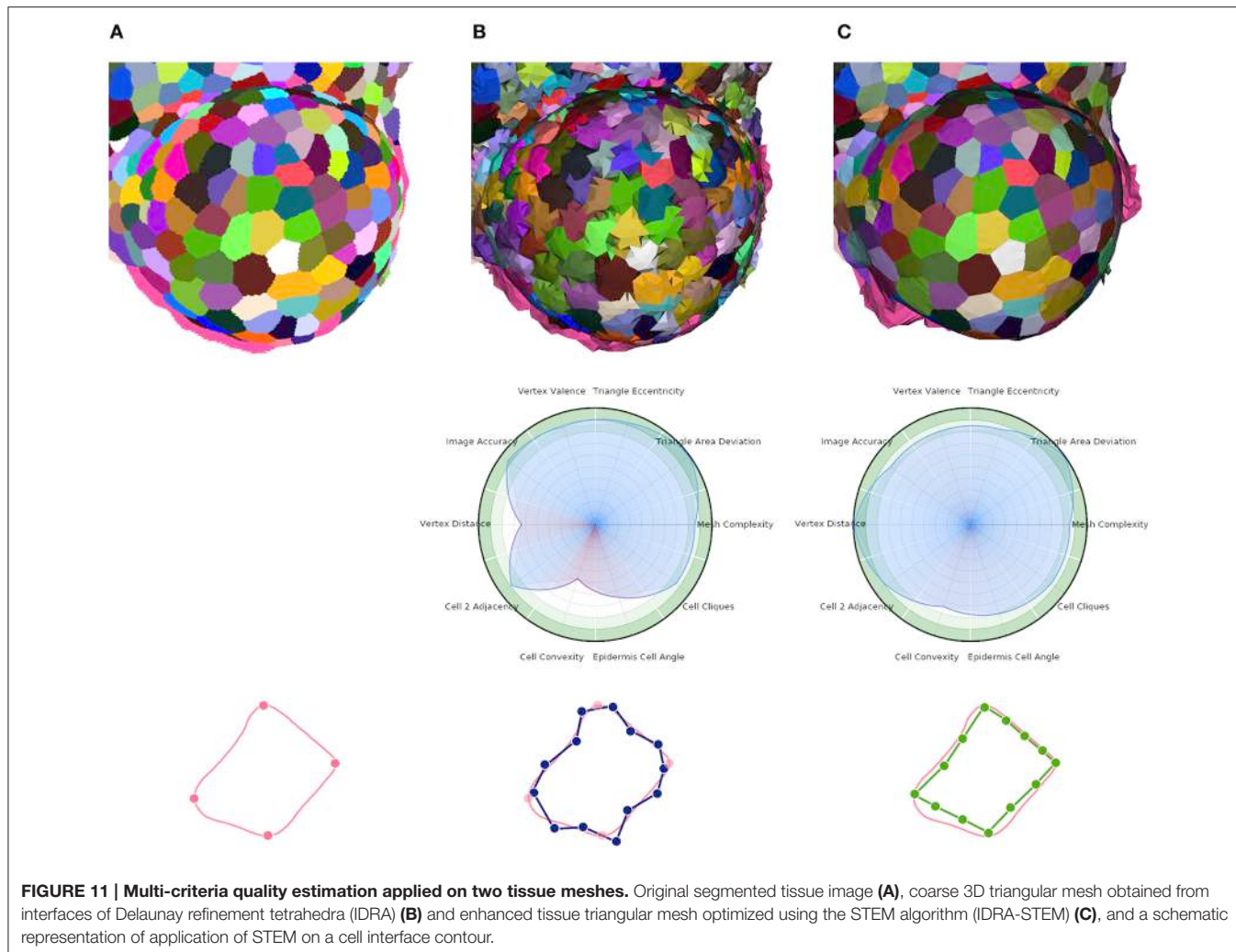
The quality of a mesh is not an unambiguously defined concept, and depends a lot on the application intended for the considered object. No unique, objective quality measure exists, it has to be defined to meet the expectations of the end-user. In our context of reconstruction of a biological entity from an input image with the

perspective of usability in FEM simulations, the notion of quality spreads over several aspects:

- **Prior consistency:** the resulting mesh should be consistent with what we expect from the tissue structure we are reconstructing, based on the hypotheses we made on tissue structure. On the geometry side, we expect to have convex cells with convex polygonal facets, and on the topology side, we assume that the mesh should be a cellular complex dualizable into a simplicial complex.
- **Image consistency:** since the mesh is based on a real acquisition, it should also correspond as well as possible to the segmented image used as input (which we consider a valid representation of the tissue, as far as possible) both geometrically (the shapes and contours of the cells) and topologically (adjacency relationships between cells).
- **Intrinsic regularity:** finally, considering the goal of using the mesh for FEM simulations, the regularity of the triangular elements of the mesh should be as high as possible for sake of numerical robustness, both geometrically (regularity and homogeneity of the triangles) and topologically (valence of the vertices).
- **Complexity:** in addition, to ensure a fast visualization and a reasonable computation time when running simulations, this multi-faceted quality should be achieved using as few triangles as possible, and we consider therefore the complexity of the mesh (in terms of number of elements) as a component of its global quality.

To obtain objective measures defining the quality of the 3D triangular meshes resulting from the DRACO-STEM pipeline, we defined a set of normalized estimators covering all these different aspects. Many of these measures have their values comprised between 0 and 1, but some do not, and we chose to normalize them by a handset “optimal” value to make a simultaneous visualization and visual comparison easier. We end up with 10 quality estimators defined as following:

- **Cell convexity** (prior global geometry): estimated for each cell in the mesh as the ratio between its volume and the volume of its convex hull, and averaged across the mesh. (*no normalization*).
- **Epidermis cell angle** (prior local geometry): computed at each surface cell junction as the absolute difference of the angles made by cells at the junction with the theoretical value of 120°, and averaged across the mesh. (*normalized by an angular deviation of 30 degrees, measured negatively from 1*).



- **Cell cliques** (prior topology): percentage of the cell junctions (mesh vertices neighboring at least 4 cells, or 3 on the surface) where strictly more than 4 (respectively 3) cells meet. (*no normalization, measured negatively from 1*).
- **Image accuracy** (image global geometry): estimated for each cell in the mesh as the Jaccard index (overlap measure) of the voxels of corresponding regions in the segmented image and in the voxelized mesh image, and averaged across the mesh. (*no normalization*).
- **Vertex distance** (image local geometry): computed for each cell junction vertex in the mesh as the distance to its corresponding point in the image, averaged across the mesh. (*normalized by  $\frac{\sqrt{3}}{4}$ , length of a voxel diagonal in an image of typical  $0.25\mu\text{m}$  resolution, measured as a reciprocal*).
- **Cell 2-adjacency** (image topology): computed as the Jaccard index (overlap measure) of the cell adjacency edges extracted from the image and those in the dual adjacency mesh. (*no normalization*).
- **Triangle area deviation** (intrinsic global geometry): estimated as the standard deviation of the mesh triangles. (*normalized by  $\sqrt{2}$  times the average area of the triangles, measured negatively from 1*).

- **Triangle eccentricity** (intrinsic local geometry): measured using the average eccentricity of the mesh triangles, computed using the sum of the sinuses of the triangle. (*normalized by 0.5, measured negatively from 1*).
- **Vertex valence** (intrinsic topology): the average absolute difference between the number of neighbors of mesh vertices and their optimal value (6 inside interfaces). (*normalized by 6, measured negatively from 1*).
- **Mesh complexity** (global complexity): estimated using the average number of triangles necessary to represent one cell. (*normalized by a reasonable number of 152, leading to a suitable total number of faces for finite element models of a 1,000-cell tissue, and corresponding to a good triangulation of the space-filling truncated octahedron, measured as a reciprocal*).

Defined this way, the quality of a mesh can conveniently be visualized on a circular plot (or spider-web) as the one shown in **Figure 11** and provide an immediate visual comparison of the

pros and cons of a meshed tissue. In this example, the first mesh has strong defects on the local cell geometry (Vertex distance) as well as on the consistency of cell geometries with biological prior (Cell convexity and Epidermis cell angle). The second mesh largely corrects this defects but actually does so by sacrificing a bit of regularity (Triangle eccentricity) and faithfulness to the image (Image accuracy).

Such a quantitative quality analysis is a precious tool to ensure the structures that are produced by the method will meet the requirements of the application it is intended for. Providing specific quality estimators along with the mesh generation algorithms is a way to guarantee the reproducibility of the presented results.

## 2.4. Implementation and Visualization

The DRACO-STEM algorithms, as well as the data structure used to represent cellular complexes are supplied as packages of the open-source plant modeling library OpenAlea (Pradal et al., 2008, 2009). This library is designed as a middleware providing tools and components to build dynamic systems implementing plant models. It is developed in Python language and is available on the GitHub software sharing platform.

OpenAlea comes with a multi-paradigm development platform called OpenAleaLab which allows modelers to integrate different sources into a unique customizable environment (Coste et al., 2014). In particular, specific component related to cell tissue modeling have been developed into a particular instance of the development environment (TissueLab) to provide easy visualization and manipulation of cell tissue structures. This way, cellular complexes representing the tissue can be visualized in interaction with tissue images, along with other useful visual components (plots, interactive console, code editor). **Figure 12** shows an example of the integration in the OpenAleaLab platform.

Using the DRACO-STEM algorithms within the OpenAlea framework is rather simple as it is integrated to work on the same data structures and with the same philosophy as the rest of the library. A specific class named **DracoMesh** is used to perform the optimization and dualization and is instantiated using an image as argument. Then three main functions applied to this object reflect the different steps of the process (Delaunay complex creation, adjacency complex optimization and dual reconstruction) and allow to manipulate parameter values. An example of a program generating a 3D tissue mesh using DRACO-STEM is given in Table 1 of Supplementary Material.

## 3. RESULTS AND DISCUSSION

### 3.1. Mesh Generation Results

We applied our evaluation method to triangular tissue meshes generated from a dataset of segmented tissue images. This dataset was composed of two time-series of a floral meristem at early developmental stages, containing respectively 3 and 10 time points. Each image contains in average around 1,000 cells, and offers a good diversity of surface curvature, and quite variable cell shapes. Using different meshing techniques and evaluating the resulting structures using the same quantitative criteria

provided us with extensive measures of the pros and cons of each method, and is the best way to assess which constitutes the best compromise. The methods we evaluated correspond to those implemented in the library we propose, and all constitute ways to reconstruct a topologically accurate tissue reconstruction:

- **Interfaces of Delaunay refinement tetrahedra** (IDRA): mesh obtained by converting the image into a coarse tetrahedral mesh using Delaunay refinement (Shewchuk, 1998), and keeping only the triangles belonging to tetrahedra of different labels.
- **Interface enhanced tissue mesh** (IDRA-STEM): same method as the previous one, except that the mesh is optimized using the STEM algorithm.
- **Voronoi Diagram of the cell centers** (Voronoi (Star)): obtained by dualization of the Delaunay tetrahedrization of the cell center points, in which the interfaces are triangulated simply by placing a vertex at the interface center and linking all interface edges to it (star triangulation).
- **Dual reconstruction using the optimized cell complex** (DRACO (Star)): obtained by dualization of the simplicial complex of adjacency optimized from the Delaunay one using the DRACO algorithm; interfaces triangulated using the star triangulation.
- **Dual reconstruction enhanced tissue mesh** (DRACO-STEM): same method as the previous one, except that the star interface mesh is remeshed locally, projected on the tissue surface and optimized using the STEM algorithm.

Concerning the other methods that could have been included, we chose to discard the standard 3D Marching Cubes (Lorensen and Cline, 1987) as well as its implementation in MorphoGraphX (Barbier de Reuille et al., 2015) because the produced meshes do not contain adjacency connections between more than two cells, and fail at representing accurately the topology of cell junctions. The Generalized Marching Cubes (Hege et al., 1997) would correct this specific problem, and so could probably the adaptive tessellation method (Chakraborty et al., 2013), but they are not available to our knowledge in any freely available package, and could therefore not be tested.

The results of the evaluation of the retained methods are presented in **Table 1** summing up the average value and standard deviation obtained for all the different quality estimators on the tested dataset.

The first conclusion to draw from these results is the clear improvement provided by the adjacency complex optimization method we introduced. When comparing the results of the meshes obtained from Delaunay (Voronoi (Star)) and the ones from the optimized complex (DRACO (Star)), triangulated using the same method, there is a clear improvement in the image consistency criteria (image accuracy:  $0.677 \rightarrow 0.790$  [ANOVA,  $p < 0.001$ ] and cell adjacency:  $0.748 \rightarrow 0.874$ , [ $p < 10^{-7}$ ]). The cell shapes are also more realistic, with a better convexity ( $0.679 \rightarrow 0.824$  [ $p < 10^{-7}$ ]). The application of DRACO therefore results in a striking improvement of the overall mesh quality ( $0.783 \rightarrow 0.865$  on average [ $p < 10^{-7}$ ]).

The other notable information is the benefit provided by our specific mesh optimization procedure STEM. Applied either on

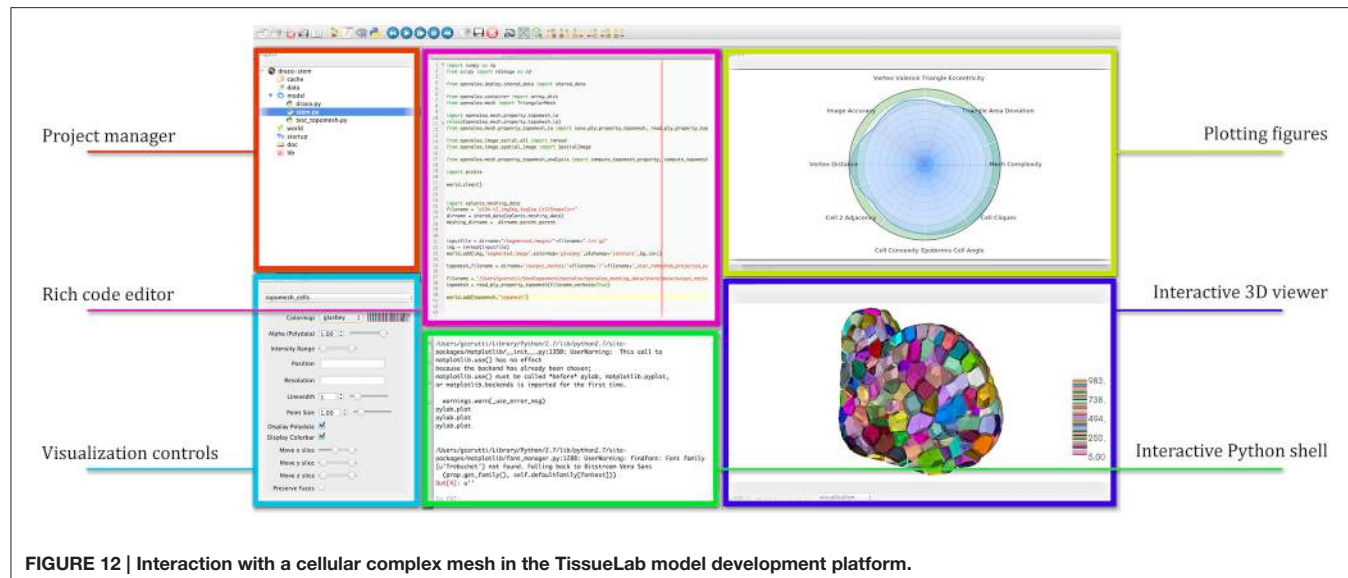


FIGURE 12 | Interaction with a cellular complex mesh in the TissueLab model development platform.

TABLE 1 | Average quality measures on meshes obtained with different generation methods: dual reconstructions from Delaunay or optimized adjacency complexes, interfaces of Delaunay refinement tetrahedra and their STEM enhanced versions.

Method	Prior Shape			Image Acc.	Dist.	2Adj.	Triangle Area	Ecc.	Val.	Mesh Cplx.	Mean	Min
	Conv.	Angle	Clique									
<b>IDRA</b>	0.526 ±0.024	0.671 ±0.011	0.872 ±0.009	0.928 ±0.002	0.634 ±0.032	0.89 ±0.011	1.0 ±0.0	0.92 ±0.001	0.888 ±0.001	0.868 ±0.04	0.82 ±0.01	0.526 ±0.024
<b>IDRA-STEM</b>	0.794 ±0.028	0.828 ±0.013	0.872 ±0.009	0.844 ±0.02	1.0 ±0.0	0.89 ±0.011	0.999 ±0.002	0.863 ±0.004	0.845 ±0.006	0.868 ±0.04	0.881 ±0.009	0.794 ±0.028
<b>Voronoi (Star)</b>	0.679 ±0.034	0.889 ±0.016	1.0 ±0.0	0.677 ±0.036	0.565 ±0.092	0.748 ±0.036	0.816 ±0.035	0.682 ±0.017	0.778 ±0.004	1.0 ±0.0	0.783 ±0.024	0.564 ±0.092
<b>DRACO (Star)</b>	0.824 ±0.034	0.898 ±0.023	1.0 ±0.0	0.79 ±0.033	1.0 ±0.0	0.874 ±0.026	0.782 ±0.042	0.703 ±0.029	0.784 ±0.005	1.0 ±0.0	0.865 ±0.014	0.702 ±0.03
<b>DRACO-STEM</b>	0.897 ±0.018	0.916 ±0.019	1.0 ±0.0	0.836 ±0.029	1.0 ±0.0	0.874 ±0.026	0.994 ±0.009	0.788 ±0.025	0.859 ±0.023	1.0 ±0.0	0.916 ±0.01	0.788 ±0.025

the IDRA or the DRACO meshes, this optimization leads to a significant increase in the average quality ( $0.82 \rightarrow 0.881$  and  $0.865 \rightarrow 0.916$  respectively [ $p < 10^{-7}$ ]) and maybe more importantly in the minimal value of the estimators, meaning that no aspect of the quality is left apart. This increase concerns first the shapes of the cells (notably cell convexity and cell angle estimators) but globally preserves the other values in the same time. The only exception is the decrease of image accuracy ( $0.928 \rightarrow 0.844$  [ $p < 10^{-7}$ ]) and triangle regularity ( $0.92 \rightarrow 0.863$  [ $p < 10^{-7}$ ]) in the case of IDRA meshes, which comes from the fact that the initial meshes have very regular triangles and are globally consistent with the image, but with very noisy cell boundaries as visible in Figure 11B, and on the vertex distance estimator. The application of STEM corrects the latter at the

expense of decreasing the regularity of the mesh elements and the volumetric consistency with the image as in Figure 11C.

Concerning the comparison between IDRA and DRACO meshing methods, their differences before any optimization appear clearly in our quality estimators. IDRA provides meshes with a very high regularity that globally fit very well the cell regions in the image, but with oscillating to spiky boundaries that make the unusable as such. DRACO meshes do not show the same regularity, in particular with the star triangulation and no remeshing (triangle eccentricity: **0.920** | 0.703, image accuracy: **0.928** | 0.790 [ $p < 10^{-7}$ ]). However in terms of the local shape of the cell interfaces and precision at the level of the cell junctions, they are clearly superior (cell convexity: 0.526 | **0.824**, vertex distance: 0.634 | **1.0** [ $p < 10^{-7}$ ]).

The necessary application of STEM, which was designed to draw meshes toward a good compromise, tends to even things up on several aspects. IDRA-STEM and DRACO-STEM meshes have close values of image consistency indicators (image accuracy: **0.844** | 0.836 [ $p > 0.1$ ], cell adjacency: **0.890** | 0.874 [ $p \approx 0.05$ ]) even if the regularity of the mesh elements remains clearly lower (triangle eccentricity: **0.863** | 0.788 [ $p < 10^{-7}$ ]). But the difference on the cell shape estimators (cell convexity: 0.794 | **0.897** [ $p < 10^{-7}$ ]) and the resulting average quality (0.881 | **0.916** [ $p < 10^{-7}$ ]) demonstrates that the DRACO-STEM algorithm provides an excellent compromise between all the desirable properties of a 3D tissue mesh.

In the end, the result of this pipeline is a mesh that corresponds as well to the image as its optimized tetrahedral mesh conversion, but with much better properties regarding the shapes and arrangement of its cells, and a regularity and size that makes it adequate for a use in biophysical simulations. The Figure 13 shows an example of such a mesh structure along with its quality evaluation.

### 3.2. Geometrical and Biological Information Projection

The mesh generation algorithms come with a complementary mesh processing library that allows in particular to compute geometrical properties on a tissue mesh. The cellular complex structure is defined in such way that several properties can be assigned to its elements of different dimensions. For instance, one can compute the volumes of the cells and the area of the interfaces, and both will be stored simultaneously in the structure along with other properties.

In particular it is possible to estimate curvature information (mean curvature, Gaussian curvature, principal directions, curvature tensor) on the surface of the mesh, measures that may be difficult to obtain using another tissue representation, but can be easily estimated on a surfacic triangular mesh (Theisel et al.,

2004). Such intrinsic geometric property of the tissue may be of great interest put in perspective with other biological measures obtained at the surface of the tissue.

The tissue structure can also be used to project external information onto a convenient spatialized visualization. For example, a fluorescence-based biological signal (hormone concentration or genetic expression) quantified from a nuclei image can be turned into a property of the cells of the tissue and visualized with the same tools. Or, given a sequence of images of the same organ with the cells tracked in time, the mesh can be used as a support for the visualization of growth rates and directions. The tissue structure constitutes then a very useful tool for the visualization and exploration of morphogenesis processes, as illustrated in Figure 14.

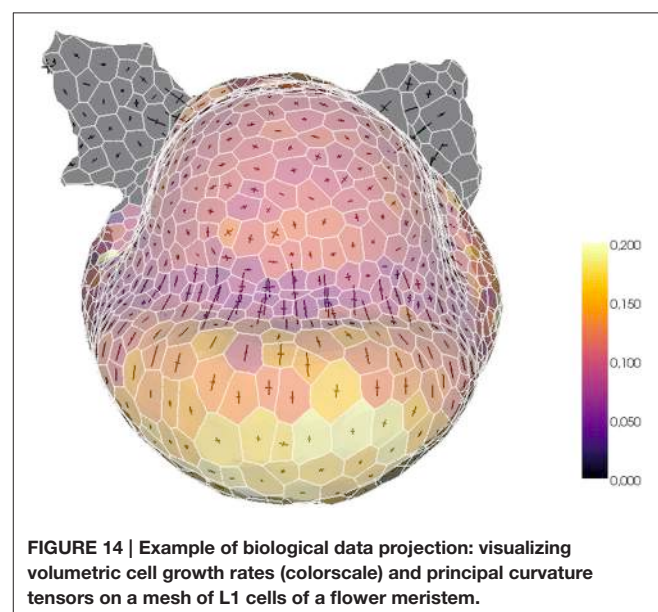


**FIGURE 14 |** Example of biological data projection: visualizing volumetric cell growth rates (colorscale) and principal curvature tensors on a mesh of L1 cells of a flower meristem.

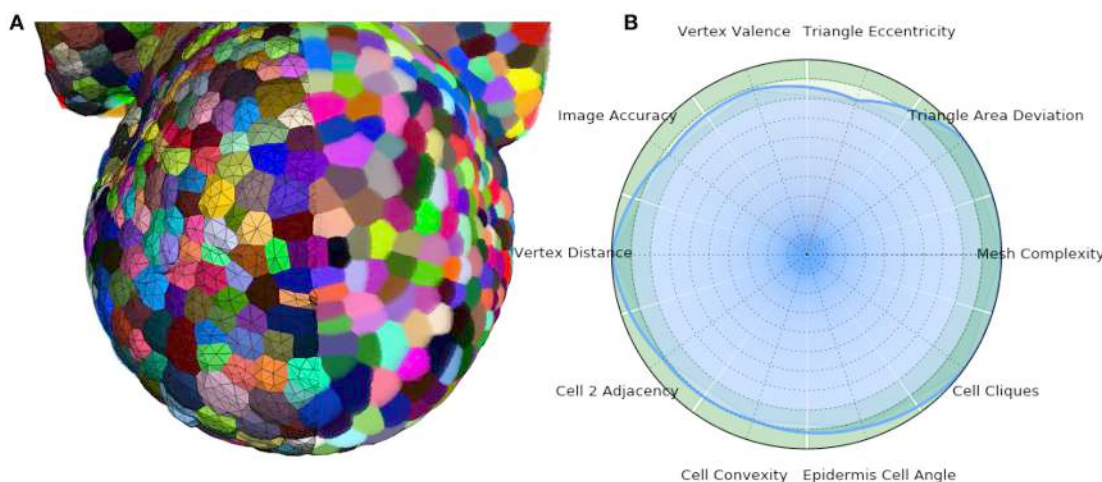


**FIGURE 13 |** 3D triangular mesh generated using the DRACO-STEM pipeline on a segmented flower meristem image (A) and its multi-criteria quality evaluation (B).

### 3.3. Biomechanical Simulations

Triangular tissue meshes produced using the DRACO-STEM pipeline have been used in the context of biomechanical simulation of cellular growth. In plants, growth can be assimilated to the yielding of cell walls under Turgor-induced stresses. It can be formalized through differential equations accounting for this yielding behavior and the mechanical equilibrium of the whole structure. Numerically, these equations can be simulated using the Finite Element Method (FEM). This approach suffers from two major bottlenecks: first, the subtle and complex shapes of organic tissues require a high quality meshing pipeline in order to generate biologically relevant structures. Second, stability of the numerical integration schemes depends heavily on the regularity in shape and size of the meshing triangles. In this perspective, tools such as the STEM optimization where the intensity of regularization can be fine tuned can really help to achieve stable and accurate simulations.

We wanted to ensure that the triangular meshes produced by DRACO were suitable for such applications and that the STEM component was pertinent in this context. Therefore, to estimate the influence of regularization on mechanical simulations, we meshed the same segmented tissue using DRACO with and without STEM optimization to compare the behavior of the numerical solver (Allard et al., 2007) and the outputs of the mechanical simulations in each case. A quick look at the smoothness of each of the meshed structures reveals much bigger local variations of the Gaussian curvature in the non-optimized structure (Figure 15A) than in the optimized one (Figure 15B).

During the simulation, the local quality of the mesh is expected to affect greatly the numerical convergence of the system toward a mechanical equilibrium. We then compared the precision of estimation of the mechanical equilibrium by monitoring the residue of the Euler implicit integration scheme. Figure 15C shows that the remaining residue is almost ten times smaller with the optimized structure compared to the more irregular one (after 1,000 iterations steps only), meaning that the optimization of the mesh makes the simulation converge much faster.

Finally, we looked at the mechanical stress amplitude distribution throughout the structure. Figures 15D,E show that, though the average stress amplitude is roughly the same for both structures, bigger variations between neighboring finite elements appears on the non-optimized structure. This is also exposed on Figure 15F where the distribution of standard deviations for the stress amplitudes within cells are displayed. While the histogram issued from the optimized structure is rather pinched a little bit below 10%, the one from the non-optimized structure is more widespread, reinforcing the idea that non-optimized structures generate highly fluctuating and less accurate stress fields.

These results validate if necessary the fact that the 3D triangular meshes constructed using our pipeline can be used directly for advanced biomechanical simulations. They constitute robust geometries on which finite element based methods can be applied safely. The study also underlines the major importance of the second geometry optimization step in order to get a better performance of the numerical solver and obtain more precise and trustworthy results out of physical simulations.

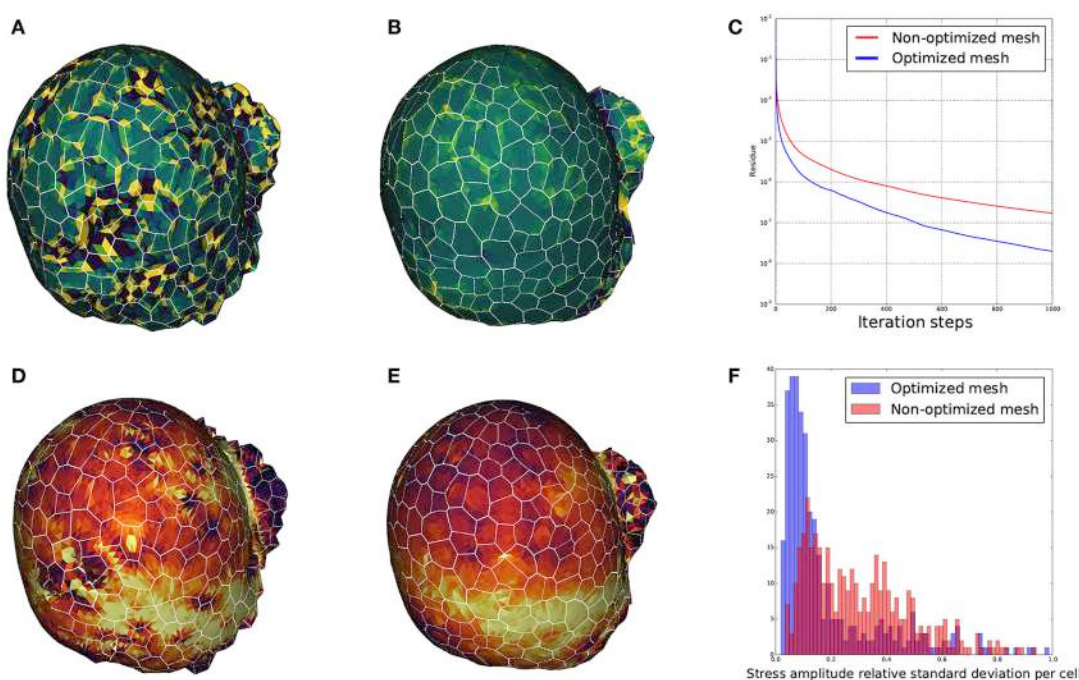


**FIGURE 15 |** Influence of mesh optimization on biomechanical simulations: comparisons between the local gaussian curvature on a non optimized DRACO mesh (**A**) and an optimized DRACO-STEM mesh (**B**), the convergence speed (error as a function of iteration steps) in an implicit Euler integration scheme in both cases (**C**), and estimation mechanical stress amplitudes respectively (**D,E**), and comparison of their cellwise standard deviations (**F**).

### 3.4. Conclusions

This computational tool provides meshing methods needed for biophysical simulations of growing SAM tissue on real-life data. The DRACO-STEM algorithm, together with 3D image processing methods provides an integrated pipeline to convert a living tissue acquired in fluorescent microscopy into a single ready-to-use data structure, combining both geometry and topology of a multi-layered tissue. Through the application of commonly defined file standards (Krupinski et al., 2015) already included in the proposed library, the produced meshes may be used in any applicative context of morphodynamic modeling.

The perspectives opened for biomechanical simulations of organ development in plants in particular are extremely promising and the first tests performed on shoot apical meristems show the pertinence of the proposed approach. The extension to other plant tissues presenting similar characteristics (approximately convex cells with flat interfaces), e.g., young leaves and root apical meristems, should in principle be possible, as these are the main assumptions made in our method. The proposed pipeline proves to supply modelers with accurate tissue geometries robust enough for numerical solvers. The availability of such a generic tool represents a key step in the development of accurate and compelling computational biophysical models of plant morphogenesis.

### AUTHOR CONTRIBUTIONS

GC and CG conceived and designed the computational framework. GC developed and implemented the mesh

### REFERENCES

- Agoston, M. (2005). *Computer Graphics and Geometric Modelling: Implementation and Algorithms*. Computer Graphics and Geometric Modeling. London: Springer Verlag.
- Allard, J., Cotin, S., Faure, F., Bensoussan, P.-J., Poyer, F., Duriez, C., et al. (2007). “SOFA - an open source framework for medical simulation,” in *MMVR 15 - Medicine Meets Virtual Reality, Volume 125 of Studies in Health Technology and Informatics* (Palm Beach), 13–18.
- Barbier de Reuille, P., Bohn-Courreau, I., Godin, C., and Traas, J. (2005). A protocol to analyse cellular dynamics during plant development. *Plant J.* 44, 1045–1053. doi: 10.1111/j.1365-313X.2005.02576.x
- Barbier de Reuille, P., Robinson, S., and Smith, R. S. (2014). “Quantifying cell shape and gene expression in the shoot apical meristem using MorphoGraphX,” in *Plant Cell Morphogenesis: Methods and Protocols*, eds V. Zarsky and F. Cvrkova (Totowa, NJ: Humana Press), 121–134. doi: 10.1007/978-1-62703-643-6\_10
- Barbier de Reuille, P., Routier-Kierzkowska, A.-L., Kierzkowski, D., Bassel, G. W., Schüpbach, T., Tauriello, G., et al. (2015). MorphoGraphX: a platform for quantifying morphogenesis in 4D. *eLife* 4:e05864. doi: 10.7554/elife.05864
- Bassel, G. W., and Smith, R. S. (2016). Quantifying morphogenesis in plants in 4D. *Curr. Opin. Plant Biol.* 29, 87–94. doi: 10.1016/j.pbi.2015.11.005
- Bassel, G. W., Stamm, P., Mosca, G., Barbier de Reuille, P., Gibbs, D. J., Winter, R., et al. (2014). Mechanical constraints imposed by 3D cellular geometry and arrangement modulate growth patterns in the arabidopsis embryo. *Proc. Natl. Acad. Sci. U.S.A.* 111, 8685–8690. doi: 10.1073/pnas.1404616111
- Botsch, M., and Kobbelt, L. (2004). “A remeshing approach to multiresolution modeling,” in *Proceedings of the Symposium on Geometry Processing* (Nice), 185–192. doi: 10.1145/1057432.1057457
- Boudon, F., Chopard, J., Ali, O., Gilles, B., Hamant, O., Bouadaoud, A., et al. (2015). A computational framework for 3D mechanical modeling of plant generation algorithms, and performed tests on segmented images. GC documented and released the code on GitHub. OA developed the mechanical framework and performed tests on the produced meshes. GC, OA, and CG wrote the manuscript.
- FUNDING**
- This work was supported by the Human Frontier Science Program (HFSP) research grant RGP0054-2013, by the Computational Biology Intitute (IBC) and by the IPL Morphogenetics.
- ACKNOWLEDGMENTS**
- Imaging: The authors thank Pradeep Das, Vincent Mirabet, Jan Traas, Henrik Larsson, Yassin Refahi, Carlos Galvan-Ampudia, Géraldine Brunoud, and Jonathan Legrand for providing confocal microscopy images of living meristems and for the segmentation of 3D tissue images. Packaging: The DRACO-STEM package provided on GitHub was built thanks to Jérôme Chopard, using the long-term support tool `pkglts`.
- SUPPLEMENTARY MATERIAL**
- The Supplementary Material for this article can be found online at: <http://journal.frontiersin.org/article/10.3389/fpls.2017.00353/full#supplementary-material>
- morphogenesis with cellular resolution. *PLoS Comput. Biol.* 11:e1003950. doi: 10.1371/journal.pcbi.1003950
- Bozorg, B., Krupinski, P., and Jönsson, H. (2014). Stress and strain provide positional and directional cues in development. *PLoS Comput. Biol.* 10:e1003410. doi: 10.1371/journal.pcbi.1003410
- Cerutti, G., and Godin, C. (2015). “Meshing meristems - an iterative mesh optimization method for modeling plant tissue at cell resolution,” in *Proceedings of the International Conference on Bioimaging*. Vol. 1, BIOIMAGING (Lisbon: BIOSTEC 2015), 23–35.
- Cerutti, G., Ribes, S., Galvan-Ampudia, C., Vernoux, T., and Godin, C. (2015). “3D tessellation of plant tissue - A dual optimization approach to cell-level meristem reconstruction from microscopy images,” in *International Conference on 3D Vision* (Lyon), 443–451.
- Chakraborty, A., Perales, M. M., Reddy, G. V., and Roy Chowdhury, A. K. (2013). Adaptive geometric tessellation for 3D reconstruction of anisotropically developing cells in multilayer tissues from sparse volumetric microscopy images. *PLoS ONE* 8:e67202. doi: 10.1371/journal.pone.0067202
- Coste, J., Baty, G., Boudon, F., Godin, C., and Pradal, C. (2014). “OpenAleaLab: an integrated multi-paradigm modelling environment,” in *EuroScipy 2014* (Cambridge, UK).
- De Berg, M., Cheong, O., Van Kreveld, M., and Overmars, M. (2008). *Computational Geometry: Algorithms and Applications*, 3rd Edn. Santa Clara, CA: Springer-Verlag TELOS. doi: 10.1007/978-3-540-77974-2
- Federici, F., Dupuy, L., Laplaze, L., Heisler, M., and Haseloff, J. (2012). Integrated genetic and computation methods for in planta cytometry. *Nat. Methods* 9, 483–485. doi: 10.1038/nmeth.1940
- Fernandez, R., Das, P., Mirabet, V., Moscardi, E., Traas, J., Verdeil, J.-L., et al. (2010). Imaging plant growth in 4D: robust tissue reconstruction and lineaging at cell resolution. *Nat. Methods* 7, 547–553. doi: 10.1038/nmeth.1472

- Hamant, O., Heisler, M. G., Jönsson, H., Krupinski, P., Uyttewaal, M., Bokov, P., et al. (2008). Developmental patterning by mechanical signals in arabidopsis. *Science* 322, 1650–1655. doi: 10.1126/science.1165594
- Hege, H.-C., Seebass, M., Stalling, D., and Zöckler, M. (1997). *A Generalized Marching Cubes Algorithm based on Non-binary Classifications*. Berlin: Tech Report, Konrad-Zuse-Zentrum für Informationstechnik.
- Jönsson, H., Gruel, J., Krupinski, P., and Troein, C. (2012). On evaluating models in computational morphodynamics. *Curr. Opin. Plant Biol.* 15, 103–110. doi: 10.1016/j.pbi.2011.09.007
- Keller, P. J. (2013). Imaging morphogenesis: technological advances and biological insights. *Science* 340. doi: 10.1126/science.1234168
- Krupinski, P., Jönsson, H., Tauriello, G., Smith, R. S., and Barbier de Reuille, P. (2015). “Exchange format for geometries” in *Sainsbury Computational Biology Workshop*. Available online at: <https://sainsburyworkshop2015.wikispaces.com/file/view/PlyFormat.pdf/557257603/PlyFormat.pdf>
- Lorensen, W. E., and Cline, H. E. (1987). “Marching cubes: a high resolution 3D surface construction algorithm,” in *Proceedings of the 14th Annual Conference on Computer Graphics and Interactive Techniques, SIGGRAPH '87* (Anaheim, CA), 163–169. doi: 10.1145/37401.37422
- Pradal, C., Boudon, F., Nouguier, C., Chopard, J., and Godin, C. (2009). PlantGL: a python-based geometric library for 3D plant modelling at different scales. *Graph. Models* 71, 1–21. doi: 10.1016/j.gmod.2008.10.001
- Pradal, C., Dufour-Kowalski, S., Boudon, F., Fournier, C., and Godin, C. (2008). OpenAlea: a visual programming and component-based software platform for plant modelling. *Funct. Plant Biol.* 35, 751–760. doi: 10.1071/FP08084
- Shapiro, B., Jönsson, H., Sahlin, P., Heisler, M., Roeder, A., Burl, M., et al. (2008). “Tessellations and pattern formation in plant growth and development,” in *Tessellations in the Sciences: Virtues, Techniques and Applications of Geometric Tilings*, eds R. Van de Weijgaert, G. Vegter, J. Ritzerveld, and V. Icke (Heidelberg: Springer-Verlag).
- Shewchuk, J. R. (1998). “Tetrahedral mesh generation by Delaunay refinement,” in *Proceedings of the Symposium on Computational Geometry, SCG '98* (Minneapolis), 86–95.
- Shewchuk, J. R. (2002). *Two Discrete Optimization Algorithms for the Topological Improvement of Tetrahedral Meshes*. Berkeley, CA: University of California at Berkeley.
- Theisel, H., Rössl, C., Zayer, R., and Seidel, H.-P. (2004). “Normal based estimation of the curvature tensor for triangular meshes,” in *Pacific Conference on Computer Graphics and Applications* (Seoul), 288–297.

**Conflict of Interest Statement:** The authors declare that the research was conducted in the absence of any commercial or financial relationships that could be construed as a potential conflict of interest.

Copyright © 2017 Cerutti, Ali and Godin. This is an open-access article distributed under the terms of the Creative Commons Attribution License (CC BY). The use, distribution or reproduction in other forums is permitted, provided the original author(s) or licensor are credited and that the original publication in this journal is cited, in accordance with accepted academic practice. No use, distribution or reproduction is permitted which does not comply with these terms.



# Modeling the Morphometric Evolution of the Maize Shoot Apical Meristem

Samuel Leiboff, Christopher K. DeAllie and Michael J. Scanlon\*

Plant Biology Section, School of Integrative Plant Science, Cornell University, Ithaca, NY, USA

The maize (*Zea mays* subsp. *mays* L.) shoot apical meristem (SAM) is a self-replenishing pool of stem cells that produces all above-ground plant tissues. Improvements in image acquisition and processing techniques have allowed high-throughput, quantitative genetic analyses of SAM morphology. As with other large-scale phenotyping efforts, meaningful descriptions of genetic architecture depend on the collection of relevant measures. In this study, we tested two quantitative image processing methods to describe SAM morphology within the genus *Zea*, represented by 33 wild relatives of maize and 841 lines from a domesticated maize by wild teosinte progenitor (MxT) backcross population, along with previously reported data from several hundred diverse maize inbred lines. Approximating the MxT SAM as a paraboloid derived eight parabolic estimators of SAM morphology that identified highly overlapping quantitative trait loci (QTL) on eight chromosomes, which implicated previously identified SAM morphology candidate genes along with new QTL for SAM morphological variation. Using a Fourier-transform related method of comprehensive shape analysis, we detected cryptic SAM shape variation that identified QTL on six chromosomes. We found that Fourier transform shape descriptors and parabolic estimation measures are highly correlated and identified similar QTL. Analysis of shoot apex contours from 73 anciently diverged plant taxa further suggested that parabolic shape may be a universal feature of plant SAMs, regardless of evolutionary clade. Future high-throughput examinations of SAM morphology may benefit from the ease of acquisition and phenotypic fidelity of modeling the SAM as a paraboloid.

## OPEN ACCESS

### Edited by:

Daniel H. Chitwood,  
Donald Danforth Plant Science  
Center, USA

### Reviewed by:

Siobhan Braybrook,  
University of Cambridge, UK  
David Jackson,  
Cold Spring Harbor Laboratory, USA

### \*Correspondence:

Michael J. Scanlon  
mjs298@cornell.edu

### Specialty section:

This article was submitted to  
Plant Biophysics and Modeling,  
a section of the journal  
*Frontiers in Plant Science*

Received: 14 July 2016

Accepted: 20 October 2016

Published: 04 November 2016

### Citation:

Leiboff S, DeAllie CK and  
Scanlon MJ (2016) Modeling  
the Morphometric Evolution of the  
Maize Shoot Apical Meristem.  
*Front. Plant Sci.* 7:1651.  
doi: 10.3389/fpls.2016.01651

**Keywords:** morphometrics, quantitative trait loci (QTL), discrete cosine transform, image analysis, *Zea*

## INTRODUCTION

The maize (*Zea mays* subsp. *mays* L.) shoot apical meristem (SAM) comprises a dome of pluripotent cells that ultimately generates all the organs of the plant shoot through regulated maintenance of stem cells and recruitment of initial cells for organogenesis (Steeves and Sussex, 1972). Mutational studies have shown that the maize shoot meristem morphology is genetically regulated (Jackson and Hake, 1999; Taguchi-Shiobara et al., 2001; Jia et al., 2009; Bommert et al., 2013; Pautler et al., 2015; Yang et al., 2015; Je et al., 2016). Although natural variation in shoot meristem morphology is associated with relatively few loci, natural variants of master regulatory genes do not appear to contribute to standing variation in SAM shape and size in domesticated maize (Thompson et al., 2014, 2015; Leiboff et al., 2015).

Recent investigations of maize meristem morphology as a quantitative trait incorporated small numbers of descriptive measurements approximating SAM shape and size for genome-wide association studies (GWAS) and quantitative trait locus (QTL) mapping (Thompson et al., 2014, 2015; Leiboff et al., 2015). Quantitative morphological analyses are highly biased by the measurement methodologies, the traits selected for analyses, and correlations between measurements (Langlade et al., 2005). Our previous study of maize inbred varieties exploited similarities between observed SAM contours and parabolic functions to estimate several shape parameters describing meristem morphology (Leiboff et al., 2015), although other models for SAM morphometrics have not been tested in quantitative genetic analyses.

Progress toward the description of complex shapes utilizing Fourier transform methods has enabled unbiased interrogations of biological shape (Dommergues et al., 2007; Klingenberg, 2010). By processing carefully placed landmarks or object outlines, Fourier transform and related methods use multiple sinusoid harmonics to reproduce highly complex shapes (Claude, 2008). High-dimensional matrices of Fourier model parameters can then be separated by principle component (PC) analysis to identify subtle, often cryptic, variations in complex plant shapes (Chitwood et al., 2014). Previous studies characterizing leaf morphology in *Antirrhinum* spp. and *Solanum* spp. have utilized Fourier shape descriptors as quantitative traits in QTL analyses of evolutionary novelty (Langlade et al., 2005; Chitwood et al., 2013, 2014).

Collectively known as teosintes, the wild members of the genus *Zea* provide a rich, highly diverse genetic system for maize genomics (Doebley, 2004; Hufford et al., 2012; Hake and Ross-Ibarra, 2015). Crosses between *Zea mays* subsp. *mays* and its progenitor, *Zea mays* subsp. *parviglumis* have been used to understand the genetic basis for striking changes in plant morphology associated with the domestication of maize (Beadle, 1980; Doebley, 2004; Hung et al., 2012; Shannon, 2012; Huang et al., 2016). Although general morphology and ontogeny of inflorescence meristem (IM) development have been reported in the genus *Zea* (Sundberg and Orr, 1986, 1990; Orr and Sundberg, 1994, 2004), little is known about variation in vegetative SAM morphology outside of domesticated maize. To date no comparative study has described the morphospace, or collection of shapes for vegetative meristems within the genus *Zea*. Indeed, no putative genetic factors underlying differences in maize and teosinte SAMs have been proposed.

Beyond the genus *Zea*, nearly all land plants and some algal relatives have shoot meristem-like structures, defined by an obligate balance of stem cell maintenance and lateral organ production (Bierhorst, 1971; Steeves and Sussex, 1972; Evert and Esau, 2006). Whereas shoot meristem cellular anatomy is notably different between many plant clades (Bierhorst, 1971; Evert and Esau, 2006), recent transcriptomic and genetic characterization has uncovered both contrasts and similarities in shoot meristem regulation pathways between disparate clades and meristem anatomy types (Frank and Scanlon, 2015; Frank et al., 2015). It is currently unclear whether analogous shoot meristem structures share quantitative morphological characteristics.

This project utilizes a maize x teosinte (MxT) backcross population to examine the genetic architecture of SAM shape and size (Hung et al., 2012; Shannon, 2012; Huang et al., 2016). We show that complex shape descriptors generated by Fourier methods detect previously undescribed, but genetically attributable minor variations in meristem shape, although the majority of the genetic loci contributing to SAM shape that are identified by Fourier analyses overlap tightly with loci identified by modeling the SAM as a paraboloid. Testing this expectation with a broad sampling of plant taxa suggests that parabolic shape may be a universal feature of plant SAMs.

## MATERIALS AND METHODS

### Plant Growth

Germplasm for all experiments was grown in 10 h-day conditions with 27°C daytime and 25°C nighttime temperatures in Percival A100 growth chambers (Percival Scientific, Perry, IA, USA). An intermediate day length was selected to promote maturation of genus *Zea* members (Emerson, 1924). Plants were watered up to twice daily. Kernels were planted with randomized positions within 98-well trays where all edge positions were filled with maize inbred B73. Soil media was a 1:1 mixture of Turface MVP (PROFILE Products LLC, Buffalo Grove, IL, USA) and LM111 (Lambert Peat Moss, Rivière-Ouelle, QC, Canada). Wild teosintes (Supplementary Data Sheet 1) were grown in 4 repeated experiments. MxT backcross lines (Supplementary Data Sheet 1) were grown in 2 repeated experiments. Plants were harvested 14 days after planting and quickly trimmed to approximately 1 cm × 1 cm × 0.5 cm SAM-containing tissue cassettes and fixed in FAA (3.7% formalin, 5% acetic acid, 50% ethanol in water) on ice, overnight.

### Histology and Image Acquisition

After overnight fixation in FAA, plant tissue was dehydrated through an ethanol dilution series, transferred to a 1:1 mix of ethanol and methyl salicylate, then transferred to methyl salicylate for clearing overnight. Fully cleared tissue was imaged by DIC with Nomarski optics on an Axio Imager.Z10 (Carl Zeiss Microscopy, LLC, Thornwood, NY, USA) with an AxioCam MRC5 camera. We captured near-median longitudinal optical sections using SAM apex contours and primordia appearance as morphological cues. To avoid the analysis of determinant, IMs in our study, we only processed images where the shoot apex displayed recent initiation of leaf primordia, a morphological marker of vegetative SAMs (Pautler et al., 2013). All MxT images were oriented so that the next primordium to initiate (P0) appeared on the left-hand side of the image.

Several shoot apex images of anciently diverged plant taxa were collected from high quality publications (Supplementary Data Sheet 1). Figures from printed texts were scanned at 300 dpi, 16-bit greyscale using an Epson Perfection 3490 photo scanner (Epson America, Long Beach, CA, USA).

A small number of shoot apex images from demonstrative plant taxa were collected from freshly fixed tissues (Supplementary Data Sheet 1). Shoot apical regions were

harvested by hand from growing tissue, fixed overnight in FAA, and stained with a modified Feulgen method (as described in 10). After a brief destain, samples were dehydrated, cleared with methyl salicylate and imaged with a Leica TCS-SP5 confocal laser scanning microscope (Leica Microsystems Exton, PA, USA) using an argon ion laser (488 nm).

## Image Processing: Parabolic Estimation and Fourier Transform

Near-median DIC images were processed by custom Image macros to extract meristem contours and measures of SAM height and SAM radius (as reported in 10). Using a custom Python script SAM height and radius were used to calculate a table of 8 parabolic estimators: height, radius, height to radius ratio (H/R), volume (Vol.), surface area (Surf. Area), arc length (Arc Len.), parabolic coefficient (Para. Coeff.), and cross-sectional area (Area) (as previously reported in 10).

Shoot apical meristem contours were digitized with an Intuos Draw Tablet (Wacom Technology Corporation, Portland, OR, USA) and used for both linear model fitting with the lm() function and Fourier transform with the Momocs package for R. All traced SAM coordinates were imported as open contours (data type Opn), thinned to 800 evenly spaced pseudo-landmarks, Procrustes aligned, and Fourier transformed by the discrete cosine transform in the Momocs package for R. Discrete cosine transform made use of 12 harmonics, the lowest number of harmonics that sufficiently recaptured variation.

## QTL Mapping

Using publically available genotype information for the MxT population from panzea.org, genotype and phenotype information were processed via the R/qt1 package for R. MxT genotypes were coded as BC2S3 and mapped using the Kosambi algorithm. Single QTL were detected using the scanone() function. We used a 95% confidence threshold generated from 10,000 permutations to determine significant QTL. Bayesian 95% confidence QTL intervals were called using the bayesint() function to estimate QTL location.

## Statistical Analysis and Plotting

Descriptive statistical analysis, correlation analysis, Wilcoxon one-sided rank sum test, and two-way ANOVA were carried out using core R packages. Raw data were summarized according to replicate by BLUP + coefficient using the nlme package in R (Leiboff et al., 2015). All correlations report Pearson's product-moment, r and were evaluated for statistical significance with the Fisher transformation. Maize inbred variety SAM shape and size data were collected from published datasets (Leiboff et al., 2015). Plots were produced using ggplot2 and R/qt1 packages in R.

## Data Availability

Supplementary Data Sheet 1 contains the source and parabolic model fit information for anciently diverged plant apex images. Supplementary Data Sheet 2 contains SAM parabolic estimates from the genus *Zea*. Supplementary Data Sheet 3 contains SAM parabolic model estimates from MxT lines in unsummarized and

BLUP+Coefficient form. Supplementary Data Sheet 4 details all significant QTL intervals as well as known GWAS candidate genes within those intervals. Supplementary Data Sheet 5 contains Fourier shape descriptor PCs in unsummarized and BLUP+Coefficient form.

## RESULTS

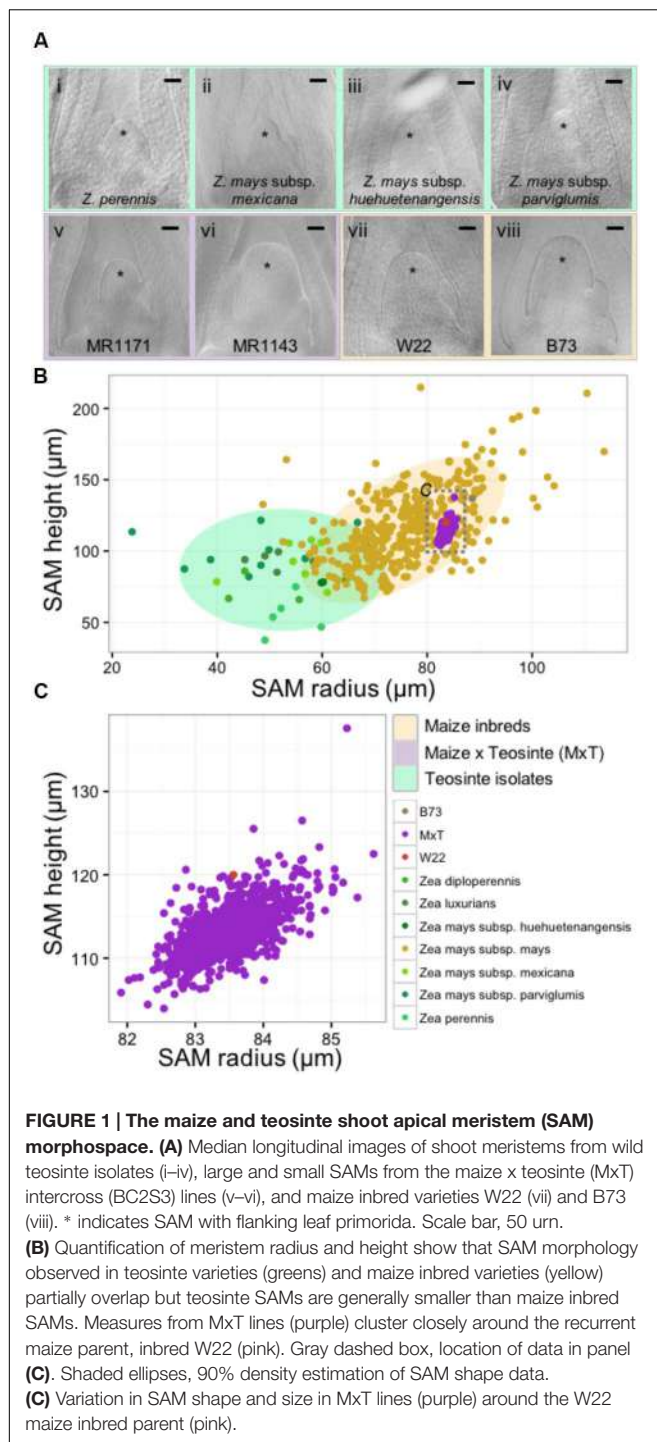
### Diversity of Shoot Meristems in the Genus *Zea*

We utilized microscopic imaging of 14-day-old seedling vegetative SAMs (described in Materials and Methods) to construct a morphospace of SAM height and radius for the genus *Zea*, which included 33 wild teosinte isolates from 3 different species (*Z. diploperennis*, *Z. luxurians*, and *Z. perennis*), 3 subspecies (*Z. mays* subsp. *huehuetenangensis*, *Z. mays* subsp. *mexicana*, and *Z. mays* subsp. *parviglumis*), 841 lines from a *Zea mays* subsp. *mays* W22 by *Zea mays* subsp. *parviglumis* backcross population (hereafter designated MxT) (Hung et al., 2012; Shannon, 2012; Huang et al., 2016), and our previously reported data on 369 diverse maize inbred lines (Figure 1; Supplementary Data Sheet 2) (Leiboff et al., 2015). Although there is a small zone of overlap between teosinte and maize inbred SAM shapes, wild teosinte meristems are significantly narrower (est. 23  $\mu\text{m}$  between medians, Wilcoxon one-sided rank sum test, *p*-value  $<2.2e-16$ ) and shorter (est. 28  $\mu\text{m}$  between medians, Wilcoxon one-sided rank sum test, *p*-value  $= 1.257e-10$ ) than meristems from domesticated maize inbred lines (Figure 1A). Measurements of MxT shoot meristems cluster around the recurrent maize parent, inbred W22 (Figure 1B), possibly reflecting the two generations of backcrosses to the maize parent that were incurred prior to analyses of SAM morphometric phenotypes (Hung et al., 2012). We detected quantitative variation in shoot meristem shape and size in SAMs isolated from MxT lines (Figures 1A,C) and focused our analysis on this population to understand the genetic architecture of maize/teosinte SAM morphometric variation.

### Parabolic Estimators of MxT Variation Identify New Meristem Morphology QTL

We used image-processing to collect two discrete measurements, SAM height and SAM radius and approximate the MxT shoot meristem as a paraboloid surface, the geometric shape yielded from revolving a parabolic curve around its central axis (additionally described in 10). Exploiting the simple geometry of a paraboloid, we used two primary measures to derive eight total parabolic shape estimators: height, radius, height to radius ratio (H/R), volume (Vol.), surface area (Surf. Area), arc length (Arc Len.), parabolic coefficient (Para. Coeff.), and cross-sectional area (Area) (Supplementary Data Sheet 3) (Leiboff et al., 2015).

Our previous study analyzed SAM volume (Figure 2A) as a quantitative trait (Leiboff et al., 2015). In this analysis we identified QTL for MxT SAM volume on chromosomes 1,



4, and 7 (**Figure 2B**). Intervals detected on chromosomes 4 and 7 were not previously implicated in natural variation of SAM morphology in 369 domesticated maize inbred varieties (Supplementary Data Sheet 4) (Leiboff et al., 2015). The large QTL interval identified on chromosome 1 contains several previously identified candidate genes for shoot meristem morphology including *ZmLAX2*, a putative auxin import protein which exhibits haplotype-specific differences in

transcript accumulation patterns in maize inbred varieties that correlate with differences in SAM size (Leiboff et al., 2015).

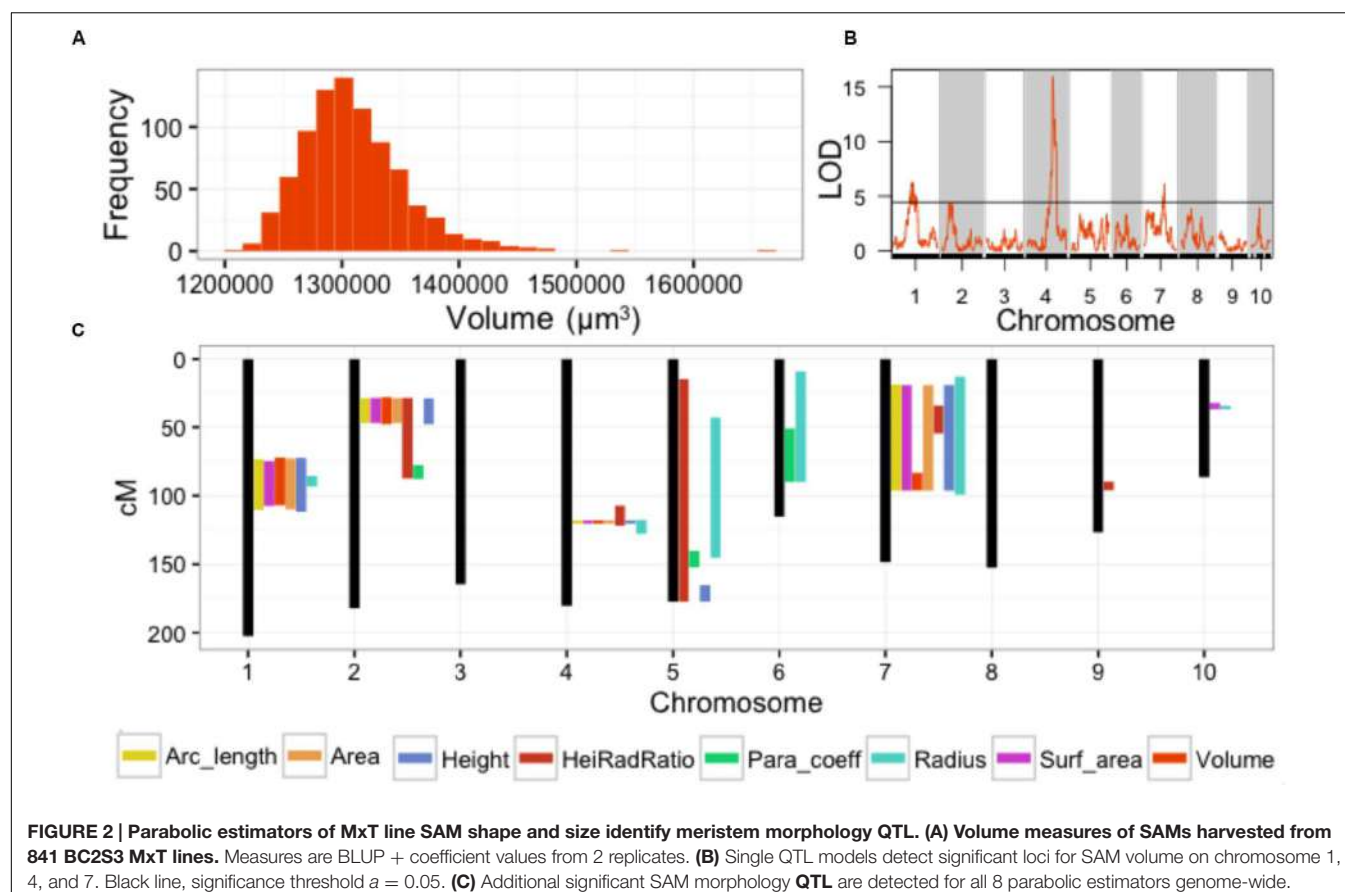
The remaining 7 parabolic estimators mapped QTL to several chromosomes (**Figure 2C**; Supplementary Data Sheet 4). Several parabolic estimators identified highly overlapping QTL intervals. Chromosome 4, for example, contains a QTL that is coincidentally associated with SAM height, radius, H/R, volume, surface area, arc length, and cross-sectional area (**Figure 2C**). All detected QTL were implicated by multiple parabolic estimators, except one QTL on chromosome 9 that is uniquely associated with SAM H/R. We find a high level of correlation between measures (Supplementary Image 1), as expected from their common derivation (see Materials and Methods).

In total, QTL intervals recaptured 11 previously identified SAM-morphology candidate genes implicated by GWAS of maize inbred varieties (Supplementary Data Sheet 4) (Leiboff et al., 2015). Intriguingly, the QTL intervals mapped on chromosomes 4, 7, and 9 have not previously been associated with SAM shape and size.

## Discrete Cosine Transform Uncovers Cryptic, Genetically Attributable Variation in MxT SAM Shape Variation

Using Fourier-related transform methods, we processed Procrustes-aligned and scaled MxT shoot meristem outlines (Supplementary Image 2) into Fourier shape PCs to comprehensively describe SAM shape variation within this population (Supplementary Data Sheet 5). Three PCs describe more than 95% of the total observed shape variation, with PC1, PC2, and PC3, explaining 85.4, 8.2, and 2.3%, respectively. Additional PCs each explained less than 1% of observed shape variation (Supplementary Data Sheet 5); we therefore chose to focus our study of SAM shape variation on PC1, PC2, and PC3. Examining raw images of SAMs, and predicted shapes at the extremes of these PCs, revealed unexpected phenotypic variance (**Figure 3**). The majority of shape variation detected in the MxT population is attributed to PC1, identifying meristems that vary in appearance from ‘post-like’ to ‘dome-like’ (**Figure 3A**). PC2 identifies meristems that vary in 2-dimensional asymmetry with respect to the plane of sample dissection, and describes variation from ‘left-leaning’ to ‘right-leaning’ SAMs (**Figure 3B**). PC3 identifies meristems that vary in slope from the SAM base to tip, and includes ‘peaked’ to ‘rounded’ shapes (**Figure 3C**).

Using PC1, PC2, and PC3 as quantitative phenotypes, we identified significant QTL for each trait: PC1 identified QTL on chromosomes 2, 4, 7, and 9 (**Figure 4A**), PC2 identified similar QTL intervals on chromosomes 2 and 4 (**Figure 4B**), whereas PC3 identified equivalent QTL intervals on chromosomes 2 and 4, in addition to different QTL on chromosomes 1 and 5 (**Figure 4C**). Despite differences in SAM measurement methods, the total QTL identified by all 8 parabolic estimators (**Figure 2C**) and 3 Fourier shape PCs overlap closely (**Figure 4D**). In a correlation analysis



of parabolic estimators and Fourier shape PCs, we find a strong, significant correlation between PC1 and several parabolic estimators, especially SAM H/R (Pearson's  $r = -0.67$ , Fisher transformation  $p$ -value  $< 2.2e-16$ ) (Figure 5A). This close association is mirrored in the tight overlap of QTL identified by PC1 and H/R (Figure 5B). Because PC1 explains the majority of shape variation in the MxT population and is correlated in both numeric value and genetic architecture to parabolic estimators, we postulated that other populations of meristems might be likewise described by quantitative parabolic models.

## Diverse Meristems and Their Parabolic Models

Despite their similar roles in stem cell maintenance and the production of lateral organs, the shoot apices of anciently diverged plant lineages have remarkable anatomical and transcriptomic differences (Figure 6A) (Bierhorst, 1971; Evert, 2006a; Frank and Scanlon, 2015; Frank et al., 2015). In an analysis of 111 images from 73 plant taxa, we find that shoot apices are well fit by a parabolic model of meristem shape (Supplementary Data Sheet 1). Linear regression of shoot apex contours with a parabolic model yielded  $R^2$  goodness-of-fit scores ranging from 0.838 to 0.997 with a mean of 0.963 and median of 0.975. Interestingly, SAM shape parameters do not

significantly separate anciently diverged evolutionary clades (ANOVA,  $p$ -value = 0.158) (Figure 6B).

## DISCUSSION

We processed SAM images from 33 wild teosintes and 841 lines from a maize by teosinte (MxT) backcross population to generate a meristem morphospace for the genus *Zea*. In our SAM morphospace, we find that teosintes and maize inbred varieties occupy partially overlapping regions of the SAM shape, where SAMs in wild teosintes are diminutive compared to SAMs observed in domesticated maize varieties. We expect this SAM morphometric gradient to reflect the effect of domestication on the flowering time of *Zea mays*. The domestication and spread of maize outside its tropical Meso-American center of origin required adaptation to flowering during long summer days. Genetic studies of flowering time in maize, teosintes, and MxT intercross populations indicate that wild teosintes repress flowering during long days (Emerson, 1924; Briggs et al., 2007; Hung et al., 2012). Allelic variants which have decreased activity of *ZmCCT* (an ortholog of rice flowering time gene, *Ghd7*) allow flowering during long days and were selected for during the domestication of maize (Briggs et al., 2007; Tsuji et al., 2011; Hung et al., 2012; Yang et al., 2013). Previous studies of natural variation in maize inbred variety SAM shape and size revealed

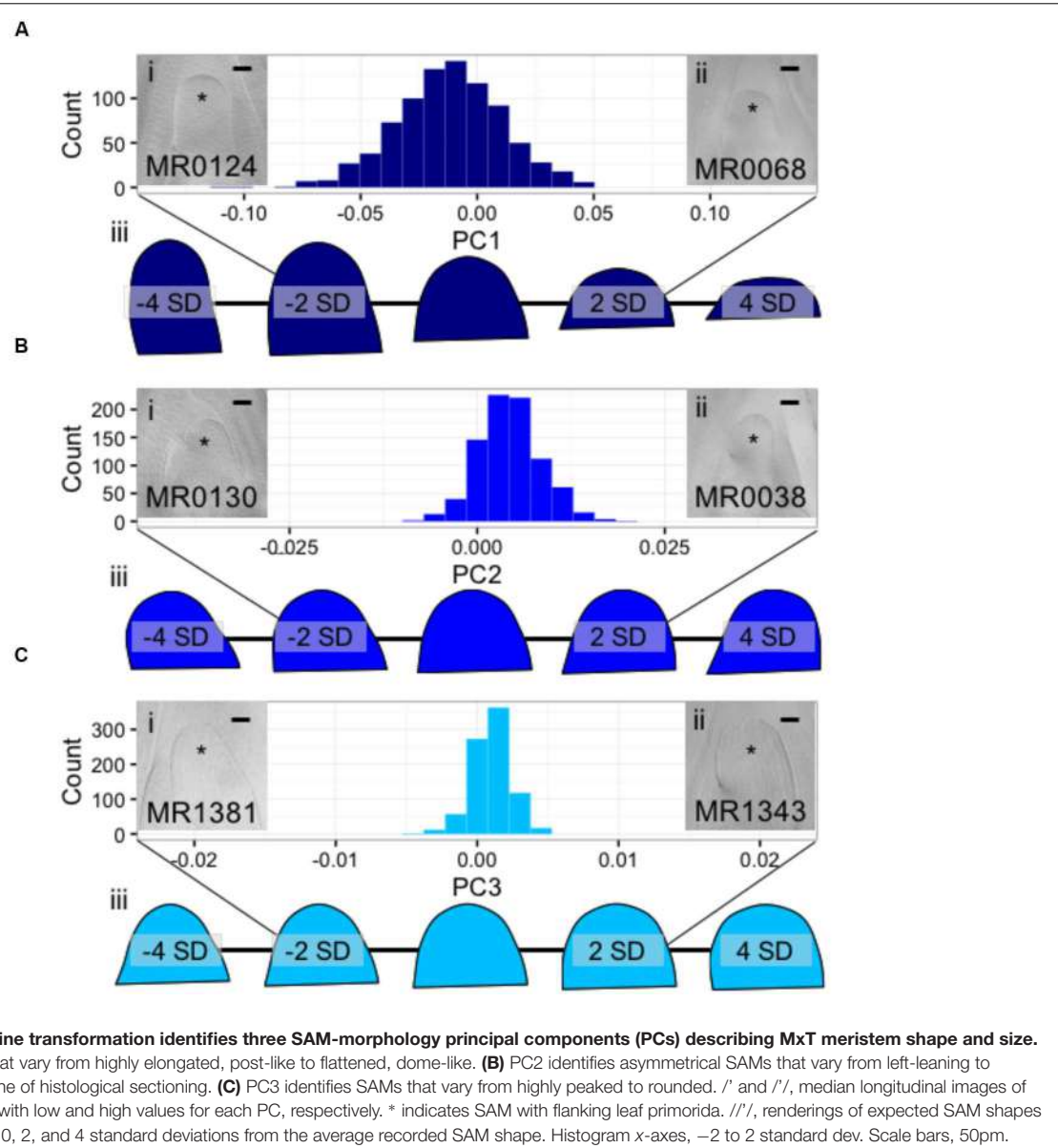


**FIGURE 3 | Discrete cosine transformation identifies three SAM-morphology principal components (PCs) describing MxT meristem shape and size.** **(A)** PC1 identifies SAMs that vary from highly elongated, post-like to flattened, dome-like. **(B)** PC2 identifies asymmetrical SAMs that vary from left-leaning to right-leaning within the plane of histological sectioning. **(C)** PC3 identifies SAMs that vary from highly peaked to rounded. // and ///, median longitudinal images of meristems from MxT lines with low and high values for each PC, respectively. \* indicates SAM with flanking leaf primordia. ///, renderings of expected SAM shapes with PC values of -4, -2, 0, 2, and 4 standard deviations from the average recorded SAM shape. Histogram x-axes, -2 to 2 standard dev. Scale bars, 50pm.

correlations between large meristem size and short flowering time (Leiboff et al., 2015; Thompson et al., 2015), reflected in GWAS candidate alleles at the *CONZ1* locus (Leiboff et al., 2015), proposed to act in a shared pathway with *ZmCCT* (Dong et al., 2012; Hung et al., 2012). QTL intervals for SAM surface area and radius on chromosome 10 include *ZmCCT*, which may contribute to differences in SAM size within the MxT population. Although the underlying mechanism that links flowering time and meristem size remains unresolved, our data agree with other reports of SAM natural variation and flowering time in maize.

Comprehensive analysis of SAM shape by Fourier methods yielded unexpected and interesting phenotypes for quantitative genetics. We note that the ‘left-leaning’ to ‘right-leaning’ asymmetry identified in PC2 (Figure 3B) only describes

asymmetry in one plane of symmetry (i.e., the midrib-margin axis), and that additional asymmetric “leanings” may in fact exist along different axes in the shoot apex. We further note that PC2 variation may be attributed to physical crowding of the shoot apex, wherein genotype specific variations in the presence of leaf primordia that are closely appressed against the SAM may contribute to variations in SAM leaning. Likewise, the “peaked versus rounded” shape variation identified in PC3 may reflect differences in biophysical forces imparted by the youngest leaf primordium at the nodal disk-of-insertion at the base of SAM, wherein the base of the SAM is “pinched” at the node in “rounded” SAMs and “unpinched” in peaked SAMs (Figure 3C). Prior implementations of Fourier methods for morphometrics have revealed genetically attributable, cryptic shape phenotypes including quantitative tissue asymmetry as

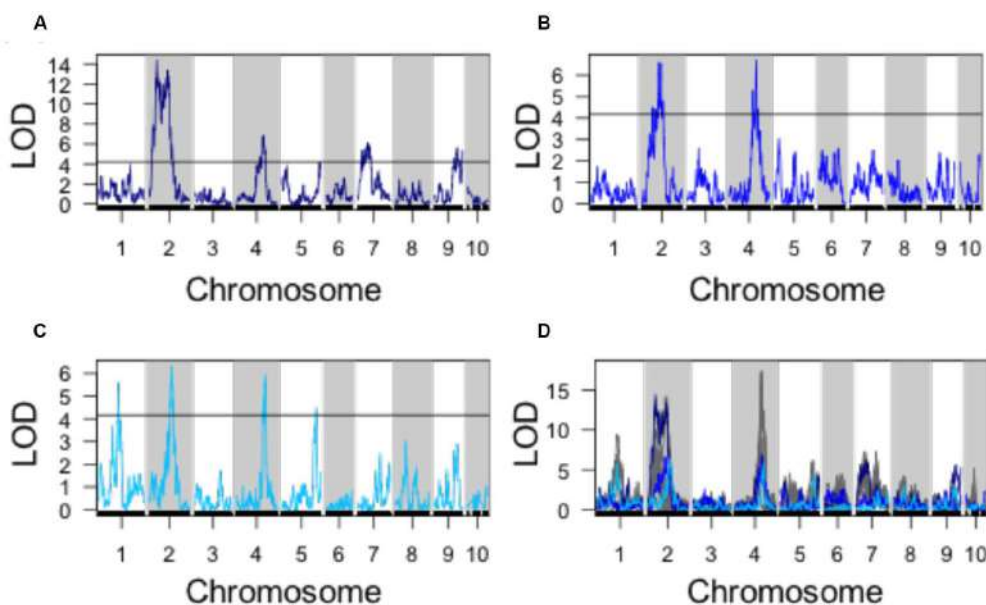


**FIGURE 4 | QTL identified for discrete cosine transform PCs. (A)** QTL for PC1. **(B)** QTL for PC2. **(C)** QTL for PC3. **(D)** Superimposed QTL profiles for discrete cosine transform descriptors (blues) and parabolic estimator phenotypes (gray). Black line, significance threshold  $a = 0.05$ .

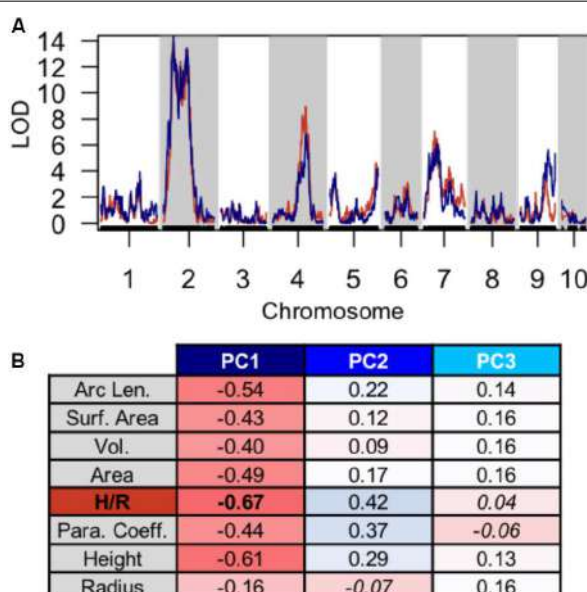


**FIGURE 5 | Discrete cosine transform PC1 recaptures QTL and phenotypic variation identified by parabolic estimators. (A)** Close overlap of QTL identified using PC1 (blue) and H/R (red). **(B)** Strong pearson correlation ( $r$ ) between PC1 and several parabolic estimator phenotypes. Correlation value, red to blue. Non-significant correlation Fischer transformation  $P > 0.05$ , italics.

we observed in PC2 (Langlade et al., 2005; Chitwood et al., 2013, 2014). Yet, because QTL identified with Fourier transform PCs overlap strongly with QTL identified by estimating the maize SAM as a paraboloid, we expect that parabolic estimation

methods are effective at representing heritable variation in SAM morphology.

Approximating SAM shape and size with a parabolic model has several advantages for quantitative genetics. Parabolic estimates of SAM morphology can be generated by collecting two simple measures, SAM height and radius, whereas Fourier methods requires the careful placement of pseudo-landmarks or outline information generated from laborious manual image tracing or automated image processing of high signal-to-noise SAM micrographs. Despite the increased sensitivity of Fourier methods, we expect that the throughput of approximating SAM morphology with a paraboloid is better suited to large-scale genetic analyses of SAM morphology in maize.

We furthermore demonstrated that shoot apical regions from diverse plant taxa are well fit by parabolic curves. The shoot apices utilized in these comparisons (especially the historical samples) were obtained from plants grown in a wide variety of environmental conditions, which may indeed influence meristem size and/or geometry (Landrein et al., 2015). Our observations suggest that parabolic meristem shape is found in all plant evolutionary clades and SAM anatomical organization types (ex. tunica-corpus, histological zonation, single apical cell, etc.), which generally correlate with evolutionary clade. Interestingly, we found that anciently diverged plant lineages have similar shoot meristem parabolic curvatures, despite rich diversity in anatomy, development, and whole-plant morphology. The universality of parabolic SAM shape in diverse lineages may, in part, be the result of biophysical forces incurred during the essential functions of the SAM. All shoot meristems maintain at least one undifferentiated stem cell initial, which divides to produce both a stem cell initial and a lateral organ initial (Steeves and Sussex, 1972; Evert,

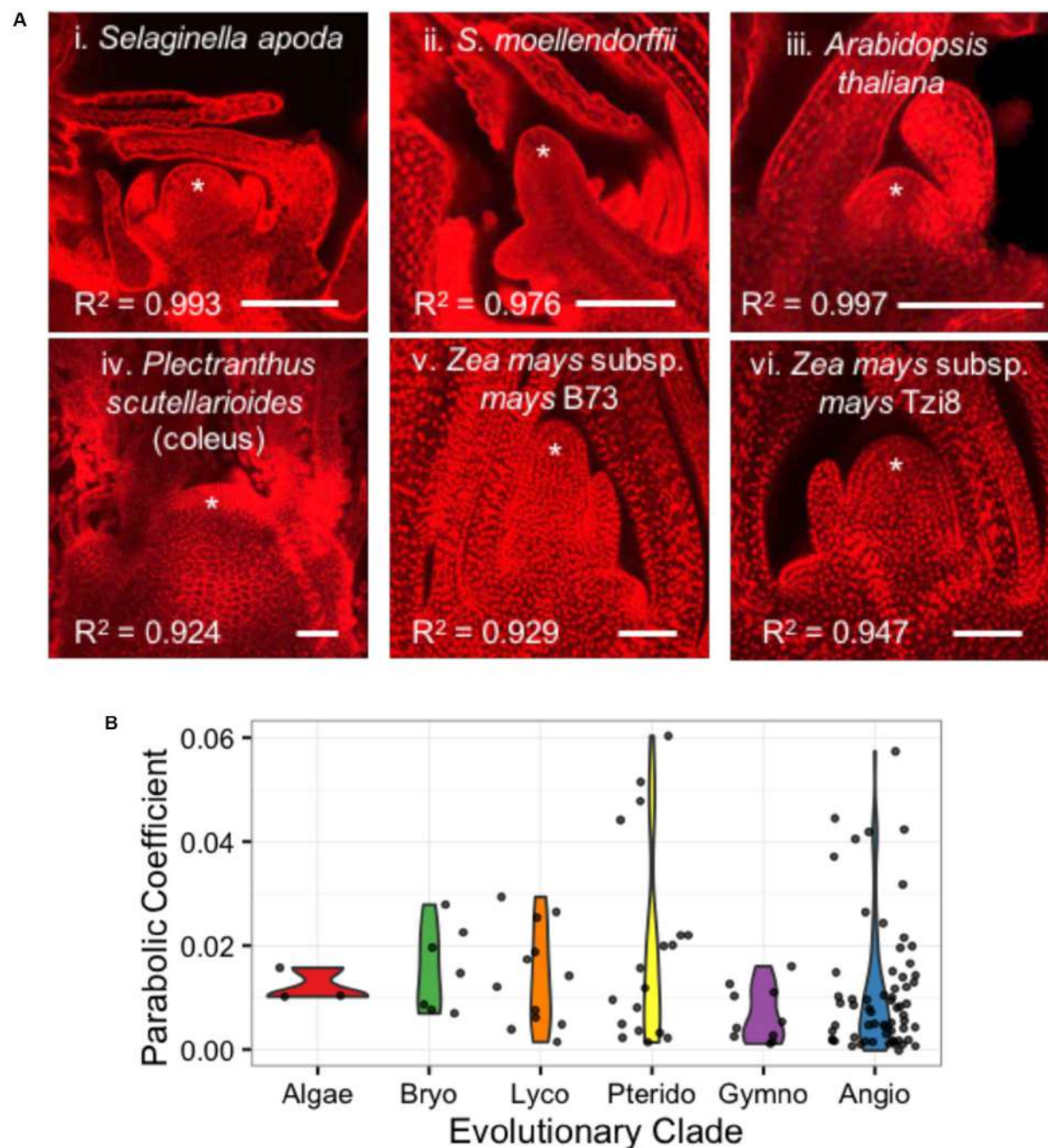


**FIGURE 6 | Diverse SAMs are well-estimated by parabolic shape models. (A)** Median optical sections of the vegetative apex from example lycophytes with a shoot meristem dominated by an inverted pyramidal cell (i, ii) and angiosperms exhibiting a ‘tunica-corpus’ shoot meristem anatomy with at least one clonal ‘tunica’ layer (iii–vi). \* indicates SAM and flanking leaf primordia. R<sup>2</sup>, goodness-of-fit of parabolic model. Bar, 50 μm. **(B)** SAMs from broadly diverse evolutionary lineages exhibit a range of parabolic coefficients.

2006a,b.). In multicellular meristems, internal cellular division from the replication of initials places stress on epidermal cell walls, deforming the shoot apical domain into a parabolic shape (Niklas and Mauseth, 1980; Green, 1999; Kwiatkowska, 2004). Whereas the angiosperm tunica-corpus-type meristem comprises an outer, epidermal layer of cells under tension

and at least one inner cell layer under compression, single apical cell-type meristems must accomplish similar geometries by portioning biophysical forces over just one cell wall and cytoplasm. Within possible parabolic shapes, our broad sampling of plant shoot meristems suggests that evolutionary clade alone is not a significant determinant of specific SAM parabolic

shape; plant taxa from disparate evolutionary clades may have similar parabolic shapes. These data, therefore, constitute robust evidence for a fundamental biophysical model of meristem morphology, which transcends not only diverse evolutionary histories, but even an anatomical transition from single-celled structure to multicellular SAM.

As previous studies in maize have uncovered statistically significant correlations between SAM size and selected adult plant traits (Leiboff et al., 2015; Thompson et al., 2015), our analyses of SAM parabolic diversity within divergent plant taxa provide a framework for future investigations as to whether a fundamental correlation between SAM architecture and adult plant morphology may extend beyond phylogenetic boundaries.

## AUTHOR CONTRIBUTIONS

MS, helped conceive and design the experiments, and edited the manuscript; SL, helped conceive and design the experiments, generated, analyzed, and interpreted the data, and wrote the manuscript. CD, performed imaging and image analyses of the teosinte SAMs.

## REFERENCES

- Beadle, G. W. (1980). The ancestry of corn. *Sci. Am.* 242, 112–119. doi: 10.1038/scientificamerican0180-112
- Bierhorst, D. W. (1971). *Morphology of Vascular Plants*. London: Macmillan.
- Bommert, P., Je, B. I., Goldshmidt, A., and Jackson, D. (2013). The maize G-alpha gene COMPACT PLANT2 functions in CLAVATA signalling to control shoot meristem size. *Nature* 502, 555–558. doi: 10.1038/nature12583
- Briggs, W. H., McMullen, M. D., Gaut, B. S., and Doebley, J. (2007). Linkage mapping of domestication loci in a large maize teosinte backcross resource. *Genetics* 177, 1915–1928. doi: 10.1534/genetics.107.076497
- Chitwood, D. H., Kumar, R., Headland, L. R., Ranjan, A., Covington, M. F., Ichihashi, Y., et al. (2013). A quantitative genetic basis for leaf morphology in a set of precisely defined tomato introgression lines. *Plant Cell* 25, 2465–2481. doi: 10.1105/tpc.113.112391
- Chitwood, D. H., Ranjan, A., Kumar, R., Ichihashi, Y., Zumstein, K., Headland, L. R., et al. (2014). Resolving distinct genetic regulators of tomato leaf shape within a heteroblastic and ontogenetic context. *Plant Cell* 26, 3616–3629. doi: 10.1105/tpc.114.130112
- Claude, J. (2008). *Morphometrics with R*. New York, NY: Springer-Verlag.
- Doebley, J. (2004). The genetics of maize evolution. *Annu. Rev. Genet.* 38, 37–59. doi: 10.1146/annurev.genet.38.072902.092425
- Dommergues, C. H., Dommergues, J. L., and Verrecchia, E. P. (2007). The discrete cosine transform, a Fourier-related method for morphometric analysis of open contours. *Math. Geol.* 39, 749–763. doi: 10.1007/s11004-007-9124-6
- Dong, Z., Danilevskaya, O., Abadie, T., Messina, C., Coles, N., and Cooper, M. (2012). A gene regulatory network model for floral transition of the shoot apex in maize and its dynamic modeling. *PLoS ONE* 7:e43450. doi: 10.1371/journal.pone.0043450
- Emerson, R. A. (1924). Control of flowering in teosinte: short-day treatment brings early flowers. *J. Hered.* 15, 41–48.
- Evert, R. F. (2006a). “Apical meristems,” in *Esau’s Plant Anatomy* (Hoboken, NJ: John Wiley & Sons, Inc.), 133–174.
- Evert, R. F. (2006b). “Meristems and differentiation,” in *Esau’s Plant Anatomy* (Hoboken, NJ: John Wiley & Sons, Inc.), 103–131.
- Evert, R. F., and Esau, K. (2006). *Esau’s Plant Anatomy?: Meristems, Cells, and Tissues of the Plant Body?: Their Structure, Function, and Development*. Hoboken, NJ: Wiley-Interscience.
- Frank, M. H., Edwards, M. B., Schultz, E. R., McKain, M. R., Fei, Z., Sørensen, I., et al. (2015). Dissecting the molecular signatures of apical cell-type shoot meristems from two ancient land plant lineages. *New Phytol.* 207, 893–904. doi: 10.1111/nph.13407
- Frank, M. H., and Scanlon, M. J. (2015). Transcriptomic evidence for the evolution of shoot meristem function in sporophyte-dominant land plants through concerted selection of ancestral gametophytic and sporophytic genetic programs. *Mol. Biol. Evol.* 32, 355–367. doi: 10.1093/molbev/msu303
- Green, P. (1999). Expression of pattern in plants: combining molecular and calculus-based biophysical paradigms. *Am. J. Bot.* 86, 1059–1076. doi: 10.2307/2656967
- Hake, S., and Ross-Ibarra, J. (2015). Genetic, evolutionary and plant breeding insights from the domestication of maize. *Elife* 2015, 1–8. doi: 10.7554/elife.05861
- Huang, C., Chen, Q., Xu, G., Xu, D., Tian, J., and Tian, F. (2016). Identification and fine mapping of quantitative trait loci for the number of vascular bundle in maize stem. *J. Integr. Plant Biol.* 58, 81–90. doi: 10.1111/jipb.12358
- Hufford, M. B., Bilinski, P., Pyhäjärvi, T., and Ross-Ibarra, J. (2012). Teosinte as a model system for population and ecological genomics. *Trends Genet.* 28, 606–615. doi: 10.1016/j.tig.2012.08.004
- Hung, H.-Y., Shannon, L. M., Tian, F., Bradbury, P. J., Chen, C., Flint-Garcia, S. A., et al. (2012). ZmCCT and the genetic basis of day-length adaptation underlying the postdomestication spread of maize. *Proc. Natl. Acad. Sci. U.S.A.* 109, E1913–E1921. doi: 10.1073/pnas.1203189109
- Jackson, D. P., and Hake, S. (1999). Control of phyllotaxy in maize by the abp11 gene. *Development* 126, 315–323.
- Je, B. I., Gruel, J., Lee, Y. K., Bommert, P., Arevalo, E. D., Eveland, A. L., et al. (2016). Signaling from maize organ primordial via FASCIALIZED EAR3 regulates stem cell proliferation and yield traits. *Nat. Genet.* 48, 785–791. doi: 10.1038/ng.3567
- Jia, Y., Lisch, D. R., Ohtsu, K., Scanlon, M. J., Nettleton, D., and Schnable, P. S. (2009). Loss of RNA-dependent RNA polymerase 2 (RDR2) function causes widespread and unexpected changes in the expression of transposons, genes, and 24-nt small RNAs. *PLoS Genet.* 5:e1000737. doi: 10.1371/journal.pgen.1000737
- Klingenberg, C. P. (2010). Evolution and development of shape: integrating quantitative approaches. *Nat. Rev. Genet.* 11, 623–635. doi: 10.1038/nrg2829
- Kwiatkowska, D. (2004). Structural integration at the shoot apical meristem: models, measurements, and experiments. *Am. J. Bot.* 91, 1277–1293. doi: 10.3732/ajb.91.9.1277

## FUNDING

This work was funded by National Science Foundation (NSF) grant IOS-1238142.

## ACKNOWLEDGMENTS

We thank L. Comai (UC Davis), for stimulating discussions of the data. We thank K. Niklas (Cornell) for strategic advice in modeling SAMs as paraboloids. Many thanks to the organizers and participants of the 2015 NIMBioS Investigative Workshop: morphological Plant Models for advice on morphometric concepts and techniques. We thank N. Ronning (Cornell) for assistance with plant harvest and image acquisition.

## SUPPLEMENTARY MATERIAL

The Supplementary Material for this article can be found online at: <http://journal.frontiersin.org/article/10.3389/fpls.2016.01651/full#supplementary-material>

- Landrein, B., Rehafi, Y., Besnard, F., Hervieux, N., Mirabet, V., Boudaoud, A., et al. (2015). Meristems size contributes to the robustness of phyllotaxis in *Arabidopsis*. *J. Exp. Bot.* 66, 1317–1324. doi: 10.1093/jxb/eru482
- Langlade, N. B., Feng, X., Dransfield, T., Copsey, L., Hanna, A. I., Thébaud, C., et al. (2005). Evolution through genetically controlled allometry space. *Proc. Natl. Acad. Sci. U.S.A.* 102, 10221–10226. doi: 10.1073/pnas.0504210102
- Leiboff, S., Li, X., Hu, H.-C., Todt, N., Yang, J., Li, X., et al. (2015). Genetic control of morphometric diversity in the maize shoot apical meristem. *Nat. Commun.* 6:8974. doi: 10.1038/ncomms9974
- Niklas, K. J., and Mauseth, J. D. (1980). Simulations of cell dimensions in shoot apical meristems: implications concerning zonate apices. *Am. J. Bot.* 67, 715–732. doi: 10.2307/2442665
- Orr, A. R., and Sundberg, M. D. (1994). Inflorescence development in a perennial teosinte: *Zea perennis* (Poaceae). *Am. J. Bot.* 81, 598–608. doi: 10.2307/2445735
- Orr, A. R., and Sundberg, M. D. (2004). Inflorescence development in a new teosinte: *Zea nicaraguensis* (Poaceae). *Am. J. Bot.* 91, 165–173. doi: 10.3732/ajb.91.2.165
- Pautler, M., Eveland, A. L., LaRue, T., Yang, F., Weeks, R., Lunde, C., et al. (2015). FASCIATED EAR4 encodes a bZIP transcription factor that regulates shoot meristem size in maize. *Plant Cell* 27, 104–120. doi: 10.1105/tpc.114.132506
- Pautler, M., Tanaka, W., Hirano, H.-Y., and Jackson, D. (2013). Grass meristems I: shoot apical meristem maintenance, axillary meristem determinacy and the floral transition. *Plant Cell Physiol.* 54, 302–312. doi: 10.1093/pcp/pct025
- Shannon, L. M. (2012). *The Genetic Architecture of Maize Domestication and Range Expansion*. Ph.D. Dissertation, University of Wisconsin, Madison, WI.
- Steeves, T. A., and Sussex, I. M. (1972). *Patterns in Plant Development*. Englewood Cliffs, NJ: Prentice-Hall.
- Sundberg, M. D., and Orr, A. R. (1986). Early inflorescence and floral development in *Zea diploperennis*, diploperennial teosinte. *Am. J. Bot.* 73, 1699–1712. doi: 10.2307/2444236
- Sundberg, M. D., and Orr, A. R. (1990). Inflorescence development in two annual teosintes: *Zea mays* subsp. *Mexicana* and *Z. mays* subsp. *Parviglumis*. *Am. J. Bot.* 77, 141–152. doi: 10.2307/2444637
- Taguchi-Shiobara, F., Yuan, Z., Hake, S., and Jackson, D. P. (2001). The fasciated ear2 gene encodes a leucine-rich repeat receptor-like protein that regulates shoot meristem proliferation in maize. *Genes Dev.* 15, 2755–2766. doi: 10.1101/gad.208501
- Thompson, A. M., Crants, J., Schnable, P. S., Yu, J., Timmermans, M. C. P., Springer, N. M., et al. (2014). Genetic control of maize shoot apical meristem architecture. *G3 (Bethesda)* 4, 1327–1337. doi: 10.1534/g3.114.011940
- Thompson, A. M., Yu, J., Timmermans, M. C. P., Schnable, P., Crants, J. C., Scanlon, M. J., et al. (2015). Diversity of maize shoot apical meristem architecture and its relationship to plant morphology. *G3* 5, 819–827. doi: 10.1534/g3.115.017541
- Tsuji, H., Taoka, K. I., and Shimamoto, K. (2011). Regulation of flowering in rice: two florigen genes, a complex gene network, and natural variation. *Curr. Opin. Plant Biol.* 14, 45–52. doi: 10.1016/j.pbi.2010.08.016
- Yang, F., Bui, H. T., Pautler, M., Llaca, V., Johnston, R., Lee, B.-H., et al. (2015). A maize glutaredoxin gene, Abphyl2, regulates shoot meristem size and phyllotaxy. *Plant Cell* 27, 121–131. doi: 10.1105/tpc.114.130393
- Yang, Q., Li, Z., Li, W., Ku, L., Wang, C., Ye, J., et al. (2013). CACTA-like transposable element in ZmCCT attenuated photoperiod sensitivity and accelerated the postdomestication spread of maize. *Proc. Natl. Acad. Sci. U.S.A.* 110, 16969–16974. doi: 10.1073/pnas.1310949110

**Conflict of Interest Statement:** The authors declare that the research was conducted in the absence of any commercial or financial relationships that could be construed as a potential conflict of interest.

Copyright © 2016 Leiboff, DeAllie and Scanlon. This is an open-access article distributed under the terms of the Creative Commons Attribution License (CC BY). The use, distribution or reproduction in other forums is permitted, provided the original author(s) or licensor are credited and that the original publication in this journal is cited, in accordance with accepted academic practice. No use, distribution or reproduction is permitted which does not comply with these terms.



# A Bistable Switch Mechanism for Stem Cell Domain Nucleation in the Shoot Apical Meristem

Dorjsuren Battogtokh<sup>1,2\*</sup> and John J. Tyson<sup>2</sup>

<sup>1</sup> Department of Theoretical Physics, The Institute of Physics and Technology, Mongolian Academy of Sciences, Ulaanbaatar, Mongolia, <sup>2</sup> Department of Biological Sciences, Virginia Polytechnic and State University, Blacksburg, VA, USA

**Keywords:** minimal model of SAM, reaction-diffusion systems, Turing instability, bistability, hormone field

## INTRODUCTION

In plants, the stem cells residing in shoot apical meristems (SAM) give rise to above-ground tissues (Aichinger et al., 2012). Hence, the maintenance of stem cell niches is of central importance to a plant's continued growth and development (Fletcher and Meyerowitz, 2000; Gordon et al., 2009). For the flowering plant *Arabidopsis thaliana*, the genetic determinants of stem cell growth, division, and localization have been identified, and negative feedback between a homeodomain transcription factor, WUSCHEL (WUS), and a receptor kinase, CLAVATA (CLV), is known to play a crucial role in controlling the reservoir of stem cells in the central domain of a SAM.

## OPEN ACCESS

### Edited by:

Alexander Bucksch,  
Georgia Institute of Technology, USA

### Reviewed by:

Alexis Maizel,  
Heidelberg University, Germany  
Luca Salerno,  
Università degli Studi Magna Græcia  
di Catanzaro, Italy

### \*Correspondence:

Dorjsuren Battogtokh  
dbattogt@vt.edu

### Specialty section:

This article was submitted to  
Plant Biophysics and Modeling,  
a section of the journal  
*Frontiers in Plant Science*

**Received:** 15 March 2016

**Accepted:** 02 May 2016

**Published:** 23 May 2016

### Citation:

Battogtokh D and Tyson JJ (2016) A Bistable Switch Mechanism for Stem Cell Domain Nucleation in the Shoot Apical Meristem. *Front. Plant Sci.* 7:674.  
doi: 10.3389/fpls.2016.00674

The morphology of plant stems and floral organs is controlled in large part by the size and stability of SAMs, which is controlled, in turn, by spatiotemporal patterns of WUS and CLV expression in meristems. For example, loss of restrictive signals in *clv* mutants of *Arabidopsis* leads to enlargement of shoot and floral meristems, resulting in extra floral organs and club-shaped siliques (Jönsson et al., 2005). The size, localization and stability of stem cell domains should be determined, in principle, by the interactions of WUS and CLV proteins, especially by their propensities to diffuse through the domain and by the rates of the molecular reactions that control their activities. Within this paradigm, reaction-diffusion (RD) models of WUS-CLV interactions have been popular mathematical models of SAM dynamics (Jönsson et al., 2005; Hohm et al., 2010; Fujita et al., 2011). In RD models, the spontaneous generation of inhomogeneous distributions of WUS and CLV in SAM domains is usually attributed to mechanisms based on a "Turing" instability (Turing, 1952; Segel and Jackson, 1972).

The generic RD equations for spatiotemporal changes in the concentrations,  $u(x,t)$  and  $v(x,t)$ , of two interacting proteins are

$$\frac{\partial u}{\partial t} = f(u, v) + D_u \frac{\partial^2 u}{\partial x^2}, \quad \frac{\partial v}{\partial t} = g(u, v) + D_v \frac{\partial^2 v}{\partial x^2},$$

where  $f(u,v)$  and  $g(u,v)$  are nonlinear functions describing their local chemical interactions. A unique, uniform, steady-state solution,  $u(x,t) = u_0 = \text{constant}$  and  $v(x,t) = v_0$ , of these equations can become unstable with respect to small, non-uniform perturbations,  $u(x,t) = u_0 + e^{\lambda t} \delta u \cos(qx)$  and  $v(x,t) = v_0 + e^{\lambda t} \delta v \cos(qx)$ ,  $\delta u \ll u_0$  and  $\delta v \ll v_0$ . The spectra of unstable modes,  $\lambda(q)$ , can be found from the characteristic equation for  $\lambda$ . A Turing instability appears for wavenumbers close to the critical wave-number defined by the equations,  $\lambda(q) \geq 0$  and  $\lambda'(q) = 0$ . The *sine qua non* for Turing patterns is the condition for diffusion coefficients:  $D_v >> D_u$ , generating standing waves of wavelength  $l \approx 2\pi/q_{crit}$  in the simulations of the RD system (Gierer and Meinhardt, 1972; Murray, 2003). At present, the diffusive lengths of CLV and WUS in SAMs have not been determined, and

there is no evidence to suggest that the Turing condition (diffusivity of CLV >> diffusivity of WUS) is satisfied in the central zone of a SAM.

In typical RD models of the SAM, as in Jönsson et al. (2005), Fujita et al. (2011) and **Figure 1**, the interactions between WUS and CLV are described by highly nonlinear terms. Consequently, these models typically display bistability in a certain range of their parameters. Interestingly, recent experimental data on cytokinin-controlled domain confinement in SAMs (Gordon et al., 2009) suggest that WUS-CLV interactions may indeed exhibit bistability (Gordon et al., 2009).

If the differential diffusivity condition is not fulfilled, domain generation is not possible in the monostable regime of a RD system. Is spontaneous domain formation possible in the bistable regime of an RD model even if the differential diffusivity condition is not fulfilled? The answer is yes, if we supplement the RD model for WUS and CLV with a third variable describing, for example, the distribution of a rapidly diffusing hormone in the SAM region. In this brief note, we propose that the bistable-switch mechanism is superior to Turing-type mechanisms of stem-cell domain nucleation in the SAM, by comparing the two mechanisms in a minimal RD model of a SAM. We prefer the bistable mechanism because it does not require artificial assumptions, such as spatial heterogeneities for parameters and variables that typically arise in fitting Turing-type models to SAM features (Jönsson et al., 2005; Fujita et al., 2011).

## DOMAIN NUCLEATION MECHANISMS

### Turing Mechanism

**Figure 1A** shows the activator-inhibitor model of SAM proposed by Fujita et al. (2011). The stable steady state undergoing Turing instability can be found at the intersection of the WUS( $u$ ) and CLV( $v$ ) nullclines, **Figure 1B** (solid and dashed lines). The linear spectrum of unstable modes can be positive,  $\lambda(q) > 0$ , and give rise to Turing patterns, if the diffusion coefficient of CLV is significantly larger than the diffusion coefficient of WUS,  $D_v >> D_u$  (see **Figure 1C**). In the resulting Turing pattern (**Figure 1D** top), the stem cell domain is the region where the level of WUS exceeds its steady state value, and other SAM domains are outside this region. In a Turing model, the size of the central domain is determined by the critical wavenumber,  $q_{crit}$ , corresponding to the maximum of  $\lambda(q)$  in **Figure 1C**. With the meristem growth, the steady state values and critical wavenumber of the Turing pattern remain the same. When the region grows to twice the original size, the number of waves in the Turing pattern doubles (**Figure 1D** bottom), which can be associated with the nucleation of new stem cell domains.

For our goal of accurate prediction of the size, location, and stability of stem cell domains in SAM, the Turing mechanism has certain limitations. First, in studying a dome-shaped SAM in two and three spatial dimensions, additional assumptions introducing spatial heterogeneity are required to localize the central domain at the apex of the SAM (Jönsson et al., 2005;

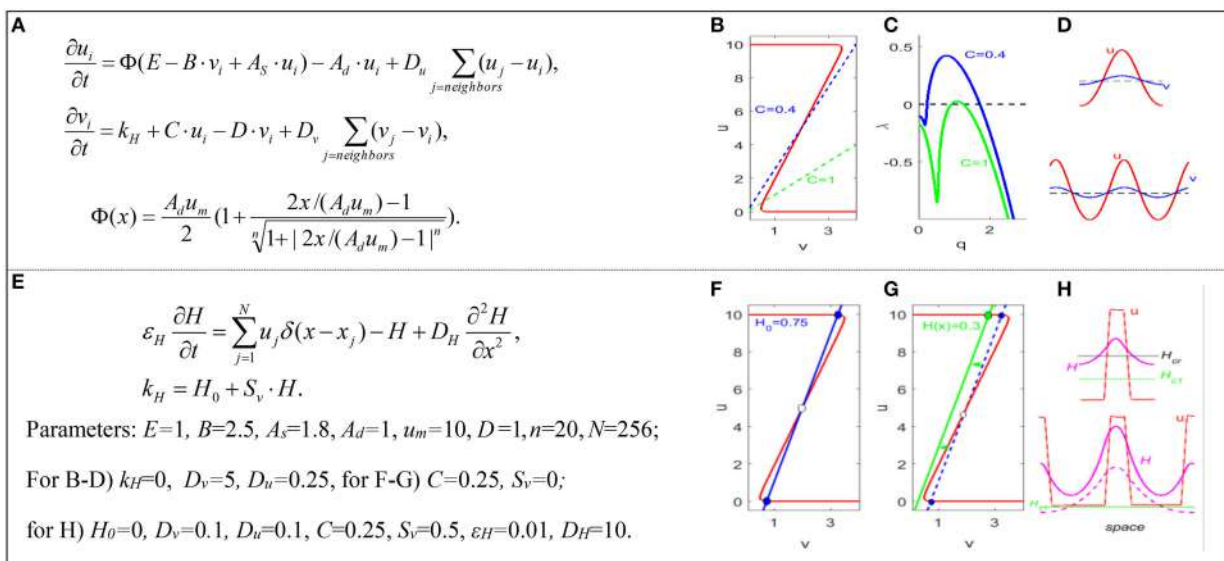


**FIGURE 1 |** Turing and bistable mechanisms of domain formation. **(A)** Fujita's model of SAM.  $u$  = WUS,  $v$  = CLV,  $i$  = cell index,  $\Phi$  is a sigmoid function. The parameters and Greek symbols are positive constants. **(B)** Nullclines. **(C)** Linear spectra of unstable modes in the continuous limit of the model. **(D)** Turing patterns (for  $C = 1$ ) in smaller (top) and larger (bottom) domains. Horizontal dashed line is the uniform steady state  $u_0 = v_0$ . **(E)** Bistable-switch model: domain patterns are controlled by the spatial distribution of "hormone" field,  $H$ .  $N$  = number of cells, and  $\delta$  = Dirac delta function. **(F)** Nullclines for a uniform  $H$  field. **(G)** Nullclines for a non-uniform  $H$  field. **(H)** Non-Turing patterns in smaller (top) and larger (bottom) domains. *Model parameters.* Function  $\Phi$  describes the synthesis rate of activator  $u$ , with basal intensity  $E$ , self-activation strength  $A_S$ , inhibitor strength  $B$ , and the maximum allowed value for activator,  $u_m$ . Parameters  $A_d$  and  $D$  describe degradation rates of activator and inhibitor. Parameter  $C$  and  $S_v$  describe the intensities of inhibitor inductions by activator and hormone.  $H_0$  is the basal synthesis rate of the inhibitor. Parameter  $\epsilon_H$  characterizes the time scale of the hormone.  $D_u$ ,  $D_v$ , and  $D_H$  are diffusion coefficients. Dirac delta function describes hormone synthesis at discrete cell locations.

Fujita et al., 2011). Under such assumptions, the size and location of domain patterns are no longer defined by the critical wavenumber of the Turing instability, but they are defined by artificial restrictions imposed on the model (Jönsson et al., 2005). Second, the value of the critical wavenumber, which determines the size of the stem cell domain in a Turing mechanism, may not depend on parameters in the manner dictated by experiments. For example, experiments (Aichinger et al., 2012) indicate that the size of the stem-cell domain increases significantly, with reduction in the rate of synthesis of CLV (the parameter C in **Figure 1A**); however,  $q_{crit}$  decreases only a little with a 2.5-fold decrease in the value of C (**Figure 1C**). Third, Turing patterns are dissipative structures subject to fluctuations depending on noise in the system, but stem-cell domains should be stable against perturbations due to mechanical pressures arising from cell growth, cell wall extension, cell division, etc. Because of these limitations we investigated whether an alternative mechanism of domain nucleation is possible in mathematical models of SAM.

## Bistable Mechanism

Depending on the parameters  $k_H$  and C, the (Fujita et al., 2011) model can exhibit a bistable regime, i.e., the nullclines of WUS( $u$ ) and CLV( $v$ ) can have three intersection points, two of which are stable steady states. Let us consider a bistable regime in the model and introduce a new diffusive variable,  $H$ , a hypothetical, rapidly diffusing hormone (Battogtokh, 2015). For simplicity, we also assume that  $H$  activity depends linearly on WUS level and that the level of CLV depends linearly on  $H$ . We redefine the parameter  $k_H$  in the equation for CLV( $v$ ) to integrate the  $H$  field into the model, see **Figure 1E**. The bistable steady states in the modified, three-variable bistable model of (Fujita et al., 2011) for uniform  $H_0$  are shown in **Figure 1F**. If we consider an initial non-uniform  $H$  field with a minimum value in the center (or apply a strong initial perturbation to the center of the system), a domain pattern as in **Figure 1H** (top) can be formed. It can be shown that for certain values of uniform  $H_0$  and nonzero  $D_u$  and  $D_v$ , the domain pattern is stable because the front solution is motionless (Tyson and Keener, 1988). The Turing condition  $D_v > D_u$  is not required for the origination and maintenance of the domain. The domain is stable even if the distribution of  $H$  is non-uniform, as long as  $H$  varies close to the value  $H_{cr}$  at which the wavefront is stationary, **Figure 1H** (top). The size and stability of the domain can be calculated from the condition of the stationary front (Battogtokh, 2015), while the location of the domain is controlled by the spatial distribution of the  $H$  field.

Spontaneous generation of new domains is possible as the system grows in size. For simplicity, let us consider growth by boundary extensions, through slow addition of new elements at the boundaries. As the system grows, the front can stay motionless, and WUS and CLV levels persist near the two stable steady-state values. However, the distribution of  $H$  may change with growth; it will stay high at the center where WUS level is high, but  $H$  level may drop in regions further away from the center. Therefore, as the system grows, the local value  $H$  may drop below the critical value  $H_{c1}$ , where there is only an upper steady state in the corresponding local system, **Figure 1G** (green

line). Thus, the drop of  $H$  below  $H_{c1}$  is accompanied by the nucleation of new domains, **Figure 1H** (bottom, dashed red line). The distance between the domains can be calculated from the model (Battogtokh, 2015).

## DISCUSSION

The framework of modeling a cell population coupled by a fast diffusive field was introduced previously by Kuramoto et al. (2000). We used the framework to model SAM cells with bistable dynamics, in the case of simple linear coupling. Exploring linear and nonlinear types of coupling with respect to experimental data may identify molecular candidates for the fast diffusive peptide-hormone. We expect that the peptide-hormone may be a member of the CLE family, for which CLV3 is one of the founding genes (Wang and Fiers, 2010; Wang et al., 2016). While in the simple three variable mathematical model considered here, the hypothetical hormone may be sufficient to drive domain nucleation, in a more realistic model (e.g., Nikolaev et al., 2007), the involvement of several members of the CLE family (e.g., CLE 19, CLE 41, etc.) and their crosstalk with phytohormones may be necessary to account for all the biological data.

We suspect that there is a close relationship between our bistable-switch mechanism and the cell-positioning mechanism in the SAM model of Nikolaev et al. (2007). However, because of the complexity of their model, bistability and front stabilization dynamics are not as apparent as in the minimal model of SAM used here.

In simulations of a lattice of hexagonal cells, representing a two-dimensional vertical section of SAM, the bistable switch mechanism can generate WUS domains at the target position near the apex; the domain size can be controlled by the synthesis rate of CLV; and the regeneration of WUS domains seen in laser-ablation experiments can be simulated (Battogtokh and Tyson, 2016).

## CONCLUSION

We believe that accurate multiscale models integrating mathematical descriptions of genomic, chemical, and mechanical processes involved in plant meristem growth and development will serve for predicting and simulating plant morphogenesis. A primary requirement for such a model is a quantitative description of the relationship between the size, location, and stability of the meristems, on one hand, and the plant's shape and phenotype, on the other hand. Therefore, identifying the correct underlying mechanism of spontaneous generation of stem-cell domain patterns is crucial for creating a mathematical model of plant growth. The most basic problem with the classic Turing mechanism for domain nucleation in the SAM is that there is no evidence for differential diffusivity of CLV (inhibitor: the complex of membrane receptor kinase CLV1 and its ligand CLV3) and WUS (activator: transcription factor) biomolecules, a necessary condition for Turing pattern formation. The bistable switch mechanism, on the contrary, is not restricted by the differential diffusivity condition. Cells in the SAM can generate

new stem cell domains by switching between the two stable steady states of WUS, depending on the local level of a hormonal field. The nucleated domain is not a dissipative structure but a stable structure; its size, location, and stability can be determined from the properties of the front solution connecting the two stable steady states (Battogtokh, 2015).

## AUTHOR CONTRIBUTIONS

DB designed and conducted the research, wrote the manuscript. JJT designed research and wrote the manuscript.

## REFERENCES

- Aichinger, E., Kornet, N., Friedrich, T., and Laux T. (2012). Plant stem cell niches. *Annu. Rev. Plant Biol.* 63, 615–636. doi: 10.1146/annurev-arplant-042811-105555
- Battogtokh, D. (2015). Domain nucleation and confinement in agent-controlled bistable systems. *Phys. Rev. E Stat. Nonlin. Soft Matter Phys.* 91:032713. doi: 10.1103/PhysRevE.91.032713
- Battogtokh, D., and Tyson, J. J. (2016). Comparison of domain nucleation mechanisms in a minimal model of shoot apical meristem. arXiv:1604.04643.
- Fletcher, J. C., and Meyerowitz, E. M. (2000). Cell signaling within the shoot meristem. *Curr. Opin. Plant Biol.* 3, 23–30. doi: 10.1016/S1369-5266(99)00033-3
- Fujita, H., Toyokura, K., Okada, K., and Kawaguchi, M. (2011). Reaction-diffusion pattern in shoot apical meristem of plants. *PLoS ONE* 6:e18243. doi: 10.1371/journal.pone.0018243
- Gierer, A., and Meinhardt, H. (1972). A theory of biological pattern formation. *Kybernetik* 12, 30–39. doi: 10.1007/BF00289234
- Gordon, S. P., Chickarmane, V. S., Ohno, C., and Meyerowitz, E. M. (2009). Multiple feedback loops through cytokinin signaling control stem cell number within the *Arabidopsis* shoot meristem. *Proc. Natl. Acad. Sci. U.S.A.* 106, 16529–16534. doi: 10.1073/pnas.0908122106
- Hohm, T., Zitzler, E., and Simon, R. (2010). A dynamic model for stem cell homeostasis and patterning in *Arabidopsis* meristems. *PLoS ONE* 5:e9189. doi: 10.1371/journal.pone.0009189
- Jönsson, H., Heisler, M., Reddy, G. V., Agrawal, V., Gor, V., Shapiro, B. E., et al. (2005). Modeling the organization of the WUSCHEL expression domain in the shoot apical meristem. *Bioinformatics* 21, i232–i240. doi: 10.1093/bioinformatics/bti1036
- Kuramoto, Y., Nakao, H., and Battogtokh, D. (2000). Multi-scaled turbulence in large populations of oscillators in a diffusive medium. *Phys. A Stat. Mech. Appl.* 288, 244–264. doi: 10.1016/S0378-4371(00)00425-8
- Murray, J. D. (2003). *Mathematical Biology II: Spatial Models and Biomedical Applications*, 3rd Edn. New York, NY: Springer-Verlag.
- Nikolaev, S. V., Penenko, A. V., Lavreha, V. V., Mjolsness, E. D., and Kolchanov N. A. (2007). A model study of the role of proteins CLV1, CLV2, CLV3, and WUS in regulation of the structure of the shoot apical meristem. *Ontogenез* 38, 457–462. doi: 10.1134/s1062360407060069
- Segel, L., and Jackson, J. L. (1972). Dissipative structure: an explanation and an ecological example. *J. Theor. Biol.* 37, 545–559. doi: 10.1016/0022-5193(72)90090-2
- Turing, A. M. (1952). The chemical basis of morphogenesis. *Philos. Trans. R. Soc. London* 237, 37–72. doi: 10.1098/rstb.1952.0012
- Tyson, J. J., and Keener, J. P. (1988). Singular perturbation theory of traveling waves in excitable media (a review). *Physica D Nonlinear Phenomena* 32, 327–361. doi: 10.1016/0167-2789(88)90062-0
- Wang, G., and Fiers, M. (2010). CLE peptide signaling during plant development. *Protoplasma* 240, 33–43. doi: 10.1007/s00709-009-0095-y
- Wang, G., Zhang, G., and Wu, M. (2016). CLE peptide signalling and crosstalk with phytohormones and environmental stimuli. *Front. Plant Sci.* 6:1211. doi: 10.3389/fpls.2015.01211

## FUNDING

Financial Assistance from the Department of Biological Sciences and the College of Science at Virginia Tech is gratefully acknowledged. DB is also partially supported by a grant of the Mongolian Foundation for Science and Technology.

## ACKNOWLEDGMENTS

The authors are grateful to Prof. Zachary L. Nimchuk for fruitful discussions. DB is thankful to Prof. Alexander S. Mikhailov and Prof. Kh. Namsrai for stimulating discussions.



# Mechanical Behavior of Cells within a Cell-Based Model of Wheat Leaf Growth

Ulyana Zubairova<sup>1\*</sup>, Sergey Nikolaev<sup>1,2\*</sup>, Aleksey Penenko<sup>3,4</sup>, Nikolay Podkolodnyy<sup>1,5,6</sup>, Sergey Golushko<sup>2,7</sup>, Dmitry Afonnikov<sup>1,8</sup> and Nikolay Kolchanov<sup>1,8</sup>

<sup>1</sup> Department of Systems Biology, Institute of Cytology and Genetics (ICG), Siberian Branch of Russian Academy of Science, Novosibirsk, Russia, <sup>2</sup> Laboratory of Analysis and Optimization of Non-Linear Systems, Institute of Computational Technologies (ICG), Siberian Branch of Russian Academy of Science, Novosibirsk, Russia, <sup>3</sup> Laboratory of Mathematical Modeling of Hydrodynamic Processes in the Environment, Institute of Computational Mathematics and Mathematical Geophysics (ICM & MG), Siberian Branch of Russian Academy of Science, Novosibirsk, Russia, <sup>4</sup> Chair of Mathematical Methods in Geophysics, Faculty of Mechanics and Mathematics, Novosibirsk State University, Novosibirsk, Russia,

<sup>5</sup> Laboratory of Mathematical Problems of Geophysics, Institute of Computational Mathematics and Mathematical Geophysics (ICM & MG), Siberian Branch of Russian Academy of Science, Novosibirsk, Russia, <sup>6</sup> Chair of Informatics Systems, Faculty of Information Technologies, Novosibirsk State University, Novosibirsk, Russia, <sup>7</sup> Chair of Mathematical Modeling, Faculty of Mechanics and Mathematics, Novosibirsk State University, Novosibirsk, Russia, <sup>8</sup> Chair of Informational Biology, Faculty of Natural Sciences, Novosibirsk State University, Novosibirsk, Russia

## OPEN ACCESS

### Edited by:

Alexander Bucksch,  
University of Georgia, USA

### Reviewed by:

Gerrit T. S. Beemster,  
University of Antwerp, Belgium  
Claudiu-Cristi Antonovici,  
Leiden University, Netherlands

### \*Correspondence:

Ulyana Zubairova  
ulyanochka@bionet.nsc.ru  
Sergey Nikolaev  
nikolaev@bionet.nsc.ru

### Specialty section:

This article was submitted to  
Plant Biophysics and Modeling,  
a section of the journal  
*Frontiers in Plant Science*

Received: 27 August 2016

Accepted: 28 November 2016

Published: 15 December 2016

### Citation:

Zubairova U, Nikolaev S, Penenko A,  
Podkolodnyy N, Golushko S,  
Afonnikov D and Kolchanov N (2016)  
Mechanical Behavior of Cells within a  
Cell-Based Model of Wheat Leaf  
Growth. *Front. Plant Sci.* 7:1878.  
doi: 10.3389/fpls.2016.01878

Understanding the principles and mechanisms of cell growth coordination in plant tissue remains an outstanding challenge for modern developmental biology. Cell-based modeling is a widely used technique for studying the geometric and topological features of plant tissue morphology during growth. We developed a quasi-one-dimensional model of unidirectional growth of a tissue layer in a linear leaf blade that takes cell autonomous growth mode into account. The model allows for fitting of the visible cell length using the experimental cell length distribution along the longitudinal axis of a wheat leaf epidermis. Additionally, it describes changes in turgor and osmotic pressures for each cell in the growing tissue. Our numerical experiments show that the pressures in the cell change over the cell cycle, and in symplastically growing tissue, they vary from cell to cell and strongly depend on the leaf growing zone to which the cells belong. Therefore, we believe that the mechanical signals generated by pressures are important to consider in simulations of tissue growth as possible targets for molecular genetic regulators of individual cell growth.

**Keywords:** wheat leaf epidermis, symplastic growth, cell mechanics, osmotic and turgor pressure, autonomous cell growth, cell-based models

## 1. INTRODUCTION

Three fundamental processes characterize the development of multicellular plants: growth, differentiation, and morphogenesis. These processes result in an increase in the size and number of cells, the appearance of the structural and functional differences between them, and the formation of functionally specialized organs in plants. Plant science has accumulated a considerable amount of information about plant growth and plant genetics. Nevertheless, the molecular genetic mechanisms that influence the growth and development of plants are still unclear. Analysis and

reconstruction of the dynamics of genetic regulatory networks are only the first steps toward understanding how genetic information determines the morphogenesis of plants (Kalve et al., 2014; Chaiwanon et al., 2016). At present, increasingly more facts demonstrate that full understanding of the mechanisms of morphogenesis requires considering the processes that occur at the tissue level in addition to the information on the expression of genes. These processes are involved in spatial pattern formation (Swarup et al., 2005; Jönsson et al., 2006; Bayer et al., 2009) and result in strains and stresses in cell walls (Green, 1999; Hamant et al., 2008). Understanding the relationships between the processes at the molecular-genetic level and at the level of cell ensembles and tissues and how these relationships result in the implementation of the biological function and morphogenesis is perhaps the most central question in systems biology (Noble, 2008).

The ability of cells to stretch and to change shape is the basis for the functional specialization of tissue and the formation of structure in plants. In contrast to animal cells, plant cells cannot migrate during tissue growth. Therefore, these cells achieve perfect control over the final shape by modulating cell division and expansion (Cosgrove, 2005). Knowledge about regulation of the biomechanical properties of the cells during these processes is now widely used in studies of plant morphogenesis. The ability of plant cells to detect mechanical stresses in a tissue and to use them as control signals is considered to be the foundation of regulated growth and morphodynamics (Ali and Traas, 2016; Braybrook and Jönsson, 2016). It is believed that management strategies based on mechanosensing include both stabilization due to the negative feedback and an increase of differences in the rates and directions of neighboring cell growth due to positive feedback (Sassi and Traas, 2015). However, despite intensive studies of such regulation (Hamant and Traas, 2010; Robinson et al., 2013; Routier-Kierzkowska and Smith, 2013), the question about the mechanisms governing the growth of the cell biomass is still open.

Experimental studies have shown a tight relationship between biomechanics and molecular-genetic processes. Such works include studies on how mechanical signals affect the cell cycle (Streichan et al., 2014), how cellular differentiation depends on the different mechanical properties of substrates (Wells, 2008; Lv et al., 2015), and how the mechanical properties of cells are involved in cancer transformation (Lekka et al., 2012). Modern experimental techniques, particularly techniques based on atomic force microscopy (Milani et al., 2011, 2013; Sugimura et al., 2016), allow for measuring the mechanical properties of the cell wall and evaluating turgor pressure in certain plant cells, which is an important factor in the internal mechano-regulation of growth processes and cell wall extension (Ali and Traas, 2016). However, experimentally studying the dynamics of mechanical parameters in individual cells in growing plant tissue is a difficult task.

Computer modeling allows the accumulated knowledge about complex spatio-temporal interactions of biomechanical and morphogenetic processes that regulate the growth and functioning of cells, tissues, organs and body to be combined

into a single conceptual scheme. Currently, cell-based models are widely used for simulating the growth of different plant organs and tissues. Examples include extensions of the cellular Potts model (Graner and Glazier, 1992; Glazier and Graner, 1993) and vertex-based model (Nagai and Honda, 2001; Merks et al., 2011; Shapiro et al., 2013). The dynamics of tissue morphology in these models is determined by the mechanics of motion of elements of cell borders (border pixels for Potts model and vertex coordinates of piecewise linear cell-cell borders for vertex-based models). In these examples, the mechanical behavior of cells is determined by setting the energy functions with respect to the “target” values of the cell volumes and boundaries. Changes of the “target” parameter may depend on time and/or state variables, which simulate cell growth. In the framework of the vertex-based models, one can describe geometric properties of the cellular structure of the tissue and the mechanical state of the cells in the tissue in terms of stretches and compressions of its volumes and boundaries. At the same time, it is impossible to explicitly express turgor and osmotic pressures in terms of the state variables of these models. Considering the importance of investigating the relationship between the mechanical properties of cells within tissues and its molecular-genetic characteristics, the development of mechanical approaches that take the internal state of the cell into account is promising for use in cell-based models of plant tissue morphodynamics.

In this paper, we propose a cell-based model for the growth of monocot leaf epidermis. The model is an extension of our previous work (Zubairova et al., 2015), which takes the difference between cell growth and division rates in different parts of the leaf growth zone into account. By taking the geometrical characteristics of tissue into account, we constructed the model state variables so that we could explicitly express turgor and osmotic pressures in the cells. This makes it possible to study the distribution of the pressures in cells of growing tissue, possible mechanisms of regulation of coordinated cellular growth, and other issues of mechanics of plant tissue growth. Using the growth of wheat leaf epidermis as an example, we showed that our model allows us to approximate the experimental cell length profile along the growth axis of the leaf (Beemster et al., 1996); at the same time, the relationship between the state variables of the model indicate significant fluctuations of pressure in the cells of the leaf growth zone. This opens up prospects for further research of the role of pressure and stress in growing cells as biomechanical regulators of molecular-genetic systems of cell morphogenesis.

The remainder of this paper is organized as follows. In Section 2 (Methods), we focus on the description of a mathematical model for the growth of wheat leaf epidermis, parameter estimation and implementation. In Section 3 (Results), we present the results of computational experiments on approximating the experimental cell length profile in a real wheat leaf and analyze the mechanical behavior of cells during symplastic growth. In Section 4 (Discussion), we discuss our simulation results with the conclusions of this work.

## 2. METHODS

### 2.1. A Mathematical Model of Symplastic Unidirectional Growth of a Linear Leaf

#### 2.1.1. Biomechanics of the Autonomous Growth of a Single Plant Cell

At present, experimental facts and theories accumulated in the literature allow us to formulate the following idea about the mechanics of plant cell growth (Equations 1–6). The concentration,  $c$ , of the dry biomass,  $m$ , in the cell changes due to the biosynthesis (growth function  $F_{grow}$ ) and by varying the cell's volume,  $V$ :

$$\frac{dc}{dt} = F_{grow} + \frac{\partial c}{\partial V} \cdot \frac{dV}{dt} \quad (1)$$

For simplicity, we assume that the cell biomass composition does not change qualitatively and that the concentration of osmolytes is proportional to the concentration of dry biomass. In particular, we can assume that this concentration is equal to  $c$ . In this case, the osmotic pressure inside the cell can be estimated from the Van't Hoff equation (Nobel, 2009):

$$P_{osm}^{in} = c R T, \quad (2)$$

where  $T$  is the absolute temperature and  $R$  is the universal gas constant.

Osmotic pressure causes the inflow of water into the cell, which simultaneously stretches the elastic cell wall. This gives rise to mechanical stress in the wall and thus to hydrostatic (turgor) pressure inside the cell:

$$\sigma_V P_{turg} = \frac{V - V_r}{V_r}, \quad (3)$$

where  $\sigma_V$  is the elastic flexibility of the cell chamber,  $V$  is the visible cell volume, and  $V_r$  is the relaxed volume of the cell chamber, i.e., the volume that will take the cell chamber bounded by the cell wall if the cell is placed into a hyperosmotic solution (in this case, the cell will lose turgor and the cell wall will cease to be in the stress-strain state).

The flow of water into the cell occurs when the difference between the osmotic pressures inside and outside the cell is greater than the turgor pressure:

$$\Psi_w = (P_{osm}^{in} - P_{osm}^{out}) - P_{turg} > 0,$$

where  $-\Psi_w$  is the water potential of the cell relative to the environment (Nobel, 2009) and  $P_{osm}^{out}$  is the osmotic pressure in the medium around the cell.

The change of the visible cell volume,  $V$ , is proportional to the water flow inside the cell:

$$\frac{dV}{dt} = S L_w \Psi_w, \quad (4)$$

where  $S$  is the cell surface area through which the water enters the cell and  $L_w$  is the hydraulic conductivity of the cell wall (Nobel,

2009). According to Ortega (2010), the relative change of the cell chamber can be represented as the sum of the irreversible changes in the volume of the cell chamber (actual growth) and its reversible elastic deformation:

$$\frac{dV}{V dt} = \phi(P_{turg} - P_c) + \sigma \frac{dP_{turg}}{dt}, \quad (5)$$

where  $\phi$  is the irreversible wall extensibility and  $P_c$  is the threshold turgor pressure.

In our model, instead of Equation (5), we introduced explicit expressions for the osmotic and turgor pressures (will be introduced below, Equations 7, 8) and postulated the following function for the cell wall growth rate. Specifically, with an increase in the turgor pressure above a certain threshold,  $P_c$  (which is different for different types of cells), the biosynthesis of the cell wall material begins (Dyson et al., 2012). This material is delivered into the wall, and it begins to grow with a rate determined by the function  $\Phi$ , dependent on the turgor pressure exceeding a certain threshold,  $P_c$ :

$$\frac{dVr}{dt} = \begin{cases} 0, & \text{if } P_{turg} \leq P_c \\ \Phi(P_{turg} - P_c), & \text{otherwise} \end{cases} \quad (6)$$

A cell of linear leaf blade epidermis is represented in the model as a parallelepiped with a volume  $V = l \cdot r_1 \cdot r_2$ . To simplify the model, we assume that the cell thickness  $r_1$  and the cell width  $r_2$  do not change during the growth process and are equal to  $r$ . Therefore, we will consider a unidirectional growth of a plant cell. This allows us to describe the mechanics of cell growth in terms of lengths as follows: visible cell length,  $l$ ; relaxed cell length (the cell wall length in the unstressed state),  $l_r$ ; and isosmotic cell length,  $l_i$ .

The isosmotic cell length,  $l_i$ , is defined as follows. As discussed above, the amount of osmolytes in the cell is equal to  $m = c \cdot V$ . Suppose that the osmotic pressure of the cell's environment is  $P_{osm}^{out}$  and that the concentration of osmolytes in the cell's environment is  $c^{out}$ . For the cell to become isotonic to the environment, the cell volume should satisfy the equality  $m = c^{out} \cdot V_i$ ; hence,  $c = c^{out} \cdot \frac{V_i}{V}$ .

In this case, the difference between osmotic pressures in and out of the cell can be expressed as follows:  $P_{osm}^{in} - P_{osm}^{out} = (c - c^{out}) R T = c^{out} R T (V_i - V)/V$ . Substituting  $V = l \cdot r^2$  and  $V_i = l_i \cdot r^2$ , we obtain

$$P_{osm} = P_{osm}^{in} - P_{osm}^{out} = \alpha \frac{l_i - l}{l}, \quad (7)$$

where  $\alpha = c^{out} R T$  is the coefficient of osmotic pressure. Note that by assuming a constant cell protoplast composition, we can write the variable  $m = c^{out} r^2 \cdot l_i$ , i.e., cell dry biomass is proportional to isosmotic length,  $l_i$ .

In the case of unidirectional growth, the turgor pressure can be expressed as follows:

$$P_{turg} = \beta \frac{l - l_r}{l_r}, \quad (8)$$

where  $\beta = \frac{S_w}{S_c} E$  is the coefficient of turgor pressure.  $S_w$  is the cross-sectional area of the cell wall, and when the cell wall thickness,  $d_w$ , is small enough,  $S_w = 4r \cdot d_w$ .  $S_c = r^2$  is the cross-sectional area of the cell across its length, and  $E$  is the Young's modulus of the cell wall material.

Suppose that water flows into the cell through the lower facet surface  $r \cdot l$ . Then, following Ortega (2010), express the growth rate of the visible cell length,  $l$ , by the following equation:

$$\frac{dl}{dt} = r \cdot l \cdot L_w \cdot (P_{osm} - P_{turg}), \quad (9)$$

or for specific growth rate:

$$\frac{dl}{l dt} = r \cdot L_w \cdot \left( \alpha \frac{li - l}{l} - \beta \frac{l - lr}{lr} \right). \quad (10)$$

Defining the function  $\Phi$  from Equation (6), we assumed that the growth rate of the relaxed cell length depends on the growth rate of the cell biomass and is identified as:

$$\frac{d lr}{dt} = \begin{cases} 0, & \text{if } P_{turg} \leq P_c \\ \eta \frac{d li}{dt} (P_{turg} - P_c)^3, & \text{otherwise,} \end{cases} \quad (11)$$

where  $\eta$  is the proportional coefficient between the cell wall and the biomass growth rates. The specific form of the regulatory function  $\Phi$  is discussed in Section 4.3.

We consider that the increase in the isolated cell dry biomass,  $m$ , under some standard conditions is described by a fixed function of time,  $m(t) = F_m(t)$ , and we will refer to it as *autonomous growth* of isolated cells. Taking the assumptions of

our model into account, we define the isosmotic cell length,  $li$ , as an explicit function of time:

$$li(t) = F_{grow}(t). \quad (12)$$

For the model of the autonomous growth of a single plant cell, we used a linear function of time for the cell isosmotic length growth,  $F_{grow}(t) = a(t - t_0) + b$ , where  $a$  is the growth rate and  $b$  is the initial cell size. The choice of a linear growth function will be explained in more detail in the Section 4. Therefore, the model of the unidirectional autonomous growth of a single plant cell is defined by Equations (10–12).

### 2.1.2. Mechanics of Symplastic Unidirectional Growth of Cells within the Leaf Epidermis

In this paper, we studied plant tissue growth based on a simplified model of wheat leaf epidermis (Figure 1A) composed of cell files consisting of similar cells. We assumed that the cells within the leaf epidermis grow in optimal conditions, its growth is described by the same time-dependent function of growth for isosmotic length as for an isolated cell, and it has the same mechanical parameters (Table 1). The only additional condition is that its walls are “glued” with walls of neighboring cells. Since neighboring cells can grow at different rates, common fragments of its walls cause additional mutual stresses within each other. Consequently, the growth rate of a cell wall fragment is actualized as being different from the free growth rates of respective cells, and hence, the growth of the cell wall can be nonuniform within the cell.

In the model, leaf epidermis is represented as a “brickwork” (Figure 1B) consisting of brick-like cells of the same type arranged in longitudinal cell files. Within each cell file, all cells have the same constant cross section and different

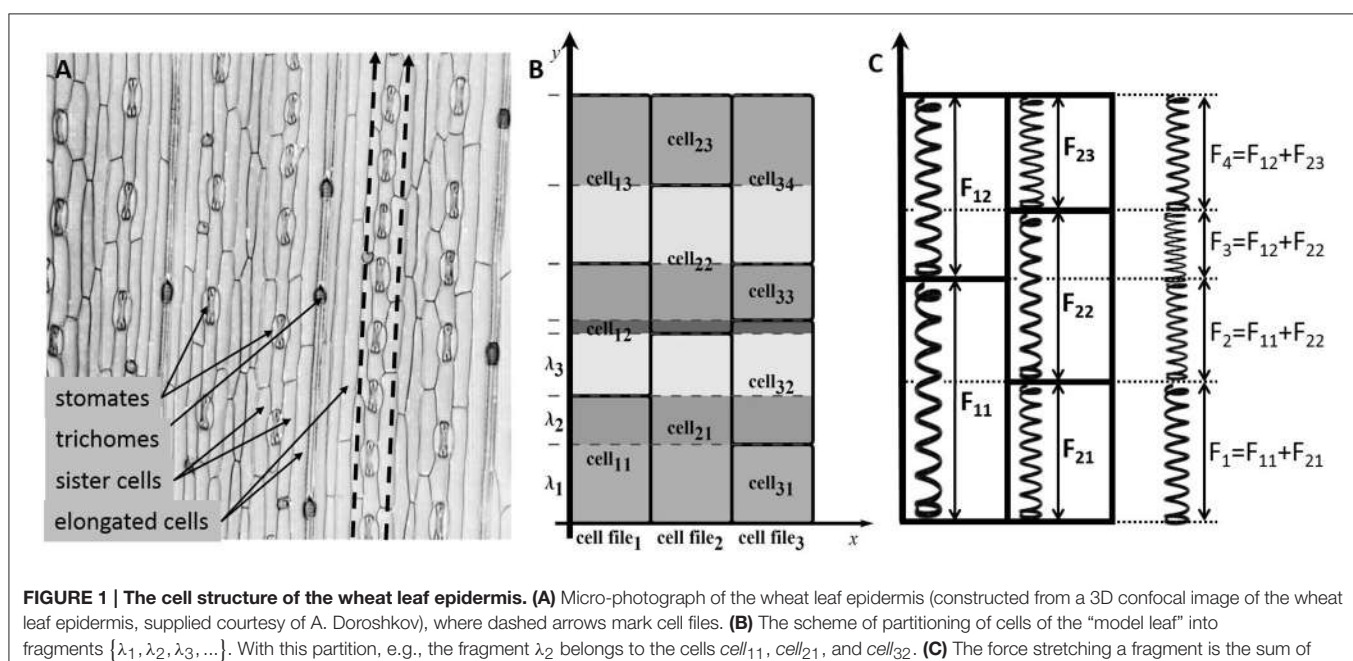


**TABLE 1 | Mechanical parameters of the model.**

Parameter	Description	Value	Sensitivity	References
$L_w$	Hydraulic conductivity of the cell wall	$40 \mu\text{m}^{-1} \cdot \text{h}^{-1} \cdot \text{bar}^{-1}$	0.00146894	Nobel, 2009
$\alpha$	Coefficient for osmotic pressure	10 bar	5.36703	Nobel, 2009
$\beta$	Coefficient for turgor pressure	100 bar	-0.000028689	Nobel, 2009; Gibson, 2012
$\eta$	Coefficient of cell wall growth rate	0.15	53.9229	Gibson, 2012
$P_c$	Threshold of turgor pressure	2 bar	-14.5014	Nobel, 2009

The symbols of the parameters are listed in the first column, a parameter description in the second column, the selected parameter value in the third column, the sensitivity of visible cell length to the parameter in the fourth column, and literature reference in the last column.

lengths (due to different growth rates of cells), and the “model leaf” has a rectangular shape in plan. Because of such a simple topology, despite the fact that we are interested in the surface of the leaf, we can consider the tissue in the model not as a two-dimensional object but as a set of one-dimensional cell chains, which are glued together. The last fact accounts for the symplastic mode of growth.

To formalize the geometric model of linear leaf epidermis, consider a rectangular compartment of rectangular cells (**Figure 1B**) in  $0xy$  coordinates. Assume that the cells grow in the  $0y$  direction. Let us mark cell files in the  $0x$  direction with index  $n$  ( $n = 1, \dots, N$ ), mark the cells in each file in the  $0y$  direction with index  $m$  ( $m = 1, \dots, M_n$ ), and designate the length of the  $m$ -th cell in the  $n$ -th file as  $l_{mn}$ . We divide each cell into fragments to take the symplastic mode of growth into account in the model. The procedure is as follows: we extend the “horizontal” border of each cell parallel to the  $0x$  axis throughout the leaf blade such that the leaf is divided into fragments in the  $0y$  direction. Index the fragments with index  $k$  ( $k = 1, \dots, K$ ) and denote the  $k$ -th fragment length as  $\lambda_k$ .

From a mechanical perspective, the fragment  $\lambda_k$  is glued fragments of different cells undergoing a force determined by the turgor pressure in the corresponding cells. Hence, the entire fragment experiences the results of all these forces (**Figure 1C**). To simplify the model, we assume that the parameters determining the mechanical behavior of the model ( $L_w, \eta, \alpha, \beta$ ) have the same values for all cells of the leaf. In this case, the next formula defines the growth rate of the common fragment for all cells contained in it.

$$\frac{d\lambda_k}{dt} = \frac{\lambda_k}{N} \sum_{n=1}^N \left( \frac{dl_{mn}}{l_{mn} dt} \right)_{\text{free}}, \quad (m : \lambda_k \in l_{mn}), \quad (13)$$

where  $l_{mn}$  is the visible length of cell  $m$  in cell file  $n$  and the expression  $\left( \frac{dl_{mn}}{l_{mn} dt} \right)_{\text{free}}$  denotes the specific growth rate of the cell visible length at the given moment if the cell would not have mechanical bonds with neighboring cells. This rate is determined by Equation (10) for the corresponding cell  $m$  in the cell file  $n$ .

The visible length of the cell,  $l_{mn}$ , within the leaf epidermis is the sum of lengths of fragments,  $\lambda_k$ , belonging to it; thus, its derivative is also equal to the sum of derivatives of fragment lengths:

$$\frac{dl_{mn}}{dt} = \sum_{\lambda_k \in l_{mn}} \frac{d\lambda_k}{dt} = \sum_{\lambda_k \in l_{mn}} \frac{\lambda_k}{N} \sum_{n=1}^N \left( \frac{dl_{mn}}{l_{mn} dt} \right)_{\text{free}} \quad (14)$$

In our model, we assume autonomous growth of the cell within the leaf epidermis; therefore, the isosmotic cell length,  $l_{mn}$ , and the relaxed cell length,  $l_{mn}$ , are regulated by each cell in the same way as for an isolated cell. The growth of the isosmotic cell length,  $l_{mn}$ , is defined by an explicit function of time and by the following initial data: the moment of time,  $t_0$ , when the cell appeared with its initial isosmotic length,  $l_{mn}^0$ .

### 2.1.3. Longitudinal Zonation Pattern of the Leaf Growth Zone

Longitudinal growth of wheat leaf occurs in a growth zone, which is a relatively short part of the leaf located at its base. The growth zone consists of a division zone (DZ), or meristem, and elongation zone (EZ) (Beemster et al., 1996). Note that the length of the meristem (DZ) is significantly smaller than the length of the elongation zone. Due to permanent division of cells in the DZ, the average length of a cell in the DZ is almost identical in space and time. With the transition into the EZ, cell proliferation stops and cells begin to stretch rapidly in the longitudinal direction. At the end of the EZ, the stretching stops. The described cell behavior is supported by the experimental measurements of cell lengths in wheat leaf (Beemster et al., 1996; Tardieu et al., 2000; Hu and Schmidhalter, 2008).

In our model of the linear leaf blade growth, we assume a stationary longitudinal zonation pattern of the leaf: a division zone (DZ) and an elongation zone (EZ). Our assumption of the stationary location of the two zones with respect to the leaf base is based on the model of switching between two zones due to morphogenetic mechanisms. For instance, such a model was used in the work of Vos et al. (2014) in the simulation of *Arabidopsis thaliana* root growth. Similar molecular mechanisms were used for justifying the stable location of the growth zone size in the shoot apical meristem of *A. thaliana* in our earlier work (Nikolaev et al., 2011). Here, we assumed that there exists some morphogen synthesized at the leaf base and propagated to the leaf tip with the constant gradient concentration providing the stable zonation pattern during leaf growth.

### 2.1.4. Division of Cells in the Division Zone

The cell in the division zone divides when its isosmotic length,  $l_{mn}$ , reaches a critical value,  $l_{max}$ . The division of the cell is described by rewriting of the cell parameters in the following way: (1) isosmotic, visible, and relaxed lengths of the mother cell are distributed between two daughter cells with the proportion of  $d/(1-d)$ , where  $d$  is the division factor; (2) the initial isosmotic lengths,  $l_{0i}$ , of daughter cells are  $d \cdot l_{max}$  and  $(1-d) l_{max}$ ; and (3) the birth time,  $t_0$ , of two daughter cells is set to  $t$ , the time of mother cell division. The division factor,  $d$ , is a random variable with the truncated normal distribution from the interval (0.1, 0.9) with mean  $\mu_d = 0.5$  and standard deviation  $\sigma_d = 0.1$ . These parameters for the division factor distribution are typical for the simulations of plant tissue growth (see, for example, Chickarmane et al., 2012).

## 2.2. Parameter Estimation and Sensitivity Analysis

### 2.2.1. Mechanical Parameters

All the parameters determining the mechanics of the cell were obtained using literature data and adopted to provide a cell cycle duration of 24.7 h (Beemster et al., 1996). The value of the hydraulic conductivity of the cell wall,  $L_w$ , was set to  $40 \mu\text{m} \cdot \text{h}^{-1} \cdot \text{bar}^{-1}$ . This estimate is within the range proposed by Nobel (2009) for  $L_w$  ( $10^{-13}$  to  $2 \cdot 10^{-12} \text{ m} \cdot \text{s}^{-1} \cdot \text{Pa}^{-1}$ , i.e.,  $36$ – $720 \mu\text{m} \cdot \text{h}^{-1} \cdot \text{bar}^{-1}$  in the units used here). Other authors suggest similar values for this parameter (Hukin et al., 2002; Mishra, 2004).

To estimate the coefficient for osmotic pressure from Equation (7),  $\alpha$ , we used equation  $\alpha = c^{out} R T$ , where  $R = 8.31446 \text{ J mol}^{-1} \text{ K}^{-1}$  is the gas constant and  $T = 300 \text{ K}$  is the temperature in Kelvin. We used  $c^{out} = 0.25 \text{ M}$ , which is close to the estimate of cell sap osmolarity as  $0.3 \text{ M}$  (Nobel, 2009), yielding  $\alpha = 10 \text{ bar}$ .

Estimates of the cell wall Young's modulus,  $E$ , from the literature vary from  $\approx 1$  to  $10,000 \text{ bar}$  (Krupinski et al., 2016); in our simulations, we used  $E = 1000 \text{ bar}$ . To estimate the coefficient for turgor pressure from Equation (8),  $\beta$ , we used equation  $\beta = \frac{S_w}{S_c} E = \frac{4r \cdot d_w}{r^2} E$ , assuming  $r = 4 \mu\text{m}$  and  $d_w = 0.1 \mu\text{m}$ . This yields  $\beta = 100 \text{ bar}$ .

The threshold of turgor pressure when the cell begins to grow,  $P_c = 2 \text{ bar}$ , is close to the values widely discussed in the literature as the "wall yield threshold" (Nobel, 2009; Dyson et al., 2012).

We have not found any estimates of the coefficient of the cell wall growth parameter,  $\eta$ , in wheat leaves in the literature. Therefore, we conducted a numerical experiment to obtain its estimate with a single cell model (see Equations 10–12). We changed the value of  $\eta$  in the range of (0, 1) and estimated the turgor and osmotic pressures in the cell during the cell cycle. The value of  $\eta = 0.15$  yielded the minimal absolute deviation of these two pressures and was chosen as the reasonable  $\eta$  estimate. We summarize the parameter values in Table 1.

To estimate the sensitivity of the cell visible length with respect to the mechanical parameters of the model, we simulated single cell growth during 24 h using Equations (10–12) with varied parameters at each run. The changes of parameters were within 10% of their estimated values with a

constant step. The sensitivity was estimated as the ratio of the visible length deviation to the deviation of the parameter value.

### 2.2.2. Kinetic Parameters

The model parameters defining the cell growth rate were obtained using experimental data on the cell length profile in a wheat leaf from Beemster et al. (1996). Beemster et al. (1996) reported the lengths of all cells along a file of sister cells (file adjacent to stomatal cell files) within wheat leaf epidermis. In their work, data were presented as follows: the individual lengths of successive cells were averaged over 0.5, 1.0, and 2.0 mm intervals in the basal part of the leaf; the next more distal; and the remaining, most distal part of the growth zone, average cell lengths in each zone, and average cell cycle for one of the leaves are summarized in Table 2.

According to our model, all cells have uniform growth rates, and individual initial sizes determine different cell cycle durations. We suppose that a cell changes its growth rate once it reaches the critical value,  $l_{max}$ , and it results in a piecewise-linear function for isosmotic length changes during cell growth (Figure 3 inset):

$$l_{mn}(t) = \begin{cases} a_1(t - t_{0mn}) + l_{mn}(t_{0mn}), & \text{if } t_{0mn} \leq t < t_{0mn} + t_{divmn} \\ a_2(t - t_{0mn} - t_{divmn}) + l_{max}, & \text{if } t_{0mn} + t_{divmn} \leq t < t_{0mn} + t_{divmn} + t_{elongmn} \end{cases} \quad (15)$$

where the coefficients  $a_1$  and  $a_2$  are the growth rates of the cells in DZ and EZ, respectively;  $t_{0mn}$  is the time point when the cell appeared;  $t_{0mn} + t_{divmn}$  is the time point when the cell isosmotic length achieves the critical value; and  $t_{0mn} + t_{divmn} + t_{elongmn}$  is the time point when the cell exited the EZ.

The critical point of the estimation is next. The experimental data are the distribution of the average visible cell lengths along the cell file (see Table 2), whereas we need to estimate the

**TABLE 2 | Experimental data on the growth of the wheat leaf from the work of Beemster et al. (1996), which were used for obtaining the model parameters.**

Parameter	Value
The average length of the growth zone (GZ), mm	23.8
The average length of the division zone (DZ), mm	3.3
The average length of the elongation zone (EZ), mm	20.5
$\hat{t}_{div}$ , the average cell cycle duration (for a cell from the division zone), hour	24.7
$\hat{t}_{elong}$ , the average elongation period (for a cell from the elongation zone), hour	71.09
$\hat{l}_0$ , the visible average initial cell length in the division zone, $\mu\text{m}$	14.74
$\hat{l}_{div}$ , the visible average final cell length in the division zone, $\mu\text{m}$	29.48
$\hat{l}_{elong}$ , the visible average final cell length in the elongation zone, $\mu\text{m}$	197.2

dynamics of the “internal” variable, the isosmotic length growth function. The experimental data provide values of the average cell cycle duration,  $\hat{t}_{div}$ ; the average elongation period,  $\hat{t}_{elong}$ ; and values of average visible length at these moments.

The coefficients  $a_1$  and  $a_2$  were obtained numerically. They are chosen to obtain the best fit between the cell length distributions in the model and real wheat leaf epidermis (Beemster et al., 1996). The cost function is based on the squared difference of the average length of the cells in the model,  $\bar{l}_{model}$ , and real leaf,  $\bar{l}_{exp}$ , within the  $i$ th interval of distance from the leaf base weighted with the scaling factor  $k_i$ :

$$F_{cost} = \sum_{i \in intervals} k_i \cdot (\bar{l}_{model} - \bar{l}_{exp})^2. \quad (16)$$

where the scaling factors,  $k_i$ , are proportional to the interval number and provide greater weight to the intervals for greater distances from the base. This weighting is introduced to balance the cost contribution from the large number of small cells in the DZ and small number of large cells at the distal part of the EZ.

The search for the  $a_1$  and  $a_2$  estimates starts from the initial values. These values were obtained by numerically solving Equations (10–12) using Mathematica software to obtain the solutions of the inverse problem for the model of a single cell growth, providing that the visible cell length at the time moments  $\hat{t}_{div}$  and  $\hat{t}_{elong}$  are equal to its experimental estimate of  $\hat{t}_{div}$  and  $\hat{t}_{elong}$  (**Table 2**). Next, we simulated the epidermis growth until its length becomes equal to that of the wheat leaf (**Table 2**). The iterative search of the minimum of the cost function Equation (16) was performed numerically by the grid enumeration of the  $a_1$  parameter with subsequent adjustment of the  $a_2$  using the golden ratio method under fixed  $a_1$ . Consequently, we obtained  $a_1 = 0.69 \mu\text{m} \cdot \text{h}^{-1}$  and  $a_2 = 5.04 \mu\text{m} \cdot \text{h}^{-1}$ .

### 2.3. Model Implementation

The computational model for the growth of wheat leaf epidermis was developed using a modified formalism of differential L-systems (DL-systems) (Lindenmayer, 1968; Prusinkiewicz et al., 1993), which we termed “glued” DL-systems. Implementation details are provided in Zubairova et al. (2015).

Briefly, the model consists of two types of DL-systems: cellular and fragmental. The first type describes the growth and division of the cells and is represented by several 1D DL-systems. Each 1D DL-system corresponds to the cell file of the 2D linear leaf blade (**Figure 1B**).  $N$  cellular DL-systems provide the cellular structure of a linear leaf blade consisting of  $N$  parallel files that cannot slide with respect to its neighbors (i.e., “glued”). The alphabet of the cellular DL-system consists of tree symbols corresponding to the cells from three zones: DZ, TZ, and EZ. Each symbol is supported by the following parameters: isosmotic length,  $l_i$ ; visible length,  $l$ ; relaxed length,  $l_r$ ; initial isosmotic length,  $l_{i0}$ ; and initial time,  $t_0$ .

The alphabet of the fragmental DL-system consists of one symbol, the cell fragment (**Figure 1B**). Its parameters are the fragment length,  $\lambda$ , and the matching vector of the fragment and cells numbers in each cell file sharing this fragment.

The dynamics of the parameters  $l_i$ ,  $l$ ,  $l_r$ , and  $\lambda$  for the corresponding cells and fragments are determined by Equations (11–14). The rewriting rules are common for cellular and fragmental DL-systems, and they come into action at the moment of division of any cell from the DZ. Thus, an additional fragmental DL-system coordinates the operation of cellular DL-systems supporting the symplastic growth of the leaf blade.

This formalism of the “glued” DL-systems results in a quasi-one-dimensional representation of the leaf blade tissue and allows one to simulate efficiently the growth of the real size leaves (see **Table 2**). It can handle the cell numbers comparable with that of the real leaf.

The computational model was implemented in an in-house-developed open source software including the implementation of algorithms in C ++ and Wolfram languages (Mathematica). The source code is available upon request.

### 2.4. Statistical Data Analysis

Descriptive statistical analysis and data visualization were performed using Mathematica 10 package. Additionally, we performed cluster analysis of the pressure profiles for the cells during the leaf growth simulation. The pressure profile is a vector of pressure values recorded for the cell from its birth until its division or until simulation stops. The size of the vector is equal to 150, which is double the maximal observed cell lifespan (75 h) during the simulation. A single element corresponds to a 1 h time interval. The first 75 numbers in the vector represent osmotic pressure values; the others represent the turgor pressure values. All the vector elements corresponding to time steps after cell division were set to 0. To determine groups of cells with similar pressure profiles, we used k-mean clustering using the Clustering Components function from the Mathematica 10 package. Clustering was applied to the set of pressure profiles using a distance function based on the number of point changes needed to go from one curve to another. The number of clusters was set to 10.

## 3. RESULTS

### 3.1. The Parameters of the Model and Its Robustness

We proposed a cell-based model for the growth of linear leaf epidermis, which is based on the explicit expression of turgor and osmotic pressures during cell growth. The model depends on the number of parameters that describe the mechanical and kinetic properties of the cells during their autonomous and symplastic growth (summarized in **Table 1**). Note that the values of the mechanical parameters of the model result in a quasi-equilibrium cell growth regime of the isolated cell when the values of turgor and osmotic pressures are practically the same and constant ( $\approx 3.6$  bar) over the cell cycle (see **Figure 2**). We performed numerical experiments to investigate the sensitivity of the visible length of an isolated growing cell just before its division. The sensitivity was studied in terms of the variation of the mechanical parameters as described in Section 2.2.1 of the Methods Section.

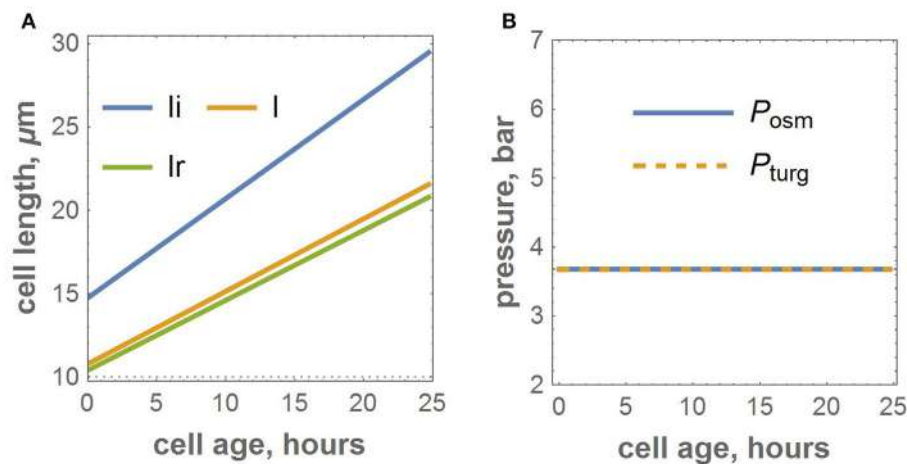


**FIGURE 2 | Numerical experiment for the growth of the isolated cell with the adopted parameters. (A)** Growth functions for isosmotic, visible, and relaxed lengths. **(B)** The dynamics of osmotic and turgor pressures.

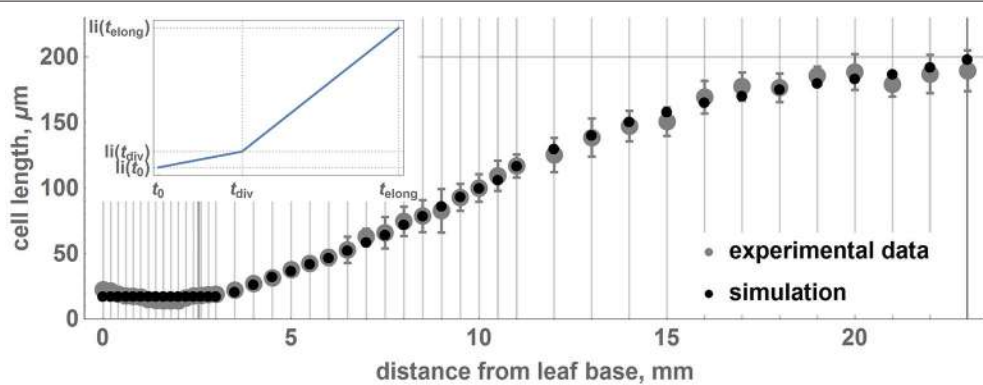


**FIGURE 3 | Relationship between average lengths of cells and distance from the leaf base: comparison between experimental data and the model.**

Points correspond to the average lengths of the cells on intervals designated by gray vertical lines. Gray points denote experimental data, and black points denote the results of the simulation with the obtained optimal parameters. The error bars denote the standard errors of the mean. The experimental points and standard errors were obtained by manual digitizing of data on leaf 1 from Beemster et al. (1996). The inset shows a piecewise linear growth function for the isosmotic length of the cell.

The results demonstrated that the sensitivity of this final cell length to all mechanical parameters decreases with increasing absolute values of the last. The largest sensitivity of the cell visible length was with respect to variation of the coefficient of cell wall growth rate,  $\eta$ . The smallest sensitivity was observed with respect to the variation of the coefficient for turgor pressure,  $\beta$  (see Table 1).

The parameters of the piecewise linear cell biomass growth function,  $a_1$  and  $a_2$  (see Equation 15), were estimated by the cell size fitting to the real data, as described in the Section 2. The estimates correspond to the minimum value of the cost function equal to  $10^{-3}$ . Figure 3 demonstrates that the two distributions coincide well, suggesting the applicability of our model to reproduce the geometric characteristics of the wheat leaf cells in the growth zone.

Stochastic cell division in the meristematic zone and cell growth mode switching affect the average cell size and its

variations over the intervals located at different distances from the leaf base. We performed 100 simulations of wheat leaf growth to estimate the influence of the fluctuation resulting from stochastic nature of the cell division  $d$  parameter on the cell length distribution along the leaf axis. Each model leaf consisted of 100 cell files with the length of the growth zone equal to that of the real leaf (Table 2). In this way, we generated 100 distributions of the cell length along the model leaf axis. We estimated the mean and the standard deviation of the cell length for each interval from the leaf base using these data. The distribution of the cell length along the axis and their standard deviations in the simulation replicates and real wheat leaf are shown in Figure 3. The figure demonstrates that the two profiles coincide well and that the model is robust with respect to stochastic fluctuations in cell division. These results suggest the applicability of our model to reproduce the geometric characteristics of the wheat leaf cells in the growth zone.

### 3.2. Mechanical Behavior of Cells during Symplastic Growth

#### 3.2.1. Increased Values of Cells Osmotic and Turgor Pressures are Characteristics of Transition Zone

In addition to reproducing the geometrical features of the growing leaf, our model is also able to calculate turgor and osmotic pressures for each cell (Equations 7, 8). During the simulation of the leaf growth, we collected information about the turgor and osmotic pressures of the cells and obtained profiles of these pressure averages for the cells at different intervals of distance from the leaf base. To estimate the variability of the pressures within the distance interval, we calculated the standard deviation of the mean for them. The profiles of the osmotic and turgor pressures along the model leaf axis are shown in **Figures 4A,B**, respectively. These plots demonstrate that in the DZ (distance from the leaf base below 3.3 mm), the average values of the osmotic and turgor pressures are constant with respect to the distance from the leaf base and is  $\approx 4$  bar (close to the value obtained for the isolated cell simulation, see **Figure 2**). At the larger distance from the base, both average pressures increase,

reaching a maximum at 7 mm ( $\approx 6$  bar for osmotic pressure and 8 bar for turgor pressure). With increasing distance from the base above 7 mm, both osmotic and turgor pressures drop to the equilibrated values ( $\approx 4$  bar) at  $\approx 12.5$  and 15 mm from the base for osmotic and turgor pressures, respectively. The pattern of pressure changes corresponds well with the leaf zonation pattern used in our model, namely, constant pressures close to the equilibrium values are observed for DZ and EZ regions; increased pressures are observed for the cells in the TZ.

The pressure variation behavior is similar to the average pressure values. It is constant at distances below 4 mm for both types of pressure. It increases at the interval from 4 to 7 mm and then decreases within the 7–15 mm interval. Interestingly, the absolute values of the turgor pressures are higher, and its variations are lower than those for the osmotic pressures (**Figures 4A,B**). Some of the cells exhibit extreme values of the turgor pressure, above 40 bar.

The pattern of the pressure values and their variations observed at the profiles (**Figures 4A,B**) are apparent from the distribution of cell pressure values in the epidermis plane

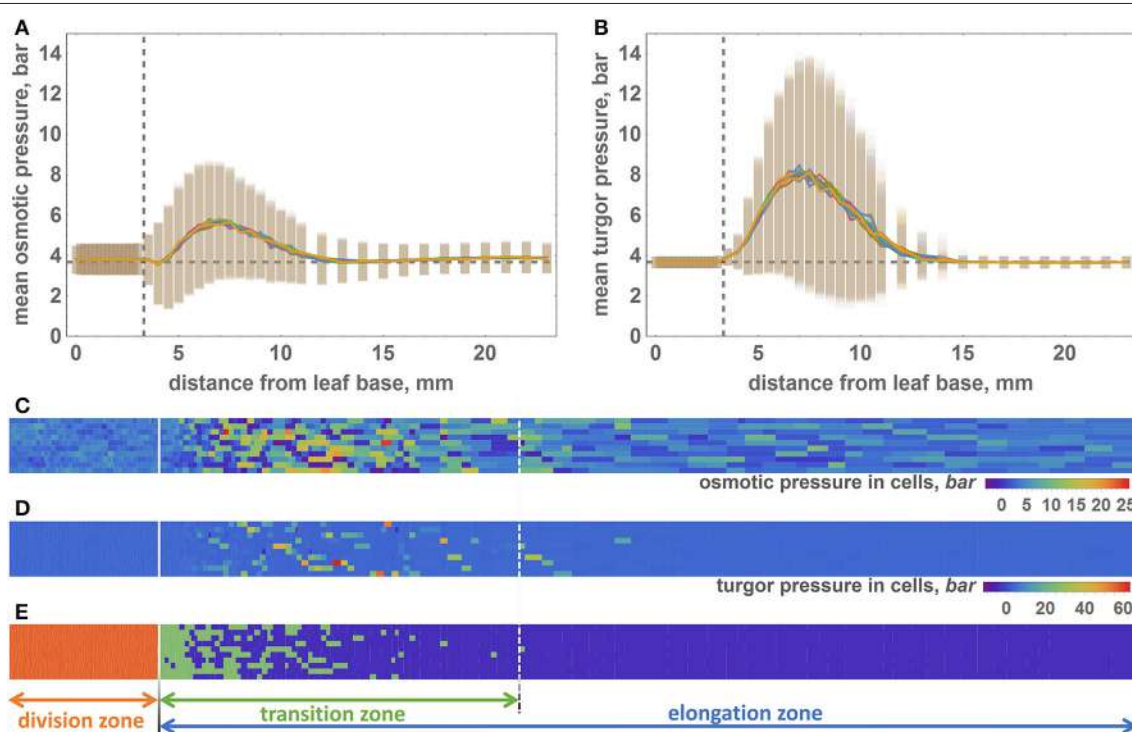


**FIGURE 4 |** The distribution of the osmotic and turgor pressures in cells along the model leaf axis. **(A)** Mean values (lines) and standard deviations (vertical bars) of the osmotic pressure (Y axis) in cells with respect to their distance from the leaf base (X axis). Vertical dashed line shows the border between the division and transition zones. Horizontal dashed line shows the equilibrium value of the osmotic pressure. **(B)** The mean values (lines) and standard deviations (vertical bars) of the turgor pressure (Y axis) in cells with respect to their distance from the leaf base (X axis). Graph notations are the same as in **(A)**. **(C)** 2D diagram of the osmotic pressure values for the epidermal cells at the time when the simulation stops. Cells represented by the rectangles, whose sizes are proportional to the cell sizes. The osmotic pressure of the cell shown by rectangle color. The color key is shown at the right bottom part of the diagram. Solid white line is the border between the DZ and TZ regions. Dashed white line is the distal border of the TZ. **(D)** 2D diagram of the turgor pressure values for the epidermal cells at the time when the simulation stops. The description of the diagram is the same as for **(C)**. **(E)** Location of cells of different types in the model leaf epidermis. The cells of different types colored by different colors: red for the DZ cells, green for the TZ cells, and violet for the EZ cells. The division of the leaf into three zones is shown by solid and dashed white lines on the diagram and by arrows below the diagram.

demonstrated in the 2D color diagrams in **Figures 4C,D** for the osmotic and turgor pressures, respectively. The zonation pattern of the high/low pressure values coincides spatially with the prevalence of the different cell types in the leaf plane (**Figure 4E**). DZ-type cells are mainly located at distances below 3.3 mm from the base, and TZ cells are located at 4–15 mm from the base. However, note that the location of the distal border of the TZ is not permanent as for the single and for different simulation runs. The majority of the EZ cells are located at distances >15 mm from the base.

### 3.2.2. Temporal Patterns of the Cell Pressure Changes during Symplastic Growth

During the leaf growth simulation, we recorded the osmotic and turgor pressure values of each cell that appeared ( $\approx 43,000$  cells in 100 cell files in total), as described in Section 2.4 of Methods. We performed cluster analysis of these profiles to reveal groups of cells with similar pressure changes during their symplastic growth. Consequently, we obtained 10 clusters of cells, for which osmotic and turgor pressure, isosmotic cell length (biomass) and visible cell length changes are shown in **Figures 5A–D**, respectively. We observed separation of all cells into groups with short (clusters 1–4), medium (clusters 5–6), and long (clusters 7–10) lifespans. Cells from the first group exhibit a short time before their division and a constant osmotic pressure during their

lifespan. These four clusters differ in turgor pressure/biomass changes. Clusters 1, 3, and 4 exhibit constant values of the turgor pressure for most of the cells. Cells from these clusters mostly reside in the DZ (**Figure 5E**). Cells from cluster 2 present an increase in both visible size and biomass (**Figures 5C,D**) at the end of their lifespan. These cells appear in the DZ a short time before the simulation finishes and are likely to enter the TZ soon after their appearance.

The cells from the second group of clusters with a medium lifespan exhibit two distinct types of behavior (**Figures 5A–D**). One part of them (cluster 5) exhibit relatively constant values of the osmotic pressure and an increase in the turgor pressure during their growth. In contrast, cells from cluster 6 present a significant increase in the osmotic pressure; however, the majority of these cells are characterized by a constant turgor pressure. The size and biomass changes (**Figure 5C**) for the cells from this group appear to be very similar: they start to increase after a short initial period of constancy. The rate of visible cell length increase is larger for the cluster 5 cells, however (**Figure 5D**). These cells are mostly located in the TZ with a slight abundance in the EZ zone (**Figure 5E**) when the simulation stops.

Long-living cells present the largest variability in pressure changes. However, there are several typical profiles represented by clusters 7, 8, 9, and 10. Interestingly, the pressure changes in cells of clusters 7 and 8 are similar to those in clusters

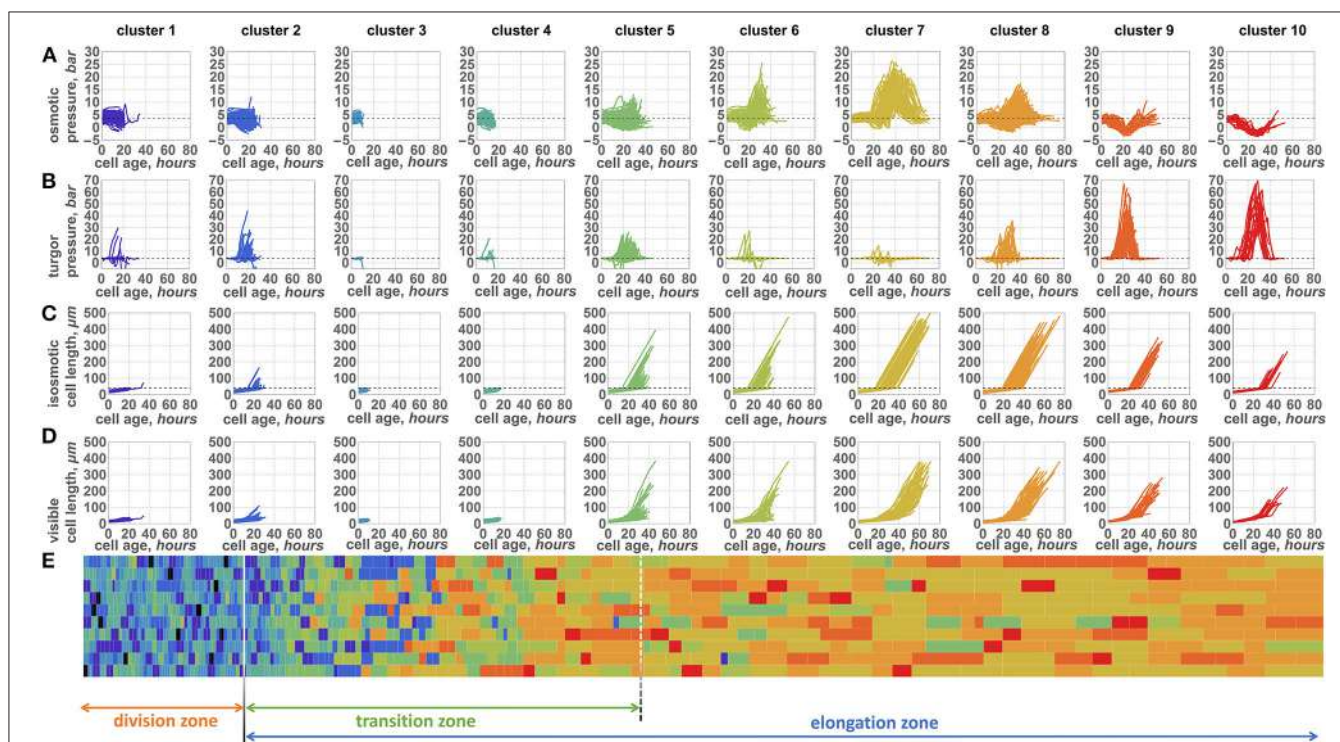


**FIGURE 5 |** Ten patterns of changes of internal parameters of the cells during symplastic growth. Plots of osmotic pressure (**A**), turgor pressure (**B**), isosmotic cell length (biomass) (**C**), and visible length (**D**) (Y axis) with respect to the cell growing time (X axes, hours) are shown. Plot columns represent parameter changes for the cells from the representative clusters 1–10 (cluster numbers shown above the plot columns). Each cluster plot has a specific color. (**E**) 2D diagram of the epidermal cells at the time when the simulation stops. Cells are represented by the rectangles, whose sizes proportional to the cell sizes. The type of the cell (cluster to which cell belongs to) is shown by the same color as the cluster plot (see **A–D**). The division of the leaf into zones is shown by arrows below the diagram.

5 and 6, respectively. The characteristics of cluster 7 are a high peak observed for the osmotic pressure with a slight variation in turgor pressure. During its growth time, the cell has passed into the elongation mode; however, some of its neighboring cells have not yet passed this mode. Therefore, the visible length of the cell increased more slowly (**Figure 5D**) than would be expected for the freely growing cell. In contrast, its isosmotic length (biomass) increases permanently (**Figure 5C**). This discrepancy between visible cell length and its biomass according to Equation (7) resulted in the sharp increase of the osmotic pressure demonstrated by the peak described above. The cluster 8 cells have a lower osmotic pressure peak but a larger variation of the turgor pressure. The cells from clusters 7 and 8 at the end of the simulation are mostly located in the EZ.

Finally, cells from clusters 9 and 10 exhibit similar behavior. They do not show any significant increase in the osmotic pressure. In contrast, a small decrease in the osmotic pressure is a characteristic of these two clusters: it is shorter in cluster 9 and longer in cluster 10. At the same time, these cells undergo a sharp increase in the turgor pressure, which is the most pronounced among the clusters. The cells from these two clusters are located far from the leaf base when the simulation stops, mostly in the elongation zone. These cells likely appear at the distal part of the division zone. They have a lower biomass growth rate at the time of their appearance (**Figure 5C**), while the cells from neighboring files entered the fast growth mode. Consequently, the cells from clusters 9 and 10 undergo stretch tension in the TZ, which results in a decrease in the osmotic pressure and an increase in the turgor pressure.

The cluster analysis demonstrates that changes of the cells pressure parameters in the growing symplastic tissues are not uniform within the cell lifespan. There are several typical patterns of the pressure changes, unlike in the independent cell growth (see **Figure 2** for comparison). The pattern of the pressure depends specifically (and stochastically) on the cell location, the initial state of the cell parameters, and the behavior of the neighboring cells. Another distinctive feature of the model is the negative relationship between turgor and osmotic pressures (for comparison, see clusters 6–10), which is the intrinsic model property due to Equations (7, 8).

## 4. DISCUSSION

### 4.1. Quasi-One-Dimensional Model of a Unidirectional Growth of Plant Tissue

Experience in the use of vertex-based models for simulating unidirectional growing tissue shows that for the generation of longitudinal rows of cells, which is in particular typical for a linear leaf, an additional constraint on the possible movement of vertices should be introduced. For example, in the model of Vos et al. (2014), vertices are constrained to move only parallel to the longitudinal axis of the root. This allows for the anisotropic elastic-plastic properties of the cell-wall material to be taken into account. In our model, anisotropy in the 2D cell pattern arises due to its quasi-one-dimensional representation (see Section 2.3 of Methods) and does not require additional constraints on the

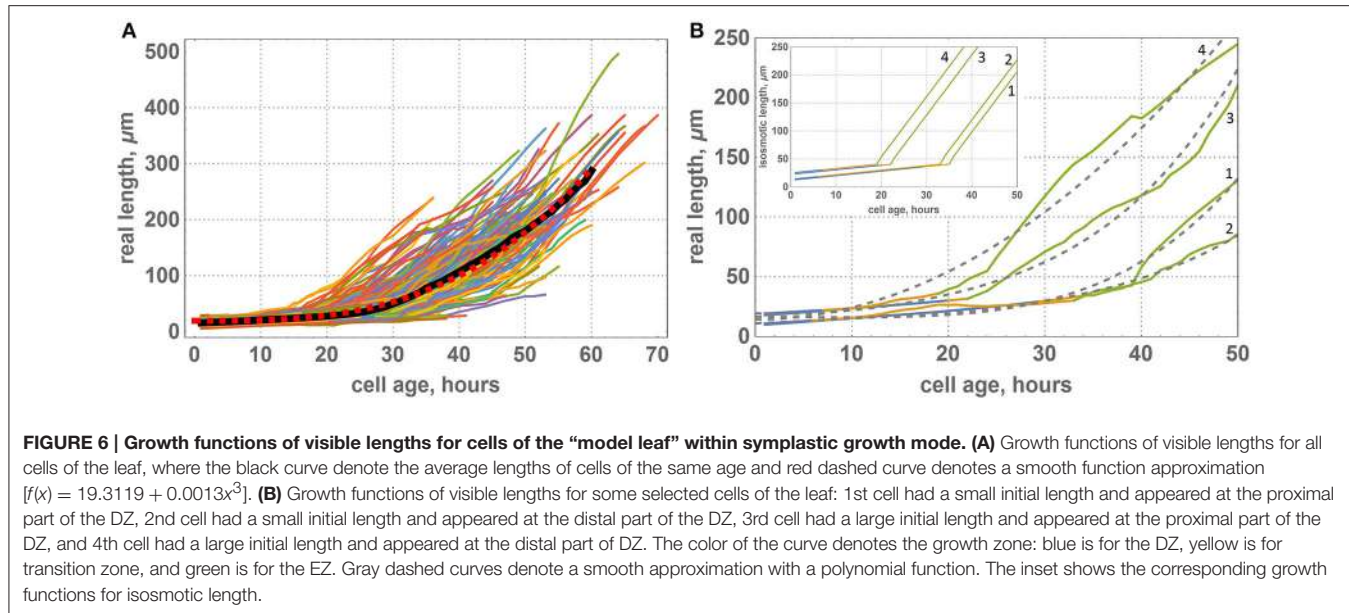
movement of vertices. We model cells rather than cell walls in the formalism of “glued” DL-systems (Zubairova et al., 2015). In this framework, the cells segments are stacked into the cell files and neighboring cell files are glued into the leaf blade. In our model, the boundaries of the stacked fragment are analogs of the vertices of cells in the vertex-based model. We store the information about the correspondence of fragments and cells to the cell fragments as a one-dimensional object (fragmental DL-system). Such a one-dimensional representation can be interpreted such that the absolute shear rigidity of the cell-wall material prevents skew deformation of the cells.

### 4.2. On Cell Growth Function

Note that in the model, we considered the growth of the cell biomass as the only “driving force” for the increase in the osmolytes concentration in the cell. This justifies the introduction of isosmotic cell length,  $l_i$ , as a model variable. Therefore, we did not consider the law of biomass conservation in our model. However, considering here the autonomous growth of cells within a tissue, we described this as function of isosmotic length (the equivalent of dry cell biomass in our model) depending on the time.

In the model, we propose a piecewise-linear function of the isosmotic cell length growth. Vos et al. (2014) also considered such a growth function (for the cell target volume) as one of the options in the vertex-based simulation of *Arabidopsis* root growth. At the same time, in a number of studies (Barlow, 1969; van der Weele et al., 2003) based on experimental data on cell length profiles along the growth axis of the *Arabidopsis* root, the authors suggested a smooth non-linear growth function for the cell length. Hu and Schmidhalter (2008) also suggested a smooth dependence of the cell length on the time using the data on the distribution of visible lengths of cells along the wheat leaf growth zone. Note that in the above papers, the authors measured the visible cell length,  $l$ , in terms of our model, and did not consider the difference between “internal” and visible sizes.

In our simulations, we set a piecewise-linear growth function of the isosmotic cell length (inset in **Figure 6B**); however, the results of our computational experiments showed a smooth non-linear function for the visible cell growth functions (**Figure 6A**). We suppose that smoothing occurs due to the fact that under the terms of symplastic growth, cells expand and contract each other due to the different growth rates of neighboring cells. As shown in **Figure 6B**, the growth functions and smooth non-linear approximations are different for various cells and depend on the cells neighborhood. **Figure 6** shows growth functions for four cells, which had different initial lengths (the 1st and the 2nd cells had a small initial length, and the 3rd and the 4th cells had a larger one) and grew under different mechanical conditions. According to our model, cells underwent the largest mechanical stress from neighbors in the transition zone between the DZ and EZ (marked in yellow on the growth curves in **Figure 6B**). The distance from the base for the cell at the time of its appearance in the DZ strongly determines the time that this cell will spend in a TZ. For example, the 1st and the 3rd cells (**Figure 6B**) appeared in the proximal part of the DZ and passed the transition zone relatively quickly. The rate of their growth is greater than the average for



the neighboring cells. Consequently, these cells are “compressed” by neighbors. This behavior is typical for the cells from clusters 6 and 7 (**Figure 5**). The 2nd and the 4th cells (**Figure 6B**) appeared in the distal part of the DZ and passed the transition zone slowly. Therefore, they grew with a lower rate in comparison with the neighbors. Hence, these cells were “stretched” by them. This behavior is typical for cells from clusters 9 and 10 (**Figure 5**).

Thus, the problem of interpreting the data on cell growth rate in the tissue requires careful consideration. The growth functions of visible lengths may also vary from cell to cell because the cells in the tissue are in the stress-strain state, which may vary depending on the environment and time. In this view, the cell typical dynamics is the time dependence of the ratio of molecular genetic markers (Sablowski and Dornelas, 2014), dry biomass dynamics, or, as in our model, the isosmotic cell length. Therefore, the question arises of which cell characteristics should be assessed in experimental observations to characterize cell growth regulation in the tissue.

#### 4.3. The Growth Function for Relaxed Cell Length and Quasi-Equilibrium Cell Growth Mode

The regulation of the synthesis of the cell-wall material is still the subject of study (Carpita and Gibeaut, 1993; Braybrook and Jönsson, 2016; Chen et al., 2016; Wang et al., 2016; Zhang et al., 2016). In this study, we proposed that the growth rate of the relaxed length is proportional to the growth rate of the isosmotic length (we can interpret  $dli/dt$  as the growth rate of dry biomass). The control function (term  $(P_{turg} - P_c)^3$  in Equation 11) determines that the threshold value of turgor pressure is the target control parameter. The 3rd power of the pressure difference in Equation (11) along with the mechanical parameter values (**Table 1**) result in a rapid growth

of the cell wall in our model. Consequently, the autonomous growth of a single cell occurs at a steady turgor pressure. These parameter values provide mechanical equilibrium when the turgor pressure is equal to the osmotic pressure in the case of isolated cells (**Figure 2**). This mode of cell growth in tissue was chosen because in the framework of vertex-based models (Nagai and Honda, 2001; Dupuy et al., 2008; Merks et al., 2011), and the computational algorithm assumes that equilibrium is achieved at each iteration step. In particular, Vos et al. (2014) used such an algorithm for modeling root growth based on the dynamics of vertices with additional constraints on its movements.

#### 4.4. The Transition between Division and Elongation Zones

Despite the simplicity of the growth zone structure for unidirectional (linear) growing plant organs (roots, hypocotyl, and leaves of monocots), there are several hypotheses about possible mechanisms for the formation of its structure (Baluska et al., 1996; Verbelen et al., 2006; Benková and Hejátko, 2009; Baluška et al., 2010; Cederholm et al., 2012; Ivanov and Dubrovský, 2013; Avramova et al., 2015). The influence of the auxin concentrations on the relative growth rate in different growth zones of the root was investigated in Chavarría-Krauser et al. (2005). The authors constructed a 1D biophysical model of auxin-related control for a single cell file. Some mechanisms of cell transition between the DZ and EZ were tested for the root growth model in Vos et al. (2014). The authors of this paper concluded that the formation of the zone size is influenced by phytohormone concentrations.

In experimental work on the maize leaf (Nelissen et al., 2012), the authors also showed that the concentrations of phytohormones may define a transition between division and elongation zones. In our model, we also assumed that gradients of morphogen substance execute patterning of the leaf growth zone

in a concentration-dependent manner and accepted a threshold mechanism of cell transition from a state of proliferation to accelerated growth while the cell size may increase tenfold. The growth and division of cells located before the cell in the same longitudinal row and the cell's own growth result in movement of the cell in the direction from the leaf base to the tip. When a cell is shifted at a certain distance from the leaf base, the concentration of morphogen substance decreases and the cell loses its ability to divide and enters the so-called transition zone, where it continues to grow with the same (slow) rate until its initial size reaches the threshold length. Subsequently, the cell turns itself into a state of expansion growth, when it begins a rapid increase in size that is likely due to the combination of endoreduplication and vacuolization (Perrot-Rechenmann, 2010; Barrada et al., 2015). Since all cells pass this switching phase asynchronously, a wide area of the leaf formed where some cells switched to fast growth and some cells continued to grow with at a slow rate (as meristematic cells). Such a neighborhood defines the transition zone (Ivanov and Dubrovsky, 2013). Furthermore, within the same cell file, the distance from the leaf base where the cell switches to another phase of growth may be different (Lück et al., 1997).

In our model, we assumed that there exists a division zone boundary defined by a concentration gradient of a morphogen. Beyond that zone, the cell continues to grow at the same slow rate as in the division zone until reaching a critical size. Then, the cell growth mode changes. Thus, the growth zone of the leaf has the following structure: the meristematic zone is in the leaf base where cells can divide, a transition zone, and then the elongation zone. This structure of leaf growth area is consistent with the structure of the growth zones for *Arabidopsis* roots and maize leaves considered in Avramova et al. (2015).

#### 4.5. The Mechanical Behavior of Cells during the Symplastic Growth of the Linear Leaf

The computational experiments considered in this paper, as well as in Vos et al. (2014), showed that it is possible to choose model parameters to reproduce the experimentally observed geometric pattern of cell tissue structure. However, the mechanical parameters of the cells during symplastic growth remain hidden because vertex-based models (Nagai and Honda, 2001; Dupuy et al., 2008; Merks et al., 2011) use abstract potential forces for simulating changes in the geometry of cells. Consequently, these potentials did not allow directly interpreting the mechanics of plant cell growth. Here, we reduced the dimension and switched to the quasi-one-dimensional model to describe the 2D leaf growth. This allowed us to explicitly link the changes in cell volume and the deformation of the cell wall. Consequently, we observed the dynamics of osmotic and turgor pressures in cells during their growth.

The significant "jumps" of pressure in the cells could be observed in the real nature. For instance, the original experimental data from Dyson et al. (2014) can serve as an indirect confirmation of such significant changes of pressure in the cells. Although, the authors conclude that the effective

(average) turgor pressure does not change throughout the different growth zones along the *Arabidopsis* root (Figure 3A from Dyson et al., 2014), their measurements indicate that pressure in individual cells of the root along the growth axis changed from 1 to 4 atm., i.e., 4 times. Note that the pressure measurements in Dyson et al. (2014) were performed in single cells for a short time only.

In our model, cells grow autonomously, but as a part of symplastic growing tissue. Note that in the framework of vertex-based models of plant tissue, the autonomous cell growth is usually accepted (Nagai and Honda, 2001; Dupuy et al., 2008). As we suppose, this could be one of the possible reasons why extreme values of pressure are observed for the cells in the transition zone between the DZ and EZ (up to 50 bar, see Figures 5A,B). Our computational experiments demonstrated that the autonomous growth of cell biomass may cause significant deformation of the cell-wall due to cell stretching/compression by the neighboring cells growing at different rates. From the other hand, extreme values of pressure are also likely to arise from the assumption of the absolute shear rigidity of the cell-wall material.

The model framework suggested here allows for the non-autonomous cell growth to be taken into account. The first step is to determine the necessity and the way the cell regulates its growth. The second step is the determination of the coordination of cells of the tissue as a whole during its growth.

#### 5. CONCLUSION

A model of the mechanics of the symplastic growth of a linear leaf is proposed. The model is a special case of a class of vertex-based models, and its parameters can be meaningfully interpreted. The biomechanical description of the autonomous growth of individual plant cells was based on explicit expressions of turgor and osmotic pressures as functions of the cell lengths. The model was developed in the framework of Lockhart (1965) and Ortega (2010) approaches. To illustrate the consequences of a widely used (in the framework of the vertex-based approach) model assumption of the autonomous growth of cells in the tissue, we used an explicit function depending only on the time for cell biomass growth.

Consideration of the geometry of the unidirectional growth of a linear leaf allowed us to bind the cell volume change with the change of the cells walls and to describe osmotic and turgor pressures in the following state variables of growing cells visible length,  $l$ , isosmotic length,  $l_i$ , and relaxed length,  $l_r$ . The model of cell growth in a plant tissue was constructed from consideration of the mechanical forces arising between cells in the symplastic growing tissue. It was shown that the proposed model of cell growth as a part of symplastic growing tissue subject to certain parameter values provides a good approximation of the experimental data on the growth of wheat leaf. At the same time, the physical interpretability of the model variables was able to reveal significant variations of turgor and osmotic pressures in cells of growing tissue. The question of accordance of such dynamics of pressures to the real situation requires experimental verification, and it is critically important for judging the adequacy

of the model, particularly the assumptions about the autonomous growth of cells and the rule of cell transition between the DZ and EZ.

To conclude, we want to emphasize the importance of cell-based biomechanical models of the plant tissue morphodynamics allowing the estimation of mechanical stress in cell walls because they can serve as regulatory signals for molecular genetic systems underlying the mechanism of the individual cell growth and formation of biomechanical properties of the cell. Such models make it possible to link biomechanical and molecular genetic levels of morphogenesis description and allow us to make a step toward a complex integrated model of morphogenesis.

## AUTHOR CONTRIBUTIONS

UZ developed the model and its computational implementation, conducted the computational experiments, wrote the manuscript, and drew the figures. SN designed the research, developed the model and its computational implementation, and wrote the manuscript. AP designed the program, ran the calculations, and provided instructive comments on the original

manuscript. NP strengthened the introduction and discussion from a biological perspective and commented on the whole manuscript. SG made substantial contributions to the model of cell biomechanics. DA and NK conceived the topic and problem and provided instructive comments on the original manuscript.

## FUNDING

The development of the model for the symplastic growth of a linear leaf accounting for the structure of the growth zone and approximation of experimental cell length profiles was supported by the Russian Science Foundation according to research project No. 14-14-00734. Simulations were performed using a program developed with support of the ICG SB RAS budget project No. 0324-2015-0003.

## ACKNOWLEDGMENTS

The authors thank Alexey Doroshkov for providing the image data of the wheat leaf epidermis used for creating **Figure 1** and Irina Penenko for revising the English version of the manuscript.

## REFERENCES

- Ali, O., and Traas, J. (2016). Force-driven polymerization and turgor-induced wall expansion. *Trends Plant Sci.* 21, 398–409. doi: 10.1016/j.tplants.2016.01.019
- Avramova, V., Spranglers, K., and Beemster, G. T. (2015). The maize leaf: another perspective on growth regulation. *Trends Plant Sci.* 20, 787–797. doi: 10.1016/j.tplants.2015.09.002
- Baluška, F., Mancuso, S., Volkmann, D., and Barlow, P. W. (2010). Root apex transition zone: a signalling-response nexus in the root. *Trends Plant Sci.* 15, 402–408. doi: 10.1016/j.tplants.2010.04.007
- Baluska, F., Volkmann, D., and Barlow, P. W. (1996). Specialized zones of development in roots: view from the cellular level. *Plant Physiol.* 112:3. doi: 10.1104/pp.112.1.3
- Barlow, P. (1969). Cell growth in the absence of division in a root meristem. *Planta* 88, 215–223.
- Barrera, A., Montané, M.-H., Robaglia, C., and Menand, B. (2015). Spatial regulation of root growth: placing the plant tor pathway in a developmental perspective. *Int. J. Mol. Sci.* 16, 19671–19697. doi: 10.3390/ijms160819671
- Bayer, E. M., Smith, R. S., Mandel, T., Nakayama, N., Sauer, M., Prusinkiewicz, P., et al. (2009). Integration of transport-based models for phyllotaxis and midvein formation. *Genes Dev.* 23, 373–384. doi: 10.1101/gad.497009
- Beemster, G. T., Masle, J., Williamson, R. E., and Farquhar, G. D. (1996). Effects of soil resistance to root penetration on leaf expansion in wheat (*Triticum aestivum* L.): kinematic analysis of leaf elongation. *J. Exp. Bot.* 47, 1663–1678.
- Benková, E., and Hejátko, J. (2009). Hormone interactions at the root apical meristem. *Plant Mol. Biol.* 69, 383–396. doi: 10.1007/s11103-008-9393-6
- Braybrook, S. A., and Jönsson, H. (2016). Shifting foundations: the mechanical cell wall and development. *Curr. Opin. Plant Biol.* 29, 115–120. doi: 10.1016/j.pbi.2015.12.009
- Carpita, N. C., and Gibeaut, D. M. (1993). Structural models of primary cell walls in flowering plants: consistency of molecular structure with the physical properties of the walls during growth. *Plant J.* 3, 1–30.
- Cederholm, H. M., Iyer-Pascuzzi, A. S., and Benfey, P. N. (2012). Patterning the primary root in *arabidopsis*. *Wiley Interdiscip. Rev.* 1, 675–691. doi: 10.1002/wdev.49
- Chaiwanon, J., Wang, W., Zhu, J.-Y., Oh, E., and Wang, Z.-Y. (2016). Information integration and communication in plant growth regulation. *Cell* 164, 1257–1268. doi: 10.1016/j.cell.2016.01.044
- Chavarría-Krauser, A., Jäger, W., and Schurr, U. (2005). Primary root growth: a biophysical model of auxin-related control. *Funct. Plant Biol.* 32, 849–862. doi: 10.1071/FP05033
- Chen, S., Jia, H., Zhao, H., Liu, D., Liu, Y., Liu, B., et al. (2016). Anisotropic cell expansion is affected through the bidirectional mobility of cellulose synthase complexes and phosphorylation at two critical residues on CESA3. *Plant Physiol.* 171, 242–250. doi: 10.1104/pp.15.01874
- Chickarmane, V. S., Gordona, S. P., Tarra, P. T., Heisler, M. G., and Meyerowitz, E. M. (2012). Cytokinin signaling as a positional cue for patterning the apical-basal axis of the growing *arabidopsis* shoot meristem. *Proc. Natl. Acad. Sci. U.S.A.* 109, 4002–4007. doi: 10.1073/pnas.1200636109
- Cosgrove, D. J. (2005). Growth of the plant cell wall. *Nat. Rev. Mol. Cell Biol.* 6, 850–861. doi: 10.1038/nrm1746
- Dupuy, L., MacKenzie, J., Rudge, T., and Haseloff, J. (2008). A system for modelling cell-cell interactions during plant morphogenesis. *Ann. Bot.* 101, 1255–1265. doi: 10.1093/aob/mcm235
- Dyson, R. J., Band, L. R., and Jensen, O. E. (2012). A model of crosslink kinetics in the expanding plant cell wall: yield stress and enzyme action. *J. Theor. Biol.* 307, 125–136. doi: 10.1016/j.jtbi.2012.04.035
- Dyson, R. J., Vizcay-Barrena, G., Band, L. R., Fernandes, A. N., French, A. P., Fozard, J. A., et al. (2014). Mechanical modelling quantifies the functional importance of outer tissue layers during root elongation and bending. *New Phytol.* 202, 1212–1222. doi: 10.1111/nph.12764
- Gibson, L. J. (2012). The hierarchical structure and mechanics of plant materials. *J. R. Soc. Interface* 9, 2749–2766. doi: 10.1098/rsif.2012.0341
- Glazier, J. A., and Graner, F. (1993). Simulation of the differential adhesion driven rearrangement of biological cells. *Phys. Rev. E* 47, 2128.
- Graner, F., and Glazier, J. A. (1992). Simulation of biological cell sorting using a two-dimensional extended potts model. *Phys. Rev. Lett.* 69, 2013.
- Green, P. B. (1999). Expression of pattern in plants: combining molecular and calculus-based biophysical paradigms. *Am. J. Bot.* 86, 1059–1076.
- Hamat, O., Heisler, M. G., Jönsson, H., Krupinski, P., Uyttewaal, M., Bokov, P., et al. (2008). Developmental patterning by mechanical signals in *arabidopsis*. *Science* 322, 1650–1655. doi: 10.1126/science.1165594
- Hamant, O., and Traas, J. (2010). The mechanics behind plant development. *New Phytol.* 185, 369–385. doi: 10.1111/j.1469-8137.2009.03100.x
- Hu, Y., and Schmidhalter, U. (2008). Spatial and temporal quantitative analysis of cell division and elongation rate in growing wheat

- leaves under saline conditions. *J. Integr. Plant Biol.* 50, 76–83. doi: 10.1111/j.1744-7909.2007.00379.x
- Hukin, D., Doering-Saad, C., Thomas, C. R., and Pritchard, J. (2002). Sensitivity of cell hydraulic conductivity to mercury is coincident with symplasmic isolation and expression of plasmalemma aquaporin genes in growing maize roots. *Planta* 215, 1047–1056. doi: 10.1007/s00425-002-0841-2
- Ivanov, V. B., and Dubrovsky, J. G. (2013). Longitudinal zonation pattern in plant roots: conflicts and solutions. *Trends Plant Sci.* 18, 237–243. doi: 10.1016/j.tplants.2012.10.002
- Jönsson, H., Heisler, M. G., Shapiro, B. E., Meyerowitz, E. M., and Mjolsness, E. (2006). An auxin-driven polarized transport model for phyllotaxis. *Proc. Natl. Acad. Sci. U.S.A.* 103, 1633–1638. doi: 10.1073/pnas.0509839103
- Kalve, S., De Vos, D., and Beemster, G. T. (2014). Leaf development: a cellular perspective. *Front. Plant Sci.* 5:362. doi: 10.3389/fpls.2014.00362
- Krupinski, P., Bozorg, B., Larsson, A., Pietra, S., Grebe, M., and Jönsson, H. (2016). A model analysis of mechanisms for radial microtubular patterns at root hair initiation sites. *Front. Plant Sci.* 7:1560. doi: 10.3389/fpls.2016.01560
- Lekka, M., Pogoda, K., Gostek, J., Klymenko, O., Prauzner-Bechcicki, S., Wiltowska-Zuber, J., et al. (2012). Cancer cell recognition–mechanical phenotype. *Micron* 43, 1259–1266. doi: 10.1016/j.micron.2012.01.019
- Lindenmayer, A. (1968). Mathematical models for cellular interaction in development, parts i and ii. *J. Theor. Biol.* 18, 280–315.
- Lockhart, J. A. (1965). An analysis of irreversible plant cell elongation. *J. Theor. Biol.* 8, 264–275.
- Lück, J., Barlow, P., and Lück, H. (1997). An automata-theoretical model of meristem development as applied to the primary root of *Zea mays* L. *Ann. Bot.* 79, 375–389.
- Lv, H., Li, L., Sun, M., Zhang, Y., Chen, L., Rong, Y., et al. (2015). Mechanism of regulation of stem cell differentiation by matrix stiffness. *Stem Cell Res. Ther.* 6:1. doi: 10.1186/s13287-015-0083-4
- Merks, R. M., Guravage, M., Inzé, D., and Beemster, G. T. (2011). Virtualleaf: an open-source framework for cell-based modeling of plant tissue growth and development. *Plant Physiol.* 155, 656–666. doi: 10.1104/pp.110.167619
- Milani, P., Braybrook, S. A., and Boudaoud, A. (2013). Shrinking the hammer: micromechanical approaches to morphogenesis. *J. Exp. Bot.* 64, 4651–4662. doi: 10.1093/jxb/ert169
- Milani, P., Gholamirad, M., Traas, J., Arnéodo, A., Boudaoud, A., Argoul, F., et al. (2011). *In vivo* analysis of local wall stiffness at the shoot apical meristem in *arabidopsis* using atomic force microscopy. *Plant J.* 67, 1116–1123. doi: 10.1111/j.1365-313X.2011.04649.x
- Mishra, S. R. (2004). *Translocation in Plants*. New Delhi: Discovery Publishing House.
- Nagai, T., and Honda, H. (2001). A dynamic cell model for the formation of epithelial tissues. *Philos. Mag. B* 81, 699–719. doi: 10.1080/13642810108205772
- Nelissen, H., Rymen, B., Jikumaru, Y., Demuyck, K., Van Lijsebettens, M., Kamiya, Y., et al. (2012). A local maximum in gibberellin levels regulates maize leaf growth by spatial control of cell division. *Curr. Biol.* 22, 1183–1187. doi: 10.1016/j.cub.2012.04.065
- Nikolaev, S. V., Zubairova, U. S., Fadeev, S. I., Mjolsness, E., and Kolchanov, N. A. (2011). Study of a one-dimensional model, accounting for cell division, of regulation of the renewing zone size in a biological tissue. *J. Appl. Ind. Math.* 4, 601–611. doi: 10.1134/S1990478911040156
- Nobel, P. (2009). *Physicochemical and Environmental Plant Physiology*. Oxford: Academic Press.
- Noble, D. (2008). *The Music of Life: Biology Beyond Genes*. Oxford: Oxford University Press.
- Ortega, J. K. (2010). Plant cell growth in tissue. *Plant Physiol.* 154, 1244–1253. doi: 10.1104/pp.110.162644
- Perrot-Rechenmann, C. (2010). Cellular responses to auxin: division versus expansion. *Cold Spring Harb. Perspect. Biol.* 2:a001446. doi: 10.1101/cshperspect.a001446
- Prusinkiewicz, P., Hammel, M., and Mjolsness, E. (1993). “Animation of plant development,” in *Proceedings of SIGGRAPH 93, In Computer Graphics Proceedings, Annual Conference Series* (Anaheim, CA: ACM SIGGRAPH), 351–360.
- Robinson, S., Burian, A., Couturier, E., Landrein, B., Louveaux, M., Neumann, E. D., et al. (2013). Mechanical control of morphogenesis at the shoot apex. *J. Exp. Bot.* 64, 4729–4744. doi: 10.1093/jxb/ert199
- Routier-Kierzkowska, A.-L., and Smith, R. S. (2013). Measuring the mechanics of morphogenesis. *Curr. Opin. Plant Biol.* 16, 25–32. doi: 10.1016/j.pbi.2012.11.002
- Sablowski, R., and Dornelas, M. C. (2014). Interplay between cell growth and cell cycle in plants. *J. Exp. Bot.* 65, 2703–2714. doi: 10.1093/jxb/ert354
- Sassi, M., and Traas, J. (2015). When biochemistry meets mechanics: a systems view of growth control in plants. *Curr. Opin. Plant Biol.* 28, 137–143. doi: 10.1016/j.pbi.2015.10.005
- Shapiro, B. E., Meyerowitz, E. M., and Mjolsness, E. (2013). Using cellzilla for plant growth simulations at the cellular level. *Front. Plant Sci.* 4:408. doi: 10.3389/fpls.2013.00408
- Streichan, S. J., Hoerner, C. R., Schneidt, T., Holzer, D., and Hufnagel, L. (2014). Spatial constraints control cell proliferation in tissues. *Proc. Natl. Acad. Sci. U.S.A.* 111, 5586–5591. doi: 10.1073/pnas.1323016111
- Sugimura, K., Lenne, P.-F., and Graner, F. (2016). Measuring forces and stresses *in situ* in living tissues. *Development* 143, 186–196. doi: 10.1242/dev.119776
- Swarup, R., Kramer, E. M., Perry, P., Knox, K., Leyser, H. M., Haseloff, J., et al. (2005). Root gravitropism requires lateral root cap and epidermal cells for transport and response to a mobile auxin signal. *Nat. Cell Biol.* 7, 1057–1065. doi: 10.1038/ncb1316
- Tardieu, F., Reymond, M., Hamard, P., Granier, C., and Muller, B. (2000). Spatial distributions of expansion rate, cell division rate and cell size in maize leaves: a synthesis of the effects of soil water status, evaporative demand and temperature. *J. Exp. Bot.* 51, 1505–1514. doi: 10.1093/jexbot/51.3 50.1505
- van der Weele, C. M., Jiang, H. S., Palaniappan, K. K., Ivanov, V. B., Palaniappan, K., and Baskin, T. I. (2003). A new algorithm for computational image analysis of deformable motion at high spatial and temporal resolution applied to root growth. Roughly uniform elongation in the meristem and also, after an abrupt acceleration, in the elongation zone. *Plant Physiol.* 132, 1138–1148. doi: 10.1104/pp.103.021345
- Verbelen, J.-P., De Cnodder, T., Le, J., Vissenberg, K., and Baluška, F. (2006). The root apex of *Arabidopsis thaliana* consists of four distinct zones of growth activities: meristematic zone, transition zone, fast elongation zone and growth terminating zone. *Plant Signal. Behav.* 1, 296–304. doi: 10.4161/psb.1.6.3511
- Vos, D. D., Vissenberg, K., Broeckhove, J., and Beemster, G. T. S. (2014). Putting theory to the test: which regulatory mechanisms can drive realistic growth of a root? *PLoS Comput. Biol.* 10:e1003910. doi: 10.1371/journal.pcbi.10 03910
- Wang, T., McFarlane, H. E., and Persson, S. (2016). The impact of abiotic factors on cellulose synthesis. *J. Exp. Bot.* 67, 543–552. doi: 10.1093/jxb/erv488
- Wells, R. G. (2008). The role of matrix stiffness in regulating cell behavior. *Hepatology* 47, 1394–1400. doi: 10.1002/hep.22193
- Zhang, Y., Nikolovski, N., Sorieul, M., Vellosillo, T., McFarlane, H. E., Dupree, R., et al. (2016). Golgi-localized stello proteins regulate the assembly and trafficking of cellulose synthase complexes in *arabidopsis*. *Nat. Commun.* 7:11656. doi: 10.1038/ncomms11656
- Zubairova, U., Golushko, S., Penenko, A., and Nikolaev, S. (2015). A computational model of the effect of symplastic growth on cell mechanics in a linear leaf blade. *J. Bioinform. Comput. Biol.* 13:1540005. doi: 10.1142/S0219720015400053
- Conflict of Interest Statement:** The authors declare that the research was conducted in the absence of any commercial or financial relationships that could be construed as a potential conflict of interest.
- Copyright © 2016 Zubairova, Nikolaev, Penenko, Podkolodnyy, Golushko, Afonnikov and Kolchanov. This is an open-access article distributed under the terms of the Creative Commons Attribution License (CC BY). The use, distribution or reproduction in other forums is permitted, provided the original author(s) or licensor are credited and that the original publication in this journal is cited, in accordance with accepted academic practice. No use, distribution or reproduction is permitted which does not comply with these terms.



# Computational Modeling of Auxin: A Foundation for Plant Engineering

Alejandro Morales-Tapia and Alfredo Cruz-Ramírez\*

Molecular and Developmental Complexity Group, Unidad de Genómica Avanzada, Langebio-Cinvestav, Irapuato, México

Since the development of agriculture, humans have relied on the cultivation of plants to satisfy our increasing demand for food, natural products, and other raw materials. As we understand more about plant development, we can better manipulate plants to fulfill our particular needs. Auxins are a class of simple metabolites that coordinate many developmental activities like growth and the appearance of functional structures in plants. Computational modeling of auxin has proven to be an excellent tool in elucidating many mechanisms that underlie these developmental events. Due to the complexity of these mechanisms, current modeling efforts are concerned only with single phenomena focused on narrow spatial and developmental contexts; but a general model of plant development could be assembled by integrating the insights from all of them. In this perspective, we summarize the current collection of auxin-driven computational models, focusing on how they could come together into a single model for plant development. A model of this nature would allow researchers to test hypotheses *in silico* and yield accurate predictions about the behavior of a plant under a given set of physical and biochemical constraints. It would also provide a solid foundation toward the establishment of plant engineering, a proposed discipline intended to enable the design and production of plants that exhibit an arbitrarily defined set of features.

**Keywords:** auxin, computational modeling, development, morphodynamics, plants

## OPEN ACCESS

**Edited by:**

Daniel H. Chitwood,  
Donald Danforth Plant Science  
Center, USA

**Reviewed by:**

Jan Petrášek,  
Charles University, Czechia  
Gerhard Buck-Sorlin,  
Agrocampus Ouest, France

**\*Correspondence:**

Alfredo Cruz-Ramírez  
alfredo.cruz@cnrs.fr

**Specialty section:**

This article was submitted to  
Plant Biophysics and Modeling,  
a section of the journal  
*Frontiers in Plant Science*

**Received:** 01 September 2016

**Accepted:** 29 November 2016

**Published:** 20 December 2016

**Citation:**

Morales-Tapia A and Cruz-Ramírez A (2016) Computational Modeling of Auxin: A Foundation for Plant Engineering. *Front. Plant Sci.* 7:1881.  
doi: 10.3389/fpls.2016.01881

## AUXIN MODELING IN AN INTRACELLULAR CONTEXT

A change in auxin concentration induces a change in the transcriptional program of the cell. Auxin response is carried out by the Auxin Response Factor (ARF) family of transcriptional regulators. Due to the variety of ARFs present in plants, the auxin signal can be interpreted differently by cells that belong to different lineages and tissues (Rademacher et al., 2011). Taking all of them into account is necessary to accurately predict a plant's phenotype, but this would require the simulation of a very complex regulation network. It has been shown, however, that this complexity can be considerably reduced if we identify the dominant players of the network and design a simplified model accordingly (Vernoux et al., 2011).

Auxin is transported from cell to cell through the action of active transporters that are present at the cell's membrane, such as those belonging to the AUX/LAX and PIN families. This enables many important developmental events (Blilou et al., 2005). These transporter proteins are commonly found polarized toward a preferred region of the membrane, as described in a mathematical model by Kleine-Vehn et al. (2011). The location of these transporters correlates with the amount of auxin present in adjacent cells. Several hypotheses have been proposed to explain this and they

have been tested through computational modeling (Wabnik et al., 2011).

A relatively simple model could account for both auxin response and transporter polarization to yield predictions on the distribution of auxin across a larger tissue. Other noteworthy phenomena that could be considered at this scale are: the diffusion of auxin within the cell (Lituviev et al., 2013); auxin transport between the cytoplasm and the nucleus (Herud et al., 2016); the feedback between auxin concentration and the amount of protein regulators like Aux/IAAs (Middleton et al., 2010) and membrane transporters like LAX3 (Mellor et al., 2015); and other mechanisms that are involved with auxin homeostasis (Mellor et al., 2016). All these examples could be integrated into a single model that describes the behavior of auxin from a cellular point of view.

## AUXIN MAXIMA

On a broader scale, as auxin travels across tissues, it tends to accumulate around localized spots which accrue a significantly higher concentration. Auxin maxima, as they are commonly known, usually precede the appearance of organs and other morphological structures, and consequently have been one of the most important traits that computational auxin models aim to recreate.

At the tip of *Arabidopsis thaliana* roots, a maximum of auxin maintains the identity of a group of cells known as the root stem cell niche (RSCN). A model by Grieneisen et al. (2007) reproduces the auxin dynamics in this region and considers auxin transport due to efflux membrane transporters (i.e., PIN proteins). The model represents the root as a 2-dimensional lattice of square cells which have different permeability values on their sides. With a similar setup, Tian et al. (2014) showed that the presence of WOX5, involved in auxin biosynthesis, is necessary for the appearance of this auxin maximum. Another study by Band et al. (2014) makes use of a realistic layout of cells and further extends the model by accounting for the effect of auxin influx transporters (i.e., AUX1/LAX).

It is crucial to consider the properties of auxin transporters when modeling the auxin flow that travels through a group of cells (Mitchison, 2015). Other mechanisms that regulate transporters themselves need to be considered as well. In *A. thaliana*, ICR1 and a family of related proteins control the deposition of PIN proteins on the cell membrane (Hazak et al., 2010). Their activity is dependent on the amount of auxin present within the cell and they are able to alter the resulting auxin distribution pattern of the tissue to which they belong (Hazak et al., 2014).

Regardless of the completeness of a single cellular model of auxin development, auxin maxima are emergent spatial features which cannot be seen if cells are considered as isolated entities. Their location, timing, and other physiological properties are the result of a complex system of cells interacting together and these characteristics are heavily influenced by the geometrical arrangement of neighboring cells and the phenomena associated with auxin transport from cell to cell.

## PATTERNING AND GROWTH

Auxin coordinates the development of many different structures that a plant needs to function, thrive, and reproduce (Vanneste and Friml, 2009). This is accomplished mainly through mechanisms that involve cell elongation, division, and differentiation; all of which are studied through computational modeling.

The distribution of cells found at the *A. thaliana* root tip can be explained by a model where cell division is controlled by a biological clock that depends on the amount of auxin present (Barrio et al., 2013), as well as specific developmental rules that seek to, among other things, balance out the total strain exerted by the growing tissue (De Vos et al., 2014).

In the *A. thaliana* RSCN, asymmetric cell division of the Cortex and Endodermis Initial (CEI) is controlled by the active form of the SCR/SRH protein complex (Di Laurenzio et al., 1996; Sabatini et al., 2003; Cui et al., 2007). RBR protein binds to, and inactivates, the SCR/SRH complex, unless prevented by CYCD6;1, which is expressed only in the CEI due to the existing auxin maximum at the RSCN. As cells move away from the auxin maximum and are, thus, exposed to a lower auxin concentration, RBR can deactivate SCR/SRH and prevent further asymmetric division of the daughter cells (Cruz-Ramírez et al., 2012).

Also in the root, the PLT family of transcription factors follows a concentration gradient that increases toward the tip and controls the growth of cells at the elongation zone. While the presence of PLT is relatively uniform and symmetric, the auxin gradient present is sensitive to changes in the physical orientation of the root structure. A model by Mähönen et al. (2014) describes how, through the integration of these two signals, the plant can effect different elongation rates on different regions of the root, allowing it to carry out an adequate gravitropic response.

Phyllotaxis is a particular pattern of organization, resembling a spiral, that is exhibited by many biological structures such as leaves, and the characteristic arrangement of seeds in a sunflower. Early studies involving auxin and its relationship with phyllotaxis have been carried out by Jönsson et al. (2006) and Smith et al. (2006). These studies locate auxin transporters within a given cell depending on the auxin concentration present in adjacent cells. This results in the repeated appearance of auxin maxima yielding a pattern that heavily resembles a phyllotactic arrangement. The phyllotactic pattern has also been found to be involved, and modeled, in the organization of floral primordia (van Mourik et al., 2012); and also influencing the development of leaves and their resulting shape (Chitwood et al., 2012).

Many other examples of computational auxin models applied to the study of patterning events exist. Jones et al. (2009) made use of a mathematical model to estimate the amount of auxin present in root hair cells; Bilsborough et al. (2011) showed how the appearance of auxin maxima spots along the edge of leaves gives rise to their resulting serration pattern; Fujita et al. (2011) explored the variety of arrangements arising from the shoot meristem of plants; Mirabet et al. (2012) studied the extent to which the phyllotactic pattern is vulnerable to naturally occurring fluctuations; Péret et al. (2013) proposed a mechanism that explains how lateral roots may emerge from the primary root

structure; and Fàbregas et al. (2015) described a model that recreates the position and number of vascular bundles that appear in the developing shoot.

All these models further push the spatial context of auxin simulations into a larger realm that allows the study of the intended physiological function of biological structures. They are also built up from a common set of premises, particularly similar in regard to how they implement auxin transport between cells. The variety of biological functions that had been reproduced using this relatively small set of rules provides a strong argument in favor of a general model of plant development that relies on auxin as a common integrating signal.

## CANALIZATION MODELS

Plants rely on specialized structures that irrigate tissues with water and nutrients in order to function properly. The organization and function of these vascular tissues is controlled by a patterning event that involves auxin and its transport. When auxin flows through a tissue, the auxin transporters in its composing cells reorient toward the direction of the broader auxin flux. This leads to the establishment of preferential canals where auxin is transported along, a phenomenon known as canalization.

Early models involving canalization were proposed by Feugier et al. (2005), Rolland-Lagan and Prusinkiewicz (2005), Fujita and Mochizuki (2006a,b), Prusinkiewicz et al. (2009), and Wabnik et al. (2010), who all showed that the venation patterns can be produced through stable and self-organizing mechanisms. With different locations for auxin sources and sinks, an extensive variety of vascular arrangements can be generated. Cell division also needs to be carefully controlled in cells that are part of the emerging canal, so as to maintain the continuity of the venation pattern (Lee et al., 2014).

Canalization models are needed to incorporate into exhaustive models of plant development, as they explain how a plant can promote and maintain its functional structures. A study by O'Connor et al. (2014), takes a step in this direction, showing how vascularization and organ initiation are closely related events carried out by the concerted action of distinct PIN proteins. This study also extends the validity of the canonical auxin/PIN mechanism into a broader phylogenetic context, since they used *Brachypodium distachyon* as the model organism.

## STRUCTURAL MECHANICS

Mechanical stress across tissues plays an important role during the life of a plant. This stress can be perceived by cells as it travels through their internal structure and it is known to induce change in the organization of the cell cytoskeleton (Hamant et al., 2008) and alter the polarization of auxin transporters (Heisler et al., 2010). Complementary to that, developmental effects resulting from auxin response alter the shape and other structural properties of a growing plant, hinting at a system where auxin and mechanical forces continuously interact with each other.

Auxin can induce changes in the pH of the apoplastic space, as thoroughly explained by a model from Steinacher et al. (2012). When the pH on the environment of a cell wall drops, its structural strength is diminished, allowing it to change its shape and yield to other forces like turgor pressure. This is a mechanism that allows the plant to control the anisotropic growth of tissues through the presence of varying concentrations of auxin (Sassi et al., 2014).

Mechanical forces are part of another theoretical layer that would greatly expand the scope of computational models of plant development. Unfortunately, accurate measurements on the mechanical properties of plant cells and tissues are still scarce. Nevertheless, recent efforts are producing valuable parameters; for example, Beauzamy et al. (2015) estimated the cell wall's stiffness and turgor pressure at the *A. thaliana* shoot meristem.

## PATHWAY CROSSTALK

Further extending the influence of auxin throughout plant development, auxin is known to interact with other hormonal pathways. For example, cytokinins (CK) are known to have a particularly close relationship with auxin. The auxin/CK antagonistic interplay has been studied by Muraro et al. (2011), who predict a dynamic which can switch from a bistable equilibrium system to a system that exhibits oscillatory changes, leading to different developmental consequences for the plant. This model was used to recreate the architecture of the *A. thaliana* root by Muraro et al. (2013). The relationship between auxin and CK also is involved with other physiological features like miRNA regulation (Muraro et al., 2014; el-Showk et al., 2015) and the geometrical distribution of the developing cells (De Rybel et al., 2014).

Auxin and brassinosteroids (BRs) work together in the formation of vascular tissue inside the *A. thaliana* shoot. This tissue is directly specified by the presence of regularly spaced auxin maxima regions along the shoot. However, with different levels of BRs, the cells at the inflorescence stem change in number and size, which influences the resulting pattern of auxin maxima and, consequently, the number of vascular bundles that appear (Ibañes et al., 2009). Strigolactone is another hormone that interacts with auxin, as it is known to promote the dissociation of PIN1 from the membrane and, thus, alter the effective rate of auxin transport. This is linked to developmental features like shoot branching in *A. thaliana* (Shinohara et al., 2013).

Sometimes, multiple hormones can interact with auxin to produce a single phenotype. For instance, at the *A. thaliana* root, the observed auxin distribution pattern is known to be affected by a complex regulation network involving CK, ethylene, and the PLS protein (Liu et al., 2010; Moore et al., 2015).

The above are all prime examples of how auxin models could be extended to incorporate other regulation mechanisms that are important for plant development. A computational model intended to reproduce as much as we know about the metabolism of plants, should consider auxin as a starting point, due to the extensive work that has been published and is available to date.

		Software Platform <sup>1</sup>									
		Root & Root Tip		Shoot & Shoot Meristem		Leaf		Flower		Other <sup>2</sup>	
		Cell	Cell	Cell	Cell	Cell	Cell	Cell	Cell	Cell	Cell
Analytic	Liu et al., 2010	COPASI Matronia									
	Middleton et al., 2010	MATLAB									
	Muraro et al., 2011	Middleton et al. 2010									
	Vernoux et al., 2011	FORTRAN Python									
	Band et al., 2012	MATLAB									
	Steinacher et al., 2012	COPASI									
	Beauzamy et al., 2015	In-House									
	Mellor et al., 2015	Python									
	Boot et al., 2016	MATLAB									
	Mellor et al., 2016	MATLAB									
1D	Muraro et al., 2013	Muraro et al. 2011									
	Ibañes et al., 2009	FORTRAN									
	Bilsborough et al., 2011	L-Studio									
	Fàbregas et al., 2015	C++ FORTRAN									
	Feugier et al., 2005	In-House									
	Rolland-Lagan and Prusinkiewicz, 2005	MATLAB									
	Fujita, Mochizuki, 2006a	In-House									
	Fujita, Mochizuki, 2006b	In-House									
	Jönsson et al., 2006	C++									
	Grieneisen et al., 2007	In-House									
1.5D	Laskowski et al., 2008	Grieneisen et al. 2007									
	Prusinkiewicz et al., 2009	In-House									
	Heisler et al., 2010	In-House									
	Wabnik et al., 2010	VirtualLeaf									
	Fujita et al., 2011	In-House									
	Kleine-Vehn et al., 2011	In-House									
	Cruz-Ramírez et al., 2012	Grieneisen et al. 2007									
	Mirabet et al., 2012	Python									
	van Mourik et al., 2012	C++									
	Barrio et al., 2013	In-House									
2D	Litulev et al., 2013	MATLAB									
	Shinohara et al., 2013	Prusinkiewicz et al. 2009									
	Band et al., 2014	In-House (SimuPlant)									
	De Rybel et al., 2014	VirtualLeaf									
	De Vos et al., 2014	VirtualLeaf									
	Hazak et al., 2014	In-House									
	Lee et al., 2014	In-House									
	Mähönen et al., 2014	Grieneisen et al. 2007									
	Muraro et al., 2014	MATLAB									
	O'Connor et al., 2014	Smith et al. 2006									
2.5D	Tian et al., 2014	VV Environment									
	el-Shawky et al., 2015	Grieneisen et al. 2007									
	Mitchinson, 2015	In-House									
	Moore et al., 2015	Grieneisen et al. 2007									
	Smith et al., 2006	VV Environment									
	Hamant et al., 2008	In-House									
	Chitwood et al., 2012	Smith et al. 2006									
	Sassi et al., 2014	SOFA									
	Swarup et al., 2005	AuxSim									
	Jones et al., 2009	AuxSim									
3D	Péret et al., 2013	MATLAB									

FIGURE 1 | Continued

**FIGURE 1 | Main features of the computational models presented.** <sup>1</sup>Software tools that were used to build the model or previous model that a particular work was based on. The term In-House is used when, to our best effort, we could not find information regarding the implementation of a particular model. We assume it had to be a unique tool that was developed strictly for the scope of the referenced study. <sup>2</sup>Other tissues or organs where the simulation takes place. The umbrella term Cell is used for intracellular dynamics that, in principle, should apply to any kind of tissue. <sup>3</sup>Crosstalk and tropisms, but also additional signals or pathways that are modeled as a result of, or coupled to, Auxin expression. <sup>4</sup>This property describes the nature of the mesh used to represent the tissue involved in the simulation. The letter S represents a static mesh established since the beginning of the model and that remains fixed throughout the whole simulation. A typical example is the lattice of square cells that is used to depict a 2D slice of the root. The letter D is used for a dynamic mesh that can deform and evolve as the simulation goes on. It can be used to represent cells which continuously change in size and geometry. <sup>5</sup>The spatial context refers to the topology of the space where the simulation takes place. Analytical solutions are considered to be dimensionless. 1.5D refers to a 1D system describing a feature that exists normally in a 2D space, for instance, the edge of a growing leaf. Similarly, a 2.5D model is essentially a 2D model projected onto a 3D space, like the surface of the developing shoot meristem. Additional references for the software tools presented: AuxSim: Kramer, 2004; Berkeley Madonna: <http://berkeleymadonna.com>; COPASI: Hoops et al., 2006; L-Studio: [http://algorithmicbotany.org/virtual\\_laboratory/](http://algorithmicbotany.org/virtual_laboratory/); SOFA: Faure et al., 2012; VirtualLeaf: Merks et al., 2011; VV Environment: Smith et al., 2004.

## TROPIC RESPONSE

Plants can sense external stimuli from their environment and react to it by changing their developmental program. For example, regarding the gravitropic response in the *A. thaliana* root, the signal originates at the root tip, increasing the local auxin concentration in the tissue following the orientation of the gravitropic stimulus. This pulse, then, travels through the root to deliver the signal to the elongation zone, where the appropriate response is carried out (Mähönen et al., 2014). Band et al. (2012) devised a mathematical model to estimate the speed of auxin redistribution in response to changes in the gravity vector. Swarup et al. (2005) showed how the auxin pulse is transported through the epidermis, due to the presence of PIN and AUX/LAX membrane transporters.

A physical deformation exerted over a tissue is enough to trigger a tropic response from the plant, as it is known that roots are more prone to spawn lateral roots in regions that were previously bent. A convincing explanation for this is given in Laskowski et al. (2008), which predicts that modifying the shape of the root at the meristematic zone leads to an increase in auxin toward the outer region of the curve. This causes an increased accumulation of AUX1 transporters in pericycle cells and induces their reprogramming into lateral root founder cells.

Tropic response in computational models provides an environmental layer which greatly influences the development of a plant. Auxin is known to play a fundamental role in the plant's response to gravity, light, humidity, and other environmental cues (Retzer et al., 2014). It would be reasonable, then, to consider auxin a fundamental signal that enables this environmental layer to interact with the remaining parts in a model of plant development.

## TOWARD A SINGLE MODEL OF PLANT DEVELOPMENT

All computational models considered in this perspective are shown in **Figure 1**, along with their properties. The vast majority of them implement auxin diffusion and transport as the core mechanism that drives the computational simulation. Only a few computational models, to date, have considered the effects

of a dynamically growing tissue together with its structural properties (e.g., Hamant et al., 2008; Barrio et al., 2013; Sassi et al., 2014).

The corpus of algorithms that the field of computational modeling of auxin has produced is enough to justify the creation of an integral model of plant development. This unified model would account, at least, for all the phenomena reviewed previously. In summary, this is how, we perceive such a model coming to existence. A single cellular layer integrates signals from physical phenomena (i.e., mechanical force, environmental stimuli) and regulatory pathways to ultimately define the metabolism of auxin and its transport. The cellular layer is then used to predict the resulting pattern of auxin present in a multi-cellular tissue which, in turn, signals the reprogramming of cells and the appearance of new organs as well as the vasculature needed to sustain them.

Studies that establish the physical constraints associated with auxin would further improve the validity of this model (Kramer et al., 2007, 2011; Beauzamy et al., 2015; Kramer and Ackelsberg, 2015; Boot et al., 2016). And, many existing software tools that deal with the acquisition of data (Schmidt et al., 2014; Barbier de Reuille et al., 2015) and its visualization (Band et al., 2014) would prove to be useful as well.

Due to its complexity, a model of this nature would have to come from a large collaborative effort among the interested scientific community. We identify two issues that could prevent this from happening, the lack of interoperation between the existing models and the difficulty of extending them with new features. This leads to most efforts producing solitary software packages that are rarely used beyond the scope of their particular study (**Figure 1**). These issues could be mitigated by the establishment of standard modeling conventions and tools, and we anticipate the need for a scientific consortium to coordinate the work of the parties concerned.

With a unified model of plant development, the scientific community would be able to evaluate *in silico* the phenotypical outcome of a given set of initial constraints. Furthermore, it would pave the way for the rational design of new biological structures and functions, a powerful paradigm that, we introduce here as plant engineering.

Plant engineering is a discipline concerned with the application of our current body of knowledge regarding plant

development to the design, improvement, and creation of plants to satisfy particular sets of requirements. While this is still a vision set in the far future, we firmly believe that the first step toward it is to establish a common and exhaustive model of plant development built over the foundation laid out by computational modeling of auxin.

## AUTHOR CONTRIBUTIONS

AM-T and AC-R conceived the layout and scope of the manuscript. AM-T wrote the manuscript with guidance and further editing by AC-R.

## REFERENCES

- Band, L. R., Wells, D. M., Fozard, J. A., Ghetiu, T., French, A. P., Pound, M. P., et al. (2014). Systems analysis of auxin transport in the *Arabidopsis* root apex. *Plant Cell* 26, 862–875. doi: 10.1105/tpc.113.119495
- Band, L. R., Wells, D. M., Larrieu, A., Sun, J., Middleton, A. M., French, A. P., et al. (2012). Root gravitropism is regulated by a transient lateral auxin gradient controlled by a tipping-point mechanism. *Proc. Natl. Acad. Sci. U.S.A.* 109, 4668–4673. doi: 10.1073/pnas.1201498109
- Barbier de Reuille, P., Routier-Kierzkowska, A.-L., Kierzkowski, D., Bassel, G. W., Schüpbach, T., Tauriello, G., et al. (2015). MorphoGraphX: a platform for quantifying morphogenesis in 4D. *eLife* 4:5864. doi: 10.7554/eLife.05864
- Barrio, R. A., Romero-Arias, J. R., Noguez, M. A., Azpeitia, E., Ortiz-Gutiérrez, E., Hernández-Hernández, V., et al. (2013). Cell patterns emerge from coupled chemical and physical fields with cell proliferation dynamics: the *Arabidopsis thaliana* root as a study system. *PLoS Comput. Biol.* 9:e1003026. doi: 10.1371/journal.pcbi.1003026
- Beauzamy, L., Louveaux, M., Hamant, O., and Boudaoud, A. (2015). Mechanically, the shoot apical meristem of *Arabidopsis* behaves like a shell inflated by a pressure of about 1 MPa. *Front. Plant Sci.* 6:1038. doi: 10.3389/fpls.2015.01038
- Bilsborough, G. D., Runions, A., Barkoulas, M., Jenkins, H. W., Hasson, A., Galinha, C., et al. (2011). Model for the regulation of *Arabidopsis thaliana* leaf margin development. *Proc. Natl. Acad. Sci. U.S.A.* 108, 3424–3429. doi: 10.1073/pnas.1015162108
- Blilou, I., Xu, J., Wildwater, M., Willemse, V., Paponov, I., Friml, J., et al. (2005). The PIN auxin efflux facilitator network controls growth and patterning in *Arabidopsis* roots. *Nature* 433, 39–44. doi: 10.1038/nature03184
- Boot, K. J. M., Hille, S. C., Libbenga, K. R., Peletier, L. A., Van Spronsen, P. C., Van Duijn, B., et al. (2016). Modelling the dynamics of polar auxin transport in inflorescence stems of *Arabidopsis thaliana*. *J. Exp. Bot.* 67, 649–666. doi: 10.1093/jxb/erv471
- Chitwood, D. H., Headland, L. R., Ranjan, A., Martinez, C. C., Braybrook, S. A., Koenig, D. P., et al. (2012). Leaf asymmetry as a developmental constraint imposed by auxin-dependent phyllotactic patterning. *Plant Cell* 24, 2318–2327. doi: 10.1105/tpc.112.098798
- Cruz-Ramírez, A., Díaz-Triviño, S., Blilou, I., Grieneisen, V. A., Sozzani, R., Zamioudis, C., et al. (2012). A bistable circuit involving SCARECROW-RETINOBLASTOMA integrates cues to inform asymmetric stem cell division. *Cell* 150, 1002–1015. doi: 10.1016/j.cell.2012.07.017
- Cui, H., Levesque, M. P., Vernoux, T., Jung, J. W., Paquette, A. J., Gallagher, K. L., et al. (2007). An evolutionarily conserved mechanism delimiting SHR movement defines a single layer of endodermis in plants. *Science* 316, 421–425. doi: 10.1126/science.1139531
- De Rybel, B., Adibi, M., Breda, A. S., Wendrich, J. R., Smit, M. E., Novak, O., et al. (2014). Integration of growth and patterning during vascular tissue formation in *Arabidopsis*. *Science* 345, 1255215–1255215. doi: 10.1126/science.1255215
- De Vos, D., Vissenberg, K., Broeckhove, J., and Beemster, G. T. S. (2014). Putting theory to the test: which regulatory mechanisms can drive realistic growth of a root? *PLoS Comput. Biol.* 10:e1003910. doi: 10.1371/journal.pcbi.1003910
- Di Laurenzio, L., Wysocka-Diller, J., Malamy, J. E., Pysh, L., Helariutta, Y., Freshour, G., et al. (1996). The SCARECROW gene regulates an asymmetric cell division that is essential for generating the radial organization of the *Arabidopsis* root. *Cell* 86, 423–433. doi: 10.1016/S0092-8674(00)80115-4
- el-Shenk, S., Help-Rinta-Rahko, H., Blomster, T., Siligato, R., Marée, A. F. M., Mähönen, A. P., et al. (2015). Parsimonious model of vascular patterning links transverse hormone fluxes to lateral root initiation: auxin leads the way, while cytokinin levels out. *PLoS Comput. Biol.* 11:e1004450. doi: 10.1371/journal.pcbi.1004450
- Fàbregas, N., Formosa-Jordan, P., Confraria, A., Siligato, R., Alonso, J. M., Swarup, R., et al. (2015). Auxin influx carriers control vascular patterning and xylem differentiation in *Arabidopsis thaliana*. *PLoS Genet.* 11:e1005183. doi: 10.1371/journal.pgen.1005183
- Faure, F., Duriez, C., Delingette, H., Allard, J., Gilles, B., Marchesseau, S., et al. (2012). “SOFA: a multi-model framework for interactive physical simulation,” in *Soft Tissue Biomechanical Modeling for Computer Assisted Surgery*, ed. Y. Payan (Berlin: Springer). doi: 10.1007/8415\_2012\_125
- Feugier, F. G., Mochizuki, A., and Iwasa, Y. (2005). Self-organization of the vascular system in plant leaves: inter-dependent dynamics of auxin flux and carrier proteins. *J. Theor. Biol.* 236, 366–375. doi: 10.1016/j.jtbi.2005.03.017
- Fujita, H., and Mochizuki, A. (2006a). Pattern formation of leaf veins by the positive feedback regulation between auxin flow and auxin efflux carrier. *J. Theor. Biol.* 241, 541–551. doi: 10.1016/j.jtbi.2005.12.016
- Fujita, H., and Mochizuki, A. (2006b). The origin of the diversity of leaf venation pattern. *Dev. Dyn.* 235, 2710–2721. doi: 10.1002/dvdy.20908
- Fujita, H., Toyokura, K., Okada, K., and Kawaguchi, M. (2011). Reaction-diffusion pattern in shoot apical meristem of plants. *PLoS ONE* 6:e18243. doi: 10.1371/journal.pone.0018243
- Grieneisen, V. A., Xu, J., Marée, A. F. M., Hogeweg, P., and Scheres, B. (2007). Auxin transport is sufficient to generate a maximum and gradient guiding root growth. *Nature* 449, 1008–1013. doi: 10.1038/nature06215
- Hamant, O., Heisler, M. G., Jönsson, H., Krupinski, P., Uyttewaal, M., Bokov, P., et al. (2008). Developmental patterning by mechanical signals in *Arabidopsis*. *Science* 322, 1650–1655. doi: 10.1126/science.1165594
- Hazak, O., Bloch, D., Porat, L., Sternberg, H., Zhang, J., Friml, J., et al. (2010). A Rho scaffold integrates the secretory system with feedback mechanisms in regulation of auxin distribution. *PLoS Biol.* 8:e1000282. doi: 10.1371/journal.pbio.1000282
- Hazak, O., Obolski, U., Prat, T., Friml, J., Hadany, L., and Yalovsky, S. (2014). Bimodal regulation of ICR1 levels generates self-organizing auxin distribution. *Proc. Natl. Acad. Sci. U.S.A.* 111, E5471–E5479. doi: 10.1073/pnas.1413918111
- Heisler, M. G., Hamant, O., Krupinski, P., Uyttewaal, M., Ohno, C., Jönsson, H., et al. (2010). Alignment between PIN1 polarity and microtubule orientation in the shoot apical meristem reveals a tight coupling between morphogenesis and auxin transport. *PLoS Biol.* 8:e1000516. doi: 10.1371/journal.pbio.1000516
- Herud, O., Weijers, D., Lau, S., and Jürgens, G. (2016). Auxin responsiveness of the MONOPTEROS-BODENLOS module in primary root initiation critically depends on the nuclear import kinetics of the Aux/IAA inhibitor BODENLOS. *Plant J.* 85, 269–277. doi: 10.1111/tpj.13108

## FUNDING

Funding for this perspective was provided by Consejo Nacional de Ciencia y Tecnología.

## ACKNOWLEDGMENTS

We appreciate the work of all people involved with computational models of auxin and apologize to the ones whose work was not included due to space constraints. We thank Mrs. Collen Beard for her help in proofreading the final version of this manuscript.

- Hoops, S., Sahle, S., Gauges, R., Lee, C., Pahle, J., Simus, N., et al. (2006). COPASI – a complex pathway simulator. *Bioinformatics* 22, 3067–3074. doi: 10.1093/bioinformatics/btl485
- Ibañes, M., Fàbregas, N., Chory, J., and Caño-Delgado, A. I. (2009). Brassinosteroid signaling and auxin transport are required to establish the periodic pattern of *Arabidopsis* shoot vascular bundles. *Proc. Natl. Acad. Sci. U.S.A.* 106, 13630–13635. doi: 10.1073/pnas.0906416106
- Jones, A. R., Kramer, E. M., Knox, K., Swarup, R., Bennett, M. J., Lazarus, C. M., et al. (2009). Auxin transport through non-hair cells sustains root-hair development. *Nat. Cell Biol.* 11, 78–84. doi: 10.1038/ncb1815
- Jönsson, H., Heisler, M. G., Shapiro, B. E., Meyerowitz, E. M., and Mjolsness, E. (2006). An auxin-driven polarized transport model for phyllotaxis. *Proc. Natl. Acad. Sci. U.S.A.* 103, 1633–1638. doi: 10.1073/pnas.0509839103
- Kleine-Vehn, J., Wabnik, K., Martinière, A., Łangowski, Ł., Willig, K., Naramoto, S., et al. (2011). Recycling, clustering, and endocytosis jointly maintain PIN auxin carrier polarity at the plasma membrane. *Mol. Syst. Biol.* 7:540. doi: 10.1038/msb.2011.72
- Kramer, E. M. (2004). PIN and AUX/LAX proteins: their role in auxin accumulation. *Trends Plant Sci.* 9, 578–582. doi: 10.1016/j.tplants.2004.10.010
- Kramer, E. M., and Ackelsberg, E. M. (2015). Auxin metabolism rates and implications for plant development. *Front. Plant Sci.* 6:150. doi: 10.3389/fpls.2015.00150
- Kramer, E. M., Frazer, N. L., and Baskin, T. I. (2007). Measurement of diffusion within the cell wall in living roots of *Arabidopsis thaliana*. *J. Exp. Bot.* 58, 3005–3015. doi: 10.1093/jxb/erm155
- Kramer, E. M., Rutschow, H. L., and Mabie, S. S. (2011). AuxV: a database of auxin transport velocities. *Trends Plant Sci.* 16, 461–463. doi: 10.1016/j.tplants.2011.05.003
- Laskowski, M., Grieneisen, V. A., Hofhuis, H., ten Hove, C. A., Hogeweg, P., Marée, A. F. M., et al. (2008). Root system architecture from coupling cell shape to auxin transport. *PLoS Biol.* 6:2721–2735. doi: 10.1371/journal.pbio.0060307
- Lee, S. W., Feugier, F. G., and Morishita, Y. (2014). Canalization-based vein formation in a growing leaf. *J. Theor. Biol.* 353, 104–120. doi: 10.1016/j.jtbi.2014.03.005
- Lituiev, D. S., Krohn, N. G., Müller, B., Jackson, D., Hellriegel, B., Dresselhaus, T., et al. (2013). Theoretical and experimental evidence indicates that there is no detectable auxin gradient in the angiosperm female gametophyte. *Development* 140, 4544–4553. doi: 10.1242/dev.098301
- Liu, J., Mehdi, S., Topping, J., Tarkowski, P., and Lindsey, K. (2010). Modelling and experimental analysis of hormonal crosstalk in *Arabidopsis*. *Mol. Syst. Biol.* 6, 3425–3441. doi: 10.1038/msb.2010.26
- Mähönen, A. P., ten Tuscher, K., Siligato, R., Smetana, O., Díaz-Triviño, S., Salojärvi, J., et al. (2014). PLETHORA gradient formation mechanism separates auxin responses. *Nature* 515, 125–129. doi: 10.1038/nature13663
- Mellor, N., Bennett, M. J., and King, J. R. (2016). GH3-mediated auxin conjugation can result in either transient or oscillatory transcriptional auxin responses. *Bull. Math. Biol.* 78, 210–234. doi: 10.1007/s11538-015-0137-x
- Mellor, N., Péret, B., Porco, S., Sairanen, I., Ljung, K., Bennett, M., et al. (2015). Modelling of *Arabidopsis* LAX3 expression suggests auxin homeostasis. *J. Theor. Biol.* 366, 57–70. doi: 10.1016/j.jtbi.2014.11.003
- Merks, R. M. H., Guravage, M., Inzé, D., and Beemster, G. T. S. (2011). VirtualLeaf: an open-source framework for cell-based modeling of plant tissue growth and development. *Plant Physiol.* 155, 656–666. doi: 10.1104/pp.110.167619
- Middleton, A. M., King, J. R., Bennett, M. J., and Owen, M. R. (2010). Mathematical modelling of the Aux/IAA negative feedback loop. *Bull. Math. Biol.* 72, 1383–1407. doi: 10.1007/s11538-009-9497-4
- Mirabet, V., Besnard, F., Vernoux, T., and Boudaoud, A. (2012). Noise and robustness in phyllotaxis. *PLoS Comput. Biol.* 8:e1002389. doi: 10.1371/journal.pcbi.1002389
- Mitchison, G. (2015). The shape of an auxin pulse, and what it tells us about the transport mechanism. *PLoS Comput. Biol.* 11:e1004487. doi: 10.1371/journal.pcbi.1004487
- Moore, S., Zhang, X., Mudge, A., Rowe, J. H., Topping, J. F., Liu, J., et al. (2015). Spatiotemporal modelling of hormonal crosstalk explains the level and patterning of hormones and gene expression in *Arabidopsis thaliana* wild-type and mutant roots. *New Phytol.* 207, 1110–1122. doi: 10.1111/nph.13421
- Muraro, D., Byrne, H., King, J., and Bennett, M. (2013). The role of auxin and cytokinin signalling in specifying the root architecture of *Arabidopsis thaliana*. *J. Theor. Biol.* 317, 71–86. doi: 10.1016/j.jtbi.2012.08.032
- Muraro, D., Byrne, H., King, J., Voß, U., Kieber, J., and Bennett, M. (2011). The influence of cytokinin-auxin cross-regulation on cell-fate determination in *Arabidopsis thaliana* root development. *J. Theor. Biol.* 283, 152–167. doi: 10.1016/j.jtbi.2011.05.011
- Muraro, D., Mellor, N., Pound, M. P., Help, H., Lucas, M., Chopard, J., et al. (2014). Integration of hormonal signaling networks and mobile microRNAs is required for vascular patterning in *Arabidopsis* roots. *Proc. Natl. Acad. Sci. U.S.A.* 111, 857–862. doi: 10.1073/pnas.1221766111
- O'Connor, D. L., Runions, A., Sluis, A., Bragg, J., Vogel, J. P., Prusinkiewicz, P., et al. (2014). A division in PIN-mediated auxin patterning during organ initiation in grasses. *PLoS Comput. Biol.* 10:e1003447. doi: 10.1371/journal.pcbi.1003447
- Péret, B., Middleton, A. M., French, A. P., Larrieu, A., Bishopp, A., Njo, M., et al. (2013). Sequential induction of auxin efflux and influx carriers regulates lateral root emergence. *Mol. Syst. Biol.* 9:699. doi: 10.1038/msb.2013.43
- Prusinkiewicz, P., Crawford, S., Smith, R. S., Ljung, K., Bennett, T., Ongaro, V., et al. (2009). Control of bud activation by an auxin transport switch. *Proc. Natl. Acad. Sci. U.S.A.* 106, 17431–17436. doi: 10.1073/pnas.0906696106
- Rademacher, E. H., Möller, B., Lokerse, A. S., Llavata-Peris, C. I., van den Berg, W., and Weijers, D. (2011). A cellular expression map of the *Arabidopsis* AUXIN RESPONSE FACTOR gene family. *Plant J.* 68, 597–606. doi: 10.1111/j.1365-313X.2011.04710.x
- Retzer, K., Korbei, B., and Luschnig, C. (2014). “Auxin and Tropisms,” in *Auxin and Its Role in Plant Development*, eds E. Zažímalová, J. Petrásek, and E. Benková (Vienna: Springer), 361–387. doi: 10.1007/978-3-7091-1526-8\_16
- Rolland-Lagan, A. G., and Prusinkiewicz, P. (2005). Reviewing models of auxin canalization in the context of leaf vein pattern formation in *Arabidopsis*. *Plant J.* 44, 854–865. doi: 10.1111/j.1365-313X.2005.02581.x
- Sabatini, S., Heidstra, R., Wildwater, M., and Scheres, B. (2003). SCARECROW is involved in positioning the stem cell niche in the *Arabidopsis* root meristem. *Genes Dev.* 17, 354–358. doi: 10.1101/gad.252503
- Sassi, M., Ali, O., Boudon, F., Cloarec, G., Abad, U., Cellier, C., et al. (2014). An auxin-mediated shift toward growth isotropy promotes organ formation at the shoot meristem in *Arabidopsis*. *Curr. Biol.* 24, 2335–2342. doi: 10.1016/j.cub.2014.08.036
- Schmidt, T., Pasternak, T., Liu, K., Blein, T., Aubry-Hivet, D., Dovzhenko, A., et al. (2014). The iRoCS Toolbox – 3D analysis of the plant root apical meristem at cellular resolution. *Plant J.* 77, 806–814. doi: 10.1111/tpj.12429
- Shinohara, N., Taylor, C., and Leyser, O. (2013). Strigolactone can promote or inhibit shoot branching by triggering rapid depletion of the auxin efflux protein PIN1 from the plasma membrane. *PLoS Biol.* 11:e1001474. doi: 10.1371/journal.pbio.1001474
- Smith, C., Prusinkiewicz, P., and Samavati, F. (2004). Local specification of surface subdivision algorithms. 3062, 313–327. doi: 10.1007/978-3-540-25959-6\_23
- Smith, R. S., Guyomarc'h, S., Mandel, T., Reinhardt, D., Kuhlemeier, C., and Prusinkiewicz, P. (2006). A plausible model of phyllotaxis. *Proc. Natl. Acad. Sci. U.S.A.* 103, 1301–1306. doi: 10.1073/pnas.0510457103
- Steinacher, A., Leyser, O., and Clayton, R. R. (2012). A computational model of auxin and pH dynamics in a single plant cell. *J. Theor. Biol.* 296, 84–94. doi: 10.1016/j.jtbi.2011.11.020
- Swarup, R., Kramer, E. M., Perry, P., Knox, K., Leyser, H. M. O., Haseloff, J., et al. (2005). Root gravitropism requires lateral root cap and epidermal cells for transport and response to a mobile auxin signal. *Nat. Cell Biol.* 7, 1057–1065. doi: 10.1038/ncb1316
- Tian, H., Wabnik, K., Niu, T., Li, H., Yu, Q., Pollmann, S., et al. (2014). WOX5-IAA17 feedback circuit-mediated cellular auxin response is crucial for the patterning of root stem cell niches in *Arabidopsis*. *Mol. Plant* 7, 277–289. doi: 10.1093/mp/sst118
- van Mourik, S., Kaufmann, K., van Dijk, A. D. J., Angenent, G. C., Merks, R. M. H., and Molenaar, J. (2012). Simulation of organ patterning on the floral meristem using a polar auxin transport model. *PLoS ONE* 7:e28762. doi: 10.1371/journal.pone.0028762
- Vanneste, S., and Friml, J. (2009). Auxin: a trigger for change in plant development. *Cell* 136, 1005–1016. doi: 10.1016/j.cell.2009.03.001

Vernoux, T., Brunoud, G., Farcot, E., Morin, V., Van den Daele, H., Legrand, J., et al. (2011). The auxin signalling network translates dynamic input into robust patterning at the shoot apex. *Mol. Syst. Biol.* 7, 508–508. doi: 10.1038/msb.2011.39

Wabnik, K., Govaerts, W., Friml, J., and Kleine-Vehn, J. (2011). Feedback models for polarized auxin transport: an emerging trend. *Mol. Biosyst.* 7, 2352–2359. doi: 10.1039/c1mb05109a

Wabnik, K., Kleine-Vehn, J., Balla, J., Sauer, M., Naramoto, S., Reinöhl, V., et al. (2010). Emergence of tissue polarization from synergy of intracellular and extracellular auxin signaling. *Mol. Syst. Biol.* 6:447. doi: 10.1038/msb.2010.103

**Conflict of Interest Statement:** The authors declare that the research was conducted in the absence of any commercial or financial relationships that could be construed as a potential conflict of interest.

Copyright © 2016 Morales-Tapia and Cruz-Ramírez. This is an open-access article distributed under the terms of the Creative Commons Attribution License (CC BY). The use, distribution or reproduction in other forums is permitted, provided the original author(s) or licensor are credited and that the original publication in this journal is cited, in accordance with accepted academic practice. No use, distribution or reproduction is permitted which does not comply with these terms.



# Morphogeometric Approaches to Non-vascular Plants

**Daniel E. Stanton<sup>1\*</sup> and Catherine Reeb<sup>2</sup>**

<sup>1</sup> Department of Ecology, Evolution and Behavior, University of Minnesota – Twin Cities, Saint Paul, MN, USA, <sup>2</sup> Institut de Systématique Évolution Biodiversité UMR 7205, UPMC, MNHN, CNRS, EPHE, Muséum National d'Histoire Naturelle, Paris, France

## OPEN ACCESS

**Edited by:**

Daniel H. Chitwood,  
Donald Danforth Plant Science  
Center, USA

**Reviewed by:**

Juan Carlos Villarreal,  
Université Laval, Canada  
Matt A. M. Renner,  
Royal Botanic Gardens and Domain  
Trust, Australia  
Jessica Budke,  
University of Tennessee, USA

**\*Correspondence:**

Daniel E. Stanton  
stan0477@umn.edu

**Specialty section:**

This article was submitted to  
Plant Biophysics and Modeling,  
a section of the journal  
*Frontiers in Plant Science*

**Received:** 17 March 2016

**Accepted:** 09 June 2016

**Published:** 27 June 2016

**Citation:**

Stanton DE and Reeb C (2016)  
Morphogeometric Approaches  
to Non-vascular Plants.  
*Front. Plant Sci.* 7:916.  
doi: 10.3389/fpls.2016.00916

Morphometric analysis of organisms has undergone a dramatic renaissance in recent years, embracing a range of novel computational and imaging techniques to provide new approaches to phenotypic characterization. These innovations have often developed piece-meal, and may reflect the taxonomic specializations and biases of their creators. In this review, we aim to provide a brief introduction to applications and applicability of modern morphometrics to non-vascular land plants, an often overlooked but evolutionarily and ecologically important group. The scale and physiology of bryophytes (mosses, liverworts, and hornworts) differ in important and informative ways from more “traditional” model plants, and their inclusion has the potential to powerfully broaden perspectives in plant morphology. In particular we highlight three areas where the “bryophytic perspective” shows considerable inter-disciplinary potential: (i) bryophytes as models for intra-specific and inter-specific phenotypic variation, (ii) bryophyte growth-forms as areas for innovation in architectural modularity, and (iii) bryophytes as models of ecophysiological integration between organs, individuals, and stands. We suggest that advances should come from two-way dialog: the translation and adoption of techniques recently developed for vascular plants (and other organisms) to bryophytes and the use of bryophytes as model systems for the innovation of new techniques and paradigms in morphogeometric approaches.

**Keywords:** geometric morphology, bryophytes, liverworts, mosses, branching patterns, modularity

## INTRODUCTION

Morphology and its geometric underpinnings have long formed an important part of our understanding of plant biology at all scales, through Goethe’s traditional work (Goethe, 1790). Traditionally considered in a structural or systematics point of view (e.g., Sneath and Sokal, 1973; Oldeman, 1977; Hallé et al., 1978; Dickinson et al., 1987; MacLeod, 2002) highlighting of geometric patterns is now built into a dynamic approach aiming to understand biological integration and modularity in the broadest sense, at all scales and levels, from development, physiological ecology to evolution (Castellanos et al., 1989; Jones, 1993; Pigliucci, 2003; Eble, 2005; Lütge, 2012; Murren, 2012; Ambruster et al., 2014; Klingenberg, 2014). Mathematical advances in the latter half of the 20th century, such as topological techniques for disentangling shape from size and multivariate statistics provided the groundwork for modern geometric morphology. Recent innovations in modeling and image analysis have greatly expanded the power of morphometric analyses (Kaandorp and Kübler, 2001; Le Bot et al., 2009; Schindelin et al., 2012; McKay, 2013), opening up new avenues for

applications such as high-throughput phenotyping and effective canopy modeling (e.g., Araus and Cairns, 2014; Bucksch et al., 2014; Puttonen et al., 2016).

The majority of recent innovations in plant geometric and morphometric analysis have focused on seed plants (angiosperms and gymnosperms). Although this bias reflects a majority of species of economic interest, it leaves aside much of the overall range in land plant morphologies and functional forms. Our objective is to provide a perspective from one of those side-lines, bryophytes, in the hope that greater attention to non-vascular plants in morphometry will not only advance studies of those overlooked groups, but also contribute novel perspectives and emphases to plant morphologists.

Although quite morphologically and taxonomically diverse (~20,000 species worldwide; Shaw et al., 2011), evolutionarily informative (Ligrone et al., 2012) and ecologically important (Lindo and Gonzalez, 2010), bryophytes are often unmentioned in modern morphometric reviews (e.g., Jensen, 2003; Diggle, 2014). This mini-review seeks to provide an overview of recent developments in the geometric and morphometric analysis of non-vascular plants. After a brief introduction to bryophytes, we present three key scales of analysis at which closer integration between plant morphometry and bryology stands to benefit both fields: organ geometry, branching patterns, and canopy-stand integration.

## WHY BRYOPHYTES?

Bryophytes are often treated as a unit; however, they are a paraphyletic group of at most three major clades (liverworts, mosses, and hornworts) that differ greatly in their morphology and physiology (Figure 1). They are united primarily by the dominance of haploid (gametophytic) stages of the life-cycle and a tendency toward poikilohydry (and often desiccation tolerance) rather than internal water conduction (with notable exceptions such as *Dendroligotrichum*; Hébant, 1977; Atala, 2011). The former may make them particularly plastic to genetic or environmental changes, while the latter encourages a wide array of morphological and physiological responses to water availability. Despite these differences, and a deep evolutionary history of divergence (~450 million years), many developmental pathways are shared with other land plants (e.g., Rensing et al., 2008; Jones and Dolan, 2012; Xu et al., 2014). Indeed, several bryophyte species have a long history of use as model systems in plant biology: the thalloid liverwort *Marchantia polymorpha* and the ephemeral moss *Physcomitrella patens* in particular have been used widely in plant molecular biology and development (e.g., Prigge and Bezanilla, 2010; Bonhomme et al., 2013; Bowman et al., 2016).

All of the above provide clear motivations for closer incorporation of bryophytes into plant morphological geometry. Morphologists may find value in the wide range of morphologies presented by bryophytes, and in the challenge of accommodating a wider spectrum of plant forms. Developmental and molecular biologists will benefit from improved phenotyping techniques for these evolutionarily important model organisms. Functional

ecologists have much to learn from groups in which morphology at multiple scales closely influences local micro-environment and poikilohydry tightly couples form to function. And lastly, bryologists will gain from the cross-application of novel techniques to what remains a small and understudied discipline.

## Geometries of Bryophyte Organs: Models for Inter- and Intra-Specific Variation

Bryophytes have long been known for their striking intra- as well as inter-specific variation, in particular in response to environment (e.g., Davy de Virville, 1927–1928; Birse, 1957). This plasticity is uneven: gametophytes often display a high degree of polymorphism while sporophytes remain less variable, being especially conserved among liverworts and hornworts (Schuster, 1966; Vanderpoorten and Goffinet, 2009). The causes of this high variability at the individual level can be linked to ecological, geographical and evolutionary factors (e.g., Forman, 1964; Glime and Raeymaekers, 1987; Vanderpoorten et al., 2003; Buryová and Shaw, 2005; Medina et al., 2012, 2015), and the majority of traditional morphometric studies focused on interpreting this variability.

Gametophytic plasticity presents a challenge to the development of clear and shared species delimitations; Schuster (1966) noted that “ideally, experimental data must be a frame of reference”, paving the way for experimental or integrative taxonomy (using “common gardens” of putatively different species to eliminate environmental effects; McQueen, 1991; Dayrat, 2005; Cano et al., 2006). At the peak of numerical taxonomy in 1970s–1980s, morphometry was a popular tool supporting morphological species delimitation (Hewson, 1970; Bischler-Causse, 1993), in particular helping to make decisions on species hypotheses for problematic taxa, where cryptic species may have been previously overlooked. In bryology, traditional morphometry involves measurements of gametophyte organs (leaves, stem, cells, including minute ornamentation), and sporophytes (seta, capsule, and peristome measurements). Measurements are made on living plants (Cano et al., 2006; Gonzalez-Mancebo et al., 2010; Yu et al., 2012), from single digitized images (De Luna and Gomez-Velasco, 2008), or from shallow image stacks (Renner et al., 2013b).

Today, at the inter-specific level, traditional morphometrics results analyzed from univariate or multivariate methods are compared to molecular species delimitations. For example, *Braunia andrieuxii* and *B. secunda* are discriminated by length of recurved margin and size of upper cells; the variation is always greater between species than within each species (De Luna and Gomez-Velasco, 2008). In the *Tortula subulata* complex, morphometrics recognize four species but not two of the previously known varieties (Cano et al., 2006). However, other species complexes show no clear morphological discontinuities (e.g., Vanderpoorten et al., 2003) and even greater intra- than interspecific variation (Renner et al., 2013a). Variations within populations of a single species (infra-specific level) have also

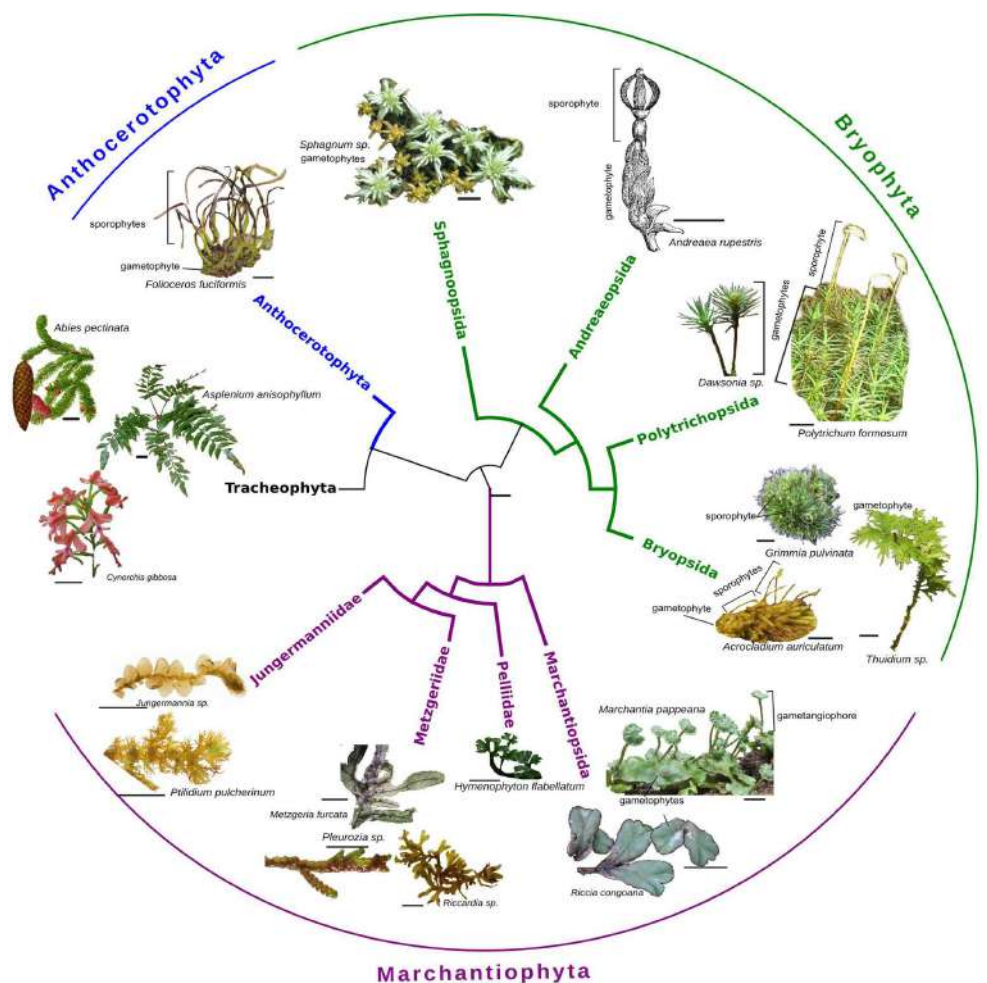


**FIGURE 1 |** Phylogenetic tree (adapted from Crandall-Stotler et al., 2008; Buck and Goffinet, 2009; Chang and Graham, 2011) showing the three main clades of bryophytes: liverworts (Marchantiophyta), mosses (Bryophyta), and hornworts (Anthocerotophyta) as well as their relationship to vascular plants (Tracheophyta). The images (scale bar 1 cm) illustrate a few examples of the wide diversity of morphologies found both within and across clades. All images by CR or DS.

been explored through traditional morphometry, showing strong correlations with geographical and ecological factors (Pereira et al., 2013). Finally, morphometrics have been incorporated into citizen science in an ongoing initiative at the Field Museum in Chicago<sup>1</sup>. From images of the leafy liverwort *Frullania*, the public is asked to measure leaves and lobules to build a huge dataset for analysis at intra- or inter-specific levels.

Geometric morphometry, which includes shape analysis through coordinates analysis of homologous points (landmarks; Bookstein, 1991) or outline analysis (elliptical Fourier analysis; Ferso et al., 1985), allows to one quantify shapes and to explore their dependence on size (allometry) via combination of quantification with multivariate analysis. We will highlight two recent applications in bryology that have used geometric morphometry to unlock nuanced evolutionary understandings

of form and development: liverwort lobules (Renner et al., 2010, 2013b; Renner, 2015) and moss sporophytes (Rose et al., 2016).

In the first example, the morphological variation in the lobule of the compound liverwort leaf, was linked to developmental heterochrony (Renner et al., 2013b), correlated with biogeographical and historical hypotheses (Renner, 2015). Beginning with species delimitation (including intra-specific variation; Renner et al., 2010) they broadened the issues to evolutionary questions, linking morphometrics to ontogenetic and phylogenetic analysis (Renner et al., 2013; Renner et al., 2013b; Renner, 2015). Univariate and multivariate analysis were combined with evolutionary methods: ontogenetic calibration, reconstruction of ancestral states for shape and duration of growth, reconstruction of phylomorphospace, and Bayesian analysis of macroevolutionary mixtures (BAMM). This led not only to confirmation of inter-specific variation but also an understanding of pitfalls associated with these methods: for example, only measurements of mature lobules

<sup>1</sup><http://microplants.fieldmuseum.org/>

recovered informative patterns. Furthermore, convergences in morphospace lead to testable hypotheses of functional and historical explanations of lobule morphologies (Renner, 2015).

In mosses, Rose et al. (2016) similarly combined geometric morphometric analyses (in this case harmonic amplitudes as descriptors of sporangium shape) with evolutionary hypothesis testing. They found strong correlations between shape and habitat indicative of repeated functional shifts. Shifts in sporangium shape were also found to correlate with increases in speciation rates, but not always in conjunction with shifts in habitat.

These adoptions of geometric morphometry in bryology show how several properties of bryophytes make them particularly amenable to such studies. The revival properties of bryophytes provide a constant and relatively easy availability of material, even from herbarium specimens; the usually huge number of objects in a single sample and the ease of manipulating digitalized images ensure perennial perspectives in morphometrics applications.

## BRANCHING PATTERNS

Above the organ-level, a different type of morphometrics, inspired by graph theory and modularity, has proven productive. Bryophytes tend to be organized into two broad morphological types: leafy, erect or prostrate shoots with associated leaf-like flattened organs (mosses and some liverworts) and thalloid, lacking the differentiation between shoots and leaves (hornworts and some liverworts). Although outwardly quite different, both of these morphologies are based in modular development, arising from repetition of the same structure at different levels.

The ontogeny of leafy bryophyte shoots, including formation of stem, leaves, and branching, has been studied for over a century (Clap, 1912; Berthier, 1970; Renzaglia, 1982; Mishler and De Luna, 1991). Branching patterns reflect ramification characteristics of shoots. They are directly linked to modularity, each ramification signaling the formation of a new module. Two types of branching patterns are recognized in bryophytes (La Farge, 1996; Goffinet and Buck, 2013): (i) sympodial, consisting of connected modules of the same level and (ii) monopodial, consisting of one module, itself connected to independent modules of different levels (**Figure 2**). Integration at the individual level, considered then as an architectural unit, defines growth-forms which depend also of perichaetial position and direction of growth (orthotropic or plagiotropic).

Modular lateral branching allows plant architecture and space filling to respond to environmental constraints, making it important to detect specific patterns (morphological modularity) in order to understand their relationship to development, environment and evolutionary history. Control of branching of the sporophyte is well known in flowering plants but conservation of the mechanisms in bryophyte gametophytes have been only briefly explored (Ashton et al., 1979; Fujita and Hasebe, 2009; Bennett et al., 2014). Using both cultivation experiments and modeling of branching patterns, Coudert et al. (2015) showed that branch initiation is patterned in the model moss *P. patens*. They highlighted regulation mechanisms by auxin, cytokinin and

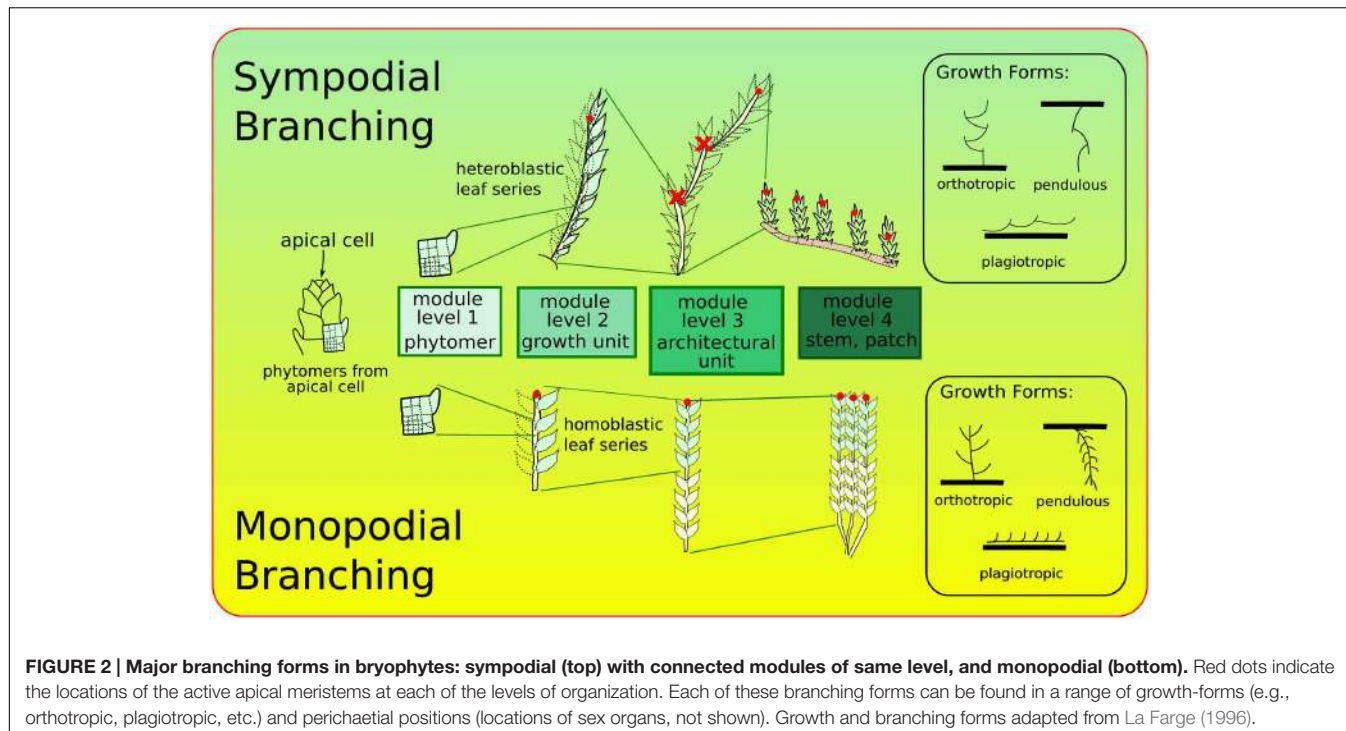
strigolactone. The moss shoot was represented as a connected graph with vertex and connecting edges (VVe modeling; see Abley et al., 2013); a vertex represents a metamer or an apex. Growth was simulated by periodically adding new vertices and by constraining different parameters: apical inhibition over branching via auxin; apical source of auxin, and transportation to neighboring metamers implying different concentrations in each metamer that can be calculated.

Analysis of branching patterns and morphometric characters can also be used for integrative taxonomy, for example in thalloid liverworts, in which phenotypic variability makes landmark-based morphogeometric approaches nearly impossible (Reeb, 2014). This approach was inspired by work on branched organisms, such as corals and sponges (Kaandorp, 1999; Kaandorp and Kübler, 2001; Kruszynski, 2010). The thallus is described as a connected graph, ordered using Horton–Strahler's law (Strahler, 1952; Tarboton, 1996) and consequently each marker is defined as either vertex (junction or apex) or edge. A thallus is considered as a tree rooted by a terminal vertex of maximum order, and branches of order  $n$  treated as sub-trees rooted by a vertex of order  $n-1$ . Following these definitions, all lengths, widths, distances, and angles can be measured on a single thallus with a precise, reliable and repeatable method. Although impossible to do by eye, two software programs (2D and LeafSnake) have been developed that automatically acquire measurements from digitized images of thalli. Statistical analysis show that specific branching patterns, typical of a species or group of species, can be identified (Reeb, 2014). These approaches are complementary to those conducted on fixed animals (Kaandorp and Kübler, 2001), but also in medicine (neuronal or blood webs, e.g., Grueber et al., 2002), in geology (river catchment areas, e.g., Zanardo et al., 2013), and even in data-mining (email networks, e.g., Guimera et al., 2006) reflecting universal and mathematical laws driving such constructions.

The branching patterns of bryophytes and other early land plants are also of interest to studies of plant allometry. Some attributes of bryophyte sporophytes scale allometrically in a manner similar to vascular plants (Niklas, 1994), but this is not universal. Vascularization imposes different constraints on tissue investment during growth, and since bryophytes vary greatly in the nature and specialization of water conducting tissues (Ligrone et al., 2000), they may not all be constrained in the same manner. Interestingly, one of the tallest moss species known, the internally conducting *Dendroligotrichum dendroides*, does show branching allometries consistent with those of other vascular plants (Atala, 2011; Atala and Alfaro, 2012).

## SHOOTS AND CANOPIES: WHOLE-PLANT APPROACHES

A key consideration in any comparison vascular and non-vascular models of plant architecture (allometric or otherwise) is that of scale. The individual modular units of bryophytes combine to determine form and function at larger physical scales, as branching patterns are integrated at the individual level ("growth-form") and at the population level ("life-form"). The



biophysical scales at which many bryophytes operate are small enough that phyllids are not adequate analogs for vascular leaves; instead, functional analogies to vascular leaves must include some combination of leaf, shoot, and canopy properties (Waite and Sack, 2010). While this may initially seem constraining, the explicit need for cross-scale integration presages some of the current directions in vascular plant modeling, where the ecophysiological and biophysical consequences of shoot and stand structure are only beginning to be considered.

The shoot and stand scales can be particularly difficult to disentangle in bryophytes. In many bryophyte species, particularly acrocarpous mosses, the individual shoots grow tightly packed into turves or cushions. These can be multiple shoots of the same individual, closely related individuals or even multi-species mixes. This life-form modifies the impact of any given shoot architecture on light penetration, water retention and gas-exchange: in a study of 22 subarctic bryophyte species, Elumeeva et al. (2011) found that shoot density was a better predictor of water retention than anatomical properties such as cell wall thickness. Shoot density can be environmentally variable within species, and the extent of its dependence on shoot architecture remains unresolved.

In cushion-forming species of mosses, the size of the cushion alone can strongly determine physiological function, determining water balance and gas exchange (Zotz et al., 2000; Rice and Schneider, 2004). Simple geometric relationships between surface area and volume allow larger cushions to remain hydrated, and, therefore, gain carbon, for much longer periods. These scaling relationships appear to be partially species-specific; cushions can vary from hemispherical (*Leucobryum glaucum*; Rice and Schneider, 2004) to flattened (*Grimmia pulvinata*; Zotz et al.,

2000). How cushion shape relates to shoot architecture and/or environment has yet to be explored more widely, despite the relative simplicity of the geometric methods required.

The surface-area relationship described by cushion size and shape is a coarse-grain simplification. The individual shoot canopies aggregate to create a rough canopy layer, analogous to that of a forest. Surface roughness has large effects on boundary-layer properties, and thus on the gas-exchange properties of a moss clump. Surface roughness has traditionally been measured by contact surface probes (Rice et al., 2001), but more efficient laser scanning methods (Rice et al., 2005) and stereoscopic image analysis (Krumnikl et al., 2010), drawing on analogies to LIDAR scanning of forests. Uptake of these methods in bryology has to date been limited (although see Acosta-Mercado et al., 2012), but their application, in conjunction with shoot- and leaf-scale architectural characterizations, shows great potential (Rice and Cornelissen, 2014).

An important distinctive feature of bryophyte canopies is that many of the surface properties are highly dynamic. Shoot and leaf structure are strongly determined by hydration state, allowing bryophytes to rapidly adjust to changing water availability. The leaves of the desert moss *Syntrichia caninervis* change angle by over 40° within seconds of rehydration, increasing exposed surface area (Wu et al., 2014). Such changes have the potential to be documented using laser-scanning approaches, as in vascular plants (Puttonen et al., 2016), providing a direct link between shoot scale dynamics and canopy surface roughness. Due to their small size, bryophytes are also particularly amenable to imaging chlorophyll fluorescence approaches (e.g., Coe et al., 2012; Stanton et al., 2014; Malenovský et al., 2015), making it possible to

combine architectural imaging and photosynthetic measurement into synchronous evaluations of physiological activity.

## PROMISING DIRECTIONS

Bryophytes offer a number of promising avenues for future research. The small size and high plasticity of bryophytes make them particularly amenable to large replication at low cost, especially as improvements in image processing allow for increasing automatization. A future expansion from two-dimensional to three-dimensional image processing and analytics will unlock applications to a wide range of organisms where branching has recently been shown to be ecologically informative, such as algae (Koehl et al., 2008; Demes et al., 2013) and lichens (Stanton and Horn, 2013; Esseen et al., 2015).

Although there have been numerous recent applications of innovative geometric approaches to bryophytes (e.g., Reeb, 2014;

Rice and Cornelissen, 2014; Coudert et al., 2015; Renner, 2015; Rose et al., 2016), the field is still very young and ripe for further exploration. We suggest that advances should come from two-way dialog: the translation and adoption of techniques developed for vascular plants (and other organisms) to bryophytes and the use of bryophytes as model systems for the innovation of new techniques and paradigms in morphogeometric approaches. This will require bryologists to adopt or adapt some terms and concepts used for vascular plants, but also for researchers more familiar with vascular plants to acknowledge and incorporate the complexity of bryophyte form and function, rather than misleadingly characterizing them as “primitive and boring”.

## AUTHOR CONTRIBUTIONS

All authors listed, have made substantial, direct and intellectual contribution to the work, and approved it for publication.

## REFERENCES

- Abley, K., De Reuille, P., Strutt, D., Bangham, A., Prunsinkiewicz, P., Marée, A., et al. (2013). An intracellular partitioning-based framework for tissue cell polarity in plants and animals. *Development* 140, 2061–2074. doi: 10.1242/dev.062984
- Acosta-Mercado, D., Cancel-Morales, N., Chinea, N., Santos-Flores, C., and De Jesus, I. (2012). Could the canopy structure of bryophytes serve as an indicator of microbial biodiversity? A test for testate amoebae and microcrustaceans from a subtropical cloud forest in Dominican Republic. *Microb. Ecol.* 65, 206–213. doi: 10.1007/s00248-011-0004-8
- Ambruster, W. S., Pélabon, C., Bolstad, G. H., and Hansen, T. F. (2014). Integrated phenotypes: understanding trait covariation in plants and animals. *Philos. Trans. R. Soc. B* 369, 1–16. doi: 10.1098/rstb.2013.0245
- Araus, J. L., and Cairns, J. E. (2014). Field high-throughput phenotyping: the new crop breeding frontier. *Trends Plant Sci.* 19, 52–61. doi: 10.1016/j.tplants.2013.09.008
- Ashton, N., Grimsley, N., and Cove, D. (1979). Analysis of gametophytic development in the moss, *Physcomitrella patens*, using auxin and cytokinin resistant mutants. *Planta* 144, 427–435. doi: 10.1007/BF00380118
- Atala, C. (2011). Water transport and gas exchange in the non-vascular plant *Dendroligotrichum dendroides* (Brid. ex Hedw.) Broth. (Polytrichaceae, Bryophyta). *Gayana Bot.* 68, 89–92. doi: 10.4067/S0717-66432011000100008
- Atala, C., and Alfaro, J. (2012). Vascular architecture of the dendroid antipodean moss *Dendroligotrichum dendroides* (Brid. ex Hedw.) Broth. (Polytrichaceae). *J. Bryol.* 34, 277–280. doi: 10.1179/1743282012Y.0000000032
- Bennett, T., Liu, M., Aoyama, T., Bierfreuer, N., Braun, M., Coudert, Y., et al. (2014). Plasma membrane-targeted PIN proteins drive shoot development in a moss. *Curr. Biol.* 24, 2776–2785. doi: 10.1016/j.cub.2014.09.054
- Berthier, J. (1970). Organisation à l'aisselle des feuilles chez les Bryophytes. *Bull. Soc. Bot. Fr.* 117, 171–182. doi: 10.1080/00378941.1970.10838824
- Birse, E. (1957). Ecological studies on growth form in bryophytes. II Experimental studies on growth form in mosses. *J. Ecol.* 45, 721–733. doi: 10.2307/2256954
- Bischler-Causse, H. (1993). *Marchantia* L. The European and African taxa. *Bryophyt. Bibl.* 45, 1–129.
- Bonhomme, S., Nogué, F., Rameau, C., and Schaefer, D. (2013). “Usefulness of *Physcomitrella patens* for studying plant organogenesis,” in *Plant Organogenesis: Methods and Protocols*, ed. I. D. Smet (New York, NY: Springer Science), 21–43.
- Bookstein, F. (1991). *Morphometric Tools for Landmark Data: Geometry and Biology*. Cambridge: Cambridge University Press.
- Bowman, J., Araki, T., and Kohchi, T. (2016). Marchantia: past, Present Future. *Plant Cell Physiol.* 57, 205–209. doi: 10.1093/pcp/pcw023
- Buck, W. B., and Goffinet, B. (2009). “Morphology and classification of mosses,” in *Bryophyte Biology*, eds. B. Goffinet and A. J. Shaw (New York, NY: Cambridge University Press), 55–138.
- Bucksch, A., Burridge, J., York, L. M., Das, A., Nord, E., Weitz, J. S., et al. (2014). Image-based high-throughput field phenotyping of crop roots. *Plant Physiol.* 166, 470–486. doi: 10.1104/pp.114.243519
- Buryová, B., and Shaw, A. J. (2005). Phenotypic plasticity in *Philonotis fontana* (Bryopsida: Bartramiales). *J. Bryol.* 27, 13–22. doi: 10.1179/174328205X40545
- Cano, M., Werner, O., and Guerra, J. (2006). A morphometric and molecular study in *Tortula subulata* complex (Pottiaceae, Bryophyta). *Bot. J. Linn. Soc.* 149, 333–350. doi: 10.1111/j.1095-8339.2005.00456.x
- Castellanos, A., Mooney, H., Bullock, H., Jones, C., and Robichaux, R. (1989). Leaf, stem, and metamer characteristics of vines in a tropical deciduous forest in Jalisco, Mexico. *Biotropica* 21, 41–49.
- Chang, Y., and Graham, S. (2011). Inferring the higher-order phylogeny of mosses (Bryophyta) and relatives using a large, multigene plastid data set. *Am. J. Bot.* 98, 839–849. doi: 10.3732/ajb.0900384
- Clap, G. (1912). The life history of *Aneura pinguis*, contribution from the Hull laboratory. *Bot. Gaz.* 14, 177–192. doi: 10.1086/330898
- Coe, K. K., Belnap, J., Grote, E. E., and Sparks, J. P. (2012). Physiological ecology of desert biocrust moss following 10 years exposure to elevated CO<sub>2</sub>: evidence for enhanced photosynthetic thermotolerance. *Physiol. Plant.* 144, 346–356. doi: 10.1111/j.1399-3054.2012.01566.x
- Coudert, Y., Palubicki, W., Ljung, K., Novak, O., Leyser, O., and Harrison, C. J. (2015). Three ancient hormonal cues co-ordinate shoot branching in a moss. *Elife* 4:e06808. doi: 10.7554/elife.06808
- Crandall-Stotler, B., Stotler, R. E., and Long, D. G. (2008). “Morphology and classification of the Marchantiophyta,” in *Bryophyte Biology*, 2nd Edn, eds B. Goffinet and A. J. Shaw (Cambridge: University Press), 155–198.
- Davy de Virville, A. D. (1927–1928). L'action du milieu sur les mousses. *Rev. Gen. Bot.* 462, 364–383; 463, 450–457; 464, 515–522; 465, 560–586; 466, 639–662; 467 711–726; 468, 768–883; 469, 30–44; 470, 95–110; 471, 156–173+18 Plates.
- Dayrat, B. (2005). Towards integrative taxonomy. *Biol. J. Linn. Soc.* 85, 407–415. doi: 10.1111/j.1095-8312.2005.00503.x
- De Luna, E., and Gomez-Velasco, G. (2008). Morphometrics and the identification of *Braunia andrieuxii* and *B. secunda* (Hedwigiaeae, Bryopsida). *Syst. Bot.* 33, 219–228. doi: 10.1600/036364408784571608
- Demes, K. W., Harley, C. D. G., Anderson, L. M., and Carrington, E. (2013). Shifts in morphological and mechanical traits compensate for performance costs of reproduction in a wave-swept seaweed. *J. Ecol.* 101, 963–970. doi: 10.1111/1365-2745.12099
- Dickinson, T. A., Parker, W. H., and Strauss, R. E. (1987). Another approach of leaf shape comparisons. *Taxon* 36, 1–20. doi: 10.2307/1221345
- Diggle, P. K. (2014). Modularity and intra-floral integration in metameric organisms: plants are more than the sum of their parts. *Philos. Trans. R. Soc. B* 369, 20130253. doi: 10.1098/rstb.2013.0253
- Eble, G. (2005). “Morphological modularity and macroevolution: conceptual and empirical aspects,” in *Modularity: Understanding the Development and*

- Evolution of Natural Complex Systems*, eds W. Callebaut and D. Rasskin-Gutman (Cambridge, MA: MIT Press), 221–238.
- Elumeeva, T., Soudzilovskaya, N., During, H. J., and Cornelissen, J. H. C. (2011). The importance of colony structure versus shoot morphology for the water balance of 22 subarctic bryophyte species. *J. Veg. Sci.* 22, 152–164. doi: 10.1111/j.1654-1103.2010.01237.x
- Esseen, P.-A., Olsson, T., Coxson, D., and Gauslaa, Y. (2015). Morphology influences water storage in hair lichens from boreal forest canopies. *Fungal Ecol.* 18, 26–35. doi: 10.1016/j.funeco.2015.07.008
- Ferso, S., Rohlf, F. J., and Koehn, R. K. (1985). Measuring shape variation of two-dimensional outlines. *Syst. Zool.* 34, 59–68. doi: 10.2307/2413345
- Forman, R. (1964). Growth under controlled conditions to explain the hierarchical distributions of a moss, *Tetraphis pellucida*. *Ecol. Monogr.* 34, 1–25. doi: 10.2307/1948461
- Fujita, T., and Hasebe, M. (2009). Convergences and divergences in polar auxin transport and shoot development in land plant evolution. *Plant Sign. Behav.* 4, 313–315. doi: 10.4161/psb.4.4.8090
- Glime, J., and Raeymaekers, G. (1987). Temperature effects on branch and rhizoid production in six species of *Fontinalis*. *J. Bryol.* 14, 779–789. doi: 10.1179/jbr.1987.14.4.779
- Goethe, J. W. (1790). *Versuch die Metamorphose der Pflanzen zu erklären*. Stuttgart: Carl Wilhelm Ettinger.
- Goffinet, B., and Buck, W. (2013). The evolution of body form in Bryophytes. *Ann. Plant Rev.* 45, 51–90.
- Gonzalez-Mancebo, J., Patino, J., Rodriguez-Romero, A., Werner, O., and Ros, R. (2010). Gymnostomiella (Pottiaceae, Bryophyta) revisited: new insights revealed by a morphometric analysis. *Nova Hedwigia* 138, 69–83.
- Grueber, W., Jan, L., and Jan, Y. (2002). Tiling of the *Drosophila epidermis* by multidendritic sensory neurons. *Development* 129, 2867–2878.
- Guimera, R., Danon, L., Diaz-Guilera, A., Giralt, F., and Arenas, A. (2006). The real communication network behind the formal chart: community structure in organizations. *J. Econ. Behav. Organ.* 61, 653–667. doi: 10.1016/j.jebo.2004.07.021
- Hallé, F., Oldeman, R., and Tomlinson, P. (1978). *Tropical Trees and Forests: An Architectural Analysis*. Dordrecht: Springer.
- Hébant, C. (1977). *The Conducting Tissues of Bryophytes*. Vaduz: J. Cramer.
- Hewson, H. J. (1970). The family Aneuraceae in Australia and New Guinea: the genus *Riccardia*. *Proc. Linn. Soc. N. S. W.* 94, 61–121.
- Jensen, R. J. (2003). - The conundrum of morphometrics. *Taxon* 52, 663–671. doi: 10.2307/3647340
- Jones, C. S. (1993). Heterochrony and heteroblastic leaf development in two subspecies of *Cucurbita argyrosperma* (Cucurbitaceae). *Am. J. Bot.* 80, 778–795. doi: 10.2307/2445598
- Jones, V. A. S., and Dolan, L. (2012). The evolution of root hairs and rhizoids. *Ann. Bot.* 110, 205–212. doi: 10.1093/aob/mcs136
- Kaandorp, J. (1999). Morphological analysis of growth forms of branching marine sessile organisms along environmental gradients. *Mar. Biol.* 134, 295–306. doi: 10.1007/s002270050547
- Kaandorp, J., and Kübler, J. (2001). *The Algorithmic Beauty of Seaweeds, Sponges and Corals*. Dordrecht: Springer.
- Klingenberg, C. P. (2014). Studying morphological integration and modularity at multiple levels: concepts and analysis. *Philos. Trans. R. Soc. B* 369:20130249. doi: 10.1098/rstb.2013.0249
- Koehl, M. A. R., Silk, W. K., Liang, H., and Mahadevan, L. (2008). How kelp produce blade shapes suited to different flow regimes: a new wrinkle. *Integr. Comp. Biol.* 48, 834–851. doi: 10.1093/icb/icn069
- Krumnikl, M., Sojka, E., Gaura, J., and Motyka, O. (2010). “Three-dimensional reconstruction of macroscopic features in biological materials,” in *BIOSTEC 2009*, eds A. Fred, J. Filipe, and H. Gamboa (Berlin: Springer-Verlag), 225–234.
- Kruszynski, K. J. (2010). *Interactive Measurements of Three-Dimensional Branching Objects*. Eindhoven: Technische Universiteit Eindhoven.
- La Farge, C. (1996). Growth form, branching pattern and perichaetal position in mosses: cladocarp and pleurocarp revisited. *Bryologist* 99, 170–186. doi: 10.2307/3244546
- Le Bot, J., Serra, V., Fabre, J., Draye, X., Adamowicz, S., and Pags, L. (2009). DART: a software to analyse root system architecture and development from captured images. *Plant Soil* 326, 261–273. doi: 10.1007/s11104-009-0005-2
- Ligrone, R., Duckett, J., and Renzaglia, K. (2000). Conducting tissues and phyletic relationships of bryophytes. *Philos. Trans. R. Soc. B* 355, 795–813. doi: 10.1098/rstb.2000.0616
- Ligrone, R., Duckett, J., and Renzaglia, K. (2012). Major transitions in the evolution of early land plants: a bryological perspective. *Ann. Bot-Lond.* 109, 851–871. doi: 10.1093/aob/mcs017
- Lindo, Z., and Gonzalez, A. (2010). The bryosphere: an integral and influential component of the earth’s biosphere. *Ecosystems* 13, 612–627. doi: 10.1007/s10021-010-9336-3
- Lüttge, U. (2012). Modularity and emergence: biology’s challenge in understanding life. *Plant Biol.* 14, 865–871. doi: 10.1111/j.1438-8677.2012.00659.x
- MacLeod, N. (2002). “Phylogenetic signals in morphometric data,” in *Morphology, Shape and Phylogeny*, eds N. MacLeod and P. L. Forey (London: Taylor and Francis).
- Malenovský, Z., Turnbull, J. D., Lucieer, A., and Robinson, S. A. (2015). Antarctic moss stress assessment based on chlorophyll content and leaf density retrieved from imaging spectroscopy data. *New Phytol.* 208, 608–624. doi: 10.1111/nph.13524
- McKay, B. D. (2013). The use of digital photography in systematics. *Biol. J. Linn. Soc.* 110, 1–13. doi: 10.1111/bij.12086
- McQueen, C. B. (1991). Laboratory and greenhouse cultures and the experimental taxonomy of bryophytes. *Adv. Bryol.* 4, 103–120.
- Medina, N., Lara, F., Mazimpaka, V., Albertos, B., and Hortal, J. (2015). Epiphytic bryophytes of *quercus* forests in central and north inland iberian peninsula. *Front. Biogeogr.* 7:21–28.
- Medina, R., Lara, F., Goffinet, B., Garilleti, R., and Mazimpaka, V. (2012). Integrative taxonomy successfully resolves the pseudo-cryptic complex of the disjunct epiphytic moss *Orthotrichum consimile* s.l. (Orthotrichaceae). *Taxon* 61, 1180–1198.
- Mishler, B., and De Luna, E. (1991). The use of ontogenetic data in phylogenetic analysis. *Adv. Bryol.* 4, 123–167.
- Murren, C. J. (2012). The integrated phenotype. *Int. Comp. Biol.* 52, 64–76. doi: 10.1093/icb/ics043
- Niklas, K. (1994). *Plant Allometry*. Chicago, IL: University of Chicago Press.
- Oldeman, R. (1977). L’architecture de la forêt Guyanaise. *Mém. l’ORSTOM* 73, 1–204.
- Pereira, M. R., de, S., Dambros, C., and Zartman, C. E. (2013). Will the real *Syrrhopodon leprieurii* please stand up? The influence of topography and distance on phenotypic variation in a widespread Neotropical moss. *Bryologist* 113, 58–64. doi: 10.1639/0007-2745-116.1.058
- Pigliucci, M. (2003). Phenotypic integration: studying the ecology and evolution of complex phenotypes. *Ecol. Lett.* 6, 265–272. doi: 10.1111/jeb.12879
- Prigge, M. J., and Bezanilla, M. (2010). Evolutionary crossroads in developmental biology: *Physcomitrella patens*. *Development* 137, 3535–3543. doi: 10.1242/dev.049023
- Puttonen, E., Briese, C., Mandlburger, G., Wieser, M., Pfennigbauer, M., Zlinszky, A., et al. (2016). Quantification of overnight movement of birch (*Betula pendula*) branches and foliage with short interval terrestrial laser scanning. *Front. Plant Sci.* 7:222. doi: 10.3389/fpls.2016.00222
- Reeb, C. (2014). *Taxonomie Intégrative du Genre Riccardia, Aneuraceae pour l’Afrique*. Dissertation. Muséum National d’Histoire Naturelle, Paris.
- Renner, M., Devos, N., and Shaw, J. (2010). *Radula splendida* sp. nov. (Radulaceae: Marchantiophyta), a polymorphic species from New Zealand. *Nova Hedwigia* 90, 105–122. doi: 10.1127/0029-5035/2010/0090-0105
- Renner, M. A. M. (2015). Lobule shape evolution in *Radula* (Jungermanniopsida): one rate fits all? *Bot. J. Linn. Soc.* 178, 222–242. doi: 10.1111/bj.12279
- Renner, M. A., Devos, N., Jairo, P., Brown, E., Orme, A., Elgey, M., et al. (2013). Integrative taxonomy resolves the cryptic and pseudo-cryptic *Radula buccinifera* complex (Porellales, Jungermanniopsida), including two reinstated and five new species. *PhytoKeys* 27, 1–113. doi: 10.3897/phytokeys.27.5523
- Renner, M. A. M., Brown, E. A., and Wardle, G. B. (2013a). Averaging v. outlier removal. Decoding variance among cryptic *Lejeunea* species (Lejeuneaceae: Jungermanniopsida) using geometric morphometrics. *Aus. Syst. Bot.* 26, 13–30. doi: 10.1071/SB12016
- Renner, M. A. M., Devos, N., Brown, E. A., and von Konrat, M. J. (2013b). Three modes of heterochrony explain lobule diversity in *Radula* subgenus Cladoradula (Porellales: Jungermanniopsida), a small lineage of early land plants today. *Bot. J. Linn. Soc.* 173, 153–175. doi: 10.1111/bj.12087

- Rensing, S. A., Lang, D., Zimmer, A. D., Terry, A., Salamov, A., Shapiro, H., et al. (2008). The physcomitrella genome reveals evolutionary insights into the conquest of land by plants. *Science* 319, 64–69. doi: 10.1126/science.1150646
- Renzaglia, K. (1982). A comparative developmental investigation of the gametophyte generation in the Metzgeriales (Hepaticophyta). *Bryophyt. Bibl.* 24, 1–234.
- Rice, S., Collins, D., and Anderson, A. (2001). Functional significance of variation in bryophyte canopy structure. *Am. J. Bot.* 88, 1568–1576. doi: 10.2307/3558400
- Rice, S., and Cornelissen, J. H. C. (2014). “Best practices for measuring photosynthesis at multiple scales,” in *Photosynthesis in Bryophytes and Early Land Plants, Advances in Photosynthesis and Respiration* 37, eds D. Hanson and S. Rice (Dordrecht: Springer), 79–93.
- Rice, S., Gutman, C., and Krouglicof, N. (2005). Laser scanning reveals bryophyte canopy structure. *New Phytol.* 166, 695–704. doi: 10.1111/j.1469-8137.2005.01327.x
- Rice, S., and Schneider, N. (2004). Cushion size, surface roughness and the control of water balance and carbon flux in the cushion moss *Leucobryum glaucum* (Leucobryaceae). *Am. J. Bot.* 91, 1164–1172. doi: 10.3732/ajb.91.8.1164
- Rose, J., Kriebel, R., and Sytsma, K. (2016). Shape analysis of moss (Bryophyta) sporophytes: insights into land plant evolution. *Am. J. Bot.* 103, 1–11. doi: 10.3732/ajb.1500394
- Schindelin, J., Arganda-Carreras, I., Frise, E., Kaynig, V., Longair, M., Pietzsch, T., et al. (2012). Fiji: an open-source platform for biological-image analysis. *Nat. Methods* 9, 676–682. doi: 10.1038/nmeth.2019
- Schuster, R. (1966). *The Hepaticae and Anthocerotae of North America*. New York, NY: Columbia University Press.
- Shaw, A. J., Szovenyi, P., and Shaw, B. (2011). Bryophyte diversity and evolution: windows into the early evolution of land plants. *Am. J. Bot.* 98, 252–369. doi: 10.3732/ajb.1000316
- Sneath, P., and Sokal, R. (1973). *Numerical Taxonomy: the Principles and Practice of Numerical Classification*. San Francisco, CA: W.H. Freeman.
- Stanton, D. E., and Horn, H. (2013). Epiphytes as “filter-drinkers”: life form changes across a fog gradient. *Bryologist* 116, 34–42. doi: 10.1639/0007-2745-116.1.034
- Stanton, D. E., Merlin, M., Bryant, G., and Ball, M. C. (2014). Water redistribution determines photosynthetic responses to warming and drying in two polar mosses. *Funct. Plant Biol.* 41, 178–186. doi: 10.1071/FP13160
- Strahler, A. (1952). Hypsometria (area-altitude) analysis of erosional topography. *Bull. Geol. Soc.* 63, 1167–1177. doi: 10.1130/0016-7606(1952)63[1117:HAAOET]2.0.CO;2
- Tarboton, D. (1996). Fractal rivers, Horton's laws and Tokunaga cyclicity. *J. Hydrol.* 187, 105–117. doi: 10.1016/S0022-1694(96)03089-2
- Vanderpoorten, A., and Goffinet, B. (2009). *Introduction to Bryophyte Biology*. Cambridge: Cambridge University Press.
- Vanderpoorten, A., Hedenäs, L., and Jacquemart, A.-L. (2003). Differentiation in DNA Fingerprinting and Morphology among Species of the Pleurocarpus Moss Genus, *Rhytidadelphus* (Hylocomiaceae). *Taxon* 52, 229–236. doi: 10.2307/3647391
- Waite, M., and Sack, L. (2010). How does moss photosynthesis relate to leaf and canopy structure? Trait relationships for 10 Hawaiian species of contrasting light habitats. *New Phytol.* 185, 156–172. doi: 10.1111/j.1469-8137.2009.03061.x
- Wu, N., Zhang, Y., Downing, A., Aanderud, Z., Tao, Y., and Steven, W. (2014). Rapid adjustment of leaf angle explains how the desert moss, *Syntrichia caninervis*, copes with multiple resource limitations during rehydration. *Funct. Plant Biol.* 41, 168–177. doi: 10.1071/FP13054
- Xu, B., Ohtani, M., Yamaguchi, M., Toyooka, K., Wakazaki, M., Sato, M., et al. (2014). Contribution of NAC transcription factors to plant adaptation to land. *Science* 343, 1505–1508. doi: 10.1126/science.1248417
- Yu, Y., Degnam, J., and Nakhleh, L. (2012). The probability of a gene tree topology within a phylogenetic network with applications to hybridization detection. *PLoS Genet.* 8:e1002660. doi: 10.1371/journal.pgen.1002660
- Zanardo, S., Zaliapin, I., and Foulaoula-Giorgio, E. (2013). Are american rivers tokunaga self-similar? New results on fluvial network topology and its climatic dependence. *J. Geophys. Res.* 118, 1–18.
- Zotz, G., Schweikert, A., Jetz, A., and Westerman, H. (2000). Water relations and carbon gain are closely related to cushion size in the moss *Grimmia pulvinata*. *New Phytol.* 148, 59–67. doi: 10.1046/j.1469-8137.2000.00745.x

**Conflict of Interest Statement:** The authors declare that the research was conducted in the absence of any commercial or financial relationships that could be construed as a potential conflict of interest.

The reviewer MR declared a past co-authorship with one of the authors CR to the handling Editor, who ensured that the process met the standards of a fair and objective review.

Copyright © 2016 Stanton and Reeb. This is an open-access article distributed under the terms of the Creative Commons Attribution License (CC BY). The use, distribution or reproduction in other forums is permitted, provided the original author(s) or licensor are credited and that the original publication in this journal is cited, in accordance with accepted academic practice. No use, distribution or reproduction is permitted which does not comply with these terms.



# Reshaping Plant Biology: Qualitative and Quantitative Descriptors for Plant Morphology

**Mathilde Balduzzi<sup>1</sup>, Brad M. Binder<sup>2</sup>, Alexander Bucksch<sup>3,4,5</sup>, Cynthia Chang<sup>6</sup>, Lilan Hong<sup>7</sup>, Anjali S. Iyer-Pascuzzi<sup>8</sup>, Christophe Pradal<sup>1,9</sup> and Erin E. Sparks<sup>10\*</sup>**

<sup>1</sup> INRIA, Virtual Plants, Montpellier, France, <sup>2</sup> Department of Biochemistry and Cellular and Molecular Biology, University of Tennessee-Knoxville, Knoxville, TN, USA, <sup>3</sup> Department of Plant Biology, University of Georgia, Athens, GA, USA, <sup>4</sup> Warnell School of Forestry and Environmental Resources, University of Georgia, Athens, GA, USA, <sup>5</sup> Institute of Bioinformatics, University of Georgia, Athens, GA, USA, <sup>6</sup> Division of Biological Sciences, University of Washington-Bothell, Bothell, WA, USA, <sup>7</sup> Weill Institute for Cell and Molecular Biology and Section of Plant Biology, School of Integrative Plant Sciences, Cornell University, Ithaca, NY, USA, <sup>8</sup> Department of Botany and Plant Pathology, Purdue University, West Lafayette, IN, USA, <sup>9</sup> CIRAD, UMR AGAP, Montpellier, France, <sup>10</sup> Department of Biology, Duke University, Durham, NC, USA

## OPEN ACCESS

**Edited by:**

Hartmut Stützel,  
Leibniz University of Hanover,  
Germany

**Reviewed by:**

Stanislaus Josef Schymanski,  
ETH Zurich, Switzerland  
Gerhard Buck-Sorlin,  
Agrocampus Ouest, France

**\*Correspondence:**

Erin E. Sparks  
[erin.sparks@duke.edu](mailto:erin.sparks@duke.edu)

**Specialty section:**

This article was submitted to  
Plant Biophysics and Modeling,  
a section of the journal  
*Frontiers in Plant Science*

**Received:** 23 August 2016

**Accepted:** 19 January 2017

**Published:** 03 February 2017

**Citation:**

Balduzzi M, Binder BM, Bucksch A, Chang C, Hong L, Iyer-Pascuzzi AS, Pradal C and Sparks EE (2017) Reshaping Plant Biology: Qualitative and Quantitative Descriptors for Plant Morphology. *Front. Plant Sci.* 8:117.  
doi: 10.3389/fpls.2017.00117

An emerging challenge in plant biology is to develop qualitative and quantitative measures to describe the appearance of plants through the integration of mathematics and biology. A major hurdle in developing these metrics is finding common terminology across fields. In this review, we define approaches for analyzing plant geometry, topology, and shape, and provide examples for how these terms have been and can be applied to plants. In leaf morphological quantifications both geometry and shape have been used to gain insight into leaf function and evolution. For the analysis of cell growth and expansion, we highlight the utility of geometric descriptors for understanding sepal and hypocotyl development. For branched structures, we describe how topology has been applied to quantify root system architecture to lend insight into root function. Lastly, we discuss the importance of using morphological descriptors in ecology to assess how communities interact, function, and respond within different environments. This review aims to provide a basic description of the mathematical principles underlying morphological quantifications.

**Keywords:** morphology, topology, geometry, leaf, hypocotyl, sepal, roots, ecology

## INTRODUCTION

The purpose of this review is to provide a common language from which biologists and mathematicians can begin a conversation on quantifying plant morphology. The idea was conceived from the National Institute for Mathematical and Biological Synthesis (NIMBioS) workshop on Plant Morphological Modeling. In this workshop, mathematicians and biologists came together to discuss how to advance the field of plant morphology. In small group discussions, we found that a substantial portion of our time was spent trying to understand what the other discipline meant when using the same words. In light of this, we decided to write a basic primer on the definition of common morphological quantifications and how they can be applied to plants. The goal of this review is to provide an introductory basis for further discussion and collaboration between math and biology.

## ONTOLOGIES FOR PLANT MORPHOLOGY

High quality morphological descriptions are critical for our understanding of biological systems, because often the appearance of a structure (e.g., leaf, cell, etc.) drives functionality (e.g., flux, nutrient transport, etc.). However, translating the visual appearance of complex organisms into qualitative and quantitative metrics remains a significant challenge in biology and mathematics. A major hurdle in advancing morphological studies is to find a common language for biologists and mathematicians to communicate. Ontologies are used to provide a common reference vocabulary (Planteome; Cooper and Jaiswal, 2016), and specific ontologies have been developed for plant structural descriptions (Plant Structural Ontologies; Ilic et al., 2007). However, these descriptions often focus on the biology and do not provide definitions for mathematical concepts. In this review we present our consensus on the definition and application of mathematical terms to describe the appearance of plant organs. While other interpretations can be considered, this review aims to provide a basic ontology of plant morphology to initiate interdisciplinary collaborations between biologists and mathematicians.

### Biological and Hierarchical Scales

Plants are complex systems and their morphology can be quantified at many different biological scales ranging from genes to organs to communities. In addition, there are hierarchical scales that encompass each of these biological scales in both space and time. Although morphology is generally quantified at a single biological scale, relating quantifications across scales is critical to improve our understanding of how morphology impacts physiology, growth, development, and ecology.

To illustrate morphological transformations across biological scales, consider how neighboring root systems influence a plant community. In response to neighbors, a plant may alter root growth and development (Chen et al., 2012). This response is mediated through multi-scale signals and transformations (Figure 1). The process begins with changes at the gene expression or protein function level as a consequence of the genotype and/or external stimuli, in this case a neighboring plant. These alterations then lead to local changes at the cellular-level. For organ growth, the cell wall properties are altered to promote or inhibit expansion. For organ development, changes at the cellular level lead to cell divisions and influence the surrounding cells to enable new organ emergence. These cellular-level changes then mediate tissue-level changes, by communication with neighboring cells. Due to the constraints imposed by a cell wall in plants, one cell cannot grow or expand without support from its neighbors. The tissue-level changes then mediate organ level changes, which translate to the phenotype of the community. The community then relays signals back to the plant to mediate changes in gene expression or function and initiate the cycle again (Figure 1). This example is an over-simplification and in reality feedback occurs at each stage of the biological scales (Figure 2). Adding to the complexity, each of these biological scales can be analyzed

on hierarchical scales of space and time (Figure 2). When designing an experiment that relies on plant morphological quantifications it is important to consider both the biological scale (from genes to ecosystems) and hierarchical scale. Later in this review we will provide specific examples at different biological scales.

### Image Acquisition and Data Reporting

Morphological measurements can be derived from different approaches including manual three-dimensional (3D) digitizing measurements (Sinoquet and Rivet, 1997; Godin et al., 1999) or image analyses (Li et al., 2014). We focus our discussion on image analysis approaches since manual measurements can be time consuming, low throughput, and subject to human error. Images can be generated in 2D or 3D, although both are generally expressed within a Cartesian coordinate system, denoted (x,y) and (x,y,z) respectively. In a 2D image, each discrete x,y coordinate is referred to as a pixel; similarly, in 3D the image coordinates are called voxels.

When considering the image acquisition system, it is first important to consider the scale of the process and resolution of the imaging system. For example, if a research question address tissue-level changes, it is likely that the resolution of digital microscopy is preferred to standard photography. In addition, the sampling frequency (static image versus time-series), physical scale (nanometers to meters), precision and accuracy required should be considered. Regardless of the image acquisition system (microscopy, X-ray tomography, photography, etc.) pre-processing is an essential first step. Pre-processing generally includes smoothing of the obtained imaging data to correct for noise of the imaging system. Once the noise has been reduced, the images can be used to extract morphological measurements. We refer the reader to the following resources for an in depth review on image processing techniques (Jain, 1989; Hartley and Zisserman, 2005), the available automation packages (Abramoff et al., 2004; Kuijken et al., 2015; Rousseau et al., 2015) and tools for computational reproducibility (Piccolo and Frampton, 2016).

After pre-processing, images may be analyzed with tools that are developed for a specific purpose or currently available. The online resource <http://www.plant-image-analysis.org> curates currently available tools for morphological plant image analysis and enables user feedback and ratings (Lobet et al., 2013). Regardless of the analysis, adhering to minimum standards for data reporting is vitally important for reproducibility. We emphasize the adoption of the Minimum Information About a Plant Phenotyping Experiment (MIAPPE; <http://www.miappe.org/>; Krajewski et al., 2015) standards.

### What is Shape?

As biologists, we often refer to the “shape” of an organ when we are describing morphology, however, this term can encompass a wide variety of mathematical parameters. Most often we are referring to the most intuitive quantification, geometry, which is used to establish measurable sizes of the plant organ surface. In this section we will define the mathematical tools that can be

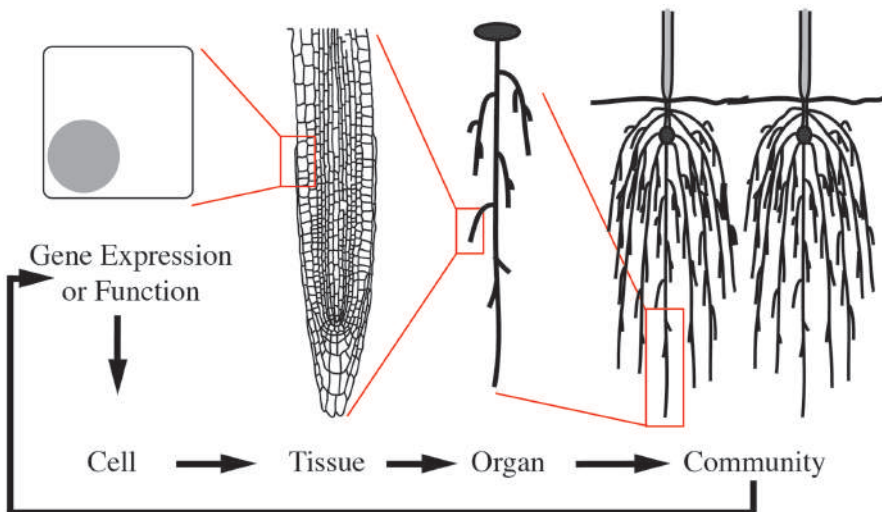
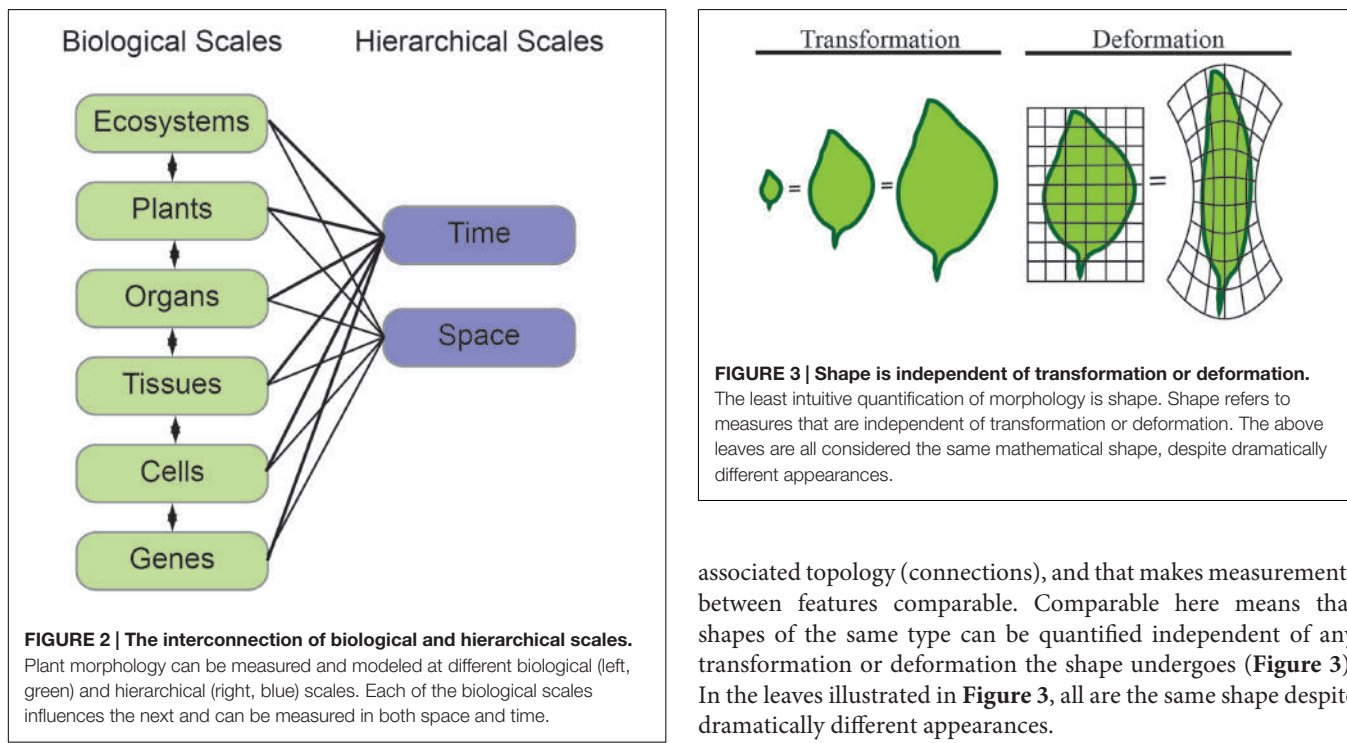
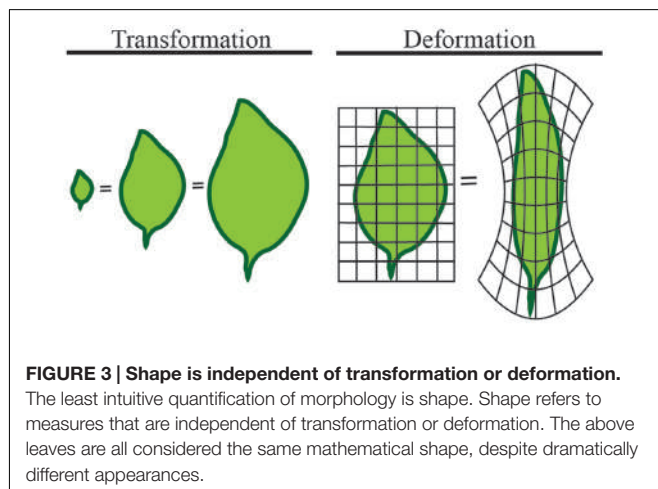


**FIGURE 1 | Morphological changes are mediated through cyclic multi-scale signals and transformations.** A multi-scale morphology transformation is illustrated by neighbor detection between root systems. Morphological changes are initiated through developmental or environmental cues that induce changes in gene expression or function. These alterations lead to local changes at the cellular-level, which are then translated to the tissue- and organ-level. Organ-level changes then lead to an altered community. The community and environmental signals then feedback to mediate gene expression or functional changes in a continuous loop.



used to describe “shape” as a frame of reference for a biologist interested in morphological analyses.

We will first define shape in mathematical terms to provide a basis for the quantitative measures to follow. The mathematical concept of shape is difficult to represent because it differs from its geometric counterpart. A shape refers to the form of an object that may have several geometric representations, but an invariant



associated topology (connections), and that makes measurements between features comparable. Comparable here means that shapes of the same type can be quantified independent of any transformation or deformation the shape undergoes (**Figure 3**). In the leaves illustrated in **Figure 3**, all are the same shape despite dramatically different appearances.

One way to overcome this challenge is to represent the shape as a set of points on the surface of the object with defined coordinates. As the shape changes each point can be tracked through the transformation process. As a result, the transformation can be expressed with a matrix, and consecutive transformations can be expressed as the product of their matrices. Transformations inherit the geometrical and algebraic properties of matrices, which has the benefit that known rules of linear algebra apply. For instance, the determinant of a  $2 \times 2$

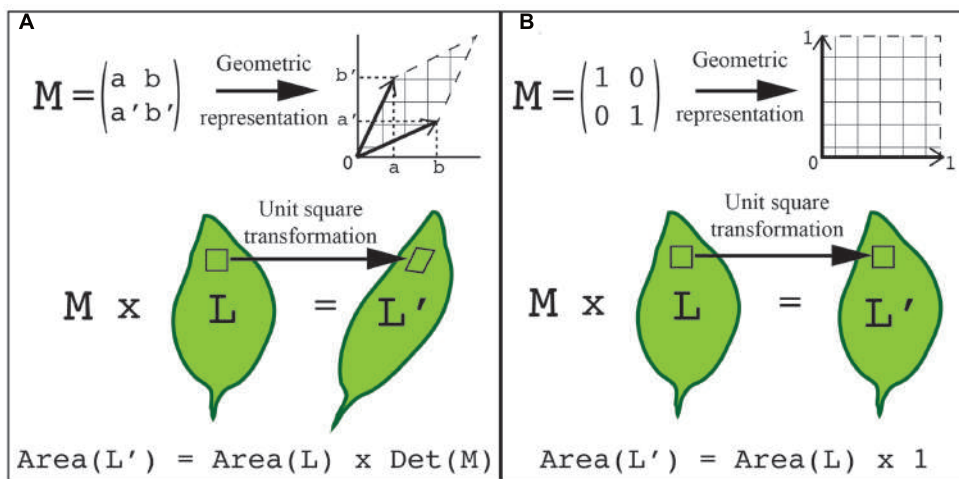


**FIGURE 4 | Using transformations to quantify shape.** The points on the surface of an object can be represented with defined coordinates. These points can then be transformed by applying a transformation matrix. **(A)** A generalized representation of applying a transformation matrix to quantify shape. **(B)** An example of a unit transformation for shape changes. **(A,B)** In both examples, a 2x2 transformation matrix, M, can be visualized as a table of two column vectors (top left) or by geometric representation (top right). This same transformation can be visualized on a leaf. Each unit square that composes the organ surface can be transformed into the geometric shape associated with the transformation matrix (middle). The total area of the transformed organ is equal to the original leaf area times the transformation matrix determinant, which is the area formed by the two vectors (bottom). In the unit transformation matrix example, the matrix determinant,  $\text{Det}(M)$ , is equal to 1.

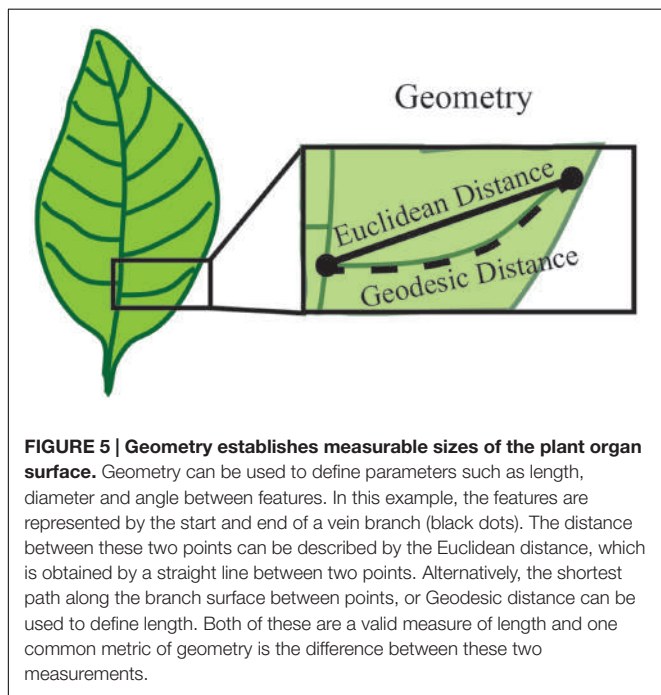


**FIGURE 5 | Geometry establishes measurable sizes of the plant organ surface.** Geometry can be used to define parameters such as length, diameter and angle between features. In this example, the features are represented by the start and end of a vein branch (black dots). The distance between these two points can be described by the Euclidean distance, which is obtained by a straight line between two points. Alternatively, the shortest path along the branch surface between points, or Geodesic distance can be used to define length. Both of these are a valid measure of length and one common metric of geometry is the difference between these two measurements.

matrix (where the determinant of matrix  $[a,b; c,d] = ad-bc$ ) is equal to the area of the parallelogram defined by the column vectors of the matrix (**Figure 4**). Consequently, the area  $A'$  of a shape transformed by a matrix M equals the area A of the original shape times the determinant of the matrix (i.e.,  $A' = A \cdot \text{det}(M)$ ). In this way, the application of two consecutive transformations represented by the two matrices

M and  $M'$  transform a shape of area A onto a shape of area  $A \cdot \text{det}(M \cdot M') = A \cdot \text{det}(M) \cdot \text{det}(M')$ . Another approach to describe a shape is to represent it as a basic geometrical model (sphere, cylinder, ruled surface, etc.). The repetition, union, or intersection of these basic building blocks can be used to describe more complex plant morphologies (Pradal et al., 2009). Later in this review, we describe how shape quantifications have been applied to gain an understanding of the genetic control of leaf morphology.

The mathematical definition of shape relies on two underlying quantifications – geometry and topology. While we will treat these quantifications as independent for the sake of simplicity, there is much overlap between these fields and the theoretical basis of each. Both approaches might characterize the same plant organ, but they refer to different types of quantifications that potentially lead to distinct biological interpretations. However, to truly understand the feedback between morphology and function, topological concepts should be viewed as complementary to the geometrical ones.

## Geometric Descriptors for Plant Morphology

Geometry is used to establish measurable sizes of the plant organ surface. Basic geometric descriptors include vector, length, width, height, diameter, angle, surface and volume. For example, when considering the vein patterning of a simple leaf, the distance from a point of vein branch emergence to the branch tip is a geometric measure of length called the Euclidean distance (**Figure 5**). To overcome the limitations of basic geometric descriptors, compound descriptors computed from these basic descriptors can be considered for complex plant forms.

Compound descriptors include density, aspect ratio and spatial distribution, which can provide a general view of plant morphology. However, their use is often dependent on the resolution of the system used to image the plants. Further, the compound nature of these descriptors leads to a loss of information, which can limit the interpretation. Alternatively, derivative descriptors can be used to expand on the basic descriptors and provide metrics for complex morphologies.

Derivative descriptors include quantifying the border of an object, a curve, or a surface. These descriptors often leverage concepts from differential geometry such as curvature, torsion of a curve or the Gaussian curvatures of a surface. Quantification of patterns (e.g., symmetry and periodicity) can also be attained through derivative descriptors. To revisit the vein patterning of a simple leaf example, the basic Euclidean distance measurement of length underestimates the total vein length because it does not account for the curvature. Instead the length could be quantified as the shortest path along the branch surface from the point of emergence and the tip, termed the geodesic distance (**Figure 5**). In this instance, the geodesic distance provides a more accurate quantification of vein length because it traces the distance along the vein surface, which is not a straight line. Further, an estimate of vein curvature could be obtained from the difference of the Euclidean and geodesic distances. While derivative descriptors provide applicable metrics for plant morphology quantifications, the accuracy of these descriptors depends on precise and high-resolution image acquisition approaches.

Thus one approach to quantify morphology is through calculating one or more geometric descriptors. Later in this review, we describe how geometric descriptors have been and could be applied to understand cell growth and expansion. Regardless of the descriptors, it is vital to include which geometry is being used and the unit (e.g., inch or cm) of measure, because infinitely many metrics exist. Further, when reporting geometries that are derived from multiple measures it is critical to make the original data available. For example, a commonly used geometric measure is specific leaf area, which is the leaf area divided by the leaf dry mass. In this case, both the leaf area and the leaf dry mass should be reported. Further, if the geometric descriptors are covariant then reporting the mean geometric measures is not sufficient and individual measurements should be reported.

## Quantifying Plant Architecture with Topology

While descriptions of shape and geometry are often applied to individual plant organs, there is significant interest in defining how these organs are connected to generate plant architectures, which ultimately impact function. For example, the spatial arrangement of shoot branches directly influences the placement of leaves and has a significant impact on photosynthetic capacity (Rameau et al., 2015). This spatial arrangement is difficult to assess with geometry even if patterning (e.g., symmetry, periodicity) can be determined. Instead, other properties within the mathematical field of topology, such as connectivity, are essential to quantify the spatial arrangement of plant organs. Topology is defined as understanding how a property persists through geometric transformation and deformation of the object of interest. The

simplest examples of topology utility are the description of branching structures (e.g., root system architecture or shoot branching architecture) and modeling connections between two objects (e.g., water flux between cells).

To understand the concept of connectedness between objects, it is important to first understand how a relationship is defined mathematically. A relationship is basically a rule that describes how elements of a set relate or interact with elements of another set. For example, a relation of connectedness (denoted by ' $\sim$ ') between branches A and B only exists if a path along the plant surface links the two (i.e.,  $A \sim B$ ). The order in which the elements are listed defines a strict relationship where  $A < B$  denotes the connectedness between user-defined reference points (e.g., tip of a branch to the base of the trunk). If we consider a tree crown, all tree branches can be ordered with regard to a defined reference point such as the point where the trunk emerges from the soil. However, if the tree is highly branched and has many ramifications, then it is often not possible to find a linear order to uniquely describe the tree crown. In this case, we can consider an additional relationship to denote the hierarchy of branches formed by the development program of the tree. If branch B emerges from branch A, we denote the emergence of a new level of branching hierarchy as  $A[B]$ . Thus, considering the whole plant, two types of connections can be defined: an object A that precedes (type ' $A < B$ ') or bears (type ' $A[B]$ ') a second object B (Godin and Caraglio, 1998; Godin, 2000).

These definitions of connectedness lead directly to the concept of graphs and of tree graphs. In mathematics, a graph is a representation of a set of objects where some objects are connected by links. Connected objects are represented by vertices (also called nodes or points), and the links that connect pairs of vertices are called edges (also called arcs or lines). Typically, a graph is depicted as a set of dots for the vertices, joined by lines or curves for the edges. Often nodes are referred to as "parents" and "children" based on the order of appearance. For example, if Node B is a main branch and Node A is a secondary branch originating from this main branch, then the parent of Node A is Node B. This can be represented as  $B < A$  or  $B[A]$ . In this example, Node A is considered the child of Node B and Node B can have many children. Thus, connectivity can be represented as a graph or a character chain (**Figure 6**). If the graph has only one parent for each node, then it is considered a tree graph. Tree graphs are convenient to describe plant architecture, because a node can represent each branch and the relationship between branches can be represented as an edge of the graph. Such a connectivity graph is often termed a skeleton if the edges and vertices can be geometrically embedded into physical branching structure captured as imaging data (Bucksch et al., 2010; Bucksch, 2014).

One type of graph is defined such that every node is on a loop or cycle. Let us again consider the venation of a simple leaf. If we want to assess the complexity of the branched pattern, we can first represent the branch junctions as features (**Figure 7**). A relationship between junctions can exist if they are connected within the graph. Typical quantifications of such a topology can give the distance between junctions, the number of loops/cycles or the average number of junctions that form a loop/cycle

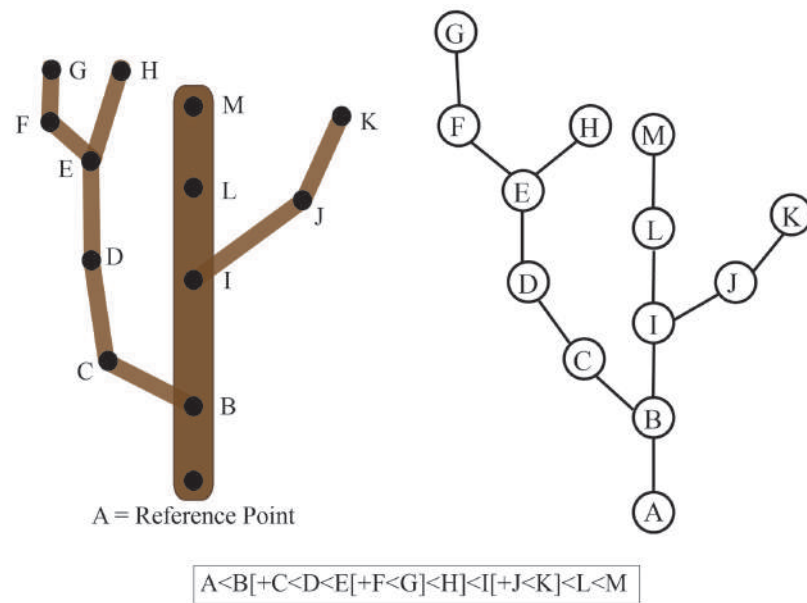


**FIGURE 6 | Connectivity of a tree branch can be represented as a graph or a character chain.** Consider the tree on the left. The reference point was chosen as the base of this main branch (A). Each branch point is represented as a node (B-K) in the graph on the right relative to the reference point A. Alternatively, branch connectivity can be represented as a character chain, where the  $C < D$  relationship indicates that C is closer to the reference point (A) than D and  $B [+ C]$  indicates that C is a child branch originating from the parent B.

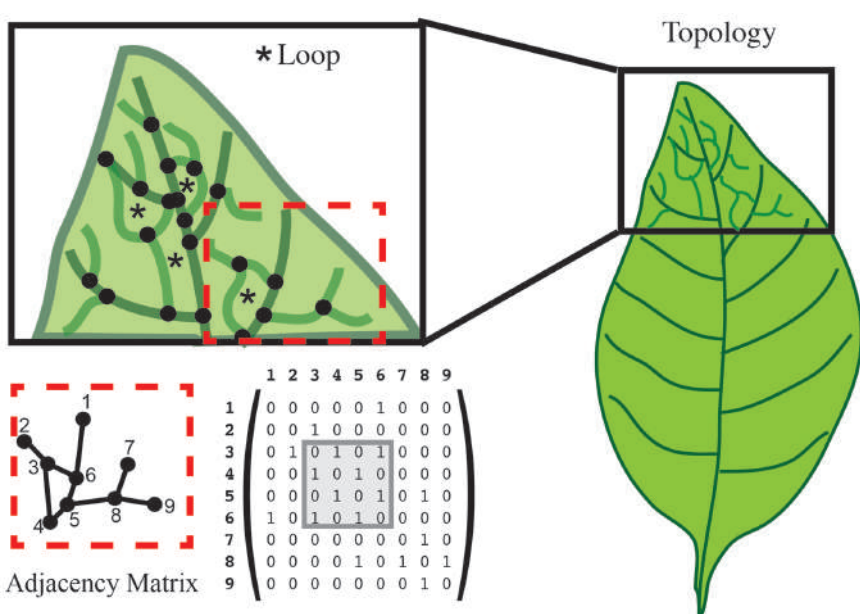


**FIGURE 7 | Topology characterizes the relationship between features.** In this leaf vein example, features are defined as the junction of branches (black dots). Topology can calculate the number of loops (asterisk in the upper left), and the number of junctions forming that loop. An adjacency matrix that defines the connection between two features can be used to represent these data. The connection between features is represented in a numerical matrix. Connected features are represented by a “1” in the adjacency matrix. Loops can be visualized within the matrix (gray box).

(Figure 7). Topologies can also be represented independent of the physical organ with a graph that describes the adjacency of loops. One possible representation of the topological graph

is adjacency matrix (Figure 7), which indicates the connection between junctions. Several types of information can be deduced directly from the adjacency matrix. For instance, two topological

graphs are isomorphic if their matrices have the same minimal polynomial, characteristic polynomial, eigenvalues, and trace. The connectedness of topological graphs can also be deduced directly from the adjacency matrix (**Figure 7**).

In addition to representing topological properties such as connectedness, graphs facilitate the extraction of other properties, such as the distance from various reference points for each node. Additional properties make it possible to model complex and dynamic systems (e.g., nutrient transport or water flux) and enable multi-scale modeling. For example, multi-scale tree graphs (MTG) are used to describe tree structures at different scales (e.g., community, individual plant, plant branches, etc.). MTG is composed of a set of graphs, where a node in one graph (e.g., one plant within the community) corresponds to another graph representing another scale (e.g., the branching pattern within that plant). Another application for MTG is to model how nutrient or water flux between cells contributes to the whole organ physiology.

Lastly, one of the most successful approaches to modeling the development of plant architecture has been Lindenmayer (L)-systems (Lindenmayer, 1968; Prusinkiewicz, 1986). L-systems employ a recursive set of rules to grow branched systems (e.g., a grammar). An L-system model begins with an initial state from which to begin construction (called axiom), and a set of rules that define how each module (i.e., plant component) transforms over time. The model is then applied step by step to simulate geometrical and topological plant development. During the last 20 years, several implementations of L-systems have been designed: cpfg (Prusinkiewicz and Lindenmayer, 1990), L+C (Prusinkiewicz et al., 2007), XL (Hemmerling et al., 2008) and L-Py (Boudon et al., 2012), among others. Each L-System language provides a dedicated modeling language that mixes classical programming languages (e.g., C, C++, Java, Python) with mathematical notation based on formal language theory. These languages have also emerged to take into account the increasing complexity of the developmental models. Some variants of the initial formalism are stochastic L-Systems (Eichhorst and Savitch, 1980), environmentally sensitive L-Systems (Prusinkiewicz et al., 2007) and relational growth grammars (Kurth et al., 2005). Independently, Godin and Caraglio (Godin and Caraglio, 1998) have introduced a multiscale formalism, the MTG, to be able to encode any type of plant architecture data at different spatial and temporal scales. While a large community has adopted this formalism, the use of multiscale modeling to simulate the dynamic development of plants is quite recent (Boudon et al., 2012; Ong et al., 2014).

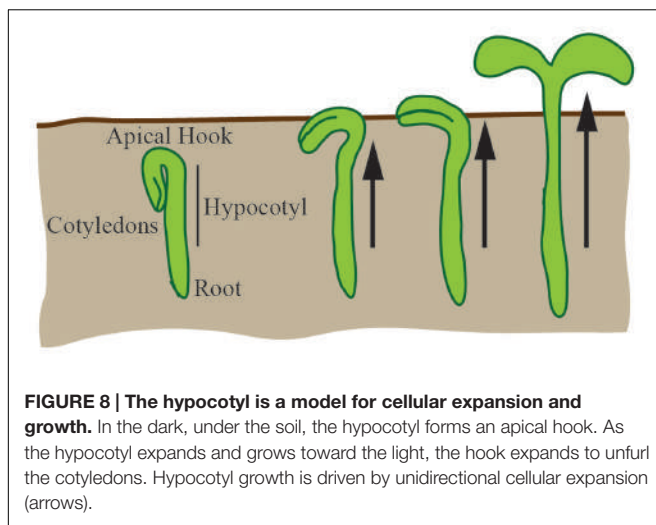
## Quantification of Changing Morphology

There is a substantial effort to assess morphology in relation to physical processes (e.g., response to biotic and abiotic environments or growth). Thus, we outline the basic concepts of comparative morphology in this section. The comparison of shapes is central to morphological quantification, and two mathematical principles exist to compare shapes. The first, reduction, relies on the removal of unimportant features and the merging of similar or equivalent features into a simplified “map.” Given a set of plant organs, the implication is that there is

an established map to perform abstraction for all plant organs. Similarly, a distinct map exists for each plant organ that will recover the original details from the reduction. Reduction stores and quantifies the difference between a given organ shape and the abstraction of the plant organ shape. The second principle, registration, reorganizes feature locations such that comparable features of two plants are aligned to the same coordinate system to minimize the distance between the features. While these principles can be applied for comparison between two objects (e.g., plants or organs), they can also be used to compare objects to a reference geometrical object modeling the shape (e.g., comparing fruit shape to a sphere). For example, given a set of leaves with different shapes, shapes can first be registered and a mean shape computed. Then for each leaf, the reduction map between this leaf and the mean leaf (abstraction) can be calculated. This map will then quantify the distance between a shape and its reduction, and provide a metric of similarity.

Measuring changes in geometry is relatively straightforward because geometry derives measurable terms. In the leaf vein example, one could compare average length of veins or vein diameter between two samples. It is important to use comparable metrics within these comparisons. For example, the Euclidean length from one sample cannot be directly compared to the geodesic length of another sample. Again with geometric quantifications it is important to indicate which metrics are being used and the units of measure.

For basic topological quantification, such as number of loops or number of junctions forming a loop, straightforward comparison can be made. However, when considering the dynamics of changing topologies, the adjacency matrices can be very useful (**Figure 7**). In an adjacency matrix, each position corresponds to the intersection of two junctions or nodes. Directly comparing adjacency matrices relies on the same order of nodes referenced at each position in the matrix. Thus, adjacency matrices are most useful for the quantification of changes within a single system. For example, when quantifying the development of veins within a leaf, node definitions are generated based on the final topology and traced back in time. This will generate equal size adjacency matrices for comparison across the development and enable quantification of new (birth-rate) and lost (death-rate) topologies at any given time. Matrix algebra applications can be applied to these matrices for comparison between plants. If instead, topological comparisons are required between systems where the nodes differ, then network alignment algorithms can be utilized. These algorithms attempt to maximize the topological similarity between two different networks, and are most frequently applied to gene-based networks (e.g., Kuchaiev et al., 2010; Milenkovic et al., 2010; Ficklin and Feltus, 2011). However, the current implementations are fraught with technical problems and the choice of algorithm can influence the outcome (e.g., Clark and Kalita, 2014). While not extensively used for morphological assays, these comparison tools can be adapted for evolutionary, cross-species, or interspecies comparisons. In the remainder of the review, we will highlight some examples of how mathematical descriptors have been and can be applied to quantify morphology in biological systems.



## Leaf Morphological Traits

We have utilized a leaf in the above illustrations, because morphological quantifications have been applied most extensively in this area. Leaf morphology is directly tied to various functions, including water uptake (e.g., Ito et al., 2015), photosynthetic capacity (e.g., Reich et al., 1998) and gas exchange (e.g., de Boer et al., 2016). However, leaf morphology is dynamic and changes in response to the environment (Chitwood and Sinha, 2016). Thus, there is an effort to quantify leaf morphology over time to lend a broader understanding into leaf function.

Two of the most common metrics for quantifying leaf morphology are the geometric measures of leaf area and specific leaf area (Kleyer et al., 2008). Leaf area is calculated as the surface area of one side of a single leaf, generally expressed as  $\text{mm}^2$ . While specific leaf area, as mentioned above, is the leaf area divided by the leaf dry mass, generally expressed as  $\text{mm}^2/\text{mg}$  (Kleyer et al., 2008). The differential use of these two metrics throughout the literature highlights the importance of reporting the original data and the geometric measure applied.

Basic geometric measures of length and width have also been applied to quantify changes in maize leaf shape, which have stereotypical linear or linear-lanceolate (pointed at both ends) leaves (Tian et al., 2011). However, for leaf shapes of increased complexity (e.g., palmate, pinnate, lobed, etc.), more sophisticated analyses have been applied. One approach, which can be applied to the same leaf changing over time or different leaves with the same type of classification (e.g., number of lobes), relies on leaf shape homology. In this approach, the same number of points are placed equidistant along the curved edge and expressed within a Cartesian coordinate system. Anchor points are defined by homologous features between leaves (e.g., base and tip) to facilitate alignment of the coordinate systems. Dimension reduction techniques (e.g., principal component analysis) are then applied to identify the points that most efficiently explain the differences in shape between the leaves (Feng et al., 2009). This approach has been successfully used to identify the genetic basis of leaf and petal shape and size in snapdragons (Langlade et al., 2005; Feng et al., 2009; Cui et al., 2010) and to characterize

the diversity and effect of climate on grape leaf morphology (Chitwood et al., 2016a,b).

An alternative approach views the leaf shape as a closed contour formed by a wave connecting back on itself. This approach is particularly suited for the comparison of leaves without homologous points. This analysis begins by converting the shape into a numeric vector called chain code, which defines a contour as a series of linear fits (Kuhl and Giardina, 1982). The chain code vector is then used to calculate Elliptical Fourier Descriptors. In the simplest terms a Fourier transform fits a series of sine waves to an object. In this case, the Elliptical Fourier Descriptor takes the Fourier transform of the boundary of the object within a closed elliptical. The Fourier transform is run at multiple Fourier coefficients to produce harmonics. The more harmonics that are utilized, the greater the complexity of the resultant curve. This approach has been successfully used to identify the genetic basis of tomato (Chitwood et al., 2012, 2013) and grape (Chitwood et al., 2014) leaf morphology.

## Modeling Cell Growth and Expansion

Changes at the cellular-level are an important mechanism by which plants grow and develop. In this section we will discuss two biological systems, the hypocotyl and floral sepals, which have been utilized to understand how growth and expansion contributes to organ morphology. The hypocotyl has been used to study cellular expansion since the mid-1800s, however, the floral sepal system is a more recently developed model.

The hypocotyl is the stem of a germinating seed that connects the cotyledons and the roots in eudicot plants. In the dark, the hypocotyl forms a hook (apical hook) that is believed to protect the cotyledons from damage as the seedling navigates through the soil; the hook subsequently opens when the seedling is exposed to light (Figure 8). Most of the hypocotyl growth in the dark derives from cell expansion primarily driven by the outer epidermal cells (Gendreau et al., 1997; Savaldi-Goldstein et al., 2007). For a cell to expand, it must balance the requirements for structural support and elasticity. At the basic level, this requires a balance between the cytoskeletal structural components and the loosening and synthesis of cell wall components (reviewed in Bashline et al., 2014). In the hypocotyl, expansion occurs along the longitudinal axis with cortical microtubules limiting cell expansion to this axis and spatially controlling cellulose synthesis (reviewed in Vandenbussche et al., 2005). Since growth of the hypocotyl is predominantly due to unidirectional cell expansion, it is an ideal system to apply basic geometric descriptors to study the control of growth.

In its simplest form, the hypocotyl (excluding the apical hook) can be viewed as a cylinder that is hydrostatically uniform and with a radial water potential gradient (Kutschera and Niklas, 2007). The rate and extent of cylinder expansion is controlled by genetic and environmental factors. Hypocotyl elongation has been primarily modeled independently of cellular morphology as an outcome of kinetic parameters written as a set of ordinary differential equations (Chew et al., 2014). It is unclear how individual cell expansions (as quantitated by geometric or shape descriptors) lead to the collective growth of the hypocotyl and

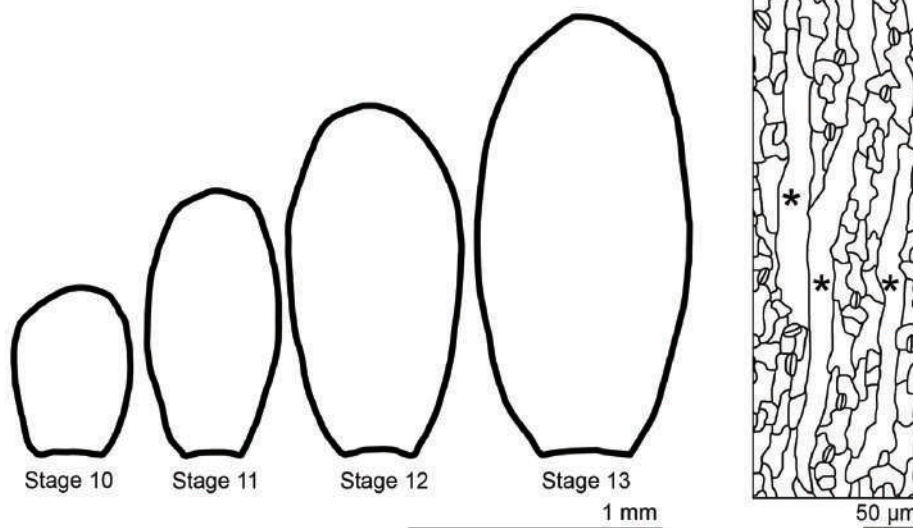


**FIGURE 9 | The morphology of sepals and their epidermal cells.** Wild-type *Arabidopsis thaliana* sepals decrease the width/length ratio as they grow. Sepal epidermal cells are highly variable in morphology, with giant pavement cells (\*) interspersed between smaller cells in a large range of sizes.

contribute to differential growth. For example, there is little known about how the apical hook is formed, maintained and opened during elongation. Additionally, nutational bending as a result of differential growth is observed, but the mechanism(s) for this are still not fully understood. These open questions could be targeted through time-series image acquisition and a temporal analysis of geometric descriptors (e.g., the aspect ratio of each cell in the hypocotyl over time). The goal of such an analysis is to identify emergent properties that could explain experimental observations (e.g., nutational bending). Thus, even in a simple and well-studied system such as the hypocotyl, the quantification of differential cell morphology has the potential to contribute to our understanding of growth control.

A more recently established system to study complex growth control is the flower sepals. In complex organs overall morphological structure is crucial for their proper function, while morphogenesis is a dynamic process in which the topology and geometry change over time. The establishment and maintenance of proper shape and size is a fundamental developmental process of all multicellular organisms, but how it is tightly regulated remains a mystery (Vogel, 2013). *Arabidopsis thaliana* sepals are used as a model to study this process because of their accessibility for live imaging and cellular growth analysis (Roeder et al., 2010, 2012; Qu et al., 2014; Tauriello et al., 2015; Hervieux et al., 2016; Hong et al., 2016).

Sepals are the outermost sterile organs of a flower, which surround and protect the developing reproductive structures inside the bud before the flower opens. The sepals start from the small dome-shaped sepal primordia initiating from a line of eight cells on the edges of the floral meristem (Bossinger and Smyth, 1996). The young sepals grow in both medial-lateral and proximal-distal directions, maintaining a relatively

low aspect ratio. Gradually, the sepals grow more in the proximal-distal direction, leading to increased aspect ratio (Figure 9). Mature sepals are roughly elliptical, approximately 2 mm long, 1 mm wide, but less than 50  $\mu\text{m}$  thick. Therefore, they are considered flat organs, and 2D geometric descriptors such as length, aspect ratio, and circularity can be used to describe their morphology.

Similar to hypocotyl growth, epidermal cells largely control sepal growth. The morphology of epidermal cells affects the overall sepal curvature and sepal shape. Through the application of a combination of quantitative and qualitative geometric descriptors, it has been shown that the abaxial sepal epidermal cells display a wide distribution of size and shape (Roeder et al., 2010). Giant pavement cells have an area up to 20,000  $\mu\text{m}^2$ , but are generally long and skinny, with high aspect ratios, whereas the smallest cells have an area less than 100  $\mu\text{m}^2$  and are more round with high circularity. These small cells can be quite irregular in shape, though they are generally less interdigitated than leaf pavement cells (Figure 9). As described above, mathematical methods such as principal component analysis and elliptical Fourier analysis have been used to describe organ shape and size (Bensmihen et al., 2008; Chitwood et al., 2013). With these approaches, a more comprehensive description of morphological change in cells and organs integrating with genetics will facilitate the understanding of the underlying mechanism of shape determination.

Besides the morphological variability, sepal pavement cells display variable growth and division as well (Roeder et al., 2010; Schiessl et al., 2014; Tauriello et al., 2015). Principal directions of growth, growth isotropism and areal increase have been used to analyze cellular growth pattern. Similar to leaves (Beemster et al., 2005), sepals have a gradient of cell growth. Young sepals have fast and anisotropic cell growth

at the tip while the growth in the lower sepals is slower and more isotropic. As the sepal grows, cell areal growth rate, growth anisotropy and cell division rate progressively decrease from the tip downward (Hervieux et al., 2016). Sepal morphology also varies across different development stages, environmental conditions, and in different genetic backgrounds. Despite high variability on the cellular level, sepals require coordinated growth to form an effective barrier to protect the meristem (Hong et al., 2016). A comprehensive analysis of morphology on the organ and cellular levels can bring insights into sepal function and the mechanisms regulating morphological diversity.

## Quantifying Root System Architecture

Root system architecture (RSA), which describes the spatial configuration of different types of roots in the root system (Lynch, 1995), is integral to water and nutrient uptake. Because of this, research has focused on imaging and quantifying RSA. Key questions include: ‘What genes underlie particular root traits (e.g., deep roots or wide root systems) and how do they function?’ ‘What root traits and architectures are optimal for specific environments?’ ‘What are the functions of different types of roots and how do they contribute to the function of the entire root system?’ Knowledge gained from addressing these questions will enhance the ability of plant breeders to develop crops with robust root systems that lead to increased crop production in harsh environments.

Root system architecture includes the topology of the root system, which describes the network and pattern of root branches (Berntson, 1997) as well as the distribution of roots, which refers to the presence of roots within a given region (Lynch, 1995; Jung and McCouch, 2013). Historically, finer features of the root system, such as root hairs, were not included in RSA (Lynch, 1995). However, more recent definitions of RSA embrace multiple scales (Smith and De Smet, 2012; Jung and McCouch, 2013; Lobet et al., 2015) and include both macroscale and microscale features such as root hairs and root diameter. Root anatomy, the internal cellular organization of the root, is not generally considered part of RSA, but recent work suggests it affects RSA (Zhu et al., 2010; Postma and Lynch, 2011; Jaramillo et al., 2013; Lynch et al., 2014; Saengwilai et al., 2014). RSA is generally divided into two broad classes, a taproot system found in most dicots and a more complex RSA found in many grass species that consists of a bushier root system with different types of roots, including shoot-borne roots.

By configuring the spatial distribution and network of roots within the soil, RSA significantly impacts the ability of roots to function in water and nutrient uptake. RSA is highly responsive to environmental signals, allowing the root system to adapt to different soil environments (Hodge, 2004; Lynch, 2011, 2013, 2014; Smith and De Smet, 2012). For example, phosphorus is concentrated in the topsoil. Thus, bean varieties more adapted to phosphate deficiency have shallower root systems, increased lateral roots in the upper region of the root system, and increased root hair density to maximize phosphate uptake (Bonser et al., 1996; Lynch and Brown, 2001; Lynch, 2011;

Peret et al., 2014; Miguel et al., 2015). Work with nitrate has provided evidence of both local and systemic nitrogen signals that impact root growth. For example, a split root experiment showed that local patches of high nitrate elicit lateral root outgrowth while root systems grown in conditions of globally high nitrate have fewer elongated laterals (Ruffel et al., 2011). In contrast, globally deficient levels of nitrate substantially increased root growth and branching, but locally deficient levels did not (Zhang et al., 1999; Ruffel et al., 2011).

Root system architecture is a complex trait controlled by a small contribution from many genes (Topp et al., 2013; Zurek et al., 2015). Due to the importance of RSA in plant growth, fitness, and defense, a major goal is to identify the genes underlying specific RSA traits. Identification of these genes requires the ability to accurately quantify the trait of interest, which in turn necessitates the ability to image and analyze root system morphology. Recent years have seen an explosion in the development of both root architecture imaging technologies (Iyer-Pascuzzi et al., 2010; Clark et al., 2011; Mairhofer et al., 2013; Rellán-Álvarez et al., 2015), and the software for quantifying RSA (Armengaud et al., 2009; French et al., 2009; Lobet et al., 2011; Galkovskyi et al., 2012; Mairhofer et al., 2012; Bucksch et al., 2014; Das et al., 2015). In addition, modeling approaches, which combine RSA under different environments, have been used to successfully predict the optimal RSA, or ideotype for specific environments (Lynch, 2007; Dray et al., 2010; Leitner et al., 2010; Pages, 2014).

Each of the growth and imaging technologies for RSA quantification has its own pros and cons (reviewed in Piñeros et al., 2016). These technologies can be destructive or non-destructive, and range from simple and inexpensive to complex and expensive. Image quantification can occur in 2D or 3D. Frequently used, more inexpensive, and non-destructive technologies include growth in gellan gum or agar (Iyer-Pascuzzi et al., 2010; Clark et al., 2011; Fang et al., 2013) or in pouches (Hund et al., 2009). In these simple systems, roots can be imaged either by scanning or imaging with a digital camera, and analyzed with any number of software packages (see again <http://www.plant-image-analysis.org> for an overview; Lobet et al., 2013). Although these systems enable inexpensive and non-destructive quantification of RSA traits, the roots are not grown in soil, which may limit the application of these results in a natural setting.

The plasticity of RSA in different environments has led to significant interest in the development of non-destructive imaging technologies that image roots grown in soil or potting mix. One such technology grows roots between two plates in soil and relies on luminescence-based reporters for visualization (Rellán-Álvarez et al., 2015). While this technology is perhaps ideal for inexpensive and non-destructive imaging of roots in soil, it is limited by the requirement for transgenic reporter plants.

An alternative approach for imaging soil-grown plants non-destructively is X-ray computed tomography (X-ray CT; Mairhofer et al., 2013). In this technique, plants are grown in soil in pots and can be imaged daily. Rates of RSA growth

and the response to environmental conditions can be observed over time, and the images can be reconstructed in 3D, which increases accuracy. Although more expensive and data-intensive, by imaging roots grown in soil, this technology promises to yield information more applicable to natural settings. One drawback of X-ray CT is the expense and the current inability to implement it in the field. In contrast, a straightforward, albeit destructive, method of field-based RSA phenotyping overcomes both of these obstacles. Termed ‘shovelomics,’ this method examines only the upper region of the root system that can be removed from the soil without much damage (Trachsel et al., 2011). Roots are washed of soil, images taken in 2D, and root traits quantified with available software packages, such as the “Digital imaging of root traits” or DIRT package (Bucksch et al., 2014; Das et al., 2015). DIRT uses an imaging pipeline to extract basic geometric root traits such as length, angle and diameter from the underlying graph representation, as well as novel descriptors of shape deformation. Recently, these descriptors were used to identify shape properties of cowpea roots that are associated with *Striga* tolerance (Burridge et al., 2016).

The ability to image, quantify, and model RSA is leading to new discoveries regarding the genes and genomic regions that control these complex traits (Topp et al., 2013; Zurek et al., 2015). Additionally, these technologies allow key questions across scales to be addressed. One such question is how (or whether) microscale features of RSA such as root hairs and root diameter impact macroscale features of RSA such as root branching. For example, root cortical aerenchyma (RCA) is open space in the root formed from the cell death of root cortex. By no longer requiring nutrients and carbon, RCA may alter the metabolic cost of root architecture such that roots can grow deeper or thicker (Lynch, 2013, 2014). SimRoot (Lynch et al., 1997) is a structural-functional model that emerged from a large amount of empirically collected data. Additionally, SimRoot incorporates physiological models of nutrient and water uptake. Software such as SimRoot can model changes in RCA and make prediction on the effects of competition in root architecture.

A recent developed software package, DynamicRoots, merges geometric and topological approaches to quantify the growth of a root system (Symonova et al., 2015). In this package 3D reconstructions of time-series RSA are first registered to the same coordinate system. These images are then converted to a series of graphs with nodes representing the voxels and edges representing the connections between neighboring voxels. Several calculations can now be derived from these graphs. For example, the addition of new edges that persist likely indicates a new branch forming and the geodesic distance between a reference point and each voxel can be used to track tip growth. Using these types of information, DynamicRoots can decompose the RSA into individual branches and extract branch-specific geometries (Symonova et al., 2015). This software is the first aimed at analyzing growing root systems from time-series data and has the potential to provide key insights into the local and global RSA impacts of changing environmental conditions.

## Morphology as a Tool for Ecology

All of the analyses highlighted above are important to contribute to our understanding of how whole communities respond, function, and interact within a particular environment. Recently, plant trait-based ecology has pushed forward many basic ecological questions. For example, quantifying plant traits helps understand variation in trait function across ecological scales (e.g., Auger and Shipley, 2012; Verheijen et al., 2013), relative importance of intra- versus inter-specific trait variation across these scales (e.g., Viole et al., 2012; Kichenin et al., 2013; Siefert et al., 2015), community assembly processes (e.g., Hille Ris Lambers et al., 2012; Laughlin and Laughlin, 2013), and eco-evolutionary dynamics (e.g., Vellend and Geber, 2005; Whitham et al., 2006; Hughes et al., 2008; Bailey et al., 2009a,b). Above- and below-ground plant traits such as leaf area and shape, root formation, and above- to below-ground biomass ratios are morphological traits that allow ecologists to make predictions about plant ecological strategies and overall community response to environmental changes (Suding et al., 2008). While genetic variation has been shown to have consequences on community and ecosystem function (e.g., Bangert et al., 2006; Crutsinger et al., 2006; Johnson et al., 2006; Lankau and Strauss, 2007), directly connecting genotypic diversity to phenotypic variation for ecologically important traits has been more difficult. The proliferation of open-source, global plant trait databases (e.g., TRY plant trait database: <https://www.try-db.org/TryWeb/Home.php>, Glopnet: <http://bio.mq.edu.au/~iwright/glopian.htm>) as well as large-scale plant phenotype databases (unPAK: <http://arabidopsis.biology.cofc.edu/>) allows plant ecologists and evolutionary biologists to quickly harness trait data to answer relevant ecological and evolutionary questions. Building these databases so that they incorporate trait data relevant across multiple scales and environments is essential to providing a holistic view of plant-environment and plant-plant interactions. Essential to the building of these databases is the rapid quantification of the plant morphological traits through the application of mathematical principles.

The establishment of larger and standardized plant trait databases would provide ecologists with the necessary amount of data to gain insight into linkages between genotype and phenotype, and the potential impact on community and ecosystem processes. Quantifying changing leaf morphology would provide insights into physiology through easier-to-measure traits such as specific leaf area. Quantifying changing topology of root formation and architecture could provide insight into drought tolerance at a single time point and eventually over time. In addition, quantifying the dynamic topology of stem elongation and branching patterns could provide insight into light acquisition under changing light environments. Finally, morphological models for above- and below-ground traits could be integrated to understand the potential links and tradeoffs under different environmental conditions. For example, these models could be instrumental in understanding tradeoffs in resource allocation between roots

and shoots, particularly in harsh conditions. Tradeoffs between above- and below-ground structures would likely differ across a light versus soil resource gradient. Together, these morphological models have the potential to help us make connections between plant genetics, morphology, physiology, and ecosystem dynamics.

## CONCLUSION

In this review we have outlined the basic principles of morphological quantification in terms of geometry, topology and shape. The choice of mathematical descriptor(s) and analysis depends heavily on the biological and hierarchical scale. We have highlighted a few examples of morphological descriptors that have been applied across biological scales. For both cellular growth and organ morphology, basic geometric descriptors and/or shape analyses can be applied to extract traits relevant to genetic, environmental, and evolutionary diversity. While these same principles can also be applied to root systems, there is an added advantage to using topological measures to quantify how individual components are connected within the whole structure. Lastly, each of these individual analyses provides important insight into the larger context of how plants function within a community. The advancement of plant morphological quantification and the interdisciplinary collaboration between biologists and mathematicians is critical to elevate our understanding of plant development, function, and evolution. It is our hope that this review will encourage more interdisciplinary interactions and promote research in the field of plant morphological modeling.

## REFERENCES

- Abramoff, M. D., Magalhães, P. J., and Ram, S. J. (2004). Image processing with ImageJ. *Biophotonics Int.* 11, 36–42.
- Armengaud, P., Zambaux, K., Hills, A., Sulpice, R., Pattison, R. J., Blatt, M. R., et al. (2009). EZ-Rhizo: integrated software for the fast and accurate measurement of root system architecture. *Plant J.* 57, 945–956. doi: 10.1111/j.1365-313X.2008.03739.x
- Auger, S., and Shipley, B. (2012). Inter-specific and intra-specific trait variation along short environmental gradients in an old-growth temperate forest. *J. Veg. Sci.* 24, 419–428. doi: 10.1111/j.1654-1103.2012.01473.x
- Bailey, J. K., Hendry, A. P., Kinnison, M. T., Post, D. M., Palkovacs, E. P., Pelletier, F., et al. (2009a). From genes to ecosystems: an emerging synthesis of eco-evolutionary dynamics. *New Phytol.* 184, 746–749. doi: 10.1111/j.1469-8137.2009.03081.x
- Bailey, J. K., Schweitzer, J. A., Ubeda, F., Koricheva, J., LeRoy, C. J., Madritch, M. D., et al. (2009b). From genes to ecosystems: a synthesis of the effects of plant genetic factors across levels of organization. *Philos. Trans. R. Soc. B* 364, 1607–1616. doi: 10.1098/rstb.2008.0336
- Bangert, R. K., Allan, G. J., Turek, R. J., Wimp, G. M., Meneses, N., Martinsen, G. D., et al. (2006). From genes to geography: a genetic similarity rule for arthropod community structure at multiple geographic scales. *Mol. Ecol.* 15, 4215–4228. doi: 10.1111/j.1365-294X.2006.03092.x
- Bashline, L., Lei, L., Li, S., and Gu, Y. (2014). Cell wall, cytoskeleton, and cell expansion in higher plants. *Mol. Plant* 7, 586–600. doi: 10.1093/mp/sss018
- Beemster, G. T. S., De Veylder, L., Vercruyse, S., West, G., Rombaut, D., Van Hummelen, P., et al. (2005). Genome-wide analysis of gene expression profiles associated with cell cycle transitions in growing organs of *Arabidopsis*. *Plant Physiol.* 138, 734–743. doi: 10.1104/pp.104.053884
- Bensmihen, S., Hanna, A. I., Langlade, N. B., Micol, J. L., Bangham, A., and Coen, E. S. (2008). Mutational spaces for leaf shape and size. *HFSP J.* 2, 110–120. doi: 10.2976/1.2836738
- Bernston, G. M. (1997). Topological scaling and plant root system architecture: developmental and functional hierarchies. *New Phytol.* 135, 621–634. doi: 10.1046/j.1469-8137.1997.00687.x
- Bonser, A. M., Lynch, J., and Snapp, S. (1996). Effect of phosphorus deficiency on growth angle of basal roots in *Phaseolus vulgaris*. *New Phytol.* 132, 281–288. doi: 10.1111/j.1469-8137.1996.tb01847.x
- Bossinger, G., and Smyth, D. R. (1996). Initiation patterns of flower and floral organ development in *Arabidopsis thaliana*. *Development* 122, 1093–1102. doi: 10.1101/tpc.1.1.37
- Boudon, F., Pradal, C., Cokelaer, T., Prusinkiewicz, P., and Godin, C. (2012). L-Py: an L-system simulation framework for modeling plant architecture development based on a dynamic language. *Front. Plant Sci.* 3:76. doi: 10.3389/fpls.2012.00076
- Bucksch, A. (2014). A practical introduction to skeletons for the plant sciences. *Appl. Plant Sci.* 2:1400005. doi: 10.3732/apps.1400005
- Bucksch, A., Burridge, J., York, L. M., Das, A., Nord, E., Weitz, J. S., et al. (2014). Image-based high-throughput field phenotyping of crop roots. *Plant Physiol.* 166, 470–486. doi: 10.1104/pp.114.243519
- Bucksch, A., Lindenbergh, R., and Menenti, M. (2010). SkelTre. *Vis. Comput.* 26, 1283–1300. doi: 10.1007/s00371-010-0520-4
- Burridge, J., Schneider, H. M., Huynh, B.-L., Roberts, P. A., Bucksch, A., and Lynch, J. P. (2016). Genome-wide association mapping and agronomic impact of cowpea root architecture. *Theor. Appl. Genet.* doi: 10.1007/s00122-016-2823-y [Epub ahead of print].

## AUTHOR CONTRIBUTIONS

Authors are listed in alphabetical order and all authors contributed equally to writing and editing the manuscript. EES coordinated and integrated individual contributions.

## FUNDING

The authors were supported by the National Institute for Mathematical and Biological Syntheses (NIMBioS) to attend the workshop on plant morphological modeling, through NSF Award #DBI-1300426, with additional support from The University of Tennessee, Knoxville. BB is supported by NSF grants IOS-1254423 and MCB-1517032. CP is partially supported by the Institute of Computational Biology (IBC) in Montpellier, France.

## ACKNOWLEDGMENTS

We gratefully acknowledge the support of the National Institute for Mathematical and Biological Syntheses (NIMBioS) for coordinating the workshop on plant morphological modeling, sponsored by the National Science Foundation through NSF Award #DBI-1300426, with additional support from The University of Tennessee, Knoxville. EES gratefully acknowledges the support of her postdoctoral mentor, Philip N. Benfey. LH thanks her postdoctoral mentor Adrienne H. K. Roeder for support.

- Chen, B. J. W., During, H. J., and Anten, N. P. R. (2012). Detect thy neighbor: identity recognition at the root level in plants. *Plant Sci.* 195, 157–167. doi: 10.1016/j.plantsci.2012.07.006
- Chew, Y. H., Smith, R. W., Jones, H. J., Seaton, D. D., Grima, R., and Halliday, K. J. (2014). Mathematical models light up plant signaling. *Plant Cell* 26, 5–20. doi: 10.1105/tpc.113.120006
- Chitwood, D. H., Headland, L. R., Kumar, R., Peng, J., Maloof, J. N., and Sinha, N. R. (2012). The developmental trajectory of leaflet morphology in wild tomato species. *Plant Physiol.* 158, 1230–1240. doi: 10.1104/pp.111.192518
- Chitwood, D. H., Klein, L. L., O'Hanlon, R., Chacko, S., Greg, M., Kitchen, C., et al. (2016a). Latent developmental and evolutionary shapes embedded within the grapevine leaf. *New Phytol.* 210, 343–355. doi: 10.1111/nph.13754
- Chitwood, D. H., Kumar, R., Headland, L. R., Ranjan, A., Covington, M. F., Ichihashi, Y., et al. (2013). A quantitative genetic basis for leaf morphology in a set of precisely defined tomato introgression lines. *Plant Cell* 25, 2465–2481. doi: 10.1105/tpc.113.112391
- Chitwood, D. H., Ranjan, A., Martinez, C. C., Headland, L. R., Thiem, T., Kumar, R., et al. (2014). A modern ampelography: a genetic basis for leaf shape and venation patterning in grape. *Plant Physiol.* 164, 259–272. doi: 10.1104/pp.113.229708
- Chitwood, D. H., Rundell, S. M., Li, D. Y., Woodford, Q. L., Yu, T. T., Lopez, J. R., et al. (2016b). Climate and developmental plasticity: interannual variability in grapevine leaf morphology. *Plant Physiol.* 170, 1480–1491. doi: 10.1104/pp.15.01825
- Chitwood, D. H., and Sinha, N. R. (2016). Evolutionary and environmental forces sculpting leaf development. *Curr. Biol.* 4, R297–R306. doi: 10.1016/j.cub.2016.02.033
- Clark, C., and Kalita, J. (2014). A comparison of algorithms for the pairwise alignment of biological networks. *Bioinformatics* 30, 2351–2359. doi: 10.1093/bioinformatics/btu307/-DC1
- Clark, R. T., MacCurdy, R. B., Jung, J. K., Shaff, J. E., McCouch, S. R., Aneshansley, D. J., et al. (2011). Three-dimensional root phenotyping with a novel imaging and software platform. *Plant Physiol.* 156, 455–465. doi: 10.1104/pp.110.169102
- Cooper, L., and Jaiswal, P. (2016). The plant ontology: a tool for plant genomics. *Methods Mol. Biol.* 1374, 89–114. doi: 10.1007/978-1-4939-3167-5\_5
- Crutsinger, G. M., Collins, M. D., Fordyce, J. A., Gompert, Z., Nice, C. C., and Sanders, N. J. (2006). Plant genotypic diversity predicts community structure and governs an ecosystem process. *Science* 313, 966–968. doi: 10.1126/science.1128326
- Cui, M. L., Copsey, L., Green, A. A., Bangham, J. A., and Coen, E. (2010). Quantitative control of organ shape by combinatorial gene activity. *PLoS Biol.* 8:e1000538. doi: 10.1371/journal.pbio.10000538
- Das, A., Schneider, H., Burridge, J., Ascano, A. K. M., Wojciechowski, T., Topp, C. N., et al. (2015). Digital imaging of root traits (DIRT): a high-throughput computing and collaboration platform for field-based root phenomics. *Plant Methods* 11:51. doi: 10.1186/s13007-015-0093-3
- de Boer, H. J., Price, C. A., Wagner-Cremer, F., Dekker, S. C., Franks, P. J., and Veneklaas, E. J. (2016). Optimal allocation of leaf epidermal area for gas exchange. *New Phytol.* 210, 1219–1228. doi: 10.1111/nph.13929
- Draye, X., Kim, Y., Lobet, G., and Javaux, M. (2010). Model-assisted integration of physiological and environmental constraints affecting the dynamic and spatial patterns of root water uptake from soils. *J. Exp. Bot.* 61, 2145–2155. doi: 10.1093/jxb/erq077
- Eichhorst, P., and Savitch, W. J. (1980). Growth functions of stochastic Lindenmayer systems. *Inform. Control* 45, 217–228. doi: 10.1016/S0019-9958(80)90593-8
- Fang, S., Clark, R. T., Zheng, Y., Iyer-Pascuzzi, A. S., Weitz, J. S., Kochian, L. V., et al. (2013). Genotypic recognition and spatial responses by rice roots. *Proc. Natl. Acad. Sci. U.S.A.* 110, 2670–2675. doi: 10.1073/pnas.1222821110
- Feng, A., Wilson, Y., Bowers, J., Kennaway, R., Bangham, A., Hannah, A., et al. (2009). Evolution of allometry in antirrhinum. *Plant Cell* 21, 2999–3007. doi: 10.1105/tpc.109.069054
- Ficklin, S. P., and Feltus, F. A. (2011). Gene coexpression network alignment and conservation of gene modules between two grass species: maize and rice. *Plant Physiol.* 156, 1244–1256. doi: 10.1104/pp.111.173047
- French, A., Ubeda-Tomás, S., Holman, T. J., Bennett, M. J., and Pridmore, T. (2009). High-throughput quantification of root growth using a novel image-analysis tool. *Plant Physiol.* 150, 1784–1795. doi: 10.1104/pp.109.140558
- Galkovskyi, T., Mileyko, Y., Bucksch, A., Moore, B., Symonova, O., Price, C. A., et al. (2012). GiA roots: software for the high throughput analysis of plant root system architecture. *BMC Plant Biol.* 12:116. doi: 10.1186/1471-2229-12-116
- Gendreau, E., Traas, J., Desnos, T., Grandjean, O., Caboche, M., and Hofte, H. (1997). Cellular basis of hypocotyl growth in *Arabidopsis thaliana*. *Plant Physiol.* 114, 295–305. doi: 10.1104/pp.114.1.295
- Godin, C. (2000). Representing and encoding plant architecture: a review. *Ann. For. Sci.* 57, 413–438. doi: 10.1051/forest:20000132
- Godin, C., and Caraglio, Y. (1998). A multiscale model of plant topological structures. *J. Theor. Biol.* 191, 1–46. doi: 10.1006/jtbi.1997.0561
- Godin, C., Costes, E., and Sinoquet, H. (1999). A method for describing plant architecture which integrates topology and geometry. *Ann. Bot.* 84, 343–357. doi: 10.1006/anbo.1999.0923
- Hartley, R., and Zisserman, A. (2005). *Multiple View Geometry in Computer Vision*. Cambridge: Cambridge University Press.
- Hemmerling, R., Kniemeyer, O., Lawwert, D., Kurth, W., and Buck-Sorlin, G. (2008). The rule-based language XL and the modelling environment GroIMP illustrated with simulated tree competition. *Funct. Plant Biol.* 35, 739–750. doi: 10.1071/FP08052
- Hervieux, N., Dumond, M., Sapala, A., Routier-Kierzkowska, A.-L., Kierzkowski, D., Roeder, A. H. K., et al. (2016). A mechanical feedback restricts sepal growth and shape in *Arabidopsis*. *Curr. Biol.* 26, 1019–1028. doi: 10.1016/j.cub.2016.03.004
- Hille Ris Lambers, J., Adler, P. B., Harpole, W. S., Levine, J. M., and Mayfield, M. M. (2012). Rethinking community assembly through the lens of coexistence theory. *Annu. Rev. Ecol. Evol. Syst.* 43, 227–248. doi: 10.1146/annurev-ecolsys-110411-160411
- Hodge, A. (2004). The plastic plant: root responses to heterogeneous supplies of nutrients. *New Phytol.* 162, 9–24. doi: 10.1111/j.1469-8137.2004.01015.x
- Hong, L., Dumond, M., Tsugawa, S., Sapala, A., Routier-Kierzkowska, A.-L., Zhou, Y., et al. (2016). Variable cell growth yields reproducible organ development through spatiotemporal averaging. *Dev. Cell* 38, 15–32. doi: 10.1016/j.devcel.2016.06.016
- Hughes, A. R., Inouye, B. D., Johnson, M. T. J., Underwood, N., and Vellend, M. (2008). Ecological consequences of genetic diversity. *Ecol. Lett.* 11, 609–623. doi: 10.1111/j.1461-0248.2008.01179.x
- Hund, A., Trachsel, S., and Stamp, P. (2009). Growth of axial and lateral roots of maize: I. development of a phenotyping platform. *Plant Soil* 325, 335–349. doi: 10.1007/s11104-009-9984-2
- Ilic, K., Kellogg, E. A., Jaiswal, P., Zapata, F., Stevens, P. F., Vincent, L. P., et al. (2007). The plant structure ontology, a unified vocabulary of anatomy and morphology of a flowering plant. *Plant Physiol.* 143, 587–599. doi: 10.1104/pp.106.092825
- Ito, F., Komatsubara, S., Shigezawa, N., Morikawa, H., Murakami, Y., Yoshino, K., et al. (2015). Mechanics of water collection in plants via morphology change of conical hairs. *Appl. Phys. Lett.* 106:133701. doi: 10.1063/1.4916213
- Iyer-Pascuzzi, A. S., Symonova, O., Mileyko, Y., Hao, Y., Belcher, H., Harer, J., et al. (2010). Imaging and analysis platform for automatic phenotyping and trait ranking of plant root systems. *Plant Physiol.* 152, 1148–1157. doi: 10.1104/pp.109.150748
- Jain, A. K. (1989). *Fundamentals of Digital Image Processing*. Upper Saddle River, NJ: Prentice-Hall, Inc.
- Jaramillo, R. E., Nord, E. A., Chimungu, J. G., Brown, K. M., and Lynch, J. P. (2013). Root cortical burden influences drought tolerance in maize. *Ann. Bot.* 112, 429–437. doi: 10.1093/aob/mct069
- Johnson, M., Lajeunesse, M. J., and Agrawal, A. A. (2006). Additive and interactive effects of plant genotypic diversity on arthropod communities and plant fitness. *Ecol. Lett.* 9, 24–34. doi: 10.1111/j.1461-0248.2005.00833.x
- Jung, J., and McCouch, S. (2013). Getting to the roots of it: genetic and hormonal control of root architecture. *Front. Plant Sci.* 4:186. doi: 10.3389/fpls.2013.00186/abstract
- Kichenin, E., Wardle, D. A., Peltzer, D. A., Morse, C. W., and Freschet, G. T. (2013). Contrasting effects of plant inter- and intraspecific variation on community-level trait measures along an environmental gradient. *Funct. Ecol.* 27, 1254–1261. doi: 10.1111/1365-2435.12116
- Kleyer, M., Bekker, R. M., Knevel, I. C., Bakker, J. P., Thompson, K., Sonnenschein, M., et al. (2008). The LEDA traitbase: a database of life-history

- traits for the Northwest European flora. *J. Ecol.* 96, 1266–1274. doi: 10.1111/j.1365-2745.2008.01430
- Krajewski, P., Chen, D., Cwiek, H., van Dijk, A. D. J., Fiorani, F., Kersey, P., et al. (2015). Towards recommendations for metadata and data handling in plant phenotyping. *J. Exp. Bot.* 66, 5417–5427. doi: 10.1093/jxb/erv271
- Kuchaiev, O., Milenkoviæ, T., Memiševiæ, V., Hayes, W., and Pržulj, N. (2010). Topological network alignment uncovers biological function and phylogeny. *J. R. Soc. Interf.* 7, 1341–1354. doi: 10.1098/rsif.2010.0063
- Kuhl, F. P., and Giardina, C. R. (1982). Elliptic fourier features of a closed contour. *Comput. Graph. Image Process.* 19, 236–258. doi: 10.1016/0146-664X(82)90034-X
- Kuijken, R. C. P., van Eeuwijk, F. A., Marcelis, L. F. M., and Bouwmeester, H. J. (2015). Root phenotyping: from component trait in the lab to breeding: Table 1. *J. Exp. Bot.* 66, 5389–5401. doi: 10.1093/jxb/erv239
- Kurth, W., Kniemeyer, O., and Buck-Sorlin, G. (2005). “Relational growth grammars—a graph rewriting approach to dynamical systems with a dynamical structure,” in *Unconventional Programming Paradigms*, eds J.-P. Banâtre, P. Fradet, J.-L. Giavitto, and O. Michel (Berlin: Springer), 56–72. doi: 10.1007/11527800\_5
- Kutschera, U., and Niklas, K. J. (2007). The epidermal-growth-control theory of stem elongation: an old and a new perspective. *J. Plant Physiol.* 164, 1395–1409. doi: 10.1016/j.jplph.2007.08.002
- Langlade, N. B., Feng, X., Dransfield, T., Copsey, L., Hanna, A. I., Thebaud, C., et al. (2005). Evolution through genetically controlled allometry space. *Proc. Natl. Acad. Sci. U.S.A.* 102, 10221–10226. doi: 10.1073/pnas.0504210102
- Lankau, R. A., and Strauss, S. Y. (2007). Mutual feedbacks maintain both genetic and species diversity in a plant community. *Science* 317, 1561–1563. doi: 10.1126/science.1147455
- Laughlin, D. C., and Laughlin, D. E. (2013). Advances in modeling trait-based plant community assembly. *Trends Plant Sci.* 18, 584–593. doi: 10.1016/j.tplants.2013.04.012
- Leitner, D., Klepsch, S., Ptashnyk, M., Marchant, A., Kirk, G. J. D., Schnepf, A., et al. (2010). A dynamic model of nutrient uptake by root hairs. *New Phytol.* 185, 792–802. doi: 10.1111/j.1469-8137.2009.03128.x
- Li, L., Zhang, Q., and Huang, D. (2014). A review of imaging techniques for plant phenotyping. *Sensors* 14, 20078–20111. doi: 10.3390/s141120078
- Lindenmayer, A. (1968). Mathematical models for cellular interaction in development, Parts I and II. *J. Theor. Biol.* 18, 280–315. doi: 10.1016/0022-5193(68)90079-9
- Lobet, G., Draye, X., and Perilleux, C. (2013). An online database for plant image analysis software tools. *Plant Methods* 9:38. doi: 10.1186/1746-4811-9-38
- Lobet, G., Pages, L., and Draye, X. (2011). A novel image-analysis toolbox enabling quantitative analysis of root system architecture. *Plant Physiol.* 157, 29–39. doi: 10.1104/pp.111.179895
- Lobet, G., Pound, M. P., Diener, J., Pradal, C., Draye, X., Godin, C., et al. (2015). Root system markup language: toward a unified root architecture description language. *Plant Physiol.* 167, 617–627. doi: 10.1104/pp.114.253625
- Lynch, J. (1995). Root architecture and plant productivity. *Plant Physiol.* 109, 7–13. doi: 10.1104/pp.109.1.7
- Lynch, J. P. (2007). Roots of the second green revolution. *Aust. J. Bot.* 55, 493–512. doi: 10.1071/BT06118
- Lynch, J. P. (2011). Root phenes for enhanced soil exploration and phosphorus acquisition: tools for future crops. *Plant Physiol.* 156, 1041–1049. doi: 10.1104/pp.111.175414
- Lynch, J. P. (2013). Steep, cheap and deep: an ideotype to optimize water and N acquisition by maize root systems. *Ann. Bot.* 112, 347–357. doi: 10.1093/aob/mcs293
- Lynch, J. P. (2014). Root phenes that reduce the metabolic costs of soil exploration: opportunities for 21st century agriculture. *Plant Cell Environ.* 38, 1775–1784. doi: 10.1111/pce.12451
- Lynch, J. P., and Brown, K. M. (2001). Topsoil foraging – an architectural adaptation of plants to low phosphorus availability. *Plant Soil* 237, 225–237. doi: 10.1023/A:1013324727040
- Lynch, J. P., Chimungu, J. G., and Brown, K. M. (2014). Root anatomical phenes associated with water acquisition from drying soil: targets for crop improvement. *J. Exp. Bot.* 65, 6155–6166. doi: 10.1093/jxb/eru162
- Lynch, J. P., Nielsen, K. L., Davis, R. D., and Jablokow, A. G. (1997). SimRoot: modelling and visualization of root systems. *Plant Soil* 188, 139–151. doi: 10.1023/A:1004276724310
- Mairhofer, S., Zappala, S., Tracy, S., Sturrock, C., Bennett, M. J., Mooney, S. J., et al. (2013). Recovering complete plant root system architectures from soil via X-ray micro-computed tomography. *Plant Methods* 9:8. doi: 10.1186/1746-4811-9-8
- Mairhofer, S., Zappala, S., Tracy, S. R., Sturrock, C., Bennett, M., Mooney, S. J., et al. (2012). RooTrak: Automated recovery of three-dimensional plant root architecture in soil from X-ray microcomputed tomography images using visual tracking. *Plant Physiol.* 158, 561–569. doi: 10.1104/pp.111.186221
- Miguel, M. A., Postma, J. A., and Lynch, J. P. (2015). Phene synergism between root hair length and basal root growth angle for phosphorus acquisition. *Plant Physiol.* 167, 1430–1439. doi: 10.1104/pp.15.00145
- Milenkovic, T., Ng, W. L., Hayes, W., and Pržulj, N. (2010). Optimal network alignment with graphlet degree vectors. *Cancer Inform.* 30, 121–137. doi: 10.4137/CIN.S4744
- Ong, Y., Streit, K., Henke, M., and Kurth, W. (2014). An approach to multiscale modelling with graph grammars. *Ann. Bot.* 114, 813–827. doi: 10.1093/aob/mcu155
- Pages, L. (2014). Branching patterns of root systems: quantitative analysis of the diversity among dicotyledonous species. *Ann. Bot.* 114, 591–598. doi: 10.1093/aob/mcu145
- Peret, B., Desnos, T., Jost, R., Kanno, S., Berkowitz, O., and Nussaume, L. (2014). Root architecture responses: in search of phosphate. *Plant Physiol.* 166, 1713–1723. doi: 10.1104/pp.114.244541
- Piccolo, S. R., and Frampton, M. B. (2016). Tools and techniques for computational reproducibility. *Gigascience* 5, 1–13. doi: 10.1186/s13742-016-0135-4
- Piñeros, M. A., Larson, B. G., Shaff, J. E., Schneider, D. J., Falcão, A. X., Yuan, L., et al. (2016). Evolving technologies for growing, imaging and analyzing 3D root system architecture of crop plants. *J. Integr. Plant Biol.* 58, 230–241. doi: 10.1111/jipb.12456
- Postma, J. A., and Lynch, J. P. (2011). Root cortical aerenchyma enhances the growth of maize on soils with suboptimal availability of nitrogen, phosphorus, and potassium. *Plant Physiol.* 156, 1190–1201. doi: 10.1104/pp.111.175489
- Pradal, C., Boudon, F., Nouguier, C., Chopard, J., and Godin, C. (2009). PlantGL: A Python-based geometric library for 3D plant modelling at different scales. *Graph. Models* 71, 1–21. doi: 10.1016/j.gmod.2008.10.001
- Prusinkiewicz, P. (1986). “Graphical applications of L-systems,” in *Proceedings of Graphics Interface '86/Vision Interface '86*, eds M. Wein and E. M. Kidd (Vancouver, BC: Canadian Information Processing Society), 247–253.
- Prusinkiewicz, P., Karwowski, R., and Lane, B. (2007). “The L+C plant modeling language,” in *Functional-Structural Plant Modeling in Crop Production*, eds J. Vos, L. F. M. Marcelis, P. H. B. de Visser, P. C. Struik, J. B. Evers, and R. J. Bogers (Wageningen: Springer), 27–42.
- Prusinkiewicz, P., and Lindenmayer, A. (1990). *The Algorithmic Beauty of Plants*. New York, NY: Springer.
- Qu, X., Chatty, P. R., and Roeder, A. H. K. (2014). Endomembrane trafficking protein SEC24A regulates cell size patterning in *Arabidopsis*. *Plant Physiol.* 166, 1877–1890. doi: 10.1104/pp.114.246033
- Rameau, C., Bertheloot, J., Leduc, N., Andrieu, B., Foucher, F., and Sakr, S. (2015). Multiple pathways regulate shoot branching. *Front Plant Sci.* 5:74. doi: 10.3389/fpls.2014.00741
- Reich, P. B., Walters, M. B., Tjoelker, M. G., Vanderklein, D., and Buschena, C. (1998). Photosynthesis and respiration rates depend on leaf and root morphology and nitrogen concentration in nine boreal tree species differing in relative growth rate. *Funct. Ecol.* 12, 395–405. doi: 10.1046/j.1365-2435.1998.00209.x
- Rellán-Álvarez, R., Lobet, G., Lindner, H., Pradier, P.-L., Sebastian, J., Yee, M.-C., et al. (2015). GLO-Roots: an imaging platform enabling multidimensional characterization of soil-grown root systems. *eLife* 4, 1–72. doi: 10.7554/eLife.07597
- Roeder, A. H. K., Chickarmane, V., Cunha, A., Obara, B., Manjunath, B. S., and Meyerowitz, E. M. (2010). Variability in the control of cell division underlies sepal epidermal patterning in *Arabidopsis thaliana*. *PLoS Biol.* 8:e1000367. doi: 10.1371/journal.pbio.1000367

- Roeder, A. H. K., Cunha, A., Ohno, C. K., and Meyerowitz, E. M. (2012). Cell cycle regulates cell type in the *Arabidopsis* sepal. *Development* 139, 4416–4427. doi: 10.1242/dev.082925
- Rousseau, D., Chéné, Y., Belin, E., Semaan, G., Trigui, G., Boudehri, K., et al. (2015). Multiscale imaging of plants: current approaches and challenges. *Plant Methods* 11:413. doi: 10.1186/s13007-015-0050-1
- Ruffel, S., Krouk, G., Ristova, D., Shasha, D., Birnbaum, K. D., and Coruzzi, G. M. (2011). Nitrogen economics of root foraging: transitive closure of the nitrate-cytokinin relay and distinct systemic signaling for N supply vs. demand. *Proc. Natl. Acad. Sci. U.S.A.* 108, 18524–18529. doi: 10.1073/pnas.1108684108
- Saengwilai, P., Nord, E. A., Chimungu, J. G., Brown, K. M., and Lynch, J. P. (2014). Root cortical aerenchyma enhances nitrogen acquisition from low-nitrogen soils in maize. *Plant Physiol.* 166, 726–735. doi: 10.1104/pp.114.241711
- Savaldi-Goldstein, S., Peto, C., and Chory, J. (2007). The epidermis both drives and restricts plant shoot growth. *Nature* 446, 199–202. doi: 10.1038/nature05618
- Schiessl, K., Muino, J. M., and Sablowski, R. (2014). *Arabidopsis* JAGGED links floral organ patterning to tissue growth by repressing Kip-related cell cycle inhibitors. *Proc. Natl. Acad. Sci. U.S.A.* 111, 2830–2835. doi: 10.1073/pnas.1320457111
- Siefert, A., Violette, C., Chalmandrier, L., Albert, C. H., Taudiere, A., Fajardo, A., et al. (2015). A global meta-analysis of the relative extent of intraspecific trait variation in plant communities. *Ecol. Lett.* 18, 1406–1419. doi: 10.1111/ele.12508
- Sinoquet, H., and Rivet, P. (1997). Measurement and visualisation of the architecture of an adult tree based on a three-dimensional digitising device. *Trees* 11, 265–270. doi: 10.1007/s004680050084
- Smith, S., and De Smet, I. (2012). Root system architecture: insights from *Arabidopsis* and cereal crops. *Philos. Trans. R. Soc. B Biol. Sci.* 367, 1441–1452. doi: 10.1098/rstb.2011.0234
- Suding, K. N., Lavorel, S., Chapin, F. S., Cornelissen, J. H. C., Diaz, S., Garnier, E., et al. (2008). Scaling environmental change through the community-level: a trait-based response-and-effect framework for plants. *Glob. Change Biol.* 14, 1125–1140. doi: 10.1111/j.1365-2486.2008.01557.x
- Symonova, O., Topp, C. N., and Edelsbrunner, H. (2015). DynamicRoots: a software platform for the reconstruction and analysis of growing plant roots. *PLoS ONE* 10:e0127657. doi: 10.1371/journal.pone.0127657
- Tauriello, G., Meyer, H. M., Smith, R. S., Koumoutsakos, P., and Roeder, A. H. K. (2015). Variability and constancy in cellular growth of *Arabidopsis* sepals. *Plant Physiol.* 169, 2342–2358. doi: 10.1104/pp.15.00839
- Tian, F., Bradbury, P. J., Brown, P. J., Hung, H., Sun, Q., Flint-Garcia, S., et al. (2011). Genome-wide association study of leaf architecture in the maize nested association mapping population. *Nat. Genet.* 43, 159–162. doi: 10.1038/ng.746
- Topp, C. N., Iyer-Pascuzzi, A. S., Anderson, J. T., Lee, C.-R., Zurek, P. R., Symonova, O., et al. (2013). 3D phenotyping and quantitative trait locus mapping identify core regions of the rice genome controlling root architecture. *Proc. Natl. Acad. Sci. U.S.A.* 110, e1695–e1704. doi: 10.1073/pnas.1304354110
- Trachsel, S., Kaepller, S. M., Brown, K. M., and Lynch, J. P. (2011). Shovelomics: high throughput phenotyping of maize (*Zea mays* L.) root architecture in the field. *Plant Soil* 341, 75–87. doi: 10.1007/s11104-010-0623-8
- Vandenbussche, F., Pierik, R., Millenaar, F. F., Voesenek, L. A., and Van Der Straeten, D. (2005). Reaching out of the shade. *Curr. Opin. Plant Biol.* 8, 462–468. doi: 10.1016/j.pbi.2005.07.007
- Vellend, M., and Geber, M. A. (2005). Connections between species diversity and genetic diversity. *Ecol. Lett.* 8, 767–781. doi: 10.1111/j.1461-0248.2005.00775.x
- Verheijen, L. M., Brokvink, V., Aerts, R., Bönnisch, G., Cornelissen, J. H. C., Kattge, J., et al. (2013). Impacts of trait variation through observed trait–climate relationships on performance of an Earth system model: a conceptual analysis. *Biogeosciences* 10, 5497–5515. doi: 10.5194/bg-10-5497-2013
- Violette, C., Enquist, B. J., McGill, B. J., Jiang, L., Albert, C. H., Hulshof, C., et al. (2012). The return of the variance: intraspecific variability in community ecology. *Trends Ecol. Evolut.* 27, 245–253. doi: 10.1016/j.tree.2011.11.014
- Vogel, G. (2013). How do organs know when they have reached the right size? *Science* 340, 1156–1157. doi: 10.1126/science.340.6137.1156-b
- Whitham, T. G., Bailey, J. K., Schweitzer, J. A., Shuster, S. M., Bangert, R. K., LeRoy, C. J., et al. (2006). A framework for community and ecosystem genetics: from genes to ecosystems. *Nat. Rev. Genet.* 7, 510–523. doi: 10.1038/nrg1877
- Zhang, H., Jennings, A., Barlow, P. W., and Forde, B. G. (1999). Dual pathways for regulation of root branching by nitrate. *Proc. Natl. Acad. Sci. U.S.A.* 96, 6529–6534. doi: 10.1073/pnas.96.11.6529
- Zhu, J., Brown, K. M., and Lynch, J. P. (2010). Root cortical aerenchyma improves the drought tolerance of maize (*Zea mays* L.). *Plant, Cell Environ.* 33, 740–749. doi: 10.1111/j.1365-3040.2009.02099.x
- Zurek, P. R., Topp, C. N., and Benfey, P. N. (2015). Quantitative trait locus mapping reveals regions of the maize genome controlling root system architecture. *Plant Physiol.* 167, 1487–1496. doi: 10.1104/pp.114.251751

**Conflict of Interest Statement:** The authors declare that the research was conducted in the absence of any commercial or financial relationships that could be construed as a potential conflict of interest.

Copyright © 2017 Balduzzi, Binder, Bucksch, Chang, Hong, Iyer-Pascuzzi, Pradal and Sparks. This is an open-access article distributed under the terms of the Creative Commons Attribution License (CC BY). The use, distribution or reproduction in other forums is permitted, provided the original author(s) or licensor are credited and that the original publication in this journal is cited, in accordance with accepted academic practice. No use, distribution or reproduction is permitted which does not comply with these terms.

# Advantages of publishing in Frontiers



## OPEN ACCESS

Articles are free to read,  
for greatest visibility



## COLLABORATIVE PEER-REVIEW

Designed to be rigorous  
– yet also collaborative,  
fair and constructive



## FAST PUBLICATION

Average 85 days from  
submission to publication  
(across all journals)



## COPYRIGHT TO AUTHORS

No limit to article  
distribution and re-use



## TRANSPARENT

Editors and reviewers  
acknowledged by name  
on published articles



## SUPPORT

By our Swiss-based  
editorial team



## IMPACT METRICS

Advanced metrics  
track your article's impact



## GLOBAL SPREAD

5'100'000+ monthly  
article views  
and downloads



## LOOP RESEARCH NETWORK

Our network  
increases readership  
for your article

## Frontiers

EPFL Innovation Park, Building I • 1015 Lausanne • Switzerland  
Tel +41 21 510 17 00 • Fax +41 21 510 17 01 • info@frontiersin.org  
[www.frontiersin.org](http://www.frontiersin.org)

## Find us on

